Methods in Molecular Biology 2216

Springer Protocols

Andreas Pohlmann
Thoralf Niendorf *Editors*

Preclinical MRI of the Kidney

Methods and Protocols

cost
EUROPEAN COOPERATION IN SCIENCE & TECHNOLOGY

OPEN ACCESS

Humana Press

METHODS IN MOLECULAR BIOLOGY

Series Editor
John M. Walker
School of Life and Medical Sciences
University of Hertfordshire
Hatfield, Hertfordshire, UK

For further volumes:
http://www.springer.com/series/7651

For over 35 years, biological scientists have come to rely on the research protocols and methodologies in the critically acclaimed *Methods in Molecular Biology* series. The series was the first to introduce the step-by-step protocols approach that has become the standard in all biomedical protocol publishing. Each protocol is provided in readily-reproducible step-by-step fashion, opening with an introductory overview, a list of the materials and reagents needed to complete the experiment, and followed by a detailed procedure that is supported with a helpful notes section offering tips and tricks of the trade as well as troubleshooting advice. These hallmark features were introduced by series editor Dr. John Walker and constitute the key ingredient in each and every volume of the *Methods in Molecular Biology* series. Tested and trusted, comprehensive and reliable, all protocols from the series are indexed in PubMed.

Preclinical MRI of the Kidney

Methods and Protocols

Edited by

Andreas Pohlmann and Thoralf Niendorf

Berlin Ultrahigh Field Facility (B.U.F.F.), Max Delbrück Center for Molecular Medicine (MDC) in the Helmholtz Association, Berlin, Germany

Humana Press

Editors
Andreas Pohlmann
Berlin Ultrahigh Field Facility (B.U.F.F.)
Max Delbrück Center for Molecular Medicine (MDC) in the Helmholtz Association
Berlin, Germany

Thoralf Niendorf
Berlin Ultrahigh Field Facility (B.U.F.F.)
Max Delbrück Center for Molecular Medicine (MDC) in the Helmholtz Association
Berlin, Germany

ISSN 1064-3745 ISSN 1940-6029 (electronic)
Methods in Molecular Biology
ISBN 978-1-0716-0977-4 ISBN 978-1-0716-0978-1 (eBook)
https://doi.org/10.1007/978-1-0716-0978-1

This Humana imprint is published by the registered company Springer Science+Business Media, LLC, part of Springer Nature.
The registered company address is: 1 New York Plaza, New York, NY 10004, U.S.A.

Preface

Preclinical MRI for Renal Health

Despite the fact that we are in an era of increased prevalence, incidence, and recognition of renal diseases, the current options for effective prophylactic and therapeutic regimens for kidney disorders are disappointingly sparse. A major obstacle is the inherent complexity of the pathophysiology in renal disease. Overcoming this requires immediate innovative action across multiple domains and requires new instruments that enable noninvasive diagnostics and monitoring of therapy during renal diseases. The upshot is that this also creates ever-increasing opportunities for discovery.

The development and validation of disruptive diagnostic approaches and strategies for early interception of renal disease and renoprotection can be brought on only with a deeper understanding of the underlying (patho)physiology. This underlines the urgent quest for emergent biomedical imaging techniques, customized for probing all stages of renal diseases. While many renal diseases involve defects at the molecular and cellular levels, these manifest themselves at the scale of the organ system. The unique function of biomedical imaging is to monitor all these levels simultaneously, connecting the view of biologists with that of clinicians *in vivo*. This asks for approaches that are noninvasive, ubiquitous, and applicable both preclinically and clinically—this is the forte of magnetic resonance imaging (MRI). An increasing body of evidence indicates that MRI biomarkers have a high potential for complementing and improving acute and chronic renal disease management. MRI is a versatile technique, and a host of functional MRI methods have emerged that are sensitive to pathophysiological changes associated with renal hemodynamics, oxygenation, fibrosis, inflammation, and microstructure. To better connect MR imaging markers with (patho)-physiology, MRI needs to be benchmarked and calibrated with integrative physiological measurements which include the use of quantitative invasive probes. Due to the enormous technical challenges involved, renal MRI biomarkers remain woefully underused in preclinical research and in clinical practice. These scientific and technical issues constitute a substantial barrier *en route* to the standardization and broad application of renal MRI.

The purpose of this book is to overcome these roadblocks by promoting an open-access collection of protocols and comprehensive recommendations for preclinical renal MRI, to be employed in translational research. The book provides answers to the common questions regarding how renal MRI technologies emerging from the research community can be translated into open-access, ready-to-go toolboxes that can be applied to human patients in a way that is standardized, highly reproducible, and harmonized across centers, with the goal of combating renal disease by substantially slowing its progression and preventing kidney injury.

With this "*from the community, to the community*" approach, the book is designed to enhance training in renal MRI sciences, to improve the reproducibility of renal imaging research, and to boost the comparability of renal MRI studies. With this mission, the book promotes an entirely unique opportunity for developing advanced *in vivo* renal phenotyping, diagnostic imaging, and therapy guidance as a link to stratified medicine. The clinical implications of this relate to a broad spectrum of physiology, nephrology, radiology,

cardiology, and other associated fields of basic science and clinical research targeting renal and cardiorenal diseases.

The chapters covered in this book are interdisciplinary in nature and bridge the gaps between physics, physiology, and medicine. The contributions are provided by leading international experts and hands-on scientists and serve as a foundation to substantially boost the development of renal imaging tools, which will increase the efficacy of diagnostics, promote the identification of new therapeutic targets and options, drive explorations into novel renoprotective strategies, and lead to enhanced prophylactic regimens. To meet this goal, the book provides chapters on the fundamental principles, detailed experimental protocols and guidelines for data analysis, to successfully unlock the full potential of renal MRI. At the same time, the book promises to help nurture a new generation of researchers with the high potential needed for the development of next-generation renal imaging technology, by addressing some crucial educational gaps.

The pace of discovery of preclinical MRI is heartening, drawing in new talent and driving the transfer of results into novel preclinical applications and into the clinical arena. The remaining challenges must be faced openly via collaborations between forward-thinking researchers, application scientists, clinicians, and the general readership of this book. These collaborations should be interdisciplinary, inter-institutional, and international, as exemplified and spearheaded by imaging networks. A prominent example of this is the renal imaging initiative PARENCHIMA, a community-driven Action of the COST (European Cooperation in Science and Technology) program of the European Union, which aims to improve the reproducibility and standardization of renal MRI biomarkers. Only because of the truly interdisciplinary nature of this work, and the essential role that having many types of expertise in close interaction has played, we got this far.

This book lives up to this mission by providing a comprehensive overview and guidance on preclinical MRI. It is intended to take this approach to the next level and to put extra weight behind finding a solution to the remaining problems in renal imaging research. With this mission, the reader will learn to make sense of the terrain we currently inhabit and to better interpret the images of the kidney that we produce using sophisticated preclinical MRI and data analysis protocols. Inevitably, there will be breakthroughs and surprises when you place next-generation imaging technologies and this book into the hands of highly creative interdisciplinary teams. However, this will only happen if we recognize that moving into the next generation of renal imaging technology is more than just a matter of buying equipment, installing it, and then trying to operate in "core facilities" where budgetary considerations, and not scientific goals, dominate. The ultimate potential of preclinical renal MRI is far greater; all that is required is the imagination to apply it, following the chapters in this book as a roadmap. We hope that the book will convey the seeds of this vision and inspire you—as it has us—to become pioneers in this amazingly promising area.

With this perspective, we are grateful to all the authors for their outstanding work, passion, dedication, and enthusiasm to drive this assembly of recommendations and open-access protocols on preclinical MRI home. We all succeeded thanks to the sheer power and momentum of interdisciplinary collaboration and teamwork. You made and make the difference. Thank you.

Berlin, Germany

Thoralf Niendorf
Andreas Pohlmann

Contents

Part V Protocols for Advanced Analyses

Contributors

Susan J. Back • *Department of Radiology, Children's Hospital of Philadelphia, Philadelphia, PA, USA*

Octavia Bane • *BioMedical Engineering and Imaging Institute, Icahn School of Medicine at Mount Sinai, New York, NY, USA; Department of Radiology, Icahn School of Medicine at Mount Sinai, New York, NY, USA*

Scott C. Beeman • *Washington University School of Medicine, St. Louis, MO, USA*

Kevin M. Bennett • *Washington University School of Medicine, St. Louis, MO, USA*

Philipp Boehm-Sturm • *Department of Experimental Neurology, Center for Stroke Research and Charité Core Facility 7T Experimental MRIs, Charité-Universitätsmedizin Berlin, Berlin, Germany*

G. Larry Bretthorst • *Washington University School of Medicine, St. Louis, MO, USA*

Kathleen Cantow • *Working Group Integrative Kidney Physiology, Institute of Physiology, Charité—University Medicine Berlin, Berlin, Germany; Institute of Physiology and Center for Cardiovascular Research, Charité – Universitätsmedizin Berlin, Berlin, Germany*

Anna Caroli • *Medical Imaging Unit, Bioengineering Department, IRCCS Istituto di Ricerche Farmacologiche Mario Negri, Bergamo, Italy*

Kai-Hsiang Chuang • *Queensland Brain Institute and Centre for Advanced Imaging, The University of Queensland, Brisbane, QLD, Australia*

Lorena Consolino • *Department of Molecular Biotechnology and Health Sciences, University of Torino, Torino, Italy*

Walter Dastrù • *Department of Molecular Biotechnology and Health Sciences, University of Torino, Torino, Italy*

Sabrina Doblas • *Laboratory of Imaging Biomarkers, Centre de Recherche sur l'Inflammation, Inserm UMR 1149, Université de Paris and AP-HP, Paris, France*

Roger G. Evans • *Cardiovascular Disease Program, Biomedicine Discovery Institute and Department of Physiology, Monash University, Melbourne, VIC, Australia*

Sean B. Fain • *Department of Radiology, University of Wisconsin, Madison, WI, USA*

Andrea Fekete • *Ist Department of Pediatrics, Semmelweis University, Budapest, Hungary*

María A. Fernández-Seara • *Radiology Department, Clínica Universidad de Navarra, University of Navarra, Pamplona, Spain*

Bert Flemming • *Working Group Integrative Kidney Physiology, Institute of Physiology, Charité—University Medicine Berlin, Berlin, Germany*

Andreia C. Freitas • *Institute for Systems and Robotics (LARSyS) and Department of Bioengineering, Instituto Superior Técnico, University of Lisbon, Lisbon, Portugal*

Iris Friedli • *Antaros Medical, BioVenture Hub, Mölndal, Sweden*

Dieter Fuchs • *FUJIFILM VisualSonics, Inc, Amsterdam, The Netherlands*

Joel R. Garbow • *Washington University School of Medicine, St. Louis, MO, USA*

Philippe Garteiser • *Laboratory of Imaging Biomarkers, Centre de Recherche sur l'Inflammation, Inserm UMR 1149, Université de Paris and AP-HP, Paris, France*

Thomas Gladytz • *Physikalisch-Technische Bundesanstalt (German Federal Metrologic Institute), Berlin, Germany*

James T. Grist • *Institute of Cancer and Genomic Sciences, University of Birmingham, Birmingham, UK*

Dirk Grosenick • *Physikalisch-Technische Bundesanstalt (German Federal Metrologic Institute), Berlin, Germany*
Bradley Hack • *Department of Radiology, NorthShore University HealthSystem, Evanston, IL, USA*
Esben Søvsø Szocska Hansen • *Department of Clinical Medicine, The MR Research Center, Aarhus University, Aarhus, Denmark*
Stefanie J. Hectors • *BioMedical Engineering and Imaging Institute, Icahn School of Medicine at Mount Sinai, New York, NY, USA; Department of Radiology, Icahn School of Medicine at Mount Sinai, New York, NY, USA; Department of Radiology, Weill Cornell Medicine, New York, NY, USA*
Adam Hosszu • *1st Department of Pediatrics, Semmelweis University, Budapest, Hungary*
Lingzhi Hu • *United Imaging Healthcare, Houston, TX, USA*
Pietro Irrera • *University of Campania "Luigi Vanvitelli", Naples, Italy*
Neil Peter Jerome • *Institute for Circulation and Diagnostic Imaging, Norwegian University of Science and Technology (NTNU), Trondheim, Norway; Department of Radiology and Nuclear Medicine, St. Olav's University Hospital, Trondheim, Norway*
Tamas Kaucsar • *1st Department of Pediatrics, Semmelweis University, Budapest, Hungary*
Ralph Kettritz • *Experimental and Clinical Research Center, Berlin, Germany*
Hahnsung Kim • *Yerkes Imaging Center, Yerkes National Primate Research Center, Emory University, Atlanta, GA, USA; Department of Radiology and Imaging Sciences, Emory University School of Medicine, Atlanta, GA, USA*
Frank Kober • *Aix-Marseille Université, CNRS UMR7339, Faculté de Médecine, Centre de Résonance Magnétique Biologique et Médicale (CRMBM), Marseille, France*
Natalie J. Korn • *Radiology and Biomedical Imaging, University of California, San Francisco, CA, USA*
Min-Chi Ku • *Berlin Ultrahigh Field Facility (B.U.F.F.), Max Delbrück Center for Molecular Medicine (MDC) in the Helmholtz Association, Berlin, Germany*
André Kühne • *MRI.TOOLS GmbH, Berlin, Germany*
Ekkehard Küstermann • *AG In vivo Imaging, University of Bremen, Bremen, Germany*
Mechthild Ladwig-Wiegard • *Institute of Animal Welfare, Animal Behavior and Laboratory Animal Science, Free University Berlin, Berlin, Germany*
Christoffer Laustsen • *Department of Clinical Medicine, The MR Research Center, Aarhus University, Aarhus, Denmark*
Lu-Ping Li • *Department of Radiology, NorthShore University HealthSystem, Evanston, IL, USA*
Alexandra Ljimani • *Department of Diagnostic and Interventional Radiology, Medical Faculty, University Dusseldorf, Dusseldorf, Germany*
Dario Livio Longo • *Institute of Biostructures and Bioimaging (IBB), Italian National Research Council (CNR), Torino, Italy*
Nuno Loução • *Philips Healthcare, Lisbon, Portugal*
Michael T. McMahon • *F.M. Kirby Research Center for Functional Brain Imaging, Kennedy Krieger Institute, Baltimore, MD, USA; Division of MR Research, The Russell H. Morgan Department of Radiology and Radiological Science, The Johns Hopkins University School of Medicine, Baltimore, MD, USA*
Martin Meier • *ZTL-Imaging Center, Hannover Medical School, Hannover, Germany; Institute for Laboratory Animal Science, Hannover Medical School, Hannover, Germany*
Sandra Meyer • *FUJIFILM VisualSonics, Inc, Amsterdam, The Netherlands*
Bastien Milani • *Département de Medecine, Service de Néphrologie, Centre Hospitalier Universitaire Vaudois, Vaud, Switzerland*

Jason M. Millward • *Berlin Ultrahigh Field Facility (B.U.F.F.), Max Delbrück Center for Molecular Medicine (MDC) in the Helmholtz Association, Berlin, Germany*
Andreas Müller • *Clinic for Diagnostic and Interventional Radiology, University of the Saarland, Homburg, Germany*
Marc Nazaré • *Medicinal Chemistry, Leibniz-Forschungsinstitut für Molekulare Pharmakologie (FMP), Berlin, Germany*
Thoralf Niendorf • *Berlin Ultrahigh Field Facility (B.U.F.F.), Max Delbrück Center for Molecular Medicine (MDC) in the Helmholtz Association, Berlin, Germany*
Rita G. Nunes • *Institute for Systems and Robotics (LARSyS) and Department of Bioengineering, Instituto Superior Técnico, University of Lisbon, Lisbon, Portugal*
Michael A. Ohliger • *Department of Radiology and Biomedical Imaging, UC San Francisco, San Francisco, CA, USA*
Gwenaël Pagé • *Laboratory of Imaging Biomarkers, Centre de Recherche sur l'Inflammation, Inserm UMR 1149, Université de Paris and AP-HP, Paris, France*
Hua Pan • *Heart Institute, Morsani College of Medicine, University of South Florida, Tampa, FL, USA*
Kowsalya Devi Pavuluri • *Division of MR Research, The Russell H. Morgan Department of Radiology and Radiological Science, The Johns Hopkins University School of Medicine, Baltimore, MD, USA*
Michael Pedersen • *Department of Clinical Medicine—Comparative Medicine Lab, Aarhus University, Aarhus, Denmark*
João S. Periquito • *Berlin Ultrahigh Field Facility (B.U.F.F.), Max Delbrück Center for Molecular Medicine (MDC) in the Helmholtz Association, Berlin, Germany*
Andreas Pohlmann • *Berlin Ultrahigh Field Facility (B.U.F.F.), Max Delbrück Center for Molecular Medicine (MDC) in the Helmholtz Association, Berlin, Germany; Siemens Healthcare, Berlin, Germany*
Pablo García Polo • *Global Research Organization (GRO), GE Healthcare, Dallas, TX, USA*
Pottumarthi V. Prasad • *Department of Radiology, NorthShore University HealthSystem, Evanston, IL, USA*
Christian Prinz • *Berlin Ultrahigh Field Facility (B.U.F.F.), Max Delbrück Center for Molecular Medicine (MDC) in the Helmholtz Association, Berlin, Germany*
Menno Pruijm • *Department of Medicine, Service of Nephrology, Lausanne University Hospital and University of Lausanne, Lausanne, Switzerland*
Paula Ramos Delgado • *Berlin Ultrahigh Field Facility (B.U.F.F.), Max Delbrück Center for Molecular Medicine (MDC) in the Helmholtz Association, Berlin, Germany*
Galen D. Reed • *GE Healthcare, Dallas, TX, USA*
Henning M. Reimann • *Berlin Ultrahigh Field Facility (B.U.F.F.), Max Delbrück Center for Molecular Medicine, Berlin, Germany*
Leili Riazy • *Experimental and Clinical Research Center, Charité—Universitätsmedizin Berlin, Berlin, Germany*
Jens Rosenberg • *The National High Magnetic Field Laboratory, Florida State University, Tallahassee, FL, USA*
Carlota M. Santos • *Institute for Systems and Robotics (LARSyS) and Department of Bioengineering, Instituto Superior Técnico, University of Lisbon, Lisbon, Portugal*
Adrian Schreiber • *Experimental and Clinical Research Center, Berlin, Germany; Department of Nephrology and Medical Intensive Care, Charité-Universitätsmedizin Berlin, Berlin, Germany*

Erdmann Seeliger • *Working Group Integrative Kidney Physiology, Institute of Physiology, Charité—University Medicine Berlin, Berlin, Germany; Department of Medicine, Service of Nephrology, Lausanne University Hospital and University of Lausanne, Lausanne, Switzerland*

Suraj D. Serai • *Department of Radiology, Children's Hospital of Philadelphia, University of Pennsylvania, Philadelphia, PA, USA*

Steven Sourbron • *Department of Infection, Immunity & Cardiovascular Disease, The University of Sheffield, Sheffield, UK*

Ludger Starke • *Berlin Ultrahigh Field Facility (B.U.F.F.), Max Delbrück Center for Molecular Medicine (MDC) in the Helmholtz Association, Berlin, Germany*

Phillip Zhe Sun • *Yerkes Imaging Center, Yerkes National Primate Research Center, Emory University, Atlanta, GA, USA; Department of Radiology and Imaging Sciences, Emory University School of Medicine, Atlanta, GA, USA; Athinoula A. Martinos Center for Biomedical Imaging, Department of Radiology, Massachusetts General Hospital and Harvard Medical School, Charlestown, MA, USA*

Karsten Tabelow • *Weierstrass Institute for Applied Analysis and Stochastics, Berlin, Germany*

Bernard E. Van Beers • *Laboratory of Imaging Biomarkers, Centre de Recherche sur l'Inflammation, Inserm UMR 1149, Université de Paris and AP-HP, Paris, France*

Daisy Villano • *Department of Molecular Biotechnology and Health Sciences, University of Torino, Torino, Italy*

Cornelius von Morze • *Mallinckrodt Institute of Radiology, Washington University, St. Louis, MO, USA; Department of Radiology, Washington University, St. Louis, MO, USA*

Helmar Waiczies • *MRI.TOOLS GmbH, Berlin, Germany*

Sonia Waiczies • *Berlin Ultrahigh Field Facility (B.U.F.F.), Max Delbrück Center for Molecular Medicine (MDC) in the Helmholtz Association, Berlin, Germany*

Zhen J. Wang • *Department of Radiology and Biomedical Imaging, UC San Francisco, San Francisco, CA, USA*

John C. Waterton • *Division of Informatics Imaging & Data Sciences, Faculty of Biology Medicine & Health, Centre for Imaging Sciences, School of Health Sciences, Manchester Academic Health Sciences Centre, University of Manchester, Manchester, UK*

Samuel A. Wickline • *Heart Institute, Morsani College of Medicine, University of South Florida, Tampa, FL, USA*

Yin Wu • *Athinoula A. Martinos Center for Biomedical Imaging, Department of Radiology, Massachusetts General Hospital and Harvard Medical School, Charlestown, MA, USA; Paul C. Lauterbur Research Center for Biomedical Imaging, Shenzhen Institutes of Advanced Technology, Chinese Academy of Sciences, Shenzhen, Guangdong, China*

Meng Yin • *Department of Radiology, Mayo Clinic, Rochester, MN, USA*

Kaixuan Zhao • *Berlin Ultrahigh Field Facility (B.U.F.F.), Max Delbrück Center for Molecular Medicine (MDC) in the Helmholtz Association, Berlin, Germany; School of Biomedical Engineering, Southern Medical University, Guangzhou, China; Guangdong Provincial Key Laboratory of Medical Image Processing, Southern Medical University, Guangzhou, China*

Frank G. Zöllner • *Computer Assisted Clinical Medicine, Medical Faculty Mannheim, Heidelberg University, Mannheim, Germany*

Part I

Introduction

Chapter 1

Recommendations for Preclinical Renal MRI: A Comprehensive Open-Access Protocol Collection to Improve Training, Reproducibility, and Comparability of Studies

Andreas Pohlmann, Susan J. Back, Andrea Fekete, Iris Friedli, Stefanie Hectors, Neil Peter Jerome, Min-Chi Ku, Dario Livio Longo, Martin Meier, Jason M. Millward, João S. Periquito, Erdmann Seeliger, Suraj D. Serai, Sonia Waiczies, Steven Sourbron, Christoffer Laustsen, and Thoralf Niendorf

Abstract

Renal MRI holds incredible promise for making a quantum leap in improving diagnosis and care of patients with a multitude of diseases, by moving beyond the limitations and restrictions of current routine clinical practice. Clinical and preclinical renal MRI is advancing with ever increasing rapidity, and yet, aside from a few examples of renal MRI in routine use, it is still not good enough. Several roadblocks are still delaying the pace of progress, particularly inefficient education of renal MR researchers, and lack of harmonization of approaches that limits the sharing of results among multiple research groups.

Here we aim to address these limitations for preclinical renal MRI (predominantly in small animals), by providing a comprehensive collection of more than 40 publications that will serve as a foundational resource for preclinical renal MRI studies. This includes chapters describing the fundamental principles underlying a variety of renal MRI methods, step-by-step protocols for executing renal MRI studies, and detailed guides for data analysis. This collection will serve as a crucial part of a roadmap toward conducting renal MRI studies in a robust and reproducible way, that will promote the standardization and sharing of data.

This chapter is based upon work from the COST Action PARENCHIMA, a community-driven network funded by the European Cooperation in Science and Technology (COST) program of the European Union, which aims to improve the reproducibility and standardization of renal MRI biomarkers.

Key words Magnetic resonance imaging (MRI), Kidney, Animals, Acute kidney injury, Chronic kidney disease, Training, Standardization

Andreas Pohlmann and Thoralf Niendorf (eds.), *Preclinical MRI of the Kidney: Methods and Protocols*, Methods in Molecular Biology, vol. 2216, https://doi.org/10.1007/978-1-0716-0978-1_1, © The Author(s) 2021

1 Who Is Pulling the Brakes in Renal MRI?

1.1 Renal MRI in Clinical Practice—Fantasy, Dream, or Reality?

Magnetic resonance imaging (MRI) of the kidney is not brain surgery—it's better! It can save lives without invasive surgery, noninvasively. This statement—a play on Donald W McRobbie's "MRI is not rocket science, it's better" in *MRI From Picture to Proton*—is one that Dr. Susan Back, radiologist and director of Pediatric Genitourinary Imaging at the Children's Hospital of Philadelphia, would sign on to without hesitation. It's Thursday afternoon and she is just running an MRI scan on a 4-year-old boy with a left kidney urinary tract dilation, which was gradually increasing on ultrasound. This is the last sequence in the MRI protocol: a contrast-enhanced dynamic 3D T_1-weighted GRE sequence with a temporal resolution of ~8 s, used for quantitative functional urography [1]. Before, an anatomic T_2-weighted MR urogram [1] was performed to identify possible anatomic causes of obstruction (Fig. 1), which are difficult to find with ultrasound. These renal MRI data play a key role in the diagnosis and treatment decisions. The configuration of the kidney on the MRI is concerning for an ureteropelvic junction obstruction because there is an abrupt transition from the renal pelvis to the proximal ureter. However, having this anatomic image and the functional information generated

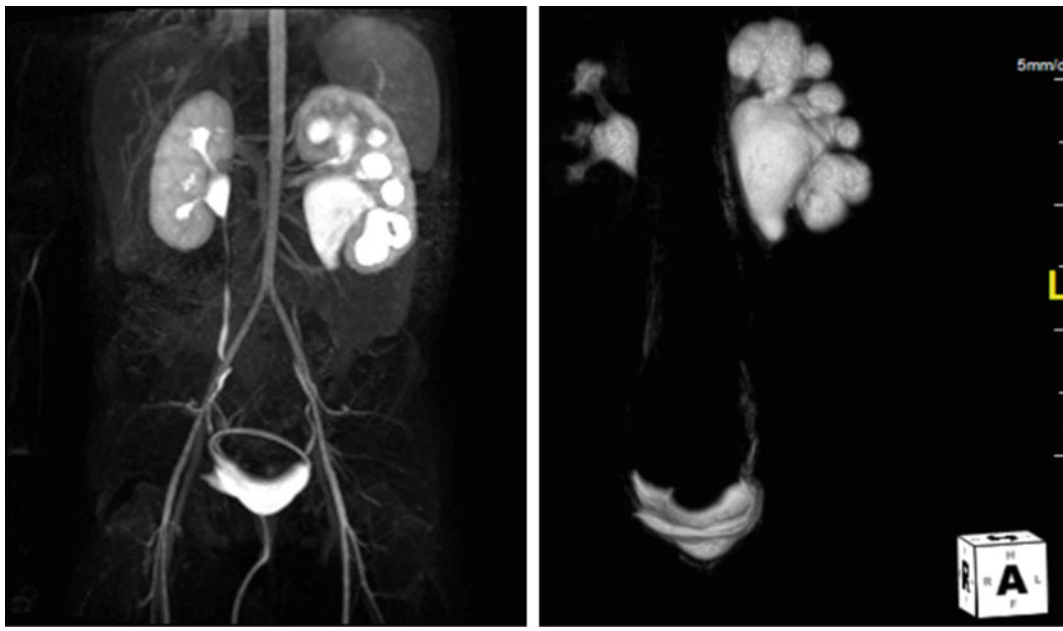

Fig. 1 Renal MRI used for diagnosis and treatment planning of a 4-year-old boy with a left kidney urinary tract dilation. The anatomic portion of the MR urogram study (left: postprocessed image created by superimposing the vascular/parenchymal enhancement phase with the renal excretion phase; right: 3D rendering) depicted the left urinary tract dilation with an abrupt transition in caliper between the dilated renal pelvis and the proximal ureter

using dynamic imaging shows good excretion and proves that the kidney is not obstructed. For the decision on whether to operate, the urologist takes a look at the quantitative functional information. Offline analysis of the dynamic data using the Parametric MRI software package (www.parametricmri.com) [2] provided a wide range of quantitative parameters for assessment of renal function, including renal transit time, calyceal transit time, volumetric differential renal function (vDRF), and Patlak differential renal function (pDRF). The other good news is that the left kidney is functioning similarly to the normal right kidney (vDRF: 48%/52%, pDRF: 49%/51%) so the urologist decides not to operate and the child would be put under observation.

While this scene of renal MRI in clinical routine use vividly illustrates the dream and ambition of many renal MRI researchers—clinicians (nephrologists, urologists, radiologists, surgeons, etc.), clinical scientists, MRI scientists, and basic scientists alike—it may, to the more realistic ones, be perhaps no more than a wild phantasy. However, for the vast majority of kidney patients worldwide, reality couldn't be more different: diagnosis and treatment decisions are predominantly based on plasma and urine parameters, that are known to be insensitive and unspecific. Information on increased serum creatinine is literally too little too late. Currently, the estimated glomerular filtration rate (eGFR; commonly calculated from serum creatinine including variables for age, gender, race) is "the best overall index of kidney function" [3], but it "is an unreliable tool to assess renal function in health and disease, as well as in clinical practice and research" [4]. It is like trying to study the complex bio system of the vast Amazon river basin solely by taking water samples at the mouth of the river.

1.2 Renal MRI, Where Are You?

Renal MRI undoubtedly holds great potential to improve diagnosis and care for millions of patients. The scientific literature reveals hundreds of renal MRI studies, both in patients and animals, aiming to demonstrate its clinical value, and to detail and validate the observed changes in functional and structural parameters. On reading the introductions of these studies we are typically being reminded of the millions of patients suffering from renal disease—acute kidney injuries (AKI) and chronic kidney diseases (CKD)—as well as the steadily growing number of diabetes patients of which many are inevitably en route to diabetic nephropathy. This is usually followed by highlighting the urgent need for more sensitive and specific bio markers, with renal MRI being a prime candidate. Yet renal MRI is still virtually absent from the radar screen of the nephrologist, and patients like those at the Children's Hospital of Philadelphia are a rare exception. What is going wrong?

1.3 Function, Function, Function

If the three most important characteristics that determine the value of a house are often considered to be "location, location, location," then the three most important characteristics of the kidney are

"function, function, function"—rather than its structure/morphology. Morphology, however, is what conventional clinical MRI is all about in the vast majority of cases. Radiologists are trained to detect and identify the subtle deviations from "normal" morphology on grayscale images with different T_1 or T_2(T_2*) weighting. This leads to three challenges for renal MRI: (1) assessing functional images, for example of perfusion or blood oxygenation, requires new training and learning of what "normality" means; (2) almost all renal MRI techniques provide "exotic" pseudocolored parametric maps rather than conventional weighted images; (3) interpreting changes in these MR parameters in the context of the complex renal physiology is anything but trivial—in other words: we don't really know what they mean.

Particularly for the last point, preclinical research is crucial because it enables researchers to obtain from the same organ MRI data together with physiological parameters from invasive probes, as well as histological data. Obvious examples are the comparison of T_1 and ADC with the degree of fibrosis from histology [5], ASL perfusion with invasively measured renal blood flow and local flux, or T_2* with invasively measured tissue oxygenation [6]. Moreover, in preclinical studies the application of (ir)reversible experimental interventions permits studying the complex relationships between MRI parameters and quantitative physiological parameters in the context of kidney-specific control of hemodynamics and oxygenation (*see* the chapter by Cantow K et al. "Reversible (Patho) Physiologically Relevant Test Interventions: Rationale and Examples"). Clearly, a lot more work needs to be done to establish and translate renal MRI into clinical practice, and preclinical research is an essential part of this process. Shedding some light on where we are with regard to research activity in MRI of the kidney may help us drive forward the development of renal MRI.

1.4 Research Activity in Renal MRI

Renal and cardiac MRI both started as niche applications, with their own unique challenges for clinical translation, ranging from acquisition to analysis and interpretation. Cardiac MRI has already become an established clinical tool, which is supported and driven by a dedicated international society (Society for Cardiovascular Magnetic Resonance (SCMR), scmr.org) and guided by >10 published consensus/position statements (scmr.org/page/guidelines). Renal MRI, on the other hand, is struggling to get off the ground.

Conceivably, this divergence is partially due to the usefulness of morphological MRI, which is rather different for both applications. Unlike cardiac MRI, with its workhorse - cardiac function assessment - being based on (cinematic) morphological images, renal MRI depends on multi-parametric structural and functional information, derived from T1, T2, BOLD, DWI, ASL, etc. A second reason might be the availability of treatment and the nature of the diseases. Due to the still rather limited treatment options for CKD, performing complicated and expensive MRI exams still seems less

critical than in cardiac disease where there are more management options. It is expected that the emergence of new CKD treatments will stimulate the interest in renal MRI.

It is interesting to consider exactly how much clinical and preclinical research activity in cardiac and renal MRI there has been, and how it has grown over the years. Using publications listed in PubMed as an indicator, we performed tailored searches with PubMed's *Medical Subject Headings* (MeSH) to obtain lists of literature on renal/cardiac MRI in humans/animals (Fig. 2, upper panels). Additionally we used PubMed's *MeSH Major Topic* to restrict the searches to papers that focus on renal/cardiac MRI while excluding articles that only mention these terms but have another focus (Fig. 2, lower panels) (*see* **Note 1**).

The number of publications in both fields has grown considerably over the years, but at very different rates. Around 1000 cardiac MRI papers per year were published during 2014–2018; the equivalent number for renal MRI papers was only around 200. After restricting the search to papers with a main focus on MRI of the kidney/heart the number of papers per year were 400 and 70, respectively. In other words, a lot more research activity in renal MRI is needed. From the number of publications one can deduce that there is considerably more clinical research than preclinical research in renal MRI. Conceivably, this is partially due to the more limited availability of preclinical MRI systems. However, preclinical renal MRI has recently seen a rapid increase to 37% of all renal MRI publications. This highlights the importance of animal research in renal MRI, considering that only 5% of cardiac MRI papers are preclinical (as of 2018).

The *renal MRI research community* is still rather small. While a recent SCMR meeting attracted more than 1900 attendees [7], international meetings on renal MRI have had approximately 150–200 attendees [8, 9]. Around 200 experts in renal MRI from 30 countries are part of PARENCHIMA (renalmri.org), a community-driven Action in the COST program of the European Union, with the aim to improve the reproducibility and standardization of renal MRI biomarkers. In fact, the number of research groups active in preclinical renal MRI is only 1/5 of those active in clinical renal MRI (*see* **Note 2**). One important conclusion from this is that accelerating the development of renal MRI will require more researchers and institutions to enter the field. We may ask ourselves, "What hurdles are slowing down progress and impeding clinical translation?"

1.5 The Usual Suspects

For a novel MRI technique, the road to routine clinical use is a stony one, involving issues such as reimbursement, available time for MRI, evidence needed that the new method is superior to existing techniques, and availability of hardware/software and trained staff. However, most renal MRI techniques are still at an early phase of development. Here, learning how to correctly

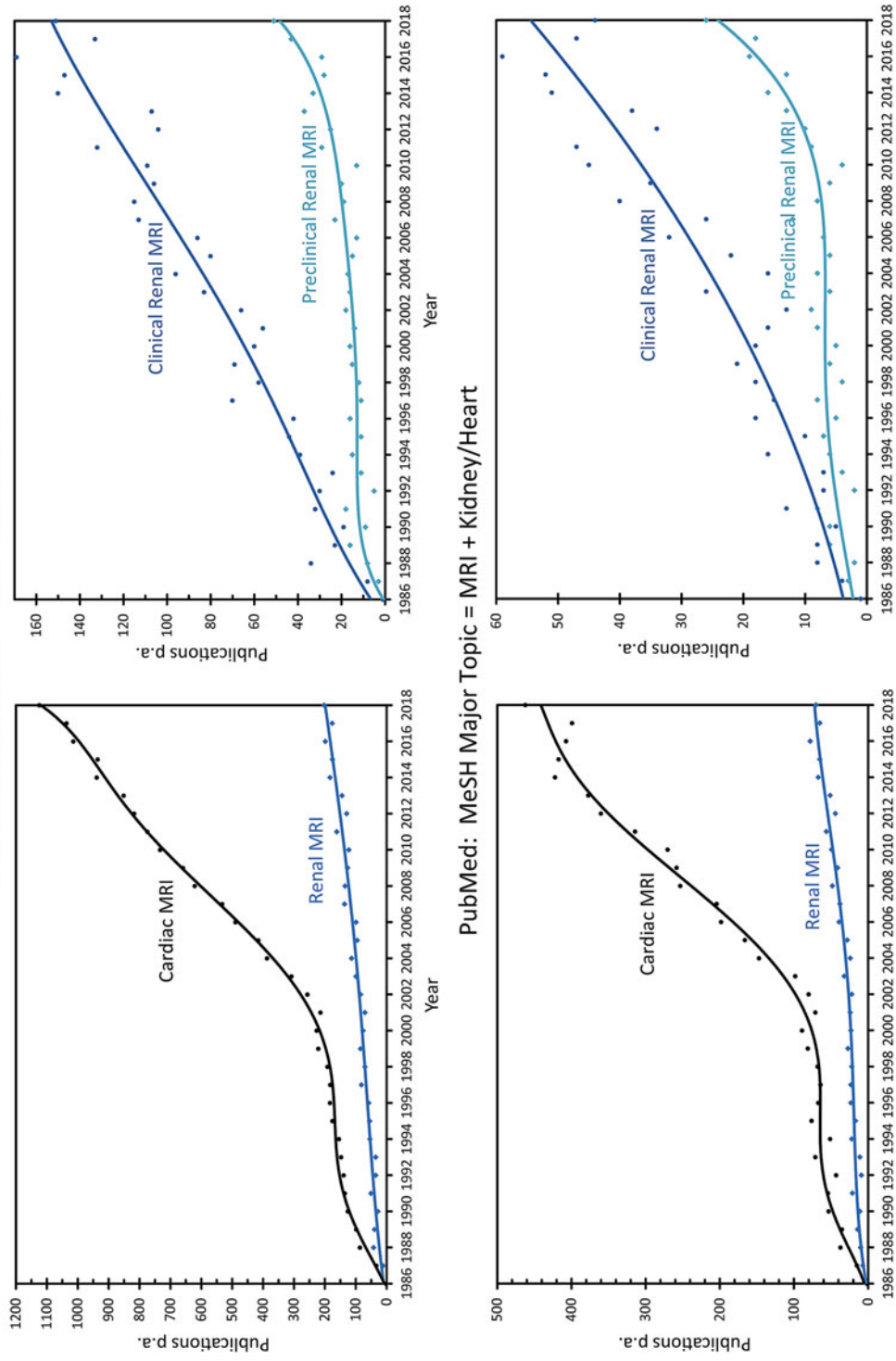

Fig. 2 Number of publications on renal or cardiac MRI over the years. Left panels: (pre)clinical renal MRI versus (pre)clinical cardiac MRI. Right panels: clinical renal MRI versus preclinical renal MRI. Lower panels: Search restricted to publications with the main focus on renal or cardiac MRI

interpret the MRI parameters (T_1, T_2*, ADC, etc.) and establishing normal ranges for these MRI parameters are only two of the items on the to-do list.

When searching for the culprits for the slow development of renal MRI, we also encounter the usual suspects: lack of training and standardization. This will sound familiar to most academic researchers. The workforce of academic research consists primarily of PhD students, who typically start their MRI research lacking the most relevant knowledge, and thus spend half or even more of their 3- to 4-year project learning the necessary theory, skills, hands-on experience and the many "secret tricks" that are essential for performing successful studies but are not found in the usual literature. This is problem #1: inefficient learning.

When designing a study, researchers encounter a further difficulty. Puzzled by the great variety of protocols (and diversity of equipment) in the literature, and often lacking an explanation for the choice of parameters, they are forced to design their study based on their own rationales and gut feelings. This is problem #2: lack of standardization. This not only hampers new researchers in setting up their studies but, even more devastatingly, has a detrimental effect on the comparability and reproducibility of research. This is a major obstacle to fast and efficient research and development.

When researchers finally publish their results, they do so in the usual format of a scientific paper, which focuses on a concise description of the problem, proposed solution, main findings, and a discussion of the meaning and limitations of the study. Important details about the practicalities of actually conducting the experiments are usually omitted. When individuals leave the lab, most of their crucial experience and expertise is lost. The cycle starts again with the next student.

2 How Can Training and Standardization Be Improved?

2.1 A Roadmap for Improved Training and Standardization of Renal MRI

Let's recap: the box of diagnostic tools available to the nephrologists is still rather poorly equipped (mostly insensitive and nonspecific plasma/urine markers), and renal MRI has the potential to be a game changer for the treatment of AKI and CKD. To address the numerous challenges of clinical translation of renal MRI, much more research activity is needed, and the community needs to grow. Among the factors preventing rapid progress are inefficient learning and lack of standardization. To overcome these roadblocks we suggest a roadmap for improving the training and standardization of preclinical and clinical renal MRI (Fig. 3). This combines protocol collections in the *Springer Protocols* book format with consensus-based technical recommendation papers based on the Delphi method.

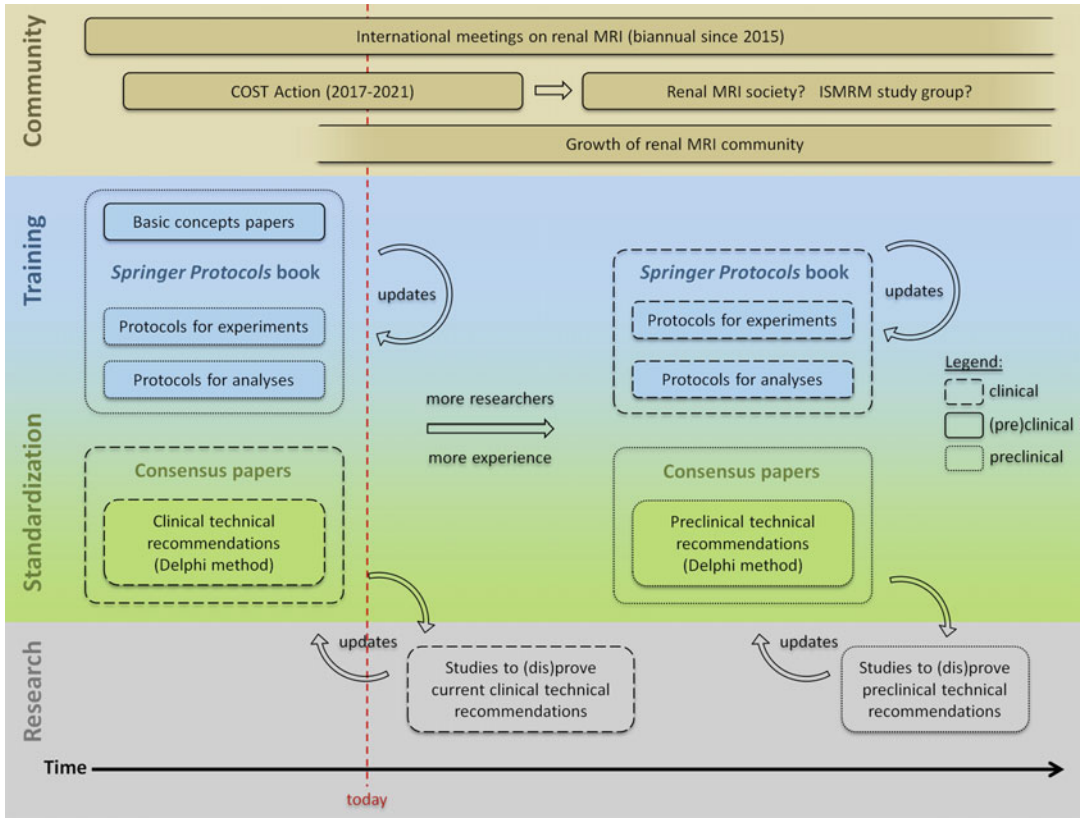

Fig. 3 Suggested roadmap for improving the training and standardization of preclinical and clinical renal MRI. It combines *Springer Protocols* books (excellent for training but also provides working protocols that help to improve comparability/standardization of future studies) with consensus-based technical recommendation papers (established tool to move toward standardization of studies). clinical = human MRI, (pre)-clinical = human and animal MRI, preclinical = animal MRI

Springer Protocols is "the world's largest collection of protocols of biomedical and life sciences," currently with over 58,000 step-by-step experimental protocols in more than 2000 books. The protocols are published individually as electronic publications in the PubMed cited journal *Methods in Molecular Biology* as well as in the form of printed books, with each book representing a collection of protocols for a specific topic. "Each protocol is provided in readily-reproducible step-by-step fashion, opening with an introductory overview, a list of the materials and reagents needed to complete the experiment, and followed by a detailed procedure that is supported with a helpful notes section offering tips and tricks of the trade as well as troubleshooting advice." [10]. This format makes *Springer Protocols* an excellent tool for training, and by providing working protocols, they also help to improve the reproducibility, comparability, and standardization of studies. Researchers are less likely to perform studies with "arbitrary" protocols and parameters when tested and proven protocols are readily available.

An established step toward standardization are consensus-based technical recommendation papers published as articles in technical journals. The process of developing expert consensus on technical aspects is a challenge. Here the Delphi method [11] can help to generate consensus statements: anonymous surveys that ensure all opinions are heard, free from peer pressure, are followed by rounds of face-to-face discussions. This iterative method permits "reaching reliable consensus in practice guidelines on health-care-related issues and on topics where there is little or no definitive evidence and where opinion is important" [12].

Because step-by-step protocols and technical recommendations address different ends of the training-standardization spectrum (Fig. 3), both perfectly complement each other. When deciding which step to take first, one needs to take into account the specific situation, that is, the size of the research community, the amount of hands-on experience available, the range of different equipment in use, the range of different subjects/objects being investigated, and so on. In these aspects clinical and preclinical renal MRI differ significantly. The number of research groups active in clinical renal MRI is five times the number of those active in preclinical renal MRI (*see* Subheading 1.4). In the clinical setting the range of setups (RF coils, field strengths) and subjects is much smaller than in preclinical settings. Even though we highlighted pediatric renal MRI in the introduction, the vast majority of renal MRI studies are performed on adult subjects at 1.5 or 3.0T. In preclinical renal MRI predominantly two species of very different size—mice and rats—are investigated at fields strengths of 3.0T, 4.7T, 7.0T, 9.4T, 11.7T, and 16.4T, with a wide range of RF coils ranging from human wrist coils to RX surface array + TX volume resonator combinations tailored for mouse or rat cardiac MRI, to cryogenically cooled TX/RX surface coils. These variations in setup influence numerous factors, including the achievable signal-to-noise ratio, the spatial resolution, and the relaxation times (T_1, T_2, T_2*), thus leading to substantially different MRI protocols. Both the great technical variety and the small size of the preclinical renal MRI community make reaching consensus-based technical recommendations particularly challenging, because many different sets of recommendations would be needed to address all commonly used study setups. Therefore, while consensus-based technical recommendations may be the natural first step for clinical renal MRI, for preclinical MRI we decided to focus instead on creating a comprehensive *Springer Protocols* collection to improve training and comparability of studies.

Both, consensus-based recommendations papers and protocols collections, can only be fully effective if they are made openly accessible. Therefore, we are very glad that it was possible to make these publications open-access thanks to support from the COST Action PARENCHIMA (renalmri.org).

2.2 Driving on the Road to more Efficient Renal MRI Research: Are We There Yet?

The answer is, of course, "not yet," as there is still some distance left to drive. But a giant leap has been made already, thanks to the COST Action PARENCHIMA (renalmri.org), which unites more than 200 experts in renal MRI from 30 countries, and the time, effort, and energy invested by more than 100 authors. After recent clinical position papers (https://academic.oup.com/ndt/issue/33/suppl_2) confirmed the demand, two projects have been implemented: The consensus-based technical recommendations for clinical translation of renal MRI (described in [12]) and the *Springer Protocols* book on preclinical renal MRI (described in Subheading 3).

Four papers present the results of applying the Delphi method to clinical renal MRI: arterial spin labeling (ASL) perfusion, blood oxygenation level dependent (BOLD) MRI, diffusion-weighed imaging (DWI), and mapping of renal T_1/T_2 [13–16]. This process generated over 160 consensus statements but also flagged topics where experts were currently unable to agree on a recommendation. These first ever technical recommendations for renal MRI should spark research into their appropriateness, with the aim to either prove or disprove specific recommendations. The findings of these future studies should then be fed back into updated and revised versions of the technical recommendations papers (Fig. 3). We hope that this approach will gradually lead to an alignment of the methods for measuring renal MRI biomarkers. It goes without saying that also the spectrum of methods covered must be extended in the future.

In the roadmap (Fig. 3), we propose to supplement these fresh off the press, already existing publications with the respective other parts, so that there will be step-by-step protocols as well as consensus-based technical recommendations available for both clinical and preclinical renal MRI. Here, the *Springer Protocols* for clinical MRI of the kidney are a placeholder for any type of protocol style journal, that is, *Methods in Molecular Biology (Springer Protocols)*, *Nature Protocols*, *Protocol Exchange*, *Journal of Visualized Experiments (JoVE)*, and so on. In contrast to the *Springer Protocols*, the latter permits independent publications on specific methods, which could be advantageous for clinical renal MRI, as it would not be necessary to publish protocols for many methods simultaneously. Needless to say, regularly updating all protocols and recommendations will be a challenging but, nevertheless, very important part of advancing the progress of renal MRI.

3 The Springer Protocols Book on Preclinical Renal MRI

Since Douglas Adams's *The Hitchhiker's Guide to the Galaxy* was first published in 1979, the number "42" has been claimed to be the answer to the question of "life, the universe, everything." After more than 2 years of hard work by 90 authors, the answer to the

question, "How can we improve the training and standardization of preclinical renal MRI?" resulted in the 42 (other) chapters of this *Springer Protocols* book Pohlmann A, Niendorf T (eds) (2020) "Preclinical MRI of the Kidney—Methods and Protocols," Springer, New York. In the following subsections we describe the tailored concept of the book and the topics covered by the chapters.

3.1 Concept and Special Features of the Book

When we started to think about the structure and content of this book on preclinical renal MRI (with main focus on small animals), it immediately became clear that a simple collection of independent chapters would not suffice, for a multitude of reasons. First, there are many important aspects involved in renal MRI that are relevant to any MRI method: it does not make sense that for every individual method the protocol would include considerations and instructions regarding the MRI hardware, animal preparation, physiological monitoring, or image slice planning and shimming. Second, due to the complexity of MRI it is very challenging to include all the information about a method in a single chapter. If the book was to become a one-stop-shop for learning renal MRI in small animals, a concept was needed. In the following we describe its concept and special features.

3.1.1 Provide all the Necessary Information for each Method

With a few exceptions, we included three chapters for each renal MRI method:

1. There is one chapter describing the **basic concepts** of the method. We believe a sound understanding of the measurement concept is essential when planning, performing, analyzing, and interpreting a study. This is complemented by a brief **overview of the preclinical renal applications**, in order to illustrate for what kind of questions and applications each technique is useful for.
2. A **step-by-step experimental protocol**, which we know from the many existing *Springer Protocols* books. These protocols are the core of the book. For less complex methods they include also instructions for data analysis.
3. Detailed **step-by-step protocols for data analysis**.

3.1.2 Generalize Protocols by Peer Review

Although we trusted that each author had extensive experience and described the protocols correctly and in an understandable manner, we endeavored to make sure these were free from lab specific techniques, assumptions and limitations, which could be due, for example, to the (un)availability of equipment or traditions. Because these **protocols should also serve to move toward the harmonization of studies**, we felt it was important to ensure that the protocols were as universal as possible and would work in many

labs and settings. For this reason we implemented a coauthor peer review process, that is, every chapter had to have one or several external coauthors from other laboratories. The roles of these coauthors are as follows:

1. To check whether the protocol would be applicable in other settings,
2. To check whether the steps and parameters are reasonable and their rationale clear and correct,
3. To add example protocols for additional lab settings.

3.1.3 Avoid Magic Numbers

Magic numbers—that is, numbers which are not explained and whose choice appears to be arbitrary—are not only a bad idea for software program codes but also for lab protocols. How often have we all read scientific publications and just could not figure out why the authors chose that particular set of measurement parameters! Was there a clever rationale behind their choice that sadly we didn't know, a lab tradition which might be reasonable but perhaps not applicable to our setting, or just a gut feeling of a student that didn't know how to make sense of all the different examples in the literature?

In any case, we wanted to reduce the magic numbers in our protocols to a minimum, so all authors were instructed to explain the rationales for their parameter choices in generic terms. If possible, advice for adapting them to other settings (other species, other field strengths) was to be given in the Notes section. Of course, example parameter sets are very valuable because they may allow readers to start straight away with a running protocol. They are also important in terms of harmonization, as mentioned. Therefore, examples of parameter sets for specific settings were requested, but separately in the Notes section, for example parameter sets for mice in a 7T MRI system and rats in a 9.4T system. For some techniques parameter sets for rats in a clinical 3T MRI system were also included.

3.1.4 Describe the Pragmatic Way for Data Analyses

It was important to us to dedicate separate chapters to the analyses because data analysis is an essential part of each study, but it is very rarely described in adequate detail. Statements like "T_2* was calculated by pixel-wise exponential fitting to the data using an in-house developed software written in MATLAB®" don't really help anyone who wants to learn how to analyze the data correctly. We are sure many of us have used similar statements in previous journal publications, but the fault is not always entirely ours: often there is simply no space (word limits!) and time to give a detailed description. Here, we wanted to make sure there was space (by having an entire chapter solely for the analysis) and time (by rewarding the effort and time spent in the detailed description with a first authorship).

It was key to present the most pragmatic approach to data analysis. What is the point in describing how to do your own code if there is established software available? So if analysis software existed, authors should describe how to get it and how to use it. Otherwise, the step-by-step instructions should focus on how to write a software program. Including pseudo code was encouraged, as well as providing downloadable code examples via GitHub or similar.

Finally, we asked to provide the readers with ideas on how to validate that their analyses give correct results. This could include for example a table of reference values or using synthetic test data.

3.1.5 Prevent Tunnel Vision—A Successful Study Needs More Than an MRI Protocol

Indeed, performing the actual MRI study is only part of the story. One must not forget that physiological MRI also requires consideration of many factors that are less important in anatomical imaging. Considerations about physiological monitoring, choosing the right animal model, measuring at the right time of the day, and using the most suitable anesthesia all have important implications.

For this reason, the first part of the book was dedicated to topics like animal models, preparation, monitoring and physiological interventions. We also questioned the need to always perform in vivo experiments on animals for training, development, and testing. Hence, one chapter provides a step-by-step protocol for the preparation of ex vivo rodent phantoms.

3.1.6 Embrace Competition—There Are Other Great Techniques Besides MRI

There are numerous questions for which it makes sense to go multimodal. Not only ultrasound and photoacoustic imaging but also invasive probes that provide quantitative physiological measurements are extremely valuable complements. Therefore, this book includes more than just MRI.

3.1.7 Make Access to This Information Free of Charge

Thanks to support from the COST Action PARENCHIMA (renalmri.org) it was possible to make all chapters open access!

3.2 Content of the Book

An overview of topics covered by the *Springer Protocols* book on preclinical renal MRI is shown in Fig. 4. Part II contains four chapters about animal models, preparation, monitoring, physiological interventions, and rodent phantoms. In Part III there are 13 chapters describing the basic concepts of the techniques, followed by Part IV with 14 step-by-step protocols for conducting experiments. Finally, Part V contains ten chapters that address data analysis; this includes the subsegmentation of the kidney into morphology-based regions of interest or concentric objects, as well as image denoising using nonlocal means (NLM) filtering.

More detailed information on the book structure and chapters is provided below by listing all chapters in the format [chapter

Topics	Part I	Part II	Part III	Part IV	Part V
Recommendations for Preclinical Renal MRI	Intro				
Animal Models of Renal Pathophysiology and Disease		Animals			
Preparation & Monitoring of Animals		Animals			
Reversible (Patho)physiological Test Interventions		Animals			
Ex Vivo Rodent Phantoms for Testing and Training		Animals			
Quantitative Physiological Measurements by Invasive Probes			Concept	Exp. Prot.	
Ultrasound & Photoacoustic Imaging			Concept		
MRI Hardware Considerations			Concept		
Essential Practical Steps (Slice Planning, Shimming)				Exp. Prot.	
Kidney Volume Measurement				Exp. Prot.	
T_1 Mapping			Concept	Exp. Prot.	Analysis
T_2 and T_2* Mapping (BOLD)			Concept	Exp. Prot.	Analysis
Diffusion (DWI, ADC, IVIM)			Concept	Exp. Prot.	Analysis
Dynamic Contrast-Enhanced (DCE)-derived Perfusion & Filtration			Concept	Exp. Prot.	Analysis
Arterial Spin Labelling (ASL) for Perfusion Measurement			Concept	Exp. Prot.	Analysis
pH Imaging by Chemical Exchange Saturation Transfer (CEST)			Concept	Exp. Prot.	Analysis
Sodium (^{23}Na) MRI			Concept	Exp. Prot.	Analysis
Hyperpolarized Carbon (^{13}C) MR			Concept	Exp. Prot.	Analysis
Fluorine (^{19}F) MR Methods for Functional Imaging			Concept		Analysis
Inflammatory Cell Assessment by Fluorine MRI				Exp. Prot.	
Oxygen Tension & Blood Volume Measurment with Fluorine MRI				Exp. Prot.	
MR Elastography			Concept	Exp. Prot.	
Subsegmentation of the Kidney (ROIs, concentric objects)					Analysis
Image Denoising for Improved Parametric Mapping					Analysis
	1	4	13	14	11

Fig. 4 Overview of topics covered by the *Springer Protocols* book on preclinical renal MRI. There are 4 chapters about animal models, preparation, monitoring, physiological interventions, and rodent phantoms; 13 chapters describing the basic concepts of the techniques; 14 chapters with step-by-step protocols for experiments, and 11 data analysis protocols

number] [chapter title] [author list]. Each chapter is PubMed-listed as an entry in *Methods Mol Biol.*

3.2.1 Part I—Introduction

1. *Recommendations for Preclinical Renal MRI: A Comprehensive Open-Access Protocol Collection to Improve Training, Reproducibility, and Comparability of Studies* (Andreas Pohlmann, Susan J. Back, Andrea Fekete, Iris Friedli, Stefanie Hectors, Neil Peter Jerome, Min-Chi Ku, Dario Livio Longo, Martin Meier, Jason M. Millward, João S. Periquito, Erdmann Seeliger, Suraj D. Serai, Sonia Waiczies, Steven Sourbron, Christoffer Laustsen, and Thoralf Niendorf).

3.2.2 Part II—Animal Models, Preparation, Monitoring, and Physiological Interventions

1. *Animal Models of Renal Pathophysiology and Disease* (Adam Hosszu, Tamas Kaucsar, Erdmann Seeliger, and Andrea Fekete).
2. *Preparation and Monitoring of Small Animals in Renal MRI* (Tamas Kaucsar, Adam Hosszu, Erdmann Seeliger, Henning M Reimann, and Andrea Fekete).

3. *Reversible (Patho)physiologically Relevant Test Interventions: Rationale and Examples* (Kathleen Cantow, Mechthild Ladwig-Wiegard, Bert Flemming, Andrea Fekete, Adam Hosszu, and Erdmann Seeliger).
4. *Preparation of Ex Vivo Rodent Phantoms for Developing, Testing, and Training MR Imaging of the Kidney and Other Organs* (Jason M. Millward, Joao Periquito, Paula Ramos Delgado, Christian Prinz, Thoralf Niendorf, and Sonia Waiczies).

3.2.3 Part III—Basic Concepts of Measurement Techniques

5. *Quantitative Assessment of Renal Perfusion and Oxygenation by Invasive Probes: Basic Concepts* (Kathleen Cantow, Roger G. Evans, Dirk Grosenick, Thomas Gladytz, Thoralf Niendorf, Bert Flemming, and Erdmann Seeliger).
6. *Ultrasound and Photoacoustic Imaging of the Kidney: Basic Concepts and Protocols* (Sandra Meyer and Dieter Fuchs Martin Meier).
7. *Hardware Considerations for Preclinical Magnetic Resonance of the Kidney* (Paula Ramos Delgado, Ekkehard Küstermann, André Kühne, Thoralf Niendorf, Andreas Pohlmann, and Martin Meier).
8. *MRI Mapping of Renal T_1: Basic Concepts* (Stefanie Hectors, Sabrina Doblas, Philippe Garteiser, Gwenaël Pagé, Bernard E. Van Beers, John C Waterton, and Octavia Bane).
9. *MRI Mapping of the Blood Oxygenation Sensitive Parameter T_2* in the Kidney: Basic Concepts* (Lu-Ping Li, Bradley Hack, Erdmann Seeliger, and Pottumarthi V. Prasad).
10. *Renal Diffusion Weighted Imaging (DWI) for Apparent Diffusion Coefficient (ADC), Intravoxel Incoherent Motion (IVIM), and Diffusion Tensor Imaging (DTI): Basic Concepts* (Neil Peter Jerome, Anna Caroli, and Alexandra Ljimani).
11. *Dynamic Contrast Enhancement (DCE) MRI–Derived Renal Perfusion and Filtration: Basic Concepts* (Michael Pedersen, Pietro Irrera, Walter Dastrù, Frank G Zöllner, Kevin M Bennett, Scott C Beeman, G Larry Bretthorst, Joel R Garbow, and Dario Livio Longo).
12. *Noninvasive Renal Perfusion Measurement Using Arterial Spin Labeling (ASL) MRI: Basic Concepts* (Min-Chi Ku, María A Fernández-Seara, Frank Kober, and Thoralf Niendorf).
13. *Renal pH Imaging Using Chemical Exchange Saturation Transfer (CEST)-MRI: Basic Concepts* (Dario Livio Longo, Pietro Irrera, Lorena Consolino, Phillip Zhe Sun, and Michael T. McMahon).
14. *Sodium (^{23}Na) MRI of the Kidney: Basic Concepts* (James T. Grist, Esben Søvsø Hansen, Frank G. Zöllner, and Christoffer Laustsen).

15. *Hyperpolarized Carbon (^{13}C) MRI of the Kidneys: Basic Concepts* (Cornelius von Morze, Galen D. Reed, Zhen J. Wang, Michael A. Ohliger, and Christoffer Laustsen).
16. *Functional Imaging Using Fluorine (^{19}F) MR Methods: Basic Concepts* (Sonia Waiczies, Christian Prinz, Ludger Starke, Jason M. Millward, Paula Ramos Delgado, Jens Rosenberg, Marc Nazaré, Helmar Waiczies, Andreas Pohlmann, and Thoralf Niendorf).
17. *MR Elastography of the Abdomen: Basic Concepts* (Suraj D. Serai and Meng Yin).

3.2.4 Part IV—Experimental Protocols

18. *Monitoring Renal Hemodynamics and Oxygenation by Invasive Probes: Experimental Protocol* (Kathleen Cantow, Mechthild Ladwig-Wiegard, Bert Flemming, Andreas Pohlmann, Thoralf Niendorf, and Erdmann Seeliger).
19. *Essential Practical Steps for MRI of the Kidney in Experimental Research* (Andreas Pohlmann, João dos Santos Periquito, and Thoralf Niendorf).
20. *Assessment of Renal Volume with MRI: Experimental Protocol* (Andreas Müller and Martin Meier).
21. *Experimental Protocols for MRI Mapping of Renal T_1* (Philippe Garteiser, Octavia Bane, Sabrina Doblas, Iris Friedli, Stefanie Hectors, Gwenaël Pagé, Bernard E. Van Beers, and John C. Waterton).
22. *Experimental Protocols for Mapping of Renal T_2* and T_2* (Andreas Pohlmann, Kaixuan Zhao, Sean B. Fain, Pottumarthi V. Prasad, and Thoralf Niendorf).
23. *Renal MRI Diffusion: Experimental Protocol* (João S. Periquito, Martin Meier, Thoralf Niendorf, Andreas Pohlmann, and Neil Peter Jerome).
24. *Dynamic Contrast Enhanced (DCE) MRI–Derived Renal Perfusion and Filtration: Experimental Protocol* (Pietro Irrera, Lorena Consolino, Walter Dastrù, Michael Pedersen, Frank G. Zöllner, and Dario Livio Longo).
25. *Renal Blood Flow Using Arterial Spin Labeling (ASL) MRI: Experimental Protocol and Principles* (Kai-Hsiang Chuang, Martin Meier, María A Fernández-Seara, Frank Kober, and Min-Chi Ku).
26. *Renal pH Mapping Using Chemical Exchange Saturation Transfer (CEST) MRI: Experimental Protocol* (Kowsalya Devi Pavuluri, Lorena Consolino, Dario Livio Longo, Pietro Irrera, Phillip Zhe Sun, and Michael T. McMahon).

27. *Sodium (^{23}Na) MRI of the Kidney: Experimental Protocol* (James T. Grist, Esben Søvsø Hansen, Frank G. Zöllner, and Christoffer Laustsen).
28. *Hyperpolarized Carbon (^{13}C) MRI of the Kidney: Experimental Protocol* (Christoffer Laustsen, Cornelius von Morze, and Galen Reed).
29. *Fluorine (^{19}F) MRI for Assessing Inflammatory Cells in the Kidney: Experimental Protocol* (Min-Chi Ku, Adrian Schreiber, Paula Ramos Delgado, Philipp Boehm-Sturm, Ralph Kettritz, Thoralf Niendorf, Andreas Pohlmann, and Sonia Waiczies).
30. *Fluorine (^{19}F) MRI to Measure Renal Oxygen Tension and Blood Volume: Experimental Protocol* (Lingzhi Hu, Hua Pan, and Samuel A. Wickline).
31. *MR Elastography of the Abdomen: Experimental Protocols* (Suraj D. Serai and Meng Yin).

3.2.5 Part V—Protocols for Advanced Analyses

32. *Subsegmentation of the Kidney in Experimental MR Images Using Morphology-Based Regions of Interest or Multiple-Layer Concentric Objects* (Leili Riazy, Bastien Milani, João S. Periquito, Kathleen Cantow, Thoralf Niendorf, Menno Pruijm, Erdmann Seeliger, and Andreas Pohlmann).
33. *Denoising for Improved Parametric MRI of the Kidney: Protocol for Nonlocal Means Filtering* (Ludger Starke, Karsten Tabelow, Thoralf Niendorf, and Andreas Pohlmann).
34. *Analysis Protocols for MRI Mapping of Renal T_1* (Philippe Garteiser, Gwenaël Pagé, Sabrina Doblas, Octavia Bane, Stefanie Hectors, Iris Friedli, Bernard E. Van Beers, and John C. Waterton).
35. *Analysis Protocols for MRI Mapping of the Blood Oxygenation Sensitive Parameters T_2* and T_2 in the Kidney* (João S. Periquito, Ludger Starke, Carlota M. Santos, Andreia C. Freitas, Nuno Loução, Pablo García Polo, Rita G. Nunes, Thoralf Niendorf, and Andreas Pohlmann).
36. *Analysis of Renal Diffusion Weighted Imaging (DWI) Using Apparent Diffusion Coefficient (ADC) and Intravoxel Incoherent Motion (IVIM) Models* (Neil Peter Jerome and João S. Periquito).
37. *Analysis Protocol for Dynamic Contrast Enhanced (DCE) MRI of Renal Perfusion and Filtration* (Frank G. Zöllner, Walter Dastrù, Pietro Irrera, Dario Livio Longo, Kevin M Bennett, Scott C. Beeman, G. Larry Bretthorst, and Joel R. Garbow).
38. *Quantitative Analysis of Renal Perfusion by Arterial Spin Labeling* (Kai-Hsiang Chuang, Frank Kober, and Min-Chi Ku).

39. *Analysis Protocol for the Quantification of Renal pH Using Chemical Exchange Saturation Transfer (CEST) MRI* (Hahnsung Kim, Yin Wu, Daisy Villano, Dario Livio Longo, Michael T. McMahon, and Phillip Zhe Sun).
40. *Analysis Protocol for Renal Sodium (^{23}Na) MR Imaging* (James T. Grist, Esben Søvsø Hansen, Frank G. Zöllner, and Christoffer Laustsen).
41. *Analysis Methods for Hyperpolarized Carbon (^{13}C) MRI of the Kidney* (Galen D. Reed, Natalie J. Korn, Christoffer Laustsen, and Cornelius von Morze).
42. *Data Preparation Protocol for Low Signal-to-Noise Ratio Fluorine-19 MRI* (Ludger Starke, Thoralf Niendorf, and Sonia Waiczies).

3.3 Mission and Vision

The mission of this book was to bring together in one collection a comprehensive assortment of protocols, methods, techniques, and recommendations that can form a cornerstone of preclinical renal MR. This collection will serve as an excellent starting point for new researchers interested in breaking into the renal MR field. Expanding the number of researchers is absolutely critical for realizing the full potential of renal MR. By providing a set of carefully constructed protocols, we can avoid the waste of time, money and resources by no longer "re-inventing the wheel." This collection will also greatly facilitate the harmonization of studies, and promote the sharing of data and results across multiple research groups, by getting everyone onto the "same page." These efforts will help us break through those bottlenecks of inefficient learning and lack of standardization. The road ahead to fully realize the scientific and clinical possibilities of renal MR remains long, but the end result will be well worth the effort.

4 Notes

1. The search string for clinical renal MRI was as follows: `(("magnetic resonance imaging"[MeSH Terms]) AND "kidney"[MeSH Terms]) AND "humans "[MeSH Terms])`. For preclinical renal MRI the last AND term was replaced with `AND "animals"[MeSH Terms]) NOT "humans"[MeSH Terms]`. For cardiac MRI the word "`kidney`" was replaced with the word "`heart`." For restricting the search to papers with a main focus on MRI of the kidney/heart `MeSH Terms` was replaced with `MeSH Major Topic`: `(("magnetic resonance imaging"[MeSH Major Topic]) AND "kidney"[MeSH Major Topic]))` …. We used PubMed's MeSH terms rather than free text search in the title/abstract to reduce the number of false positive/negative search results. However, a

drawback of using MeSH terms is that the indexing process takes rather long (several studies reported average delays of 100–150 days), but it may take significantly longer in some cases. For example, we found that several of our publications from 2017 and after were not yet MeSH indexed. Hence, the presented publication statistics can only be rough estimates of the true numbers of publications. Data for the year 2019 was excluded, because most PubMed listed publications on renal MRI had not been indexed with MeSH Terms yet.

2. We further exploited the publication lists obtained from the above PubMed's searches. We defined *active researchers* as anyone who published on renal MRI since 2015. After exporting the date-restricted publications lists from PubMed in XML format, we used an in-house developed software to extract the affiliations of the first and last authors—these research groups (departments of hospitals and academic institutions were counted individually) were considered to be *active players in renal MRI*. Duplicates were removed automatically (using Matlab's *unique()* function) and manually. The limitations mentioned in **Note 1** also apply here: due to the incomplete MeSH indexing the derived statistics are only rough estimates and data of 2019 could not be included.

Acknowledgments

This work was funded, in part (Thoralf Niendorf, Sonia Waiczies, Andreas Pohlmann, Erdmann Seeliger and Joao Periquito), by the German Research Foundation (Gefoerdert durch die Deutsche Forschungsgemeinschaft (DFG), Projektnummer 394046635, SFB 1365, RENOPROTECTION. Funded by the Deutsche Forschungsgemeinschaft (DFG, German Research Foundation), Project number 394046635, SFB 1365, RENOPROTECTION).

This chapter is based upon the work from COST Action PARENCHIMA, supported by European Cooperation in Science and Technology (COST). COST (www.cost.eu) is a funding agency for research and innovation networks. COST Actions help connect research initiatives across Europe and enable scientists to enrich their ideas by sharing them with their peers. This boosts their research, career, and innovation.

PARENCHIMA (renalmri.org) is a community-driven Action in the COST program of the European Union, which unites more than 200 experts in renal MRI from 30 countries with the aim to improve the reproducibility and standardization of renal MRI biomarkers.

References

1. Dickerson EC, Dillman JR, Smith EA, DiPietro MA, Lebowitz RL, Darge K (2015) Pediatric MR urography: indications, techniques, and approach to review. Radiographics 35 (4):1208–1230. https://doi.org/10.1148/rg.2015140223
2. Khrichenko D, Darge K (2010) Functional analysis in MR urography—made simple. Pediatr Radiol 40(2):182–199. https://doi.org/10.1007/s00247-009-1458-4
3. National Kidney Foundation NY, USA. https://www.kidney.org/professionals/kdoqi/gfr_calculator. Accessed 07 Jan 2020
4. Porrini E, Ruggenenti P, Luis-Lima S, Carrara F, Jimenez A, de Vries APJ, Torres A, Gaspari F, Remuzzi G (2019) Estimated GFR: time for a critical appraisal. Nat Rev Nephrol 15(3):177–190. https://doi.org/10.1038/s41581-018-0080-9
5. Friedli I, Crowe LA, Berchtold L, Moll S, Hadaya K, de Perrot T, Vesin C, Martin PY, de Seigneux S, Vallee JP (2016) New magnetic resonance imaging index for renal fibrosis assessment: a comparison between diffusion-weighted imaging and T1 mapping with histological validation. Sci Rep 6:30088. https://doi.org/10.1038/srep30088
6. Pohlmann A, Arakelyan K, Hentschel J, Cantow K, Flemming B, Ladwig M, Waiczies S, Seeliger E, Niendorf T (2014) Detailing the relation between renal T2* and renal tissue pO2 using an integrated approach of parametric magnetic resonance imaging and invasive physiological measurements. Investig Radiol 49(8):547–560. https://doi.org/10.1097/RLI.0000000000000054
7. SCMR (2018) The Society for Cardiovascular Magnetic Resonance—News 2018. scmr.org/page/CMR2018news. Accessed 07 Jan 2020
8. Pohlmann A, Seeliger E, Grosenick D, Waiczies S, Cantow K, Persson PB, Niendorf T (2017) 2nd International Scientific Symposium on Functional Renal Imaging: Where Physiology, Nephrology, Radiology and Physics Meet. www.mdc-berlin.de/renal. Accessed 07 Feb 2020
9. Francis S, Taal M, Selby N (2019) 3rd International Symposium on Functional Renal Imaging. www.nottingham.ac.uk/go/3rdrenalmri. Accessed 07 Feb 2020
10. SpringerNature Springer Protocols. www.springernature.com/gp/librarians/products/product-types/database/springerprotocols. Accessed 10 Feb 2020
11. Dalkey N, Helmer O (1963) An experimental application of the DELPHI method to the use of experts. Manag Sci 9(3):458–467. https://doi.org/10.1287/mnsc.9.3.458
12. Mendichovszky I, Pullens P, Dekkers I, Nery F, Bane O, Pohlmann A, de Boer A, Ljimani A, Odudu A, Buchanan C, Sharma K, Laustsen C, Harteveld A, Golay X, Pedrosa I, Alsop D, Fain S, Caroli A, Prasad P, Francis S, Sigmund E, Fernandez-Seara M, Sourbron S (2020) Technical recommendations for clinical translation of renal MRI: a consensus project of the cooperation in science and technology action PARENCHIMA. MAGMA 33 (1):131–140. https://doi.org/10.1007/s10334-019-00784-w
13. Nery F, Buchanan CE, Harteveld AA, Odudu A, Bane O, Cox EF, Derlin K, Gach HM, Golay X, Gutberlet M, Laustsen C, Ljimani A, Madhuranthakam AJ, Pedrosa I, Prasad PV, Robson PM, Sharma K, Sourbron S, Taso M, Thomas DL, Wang DJJ, Zhang JL, Alsop DC, Fain SB, Francis ST, Fernandez-Seara MA (2020) Consensus-based technical recommendations for clinical translation of renal ASL MRI. MAGMA 33 (1):1–21. https://doi.org/10.1007/s10334-019-00800-z
14. Bane O, Mendichovszky IA, Milani B, Dekkers IA, Deux JF, Eckerbom P, Grenier N, Hall ME, Inoue T, Laustsen C, Lerman LO, Liu C, Morrell G, Pedersen M, Pruijm M, Sadowski EA, Seeliger E, Sharma K, Thoeny H, Vermathen P, Wang ZJ, Serafin Z, Zhang JL, Francis ST, Sourbron S, Pohlmann A, Fain SB, Prasad PV (2020) Consensus-based technical recommendations for clinical translation of renal BOLD MRI. MAGMA 33(1):199–215. https://doi.org/10.1007/s10334-019-00802-x
15. Ljimani A, Caroli A, Laustsen C, Francis S, Mendichovszky IA, Bane O, Nery F, Sharma K, Pohlmann A, Dekkers IA, Vallee JP, Derlin K, Notohamiprodjo M, Lim RP, Palmucci S, Serai SD, Periquito J, Wang ZJ, Froeling M, Thoeny HC, Prasad P, Schneider M, Niendorf T, Pullens P, Sourbron S, Sigmund EE (2020) Consensus-based technical recommendations for clinical translation of renal diffusion-weighted MRI.

MAGMA 33(1):177–195. https://doi.org/10.1007/s10334-019-00790-y

16. Dekkers IA, de Boer A, Sharma K, Cox EF, Lamb HJ, Buckley DL, Bane O, Morris DM, Prasad PV, Semple SIK, Gillis KA, Hockings P, Buchanan C, Wolf M, Laustsen C, Leiner T, Haddock B, Hoogduin JM, Pullens P, Sourbron S, Francis S (2020) Consensus-based technical recommendations for clinical translation of renal T1 and T2 mapping MRI. MAGMA 33(1):163–176. https://doi.org/10.1007/s10334-019-00797-5

Part II

Animal Models, Preparation, Monitoring, and Physiological Interventions

Chapter 2

Animal Models of Renal Pathophysiology and Disease

Adam Hosszu, Tamas Kaucsar, Erdmann Seeliger, and Andrea Fekete

Abstract

Renal diseases remain devastating illnesses with unacceptably high rates of mortality and morbidity worldwide. Animal models are essential tools to better understand the pathomechanisms of kidney-related illnesses and to develop new, successful therapeutic strategies. Magnetic resonance imaging (MRI) has been actively explored in the last decades for assessing renal function, perfusion, tissue oxygenation as well as the degree of fibrosis and inflammation. This chapter aims to provide a comprehensive overview of animal models of acute and chronic kidney diseases, highlighting MRI-specific considerations, advantages, and pitfalls, and thus assisting the researcher in experiment planning.

This publication is based upon work from the COST Action PARENCHIMA, a community-driven network funded by the European Cooperation in Science and Technology (COST) program of the European Union, which aims to improve the reproducibility and standardization of renal MRI biomarkers.

Key words Kidney disease, Magnetic resonance imaging (MRI), Animal models, Rodents

1 Introduction

Renal diseases remain devastating illnesses with unacceptably high rates of mortality and morbidity worldwide. The prevalence of end stage kidney disease is currently between 8% and 16% and is rapidly increasing; the number of patients increased tenfold in the last four decades [1].

Kidney diseases generate a major drain on health and productivity-related resources for healthcare systems; thus, prevention and early treatment would have an enormous social and economic impact.

Understanding the pathologic mechanisms of renal injury is essential for finding new targets for intervention and developing effective treatments for patients with kidney disease [2]. Landmark publications have outlined key areas in which progress is necessary, specifically highlighting the need for superior diagnostic tools [3].

At present, diagnosis of kidney disease is difficult and often involves invasive procedures such as biopsy. Conventional markers of renal function such as serum creatinine and blood urea nitrogen

Andreas Pohlmann and Thoralf Niendorf (eds.), *Preclinical MRI of the Kidney: Methods and Protocols*, Methods in Molecular Biology, vol. 2216, https://doi.org/10.1007/978-1-0716-0978-1_2,

are poorly sensitive and poorly selective. The levels of these biomarkers can take several hours or days to reach a new steady state and thus represent a delayed indication of functional change that lags behind structural deterioration during the early stage of acute kidney injury (AKI). In addition, the imbalance between oxygen supply and demand in kidney tissue is the initiating step in the pathophysiology of renal ischemia–reperfusion injury (IRI), and a pivotal early element in the pathophysiology of AKI of other origins. Currently kidney biopsy is the only available method to assess renal microstructure, but it has several disadvantages, including its invasive nature and susceptibility to sampling bias. Thus, noninvasive, in vivo imaging methods such as MRI are indispensable for the adequate assessment of kidney function, oxygenation, and structure in both preclinical and clinical setups. Importantly, several novel techniques are available to generate MRI data by measuring tissue properties linked to filtration, tissue oxygenation, perfusion, fibrosis, inflammation, or tissue edema that can be used as biomarkers of renal disease [4]. MRI affords full kidney coverage, soft tissue contrast that helps to differentiate the renal layers, second-to-minute temporal resolution, support of longitudinal studies, and high anatomical detail without the use of ionizing radiation [5, 6].

Drug discovery is a time-consuming, expensive, and high-risk process. In order to develop one FDA approved drug in the preclinical phase thousands of compounds have to be tested from which only dozens end up in clinical trials [7]. Conducting studies on animal models is a valuable strategy in the preparation for clinical trials because of the high similarity between some animals and humans in their genetics, physiology, diseases, and diagnostic tools. Without doubt the translatability of results obtained in animal models to humans has numerous limitations, but often they represent an indispensable approach for trying to predict the effects of a drug in the complex human system, and also for deciding on an appropriate dose regime for the clinical trial(s) that balances efficacy and safety. Many mechanistic questions can be answered only through invasive procedures or extreme exposures possible only in animals. Moreover, due to the fact that decades may elapse between the onset and clinical manifestations of renal diseases in humans (e.g., diabetic kidney disease), rodent models offer a more feasible means of experimentation because the timeline of pathogeneses are typically much shorter (either naturally or due to tailored disease induction).

An ideal disease model accurately mimics the human condition genetically, experimentally and/or physiologically, but unfortunately such models do not exist. One reason for the poor outcomes in clinical trials is that most animal models do not fully recapitulate the pathological mechanisms underlying human diseases. Human diseases are very complex, but specific factors of a disease are relatively easy to model, which is an advantage and disadvantage

at the same time. All of the widely used animal models have their particular limitations; therefore, the model used should be appropriate for the question being addressed [8].

The present chapter summarizes animal models of renal diseases highlighting MRI-specific considerations, advantages, and pitfalls with an aim to assist the researcher in planning an experiment and choosing the best species/strain/model to address the question being asked.

This chapter is part of the book Pohlmann A, Niendorf T (eds) (2020) Preclinical MRI of the Kidney—Methods and Protocols. Springer, New York.

2 Ethical Issues

A wide range of positions exist on the debate over the ethics of animal experiments. On one end of the spectrum people argue that an animal should have as much right to live out a full life, free of suffering as a human and thus all animal experimentation should end. Others argue that while the unnecessary abuse of animals is clearly wrong, animal experimentation must continue because of the enormous scientific resource that animal models provide. A detailed discussion of the growing scholarly literature in animal research ethics is beyond the scope of this chapter; however, the authors feel obliged to provide some fundamental guidelines for conduct of ethical research. The authors of this chapter believe that biomedical animal research is founded on a pivotal ethical principle: "*It is among the most noble and indeed imperative of human endeavors to employ scientific research to prevent, alleviate, and cure the pain, suffering, distress, fear, anxiety, disability, infirmity and death associated with human disease*" [9]. Because the use of animal models to understand human disease is motivated by such a high ethical ideal, we must aim to adhere to the highest ethical standards when conducting research.

When designing a study applying the principles of 3Rs: replacement, reduction, and refinement is advised to provide a framework for performing the most humane animal research possible. *Replacement* means the substitution of animals with alternative techniques or avoid the use of animals altogether. Alternative methods such as cell cultures or novel approaches such as stem cell technologies, tissue engineering, or modeling using artificial intelligence show promise for replacing animals in many areas of research but often give limited information about what happens in the whole living animal. *Reduction* means to obtain information of given amount and precision from fewer animals or more information from the same number of animals. Proper experimental design and statistical analysis of the proposed project is pivotal in using the optimal number of animals. If more animals are used than is necessary for

obtaining reliable results, then animal lives are wasted. On the other hand, if too few animals are used then the results can be unreliable and the experiment has to be repeated, using more animals in total. *Refinement* means minimizing the incidence or severity of procedures that result in distress or suffering of animals which still have to be used. Refinement can also improve the quality of research by reducing stress in animals. By law, any suffering or pain to an animal must be minimized. Animals must be anaesthetized for surgery, and, if necessary, analgesics must be administered afterward, which will be discussed in detail in the chapter by Kaucsar T et al. "Preparation and Monitoring of Small Animals in Renal MRI."

3 General Guidelines for Choosing an Animal Model

3.1 Rat or Mouse?

The first major decision when designing a study using an animal model is to choose the most suitable species. Rodent models are the most popular to resemble human disease for a number of reasons: 90% of genes are orthologous in the rat, murine, and human genomes, small size and fast reproduction of rodents facilitates high-throughput studies, and a very good genetic/molecular tool box is available.

Differences within rodents must not be underestimated when designing experiments. Inbred mouse strains are more stable, uniform, repeatable, and better defined than outbred rat strains such as Wistar or Sprague-Dawley where the exact genetic background of each animal is unknown [10].

While rats used to be the preferred rodent in kidney research, this changed with the advent of murine transgenic and knockout technologies in the past decades. Genetically modified mice provide unique opportunities for targeted research of the impact of individual proteins on phenotype and responsiveness to therapeutic interventions. Gene deletion or overexpression generally results in very predictable and precise phenotypes in mice. Furthermore, due to their small size many more mice can be housed in a small space than rats and are therefore cheaper to maintain; they have a short reproductive cycle and accelerated life span.

Murine models of kidney disease do have some limitations and disadvantages that are worth considering. Surgical procedures such as ureteric obstruction, renal ischemia, or kidney transplantation are widely used to model human disease. Surgical manipulations and micropuncture studies are technically much easier to perform in larger animals such as rats.

Moreover, the pathophysiology in rat models is often not replicated in mice. For example, while humans and rats have only one copy of the renin gene, mice either have a single gene or two copies at the renin locus. This may be an important confounding variable considering the central role of the renin–angiotensin–aldosterone system in renal disease and that the plasma renin activity of mice

with two renin genes is tenfold higher than their single-gene counterparts [11].

Hypertension is a leading cause of kidney failure; thus, noninvasive blood pressure measurements are a crucial component of studies in the field. While the technique is fairly routine in rats, it has been proven to be rather challenging in mice [12].

Finally, the smaller size of mice means smaller amounts of experimental material to work with. The fundamental limitation in MRI is signal-to-noise ratio, which is in direct correlation with the volume of the subject. Acquiring high-resolution images of relatively small mouse kidneys could be challenging using lower field strength MRI machines. Furthermore, concurrent measurement of multiple variables such as RNA expression, protein levels, histology, and metabolic processes from individual animals can be challenging.

3.2 Which Strain?

The choice of the right strain is essential since disease phenotypes in rodents are strongly influenced by species and strain. For example, there are distinct differences in the susceptibility to ischemic AKI among various mouse strains or even different colonies of the same strain. 129/Sv and National Institute of Health Swiss mice have been shown to be less sensitive to ischemic injury than C57BL/6 or BALB/c mice [13, 14]. Most transgenic models are described to have comparable genetic background with wild-type strains such as C57BL/6 after at least five generations of backcross; however, the wild-type mice from the same transgenic models may differ significantly from ordinary C57BL/6 mice. Similarly, Brown-Norway rats have been found to be almost completely protected against several manifestations of IRI when compared with the commonly used Sprague-Dawley rat model [15]. In conclusion, pilot experiments always have to be performed to determine the appropriate duration of ischemia for a new strain to be studied.

The C57BL/6 mouse strain is also relatively resistant to the development of diabetic kidney disease (DKD). C57BL/6 mice develop significantly less albuminuria and renal histopathological changes than DBA/2J and KK/HIJ mice [16]. Sprague-Dawley rats are far more sensitive to streptozotocin-induced diabetes than nude rats [17].

The remnant kidney model or 5/6 nephrectomy model has been used extensively in rats to study the pathogenesis of glomerulosclerosis. In contrast, mouse strains such as C57BL/6 and C57BLX Swiss-Webster mice do not develop significant glomerulosclerosis or increased systolic blood pressure and proteinuria in this model. C57BL/6 mice and Wistar rats are less susceptible to deoxycorticosterone acetate (DOCA) salt-induced hypertension than 129/Sv mice or Sprague-Dawley rats respectively [18, 19]. Thus, the more susceptible 129/Sv strain is

recommended to study hypertension-associated glomerulosclerosis in mice [20].

3.3 Sex

The anatomical structure of the healthy kidney is different in the two sexes. Females have more glomeruli in the kidneys, higher renovascular resistance, lower absolute GFR, and lower renal plasma flow. There are differences on the cellular level as well: males have larger mitochondria and more lysosomes and ribosomes in their proximal tubular cells. Although estrogen and androgen receptors are found in renal tissue in both sexes, animal experimental models (e.g., castration, ovariectomy) suggest that sex hormones are involved in the sexual dimorphism of the kidney [21].

Female sex is a protective factor in several renal diseases which disappear after menopause. Not only the outcome of AKI is better in females [22, 23], but the progression of renal function deterioration during the aging process [24] as well as other chronic renal diseases [25] is also slower in females compared to males. Some studies support the protective role of female hormones (17-β-estradiol, progesterone) [26–28]. Others highlight the negative effect of testosterone: Park et al. found more severe renal injury after testosterone therapy in female, ovariectomized, and castrated male mice [29].

For the aforementioned reasons the use of female rodents is only advised if the study specifically aims to investigate sex differences or the role of sex hormones. Duration of the estrous cycle is 4–5 days in both rats and mice; a vaginal smear has to be obtained and stages of the estrous cycle have to be identified before starting an experiment. C. Caligioni provides a detailed description of assessing the reproductive status of mice [30].

3.4 Other Species

Some nonrodent species are also used, although less frequently. In theory, nonhuman primates are the most similar to human biology, but the heterogeneity is huge among species. Close approximation of genetic, structural, and functional features of nonhuman primates to humans make them ideal experimental models; however, specific ethical considerations are essential [31]. These animals are likely to sense pain, distress, and social relationships in the same way as humans. Moreover, they are expensive to obtain and house, may transmit diseases to humans, and can be difficult to handle due to their strength and intelligence. Experiments with nonhuman primates are limited to a very small number of animals compared to rodents; thus, their statistical value can be doubtful.

Work using dogs played an enormous role in the early advancement of dialysis and transplantation techniques, or the use of azathioprine in immunosuppression, and others [32]. However, ethical considerations and strong feelings of the public have substantially limited the use of companion animals for research purposes.

Farm animals such as pigs are fairly similar to humans in renal anatomy, size, and metabolism. Pigs are the subject of extensive research especially as a potential source of kidneys for xenotransplantation [33]. The size of fully grown pigs limits routine laboratory use; moreover, potential virus or prion transmission from pigs to humans will possibly reduce their use as xenograft sources.

4 Models of AKI

4.1 Ischemia–Reperfusion Injury

Renal IRI is the most common cause of AKI in patients and temporary occlusion of renal blood flow is unavoidable during kidney transplantation. Therefore, models that accurately and reproducibly replicate renal IRI are indispensable for investigating the pathomechanism of AKI and for the development of novel therapeutic agents. There are three commonly used models of IRI: (1) bilateral clamping of renal arteries and veins; (2) unilateral clamping; and (3) unilateral clamping with contralateral nephrectomy [34]. The bilateral model is regularly used because it is considered most relevant to human pathology where blood supply is typically affected in both kidneys. Some studies performed decapsulation prior to renal ischemia that may have renoprotective effects, as reported earlier [35]. However, decapsulation was not conducted in the majority of published studies. Unilateral IRI models without contralateral nephrectomy leave animals with a healthy kidney which takes over the excretory function. Consequently, this model allows for the study of the effect of prolonged ischemia times without excessive postprocedure lethal outcomes. On the other hand, this model does not allow the study of filtration and excretory function of the affected kidney after IRI because of the compensation achieved by the unaffected healthy kidney. In the third model right nephrectomy is performed at the time of left kidney IRI. Tissue from the removed right kidney can be used as highly valuable control in studies where pretreatment that induces or suppresses specific gene or protein expression is involved. Thus, changes in the molecule of interest can be confirmed and quantified in each individual animal used in the experiment. This model is most useful when the researcher aims to test the effect of drugs or compounds administered prior to the induction of IRI, furthermore overall survival is more reliable than with bilateral clamping and this model closely mimics the situation occurring in renal transplantation. Several studies suggest the protective potential of contralateral nephrectomy against IRI by increasing blood flow and other beneficial pleotropic effects (e.g., antiapoptotic, proliferative, vasodilatory) in the remaining kidney [36], which should be taken into consideration when designing an experiment.

The pathological consequences of renal IRI are proportional to the period of ischemia which has to be determined for the

individual species, strain, sex, and age. Shorter ischemia causes subclinical AKI, with minor histologic change and without any functional deterioration as assessed by serum creatinine and BUN [37]. As ischemia duration increases clinical AKI develops with moderate renal damage accompanied by renal failure. If the extent of injury is mild, then the full recovery of renal function can be expected. However, longer ischemia generally leads to lethal kidney damage, with continuously deteriorating kidney function and the animals die due to uremia [38]. As a guide, 30–50 min and 20–35 min of occlusion respectively is generally used in rats and mice. Clamping time, maintenance of body temperature, and the type of anesthesia are key parameters to be standardized for reproducibility.

4.2 Renal Transplantation

Renal transplantation is predominantly performed in rats due to the challenging microsurgical techniques involved. Depending on the aim of the study various combinations of inbred and outbred strains model various complications of kidney transplantation such as IRI, acute rejection, or chronic allograft nephropathy [39]. Autotransplantation models are ideal for the study of alloantigen-independent mechanisms such as IRI or the effect of cold storage on the organ. Fisher and Lewis rat strains differ at the major histocompatibility loci I and II which results in chronic allograft nephropathy if no immunosuppression is applied. Thus, transplantation from a Fisher donor to a Lewis recipient is the most commonly used model of chronic allograft nephropathy [40]. Other strains—both as donor and recipient—include outbred strains: Sprague-Dawley, Wistar, and Long-Evans; or inbred strains: Lewis, Brown-Norway, and Dark Agouti [41–43].

A large number of different surgical techniques have been reported, probably due to the technical difficulties associated with rat renal transplantation. Detailed procedures are available in an excellent review by Schumacher et al. which describes all technical aspects, different techniques of vascular anastomosis, strain selection, and more [44].

4.3 Sepsis-Induced AKI

Sepsis is a complex disease that involves at least two stages, which should ideally be reproduced in animal models. An initial proinflammatory burst resulting in hypodynamic circulation with hypotension and organ dysfunction is followed by compensatory immune depression, with hyperdynamic circulation, but these can overlap. There are three types of sepsis animal models: exogenous toxin (e.g., LPS)-induced; alteration of endogenous protective barriers (e.g., cecal ligation and puncture (CLP) or colon ascendens stent peritonitis (CASP)); or exogenous bacteria-induced. The LPS model is predominantly used in rodents as the standard CLP model does not develop AKI, while bacterial infusion models are established mainly in larger animals such as dogs and sheep. C. N. May's

group established a model of hyperdynamic sepsis in conscious sheep. In this model sepsis is induced by intravenous infusion of live *Escherichia coli* and is characterized by hypotension, tachycardia, peripheral vasodilation, and AKI [45].

Advantages of LPS injection are that its simple, sterile, and induces systemic inflammation that has many similarities with hypodynamic sepsis pathophysiology in humans. The disadvantage is that early and transient proinflammatory mediator production is more intense than in humans. LPS causes decreased GFR, increased BUN levels, and neutrophil infiltration in the kidney [46]. LPS dose can be titrated to mimic different aspects of sepsis: typical LPS doses cause systemic hypotension and decreased glomerular perfusion, while lower doses do not cause systemic hypotension but decrease glomerular perfusion [47].

4.4 Toxin-Induced AKI

4.4.1 Cisplatin

Cisplatin is a widely used anticancer drug; however, high doses have significant toxic effects on proximal tubules. Cisplatin treatment leads to inflammation and interstitial fibrosis, moreover renal blood flow is also altered. Most studies use a single *i.p.* injection of 6–20 mg/kg cisplatin in rats, which induces AKI within 72 h and both pathology and recovery phase are comparable to those of humans [48]. Higher doses are also used, albeit less frequently [49, 50].

4.4.2 Contrast-Induced AKI (CIAKI)

Intravascular administration of iodinated X-ray contrast media (CM) for computer tomography, MRI or angiography can induce AKI characterized by renal tissue hypoxia due to reduced renal blood flow and consequent oxidative stress [51]. Incidence varies between 3% and 25% depending on several factors. Firstly, the potential to cause CIAKI is less when CM are given intravenously (typically in lower doses, e.g., for computed tomography or urography) than intra-arterially (often in higher doses, e.g., for cardiac procedures), because the renal first-pass concentration is higher for the latter route of administration. Secondly, physicochemical properties of CM solutions such as osmolality and viscosity impinge on their different safety profiles. Thirdly, hydration status of the patient plays an important role. Finally, preexisting conditions such as endothelial dysfunction, for example related to diabetes mellitus, and impaired renal function increase the risk of CIAKI [51].

There are a number of models that reliably induce CIAKI in otherwise healthy animals. The clinical setting of cardiac procedures is emulated by a model, in which a 1.5 mL bolus of a high viscous CM (iodixanol 320 mg iodine/mL) is injected into the thoracic aorta of naïve rats [52–54]. A high dose of intravenously administered iodixanol (rat: 4 g iodine/kg body weight; rabbit: 5 g iodine/kg body weight) also induces CIAKI [55, 56].

In order to emulate conditions of patients who are at increased risk for CIAKI, several animal models employing a combination of contrast agent injection and other injuries (e.g., vasodilator inhibition, dehydration, IRI, diabetes) have been studied. Vasoconstriction induced by inhibition of nitric oxide synthase (e.g., L-NAME, 10 mg/kg body weight) combined with prostaglandin synthesis inhibition (indomethacin, 10 mg/kg body weight) prior to CM administration (iohexol, 1 g iodine/kg body weight) has been employed in rats and mice [57]. Another reliable murine model of CIAKI includes 30 min bilateral renal ischemia and CM administration 24 h after reperfusion [58].

4.4.3 Aristolochic Acid and Folic Acid

Both models are useful to study AKI to chronic kidney disease (CKD) transition. Aristolochic acid nephropathy is characterized by proximal tubular injury, necrosis and oxidative stress resulting in progressive interstitial fibrosis [59]. Aristolochic acid is the underlying cause of Balkan nephropathy and Chinese Herb nephropathy [60].

In folic acid nephropathy folic acid crystal deposits appear in the tubular lumen resulting in obstruction and subsequent acute tubular necrosis, tubular dilatation and cast formation. Mitochondrial dysfunction and early renal fibrosis are typical features of folic acid nephropathy as well.

4.4.4 Glycerol

In rhabdomyolysis skeletal muscle breakdown leads to the release of intracellular proteins and toxic compounds into circulation. AKI is a recurrent complication of rhabdomyolysis, mainly caused by inflammation and oxidative stress. Human symptoms are reproduced in rodents by water deprivation for 24 h followed by glycerol administration into the hindlimb muscle [61]. Elevated BUN and serum creatinine levels in this model are not exclusively the result of declined renal function, but rhabdomyolysis as well, thus GFR or creatinine clearance measurement should be preferred.

5 Models of CKD

5.1 Unilateral Ureteral Obstruction (UUO)

Renal fibrosis is the hallmark of progressive kidney disease that involves glomerular sclerosis tubulointerstitial fibrosis and atherosclerosis. UUO in rodents can be experimentally manipulated with respect to timing, severity and duration, while reversal of the obstruction allows the study of recovery. Complete UUO results in reduced renal blood flow and GFR within 24 h, followed by hydronephrosis, inflammation and tubular cell death within days. In 1–2 weeks severe hydronephrosis and severe fibrosis develops. The surgical procedure is relatively straightforward. Animals undergo a midline incision, the left ureter is located and then ligated [62]. Because clinical congenital obstructive nephropathy involves

only partial obstruction, models of partial UUO have been developed in neonatal mice or rats. These models are, however, technically challenging and meticulous technique is essential. In one method a piece of silicone tubing is slit and longitudinally fitted around the ureter forming a sleeve. Another recommended technique involves placement of a fine stainless-steel wire parallel to the ureter. After ligation the wire is pulled out leaving a partial obstruction. The ligature can then be removed at various time points to study recovery mechanisms. Due to functional and cellular compensatory mechanisms we recommend using sham-operated animals as controls instead of the contralateral kidney (unless comparing a therapeutic intervention on the obstructed kidney).

5.2 5/6 Nephrectomy

The 5/6 nephrectomy model mimics progressive renal failure after loss of renal mass in humans. The recommended approach is removal of the right kidney and resection of the upper and lower poles of the left kidney (2/3 of the kidney) [63]. The approach where branches of the renal artery are ligated is not feasible in mice due to their limited renal artery branching. Remnant kidneys develop glomerulosclerosis, tubulointerstitial fibrosis, renal atrophy and proteinuria. Susceptibility to renal injury in the 5/6 nephrectomy model is highly variable between different strains. C57BL/6 mice are resistant compared to 129/Sv or Swiss Webster mice.

5.3 Models of DKD

DKD is the leading cause of end-stage kidney disease worldwide. Unfortunately, animal models that replicate all important functional, structural and molecular features of human DKD are lacking. In both mice and rats, type 1 diabetes mellitus (T1DM) can be induced by streptozotocin, which is transported by GLUT2 transporter and destroys pancreatic beta cells. Renal and hepatic cells also express GLUT2, thus streptozotocin has additional direct nephrotoxic and hepatotoxic effects apart from the injury induced by diabetes [64]. Genetic models of T1DM such as Akita and OVE26 mice are also available [65]. T1DM can be induced by streptozotocin injection in DBA/2J mice, which are susceptible to nephropathy [16]. Streptozotocin induces T1DM with hyperlipidemia in ApoE$^{-/-}$ mice [66].

Models of type 2 diabetes mellitus (T2DM) utilize genetically obese rodents such as ob/ob mice, db/db mice, or Zucker rats [67, 68]. These animals are either leptin deficient or have inactivating mutations in the leptin receptor. High-fat diet can be useful to investigate the mechanisms of insulin resistance, even though the animals do not exhibit classical features of human DKD, they rarely become hyperglycemic and high-fat diet alone may cause renal injury. MKR mice can be used in a nonobese model of T2DM because the insulin receptor is dysfunctional resulting in insulin resistance, hyperglycemia and hyperlipidemia [69].

5.4 Models of Polycystic Kidney Disease

Polycystic kidney disease (PKD) is a genetic disorder associated with cystic bile ducts, bile duct proliferation, and cystic pancreatic ducts. There are two types of PKD in humans: the autosomal dominant PKD (ADPKD) caused by mutations in the PKD1 or PKD2 gene, and autosomal recessive PKD (ARPKD) caused by a mutation in the PKHD1 gene. In ADPKD the renal parenchyma is replaced by cysts originating from all segments of the nephron, collecting tubules, and ducts. In ARPKD cysts originate only from dilated collecting tubules and ducts.

In spontaneous hereditary models of PKD animals have obvious PKD phenotypes, but the responsible genes are not necessarily orthologous with the human genes. Examples of such models are Han:SPRD-Cy rats [70], PCK rats [71], Pcy mice [72], and Jck mice [73].

Transgenic mouse models have also been developed. Thivierge et al. produced a model with a bacterial artificial chromosome in which PKD1 gene expression is increased in the kidney, heart and liver, and the gene product PC1 is overexpressed in renal cysts [74]. Several transgenic models have been developed by deletion of human orthologous genes *Pkd1* [75], *Pkd2* [76] or *Pkhd1* [77]. Nagao et al. published a detailed review of PKD models [78].

5.5 Models of Hypertension

5.5.1 Spontaneously Hypertensive Rats (SHR)

The SHR rat strain was generated by protracted rounds of breeding and selection for high blood pressure. SHR rats develop hypertension at 5–6 weeks of age and systolic blood pressure of 180–200 mmHg by adulthood with high renin levels. Proteinuria increases from 6 weeks of age, GFR decreases by 20% by 15 weeks of age and glomerulosclerosis and tubulointerstitial fibrosis develops at around 50 weeks of age. Progression of hypertensive renal damage in this model mirrors that seen in human hypertension [79]. Unilateral nephrectomy may be required to induce significant renal injury [80].

5.5.2 Deoxycorticosterone Acetate (DOCA)–Salt Hypertension

The subcutaneous implantation of a DOCA pellet, uninephrectomy, and supplementation of 1% NaCl in drinking water or high-salt diet induces moderate-to-severe hypertension with renal injury and low renin levels [81]. Angiotensin II administration can aggravate renal injury. Renal pathological changes include proteinuria, fibrotic alterations, and impaired endothelium-dependent relaxation.

5.6 Podocyte Injury Models

Focal segmental glomerulosclerosis (FSGS) is the primary cause of glomerular diseases, characterized by proteinuria or nephrotic syndrome. Fibrotic lesions in some glomeruli (focal) or in specific parts of a single glomerulus (segmental) are the histological features of the disease.

In animal models FSGS can be induced by podocyte toxins such as puromycin, aminonucleoside or adriamycin [82]. The main disadvantage of drug-induced models is the uncertainty of

their similarity to human pathology of the disease as well as a robust variability between rodent strains in susceptibility (e.g., C57BL/6 mice are far more resistant than BALB/c) [83].

Spontaneous FSGS models include the Buffalo/MWF and Munich Wistar Fromter rat models [84, 85]. Excellent transgenic models include the Nep25 mouse model [86], the diphtheria toxin rat model, the Thy-1.1 mouse model [87], and others. Genetically engineered mouse models give valuable insight to protein–protein interactions and their role in the prognosis of FSGS. Yang et al. provide a comprehensive review of FSGS rodent models [88].

6 Humanized Mouse Models

Many elements of mouse biological systems are different from those of humans, especially their immune system. Humanized mice have become important preclinical tools to accurately recapitulate human biological systems. Presently there are three widely used strains of immunodeficient mice: NOD.Cg-Prkdc^{scid}Il2rg^{tm1Wjl} (NSG), NODShi.Cg-Prkdc^{scid}Il2rg^{tm1Sug} (NOG) and C;129S4-Rag2^{tm1Flv}Il2rg^{tm1Flv} (BRG), which lack T, B, and NK cells and have functionally impaired dendritic cells and macrophages. These mice are engrafted with human transplants including peripheral blood mononuclear cells, a combination of bone marrow, liver, and thymus, or hematopoietic stem cells [89]. Humanized mouse models have tremendous potential in the study of the mechanisms of allograft rejection during transplantation or immune-mediated renal diseases such as T1DM [90, 91].

Acknowledgments

This work was funded in part (Erdmann Seeliger) by the German Research Foundation (Gefoerdert durch die Deutsche Forschungsgemeinschaft (DFG), Projektnummer 394046635, SFB 1365, RENOPROTECTION. Funded by the Deutsche Forschungsgemeinschaft (DFG, German Research Foundation), Project number 394046635, SFB 1365, RENOPROTECTION).

This publication is based upon work from COST Action PARENCHIMA, supported by European Cooperation in Science and Technology (COST). COST (www.cost.eu) is a funding agency for research and innovation networks. COST Actions help connect research initiatives across Europe and enable scientists to enrich their ideas by sharing them with their peers. This boosts their research, career, and innovation.

PARENCHIMA (renalmri.org) is a community-driven Action in the COST program of the European Union, which unites more than 200 experts in renal MRI from 30 countries with the aim to improve the reproducibility and standardization of renal MRI biomarkers.

References

1. US Renal Data System Annual Report 2016. (2016). https://www.usrds.org/adr.aspx
2. Liu Y (2006) Renal fibrosis: new insights into the pathogenesis and therapeutics. Kidney Int 69(2):213–217. https://doi.org/10.1038/sj.ki.5000054
3. Levin A, Tonelli M, Bonventre J, Coresh J, Donner JA, Fogo AB, Fox CS, Gansevoort RT, Heerspink HJL, Jardine M, Kasiske B, Kottgen A, Kretzler M, Levey AS, Luyckx VA, Mehta R, Moe O, Obrador G, Pannu N, Parikh CR, Perkovic V, Pollock C, Stenvinkel P, Tuttle KR, Wheeler DC, Eckardt KU (2017) Global kidney health 2017 and beyond: a roadmap for closing gaps in care, research, and policy. Lancet 390(10105):1888–1917. https://doi.org/10.1016/S0140-6736(17)30788-2
4. Selby NM, Blankestijn PJ, Boor P, Combe C, Eckardt KU, Eikefjord E, Garcia-Fernandez N, Golay X, Gordon I, Grenier N, Hockings PD, Jensen JD, Joles JA, Kalra PA, Kramer BK, Mark PB, Mendichovszky IA, Nikolic O, Odudu A, Ong ACM, Ortiz A, Pruijm M, Remuzzi G, Rorvik J, de Seigneux S, Simms RJ, Slatinska J, Summers P, Taal MW, Thoeny HC, Vallee JP, Wolf M, Caroli A, Sourbron S (2018) Magnetic resonance imaging biomarkers for chronic kidney disease: a position paper from the European Cooperation in Science and Technology Action PARENCHIMA. Nephrol Dial Transplant 33(suppl_2):ii4–ii14. https://doi.org/10.1093/ndt/gfy152
5. Prasad PV (2006) Functional MRI of the kidney: tools for translational studies of pathophysiology of renal disease. Am J Physiol Renal Physiol 290(5):F958–F974. https://doi.org/10.1152/ajprenal.00114.2005
6. Haque M, Franklin T, Prasad P (2011) Renal oxygenation changes during water loading as evaluated by BOLD MRI: effect of NOS inhibition. J Magn Reson Imaging 33(4):898–901. https://doi.org/10.1002/jmri.22509
7. DiMasi JA, Grabowski HG, Hansen RW (2016) Innovation in the pharmaceutical industry: new estimates of R&D costs. J Health Econ 47:20–33. https://doi.org/10.1016/j.jhealeco.2016.01.012
8. Justice MJ, Dhillon P (2016) Using the mouse to model human disease: increasing validity and reproducibility. Dis Model Mech 9(2):101–103. https://doi.org/10.1242/dmm.024547
9. Tannenbaum J (2017) Ethics in biomedical animal research: the key role of the investigator. In: Conn PM (ed) Animal models for the study of human disease, 2edn edn. Academic Press, Cambridge, Massachusetts, pp 1–44. https://doi.org/10.1016/B978-0-12-809468-6.00001-2
10. Festing MF (2010) Inbred strains should replace outbred stocks in toxicology, safety testing, and drug development. Toxicol Pathol 38(5):681–690. https://doi.org/10.1177/0192623310373776
11. Nishino T, Sasaki N, Nagasaki K, Ahmad Z, Agui T (2010) Genetic background strongly influences the severity of glomerulosclerosis in mice. J Vet Med Sci 72(10):1313–1318. https://doi.org/10.1292/jvms.10-0144
12. Feng M, DiPetrillo K (2009) Non-invasive blood pressure measurement in mice. Methods Mol Biol 573:45–55. https://doi.org/10.1007/978-1-60761-247-6_3
13. Brune S, Pricl S, Wunsch B (2013) Structure of the sigma1 receptor and its ligand binding site. J Med Chem 56(24):9809–9819. https://doi.org/10.1021/jm400660u
14. Lu X, Li N, Shushakova N, Schmitt R, Menne J, Susnik N, Meier M, Leitges M, Haller H, Gueler F, Rong S (2012) C57BL/6 and 129/Sv mice: genetic difference to renal ischemia-reperfusion. J Nephrol 25(5):738–743. https://doi.org/10.5301/jn.5000053
15. Basile DP, Donohoe D, Cao XIA, Van Why SK (2004) Resistance to ischemic acute renal failure in the Brown Norway rat: a new model to study cytoprotection. Kidney Int 65(6):2201–2211. https://doi.org/10.1111/j.1523-1755.2004.00637.x
16. Qi Z, Fujita H, Jin J, Davis LS, Wang Y, Fogo AB, Breyer MD (2005) Characterization of susceptibility of inbred mouse strains to diabetic nephropathy. Diabetes 54(9):2628–2637. https://doi.org/10.2337/diabetes.54.9.2628
17. Mahmoud Abu Abeeleh ZBI, Alzaben KR, Abu-Halaweh SA, Al-Essa MK, Abuabeeleh J, Alsmady MM (2009) Induction of diabetes mellitus in rats using intraperitoneal streptozotocin: a comparison between 2 strains of rats. European J Sci Res 32(3):398–402
18. Hartner A, Cordasic N, Klanke B, Veelken R, Hilgers KF (2003) Strain differences in the development of hypertension and glomerular lesions induced by deoxycorticosterone acetate salt in mice. Nephrol Dial Transplant 18(10):1999–2004. https://doi.org/10.1093/ndt/gfg299

19. Erdely A, Freshour G, Tain YL, Engels K, Baylis C (2007) DOCA/NaCl-induced chronic kidney disease: a comparison of renal nitric oxide production in resistant and susceptible rat strains. Am J Physiol Renal Physiol 292 (1):F192–F196. https://doi.org/10.1152/ajprenal.00146.2006
20. Ma LJ, Fogo AB (2003) Model of robust induction of glomerulosclerosis in mice: importance of genetic background. Kidney Int 64(1):350–355. https://doi.org/10.1046/j.1523-1755.2003.00058.x
21. Hutchens MP, Dunlap J, Hurn PD, Jarnberg PO (2008) Renal ischemia: does sex matter? Anesth Analg 107(1):239–249. https://doi.org/10.1213/ane.0b013e318178ca42
22. Muller V, Losonczy G, Heemann U, Vannay A, Fekete A, Reusz G, Tulassay T, Szabo AJ (2002) Sexual dimorphism in renal ischemia-reperfusion injury in rats: possible role of endothelin. Kidney Int 62(4):1364–1371. https://doi.org/10.1111/j.1523-1755.2002.kid590.x
23. Mehta RL, Pascual MT, Soroko S, Chertow GM (2002) Diuretics, mortality, and nonrecovery of renal function in acute renal failure. JAMA 288(20):2547–2553
24. Berg UB (2006) Differences in decline in GFR with age between males and females. Reference data on clearances of inulin and PAH in potential kidney donors. Nephrol Dial Transplant 21 (9):2577–2582. https://doi.org/10.1093/ndt/gfl227
25. Kummer S, von Gersdorff G, Kemper MJ, Oh J (2012) The influence of gender and sexual hormones on incidence and outcome of chronic kidney disease. Pediatr Nephrol 27 (8):1213–1219. https://doi.org/10.1007/s00467-011-1963-1
26. Hosszu A, Antal Z, Veres-Szekely A, Lenart L, Balogh DB, Szkibinszkij E, Illesy L, Hodrea J, Banki NF, Wagner L, Vannay A, Szabo AJ, Fekete A (2018) The role of Sigma-1 receptor in sex-specific heat shock response in an experimental rat model of renal ischaemia/reperfusion injury. Transpl Int 31(11):1268–1278. https://doi.org/10.1111/tri.13293
27. Aufhauser DD Jr, Wang Z, Murken DR, Bhatti TR, Wang Y, Ge G, Redfield RR 3rd, Abt PL, Wang L, Svoronos N, Thomasson A, Reese PP, Hancock WW, Levine MH (2016) Improved renal ischemia tolerance in females influences kidney transplantation outcomes. J Clin Invest 126(5):1968–1977. https://doi.org/10.1172/jci84712
28. Satake A, Takaoka M, Nishikawa M, Yuba M, Shibata Y, Okumura K, Kitano K, Tsutsui H, Fujii K, Kobuchi S, Ohkita M, Matsumura Y (2008) Protective effect of 17beta-estradiol on ischemic acute renal failure through the PI3K/Akt/eNOS pathway. Kidney Int 73 (3):308–317. https://doi.org/10.1038/sj.ki.5002690
29. Park KM, Kim JI, Ahn Y, Bonventre AJ, Bonventre JV (2004) Testosterone is responsible for enhanced susceptibility of males to ischemic renal injury. J Biol Chem 279 (50):52282–52292. https://doi.org/10.1074/jbc.M407629200
30. Caligioni CS (2009) Assessing reproductive status/stages in mice. Curr Protoc Neurosci. https://doi.org/10.1002/0471142301.nsa04is48
31. Coors ME, Glover JJ, Juengst ET, Sikela JM (2010) The ethics of using transgenic non-human primates to study what makes us human. Nat Rev Genet 11(9):658–662. https://doi.org/10.1038/nrg2864
32. Yarger WE, Griffith LD (1974) Intrarenal hemodynamics following chronic unilateral ureteral obstruction in the dog. Am J Phys 227(4):816–826. https://doi.org/10.1152/ajplegacy.1974.227.4.816
33. Giraud S, Favreau F, Chatauret N, Thuillier R, Maiga S, Hauet T (2011) Contribution of large pig for renal ischemia-reperfusion and transplantation studies: the preclinical model. J Biomed Biotechnol 2011:532127. https://doi.org/10.1155/2011/532127
34. Wei Q, Dong Z (2012) Mouse model of ischemic acute kidney injury: technical notes and tricks. Am J Physiol Renal Physiol 303(11): F1487–F1494. https://doi.org/10.1152/ajprenal.00352.2012
35. Stone HH, Fulenwider JT (1977) Renal decapsulation in the prevention of post-ischemic oliguria. Ann Surg 186(3):343–355. https://doi.org/10.1097/00000658-197709000-00012
36. Kierulf-Lassen C, Nielsen PM, Qi H, Damgaard M, Laustsen C, Pedersen M, Krag S, Birn H, Norregaard R, Jespersen B (2017) Unilateral nephrectomy diminishes ischemic acute kidney injury through enhanced perfusion and reduced pro-inflammatory and pro-fibrotic responses. PLoS One 12(12): e0190009. https://doi.org/10.1371/journal.pone.0190009
37. Kaucsar T, Godo M, Revesz C, Kovacs M, Mocsai A, Kiss N, Albert M, Krenacs T, Szenasi G, Hamar P (2016) Urine/plasma neutrophil gelatinase associated Lipocalin ratio is a sensitive and specific marker of subclinical acute kidney injury in mice. PLoS One 11(1):e0148043. https://doi.org/10.1371/journal.pone.0148043

38. Kaucsar T, Revesz C, Godo M, Krenacs T, Albert M, Szalay CI, Rosivall L, Benyo Z, Batkai S, Thum T, Szenasi G, Hamar P (2013) Activation of the miR-17 family and miR-21 during murine kidney ischemia-reperfusion injury. Nucleic Acid Ther 23 (5):344–354. https://doi.org/10.1089/nat.2013.0438
39. Shrestha B, Haylor J (2014) Experimental rat models of chronic allograft nephropathy: a review. Int J Nephrol Renovasc Dis 7:315–322. https://doi.org/10.2147/ijnrd.S65604
40. White E, Hildemann WH, Mullen Y (1969) Chronic kidney allograft reactions in rats. Transplantation 8(5):602–617
41. Frodin L, Engberg A (1975) Renal transplantation in the rat. I. Studies concerning the ureteral anastomosis with special reference to the end-to-end technique. Urol Res 3(2):87–90
42. Bramis JP, Schanzer H, Taub RN (1977) Prolongation of rat renal allograft survival by cyclophosphamide and intravenous donor-specific antigens. Eur Surg Res 9(2):140–154. https://doi.org/10.1159/000127934
43. Harvig B, Norlen BJ (1980) A technique for in vivo and in vitro studies on the preserved and transplanted rat kidney. Urol Res 8 (2):107–112
44. Schumacher M, Van Vliet BN, Ferrari P (2003) Kidney transplantation in rats: an appraisal of surgical techniques and outcome. Microsurgery 23(4):387–394. https://doi.org/10.1002/micr.10139
45. Lankadeva YR, Kosaka J, Evans RG, May CN (2018) An ovine model for studying the pathophysiology of septic acute kidney injury. Methods Mol Biol 1717:207–218. https://doi.org/10.1007/978-1-4939-7526-6_16
46. Cunningham PN, Wang Y, Guo R, He G, Quigg RJ (2004) Role of toll-like receptor 4 in endotoxin-induced acute renal failure. J Immunol 172(4):2629–2635. https://doi.org/10.4049/jimmunol.172.4.2629
47. Wang W, Falk SA, Jittikanont S, Gengaro PE, Edelstein CL, Schrier RW (2002) Protective effect of renal denervation on normotensive endotoxemia-induced acute renal failure in mice. Am J Physiol Renal Physiol 283(3): F583–F587. https://doi.org/10.1152/ajprenal.00270.2001
48. Ko JW, Lee IC, Park SH, Moon C, Kang SS, Kim SH, Kim JC (2014) Protective effects of pine bark extract against cisplatin-induced hepatotoxicity and oxidative stress in rats. Lab Anim Res 30(4):174–180. https://doi.org/10.5625/lar.2014.30.4.174
49. Mitazaki S, Kato N, Suto M, Hiraiwa K, Abe S (2009) Interleukin-6 deficiency accelerates cisplatin-induced acute renal failure but not systemic injury. Toxicology 265(3):115–121. https://doi.org/10.1016/j.tox.2009.10.005
50. Zhang J, Rudemiller NP, Patel MB, Wei Q, Karlovich NS, Jeffs AD, Wu M, Sparks MA, Privratsky JR, Herrera M, Gurley SB, Nedospasov SA, Crowley SD (2016) Competing actions of type 1 angiotensin II receptors expressed on T lymphocytes and kidney epithelium during cisplatin-induced AKI. J Am Soc Nephrol 27(8):2257–2264. https://doi.org/10.1681/asn.2015060683
51. Fahling M, Seeliger E, Patzak A, Persson PB (2017) Understanding and preventing contrast-induced acute kidney injury. Nat Rev Nephrol 13(3):169–180. https://doi.org/10.1038/nrneph.2016.196
52. Arakelyan K, Cantow K, Hentschel J, Flemming B, Pohlmann A, Ladwig M, Niendorf T, Seeliger E (2013) Early effects of an x-ray contrast medium on renal T(2) */T (2) MRI as compared to short-term hyperoxia, hypoxia and aortic occlusion in rats. Acta Physiol (Oxf) 208(2):202–213. https://doi.org/10.1111/apha.12094
53. Seeliger E, Becker K, Ladwig M, Wronski T, Persson PB, Flemming B (2010) Up to 50-fold increase in urine viscosity with iso-osmolar contrast media in the rat. Radiology 256 (2):406–414. https://doi.org/10.1148/radiol.10091485
54. Seeliger E, Cantow K, Arakelyan K, Ladwig M, Persson PB, Flemming B (2014) Low-dose nitrite alleviates early effects of an X-ray contrast medium on renal hemodynamics and oxygenation in rats. Investig Radiol 49(2):70–77. https://doi.org/10.1097/RLI.0b013e3182a6fea6
55. Lenhard DC, Frisk AL, Lengsfeld P, Pietsch H, Jost G (2013) The effect of iodinated contrast agent properties on renal kinetics and oxygenation. Investig Radiol 48(4):175–182. https://doi.org/10.1097/RLI.0b013e31827b70f9
56. Lauver DA, Carey EG, Bergin IL, Lucchesi BR, Gurm HS (2014) Sildenafil citrate for prophylaxis of nephropathy in an animal model of contrast-induced acute kidney injury. PLoS One 9(11):e113598. https://doi.org/10.1371/journal.pone.0113598
57. Kiss N, Hamar P (2016) Histopathological evaluation of contrast-induced acute kidney injury rodent models. Biomed Res Int 2016:3763250. https://doi.org/10.1155/2016/3763250
58. Linkermann A, Heller JO, Prokai A, Weinberg JM, De Zen F, Himmerkus N, Szabo AJ,

Brasen JH, Kunzendorf U, Krautwald S (2013) The RIP1-kinase inhibitor necrostatin-1 prevents osmotic nephrosis and contrast-induced AKI in mice. J Am Soc Nephrol 24 (10):1545–1557. https://doi.org/10.1681/asn.2012121169

59. Nortier J, Pozdzik A, Roumeguere T, Vanherweghem JL (2015) Aristolochic acid nephropathy ("Chinese herb nephropathy"). Nephrol Ther 11(7):574–588. https://doi.org/10.1016/j.nephro.2015.10.001
60. De Broe ME (2012) Chinese herbs nephropathy and Balkan endemic nephropathy: toward a single entity, aristolochic acid nephropathy. Kidney Int 81(6):513–515. https://doi.org/10.1038/ki.2011.428
61. Geng Y, Zhang L, Fu B, Zhang J, Hong Q, Hu J, Li D, Luo C, Cui S, Zhu F, Chen X (2014) Mesenchymal stem cells ameliorate rhabdomyolysis-induced acute kidney injury via the activation of M2 macrophages. Stem Cell Res Ther 5(3):80. https://doi.org/10.1186/scrt469
62. Chevalier RL, Forbes MS, Thornhill BA (2009) Ureteral obstruction as a model of renal interstitial fibrosis and obstructive nephropathy. Kidney Int 75(11):1145–1152. https://doi.org/10.1038/ki.2009.86
63. He J, Wang Y, Sun S, Yu M, Wang C, Pei X, Zhu B, Wu J, Zhao W (2012) Bone marrow stem cells-derived microvesicles protect against renal injury in the mouse remnant kidney model. Nephrology (Carlton) 17 (5):493–500. https://doi.org/10.1111/j.1440-1797.2012.01589.x
64. Hewitson TD, Ono T, Becker GJ (2009) Small animal models of kidney disease: a review. Methods Mol Biol 466:41–57. https://doi.org/10.1007/978-1-59745-352-3_4
65. Graham ML, Schuurman HJ (2015) Validity of animal models of type 1 diabetes, and strategies to enhance their utility in translational research. Eur J Pharmacol 759:221–230. https://doi.org/10.1016/j.ejphar.2015.02.054
66. Lassila M, Seah KK, Allen TJ, Thallas V, Thomas MC, Candido R, Burns WC, Forbes JM, Calkin AC, Cooper ME, Jandeleit-Dahm KA (2004) Accelerated nephropathy in diabetic apolipoprotein e-knockout mouse: role of advanced glycation end products. J Am Soc Nephrol 15(8):2125–2138. https://doi.org/10.1097/01.Asn.0000133025.23732.46
67. Chua SC Jr, Chung WK, Wu-Peng XS, Zhang Y, Liu SM, Tartaglia L, Leibel RL (1996) Phenotypes of mouse diabetes and rat fatty due to mutations in the OB (leptin) receptor. Science 271(5251):994–996
68. Zucker LM, Antoniades HN (1972) Insulin and obesity in the Zucker genetically obese rat "fatty". Endocrinology 90(5):1320–1330. https://doi.org/10.1210/endo-90-5-1320
69. Mallipattu SK, Gallagher EJ, LeRoith D, Liu R, Mehrotra A, Horne SJ, Chuang PY, Yang VW, He JC (2014) Diabetic nephropathy in a non-obese mouse model of type 2 diabetes mellitus. Am J Physiol Renal Physiol 306(9): F1008–F1017. https://doi.org/10.1152/ajprenal.00597.2013
70. Kaspareit-Rittinghausen J, Rapp K, Deerberg F, Wcislo A, Messow C (1989) Hereditary polycystic kidney disease associated with osteorenal syndrome in rats. Vet Pathol 26 (3):195–201. https://doi.org/10.1177/030098588902600302
71. Katsuyama M, Masuyama T, Komura I, Hibino T, Takahashi H (2000) Characterization of a novel polycystic kidney rat model with accompanying polycystic liver. Exp Anim 49 (1):51–55. https://doi.org/10.1538/expanim.49.51
72. Takahashi H, Calvet JP, Dittemore-Hoover D, Yoshida K, Grantham JJ, Gattone VH 2nd (1991) A hereditary model of slowly progressive polycystic kidney disease in the mouse. J Am Soc Nephrol 1(7):980–989
73. Atala A, Freeman MR, Mandell J, Beier DR (1993) Juvenile cystic kidneys (jck): a new mouse mutation which causes polycystic kidneys. Kidney Int 43(5):1081–1085
74. Thivierge C, Kurbegovic A, Couillard M, Guillaume R, Cote O, Trudel M (2006) Overexpression of PKD1 causes polycystic kidney disease. Mol Cell Biol 26(4):1538–1548. https://doi.org/10.1128/mcb.26.4.1538-1548.2006
75. Muto S, Aiba A, Saito Y, Nakao K, Nakamura K, Tomita K, Kitamura T, Kurabayashi M, Nagai R, Higashihara E, Harris PC, Katsuki M, Horie S (2002) Pioglitazone improves the phenotype and molecular defects of a targeted Pkd1 mutant. Hum Mol Genet 11 (15):1731–1742. https://doi.org/10.1093/hmg/11.15.1731
76. Wu G, Somlo S (2000) Molecular genetics and mechanism of autosomal dominant polycystic kidney disease. Mol Genet Metab 69(1):1–15. https://doi.org/10.1006/mgme.1999.2943
77. Williams SS, Cobo-Stark P, James LR, Somlo S, Igarashi P (2008) Kidney cysts, pancreatic cysts, and biliary disease in a mouse model of autosomal recessive polycystic kidney disease. Pediatr Nephrol 23(5):733–741. https://doi.org/10.1007/s00467-007-0735-4

78. Nagao S, Kugita M, Yoshihara D, Yamaguchi T (2012) Animal models for human polycystic kidney disease. Exp Anim 61(5):477–488. https://doi.org/10.1538/expanim.61.477
79. Hultstrom M (2012) Development of structural kidney damage in spontaneously hypertensive rats. J Hypertens 30(6):1087–1091. https://doi.org/10.1097/HJH.0b013e328352b89a
80. Zhong F, Mallipattu SK, Estrada C, Menon M, Salem F, Jain MK, Chen H, Wang Y, Lee K, He JC (2016) Reduced Kruppel-like factor 2 aggravates glomerular endothelial cell injury and kidney disease in mice with unilateral nephrectomy. Am J Pathol 186 (8):2021–2031. https://doi.org/10.1016/j.ajpath.2016.03.018
81. Rabe M, Schaefer F (2016) Non-transgenic mouse models of kidney disease. Nephron 133(1):53–61. https://doi.org/10.1159/000445171
82. Grond J, Muller EW, van Goor H, Weening JJ, Elema JD (1988) Differences in puromycin aminonucleoside nephrosis in two rat strains. Kidney Int 33(2):524–529. https://doi.org/10.1038/ki.1988.29
83. LEE VW, HARRIS DC (2011) Adriamycin nephropathy: a model of focal segmental glomerulosclerosis. Nephrology 16(1):30–38. https://doi.org/10.1111/j.1440-1797.2010.01383.x
84. Akiyama K, Morita H, Suetsugu S, Kuraba S, Numata Y, Yamamoto Y, Inui K, Ideura T, Wakisaka N, Nakano K, Oniki H, Takenawa T, Matsuyama M, Yoshimura A (2008) Actin-related protein 3 (Arp3) is mutated in proteinuric BUF/Mna rats. Mamm Genome 19(1):41–50. https://doi.org/10.1007/s00335-007-9078-5
85. Fassi A, Sangalli F, Maffi R, Colombi F, Mohamed E, Brenner BM, Remuzzi G, Remuzzi A (1998) Progressive Glomerular Injury in the MWF Rat is predicted by Inborn Nephron Deficit. J Am Soc Nephrol 9 (8):1399–1406
86. Matsusaka T, Xin J, Niwa S, Kobayashi K, Akatsuka A, Hashizume H, Wang Q-c, Pastan I, Fogo AB, Ichikawa I (2005) Genetic engineering of glomerular sclerosis in the mouse via control of onset and severity of podocyte-specific injury. J Am Soc Nephrol 16(4):1013–1023. https://doi.org/10.1681/asn.2004080720
87. Assmann KJM, Van Son JPHF, Dïjkman HBPM, Mentzel S, Wetzels JFM (2002) Antibody-induced albuminuria and accelerated focal glomerulosclerosis in the Thy-1.1 transgenic mouse. Kidney Int 62(1):116–126. https://doi.org/10.1046/j.1523-1755.2002.00428.x
88. Yang JW, Dettmar A, Kronbichler A, Yung Gee H, Saleem M, Heon Kim S, Shin JI (2018) Recent advances of animal model of focal segmental glomerulosclerosis. Clin Exp Nephro 22(4):752–763. https://doi.org/10.1007/s10157-018-1552-8
89. Ito R, Takahashi T, Ito M (2018) Humanized mouse models: application to human diseases. J Cell Physiol 233(5):3723–3728. https://doi.org/10.1002/jcp.26045
90. Kenney LL, Shultz LD, Greiner DL, Brehm MA (2016) Humanized mouse models for transplant immunology. Am J Transplant 16 (2):389–397. https://doi.org/10.1111/ajt.13520
91. Tan S, Li Y, Xia J, Jin CH, Hu Z, Duinkerken G, Li Y, Khosravi Maharlooei M, Chavez E, Nauman G, Danzl N, Nakayama M, Roep BO, Sykes M, Yang YG (2017) Type 1 diabetes induction in humanized mice. Proc Natl Acad Sci U S A 114(41):10954–10959. https://doi.org/10.1073/pnas.1710415114

Chapter 3

Preparation and Monitoring of Small Animals in Renal MRI

Tamas Kaucsar, Adam Hosszu, Erdmann Seeliger, Henning M. Reimann, and Andrea Fekete

Abstract

Renal diseases remain devastating illnesses with unacceptably high rates of mortality and morbidity worldwide. Animal models are essential tools to better understand the pathomechanism of kidney-related illnesses and to develop new, successful therapeutic strategies. Magnetic resonance imaging (MRI) has been actively explored in the last decades for assessing renal function, perfusion, tissue oxygenation as well as the degree of fibrosis and inflammation. This chapter aims to provide an overview of the preparation and monitoring of small animals before, during, and after surgical interventions or MR imaging. Standardization of experimental settings such as body temperature or hydration of animals and minimizing pain and distress are essential for diminishing nonexperimental variables as well as for conducting ethical research.

This publication is based upon work from the COST Action PARENCHIMA, a community-driven network funded by the European Cooperation in Science and Technology (COST) program of the European Union, which aims to improve the reproducibility and standardization of renal MRI biomarkers.

Key words Magnetic resonance imaging (MRI), Kidney, Rodent surgery, Anesthesia

1 Introduction

Renal diseases are devastating illnesses with unacceptably high rates of mortality and morbidity worldwide. End-stage renal disease is the final stage of chronic kidney disease (CKD) characterized by complete loss of kidney function. Global prevalence is estimated to be 8–16% and the overall years of life lost due to premature death is third behind AIDS and diabetes mellitus [1]. Kidney diseases create a huge burden on healthcare systems; thus, the social and economic impact of prevention and early treatment would be enormous. Several publications have highlighted the need for new, effective therapies as well as superior diagnostic tools.

At present, diagnosis of kidney disease is difficult and often involves invasive procedures. Conventional markers of renal function such as serum creatinine and blood urea nitrogen are poorly sensitive and poorly selective, as they represent a delayed indication

Andreas Pohlmann and Thoralf Niendorf (eds.), *Preclinical MRI of the Kidney: Methods and Protocols*, Methods in Molecular Biology, vol. 2216, https://doi.org/10.1007/978-1-0716-0978-1_3,

of functional change that lags behind structural deterioration during the early stage of acute kidney injury (AKI). Currently kidney biopsy is the single method to assess renal microstructure in humans, but it is an invasive procedure and sampling bias can alter results. Thus, noninvasive, in vivo imaging methods are crucial for the adequate assessment of kidney function, oxygenation, and structure in both preclinical and clinical setups. Importantly, state-of-the-art functional MRI techniques are available to determine tissue oxygenation, perfusion, fibrosis, inflammation, or tissue edema that can be used as biomarkers of renal disease [2]. MRI affords full kidney coverage, soft tissue contrast that helps to differentiate the renal layers, second-to-minute temporal resolution, support of longitudinal studies and high anatomical detail without the use of ionizing radiation [3, 4].

However, imaging rodents can be challenging because in contrast to human studies, imaging of animals requires anesthesia to physically restrain the animals and minimize their gross motion. Anesthetic agents can profoundly alter physiology of the experimental animal and may thus influence the image data acquired. It is therefore necessary to use the most appropriate anesthetic compound and to monitor the physiology of anesthetized animals during image acquisition [5–7].

It is essential that researchers use animals in scientifically, technically, and humanely appropriate ways. Effective and appropriate animal care before, during, and after experimentation not only is important for the enhancement of animal well-being but can also have a major effect on the quality of research. Hydration status, the type of anesthesia used, or body temperature of the animals during surgery or MRI measurements, as well as postoperative care are all factors that can affect results, and thus should be carefully planned prior to the intervention. Standard protocols can be modified, but should not compromise the well-being of the animals.

This chapter summarizes preoperative procedures, advantages and disadvantages of different anesthetic agents, monitoring of physiological functions during surgical or imaging procedures, and how these challenges can be successfully addressed.

This chapter is part of the book Pohlmann A, Niendorf T (eds) (2020) Preclinical MRI of the Kidney—Methods and Protocols. Springer, New York.

2 Hydration

Animals can experience considerable fluid loss during surgery mainly due to evaporation from open body cavities or blood loss. Rodents are particularly vulnerable to intraoperative fluid loss because of their small size and relatively small total body fluid content. Warm, sterile isotonic fluids should be administered at 3–5% of the body weight subcutaneously or intraperitoneally

prior to and at the end of surgery. Alternatively, isotonic fluid can be continuously administered via intravenous infusion or even via intra-arterial infusion in case a catheter has already been placed into an artery for monitoring of blood pressure and heart rate. The operative field should be irrigated with warm saline and drying out of tissues should be avoided [8, 9]. In any case, quantity of hydration has to be logged and/or standardized to eliminate non-experimental variable factors. For example, with proper hydration tubular reabsorption, an energy-dependent process can be spared. Hence, some procedures such as ischemia will have less effect on renal injury in well hydrated animals. Intraoperative fluid replacement is also important because during the recovery phase water intake is usually reduced, even though ad libitum water access is usually ensured after surgery.

An ophthalmic lubricating ointment should be applied to the eyes to protect the cornea from drying out.

3 Anesthesia

The use of anesthetics for surgical or in vivo imaging procedures comes with an inevitable autonomic nervous system depression, causing cardiovascular and respiratory depression, hypothermia, and altered metabolism [10]. Different anesthetics influence these physiological processes differently; thus, various anesthetic agents should be selected for different experimental models. For example, anesthesia used during renal ischemia–reperfusion injury (IRI) surgery has an important impact on the extent of injury. Numerous studies showed that anesthetics are renoprotective due to their anti-inflammatory, antiapoptotic, or antinecrotic effect, independently of the way of administration. Also different anesthetics impose different effects on vasomotion (dilation and constriction). Vasomotion, in turn, has a direct impact on local renal blood volume fraction, which affects the measure T_2*. Furthermore, it influences perfusion, which affects the blood oxygenation and ultimately T_2* as well. R_2*—the transverse relaxation rate—can vary by more than 100% depending on the anesthetic regimen [11]. In animal experiments inhalable and injectable anesthetics are both popular. Advantage of inhalable anesthetics (e.g., halothane or fluranes) are that they are rapidly eliminated through the lungs; therefore, incidence of fatal events is lower and fast recovery can be achieved. On the other hand, they are frequently irritant, and it is hard to set a precise dosage; hence, it is easier to cause hypoxia, and if apnea occurs loss of consciousness will last longer. Injectable anesthetics (barbiturates, ketamine, propofol, etc.) promote a quick loss of consciousness with better control of cardiopulmonary function and induce anesthesia at a lower dose. They frequently influence blood pressure, and hypothermia can also develop. Although barbiturates can be precisely dosed through intravenous administration, the

intraperitoneal, subcutaneous, or intramuscular injection of other injectable anesthetics may lead to variable levels of anesthesia. Because of the short time of action (with the exception of urethane) repeated dosing or constant infusion of injectable anesthetics is sometimes needed, prolonging recovery time [12]. During procedures respiratory rate and alertness of the animal should be followed. Anesthesia should be intensified at the first signs of alertness such as movement of whiskers or reflex triggered by pinching the toes outside the MR environment. It should be noted that deeper anesthesia is needed for surgical interventions than for MRI alone.

3.1 Injectable Anesthetics

Ketamine is one of the safest and most widely used injectable anesthetics in animal surgeries because it does not require intravenous access and cardiorespiratory depression occurs only at a much higher dose than what is needed for anesthesia [13]. Ketamine is frequently used in combination with other anesthetics like α2 agonists (xylazine) or benzodiazepines to prevent muscle rigidity and produce more stable anesthesia [7]. In these cases, the dose of ketamine can be reduced. However, ketamine may reduce IRI in rats in low doses, when its antioxidant capacity is the greatest [14]. On the other hand, ketamine may be harmful at higher doses due to its sympathomimetic effect [15]. Despite the low cardiovascular and respiratory influence of ketamine alone [16], cardiac influences, like hypotension with minimal respiratory depression must also be considered when using ketamine together with xylazine [17]. Substantial cardiovascular effects (bradycardia, hypotension) were observed when acepromazine, buprenorphine, or carprofen was also added to the ketamine–xylazine combination. Nevertheless, the addition of acepromazine led to stable hemodynamic parameters while sustaining adequate anesthesia for performing surgical procedures [18]. Cerebral hemodynamics are also affected by ketamine–xylazine combinations, which may cause reduction of cerebral blood flow thus affecting brain oxygenation and leading to interferences with several imaging procedures [19]. Metabolic changes could also occur during ketamine–xylazine anesthesia. Decreased insulin secretion by pancreatic β cells together with the blockade of ATP-dependent potassium channels may cause elevated levels of blood glucose and potassium [20].

Short and ultrashort acting barbiturates (pentobarbital and thiopental, respectively) are also frequently used in animal experiments. They are relatively inexpensive and have a rapid and smooth onset of action as well as recovery [21]. On the other hand, they have small therapeutic margin and even though they can be precisely dosed via intravenous administration, the risk of fatal events is much higher than for ketamine [22]. However, their use is limited in renal ischemia–reperfusion surgery, since they reduce blood pressure and thus blood flow to the kidney. Although by lowering pentobarbital dose there are less cardiovascular side effects, poor anesthetic depth, and serious respiratory depression with low

oxygen saturation can be expected during pentobarbital monoanesthesia [17]. Thiopental decreased malondialdehyde levels and reduced histopathologic damage to the kidneys after IRI in subanesthetic doses [15]. Moreover, clinically high doses of thiopental effectively protected against renal IRI [23]. What may lie behind this renoprotective effect is that thiopental is also an antioxidant [24] and inhibits neutrophil function [25]. Thiopental might also depress brain metabolism and thus elevate brain glucose content in the cortex [26]; however, pentobarbital has no effect on blood glucose levels [20].

Propofol is a rapid acting anesthetic, with short recovery duration, thus convenient for short procedures [10]. Propofol has a serious respiratory depressant effect and decrease in cerebral blood flow and intracranial pressure have also been reported [27]. The renoprotective effect of propofol via reduced production of proinflammatory cytokines, less neutrophil infiltration, and hence lower reactive oxygen species accumulation is well documented [15, 28, 29]. Due to its renoprotective effect, propofol is currently not used in experimental models of renal injury.

Urethane is extensively used alone or in combination with ketamine and xylazine in nonrecovery procedures. Advantages are its long-lasting (several hours) surgical plane of anesthesia [30, 31] and least effects on cardiovascular and respiratory control compared to other anesthetics [32, 33]. At least 8 h of fasting of the animals is recommended before urethane anesthesia.

3.2 Inhalable Anesthetics

Halogenated ethers are the preferred volatile anesthetics during animal experiments. Due to their rapid onset and short recovery time and low metabolism the side effects of inhalation anesthesia can be well controlled [10]. For example, isoflurane is preferred in cardiovascular studies, since it causes less hemodynamic depression than injectable anesthetics [17, 34]. It also reduces peripheral resistance thus hypotension might occur [35]. On the other hand, the rate of respiratory depression is higher than by injectable anesthetics; therefore, respiratory rate monitoring is indispensable when adjusting gas concentration. By maintaining high tidal volumes a stable oxygen saturation may be achieved during isoflurane anesthesia [17]. Yet isoflurane-induced respiratory depression results in hypercapnia, leading to substantial vasodilation in the brain and increased baseline cerebral blood flow [36]. To maintain physiological cerebral blood flow mechanical ventilation of the animal is recommended. In contrast, hypercapnia has only negligible effects on vasomotion in the kidney [37]. However, vasodilatory effects of isoflurane may be reflected in renal T_2* that has been found substantially higher compared to other anesthetics [11]. Metabolic changes have also been reported: isoflurane decreases insulin production, thus leads to higher blood glucose levels [20].

There is increasing evidence that halogenated ethers provide significant protection against renal IRI, which effect is differential: desflurane being less protective than isoflurane or sevoflurane [38]. Moreover, anesthesia with isoflurane has a preconditioning effect on renal IRI, with the involvement of JNK and ERK protein kinases [39]. When compared to propofol, isoflurane provided the same level of protection against ischemia reperfusion injury and therefore should be used with caution [40].

4 Physiological Monitoring

4.1 Body Temperature

Due to their large surface to body weight ratio rodents lose heat rapidly especially if the abdominal cavity is exposed. Hypothermia might further be exacerbated by the use of cold, dry gases, hair clipping, or the administration of cold fluids. Hairless strains and neonates which are considered exothermic in the early stages of life are especially susceptible to hypothermia because of their diminished insulation. Hypothermia poses multiple risks during anesthesia and recovery, including infection, bleeding complications and cardiac dysfunction. These factors may be the difference between life and death and if the animal survives, the difference between good and unreliable data; therefore, it is highly recommended that an external heat source be used during surgery. Adjustable heating pads or circulating warm water blankets usually allow a good maintenance of body temperature. Homogeneous warming of large surface areas of the animal's body—instead of using planar heating pads that provide comparably smaller contact areas—permits to reduce the heating temperature and allows for better maintenance of overall physiological body temperature [41]. For accurate control, a thermometer should be used to measure the temperature rectally and—if abdominal surgery is part of the procedure—also a second temperature probe placed close to the kidney should be used. Here it is important to consider the possible interactions of the temperature probe with the MRI. Conventional resistive probes with metallic cables may suffer from electrical currents induced by the time-varying magnetic field gradients used during imaging. This might disturb the temperature measurement and even heat up the cables. Use of fiber optical probes helps to avoid these issues but some optical probes experience a sizable offset in the measured temperature with a very strong magnetic field. For instance, a negative offset of 4.7 °C at a magnetic field strength of 9.4T was observed with GaAs-based probes. Some heating pads can automatically regulate the temperature with the help of a thermostat [42]. Too high temperatures can cause protein denaturation and tissue injury, which might result in death.

Kidney temperature during ischemia significantly influences IRI. Body temperature drops after anesthesia, which mitigates IRI

[9]. Therefore, close control and maintenance of body temperature is needed in order to perform reproducible AKI. Ischemia should only be initiated if the desired stable temperature is set and maintained.

4.2 Respiration

Respiratory monitoring can be achieved by observation of chest motion, depth and character of respiration during surgical interventions. Direct visualization of the animal is not feasible during imaging; therefore, respiratory motion detection systems that are compatible with and safe to use for most imaging modalities should be employed. These systems typically detect breathing motion by compressions of a respiratory sensor placed in contact with the chest.

During MRI, breathing often causes motion artefacts, which can severely compromise imaging acquisitions and hence measures to reduce or eliminate such artefacts should be taken. Gating techniques allow for the synchronization of data acquisition with the respiratory cycle. The largest movement of the abdomen occurs between inspiration and expiration; therefore, this period should be excluded from data acquisition.

4.3 Cardiovascular System

Heart rate can be monitored using an electrocardiograph system. Heart rate usually correlates with anesthetic depth. A pulse oximeter can be used to measure arterial O_2 saturation, pulse strength, breath rate and blood flow in real time, and can thus detect hypoventilation, airway obstruction, or other problems during anesthesia. Pulse oximeters are not remarkably accurate in rodents, but can detect trends and are nevertheless valuable tools. Whenever possible, cardiovascular monitoring should include continuous blood pressure measurement. For nonrecovery experiments, direct blood pressure (and heart rate) monitoring via a catheter in the femoral or carotid artery connected to a pressure transducer is preferred. Alternatively, an inflatable tail pressure cuff can be used noninvasively [10].

5 Recovery

Proper postoperative care is needed to minimize the loss of animals, to reduce intraexperimental variation and to offer humane conditions for recovery [8]. Body temperature should be maintained within physiological limits until the end of anesthesia, when the animal starts to be active.

5.1 Analgesia

If activity is resumed, analgesics may be given without the risk of further respiratory depression. Opioids are most commonly used for this purpose [9]; however, some of them can protect against IRI. For example, morphine and naloxone inhibited superoxide

anion production after renal IRI in rabbits [43] and naloxone alone can also improve warm renal IRI in dogs [44]. However, buprenorphine, a mixed partial μ-opioid receptor agonist and κ-and δ-opioid receptor antagonist improved animal health by reducing postsurgical stress response, without interfering with renal IRI [45].

Other analgesics, like α2-agonists are proven to have benefic effect on renal IRI [46, 47]. Nonsteroidal anti-inflammatory drugs also interfere with the renal IRI model [48, 49].

.

5.2 Antibiotics

Although there is a risk for postoperative infections after surgery, there is no indication for empiric use of antibiotic prevention [50]. Focus has to be placed on aseptic surgical infrastructure, cautious animal handling, and well-managed animal facilities (SPF, etc.). If systemic antibiotic use is inevitable, then fluoroquinolones and the trimethoprim–sulfonamide combination are generally recommended, since they are not harmful to the symbiotic intestinal bacterial population of mice [51]. Gentamicin is reported to ameliorate IRI mostly during the reperfusion phase and should not be used in such experiments [52]. Antibiotic administration should be delayed until complete anesthetic recovery takes place because of hypotension and prolonged anesthesia due to their calcium blocking action [51].

Acknowledgments

This chapter is based upon work from COST Action PARENCHIMA, supported by European Cooperation in Science and Technology (COST). COST (www.cost.eu) is a funding agency for research and innovation networks. COST Actions help connect research initiatives across Europe and enable scientists to enrich their ideas by sharing them with their peers. This boosts their research, career, and innovation.
PARENCHIMA (renalmri.org) is a community-driven Action in the COST program of the European Union, which unites more than 200 experts in renal MRI from 30 countries with the aim to improve the reproducibility and standardization of renal MRI biomarkers.

References

1. US Renal Data System Annual Report 2016. (2016). https://www.usrds.org/adr.aspx
2. Selby NM, Blankestijn PJ, Boor P, Combe C, Eckardt KU, Eikefjord E, Garcia-Fernandez N, Golay X, Gordon I, Grenier N, Hockings PD, Jensen JD, Joles JA, Kalra PA, Kramer BK, Mark PB, Mendichovszky IA, Nikolic O, Odudu A, Ong ACM, Ortiz A, Pruijm M, Remuzzi G, Rorvik J, de Seigneux S, Simms RJ, Slatinska J, Summers P, Taal MW, Thoeny HC, Vallee JP, Wolf M, Caroli A, Sourbron S (2018) Magnetic resonance imaging biomarkers for chronic kidney disease: a position paper from the European Cooperation in

Science and Technology Action PARENCHIMA. Nephrol Dial Transplant 33(suppl_2): ii4–ii14. https://doi.org/10.1093/ndt/gfy152

3. Prasad PV (2006) Functional MRI of the kidney: tools for translational studies of pathophysiology of renal disease. Am J Physiol Renal Physiol 290(5):F958–F974. https://doi.org/10.1152/ajprenal.00114.2005
4. Haque M, Franklin T, Prasad P (2011) Renal oxygenation changes during water loading as evaluated by BOLD MRI: effect of NOS inhibition. J Magn Reson Imaging 33 (4):898–901. https://doi.org/10.1002/jmri.22509
5. Tremoleda JL, Macholl S, Sosabowski JK (2018) Anesthesia and monitoring of animals during MRI studies. Methods Mol Biol 1718:423–439. https://doi.org/10.1007/978-1-4939-7531-0_25
6. Herrmann K, Flecknell P (2019) Retrospective review of anesthetic and analgesic regimens used in animal research proposals. ALTEX 36 (1):65–80. https://doi.org/10.14573/altex.1804011
7. Reimann HM, Niendorf T (2020) The (un)conscious mouse as a model for human brain functions: key principles of anesthesia and their impact on translational neuroimaging. Front Syst Neurosci 14:8. https://doi.org/10.3389/fnsys.2020.00008
8. Wei Q, Dong Z (2012) Mouse model of ischemic acute kidney injury: technical notes and tricks. Am J Physiol Renal Physiol 303(11): F1487–F1494. https://doi.org/10.1152/ajprenal.00352.2012
9. Le Clef N, Verhulst A, D'Haese PC, Vervaet BA (2016) Unilateral renal ischemia-reperfusion as a robust model for acute to chronic kidney injury in mice. PLoS One 11 (3):e0152153. https://doi.org/10.1371/journal.pone.0152153
10. Tremoleda JL, Kerton A, Gsell W (2012) Anaesthesia and physiological monitoring during in vivo imaging of laboratory rodents: considerations on experimental outcomes and animal welfare. EJNMMI Res 2(1):44. https://doi.org/10.1186/2191-219x-2-44
11. Niles DJ, Gordon JW, Fain SB (2015) Effect of anesthesia on renal R2 * measured by blood oxygen level-dependent MRI. NMR Biomed 28(7):811–817. https://doi.org/10.1002/nbm.3314
12. Furtado KS, Andrade FO (2013) Comparison of the beneficial and adverse effects of inhaled and injectable anaesthetics: a mini-review. OA Anaesthetics 1(2):20. https://doi.org/10.13172/2052-7853-1-2-1006
13. Hedenqvist P, Hellebrekers L (2003) Laboratory animal analgesia, anesthesia, and euthanasia
14. Demirkiran H, Senoglu N, Oksuz H, Dogan Z, Yüzbaşıoğu F, Bulbuloglu E, Inanc Tolun F, Aral M, Ciralik H, Goksu M, Yardimci C (2019) The effects of different doses ketamine on the renal ischemia/reperfusion injury in rats. Eastern J Med 24(2):194–199. https://doi.org/10.5505/ejm.2019.48658
15. Yuzer H, Yuzbasioglu MF, Ciralik H, Kurutas EB, Ozkan OV, Bulbuloglu E, Atlı Y, Erdogan O, Kale IT (2009) Effects of intravenous anesthetics on renal ischemia/reperfusion injury. Ren Fail 31(4):290–296. https://doi.org/10.1080/08860220902779962
16. Hau J, Schapiro SJ (2010) Handbook of laboratory animal science, volume I: essential principles and practices. CRC Press, Boca Raton
17. Tsukamoto A, Serizawa K, Sato R, Yamazaki J, Inomata T (2015) Vital signs monitoring during injectable and inhalant anesthesia in mice. Exp Anim 64(1):57–64. https://doi.org/10.1538/expanim.14-0050
18. Buitrago S, Martin TE, Tetens-Woodring J, Belicha-Villanueva A, Wilding GE (2008) Safety and efficacy of various combinations of injectable anesthetics in BALB/c mice. J Am Assoc Lab Anim Sci 47(1):11–17
19. Lei H, Grinberg O, Nwaigwe CI, Hou HG, Williams H, Swartz HM, Dunn JF (2001) The effects of ketamine-xylazine anesthesia on cerebral blood flow and oxygenation observed using nuclear magnetic resonance perfusion imaging and electron paramagnetic resonance oximetry. Brain Res 913(2):174–179. https://doi.org/10.1016/s0006-8993(01)02786-x
20. Ochiai Y, Iwano H, Sakamoto T, Hirabayashi M, Kaneko E, Watanabe T, Yamashita K, Yokota H (2016) Blood biochemical changes in mice after administration of a mixture of three anesthetic agents. J Vet Med Sci 78(6):951–956. https://doi.org/10.1292/jvms.15-0474
21. Ilkiw JE (1992) Advantages and guidelines for using ultrashort barbiturates for induction of anesthesia. Vet Clin North Am Small Anim Pract 22(2):261–264
22. Lopez-Munoz F, Ucha-Udabe R, Alamo C (2005) The history of barbiturates a century after their clinical introduction. Neuropsychiatr Dis Treat 1(4):329–343
23. Dogan Z, Yuzbasioglu MF, Kurutas EB, Yildiz H, Coskuner I, Senoglu N, Oksuz H, Bulbuloglu E (2010) Thiopental improves renal ischemia-reperfusion injury. Ren Fail 32 (3):391–395. https://doi.org/10.3109/08860221003611752

24. Almaas R, Saugstad OD, Pleasure D, Rootwelt T (2000) Effect of barbiturates on hydroxyl radicals, lipid peroxidation, and hypoxic cell death in human NT2-N neurons. Anesthesiology 92(3):764–774. https://doi.org/10.1097/00000542-200003000-00020
25. Nishina K, Akamatsu H, Mikawa K, Shiga M, Maekawa N, Obara H, Niwa Y (1998) The inhibitory effects of thiopental, midazolam, and ketamine on human neutrophil functions. Anesth Analg 86(1):159–165. https://doi.org/10.1097/00000539-199801000-00032
26. Lei H, Duarte JM, Mlynarik V, Python A, Gruetter R (2010) Deep thiopental anesthesia alters steady-state glucose homeostasis but not the neurochemical profile of rat cortex. J Neurosci Res 88(2):413–419. https://doi.org/10.1002/jnr.22212
27. Bruns A, Kunnecke B, Risterucci C, Moreau JL, von Kienlin M (2009) Validation of cerebral blood perfusion imaging as a modality for quantitative pharmacological MRI in rats. Magn Reson Med 61(6):1451–1458. https://doi.org/10.1002/mrm.21779
28. Yuzbasioglu MF, Aykas A, Kurutas EB, Sahinkanat T (2010) Protective effects of propofol against ischemia/reperfusion injury in rat kidneys. Ren Fail 32(5):578–583. https://doi.org/10.3109/08860220903548940
29. Sanchez-Conde P, Rodriguez-Lopez JM, Nicolas JL, Lozano FS, Garcia-Criado FJ, Cascajo C, Gonzalez-Sarmiento R, Muriel C (2008) The comparative abilities of propofol and sevoflurane to modulate inflammation and oxidative stress in the kidney after aortic cross-clamping. Anesth Analg 106 (2):371–378, table of contents. https://doi.org/10.1213/ane.0b013e318160580b
30. Liu X, Li R, Yang Z, Hudetz AG, Li SJ (2012) Differential effect of isoflurane, medetomidine, and urethane on BOLD responses to acute levo-tetrahydropalmatine in the rat. Magn Reson Med 68(2):552–559. https://doi.org/10.1002/mrm.23243
31. Aizawa N, Ogawa S, Sugiyama R, Homma Y, Igawa Y (2015) Influence of urethane-anesthesia on the effect of resiniferatoxin treatment on bladder function in rats with spinal cord injury. Neurourol Urodyn 34 (3):274–279. https://doi.org/10.1002/nau.22549
32. Maggi CA, Meli A (1986) Suitability of urethane anesthesia for physiopharmacological investigations in various systems. Part 1: general considerations. Experientia 42 (2):109–114. https://doi.org/10.1007/bf01952426
33. Ganjoo P, Farber NE, Schwabe D, Kampine JP, Schmeling WT (1996) Desflurane attenuates the somatosympathetic reflex in rats. Anesth Analg 83(1):55–61. https://doi.org/10.1097/00000539-199607000-00010
34. Kober F, Iltis I, Cozzone PJ, Bernard M (2004) Cine-MRI assessment of cardiac function in mice anesthetized with ketamine/xylazine and isoflurane. MAGMA 17 (3–6):157–161. https://doi.org/10.1007/s10334-004-0086-0
35. Kersten JR, Lowe D, Hettrick DA, Pagel PS, Gross GJ, Warltier DC (1996) Glyburide, a KATP channel antagonist, attenuates the cardioprotective effects of isoflurane in stunned myocardium. Anesth Analg 83(1):27–33. https://doi.org/10.1097/00000539-199607000-00006
36. van Alst TM, Wachsmuth L, Datunashvili M, Albers F, Just N, Budde T, Faber C (2019) Anesthesia differentially modulates neuronal and vascular contributions to the BOLD signal. NeuroImage 195:89–103. https://doi.org/10.1016/j.neuroimage.2019.03.057
37. Grosenick D, Cantow K, Arakelyan K, Wabnitz H, Flemming B, Skalweit A, Ladwig M, Macdonald R, Niendorf T, Seeliger E (2015) Detailing renal hemodynamics and oxygenation in rats by a combined near-infrared spectroscopy and invasive probe approach. Biomed Opt Express 6 (2):309–323. https://doi.org/10.1364/BOE.6.000309
38. Lee HT, Ota-Setlik A, Fu Y, Nasr SH, Emala CW (2004) Differential protective effects of volatile anesthetics against renal ischemia-reperfusion injury in vivo. Anesthesiology 101 (6):1313–1324. https://doi.org/10.1097/00000542-200412000-00011
39. Hashiguchi H, Morooka H, Miyoshi H, Matsumoto M, Koji T, Sumikawa K (2005) Isoflurane protects renal function against ischemia and reperfusion through inhibition of protein kinases, JNK and ERK. Anesth Analg 101 (6):1584–1589. https://doi.org/10.1213/01.Ane.0000184044.51749.B8
40. Carraretto AR, Vianna Filho PT, Castiglia YM, Golim Mde A, Souza AV, Carvalho LR, Deffune E, Vianna PT (2013) Do propofol and isoflurane protect the kidney against ischemia/reperfusion injury during transient hyperglycemia? Acta Cir Bras 28(3):161–166
41. Reimann HM, Hentschel J, Marek J, Huelnhagen T, Todiras M, Kox S, Waiczies S, Hodge R, Bader M, Pohlmann A, Niendorf T (2016) Normothermic mouse functional MRI of acute focal Thermostimulation for probing

nociception. Sci Rep 6:17230. https://doi.org/10.1038/srep17230

42. Delbridge MS, Shrestha BM, Raftery AT, El Nahas AM, Haylor JL (2007) The effect of body temperature in a rat model of renal ischemia-reperfusion injury. Transplant Proc 39(10):2983–2985. https://doi.org/10.1016/j.transproceed.2007.04.028
43. Blaszczyk J, Kedziora J, Luciak M, Sibinska E, Trznadel K, Pawlicki L (1994) Effect of morphine and naloxone on oxidative metabolism during experimental renal ischemia and reperfusion. Exp Nephrol 2(6):364–370
44. Elkadi HK, Nghiem DD, Southard JH, Kelly KM, Olson CL (1987) Naloxone in renal ischemia: a functional and microanatomical study. J Surg Res 42(6):675–692
45. Deng J, St Clair M, Everett C, Reitman M, Star RA (2000) Buprenorphine given after surgery does not alter renal ischemia/reperfusion injury. Comp Med 50(6):628–632
46. Gonullu E, Ozkardesler S, Kume T, Duru LS, Akan M, Guneli ME, Ergur BU, Meseri R, Dora O (2014) Comparison of the effects of dexmedetomidine administered at two different times on renal ischemia/reperfusion injury in rats. Braz J Anesthesiol 64(3):152–158. https://doi.org/10.1016/j.bjane.2013.06.002
47. Ma J, Chen Q, Li J, Zhao H, Mi E, Chen Y, Yi B, Ning J, Ma D, Lu K, Gu J (2018) Dexmedetomidine-mediated prevention of renal ischemia-reperfusion injury depends in part on cholinergic anti-inflammatory mechanisms. Anesth Analg 130(4):1054–1062. https://doi.org/10.1213/ANE.0000000000003820
48. Zhu SH, Zhou LJ, Jiang H, Chen RJ, Lin C, Feng S, Jin J, Chen JH, Wu JY (2014) Protective effect of indomethacin in renal ischemia-reperfusion injury in mice. J Zhejiang Univ Sci B 15(8):735–742. https://doi.org/10.1631/jzus.B1300196
49. Calistro Neto JP, Torres Rda C, Goncalves GM, Silva LM, Domingues MA, Modolo NS, Barros GA (2015) Parecoxib reduces renal injury in an ischemia/reperfusion model in rats. Acta Cir Bras 30(4):270–276. https://doi.org/10.1590/S0102-865020150040000006
50. Narver HL (2017) Antimicrobial stewardship in laboratory animal facilities. J Am Assoc Lab Anim Sci 56(1):6–10
51. Gargiulo S, Greco A, Gramanzini M, Esposito S, Affuso A, Brunetti A, Vesce G (2012) Mice anesthesia, analgesia, and care, part II: anesthetic considerations in preclinical imaging studies. ILAR J 53(1):E70–E81. https://doi.org/10.1093/ilar.53.1.70
52. Zager RA (1992) Gentamicin effects on renal ischemia/reperfusion injury. Circ Res 70(1):20–28. https://doi.org/10.1161/01.res.70.1.20

Chapter 4

Reversible (Patho)Physiologically Relevant Test Interventions: Rationale and Examples

Kathleen Cantow, Mechthild Ladwig-Wiegard, Bert Flemming, Andrea Fekete, Adam Hosszu, and Erdmann Seeliger

Abstract

Renal tissue hypoperfusion and hypoxia are early key elements in the pathophysiology of acute kidney injury of various origins, and may also promote progression from acute injury to chronic kidney disease. Here we describe test interventions that are used to study the control of renal hemodynamics and oxygenation in experimental animals in the context of kidney-specific control of hemodynamics and oxygenation. The rationale behind the use of the individual tests, the physiological responses of renal hemodynamics and oxygenation, the use in preclinical studies, and the possible application in humans are discussed.

This chapter is based upon work from the COST Action PARENCHIMA, a community-driven network funded by the European Cooperation in Science and Technology (COST) program of the European Union, which aims to improve the reproducibility and standardization of renal MRI biomarkers.

Key words Renal hemodynamics and oxygenation, In vivo methods, Rats, Test interventions

1 Introduction

Kidney diseases are a global health burden with steadily increasing incidence and prevalence [1–5]. Animal studies indicate that acute kidney injuries (AKI) of various origins share one common link in the pathophysiological chain of events, ultimately leading to AKI, as well as to progression from AKI to chronic kidney diseases (CKD): imbalance between renal oxygen delivery and oxygen demand [6–14]. Renal tissue hypoperfusion and hypoxia have also been suggested to play a pivotal role in the pathophysiology of other kidney diseases including diabetic kidney disease [15–19]. These pathophysiological concepts have largely been generated by preclinical studies that used either invasive quantitative probes or noninvasive functional magnetic resonance imaging (MRI) techniques to gain insight into renal hemodynamics and oxygenation. Thus, making ultimate statements on the role of renal hypoperfusion and hypoxia for these renal disorders is elusive

Andreas Pohlmann and Thoralf Niendorf (eds.), *Preclinical MRI of the Kidney: Methods and Protocols*, Methods in Molecular Biology, vol. 2216, https://doi.org/10.1007/978-1-0716-0978-1_4,

because in vivo assessment of renal hemodynamics and oxygenation constitutes a challenge.

All modalities available in today's experimental and translational research practice have inherent shortcomings and methodological constraints. Invasiveness is the major disadvantage of the gold standard physiological probes such as perivascular flow probes for measurement of total renal blood flow, laser-Doppler-optodes for assessment of local tissue perfusion, and Clark-type electrodes or fluorescence-quenching optodes for measurements of local tissue partial pressure of oxygen (pO_2), which precludes their use in humans. While functional MRI including blood oxygenation-sensitized T_2* (aka blood oxygenation level-dependent MRI; BOLD-MRI) offers noninvasive techniques to obtain insight into renal perfusion and oxygenation, its major weakness is its qualitative nature. Before it can be used for quantitative characterization of renal tissue perfusion and oxygenation, it needs to be calibrated with the gold standard invasive techniques in various (patho)-physiological scenarios [20–24].

The control of renal hemodynamics and oxygenation under physiological as well as under pathophysiological conditions is complex and differs considerably from nonrenal tissue [8, 21, 23, 25–27]. Due to the considerable capacity of the organism's homeostatic control systems to—at least partially—compensate for disturbances of, or injury to, certain control elements, these alterations are often not easily detectable when studied by measuring baseline data only. In order to disentangle these complexities, dedicated reversible test interventions are conceptually appealing. In fact, such interventions can serve three main purposes. First, they are used to gain more insight into the control of renal hemodynamics and oxygenation in healthy animals and in animal models of various kidney diseases [8, 12, 25, 28–37]. Second, the tests are used to assess whether a given drug or contrast agent has beneficial or unwarranted effects on the control of renal hemodynamics and oxygenation [38–40]. Finally, dedicated reversible tests are used to achieve calibration of functional MRI data [22, 23].

In this chapter, specifics of the control of renal hemodynamics and oxygenation are outlined first. Then, the individual test procedures are described, and the rationale behind their use, the physiological response of renal hemodynamics and oxygenation, the use in preclinical studies and the possible application in humans are discussed.

This chapter is part of the book Pohlmann A, Niendorf T (eds) (2020) Preclinical MRI of the Kidney—Methods and Protocols. Springer, New York.

2 Specifics of Renal Hemodynamics and Oxygenation

Renal hemodynamics and oxygenation offer a number of striking differences when compared to nonrenal tissue. First, total renal blood flow (RBF) is huge when compared to virtually all other organs on a per gram basis: the kidneys receive about 20% of the cardiac output under resting conditions. Yet the distribution of blood perfusion differs substantially between the layers: while 100% of blood flowing into the kidney reaches the cortex, only 15% of blood that previously passes through the cortex, will reach the medulla. Even intralayer (cortex, outer medulla, and inner medulla) perfusion is quite heterogeneous [8, 41, 42]. In accordance with the high total RBF, the kidneys' oxygen extraction (the difference between the O_2 content in the renal arterial and the renal venous blood) is low as compared to the majority of nonrenal tissues. Yet the partial pressure of oxygen (pO_2) is low in the medulla and also varies considerably within the respective layers, in accordance with the different blood flow distribution [21, 23, 26, 43–47].

Second, the kidney differs from all other organs with regard to the relationship between metabolism and perfusion. More than 26 thousand millimoles of sodium (Na^+) are filtered in the human glomeruli every day, equivalent to more than 1.5 kg of table salt. To achieve sodium balance, the amount of salt excreted by the kidneys must exactly match the amount of ingested salt minus the amount of extrarenal loss. Thus, more than 99% of the filtered sodium must usually be reabsorbed from the tubules. Tubular resorption relies on active transport processes, which account for about 85% of the kidney's energy expenditure and therefore its O_2 consumption. The more sodium is filtered in the glomeruli, the more must be reabsorbed. As glomerular filtration rate (GFR), under the majority of circumstances, increases with increasing RBF, renal O_2 consumption also usually increases with increasing renal perfusion. This is in contradistinction to all other organs, where metabolism determines perfusion [8, 48].

Third, hormones such as angiotensin II and epinephrine, sympathetic vasomotor nerves, and paracrine mediators such as nitric oxide or adenosine, that control resistance vessels in nonrenal tissues, impinge on intrarenal resistance vessels too, thereby altering renal O_2 delivery. However, in the kidney, they additionally affect tubular sodium resorption and thus O_2 consumption. Furthermore, their effect on postglomerular vessels can result in divergent responses of RBF and GFR. Finally, adenosine exerts vasodilation in virtually all nonrenal vascular beds, but vasoconstriction in the renal cortex [8, 25, 48, 49].

Fourth, the kidney is equipped with efficient mechanisms of autoregulation, that is, the ability to dampen or even to abolish the

effects that changes in renal arterial pressure would otherwise inevitably have on RBF and GFR. The almost perfect autoregulation of RBF and GFR probably relies on the fact that not just one, but three mechanisms are involved. The first one, the myogenic response (aka Bayliss effect) acts not only on renal resistance vessels but also on brain and gut vessels. The second mechanism, the tubuloglomerular feedback (TGF), and the third one, hitherto just named "third mechanism", are kidney-specific. Renal autoregulatory mechanisms, in particular the TGF and the third mechanism, have been suggested to serve the purpose of balancing O_2 delivery, that is, RBF with metabolic and O_2 demands arising from tubular reabsorption. The outer medulla is particularly prone to imbalance between O_2 delivery and demand since this layer exhibits a high O_2 demand but low pO_2 [21, 34, 35, 50–52].

Fifth, intrarenal perfusion is also affected by changes in tubular volume. The tubular volume fraction is quite large and can rapidly change due to alterations in GFR, in tubular outflow toward the pelvis, in tubular fluid resorption, and modulation of the transmural pressure gradient. Since the renal capsule is rather tough, changes in tubular volume will result in circular distension or compression of intrarenal vessels [23, 36].

Finally, in addition to the heterogeneous intrarenal blood perfusion, three other factors substantially contribute to the low tissue pO_2 and, in particular, to the "physiological hypoxia" in the medulla. First, there is a considerable shunt diffusion of O_2 from arteries to veins in the cortex and from descending to ascending vasa recta in the medulla [53–55]. Second, the Fåhræus–Lindqvist effect lowers the hematocrit in the vasa recta supplying the medulla, which lowers the O_2 content of blood perfusing parts of the medulla [41, 42]. Third, plasma skimming at intrarenal vessel branches results in different hematocrit and therefore O_2 content of blood perfusing the daughter vessels [41, 56].

3 Dedicated Reversible Test Interventions

3.1 Short Periods of Occlusion of the Renal Artery or Renal Vein

Occlusions of the renal artery (alternatively: the suprarenal aorta) or of the renal vein emulate clinical conditions in which deficient renal perfusion results in deterioration of intrarenal oxygenation. If maintained for longer periods of time these conditions can cause AKI [57–59]. The rationale for performing both of these tests is that renal arterial occlusion and renal venous occlusion have similar effects with regard to renal perfusion and oxygenation, yet opposing effects with regard to intrarenal blood volume. With the onset of aortic occlusion, the inflow of blood into the kidney is abruptly stopped while outflow via the renal vein continues until pressures in intrarenal vessels and in the vena cava are equalized. With the onset of renal venous occlusion, outflow of blood is abruptly stopped

while inflow via the artery does not cease until the arterial pressure-induced distension of intrarenal vessels is counterbalanced by the resistance of the renal tissue including the rather tough capsule [22, 39, 60].

In both cases, renal tissue perfusion rapidly decreases and eventually approaches zero flow. As renal O_2 consumption remains unaltered at the early stage of occlusions, a rapid and massive decline in renal tissue pO_2 results, which, in turn, also reduces blood pO_2 and the O_2 saturation of hemoglobin (StO_2) in the intrarenal (micro)vasculature. This intrarenal deoxygenation of hemoglobin (Hb) is aggravated by a progressive rightward shift of the oxyHb dissociation curve during the occlusion due to the intrarenal accumulation of carbon dioxide (CO_2) [22, 39, 60].

Yet the opposing changes of renal blood volume have an impact on renal tissue oxygenation. The decrease in tissue pO_2 at the onset of the venous occlusion is much slower than at the onset of the arterial occlusion. While renal O_2 consumption is similar during both kinds of occlusions, the transiently maintained inflow of oxygenated blood at the onset of venous occlusion increases the intrarenal reservoir of O_2 [22, 39, 60].

The opposing changes in renal blood volume have a massive impact on the changes in blood oxygenation-sensitized T_2^* (and its reciprocal value, R_2^*), because T_2^* reflects the amount of deoxygenated Hb (deoxyHb) per tissue volume (voxel) [23]. In case of the venous occlusion with its increase in the vascular volume fraction and thus the increasing amount of deoxyHb per volume, tissue T_2^* massively decreases [60]. With the arterial occlusion's decrease of deoxyHb per volume, the decrease in T_2^* is small. In fact, it was found significantly smaller than the decrease in T_2^* measured during hypoxemia (8% inspiratory oxygen fraction), which is diametrically opposed to the effects of arterial occlusion versus hypoxemia on tissue pO_2 (*see* Fig. 1) [22, 23, 36].

Short-time (1–3 min) occlusions of the renal artery (or of the suprarenal aorta) have been used in several studies for different scientific purposes. In order to gauge the effects on T_2^* and T_2 of bolus injections of an X-ray contrast medium into the thoracic aorta of healthy rats, the effect of arterial occlusion (and that of hypoxemia) was quantified in the same rats [36]. En route to calibration of T_2^* with quantitative physiological measurements by means of a dedicated hybrid MR-PHYSIOL setup (*see* the chapter by Cantow K et al. "Monitoring Renal Hemodynamics and Oxygenation by Invasive Probes: Experimental Protocol"), suprarenal aortic occlusion was used [22]. In order to ascertain that the superparamagnetic iron oxide nanoparticle (USPIO) preparation, ferumoxytol is suitable as a contrast medium for MR-based assessment of the renal blood volume fraction; its possible unwarranted effects on control of renal hemodynamics and oxygenation were tested by interventions including suprarenal aortic occlusion in rats (*see* Fig. 2)

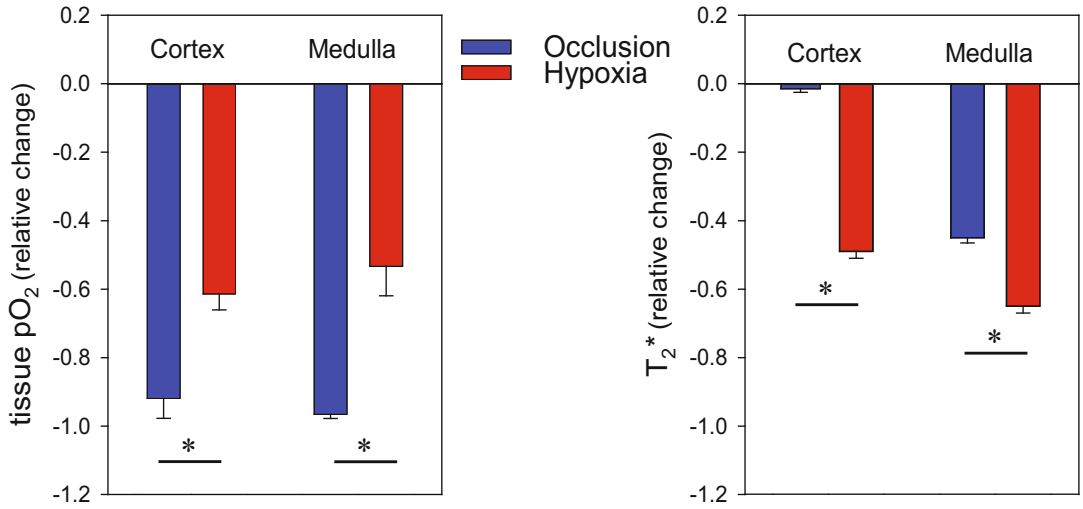

Fig. 1 Comparison of relative changes in renal cortical and medullary tissue pO_2 quantified by invasive gold standard fluorescence quenching optodes (left panel) versus relative changes in renal cortical and medullary T_2* (so-called BOLD-MRI, right panel), during short-term occlusion of the suprarenal aorta and short-term hypoxia (8% inspiratory O_2 fraction), respectively, in anesthetized rats. Data are mean ± SEM, redrawn from Refs. 22, 36

[38]. Implementing a setup that combines classical invasive probes for RBF, tissue perfusion, and pO_2 with newly developed near infrared spectroscopy (NIRS) techniques that enable monitoring of the amount of Hb per tissue volume and the O_2 saturation of Hb (StO_2) of intrarenal blood (termed PHYSIOL-NIRS), aortic occlusion was used as one of the test interventions [39]. By means of a dedicated deconvolution procedure developed by our group, the time course of RBF upon the release of the occlusion can be analyzed. This "step-response" analysis allows us to determine the strength of each of the three mechanisms of RBF autoregulation in the whole kidney in vivo, in both healthy rats and rat models of AKI [30, 34, 35].

Short-time (1–3 min) occlusions of the renal vein were also used for different purposes. In order to establish an optimum dose of the USPIO ferumoxytol in rats for the purpose of T_2*-based quantification of the renal blood volume fraction in a 9.4T small animal scanner, renal venous occlusion was chosen as the combined effects of the decrease in O_2 delivery and the increase in the blood volume fraction; thus, deoxyHb per volume was expected to result in a most prominent decrease in T_2* (*see* Fig. 3) [60].

Both renal arterial occlusion and renal venous occlusion was performed in the same healthy rats in the PHYSIOL-NIRS setup in order to directly compare their effects [39].

As the implementation of vascular occluders necessitates invasive techniques, these tests can be performed in preclinical studies only.

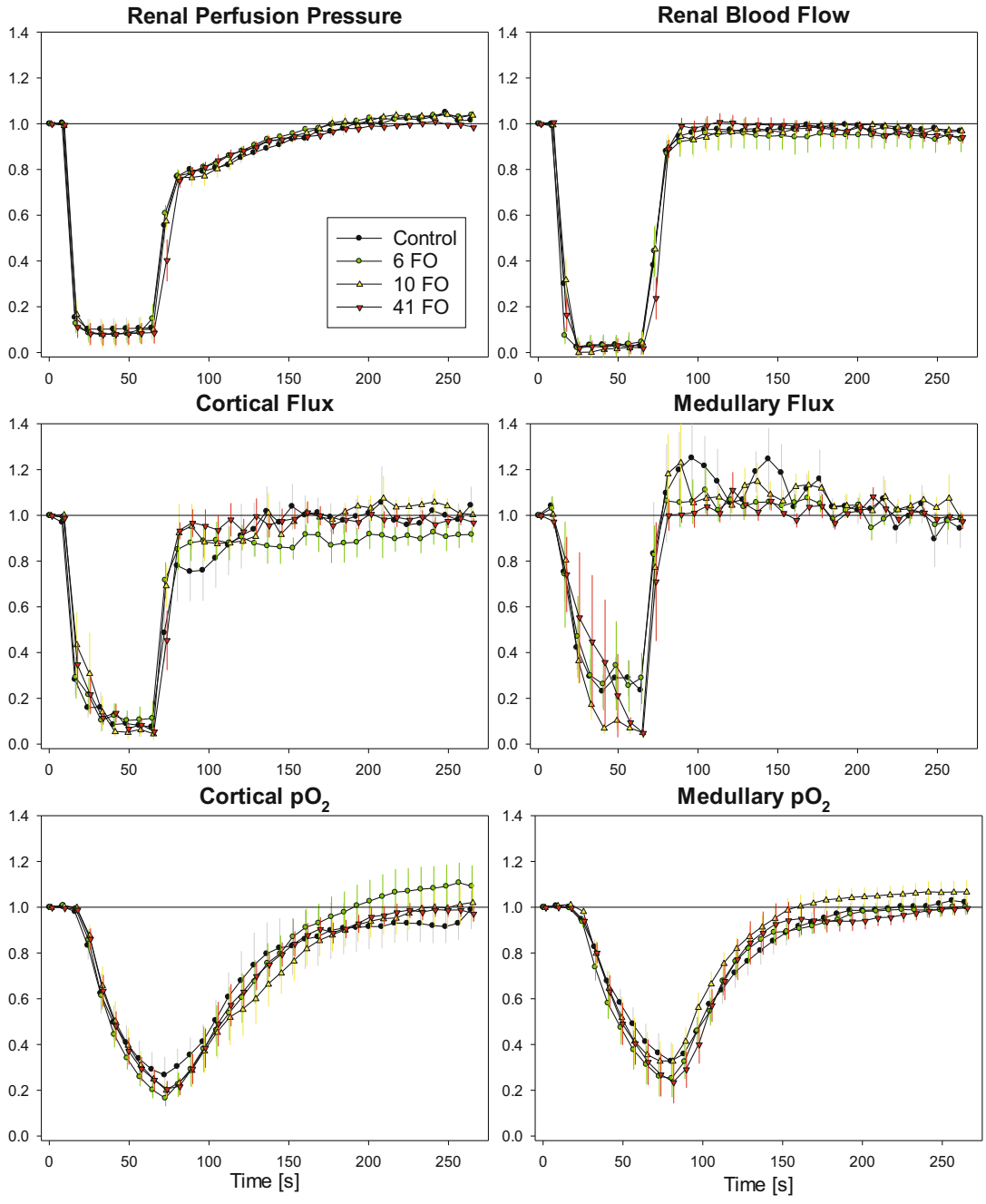

Fig. 2 In order to study whether the USPIO preparation, ferumoxytol (FO), exerts unwarranted effects on regulation of renal hemodynamics and oxygenation, a short-term suprarenal aortic occlusion was employed as test intervention in anesthetized rats [38]. Here, the relative changes (mean ± SEM) in hemodynamics and tissue oxygenation are depicted with FO dosages of 6, 10, and 41 mg Fe/kg body mass, or vehicle (Control)

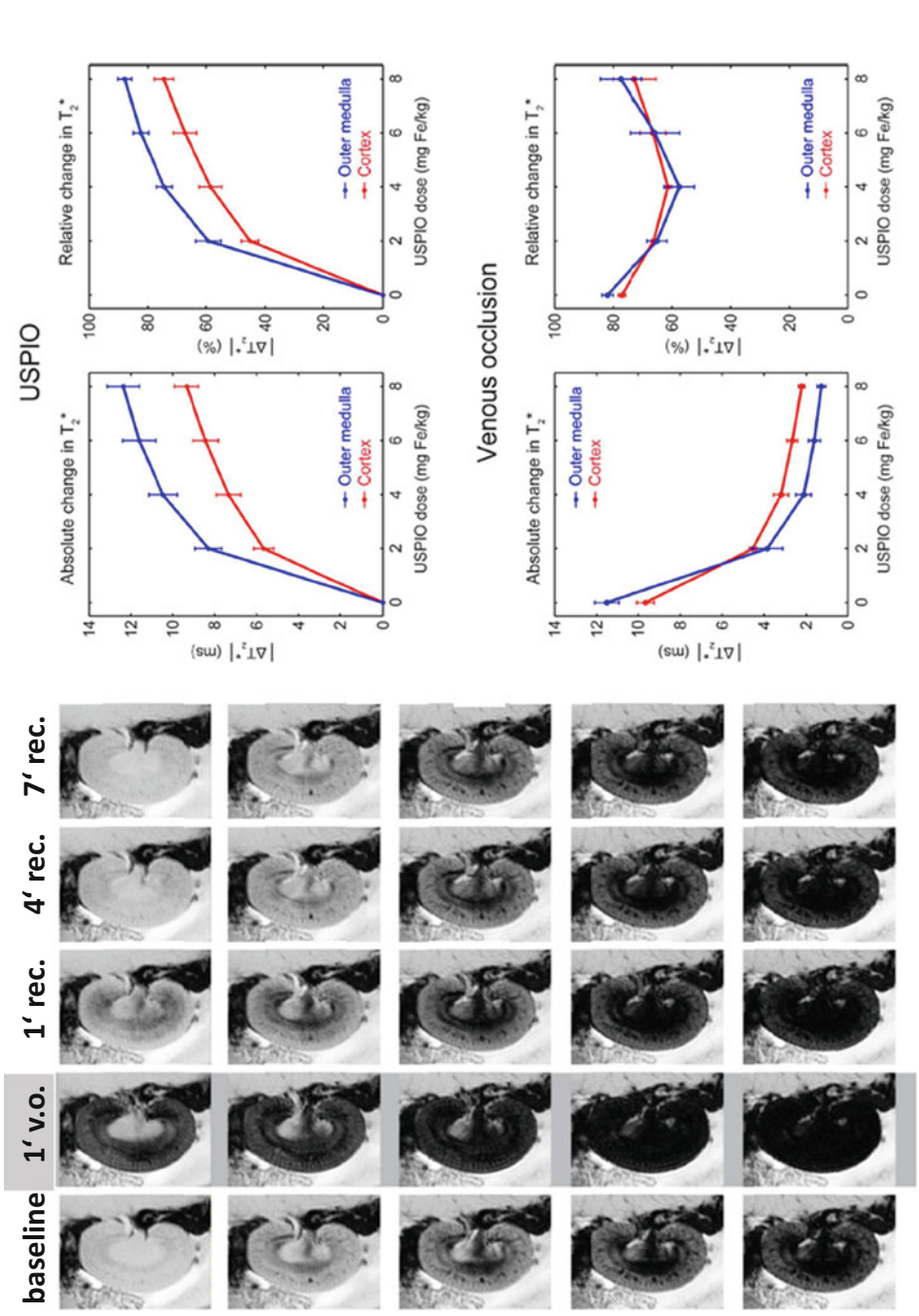

Fig. 3 Left panel: T_2*-weighted images (echo time = 3.6 ms, spatial resolution = 226 × 422 µm) obtained by a 9.4 T small animal MR scanner (Bruker Biospin, Biospec 94/20) of a rat kidney in vivo at baseline, during occlusion of the renal vein (v.o.), and at the beginning of the recovery phase (rec.) without the USPIO ferumoxytol (top row), and with four increasing doses of ferumoxytol [60]. Right panels: Comparison of the renal cortical and medullary T_2* sensitivity to USPIO injection and the T_2* sensitivity to the venous occlusion at different USPIO doses. Data are mean ± SEM (n = 4 rats) of cortical and medullary ROIs [60]

3.2 Servocontrolled Changes in Renal Arterial Pressure

Dynamic changes in renal arterial pressure according to different time courses of pressure reduction followed by pressure restoration—be it staircasewise or rampwise changes—enable insights into control of renal hemodynamics and oxygenation including the degree of autoregulation's efficiency and the contributions of the three autoregulatory mechanisms in vivo. This is achieved by a servocontrol system developed by our group, that was utilized to help disentangle the complexities of renal physiology and pathophysiology [30, 31, 33, 34]. Moreover, a study that employed such an intervention in a rat model that emulates an early stage of diabetic kidney disease (a type 1 diabetes mellitus–like model induced by administration of streptozotocin 4 weeks before obtaining the data on renal perfusion and oxygenation) unmasked alterations in the control of renal perfusion and oxygenation that would have gone undetected when only baseline data had been obtained [32]. Data on medullary tissue pO_2 obtained by invasive probes in this model have been inconsistent, which, among other reasons, may be caused by the spatial heterogeneity of pO_2 within the renal medulla [15–17]. A recent study did not find any significant differences in baseline data on RBF and cortical and medullary tissue pO_2 among healthy control rats, diabetic rats, and diabetic rats treated with the antidiabetic liraglutide (a glucagon-like peptide 1 agonist approved for patients suffering from type 2 diabetes). However, as depicted by Fig. 4, the response to ramp-wise reduction and restoration of renal arterial pressure differed considerably among these groups [32].

Again, as the implementation of a vascular occluder necessitates invasive techniques, such studies can be performed in preclinical studies only.

3.3 Short Periods of Changes in the Inspiratory Gas Mixture

Hyperoxia, hypoxia, and hypercapnia primarily alter blood oxygenation. Renal O_2 delivery is determined by renal perfusion and by the arterial O_2 content. The latter is determined, among other factors, by the inspiratory fraction of oxygen (FiO_2), and, due to the effect of CO_2 on the oxyHb dissociation curve, also by the inspiratory fraction of CO_2 ($FiCO_2$).

Increasing the FiO_2 from 21% (normoxia) to 100% (hyperoxia) results in a substantial increase in arterial pO_2 (usually four- to fivefold), whereas the increase in arterial O_2 content is very small, because most of the Hb in arterial blood is already O_2 saturated under normoxic conditions. Yet the increase in arterial pO_2 enhances the driving force for diffusion of O_2 from intrarenal vessels to tissue as well as from intrarenal arteries to veins. As a consequence, the increase in renal tissue pO_2 is substantial, whereby medullary pO_2 increases less than cortical pO_2, due to arteriovenous diffusive O_2 shunting, which reduces the O_2 content of arterial blood that perfuses the medulla [22, 26, 39, 53–55]. Renal T_2* changes exerted by hyperoxia are small

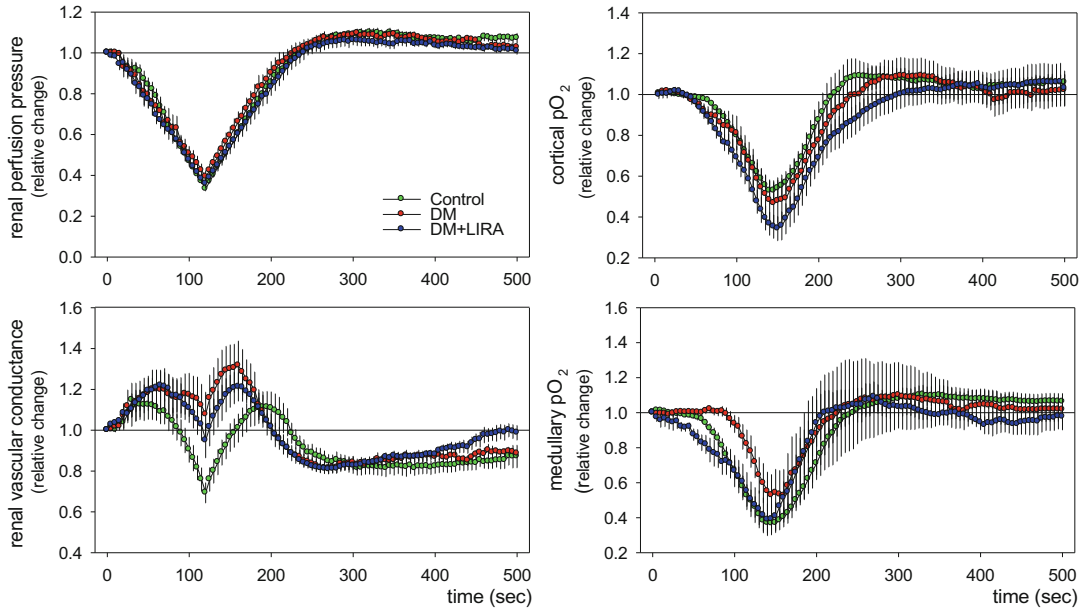

Fig. 4 Changes of invasively measured parameters of renal hemodynamics and oxygenation during ramp-wise reduction in renal perfusion pressure followed by ramp-wise pressure restoration in anesthetized rats. Conductance values (the reciprocal of vascular resistance) were calculated by dividing the respective perfusion values by renal perfusion pressure, in order to distinguish flow changes that result from passive circular distension/compression of vessels from those actively exerted by vascular smooth muscles. Three groups were studied: a healthy control group, a group in which a diabetes mellitus type 1-like disorder (DM) was induced by streptozotocin 4 weeks before obtaining the data, and a third group in which DM was induced and the antidiabetic liraglutide administered for 3 weeks (DM + LIRA). Values (mean ± SEM) are given as relative changes from baseline [32]

[22]. While the amount of deoxyHb in arterial blood is barely changed, the increase in blood pO_2 in intrarenal veins that results from the higher arteriovenous pO_2 difference decreases venous deoxyHb. While primarily altering blood oxygenation, the hyperoxic stimulus has also secondary effects: it results in vasoconstriction, preferentially in nonrenal vascular beds, which leads to an increase in arterial pressure [22, 31, 39].

The primary effect of reducing the FiO_2 (typically to either 8% or 10%, with durations of 3–12 min, in rat studies) is a decrease in oxygenation of arterial blood (hypoxemia) with the consequent reduction in renal O_2 supply. With ongoing O_2 consumption, this does per se result in a decrease in renal tissue pO_2. Yet renal O_2 supply is further diminished by hypoxia-induced extrarenal vasodilation that results in a drop in arterial pressure with ensuing decrease in RBF [22, 31, 39, 59]. Whether this is aggravated of alleviated by constriction or dilation, respectively, of the renal vasculature depends on the degree of hypoxia: in anesthetized rats, FiO_2 of 8% results in renal vasoconstriction while 10% results in vasodilation [22, 31, 39]. The combined effect of hypoxemia and

reduced RBF on renal O_2 supply leads to a major mismatch with O_2 consumption, that massively reduces tissue pO_2 as well as T_2* (*see* Fig. 1) [22, 39]. A further secondary effect of arterial hypoxemia is increased ventilation triggered by arterial chemoreceptors. The ensuing decrease in arterial pCO_2 shifts the oxyHb dissociation curve to the left, that is, O_2 is hindered from being released by Hb, which further aggravates the tissue hypoxia [61, 62].

With the hypercapnic stimulus (increasing $FiCO_2$ to 5%) the opposite effect is achieved, namely a rightward shift of the oxyHb dissociation curve. This would per se result in a decrease in StO_2 and an increase in blood and tissue pO_2. However, while the increase in tissue pO_2 is substantial, the StO_2 decrease is meagre [39]. The major reason that StO_2 does not decrease much is that increased pCO_2 of arterial blood is a very strong stimulus for ventilation, again mediated by arterial chemoreceptors [61, 62].

Hyperoxic, hypoxic, and hypercapnic tests have been used in a multitude of preclinical in vivo studies. With regard to the kidney this includes but is not limited to studies on the control of renal hemodynamics and oxygenation in healthy animals and models of kidney diseases [26, 27, 31, 53–55, 59], experiments that aimed at calibration of T_2* by means of the MR-PHYSIOL setup (*see* Fig. 5), [22] studies on the T_2* effect of an X-ray contrast medium, [36] assessment of possible unwarranted effects of the USPIO ferumoxytol, [38] and experiments en route to the PHYSIOL-NIRS setup [39].

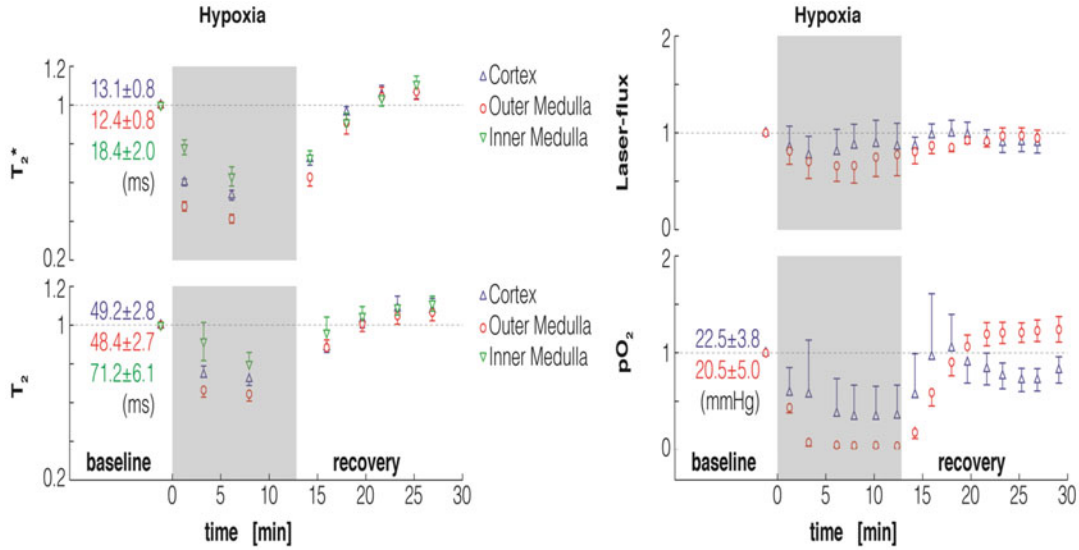

Fig. 5 Time courses of selected invasively measured data and MR parameters acquired simultaneously throughout baseline, a period of hypoxia (FiO_2 = 8%), and recovery in anesthetized rats by means of a dedicated MR-PHYSIOL hybrid setup (for details see text). Data (mean ± SEM) are relative changes from baseline, redrawn from Ref. 22

Given the broad therapeutic use of pure oxygen, short-term tests with 100% FiO_2 should pose no problem for studies in humans, whereas hypoxic challenges are precluded in humans, for obvious ethical reasons. Hypercapnia has been used for decades in humans, in particular, for the study of cerebrovascular reactivity, and should thus be employed in preclinical and clinical studies on renal hemodynamics and oxygenation as well [63, 64].

3.4 Administration of Drugs and Endogenous Vasoactive Substances

Furosemide is the "classic" loop diuretic: its major action is the inhibition of the sodium–potassium–two-chloride cotransporter in the apical membrane of tubular epithelial cells of the thick ascending limb of Henle's loop. The primary effect is an increase in urine flow rate and in urinary sodium and potassium excretion. As less tubular resorption necessitates less renal O_2 consumption, administration of furosemide leads to an increase in renal tissue pO_2 [65, 66]. In accordance, increases in renal T_2* (or decreases in its reciprocal value R_2*) have been observed in a multitude of preclinical as well as clinical studies (*see* Fig. 6) [37, 66–69]. It must be noted, however, that the increase in T_2* upon furosemide does not solely rely on improved oxygenation. First, the increase in tubular fluid downstream of the thick ascending limb will increase the transmural pressure gradient, thereby compressing intrarenal

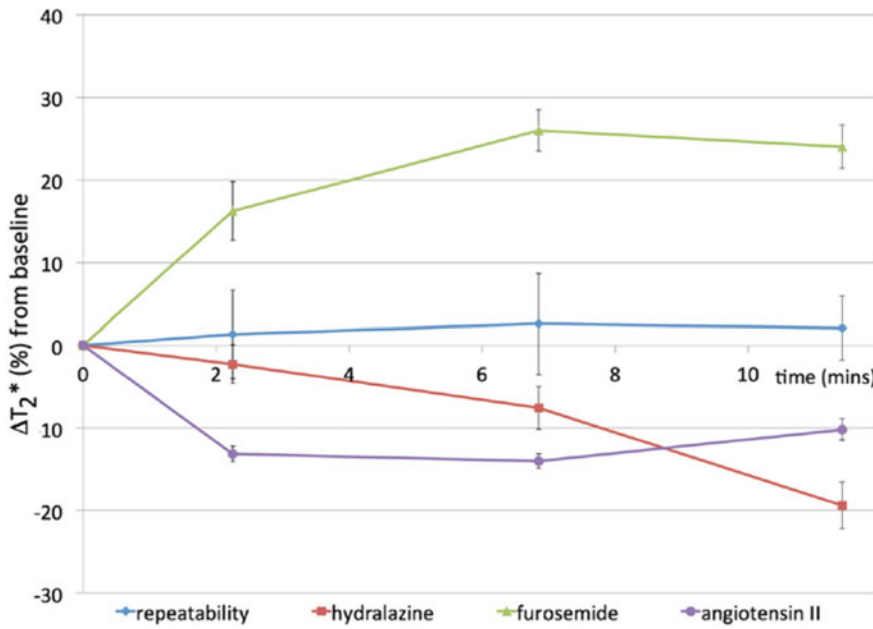

Fig. 6 Effect of injections of furosemide (5 mg/kg body mass), hydralazine (5 mg/kg), angiotensin II (0.5 μg/min/kg), and saline (repeatability) on renal BOLD as recorded by means of a 1.5 T clinical MR scanner (Magnetom Avanto, Siemens Healthcare), using a multiple gradient echo sequence (TR = 300 ms, TE = 5, 10, 20, 30, and 40 ms, voxel size 0.6 × 0.6 mm in-plane and 5 mm slice thickness) in rats in vivo. Data are mean ± SEM of median ROI values [37]

vessels with the ensuing decrease in the amount of deoxyHb per tissue volume. Second, furosemide inhibits the TGF, thereby compromising renal autoregulation with the possible consequence of an increase in RBF [34, 35, 50].

The use of the furosemide test in both preclinical and clinical MR studies is nowadays as widespread that it is almost regarded as a gold standard. However, whether it fulfils all expectations regarding its use as a diagnostic tool in patients suffering from various kidney diseases, remains to be seen [68].

Administration of furosemide is a reversible intervention insofar as its direct effects vanish with the excretion of the drug. However, it leaves the organism with deficits in water, sodium, and potassium. These should ideally be replenished—be it per os or by means of infusions of a balanced electrolyte solution.

Bolus injections of adenosine cause a rapid drop in arterial pressure due to its vasodilatory effect on nonrenal resistance vessels. In the renal cortical vascular bed, it exerts vasoconstriction [39, 49]. The consequence of these two effects is a substantial decrease in RBF followed by a smaller decrease in cortical tissue pO_2. All these effects vanish rapidly, lasting less than a minute for the hemodynamics and less than 2 min for the cortical pO_2 in rats [39].

Whereas the role of adenosine in various renal control mechanisms including the TGF as well as the potentially beneficial effect of adenosine receptor antagonists for prevention of X-ray contrast media-induced AKI have been intensively studied, [49, 70] the adenosine test has seldom been used to study renal hemodynamics and oxygenation. This may appear surprising, as injections of adenosine—be it intravenously or into coronary arteries—in patients suffering from coronary disease is quite established [71, 72]. While the risk for a decrease in renal cortical pO_2 in patients must not be ignored—even if it is lasting less than 2 min, the test should at least find wider use in preclinical studies.

Acknowledgments

This work was funded, in part (Kathleen Cantow and Erdmann Seeliger) by the German Research Foundation (Gefoerdert durch die Deutsche Forschungsgemeinschaft (DFG), Project number/Projektnummer 394046635, SFB 1365, RENOPROTECTION). The authors wish to thank Ariane Anger and Andrea Gerhardt for expert technical assistance.

This chapter is based upon work from COST Action PAR ENCHIMA, supported by European Cooperation in Science and Technology (COST). COST (www.cost.eu) is a funding agency for research and innovation networks. COST Actions help connect research initiatives across Europe and enable scientists to enrich

their ideas by sharing them with their peers. This boosts their research, career, and innovation.

PARENCHIMA (renalmri.org) is a community-driven Action in the COST program of the European Union, which unites more than 200 experts in renal MRI from 30 countries with the aim to improve the reproducibility and standardization of renal MRI biomarkers.

References

1. Fortrie G, de Geus HRH, Betjes MGH (2019) The aftermath of acute kidney injury: a narrative review of long-term mortality and renal function. Crit Care 23(1):24. https://doi.org/10.1186/s13054-019-2314-z
2. Selby NM, Taal MW (2019) Long-term outcomes after AKI-a major unmet clinical need. Kidney Int 95(1):21–23. https://doi.org/10.1016/j.kint.2018.09.005
3. Zuk A, Bonventre JV (2019) Recent advances in acute kidney injury and its consequences and impact on chronic kidney disease. Curr Opin Nephrol Hypertens 28(4):397–405. https://doi.org/10.1097/mnh.0000000000000504
4. Levin A, Tonelli M, Bonventre J, Coresh J, Donner JA, Fogo AB, Fox CS, Gansevoort RT, Heerspink HJL, Jardine M, Kasiske B, Kottgen A, Kretzler M, Levey AS, Luyckx VA, Mehta R, Moe O, Obrador G, Pannu N, Parikh CR, Perkovic V, Pollock C, Stenvinkel P, Tuttle KR, Wheeler DC, Eckardt KU (2017) Global kidney health 2017 and beyond: a roadmap for closing gaps in care, research, and policy. Lancet 390(10105):1888–1917. https://doi.org/10.1016/s0140-6736(17)30788-2
5. Bello AK, Levin A, Tonelli M, Okpechi IG, Feehally J, Harris D, Jindal K, Salako BL, Rateb A, Osman MA, Qarni B, Saad S, Lunney M, Wiebe N, Ye F, Johnson DW (2017) Assessment of global kidney health care status. JAMA 317(18):1864–1881. https://doi.org/10.1001/jama.2017.4046
6. Brezis M, Rosen S (1995) Hypoxia of the renal medulla--its implications for disease. N Engl J Med 332:647–655
7. Seeliger E, Sendeski M, Rihal CS, Persson PB (2012) Contrast-induced kidney injury: mechanisms, risk factors, and prevention. Eur Heart J 33(16):2007–2015
8. Evans RG, Ince C, Joles JA, Smith DW, May CN, O'Connor PM, Gardiner BS (2013) Haemodynamic influences on kidney oxygenation: the clinical implications of integrative physiology. Clin Exp Pharmacol Physiol 40:106–122
9. Evans RG, Ow CP, Bie P (2015) The chronic hypoxia hypothesis: the search for the smoking gun goes on. Am J Physiol Renal Physiol 308 (2):F101–F102
10. Shu S, Wang Y, Zheng M, Liu Z, Cai J, Tang C, Dong Z (2019) Hypoxia and hypoxia-inducible factors in kidney injury and repair. Cell 8(3):207. https://doi.org/10.3390/cells8030207
11. Hultstrom M, Becirovic-Agic M, Jonsson S (2018) Comparison of acute kidney injury of different etiology reveals in-common mechanisms of tissue damage. Physiol Genomics 50 (3):127–141. https://doi.org/10.1152/physiolgenomics.00037.2017
12. Calzavacca P, Evans RG, Bailey M, Bellomo R, May CN (2015) Cortical and medullary tissue perfusion and oxygenation in experimental septic acute kidney injury. Crit Care Med 43 (10):e431–e439
13. Fähling M, Seeliger E, Patzak A, Persson PB (2017) Understanding and preventing contrast-induced acute kidney injury. Nat Rev Nephrol 13(3):169–180
14. Ma S, Evans RG, Iguchi N, Tare M, Parkington HC, Bellomo R, May CN, Lankadeva YR (2019) Sepsis-induced acute kidney injury: a disease of the microcirculation. Microcirculation 26(2):e12483. https://doi.org/10.1111/micc.12483
15. Palm F, Carlsson PO, Hansell P, Hellberg O, Nygren A, Liss P (2003) Altered response in renal blood flow and oxygen tension to contrast media in diabetic rats. Acta Radiol 44 (3):347–353
16. Palm F, Cederberg J, Hansell P, Liss P, Carlsson PO (2003) Reactive oxygen species cause diabetes-induced decrease in renal oxygen tension. Diabetologia 46(8):1153–1160
17. dos Santos EA, Li LP, Ji L, Prasad PV (2007) Early changes with diabetes in renal medullary hemodynamics as evaluated by fiberoptic probes and BOLD magnetic resonance imaging. Investig Radiol 42(3):157–162. https://

doi.org/10.1097/01.rli.0000252492.96709.36

18. Calvin AD, Misra S, Pflueger A (2010) Contrast-induced acute kidney injury and diabetic nephropathy. Nat Rev Nephrol 6 (11):679–688
19. Hansell P, Welch WJ, Blantz RC, Palm F (2013) Determinants of kidney oxygen consumption and their relationship to tissue oxygen tension in diabetes and hypertension. Clin Exp Pharmacol Physiol 40(2):123–137
20. Evans RG, Gardiner BS, Smith DW, O'Connor PM (2008) Methods for studying the physiology of kidney oxygenation. Clin Exp Pharmacol Physiol 35(12):1405–1412
21. Pohlmann A, Cantow K, Hentschel J, Arakelyan K, Ladwig M, Flemming B, Hoff U, Persson PB, Seeliger E, Niendorf T (2013) Linking non-invasive parametric MRI with invasive physiological measurements (MR-PHYSIOL): towards a hybrid and integrated approach for investigation of acute kidney injury in rats. Acta Physiol (Oxf) 207 (4):673–689
22. Pohlmann A, Arakelyan K, Hentschel J, Cantow K, Flemming B, Ladwig M, Waiczies S, Seeliger E, Niendorf T (2014) Detailing the relation between renal T2* and renal tissue pO2 using an integrated approach of parametric magnetic resonance imaging and invasive physiological measurements. Investig Radiol 49(8):547–560
23. Niendorf T, Pohlmann A, Arakelyan K, Flemming B, Cantow K, Hentschel J, Grosenick D, Ladwig M, Reimann H, Klix S, Waiczies S, Seeliger E (2015) How BOLD is blood oxygenation-dependent (BOLD) magnetic resonance imaging of the kidney? Opportunities, challenges and future directions. Acta Physiol (Oxf) 213(1):19–38
24. Hirakawa Y, Tanaka T, Nangaku M (2017) Renal hypoxia in CKD; pathophysiology and detecting methods. Front Physiol 8:99. https://doi.org/10.3389/fphys.2017.00099
25. Calzavacca P, Evans RG, Bailey M, Bellomo R, May CN (2015) Variable responses of regional renal oxygenation and perfusion to vasoactive agents in awake sheep. Am J Physiol Regul Integr Comp Physiol 309(10):R1226–R1233
26. Evans RG, Gardiner BS, Smith DW, O'Connor PM (2008) Intrarenal oxygenation: unique challenges and the biophysical basis of homeostasis. Am J Physiol Renal Physiol 295 (5):1259–1270
27. Evans RG, Goddard D, Eppel GA, O'Connor PM (2011) Factors that render the kidney susceptible to tissue hypoxia in hypoxemia. Am J Physiol Regul Integr Comp Physiol 300(4): R931–R940
28. Emans TW, Janssen BJ, Pinkham MI, Ow CP, Evans RG, Joles JA, Malpas SC, Krediet CT, Koeners MP (2016) Exogenous and endogenous angiotensin-II decrease renal cortical oxygen tension in conscious rats by limiting renal blood flow. J Physiol 594(21):6287–6300. https://doi.org/10.1113/jp270731
29. Evans RG, Madden AC, Denton KM (2000) Diversity of responses of renal cortical and medullary blood flow to vasoconstrictors in conscious rabbits. Acta Physiol Scand 169 (4):297–308
30. Seeliger E, Flemming B, Wronski T, Ladwig M, Arakelyan K, Godes M, Mockel M, Persson PB (2007) Viscosity of contrast media perturbs renal hemodynamics. J Am Soc Nephrol 18 (11):2912–2920
31. Flemming B, Seeliger E, Wronski T, Steer K, Arenz N, Persson PB (2000) Oxygen and renal hemodynamics in the conscious rat. J Am Soc Nephrol 11(1):18–24
32. Ferrara F, Cantow K, Flemming B, Skalweit A, Ladwig M, Fähling M, Seeliger E (2017) Effects of liraglutide on control of renal hemodynamics and oxygenation in diabetic rats. Acta Physiol (Oxf) 219(Suppl. 711):38
33. Flemming B, Arenz N, Seeliger E, Wronski T, Steer K, Persson PB (2001) Time-dependent autoregulation of renal blood flow in conscious rats. J Am Soc Nephrol 12(11):2253–2262
34. Seeliger E, Wronski T, Ladwig M, Dobrowolski L, Vogel T, Godes M, Persson PB, Flemming B (2009) The renin-angiotensin system and the third mechanism of renal blood flow autoregulation. Am J Physiol Renal Physiol 296(6):F1334–F1345
35. Wronski T, Seeliger E, Persson PB, Forner C, Fichtner C, Scheller J, Flemming B (2003) The step response: a method to characterize mechanisms of renal blood flow autoregulation. Am J Physiol Renal Physiol 285(4): F758–F764
36. Arakelyan K, Cantow K, Hentschel J, Flemming B, Pohlmann A, Ladwig M, Niendorf T, Seeliger E (2013) Early effects of an x-ray contrast medium on renal T_2*/T_2 MRI as compared to short-term hyperoxia, hypoxia and aortic occlusion in rats. Acta Physiol 208(2):202–213
37. Jerome NP, Boult JK, Orton MR, d'Arcy J, Collins DJ, Leach MO, Koh DM, Robinson SP (2016) Modulation of renal oxygenation and perfusion in rat kidney monitored by quantitative diffusion and blood oxygen level dependent magnetic resonance imaging on a

clinical 1.5T platform. BMC Nephrol 17 (1):142. https://doi.org/10.1186/s12882-016-0356-x

38. Cantow K, Pohlmann A, Flemming B, Ferrara F, Waiczies S, Grosenick D, Niendorf T, Seeliger E (2016) Acute effects of ferumoxytol on regulation of renal hemodynamics and oxygenation. Sci Rep 6:29965. https://doi.org/10.1038/srep29965
39. Grosenick D, Cantow K, Arakelyan K, Wabnitz H, Flemming B, Skalweit A, Ladwig M, Macdonald R, Niendorf T, Seeliger E (2015) Detailing renal hemodynamics and oxygenation in rats by a combined near-infrared spectroscopy and invasive probe approach. Biomed Opt Express 6(2):309–323
40. Seeliger E, Cantow K, Arakelyan K, Ladwig M, Persson PB, Flemming B (2014) Low-dose nitrite alleviates early effects of an X-ray contrast medium on renal hemodynamics and oxygenation in rats. Investig Radiol 49(2):70–77
41. Edwards A, Silldorff EP, Pallone TL (2000) The renal medullary microcirculation. Front Biosci 5:E36–E52
42. Zimmerhackl BL, Robertson CR, Jamison RL (1987) The medullary microcirculation. Kidney Int 31(2):641–647
43. Schurek HJ (1988) Kidney medullary hypoxia: a key to understanding acute renal failure? die Nierenmarkhypoxie: ein Schlussel zum Verstandnis des akuten Nierenversagens? Klin Wochenschr 66(18):828–835
44. Baumgartl H, Leichtweiss HP, Lubbers DW, Weiss C, Huland H (1972) The oxygen supply of the dog kidney: measurements of intrarenal pO_2. Microvasc Res 4(3):247–257
45. Lubbers DW, Baumgartl H (1997) Heterogeneities and profiles of oxygen pressure in brain and kidney as examples of the pO_2 distribution in the living tissue. Kidney Int 51(2):372–380
46. Evans RG, Ow CPC (2018) Heterogeneity of renal cortical oxygenation: seeing is believing. Kidney Int 93(6):1278–1280. https://doi.org/10.1016/j.kint.2018.01.039
47. Hirakawa Y, Mizukami K, Yoshihara T, Takahashi I, Khulan P, Honda T, Mimura I, Tanaka T, Tobita S, Nangaku M (2018) Intravital phosphorescence lifetime imaging of the renal cortex accurately measures renal hypoxia. Kidney Int 93(6):1483–1489. https://doi.org/10.1016/j.kint.2018.01.015
48. Evans RG, Harrop GK, Ngo JP, Ow CP, O'Connor PM (2014) Basal renal O_2 consumption and the efficiency of O_2 utilization for Na^+ reabsorption. Am J Physiol Renal Physiol 306(5):F551–F560
49. Vallon V, Muhlbauer B, Osswald H (2006) Adenosine and kidney function. Physiol Rev 86(3):901–940
50. Just A (2007) Mechanisms of renal blood flow autoregulation: dynamics and contributions. Am J Physiol Regul Integr Comp Physiol 292 (1):R1–R17
51. O'Connor PM (2006) Renal oxygen delivery: matching delivery to metabolic demand. Clin Exp Pharmacol Physiol 33(10):961–967
52. Blantz RC, Weir MR (2004) Are the oxygen costs of kidney function highly regulated? Curr Opin Nephrol Hypertens 13(1):67–71
53. Schurek HJ, Jost U, Baumgartl H, Bertram H, Heckmann U (1990) Evidence for a preglomerular oxygen diffusion shunt in rat renal cortex. Am J Physiol 259(6 Pt 2):F910–F915
54. Ngo JP, Ow CP, Gardiner BS, Kar S, Pearson JT, Smith DW, Evans RG (2016) Diffusive shunting of gases and other molecules in the renal vasculature: physiological and evolutionary significance. Am J Physiol Regul Integr Comp Physiol 311(5):R797–r810. https://doi.org/10.1152/ajpregu.00246.2016
55. Leong CL, Anderson WP, O'Connor PM, Evans RG (2007) Evidence that renal arterial-venous oxygen shunting contributes to dynamic regulation of renal oxygenation. Am J Physiol Renal Physiol 292:F1726–F1733
56. Pappenheimer JR, Kinter WB (1956) Hematocrit ratio of blood within mammalian kidney and its significance for renal hemodynamics. Am J Physiol 185:377
57. Hoff U, Lukitsch I, Chaykovska L, Ladwig M, Arnold C, Manthati VL, Fuller TF, Schneider W, Gollasch M, Muller DN, Flemming B, Seeliger E, Luft FC, Falck JR, Dragun D, Schunck WH (2011) Inhibition of 20-HETE synthesis and action protects the kidney from ischemia/reperfusion injury. Kidney Int 79(1):57–65
58. Hosszu A, Antal Z, Lenart L, Hodrea J, Koszegi S, Balogh DB, Banki NF, Wagner L, Denes A, Hamar P, Degrell P, Vannay A, Szabo AJ, Fekete A (2017) sigma1-receptor Agonism protects against renal ischemia-reperfusion injury. J Am Soc Nephrol 28(1):152–165. https://doi.org/10.1681/asn.2015070772
59. Cantow K, Flemming B, Ladwig-Wiegard M, Persson PB, Seeliger E (2017) Low dose nitrite improves reoxygenation following renal ischemia in rats. Sci Rep 7(1):14597–15058
60. Pohlmann A, Cantow K, Huelnhagen T, Grosenick D, Dos Santos PJ, Boehmert L, Gladytz T, Waiczies S, Flemming B, Seeliger E, Niendorf T (2017) Experimental MRI monitoring of renal blood volume

fraction variations En route to renal magnetic resonance oximetry. Tomography 3 (4):188–200. https://doi.org/10.18383/j.tom.2017.00012

61. Kumar P (2009) Systemic effects resulting from carotid body stimulation-invited article. Adv Exp Med Biol 648:223–233. https://doi.org/10.1007/978-90-481-2259-2_26
62. Lahiri S, Forster RE 2nd (2003) CO_2/H(+) sensing: peripheral and central chemoreception. Int J Biochem Cell Biol 35 (10):1413–1435
63. Catchlove SJ, Pipingas A, Hughes ME, Macpherson H (2018) Magnetic resonance imaging for assessment of cerebrovascular reactivity and its relationship to cognition: a systematic review. BMC Neurosci 19(1):21. https://doi.org/10.1186/s12868-018-0421-4
64. Corfield DR, McKay LC (2016) Regional cerebrovascular responses to hypercapnia and hypoxia. Adv Exp Med Biol 903:157–167. https://doi.org/10.1007/978-1-4899-7678-9_11
65. Brezis M, Agmon Y, Epstein FH (1994) Determinants of intrarenal oxygenation. I. Effects of diuretics. Am J Physiol 267(6 Pt 2): F1059–F1062. https://doi.org/10.1152/ajprenal.1994.267.6.F1059
66. Warner L, Glockner JF, Woollard J, Textor SC, Romero JC, Lerman LO (2011) Determinations of renal cortical and medullary oxygenation using blood oxygen level-dependent magnetic resonance imaging and selective diuretics. Investig Radiol 46(1):41–47. https://doi.org/10.1097/RLI.0b013e3181f0213f
67. Prasad PV, Edelman RR, Epstein FH (1996) Noninvasive evaluation of intrarenal oxygenation with BOLD MRI. Circulation 94 (12):3271–3275. https://doi.org/10.1161/01.cir.94.12.3271
68. Palmucci S, Mammino L, Caltabiano DC, Costanzo V, Foti PV, Mauro LA, Farina R, Profitta ME, Sinagra N, Ettorre GC, Veroux M, Basile A (2019) Diffusion-MR in kidney transplant recipients: is diuretic stimulation a useful diagnostic tool for improving differentiation between functioning and non-functioning kidneys? Clin Imaging 53:97–104. https://doi.org/10.1016/j.clinimag.2018.10.003
69. Haddock B, Larsson HBW, Francis S, Andersen UB (2019) Human renal response to furosemide: simultaneous oxygenation and perfusion measurements in cortex and medulla. Acta Physiol (Oxf) 227:e13292. https://doi.org/10.1111/apha.13292
70. Welch WJ (2002) Adenosine A1 receptor antagonists in the kidney: effects in fluid-retaining disorders. Curr Opin Pharmacol 2 (2):165–170
71. Gili S, Barbero U, Errigo D, De Luca G, Biondi-Zoccai G, Leone AM, Iannaccone M, Montefusco A, Omede P, Moretti C, D'Amico M, Gaita F, D'Ascenzo F (2018) Intracoronary versus intravenous adenosine to assess fractional flow reserve: a systematic review and meta-analysis. J Cardiovasc Med (Hagerstown) 19(6):274–283. https://doi.org/10.2459/jcm.0000000000000652
72. Solerno R, Pedroni P, Mariani J, Sarmiento R (2018) Comparison of sodium nitroprusside and adenosine for fractional flow reserve assessment: a systematic review and meta-analysis. Expert Rev Cardiovasc Ther 16(10):765–770. https://doi.org/10.1080/14779072.2018.1513789

Chapter 5

Preparation of Ex Vivo Rodent Phantoms for Developing, Testing, and Training MR Imaging of the Kidney and Other Organs

Jason M. Millward, João S. Periquito, Paula Ramos Delgado, Christian Prinz, Thoralf Niendorf, and Sonia Waiczies

Abstract

Here we describe a simple and inexpensive protocol for preparing ex vivo rodent phantoms for use in MR imaging studies. The experimental animals are perfused and fixed with formaldehyde, and then wrapped with gauze and sealed with liquid latex. This yields a phantom that preserves all organs in situ, and which avoids the need to keep fixed animals and organs in containers that have dimensions very different from living animals. This is especially important for loading in MR detectors, and specifically the RF coils, they are usually used with. The phantom can be safely stored and conveniently reused, and can provide MR scientists with a realistic phantom with which to establish protocols in preparation for preclinical in vivo studies—for renal, brain, and body imaging. The phantom also serves as an ideal teaching tool, for trainees learning how to perform preclinical MRI investigations of the kidney and other target organs, while avoiding the need for handling living animals, and reducing the total number of animals required.

This protocol chapter is part of the PARENCHIMA initiative "MRI Biomarkers for CKD" (CA16103), a community-driven Action of the European Cooperation in Science and Technology (COST) program of the European Union, which aims to improve the reproducibility and standardization of renal MRI biomarkers.

Key words Ex vivo methods, Rat, Mouse, Phantom, Magnetic resonance imaging (MRI), Kidney

1 Introduction

Prior to starting any preclinical in vivo MRI study, it is essential to invest time to test novel imaging techniques, optimize MR pulse sequence parameters and develop a workflow tailored to address the specific scientific questions at hand [1]. Much of this work can be done without using living animals, by constructing synthetic phantoms using materials that have similar MR properties as the tissue of interest (e.g., agarose). Ultimately, a point is reached when the limitations of synthetic phantoms impede progress, and phantoms that are more biologically realistic are needed. In some cases this

Andreas Pohlmann and Thoralf Niendorf (eds.), *Preclinical MRI of the Kidney: Methods and Protocols*, Methods in Molecular Biology, vol. 2216, https://doi.org/10.1007/978-1-0716-0978-1_5,

can be accomplished using ex vivo tissue samples removed from experimental animals postmortem. The tissues are chemically fixed (usually with formaldehyde), and samples embedded in tubes or containers for imaging. However, this removes the organs from their surrounding environment. In the case of renal MR, it is advantageous to image the kidney in situ, within its biological context, including the surrounding organs and perirenal fat. The typical solution for this problem is to use ex vivo phantoms, which consist of the intact experimental animal (usually rats or mice) placed inside a sealed container along with the fixation solution. This solution is suboptimal. The containers used generally have a cylindrical or rectangular shape, which is substantially different from the shape of an animal. This can be problematic given the space constraints of the MR hardware (e.g., RF coil diameter, size of the animal holding bed). In some cases the container size may mean that a larger field of view needs to be acquired than would otherwise be necessary for a living animal. It may also be difficult, or impossible, to use surface RF coils to scan samples embedded in a container. For example, when scanning the brain or the kidney, positioning the sample such that the target organ is as close as possible to the RF coil could be problematic if the container is in the way. Furthermore, the additional mass of the fixation liquid in a container with a rat or mouse body can substantially change the loading in the coil, which could cause problems with matching and tuning. The shape of the container can also cause other problems; the curved and conical shapes of typical laboratory plastic tubes can interfere with shimming the main magnetic field B_0.

Here we describe a simple and inexpensive method to prepare ex vivo phantoms using mice or rats that are perfused and chemically fixed, covered in gauze and sealed with latex. This solution results in a phantom that preserves the biological context of the organs of interest, and which is much more similar to the original animal in terms of dimensions and loading. It avoids the use of containers of toxic formaldehyde solution. The phantoms can be readily used by imaging scientists and scientists from related fields who are not trained in the handling of living experimental animals. This makes the phantom an ideal teaching tool for educating trainees learning how to perform preclinical studies, while also avoiding the confounding effects of motion artifacts. Finally, the phantoms can be easily stored and reused for extended periods of time. This will substantially reduce the total number of animals required for developing new MRI methods, and will facilitate more efficient and effective in vivo studies, thus consistent with the 3R principles of animal research [2, 3].

This chapter is part of the book Pohlmann A, Niendorf T (eds) (2020) Preclinical MRI of the Kidney—Methods and Protocols. Springer, New York.

2 Materials

2.1 Animals

The method described here can be used for any animal strain. The choice of strain depends on the specific needs of the researcher. Ideally, the specific rat or mouse strain should be consistent with the strain that will be used for the corresponding in vivo experiments. Most importantly the size and geometry of the animal should be comparable to that of the animal used for in vivo experiments, to ensure that the loading will be similar between phantom and in vivo experiments.

2.2 Perfusion and Dissection

All steps of the protocol should be conducted in accordance with procedures approved by the local Animal Welfare Department and authorities and conform to guidelines to minimize discomfort to animals (86/609/EEC).

The perfusion should be done in a lab environment equipped for dealing with hazardous fumes, using a chemical fume hood (alternatively fume extraction dome hoods) due to the respiratory hazards of formaldehyde. The lab should also have appropriate mechanisms in place for disposing of formaldehyde liquid waste, solid materials contaminated with formaldehyde (e.g., paper tissues), as well as animal carcasses (e.g., freezer for temporary storage; capacity for incineration).

1. Anesthesia (e.g., ketamine–xylazine various suppliers). Or alternative for terminal anesthesia, as per individual institutional experimental animal use guidelines.
2. Surgical instruments (scissors, rongeurs, forceps, hemostat).
3. Syringes (1 ml, 20 ml, 60 ml); needles (26 Gauge, 23 Gauge Butterfly).
4. 70% ethanol in a spray bottle.
5. Solutions for perfusion: phosphate buffered saline (PBS); formaldehyde solution (e.g., 4% aq. paraformaldehyde [PFA]).
6. Airtight plastic container for storage of the animal during the post-fixation step (*see* **Note 1**).

2.3 Latex Covering

1. Liquid latex (e.g., 0.3% ammonia prevulcanized, low-viscosity—various suppliers).
2. Surgical gauze.
3. 3-O surgical suture (e.g., Ethicon.com, product code C003D).
4. Fine paintbrushes.
5. Hair dryer.

3 Methods

3.1 Perfusion and Fixation

1. Administer a terminal dose of anesthetic—here we used an intraperitoneal injection of a mixture of ketamine (100 mg/kg) and xylazine (5 mg/kg) diluted in 0.9% NaCl. We used the same dose for mouse and rat, adjusted for individual body weight.
2. Confirm that the animal has reached the required depth of anesthesia, for example by checking for absence of a reflex response to stimulation of the hind paws.
3. Place the animal in supine position on a work surface (e.g., Styrofoam covered with aluminum foil), and fix the extremities of the animal to the surface.
4. Apply 70% ethanol to the ventral surface, taking care not to spray the facial region.
5. With forceps, grasp the sternum, and make an incision into the thoracic cavity with large scissors.
6. Carefully expand the thoracic space with the scissors, taking care not to cut any major blood vessels. Cut down the ribs at the lateral sides to allow for blood drainage. Carefully separate the heart from the surrounding connective tissue. Cut through the diaphragm, and expose the inferior vena cava and the descending aorta. Attach a hemostat clamp to the sternum, and reflect backward to reveal the now opened thoracic cavity.
7. Visualize the separation between the left and right ventricles (slight color difference). Insert the needle into the **left ventricle** of the heart. Take care not to insert the needle too far, or you will enter the right ventricle. *MOUSE—inject a total volume of 20 ml PBS, using a 20 ml syringe with a 26G needle. *RAT—inject a total volume of 180 ml PBS, using 60 ml syringes attached to a tube connected to a 23G butterfly needle. After inserting the needle into the heart, use a hemostat to clamp the butterfly needle. Cut the inferior vena cava.
8. Start PBS perfusion by slowly depressing the plunger, alternatively use a perfusion pump if available. Observe the color change in the liver: as a sign that the perfusion is correct, the deep red color changes to dull brown as the blood is drained (*see* **Note 2**) *RAT—after finishing with the first 60 ml syringe, replace the empty syringe with a filled one. Repeat with a third syringe to complete the full 180 ml volume.
9. Start fixation by perfusing with 4% PFA (*see* **Note 3**) (this step should be done under a ventilation system, to avoid exposure to the hazardous PFA fumes). *MOUSE—switch from the 20 ml PBS syringe to a syringe filled with 20 ml PFA. Reinsert the needle in the left ventricle, into the same injection point,

used by the previous needle (look for a small dark spot). *RAT—attach the 60 ml syringe with PFA directly to the tube connected to the butterfly needle. At this point the exsanguination and perfusion is complete.

10. Postfixation. Place the animal body into a sealable plastic container and fill with PFA and stored at room temperature for approximately 1 week (*see* **Note 1**).

3.2 Disarticulation

Removal of the extremities (disarticulation) can be performed at the discretion of the researcher, depending on the objective, and depending on the space constraints of the specific hardware (RF coil diameter, dimensions of the animal holding bed) that the animal phantom is to be used with. In some cases it may be sufficient to secure the forelimb and hind limb into position by suturing them to the body, before wrapping the body with gauze. Regardless, the tail should be removed. In addition, it may be necessary to remove the skin, in order to tailor the size of the phantom to the hardware dimensions. Here we describe in detail how to perform the disarticulation on a rat. In the mouse, this is easily accomplished using standard surgical scissors.

1. Remove the skin around the joint of the forelimb and the shoulder (scapular joint) with surgical scissors. Using a scalpel, dissect the musculature around the scapula (Fig. 1a). Using the fingers, feel for the location of the joint (Fig. 1b). When the joint is exposed, use rongeurs to separate the scapula, and remove the entire forelimb (Fig. 1c). Repeat the process on the other side.
2. The procedure for the hind limbs is similar. Remove the skin around the joint of the femur and hip. Using a scalpel, dissect the musculature around the femur, and feel for the location of the ball and socket hip joint (where the femur fits in the acetabulum of the pelvis). When the joint is exposed, cut the tendons with a scalpel, or cut the bone directly using rongeurs (Fig. 1a). Repeat on the other side.
3. Use a scalpel to dissect the musculature of the tail at the proximal end. Expose the coccyx, and separate the tail using rongeurs. The disarticulation is now complete.
4. Proceed with removing the skin of the remaining body. Using scissors, cut through the skin at the level of the neck—the skin of the head can remain in place. Remove the skin and any extraneous tissue from the exposed thoracic cavity and the dorsal thoracic region. Use the fingers to separate the skin and expand the subcutaneous space in the dorsal lumbar region. Make a midline cut of the skin with scissors, and use a scalpel to separate the rest of the skin from the underlying

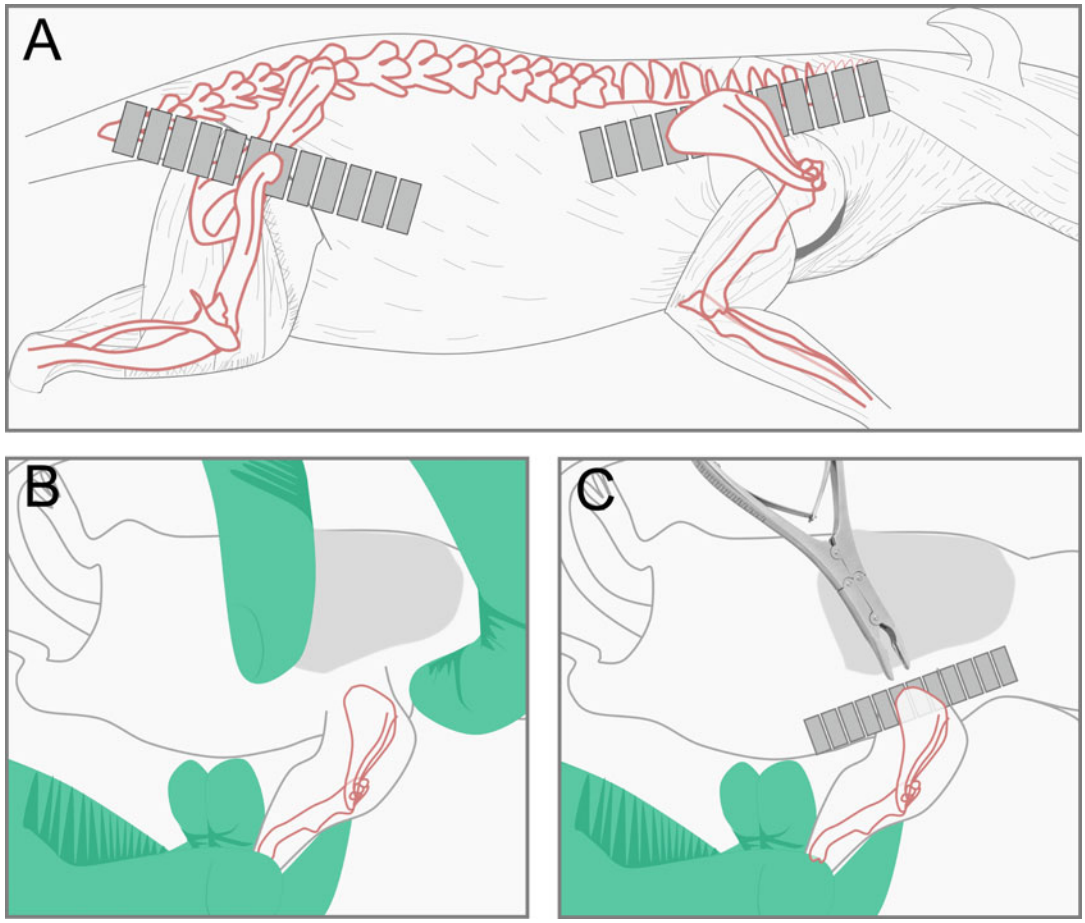

Fig. 1 Schematic for disarticulation. The location of the cut-points for removing the forelimb and hind limb is depicted by the gray lines (**a**). After cutting the overlying musculature, the joint of the scapula can be visualized (**b**). The forelimb is reflected back, and the joint cut using rongeurs (**c**)

tissue. Continue removing skin from the ventral lumbar region, taking care not to pierce the peritoneum.

5. The skin of the head can remain in place, since the head will not be covered with gauze. Remove the ears (exposing the auditory cavity), trim the whiskers and remove extraneous tissue from the lower mandible region.

3.3 Coating with Gauze and Latex

In the next steps the fixed and disarticulated body will be wrapped in gauze and covered in liquid latex.

1. Starting from the neck, tightly wrap the thoracic region with gauze. It may be necessary to fill part of the thoracic cavity that was opened during the perfusion step with gauze, in order to eliminate empty space and have a securely wrapped phantom. Continue wrapping the lumbar/sacral region with gauze; a

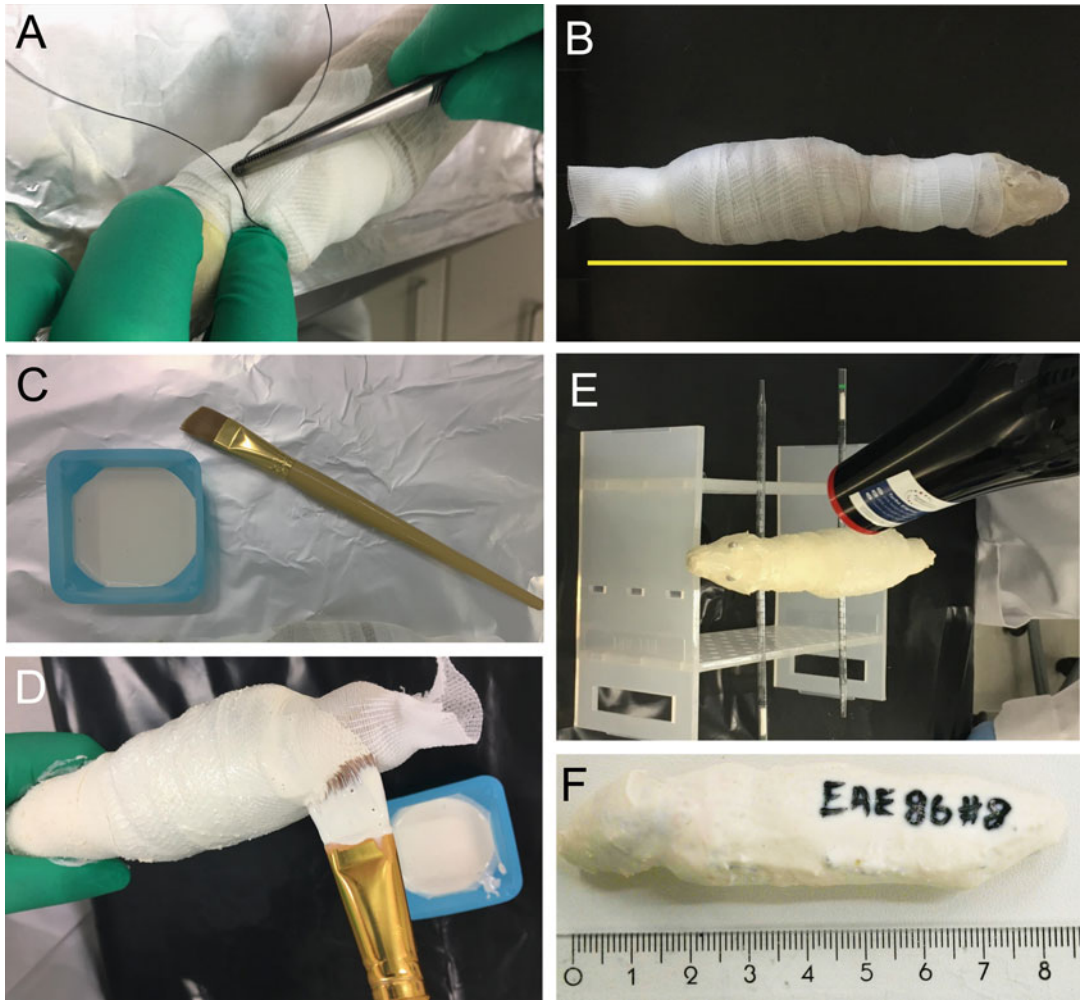

Fig. 2 Workflow for preparation of the phantom. The rat body is wrapped tightly with gauze, which is then fixed securely to the underlying musculature using surgical sutures (**a**). The entire body is covered with gauze, except for the head, which remains unwrapped (scale bar = 22 cm) (**b**). Liquid latex is applied directly to the surface of the phantom using a paintbrush (**c**, **d**). The phantom is place on an improvised holder, here a laboratory tube rack with pipettes. A hair dryer is used to accelerate the drying process (**e**). An example of a completed, labeled mouse phantom (**f**)

small extension of gauze can remain at the posterior end to serve as a grip when applying the latex.

2. Firmly attach the gauze to the underlying muscle tissue using standard surgical sutures (Fig. 2a). The phantom is now ready to be covered with latex (Fig. 2b).
3. Pour some liquid latex into a suitable container; for example, a plastic weigh boat used with a standard laboratory scale is ideal. Using a flat paintbrush, apply the first coat of latex directly to the gauze (Fig. 2b, c). All surfaces should be completely

covered, although avoid excessive latex. It is preferable to apply the latex with a brush, rather than simply submerging the phantom in latex.

4. Generously apply latex to the head, taking care to fill the auditory cavity and the oral cavity.
5. Place the phantom on a support to dry, allowing air to circulate. Here we improvised a support using a laboratory tube rack and pipettes (Fig. 2d).
6. Use a standard hair dryer to apply warm air (c. 5–10 min), to accelerate the drying of the latex (Fig. 2d). Allow additional time (c. 20 min) to dry at room temperature.
7. The phantom will be easier to handle once the first coat of latex is dry. Then, apply a second coat of liquid latex, ensuring that all gaps are completely covered. Make sure that the oral cavity is completely sealed. Apply the latex generously; the objective is to ensure that there is a complete watertight seal over the entire surface. Repeat the drying process with the hair dryer, and allow to air dry completely at room temperature.
8. The phantom is now finished. It is possible to write on the surface of the dry latex with a permanent felt-tipped marker, for example to record useful information about the animal (Fig. 2f).
9. The phantom can be used at room temperature, for example inside the MRI scanner, for extended periods. Long-term storage should be at 4 °C.

4 Example Images

In Fig. 3 we show representative images of MRI scans of the ex vivo phantoms. These scans were performed on a Bruker Biospec 9.4 Tesla USR94/20 animal MRI scanner (Bruker Biospin, Ettlingen, Germany).

4.1 Rat

MRI scans targeting the rat kidney were acquired in the coronal (Fig. 3a, b) and sagittal (Fig. 3d, e) planes. The identical MRI hardware setup (including the RF coils) and pulse sequence parameters were used to acquire the images of the ex vivo phantom (Fig. 3a, d) and an in vivo rat of the same strain and approximate mass as the animal used to prepare the phantom (Fig. 3b, e). The in vivo scans were done as described in the chapter by Pohlmann A et al. "Experimental Protocol for MRI Mapping of the Blood Oxygenation-Sensitive Parameters T_2^* and T_2 in the Kidney." The ex vivo and in vivo scans show a comparable level of detail, and the kidneys (denoted by "K") can be seen in relation to the surrounding tissues. MRI sequence parameters are listed in **Note 4**.

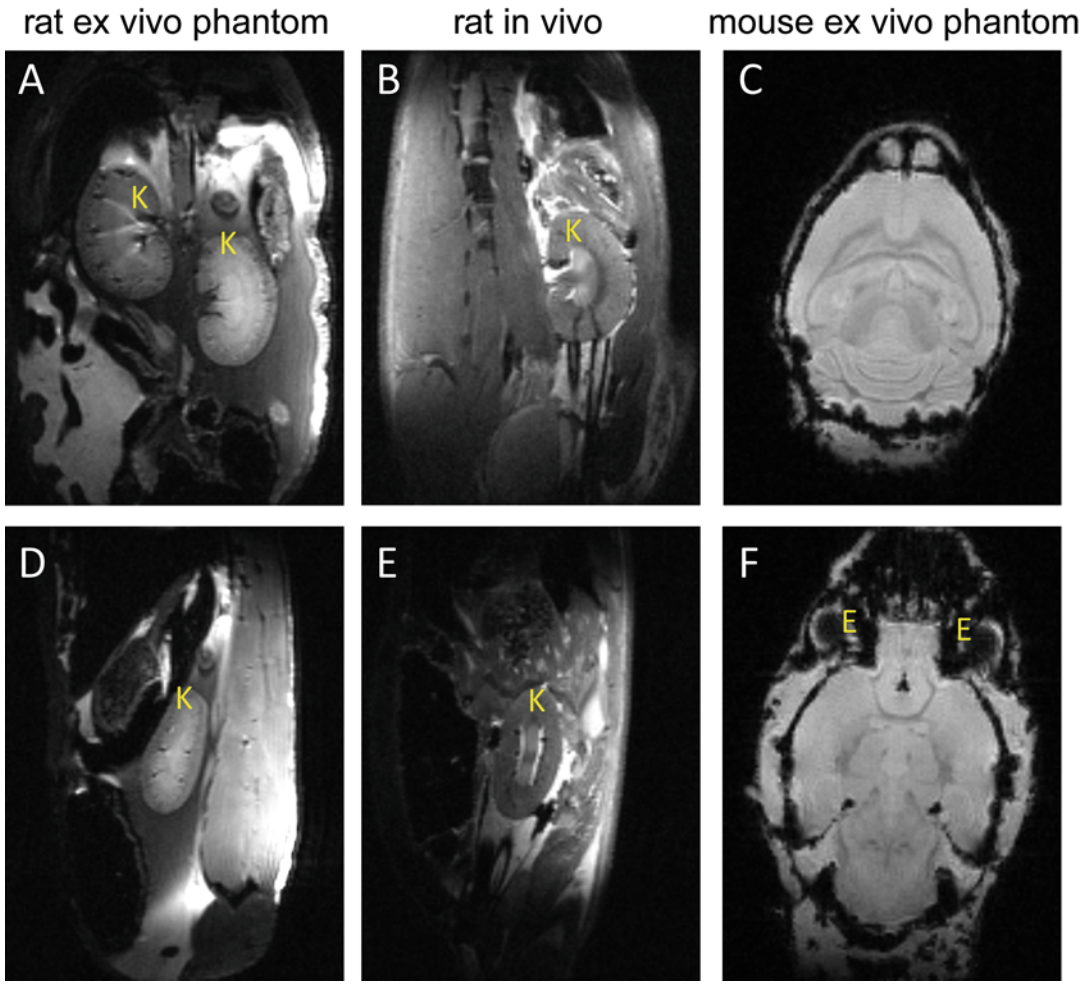

Fig. 3 Representative ex vivo and in vivo MR images. MRI scans targeting the rat kidney were acquired in the coronal (**a**, **b**) and sagittal (**d**, **e**) planes. Identical MRI hardware and pulse sequence parameters were used to acquire the images of the ex vivo phantom (**a**, **d**) and in vivo images of a rat of the same strain and approximate mass as the animal used to prepare the phantom (**b**, **e**). The kidneys are denoted by "K." MRI scans targeting the mouse brain were acquired in the coronal plane in the ex vivo phantom (**c**, **f**). Images show the brain in relation to surrounding structures such as the skull, and the eyes (denoted by "**e**")

4.2 Mouse

MRI scans targeting the mouse brain were acquired in the coronal plane in the ex vivo phantom (Fig. 3c, f). A mid-brain slice shows good contrast between gray matter and white matter structures, and the skull can be seen on the exterior of the brain (Fig. 3c). A lower brain slice (from a more inferior level) shows the brain in relation to surrounding tissue structures, for example the eyes (denoted by "E") (Fig. 3f). MRI sequence parameters are listed in **Note 5**.

5 Notes

1. The container should be large enough that the animal is completely submerged in the formaldehyde solution and also suited for preserving the shape of the animal (e.g., curvature of the body) during postfixation.
2. Ensure that no PBS leaks from the mouth and nose region: this is a sign that the needle has shifted position into the right ventricle (and that the PBS is being perfused into the respiratory circulation, not the systemic circulation). If this occurs, remove the needle and reposition into the left ventricle.
3. Formaldehyde fixation solutions such as 4% aq. PFA or 10% neutral buffered formalin are widely used, but other fixation solutions may be substituted, as suit the needs of the experimenter. One variation is to add 8 mM of gadolinium-based contrast agent, to change the relaxation properties of the tissue in the ex vivo preparation [4]. Another alternative is to use a zinc-based fixation solution [5].
4. MR images of the rat ex vivo and in vivo were acquired using a RARE sequence: TR = 540 ms, TE = 12 ms, FOV = 70 × 52 × 35 mm, matrix = 128 × 172 × 5, number of averages = 4, slice thickness = 0.7 mm. acquisition time = 1 min 9 s.
5. MR images of the mouse ex vivo phantom were acquired using a FLASH sequence: TR = 50 ms, TE = 8 ms, FOV = 20 × 20 × 12 mm, matrix = 160 × 160 × 96, number of averages = 4, slice thickness = 12 mm, acquisition time = 56 min 32 s.

Acknowledgments

This work was funded in part (Thoralf Niendorf, Sonia Waiczies, Joao Periquito) by the German Research Foundation (Gefoerdert durch die Deutsche Forschungsgemeinschaft (DFG), Projektnummer 394046635, SFB 1365, RENOPROTECTION. Funded by the Deutsche Forschungsgemeinschaft (DFG, German Research Foundation), Project number 394046635, SFB 1365, RENOPROTECTION).
This chapter is based upon work from COST Action PARENCHIMA, supported by European Cooperation in Science and Technology (COST). COST (www.cost.eu) is a funding agency for research and innovation networks. COST Actions help connect research initiatives across Europe and enable scientists to enrich their ideas by sharing them with their peers. This boosts their research, career, and innovation.

PARENCHIMA (renalmri.org) is a community-driven Action in the COST program of the European Union, which unites more than 200 experts in renal MRI from 30 countries with the aim to improve the reproducibility and standardization of renal MRI biomarkers.

References

1. Cunha L, Horvath I, Ferreira S, Lemos J, Costa P, Vieira D, Veres DS, Szigeti K, Summavielle T, Mathe D, Metello LF (2014) Preclinical imaging: an essential ally in modern biosciences. Mol Diagn Ther 18(2):153–173. https://doi.org/10.1007/s40291-013-0062-3
2. Graham ML, Prescott MJ (2015) The multifactorial role of the 3Rs in shifting the harm-benefit analysis in animal models of disease. European J Pharmacol 759:19–29. https://doi.org/10.1016/j.ejphar.2015.03.040
3. Russell WMS, Burch RL (1959) The principles of humane experimental technique. Methuen & Co. Ltd., London
4. Cleary JO, Wiseman FK, Norris FC, Price AN, Choy M, Tybulewicz VL, Ordidge RJ, Brandner S, Fisher EM, Lythgoe MF (2011) Structural correlates of active-staining following magnetic resonance microscopy in the mouse brain. NeuroImage 56(3):974–983. https://doi.org/10.1016/j.neuroimage.2011.01.082
5. Mori H, Soonsawad P, Schuetter L, Chen Q, Hubbard NE, Cardiff RD, Borowsky AD (2015) Introduction of zinc-salt fixation for effective detection of immune cell-related markers by immunohistochemistry. Toxicol Pathol 43(6):883–889. https://doi.org/10.1177/0192623315587593

Part III

Basic Concepts of Measurement Techniques

Chapter 6

Quantitative Assessment of Renal Perfusion and Oxygenation by Invasive Probes: Basic Concepts

Kathleen Cantow, Roger G. Evans, Dirk Grosenick, Thomas Gladytz, Thoralf Niendorf, Bert Flemming, and Erdmann Seeliger

Abstract

Renal tissue hypoperfusion and hypoxia are early key elements in the pathophysiology of acute kidney injury of various origins, and may also promote progression from acute injury to chronic kidney disease. Here we describe basic principles of methodology to quantify renal hemodynamics and tissue oxygenation by means of invasive probes in experimental animals. Advantages and disadvantages of the various methods are discussed in the context of the heterogeneity of renal tissue perfusion and oxygenation.

This chapter is based upon work from the COST Action PARENCHIMA, a community-driven network funded by the European Cooperation in Science and Technology (COST) program of the European Union, which aims to improve the reproducibility and standardization of renal MRI biomarkers. This introduction chapter is complemented by a separate chapter describing the experimental procedure and data analysis.

Key words Renal hemodynamics and oxygenation, In vivo methods, Quantitative invasive probes

1 Introduction

Kidney diseases are a global health burden with steadily increasing prevalence and incidence [1–5]. Animal studies have provided evidence that acute kidney injury (AKI) of various origins shares a common link in the pathophysiological chain of events, ultimately leading to AKI, as well as to progression from AKI to chronic kidney disease (CKD): imbalance between renal oxygen delivery and oxygen demand [3, 6–13]. Renal tissue hypoperfusion and hypoxia have also been suggested to play a pivotal role in the pathophysiology of other kidney diseases including diabetic kidney disease [14–16].

The majority of the preclinical studies that generated this concept utilized a set of invasive probes to measure renal hemodynamics and oxygenation in anesthetized animals [12, 14, 17–20]. These methods have also been used (1) to study mechanisms of

Andreas Pohlmann and Thoralf Niendorf (eds.), *Preclinical MRI of the Kidney: Methods and Protocols*, Methods in Molecular Biology, vol. 2216, https://doi.org/10.1007/978-1-0716-0978-1_6,

physiological control of renal hemodynamics and oxygenation and (2) the effects of various substances on this control in healthy animals, (3) to test several putative preventive or therapeutic approaches for AKI and CKD in animal models, and (4) for the purpose of calibrating functional magnetic resonance imaging (MRI) including renal blood oxygenation level-dependent MRI (BOLD-MRI) that makes use of the quantitative MR parameter T_2*, which is a surrogate for blood oxygenation [18–28].

The invasive probes typically include (1) a perivascular flow probe for measurement of total renal blood flow, (2) laser-Doppler-optodes for assessment of local tissue perfusion, (3) Clark-type electrodes or fluorescence-quenching optodes for measurements of local tissue partial pressure of oxygen (pO_2), and (4) devices for invasive measurement of arterial blood pressure. These methods are considered the gold standard for the study of renal hemodynamics and oxygenation, because the methods, with the exception of the laser-Doppler fluxmetry, provide calibrated quantitative data [25, 29, 30]. Step-by-step protocols for application of these techniques in two setups, one for stand-alone experiments in laboratories for integrative physiology, and the other for experiments within small-animal MR scanners by use of a hybrid setup, are provided in the chapter by Cantow K et al. "Monitoring Renal Hemodynamics and Oxygenation by Invasive Probes: Experimental Protocol".

As with all established modalities available in today's experimental and translational research, these techniques have shortcomings and methodological limitations. In particular, their invasiveness, for obvious ethical reasons, precludes their use in humans. The invasiveness is, furthermore, a considerable hurdle for implementation of these methods in long-term and longitudinal studies: although invasive probes have been used in conscious, chronically instrumented animals [22, 24, 31–37], the vast majority of studies has been performed in "terminal experiments" in anesthetized animals. This is a major limitation of all invasive techniques because the measurements are by necessity potentially confounded by the effects of anesthesia (*see* the chapter by Kaucsar T et al. "Preparation and Monitoring of Small Animals in Renal MRI").

The measurement of intrarenal tissue perfusion and tissue oxygenation is quite challenging, because of their vast spatial heterogeneity both among the renal layers (cortex, outer medulla, and inner medulla) and within the layers. In this chapter, the causes and the degree for this spatial variability are outlined first, before the basic principles of methodology to quantify renal hemodynamics and oxygenation by means of invasive probes in experimental animals are described together with a discussion of the pros and cons of the various methods.

This introduction chapter is complemented by a separate chapter describing the experimental procedure, which is part of this book.

This chapter is part of the book Pohlmann A, Niendorf T (eds) (2020) Preclinical MRI of the Kidney—Methods and Protocols. Springer, New York.

2 Heterogeneity of Intrarenal Perfusion and Oxygenation—Causes and Degree of Variability

Intrarenal local tissue pO_2 is determined by the balance between local O_2 supply and local O_2 consumption. Additionally, determinants of local O_2 diffusion play a role. Local O_2 supply depends on local blood perfusion, local vessel density, and local blood pO_2 and blood O_2 content. Local O_2 consumption is foremost determined by local metabolic demand. Blood perfusion within the kidney is much more heterogeneous than within most other organs, due to its particular vascular architecture [8, 38–40].

From the branches of the renal artery that enter the kidney at its hilus, interlobar arteries arise, which align with the medullary–cortical axis. From interlobar arteries emerge arcuate arteries that run along the boundary between the cortex and the medulla, that is, perpendicular to the medullary–cortical axis. From the latter, interlobular arteries branch off at regular intervals at angles of about 90 degrees, so that they all enter the renal cortex. For this reason, virtually all the blood flowing into the kidney perfuses the cortex first [8, 25, 38, 41–43]. The interlobular arteries are in close proximity to interlobular veins, together forming what might be called "vascular bundles" that run in parallel at regular distances from the corticomedullary boundary toward the capsule. Within the cortex, interlobular arteries branch off into afferent (preglomerular) arterioles, from which glomerular capillaries arise that, in turn, rejoin into efferent (postglomerular) arterioles. The efferent arterioles from the subcapsular and mid-cortical glomeruli branch off into networks of peritubular capillaries. The efferent arterioles of the deep cortical (juxtamedullary) glomeruli, however, branch off at about the corticomedullary boundary to form capillary-like vessels, the descending vasa recta [38–40]. These very straight and exceptionally long vessels descend toward the papilla. The descending vasa recta provide virtually all blood that perfuses the medulla. As a consequence, only 10–15% of blood that previously passes through the cortex, will reach the medulla, and the vascular density is much lower in the medulla than the cortex [8, 25, 38, 41–43]. The descending vasa recta are in close proximity with the ascending vasa recta, thus forming distinct "vascular bundles" that run in parallel at regular distances through the medulla [38–40].

These particularities of the intrarenal vascular architecture have a number of salient consequences with regard to local blood

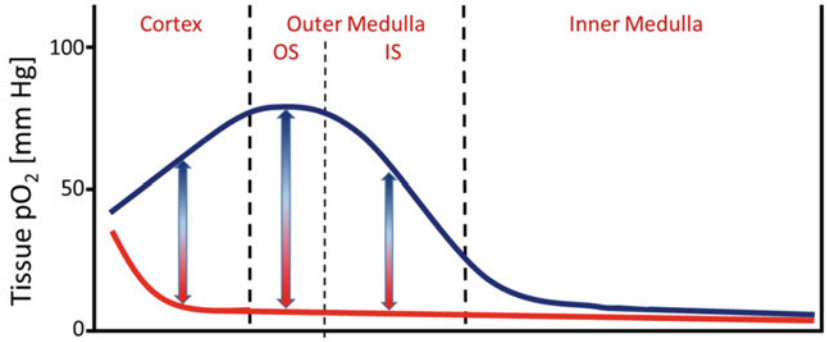

Fig. 1 Scheme depicting the range of intrarenal tissue partial pressure of oxygen (pO_2). The red curve depicts values at the greatest distance from two neighboring "vascular bundles," the blue one that directly adjacent to "vascular bundles" (for details see text); OS (outer stripe), IS (inner stripe). Original data were obtained by measurements in in anesthetized dogs and rats [43–45]

perfusion and thus the local O_2 supply. First, the striking difference in the quantity of blood perfusion between the cortex and the medulla, together with the difference in their vascular densities, is one of the major reasons for the low tissue pO_2 in the medulla. Second, the Fåhræus–Lindqvist effect that lowers the hematocrit and thereby the O_2 content of blood in the vasa recta that supply the medulla, contributes to low medullary O_2 delivery [39, 40]. Third, diffusive shunting of O_2 between the arcuate and interlobular arteries and their respective veins in the cortex as well as between the descending and ascending vasa recta in the medulla, owing to the close proximities of the respective vessels, are a further major reason behind the "physiological hypoxia" of the medulla. Thus, blood pO_2 is higher in the venous vessels than in the capillaries these venous vessels drain. Fourth, due to the particular vascular architecture with distinct "vascular bundles" that comprise arterial vessels with high pO_2 and venous vessels with relatively high pO_2 (due mainly to the low fractional O_2 extraction of the renal tissue), there are huge differences in local pO_2 even within a given renal layer under physiological conditions [25, 41, 43–47]. Fifth, plasma skimming at intrarenal vessel branches results in different hematocrit and therefore O_2 content of blood perfusing the daughter vessels, which also contributes to the local pO_2 differences [39, 48].

The schematic shown in Fig. 1 depicts the range of local pO_2 values as measured by invasive Clark-type electrodes in the kidneys of rats and dogs under physiological conditions in vivo [43–45]. These measurements reveal that local tissue pO_2 levels in the cortex vary dramatically, foremost according to the distance to the "vascular bundles" of interlobular arteries and veins: pO_2 values range from 10 mmHg at the greatest distance from two neighboring "bundles," to up to 70 mmHg around the "bundles." In

addition, local cortical tissue pO_2 varies with the distance to the arcuate arteries located at the corticomedullary boundary. Also, the range of tissue pO_2 variability in the outer medulla is huge (*see* Fig. 1): whereas pO_2 is less than 10 mmHg in locations at maximum distance from the "vascular bundles" of descending and ascending vasa recta, pO_2 is up to 75 mmHg in close proximity to these "bundles." In the inner medulla, tissue pO_2 is rather homogenous: in general, it usually amounts to less than 15 mmHg.

The huge differences in tissue pO_2 among the renal layers not only reflect the differences in O_2 supply but also the different O_2 consumption of the distinct sections of the tubules located in the respective renal layers. Tubular resorption relies on active transport processes, which account for about 85% of the kidney's energy expenditure and, therefore, its O_2 consumption [8, 49]. The proximal tubule and the distal convoluted tubule, which constitute the majority of tubular segments within the cortex, consume much O_2 because a huge amount of osmolytes is resorbed by active transport in these segments. On the other hand, tubular sections such as the thin descending and the thin ascending limbs of Henle's loop and the medullary collecting duct, which are the most abundant tubular sections within the medulla, feature very low to nonexisting active transport. Yet the thick ascending limbs of Henle's loop, which are located in the outer medulla, consume much O_2, because of their active resorption of osmolytes [8, 25, 41, 43–47, 50]. The high O_2 demands of the thick ascending limbs in relation to the rather low O_2 supply of the outer medulla, consequent to its particular vascular architecture, exposes this renal layer to the greatest risk for hypoxic tissue damage [6–14, 43, 51, 52].

3 Methods: Methodologic Principles, Advantages, and Disadvantages

Techniques for invasive measurements of renal hemodynamics and oxygenation comprise readily (commercially) available methods and devices that are employed in many laboratories of integrative kidney physiology worldwide, but also techniques that are established only in one or a few laboratories. The widely used methods are described first. They include (1) perivascular flow probes for measurement of total renal blood flow, (2) laser-Doppler-optodes for assessment of local tissue perfusion, (3) Clark-type electrodes for measurements of local tissue pO_2, (4) fluorescence-quenching optodes for the same purpose, (5) devices for invasive measurement of arterial blood pressure, and (6) pimonidazole adduct immunohistochemistry for assessment of renal tissue hypoxia.

The pimonidazole technique is included here because of its widespread usage, although it is an exceptional case for two reasons. First, in contrast to the other techniques, this approach does not allow investigators to monitor a given parameter over time, but

only provides a snapshot: Pimonidazole is injected at a single time point in vivo, and pimonidazole adducts formed in severely hypoxic tissue are visualized in ex vivo samples [53–55]. Second, although the technique has been used for two decades, it was subjected to close scrutiny only recently [55]. Upon this careful investigation major pitfalls were identified and detailed—which, at least in part, cast doubts on the reliability of previously published results—and methods to address and overcome these issues have been proposed [55].

In the final part of this chapter, a few selected examples of methods are discussed that are not (yet) generally available but presently established in only one or a few laboratories.

3.1 Transonic Flow Probes

Today's gold standard for whole kidney blood flow measurements is a flow probe attached to the renal artery or to the renal vein that makes use of ultrasound transit time differences. This method was established in the late 1970s and provides continuous absolute measurements of blood flow (in mL per min) independent of the actual flow velocity profile, the actual vessel diameter, and the actual hematocrit [56]. The commercially available device (Transonic™, Transonic Systems Inc.) comprises an electronic flow detection unit (flowmeter) and perivascular probes [57, 58]. The flow probe consists of two ultrasonic transducers and a fixed acoustic reflector (*see* Fig. 2a). The flow probe is positioned on the blood vessel so that the vessel lies within the acoustic sensing window defined by

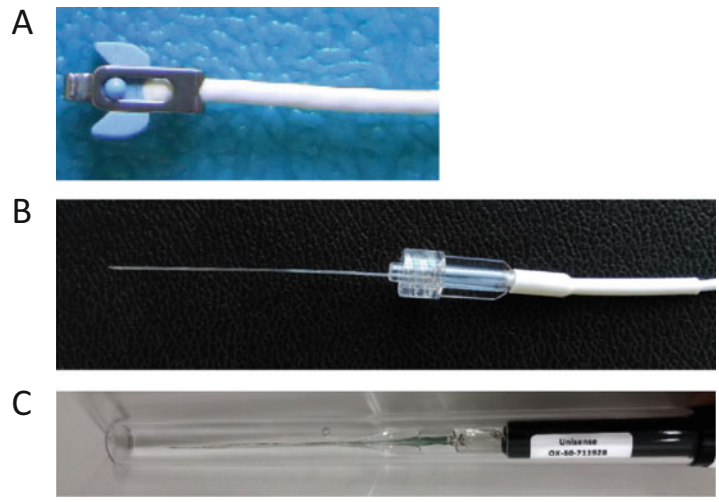

Fig. 2 Photographs of typical probes for invasive measurements. (**a**) Perivascular Transonic™ flow probe for measurement of total renal blood flow. (**b**) Combined fluorescence-quenching-laser-Doppler probe (OxyLite/OxyFlo™) for simultaneous measurements of local tissue pO_2 and assessment of local tissue perfusion in the same circumscribed area. (**c**) Clark-type electrode for measurement of local tissue pO_2

the transducers and the metallic reflector. Probes are available in various sizes to fit the dimensions of the blood vessel of interest.

The flowmeter directs the flow probe through measurement cycles [57, 58]. First, a wide beam of ultrasound is emitted by the downstream transducer. It intersects the vessel in the upstream direction, is reflected by the acoustic reflector, then intersects the vessel again before being received by the upstream transducer. The flowmeter records the transit time. Then, the transit–receive sequence is repeated, but with the transmitting and receiving functions of the transducers reversed, that is, the vessel is bisected by the beam in the downstream direction. The transit time during the upstream cycle is higher than during the downstream cycle, because the ultrasound beam travels against the blood flow in the first, and with the blood flow in the latter cycle. The difference in the transit times is directly proportional to blood volume flow. Due to the wide ultrasonic beams, all flowing blood is accounted for; thus, the transit time is sampled at all points across the vessel diameter, and the volume flow measurement is independent of the flow velocity profile [57, 58].

An accurate measure of volumetric flow is obtained by the perivascular probes even when the vessel is smaller than the acoustic window, because the parts of the ultrasonic beam that do not intersect the vessel do not contribute to the signal [57, 58]. However, air effectively blocks ultrasound transmission, and even small air bubbles compromise measurement accuracy. Therefore, all spaces between the vessel and probe must be filled with a suitable acoustic coupling agent. In case of "terminal experiments" in anesthetized animals, where the abdomen is opened, this can be achieved by simply filling the abdominal cavity with isotonic saline (at 37 °C) [27]. Acoustic coupling gels can also be used and are available from the supplier of the probes. Fatty tissue also affects the ultrasonic beam; thus, the vessel of interest must be thoroughly prepared by gently removing fatty tissue [27].

Measurements of total renal blood flow by means of Transonic™ devices have also been performed in chronically instrumented animals [22, 31, 33, 58, 59]. Here, the perivascular probe becomes encapsulated by tissue, which stabilizes its position. En route to calibration of functional MRI for the study of renal hemodynamics and oxygenation, an integrated multimodality approach was developed that enables measurements of invasive gold standard parameters and functional MR parameters simultaneously for the same kidney in an ultrahigh field small animal scanner (MR-PHYSIOL) [25–28]. For such a setup, a special Transonic™ flow probe is used: its acoustic reflector is made of Macor ceramics instead of stainless steel or brass to meet the safety and compatibility requirements of MRI (*see* the chapter by Cantow K et al. "Monitoring Renal Hemodynamics and Oxygenation by Invasive Probes: Experimental Protocol").

With the introduction of the Transonic™ technique, all other methods used for quantitative assessment of total renal blood flow in experimental animals including but not limited to electromagnetic probes and microsphere techniques were rendered obsolete.

3.2 Laser-Doppler Optodes

In the 1970s, laser-Doppler probes were developed that estimate local blood perfusion within circumscribed areas of tissue [60, 61]. For this purpose, pulsed light of a distinct wavelength (e.g., 785 nm) is guided via an optical fiber into the tissue subjacent to the tip of the fiber, where it is scattered within the tissue. A fraction of the light encounters erythrocytes, is reflected, and is fed back via the fiber to the photodetecting device of the apparatus. From the amount of reflected light the concentration of erythrocytes per tissue volume is estimated. Because erythrocytes move with the bloodstream, the reflected light becomes frequency shifted due to the Doppler effect. The photodetected signal comprises a broad spectrum of Doppler frequency shifted signals from which the average velocity of erythrocytes is derived. An estimate of microvascular blood perfusion is than calculated by the apparatus as the product of mean erythrocyte velocity and mean erythrocyte concentration in the volume of tissue under illumination from the probe [61].

The most important limitation of the laser-Doppler technique is that it can only provide arbitrary, nonabsolute, units for blood perfusion rather than an absolute value of blood flow, which is why the method is often termed laser-Doppler-fluxmetry [25]. This is due to the fact that the actual sampling volume could only be determined if it were possible to identify which erythrocytes have interacted with the light reflected from the tissue. The latter depends on the optical scattering and absorption coefficients of the tissue. Since these coefficients vary considerably with regard to the local microvasculature and its perfusion at the time of measurement, it is impossible to determine the actual sampling volume and thus the blood flow in absolute terms [61].

Estimated mean sampling depths for mammal tissues range from 0.5–1.5 mm, corresponding to "captured" volumes of roughly 1 mm^3 of tissue. However, these values must be lower in regions with large light absorption due to large amounts of erythrocytes per volume such as the renal cortex, and lower in the inner medulla with its low amount of erythrocytes per volume [38–40, 61].

Considering the rather small volume of tissue for which the laser-Doppler data are obtained versus the heterogeneity of intrarenal perfusion, extrapolation of the results of one area to other areas, even of the same renal layer, is unfeasible. Because of the impossibility to provide absolute data, laser-Doppler-fluxmetry allows investigators only to report relative changes occurring while the optode is fixed in place. Therefore, only continuous and

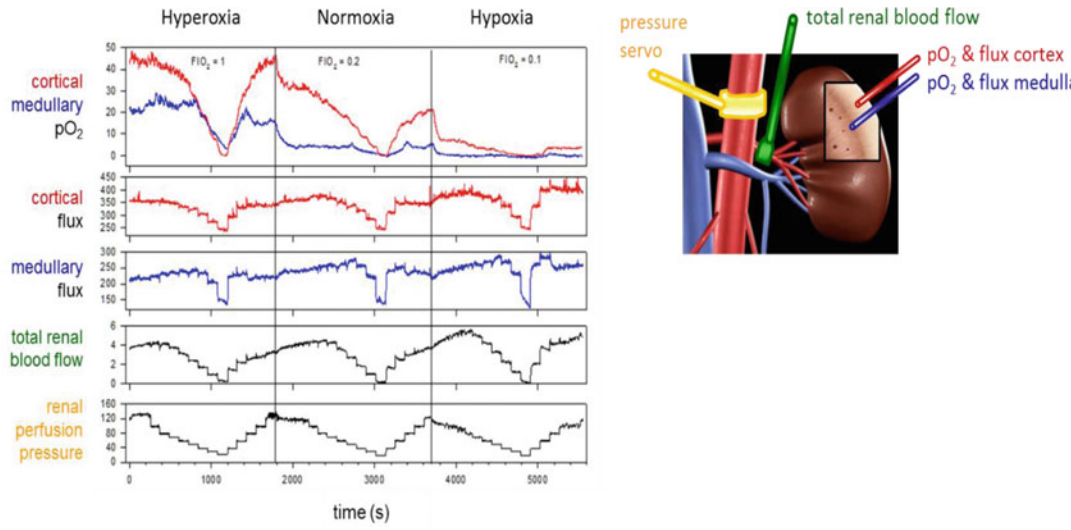

Fig. 3 Original tracings of invasively measured parameters of renal hemodynamic and oxygenation in an anesthetized rat (left panel) and sketch of the left kidney with the locations of the used probes (right panel). The rat was exposed to staircasewise reductions in renal perfusion pressure followed by staircasewise pressure restorations performed by means of a servo-controlled inflatable occluder placed around the suprarenal aorta (pressure servo) [22]. This was done under normoxic (inspiratory fraction of O_2, $FiO_2 = 0.2$), hyperoxic ($FiO_2 = 1.0$), and hypoxic ($FiO_2 = 0.1$) conditions

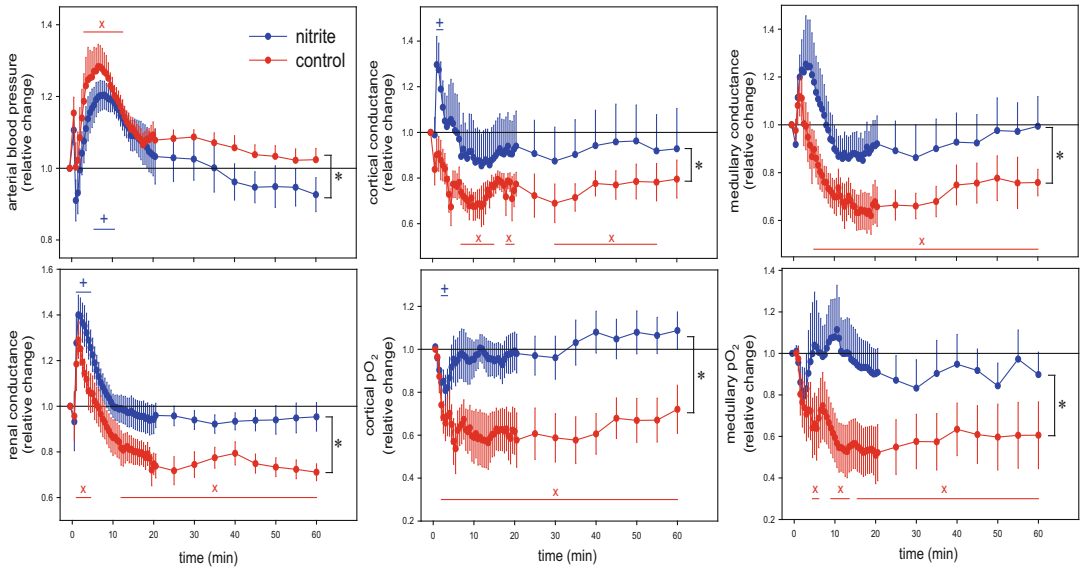

Fig. 4 Time courses of invasively measured parameters of renal hemodynamics and oxygenation in two groups of anesthetized rats that both received a 1.5 mL bolus injection of an X-ray contrast medium (iodixanol 320 mg iodine per mL) into the thoracic aorta at time 0. In the blue group, a low dose of nitrite was administered by continuous infusion, while in the red group saline was infused (control). Conductance values (the reciprocal of vascular resistance) were calculated by dividing the respective perfusion values by arterial blood pressure, in order to distinguish flow changes that result from passive circular distension/compression of vessels from those actively exerted by vascular smooth muscles. Values (mean ± SEM) are given as relative changes from baseline. Redrawn from Ref. 20

quantifiable changes relative to baseline (control) measurements are recorded, typically induced by acute interventions such as changes in renal arterial pressure or the inspiratory O_2 fraction, or by the administration of drugs (*see* Figs. 3 and 4) [18–20, 22, 23, 25, 28, 62]. Yet even interpretation of changes in laser-Doppler data recorded during such maneuvers must be done with due caution: they could rely on changes in local hematocrit, for example, due to changes in plasma skimming, rather than changes in blood flow [25, 39, 48].

In many studies on renal hemodynamics, data from two probes are recorded, one placed within the cortex and the other one in the (outer) medulla. This approach has been also employed in chronically instrumented rats [22]. It must be noted, that the potential tissue injury inflicted by the insertion of the optodes (usual tip diameters range from 50 to 300 μm) may confound the results. Laser-Doppler fluxmetry devices are supplied by various manufacturers. Oxford Optronics, Ltd., provides combined fluorescence-quenching and laser-Doppler optodes (OxyLite/OxyFlo™) that enable simultaneous recordings of local tissue pO_2 (vide infra) and of relative changes in local tissue perfusion in the same circumscribed area of renal tissue (*see* Fig. 2b).

3.3 Clark-Type Electrodes

These polarographic electrodes were developed in the 1950s by Clark and colleagues [63]. The electrodes consist of a noble metal (e.g., silver, gold, platinum) which reduces O_2 due to a negative polarizing voltage. The difference in voltage between the reference electrode (anode) and the measuring electrode (cathode) is proportional to the amount of O_2 molecules being reduced on the cathode. This enables quantification of tissue pO_2 (absolute values in mmHg). The critical technical advance was electrical insulation of the anode and cathode with a gas-permeable but liquid-impermeable membrane. This approach provided the foundation for the development of miniaturized versions (*see* Fig. 2c) with tips as small as 1–5 μm, that enable quantification of pO_2 even in specific vascular and tubular elements of the kidney [64, 65]. Using such small electrodes, Lübbers, Baumgärtl, and colleagues were the first to document the vast heterogeneity of renal tissue pO_2 among as well as within the renal layers that is depicted by Fig. 1 [43–45]. These authors generated "spatial maps" with the frequency distribution of pO_2 values ("pO_2 histograms") from the cortex to the inner medulla, by moving the electrodes through the renal tissues using a nanostepper technique (step width 50 μm).

While "pO_2 histograms" have also been obtained in a few recent studies [66, 67], the majority of studies uses fixed electrodes, making sure that the tips remain at the same location within the kidney throughout the experiment. Often, one electrode is placed within the cortex and the other one in the (outer) medulla. The

tissue volume that is "captured" by the electrodes has probably about the same diameter as the tip of the electrode; thus, standard electrodes of $\leq$10 μm diameter obtain pO_2 values that are representative for a relatively small tissue volume only [67]. In the face of the spatial heterogeneity of intrarenal pO_2, this constitutes a major limitation of this technique. On the other hand, the potential tissue injury inflicted by the insertion of these small electrodes is less than with bigger electrodes or fluorescence quenching optodes that enable better "spatial averaging" (vide infra) [24, 35, 67]. Another drawback of Clark-type electrodes is O_2 consumption due to their electrochemical reduction, which is particularly unfavorable in areas with a fragile balance between O_2 delivery and demand such as the renal medulla [67–70].

Furthermore, it is not technically feasible to make repeated measurements in the same anesthetized animal over time-frames longer than a few hours. Yet, recently, a telemetric method using carbon paste electrodes has been developed that allows assessment of renal tissue pO_2 in conscious rats [35]. This method provides exquisite temporal resolution [24]. The major limitations of the method are (1) that it requires considerable skill and expertise to construct and implant the devices, (2) that tissue pO_2 can only be monitored at a single location in each animal, and (3) that only relative changes in tissue pO_2, rather than absolute levels are measured.

3.4 Fluorescence-Quenching Optodes

In the 1990s, a fiber-optic oxygen-sensing device was developed that measures pO_2 from the lifetime of fluorescence of a (ruthenium- or platinum-based) luminophore at the tip of an optode [70, 71]. The probe is connected to a pO_2 meter developed by Oxford Optronics, Ltd., that generates short pulses of blue LED light, which are transmitted via the fiber to the tip of the optode [70]. The resulting emission of fluorescent light is quenched by the presence of O_2 molecules. The OxyLite™ instrument measures the lifetime of each pulse of fluorescence, which is approximately inversely proportional to the pO_2 according to the Stern-Volmer equation at pO_2 values between 0 and 100 mmHg [68, 71].

Direct comparisons between Clark-type electrodes and quenching optodes reveal their respective advantages and disadvantages [67, 68, 70]. Both techniques share the disadvantage of invasiveness, and the advantage of enabling absolute quantification of pO_2 (in mmHg). Advantages of the optode include the absence of O_2 consumption and a greater accuracy at low pO_2, which is of particular importance when it comes to measurements in the renal medulla. In contrast to the electrodes that "capture" a tissue volume that is approximately equal to their tip diameter, optodes do not "capture" a proper volume. The pO_2 measured by the optodes is that within the probe-head (at the tip) of the optode itself, which covers a circular area of 230 μm diameter [67, 68, 70]. The larger

diameter of the optodes as compared with that of standard pO_2 electrodes increases the risk for tissue damage. On the other hand, it facilitates a favorable "spatial averaging" of renal tissue pO_2 values in the face of their huge spatial heterogeneity. In fact, "pO_2histograms" of renal cortical pO_2 obtained in rabbits by a fluorescence optode were more tightly distributed than those provided by a Clark-type electrode, which may aid detection of (patho)-physiologically significant changes in intrarenal oxygenation [67]. Finally, the optodes have been proven to be MR compatible and MR safe [25, 26].

As mentioned earlier, combined fluorescence-quenching-laser-Doppler probes (OxyLite/OxyFlo™) enable simultaneous measurements of local tissue pO_2 and assessment of local tissue perfusion in the same circumscribed area (*see* Fig. 2b).

3.5 Monitoring of Arterial Blood Pressure

It is mandatory for in vivo studies in anesthetized experimental animals, be it studies on control of renal hemodynamics and oxygenation or on every other functional parameter, to monitor cardiovascular variables such as arterial blood pressure and heart rate throughout the experiment in order to ascertain that physiological cardiovascular control is maintained. In anesthetized animals this is best achieved by use of invasive techniques: a fluid-filled catheter inserted into a conduit artery (e.g., femoral or carotid arteries) connected to one of the various commercially available pressure transducers and quantitatively calibrated via a recording device (*see* the chapter by Cantow K et al. "Monitoring Renal Hemodynamics and Oxygenation by Invasive Probes: Experimental Protocol").

Direct intra-arterial measurements in unanesthetized animals is the most physiologically relevant means of arterial pressure determination. Telemetric pressure monitoring is the gold standard in conscious animals, and various telemetric devices are commercially available [72, 73]. A limitation of this technique is that implantation surgery and maintenance of catheters require considerable skill [72]. The tail-cuff method is a simple noninvasive plethysmographic technique to assess arterial pressure in conscious rats and mice [74, 75]. Since the conditions for tail-cuff measurements necessarily involve heating and restraint of the animal, which almost inevitably alter the measured parameter (arterial pressure), the physiological meaningfulness of the results is questionable [73].

3.6 Pimonidazole Adduct Immunohistochemistry

This method was originally developed for detection of hypoxia in tumors, but subsequently adapted for use in the kidney [53]. For this technique, pimonidazole (usually 60 mg/kg of body mass) is administered to the experimental animal in vivo [54]. Pimonidazole forms adducts within hypoxic (<approximately 10 mmHg) cells. These adducts are immunohistochemically visualized in ex vivo samples of the kidney. The advantage of this technique is that it provides good spatial resolution of renal tissue hypoxia at the

cellular level. Its major limitations include (1) that it detects severe hypoxia only, with a cutoff of about 10 mmHg, (2) that hypoxia can only be assessed postmortem, and (3) only at a single time point. Those using this technique must also be aware of two major sources of false-positive detection of hypoxia, as recently revealed [55]. Firstly, pimonidazole adducts can form postmortem in cells that were not hypoxic in the living animal. For this reason, it is recommended that kidney tissue be perfusion fixed, rather than immersion fixed. Secondly, when the standard (mouse) monoclonal antibody is used, false positive staining has been observed in damaged rat kidney tissue, presumably as a result of the anti-mouse secondary antibody binding to mouse-like antigens in the damaged tissue. This problem can be avoided by use of a newly commercially available polyclonal anti-pimonidazole antibody raised in rabbits [55].

3.7 Examples of Methods That Are Not Generally Available

3.7.1 Bladder pO_2

It is not technically feasible to measure renal tissue pO_2 in humans. It can also be technically difficult to measure renal tissue pO_2 in experimental animals unless they are deeply anesthetized. However, it is technically feasible to measure the pO_2 of urine in both experimental animals and man. There has been a long history of interest in this approach for monitoring renal medullary tissue oxygenation [76]. However, with the recent development of fiber-optic probes that can be inserted into a standard Foley bladder catheter, it has been possible to subject this method to close scrutiny [77]. Available evidence now indicates that urinary pO_2 can provide a good estimate of renal medullary pO_2 [77]. Because this technique can be deployed in humans equipped with a bladder catheter, it provides a translational pathway for development of approaches to improve renal medullary oxygenation in human patients at risk of AKI. It is also noteworthy that low urinary pO_2 during cardiac surgery requiring cardiopulmonary bypass predicts development of postoperative AKI. In light of this, urinary pO_2 measurements may provide a real-time measure of medullary oxygenation and predict the risk of AKI in critically ill patients. The major limitation of this approach is that the combination of low urine flow and high arterial pO_2 can confound the relationship between urinary pO_2 and medullary pO_2 [77].

3.7.2 Near Infrared Spectroscopy

Near infrared spectroscopy (NIRS), together with models for diffuse optical imaging affords the measurement of (1) tissue concentrations of oxygenated hemoglobin (oxyHb) and deoxygenated hemoglobin (deoxyHb), (2) oxygen saturation of Hb (StO_2) within tissues, and (3) tissue blood volume fraction in vivo. In particular, spatially resolved reflectance NIRS (SRR-NIRS), together with Monte-Carlo simulations of diffuse light propagation, has been applied to monitor these parameters within renal

cortical tissue [78]. Quantification of the underlying absorption and reduced scattering coefficients of the tissue is based on analyzing the decrease of the intensity of diffusely remitted light with increasing distance from the light injection point. Recording techniques for the renal cortex of anesthetized rats have been established, with a linear fiber array placed on the ventral surface of the exposed kidney. Measurements have been done at selected near-infrared wavelengths between about 670 and 850 nm by multiplexing millisecond pulses from the different laser sources in time. In this way, quantitative measurements of renal cortex parameters have been achieved at a repetition rate of multiple Hz [78].

SRR-NIRS has been successfully combined with "classical" invasive techniques to study renal hemodynamics and oxygenation in rats [78]. Thus, SRR-NIRS-derived parameters such as the amount of Hb per tissue volume and StO_2 were obtained simultaneously with parameters including total renal blood flow, local cortical tissue perfusion and tissue pO_2 in the same kidney. Control of renal hemodynamics and oxygenation was studied by dedicated reversible test interventions including brief occlusions of the renal artery or the renal vein, short-term hypoxia, hyperoxia, and hypercapnia, and administration of adenosine. The results demonstrate that the combined approach, by providing different but complementary information, enables a more comprehensive characterization of renal hemodynamics and oxygenation [78].

The SRR-NIRS technique could also serve to help calibrate renal T_2* MRI. This MR surrogate parameter for blood oxygenation is related to the amount of deoxyHb per tissue volume. Confounders of the T_2* to tissue pO_2 relationship include the vascular volume fraction, the local hematocrit, and shifts of the oxyHb dissociation curve [25–28]. Since SRR-NIRS enables quantitative monitoring of the amount of Hb per tissue volume and of StO_2 it is an ideal candidate to unravel and quantify the contributions of confounding factors to renal T_2* MRI.

By extending the wavelength range beyond 900 nm, the tissue water content can additionally be assessed, which, together with the reduced scattering coefficients at the different wavelengths, can serve as a surrogate for other (patho)physiologically relevant parameters such as the tubular volume fraction.

Application of SRR-NIRS in reflection mode constrains measurements to the renal cortex of rats. Recently it was demonstrated that changes of rat medullary Hb parameters can also be assessed by SRR-NIRS in transmission mode using an additional fiber placed on the dorsal surface of the kidney [79].

3.7.3 *Intravital Microscopy*

Perhaps the "final frontier" in methods for assessing renal oxygenation are techniques that provide cellular resolution, in real time, in living animals. Hirakawa and colleagues have recently reported use

of a technique they call "intravital phosphorescence lifetime imaging microscopy" [47]. This technique allows cellular pO_2 in the renal cortex of live animals to be resolved to the level of individual tubular cross-sections. It requires injection of a molecule whose phosphorescence is quenched by O_2. Thus, pO_2 can be measured by assessing the decay curve of the phosphorescence. Such probes are available that accumulate intracellularly or are retained within the vasculature. Thus, it is possible to use this approach to assess the heterogeneity of renal blood and tissue pO_2 in real time with unprecedented cellular resolution. Currently, the technique is limited for use in the superficial cortex.

Acknowledgments

This work was funded, in part (Kathleen Cantow, Thoralf Niendorf, and Erdmann Seeliger), by the German Research Foundation (Gefoerdert durch die Deutsche Forschungsgemeinschaft (DFG), Projektnummer/Project number 394046635, SFB 1365, RENOPROTECTION).

The authors wish to thank Ariane Anger and Andrea Gerhardt for expert technical assistance and Dr. Connie Ow for the image shown in Fig. 2c.

This chapter is based upon work from COST Action PARENCH IMA, supported by European Cooperation in Science and Technology (COST). COST (www.cost.eu) is a funding agency for research and innovation networks. COST Actions help connect research initiatives across Europe and enable scientists to enrich their ideas by sharing them with their peers. This boosts their research, career, and innovation.

PARENCHIMA (renalmri.org) is a community-driven Action in the COST program of the European Union, which unites more than 200 experts in renal MRI from 30 countries with the aim to improve the reproducibility and standardization of renal MRI biomarkers.

References

1. Fortrie G, de Geus HRH, Betjes MGH (2019) The aftermath of acute kidney injury: a narrative review of long-term mortality and renal function. Crit Care 23(1):24. https://doi.org/10.1186/s13054-019-2314-z
2. Selby NM, Taal MW (2019) Long-term outcomes after AKI-a major unmet clinical need. Kidney Int 95(1):21–23. https://doi.org/10.1016/j.kint.2018.09.005
3. Zuk A, Bonventre JV (2019) Recent advances in acute kidney injury and its consequences and impact on chronic kidney disease. Curr Opin Nephrol Hypertens 28(4):397–405. https://doi.org/10.1097/mnh.0000000000000504
4. Levin A, Tonelli M, Bonventre J, Coresh J, Donner JA, Fogo AB, Fox CS, Gansevoort RT, Heerspink HJL, Jardine M, Kasiske B, Kottgen A, Kretzler M, Levey AS, Luyckx VA, Mehta R, Moe O, Obrador G, Pannu N, Parikh CR, Perkovic V, Pollock C, Stenvinkel P, Tuttle KR, Wheeler DC, Eckardt KU (2017) Global kidney health 2017 and beyond: a roadmap for closing gaps in care, research, and policy. Lancet 390(10105):1888–1917. https://doi.org/10.1016/s0140-6736(17)30788-2

5. Bello AK, Levin A, Tonelli M, Okpechi IG, Feehally J, Harris D, Jindal K, Salako BL, Rateb A, Osman MA, Qarni B, Saad S, Lunney M, Wiebe N, Ye F, Johnson DW (2017) Assessment of global kidney health care status. JAMA 317(18):1864–1881. https://doi.org/10.1001/jama.2017.4046
6. Brezis M, Rosen S (1995) Hypoxia of the renal medulla--its implications for disease. N Engl J Med 332:647–655
7. Fähling M, Seeliger E, Patzak A, Persson PB (2017) Understanding and preventing contrast-induced acute kidney injury. Nat Rev Nephrol 13(3):169–180
8. Evans RG, Ince C, Joles JA, Smith DW, May CN, O'Connor PM, Gardiner BS (2013) Haemodynamic influences on kidney oxygenation: the clinical implications of integrative physiology. Clin Exp Pharmacol Physiol 40:106–122
9. Evans RG, Ow CP, Bie P (2015) The chronic hypoxia hypothesis: the search for the smoking gun goes on. Am J Physiol Renal Physiol 308 (2):F101–F102
10. Shu S, Wang Y, Zheng M, Liu Z, Cai J, Tang C, Dong Z (2019) Hypoxia and hypoxia-inducible factors in kidney injury and repair. Cell 8(3). https://doi.org/10.3390/cells8030207
11. Hultstrom M, Becirovic-Agic M, Jonsson S (2018) Comparison of acute kidney injury of different etiology reveals in-common mechanisms of tissue damage. Physiol Genomics 50 (3):127–141. https://doi.org/10.1152/physiolgenomics.00037.2017
12. Calzavacca P, Evans RG, Bailey M, Bellomo R, May CN (2015) Cortical and medullary tissue perfusion and oxygenation in experimental septic acute kidney injury. Crit Care Med 43 (10):e431–e439
13. Ma S, Evans RG, Iguchi N, Tare M, Parkington HC, Bellomo R, May CN, Lankadeva YR (2019) Sepsis-induced acute kidney injury: a disease of the microcirculation. Microcirculation 26(2):e12483. https://doi.org/10.1111/micc.12483
14. dos Santos EA, Li LP, Ji L, Prasad PV (2007) Early changes with diabetes in renal medullary hemodynamics as evaluated by fiberoptic probes and BOLD magnetic resonance imaging. Investig Radiol 42(3):157–162. https://doi.org/10.1097/01.rli.0000252492.96709.36
15. Calvin AD, Misra S, Pflueger A (2010) Contrast-induced acute kidney injury and diabetic nephropathy. Nat Rev Nephrol 6 (11):679–688
16. Hansell P, Welch WJ, Blantz RC, Palm F (2013) Determinants of kidney oxygen consumption and their relationship to tissue oxygen tension in diabetes and hypertension. Clin Exp Pharmacol Physiol 40(2):123–137
17. Seeliger E, Flemming B, Wronski T, Ladwig M, Arakelyan K, Godes M, Mockel M, Persson PB (2007) Viscosity of contrast media perturbs renal hemodynamics. J Am Soc Nephrol 18 (11):2912–2920
18. Hoff U, Lukitsch I, Chaykovska L, Ladwig M, Arnold C, Manthati VL, Fuller TF, Schneider W, Gollasch M, Muller DN, Flemming B, Seeliger E, Luft FC, Falck JR, Dragun D, Schunck WH (2011) Inhibition of 20-HETE synthesis and action protects the kidney from ischemia/reperfusion injury. Kidney Int 79(1):57–65
19. Cantow K, Flemming B, Ladwig-Wiegard M, Persson PB, Seeliger E (2017) Low dose nitrite improves reoxygenation following renal ischemia in rats. Sci Rep 7(1):14597–15058
20. Seeliger E, Cantow K, Arakelyan K, Ladwig M, Persson PB, Flemming B (2014) Low-dose nitrite alleviates early effects of an X-ray contrast medium on renal hemodynamics and oxygenation in rats. Investig Radiol 49(2):70–77
21. Seeliger E, Wronski T, Ladwig M, Dobrowolski L, Vogel T, Godes M, Persson PB, Flemming B (2009) The renin-angiotensin system and the third mechanism of renal blood flow autoregulation. Am J Physiol Renal Physiol 296(6):F1334–F1345
22. Flemming B, Seeliger E, Wronski T, Steer K, Arenz N, Persson PB (2000) Oxygen and renal hemodynamics in the conscious rat. J Am Soc Nephrol 11(1):18–24
23. Cantow K, Pohlmann A, Flemming B, Ferrara F, Waiczies S, Grosenick D, Niendorf T, Seeliger E (2016) Acute effects of ferumoxytol on regulation of renal hemodynamics and oxygenation. Sci Rep 6:29965. https://doi.org/10.1038/srep29965
24. Emans TW, Janssen BJ, Pinkham MI, Ow CP, Evans RG, Joles JA, Malpas SC, Krediet CT, Koeners MP (2016) Exogenous and endogenous angiotensin-II decrease renal cortical oxygen tension in conscious rats by limiting renal blood flow. J Physiol 594(21):6287–6300. https://doi.org/10.1113/jp270731
25. Pohlmann A, Cantow K, Hentschel J, Arakelyan K, Ladwig M, Flemming B, Hoff U, Persson PB, Seeliger E, Niendorf T (2013) Linking non-invasive parametric MRI with invasive physiological measurements (MR-PHYSIOL): towards a hybrid and integrated approach for investigation of acute

kidney injury in rats. Acta Physiol (Oxf) 207 (4):673–689

26. Niendorf T, Pohlmann A, Arakelyan K, Flemming B, Cantow K, Hentschel J, Grosenick D, Ladwig M, Reimann H, Klix S, Waiczies S, Seeliger E (2015) How BOLD is blood oxygenation level-dependent (BOLD) magnetic resonance imaging of the kidney? Opportunities, challenges and future directions. Acta Physiol (Oxf) 213(1):19–38
27. Cantow K, Arakelyan K, Seeliger E, Niendorf T, Pohlmann A (2016) Assessment of renal hemodynamics and oxygenation by simultaneous magnetic resonance imaging (MRI) and quantitative invasive physiological measurements. Methods Mol Biol 1397:129–154. https://doi.org/10.1007/978-1-4939-3353-2_11
28. Pohlmann A, Arakelyan K, Hentschel J, Cantow K, Flemming B, Ladwig M, Waiczies S, Seeliger E, Niendorf T (2014) Detailing the relation between renal T2* and renal tissue pO_2 using an integrated approach of parametric magnetic resonance imaging and invasive physiological measurements. Investig Radiol 49(8):547–560
29. Evans RG, Gardiner BS, Smith DW, O'Connor PM (2008) Methods for studying the physiology of kidney oxygenation. Clin Exp Pharmacol Physiol 35(12):1405–1412
30. Hirakawa Y, Tanaka T, Nangaku M (2017) Renal hypoxia in CKD; pathophysiology and detecting methods. Front Physiol 8:99. https://doi.org/10.3389/fphys.2017.00099
31. Flemming B, Arenz N, Seeliger E, Wronski T, Steer K, Persson PB (2001) Time-dependent autoregulation of renal blood flow in conscious rats. J Am Soc Nephrol 12(11):2253–2262
32. Calzavacca P, Evans RG, Bailey M, Bellomo R, May CN (2015) Variable responses of regional renal oxygenation and perfusion to vasoactive agents in awake sheep. Am J Physiol Regul Integr Comp Physiol 309(10):R1226–R1233
33. Calzavacca P, Evans RG, Bailey M, Lankadeva YR, Bellomo R, May CN (2015) Long-term measurement of renal cortical and medullary tissue oxygenation and perfusion in unanesthetized sheep. Am J Physiol Regul Integr Comp Physiol 308(10):R832–R839
34. Evans RG, Madden AC, Denton KM (2000) Diversity of responses of renal cortical and medullary blood flow to vasoconstrictors in conscious rabbits. Acta Physiol Scand 169 (4):297–308
35. Koeners MP, Ow CP, Russell DM, Abdelkader A, Eppel GA, Ludbrook J, Malpas SC, Evans RG (2013) Telemetry-based oxygen sensor for continuous monitoring of kidney oxygenation in conscious rats. Am J Physiol Renal Physiol 304(12):F1471–F1480
36. Koeners MP, Ow CPC, Russell DM, Evans RG, Malpas SC (2016) Prolonged and continuous measurement of kidney oxygenation in conscious rats. Methods Mol Biol 1397:93–111. https://doi.org/10.1007/978-1-4939-3353-2_9.:93-111
37. Lankadeva YR, Kosaka J, Evans RG, Bailey SR, Bellomo R, May CN (2016) Intrarenal and urinary oxygenation during norepinephrine resuscitation in ovine septic acute kidney injury. Kidney Int 90(1):100–108
38. Pitts RF (1974) Anatomy of the kidney. In: Pitts RF (ed) Physiology of the kidney and body fluids. Year Book Medical Publishers, Inc., Chicago
39. Edwards A, Silldforff EP, Pallone TL (2000) The renal medullary microcirculation. Front Biosci 5:E36–E52
40. Zimmerhackl BL, Robertson CR, Jamison RL (1987) The medullary microcirculation. Kidney Int 31(2):641–647
41. Evans RG, Gardiner BS, Smith DW, O'Connor PM (2008) Intrarenal oxygenation: unique challenges and the biophysical basis of homeostasis. Am J Physiol Renal Physiol 295 (5):1259–1270
42. Niendorf T, Pohlmann A, Arakelyan K, Flemming B, Cantow K, Hentschel J, Grosenick D, Ladwig M, Reimann H, Klix S, Waiczies S, Seeliger E (2015) How BOLD is blood oxygenation-dependent (BOLD) magnetic resonance imaging of the kidney? Opportunities, challenges and future directions. Acta Physiol (Oxf) 213(1):19–38
43. Schurek HJ (1988) Kidney medullary hypoxia: a key to understanding acute renal failure? Klin Wochenschr 66(18):828–835
44. Baumgartl H, Leichtweiss HP, Lubbers DW, Weiss C, Huland H (1972) The oxygen supply of the dog kidney: measurements of intrarenal pO_2. Microvasc Res 4(3):247–257
45. Lubbers DW, Baumgartl H (1997) Heterogeneities and profiles of oxygen pressure in brain and kidney as examples of the pO_2 distribution in the living tissue. Kidney Int 51(2):372–380
46. Evans RG, Ow CPC (2018) Heterogeneity of renal cortical oxygenation: seeing is believing. Kidney Int 93(6):1278–1280. https://doi.org/10.1016/j.kint.2018.01.039
47. Hirakawa Y, Mizukami K, Yoshihara T, Takahashi I, Khulan P, Honda T, Mimura I, Tanaka T, Tobita S, Nangaku M (2018) Intravital phosphorescence lifetime imaging of the renal cortex accurately measures renal hypoxia.

Kidney Int 93(6):1483–1489. https://doi.org/10.1016/j.kint.2018.01.015

48. Pappenheimer JR, Kinter WB (1956) Hematocrit ratio of blood within mammalian kidney and its significance for renal hemodynamics. Am J Physiol 185:377
49. Evans RG, Harrop GK, Ngo JP, Ow CP, O'Connor PM (2014) Basal renal O_2 consumption and the efficiency of O_2 utilization for Na^+ reabsorption. Am J Physiol Renal Physiol 306(5):F551–F560
50. Pitts RF (1974) Mechanisms of reabsorption and excretion of salt and water. In: Pitts RF (ed) Physiology of the kidney and body fluids. Year Book Medical Publishers, Inc., Chicago
51. Palm F, Carlsson PO, Hansell P, Hellberg O, Nygren A, Liss P (2003) Altered response in renal blood flow and oxygen tension to contrast media in diabetic rats. Acta Radiol 44 (3):347–353
52. Palm F, Cederberg J, Hansell P, Liss P, Carlsson PO (2003) Reactive oxygen species cause diabetes-induced decrease in renal oxygen tension. Diabetologia 46(8):1153–1160
53. Zhong Z, Arteel GE, Connor HD, Yin M, Frankenberg MV, Stachlewitz RF, Raleigh JA, Mason RP, Thurman RG (1998) Cyclosporin a increases hypoxia and free radical production in rat kidneys: prevention by dietary glycine. Am J Physiol 275(4):F595–F604. https://doi.org/10.1152/ajprenal.1998.275.4.F595
54. Rosenberger C, Rosen S, Paliege A, Heyman SN (2009) Pimonidazole adduct immunohistochemistry in the rat kidney: detection of tissue hypoxia. Methods Mol Biol 466:161–174. https://doi.org/10.1007/978-1-59745-352-3_12
55. Ow CPC, Ullah MM, Ngo JP, Sayakkarage A, Evans RG (2019) Detection of cellular hypoxia by pimonidazole adduct immunohistochemistry in kidney disease: methodological pitfalls and their solution. Am J Physiol Renal Physiol 317(2):F322. https://doi.org/10.1152/ajprenal.00219.2019
56. Drost CJ (1978) Vessel diameter-independent volume flow measurements using ultrasound. In: Proceedings of San Diego Biomedical Symposium, vol 17. San Diego Biomedical Society, San Diego, CA, pp 299–302
57. Dean DA, Jia CX, Cabreriza SE, D'Alessandro DA, Dickstein ML, Sardo MJ, Chalik N, Spotnitz HM (1996) Validation study of a new transit time ultrasonic flow probe for continuous great vessel measurements. ASAIO J 42(5): M671–M676
58. Charbel FT, Hoffman WE, Misra M, Ostergren L (1998) Ultrasonic perivascular flow probe: technique and application in neurosurgery. Neurol Res 20(5):439–442
59. Lankadeva YR, Cochrane AD, Marino B, Iguchi N, Hood SG, Bellomo R, May CN, Evans RG (2019) Strategies that improve renal medullary oxygenation during experimental cardiopulmonary bypass may mitigate postoperative acute kidney injury. Kidney Int 95(6):1338–1346. https://doi.org/10.1016/j.kint.2019.01.032
60. Stern MD, Bowen PD, Parma R, Osgood RW, Bowman RL, Stein JH (1979) Measurement of renal cortical and medullary blood flow by laser-Doppler spectroscopy in the rat. Am J Physiol 236(1):F80–F87. https://doi.org/10.1152/ajprenal.1979.236.1.F80
61. Obeid AN, Barnett NJ, Dougherty G, Ward G (1990) A critical review of laser Doppler flowmetry. J Med Eng Technol 14(5):178–181
62. Ferrara F, Cantow K, Flemming B, Skalweit A, Ladwig M, Fähling M, Seeliger E (2017) Effects of liraglutide on control of renal hemodynamics and oxygenation in diabetic rats. Acta Physiol (Oxf) 219(Suppl. 711):38
63. Clark LC Jr, Misrahy G, Fox RP (1958) Chronically implanted polarographic electrodes. J Appl Physiol 13(1):85–91. https://doi.org/10.1152/jappl.1958.13.1.85
64. Whalen WJ, Riley J, Nair P (1967) A microelectrode for measuring intracellular PO2. J Appl Physiol 23(5):798–801. https://doi.org/10.1152/jappl.1967.23.5.798
65. Welch WJ, Baumgartl H, Lubbers D, Wilcox CS (2001) Nephron pO_2 and renal oxygen usage in the hypertensive rat kidney. Kidney Int 59(1):230–237. https://doi.org/10.1046/j.1523-1755.2001.00483.x
66. Ow CPC, Ngo JP, Ullah MM, Barsha G, Meex RC, Watt MJ, Hilliard LM, Koeners MP, Evans RG (2018) Absence of renal hypoxia in the subacute phase of severe renal ischemia-reperfusion injury. Am J Physiol Renal Physiol 315(5):F1358–f1369. https://doi.org/10.1152/ajprenal.00249.2018
67. Leong CL, O'Connor PM, Eppel GA, Anderson WP, Evans RG (2008) Measurement of renal tissue oxygen tension: systematic differences between fluorescence optode and microelectrode recordings in anaesthetized rabbits. Nephron Physiol 108(2):11–17
68. Shaw AD, Li Z, Thomas Z, Stevens CW (2002) Assessment of tissue oxygen tension: comparison of dynamic fluorescence quenching and polarographic electrode technique. Crit Care 6(1):76–80
69. Carreau A, El Hafny-Rahbi B, Matejuk A, Grillon C, Kieda C (2011) Why is the partial

oxygen pressure of human tissues a crucial parameter? Small molecules and hypoxia. J Cell Mol Med 15(6):1239–1253. https://doi.org/10.1111/j.1582-4934.2011.01258.x

70. Griffiths JR, Robinson SP (1999) The OxyLite: a fibre-optic oxygen sensor. Br J Radiol 72 (859):627–630. https://doi.org/10.1259/bjr.72.859.10624317
71. Young WK, Vojnovic B, Wardman P (1996) Measurement of oxygen tension in tumours by time-resolved fluorescence. British J Cancer Suppl 27:S256–S259
72. Sponer G, Müller-Beckmann B, Martin U (1993) Blood pressure recording in rats: pitfalls and problems. In: Gretz N, Strauch M (eds) Experimental and genetic rat models of chronic renal failure. Karger, Basel, pp 319–330
73. Nalivaiko E (2011) Animal models of psychogenic cardiovascular disorders: what we can learn from them and what we cannot. Clin Exp Pharmacol Physiol 38(2):115–125. https://doi.org/10.1111/j.1440-1681.2010.05465.x
74. Byrom FB, Wilson C (1938) A plethysmographic method for measuring systolic blood pressure in the intact rat. J Physiol 93 (3):301–304. https://doi.org/10.1113/jphysiol.1938.sp003641
75. Krege JH, Hodgin JB, Hagaman JR, Smithies O (1995) A noninvasive computerized tail-cuff system for measuring blood pressure in mice. Hypertension 25(5):1111–1115. https://doi.org/10.1161/01.hyp.25.5.1111
76. Aperia AC, Liebow AA (1964) Implications of urinary pO2 for renal medullary blood flow. Am J Physiol 206:499–504
77. Ngo JP, Lankadeva YR, Zhu MZL, Martin A, Kanki M, Cochrane AD, Smith JA, Thrift AG, May CN, Evans RG (2019) Factors that confound the prediction of renal medullary oxygenation and risk of acute kidney injury from measurement of bladder urine oxygen tension. Acta Physiol (Oxf) 227(1):e13294. https://doi.org/10.1111/apha.13294
78. Grosenick D, Cantow K, Arakelyan K, Wabnitz H, Flemming B, Skalweit A, Ladwig M, Macdonald R, Niendorf T, Seeliger E (2015) Detailing renal hemodynamics and oxygenation in rats by a combined near-infrared spectroscopy and invasive probe approach. Biomed Opt Express 6(2):309–323
79. Gladytz T, Cantow K, Flemming B, Pohlmann A, Niendorf T, Seeliger E, Grosenick D Towards depth-resolved characterization of hemodynamics and oxygenation in the rat kidney. In Proc SPIE, 2019. vol 11074, pp 1107415-1107411-1107415–1107413

Chapter 7

Ultrasound and Photoacoustic Imaging of the Kidney: Basic Concepts and Protocols

Sandra Meyer, Dieter Fuchs, and Martin Meier

Abstract

Noninvasive, robust, and reproducible methods to image kidneys are provided by different imaging modalities. A combination of modalities (multimodality) can give better insight into structure and function and to understand the physiology of the kidney. Magnetic resonance imaging can be complemented by a multimodal imaging approach to obtain additional information or include interventional procedures. In the clinic, renal ultrasound has been essential for the diagnosis and management of kidney disease and for the guidance of invasive procedures for a long time. Adapting ultrasound to preclinical requirements and for translational research, the combination with photoacoustic imaging expands the capabilities to obtain anatomical, functional, and molecular information from animal models. This chapter describes the basic concepts of how to image kidneys using different and most appropriate modalities.

This chapter is based upon work from the COST Action PARENCHIMA, a community-driven network funded by the European Cooperation in Science and Technology (COST) program of the European Union, which aims to improve the reproducibility and standardization of renal MRI biomarkers. This introduction chapter is complemented by two separate chapters describing the experimental procedure and data analysis.

Key words Magnetic resonance imaging (MRI), Kidney, Ultrasound imaging (US), Photoacoustic imaging (PA), Multimodality, Doppler, Contrast, Animals, Rats, Mice

1 Introduction

Magnetic resonance imaging, while very powerful by itself, can be complemented by a multimodal imaging approach to streamline workflow processes, obtain additional information, or include interventional procedures. Ultrasound and computed tomography are modalities of primary choice in renal imaging on patients, with the disadvantage of computed tomography exposing the body to harmful irradiation. Due to its fast, cost-effective, versatile, and nonionizing characteristics, ultrasound imaging is well-established in the clinical practice, often used for first-line diagnostics and follow-ups and as a complementary method to MRI.

Andreas Pohlmann and Thoralf Niendorf (eds.), *Preclinical MRI of the Kidney: Methods and Protocols*, Methods in Molecular Biology, vol. 2216, https://doi.org/10.1007/978-1-0716-0978-1_7,

In the clinic, renal ultrasound has been essential for the diagnosis and management of kidney disease and for the guidance of invasive procedure for decades. Nevertheless, new developments to advance clinical diagnostics and medical treatments are required and strongly rely on appropriate preclinical models. Adapting the ultrasound technology to match preclinical requirements for translational studies and combining it with photoacoustic imaging, expands the researchers' capabilities to obtain anatomical, functional, and molecular information from their animal models.

MRI has the advantage of superior soft-tissue contrast, which facilitates and enables the detection and characterization of renal lesions. This chapter will give an introduction to how detailed kidney images can be created, blood flow visualized and quantified, and capillary as well as renal function assessed in vivo, noninvasively, and in real time using high-frequency ultrasound.

This introduction chapter is complemented by two separate chapters describing the experimental procedure and data analysis, which are part of this book.

This chapter is part of the book Pohlmann A, Niendorf T (eds) (2020) Preclinical MRI of the Kidney—Methods and Protocols. Springer, New York.

2 Measurement Concepts of Ultrasound and Photoacoustics

The basic principle of ultrasound imaging relies on detecting differences in tissue density by using sound waves with frequencies above the range of human hearing—typically in the MHz range. Using piezoelectric elements short, harmless ultrasound pulses are sent into the body. These sound waves are partially reflected back to the transducer by different layers of tissue and the return signals (often referred to as "echo"—hence the term "echography" which is used as a synonym to ultrasound) are recorded. Based on the time it takes for the echo to travel into the tissue and back and the strength of the signal, an image can be computed and displayed in real time. The resulting two-dimensional, grayscale image of an area of interest is referred to as Brightness Mode or B-Mode. Tissue closest to the transducer is displayed at the top and structures further away are shown below; a scale provides depth and size information in real time. With increasing density more echo is recorded resulting in a brighter signal on the screen; therefore, dense structures (e.g., skin) are represented in white and light gray tones, whereas ultrasound gel used for coupling and fluid-filled structures inside the body appear black. Most tissues and organs are displayed in a range of grayscales in between and have a characteristic appearance ("speckle pattern") that aids in their identification. B-Mode is the standard imaging mode on ultrasound systems and worked with the most because it allows for effective visualization of anatomical structures. It can be complemented by additional imaging modes to obtain functional information which are outlined in more detail in Subheading 3.

In ultrasound, the frequency of the sound waves sent into the tissue is of importance as it determines image resolution and penetration depth. In a clinical setting, renal ultrasound scans on adult patients are normally performed with a 3–6 MHz curved array transducer where the term "curved" describes the shape of the transducer surface. Routine measurements include determining the length of the kidney in a sagittal view, the measurement of cortex thickness and of blood flow in the renal and interlobar arteries [1].

By using an appropriate setup and ultrasound imaging system, these parameters and a variety of others can be obtained in preclinical animal models. Dedicated small-animal micro-ultrasound systems provide high spatial resolution down to 30 μm by employing higher frequencies of up to 70 MHz. While early systems for small animal imaging were equipped with mechanical probes, state-of-the-art micro-ultrasound systems are working with digital linear array (flat transducer surface) probes and are suitable for a broad range of applications [2]. In addition to providing higher resolution than clinical machines, ultrasound systems dedicated to preclinical research also:

1. Allow for controlled transducer positioning (Fig. 1a, c) and include a setup for image-guided injections. While clinical ultrasound and also injections are performed handheld, a stationary setup is superior in most preclinical applications.
2. Include an integrated animal handling solution for physiological monitoring and anesthesia. These are crucial components for any kind of imaging focusing on functional analysis (blood flow, perfusion, etc.) and should be controlled and recorded carefully at all times to ensure reproducibility. However, some ultrasound applications to evaluate anatomy can be performed on conscious animals when appropriately restrained or trained.

Since ultrasound relies on the detection of soundwaves, no contrast agent is required to visualize anatomical structures, 3D volumes, or to assess blood flow velocities. It is noteworthy that anatomical structures and volumes measured with dedicated small animal ultrasound match results acquired with dedicated small animal MRI or μCT systems [3].

Above and beyond the capabilities of micro-ultrasound to gather anatomical and functional information, photoacoustic imaging can also be applied in a preclinical setting to add molecular information. Photoacoustic imaging is a hybrid imaging modality that combines the strengths of optical and ultrasound imaging and can be used to monitor endogenous parameters such as blood content or oxygen saturation or various exogenous contrast agents.

In this imaging approach (Fig. 2), short (a few nanoseconds) pulses of near-infrared laser light are transmitted into the tissue and

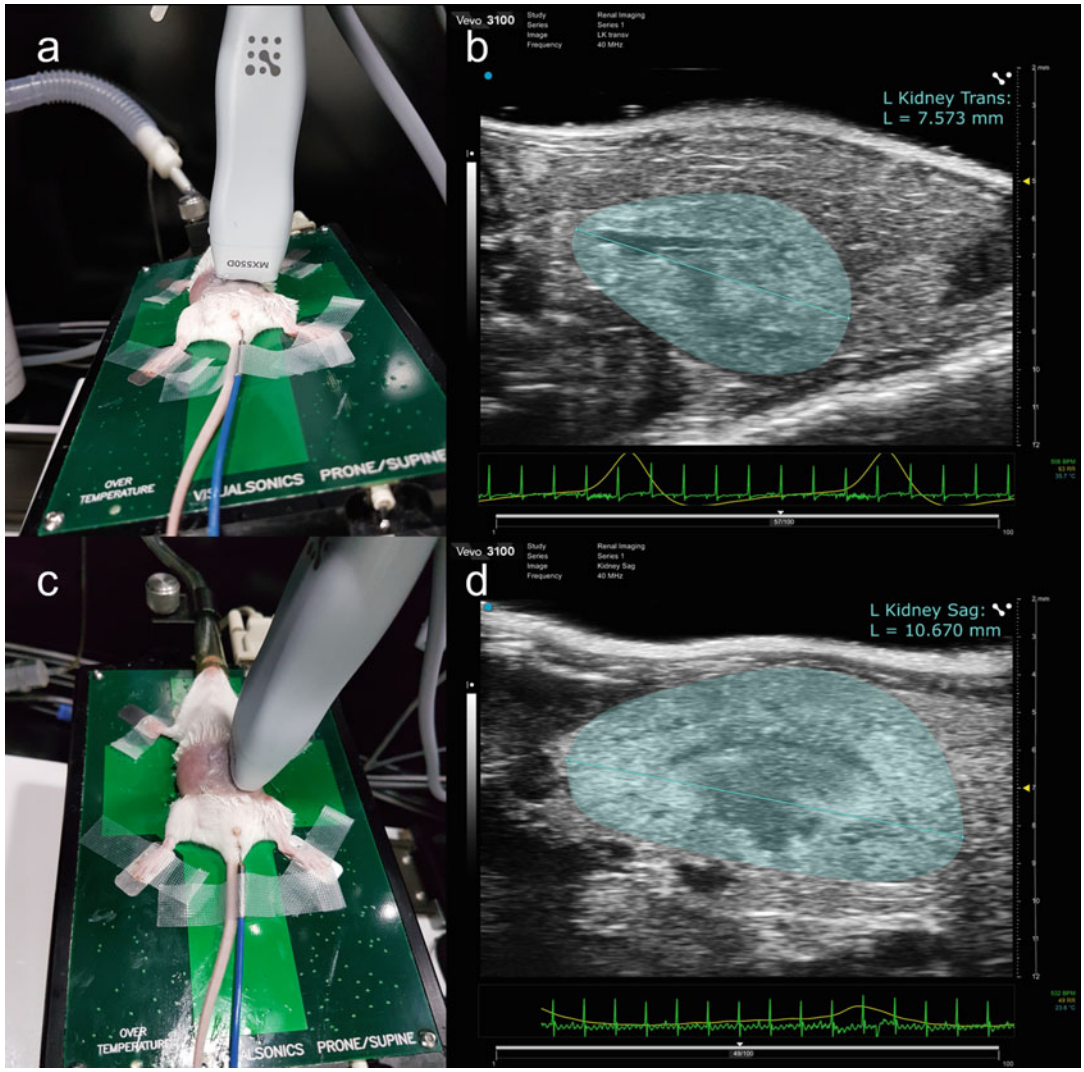

Fig. 1 Standard renal exam: animal and transducer positioning; (**a**) transverse position for left kidney imaging, (**b**) transverse US B-Mode image of the left kidney with length measurement, (**c**) sagittal position for left kidney imaging, (**d**) sagittal US B-Mode image of the left kidney with length measurement. Note the millimeter scale on the right and the physiological monitoring (ECG in green, respiration in yellow) below the US images

are selectively absorbed according to the optical properties of the tissue components. Light absorption results in a thermoelastic expansion creating a sound wave that can be localized by the ultrasound transducer and at the same resolution as the ultrasound image [4].

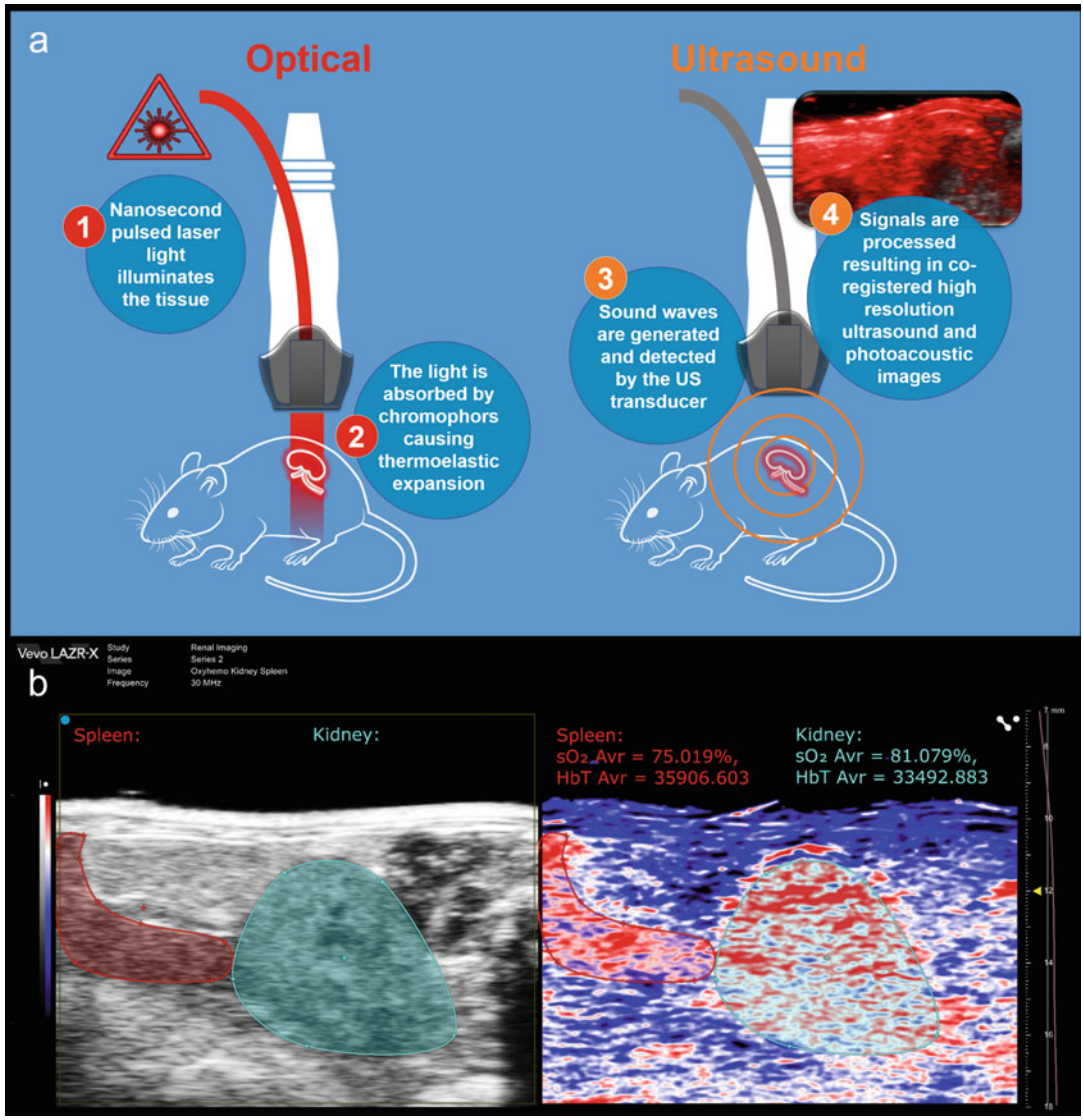

Fig. 2 Photoacoustic imaging; (**a**) the photoacoustic effect, (**b**) coregistered B-Mode image providing anatomical information (left) and photoacoustic image displaying oxygen saturation (right) in the spleen and left kidney

3 Overview of Applications

This section provides an overview of applications of high-frequency ultrasound and photoacoustic imaging in preclinical renal research. Examples of specific disease models and how multimodal imaging is applied are summarized in a brief review of selected publications in Table 1.

Table 1
Examples of specific disease models and how multimodal imaging is applied

Disease (animal model)	Usage of US and PA	Findings and Remarks	References
Polycystic kidney disease (PCK rats)	• Cyst detection • Kidney and cyst volume	Evaluation of kidneys in B-mode, power Doppler, and 3D • Quantification of kidney volume, number of cysts and cyst volume • US-based kidney volumes correlated strongly with kidney weights • US provided superior information in comparison to microscopic analysis of stained kidney sections	[12]
Type 2 diabetes (leptin-deficient (Ob/Ob) mice	• Anatomical and blood flow analysis • Renal RI and PI;	• RI and PI were higher in the ob/ob mice (RI 1.50; PI 0.81) at 21 weeks compared to lean controls (RI 0.69; PI 1.18) • Includes echocardiography and coronary flow reserve data	[13]
Orthotopic renal cell carcinoma (athymic nude mice)	• Tumor volume	• Validation of noninvasive imaging tools for monitoring of tumor growth in an orthotopic renal cell carcinoma xenograft • Tumor volumes determined by hrUS, μCT, and MRI showed a very good correlation with each other and with caliper measurements at autopsy • US examination time was very short (5 min)	[3]
Metastatic tumor xenografts Immunodeficient mice (NOD-SCID)	• Image-guided injections • Tumor localization and sizing	• To establish orthotopic xenograft models by ultrasound-guided injections into the adrenal gland and kidney (subcapsular) • Tumor location, size, and relation to the adrenal gland and kidney were monitored accurately and weekly in US • Technique is efficient, with up to 10 mice injected per 2-h session • Mice had fast recovery times of less than 15 min without procedure-related morbidity or mortality	[10]
Hydronephrosis/congenital obstructive nephropathy (megabladder (mgb) mouse)	Evaluate hydronephrosis	• Total renal length (RL) and renal pelvic anterior–posterior diameter (APD) were measured. Hydronephrosis was scored by the ratio of APD to RL • US permits easy stratification of mice into consistent pathological study groups composed of mild, moderate, and severe kidneys. This approach significantly improves the utility of this animal model	[14]

(continued)

Table 1
(continued)

Disease (animal model)	Usage of US and PA	Findings and Remarks	References
Hydronephrosis and underlying etiologies in (aging mice)	• Detection of hydronephrosis • Identification of concurrent abdominal lesions	• Underlying etiologies included pyelonephritis secondary to a preputial gland abscess and ascending urinary tract infections; cystolithiasis, infiltrative abdominal neoplasia with invasion of the renal pelvis, hilum, and parenchyma and surrounding lymph nodes; mouse urologic syndrome, and a case of spontaneous hydronephrosis with ureteritis	[6]
Acute kidney ischemia (induced by unilateral clamping in mice)	• Oxygen saturation measurements	• Longitudinal measurement of oxygen saturation shows differences between mild and severe renal injury • Kidney volume was also determined • PA provided a sensitive measure of change in sO_2 in the acute phase of AKI, with the sO_2 at 24 h after AKI being predictive of renal function in the chronic phase	[15]
Acute kidney injury (bilateral renal ischemia induced by clamping in mice)	• Renal microperfusion imaging	• Contrast-enhanced ultrasonography with high-resolution parametric perfusion maps can monitor changes in renal microvascular perfusion in space and time in mice	[16]
Acute renal ischemia induced by systemic hypoperfusion (Sprague-Dawley rats)	• Study hemorrhagic shock changes with microimaging	• After 1 h of ischemia, B-mode images documented slight changes in kidney echogenicity • Color and PW-Doppler analysis showed a reduction in renal blood flow in kidneys during the hypoperfusion with a progressive and significant change from baseline values of resistive index	[17]
Vesicoureteral reflux (C57BL6/J and C3H/HeJ inbred mice)	Monitor reflux with US contrast	• Reflux was detected in the proximal ureters and the renal pelvis bilaterally in C3H/HeJ mice • Contrast-enhanced ultrasound cystograms were established in-vivo	[18]
BALB mice	Contrast agent biodistribution in US and photoacoustic imaging	• A dual imaging contrast agent was developed to monitor kidney perfusion and organ distribution as well as whole-body biodistribution	[9]
Chronic kidney disease and cardiovascular disease (induced in C57BL/6J mice by 5/6 nephrectomy)	Assess cardiac dimensions and function	• Cardiac dysfunction and dilatation of the left ventricle was observed 8 weeks after partial nephrectomy • A treatment reversed cardiac dilatation and significantly improved cardiac dysfunction	[19]

3.1 Evaluating Kidney Size and Anatomy

B-Mode, as introduced in Measurement concepts (2.), is used to locate the kidneys in the abdomen, observe the surrounding tissue and anatomical structure and to obtain organ size.

When viewed using ultrasound, the kidneys are located lateral of the abdominal aorta. The right kidney is positioned slightly more cranial in the thoracic cavity then the left kidney, and both can be identified by their characteristic appearance in ultrasound: the medulla in the medial portion of the kidney is darker than the cortex and surrounding the cortex, the kidney capsule appears as a bright thin line. Once the appearance of kidneys and surrounding in ultrasound are familiar, it is easy to identify any changes: Cysts are liquid-filled structures and therefore are visible as black, round structures with in the tissue. Hydronephrosis is qualitatively recognized as distension and dilatation of the renal pelvis and a method to quantify hydronephrosis based on the proportion of renal parenchyma in a longitudinal ultrasound image as been established [5] and underlying etiologies have been studied [6]. Tumor masses will appear in a different grayscale than the surrounding tissue and when becoming larger will distort the regular bean shaped form of the kidney. The observation and sizing of the kidney in 2D images can be performed in the transverse (Fig. 1a, b) and sagittal imaging (Fig. 1c, d) plane as required, based on preference. Moving through the whole organ in in both imaging planes in 2D allows to systematically screen for changes inside and also in the surroundings (e.g., ascites in the peritoneum). In addition, ultrasound imaging also may be used to study cardiovascular disease linked to chronic kidney disease [19].

Most preclinical ultrasound systems also allow to gather three-dimensional information. The principle for 3D image acquisition is similar between ultrasound and MRI where both acquire sequential 2D images with a known distance between them, determining the resolution along the *z*-axis (slice thickness). In ultrasound imaging a motor needs to be attached to move the probe across the area of interest along the *z*-axis and acquire a stack of images (Fig. 3). The consecutive 2D slices can be compiled into a 3D view, displayed in various ways, and analyzed to obtain accurate volume information of the kidneys and also cysts or tumor masses within.

3.2 Visualization of Blood Flow

When ultrasound waves are reflected by moving blood a frequency shift (Doppler shift) of the return ultrasound signal is induced that allows to display and measure blood flow. Most ultrasound systems are equipped with several imaging modes that use this Doppler effect to display blood flow in 2D images and allow for measuring blood flow velocities.

Color Doppler mode, overlaid on top of a B-Mode image for anatomical reference, displays blood flow in the area of interest in gradients of red and blue (Fig. 4b). The color gradients indicate both the direction and mean velocity of the Doppler shift: blood

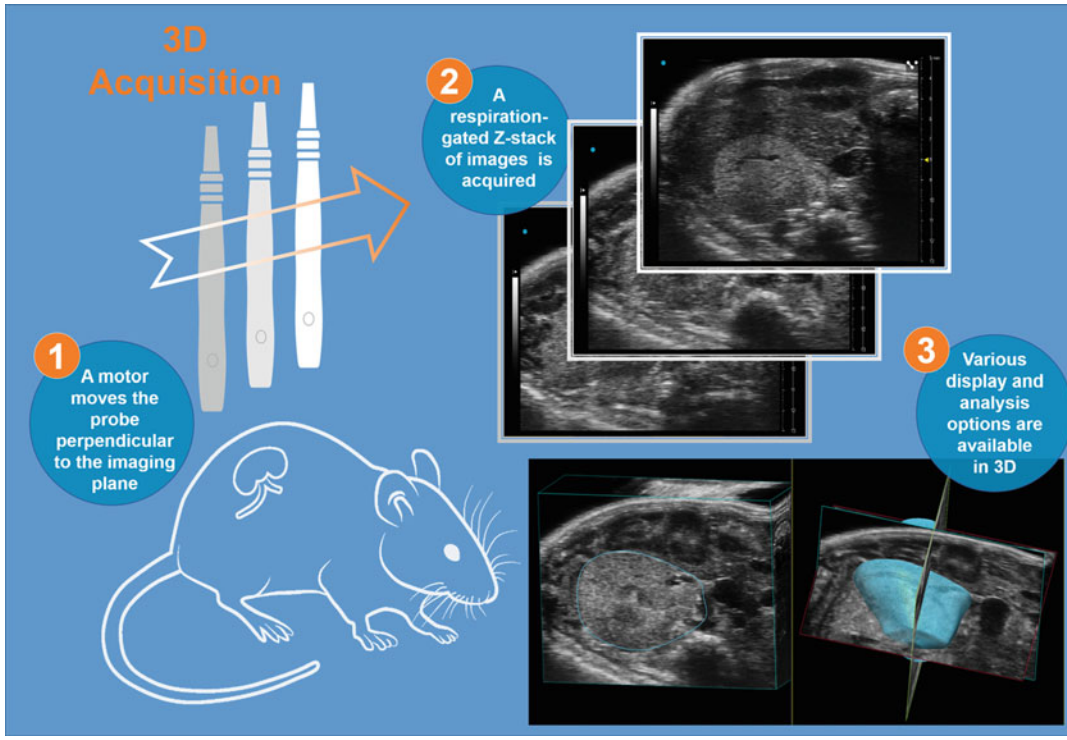

Fig. 3 Schematic workflow for 3D US image acquisition and processing

flowing toward the transducer is represented by a gradient between red (lowest velocity) and white (highest velocity) and blood flowing away from the transducer is represented by a gradient between blue (lowest velocity) and white (highest velocity). BART is an acronym commonly used to remember the colors associated with the direction of flow: Blue Away, Red Toward. Color Doppler mode is a very useful tool to identify the major and cortical vessels in the kidney and accurately guide the positioning for flow measurements, which are performed in pulsed-wave (PW) Doppler mode. To obtain a measurement, a Doppler sample volume (point where the blood flow should be measured) is placed within the vessel and the system generates a PW Doppler spectrum that displays time on the *x*-axis and flow velocity on the *y*-axis (Fig. 4d). Once PW Doppler spectrums of the renal artery and vein have been recorded, velocity measurements such as peak systolic velocity (PSV), end-diastolic velocity (EDV), and the velocity time integral (VTI) can be added. Based on these measurements, relevant parameters will be calculated as an indicator for vascular function.

- The resistive index (RI) is an example of additional analysis that may be useful. A RI of 0 is calculated for continuous flow patterns and an RI of 1 indicates a strongly pulsating flow with no flow during diastole. In the clinic an RI of the renal

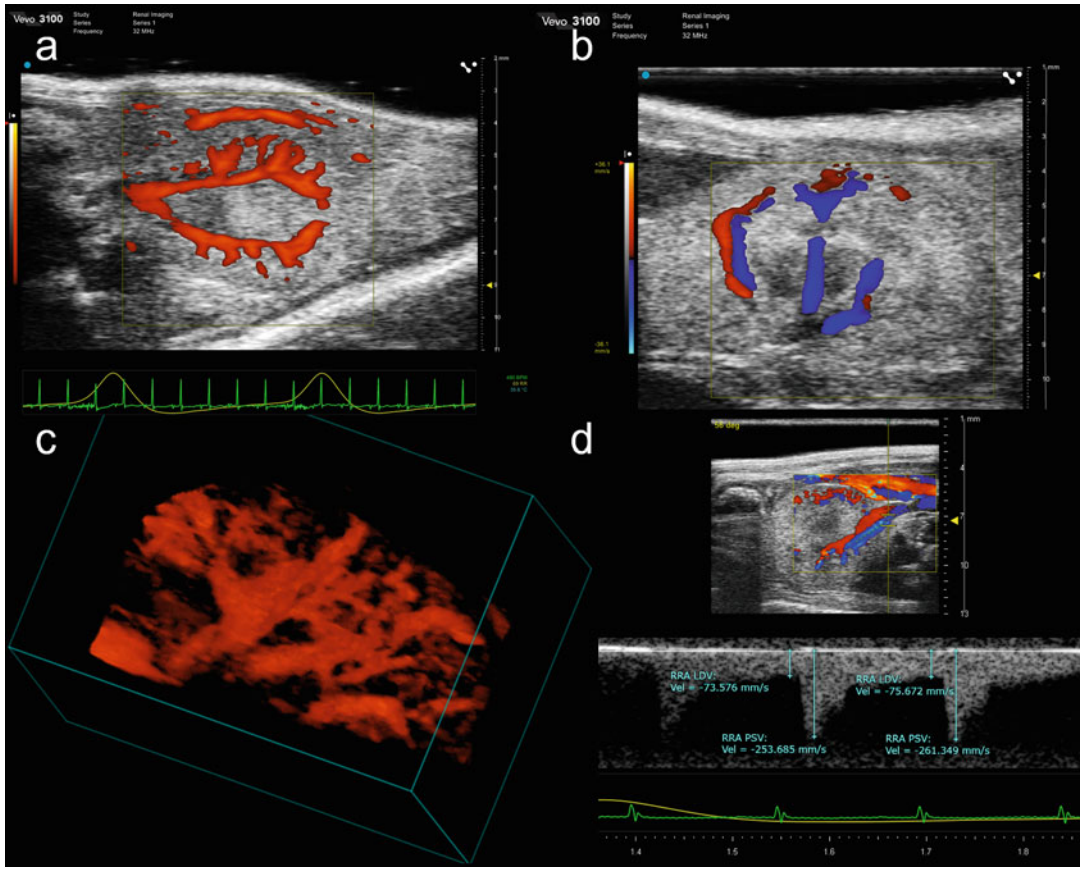

Fig. 4 Assessment of blood flow; (**a**) power Doppler signal in transverse view of the left kidney is overlaid with the B-mode image, (**b**) Blood flow in the interlobal vessels as visualized in Color Doppler Mode, in this image red and blue colors indicate arterial and venous flow, respectively; (**c**) three-dimensional rendering of Power Doppler signal of a healthy kidney, (**d**) pulse-waved Doppler profile of renal artery flow, peak systolic (PSV), and lowest diastolic velocity (LDV) measurements are shown, the sample positioning is indicated in the scout image above the flow profile

artery = 0.6 is observed in healthy adults and a rise in RI is seen as an indicator for renal disease.

$$\mathrm{RI} = \frac{\mathrm{PSV} - \mathrm{EDV}}{\mathrm{PSV}}$$

- The pulsatility index (PI) is another parameter often calculated in clinical renal diagnosis.

$$\mathrm{PI} = \frac{\mathrm{PSV} - \mathrm{EDV}}{\mathrm{VTI\ mean\ velocity}}$$

Power Doppler mode is another tool used to display and analyze blood flow within an area of interest. It is similar to color Doppler mode in detecting the occurring Doppler shift, but instead

of displaying blood flow direction, it color-codes flow from orange to yellow according to signal intensity and is most useful for smaller vessels having slower blood flow (Fig. 4a).

It is crucial for PW Doppler mode and all other Doppler imaging modes, that an appropriate angle is achieved between the transmitted ultrasound beam and the blood flowing through the vessel; the imaging plane should be adjusted such that the angle between these two is less than 60 ° to provide an accurate velocity measurement.

Color and power Doppler information can also be acquired in 3D, visualizing the blood vessel structure in the entire organ (Fig. 4c). The amount of Doppler signal in a 3D volume can then be calculated. With the right animal setup, imaging both kidneys at the same time is feasible.

3.3 Perfusion Imaging

While Doppler imaging can be used to visualize blood flow in the renal artery and vein and also in the interlobar and arcuate vessels, monitoring perfusion of the kidney at capillary level requires the use of ultrasound contrast agents. Ultrasound contrast agents are very small gas bubbles (microbubbles) about 2–3 μm in diameter and encapsulated by a polymer or lipid shell (Fig. 5a). Several contrast imaging modes can be used for the detection of these microbubbles in the area of interest. Linear contrast enhanced ultrasound, the first contrast mode used at frequencies above 15 MHz, primarily relies on subtraction of background information to display the increase in echo due to the wash-in of contrast agent. Newer generation systems allow to monitor perfusion in real-time based on nonlinear fundamental detection with amplitude modulation, resulting in a higher sensitivity [7].

While ultrasound imaging to monitor perfusion requires a contrast agent and therefore intravenous access, photoacoustic imaging allows for the detection of hemoglobin and its oxygen saturation status (Fig. 2). Based on the change of hemoglobin's optical properties dependent on oxygen bound to the heme group, one can assess tissue oxygenation at a level matching BOLD (blood oxygen level–dependent) MRI [8]. It should be noted that ultrasound contrast agent and photoacoustic imaging of hemoglobin are nontoxic and harmless to the animal.

3.4 Molecular Information

Ultrasound and photoacoustic contrast agents can also be used for molecular imaging. Ultrasound contrast agents can be targeted to assess biomarker expression (Fig. 5c) but are exclusively tailored to vascular endothelium as the contrast agent does not leave the vasculature. Photoacoustic contrast agents, dyes or nanometer-sized particles, can be used for specifically targeting extravascular targets or for assessing glomeruli function and to study biodistribution [9].

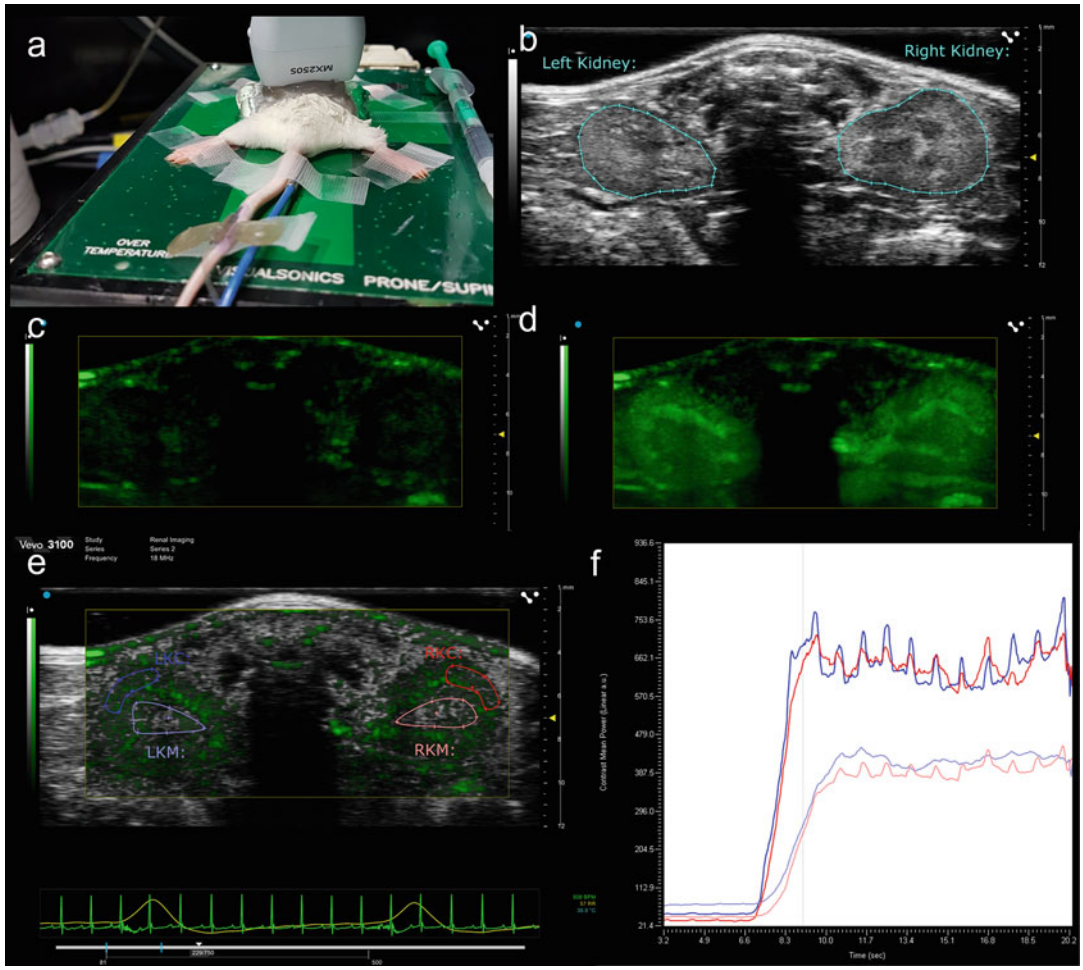

Fig. 5 Perfusion assessment of both mouse kidneys; (**a**) schematic model of a microbubble used for US contrast imaging; (**b**) animal and transducer position, (**c**) B-mode image, left and right kidney are outlined; (**d**) schematic binding of targeted contrast agent to a biomarker; Non-linear contrast image of both kidneys before (**e**) and after contrast injection (**f**). After contrast injection; for analysis, regions of interest in cortex and medulla of left (blue) and right (red) kidney are selected (**g**); a graph displays the contrast signal in these regions of interest (**h**)

3.5 Interventional Procedures

In contrast to other imaging modalities, in ultrasound and photoacoustic imaging the animal is accessible throughout the imaging session, allowing for various interventional procedures to be performed during an imaging session (Fig. 6). Using a so-called in-plane needle visualization technique, it is possible to follow the movement of a needle inside the animal in B-mode and ensure accurate placement of the needle tip for injections or aspiration. Image guided injections allow to place cells to create orthotopic tumor models or apply drug treatments precisely without the need for more invasive surgery [10]. Switching to image guided injections is an important step in the refinement of animal procedures and helps to shorten recovery time and minimize discomfort and

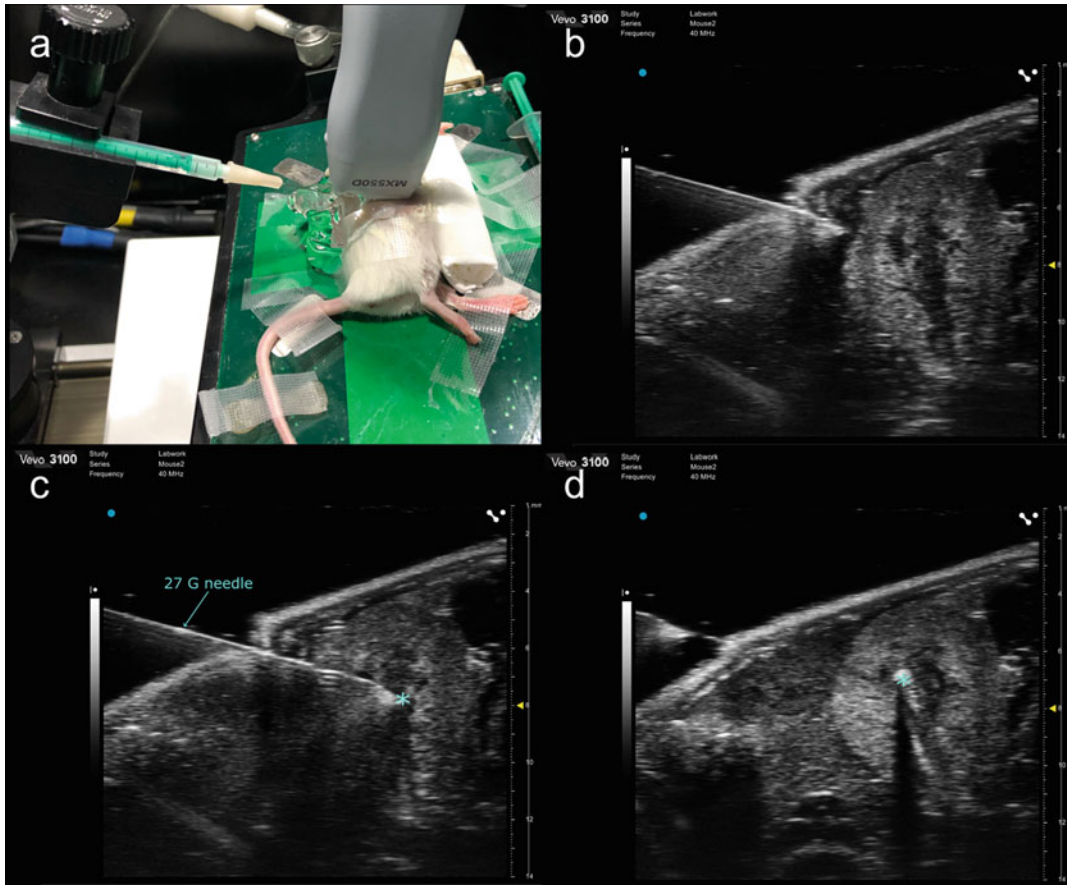

Fig. 6 Image guided injection into the left kidney of a mouse; (**a**) animal and needle positioning, (**b**) penetration of the skin, (**c**) the needle tip (marked with an asterisk) is positioned in the medulla of the kidney, (**d**) after injection of US contrast agent and needle retraction, injection site is marked with an asterisk

complications as the procedure can be performed with only light anesthesia and the procedure itself does not require postoperative analgesia. In addition the success of any given injection or aspiration can be verified in real time.

4 Protocols

4.1 Standard Renal Exam

The protocol outlined below depicts a standard renal ultrasound exam that can be performed on various ultrasound systems. If available, a system dedicated for small animal imaging using high-frequency linear transducers is be preferred due its superior resolution and sensitivity. For rats a transducer with a 50 or 75 μm resolution is appropriate and for mice a transducer with 40 μm resolution should be used. Despite the similar principle of various ultrasound systems, the availability of imaging modes, settings and

analysis tools may vary. Please refer to instructions provided by the manufacturer for system-specific information and tailored work protocols.

While some brief ultrasound scans (e.g., for linear measurements, screening for pathologies or anatomical alterations) can be performed on awake animals, more comprehensive renal exams including flow measurements or volumetric analysis normally require the use of anesthesia. A brief description of isoflurane anesthesia is included below, but researchers should always carefully follow local rules and regulations.

In order to ensure reproducibility and to streamline workflow in longitudinal studies, it is recommended to store settings for all imaging modes and applications, stick to the same anesthesia type and level, as well as monitor the animal's physiologic parameters.

1. Switch on the flow of oxygen or medical air (the latter preferred for contrast enhanced ultrasound imaging) and set it to 1 L/min, place the animal in the induction box and turn on isoflurane at 4–5% until anesthesia is induced. Once a sufficient level of anesthesia is reached (loss of righting reflex), transfer the animal onto the imaging table and reduce isoflurane to 1.5–2% during imaging (depending on the animal model), or higher for interventional procedures. Make sure to switch the flow of anesthesia gas from the knock out box to the mask.
2. Place the animal in supine position if the renal exam is part of an abdominal scan; a prone position may be used to evaluate kidney structure, dimensions and volume, this position is also more suitable for image-guided injections.
3. Prepare the animal: apply eye ointment, tape the paws to the ECG leads using a small amount of ECG gel for coupling, insert a rectal probe to monitor body temperature and remove the hair in the area of interest. Animal physiology should be carefully monitored throughout the imaging session and adjustments made as necessary; for example, an additional heat lamp can be used to maintain body temperature.
4. Remove hair from the area of interest using a dedicated clipper and/or hair removal cream.
5. Apply a sufficient amount of prewarmed ultrasound gel, place the transducer in transverse position below the ribcage and start imaging in B-mode. Check the transducer orientation. In a supine position the imaging convention needs to be followed similar to MRI imaging, that is, with a transverse imaging plane the head should be behind the image, tail toward the viewer, animal's left on the right side of the screen.
6. Locate the area of interest by moving from the lower end of the ribcage toward the lower abdomen. The right kidney can be localized caudally of and adjacent to the liver. The left kidney is

located caudally of the stomach and in close proximity to spleen and the tail of the pancreas (Fig. 1a).

7. The image can be optimized by adjusting the field of view to fit the kidney, focus and gain. Localize the widest, middle part of the kidney and center the organ on the screen using the micromanipulators of the animal station. When imaging in a supine position, the animal table may be tilted sideways to bring the kidney closer to the transducer and remove shadowing caused by the intestinal tract. Save a B-Mode video clip of the transverse view for analysis (Fig. 1b).
8. Switch on color Doppler to display the blood flow in the renal artery and vein. Adjust the Doppler window to fit the position and size of the organ and fine-tune the transducer position to locate the vessels. Save a video clip, then activate pulsed-wave Doppler mode to measure blood flow in the renal artery by placing the Sample Volume gate within the artery. Align the angle of the PW Doppler with the direction of blood flow as indicated by color Doppler mode—you may need to reposition the transducer to obtain an angle smaller than 60°. Velocity, gain and baseline may be adjusted to display the flow profile and should be saved as presets in longitudinal studies. Save the blood flow profile for analysis (Fig. 4d).
9. With the transverse view centered on the screen, the sagittal view of the kidney can be displayed by rotating the transducer 90°. Confirm the longest extension of the kidney is displayed by a mid-lateral movement and save a B-Mode video clip of the sagittal view for analysis (Fig. 1d).
10. If required, intrarenal flow in the interlobar arteries can also be displayed and measured. Starting from the sagittal view, the transducer should be adjusted to the coronal plane. Fine-tune the positioning until the vessel structure (in B-Mode) and flow pattern (in color Doppler mode, Fig. 4b)) can be visualized, then switch on pulse-waved Doppler to record the flow pattern.
11. In addition a 3D data set of the area of interest can be obtained either in the transverse or sagittal view. Most commonly a 3D motor is used to move the transducer perpendicular to the imaging plane to acquire a stack of images (Fig. 3). Select a start and end position or scanning range and start 3D acquisition. Respiration gating may be applied to avoid movement artifacts due to the breathing of the animal. Once completed the data set can be processed to display a 3D view of the organ and saved for analysis.
12. A combined 3D acquisition of B-Mode and power Doppler or color Doppler may be used to also obtain blood flow information for the whole organ (Fig. 4c). In this case, power or color

Doppler should be activated before starting the 3D acquisition and the size of the window should be enlarged to cover the region of interest, the use of respiration gating and a wall filter is recommended to avoid respiration artifacts.

13. Confirm all images required for analysis have been saved. Wipe off the ultrasound gel, turn off the isoflurane and release the animal from the mouse handling table. Monitor the animal until fully recovered.

4.2 Perfusion Studies

Studying kidney perfusion in ultrasound imaging requires the intravenous injection of a contrast agent. Administration can be performed either as a continuous infusion using a pump, or as bolus injection, which can be delivered by hand but using a pump is recommended to ensure reproducibility. In addition it is possible to study reperfusion by applying a short ultrasound pulse to destroy the contrast agent within the field of view and record subsequent reperfusion. Here we would like to outline a basic perfusion study that can be included in an imaging session in combination with the standard exam. To allow for comparison, the imaging procedure should be standardized as much as possible. For a detailed review of contrast imaging in small animals and various parameters that should be considered, please refer to [11].

1. Before anesthetizing the animal, follow the instructions provided by the manufacturer to reconstitute the US contrast agent. Prepare a tail vein catheter (butterfly needle suitable for the contrast agent, fine tubing connected to syringe filled with saline).
2. Start animal anesthesia as described above. Once the animal has been moved to the animal table and eye ointment has been applied, insert the saline filled butterfly needle into the tail vein and fix the catheter with tape or tissue glue. Position and prepare the animal for imaging to obtain anatomical and blood flow information as described above using the 22–55 MHz probe (*see* Subheading 4.1).
3. Switch ultrasound transducer if required for high sensitivity detection (e.g., 15–24 MHz transducer for 2–3 μm phospholipid shell bubbles). Contrast imaging for one kidney can be performed in various positions, if perfusion of both kidneys should be observed at the same time, a prone position may be used (Fig. 5c, d). Position the animal as required and apply a small amount of gel. Avoid air bubbles as these may cause artifacts.
4. Start the nonlinear contrast (NLC) mode, adjust the imaging window, and adjust the gain so that a small amount of background signal is visible in the area of interest (Fig. 5e). Check the frame rate of the image acquisition and adjust the video clip

length to allow for sufficient acquisition time (e.g., 30 s), locate the prospective saving option on the system. If required, acquire a 3D data set before contrast injection and do not move the animal or transducer. Once the settings have been optimized it is advised to store the settings as presets.

5. Fill a new syringe with contrast agent, flush the catheter with 15 μL of saline and change to the syringe containing the contrast agent. Start the video clip with automatic storage option. After 3 s inject the bolus of 50 μL of contrast agent within 3 s using a pump for accurate injection rates. Within a few seconds a signal increase in the area of interest should be visible and the video clip will be stored automatically (Fig. 5f).
6. Change back to the syringe containing saline and flush the catheter with 15 μL and if required, record a second 3D data set using the previous settings. Circulating contrast agent will be observed for approximately 10–15 min. Once the contrast agent has been cleared a second bolus injection can be performed if required. After completing the contrast acquisition end the exam (*see* Subheading 4.1) or continue with one of the options described below.

4.3 Photoacoustic Exam to Monitor Oxygen Saturation

In addition to 2D and 3D ultrasound imaging showing renal anatomy, blood flow, and perfusion, photoacoustic (PA) imaging can add additional information by visualizing endogenous as well as exogenous contrast agents.

1. Anesthesia and animal preparation for PA imaging are identical to the procedure described above, but in order to obtain the best possible PA images the animal should be placed either in a lateral decubitus position or prone position to image both kidneys. In a prone position white gauze may be placed underneath the flanks of the animal to ensure reproducible positioning as well as optimizing light delivery.
2. Depending on the system, choose the appropriate photoacoustic transducer or the ultrasound transducer with laser fiber combination. Apply enough gel to the recess of the transducer so that it is overflowing and ensure that no bubbles are present.
3. Apply a generous amount of prewarmed, bubble-free gel to the animal. Lower the transducer into the gel just until contact is made and an image appears in B-Mode. Position the animal or transducer such that the skin line appears horizontal and at the recommended distance from the transducer. This ensures optimized and reproducible light delivery into the tissue, resulting in accurate photoacoustic data.
4. To limit the field of view to the target, adjust image depth, depth offset, and image width. If required, record ultrasound images in B-Mode or Doppler modes as described above.

5. Switch from B-mode to PA-mode, and start imaging at a single wavelength (e.g., 800 nm). First, increase the PA gain to determine if there is any signal present that may be missed with lower gain. Adjust the gain so that low-level signal can still be seen while keeping background signal (often referred to as "noise") to a minimum.
6. To compensate for light attenuation at depth, adjust the time gain compensation or fluence correction. Try to "even out" the signal throughout the depth of the image. For example, the signal at the surface of the skin can be quenched while applying a slight boost with increasing depth. All settings should be saved and reapplied in future imaging sessions.
7. Switch to oxygen detection and record a video clip for Oxygen Saturation analysis, a 3D data set may also be obtained.
8. If required, also obtain a spectral scan or a multiwavelength scans in 2D and 3D based on previously established protocols for imaging exogenous contrast agents such as dyes (e.g., Evans Blue) or nanoparticles.
9. End the exam as described above or continue to perform an interventional procedure.

4.4 Image Guided Needle Injections

Image guided interventions can be added to any imaging session as an additional step to locally administer a drug or implement cells. This procedure can be performed independently and is a fast and reliable procedure to replace a surgical intervention. Please refer to Subheading 4.1 for instructions on anesthesia, animal preparation, and imaging and follow these additional steps:

1. An analgesic treatment may be applied before the start of the procedure.
2. Prepare a syringe for injection and attach a 30G 1 in. needle. If the use of a different needle is required, please ensure the length of the shaft is sufficient for the needle to pass under the probe without the needle hub pressing against the probe casing. Fix the syringe in an injection mount to allow for precise control of the needle movement directly under the transducer, for best visualization of the needle tip the bevel should be facing upward.
3. If available, an additional micromanipulator can be placed between transducer and transducer mount, this allows to fine-tune the probe position for clear identification of the needle tip during the procedure.
4. Adjust the positioning of the needle and transducer. The needle should be aligned with and parallel to the ultrasound beam, which can be checked by placing the needle in some ultrasound gel and lowering the transducer into it (Fig. 6c). When

positioned correctly, the whole length and tip of the needle should be visible on the live image as a bright line. Once a good alignment has been achieved, movement of the needle and probe in the Y-axis should be avoided.

5. The animal may be taped to the electrodes in a prone position or in a lateral decubitus position (Fig. 6a) to inject into the contralateral kidney. In this case, taping the lower front and hind paw and tail to the electrodes will allow to monitor the animal's physiology.
6. Apply a generous amount of bubble-free gel to the area of interest. Lower transducer into the gel and bring the kidney into view. Adjust the position to have some space on the left for needle positioning.
7. If desired, set the ultrasound system up to record a long video clip by adjusting the length of the video and enable prospective saving, start recording before inserting the needle or injection as required.
8. Advance the needle forward into the gel until it is visible. By tilting and moving it up or down, the projected needle path should point to the target area within the kidney. If large blood vessels or critical organs lie within the needle pathway, reposition the animal to avoid unnecessary damage of tissue.
9. Advance the needle quickly to push through the skin, then gently move forward to place the needle tip in the target structure (Fig. 6b). If the needle slightly bends out of view during the injection, the Υ-axis micromanipulator can be used to readjust the image. Perform the injection and wait shortly to allow for distribution then slowly retract the needle (Fig. 6d). If desired, save a video clip of the procedure.
10. End the ultrasound exam as described above and monitor the recovery of the animal. Check the animal for signs of pain or complications in regular intervals as indicated in the animal protocol (i.e., up to 24 h after injection).

4.5 Analysis

All commercially available ultrasound systems dedicated to in vivo imaging provide measurement tools for comprehensive image analysis that cover a broad range of standard applications. As data is mostly stored in proprietary file formats, analysis tools are a fundamental part of the system capabilities and convenient to use, no other third party or open source software is normally used for standard analysis. Therefore no detailed step-by-step instructions are given below. Instead the type of measurements routinely performed are outlined below and were applicable, calculations are mentioned. Depending on the ultrasound system that is used, measurements will either be added directly during the exam, afterward on the ultrasound system itself or on a dedicated offline

analysis software. Please refer to the user instructions to ensure all data required for analysis is saved. Modern preclinical ultrasound and photoacoustic equipment allow for extracting the image data as DICOM or raw formats, making the data accessible in nonproprietary image analysis programs.

1. The length of the kidney in a sagittal and transverse 2D B-Mode images can be measured in mm using a line measurement.
2. In standard clinical exams, kidney volume is often calculated using the ellipsoid formula: Length × Width × Depth × 0.523. Using a 3D motor and appropriate settings a more accurate volume of the kidneys can be obtained. Depending on the software, various ways of volume reconstructions are available. Mostly the user is required to outline the organ in a few, selected frames on either the video clip or reconstructed 3D view. Based on this information an outline of the organ is created and the volume calculated. In addition to the total kidney volume, sub-volumes can be added to measure cysts, tumors or other anatomical structures. Most software packages also allow to copy volume reconstructions between imaging modes and will quantify additional parameters. In 3D Power and Color Doppler images, percent vascularity can be measured in the volume of interest. Various display options are available to visualize results.
3. In PA imaging, the PA signal intensity can be measured within an area of interest at a single wavelength and build in algorithms allow to also calculate oxygen saturation and hemoglobin content in 2D and 3D. If required, signal from endogenous or exogenous contrast agents can be separated from background using automated spectral unmixing tools.
4. Flow analysis of the renal artery or intrarenal arteries routinely include measuring peak systolic (PSV) and lowest diastolic (LDV) as well as the velocity-time-integral. If not automated in the analysis software, the Resistive Index can be calculated manually based on the first two parameters: (PSV − LDV)/PSV.
5. A basic perfusion analysis includes outlining areas of interest, for example in the kidney cortex, medulla or a tumor, to display the wash in curve of the contrast agent. Based on this curve, the time to peak, a relative measure for blood flow, and peak enhancement, a relative measure for blood volume, can be measured. If 3D data is recorded, it is also possible to observe the contrast signal before and after contrast injection and calculate the parameter percent agent.
6. For presentation purposes, ultrasound and photoacoustic imaging analysis software allows for annotations and color

coding of anatomical structures and further editing for educational purposes or publishing.

Acknowledgments

This chapter is based upon work from COST Action PARENCHIMA, supported by European Cooperation in Science and Technology (COST). COST (www.cost.eu) is a funding agency for research and innovation networks. COST Actions help connect research initiatives across Europe and enable scientists to enrich their ideas by sharing them with their peers. This boosts their research, career, and innovation.
PARENCHIMA (renalmri.org) is a community-driven Action in the COST program of the European Union, which unites more than 200 experts in renal MRI from 30 countries with the aim to improve the reproducibility and standardization of renal MRI biomarkers.

References

1. Hansen K, Nielsen M, Ewertsen C (2015) Ultrasonography of the kidney: a pictorial review. Diagnostics 6:2
2. Foster FS, Hossack J, Adamson SL (2011) Micro-ultrasound for preclinical imaging. Interface Focus 1:576–601
3. Linxweiler J, Körbel C, Müller A et al (2017) Experimental imaging in orthotopic renal cell carcinoma xenograft models: comparative evaluation of high-resolution 3D ultrasonography, in-vivo micro-CT and 9.4T MRI. Sci Rep 7:1–10
4. Needles A, Heinmiller A, Sun J et al (2013) Development and initial application of a fully integrated photoacoustic micro-ultrasound system. IEEE Trans Ultrason Ferroelectr Freq Control 60:888–897
5. Carpenter AR, Becknell B, Ingraham SE, McHugh KM (2012) Ultrasound imaging of the murine kidney. In: Michos O (ed) Kidney development. Methods in molecular biology, vol 886. Humana Press, Totowa, NJ
6. Springer DA, Allen M, Hoffman V et al (2014) Investigation and identification of etiologies involved in the development of acquired hydronephrosis in aged laboratory mice with the use of high-frequency ultrasound imaging. Pathobiol Aging Age Relat Dis 4:1–14
7. Needles A, Arditi M, Rognin NG et al (2010) Nonlinear contrast imaging with an array-based micro-ultrasound system. Ultrasound Med Biol 36:2097–2106
8. Rich LJ, Seshadri M (2015) Photoacoustic imaging of vascular hemodynamics: validation with blood oxygenation level–dependent MR imaging. Radiology 275:110–118
9. Toumia Y, Cerroni B, Trochet P et al (2018) Performances of a pristine graphene-microbubble hybrid construct as dual imaging contrast agent and assessment of its biodistribution by photoacoustic imaging. Part Part Syst Charact 35:1800066
10. Noord RAVAN, Thomas T, Krook M et al (2017) Tissue-directed implantation using ultrasound visualization for development of biologically relevant metastatic tumor xenografts. In Vivo 791:779–791
11. Hyvelin J, Tardy I, Arbogast C et al (2013) Use of ultrasound contrast agent microbubbles in preclinical research. Investig Radiol 48:1–14
12. Kapoor S, Rodriguez D, Mitchell K et al (2016) High resolution ultrasonography for assessment of renal cysts in the PCK rat model of autosomal recessive polycystic kidney disease. Kidney Blood Press Res 41:186–196
13. Westergren HU, Grönros J, Heinonen SE et al (2015) Impaired coronary and renal vascular function in spontaneously type 2 diabetic leptin-deficient mice. PLoS One 10:e0130648
14. Ingraham SE, Saha M, Carpenter AR et al (2010) Pathogenesis of renal injury in the Megabladder mouse: a genetic model of congenital obstructive nephropathy. Pediatr Res 68:500–507

15. Okumura K, Matsumoto J, Iwata Y et al (2018) Evaluation of renal oxygen saturation using photoacoustic imaging for the early prediction of chronic renal function in a model of ischemia-induced acute kidney injury. PLoS One 13:e0206461
16. Fischer K, Meral FC, Zhang Y et al (2016) High-resolution renal perfusion mapping using contrast-enhanced ultrasonography in ischemia-reperfusion injury monitors changes in renal microperfusion. Kidney Int 89:1388–1398
17. Iacobellis F, Segreto T, Berritto D et al (2018) A rat model of acute kidney injury through systemic hypoperfusion evaluated by micro-US, color and PW-Doppler. Radiol Med 124 (5):323–330
18. Paredes J, Sims-Lucas S, Wang H et al (2011) Assessing vesicoureteral reflux in live inbred mice via ultrasound with a microbubble contrast agent. AJP Ren Physiol 300: F1262–F1265
19. Yoshida A, Kanamori H, Naruse G et al (2019) (pro)renin receptor blockade ameliorates heart failure caused by chronic kidney disease. J Card Fail 25:286–300

Chapter 8

Hardware Considerations for Preclinical Magnetic Resonance of the Kidney

Paula Ramos Delgado, Ekkehard Küstermann, André Kühne, Jason M. Millward, Thoralf Niendorf, Andreas Pohlmann, and Martin Meier

Abstract

Magnetic resonance imaging (MRI) is a noninvasive imaging technology that offers unparalleled anatomical and functional detail, along with diagnostic sensitivity. MRI is suitable for longitudinal studies due to the lack of exposure to ionizing radiation. Before undertaking preclinical MRI investigations of the kidney, the appropriate MRI hardware should be carefully chosen to balance the competing demands of image quality, spatial resolution, and imaging speed, tailored to the specific scientific objectives of the investigation. Here we describe the equipment needed to perform renal MRI in rodents, with the aim to guide the appropriate hardware selection to meet the needs of renal MRI applications.

This publication is based upon work from the COST Action PARENCHIMA, a community-driven network funded by the European Cooperation in Science and Technology (COST) program of the European Union, which aims to improve the reproducibility and standardization of renal MRI biomarkers. This chapter on hardware considerations for renal MRI in small animals is complemented by two separate publications describing the experimental procedure and data analysis.

Key words Magnetic Resonance Imaging (MRI), Kidney, Mice, Rats, Hardware, RF coils, Renal MRI

1 Introduction

The detection, staging, and monitoring of kidney diseases (KD) using measurements of renal function and structure is critical in clinical nephrology. The use of animal models in kidney research promotes the understanding of disease and therapy mechanisms. While current imaging modalities such as computed tomography or ultrasound can provide some information on structural changes in the kidney, these approaches offer limited insights into functional changes.

Magnetic resonance imaging (MRI) is a noninvasive imaging technology that offers an unparalleled level of anatomical and functional detail, along with diagnostic sensitivity. MRI is suitable

Andreas Pohlmann and Thoralf Niendorf (eds.), *Preclinical MRI of the Kidney: Methods and Protocols*, Methods in Molecular Biology, vol. 2216, https://doi.org/10.1007/978-1-0716-0978-1_8,

for longitudinal studies due to the lack of exposure to ionizing radiation. Together with established imaging techniques, novel approaches such as dynamic contrast-enhanced MRI (DCE-MRI), arterial spin labeling (ASL), blood oxygen level dependent MRI (BOLD), and diffusion-weighted imaging (DWI) can provide a broad characterization of the kidney, including renal vascular perfusion, oxygenation, and glomerular filtration rate.

For performing dedicated MR measurements of the kidney, the appropriate MRI hardware should be carefully chosen to balance the competing demands of image quality, spatial resolution and imaging speed, tailored to the specific scientific objectives of the investigation. This chapter is intended to outline the key hardware components of an MRI scanner and to provide an overview of currently established technologies, with the goal to guide the appropriate hardware selection that meets the needs of preclinical MRI of the kidney.

This chapter on hardware considerations for renal MRI in small animals is part of the book Pohlmann A, Niendorf T (eds) (2020) Preclinical MRI of the Kidney–Methods and Protocols. Springer, New York.

2 Static Magnetic Field Strength (B_0)

A superconducting magnet that generates a constant homogeneous magnetic field is the core hardware component of an MRI scanner. This strength of this static magnetic field (B_0) is proportional to the net polarization produced within the sample. The detected MR signal on a receive RF coil depends on B_0^2, whereas the noise increases linearly with B_0 [1]. B_0 governs the signal-to-noise ratio (SNR), which is the currency for MR image quality. This provides strong motivation and momentum to move to increasingly higher magnetic field strengths for preclinical and clinical renal MRI applications [2–4]. The proportionality of SNR with B_0 is linear in the quasi-static regime, as demonstrated theoretically [5, 6] and experimentally [7]. For higher magnetic field strengths, wave propagation and the increasing resonance frequencies must be considered [2]. Additionally, an experimental study on intrinsic SNR behaviour with increasing B_0 field strengths (3.0, 7.0, and 9.4 T) in the human brain reported a superlinear increase in SNR ($SNR \propto B_0^{1.65}$) [7]. This observation was also confirmed in a simulation study [8].

Relaxation time constants of biological tissues also change with the magnetic field strength, thus influencing the SNR as well as the contrast-to-noise ratio (CNR), which ultimately has an impact on the image quality. The longitudinal relaxation time (T_1) increases nonlinearly with increasing B_0 [1, 9–11]. The transversal relaxation (T_2) and T_2^* decrease at different slopes linearly [1, 9, 12–14]. These dependencies on B_0 are responsible for the reduced

T_1-weighted contrast and increased BOLD effect at higher magnetic field strengths (*see* **Note 1**). MRI methods based on T_2*-weighting (e.g., susceptibility weighted imaging, BOLD) will benefit from the T_2* shortening, and thus increase in sensitivity at high magnetic field strengths, which underlies their broad application in renal MRI. An example of renal T_2*-mapping ($R_2^* = 1/T_2^*$) is the study of oxygenation and haemodynamics in renal disorders (for a review *see* [15]). MR spectroscopy also benefits from the enhanced signal dispersion achieved at higher magnetic field strengths, which results in better resolved spectra, and permits improved accuracy of metabolite identification and quantification [1, 16].

However, MRI at high magnetic field strengths is susceptible to more severe B_0 and B_1 inhomogeneities, compared to lower field strengths. These inhomogeneities are primarily due to differences in the magnetic susceptibility at tissue interfaces. Susceptibility artifacts present themselves as T_2*-induced signal losses (or even signal voids) in areas with very high B_0 gradients, low phase-encoding bandwidth-related image distortion and off-resonance effects caused by ΔB_0-induced frequency dispersions. MRI of the kidney poses additional challenges due to the anatomical context. The kidneys are adjacent to bowels, in close proximity to skin/fat/muscle boundaries (e.g., perirenal fat) or in areas containing cavities might be particularly prone to susceptibility artifacts.

Artifacts are visible as signal losses at interfaces between fat and tissue or air and tissue (susceptibility artifacts), image blurring, image distortion, and broadening of spectral lines in MRS, which interferes with the reliable differentiation of metabolites. B_0 inhomogeneities can be mitigated using B_0 shimming (*see* Subheading 3).

B_1 inhomogeneities lead to variations in the flip angle driven by the RF pulse excitation. B_1 inhomogeneities affect tissue contrast and SNR, appearing as signal intensity variations or losses across the field of view. Nonuniformities in B_1 are caused by the RF coil (e.g., surface RF coil, *see* Subheading 4) or by the creation of standing waves and constructive/destructive interferences within the object under investigation, due to the reduction of the effective wavelength which at higher field strengths becomes shorter, and can approach the dimensions of the specific anatomical structures under study [17]. While the RF wavelength inside tissue at 3.0 T (~128 MHz) is about 30 cm, at 7.0 T (~300 MHz) it is reduced to about 13 cm [18] and to 6.5 cm at 14.0 T (~600 MHz). In preclinical renal MRI, this is not a major concern, as the size of the abdomen in small animals is typically much smaller than the RF wavelength.

RF power requirements for spin excitation increase quadratically with B_0. This imposes major concerns, especially for human applications, since the RF power deposition can easily reach the regulatory limits specified by IEC guidelines for the specific

absorption rate (SAR) [16]. This constraint can be adressed by modification and adaptation of MR pulse sequences, acquisition strategies, and RF coils [18, 19]. In the case of preclinical studies, these issues have received less attention since there are no enforced SAR guidelines for small animals. Nevertheless, the physiological effects of tissue heating due to heavy RF deposition in experimental animals could be a serious confounding factor in preclinical studies that should not be ignored.

2.1 SNR Comparison for Magnetic Field Strength

The SNR gains resulting from increasing B_0, field have been computationally estimated for brain MRI to range from $B_0^{1.2}$ (close to the brain surface) up to $B_0^{2.1}$ (at the center of the head) [8]. Pohmann et al. [7] investigated the field dependence of SNR for magnetic field strengths ranging between 3.0 T and 9.4 T using gradient echo techniques, and reported that SNR increases supralinearly ($B_0^{1.65}$). Using this relationship, the calculated relative SNR (normalized for the typical case of a 3.0 T scanner) and resolution gains (in μm, in-plane resolution 1 mm) corresponding to all static magnetic field strengths from 1.5 T to 21.1 T are shown in Table 1.

The increase in SNR provided by higher magnetic field strengths can be invested in enhanced spatial resolution or improvements in imaging speed. The triad of B_0, spatial resolution, and imaging speed form the so-called SNR conundrum in which the competing constraints of SNR, CNR, spatial resolution, and imaging speed govern the image quality. For example, increasing the matrix size for a certain field of view will increase the spatial resolution—which will permit the visualization of more subtle anatomical structures in the kidney—but at a cost of reducing the SNR, or signal intensity per pixel/voxel. Although resolution in the frequency-encoding direction can be conveniently enhanced by increasing the matrix size without major scan time penalty, increasing spatial resolution along the phase-encoding direction substantially prolongs the scan time. Boosting the SNR is also possible by modifying the size of the field of view or the slice thickness: the larger these parameters are, the more signal is acquired. Another way to further increase SNR is signal averaging, which reduces the noise but comes at the cost longer scan times. Depending on the individual experimental context, longer scan times may be a reasonable price to pay (especially for ex vivo studies). For in vivo studies, animal welfare considerations call for the minimum scan time possible to achieve the scientific objective, and shorter scans promote higher throughput of individual animals to improve the experimental sample size.

Additional strategies to gain SNR include the use of SNR-promoting rapid imaging techniques such as RARE imaging, and dedicated RF coil technology, including cryogenically cooled RF coils (*see* Subheading 4).

Table 1
Relative SNR and resolution gain with increasing static magnetic field strength

Magnetic field, B_0 (T)	Relative SNR gain	Resolution gain (in-plane 1 mm) (μm^2)
1.5	0.3	(1550 × 1550)
3.0	1.0	(495 × 495)
4.7	2.1	(235 × 235)
7.0	4.0	(122 × 122)
9.4	6.6	(75 × 75)
11.7	9.4	(52 × 52)
14.0	12.7	(39 × 39)
16.4	16.5	(30 × 30)
17.6	18.5	(27 × 27)
21.1	25.0	(20 × 20)

SNR values were computed as proportional to $B^{1.65}$. The relative SNR gain was calculated relative to that of 3.0 T

2.2 Magnetic Field Strengths Used in Recently Published Studies

To provide guidance as to which B_0 is necessary or sufficient for preclinical MRI of the kidney, a total of 121 publications published over the past 10 years were reviewed. Of these, 66 publications reported on renal MRI in rats, and 55 in mice. Figure 1 shows the number of publications found per magnetic field strength for renal MRI in rats and mice. In rats, a total of 25 publications (38%) were performed at 3.0 T, closely followed by 9.4 T with 20 papers (30%). In mice the preferred magnetic field strength was 7.0 T (25 publications, 46%). The magnetic field strengths of 9.4 T (8 papers, 15%), 3.0 T (7 papers, 13%), and 11.7 T (6 publications, 11%) were also used for MRI studies of mouse kidney.

Figure 2 illustrates the number of publications per magnetic field strength, listed by year for rats and mice. In rats, the number of studies performed at 3.0 and 9.4 T was quite stable for the last 7 years. Studies at 4.7 T (7 papers, 11%) were also widely reported, as shown in the trends displayed since 2009. The use of field strengths of 1.5 and 7.0 T (7 and 6 publications, respectively) varied during the period under investigation. In contrast, 7.0 T was established as the typical magnetic field strength for preclinical MRI of the kidney in mice during this period. In the last few years, 11.7 T and 16.4 T have also emerged as MR systems suitable for the study of the mouse kidney.

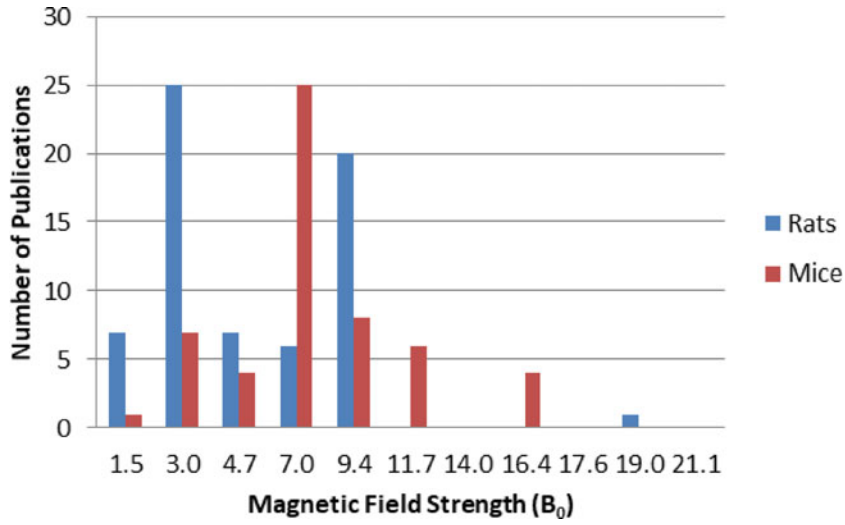

Fig. 1 Number of publications per magnetic field strength for renal MRI in rats and mice, within a total of 121 reports on preclinical renal MRI published in the past 10 years

3 Gradient Systems

To enable the spatial localisation of the MR signal, magnetic field gradients are used, which are provided by gradient coils. Gradient coils produce a linear variation of the magnetic field as a function of the spatial position (X-, Y-, and Z-direction) modifying the resonance frequency for spatial encoding of the MR signal.

Typical parameters governing the performance of the gradient system are the peak gradient strength, the rise time, and the slew rate. The peak gradient strength is the maximum achievable gradient strength (in mT/m). Typical peak gradient amplitudes in preclinical scanners are in the range of 200–1000 mT/m. Clinical scanners used for preclinical MRI of the kidney provide maximum gradient amplitudes ranging between 45 mT/m and 82 mT/m. The gradient rise time is the time needed to change the gradient field from zero to the peak amplitude (in ms). The gradient slew rate is the most important parameter, and refers to the speed at which a gradient can be switched. It is defined as the peak gradient strength divided by the gradient rise time (in T/m/s). This defines the maximum scanning speed, since it influences the minimum achievable repetition time (TR) and echo time (TE), as well as the echo spacing in fast imaging techniques such as RARE or EPI (*see* **Note 2**). Typical slew rates in preclinical scanners are in the range of 640–9000 T/m/s. Clinical scanners used for preclinical MRI of the kidney offer slew rates ranging between 150 T/m/s and 200 T/m/s. Gradient coils can be driven in two modes: (a) constant rise time, in which the slew rate is adapted for each gradient amplitude and (b) maximum slew rate, where the rise is adjusted for each gradient amplitude.

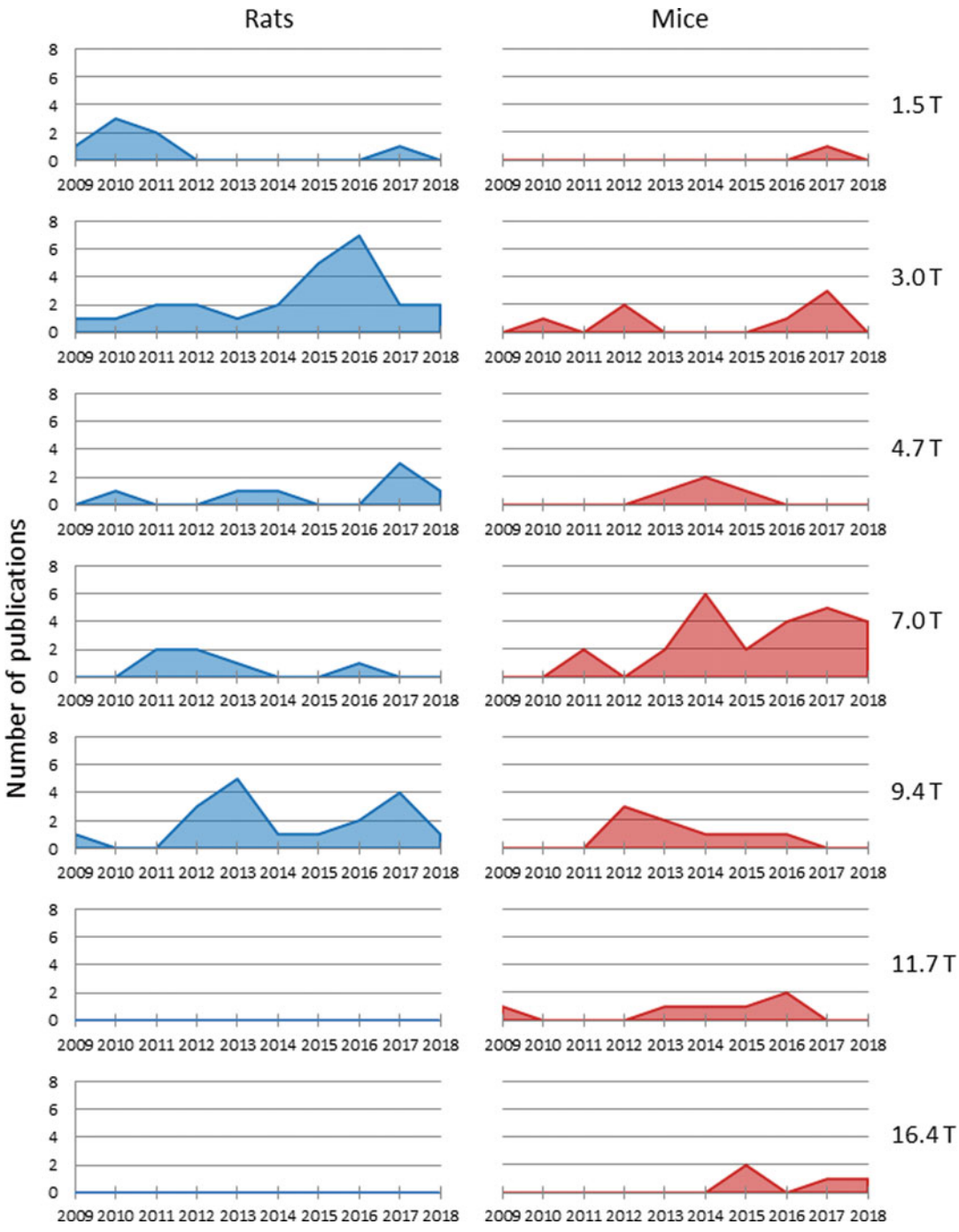

Fig. 2 Number of selected publications ordered by magnetic field strength and year, within a total of 121 reports published in the past 10 years (2009–2018) for preclinical renal MRI in rats and mice

The duty cycle defines the amount of time during which the gradient system can be run at maximum power amplitude (in % time). This parameter depends not only on the gradient system specifications mentioned above but also on the specific MR imaging technique used. Typical duty cycles in existing preclinical scanners can reach almost 100%. For this purpose, gradient coils are water-cooled to ensure proper heat dissipation and temperature management.

The accuracy of the spatial representation depends on the quality of the linear magnetic field gradients and on the homogeneity of the static magnetic field (typically given in parts per million, ppm). Any deviation will appear as object distortion in the image, and thus a correction procedure called "shimming" is typically performed. During system installation, the manufacturer places small metal plates inside the scanner bore to improve the uniformity of the main magnetic field in a static and permanent manner—this is "passive" shimming. The distribution of these ferromagnetic pieces is adjusted over several iterations until the achieved magnetic field uniformity meets the vendor's specification. In addition to passive shimming, resistive shim coils are used for B_0 homogenization. These adjustments are performed with a shim calibration tool on an empty magnet, and therefore the B_0 homogeneity becomes impaired as soon as a sample or subject (human or animal) is placed inside the magnet bore.

An "active" shimming procedure can be conducted during measurement adjustments with every MR scan. This is crucial for techniques such as fat suppression or MR spectroscopy, since the introduction of any matter—an object or animal—inevitably introduces local magnetic field perturbations of the main static magnetic field, which then must be actively compensated for. Especially at the boundaries between tissue and air-filled areas, where magnetic field distortions are pronounced due to the different magnetic susceptibility which can cause severe signal losses and image distortions. Corrective magnetic fields produced by electrical RF coils, designated as shim gradients [20] which are superimposed upon the main magnetic field. Typically, the shim gradient system contains a set of first-order gradients which impose linear field changes in the X-, Y-, and Z-directions, and some second order gradients, which create spherical harmonics in the Z^2, ZX, ZY X^2-Y^2, and XY directions [21]. Some MR systems are also equipped with more sophisticated shim gradients which provide third and fourth order correction terms [22].

Depending on the specific pulse sequence and imaging technique used, the scientist has to adjust these magnetic field corrections to meet certain quality prequisites. Especially with T_2*-weighted sequences (e.g., gradient-echo or EPI sequences) the image quality improves with improved B_0 homogeneity. MR spectroscopic methods are even more demanding [23]. Usually,

state-of-the-art MR systems provide automated methods to perform the B_0 shimming task, but the user still needs to check the performance and correct the shim settings manually if necessary.

For B_0 shimming a global approach covering the entire FOV, or a localized shim covering a target area can be used. In general, the smaller the region of interest the better the achievable B_0 homogeneity. In the case of renal MRI, the B_0 homogeneity achieved after shimming across one kidney will be better than that for the whole abdomen, with air-filled lungs and gut. In the case of tissues that are moving due to respiration, cardiac activity or peristaltic motion, the magnetic field distortions change over time, which require different strategies. The time-averaged global shim would be the fastest and easiest solution, if this is sufficient. Alternatively, shimming—and also data acquisition—would be performed in synchrony with the breathing by using a trigger signal from a physiological monitor [24].

4 Radio Frequency (RF) Coils

Besides the static magnetic field and the spatial encoding with the gradient system, MRI requires transmission of RF pulses and reception of the MR signal from the sample or subject.

For signal excitation, the RF transmit resonator, or RF coil, sends RF pulses with a particular frequency, bandwidth, shape, duration, amplitude, and phase modulation to tilt the net magnetization vector oriented in parallel with the main magnetic field during equilibrium. B_0 (typically assigned as the Z-direction), is tilted into the perpendicular transverse (X-Y) plane by a given flip angle α. After excitation, the magnetization precesses back to equilibrium and induces a signal in the RF receive coil (for a comprehensive review *see* [25]).

Depending on the transmission and reception capabilities, three general types of RF coils are commonly used: (1) transmit-receive (Tx/Rx) or transceiver RF coils, (2) transmit-only (Tx) RF coils, and (3) receive-only (Rx) RF coils. These generally have two types of geometry: (1) volume RF coils and (2) surface RF coils. Both RF coil types and geometries determine the amount of tissue or organ coverage and sensitivity to the MR signal.

Volume RF resonators are designed to produce a uniform RF field over a large field-of-view (FOV), and are typically used as transmit-receive RF coils or transmit RF coils (using a surface RF coil for reception). The most widely used type of volume RF coils in both human and preclinical MRI are birdcage resonators [26, 27] driven in quadrature mode. This means that two spatially orthogonal RF channels are used for RF transmission as well as signal reception. This RF coil configuration provides a 41.4% SNR gain over simple single channel or "linear" RF coils, due to the coherent

signal increases which scale linearly with the number of channels, while the incoherent noise increases with the square root of the number of channels. For example, Chang et al. [28] used this RF coil setup in a renal hypoxia study in a mouse model after myocardial infarction of different sizes using BOLD MRI. Other types of volume resonators include saddle RF coils, Helmholtz RF coils, and the transverse electromagnetic (TEM) resonators, among others.

Smaller anatomical coverage and FOVs, but enhanced SNR, are provided by surface RF coils. Due to the principle of reciprocity, the closer the position of the RF coil is to the tissue of interest, the higher is the attainable SNR. However, the sensitivity drops with increasing distance to the RF coil surface, which thus results in a reduced FOV, and an inhomogeneous sensitivity profile [29]. Within a short distance of typically up to ~1 cm, a surface RF coil outperforms a volume RF coil in terms of sensitivity. Since the kidneys are located beneath the skin, surface RF coils positioned directly above are used for optimal signal reception in renal MRI. This is advantageous not only for X-nuclei MR imaging (*see* Subheading 5) but also for other applications with low SNR, such as perfusion or diffusion-weighted imaging.

Surface RF coils may be used as transmit/receive devices or as receive-only RF coils in conjunction with a volume RF coil used for homogeneous RF transmission. The first option is technically very simple since only one RF coil is necessary, which occupies less space. In the case of small animal imaging, it is most likely a simple single-turn loop with at least two tunable capacitances for tuning and matching. Images will show a strong spatially varying SNR decay, due to the addition of the inhomogeneous excitation and reception profiles [30]. This effect may be mitigated, for example, by using adiabatic excitation RF pulses [31].

The second option involves the use of two RF coils (Tx: volume RF coil, Rx: surface RF coil) which are tuned to the same resonant frequency. To avoid RF coupling between both coils, the surface RF coil must be detuned during transmission while the volume RF coil must be detuned during reception. Thus, both RF coils must include an option, using active and passive diodes, to allow for tuning and detuning during the MR experiment. This is the most common setup, since it improves the SNR in comparison with a Tx/Rx volume RF coil, while still maintaining a homogeneous B_1. For example, Hüper et al. [32] used a four-element quadrature surface receive RF coil in combination with a transmit volume RF coil to investigate renal perfusion in acute and chronic renal allograft rejection in translational mouse models. The use of the surface RF coil improved the SNR from 15 (with a standard transceive volume RF coil) to 35.

Further SNR gains in small animal MRI are achieved with arrays of surface RF coils for signal reception [33], which are typically used together with a volume RF coil for signal excitation

(*see* **Notes 3** and **4**). The use of RF coil arrays for brain imaging is especially widespread, and these are routinely offered by manufacturers. State-of-the-art small-animal MRI systems are usually equipped with 4–16 Rx channels, to which custom-tailored RF coils may be connected. Less popular are metamaterial-inspired RF coils, which have been developed for superficial tissue imaging in order to provide the best compromise of high SNR over a large FOV, while using only one receive channel [34].

Depending on the size of the sample and the RF coil, and their corresponding temperatures and resistances, their noise electronic contribution varies [35–37]. This factor is even more crucial in preclinical applications where the noise contribution of the RF coil, capacitors, sample, shield, receive electronics, and transmission lines are important [26]. This fact is exploited in small-animal imaging by the use of cryogenically cooled (cryo-cooled) RF coils. By lowering the temperature of the receiver chain, the noise contributions corresponding to temperatures and resistances can be reduced [38–40], thus achieving a significant increase in SNR, which has been reported in the literature (for a review *see* [15]). Unfortunately, only negligible effects are achieved in human MR [15, 41]. With increasing size of the sample, the relative contribution to the noise increases, and eventually becomes the dominating noise source—this is the default situation for human MR. Thus, only small animal MR applications will benefit from this cooling approach, since the noise contributions from the sample and RF coil are in the same order of magnitude. The SNR gain achieved with such cryo-cooled RF coils is higher at lower static magnetic fields [15, 26, 42]. A recognized limitation of cryo-cooled surface RF coils is that only transceive capabilities are supported, resulting in nonuniform excitation and reception profiles, which might hamper quantitative measurements.

Another option for the small-animal MR imaging of the kidney is the use of clinical scanners together with RF coils tailored for the human hand/wrist or knee. These are typically 8- to 16-element RF coil arrays which provide quasi-homogeneous excitation and reception profiles. Although these RF coils have a small size, they are not optimized for small-animal imaging and are not designed with matching/tuning capabilities. Moreover, RF coils tailored for rodent imaging are designed for a broad range of loadings (i.e., from almost empty to full loading, with a typical frequency-diameter product in the range 2–30 MHz · m [26]), in comparison to the clinical setups. Therefore, these clinical RF coils will achieve a lower efficiency than that of dedicated RF coils designed for preclinical MR systems. Alternatively, RF coils tailored for renal MRI of small rodents provided by RF coil manufactures can be connected with clinical MR scanners to enhance the fill factor and SNR.

In the following subsections, examples of possible RF coil setups are shown from different vendors. A list of the available MR system and RF coil vendors can be found in Table 2.

4.1 Commercially Available RF Coils Suitable for Kidney MRI in Rats

Due to the considerable anatomical homology with humans, rats have become one of the most commonly use rodents in animal research, particularly, in preclinical MRI. With a weight of 150–450 g, both clinical and preclinical MR systems and RF coils can be used to perform renal MR experiments:

Clinical MR System
- Tx/Rx wrist RF coil (e.g., Siemens eight-channel wrist RF coil, Fig. 3A).
- Tx/Rx knee RF coil (e.g., Siemens 15-channel knee RF coil, Fig. 3B).

Preclinical MR System
- Tx/Rx volume resonator (e.g., Bruker Biospin, Ettlingen, Germany, quadrature rat body RF coil with inner diameter (ID) = 72 mm (Fig. 3C), 82 mm or 86 mm; RAPID Biomed, Rimpar, Germany 2 × 4-channel volumetric rat array with ID = 72 mm).
- Tx/Rx quadrature volume resonator (e.g., MRI.TOOLS GmbH, Berlin, Germany, supporting an ID ranging from 54 mm to 86 mm and magnetic field strengths of 3.0 T, 4.7 T, 7.0 T, 9.4 T, and 11.T (Fig. 3D).
- Rx surface RF coil (e.g., 2 × 2 RAPID Biomed, Rimpar, Germany) rat cardiac surface array RF coil; 4 × 1 element (e.g., Bruker Biospin, Ettlingen, Germany) rat cardiac surface array RF coil, Fig. 3E) in combination with Tx volume resonator (e.g., Bruker rat body RF coils with ID 72 mm (Fig. 3F), 82 mm or 86 mm).

4.2 Commercially Available RF Coils Suitable for Kidney MRI in Mice

Mice are the most commonly used rodent in biomedical research. Their genetic similarity to humans has made them extremely useful, allowing the development of mouse models of many human diseases. Mice have an average weight of 15–40 g, making them too small for standard human RF coils:

Clinical System
- There are no standard human RF coils that are small enough to be suitable for mice MRI. Alternatively, a Tx/Rx quadrature volume resonator (MRI.TOOLS GmbH, Berlin, Germany), supporting an ID ranging from 30 mm to 45 mm and magnetic field strengths of 3.0 and 7.0 T can be used for renal MRI with clinical MR scanners (Fig. 4A).

Table 2
List of vendors of MR equipment and RF coils

	Vendor	Website
Clinical MRI	Canon Medical Systems	us.medical.canon
	General Electric Medical Systems Inc.	www.gehealthcare.com
	MRI Devices Corp.	www.allmri.com
	MR Instruments Inc.	www.mrinstruments.com
	MRI.TOOLS GmbH	www.mritools.de
	NOVA Medical Inc.	www.novamedical.com
	RAPID Biomedical GmbH	www.rapidbiomed.de
	Philips Medical Systems	www.medical.philips.com
	ScanMed	www.scanmed.com
	Siemens Medical Systems	www.siemens-healthineers.com
	Tesla Engineering Limited	www.tesla.co.uk
Preclinical MRI	Bruker BioSpin MRI GmbH	www.bruker.com
	Doty Scientific, Inc.	www.dotynmr.com
	MR Solutions	www.mrsolutions.com
	MRI.TOOLS GmbH	www.mritools.de
	RAPID Biomedical GmbH	www.rapidbiomed.de

Preclinical System

- Tx/Rx volume resonator (Bruker Biospin, Ettlingen, Germany) quadrature mouse body RF coil with ID = 35 mm, Fig. 4B); 2 × 4 -channel volumetric mouse array (RAPID Biomed, Rimpar, Germany) with 35 mm ID.
- Tx/Rx quadrature volume resonator (MRI.TOOLS GmbH, Berlin, Germany, supporting an ID ranging from 30 mm to 45 mm and magnetic field strengths of 3.0 T, 4.7 T, 7.0 T, 9.4 T, and 11.T (Fig. 4A).
- Rx surface RF coil (e.g., RAPID Biomed, Rimpar, Germany) 2 × 2 mouse cardiac surface array RF coil; 2 × 2 element mouse cardiac surface array RF coil (e.g., Bruker Biospin, Ettlingen, Germany, Fig. 4B) in combination with Tx volume resonator (e.g., Bruker Biospin, Ettlingen, Germany) quadrature mouse body RF coils with ID 72 mm (as shown in Fig. 4E), 82 mm or 86 mm).
- Tx/Rx 2 × 2 element array rat/mouse CryoProbe (e.g., Bruker Biospin, Ettlingen, Germany, Fig. 4C).

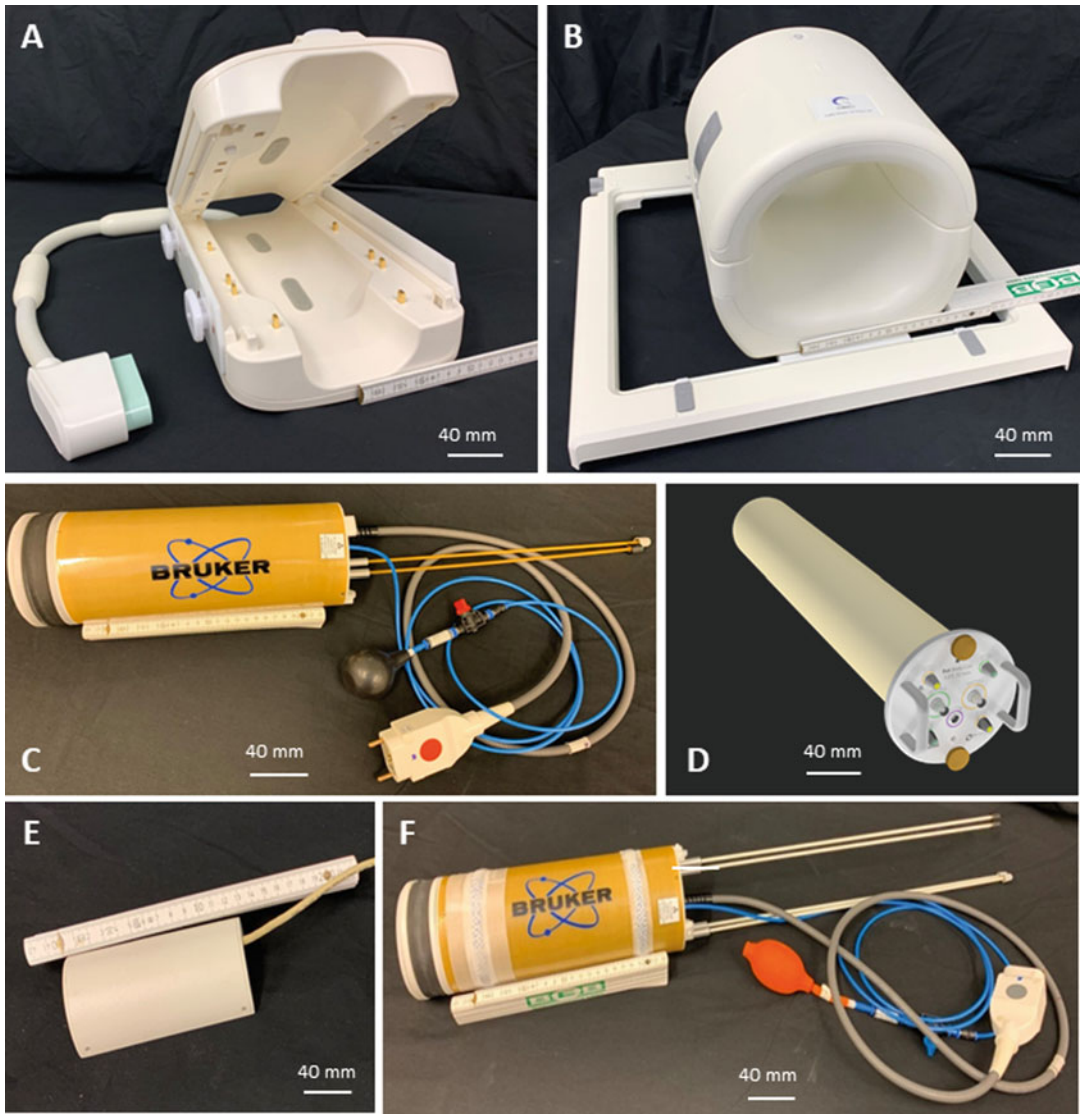

Fig. 3 Example RF coils suitable for kidney MRI of the rat. (**a**) Siemens 8-channel wrist RF coil, (**b**) Siemens 15-channel knee RF coil, (**c**) Bruker quadrature rat body RF coil with inner diameter (ID) 72 mm, (**d**) MRI.TOOLS GmbH quadrature rat body RF coil with ID of 72 mm, (**e**) 4 × 1 element Bruker rat cardiac Rx surface array RF coil, (**f**) Bruker rat body Tx volume resonator with ID 72 mm.

5 Multinuclear Imaging

The most frequent MRI method in biomedical research is proton (^{1}H) imaging. Hydrogen is the most abundant nucleus in living organisms. It also is the nucleus which is the most sensitive to interactions with an external magnetic field, due to its high gyromagnetic ratio ($\gamma = 42.576$ MHz/T).

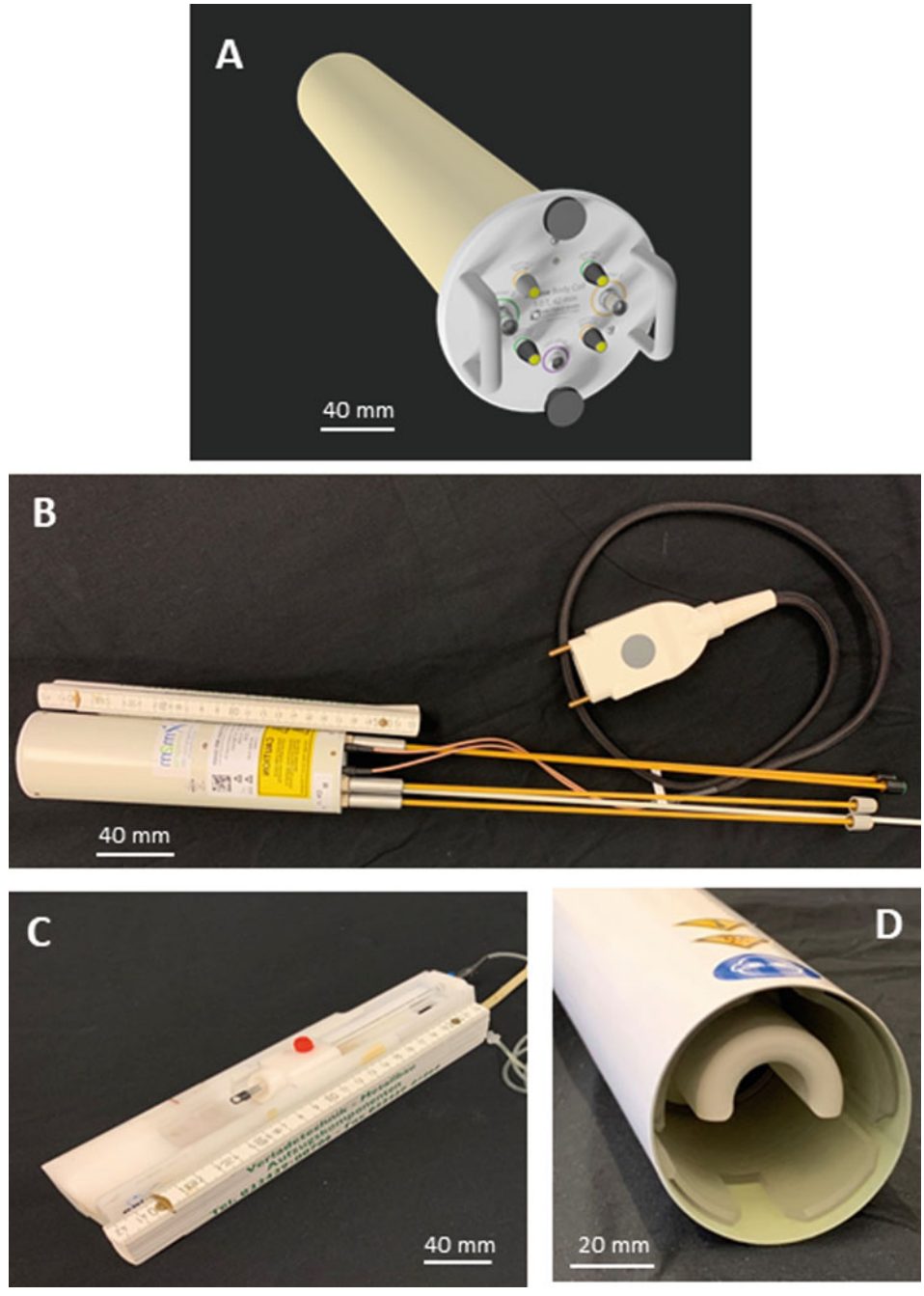

Fig. 4 Example RF coils suitable for kidney MRI of the mouse. (**a**) MRI.TOOLS GmbH quadrature mouse body RF coil with an ID = 42 mm, (**b**) Bruker quadrature mouse body RF coil with 35 mm ID, (**c**) Bruker 2 × 2 element mouse cardiac surface array RF coil, (**d**) Tx/Rx quadrature surface RF coil with cryo-cooling technology (CryoProbe)

In preclinical renal MRI, structural and functional information is typically investigated using in vivo ^{1}H MR imaging of the kidney. Techniques such as T_2/T_2* mapping, arterial spin labeling (ASL), dynamic contrast-enhanced imaging (DCE-MRI) or diffusion-weighted imaging (DWI) are performed in order to study the oxygenation, perfusion, clearance rate, and water and metabolite motion within the kidneys.

Physiometabolic probing is supported by imaging and spectroscopic applications of other nuclei such as ^{13}C, ^{17}O, ^{23}Na, ^{35}Cl, ^{39}K, ^{31}P, and ^{19}F [43]. The detection of X-nuclei is challening because of the low intrinsic SNR due to the smaller γ, compared to ^{1}H, and by the lower abundance of these nuclei in biological tissues.

Increasing B_0 is the most effective way to increase sensitivity—the benefits of higher B_0 are unique metabolic and functional information, as well as outstanding anatomical detail [44–47]. X-nuclei MR also benefits from the increase in SNR achieved with cryo-cooled transceive surface RF coils, which are currently available for ^{13}C, ^{31}P, ^{19}F, and ^{1}H [48, 49].

Changes in the biodistribution of endogenous metabolites that can be detected with ^{23}Na- or ^{31}P-MR have been demonstrated to be markers of renal disease [50–53]. For more details on preclinical ^{23}Na-MRI protocols, see the chapters by Grist JT et al. "Sodium (^{23}Na) MRI of the Kidney: Basic Concept" and "Sodium (^{23}Na) MRI of the Kidney: Experimental Protocol." Similarly, renal perfusion, oxygenation, and inflammatory cell infiltration can be investigated using ^{19}F-MRI [54–57]. *See* the chapters by Grist JT et al. "Sodium (^{23}Na) MRI of the Kidney: Basic Concept" and "Sodium (^{23}Na) MRI of the Kidney: Experimental Protocol" on how to perform ^{19}F-MRI renal studies in rodents.

Hyperpolarization techniques have great potential for explorations into renal metabolic diseases (e.g., hyperpolarized ^{13}C-MRI), where SNR is boosted up to a 20,000-fold compared to conventional ^{13}C-MRI [58]. Experimental protocols to perform hyperpolarized ^{13}C-MRI in preclinical studies are provided in the chapters by von Morze C et al. "Hyperpolarized Carbon (^{13}C) MRI of the Kidneys: Basic Concept" and by Laustsen C et al. "Hyperpolarized Carbon (^{13}C) MRI of the Kidney: Experimental Protocol."

6 Physiological Monitoring

A major difference between clinical and preclinical MRI is the need to anesthetize the animals prior to imaging. Since most anaesthetic drugs produce physiological changes (temperature decrease, depression of cardiorespiratory function, etc.), monitoring the anaesthetized animals is a very crucial aspect in preclinical MRI studies. Even in the most simple case, that is, the scanning of spontaneously breathing animals without any further intervention

or treatment, respiration and temperature of the animal has to be monitored continuously during the scan in order to guarantee the appropriate anaesthetic status and to avoid hypothermia. In particular, hypothermia is a critical issues in rodent imaging, since mice have a low mass vs. a large surface which promotes heat loss [59, 60]. This problem is less severe in rats due to their larger weight, but it is not negligible [61]. Heating systems must be therefore used to maintain temperature homeostasis.

Physiological monitoring of the animal is even more essential in functional MR imaging, since changes may produce confounding effects on the outcome of the MR experiment [62]. Careful monitoring and recording of physiological data should be performed at all times during the experiment to ensure the validity of the results and their reproducibility. The frequency of physiological monitoring depends on the invasiveness of the experimental procedure as well as the time after induction of anaesthesia. As a rule of thumb, the more invasive the procedure and the longer the time under anaesthesia, the more frequent the physiological monitoring of the animal should be performed. Additionally, the correct positioning of the animals on the animal bed systems, along with careful intubation (if needed) are essential to ensure respiratory and circulatory comfort during imaging, and to promote recovery of the animal after the experiment.

Typical physiological parameters monitored during MR experiments include temperature, heart rate, and respiration rate. Many manufacturers already offer these three monitoring channels, and are ready to use these signals for the purpose of gating or triggering the MR imaging techniques. Additionally, information on blood pressure, blood oxygen saturation, transcutaneous pCO_2, or pH can also be collected. In some cases, invasive withdrawal of blood samples is necessary—this is a very difficult task since the sampling has to be executed using long tubes with considerable dead volumes and very limited visual control.

Finally, all equipment must allow for remote physiological monitoring, and strictly comply with MR safety requirements. Several integrated animal handling solutions for physiological monitoring and anaesthesia are commercially available. Examples are given in Table 3.

7 Practical Points to Consider When Planning a Study

The aim of this chapter is to outline the main hardware components required for preclinical MRI of the kidney and to guide the appropriate hardware selection to meet the individual needs.

This section is intended to provide a summary of the prequisites needed and to help prepare for preclinical renal MR applications:

Table 3
Examples of commercially available equipment for physiological monitoring in preclinical MRI

Physiological parameter (s)	Examples of vendor equipment
Temperature	Omniflex (Neoptix, Inc., Canada) Fiber optic temperature probes (SA Instruments, Inc. Stony Brook, NY, USA) RightTemp (Kent Scientific Corp., Torrington, CT, USA) MultiSens (Opsens Solutions, Canada)
Respiration rate/ECG and gating	BioVet (m2m imaging, Cleveland, OH, USA) Model 1030 Monitoring & Gating system (Small Animall Instruments, Inc. Stony Brook, NY, USA)
Blood pressure	CODA monitor (Kent Scientific Corp., Torrington, CT, USA)
Blood oxygen saturation, heart rate	Pulse oximeter (SA Instruments, Inc. Stony Brook, NY, USA) MouseOx (STARR Life Sciences Corp., USA)
Transcutateous pCO_2	Capnograph (SA Instruments, Inc. Stony Brook, NY, USA) CapnoScan (Kent Scientific Corp., Torrington, CT, USA)
Several	PhysioSuite (Kent Scientific Corp., Torrington, CT, USA) PLUGSYS (Harvard Apparatus, Holliston, MA, USA)

7.1 MRI System

7.1.1 Clinical or Preclinical?

With a 3.0 T clinical MR system, renal MRI of rats is feasible with acceptable image quality and spatial resolution. However, if possible, we recommend to use a dedicated ultrahigh field MR system tailored for small-animal imaging with a magnetic field strength of 7.0 or 9.4 T. The reason is that the SNR gain achieved with preclinical MR scanners compared to that at lower B_0 is instrumental for achieving good spatial and temporal resolution, as well as for reducing the scan times needed to perform MR examinations.

7.1.2 Should I Consider Moving to a High Magnetic Field Strength?

As discussed above (*see* Subheading 2), the use of a higher magnetic field strength results in an increase in SNR proportional to B_0 ($SNR \propto B_0^{1.65}$). This means that renal MR images will achieve greater SNR that can be traded off for to achieve higher spatial resolution or reduced scan time as needed (*see* Table 1). Also, higher B_0 increases the BOLD effect. In general, all methods based on T_2*-weighting will benefit from an increase in the magnetic field strength. MR spectroscopy applications also profit from the increased B_0. Therefore, we strongly recommend the use of a high B_0 for these MR applications. However, not all facilities have such high field MR scanners readily available, in which case it might be advisable to perform the experiments using a lower magnetic field system, as opposed to moving animals, equipment, and personnel to another facility.

7.1.3 Higher Magnetic Fields Are All Rainbows and Unicorns, and Should Always Be Used, Right?

Not necessarily! Be aware that higher magnetic field strengths suffer from greater B_0 and B_1 inhomogeneities than lower field strengths, which must be corrected in order to fully benefit from the boost in SNR. Also, due to the B_0-dependent changes of the relaxation properties, the method-specific and protocol-specific imaging parameters have to be adopted in order to generate similar image contrasts that are comparable to those achieved at lower B_0. If the focus is the transfer of MR methods from preclinical models to clinical applications, use of the same static magnetic field strength is advisable. The "loss" of SNR may be partially compensated for by the use of cryo-cooled RF coils, which would be more cost-effective than the procurement of a high field small animal MR scanner.

7.1.4 OK, But ... Which B_0 Is Everyone Else Using?

The move to higher magnetic field strengths is supported by a large body of literature (see Figs. 1 and 2) which reports the most typical magnetic field strengths for rats to be 3.0 and 9.4 T and for mice to be 7.0 and 9.4 T. The continued use of 3.0 T scanners for rats is mainly due to the use of readily available clinical MR systems, which are then adapted for rat MR experiments. However, these are typically performed using hand/wrist or knee RF coils tailored for clinical applications in humans, and are not optimized for animal imaging, with the main disadvantages being a loss of signal due to incorrect loading, and the inability to match and tune the RF coil.

7.1.5 What About the Gradient System?

Depending on the MR application of your choice, a high gradient slew rate might be needed. Fast imaging techniques need fast gradient switching speeds, since this parameter influences the minimum achievable repetition time (TR), echo time (TE), and the echo spacing. However, a higher slew rate means a greater monetary investment will be needed at the acquisition of a new MR scanner. Equally, the duty cycle is a crucial parameter in hardware-demanding sequences, which generally includes all fast imaging techniques. We recommend the procurement of a gradient system tailored according to the individual experimental needs.

7.2 RF Coil Setup

7.2.1 Which Kind of RF Coil Should I Use to Get the Most Juice from My Clinical MR Scanner?

The best option is to use a hand/wrist RF coil; a knee RF coil is a second-best option. Both of these are RF coil arrays which provide high SNR and full FOV coverage. However, these RF coils are tailored for clinical applications in humans and are not optimized for animal imaging, with the main disadvantages being a loss of signal due to incorrect loading and the inability to match and tune the RF coil. Also, the clinical MR system must be adapted for rat MR experiments (mice are too small and do not provide enough loading in clinical systems). Alternatively, dedicated RF coils provided by RF coil vendors which are customized for renal MRI of rats can be connected to the clinical MR scanner.

7.2.2 Which RF Coil Setups Are the Most Suitable for Renal Applications in My Preclinical MR Scanner?

The anatomical position of the kidneys suggests placement of the RF coil in close proximity to the dorsal skin of the animal. We recommend the use of a surface RF coil for signal reception together with a volume RF coil for excitation. This is the most common setup since it improves the SNR in comparison with a Tx/Rx volume RF coil, while still maintaining a homogeneous B_1. Also, be aware that this setup needs the synchronized detuning of the RF coils in turns in order to avoid RF coupling between the two coils (the surface RF coil must be detuned during transmission while the volume RF coil must be detuned during reception).

7.3 X-Nuclei

7.3.1 What If I Want to Perform X-Nuclei MRI/MRS?

Broadband RF chains, including the transmission path and the receive path, together with RF coils specifically tailored for X-nuclei are needed. Due to the typically low SNR inherent to X-nuclei MR applications, a good option would be the use of a cryo-cooled RF coil. Imaging of a single kidney can be performed in mice using a mouse cryo-cooled RF coil. To image both kidneys simultaneously in mice, a rat cryo-cooled RF coil could be used. However, bear in mind that cryo-cooled RF coils are designed as transceive surface RF antennae, and provide inhomogeneous transmit and sensitivity profiles. Therefore, if your MR application needs exact T_1 contrasts or quantification based on absolute signal intensities, a B_1 correction must be performed.

7.4 Animal Handling and Physiological Monitoring

Please also *see* the chapter by Kaucsar T et al. "Preparation and Monitoring of Small Animals in Renal MRI."

7.4.1 How Should I Position the Rodent in the Animal Bed Prior to the Experiment?

This depends on the kind of RF coil being used. Typically, the kidneys are measured from the dorsal side using a combination of a volume RF coil for RF pulse transmission and a surface RF coil to receive the MR signal. The volume RF coil will be placed inside the bore and fixed, while the surface RF coil is typically displaceable or is fixed on the animal bed. The position of the animal will then be adapted according to this setup.

7.4.2 What Is the Essential Physiological Monitoring that Should Be Performed During Small-Animal Renal MR Experiments?

The essential physiological monitoring includes respiration, which is also used for triggering, and body temperature, which should be maintained at a normal level.

7.4.3 What Other Physiological Parameters Can I Measure, and Which Equipment Should I Use?

A wide variety of MR compatible equipment exists in the market that allows for measurement of temperature, respiration rate, blood pressure, blood oxygen saturation and respiration rate, and transcutaneous pCO_2, among others. *See* Table 3 for exemples of commercially available equipment for physiological monitoring in preclinical MRI.

7.5 Image Acquisition

7.5.1 Should I Perform B_0 Shimming in Every MR Study?

Preferably, yes. Active shimming protocols homogenize the B_0 field in a small region of interest, and help to improve the performance of T_2*-weighted MR protocols such as EPI. For performing MRS of the kidney (or any other organ), shimming should always be completed during the MR study adjustments. In general, we recommend to always perform shimming in every renal MR study.

7.5.2 Should I Always Do Triggering of the Signal? What Are my Options?

Renal MR imaging should be synchronized with animal respiration, preferably triggered to the exhalation phase [32, 63]. If possible, the animals should be allowed to breathe spontaneously under anaesthesia.

8 Notes

1. After the decade of the brain and the (re)discovery of the brain–heart–kidney network, a new era of kidney imaging is expected. The most important brain research tool is fMRI, and it has served as strong motivation for continued technological improvements in hardware development. Similar techniques are valuable for renal imaging. BOLD-based and BV/BF-based techniques greatly benefit from higher magnetic fields, providing a higher SNR, a higher CNR, and better spatial resolution. Nevertheless, the use of higher magnetic fields brings new problems that call for new hardware solutions.
2. Although there is an increased demand on gradient performance, this will exacerbate the problems associated with acoustic noise. New gradient designs should take into account the acoustic noise pressure level as a parameter. Gradient systems that are targeted to the region of interest only may be a solution. The higher gradient performance with increased bandwidth, as well as the increased physiological noise, reduce the gain in the SNR. A limit of the tissue contribution to thermal noise may be found by new RF coil designs.
3. Modern MRI systems come equipped with multiple receiver units allowing parallel acquisition. A combination of small, multielement receive-only RF coils with parallel imaging is a game changer in the way MRI data are acquired. Reducing the RF coil size will allow for the acquisition of data from a small region of interest with higher sensitivity, because of the close proximity of the RF coil to the region, and thus limited noise contribution from tissue. The use of multiple elements, which are decoupled from each other, will help to achieve extended tissue coverage.
4. A problem associated with parallel imaging arises in the storage and processing of large amounts of data. Therefore, considerable effort must be invested into the handling of "Big Data." Boosting the data transfer rate, the use of array processors and the application of renal MRI will push the limits of data science.

Acknowledgments

This work was funded in part (Thoralf Niendorf, Andreas Pohlmann) by the German Research Foundation (Gefoerdert durch die Deutsche Forschungsgemeinschaft (DFG), Projektnummer 394046635, SFB 1365, RENOPROTECTION. Funded by the Deutsche Forschungsgemeinschaft (DFG, German Research Foundation), Project number 394046635, SFB 1365, RENOPROTECTION).

This publication is based upon work from COST Action PARENCHIMA, supported by European Cooperation in Science and Technology (COST). COST (www.cost.eu) is a funding agency for research and innovation networks. COST Actions help connect research initiatives across Europe and enable scientists to enrich their ideas by sharing them with their peers. This boosts their research, career, and innovation.

PARENCHIMA (renalmri.org) is a community-driven Action in the COST program of the European Union, which unites more than 200 experts in renal MRI from 30 countries with the aim to improve the reproducibility and standardization of renal MRI biomarkers.

References

1. de Graaf RA, Brown PB, McIntyre S, Nixon TW, Behar KL, Rothman DL (2006) High magnetic field water and metabolite proton T_1 and T_2 relaxation in rat brain in vivo. Magn Reson Med 56(2):386–394. https://doi.org/10.1002/mrm.20946
2. Ladd ME (2018) The quest for higher sensitivity in MRI through higher magnetic fields. Z Med Phys 28(1):1–3. https://doi.org/10.1016/j.zemedi.2017.12.001
3. Moser E, Laistler E, Schmitt F, Kontaxis G (2017) Ultra-high field NMR and MRI—the role ofmagnet technology to iIncrease sensitivity and specificity. Front Phys 5:33. https://doi.org/10.3389/fphy.2017.00033
4. Niendorf T, Barth M, Kober F, Trattnig S (2016) From ultrahigh to extreme field magnetic resonance: where physics, biology and medicine meet. MAGMA 29(3):309–311. https://doi.org/10.1007/s10334-016-0564-1
5. Hoult DI (2000) Sensitivity and power deposition in a high-field imaging experiment. J Magn Reson Imaging 12:46–67. https://doi.org/10.1002/1522-2586(200007)12:1<46::AID-JMRI6>3.0.CO;2-D
6. Hoult DI, Richards RE (1976) The signal-to-noise ratio of the nuclear magnetic resonance experiment. J Magn Reson 24(1):71–85. https://doi.org/10.1016/0022-2364(76)90233-X
7. Pohmann R, Speck O, Scheffler K (2016) Signal-to-noise ratio and MR tissue parameters in human brain imaging at 3, 7, and 9.4 Tesla using current receive coil array. Magn Reson Med 75:801–809. https://doi.org/10.1002/mrm.25677
8. Guérin B, Villena JF, Polimeridis AG, Adalsteinsson E, Daniel L, White JK, Wald LL (1980) The ultimate signal-to-noise ratio in realistic body models. Magn Reson Med 78:1969–1980. https://doi.org/10.1002/mrm.26564
9. Merkle EM, Dale BM (2005) Abdominal MRI at 3.0 T: the basics revisited. Am J Roentgenol 186(6):1524–1532. https://doi.org/10.2214/AJR.05.0932
10. Rooney WD, Johnson G, Li X, Cohen ER, Kim SG, Ugurbil K, Springer CS (2007) Magnetic field and tissue dependencies of human brain longitudinal ^1H_2O relaxation *in vivo*. Magn Reson Med 57(2):308–318. https://doi.org/10.1002/mrm.21122
11. Seehafer JU, Kalthoff D, Farr TD, Wiedermann D, Hoehm M (2010) No increase of the blood oxygenation level-dependent functional magnetic resonance imaging signal with higher field strength: implications for

brain activation studies. J Neurosci 30 (15):5234–5241. https://doi.org/10.1523/JNEUROSCI.0844-10.2010

12. Schenck JF (1995) Imaging of brain iron by magnetic resonance: T_2 relaxation at different field strengths. J Neurol Sci 134:10–18. https://doi.org/10.1016/0022-510X(95)00203-E
13. Duyn JH (2012) The future of ultra-high field MRI and fMRI for study of the human brain. NeuroImage 62:1241–1248. https://doi.org/10.1016/j.neuroimage.2011.10.065
14. Baldanchani P, Naidich TP (2015) Ultra-high-field MR neuroimaging. Am J Neuroradiol 36 (7):1204–1215. https://doi.org/10.3174/ajnr.A4180
15. Niendorf T, Pohlmann A, Reimann HM, Waiczies H, Peper E, Huelnhagen T, Seeliger E, Schreiber A, Kettritz R, Strobel K, Ku MC, Waiczies S (2015) Advancing cardiovascular, neurovascular, and renal magnetic resonance imaging in small rodents using cryogenic radiofrequency coil technology. Front Pharmacol 6:255. https://doi.org/10.3389/fphar.2015.00255
16. Schick F (2005) Whole-body MRI at high field: technical limits and clinical potential. Eur Radiol 15(5):946–959. https://doi.org/10.1007/s00330-005-2678-0
17. Van de Moortele PF, Akgun C, Adriany G, Moeller S, Ritter J, Collins CM, Smith MB, Vaughan JT, Ugurbil K (2005) B_1 destructive interferences and spatial phase patterns at 7 T with a head transceiver array RF coil. Magn Reson Med 54:1503–1518. https://doi.org/10.1002/mrm.20708
18. Niendorf T, Graessl A, Thalhammer C, Dieringer MA, Kraus O, Santoro D, Fuchs K, Hezel F, Waiczies S, Ittermann B, Winter L (2013) Progress and promises of human cardiac magnetic resonance at ultrahigh fields: a physics perspective. J Magn Reson 229:208–222. https://doi.org/10.1016/j.jmr.2012.11.015
19. Fiedler T, Ladd ME, Bitz AK (2017) SAR simulations & safety. NeuroImage 168:33–58. https://doi.org/10.1016/j.neuroimage.2017.03.035
20. Stockmann JP, Wald LL (2018) In vivo B_0 field shimming methods for MRI at 7T. NeuroImage 168:71–87. https://doi.org/10.1016/j.neuroimage.2017.06.013
21. Juchem C, de Graaf RA (2016) B_0 magnetic field homogeneity and shimming for *in vivo* magnetic resonance spectroscopy. Anal Biochem 529:17–29. https://doi.org/10.1016/j.ab.2016.06.003
22. Pan JW, Lo KM, Hetherington HP (2012) Role of very high order and degree B_0 shimming for spectroscopic imaging of the human brain at 7 Tesla. Magn Reson Med 68 (4):1007–1017. https://doi.org/10.1002/mrm.24122
23. Motyka S, Moser P, Hingerl L, Hangel G, Heckova E, Strasser B, Eckstein K, Robinson SD, Poser BA, Gruber S, Trattnig S, Bogner W (2019) The influence of spatial resolution on the spectral quality and quantification accuracy of whole-brain MRSI at 1.5T, 3T, 7T, and 9.4T. Magn Reson Med 82(2):551–565. https://doi.org/10.1002/mrm.27746
24. Meyer A, Stolz K, Dreher W, Bergemann J, Thimmashetty VH, Lueschen N, Azizi Z, Khobragade V, Maedler K, Kuestermann E (2015) Manganese-mediated MRI signals correlate with functional β-cell mass during diabetes progression. Diabetes 64(6):2138–2147. https://doi.org/10.2337/db14-0864
25. Gruber B, Froeling M, Leiner T, Klomp DWJ (2018) RF coils: a practical guide for nonphysicists. J Magn Reson Imaging 48:590–604. https://doi.org/10.1002/jmri.26187
26. Doty FD, Entzminger G, Kulkarni J, Pamarthy K, Staab JP (2007) Radio frequency coil technology for small-animal MRI. NMR Biomed 20:304–325. https://doi.org/10.1002/nbm.1149
27. Lopez Rios N, Pouliot P, Papoutsis K, Foias A, Stikov N, Lesage F, Dehaes M, Cohen-Adad J (2018) Design and construction of an optimized transmit/receive hybrid birdcage resonator to improve full body images of medium-sized animals in 7T scanner. PLoS One 13(2): e0192035. https://doi.org/10.1371/journal.pone.0192035
28. Chang D, Wang YC, Xu TT, Peng XG, Cai Y, Wang L, Bai YY, Ju S (2017) Noninvasive identification of renal hypoxia in experimental myocardial infarctions of different sizes by using BOLD MR imaging in a mouse model. Radiology 286(1):129–139. https://doi.org/10.1148/radiol.2017161998
29. Wallner BK, Edelman RR, Bajakian RL, Kleefield J, Atkinson DJ, Mattle HP (1990) Signal normalization in surface-RF coil MR imaging. Am J Neuroradiol 11(6):1271–1272
30. Hayes CE, Axel L (1985) Noise performance of surface RF coils for magnetic resonance imaging at 1.5 T. Med Phys 12(5):604–607. https://doi.org/10.1118/1.595682
31. Garwood M, DelaBarre L (2001) The return of the frequency sweep: designing adiabatic pulses for contemporary NMR. J Magn Reson 153 (2):155–177. https://doi.org/10.1006/jmre.2001.2340

32. Hueper K, Schmidbauer M, Thorenz A, Bräsen JH, Gutberlet M, Mengel M, Hartung D, Chen R, Meier M, Haller H, Wacker F, Rong S, Gueler F (2017) Longitudinal evaluation of perfusion changes in acute and chronic renal allograft rejection using arterial spin labeling in translational mouse models. J Magn Reson Imaging 46(6):1664–1672. https://doi.org/10.1002/jmri.25713
33. Gareis D, Wichmann T, Lanz T, Melkus G, Horn M, Jakob PM (2007) Mouse MRI using phased-array RF coils. NMR Biomed 20 (3):326–334. https://doi.org/10.1002/nbm.1156
34. Zubkov M, Hurshkainen AA, Brui EA, Glybovski SB, Gulyaev V, Anisimov NV, Volkov DV, Pirogov YA, Melchakova IV (2018) Small-animal, whole-body imaging with metamaterial-inspired RF coil. NMR Biomed 31:e3952. https://doi.org/10.1002/nbm.3952
35. Hoult DI, Lauterbur PC (1979) The sensitivity of the zeugmatographic experiment involving human sample. J Magn Reson 34(2):425–433. https://doi.org/10.1016/0022-2364(79)90019-2
36. Edelstein WA, Glover GH, Hardy CJ, Redington RW (1986) The intrinsic signal-to-noise ratio in NMR imaging. Magn Reson Med 3 (4):604–618. https://doi.org/10.1002/mrm.1910030413
37. Marques JP, Simonis FFJ, Webb AG (2019) Low-field MRI: an MR physics perspective. J Magn Reson Imaging 49:1528–1542. https://doi.org/10.1002/jmri.26637
38. Kovacs H, Moskau D, Spraul M (2005) Cryogenically cooled probes—a leap in NMR technology. Prog Nucl Magn Reson Spectrosc 46:131–155. https://doi.org/10.1016/j.pnmrs.2005.03.001
39. Ratering D, Baltes C, Nordmeyer-Massner J, Marek D, Rudin M (2008) Performance of a 200-MHz cryogenic RF probe designed for MRI and MRS of the murine brain. Magn Reson Med 59:1440–1447. https://doi.org/10.1002/mrm.21629
40. Baltes C, Radzwill N, Bosshard S, Marek D, Rudin M (2009) Micro MRI of the mouse brain using a novel 400MHz cryogenic quadrature RF probe. NMR Biomed 22:834–842. https://doi.org/10.1002/nbm.1396
41. Xie L, Layton AT, Wang N, Larson PEZ, Zhang JL, Lee VS, Liu C, Johnson GA (2016) Dynamic contrast-enhanced quantitative susceptibility mapping with ultrashort echo time MRI for evaluating renal function. Am J Physiol Ren Physiol 310(2):F174–F182. https://doi.org/10.1152/ajprenal.00351.2015
42. Poirier-Quinot M, Ginefri JC, Girard O, Robert P, Darrasse L (2008) Performance of a miniature high-temperature superconducting (HTS) surface RF coil for in vivo microimaging of the mouse in a standard 1.5T clinical whole-body scanner. Magn Reson Med 60 (4):917–927. https://doi.org/10.1002/mrm.21605
43. Hu R, Kleimaier D, Malzacher M, Hoesl MAU, Paschke NK, Schad LR (2019) X-nuclei imaging: current state, technical challenges, and future directions. J Magn Reson Imaging 51(2):355–376. https://doi.org/10.1002/jmri.26780
44. Nagel AM, Umathum R, Rösler MB, Ladd ME, Litvak I, Gor'kov PL, Brey WW, Schepkin VD (2016) ^{39}K and ^{23}Na relaxation times and MRI of rat head at 21.1T. NMR Biomed 29:759–766. https://doi.org/10.1002/nbm.3528
45. Schepkin VD, Brey WW, Gor'kov PL, Grant SC (2010) Initial *in vivo* rodent sodium and proton MR imaging at 21.1 T. Magn Reson Imaging 28(3):400–407. https://doi.org/10.1016/j.mri.2009.10.002
46. Schepkin VD, Elumalai M, Kitchen JA, Qian C, Gor'kov PL, Brey WW (2014) In vivo chlorine and sodium MRI of rat brain at 21.1 T. MAGMA 27:63–70. https://doi.org/10.1007/s10334-013-0387-2
47. Waiczies S, Rosenberg JT, Kuehne A, Starke L, Ramos Delgado P, Millward JM, Prinz C, Periquito J, Pohlmann A, Niendorf T (2019) Fluorine19 MRI at 21.1 T: enhanced spin–lattice relaxation of perfluoro15crown5ether and sensitivity as demonstrated in *ex vivo* murine neuroinflammation. MAGMA 32:37–49. https://doi.org/10.1007/s10334-018-0710-z
48. Waiczies S, Millward JM, Starke L, Ramos Delgado P, Huelnhagen T, Prinz C, Marek D, Wecker D, Wissmann R, Koch S, Boehm-Sturm P, Waiczies H, Niendorf T, Pohlmann A (2017) Enhanced fluorine-19 MRI sensitivity using a cryogenic radiofrequency probe: technical developments and *ex vivo* demonstration in a mouse model of neuroinflammation. Sci Rep 7:9808. https://doi.org/10.1038/s41598-017-09622-2
49. Sack M, Wetterling F, Sartorius A, Ende G, Weber-Fahr W (2014) Signal-to-noise ratio of a mouse brain ^{13}C CryoProbe™ system in comparison with room temperature coils: spectroscopic phantom and *in vivo* results. NMR Biomed 27:709–715. https://doi.org/10.1002/nbm.3110

50. Boska MD, Meyerhoff DJ, Twieg DB, Karczmar GS, Matson GB, Weiner MW (1990) Image-guided ^{31}P magnetic resonance spectroscopy of normal and transplanted human kidneys. Kidney Int 38:294–300. https://doi.org/10.1038/ki.1990.199
51. Klemm A, Rzanny R, Fünfstück R, Werner W, Schubert J, Kaiser WA, Stein G (1998) ^{31}P-magnetic resonance spectroscopy (^{31}P-MRS) of human allografts after renal transplantation. Nephrol Dial Transplant 13 (12):3147–3152. https://doi.org/10.1093/ndt/13.12.3147
52. Maril N, Margalit R, Mispelter J, Degani H (2004) Functional sodium magnetic resonance imaging of the intact rat kidney. Kidney Int 65:927–935. https://doi.org/10.1111/j.1523-1755.2004.00475.x
53. Kalayciyan R, Wetterling F, Neudecker S, Haneder S, Gretz N, Schad LR (2013) Bilateral kidney sodium-MRI: enabling accurate quantification of renal sodium concentration through a two-element phased array system. J Magn Reson Imaging 38(3). https://doi.org/10.1002/jmri.24024
54. Pohlmann A, Schreiber A, Ku MC, Waiczies H, Kox S, Kettritz R, Waiczies S, Niendorf T (2014) Assessment of renal inflammatory cell infiltration in a murine ANCA-induced glomerulonephritis model by 19F-MRI. In: Joint Annual Meeting ISMRM-ESMRMB 2014, Milan, Italy. https://doi.org/10.13140/RG.2.1.4143.4326
55. Ruiz-Cabello J, Barnett BP, Bottomley PA, Bulte JWM (2011) Fluorine (^{19}F) MRS and MRI in biomedicine. NMR Biomed 24 (2):114–129. https://doi.org/10.1002/nbm.1570
56. Hitchens TK, Ye Q, Eytan DF, Janjic JM, Ahrens ET, Ho C (2011) ^{19}F MRI detection of acute allograft rejection with in vivo perfluorocarbon labeling of immune cells. Magn Reson Med 65(4):1144–1153. https://doi.org/10.1002/mrm.22702
57. Hu L, Chen J, Yang X, Senpan A, Allen JS, Yanaba N, Caruthers SD, Lanza GM, Hammerman MR, Wickline SA (2014) Assessing intrarenal nonperfusion and vascular leakage in acute kidney injury with multinuclear ^{1}H/^{19}F MRI and perfluorocarbon nanoparticles. Magn Reson Med 71:2186–2196. https://doi.org/10.1002/mrm.24851
58. Pedersen M, Ursprung S, Jensen JD, Jespersen B, Gallagher F, Lautsten C (2019) Hyperpolarised ^{13}CMRI metabolic and functional imaging: an emerging renal MR diagnostic modality. MAGMA 33(1):23–32. https://doi.org/10.1007/s10334-019-00801-y
59. Gordon CJ (2017) The mouse thermoregulatory system: its impact on translating biomedical data to humans. Physiol Behav 179:55–66. https://doi.org/10.1016/j.physbeh.2017.05.026
60. Reimann HM, Hentschel J, Marek J, Huelnhagen T, Todiras M, Kox S, Waiczies S, Hodge R, Bader M, Pohlmann A, Niendorf T (2016) Normothermic mouse functional MRI of acute focal thermostimulation for probing nociception. Sci Rep 6:17230. https://doi.org/10.1038/srep17230
61. Hitt BA, Mazze RI, Cook TL, Beppu WJ, Kosek JC (1977) Thermoregulatory defect in rats during anesthesia. Anesth Analg 56 (1):9–15. https://doi.org/10.1213/00000539-197701000-00006
62. Niles DJ, Gordon JW, Fain SB (2016) Effect of anesthesia on renal R_2* measured by blood oxygen level-dependent MRI. NMR Biomed 28(7):811–817. https://doi.org/10.1002/nbm.3314
63. Nikken JJ, Krestin GP (2007) MRI of the kidney-state of the art. Eur Radiol 17 (11):2780–2793. https://doi.org/10.1007/s00330-007-0701-3

Chapter 9

MRI Mapping of Renal T_1: Basic Concept

Stefanie J. Hectors, Philippe Garteiser, Sabrina Doblas, Gwenaël Pagé, Bernard E. Van Beers, John C. Waterton, and Octavia Bane

Abstract

In renal MRI, measurement of the T_1 relaxation time of water molecules may provide a valuable biomarker for a variety of pathological conditions. Due to its sensitivity to the tissue microenvironment, T_1 has gained substantial interest for noninvasive imaging of renal pathology, including inflammation and fibrosis. In this chapter, we will discuss the basic concept of T_1 mapping and different T_1 measurement techniques and we will provide an overview of emerging preclinical applications of T_1 for imaging of kidney disease.

This chapter is based upon work from the COST Action PARENCHIMA, a community-driven network funded by the European Cooperation in Science and Technology (COST) program of the European Union, which aims to improve the reproducibility and standardization of renal MRI biomarkers. This introduction chapter is complemented by two separate chapters describing the experimental procedure and data analysis.

Key words Magnetic resonance imaging (MRI), Parametric imaging, T_1 mapping, Kidney, Preclinical

1 Introduction

Renal pathologies may result in structural and functional changes that could possibly be noninvasively detected by magnetic resonance imaging (MRI) [1]. While the MRI relaxometry parameter T_1, that is, the longitudinal relaxation time, is used quite extensively for assessment of other organs, for example in cardiac and brain MRI, its application for the assessment of renal pathology is relatively scarcely used. Several reports, both in the clinical [1] and preclinical setting [2–5], have shown promise of T_1 for detection and characterization of renal pathologies, including inflammation and fibrosis. These results warrant further investigation of this relaxation parameter for evaluation of renal pathology. In this chapter, we will discuss the basic concept of T_1 as well as emerging applications of this MRI parameter for noninvasive characterization of renal pathologies.

This introduction chapter is complemented by two separate chapters describing the experimental procedure and data analysis, which are part of this book.

Andreas Pohlmann and Thoralf Niendorf (eds.), *Preclinical MRI of the Kidney: Methods and Protocols*, Methods in Molecular Biology, vol. 2216, https://doi.org/10.1007/978-1-0716-0978-1_9,

This chapter is part of the book Pohlmann A, Niendorf T (eds) (2020) Preclinical MRI of the Kidney—Methods and Protocols. Springer, New York.

2 Measurement Concept

2.1 Basic Concept of T_1 Mapping

Magnetic resonance imaging (MRI) is based on the interaction of nuclear spins with three types of magnetic fields: main field B_0, radiofrequency field B_1, and linear gradient fields. MRI signal relies on the physical properties of atoms with an odd number of protons or neutrons, which possess a nuclear angular momentum (spin), that gives rise to a magnetic dipole moment. Using classical physics, the atom can be described as a charged sphere spinning about its axis and giving rise to a current loop that creates the magnetic dipole moment. Since MRI is concerned with the spin property of protons and neutrons, and their interactions with a large magnetic field, these particles will be referred to as "spins". Most MRI applications in biological specimens generate signal by manipulating the spin of single proton hydrogen (^{1}H), although it is feasible to generate MR images in biological samples from the signal of other nuclei such as sodium [6], or hyperpolarized gases.

$$\boldsymbol{\omega}_0 = \boldsymbol{\gamma}\, \mathbf{B}_0 \tag{1}$$

In the absence of a magnetic $\mathbf{B_0}$ field, nuclear spins are oriented randomly. The presence of an external magnetic field ($\mathbf{B_0}$) will have two effects on the spins: they will tend to align with the main magnetic field $\mathbf{B_0}$, to create a net macroscopic magnetic moment $\mathbf{M_0}$ in the direction of the field (the longitudinal direction, or conventionally, the z-direction), and they will precess around the main magnetic field at a well-defined frequency called the Larmor frequency (Eq. 1, Fig. 1) where γ, the gyromagnetic ratio, is a constant specific to each atom. Thus, a ^{1}H atom in a magnetic field of 1 tesla (T) = 10^4 gauss will precess about the field with a Larmor frequency of $\gamma/2\pi = 42.58$ MHz/tesla [7, 8].

The presence of the static magnetic field B_0 polarizes the sample of protons to a net magnetization $\mathbf{M_0}$ in the longitudinal direction. However, polarization is not sufficient to obtain a large, coherent MR signal for image reconstruction. To obtain the MR signal, a radiofrequency field $\mathbf{B_1}$ is applied as a pulse of a few milliseconds in the xy (transverse) plane. $\mathbf{B_1}$ is tuned to the resonant Larmor frequency of the spins, so it excites the spins out of equilibrium, tipping the $\mathbf{M_0}$ vector away from the z-axis by an angle known as flip angle, which is dependent on the amplitude and duration of the RF pulse (Fig. 2) [8]. The $\mathbf{B_1}$ induced rotation of the magnetization toward the transverse plane causes the longitudinal component of magnetization to decrease, and the transverse component to increase.

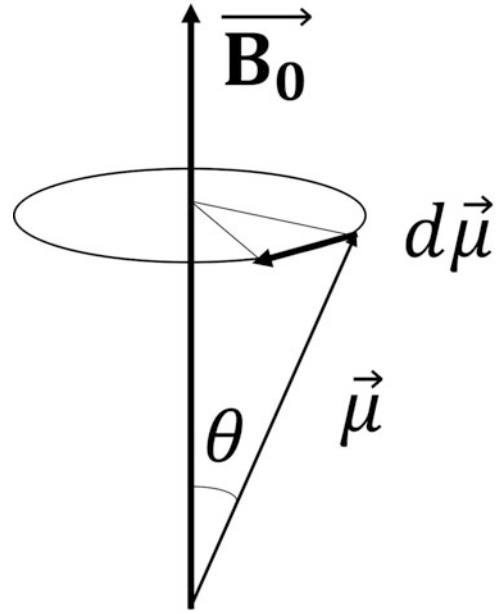

Fig. 1 B_0 interacts with the nuclear magnetic moment μ, producing a torque that causes the protons to precess around B_0. (From Dwight Nishimura, "Principles of Magnetic Resonance Imaging," Stanford University Press, Palo Alto, CA, 2010)

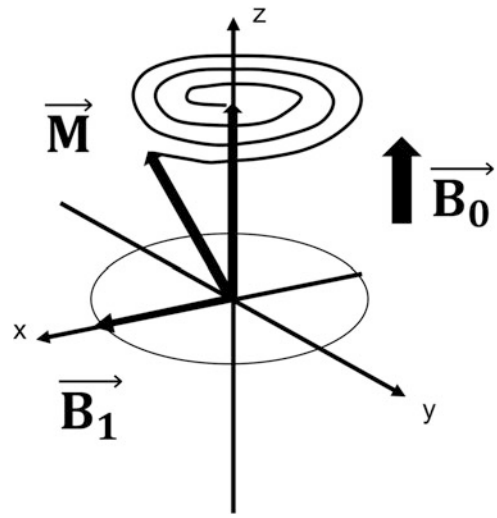

Fig. 2 Nutation at Larmor frequency of the magnetization vector around the RF pulse B_1 applied in the transverse plane. (From Dwight Nishimura, "Principles of Magnetic Resonance Imaging," Stanford University, Palo Alto, CA 2010)

When the RF $\mathbf{B_1}$ pulse is turned off, the magnetization precesses back to its equilibrium state, and the longitudinal component recovers, while the transverse component decays. The Bloch equation describes the behavior of the magnetization vector **M,** based on the T_1 and T_2 relaxation time constants and the magnetic fields applied:

$$\frac{d\mathbf{M}}{dt} = \mathbf{M} \times \gamma\mathbf{B} - \frac{M_x\mathbf{i} + M_y\mathbf{j}}{T_2} - \frac{(M_z - M_0)\mathbf{k}}{T_1} \quad (2)$$

Solving the z-axis component of the Bloch equation, we obtain an exponential expression for the recovery of M_z to the equilibrium M_0 magnetization (Eq. 3). The time constant T_1 is known as the spin-lattice or longitudinal relaxation time.

$$M_z(t) = M_0 + \left(M_{z\,(t=0)} - M_0\right) \exp\left(-\frac{t}{T_1}\right) \quad (3)$$

The reference standard method for measuring T_1 is the inversion-recovery spin echo method (IR-SE; see IR-SE signal curve in Fig. 3 top) that originated from early NMR experiments [9, 10]. It involves inversion of the magnetization M_0 by a 180° RF pulse in the z direction, followed by a time delay known as inversion time (TI) during which the equilibrium magnetization is allowed to decay. The TI ends after the application of a 90° RF pulse, which tips the magnetization in the x-y (transverse) plane for MR signal readout (receiving). A 180 pulse is then applied in the x direction, to rephase the precessing spins in a "spin echo" occurring at a fixed echo time TE.

After a long repetition time (TR) that allows for the magnetization to recover to equilibrium, the IR preparation is repeated with different subsequent inversion times. For accurate work, between 4 and 10 TI values should be used, although a T_1 can be calculated with as few as two TI values. TR is chosen to be much longer than the longest expected T_1 of interest in the tissue, in order to allow the magnetization to fully recover to equilibrium. For very accurate work this ratio TI/T_1 is as high as 5 or even 7, although for in vivo work 3 is more common. Signal decay and recovery can be observed on the images acquired with different TI's (Fig. 3 top), with signal nulling at $TI_{null} = T_1 \ln 2$, when the inversion preparation pulse is exactly 180° and the $TR >> T_1$ of tissue. If expected T_1 of the tissue is known, choosing a range of TI's before and after TI_{null} allows for acquisition of enough data points to fit the signal decay and recovery curve. Alternatively, performing a series of preliminary IR-SE experiments allows identification of the signal nulling time in the tissue of interest (TI_{null}), and choice of optimal range of TI values for measuring T_1.

IR-SE pulse sequences used currently in animal [2, 3] and human imaging differ from the reference standard IR-SE experiment described above by use of fast readout techniques. There are

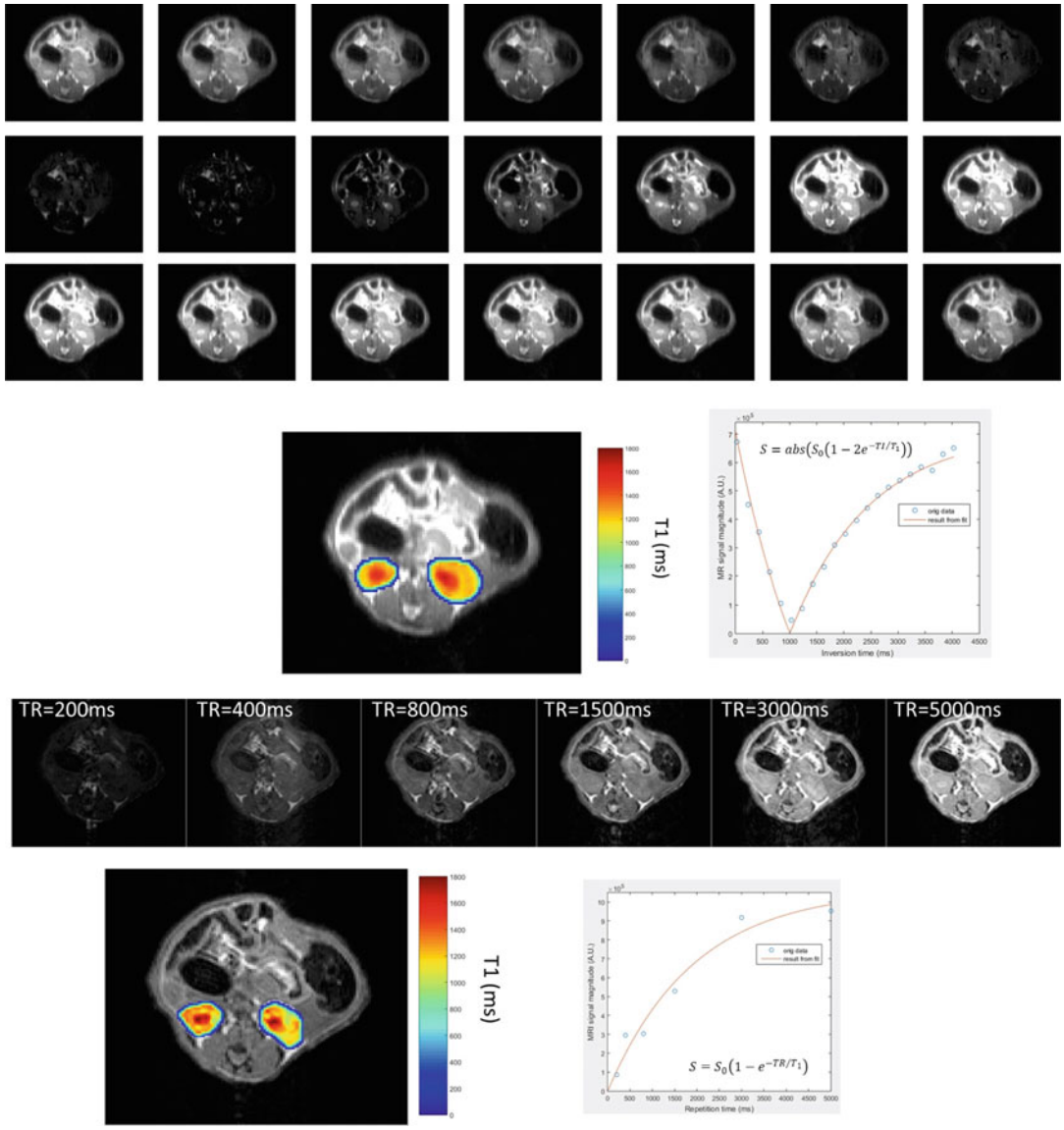

Fig. 3 T_1 mapping examples in the kidneys of a control mouse (c57bl6) imaged on a 7 T Bruker Pharmascan. Top: Inversion recovery experiment with a FAIR RARE pulse sequence, showing sequence of inversion times, T_1 color map and signal recovery curve: TE = 35.8 ms; recovery time = 10 s; NEX = 2; scan time 8 min 33 s; 21 inversion times (TI = 30 + $n \times$ 200 ms, $n = 0 \ldots 20$); nonselective inversion slice; matrix 128 $\times$ 100; FOV 40 $\times$ 30 mm; single 1 mm-thick slice. Bottom: Variable TR experiment with a RARE VTR pulse sequence, showing 8 variable repetition times (200, 400, 800, 1500, 3000, 5000 ms), T_1 color map and signal recovery curve: TE 11 ms; NEX = 1; scan time 8 min 43 s; matrix 128 $\times$ 96; FOV = 40 $\times$ 30 mm; single 1 mm-thick slice; no fat suppression; shallow breathing; no motion compensation

various fast readout techniques that have been introduced for both inversion and saturation recovery pulse sequences:

1. The **Ra**pid Imaging with **R**efocused **E**choes (RARE) readout, also called fast or turbo spin-echo readout by clinical scanner manufacturers, uses several 180° refocusing pulses within the same TR to create an echo train. Within the echo train, each 180 pulse induces a refocused echo, comprising spin-echo and stimulated echo contributions, which is digitized, and each echo is acquired with a different phase encoding gradient, so that multiple lines of k-space (multiple phase encoding steps) can be acquired within the same TR. The number of 180° pulses is called the echo train length (ETL) or RARE factor: a typical value is 8.
2. **E**cho **p**lanar **i**maging (EPI) uses a single RF preparation (in the case of IR, 180°-TI-90°) and then acquire multiple gradient echoes by combining a high amplitude bipolar oscillating frequency encoding gradient with a low amplitude monopolar blip phase encoding gradient. This approach permits fast acquisition of k-space data in a single shot (all lines of k-space in the 2D plane are acquired for each RF preparation), or a few multiple shots (groups of k-space lines are acquired for each RF preparation).
3. A derivative of the IR methods, the Look–Locker inversion recovery (LL-IR) method, samples the magnetization recovery using rapid, small flip angle imaging readouts. More details and caveats on data acquisition and analysis with this method can be found in the chapters by Garteiser P et al. "Experimental Protocols for MRI Mapping of Renal T_1" and "Analysis Protocols for MRI Mapping of Renal T_1." In addition to EPI, LL-IR pulse sequences can employ other readout methods:
   - **F**ast **l**ow **a**ngle **s**hots (FLASH) tips the magnetization to the transverse xy plane during the recovery period by a small angle, in order to sample it. Magnetization is spoiled before subsequent RF pulses. This readout method has the advantage of a short TR (~3 ms) that is compatible with low flip angles (<10°) [11]. As such, the longitudinal regrowth of the magnetization is perturbed only to a small extent. Use of a FLASH readout requires fitting the data with a modified version of the IR-SE equation, the Look–Locker equation (chapter by Garteiser P et al. "Analysis Protocols for MRI Mapping of Renal T_1"). FLASH can also be used in T_1 mapping methods that do not employ an inversion pulse, like variable flip angle (see next section).
   - Balanced readouts such as **s**teady-**s**tate **f**ree **p**recession (SSFP) can also be used, as they tend to yield higher signal to noise due to the reuse of magnetization from preceding shots [12]. Use of these types of readouts also requires

fitting the data with a Look–Locker equation or more complex equations that take into account the dependence of signal on both T_1 and T_2 decay. Details on acquisition and analysis with pulse sequences using an SSFP or FISP readout method can be found in the chapters by Garteiser P et al. "Experimental Protocols for MRI Mapping of Renal T_1" and "Analysis Protocols for MRI Mapping of Renal T_1."

2.2 Overview of T_1 Mapping Techniques

The longitudinal relaxation time T_1 can be measured by a variety of methods [13, 14]. The multiple delay inversion-recovery (IR) method can measure T_1 with high accuracy, however, it has long acquisition times (10–15 min with current EPI readouts [2, 3]), which makes it impractical for in vivo settings. There are several methods that have been developed for faster T_1 measurement: the saturation recovery or variable TR (VTR) method, the variable flip angle (VFA), the Look–Locker modified IR, and the proton density (PD) method. Comprehensive description of the most common pulse sequence implementations for each T_1 measurement method, acquisition protocols and corresponding analysis workflows for preclinical and clithe chapters by Garteiser P et al. "Experimental Protocols for MRI Mapping of Renal T_1" and "Analysis Protocols for MRI Mapping of Renal T_1."

2.2.1 The Saturation Recovery or VTR Method

The saturation recovery or variable TR (VTR) method, in which T_1-weighted signal is acquired with multiple TR values (Fig. 3b) shares the same limitations of limited spatial coverage and resolution as the IR method but allows shorter overall scan times [15]. The magnetization is tipped 90° (from the z to the xy plane) and the recovery is usually sampled by a RARE readout over several repetition times TR of different durations (Fig. 3b).

2.2.2 The VFA Method

In variable flip angle (VFA) methods [14–17], the RF flip angle is varied while keeping the TR constant in a 2D or 3D spoiled gradient echo (SPGR) acquisition. VFA is particularly useful in dynamic contrast-enhanced MRI (DCE-MRI) experiments, as VFA measurements allow for voxel-based baseline (precontrast enhancement) T_1 mapping with the same spatial resolution and coverage as the DCE-MRI scan in a short amount of time.

2.2.3 The Look–Locker Modified IR Method

The Look–Locker modified IR [18–21], decreases the acquisition time by sampling the signal recovery curve multiple times per TR after application of several low flip angle pulses during the acquisition. Despite shortened acquisition time, Look–Locker IR methods are still limited in spatial coverage.

2.2.4 The PD Method

In the proton density (PD) approach [22], T_1 is derived by comparing PD-weighted images with DCE baseline (precontrast) images acquired with an SPGR pulse sequence. More information on the use of T_1 for quantitative DCE-MRI measurements can be

found in the chapters by Li L-P et al. "MRI Mapping of the Blood Oxygenation Sensitive Parameter T_2* in the Kidney: Basic Concept"; by Chuang K-H et al. "Renal Blood Flow Using Arterial Spin Labeling (ASL) MRI: Experimental Protocol and Principles"; and by Grist JT et al. "Analysis Protocol for Renal Sodium (23Na) MR Imaging," which cover the basic concept, experimental protocols, and analysis techniques of DCE-MRI, respectively.

2.2.5 MR Fingerprinting

Next to conventional T_1 mapping techniques, T_1 can also be extracted from magnetic resonance fingerprinting techniques, a novel MRI method that uses a pseudorandomized acquisition scheme to generate unique signal evolutions (or "fingerprints") for each tissue voxel dependent on the relaxation parameters [23].

3 Overview of Applications on Preclinical and Clinical MR Instruments

T_1 differs between different kidney components (cortex, medulla, urine, etc.); it decreases when paramagnetic contrast agents such as gadolinium chelates or oxygen (O_2) are present, and it may increase or decrease with pathology. In addition T_1 tends to increase with B_0, an important consideration since animal studies have been performed over more than an order of magnitude range in B_0.

The sensitivity of T_1 to the tissue microenvironment has been employed quite extensively to assess renal structure and function, both in clinical and preclinical studies. A comprehensive review of clinical T_1 (and T_2) applications in the kidney can be found here [24]. The use of T_1 for noninvasive assessment of renal pathology in preclinical models has already been explored in the 1980s, showing that various effects including ischemia, tubular obstruction and renal congestion may attribute to T_1 differences in rat models of acute and chronic renal failure [25, 26]. T_1 values can be affected by a wide variety of changes in the tissue environment, including inflammation and fibrosis. Inflammation can coexist with fibrosis in the kidney tissue [27], for example during rejection of transplanted kidneys. While clinical MRI studies are valuable for, for example, the grading of renal fibrosis in patients, preclinical studies with well-established animal models have the advantage of the possibility to assess dynamic changes in T_1 after the onset of pathology.

Hueper et al. performed longitudinal T_1 measurements on a 7 Tesla dedicated animal MR scanner in mice after transient unilateral clamping of the renal pedicle, causing moderate or severe acute kidney injury (AKI) dependent on the ischemia time [3]. T_1 values were significantly elevated after AKI, with a peak at 7 days after the ischemic event. In mice with severe AKI, the T_1 elevation persisted until at least a month after surgery. The initial peak in T_1 values is likely attributed to increased water content due to an acute

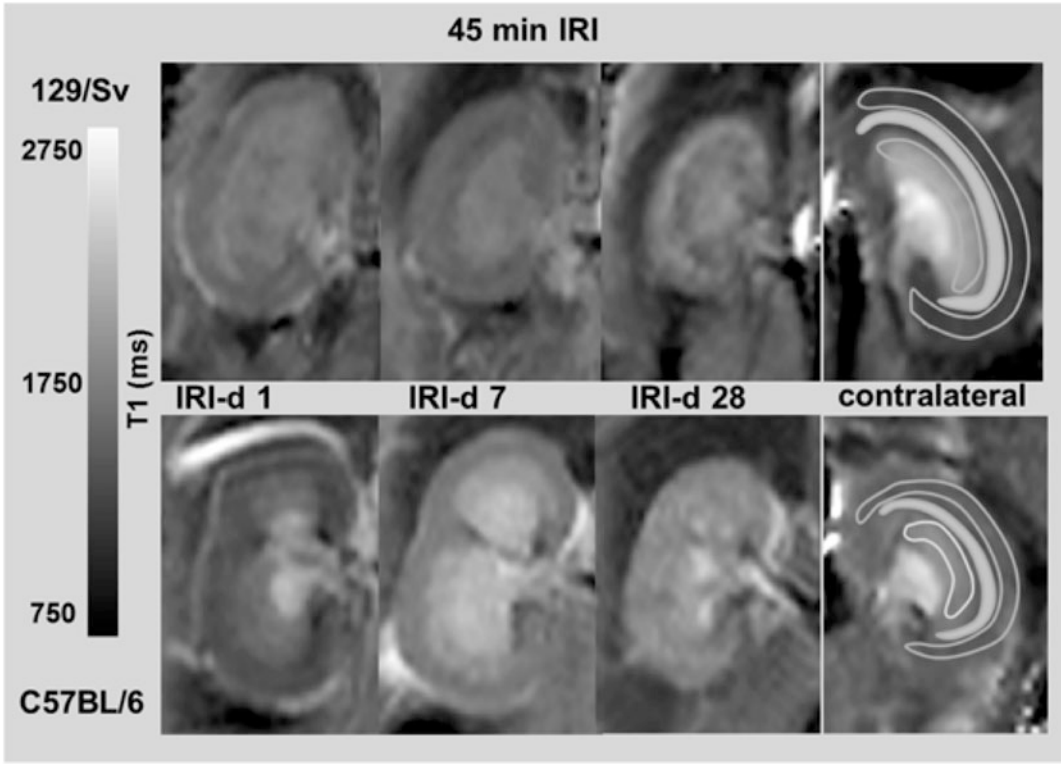

Fig. 4 T_1 maps after 45 min ischemia reperfusion injury (IRI) for 129/Sv (upper row) and C57BL/6 mice (lower row) at day 1, day 7 and day 28 are shown. In T_1 maps spatial differences can be measured by placing ROIs in the cortex and the outer stripe (OSOM) and inner stripe (ISOM) of the outer medulla, which is illustrated in the contralateral normal kidney. After severe acute kidney injury, differences of T_1-values between the two mouse strains were most pronounced on day 7: this example shows higher T_1-values in the ISOM and lower T_1-values in the renal cortex of C57BL/6 compared to 129/Sv mice. (Adapted from Tewes et al., "Functional MRI for characterization of renal perfusion impairment and edema formation due to acute kidney injury in different mouse strains" PloS One)

inflammation response. The persisting T_1 increase in severe AKI may at least partly be explained by development of fibrosis due to inadequate renal tissue regeneration and incomplete tubular repair. In a follow-up study, changes in T_1 (and arterial spin labeling perfusion parameters) after AKI was assessed in two mouse strains (C57BL/6 and 129/Sv) to investigate potential effects of different genetic backgrounds on the experimental study [5]. Overall, similar trends of increased T_1 were found in both animal models, except for a significantly higher T_1 increase in the cortex and outer stripe of the outer medulla (OSOM) of the 129/Sv vs. C57BL/6 mice at day 1 after moderate AKI and higher relative T_1 values in the cortex and lower relative T_1 values in the inner stripe of the outer medulla (ISOM) at day 7 after severe AKI in 129/Sv mice (Fig. 4) The same research team also assessed multiparametric MRI parameters, including T_1, in mouse models of allogenic and isogenic renal

transplantation [2]. Acute allograft rejection was observed in allogenic kidney transplants. T_1 was significantly elevated in allogenic vs. isogenic allografts. Histopathological evaluation showed signification strong correlations of T_1 with presence of macrophages, T-cells and fibrosis (correlation coefficient r range 0.78–0.91, $P < 0.01$). These studies show that kidney T_1 is sensitive to several pathophysiological processes, including inflammation and fibrosis, which may occur simultaneously in events of kidney injury and rejection.

The findings of the group of Hueper et al. have also been observed by other research groups in independent studies. Jiang et al. employed longitudinal multiparametric MRI, including T_1 for evaluation of folic acid-induced AKI in mice [4]. The experiments were performed at a 16.4 T dedicated animal MR system (Bruker). T_1 was found to increase in both the renal cortex and medulla, most prominently at 2 weeks after treatment, while T_1 tended to regress at 4 weeks after treatment. Histopathological evaluation showed increased fluid content and association of tubular dilation at 2 weeks after treatment, explaining the T_1 elevation.

While dedicated preclinical MRI systems are highly suitable for high-resolution imaging of kidneys in small animals, clinical systems could also be used for preclinical renal T_1 studies. Ko et al. performed a longitudinal multiparametric MRI study after severe bilateral ischemic-reperfusion AKI in rat kidneys on a clinical 3 T MR scanner [28]. T_1 values were elevated in both the cortex and medulla after AKI, similar as reported in previous studies. No significant correlations of T_1 with histopathological evaluation of different markers including macrophages and collagen deposition were observed, possibly owing to complex pathological changes after AKI and multiple factors attributing to the T_1 changes. Hu et al. found significant positive correlations of T_1 with histological expression of Masson's trichrome (collagen) and alpha-smooth muscle actin in a multiparametric MRI study in a rat model of unilateral ureteral obstruction performed on a clinical 3 T MRI system [29]. Friedli et al. also found significant correlations of T_1 with histopathological inflammation and fibrosis in a rat model of unilateral ureteral obstruction. The latter study was performed on a 3 T MR system [20].

Gao et al. have reported feasibility of MR fingerprinting for imaging of healthy mouse kidneys on a preclinical 7 T MR system, showing inherent resistance of the MR fingerprinting technique to respiratory motion artifacts [30].

T_1 may also be used as baseline measurement for DCE-MRI acquisitions. More information on the use of T_1 for quantitative DCE-MRI measurements can be found in the chapters by Pedersen M et al. "Dynamic Contrast Enhancement (DCE) MRI–Derived Renal Perfusion and Filtration: Basic Concepts"; by Irrera P et al. "Dynamic Contrast Enhanced (DCE) MRI-Derived Renal

Perfusion and Filtration: Experimental Protocol"; and by Zöllner FG et al. "Analysis Protocol for Dynamic Contrast Enhanced (DCE) MRI of Renal Perfusion and Filtration," which cover the basic concept, experimental protocols, and analysis techniques of DCE-MRI, respectively.

In summary, several studies have demonstrated suitability of T_1 for assessment of renal pathology in preclinical models. These promising results warrant further investigation of this MRI relaxation technique both in the preclinical and clinical settings.

Acknowledgement

The experiments shown in Fig. 3 were performed on a platform member of France Life Imaging network (grant ANR-11-INBS-0006).

This chapter is based upon work from COST Action PARENCHIMA, supported by European Cooperation in Science and Technology (COST). COST (www.cost.eu) is a funding agency for research and innovation networks. COST Actions help connect research initiatives across Europe and enable scientists to enrich their ideas by sharing them with their peers. This boosts their research, career, and innovation.

PARENCHIMA (renalmri.org) is a community-driven Action in the COST program of the European Union, which unites more than 200 experts in renal MRI from 30 countries with the aim to improve the reproducibility and standardization of renal MRI biomarkers.

References

1. Selby NM, Blankestijn PJ, Boor P, Combe C, Eckardt KU, Eikefjord E, Garcia-Fernandez N, Golay X, Gordon I, Grenier N, Hockings PD, Jensen JD, Joles JA, Kalra PA, Kramer BK, Mark PB, Mendichovszky IA, Nikolic O, Odudu A, Ong ACM, Ortiz A, Pruijm M, Remuzzi G, Rorvik J, de Seigneux S, Simms RJ, Slatinska J, Summers P, Taal MW, Thoeny HC, Vallee JP, Wolf M, Caroli A, Sourbron S (2018) Magnetic resonance imaging biomarkers for chronic kidney disease: a position paper from the European Cooperation in Science and Technology action PARENCHIMA. Nephrol Dial Transplant 33(suppl_2):ii4–ii14. https://doi.org/10.1093/ndt/gfy152
2. Hueper K, Hensen B, Gutberlet M, Chen R, Hartung D, Barrmeyer A, Meier M, Li W, Jang MS, Mengel M, Wacker F, Rong S, Gueler F (2016) Kidney transplantation: multiparametric functional magnetic resonance imaging for assessment of renal allograft pathophysiology in mice. Investig Radiol 51(1):58–65. https://doi.org/10.1097/RLI.0000000000000205
3. Hueper K, Peperhove M, Rong S, Gerstenberg J, Mengel M, Meier M, Gutberlet M, Tewes S, Barrmeyer A, Chen R, Haller H, Wacker F, Hartung D, Gueler F (2014) T1-mapping for assessment of ischemia-induced acute kidney injury and prediction of chronic kidney disease in mice. Eur Radiol 24(9):2252–2260. https://doi.org/10.1007/s00330-014-3250-6
4. Jiang K, Ponzo TA, Tang H, Mishra PK, Macura SI, Lerman LO (2018) Multiparametric MRI detects longitudinal evolution of folic acid-induced nephropathy in mice. Am J Physiol Renal Physiol 315(5):F1252–F1260. https://doi.org/10.1152/ajprenal.00128.2018

5. Tewes S, Gueler F, Chen R, Gutberlet M, Jang MS, Meier M, Mengel M, Hartung D, Wacker F, Rong S, Hueper K (2017) Functional MRI for characterization of renal perfusion impairment and edema formation due to acute kidney injury in different mouse strains. PLoS One 12(3):e0173248. https://doi.org/10.1371/journal.pone.0173248
6. Maril N, Margalit R, Rosen S, Heyman SN, Degani H (2006) Detection of evolving acute tubular necrosis with renal 23Na MRI: studies in rats. Kidney Int 69(4):765–768. https://doi.org/10.1038/sj.ki.5000152
7. Haacke EM, Brown RW, Thompson MR, Venkatesan R (1999) Magnetic resonance imaging: physical principles and sequence design. Wiley, New York
8. Nishimura DG (1996) Principles of magnetic resonance imaging. Stanford University, Stanford, CA
9. Brown RW, Cheng Y-CN, Haacke EM, Thompson MR, Venkatesan R (2014) Magnetic resonance imaging: physical principles and sequence design, 2nd edn. Wiley-Blackwell, New York, NY
10. Berger S, Braun S (2004) 200 and more NMR experiments: a practical course, 1st edn. Wiley-VCH
11. Kierulf-Lassen C, Nielsen PM, Qi H, Damgaard M, Laustsen C, Pedersen M, Krag S, Birn H, Norregaard R, Jespersen B (2017) Unilateral nephrectomy diminishes ischemic acute kidney injury through enhanced perfusion and reduced pro-inflammatory and pro-fibrotic responses. PLoS One 12(12):e0190009. https://doi.org/10.1371/journal.pone.0190009
12. Little RA, Jamin Y, Boult JKR, Naish JH, Watson Y, Cheung S, Holliday KF, Lu H, McHugh DJ, Irlam J, West CML, Betts GN, Ashton G, Reynolds AR, Maddineni S, Clarke NW, Parker GJM, Waterton JC, Robinson SP, O'Connor JPB (2018) Mapping hypoxia in renal carcinoma with oxygen-enhanced MRI: comparison with intrinsic susceptibility MRI and pathology. Radiology 288(3):739–747. https://doi.org/10.1148/radiol.2018171531
13. Kingsley P (1999) Methods of measuring spin-lattice (t1) relaxation times: an annotated bibliography. Concepts Magn Reson 11:243–276. https://doi.org/10.1002/(SICI)1099-0534
14. Stikov N, Boudreau M, Levesque IR, Tardif CL, Barral JK, Pike GB (2015) On the accuracy of T1 mapping: searching for common ground. Magn Reson Med 73(2):514–522. https://doi.org/10.1002/mrm.25135
15. Fennessy FM, Fedorov A, Gupta SN, Schmidt EJ, Tempany CM, Mulkern RV (2012) Practical considerations in T1 mapping of prostate for dynamic contrast enhancement pharmacokinetic analyses. Magn Reson Imaging 30(9):1224–1233. https://doi.org/10.1016/j.mri.2012.06.011
16. Aryal MP, Chenevert TL, Cao Y (2016) Impact of uncertainty in longitudinal T1 measurements on quantification of dynamic contrast-enhanced MRI. NMR Biomed 29(4):411–419
17. Schabel MC, Parker DL (2008) Uncertainty and bias in contrast concentration measurements using spoiled gradient echo pulse sequences. Phys Med Biol 53(9):2345–2373. https://doi.org/10.1088/0031-9155/53/9/010
18. Raman FS, Kawel-Boehm N, Gai N, Freed M, Han J, Liu CY, Lima JA, Bluemke DA, Liu S (2013) Modified Look-Locker inversion recovery T1 mapping indices: assessment of accuracy and reproducibility between magnetic resonance scanners. J Cardiovasc Magn Reson 15:64. https://doi.org/10.1186/1532-429x-15-64
19. Roujol S, Weingartner S, Foppa M, Chow K, Kawaji K, Ngo LH, Kellman P, Manning WJ, Thompson RB, Nezafat R (2014) Accuracy, precision, and reproducibility of four T1 mapping sequences: a head-to-head comparison of MOLLI, ShMOLLI, SASHA, and SAPPHIRE. Radiology 272(3):683–689. https://doi.org/10.1148/radiol.14140296
20. Friedli I, Crowe LA, Berchtold L, Moll S, Hadaya K, de Perrot T, Vesin C, Martin PY, de Seigneux S, Vallee JP (2016) New magnetic resonance imaging index for renal fibrosis assessment: a comparison between diffusion-weighted imaging and T1 mapping with histological validation. Sci Rep 6:30088. https://doi.org/10.1038/srep30088
21. Look DC, Locker D (1970) Time saving in measurement of NMR and EPR relaxation times. Rev Sci Instrum 41:250–251
22. Huang W, Wang Y, Panicek DM, Schwartz LH, Koutcher JA (2009) Feasibility of using limited-population-based average R10 for pharmacokinetic modeling of osteosarcoma dynamic contrast-enhanced magnetic resonance imaging data. Magn Reson Imaging 27(6):852–858. https://doi.org/10.1016/j.mri.2009.01.020
23. Ma D, Gulani V, Seiberlich N, Liu K, Sunshine JL, Duerk JL, Griswold MA (2013) Magnetic resonance fingerprinting. Nature 495(7440):187–192. https://doi.org/10.1038/nature11971

24. Wolf M, de Boer A, Sharma K, Boor P, Leiner T, Sunder-Plassmann G, Moser E, Caroli A, Jerome NP (2018) Magnetic resonance imaging T1- and T2-mapping to assess renal structure and function: a systematic review and statement paper. Nephrol Dial Transplant 33(suppl_2):ii41–ii50. https://doi.org/10.1093/ndt/gfy198
25. Abrashkin S, Weininger J, Griffel L, Schneider R, Iaina A (1987) Proton magnetic resonance in experimental acute and chronic renal failure in rats. Ren Fail 10(1):21–27
26. Iaina A, Abrashkin S, Weininger J (1986) Proton MR study of different types of experimental acute renal failure in rats. Magn Reson Imaging 4(3):241–244
27. Loupy A, Haas M, Solez K, Racusen L, Glotz D, Seron D, Nankivell BJ, Colvin RB, Afrouzian M, Akalin E, Alachkar N, Bagnasco S, Becker JU, Cornell L, Drachenberg C, Dragun D, de Kort H, Gibson IW, Kraus ES, Lefaucheur C, Legendre C, Liapis H, Muthukumar T, Nickeleit V, Orandi B, Park W, Rabant M, Randhawa P, Reed EF, Roufosse C, Seshan SV, Sis B, Singh HK, Schinstock C, Tambur A, Zeevi A, Mengel M (2017) The Banff 2015 kidney meeting report: current challenges in rejection classification and prospects for adopting molecular pathology. Am J Transplant 17(1):28–41. https://doi.org/10.1111/ajt.14107
28. Ko SF, Yip HK, Zhen YY, Lee CC, Lee CC, Huang SJ, Huang CC, Ng SH, Lin JW (2017) Severe bilateral ischemic-reperfusion renal injury: hyperacute and acute changes in apparent diffusion coefficient, T1, and T2 mapping with immunohistochemical correlations. Sci Rep 7(1):1725. https://doi.org/10.1038/s41598-017-01895-x
29. Hu G, Liang W, Wu M, Lai C, Mei Y, Li Y, Xu J, Luo L, Quan X (2018) Comparison of T1 mapping and T1rho values with conventional diffusion-weighted imaging to assess fibrosis in a rat model of unilateral ureteral obstruction. Acad Radiol 26(1):22–29. https://doi.org/10.1016/j.acra.2018.03.023
30. Gao Y, Chen Y, Ma D, Jiang Y, Herrmann KA, Vincent JA, Dell KM, Drumm ML, Brady-Kalnay SM, Griswold MA, Flask CA, Lu L (2015) Preclinical MR fingerprinting (MRF) at 7 T: effective quantitative imaging for rodent disease models. NMR Biomed 28(3):384–394. https://doi.org/10.1002/nbm.3262

Chapter 10

MRI Mapping of the Blood Oxygenation Sensitive Parameter T_2* in the Kidney: Basic Concept

Lu-Ping Li, Bradley Hack, Erdmann Seeliger, and Pottumarthi V. Prasad

Abstract

The role of hypoxia in renal disease and injury has long been suggested but much work still remains, especially as it relates to human translation. Invasive pO_2 probes are feasible in animal models but not for human use. In addition, they only provide localized measurements. Histological methods can identify hypoxic tissue and provide a spatial distribution, but are invasive and allow only one-time point. Blood oxygenation level dependent (BOLD) MRI is a noninvasive method that can monitor relative oxygen availability across the kidney. It is based on the inherent differences in magnetic properties of oxygenated vs. deoxygenated hemoglobin. Presence of deoxyhemoglobin enhances the spin–spin relaxation rate measured using a gradient echo sequence, known as R_2* (= $1/T_2$*). While the key interest of BOLD MRI is in the application to humans, use in preclinical models is necessary primarily to validate the measurement against invasive methods, to better understand physiology and pathophysiology, and to evaluate novel interventions. Application of MRI acquisitions in preclinical settings involves several challenges both in terms of logistics and data acquisition. This section will introduce the concept of BOLD MRI and provide some illustrative applications. The following sections will discuss the technical issues associated with data acquisition and analysis.

This chapter is based upon work from the COST Action PARENCHIMA, a community-driven network funded by the European Cooperation in Science and Technology (COST) program of the European Union, which aims to improve the reproducibility and standardization of renal MRI biomarkers. This introduction chapter is complemented by two separate chapters describing the experimental procedure and data analysis.

Key words Magnetic resonance imaging (MRI), Kidney, Mice, Rats, Blood oxygenation level dependent (BOLD) MRI, Hypoxia

1 Introduction

All organs exist in a state of dynamically balanced oxygen supply as determined by blood flow and arterial oxygen content and demand as determined by metabolism. Yet renal hemodynamics and oxygenation offer a number of striking differences vs. nonrenal tissues. Most organs extract approximately 45% of available oxygen (i.e., difference between arterial and venous blood) while the kidney only

Andreas Pohlmann and Thoralf Niendorf (eds.), *Preclinical MRI of the Kidney: Methods and Protocols*, Methods in Molecular Biology, vol. 2216, https://doi.org/10.1007/978-1-0716-0978-1_10,

extracts 10–15% of available oxygen. This is in part because, on a per gram basis, whole-kidney blood flow is higher than that of most other tissues. The kidneys while receiving 20–25% of cardiac output under resting conditions, only consume about 7% of the body's total oxygen. The major determinant of renal O_2 consumption is energy-dependent tubular sodium reabsorption. Whereas O_2 consumption determines perfusion in nonrenal tissues, renal O_2 consumption is largely determined by perfusion. Increased renal blood flow is, in general, accompanied by increased glomerular filtration rate, and therefore necessitates increased energy-dependent tubular sodium reabsorption. Another particularity is the highly heterogeneous blood perfusion and oxygenation within the kidney. Virtually all of the blood flowing into the kidney perfuses the cortex. The medulla is perfused by a small fraction (about 10% of total renal blood flow) of blood that had traversed the cortex. In accordance, tissue partial pressure of oxygen (pO_2) is very low in the medulla. Three additional mechanisms substantially contribute to low renal tissue pO_2. (a) The particular architecture of the intrarenal vasculature enables shunt diffusion of O_2 from arteries to veins in the cortex as well as from descending to ascending vasa recta in the medulla. (b) The vascular architecture also promotes differential distribution of erythrocytes and plasma at certain vessel branches (plasma skimming), which results in different hematocrit and O_2 content of blood perfusing the daughter vessels. (c) The Fåhræus–Lindqvist effect lowers the hematocrit in the long and narrow vasa recta supplying the medulla, which lowers the O_2 content of blood perfusing the medulla. At the same time, a rather high metabolic rate and thus O_2 demand is required to support active reabsorption of sodium along medullary thick ascending limbs of Henle's loop (mTAL) [1]. For a comprehensive description of the causes and the degree of the heterogeneity of intrarenal perfusion and oxygenation *see* the chapter by Cantow K et al. "Quantitative Assessment of Renal Perfusion and Oxygenation by Invasive Probes: Basic Concepts."

Given these particularities in renal oxygenation, there is an interest in understanding the physiological mechanisms involved in maintaining the oxygenation status within the medulla in health and how they may be affected in disease. Acute changes to intrarenal O_2 can be caused by both changes in O_2 supply due to changes in arterial O_2 content or perfusion, changes in O_2 consumption, or a combination of the two. For example, nitric oxide (NO) regulates blood supply by relaxing smooth muscle tension of resistance vessels and inhibitors of NO formation such as L-NAME reduce renal blood flow. The resulting reduction in renal O_2 supply decreases renal tissue oxygenation as evaluated by BOLD-MRI [2]. Alternatively, loop diuretics like furosemide block the sodium–potassium–chloride transporter in the mTAL. Inhibiting this secondary active transport decreases the load of the primary active sodium–

potassium pump (Na^+/K^+ ATPase) in the mTAL. The ensuing decrease in O_2-dependent sodium reabsorption results in an increase in outer medullary pO_2. Thus, administration of furosemide is most commonly used both as a validation of the measurements [3, 4] and as a tubular functional paradigm in the clinic [5]; for detailed discussion of the pros and cons *see* the chapter by Cantow K et al. "Reversible (Patho)Physiologically Relevant Test Interventions: Rationale and Examples." Early work using atrial natriuretic peptide (ANP), which was expected to cause some increase in blood flow, caused a significant decrease in both cortical and medullary O_2 due to the net increase in O_2 consumption related to sodium transport [6]. This illustrates the distinction between monitoring oxygenation vs. perfusion or blood flow and is especially relevant in the kidney.

In the setting of kidney disease, deregulation of O_2 balance has long been studied. A recent review [7] of gene responses in six different models of acute kidney injury (gram-negative sepsis, gram-positive sepsis, ischemia reperfusion, malignant hypertension, rhabdomyolysis, and cisplatin nephrotoxicity) found that hypoxia along with oxidative stress and inflammation was the common feature of all the disease models. These acute injuries may lead to tubule cell death by apoptosis or necrosis and injured cells frequently dedifferentiated into fibroblasts. This fibrosis can lead to tubular atrophy and reduction in function, forcing the remaining tubules to use more oxygen which can cause further injury [7].

Understanding the relationship between renal oxygenation and kidney disease was predominantly based on data obtained from preclinical models with tissue pO_2 measurements using invasive microprobes [3, 6, 8]. These probes were inserted in the kidney to provide local and acute pO_2 readings. Probe position is critical and can be difficult to maintain in small animals. Alternately, pimonidazole [9] can be used to stain tissue at severe hypoxia. This histological staining method only captures hypoxia present at the moment of tissue sampling. For detailed discussion of the advantages and disadvantages of these methods *see* the chapter by Cantow K et al. "Quantitative Assessment of Renal Perfusion and Oxygenation by Invasive Probes: Basic Concepts." BOLD MRI is a noninvasive imaging technique that can be used to estimate the relative oxygen availability in tissue. It offers both spatial information (at reduced spatial resolution compared to histology) and temporal resolution (typically lower than microprobes). Figure 1 illustrates the similarity and differences between histological, microprobe, and BOLD-MRI measurements. BOLD MRI allows for longitudinal follow-up because of its noninvasive nature.

In this chapter, we will provide an overview of BOLD MRI including the basic concept involved, and a few illustrative applications of renal BOLD MRI in rodents.

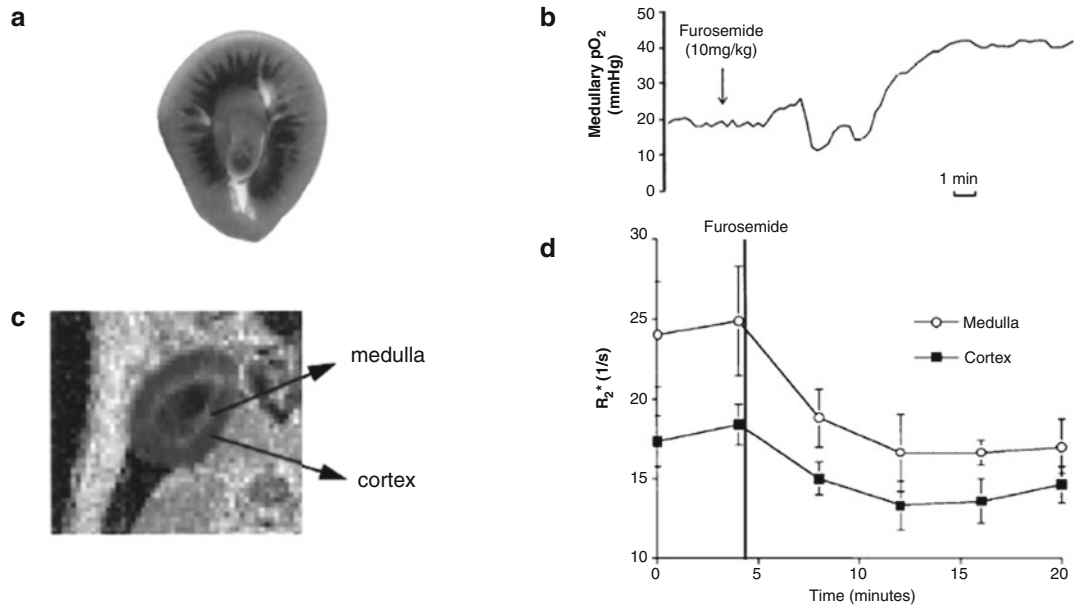

Fig. 1 (**a**) [10] A slice of rat kidney histologically stained for pimonidazole, showing the corticomedullary differences. Higher staining in the medulla is related to the increased hypoxia. This method can capture the spatial distribution of severe hypoxia within the kidney at the time of tissue sampling. (Reproduced from Zhong Z et al., *Am. J. Physiol.* 275 (*Renal Physiol.* 44): F595–F604, 1998 with permission from American Physiological Society). (**b**) [3] pO_2 microelectrode data showing the temporal changes in renal medullary pO_2 in a rat kidney and illustrates the increase in pO_2 following administration of furosemide. (Reproduced from Brezis M et al., *Am. J. Physiol.* 267 (*Renal Fluid Electrolyte Physiol.* 36): F1059–F1062, 1994 with permission from American Physiological Society). (**c**) [11] A representative slice of R_2* map in a rat kidney showing corticomedullary differences, even though the contrast is opposite compared to (**a**). The spatial resolution is also obviously lower compared to (**a**). (**d**) [11] Shows the changes in R_2* in the outer medulla and cortex after injection of furosemide. The first two points for both curves are baseline (preinjection). Both medullary and cortical R_2* drop after the injection of furosemide and stay relatively constant over the 20-min period of observation. Error bars represent standard deviation in the individual ROI measurements. This figure illustrates the merits of BOLD MRI in terms of providing both spatial and temporal information of pO_2 changes in kidneys. (Reproduced from Prasad PV et al., *J. Magn. Reson. Imaging* 1999; 9:842–846 with permission from John Wiley & Sons)

This introduction chapter is complemented by two separate chapters describing the experimental procedure and data analysis, which are part of this book.

This chapter is part of the book Pohlmann A, Niendorf T (eds) (2020) Preclinical MRI of the Kidney—Methods and Protocols. Springer, New York.

2 Measurement Concept

2.1 Basic Concept of BOLD Contrast

BOLD MRI technique uses deoxyhemoglobin (deoxyHb) as an intrinsic (or endogenous) contrast mechanism. Hemoglobin (Hb) is the primary vehicle for transporting O_2 in the blood. When O_2 is bound to Hb, it becomes oxyhemoglobin (oxyHb)

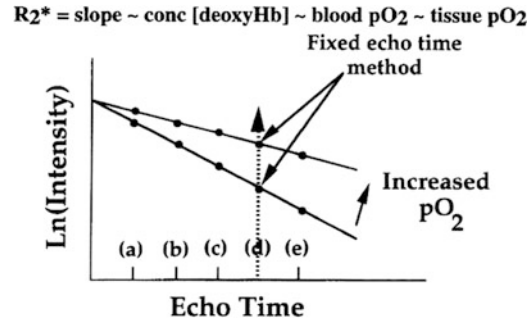

Fig. 2 [13]: Blood oxygenation level-dependent (BOLD) MRI changes qualitatively with pO_2. The deoxygenation of hemoglobin changes its magnetic characteristics, leading to changes in a parameter of magnetic resonance called R_2* (apparent spin–spin relaxation rate). R_2* can be estimated from signal intensity measurements made at several different echo times (**a**–**e**). The slope of Ln (intensity) vs. echo time determines R_2* and is directly related to the amount of deoxygenated blood. A decrease in the slope implies an increase in the pO_2 of blood. We can either measure the slope or obtain intensity measurements at a single echo time (e.g., **d**) to detect a difference in pO_2. Because blood pO_2 is thought to be in rapid equilibrium with tissue pO_2, changes in BOLD signal intensity or R_2* should reflect changes in the pO_2 of the tissue. (Reproduced from Prasad PV et al., Circulation. 1996 Dec 15; 94: 3271–5 with permission from American Heart Association)

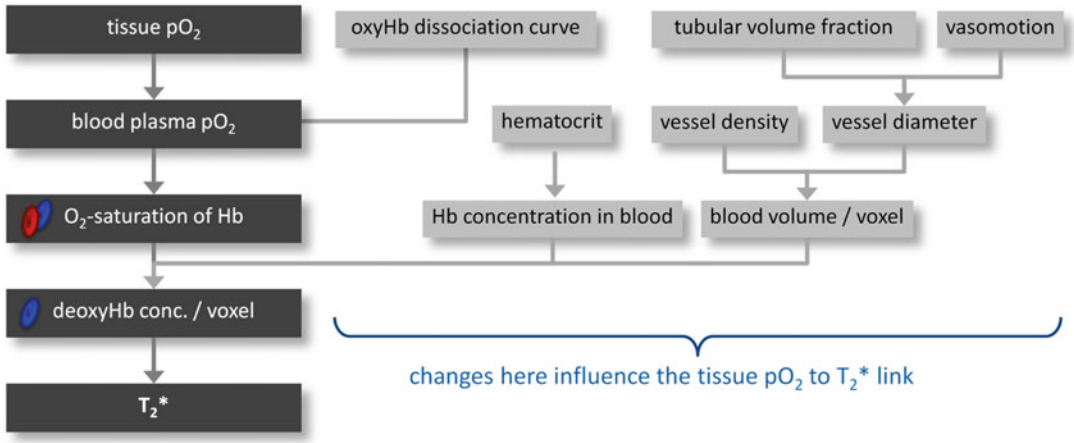

Fig. 3 [14]: Link between tissue pO_2 and T_2* (or R_2*), together with the potentially confounding factors

which is diamagnetic. When O_2 is released from Hb, it becomes deoxyhemoglobin (deoxyHb) which behaves as a paramagnet [12]. Since Hb is compartmentalized to the vascular system, the presence of deoxyHb creates local magnetic susceptibility gradients in and around blood vessels. This induces spin-dephasing so that the effective spin–spin relaxation decay of the MR signal governed by the relaxation time T_2* will be shortened when the local

deoxyHb concentration is increased. This results in signal loss in T_2*-weighted imaging (e.g., gradient echo (GRE) imaging) in areas of increased deoxyHb concentration. The BOLD signal is quantitatively measured by either the effective relaxation time T_2* (s) OR relaxation rate R_2* ($= 1/T_2$* and expressed in s^{-1}). T_2* and R_2* can be calculated based on GRE data acquired at different echo times (TE) and determining the slope of Ln (signal intensity) vs. TE (Fig. 2). With the assumption that hematocrit and local blood volume fraction remain unchanged (in fact, they might vary significantly), a decrease of R_2* corresponds to an increase of O_2 saturation of Hb and, assuming an unchanged oxyHb dissociation curve, in blood pO_2. Under "perfect" physiological conditions the pO_2 of capillary blood is thought to be in equilibrium with the surrounding tissue, and changes in observed R_2* could be interpreted as an indicator of changes in tissue pO_2. In many (patho)physiological scenarios however, the link between R_2* (T_2*), O_2 saturation of Hb, and tissue pO_2 is confounded by changes in various factors, which are illustrated in Fig. 3 and detailed in Subheading 2.3 [14].

The ratio of oxyHb to deoxyHb (which is the major determinant of % O_2 saturation of Hb under physiological conditions) is related to the pO_2 of blood and is governed by the oxyHb dissociation curve [15]. The renal medullary pO_2 is in the lower range of the curve. Hence a change in pO_2 will result in relatively larger change in the ratio of oxyHb to deoxyHb compared to a similar change in pO_2 of cortex. This makes BOLD MRI sensitive for following changes in pO_2 in the medulla.

2.2 BOLD MRI Acquisition Methods and Strategies for Kidney Oxygenation Measurement in Rodents

Two MR imaging techniques are used for renal BOLD MRI, namely, single shot echo planar imaging (EPI) [13] and multiple gradient echo (mGRE) sequences [4]. Functional imaging of the human brain predominantly uses single shot EPI due to the need for high temporal resolution and/or signal averaging. The ultrafast nature of EPI makes it ideal for abdominal imaging to freeze motion. It is suitable for applications with rapid changes in oxygenation and where R_2* mapping is not necessary [16]. However, it is highly sensitive to bulk magnetic susceptibility artifacts which results in image blurring, geometrical distortion, signal loss, and limited spatial resolution. The image distortion is amplified in regions with poor magnetic field homogeneity such as in the vicinity of bowels filled with gas. It is hardly used in preclinical setting, especially when using high field strength MR scanners.

mGRE sequence is currently the most widely utilized acquisition method both for human [4] and preclinical [11] applications of renal BOLD MRI. It acquires signals at multiple echo times after each excitation pulse. R_2* calculated as the slope of the straight line fitting of Ln(SI) vs. TE or by fitting the SI vs. TE data to a single decay monoexponential function. mGRE acquisitions provide improved SNR (signal-to-noise ratio), spatial resolution, and

image quality compared to single shot EPI method. However, longer echo times with mGRE sequence also suffer from bulk susceptibility artifacts. In preclinical setting, motion artifacts are usually minimized using multiple averages. mGRE can suffer from phase variations between odd and even echoes when both water and fat components are present in renal tissue. Choice of echo times corresponding to in-phase or out-of-phase can minimize such artifacts. In the presence of flow, use of even echoes may be preferred.

2.3 Limitations of BOLD MRI for Absolute pO_2 Measurement

R_2* inherently depends on many parameters, primarily including R_2 the natural spin–spin relaxation rate and a susceptibility weighted component termed R_2' ($R_2^* = R_2 + R_2'$). R_2' is determined by the susceptibility component. In the context of BOLD MRI, it depends on the amount of deoxyHb present within the voxel which is determined by the combination of fractional blood volume (fraction of the voxel occupied by blood), hematocrit, and O_2 saturation of hemoglobin.

The factors confounding the relationship between R_2^*(or T_2^*) and intrarenal blood pO_2 are listed in Table 1.

BOLD MRI is inherently best suited to monitor changes in regional pO_2 which is assumed to be in a dynamic equilibrium with O_2 saturation of Hb. This inherently assumes that there are no concomitant changes in fractional blood volume, the oxyHb dissociation curve, and hematocrit. While this may be valid with certain pharmacological maneuvers, one or more of these confounders will change in various acute scenarios. Any vasodilation or vasoconstriction, either induced by pharmacologic maneuvers or by endogenous control of renal vessels, alters the blood volume fraction. Besides the vasculature, the interstitial and the tubular compartments can also experience rapid volume changes and, given the rather rigid renal capsule, can therefore modulate the blood volume fraction. The tubular volume fraction is a unique feature of the kidney; it is quite large and can rapidly change due to (a) changes in glomerular filtration, (b) alterations in tubular outflow toward the pelvis, (c) modulation of the transmural pressure gradient, and (d) changes in resorption. This is partly the motivation to establish R_2^* vs. tissue pO_2 calibration relationship. However, such calibration is strictly valid only in the model it was established in, for example, healthy animals and cannot be generalized to disease models and other species including humans. Mathematical analytical methods can be used to model the relationship between R_2' and O_2 saturation of Hb [17, 18]. However, these will require knowledge of fractional blood volume and regional hematocrit for the individual kidney. In kidneys, it is known that hematocrit is lower in the inner medulla [19]. This explains why inner medulla in rodents usually have low R_2^* values (typically lower than the cortex and erroneously indicating more availability of oxygen). Fractional blood volume is inherently an imaging specific concept and so

Table 1
Factors confounding the relationship between R_2*(or T_2*), oxygen saturation of hemoglobin, and blood pO_2

Confounding factor	Direction of effect	Examples scenarios
Blood volume fraction	Positive	Vasodilation/constriction, change in tubular volume fraction
Hematocrit	Positive	Plasma skimming, hemodilution
Oxygen–hemoglobin dissociation curve		Changes in pH, pCO_2, or temperature
Magnetic field (B_0) inhomogeneity	Positive	Bowel gas, poor shim
T_2	Positive	Edema

A "positive" direction of the effect means that an increase in the confounding factor leads to an increase in R_2* (decrease in T_2*) and hence an overestimation of the hypoxia

there is very little literature on its measurement. The ideal method to estimate fractional blood volume is by using an intravascular contrast agent such as ultrasmall paramagnetic iron oxide (USPIO) [20, 21]. Oxygen saturation of Hb is related to the pO_2 of blood by the oxyHb dissociation curve which is influenced by factors such as pH, pCO_2, and temperature. Further the inherent assumption that blood pO_2 is in a dynamic equilibrium with surrounding tissue pO_2 may not hold in disease [22]. These limitations of BOLD MRI need to be taken in to account when interpreting experimental findings as illustrated recently [14]. In order to study the detailed link between renal tissue pO_2 and T_2* in vivo, an integrated approach that combines parametric MRI and quantitative physiological measurements (MR-PHYSIOL) was proposed [23]. The MR-PHYSIOL setup was used to study the relationship between renal T_2* and tissue pO_2 and perfusion in rats. The findings indicate that changes in T_2* qualitatively reflect changes in renal tissue pO_2 induced by maneuvers including hyperoxia, suprarenal aortic occlusion, and hypoxia. Yet a closer examination of the quantitative relationships between relative changes in T_2* and in tissue pO_2 revealed discrepancies, indicating that, due to the differential changes in one or more of the confounders, simple translation of quantitative results obtained for one intervention of renal hemodynamics and oxygenation to another intervention is falling short of being appropriate. Also, taking the perfusion and oxygenation heterogeneity among the kidney layer into account, extrapolation of results obtained for one layer to others must be made with due caution [24].

2.3.1 R_2' Measurement

Given the specific interest in the susceptibility component of spin–spin relaxation rate for BOLD MRI, measurement of R_2' is desired. While there has been some effort in directly estimating R_2' using

asymmetric spin-echo sequences [25], a simpler and practical method may be to perform a gradient echo and spin echo measurement to estimate R_2* and R_2 separately then calculate the difference [26]. Since R_2 can independently vary with certain pharmacological maneuvers (e.g., following L-NAME [21]), using R_2' as the BOLD MRI parameter may be more specific to the oxygenation related changes. A recent study illustrated the feasibility of using R_2' measurements to estimate blood oxygenation in rat kidneys [17]. While R_2 is not directly sensitive to BOLD effects, there is actually an indirect dependence due to diffusion effects of spins experiencing the field gradients generated by the presence of deoxyHb in the microvasculature. In this regard, R_2 has been shown to be more specific to small vessels [27], while R_2* is typically weighted by larger vessels.

2.4 Considerations Regarding Animal Preparation

- Bowel gas can create susceptibility artifacts in renal R_2* map, right lateral position helps minimize susceptibility artifacts from bowel gas.
- Respiratory motion could create artifacts and usually multiple measurements for averaging purposes can be used to minimize these. Alternately, respiratory triggering could be used but may increase the acquisition times.
- Studies indicate the choice of anesthesia has a large influence on renal R_2* [28]. This may be partly due to known effects of anesthesia on respiration, temperature, blood pressure, and hence pO_2.

3 Overview of Preclinical Applications

Noninvasive BOLD MRI is primarily attractive for the use in humans. However, there is a need for preclinical applications of the method primarily to validate the technique against invasive measures and better understand changes in different diseases.

Validation of renal BOLD MRI measurements is mostly carried out by comparing the responses to certain (patho)physiologically relevant test interventions or pharmacological maneuvers against pO_2 measurements using invasive microprobes [2, 29]. BOLD data was compared with pimonidazole staining in 10-week-old mice [30]. Interestingly, pimonidazole staining did not show differences between db/db and db/m mice, even though BOLD MRI showed significant differences (Fig. 4). This is probably related to the fact that pimonidazole detects severe hypoxia, typically $pO_2 < 10$ mmHg. There was one study in swine where the invasive probe was placed in the contralateral kidney compared to the one where BOLD MRI measurements were made [31]. This study

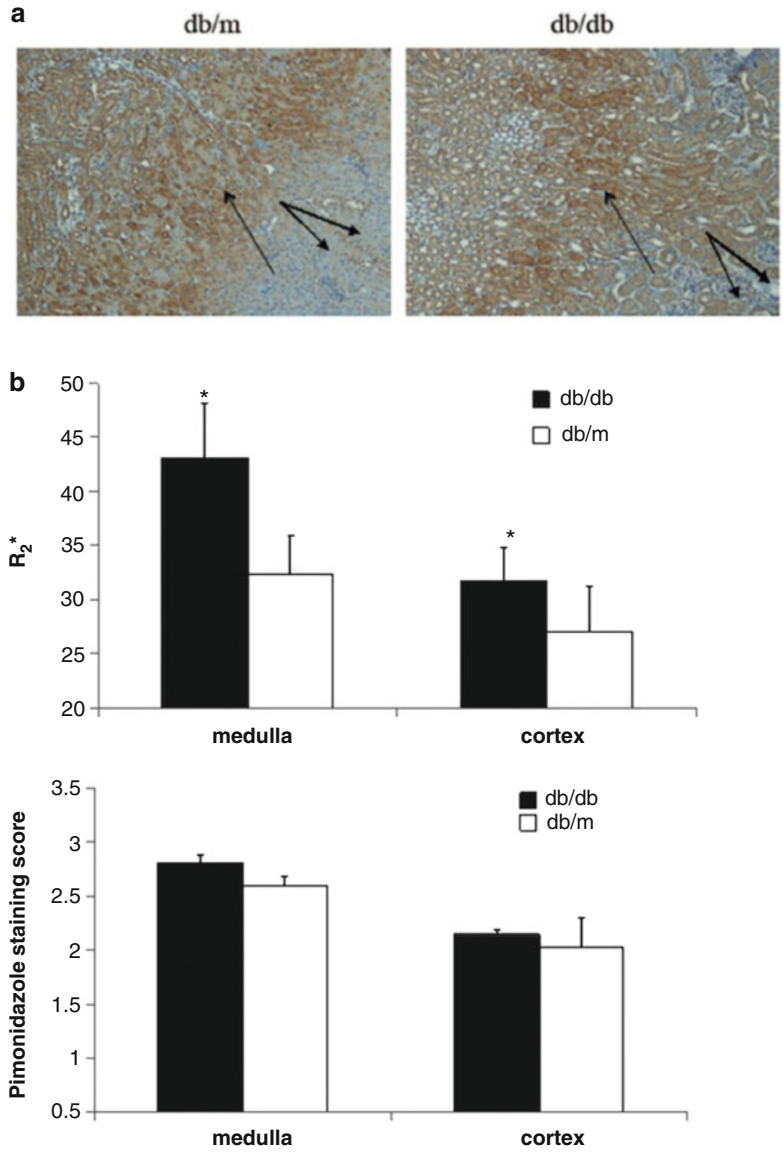

Fig. 4 [30]: (**a**) Pimonidazole immunohistochemical staining of the kidney of db/m and db/db mouse (magnification 100×). Strong pimonidazole (brown) staining of renal tubules was observed mainly in the outer medulla (single arrows) both from db/m and db/db mouse. Weaker staining was seen in the cortex of both db/db and db/m mice (double arrows). (**b**) A summary of R_2* values obtained by BOLD MRI in the medulla and cortex of 10-week-old db/db and db/m mice (upper panel). R_2* is higher in medulla than cortex in both db/db and db/m reflecting lower oxygenation in the medulla. The asterisk denotes a significant difference in R_2* between db/db and db/m in both cortex ($P < 0.04$) and medulla ($P < 0.001$). The lower panel shows the pimonidazole staining score for db/db and db/m mice of similar age (10 weeks old). The medulla had stronger staining than the cortex in both db/db and db/m reflecting increased hypoxia. No significant differences were found in the pimonidazole staining of the medulla and cortex between db/db and the db/m mice. The lack of significance with pimonidazole may be partly related to the fact that it is only sensitive to severe hypoxia, that is, $pO_2 < 10$ mmHg. (Reproduced from Prasad PV et al., Invest Radiol 2010; 45: 819–822 with permission from Wolters Kluwers Health Inc.)

proposed the use of R_2* vs. pO_2 as a calibration curve for translating BOLD MRI measurements in to pO_2 estimates. More recently, true simultaneous measurements with both BOLD MRI and invasive probes were demonstrated in rats [23]. Interventions such as hypoxia, hyperoxia, and suprarenal aortic occlusion were studied by use of this MR-PHYSIOL setup [24]. Use of high field small animal scanners is ideal for rodent applications in terms of signal-to-noise ratios. However, renal BOLD MRI can also be effectively conducted in rats using whole body scanners at both 1.5 [11] and 3 T [32] routinely used in humans which have more widespread availability. Renal BOLD MRI in mice has been shown to be feasible at 3 T using a custom surface radiofrequency loop coil for signal reception [30, 33].

Early application of renal BOLD MRI was primarily to evaluate acute effects of physiological or pharmacological maneuvers. Administration of furosemide increased medullary oxygenation predominantly due to reduction in O_2 consumption [3, 6]. Given the role of NO in essential hypertension, we have also observed differential response to administration of L-NAME in healthy rats compared to spontaneously hypertensive rats (SHR) [34]. Because the reduced NO availability in SHR is related to oxidative stress, we also observed a differential response to free radical scavenger (tempol) in SHR rats compared to controls [35].

3.1 Application to Disease Models

Acute kidney injury (AKI) is a sudden episode of kidney failure or kidney damage that happens within a few hours or a few days of an insult such as administration of nephrotoxins. AKI is common in patients who are hospitalized, patients who have underlying kidney disease, and especially in older adults. Medullary hypoxic injury plays a major role in the pathogenesis of AKI [7], as has been studied by both invasive probes and BOLD MRI in rat models of X-ray contrast induced AKI and renal ischemia/reperfusion injury [36–38].

Given the role of endothelial dysfunction in the susceptibility to contrast induced AKI, we have studied the additive effects of L-NAME, indomethacin (prostaglandin inhibitor) followed by iodinated radio-contrast medium iothalamate (Fig. 5) [32]. Using this AKI model, we compared the effects of different contrast media based on different physicochemical properties, observed large increases in R_2* in the inner-stripe of outer medulla [39]. In a similar model, we evaluated potential preventative maneuvers such as preadministration of furosemide or N-acetylcysteine (NAC, an antioxidant). We found that furosemide was effective in abolishing the increase in R_2* post-radiocontrast [40]. These observations matched with a decrease in urinary neutrophil gelatinase associated lipocalin (NGAL) measurements, a marker of tubular injury.

Unilateral ureteral obstruction (UUO) is a commonly used model of renal fibrosis [41]. However, permanent ligation of ureter

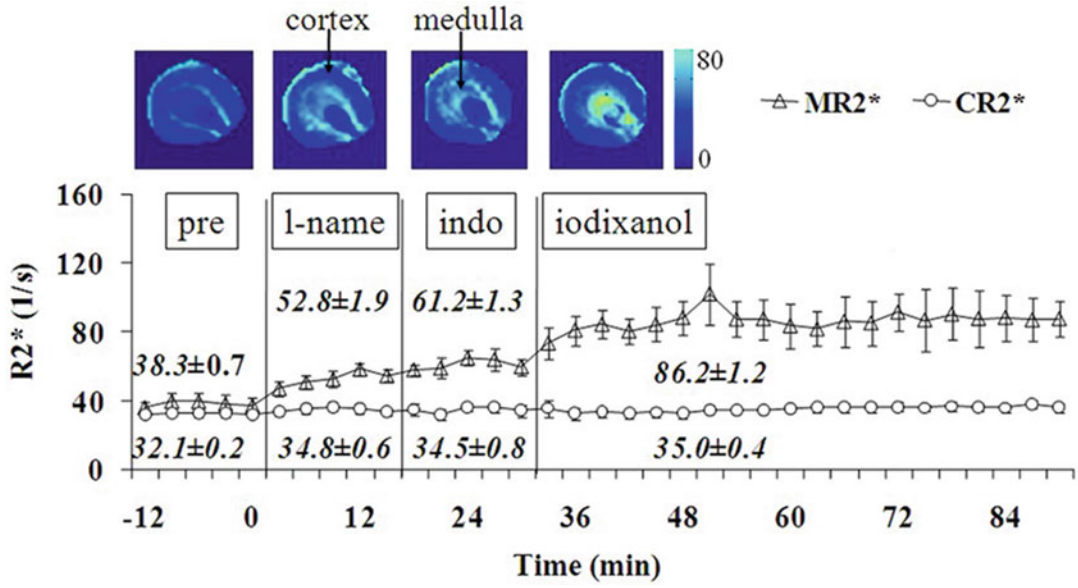

Fig. 5 [32]: Averaged (mean ± SE) renal R_2* time course from six rats in renal medulla and cortex following the administration of L-NAME, indomethacin, and radio-contrast iodixanol. The vertical lines indicate the time of administration of each of chemicals. Pre: baseline; l-name: L-NAME; indo: indomethacin. Error bars represent standard error among rats. On the top are R_2* maps generated using custom Matlab (Mathworks, Natick, MA, USA) code in one representative rat. The relative brightness in renal outer medulla suggests low oxygenation level compared to cortex. The window settings were the same in all maps. The brightness in renal outer medulla increases gradually after each chemical, suggesting the progressively decreasing of oxygenation. The R_2* maps are from baseline, following administration of L-NAME, indomethacin, and iodixanol. The arrows show the renal outer medulla and cortex where the ROIs were placed. The renal outer medulla is relatively brighter than renal cortex in baseline R_2* map, suggesting lower oxygenation level there. Each chemical contributes to the additional increased brightness in R_2* maps in the renal outer medulla, suggesting progressive hypoxia in the renal outer medulla. Bottom: shows the corresponding plot of R_2* vs. time. (Reproduced from Prasad PV et al., J. Magn. Reson. Imaging 2012; 36:1162–1167 with permission from John Wiley & Sons)

results in complete loss of renal parenchyma within couple of weeks. A reversible unilateral ureteral obstruction (rUUO) was proposed as a more representative model of chronic kidney disease (CKD) [42]. In rUUO model, the microvascular clip used to ligate the ureter is moved distally every 2 days for 6 days and then removed. BOLD MRI was used to monitor the longitudinal changes at 2 and 28 days following reversal of the UUO [43]. This application is an illustration of the advantage of a noninvasive imaging method in performing longitudinal studies within the same animal.

Acknowledgments

Work supported, in part, by grant funding from the National Institutes of Health (R01 DK093793 and R01 DK106557).
This publication is based upon work from COST Action PARENCHIMA, supported by European Cooperation in Science and Technology (COST). COST (www.cost.eu) is a funding agency for research and innovation networks. COST Actions help connect research initiatives across Europe and enable scientists to enrich their ideas by sharing them with their peers. This boosts their research, career, and innovation.
PARENCHIMA (renalmri.org) is a community-driven Action in the COST program of the European Union, which unites more than 200 experts in renal MRI from 30 countries with the aim to improve the reproducibility and standardization of renal MRI biomarkers.

References

1. Brezis M, Rosen S (1995) Hypoxia of the renal medulla--its implications for disease. N Engl J Med 332(10):647–655. https://doi.org/10.1056/NEJM199503093321006
2. Li LP, Ji L, Santos EA, Dunkle E, Pierchala L, Prasad P (2009) Effect of nitric oxide synthase inhibition on intrarenal oxygenation as evaluated by blood oxygenation level-dependent magnetic resonance imaging. Investig Radiol 44(2):67–73. https://doi.org/10.1097/RLI.0b013e3181900975
3. Brezis M, Agmon Y, Epstein FH (1994) Determinants of intrarenal oxygenation. I. Effects of diuretics. Am J Physiol 267(6 Pt 2): F1059–F1062
4. Prasad PV, Chen Q, Goldfarb JW, Epstein FH, Edelman RR (1997) Breath-hold R2* mapping with a multiple gradient-recalled echo sequence: application to the evaluation of intrarenal oxygenation. J Magn Reson Imaging 7(6):1163–1165
5. Prasad PV, Li LP, Thacker JM, Li W, Hack B, Kohn O, Sprague SM (2019) Cortical perfusion and tubular function as evaluated by magnetic resonance imaging correlates with annual loss in renal function in moderate chronic kidney disease. Am J Nephrol 49(2):114–124. https://doi.org/10.1159/000496161
6. Brezis M, Heyman SN, Epstein FH (1994) Determinants of intrarenal oxygenation. II. Hemodynamic effects. Am J Physiol 267 (6 Pt 2):F1063–F1068
7. Hultstrom M, Becirovic-Agic M, Jonsson S (2018) Comparison of acute kidney injury of different etiology reveals in-common mechanisms of tissue damage. Physiol Genomics 50 (3):127–141. https://doi.org/10.1152/physiolgenomics.00037.2017
8. Aukland K, Krog J (1960) Renal oxygen tension. Nature 188:671. https://doi.org/10.1038/188671a0
9. Rosenberger C, Rosen S, Paliege A, Heyman SN (2009) Pimonidazole adduct immunohistochemistry in the rat kidney: detection of tissue hypoxia. Methods Mol Biol 466:161–174. https://doi.org/10.1007/978-1-59745-352-3_12
10. Zhong Z, Arteel GE, Connor HD, Yin M, Frankenberg MV, Stachlewitz RF, Raleigh JA, Mason RP, Thurman RG (1998) Cyclosporin A increases hypoxia and free radical production in rat kidneys: prevention by dietary glycine. Am J Phys 275(4):F595–F604. https://doi.org/10.1152/ajprenal.1998.275.4.F595
11. Priatna A, Epstein FH, Spokes K, Prasad PV (1999) Evaluation of changes in intrarenal oxygenation in rats using multiple gradient-recalled echo (mGRE) sequence. J Magn Reson Imaging 9(6):842–846
12. Buxton RB (2013) The physics of functional magnetic resonance imaging (fMRI). Rep Prog Phys 76(9):096601. https://doi.org/10.1088/0034-4885/76/9/096601
13. Prasad PV, Edelman RR, Epstein FH (1996) Noninvasive evaluation of intrarenal oxygenation with BOLD MRI. Circulation 94 (12):3271–3275. https://doi.org/10.1161/01.cir.94.12.3271

14. Niendorf T, Pohlmann A, Arakelyan K, Flemming B, Cantow K, Hentschel J, Grosenick D, Ladwig M, Reimann H, Klix S, Waiczies S, Seeliger E (2015) How bold is blood oxygenation level-dependent (BOLD) magnetic resonance imaging of the kidney? Opportunities, challenges and future directions. Acta Physiol 213(1):19–38. https://doi.org/10.1111/apha.12393
15. Severinghaus JW (1979) Simple, accurate equations for human blood O2 dissociation computations. J Appl Physiol Respir Environ Exerc Physiol 46(3):599–602. https://doi.org/10.1152/jappl.1979.46.3.599
16. Schachinger H, Klarhofer M, Linder L, Drewe J, Scheffler K (2006) Angiotensin II decreases the renal MRI blood oxygenation level-dependent signal. Hypertension 47 (6):1062–1066. https://doi.org/10.1161/01.HYP.0000220109.98142.a3
17. Thacker J, Zhang JL, Franklin T, Prasad P (2017) BOLD quantified renal pO2 is sensitive to pharmacological challenges in rats. Magn Reson Med 78(1):297–302. https://doi.org/10.1002/mrm.26367
18. Zhang JL, Morrell G, Rusinek H, Warner L, Vivier PH, Cheung AK, Lerman LO, Lee VS (2014) Measurement of renal tissue oxygenation with blood oxygen level-dependent MRI and oxygen transit modeling. Am J Physiol Renal Physiol 306(6):F579–F587. https://doi.org/10.1152/ajprenal.00575.2013
19. Zimmerhackl B, Robertson CR, Jamison RL (1985) The microcirculation of the renal medulla. Circ Res 57(5):657–667
20. Pohlmann A, Cantow K, Huelnhagen T, Grosenick D, Dos Santos PJ, Boehmert L, Gladytz T, Waiczies S, Flemming B, Seeliger E, Niendorf T (2017) Experimental MRI monitoring of renal blood volume fraction variations en route to renal magnetic resonance oximetry. Tomography 3(4):188–200. https://doi.org/10.18383/j.tom.2017.00012
21. Storey P, Ji L, Li LP, Prasad PV (2011) Sensitivity of USPIO-enhanced R2 imaging to dynamic blood volume changes in the rat kidney. J Magn Reson Imaging 33(5):1091–1099. https://doi.org/10.1002/jmri.22526
22. Evans RG, Leong CL, Anderson WP, O'Connor PM (2007) Don't be so BOLD: potential limitations in the use of BOLD MRI for studies of renal oxygenation. Kidney Int 71 (12):1327–1328; author reply 1328. https://doi.org/10.1038/sj.ki.5002321
23. Cantow K, Arakelyan K, Seeliger E, Niendorf T, Pohlmann A (2016) Assessment of renal hemodynamics and oxygenation by simultaneous magnetic resonance imaging (MRI) and quantitative invasive physiological measurements. Methods Mol Biol 1397:129–154. https://doi.org/10.1007/978-1-4939-3353-2_11
24. Pohlmann A, Arakelyan K, Hentschel J, Cantow K, Flemming B, Ladwig M, Waiczies S, Seeliger E, Niendorf T (2014) Detailing the relation between renal T2* and renal tissue pO2 using an integrated approach of parametric magnetic resonance imaging and invasive physiological measurements. Investig Radiol 49(8):547–560. https://doi.org/10.1097/RLI.0000000000000054
25. Zhang X, Zhang Y, Yang X, Wang X, An H, Zhang J, Fang J (2013) Feasibility of noninvasive quantitative measurements of intrarenal R (2)' in humans using an asymmetric spin echo echo planar imaging sequence. NMR Biomed 26(1):91–97. https://doi.org/10.1002/nbm.2823
26. Yang X, Cao J, Wang X, Li X, Xu Y, Jiang X (2008) Evaluation of renal oxygenation in rat by using R2' at 3-T magnetic resonance: initial observation. Acad Radiol 15(7):912–918. https://doi.org/10.1016/j.acra.2008.01.015
27. Boxerman JL, Hamberg LM, Rosen BR, Weisskoff RM (1995) MR contrast due to intravascular magnetic susceptibility perturbations. Magn Reson Med 34(4):555–566
28. Niles DJ, Gordon JW, Fain SB (2015) Effect of anesthesia on renal R2 * measured by blood oxygen level-dependent MRI. NMR Biomed 28(7):811–817. https://doi.org/10.1002/nbm.3314
29. dos Santos EA, Li LP, Ji L, Prasad PV (2007) Early changes with diabetes in renal medullary hemodynamics as evaluated by fiberoptic probes and BOLD magnetic resonance imaging. Investig Radiol 42(3):157–162. https://doi.org/10.1097/01.rli.0000252492.96709.36
30. Prasad P, Li LP, Halter S, Cabray J, Ye M, Batlle D (2010) Evaluation of renal hypoxia in diabetic mice by BOLD MRI. Invest Radiol 45 (12):819–822. https://doi.org/10.1097/RLI.0b013e3181ec9b02
31. Pedersen M, Dissing TH, Morkenborg J, Stodkilde-Jorgensen H, Hansen LH, Pedersen LB, Grenier N, Frokiaer J (2005) Validation of quantitative BOLD MRI measurements in kidney: application to unilateral ureteral obstruction. Kidney Int 67(6):2305–2312. https://doi.org/10.1111/j.1523-1755.2005.00334.x
32. Li LP, Franklin T, Du H, Papadopoulou-Rosenzweig M, Carbray J, Solomon R, Prasad PV (2012) Intrarenal oxygenation by blood

oxygenation level-dependent MRI in contrast nephropathy model: effect of the viscosity and dose. J Magn Reson Imaging 36 (5):1162–1167. https://doi.org/10.1002/jmri.23747

33. Li LP, Ji L, Lindsay S, Prasad PV (2007) Evaluation of intrarenal oxygenation in mice by BOLD MRI on a 3.0T human whole-body scanner. J Magn Reson Imaging 25 (3):635–638. https://doi.org/10.1002/jmri.20841
34. Li L, Storey P, Kim D, Li W, Prasad P (2003) Kidneys in hypertensive rats show reduced response to nitric oxide synthase inhibition as evaluated by BOLD MRI. J Magn Reson Imaging 17(6):671–675. https://doi.org/10.1002/jmri.10301
35. Li LP, Li BS, Storey P, Fogelson L, Li W, Prasad P (2005) Effect of free radical scavenger (tempol) on intrarenal oxygenation in hypertensive rats as evaluated by BOLD MRI. J Magn Reson Imaging 21(3):245–248. https://doi.org/10.1002/jmri.20260
36. Hoff U, Lukitsch I, Chaykovska L, Ladwig M, Arnold C, Manthati VL, Fuller TF, Schneider W, Gollasch M, Muller DN, Flemming B, Seeliger E, Luft FC, Falck JR, Dragun D, Schunck WH (2011) Inhibition of 20-HETE synthesis and action protects the kidney from ischemia/reperfusion injury. Kidney Int 79(1):57–65. https://doi.org/10.1038/ki.2010.377
37. Arakelyan K, Cantow K, Hentschel J, Flemming B, Pohlmann A, Ladwig M, Niendorf T, Seeliger E (2013) Early effects of an x-ray contrast medium on renal T2 */T2 MRI as compared to short-term hyperoxia, hypoxia and aortic occlusion in rats. Acta Physiol 208(2):202–213. https://doi.org/10.1111/apha.12094
38. Seeliger E, Flemming B, Wronski T, Ladwig M, Arakelyan K, Godes M, Mockel M, Persson PB (2007) Viscosity of contrast media perturbs renal hemodynamics. J Am Soc Nephrol 18 (11):2912–2920. https://doi.org/10.1681/ASN.2006111216
39. Li LP, Lu J, Zhou Y, Papadopoulou MV, Franklin T, Bokhary U, Solomon R, Sen A, Prasad PV (2014) Evaluation of intrarenal oxygenation in iodinated contrast-induced acute kidney injury-susceptible rats by blood oxygen level-dependent magnetic resonance imaging. Invest Radiol 49:403–410. https://doi.org/10.1097/RLI.0000000000000031
40. Li LP, Thacker J, Lu J, Franklin T, Zhou Y, Papadopoulou MV, Solomon R, Prasad PV (2014) Efficacy of preventive interventions for iodinated contrast-induced acute kidney injury evaluated by intrarenal oxygenation as an early marker. Invest Radiol 49(10):647–652. https://doi.org/10.1097/RLI.0000000000000065
41. Togao O, Doi S, Kuro-o M, Masaki T, Yorioka N, Takahashi M (2010) Assessment of renal fibrosis with diffusion-weighted MR imaging: study with murine model of unilateral ureteral obstruction. Radiology 255 (3):772–780. https://doi.org/10.1148/radiol.10091735
42. Puri TS, Shakaib MI, Chang A, Mathew L, Olayinka O, Minto AW, Sarav M, Hack BK, Quigg RJ (2010) Chronic kidney disease induced in mice by reversible unilateral ureteral obstruction is dependent on genetic background. Am J Physiol Renal Physiol 298(4): F1024–F1032. https://doi.org/10.1152/ajprenal.00384.2009
43. Haque ME, Franklin T, Bokhary U, Mathew L, Hack BK, Chang A, Puri TS, Prasad PV (2014) Longitudinal changes in MRI markers in a reversible unilateral ureteral obstruction mouse model: preliminary experience. J Magn Reson Imaging 39(4):835–841. https://doi.org/10.1002/jmri.24235

Chapter 11

Renal Diffusion-Weighted Imaging (DWI) for Apparent Diffusion Coefficient (ADC), Intravoxel Incoherent Motion (IVIM), and Diffusion Tensor Imaging (DTI): Basic Concepts

Neil Peter Jerome, Anna Caroli, and Alexandra Ljimani

Abstract

The specialized function of the kidney is reflected in its unique structure, characterized by juxtaposition of disorganized and ordered elements, including renal glomerula, capillaries, and tubules. The key role of the kidney in blood filtration, and changes in filtration rate and blood flow associated with pathological conditions, make it possible to investigate kidney function using the motion of water molecules in renal tissue. Diffusion-weighted imaging (DWI) is a versatile modality that sensitizes observable signal to water motion, and can inform on the complexity of the tissue microstructure. Several DWI acquisition strategies are available, as are different analysis strategies, and models that attempt to capture not only simple diffusion effects, but also perfusion, compartmentalization, and anisotropy. This chapter introduces the basic concepts of DWI alongside common acquisition schemes and models, and gives an overview of specific DWI applications for animal models of renal disease.

This chapter is based upon work from the COST Action PARENCHIMA, a community-driven network funded by the European Cooperation in Science and Technology (COST) program of the European Union, which aims to improve the reproducibility and standardization of renal MRI biomarkers. This introduction chapter is complemented by two separate chapters describing the experimental procedure and data analysis.

Key words MRI, Kidney, Diffusion, Diffusion-weighted imaging (DWI), Apparent diffusion coefficient (ADC), Intravoxel incoherent motion (IVIM), Mouse, Rat

1 Introduction

The dominant role of magnetic resonance imaging (MRI), and in particular diffusion-weighted imaging (DWI), in the diagnosis and monitoring of renal disease is driven by the ability to provide simultaneous assessment of kidney anatomy and function. In addition to the potential to avoid or reduce the need for biopsy, which is invasive and subject to sampling bias, the use of functional imaging techniques such as DWI allow examination of tissue microstructure in vivo as well as the potential for challenge protocols using administered agents. In particular, in view of the controversial study on

Andreas Pohlmann and Thoralf Niendorf (eds.), *Preclinical MRI of the Kidney: Methods and Protocols*, Methods in Molecular Biology, vol. 2216, https://doi.org/10.1007/978-1-0716-0978-1_11,

gadolinium-containing MR contrast agents with regard to nephrogenic systemic fibrosis (NSF) [1] or possible gadolinium deposits in the central nervous system (CNS) [2], contrast-free examination techniques are to be preferred, especially in patients with impaired renal function.

Diffusion-weighted imaging comes in many variants, from simple to complex schemes, all based on indirect observation of water molecular motion, that are sensitive to changes in renal perfusion and tubular flow, alterations of cellularity arising from inflammation, edema, or hyperplasia, and from fibrosis. A recent review of the application of renal DWI in humans [3] gives an overview of research performed so far and illustrates renal DWI potential in the clinic. The authors in particular conclude that DWI is well-placed to investigate decline of renal function as well as to monitor disease progression in both acute and chronic kidney diseases, while noting that complexity of the diffusion signal makes biological validation difficult.

The strengths of DWI are not without accompanying drawbacks, however, which include the relatively long acquisition times required for advanced DWI protocols, an increased susceptibility to image artifacts, and an overall decreased spatial resolution due to the imaging sequences used. Careful consideration of both the research question to be addressed and the optimal acquisition parameters to be used, together with acquisition of complementary MRI modalities, can ameliorate some of these issues.

This chapter discusses the underlying phenomena and contrast mechanisms of diffusion-weighted imaging. It is complemented by two separate chapters describing experimental procedure and data analysis, which are part of this book.

This chapter is part of the book Pohlmann A, Niendorf T (eds) (2020) Preclinical MRI of the Kidney—Methods and Protocols. Springer, New York.

2 Diffusion Weighted Imaging Concepts

2.1 Fundamental Concept

MRI signal arising from water protons in vivo is sensitive to the exact nature of the tissue, including not only how the spins interact with the tissue lattice and other spins through T_1 and T_2 relaxation mechanisms, but also the tendency of water molecules to physically move around, or diffuse, over time. The use of the term diffusion-weighted imaging is a general catch-all term for any imaging using pulsed field gradients for motion sensitization. DWI is sensitive to the nature and degree of proton movement, which depends on tissue microstructure, therefore representing an informative component of research and clinical MRI protocols.

The use of pulsed gradient fields added to a MRI readout sequence, in a dephase-rephase cycle commonly implemented as a polarity-reversed pair or as equal pulses placed either side of a spin-echo pulse, causes a loss of the MRI signal proportional to the

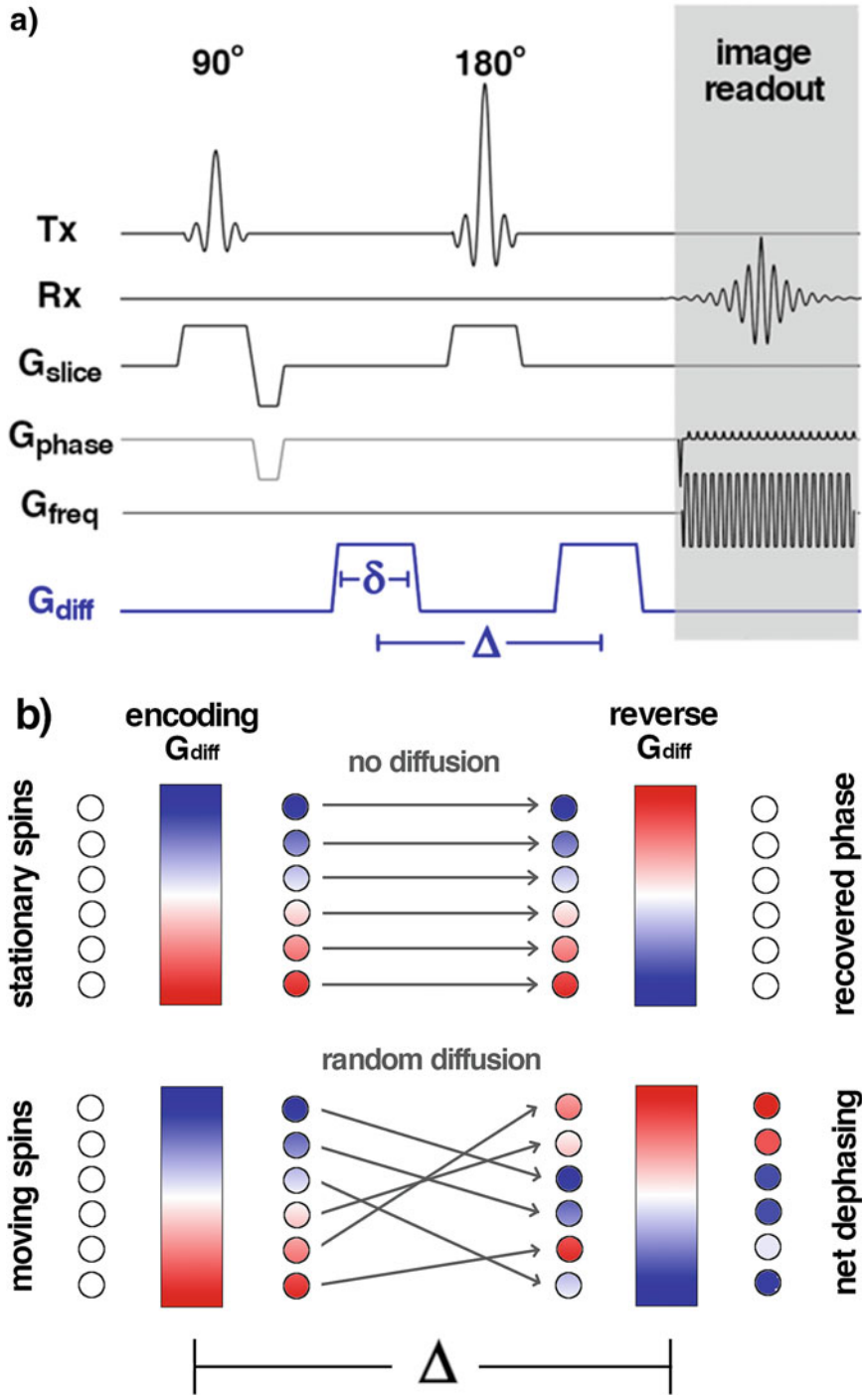

Fig. 1 Illustration of (**a**) DWI pulse sequence, showing the diffusion gradients (lower line, in blue) for a spin-echo echo-planar readout sequence. (**b**) Schematic one-dimensional illustration of the net dephasing of spins dependent on their motion. The initial gradient pulse adds an additional phase (red and blue being +/− additions to the static magnetic field) by transiently modulating the Larmor frequency of the spins. The amount of additional phase is defined by the spin location along the gradient pulse direction (here up/down for simplicity). During the diffusion time Δ, spins have an opportunity to diffuse according to their tissue environment. The reverse pulse (in practice the same polarity, but acting as reversed in combination with the 180° spin-echo pulse) restores the phase offset for spins that have not moved (upper section), whereas moving spins do not receive equal dephase and rephase shifts, leading to a net phase shift (indicated by remaining color) and an overall signal loss

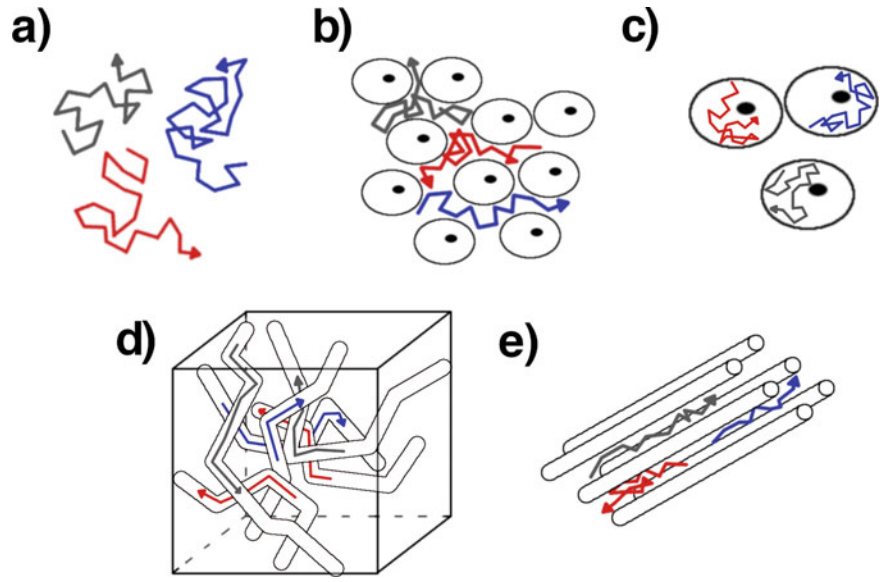

Fig. 2 Schematic summary of motion types that can be investigated by diffusion imaging. Illustrative paths for water molecules are shown for: (**a**) free diffusion, also called Gaussian or true diffusion, that is a random motion; (**b**) apparent hindered diffusion in the tissue, where the microstructure alter true diffusion by introducing barriers; (**c**) apparent diffusion restriction, for example within cells (**d**) pseudodiffusion, denoting motion due to flow in vessels or tubules; and (**e**) diffusion directionality caused by structural elements

overall mis-match of the pulses experienced by spins that have changed location (Fig. 1). The larger the distance covered by water molecules (and the proton spins therein) between the gradient pulses, the greater the mismatch of pulses experienced by the spins, and the greater the overall signal destruction from the net spin dephasing. Over time, this basic DWI concept has been implemented into a raft of specialized sequences, targeted and optimized for different applications.

2.2 Water Motion and Relation to Microstructure

In a large, single-compartment system, free diffusion of water molecules is a truly chaotic, random phenomenon known as Brownian motion, and might go on indefinitely (Fig. 2a). Here, the average displacement of molecules over time is described by an increasingly wide distribution, Gaussian (or normal) in nature, centered on the starting position and characterized by a *diffusion coefficient*. In biological tissues, water molecules interact with surrounding structures (cell walls, extracellular matrix, and so forth), which act as barriers causing an alteration and possible restriction in diffusion (Fig. 2b, c). Tissue microstructure may also contain flow elements, or structure with directional preference (Fig. 2d, e). The observed diffusion coefficient from an imaging voxel, which may contain a complex mix of diffusion environments, is thus an empirical parameter, the *apparent diffusion coefficient (ADC)* measured in mm^2/s. Since tissue microstructure is a major determinant of apparent diffusion, pathological conditions affecting microstructure cause an alteration in ADC.

The length scale of diffusion imaging, that is the average distance covered by water molecules during the DWI experiment, is determined as a balance of the average speed of the water molecules in their environment and the diffusion time allowed in the acquisition. Moreover, it is possible to see signal characteristic of molecules whose motion is restricted to certain structures if the length scale exceeds the structure dimensions. This, for example, allows for the inference of intracellular water motion and thus cell size in appropriately designed DWI protocols [4].

In the kidney, nonrandom perfusion and tubular flow, which manifest as pseudodiffusion processes, as well as the high degree of directional order in the renal structure, add complexity to the investigation of water molecule motion. Specific signal interpretation models have been developed to account for an additional (or sometimes more than one) pseudodiffusion compartment, generally possessing a pseudodiffusion coefficient of a higher magnitude than that of true diffusion. Similarly, additional models assessing diffusion along multiple explicit directions have been developed to provide information on directional motion as well as on the relative anisotropy of the tissue.

Since the complexity of diffusion signal interpretation models is intrinsically tied to the complexity of image acquisition protocols, DWI acquisition and analysis cannot be considered and discussed independently (*see* **Note 1**). The choice of acquisition parameters will determine and/or limit the possible signal interpretation models, and therefore acquisition must be carefully designed, with the expected analysis in mind. In particular, DWI acquisitions are often lengthy, and there is always pressure to limit their duration when transferred to clinical practice to minimize patient discomfort. When planning renal DWI studies in the preclinical setting, it is thus important to consider also their translational potential, and the additional value that more complex acquisitions offer in relation to the extra scan time required.

3 Diffusion Modeling

The degree of diffusion weighting applied to an image is conventionally reported as its *b*-value, where *b* is a compound parameter, expressed in s/mm^2, arising from the specifics of the pulsed gradients used to sensitize the signal to spin motion. The *b*-value is limited by the gradient hardware, but values of several thousand are commonly achievable. Given that the incomplete rephasing of displaced water molecules explicitly leads to a loss of signal, increased diffusion weighting is ultimately limited by signal-to-noise and in general is performed with a lower spatial resolution than images acquired using other MRI modalities. Sufficiently high *b*-values may reduce the signal to the level of background noise, and in these cases either these data can be excluded, or an explicit noise term added to the analysis.

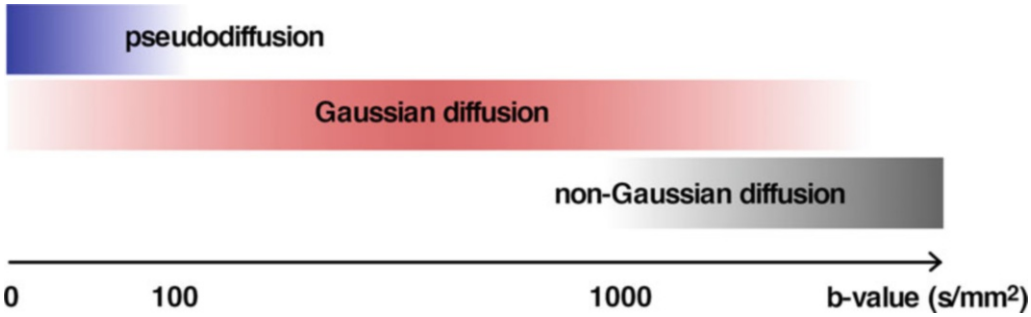

Fig. 3 Different diffusion weightings, summarized by the compound parameter *b*-value, give rise to diffusion signal that is influenced by different diffusion regimes. Intuitive, though necessarily simplified, interpretations of these diffusion phenomena include (1) pseudodiffusion, observed at low *b*-values and reflecting vessel and tubular flow; (2) Gaussian (or random) diffusion, reflecting diffusion of water molecules in the renal tissue and thus informing on renal microstructure and cellularity; and (3) non-Gaussian diffusion, observed at high *b*-values and providing additional information on tissue microstructure. In addition to *b*-value, diffusion time, delay, and direction parameters influence the observed DWI signal

The range of *b*-values used in a diffusion imaging protocol defines which diffusion components will be present and/or dominate the signal, and thus will influence the analysis. The simplified illustration in Fig. 3 gives a rough guideline to the *b*-value ranges where different diffusion phenomena can be detected, though it is important to appreciate the simplifications made when attempting to model diffusion processes in tissue, and that *b*-value magnitude alone is not sufficient to describe the experiment.

In some circumstances, such as the spatial localization of tumors, it may be sufficient to simply observe the hyperintense signal of highly cellular regions on a single diffusion-weighted image of sufficient *b*-value to provide increased contrast (although at lower overall signal). Diffusion-weighted images have an underlying T_2 weighting arising from the longer TE required to allow for inclusion of the diffusion-sensitizing pulses, which can be confounding where long-T_2 regions (e.g., free water) can be mistaken for low diffusion areas—this is known as the T_2 *shine-through* effect [5]. In most applications, however, modeling of the DWI signal behavior, across a set of matched images varying only in the applied *b*-values, removes the T_2 influence and gives quantitative parameters that are, in theory, comparable across studies (*see* **Note 2**).

In the following sections, several diffusion signal interpretation models relevant to renal studies are described, though this is far from an exhaustive list of models or mathematical representations available. Choice of DWI protocols are often selected in terms of the additional value that they may offer in relation to their additional complexity and duration, and with a particular diffusion model and analysis scheme in mind (*see* **Note 3**).

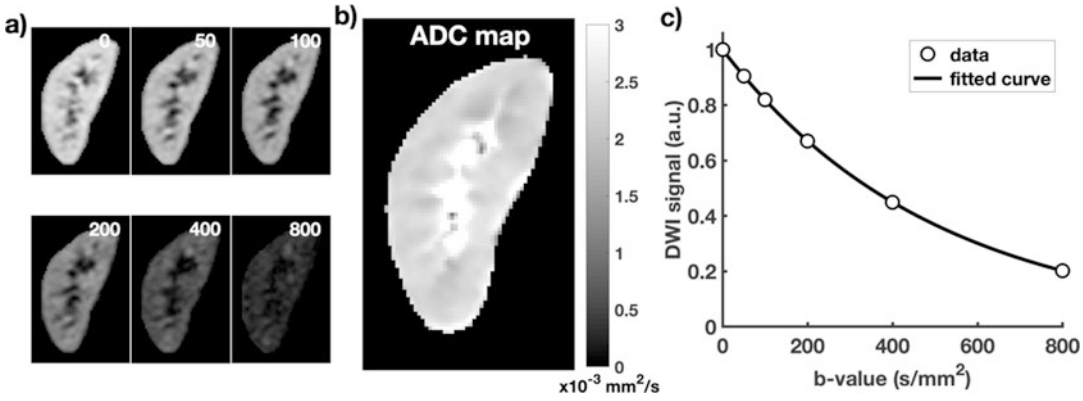

Fig. 4 Monoexponential ADC model. (**a**) Example DWI images acquired with different *b*-values (given in s/mm^2) from a healthy kidney, and (**b**) the ADC map resulting from fitting a monoexponential model. Signal-to-noise ratio, depending on T_2, spatial resolution, and the underlying diffusion itself, decreases with the increase in *b*-value. (**c**) Schematic illustration of an ideal ADC curve fit to noiseless data. Analysis methods are discussed in detail in the chapter by Jerome NP et al. "Analysis of Renal Diffusion-Weighted Imaging (DWI) Using Apparent Diffusion Coefficient (ADC) and Intravoxel Incoherent Motion (IVIM) Models"

3.1 Monoexponential Apparent Diffusion Coefficient (ADC)

The simplest and most widely used model to interpret the DWI signal is a single compartment model, summarizing all motion components (from diffusion, flow, etc.) in a single coefficient (ADC, *see* **Note 4**). The resulting ADC maps (*see* Fig. 4) are derived from the fitting of the DWI signal, across all *b*-values on a voxel-wise basis, of a single-exponential model according to the following formula:

$$S_{(\mathrm{b})} = S_{(\mathrm{total})} . \exp\left(-\frac{\mathrm{TE}}{T_2}\right) . \exp\left(-b.\mathrm{ADC}\right) \qquad (1)$$

where $S_{(\mathrm{b})}$ and $S_{(\mathrm{total})}$ represent the signal observed at a particular *b*-value, and the overall equilibrium signal (at $b = 0$ s/mm^2 and TE = 0 ms) respectively. Since the echo time TE is usually not varied across images with different diffusion weightings, the first two terms are often summarized as S_0, the signal at a *b*-value of zero, and the formula simplifies as follows:

$$S_{(\mathrm{b})} = S_0 . \exp\left(-b.\mathrm{ADC}\right) \qquad (2)$$

Despite the DWI signal not being truly monoexponential, and ADC being a purely empirical parameter summarizing different factors contributing to the diffusion signal, ADC can still be considered as a sensitive and useful biomarker [6, 7].

The monoexponential model requires acquisition of a minimum of 2 *b*-values. The lower value is commonly set as zero by default, although this leads to what is known as a perfusion-sensitive ADC; choosing a minimum *b*-value of approximately

100–200 s/mm^2 removes this influence to give a perfusion-insensitive ADC. The highest *b*-value is normally chosen as the maximum value while retaining sufficient signal, commonly in the range 700–1000 s/mm^2 [8], although non-Gaussian processes may become relevant at this upper limit (Fig. 3). The coefficient derived from the analysis is always referred to as ADC, although it is important to note that if the underlying signal curve is not mono-exponential the measured ADC strongly depends on the *b*-values chosen [9], and so is not necessarily comparable across studies. Main advantages of the simple monoexponential equation is the short acquisition time required, and the general robustness of ADC as a marker of diffusion [10]. The monoexponential model is also suited to DWI studies with multiple *b*-values, with additional data points allowing for estimation of ADC uncertainties.

3.2 Intravoxel Incoherent Motion (IVIM)

One advanced model to interpret the diffusion imaging signal is the intravoxel incoherent motion (IVIM) model. Originally proposed by Le Bihan for the assessment of microcapillary perfusion in the brain [11], the model is generally applicable if a number of assumptions are fulfilled, and represents a popular choice for attempting to separate diffusion from flowing components [12].

In this model, a second compartment is included in the signal interpretation to describe the flow-based motion of water molecules in blood capillaries and tubules that, if assumed to randomly occur in all directions, appears as an accelerated diffusion process (Fig. 5).

The pseudodiffusion component associated with flow is described by the pseudodiffusion coefficient D^* that, since flow is faster than diffusion, is approximately an order of magnitude larger

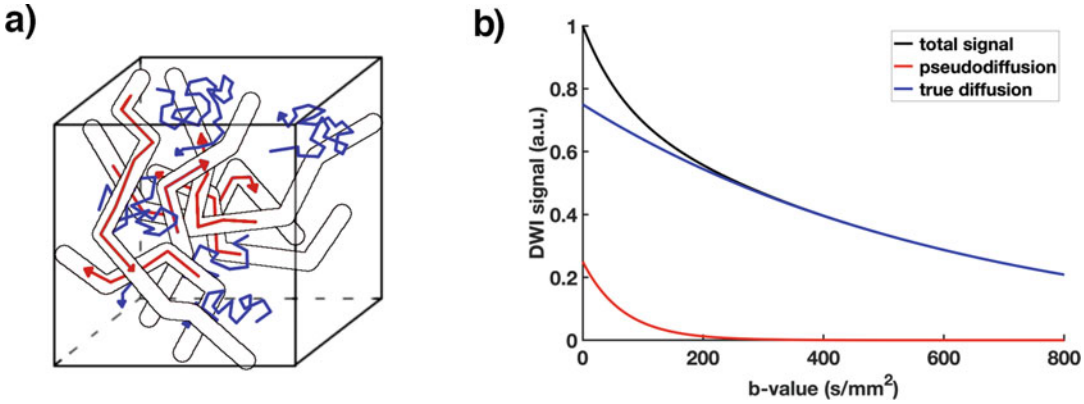

Fig. 5 IVIM model. (**a**) Schematic representation of random water motion in a voxel of renal tissue, where free diffusion component (in blue, described by the diffusion coefficient *D*) is complemented by fluid flowing in capillaries and tubules (in red, described by the pseudodiffusion coefficient *D**). (**b**) Contributions of true diffusion and pseudodiffusion to the observed diffusion signal decay—pseudodiffusion is substantially faster than true diffusion, and so is only observed at low *b*-values

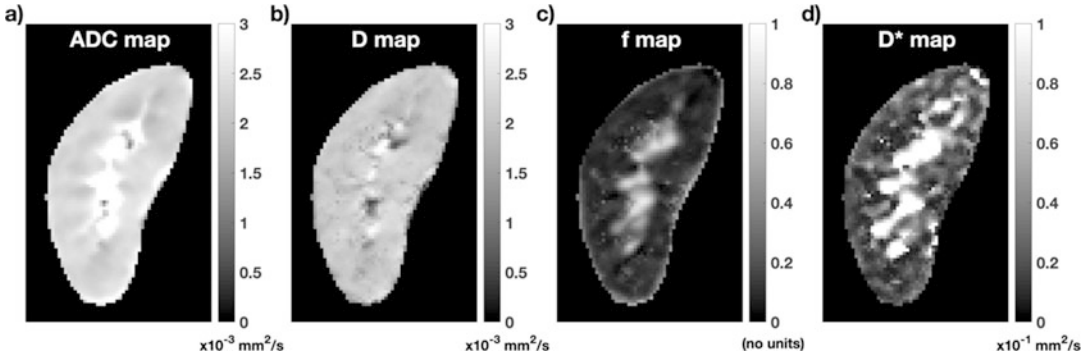

Fig. 6 Representative parametric maps resulting from DWI model fitting. (**a**) ADC map, resulting from monoexponential model fitting. (**b**) Pure diffusion *D*, (**c**) pseudodiffusion fraction *f*, and (**d**) pseudodiffusion *D** maps, resulting from IVIM model fitting over several *b*-values. DWI-based parameters show contrast between the cortex, medulla, and renal hilum. Some extreme values are seen as a consequence of respiratory motion at the lower boundary of the kidney. Parameters associated with pseudodiffusion, *f* and *D**, commonly give maps with higher noise

than the true diffusion coefficient *D*. The components have relative signal contributions given by the pseudodiffusion fraction (f), and the overall IVIM model is described by the following equation:

$$S_{(b)} = S_0.((1-f).\exp(-b.D) + f.\exp(-b.D^*)) \qquad (3)$$

implicitly assuming that there is no exchange between the compartments, and that the associated compartmental T_2 values are the same. Since this is known not to be true in certain circumstances [13, 14], it is important to note that the derived pseudodiffusion coefficient D^* and pseudodiffusion fraction f are nevertheless empirical and should strictly be considered reflective of and not, as often stated, a direct measure of perfusion or flow.

The use of the IVIM model requires substantially more complex analyses than the monoexponential model (analyses are discussed in the chapter by Jerome NP et al. "Analysis of Renal Diffusion-Weighted Imaging (DWI) Using Apparent Diffusion Coefficient (ADC) and Intravoxel Incoherent Motion (IVIM) Models"), and more care to reliably separate pure diffusion from pseudodiffusion components. IVIM analysis tools are increasingly being offered by MRI manufacturers, although the choice of model fitting methods may significantly influence the derived parameters from the more complex model [15, 16]. Parametric maps resulting from IVIM analysis show the similarity of *D* coefficient with ADC, and the increased noise that is characteristic of the pseudodiffusion parameters *f* and *D** (Fig. 6).

The main feature of any DWI acquisition intended for IVIM analysis is the increased number of *b*-values required, especially low *b*-values that sample the signal curve before the pseudodiffusion component has decayed (Fig. 5). Simplified versions of the IVIM

approach usually attempt to limit the acquisition time by using fewer *b*-values, the minimum being three for a segmented fitting that does not attempt to measure D^* [15, 17–19]. Additional complications of multiple *b*-value acquisitions are the increased sensitivity to movement, and the known difficulty of providing repeatable pseudodiffusion parameters compared to diffusion [20–22].

3.3 Diffusion Tensor Imaging (DTI)

If the directionality (or loss thereof) of diffusion arising from tissue structure is of interest, for example as an indication of loss of function or invasion of relevant tissue, consideration of the diffusion signal decay along specified direction, expressed as a tensor, allows calculation of an ellipsoid that represents the diffusion propagator in three dimensions. In the simplified case of isotropic diffusion, diffusion is equal in all directions and the ellipsoid is a sphere. Diffusion isotropy is assumed, though often unstated, in both the monoexponential and IVIM models described above. Conversely, in diffusion tensor imaging (DTI), diffusion-sensitizing gradients are applied along a number of prespecified directions, which are included in the model used to interpret the diffusion imaging signal. In DTI, the diffusion is assumed to be Gaussian and to follow a monoexponential signal decay.

The degree of direction-dependency of the diffusion signal is captured by the fractional anisotropy (*FA*) parameter, ranging from 0 (complete isotropy) to 1 (complete anisotropy) and derived from the relative dimensions of the diffusion ellipsoid according to the following equation:

$$\mathrm{FA} = \sqrt{\frac{3\left[(\lambda_1 - \mathrm{MD})^2 + (\lambda_2 - \mathrm{MD})^2 + (\lambda_3 - \mathrm{MD})^2\right]}{2\left({\lambda_1}^2 + {\lambda_2}^2 + {\lambda_3}^2\right)}} \tag{4}$$

where λ_i represent the eigenvalues of the corresponding diffusion eigenvectors, meaning diffusion coefficients along each of the principal ellipsoid axes, and MD represents mean diffusivity, given by the following:

$$\mathrm{MD} = (\lambda_1 + \lambda_2 + \lambda_3)/3 \tag{5}$$

Directional diffusion coefficients can be reported for each individual direction (λ_i) or along the major and minor axes of the ellipsoid (λ_1 and λ_{trans}, the latter computed as average of the transverse axes coefficients). Given their complexity and alternative formulations, DTI equations used in any study should be clearly stated [23, 24].

Similar to IVIM, DTI requires the acquisition of substantially more images than the basic DWI scheme, although for DTI the number of directions of the applied diffusion-sensitizing gradients is increased rather than the number of *b*-values. In order to define

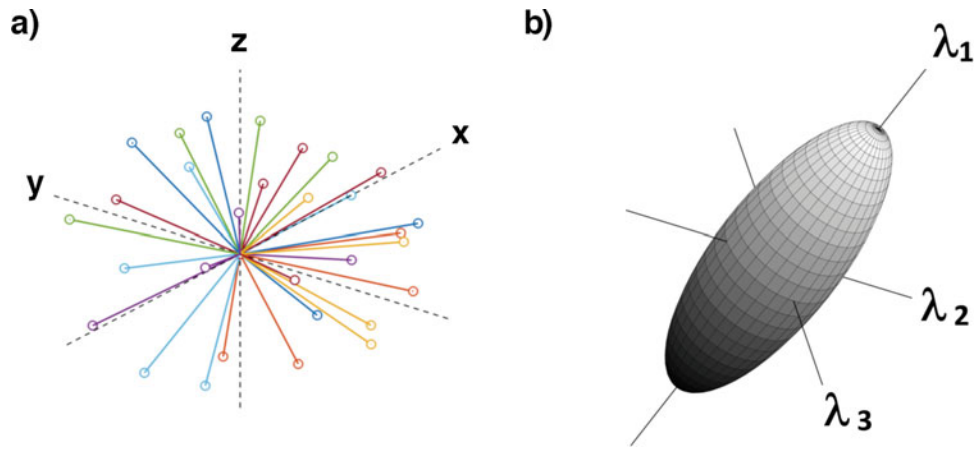

Fig. 7 Illustration of diffusion tensor imaging principles. (**a**) Diffusion vectors in q-space, representing diffusion gradients of equal magnitude applied along different directions (in this case $n = 30$) to investigate tissue anisotropy. (**b**) Corresponding diffusion propagator ellipsoid, where λ_i represent diffusion magnitude along each of the principal ellipsoid axes (i.e., eigenvalues of the principal eigenvectors). Measures of anisotropy, derived from these eigenvalues, are able to describe diffusion with directional preference

the tensor, a minimum of six different directions must be acquired alongside the $b = 0$ image (which, not being diffusion-weighted, has no directionality), but to reduce noise sensitivity it is common to acquire more, up to 30 or even 60 directions. Diffusion directions are usually equally distributed over the surface of a sphere, forming a "shell" in diffusion space (also called q-space), although user-defined vector sets are acceptable as long as there is sufficient sampling of the diffusion directions (Fig. 7).

The DTI technique was developed for application in the brain, but can provide relevant information in the kidney as well. Color and brightness of fractional anisotropy maps indicate orientation and degree of anisotropic diffusion, and can be portrayed as small ellipsoids, which are oriented and color-coded according to the direction of strongest diffusion, to illustrate tissue structure (similar to tractography in brain white matter). Maps of mean diffusivity resemble conventional diffusion coefficient maps (Fig. 8).

Given the large number of images required for DTI analysis, it is common to acquire only one shell in q-space, corresponding to a single non-zero *b*-value chosen based on the target tissue and expected signal-to-noise ratio. For body applications, this is much lower than for the brain, and is commonly within the range 500–1000 s/mm^2. More complex acquisition strategies are available, including multiple shells, as well as the option to retroactively ignore the directional information and calculate ADC.

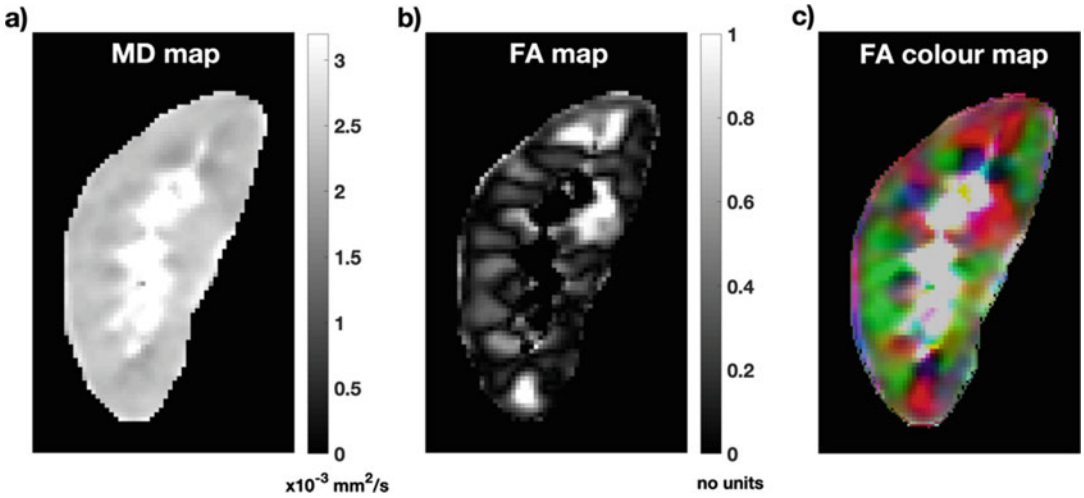

Fig. 8 Representative parametric maps resulting from diffusion tensor imaging analysis of a healthy kidney. (**a**) Mean diffusion (MD) map. (**b**) Fractional anisotropy (FA) map in gray scale. (**c**) FA map in color scale, illustrating the direction of the λ_1 eigenvector

4 Diffusion Imaging in the Kidney

A more detailed review of the applications of renal diffusion imaging in humans was recently conducted by the international COST Action PARENCHIMA [3]. Much of the literature summarized therein, predominantly using the most established ADC but also including IVIM and DTI measures, reports a correlation between diffusion metrics and eGFR decline [25–29] or fibrosis [30–32], in patients with diabetes and other chronic kidney disease (CKD) [33–38], as well as in kidney allograft recipients [30, 39, 40].

Preclinical studies also demonstrate the broad connection of ADC with renal disease, with both ADC and DTI studies having links to renal fibrosis from acute ureteral obstruction [41–45] and diabetes [46, 47]. Preclinical studies also allow for study of the effects of potential contrast agents [48–50]. The development of novel DWI-based biomarkers may yet rely on biological validation and an improvement in specificity [51].

5 Diffusion Acquisition Considerations

In diffusion imaging, most trade-offs are about keeping the acquisition time reasonable and, similar to other MRI modalities, acquiring signal-to-noise ratio sufficient to provide reliable results. Preclinical imaging protocols are less constrained by time than clinical protocols, and so allow for longer scanning that may take advantage of increased averaging or alternate acquisition schemes.

Since increasing the number of acquired averages to give sufficient signal-to-noise quickly becomes prohibitive, DWI is normally acquired with lower spatial resolution than anatomical T_1- or T_2-weighted images. Number and repeats of each *b*-value depend on time available and intended analysis strategy, and are thus specific to each study and/or scanner. By default, most MR scanners will acquire three orthogonal directions (which may or may not be available as separate images [52]) for all nonzero *b*-values in order to calculate the *trace image*, implicitly assuming isotropic diffusion. Such schemes ultimately determine the exact sampling and thus the format of the resulting data. Furthermore, most diffusion imaging sequences allow for specification of several diffusion schemes (often with vendor-specific names and implementations), which trade-off between image quality and diffusion direction specifics. Such schemes may involve multiple "shots" to acquire k-space [31, 53], smaller field-of-view excitation through combination pulses [54], as well as variations on the gradient scheme such as bipolar encoding, designed to reduce distortion from eddy currents [55, 56]. In general, diffusion-weighted images may require an explicit postprocessing protocol as part of the analysis (*see* **Note 5**).

Since the acquisition of high *b*-values requires a larger TE in order to accommodate the pulses, the choice of the maximum *b*-value is a compromise between precision of diffusion estimates over a suitably chosen *b*-value range, and the available signal (*see* **Note 6**). DWI sequence variants that explicitly probe the effects of the diffusion time Δ as well as TE illustrate the importance of not neglecting potential influences of the acquisition parameters on the diffusion signal [13, 57].

Other significant factors in diffusion imaging arise directly from the use of echo-planar imaging (EPI) readout sequences, which although suitably fast gives images which are susceptible to distortion artifacts arising from high use of gradients (finite slew rates, eddy currents, nonlinearity, and so forth) and local susceptibility differences at tissue boundaries (and especially at tissue–air boundaries). Distortion correction can thus be necessary in diffusion imaging, and may involve prospective planning (e.g., phase-reversal images) [58] as well as retrospective processing (e.g., registration) [59].

Additional DWI protocols, such as those including flow compensation [60], alternate strategies to EPI readout [53, 61], and steady-state free precession sequences [62–64] and the influence of physiological factors on the DWI [65], have been reported in literature and may provide tools for ameliorating specific physiological and instrumental factors.

6 Notes

1. The specifics of diffusion imaging data acquisition and intended analysis strongly influence each other, and thus both should be borne in mind while planning a new study. Whenever possible, overly specific acquisition protocols should be avoided to allow for data reuse through additional retrospective analysis, and cross-study comparisons.
2. Many acquisition parameters influence the resulting diffusion-related parameters, making comparison across studies challenging. In the absence of widely accepted standardized protocols, it may be advantageous to consider the extent to which comparison with other studies will be possible.
3. As with all MRI studies, but of particular importance in diffusion imaging, care should be taken to report the adopted protocol as completely as possible. This necessarily includes the acquisition scheme and parameters, but also extends to the analysis algorithms.
4. The majority of diffusion models contain a parameter that attempts to capture the underlying tissue diffusion—ADC, (IVIM) *D*, (DTI) MD, and so on. While superficially similar and reflective of tissue structure, they are not precisely equivalent given the different assumptions implicit in the models they derive from.
5. The most common readout for diffusion imaging is the echo planar imaging (EPI) sequence, which is susceptible to artifacts and distortion; an adequate post-processing scheme is required. Analysis of DWI is discussed in more detail in the chapter by Jerome NP et al. "Analysis of Renal Diffusion-Weighted Imaging (DWI) Using Apparent Diffusion Coefficient (ADC) and Intravoxel Incoherent Motion (IVIM) Models."
6. Since diffusion contrast is created by deliberate dephasing and thus loss of the MR signal, sufficient signal-to-noise ratio is critical to ensure good quality data and successful analysis. Failure to assess the signal-to-noise ratio or account for the noise floor may introduce bias in the estimate of diffusion parameters.

Acknowledgments

NPJ wishes to acknowledge support from the liaison Committee between the Central Norway Regional Health Authority and the Norwegian University of Science and Technology (Project nr. 90065000).

This chapter is based upon work from COST Action PARENCHIMA, supported by European Cooperation in Science and Technology (COST). COST (www.cost.eu) is a funding agency for research and innovation networks. COST Actions help connect research initiatives across Europe and enable scientists to enrich their ideas by sharing them with their peers. This boosts their research, career, and innovation.
PARENCHIMA (renalmri.org) is a community-driven Action in the COST program of the European Union, which unites more than 200 experts in renal MRI from 30 countries with the aim to improve the reproducibility and standardization of renal MRI biomarkers.

References

1. Roditi G, Maki JH, Oliveira G, Michaely HJ (2009) Renovascular imaging in the NSF era. J Magn Reson Imaging 30:1323–1334
2. Olchowy C, Cebulski K, Łasecki M et al (2017) The presence of the gadolinium-based contrast agent depositions in the brain and symptoms of gadolinium neurotoxicity-a systematic review. PLoS One 12:1–14
3. Caroli A, Schneider M, Friedli I et al (2018) Diffusion-weighted magnetic resonance imaging to assess diffuse renal pathology: a systematic review and statement paper. Nephrol Dial Transplant 33:ii29–ii40
4. Panagiotaki E, Chan RW, Dikaios N et al (2015) Microstructural characterization of normal and malignant human prostate tissue with vascular, extracellular, and restricted diffusion for cytometry in tumours magnetic resonance imaging. Investig Radiol 50:218–227
5. Cheng L, Blackledge MD, Collins DJ et al (2016) T2-adjusted computed diffusion-weighted imaging: a novel method to enhance tumour visualisation. Comput Biol Med 79:92–98
6. Eisenberger U, Theony HC, Boesch C et al (2014) Living renal allograft transplantation : diffusion-weighted MR imaging in longitudinal follow-up of the donated and the remaining kidney. Radiology 270:800–808
7. Thoeny HC, De Keyzer F (2011) Diffusion-weighted MR imaging of native and transplanted kidneys. Radiology 259:25–38
8. Saritas EU, Lee JH, Nishimura DG (2011) SNR dependence of optimal parameters for apparent diffusion coefficient measurements. IEEE Trans Med Imaging 30:424–437
9. Zhang JL, Sigmund EE, Rusinek H et al (2012) Optimization of b-value sampling for diffusion-weighted imaging of the kidney. Magn Reson Med 67:89–97
10. Winfield JM, Tunariu N, Rata M et al (2017) Extracranial soft-tissue tumors: repeatability of apparent diffusion coefficient estimates from diffusion-weighted MR imaging. Radiology 284:88–99
11. Le Bihan D, Breton E, Lallemand D et al (1988) Separation of diffusion and perfusion in intravoxel incoherent motion MR imaging. Radiology 168:497–505
12. Ljimani A, Lanzman RS, Müller-Lutz A et al (2018) Non-gaussian diffusion evaluation of the human kidney by Padé exponent model. J Magn Reson Imaging 47:160–167
13. Jerome NP, D'Arcy JA, Feiweier T et al (2016) Extended T2-IVIM model for correction of TE dependence of pseudo-diffusion volume fraction in clinical diffusion-weighted magnetic resonance imaging. Phys Med Biol 61: N667–N680
14. Lemke A, Laun FB, Simon D et al (2010) An in vivo verification of the intravoxel incoherent motion effect in diffusion-weighted imaging of the abdomen. Magn Reson Med 64:1580–1585
15. Meeus EM, Novak J, Withey SB et al (2017) Evaluation of intravoxel incoherent motion fitting methods in low-perfused tissue. J Magn Reson Imaging 45:1325–1334
16. Vidić I, Jerome NP, Bathen TF et al (2019) Accuracy of breast cancer lesion classification using intravoxel incoherent motion diffusion-weighted imaging is improved by the inclusion of global or local prior knowledge with bayesian methods. J Magn Reson Imaging 50:1478–1488
17. Cho GY, Moy L, Zhang JL et al (2015) Comparison of fitting methods and b-value

sampling strategies for intravoxel incoherent motion in breast cancer. Magn Reson Med 74:1077–1085

18. Gurney-Champion OJ, Klaassen R, Froeling M et al (2018) Comparison of six fit algorithms for the intravoxel incoherent motion model of diffusionweighted magnetic resonance imaging data of pancreatic cancer patients. PLoS One 13:1–18
19. Jalnefjord O, Andersson M, Montelius M et al (2018) Comparison of methods for estimation of the intravoxel incoherent motion (IVIM) diffusion coefficient (D) and perfusion fraction (f). MAGMA 31(6):715–723. https://doi.org/10.1007/s10334-018-0697-5
20. Jerome NP, Boult JKR, Orton MR et al (2016) Modulation of renal oxygenation and perfusion in rat kidney monitored by quantitative diffusion and blood oxygen level dependent magnetic resonance imaging on a clinical 1.5T platform. BMC Nephrol 17:142
21. Jerome NP, Miyazaki K, Collins DJ et al (2016) Repeatability of derived parameters from histograms following non-Gaussian diffusion modelling of diffusion-weighted imaging in a paediatric oncological cohort. Eur Radiol 27:345–353
22. Orton MR, Jerome NP, Rata M, Koh D-M (2018) IVIM in the body: a general overview. In: Le Bihan D, Iima M, Federau C, Sigmund EE (eds) Intravoxel incoherent motion MRI Princ. Appl. Pan Stanford Publishing Pte. Ltd., pp 145–174
23. Kingsley PB (2006) Introduction to diffusion tensor imaging mathematics : part II. Anisotropy, diffusion- weighting factors, and gradient encoding schemes. Concepts Magn Reson Part A 28A:123–154
24. Kingsley PB (2006) Introduction to diffusion tensor imaging mathematics: part I. tensors, rotations, and eigenvectors. Concepts Magn Reson Part A 28A:101–122
25. Ding J, Chen J, Jiang Z et al (2016) Is low b-factors-based apparent diffusion coefficient helpful in assessing renal dysfunction? Radiol Med 121:6–11
26. Ding J, Chen J, Jiang Z et al (2016) Assessment of renal dysfunction with diffusion-weighted imaging: comparing intra-voxel incoherent motion (IVIM) with a mono-exponential model. Acta Radiol 57:507–512
27. Li Q, Wu X, Qiu L et al (2013) Diffusion-weighted MRI in the assessment of split renal function: comparison of navigator-triggered prospective acquisition correction and breath-hold acquisition. Am J Roentgenol 200:113–119
28. Prasad PV, Thacker J, Li LP et al (2015) Multi-parametric evaluation of chronic kidney disease by MRI: a preliminary cross-sectional study. PLoS One 10:1–14
29. Özçelik Ü, Çevik H et al (2017) Evaluation of transplanted kidneys and comparison with healthy volunteers and kidney donors with diffusion-weighted magnetic resonance imaging: initial experience. Exp Clin Transplant. https://doi.org/10.6002/ect.2016.0341
30. Friedli I, Crowe LA, Berchtold L et al (2016) New magnetic resonance imaging index for renal fibrosis assessment: a comparison between diffusion-weighted imaging and T1 mapping with histological validation. Sci Rep 6:1–15
31. Friedli I, Crowe LA, de Perrot T et al (2017) Comparison of readout-segmented and conventional single-shot for echo-planar diffusion-weighted imaging in the assessment of kidney interstitial fibrosis. J Magn Reson Imaging 46:1631–1640
32. Zhao J, Wang ZJ, Liu M et al (2014) Assessment of renal fibrosis in chronic kidney disease using diffusion-weighted MRI. Clin Radiol 69:1117–1122
33. Inoue T, Kozawa E, Okada H et al (2011) Noninvasive evaluation of kidney hypoxia and fibrosis using magnetic resonance imaging. J Am Soc Nephrol 22:1429–1434
34. Liu Z, Xu Y, Zhang J et al (2015) Chronic kidney disease: pathological and functional assessment with diffusion tensor imaging at 3T MR. Eur Radiol 25:652–660
35. Rona G, Pasaoglu L, Ozkayar N et al (2016) Functional evaluation of secondary renal amyloidosis with diffusion-weighted MR imaging. Ren Fail 38:249–255
36. Wang WJ, Pui MH, Guo Y et al (2014) 3T magnetic resonance diffusion tensor imaging in chronic kidney disease. Abdom Imaging 39:770–775
37. Emre T, Kiliçkesmez Ö, Büker A et al (2016) Renal function and diffusion-weighted imaging: a new method to diagnose kidney failure before losing half function. Radiol Med 121:163–172
38. Çakmak P, Yağci AB, Dursun B et al (2014) Renal diffusion-weighted imaging in diabetic nephropathy: correlation with clinical stages of disease. Diagnostic Interv Radiol 20:374–378
39. Palmucci S, Cappello G, Attinà G et al (2015) Diffusion weighted imaging and diffusion tensor imaging in the evaluation of transplanted kidneys. Eur J Radiol Open 2:71–80

40. Hueper K, Khalifa AA, Bräsen JH et al (2016) Diffusion-weighted imaging and diffusion tensor imaging detect delayed graft function and correlate with allograft fibrosis in patients early after kidney transplantation. J Magn Reson Imaging 44:112–121
41. Haque ME, Franklin T, Bokhary U et al (2014) Longitudinal changes in MRI markers in a reversible unilateral ureteral obstruction mouse model: preliminary experience. J Magn Reson Imaging 39:835–841
42. Hu G, Yang Z, Liang W et al (2019) Intravoxel incoherent motion and arterial spin labeling MRI analysis of reversible unilateral ureteral obstruction in rats. J Magn Reson Imaging 50:288–296
43. Togao O, Doi S, Kuro-o M et al (2010) Assessment of renal fibrosis with diffusion-weighted MR Imaging: study with murine model purpose: methods: results: conclusion. Radiology 255:772–780
44. Wang F, Takahashi KK, Li H et al (2018) Assessment of unilateral ureter obstruction with multi-parametric MRI. Magn Reson Med 79:2216–2227
45. Pons M, Leporq B, Ali L et al (2018) Renal parenchyma impairment characterization in partial unilateral ureteral obstruction in mice with intravoxel incoherent motion-MRI. NMR Biomed 31:1–9
46. Kaimori JY, Isaka Y, Hatanaka M et al (2017) Visualization of kidney fibrosis in diabetic nephropathy by long diffusion tensor imaging MRI with spin-echo sequence. Sci Rep 7:2–9
47. Yan YY, Hartono S, Hennedige T et al (2017) Intravoxel incoherent motion and diffusion tensor imaging of early renal fibrosis induced in a murine model of streptozotocin induced diabetes. Magn Reson Imaging 38:71–76
48. Jost G, Lenhard DC, Sieber MA et al (2011) Changes of renal water diffusion coefficient after application of iodinated contrast agents: effect of viscosity. Investig Radiol 46:796–800
49. Wang Y, Ren K, Liu Y et al (2017) Application of BOLD MRI and DTI for the evaluation of renal effect related to viscosity of iodinated contrast agent in a rat model. J Magn Reson Imaging 46:1320–1331
50. Liang L, Chen WB, KWY C et al (2016) Using intravoxel incoherent motion MR imaging to study the renal pathophysiological process of contrast-induced acute kidney injury in rats: comparison with conventional DWI and arterial spin labelling. Eur Radiol 26:1597–1605
51. Thoeny HC, Grenier N (2010) Science to practice: can diffusion-weighted MR imaging findings be used as biomarkers to monitor the progression of renal fibrosis? Radiology 255:667–668
52. Jerome NP, Orton MR, D'Arcy JA et al (2015) Use of the temporal median and trimmed mean mitigates effects of respiratory motion in multiple-acquisition abdominal diffusion imaging. Phys Med Biol 60:N9–N20
53. Wu CJ, Wang Q, Zhang J et al (2016) Readout-segmented echo-planar imaging in diffusion-weighted imaging of the kidney: comparison with single-shot echo-planar imaging in image quality. Abdom Radiol 41:100–108
54. He YL, Hausmann D, Morelli JN et al (2016) Renal zoomed EPI-DWI with spatially-selective radiofrequency excitation pulses in two dimensions. Eur J Radiol 85:1773–1777
55. Furuta A, Isoda H, Yamashita R et al (2014) Comparison of monopolar and bipolar diffusion weighted imaging sequences for detection of small hepatic metastases. Eur J Radiol 83:1626–1630
56. Kyriazi S, Blackledge M, Collins DJ, Desouza NM (2010) Optimising diffusion-weighted imaging in the abdomen and pelvis: comparison of image quality between monopolar and bipolar single-shot spin-echo echo-planar sequences. Eur Radiol 20:2422–2431
57. Clark CA, Hedehus M, Moseley ME (2001) Diffusion time dependence of the apparent diffusion tensor in healthy human brain and white matter disease. Magn Reson Med 45:1126–1129
58. Holland D, Kuperman JM, Dale AM (2010) Efficient correction of inhomogeneous static magnetic field-induced distortion in echo planar imaging. NeuroImage 50:175–183
59. Guyader J-M, Bernardin L, Douglas NHM et al (2015) Influence of image registration on apparent diffusion coefficient images computed from free-breathing diffusion MR images of the abdomen. J Magn Reson Imaging 42:315–330
60. Wetscherek A, Stieltjes B, Laun FB (2015) Flow-compensated intravoxel incoherent motion diffusion imaging. Magn Reson Med 74:410–419
61. Friedli I, Crowe LA, Viallon M et al (2015) Improvement of renal diffusion-weighted magnetic resonance imaging with readout-segmented echo-planar imaging at 3T. Magn Reson Imaging 33:701–708

62. Delalande C, De Zwart JA, Trillaud H et al (1999) An echo-shifted gradient-echo MRI method for efficient diffusion weighting. Magn Reson Med 41:1000–1008
63. Ding S, Trillaud H, Yongbi M et al (1995) High resolution renal diffusion imaging using a modified steady-state free precession sequence. Magn Reson Med 34:586–595
64. Lu L, Erokwu B, Lee G et al (2012) Diffusion-prepared fast imaging with steady-state free precession (DP-FISP): a rapid diffusion MRI technique at 7 T. Magn Reson Med 68:868–873
65. Lanzman RS, Ljimani A, Müller-Lutz A et al (2019) Assessment of time-resolved renal diffusion parameters over the entire cardiac cycle. Magn Reson Imaging 55:1–6

Chapter 12

Dynamic Contrast Enhancement (DCE) MRI–Derived Renal Perfusion and Filtration: Basic Concepts

Michael Pedersen, Pietro Irrera, Walter Dastrù, Frank G. Zöllner, Kevin M. Bennett, Scott C. Beeman, G. Larry Bretthorst, Joel R. Garbow, and Dario Livio Longo

Abstract

Dynamic contrast-enhanced (DCE) MRI monitors the transit of contrast agents, typically gadolinium chelates, through the intrarenal regions, the renal cortex, the medulla, and the collecting system. In this way, DCE-MRI reveals the renal uptake and excretion of the contrast agent. An optimal DCE-MRI acquisition protocol involves finding a good compromise between whole-kidney coverage (i.e., 3D imaging), spatial and temporal resolution, and contrast resolution. By analyzing the enhancement of the renal tissues as a function of time, one can determine indirect measures of clinically important single-kidney parameters as the renal blood flow, glomerular filtration rate, and intrarenal blood volumes. Gadolinium-containing contrast agents may be nephrotoxic in patients suffering from severe renal dysfunction, but otherwise DCE-MRI is clearly useful for diagnosis of renal functions and for assessing treatment response and posttransplant rejection.

Here we introduce the concept of renal DCE-MRI, describe the existing methods, and provide an overview of preclinical DCE-MRI applications to illustrate the utility of this technique to measure renal perfusion and glomerular filtration rate in animal models.

This publication is based upon work from the COST Action PARENCHIMA, a community-driven network funded by the European Cooperation in Science and Technology (COST) program of the European Union, which aims to improve the reproducibility and standardization of renal MRI biomarkers. This introduction is complemented by two separate publications describing the experimental procedure and data analysis.

Key words Magnetic resonance imaging (MRI), Dynamic contrast-enhanced (DCE), Kidney, Mice, Rats, T_1 mapping, Contrast agent, Perfusion, Glomerular filtration rate (GFR)

1 Introduction

Glomerular filtration rate (GFR) is a standard measure of kidney function. In past decades, simplified plasma clearance employing radiopharmaceuticals (51Cr-EDTA, 125I-iothalamate, 99mTc-DTPA) was introduced and validated to provide very accurate estimates of total GFR [1–4]. Later, alternative techniques have

Andreas Pohlmann and Thoralf Niendorf (eds.), *Preclinical MRI of the Kidney: Methods and Protocols*, Methods in Molecular Biology, vol. 2216, https://doi.org/10.1007/978-1-0716-0978-1_12,

been evaluated, using minute doses of nonradioactive contrast agents, including iothalamate and iohexol [5]. Plasma clearance of such compounds has also been applied to measure renal function. Renal blood flow (RBF) is another important measure of the functional status of a kidney. The standard tracer-based technique for quantifying RBF is to measure clearance of substances such as hippurate or of radiopharmaceuticals [6].

Dynamic contrast enhanced (DCE-MRI) is an alternative to these techniques that uses gadolinium chelates as contrast agents (CAs), providing functional information analogous to that obtained from radionuclide studies [7, 8]. These chelates are generally considered glomerular filtration markers, since they are removed from the circulation exclusively by glomerular filtration.

DCE-MRI measures T_1-weighted signal intensity changes in tissues over time after bolus administration of a contrast agent. Dynamic data acquisition allows for monitoring of the contrast agent in the renal cortex, the medulla, and the collecting system, providing a renographic representation with underlying information about the renal perfusion, filtration, and vascularization [9–12]. Postprocessing analyses of these signal-vs-time curves reveal kidney functionality in terms of filtration and perfusion, including both heuristic nonmodel approaches and model-based quantitative methods [13, 14]. However, while DCE-MRI is a promising tool in animal models, its clinical utility is hampered by the risk of developing nephrogenic systemic fibrosis in renal patients with severely reduced glomerular filtration capacity [15]. In this chapter, we will address the basic concept of DCE-MRI with the emphasis on kidney disease models in rodents.

This introduction chapter is complemented by two separate chapters describing the experimental procedure and data analysis, which are part of this book.

This chapter is part of the book Pohlmann A, Niendorf T (eds) (2020) Preclinical MRI of the Kidney—Methods and Protocols. Springer, New York.

2 Measurement Concept

2.1 Basic Concept of DCE

The standard acquisition scheme of a DCE-MRI experiment is based on repeated T_1-weighted images before and after the injection of a Gadolinium-based CA. In this way, a dynamic curve of the signal enhancement in the kidney is recorded in a time window wide enough (5–10 min) to see the contrast range from the vascular peak enhancement to the wash-out phase. An injection dose of 0.1 mmol Gd/kg is considered standard [16], and lower doses are occasionally exploited to reduce concomitant T_2* effects in vessels.

2.2 Gadolinium-Based Contrast Agents

In DCE-MRI, the gadolinium agents have two main advantages, one attributed to the properties of the gadolinium-ion in response to a magnetic field, and one attributed to the chelate that has a biodistribution in the body which favors measurements of renal clearance. In physical terms, the gadolinium ion is chosen having seven unpaired electrons in its orbitals resulting in strong paramagnetism [17–19]. Furthermore, the symmetry of the electron configuration of the trivalent gadolinium ion is a hospitable environment for electron spins, contributing to the rise of the crucial nuclear magnetic resonance parameter called relaxation. For these reasons, gadolinium (Gd^{3+}) is the most common metal ion used in paramagnetic contrast agent and its relationship is given by $1/T_{1\ (\text{Measured})} = 1/T_{1\ (\text{Water})} + r_1\,[\text{Gd}]$. The relaxivity is dependent on the magnetic field and temperature [20–22]. Due to its toxicity as free ion, Gd is trapped in a molecular structure defined by the closed/open ring that chelates the metal. These macrocyclic and linear CAs may possess different r_1, osmolarity, and molecular size [23–25]. In addition to clinical contrast agents, several other Gd complexes have been investigated for providing higher relaxivity or contrast efficiency [26–31]. All the contrast agents used for mapping kidney perfusion are small molecular weight extracellular agents and are administered intravenously [32].

2.3 Conversion of Signal into Contrast Agent Concentration

Contrary to nuclear medicine modalities, MRI unfortunately does not measure changes in signal intensity in a straightforward way. This means that measurements of injected contrast agent concentration is difficult, which again severely hinders the possibility to calculate important parameters in absolute units such as ml/min or ml/min/g. Previous studies have taken this constraint into account in three different ways: (1) by assuming that the signal intensity is linearly related to the concentration of contrast agent, (2) by making calibration of water doped with contrast agent and then assume the same signal-vs-concentration can be applied in the living tissue, and (3) by introducing the mathematical complex relationship between signal and concentration. These three approaches are here ordered with increasing difficulties in which they can be performed, meaning that the third method is by far the most ambitious. To be able to convert signal intensities into concentration, we present a step-by-procedure. First, the mathematical equation that relates the signal into concentration relies on both well-known constants, the employed MR imaging technique and the pulse sequence parameters (echo-time, recovery time, flip angle, etc.). Due to the paramagnetic properties of the contrast agent, the magnetic relaxation time (T_1) decreases in the presence of the contrast agent. Conversion of acquired signal (enhancement) to changes in T_1 needs some mathematical understanding. In a simple setup, DCE-MRI is performed with a T_1-weighted-2D-spoiled gradient-echo train (Fig. 1).

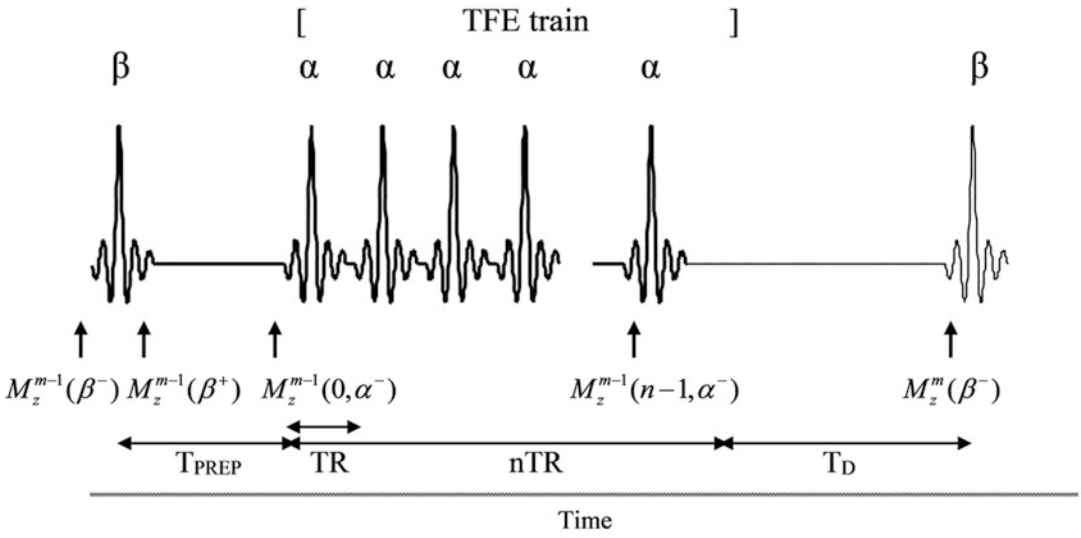

Fig. 1 Pulse train for dynamic MRI using a spoiled gradient-echo sequence

First, we consider the spoiled gradient echo sequence (TFE) without prepulses. The longitudinal component of the magnetization is denoted M_z, which relaxes back to its equilibrium M_0 due to a characteristic relaxation time (T_1). The magnetization M_z is derived by the Bloch equation, given as follows:

$$\frac{dM_z}{dt} = \frac{M_0 - M_z}{T_1} \tag{1}$$

where M_0 denotes the bulk longitudinal magnetization, and T_1 is the longitudinal relaxation time. Integration of Eq. 1 returns the time-dependent $M_z(t)$:

$$\int_0^{M_z} \frac{dM_z}{M_0 - M_z} = \int_0^t \frac{dt}{T_1} \Rightarrow M_z(t) - M_0 = Ae^{-t/T_1} \tag{2}$$

Giving the notation that $M_z(t = 0)$ is $M_z(0)$, we define the constraint:

$$M_z(0) = M_0 + A \Rightarrow A = M_z(0) - M_0 \tag{3}$$

Resolving Eq. 2 gives the following:

$$\begin{aligned} M_z(t) &= M_0 + [M_z(0) - M_0]e^{-t/T_1} \\ &= M_0\left[1 - e^{-t/T_1}\right] + M_z(0^+)e^{-t/T_1} \end{aligned} \tag{4}$$

The magnetization just before the n'th pulse (denoted as $n\text{TR}^-$) can now be determined:

$$\begin{aligned} M_z(n\mathrm{TR}^-) &= M_0\left[1-e^{-\mathrm{TR}/T_1}\right] + M_z\left((n-1)\mathrm{TR}^+\right)e^{-\mathrm{TR}/T_1} \\ &= M_0[1-E_1] + M_z((n-1)\mathrm{TR}^-)\cos\alpha E_1 \end{aligned} \tag{5}$$

where $E = e^{-\mathrm{TR}/T_1}$, and $M_z((n-1)\mathrm{TR}^-)$ represents the magnetization just after a time $(n-1)$TR. Eq. 5 can be developed recursively:

$$\begin{aligned} M_z(n\mathrm{TR}^-) &= M_0[1-E_1] + [M_0[1-E_1] + M_z((n-2)\mathrm{TR}^-)\cos\alpha E_1]\cos\alpha E_1 \\ &= M_0[1-E_1] + M_0[1-E_1]\cos\alpha E_1 + M_z((n-2)\mathrm{TR}^-)[\cos\alpha E_1]^2 \\ &= \sum_{i=0}^{n-1} M_0[1-E_1][\cos\alpha E_1]^i + M_z(0^-)[\cos\alpha E_1]^n \\ &= M_0[1-E_1]\frac{1-[\cos\alpha E_1]^n}{1-\cos\alpha E_1} + M_0^{\mathrm{eq}}[\cos\alpha E_1]^n \end{aligned} \tag{6}$$

Herein, the geometric series is assumed:

$$M_z^{\mathrm{eq}} = \lim_{n\to\infty} M_z(n\mathrm{TR}) \to M_0\frac{1-E_1}{1-\cos\alpha E_1} \tag{7}$$

The steady-state condition can then be described as follows:

$$M_z^{\mathrm{eq}} = M_0^{\mathrm{eq}}\frac{1-E_1}{1-E_1\cos\alpha} \tag{8}$$

Taking into account that steady-state condition must be fulfilled in presence of a delay T_{D}, employed between the TFE train and the subsequent RF pulse, the following must apply:

$$M_z^{\mathrm{eq}} = M_z^{\mathrm{eq},0}\left[1-e^{-T_{\mathrm{D}}/T1}\right] + M_z^{\mathrm{eq}}e^{-T_{\mathrm{D}}/T1} \tag{9}$$

Now, let us introduce the preparation pulse (with flip-angle β) applied a time T_{PREP} before the excitation pulse. M_0^{eq} is taken into account by solving:

$$M_z^0 = M_0^{\mathrm{eq}}\left[1-e^{-T_{\mathrm{PREP}}/T1}\right] + M_z(\beta^+)e^{-T_{\mathrm{PREP}}/T1} \tag{10}$$

where $M_z(\beta^+)$ represents the magnetization just after the β pulse. The magnetization before the n'th α-pulse, denoted as $M_z(n,\alpha^-)$, is given as the combination of Eqs. 6 and 10:

$$\begin{aligned} M_z^-(n,\alpha) = &\left[M_0^{\mathrm{eq}}\left(1-e^{-T_{\mathrm{PREP}}/T1}\right) + M_z^{\mathrm{eq},0}e^{-T_{\mathrm{PREP}}/T1}\cos\beta\right][E_1\cos\alpha]^n \\ &+ M_0^{\mathrm{eq}}[1-E_1]\frac{1-[E_1\cos\alpha]^n}{1-E_1\cos\alpha} \end{aligned} \tag{11}$$

Therefore, using a heavily T_1-weighted pulse sequence, changes in signal intensity are then almost entirely dependent on changes of T_1. In these circumstances, it can be shown that M_z^{eq} is almost linearly dependent on T_1 relaxation rate. Note again that the

specific magnetic relaxivity of the gadolinium-agent (r) defines the characteristic enhancement property by the equation: $[\mathrm{Gd}] = (1/T_1 - 1/T_{1(0)})/r$, where $T_{1(0)}$ is the bulk relaxation time in the tissue without the presence of contrast agent, and [Gd] is the concentration of contrast (gadolinium) agent. In principle, this means that a precontrast measurement of T_1 (T_1-mapping) should be performed before injection of the contrast agent. One important factor contributing to erroneous measurements of $T_{1(0)}$ of blood is the inflow effect, because the coherent movement of flowing fluid can alter T_1 of the signal arising from spins therein. Placing the central-encoding lines within the low blood flow window within the cardiac cycle can, to some extent, minimize the problems of the inflow effect.

2.4 Imaging Readout

For dynamic acquisitions, two factors must be taken into consideration: the time resolution and the contrast resolution required. For quantitative studies of renal perfusion and GFR, based on the first-pass of the contrast agent, a high temporal resolution is particularly important to accurately sample the vascular phase of the kidney (especially for renal perfusion studies) in order to measure the arterial input function (AIF). The AIF is the signal-time-curve usually observed in the suprarenal abdominal aorta or in a renal artery and is used in different kinetic models in order to compensate for the non-instantaneous bolus injected into the blood. The request for a high temporal resolution explains why some studies have been performed using a single slice acquisition scheme and not as multislice or 3D techniques. However, the required extrapolation of functional data from one slice to the whole kidney is not always valid if the renal disease is irregularly or focally distributed.

Most of the exploited sampling techniques are gradient echo imaging, echo-planar imaging and spiral imaging. Differences in the sequence are represented by the ability to cover the image space, from conventional approaches that acquire a portion of the space every TR to entire space acquisition in every TR step. Among them, other subtechniques exist with little changes in the sampling approach like spoiled gradient echo, segmental echo planar imaging, keyhole imaging or parallel imaging [33].

2.4.1 Gradient-Echo

Gradient echo (also "gradient recalled echo," GRE)-based sequences are the most commonly used sequences for DCE-MRI studies, where fast GRE sequences can be implemented in different ways, including unbalanced, balanced steady-state, and RF-spoiled sequences [34]. Notably, standard (unbalanced) and balanced gradient echo sequences are sensitive to T_2 effects that result in signal decreases upon the accumulation of the contrast agent in the region of interest. Therefore, spoiled GRE sequences are mostly used since they are more sensitive to T_1 effects leading to higher contrast enhancements. A drawback of these sequences is the low SNR (signal to noise ratio) that can be compensated by the use of 3D acquisitions.

2.4.2 Echo-Planar Imaging

Echo planar imaging (EPI) allows fast image acquisition in combination with high temporal and spatial resolution, with acquisition of several images per second [35]. On the other hand, EPI sequences are difficult to exploit in abdomen and thorax regions since they are sensitive to susceptibility and motion effects. These artifacts can however be reduced by using segmented EPI sequences with a concomitant loss in temporal resolution.

2.4.3 Keyhole Imaging

Since central lines of the K-space are more sensitive to image contrast in comparison to peripheral lines, keyhole imaging is exploited for accelerating imaging acquisition by acquiring multiple central K-space lines. This high-contrast but low-spatial resolution image can then be combined with a high-resolution image to restore the spatial information. Consequently, temporal resolution can be increased up to three- to fourfold, despite some problems that can be encountered in areas with large physiological movements. Several partial K-space sampling techniques have been developed and exploited in a variety of applications [36].

2.5 T_1 Mapping

T_1 measurements can be performed along the dynamic acquisition (precontrast and postcontrast) at every repetition time or before and after the bolus administration using T_1 mapping techniques. Applying a radiofrequency (RF) pulse, spins will change their magnetization status according to the design of the pulse. The magnetization can be inverted or saturated (nulled), and T_1-weighted images are acquired after the inversion or time after saturation pulse. Since the T_1 calculation is the time that magnetization takes to restore to its equilibrium (which is considered fully restored after 5 times the T_1), the two models of RF pulses are called inversion recovery and saturation recovery. Another way to perturb the magnetization is achieved by manipulating the flip angle of the RF pulse at every sequence acquisition, sampling the T_1 relaxation for different angle values.

2.5.1 Saturation Recovery

A 90° saturation pulse effectively nulls the magnetization independently of its state before the saturation pulse. In this way, keeping the repetition time lower than the T_1, the system is unable to fully recover to equilibrium and is said to be saturated. Thus, the T_1 measurements are performed by varying the TR constantly ranging from 0 to, at least, 2–3 times the longest T_1 value expected in the sample. The result is that saturation recovery is a very fast method but with the drawback of a limited dynamic range and limited T_1 range.

2.5.2 Inversion Recovery

Inversion recovery consists of a 180° inversion pulse which rotates the longitudinal magnetization to give the classical decay with a 90° pulse. The inversion recovery pulse sequence is repeated continuously, each time applying the same inversion pulse, followed by

different waiting times (time of inversion). The principle of this method implies that the repetition time of the sequence must be greater than the longest T_1 since the magnetization needs to be fully recovered before applying another inversion pulse. Inversion recovery is a method for T_1 map acquisition which produces maps with good accuracy and intensity dynamic range but with the drawback of being time-consuming.

2.5.3 Variable Flip Angle (VFA)

Variable flip angle is used to acquire 3D T_1 maps, and the technique uses two or more repeated sequences with different flip angles (ranging from a few degrees to even more than 90°), sampling the T_1 relaxation for different angle values. The method is relatively sensitive to B_1 inhomogeneities; hence a field map should be acquired. Recently, magnetization transfer effects were identified as an additional source of variability in the obtained VFA data, which can be reduced dramatically by use of tailored composite RF pulses that apply the same power to the bound proton pool for all flip angles [37].

2.6 Renal Handling of Contrast Agents

Before analysis of the acquired DCE-MRI data, it is important to understand how the renal segments handle the gadolinium agent during DCE-MRI. Following an i.v. (intravenous) bolus of contrast agent, the arterial concentration is promptly increased following a steady decline over time, reflecting the input and output of the agent over time. Figure 2 shows an example of dynamic

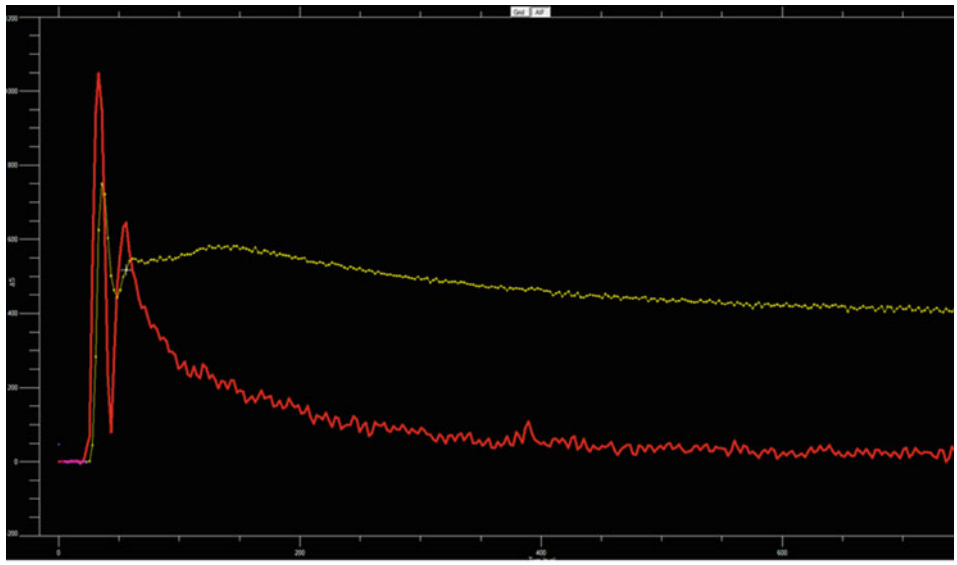

Fig. 2 Dynamic uptake curve (enhancement) in the aorta (red) and renal whole-parenchyma (yellow) following iv bolus of a gadolinium agent. Purple dots indicate baseline values prior to bolus administration. *See* Fig. 3 text for MRI sequence parameters. The aorta curve shows a rapid increase followed by a decline over time (0–800 s). The renal curve shows a first-pass vascular uptake, followed by a pattern with decreasing vascular gadolinium-content combined with a glomerular handling of the contrast agent

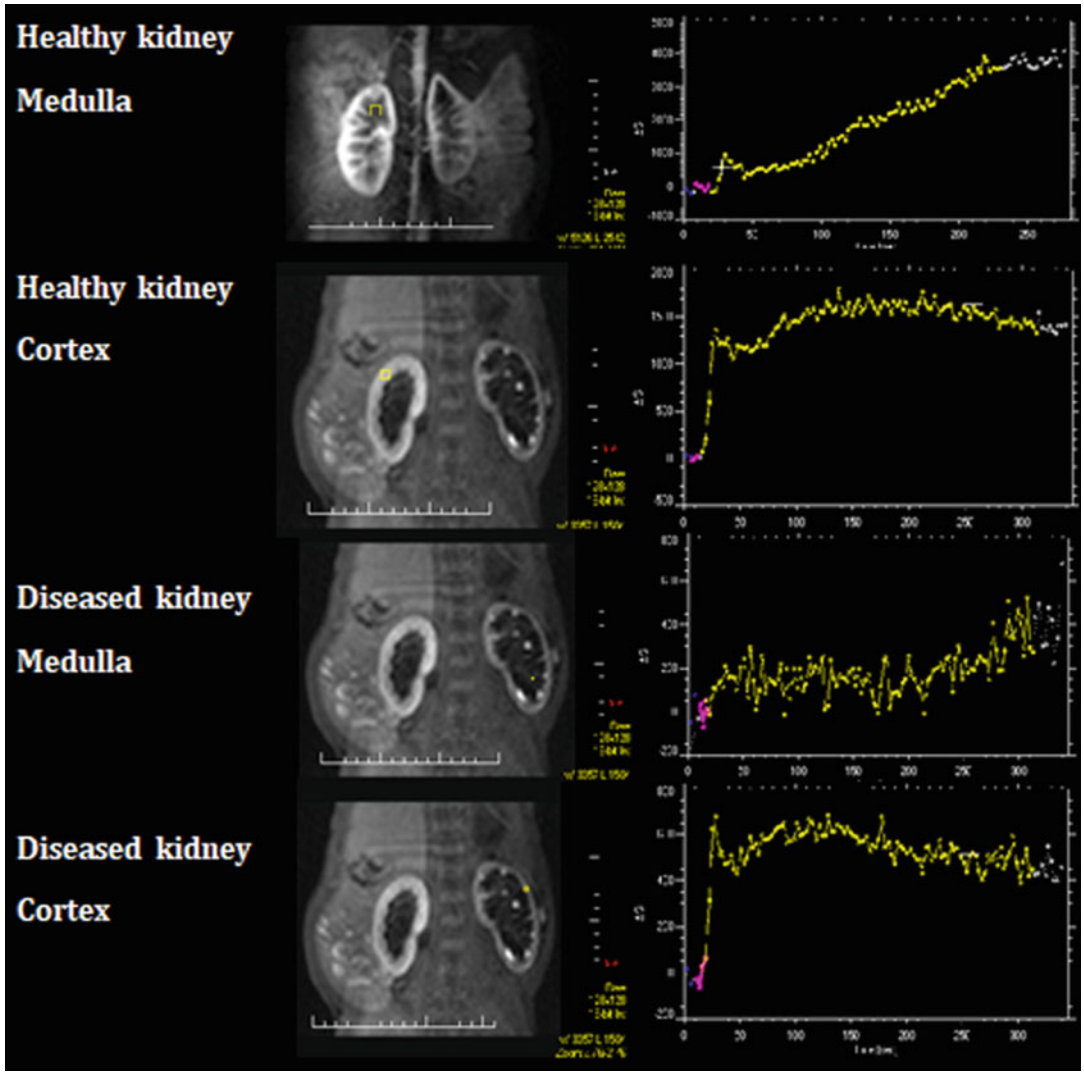

Fig. 3 Example of MR renogram, the result of DCE-MRI of pig kidneys with healthy (left) and diseased (right) kidneys. The yellow ROIs are shown to illustrate where the dynamic curves were drawn. The data were obtained as follows: the anaesthetized pig was placed supine in the magnet, and a surface radiofrequency coil was used for data reception. Fast multislice anatomical images were initially acquired to localize both kidneys. Next, an MRI renography pulse sequence was employed. The whole kidney was covered using a mutlislice (3.0 mm thickness with zero gap) fast 3D gradient echo sequence. Other parameters included: matrix = 128 × 128, field of view = 220 × 220 mm^2, TR = 4.3 ms, TE = 1.5 ms. This scan was accompanied by an intravenous injection of 0.05 ml/kg of Gd-DTPA-BMA (Omniscan®; GE Healthcare, Oslo, Norway) was performed as a single bolus administered by hand 10 s after start of a dynamic gradient-echo sequence, with a single phase acquisition time of 2.2 s. A total of 700 dynamic phases were acquired during 7 min

enhancement following a bolus of a gadolinium agent, and Fig. 3 shows the handling of a gadolinium agent in the healthy and diseased (ureteric obstructed) kidneys. Graphical presentation of the renal enhancement is denoted as an MR renogram.

The MR renogram typically consists of vascular, parenchymal, and excretory phases [38]. The vascular phase occurs almost immediately after contrast injection and provides the first segment of the renographic curve, which is reflected by a steep linear rise. In the cortex, this is followed by the parenchymal phase, characterized by continuous uptake, which is represented in the intensity–time curve as a slower linear increase up to a second peak. In the excretory phase, contrast material is released into the collecting system calices and constitutes the third segment of the renographic curve.

2.7 Analysis Methods

While the experimental design of DCE-MRI is simple, extracting true morphological or physiological parameters from a DCE time course is extraordinarily difficult, due to a number of factors, including intravoxel heterogeneity in tissue microstructure and the need for pharmacokinetic (model-based) or empirical (non-model based) modeling of the DCE-MRI signal [16, 38]. Tissue heterogeneity depends upon the organ of interest and image resolution, which are typically not varied in a single experiment. Pharmacokinetic and empirical modeling, however, are active areas of investigation.

2.7.1 Semiquantitative Analysis

As a descriptive approach, the dynamic time-vs-time curve of DCE-MRI data provides information with parameters like time-to-peak enhancement, uptake slope, area-under-the-curve and wash-out rate. These heuristic enhancement parameters may have some relation to physiologic parameters although they also depend on the particular MRI system and acquisition settings, including pulse sequence, sequence parameters, system manufacturer, and contrast agent employed [39]. Figure 4 shows an example of such parameters.

2.7.2 Quantitative—Pharmacokinetic Models

Alternatively, various physiological pharmacokinetic models have been proposed, usually based on long-term experiences in nuclear medicine. These models are often attributed to situations where the capillary bed (e.g., the blood–brain barrier) is compromised, resulting in extravasation of the contrast agent through the leaky capillaries. For example, modeling the dynamic extravasation of MRI contrast agent can provide a measure of the extravascular uptake. Overall, applying pharmacokinetic models allow calculation of several measures: (1) physiologic properties (transendothelial permeability, capillary surface area, lesion leakage space), (2) pharmacokinetic parameters (compartmental transfer and rate constants, leakage space), and (3) pathological measures (microvessel density and vascular endothelial growth factor) [13, 16]. Measurements of these parameters using modeling are now considered diagnostically important in tumor evaluation (grade classification) and to recognize the onset of stroke by indirect measurements of rCBF, rCBV, and MTT, although they usually provide limited

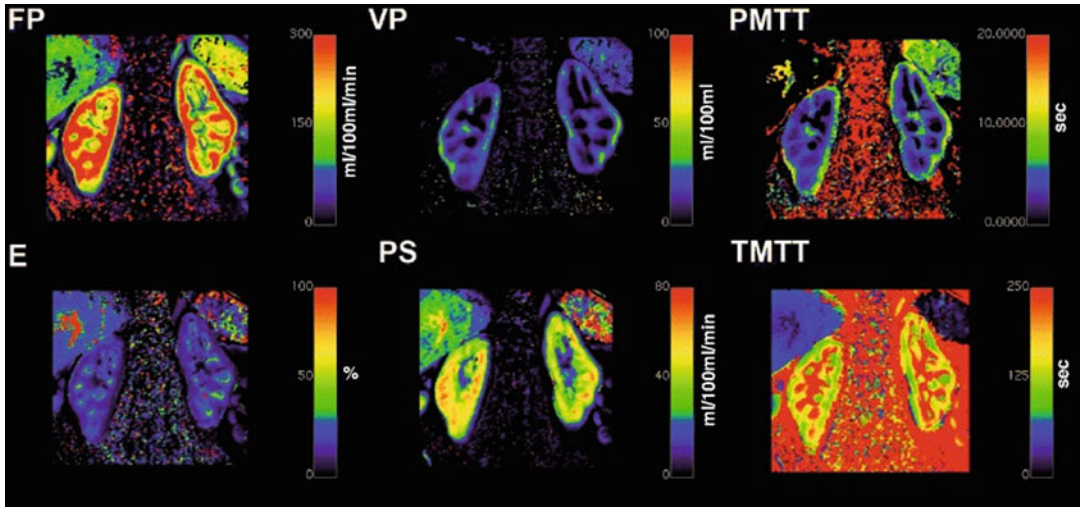

Fig. 4 Example of parameters estimated from DCE-MRI in kidneys. Top row from left to right: plasma flow (FP), plasma volume (VP), plasma mean transit time (PMTT). Lower row from left to right: extraction fraction (E), permeable surface area product (PS), and tubular mean transit time (TMMT). The maps are reproduced with permission from Zöllner et al. [39]

insight into the underlying pathophysiology of the brain tumor or stroke [40]. It is therefore likely that similar parameters can be measured in the kidney. The quantitative models require additional postprocessing steps, including contrast agent concentration calculation (e.g., based on linearity assumption between concentration and signal changes or in previously acquired T_1 maps), selection of a major artery to derive the AIF curve, selection of the pharmacokinetic model (as well as of the number of the compartments and how they are connected) to be used. In addition, the focus of the application as well as the quality of the data will guide the selection of the more appropriate model. Besides, the temporal resolution, protocol injection, and acquisition time can influence the quality of the outcomes, making it necessary to have appropriate and optimized measurement protocols.

2.7.3 *Model Selection*

All data analysis, including analysis of DCE-MRI data, involves either explicit or implicit comparison to a model. The data are typically considered to be the sum of the signal and noise, and the estimated signal model parameters are of primary interest. In the ideal case, the underlying principles of the measurement and the signal response form the basis of the signal model. Often, however, there are several potential signal models. The analyst must decide which of these competing models best represents the data without "over fitting" (i.e., fitting the noise). Even when the correct signal model is known, the signal-to-noise ratio of the data may not support the complexity of the correct model, requiring that simpler models be considered.

Here, we consider the problem of model selection in DCE-MRI experiments in the kidney. The importance of selecting an appropriate DCE tracer kinetic model to measure tissue perfusion and capillary permeability has already been examined in tumors in previous reports [41, 42]. Model selection algorithms, including Chi-square [43], Akaike information criterion (AIC) [44–46], F-test [47–49], and the Durbin–Watson statistic [45, 50], have been applied to evaluate tracer kinetic models commonly used in DCE-MRI.

2.7.4 Bayesian Probability Theory

An elegant solution to the model selection problem using Bayesian probability theory-based methods has recently been described [51–53]. Bayesian probability theory [54] provides a rigorous formalism for model selection. To determine the optimal model amongst a cohort of competing models, it is necessary to balance the accuracy with which the model recapitulates the data (the goodness of fit, characterized by the residuals) against the number of free parameters in each model (the complexity). Cox's theorem [55] and its further elaboration by Jaynes [56], state that Bayesian probability theory is the only method of ranking hypotheses concerning model selection that is consistent and can incorporate all of the available prior information. Advances in computational power and the development of Markov-chain Monte Carlo (MCMC) methods have greatly increased the applicability of Bayesian inference to a range of problems.

Bayesian probability theory seeks to assign a probability to the truth of a specific hypothesis. Using a Bayesian approach, the model selection problem treats the model itself as a parameter, for which the posterior probability of a model, given the data and prior information, is computed [51–53]. The posterior probability of each model is calculated by:

$$P(M|DI) = \frac{P(M|I)P(D|MI)}{P(D|I)} \tag{12}$$

where $P(M|DI)$ is the posterior probability for any one of M models. The vertical bar "|" means "given the data, D and the prior information, I." On the right-hand side, $P(M|I)$ is the prior probability for each of the M different models, assigned in this calculation as a uniform prior probability. $P(D|MI)$ is the probability for the data, given model M and prior information I. Finally, the denominator, $P(D|I)$ is a normalization constant that ensures the total probability over all of the models sums to one.

An example of a joint Bayesian approach to model selection in DCE-MRI was described recently by Beeman et al. [57], applied to models of blood flow in cortex in a mouse model of three different renal perfusion rates. The three cohorts of mice studied were: (1) Control; (2) Losartan-treated (high renal blood flow); (3) L-NAME-treated (low renal blood flow). DCE-MRI data were analyzed on a voxel-

by-voxel basis. Four models and model parameters were compared in each voxel. Two of the models, the Patlak–Rutland model [58] and the two-compartment model were pharmacokinetic and two, the cumulative log-logistic model with either monoexponential decay with a constant offset or biexponential decay, were empirical. A Markov-chain Monte Carlo simulation was run to compute the posterior probability for the parameters and the model. The estimated probabilities of the parameters of the biexponential model, obtained using this approach, are shown in Fig. 5.

The importance of signal-to-noise in model selection in DCE-MRI was described recently by Duan et al. [51] In their paper, the authors considered four established kinetic models for analyzing DCE-MRI data collected from patients enrolled in the EMBRACE study, an international study of MRI-guided brachytherapy in locally advanced cervical cancer. The models were (1) Toft's (TM), (2) Extended Toft's (ETM), (3) Two-Site Exchange (2CXM), and (4) Compartment Tissue Uptake (CTUM). To demonstrate the importance of signal-to-noise in DCE data analysis, noise-free in silico DCE data sets were generated for each of the four models. The temporal resolution and total data acquisition times were identical to those of the clinical DCE-MRI protocol, using patient-derived tissue parameters.

As expected, Bayesian model selection chose the "correct" signal model for each of these noise-free data sets. Increasing amounts of normally distributed (Gaussian) noise were then added to each data set. At each noise power, 100 independent MCMC simulations (i.e., different noise sets) were performed and the number of "correct" selections, in which model selection chose the model used to simulate the data, was recorded. The number of correct model selections varied as a function of both model complexity and noise power. With increasing levels of noise, simpler data representations were preferred relative to more complex models (Fig. 6a). Figure 6b shows model selection results for in silico data created based on the 2XCM. The number of correct model selections dropped rapidly with increasing noise, with a concomitant increase in the selection of the CTUM, a simplified version of the 2XCM. Figure 6c, d shows how the accuracy and uncertainty of estimations of extravascular, extracellular volume (ve), the only common parameter between the simplest model (TM) and the most complex model (2XCM), vary with added noise. At every noise level, the uncertainties of the estimated ve are much smaller for the TM, relative to the 2CXM.

2.8 Practical Considerations

The main advantage of T_1-weighted DCE-MRI is that both tissue blood flow and filtration (permeability surface) can be measured simultaneously. One important element in the T_1-weighted DCE-MRI is the underlying model from which the calculated parameters are derived. Many assumptions about the tissue system

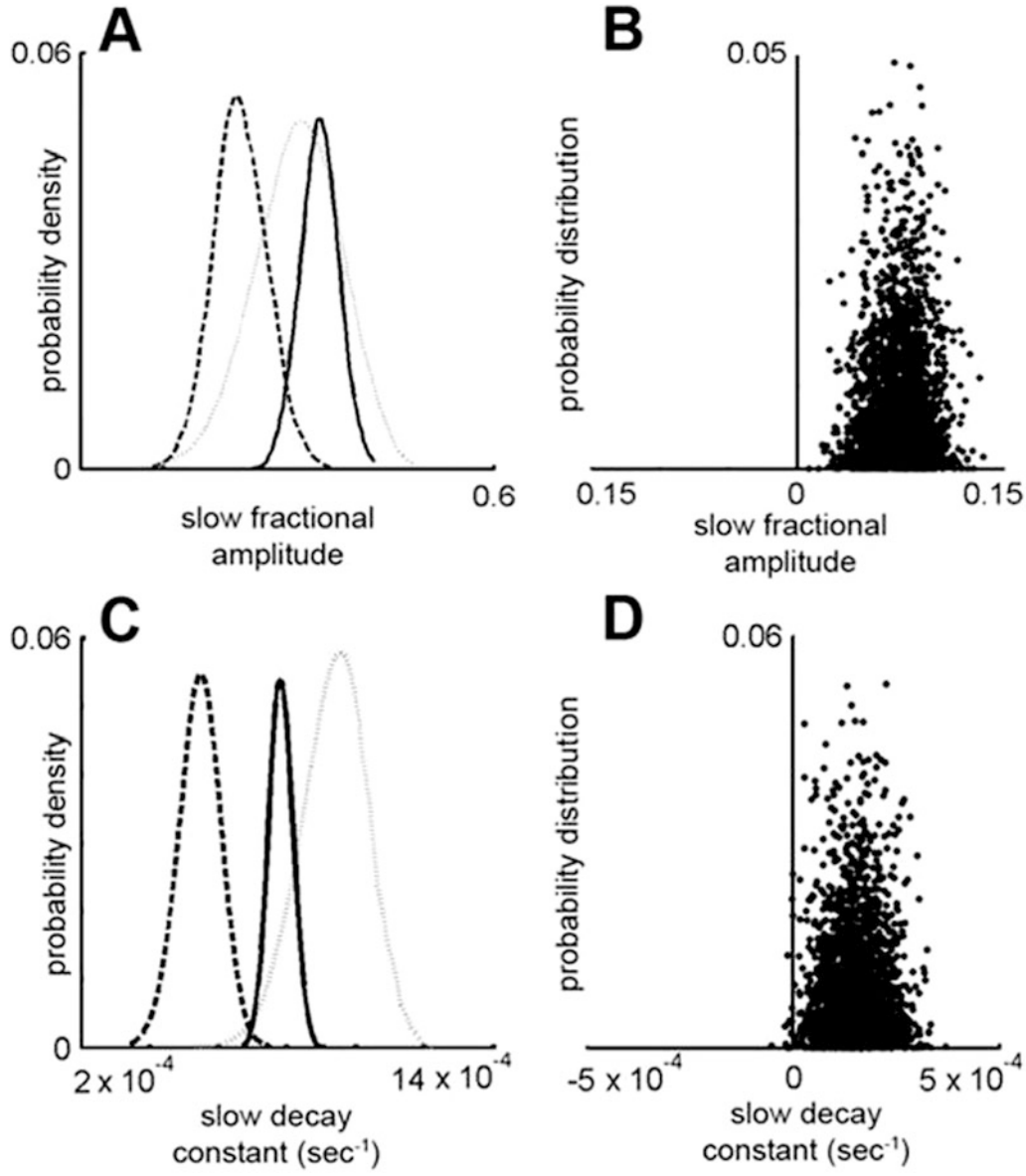

Fig. 5 (**a**, **c**) Bayesian-estimated posterior probability densities of the empirical biexponential model's joint fractional amplitudes of the washout and joint slow decay-rate constants, respectively, for each cohort. The Losartan-treated (high renal blood flow) group is represented by the solid black line, the L-NAME (low renal blood flow group) by the dashed black line, and the control group by the dotted gray line. (**b**, **d**) The difference in the posterior probability distributions for the joint fractional amplitudes of the washout and joint slow decay-rate constants, respectively, calculated on the high and low flow cohorts. From among the empirical/biexponential model joint parameter estimates, the fractional amplitudes of the washout terms (**a**) and the slow decay-rate constants (**c**) differed between mouse cohorts of high and low flow; that is, the 95% confidence interval of the difference in the probability distributions did not overlap with 0 (**b** and **d**). (Adapted, with permission, from Beeman, et al. [57])

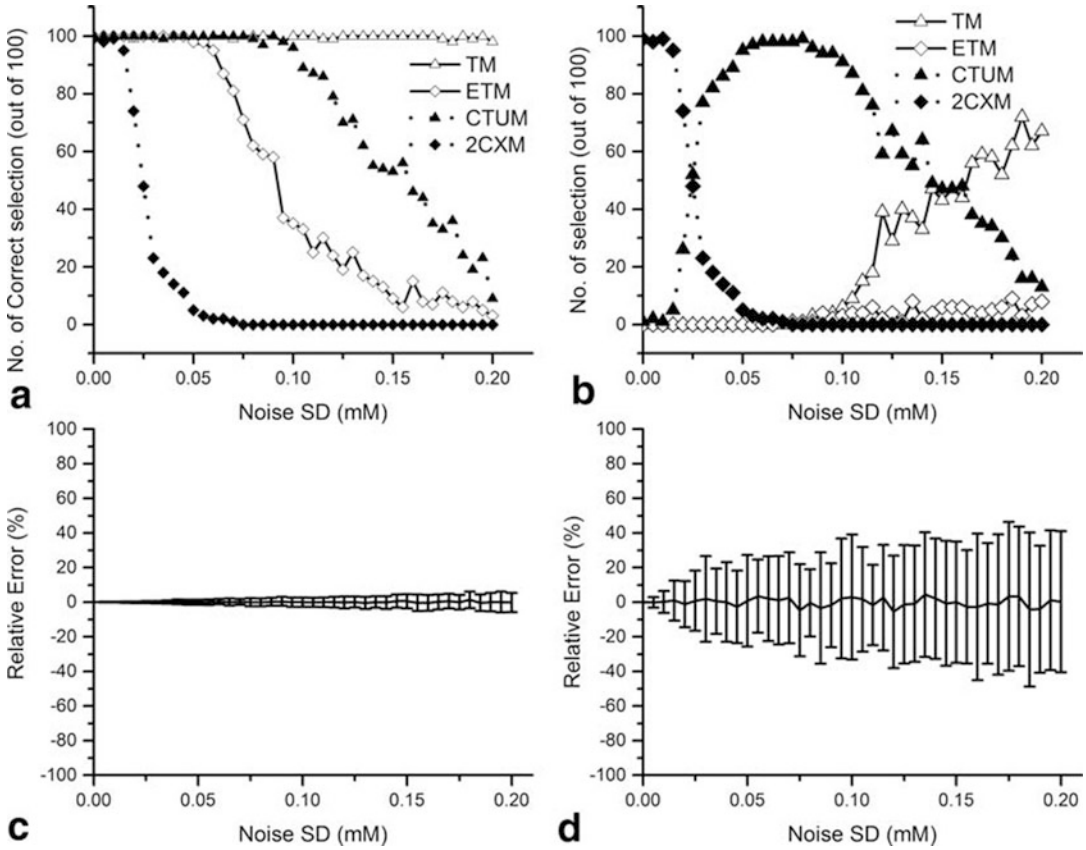

Fig. 6 Bayesian DCE-MRI model-selection and parameter-estimation results for in silico datasets created based on the whole-tumor averaged ROI DCE time course from a single patient in the EMBRACE study. (**a**) For each of the four in silico DCE-MRI data models, the number of "correct" model selections (out of 100 different noise representations), as a function of the noise standard deviation (SD). (**b**) For the two-compartment exchange in silico DCE-MRI data model (the most complex model of the four models examined), the number of times a given model was selected (out of 100 different noise representations) as a function of the noise SD. (**c**, **d**) Relative percent error of v_e (extracellular-extravascular volume fraction) estimated from initially noiseless simulated TM (**c**) and 2CXM (**d**) data as a function of added noise. (Adapted with permission from Duan et al. [51])

are made with respect to the nature of contrast agent kinetic modeling, and these assumptions may affect the accuracy of the parameter calculations. In practice, a compromise must be struck between reality and the precision of the measured data (signal-to noise ratio, temporal resolution, etc.). The different models proposed by leading experts in this field have unfortunately been presented with a variety of quantities, meaning that comparisons between different groups are almost impossible. Consequently, a standardization of quantities associated with analysis of T_1-weighted DCE-MRI has been proposed in the review by Tofts et al. [59], and later by Sourbron [42] as part of building up a common language for the estimation and description of physiologic parameters in the kidney.

For all methods proposed, the calculation of renal parameters requires knowledge of the arterial input function, which in practice is derived from the abdominal aorta or a renal artery with the assumption that this represents the exact input to the renal tissue. Delay and dispersion of the bolus that are introduced during its passage from the site of arterial input function estimation to the renal tissue will therefore introduce an error in the quantification of RBF or GFR, and this error could very well vary from one region to another because of the differences in the amount of delay and dispersion for different kidney regions. Thus, some general approximations seem useful: (1) DCE-MRI is performed under a steady-state condition. (2) The renal relaxivity of the gadolinium-agent is known. (3) Some conversion to gadolinium concentration can be made. (4) An input curve is defined. (5) A mathematical analytical model can be approximated.

Today, little is known about the potential of gadolinium-enhanced MRI for the assessment of the regional renal blood flow and the regional glomerular filtration rate. Nor do we know the limitations and accuracy of this technique under different pathological and pathophysiological conditions. Thirdly, we do not know the clinical applicability of DCE-MRI and the role it may have in clinical diagnosis. A step-by-step procedure should therefore be initiated to exploit the abovementioned fundamental questions: (1) The methodologies should be further validated against standard methods to obtain reproducible results in agreements to those obtained by clinical non-MRI techniques. (2) Further animal studies should be performed to examine the accuracy and availability under different pathological and pathophysiological conditions. (3) Experimental studies in humans, where the DCE-MRI methods are validated against a standard reference method.

3 Overview of Applications

3.1 DCE-MRI Validation Studies in Animal Models

Several studies investigated DCE-MRI approaches for assessing renal filtration in animal models. Annet et al. estimated the GFR in rabbit kidneys by applying a compartment model and compared the MRI-derived estimate with the measured plasma clearance of 51Cr-EDTA [60]. Although MRI-based GFR values were lower than those measured experimentally, a marked correlation was observed between the two techniques. Winter et al. compared renal perfusion values obtained by arterial spin labeling (ASL) or DCE-MRI in healthy rats, with absolute renal cortex perfusion estimates in close agreement with those obtained by ASL [61].

Zimmer et al. performed an inter- and intramethodical comparison by measuring differences in renal blood flow (RBF) in five rats with unilateral ischemic acute kidney injury with both ASL and DCE-MRI. Both, the FAIR-ASL approach and DCE-MRI

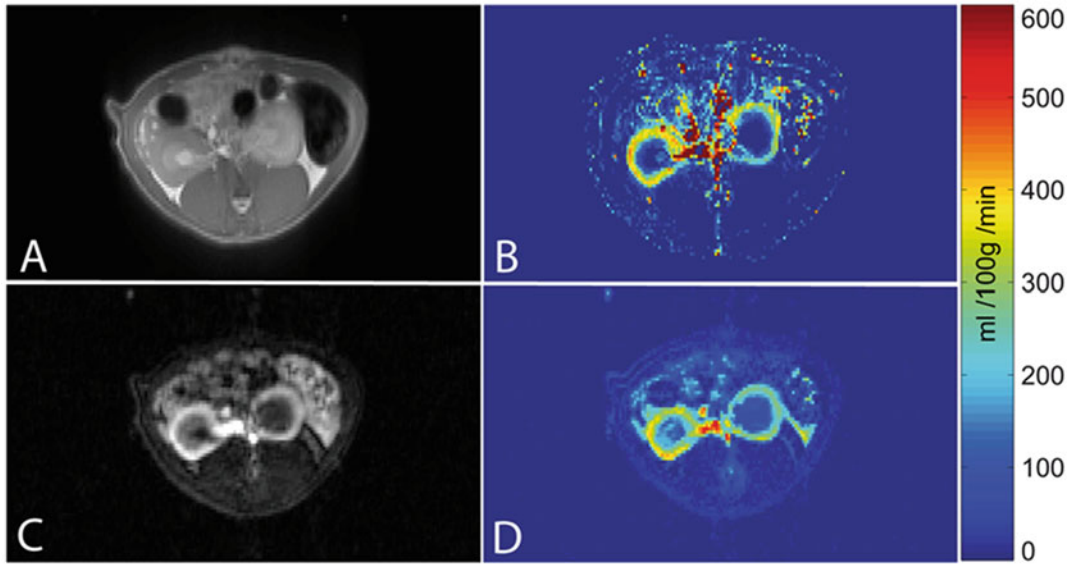

Fig. 7 Exemplary illustration of perfusion MRI of a rat with left-side AKI and perfusion maps. (**a**) True-FISP M_0 image of an ASL measurement and the corresponding perfusion map (**b**). (**c**) TWIST post–contrast agent injection image and the corresponding RBF map (**d**). All drawings show the same rat and the same axial slice. Differences between the kidney with AKI and the contralateral kidney are clearly visible on the MRI images as well as on the perfusion maps. (Reproduced with permission from Zimmer et al. [62])

deconvolution technique showed significant differences in RBF between healthy and diseased kidneys as shown in Fig. 7 [62]. The validation of MRI-based GFR estimation by optical imaging was proposed by Sadick et al. [63]. GFR estimation was performed by DCE-MRI on a 3 T whole body scanner using a dedicated animal rat volume coil and by clearance using a fluorescent tracer (FITC-sinistrin) and an optical imaging device. However, the correlation between optical GFR and MRI-based GFR was poor, probably due to the fact that measurements were performed on different days involving two anesthesia thus affecting the physiology of the animals. Zöllner et al. recently showed a simultaneous measurement of optical and MR-based GFR in healthy rats and rats with unilateral nephrectomy (UNX) [64]. A two-compartment filtration model was employed to calculate a map of the tubular flow. Subsequent, taking the cortex volume into account single kidney GFR values were calculated with a good correlation observed between the two methods. The reduction of GFR in the UNX rats was about 50% and observed for both techniques.

The role played by the binding to serum proteins in the calculation of DCE-MRI derived estimates was investigated by Notohamiprodjo et al. by administering Gadolinium-based contrast agents with different chemical structure [65]. The two investigated contrast agents, Gd-BOPTA and Gd-DTPA differ in their binding affinity toward serum albumin, hence affecting both the

relaxivity and the pharmacokinetic properties [66–68]. In fact, binding to the serum protein results in longer circulation times (hence reduced filtration) and higher contrast capability that are easily observed at low magnetic fields (0.5–1.5 T) [69–73]. Therefore, whereas similar renal perfusion values were obtained by both the two contrast agents, GFR estimates were not accurate when obtained with the albumin-binding one (Gd-BOPTA), thus indicating that even low albumin binding may affect GFR estimates.

3.2 DCE-MRI for Assessing Kidney Damages in Animal Models

In the preclinical panorama, DCE-MRI has been widely used to assess kidney function in renovascular and parenchymal diseases that may lead to chronic kidney failure but also in acute events like ischemia–reperfusion, toxicity, infections, or surgery. Thus, different animal models have been explored ranging from classical acute kidney injury (AKI) and chronic kidney disease (CKD) to posttransplant rejection, nephrectomy, and assessment of drug treatment [74–80]. In a murine model of unilateral renal artery stenosis (RAS), measurements of single kidney GFR and perfusion by a modified two-compartment model were compared to those obtained from fluorescein isothiocyanate (FITC)-inulin clearance and ASL, respectively. Both renal GFR and perfusion measurements were in close agreement with the FITC-inulin clearance and ASL methods, with a marked reduction in GFR and perfusion estimates for the stenotic as compared to the control kidneys [81]. Ischemia–reperfusion injury has been exploited to model acute kidney damages and DCE-MRI approaches have been investigated for assessing single-kidney function in both mice and rats [82, 83]. Significant reduction in single kidney GFR (calculated by applying a two compartment renal filtration model) was observed for ischemic kidneys in comparison to contralateral ones in rats [84]. Conversely, for all the other DCE-MRI derived functional parameters (mean transit times and renal blood volume) differences were present, but were not significant between diseased and contralateral kidneys of ischemic rats.

DCE-MRI studies have also been exploited in murine renal transplantations studies for assessing acute rejection and evaluation of immunosuppressive therapy [85]. In this study, a deconvolution approach was applied to the DCE-MRI data and the plasma flow estimate provided restored organ perfusion under Ciclosporin A therapy in syngeneic transplants compared to controls.

Acknowledgments

The Italian Ministry for Education and Research (MIUR) is gratefully acknowledged for yearly FOE funding to the Euro-BioImaging Multi-Modal Molecular Imaging Italian Node (MMMI).

This publication is based upon work from COST Action PARENCHIMA, supported by European Cooperation in Science and Technology (COST). COST (www.cost.eu) is a funding agency for research and innovation networks. COST Actions help connect research initiatives across Europe and enable scientists to enrich their ideas by sharing them with their peers. This boosts their research, career, and innovation.
PARENCHIMA (renalmri.org) is a community-driven Action in the COST program of the European Union, which unites more than 200 experts in renal MRI from 30 countries with the aim to improve the reproducibility and standardization of renal MRI biomarkers.

References

1. Hauser W, Atkins HL, Nelson KG, Richards P (1970) Technetium-99m DTPA: a new radiopharmaceutical for brain and kidney scanning. Radiology 94(3):679–684. https://doi.org/10.1148/94.3.679
2. Taylor A (1999) Radionuclide renography: a personal approach. Semin Nucl Med 29 (2):102–127
3. Gaspari F, Perico N, Remuzzi G (1997) Measurement of glomerular filtration rate. Kidney Int Suppl 63:S151–S154
4. Barbour GL, Crumb CK, Boyd CM, Reeves RD, Rastogi SP, Patterson RM (1976) Comparison of inulin, iothalamate, and 99mTc-DTPA for measurement of glomerular filtration rate. J Nucl Med 17(4):317–320
5. Soveri I, Berg UB, Bjork J, Elinder CG, Grubb A, Mejare I, Sterner G, Back SE, SBU GFR Review Group (2014) Measuring GFR: a systematic review. Am J Kidney Dis 64 (3):411–424. https://doi.org/10.1053/j.ajkd.2014.04.010
6. Peters AM (1991) Quantification of renal haemodynamics with radionuclides. Eur J Nucl Med 18(4):274–286
7. Suto Y, Caner BE, Tamagawa Y, Matsuda T, Nakashima T, Matsushita T, Odori T, Ishii Y, Torizuka K (1989) Assessment of magnetic resonance contrast enhancement with Gd-DTPA: comparison with the uptake of Tc-99m-DTPA. Radiat Med 7(5):209–213
8. Prato FS, Wisenberg G, Marshall TP, Uksik P, Zabel P (1988) Comparison of the biodistribution of gadolinium-153 DTPA and technetium-99m DTPA in rats. J Nucl Med 29(10):1683–1687
9. Choyke PL, Frank JA, Girton ME, Inscoe SW, Carvlin MJ, Black JL, Austin HA, Dwyer AJ (1989) Dynamic Gd-DTPA-enhanced MR imaging of the kidney: experimental results. Radiology 170(3 Pt 1):713–720. https://doi.org/10.1148/radiology.170.3.2916025
10. Fransen R, Muller HJ, Boer WH, Nicolay K, Koomans HA (1996) Contrast-enhanced dynamic magnetic resonance imaging of the rat kidney. J Am Soc Nephrol 7(3):424–430
11. Wen JG, Chen Y, Ringgaard S, Frokiaer J, Jorgensen TM, Stodkilde-Jorgensen H, Djurhuus JC (2000) Evaluation of renal function in normal and hydronephrotic kidneys in rats using gadolinium diethylenetetramine-pentaacetic acid enhanced dynamic magnetic resonance imaging. J Urol 163(4):1264–1270
12. Kikinis R, von Schulthess GK, Jager P, Durr R, Bino M, Kuoni W, Kubler O (1987) Normal and hydronephrotic kidney: evaluation of renal function with contrast-enhanced MR imaging. Radiology 165(3):837–842. https://doi.org/10.1148/radiology.165.3.3685363
13. Sourbron SP, Michaely HJ, Reiser MF, Schoenberg SO (2008) MRI-measurement of perfusion and glomerular filtration in the human kidney with a separable compartment model. Investig Radiol 43(1):40–48. https://doi.org/10.1097/RLI.0b013e31815597c5
14. Pedersen M, Shi Y, Anderson P, Stodkilde-Jorgensen H, Djurhuus JC, Gordon I, Frokiaer J (2004) Quantitation of differential renal blood flow and renal function using dynamic contrast-enhanced MRI in rats. Magn Reson Med 51(3):510–517. https://doi.org/10.1002/mrm.10711
15. Elmholdt TR, Pedersen M, Jorgensen B, Sondergaard K, Jensen JD, Ramsing M, Olesen AB (2011) Nephrogenic systemic fibrosis is found only among gadolinium-exposed patients with renal insufficiency: a case-control study from Denmark. Br J Dermatol 165

(4):828–836. https://doi.org/10.1111/j.1365-2133.2011.10465.x

16. Grenier N, Mendichovszky I, de Senneville BD, Roujol S, Desbarats P, Pedersen M, Wells K, Frokiaer J, Gordon I (2008) Measurement of glomerular filtration rate with magnetic resonance imaging: principles, limitations, and expectations. Semin Nucl Med 38(1):47–55. https://doi.org/10.1053/j.semnuclmed.2007.09.004
17. Aime S, Botta M, Terreno E (2005) Gd(III)-based contrast agents for MRI. Adv Inorg Chem 57(57):173–237. https://doi.org/10.1016/S0898-8838(05)57004-1
18. Caravan P, Ellison JJ, McMurry TJ, Lauffer RB (1999) Gadolinium(III) chelates as MRI contrast agents: structure, dynamics, and applications. Chem Rev 99(9):2293–2352
19. Aime S, Botta M, Fasano M, Crich SG, Terreno E (1996) Gd(III) complexes as contrast agents for magnetic resonance imaging: a proton relaxation enhancement study of the interaction with human serum albumin. J Biol Inorg Chem 1(4):312–319. https://doi.org/10.1007/s007750050059
20. Lauffer RB (1987) Paramagnetic metal complexes as water proton relaxation agents for NMR imaging: theory and design. Chem Rev 87(5):901–927
21. Werner EJ, Datta A, Jocher CJ, Raymond KN (2008) High-relaxivity MRI contrast agents: where coordination chemistry meets medical imaging. Angew Chem Int Ed Engl 47 (45):8568–8580. https://doi.org/10.1002/anie.200800212
22. Burtea C, Laurent S, Vander Elst L, Muller RN (2008) Contrast agents: magnetic resonance. Handb Exp Pharmacol (185 Pt 1):135-165. https://doi.org/10.1007/978-3-540-72718-7_7
23. Aime S, Caravan P (2009) Biodistribution of gadolinium-based contrast agents, including gadolinium deposition. J Magn Reson Imaging 30(6):1259–1267. https://doi.org/10.1002/jmri.21969
24. Baranyai Z, Palinkas Z, Uggeri F, Maiocchi A, Aime S, Brucher E (2012) Dissociation kinetics of open-chain and macrocyclic gadolinium (III)-aminopolycarboxylate complexes related to magnetic resonance imaging: catalytic effect of endogenous ligands. Chemistry 18 (51):16426–16435. https://doi.org/10.1002/chem.201202930
25. Baranyai Z, Uggeri F, Giovenzana GB, Benyei A, Brucher E, Aime S (2009) Equilibrium and kinetic properties of the lanthanoids (III) and various divalent metal complexes of the heptadentate ligand AAZTA. Chemistry 15 (7):1696–1705. https://doi.org/10.1002/chem.200801803
26. Sherry AD, Caravan P, Lenkinski RE (2009) Primer on gadolinium chemistry. J Magn Reson Imaging 30(6):1240–1248. https://doi.org/10.1002/jmri.21966
27. Wahsner J, Gale EM, Rodriguez-Rodriguez A, Caravan P (2019) Chemistry of MRI contrast agents: current challenges and new frontiers. Chem Rev 119(2):957–1057. https://doi.org/10.1021/acs.chemrev.8b00363
28. Dastru W, Longo D, Aime S (2011) Contrast agents and mechanisms. Drug Discov Today 8 (2–4):e109–e115. https://doi.org/10.1016/j.ddtec.2011.11.013
29. Terreno E, Dastru W, Delli Castelli D, Gianolio E, Geninatti Crich S, Longo D, Aime S (2010) Advances in metal-based probes for MR molecular imaging applications. Curr Med Chem 17(31):3684–3700
30. Avedano S, Botta M, Haigh JS, Longo DL, Woods M (2013) Coupling fast water exchange to slow molecular tumbling in Gd3+ chelates: why faster is not always better. Inorg Chem 52 (15):8436–8450. https://doi.org/10.1021/ic400308a
31. Longo DL, Arena F, Consolino L, Minazzi P, Geninatti-Crich S, Giovenzana GB, Aime S (2016) Gd-AAZTA-MADEC, an improved blood pool agent for DCE-MRI studies on mice on 1 T scanners. Biomaterials 75:47–57. https://doi.org/10.1016/j.biomaterials.2015.10.012
32. Pierre VC, Allen MJ, Caravan P (2014) Contrast agents for MRI: 30+ years and where are we going? J Biol Inorg Chem 19(2):127–131. https://doi.org/10.1007/s00775-013-1074-5
33. Paschal CB, Morris HD (2004) K-space in the clinic. J Magn Reson Imaging 19(2):145–159. https://doi.org/10.1002/jmri.10451
34. Markl M, Leupold J (2012) Gradient echo imaging. J Magn Reson Imaging 35 (6):1274–1289. https://doi.org/10.1002/jmri.23638
35. Tsao J (2010) Ultrafast imaging: principles, pitfalls, solutions, and applications. J Magn Reson Imaging 32(2):252–266. https://doi.org/10.1002/jmri.22239
36. Oesterle C, Strohschein R, Kohler M, Schnell M, Hennig J (2000) Benefits and pitfalls of keyhole imaging, especially in first-pass perfusion studies. J Magn Reson Imaging 11 (3):312–323
37. Teixeira RPAG, Malik SJ, Hajnal JV (2019) Fast quantitative MRI using controlled

saturation magnetization transfer. Magn Reson Med 81(2):907–920. https://doi.org/10.1002/mrm.27442

38. Grenier N, Pedersen M, Hauger O (2006) Contrast agents for functional and cellular MRI of the kidney. Eur J Radiol 60 (3):341–352. https://doi.org/10.1016/j.ejrad.2006.06.024
39. Zollner FG, Daab M, Sourbron SP, Schad LR, Schoenberg SO, Weisser G (2016) An open source software for analysis of dynamic contrast enhanced magnetic resonance images: UMM-Perfusion revisited. BMC Med Imaging 16:7. https://doi.org/10.1186/s12880-016-0109-0
40. Roldan-Valadez E, Gonzalez-Gutierrez O, Martinez-Lopez M (2012) Diagnostic performance of PWI/DWI MRI parameters in discriminating hyperacute versus acute ischaemic stroke: finding the best thresholds. Clin Radiol 67(3):250–257. https://doi.org/10.1016/j.crad.2011.08.020
41. Ewing JR, Bagher-Ebadian H (2013) Model selection in measures of vascular parameters using dynamic contrast-enhanced MRI: experimental and clinical applications. NMR Biomed 26(8):1028–1041. https://doi.org/10.1002/nbm.2996
42. Sourbron SP, Buckley DL (2013) Classic models for dynamic contrast-enhanced MRI. NMR Biomed 26(8):1004–1027. https://doi.org/10.1002/nbm.2940
43. Abrikossova N, Skoglund C, Ahren M, Bengtsson T, Uvdal K (2012) Effects of gadolinium oxide nanoparticles on the oxidative burst from human neutrophil granulocytes. Nanotechnology 23(27):275101. https://doi.org/10.1088/0957-4484/23/27/275101
44. Kallehauge JF, Tanderup K, Duan C, Haack S, Pedersen EM, Lindegaard JC, Fokdal LU, Mohamed SM, Nielsen T (2014) Tracer kinetic model selection for dynamic contrast-enhanced magnetic resonance imaging of locally advanced cervical cancer. Acta Oncol 53 (8):1064–1072. https://doi.org/10.3109/0284186X.2014.937879
45. Li X, Welch EB, Chakravarthy AB, Xu L, Arlinghaus LR, Farley J, Mayer IA, Kelley MC, Meszoely IM, Means-Powell J, Abramson VG, Grau AM, Gore JC, Yankeelov TE (2012) Statistical comparison of dynamic contrast-enhanced MRI pharmacokinetic models in human breast cancer. Magn Reson Med 68(1):261–271. https://doi.org/10.1002/mrm.23205
46. Naish JH, Kershaw LE, Buckley DL, Jackson A, Waterton JC, Parker GJ (2009) Modeling of contrast agent kinetics in the lung using T1-weighted dynamic contrast-enhanced MRI. Magn Reson Med 61 (6):1507–1514. https://doi.org/10.1002/mrm.21814
47. Bagher-Ebadian H, Jain R, Nejad-Davarani SP, Mikkelsen T, Lu M, Jiang Q, Scarpace L, Arbab AS, Narang J, Soltanian-Zadeh H, Paudyal R, Ewing JR (2012) Model selection for DCE-T1 studies in glioblastoma. Magn Reson Med 68 (1):241–251. https://doi.org/10.1002/mrm.23211
48. Chwang WB, Jain R, Bagher-Ebadian H, Nejad-Davarani SP, Iskander AS, VanSlooten A, Schultz L, Arbab AS, Ewing JR (2014) Measurement of rat brain tumor kinetics using an intravascular MR contrast agent and DCE-MRI nested model selection. J Magn Reson Imaging 40(5):1223–1229. https://doi.org/10.1002/jmri.24469
49. Donaldson SB, West CM, Davidson SE, Carrington BM, Hutchison G, Jones AP, Sourbron SP, Buckley DL (2010) A comparison of tracer kinetic models for T1-weighted dynamic contrast-enhanced MRI: application in carcinoma of the cervix. Magn Reson Med 63 (3):691–700. https://doi.org/10.1002/mrm.22217
50. Draper NR, Smith H (1998) Applied regression analysis, 3rd edn. Wiley, New York
51. Duan C, Kallehauge JF, Bretthorst GL, Tanderup K, Ackerman JJ, Garbow JR (2017) Are complex DCE-MRI models supported by clinical data? Magn Reson Med 77 (3):1329–1339. https://doi.org/10.1002/mrm.26189
52. Meinerz K, Beeman SC, Duan C, Bretthorst GL, Garbow JR, Ackerman JJH (2018) Bayesian modeling of NMR data: quantifying longitudinal relaxation in vivo, and in vitro with a tissue-water-relaxation mimic (crosslinked bovine serum albumin). Appl Magn Reson 49 (1):3–24
53. Quirk JD, Bretthorst GL, Garbow JR, Ackerman JJ (2019) Magnetic resonance data modeling: the Bayesian analysis toolbox. Concepts Magn Reson Part A 47A:e21467
54. Bayes T, Price R (1763) An essay toward solving a problem in the doctrine of chance. Philos Trans R Soc Lond 53:370–418
55. Cox RT (1961) The algebra of probable inference. Johns Hopkins University Press, Baltimore, MD
56. Jaynes ET (1988) Optimal information-processing and Bayes theorem - comment. Am Stat 42(4):280–281. https://doi.org/10.2307/2685144

57. Beeman SC, Osei-Owusu P, Duan C, Engelbach J, Bretthorst GL, Ackerman JJH, Blumer KJ, Garbow JR (2015) Renal DCE-MRI model selection using Bayesian probability theory. Tomography 1(1):61–68. https://doi.org/10.18383/j.tom.2015.00133
58. Patlak CS, Blasberg RG, Fenstermacher JD (1983) Graphical evaluation of blood-to-brain transfer constants from multiple-time uptake data. J Cereb Blood Flow Metab 3(1):1–7. https://doi.org/10.1038/jcbfm.1983.1
59. Tofts PS, Brix G, Buckley DL, Evelhoch JL, Henderson E, Knopp MV, Larsson HB, Lee TY, Mayr NA, Parker GJ, Port RE, Taylor J, Weisskoff RM (1999) Estimating kinetic parameters from dynamic contrast-enhanced T(1)-weighted MRI of a diffusable tracer: standardized quantities and symbols. J Magn Reson Imaging 10(3):223–232. https://doi.org/10.1002/(SICI)1522-2586(199909)10:3<223::AID-JMRI2>3.0.CO;2-S
60. Annet L, Hermoye L, Peeters F, Jamar F, Dehoux JP, Van Beers BE (2004) Glomerular filtration rate: assessment with dynamic contrast-enhanced MRI and a cortical-compartment model in the rabbit kidney. J Magn Reson Imaging 20(5):843–849. https://doi.org/10.1002/jmri.20173
61. Winter JD, St Lawrence KS, Cheng HL (2011) Quantification of renal perfusion: comparison of arterial spin labeling and dynamic contrast-enhanced MRI. J Magn Reson Imaging 34(3):608–615. https://doi.org/10.1002/jmri.22660
62. Zimmer F, Zollner FG, Hoeger S, Klotz S, Tsagogiorgas C, Kramer BK, Schad LR (2013) Quantitative renal perfusion measurements in a rat model of acute kidney injury at 3T: testing inter- and intramethodical significance of ASL and DCE-MRI. PLoS One 8(1):e53849. https://doi.org/10.1371/journal.pone.0053849
63. Sadick M, Attenberger U, Kraenzlin B, Kayed H, Schoenberg SO, Gretz N, Schock-Kusch D (2011) Two non-invasive GFR-estimation methods in rat models of polycystic kidney disease: 3.0 tesla dynamic contrast-enhanced MRI and optical imaging. Nephrol Dial Transplant 26(10):3101–3108. https://doi.org/10.1093/ndt/gfr148
64. Zollner FG, Schock-Kusch D, Backer S, Neudecker S, Gretz N, Schad LR (2013) Simultaneous measurement of kidney function by dynamic contrast enhanced MRI and FITC-sinistrin clearance in rats at 3 tesla: initial results. PLoS One 8(11):e79992. https://doi.org/10.1371/journal.pone.0079992
65. Notohamiprodjo M, Pedersen M, Glaser C, Helck AD, Lodemann K-P, Jespersen B, Fischereder M, Reiser MF, Sourbron SP (2011) Comparison of Gd-DTPA and Gd-BOPTA for studying renal perfusion and filtration. J Magn Reson Imaging 34(3):595–607. https://doi.org/10.1002/jmri.22640
66. Laurent S, Elst LV, Muller RN (2006) Comparative study of the physicochemical properties of six clinical low molecular weight gadolinium contrast agents. Contrast Media Mol Imaging 1(3):128–137. https://doi.org/10.1002/cmmi.100
67. Caravan P, Cloutier NJ, Greenfield MT, McDermid SA, Dunham SU, Bulte JW, Amedio JC Jr, Looby RJ, Supkowski RM, Horrocks WD Jr, McMurry TJ, Lauffer RB (2002) The interaction of MS-325 with human serum albumin and its effect on proton relaxation rates. J Am Chem Soc 124(12):3152–3162
68. Aime S, Barge A, Botta M, Terreno E (2003) Interactions of lanthanides and their complexes with proteins. Conclusions regarding magnetic resonance imaging. Met Ions Biol Syst 40:643–682
69. Caravan P, Parigi G, Chasse JM, Cloutier NJ, Ellison JJ, Lauffer RB, Luchinat C, McDermid SA, Spiller M, McMurry TJ (2007) Albumin binding, relaxivity, and water exchange kinetics of the diastereoisomers of MS-325, a gadolinium(III)-based magnetic resonance angiography contrast agent. Inorg Chem 46(16):6632–6639. https://doi.org/10.1021/ic700686k
70. Botta M, Avedano S, Giovenzana GB, Lombardi A, Longo D, Cassino C, Tei L, Aime S (2011) Relaxometric study of a series of monoaqua Gd-III complexes of rigidified EGTA-like chelators and their noncovalent interaction with human serum albumin. Eur J Inorg Chem (6):802–810. https://doi.org/10.1002/ejic.201001103
71. Gianolio E, Giovenzana GB, Longo D, Longo I, Menegotto I, Aime S (2007) Relaxometric and modelling studies of the binding of a lipophilic Gd-AAZTA complex to fatted and defatted human serum albumin. Chemistry 13(20):5785–5797. https://doi.org/10.1002/chem.200601277
72. Avedano S, Tei L, Lombardi A, Giovenzana GB, Aime S, Longo D, Botta M (2007) Maximizing the relaxivity of HSA-bound gadolinium complexes by simultaneous optimization of rotation and water exchange. Chem Commun (Camb) (45):4726–4728. https://doi.org/10.1039/b714438e

73. Aime S, Gianolio E, Longo D, Pagliarin R, Lovazzano C, Sisti M (2005) New insights for pursuing high relaxivity MRI agents from modelling the binding interaction of Gd(III) chelates to HSA. Chembiochem 6 (5):818–820. https://doi.org/10.1002/cbic.200400364
74. Egger C, Cannet C, Gérard C, Debon C, Stohler N, Dunbar A, Tigani B, Li J, Beckmann N (2015) Adriamycin-induced nephropathy in rats: functional and cellular effects characterized by MRI. J Magn Reson Imaging 41 (3):829–840. https://doi.org/10.1002/jmri.24603
75. Laurent D, Poirier K, Wasvary J, Rudin M (2002) Effect of essential hypertension on kidney function as measured in rat by dynamic MRI. Magn Reson Med 47(1):127–134
76. Hermoye L, Annet L, Lemmerling P, Peeters F, Jamar F, Gianello P, Van Huffel S, Van Beers BE (2004) Calculation of the renal perfusion and glomerular filtration rate from the renal impulse response obtained with MRI. Magn Reson Med 51(5):1017–1025. https://doi.org/10.1002/mrm.20026
77. Zhang YD, Wang J, Zhang J, Wang X, Jiang X (2014) Effect of iodinated contrast media on renal function evaluated with dynamic three-dimensional MR renography. Radiology 270 (2):409–415. https://doi.org/10.1148/radiol.13122495
78. Liu X, Murphy MP, Xing W, Wu H, Zhang R, Sun H (2018) Mitochondria-targeted antioxidant MitoQ reduced renal damage caused by ischemia-reperfusion injury in rodent kidneys: longitudinal observations of T. Magn Reson Med 79(3):1559–1567. https://doi.org/10.1002/mrm.26772
79. Sari-Sarraf F, Pomposiello S, Laurent D (2008) Acute impairment of rat renal function by L -NAME as measured using dynamic MRI. MAGMA 21(4):291–297. https://doi.org/10.1007/s10334-008-0130-6
80. Privratsky JR, Wang N, Qi Y, Ren J, Morris BT, Hunting JC, Johnson GA, Crowley SD (2019) Dynamic contrast-enhanced MRI promotes early detection of toxin-induced acute kidney injury. Am J Physiol Renal Physiol 316(2): F351–F359. https://doi.org/10.1152/ajprenal.00416.2018
81. Jiang K, Tang H, Mishra PK, Macura SI, Lerman LO (2017) Measurement of murine single-kidney glomerular filtration rate using dynamic contrast-enhanced MRI. Magn Reson Med 79(6):2935–2943. https://doi.org/10.1002/mrm.26955
82. Zollner FG, Zimmer F, Klotz S, Hoeger S, Schad LR (2014) Renal perfusion in acute kidney injury with DCE-MRI: deconvolution analysis versus two-compartment filtration model. Magn Reson Imaging 32(6):781–785. https://doi.org/10.1016/j.mri.2014.02.014
83. Oostendorp M, de Vries EE, Slenter JM, Peutz-Kootstra CJ, Snoeijs MG, Post MJ, van Heurn LW, Backes WH (2011) MRI of renal oxygenation and function after normothermic ischemia-reperfusion injury. NMR Biomed 24 (2):194–200. https://doi.org/10.1002/nbm.1572
84. Zöllner FG, Zimmer F, Klotz S, Hoeger S, Schad LR (2015) Functional imaging of acute kidney injury at 3 tesla: investigating multiple parameters using DCE-MRI and a two-compartment filtration model. Z Med Phys 25(1):58–65. https://doi.org/10.1016/j.zemedi.2014.01.002
85. Notohamiprodjo M, Kalnins A, Andrassy M, Kolb M, Ehle B, Mueller S, Thomas MN, Werner J, Guba M, Nikolaou K, Andrassy J (2016) Multiparametric functional MRI: a tool to uncover subtle changes following allogeneic renal transplantation. PLoS One 11 (11):e0165532. https://doi.org/10.1371/journal.pone.0165532

Chapter 13

Noninvasive Renal Perfusion Measurement Using Arterial Spin Labeling (ASL) MRI: Basic Concept

Min-Chi Ku, María A. Fernández-Seara, Frank Kober, and Thoralf Niendorf

Abstract

The kidney is a complex organ involved in the excretion of metabolic products as well as the regulation of body fluids, osmolarity, and homeostatic status. These functions are influenced in large part by alterations in the regional distribution of blood flow between the renal cortex and medulla. Renal perfusion is therefore a key determinant of glomerular filtration. Therefore the quantification of regional renal perfusion could provide important insights into renal function and renal (patho)physiology. Arterial spin labeling (ASL) based perfusion MRI techniques, can offer a noninvasive and reproducible way of measuring renal perfusion in animal models. This chapter addresses the basic concept of ASL-MRI.

This chapter is based upon work from the COST Action PARENCHIMA, a community-driven network funded by the European Cooperation in Science and Technology (COST) program of the European Union, which aims to improve the reproducibility and standardization of renal MRI biomarkers. This introduction chapter is complemented by two separate chapters describing the experimental procedure and data analysis.

Key words Magnetic resonance imaging (MRI), Renal, Perfusion, Arterial spin labeling (ASL), Kidney, Mice, Rats

1 Introduction

Kidneys are highly perfused organs in the body as they receive 20–25% blood of the resting cardiac output. High blood flow to the kidneys ensures adequate delivery of plasma to be filtered by the glomeruli, a physiological process necessary for the regulation of homeostasis. Therefore, the changes in renal blood flow (RBF) will also change the glomerular filtration rate (GFR) and, consequently, the volume and composition of body fluids. Thus, even a slight change in renal perfusion that exceeds renal autoregulation can have a significant impact on the kidney function. The complex interaction between RBF, renal oxygen delivery, renal oxygen consumption, and GFR made measuring of renal perfusion an

Andreas Pohlmann and Thoralf Niendorf (eds.), *Preclinical MRI of the Kidney: Methods and Protocols*, Methods in Molecular Biology, vol. 2216, https://doi.org/10.1007/978-1-0716-0978-1_13,

attractive target to understand the regulation and homeostasis of renal tissue in health and disease.

Renal perfusion, defined as the blood flow that passes through a unit mass of renal tissue within a given time (mL/min/g) that is also a key determinant of glomerular filtration. A unique aspect of the renal perfusion is that the blood flow is regionally specific. Due to the lack of a reliable technic which allowed to precisely measure the regional RBF, it is roughly estimated that 80–85% of the total renal blood flow supplies renal cortex, 10–15% outer medulla and only 1–5% inner medulla [1].The cortical blood flow is tightly regulated by well-documented mechanisms. Conversely, medullary blood flow regulation is less understood and difficult to measure [2]. The capillary density and surface area is higher in the medulla than in the cortex at least in the mice. It is very challenging to measure the medulla renal perfusion because of the complexity of the microcirculation and its tight connection of arterioles from the cortex. Although inner renal medulla receives less than 1–5% of the total renal blood flow, but changes in this region can still have major effect on electros and water homeostasis and control of arterial blood pressure [3]. Regardless, to understand the physiological regulation of renal perfusion and the role of its dysregulation in separate regions will require methods that allow quantification of renal perfusion both at the whole organ level and at the local tissue level. Most of the imaging techniques for assessing renal perfusion that have been used in humans and animals have significant limitations (Table 1) and by far there is still no gold-standard technique available. For instance, renal perfusion can be measured with dynamic contrast-enhanced MRI (DCE-MRI). However, the major drawback of DCE-MRI is the involvement of contrast media for the measurement of perfusion. The contrast media are easily filtered by renal glomeruli and hence it is difficult to obtain absolute quantification. Other known side effects, such as the development of nephrogenic systemic fibrosis, also limit their application to patients with renal deficits.

A noninvasive, practical, robust, and reproducible method to measure renal perfusion is of great interest but remains elusive, both in the clinic and basic research. The Arterial spin labeling (ASL) MRI technique introduced three decades ago for quantifying tissue perfusion [6, 7], is potentially the only available technique to meet all these needs. ASL is a MRI method generating endogenous contrast specifically related to capillary blood flow. It is therefore free of exogenous contrast media. By magnetically labeling arterial blood proton spins with inversion or saturation as a freely diffusible endogenous tracer, ASL allows for the measurement of RBF. Originally developed for measuring cerebral perfusion, the use of endogenous blood signal to obtain tissue perfusion information is particularly relevant for multiple and longitudinal imaging of patients. This attribute is also important for preclinical

Table 1
Overview of methods for monitoring renal blood flow [4, 5]

Invasive	Noninvasive
Scintigraphy	Doppler ultrasound
Positron-emission tomography (PET)	Cine phase-contrast MRI
Multidetector computed tomography (CT)	Arterial spin labeling (ASL) MRI
Contrast-enhanced ultrasound (Sonography)	
Dynamic contrast-enhanced MRI (DCE-MRI)	

imaging applications, as multiple tail-vein injections and/or catheterizations can cause local inflammation and necrosis resulting in reduced access to veins. The mature and reliable animal models combined with reproducible imaging techniques are an indispensable part of scientifically designed kidney disease studies, and play an important role in resolving the general bottleneck in renal disease treatment that is usually delayed due to difficulties in imaging disease progression.

The ASL approach has been rigorously studied in various preclinical applications including correlating the degree of acute rejection and renal cortical blood flow in rat allograft model [8], comparison of imaging results with histologic examination in ischemia-induced acute kidney injury (AKI) [9], early detection of antiangiogenic treatment responses in a mouse xenograft tumor model [10] and validation of the pathophysiological process of contrast-induced acute kidney injury in rats [11]. In this chapter, we address the basic concept and the developments of renal ASL with the emphasis on kidney disease models in rodents.

This introduction chapter is complemented by two separate chapters describing the experimental procedure and data analysis, which are part of this book.

This chapter is part of the book Pohlmann A, Niendorf T (eds) (2020) Preclinical MRI of the Kidney—Methods and Protocols. Springer, New York.

2 Measurement Concept

2.1 Basic Concept of ASL-MRI

ASL provides quantitative parametric images of tissue perfusion. It uses a modified proton magnetization of arterial blood as an endogenous, freely diffusible contrast medium which determines the delivery rate of oxygen and nutrients to the capillary bed and is expressed as the volume of blood traveling through a gram of tissue per minute (mL 100 g^{-1} min^{-1}). The basic ASL experiment collects two image types, referred to as the "label" (or tag) and "control" (or nonlabeled) image respectively. The label is applied

Fig. 1 Left: All ASL pulse sequences consist of two modules: a preparation module to magnetically label flowing blood, and a readout module to generate paired images. Right: Schematic showing different labeling modules. A single or a train of radiofrequency pulse for labeling followed by a postlabel delay before the image is acquired within one TR.

using radiofrequency (RF) pulses to alter the longitudinal magnetization of protons in the arterial blood before it enters the desired imaging plane, and an image is collected after a time delay. The control image is acquired at the same time delay without labeling the arterial blood protons. Provided that the inverted magnetization of the inflowing blood is the only difference between the control and label images, a simple subtraction of the label from the control image yields a perfusion-weighted image in which signal intensity is proportional to perfusion. All ASL pulse sequences consist of two components: (1) a preparation module to magnetically label inflowing blood, and (2) an imaging readout scheme to generate paired images of the target tissue under "control" and "tagged" conditions. ASL methods may be classified as to how each of these modules is constructed (Fig. 1).

2.2 Labeling Methods and Strategies for Kidney perfusion Measurement in Rodents

There are two main labeling strategies that have been developed: pulsed ASL (PASL) [12] and continuous ASL (CASL) (Fig. 1, left). Pulsed and continuous ASL labeling methods differ fundamentally in both the spatial extent and the duration of the labeling (Fig. 1, right), and these differences give rise to the strengths and weaknesses of each approach [13]. PASL uses a single short pulse or a limited number of pulses, to invert a thick slab of arterial water spins. It can be further divided into those that label spins asymmetrically with respect to the plane of imaging (Signal Targeting by Alternating Radiofrequency pulses; **STAR** [14] and Proximal Inversion with Control of Off-Resonance Effects; **PICORE** [15] or symmetrically (Flow-sensitive Alternating Inversion Recovery; **FAIR**) [16]. In contrast, CASL techniques use a continuous radiofrequency wave in a plane upstream of the imaging volume for generating a flow-driven inversion of arterial blood flowing through that plane. Later, a modified form called pseudo-continuous arterial spin labeling (pCASL) has been developed, that uses a long series of short RF-pulses together with a strong slice-selection gradient, also resulting in a flow-driven inversion of upstream blood proton spins. pCASL thus combines favorable features of CASL (high signal-to-noise) with those of PASL

Table 2
Overview of renal ASL studies in rodents

Reference	Scanner	ASL labeling	Image readout	Animal model
[9]	7.0 T (Bruker)	FAIR	EPI	Mouse
[10, 17]	7.0 T (Bruker)	FAIR	SE-EPI	Mouse
[18]	11.5 T (Bruker)	FAIR	SE-EPI	Mouse
[19]	11.5 T (Bruker)	pCASL	bSSFP	Mouse
[20]	7.0 T (Bruker)	FAIR	bSSFP	Mouse
[21]	3.0 T clinical whole body (Siemens)	FAIR	bSSFP	Rat
[22]	3.0 T clinical whole body (Siemens)	FAIR	bSSFP	Rat
[23]	3.0 T clinical whole body (Siemens)	FAIR	bSSFP	Rat

(lower energy deposition). Today most commercially available ASL products are based on pCASL or a PASL variant. Table 2 shows examples of preclinical studies using ASL for measuring RBF in animal models and list each of the labeling and readout methods.

2.2.1 Pulsed ASL (PASL)

The PASL variant (FAIR) is the major method used for measuring renal perfusion in rodents due to its ease of implementation. FAIR uses a single long-duration RF pulse which is applied to invert the arterial magnetization as blood flows through the labeling plane while a gradient is applied in the direction of arterial flow. In FAIR ASL the magnetization is usually prepared using a global inversion which is referred to as the "labeling" and a slice selective inversion which is referred to as "control." The sequence begins with a spatially selective inversion pulse limited to a small region in and around the imaged slice. In the standard labeling scheme the selective inversion slice (control) is in the same plane as the imaging slice with a thickness of 1.5–5 times the thickness of the imaging slice. The inversion pulse is usually slightly wider than the imaging slice to minimize artifacts and ensure uniform inversion. For the "labeling," the same inversion pulse is applied but without the slice-selection gradient. This causes an inversion of spins within the entire sensitive volume of the RF coil (Fig. 2a). By subtracting the control image from the labeling image, a perfusion-weighted image (PWI) is formed, which with the appropriate modeling can be quantified using a perfusion map in units of mL/100 g/min. In various preclinical MRI situations, for instance with dedicated small brain birdcage transmit/receive (TX/RX) resonators, the transmit coil used may not be long enough to provide a sufficiently global inversion for FAIR perfusion measurements.

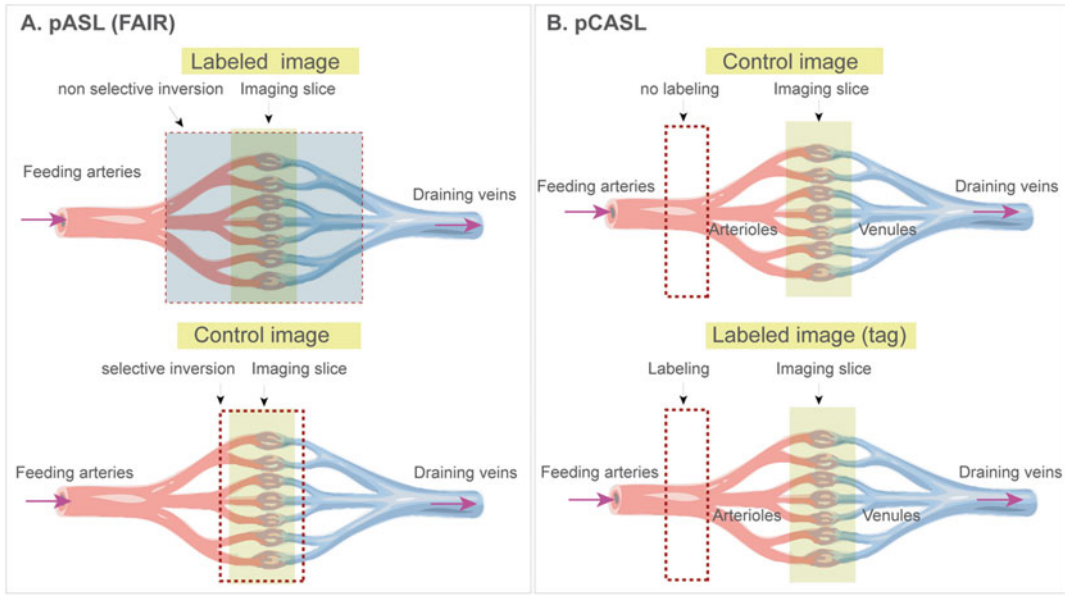

Fig. 2 Basic principle of arterial spin labeling (ASL) acquisition. It consists of a differential technique during which two acquisitions are carried out: one with the labeling of arterial protons (label image) and a control image. Arterial blood is labelled by inverting its magnetization. After an inflow time (inversion time), which allows the labeled blood to flow into the tissue of interest, an image is acquired with an appropriate readout sequence. (**a**) FAIR uses a nonselective inversion pulse for the labeled images that becomes selective with the addition of a slice selection gradient for the control. (**b**) The magnetic labeling of arterial protons is carried out upstream from the volume of interest, by radiofrequency pulses. The labeled protons then migrate via the arterial vessels toward the tissue where they pass from the capillary compartment to the extravascular compartment (example shown: pCASL)

2.2.2 Continuous ASL (CASL) and Pseudo-Continuous ASL (pCASL)

CASL uses a continuous flow-driven radiofrequency inversion of blood upstream of the imaging volume. The radiofrequency wave is transmitted either by a dedicated, separate labeling coil or by the volume transmit coil that is also used for imaging. The latter approach has the advantage that no special hardware components are required but the disadvantage of depositing high amounts of RF energy leading to magnetization transfer contrast that has to be properly corrected. One drawback of CASL labeling approach is the consequently high transmitter duty-cycle requirement.

The pCASL technique has evolved from the original CASL technique in both, brain and kidney applications [24]. pCASL uses series of short and high-power RF and gradient pulses instead of the long RF pulses used in CASL to generate a flow-driven inversion. Compared to FAIR, pseudo-continuous ASL (pCASL) provides significant advantages such as increased SNR and better definition of the labeling bolus. FAIR (pulsed ASL) may be attractive for renal imaging because it can label closer to the tissue, but pCASL offers the potential advantage of high SNR of the kidneys

and the whole abdomen, which would be desirable in some specific applications (e.g., metastatic). An earlier study compared the performances of FAIR and pCASL in terms of sensitivity, absolute quantification, reproducibility, and flexibility of implementation using healthy mice [18]. It was reported that the application of pCASL at 11.75 T scanner had higher sensitivity compared to FAIR (> þ20%). Finally, since pCASL can be straightforwardly used in multislice mode and in any imaging orientation, it may be considered as a method of choice for mouse kidney perfusion studies.

2.3 Imaging Readout

A typical ASL MRI acquisition combines an ASL magnetization preparation module (labeling methods) followed by a subsequent rapid imaging module (readouts) to capture the blood flow–weighted contrast. These two aspects of the acquisition are independent of each other. It is important to note that the majority of the ASL imaging developments has focused on the optimization of preparation module of the ASL acquisition [20].

An important prerequisite for successful kidney imaging is the ability to get fast imaging to limit the sensitivity to motion [19]. As such, ASL has been implemented with a wide variety of fast image readout techniques, which in turn can be optimized according to a specific application. The fast image readout techniques can be broadly classified as two-dimensional (2D) or 3D acquisition schemes. Whereas 3D readouts are generally recommended for brain ASL, a consensus of the optimal readout module for renal applications has yet to be established. This consideration has been recently achieved to recommend a 2D readout in humans (unpublished by PARENCHIMA ASL expert panel).

With respect to 2D readouts, to determine the optimal readout for renal ASL, a number of factors should be considered. The optimal readout should have a short echo time (TE) in order to provide the highest image signal-to-noise ratio (SNR), and to reduce the amount of signal dephasing and distortion. At longer TEs, the short tissue intrinsic T_2 and T_2^* in the abdomen leads to rapid signal drop and the loss of perfusion signal. The ideal readout should be collected in a short shot length to enable multiple slices through the kidney to be acquired prior to the decay of the ASL label, thus enabling whole-kidney perfusion assessment [25]. Many ASL MRI studies have utilized either echo-planar imaging (EPI) or true fast imaging with steady-state free precession (bSSFP; True FISP) readouts [20] though the readout of ASL can be measured with any method. Both EPI and bSSFP readouts are prone to off-resonance artifacts on high field MRI scanners [20] where the majority of animal studies are done by using such high field or ultra-high field (> = 7 T) scanners. Specifically, B0 inhomogeneity results in increased distortion / ghosting and banding artifacts from EPI and True FISP imaging readouts. These artifacts are particularly problematic for abdominal imaging applications such

as kidney where cardiac and respiratory motions well as adipose tissue can make precise shimming difficult. In addition, the increase in T1 relaxation times which is proportional with the field strength can result in spoiled gradient echo images with a lower signal-to-noise ratio (SNR) relative to these other imaging readouts. The low SNR is specifically problematic for ASL MRI techniques as the differential blood flow signal is typically less than 10% of the mean tissue signal.

Though the optimization of EPI acquisitions allow for whole-kidney coverage but nevertheless provide sub-optimal and slice-dependent perfusion-weighted SNR and is susceptible to off-resonance conditions mentioned above. There is an urgent need to develop a rapid and robust ASL MRI imaging readout that is balanced on blood flow labeling from the ASL labeling module and also avoid B0 inhomogeneities and motion artifacts on high field preclinical MRI scanners.

While several groups independently optimize the bSSFP image readout and shown the advantage over EPI readouts [25], more advanced methods now provide alternative readouts, such as 3D gradient and spin echo (GRASE) [26, 27]. 3D GRASE has superior SNR compared to 2D acquisitions. An alternative to 3D GRASE is 3D rapid acquisition with relaxation enhancement (RARE) combined with a spiral readout trajectory (shorter echo times and superior SNR), but can introduce through-plane blurring due to long readout times.

3 Overview of Applications

3.1 ASL for Measuring Kidney Perfusion in Animal Models

The encouraging results using ASL for measuring human renal perfusion mandate further validation of renal ASL measurements using animal models. For example, in vivo interventional swine model has been used with FAIR-ASL technique to track cortical perfusion changes during pharmacologic and physiologic alterations in renal blood flow [28]. For measuring renal hemodynamics and oxygenation in X-ray contrast agent induced acute kidney injury (CIAKI), a rat model was used. Rats were injected with contrast media and followed by ASL measurements [29]. Other models, for instance ischemia induced AKI in mice, was done by transient unilateral clamping of the renal pedicle for either 35 min for moderate AKI or 45 min for severe AKI. Using ASL, renal perfusion impairment was found more pronounced in severe compared to moderate AKI, with severe AKI causing a 33% reduction in renal perfusion [9]. In addition, ASL can be useful for longitudinal assessment of renal perfusion impairment due to acute and chronic renal allograft rejection in translational mouse models [30]. By combining with the histological assessment, perfusion impairment can be validated and revealed its relationship to the severity of

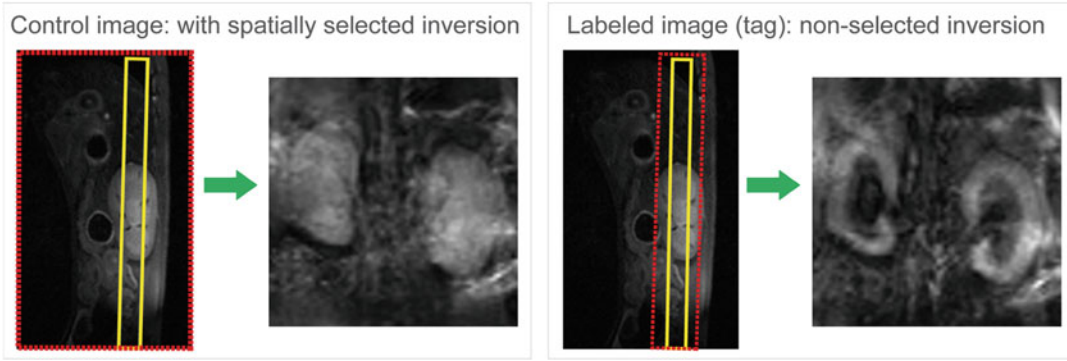

Fig. 3 An example of arterial spin labeling (ASL) acquisition using FAIR-EPI

vascular changes and renal damage. Other applications such as exploring the renoprotective efficacy of drug treatment in ischemia-induced AKI or in renal allograft recipients revealed that the renoprotective effect of the drug was associated with improved renal perfusion [22]. Thus, noninvasive perfusion imaging might provide insights into the underlying disease mechanisms in acute and chronic renal allograft rejection and might facilitate monitoring of novel treatment strategies. Similar approach can be applied to monitor kidney function of most common kidney diseases, such as CIAKI, diabetic nephropathy, and kidney transplant. In addition, ASL techniques can also be used to monitor the therapeutic responses of treatments to common renal hypoxia disease. Figure 3 is an example of ASL measurement using FAIR for labeling and EPI for image readout in a healthy mouse. Table 2 lists all examples of preclinical studies using ASL for measuring RBF in rodent models.

Acknowledgments

This work was funded in part (Thoralf Niendorf, Sonia Waiczies, Andreas Pohlmann, and Joao Periquito) by the German Research Foundation (Gefoerdert durch die Deutsche Forschungsgemeinschaft (DFG), Projektnummer 394046635, SFB 1365, RENOPROTECTION. Funded by the Deutsche Forschungsgemeinschaft (DFG, German Research Foundation), Project number 394046635, SFB 1365, RENOPROTECTION).
This chapter is based upon work from COST Action PARENCHIMA, supported by European Cooperation in Science and Technology (COST). COST (www.cost.eu) is a funding agency for research and innovation networks. COST Actions help connect research initiatives across Europe and enable scientists to enrich their ideas by sharing them with their peers. This boosts their research, career, and innovation.
PARENCHIMA (renalmri.org) is a community-driven Action in the COST program of the European Union, which unites more

than 200 experts in renal MRI from 30 countries with the aim to improve the reproducibility and standardization of renal MRI biomarkers.

References

1. Wentland AL, Artz NS, Fain SB, Grist TM, Djamali A, Sadowski EA (2012) MR measures of renal perfusion, oxygen bioavailability and total renal blood flow in a porcine model: non-invasive regional assessment of renal function. Nephrol Dial Transplant 27:128–135
2. Kennedy-Lydon TM, Crawford C, Wildman SS, Peppiatt-Wildman CM (2013) Renal pericytes: regulators of medullary blood flow. Acta Physiol 207:212–225
3. Cowley AW Jr, Mattson DL, Lu S, Roman RJ (1995) The renal medulla and hypertension. Hypertension 25:663–673
4. Schneider AG, Goodwin MD, Bellomo R (2013) Measurement of kidney perfusion in critically ill patients. Crit Care 17:220
5. Lemoine S, Papillard M, Belloi A, Rognant N, Fouque D, Laville M, Rouviere O, Juillard L (2011) Renal perfusion: noninvasive measurement with multidetector CT versus fluorescent microspheres in a pig model. Radiology 260:414–420
6. Detre JA, Leigh JS, Williams DS, Koretsky AP (1992) Perfusion imaging. Magn Reson Med 23:37–45
7. Williams DS, Detre JA, Leigh JS, Koretsky AP (1992) Magnetic resonance imaging of perfusion using spin inversion of arterial water. Proc Natl Acad Sci U S A 89:212–216
8. Wang JJ, Hendrich KS, Jackson EK, Ildstad ST, Williams DS, Ho C (1998) Perfusion quantitation in transplanted rat kidney by MRI with arterial spin labeling. Kidney Int 53:1783–1791
9. Hueper K, Gutberlet M, Rong S, Hartung D, Mengel M, Lu X, Haller H, Wacker F, Meier M, Gueler F (2014) Acute kidney injury: arterial spin labeling to monitor renal perfusion impairment in mice-comparison with histopathologic results and renal function. Radiology 270:117–124
10. Rajendran R, Huang W, Tang AM, Liang JM, Choo S, Reese T, Hentze H, van Boxtel S, Cliffe A, Rogers K, Henry B, Chuang KH (2014) Early detection of antiangiogenic treatment responses in a mouse xenograft tumor model using quantitative perfusion MRI. Cancer Med 3:47–60
11. Liang L, Chen WB, Chan KW, Li YG, Zhang B, Liang CH, Liu GS, Zhang SX (2016) Using intravoxel incoherent motion MR imaging to study the renal pathophysiological process of contrast-induced acute kidney injury in rats: comparison with conventional DWI and arterial spin labelling. Eur Radiol 26:1597–1605
12. Kwong KK, Belliveau JW, Chesler DA, Goldberg IE, Weisskoff RM, Poncelet BP, Kennedy DN, Hoppel BE, Cohen MS, Turner R et al (1992) Dynamic magnetic resonance imaging of human brain activity during primary sensory stimulation. Proc Natl Acad Sci U S A 89:5675–5679
13. Nery F, Gordon I, Thomas DL (2018) Non-invasive renal perfusion imaging using arterial spin labeling MRI: challenges and opportunities. Diagnostics 8:2
14. Edelman RR, Siewert B, Adamis M, Gaa J, Laub G, Wielopolski P (1994) Signal targeting with alternating radiofrequency (STAR) sequences: application to MR angiography. Magn Reson Med 31:233–238
15. Wong EC, Buxton RB, Frank LR (1997) Implementation of quantitative perfusion imaging techniques for functional brain mapping using pulsed arterial spin labeling. NMR Biomed 10:237–249
16. Kim SG (1995) Quantification of relative cerebral blood flow change by flow-sensitive alternating inversion recovery (FAIR) technique: application to functional mapping. Magn Reson Med 34:293–301
17. Rajendran R, Lew SK, Yong CX, Tan J, Wang DJ, Chuang KH (2013) Quantitative mouse renal perfusion using arterial spin labeling. NMR Biomed 26:1225–1232
18. Duhamel G, Prevost V, Girard OM, Callot V, Cozzone PJ (2014) High-resolution mouse kidney perfusion imaging by pseudo-continuous arterial spin labeling at 11.75T. Magn Reson Med 71:1186–1196
19. Prevost VH, Girard OM, Callot V, Cozzone PJ, Duhamel G (2015) Fast imaging strategies for mouse kidney perfusion measurement with pseudocontinuous arterial spin labeling (pCASL) at ultra high magnetic field (11.75 tesla). J Magn Reson Imaging 42:999–1008
20. Gao Y, Goodnough CL, Erokwu BO, Farr GW, Darrah R, Lu L, Dell KM, Yu X, Flask CA (2014) Arterial spin labeling-fast imaging with steady-state free precession (ASL-FISP): a

rapid and quantitative perfusion technique for high-field MRI. NMR Biomed 27:996–1004

21. Zimmer F, Zollner FG, Hoeger S, Klotz S, Tsagogiorgas C, Kramer BK, Schad LR (2013) Quantitative renal perfusion measurements in a rat model of acute kidney injury at 3T: testing inter- and intramethodical significance of ASL and DCE-MRI. PLoS One 8: e53849
22. Klotz S, Pallavi P, Tsagogiorgas C, Zimmer F, Zollner FG, Binzen U, Greffrath W, Treede RD, Walter J, Harmsen MC, Kramer BK, Hafner M, Yard BA, Hoeger S (2016) N-octanoyl dopamine treatment exerts renoprotective properties in acute kidney injury but not in renal allograft recipients. Nephrol Dial Transplant 31:564–573
23. Tan H, Thacker J, Franklin T, Prasad PV (2015) Sensitivity of arterial spin labeling perfusion MRI to pharmacologically induced perfusion changes in rat kidneys. J Magn Reson Imaging 41:1124–1128
24. Roberts DA, Detre JA, Bolinger L, Insko EK, Lenkinski RE, Pentecost MJ, Leigh JS Jr (1995) Renal perfusion in humans: MR imaging with spin tagging of arterial water. Radiology 196:281–286
25. Buchanan CE, Cox EF, Francis ST (2018) Evaluation of 2D imaging schemes for pulsed arterial spin labeling of the human kidney cortex. Diagnostics 8:43
26. Robson PM, Madhuranthakam AJ, Smith MP, Sun MR, Dai W, Rofsky NM, Pedrosa I, Alsop DC (2016) Volumetric arterial spin-labeled perfusion imaging of the kidneys with a three-dimensional fast spin echo acquisition. Acad Radiol 23:144–154
27. Cutajar M, Thomas DL, Banks T, Clark CA, Golay X, Gordon I (2012) Repeatability of renal arterial spin labelling MRI in healthy subjects. MAGMA 25:145–153
28. Artz NS, Wentland AL, Sadowski EA, Djamali A, Grist TM, Seo S, Fain SB (2011) Comparing kidney perfusion using noncontrast arterial spin labeling MRI and microsphere methods in an interventional swine model. Investig Radiol 46:124–131
29. Chen WB, Liang L, Zhang B, Liu CL, Liu HJ, Luo HY, Zeng QX, Liang CH, Liu GS, Zhang SX (2015) To evaluate the damage of renal function in CIAKI rats at 3T: using ASL and BOLD MRI. Biomed Res Int 2015:593060
30. Hueper K, Schmidbauer M, Thorenz A, Brasen JH, Gutberlet M, Mengel M, Hartung D, Chen R, Meier M, Haller H, Wacker F, Rong S, Gueler F (2017) Longitudinal evaluation of perfusion changes in acute and chronic renal allograft rejection using arterial spin labeling in translational mouse models. J Magn Reson Imaging 46:1664–1672

Chapter 14

Renal pH Imaging Using Chemical Exchange Saturation Transfer (CEST) MRI: Basic Concept

Dario Livio Longo, Pietro Irrera, Lorena Consolino, Phillip Zhe Sun, and Michael T. McMahon

Abstract

Magnetic Resonance Imaging (MRI) has been actively explored in the last several decades for assessing renal function by providing several physiological information, including glomerular filtration rate, renal plasma flow, tissue oxygenation and water diffusion. Within MRI, the developing field of chemical exchange saturation transfer (CEST) has potential to provide further functional information for diagnosing kidney diseases. Both endogenous produced molecules as well as exogenously administered CEST agents have been exploited for providing functional information related to kidney diseases in preclinical studies. In particular, CEST MRI has been exploited for assessing the acid-base homeostasis in the kidney and for monitoring pH changes in several disease models. This review summarizes several CEST MRI procedures for assessing kidney functionality and pH, for monitoring renal pH changes in different kidney injury models and for evaluating renal allograft rejection.

This chapter is based upon work from the COST Action PARENCHIMA, a community-driven network funded by the European Cooperation in Science and Technology (COST) program of the European Union, which aims to improve the reproducibility and standardization of renal MRI biomarkers. This introduction chapter is complemented by two separate chapters describing the experimental procedure and data analysis.

Key words Magnetic resonance imaging (MRI), Kidney, Mice, Rats, pH, Iopamidol, Chemical exchange saturation transfer (CEST), Acute kidney injury, Ischemia–reperfusion injury, Renal damage

1 Introduction

Renal dysfunction is recognized as a significant health problem originating from a variety of causes leading to acute or chronic kidney diseases. Predisposition to acute kidney injury and premature mortality are frequent outcomes for chronic kidney diseases [1]. Moreover, according to the Global Burden of Disease 2013 study, the age-standardized death rates for chronic kidney diseases showed one of the highest increases in the last two decades [2]. Therefore, reliable and early diagnosis of acute and chronic kidney diseases is needed to preserve renal functionality and

Andreas Pohlmann and Thoralf Niendorf (eds.), *Preclinical MRI of the Kidney: Methods and Protocols*, Methods in Molecular Biology, vol. 2216, https://doi.org/10.1007/978-1-0716-0978-1_14,

improve patients' outcome. Despite these premises, current clinical evaluation of renal function is still based on measurement of serum creatinine, which is well known to have several limitations. In fact, an elevated serum creatinine concentration is only discovered at late stages of the disease when renal functionality is already compromised. Therefore, novel noninvasive imaging approaches are needed for a more accurate and early diagnosis of renal physiology. Magnetic resonance imaging (MRI) has been exploited for tissue anatomic imaging, owing to the high spatial resolution and lack of ionizing radiation. In research, novel MRI techniques have been investigated for assessing multiple functional parameters of the kidneys, including perfusion, filtration, oxygenation and tissue elasticity [3–11]. Several reviews covering the role of these MRI approaches for assessing renal functionality have been published [12–15]. This additional information should enable a better characterization of acute and chronic kidney diseases in comparison to standard urine and serum-based assays.

Recently, Chemical Exchange Saturation Transfer (CEST) MRI has emerged as a novel approach for functional and molecular imaging with great promise for clinical translation [16–18]. In addition, CEST MRI pH imaging has emerged as a valuable approach for assessing extracellular pH values in several tissues, including kidneys and tumors, providing the highest accuracy and spatial resolution achievable so far [19]. Owing to the key role of the kidneys in maintaining the acid-base homeostasis, CEST MRI pH mapping has emerged as a novel and promising approach in monitoring kidney functionality.

In this chapter, we will address the basic concept and the developments of renal CEST pH imaging with the emphasis on kidney disease models in rodents.

This introduction chapter is complemented by two separate chapters describing the experimental procedure and data analysis, which are part of this book.

This chapter is part of the book Pohlmann A, Niendorf T (eds) (2020) Preclinical MRI of the Kidney—Methods and Protocols. Springer, New York.

2 Measurement Concept

2.1 Basic Concept of Chemical Exchange Saturation Transfer (CEST) Imaging

CEST is a new technique that enables the indirect detection of molecules possessing mobile protons in exchange with water [20]. Because of this, CEST makes MRI sensitive to endogenous or exogenous molecules that possess suitable protons [21–32]. The generation of contrast is based on a selective irradiation with a radiofrequency pulse at the specific absorption frequency of the exchanging proton, followed by a subsequent transfer, due to chemical exchange with bulk water, of the saturated signal. Upon the application of a long saturation RF (radiofrequency) pulse, the

water signal decreases, allowing the amplification of the labeled protons from the molecule to water. As a consequence, low concentration molecules can be specifically and indirectly detected, owing to the frequency selective irradiation of their mobile proton pool(s) [33–38].

2.2 CEST Contrast Agents for Imaging Kidneys and Mapping pH

Several classes of CEST contrast agents can be used as pH responsive agents and exploited for in vivo experiments.

2.2.1 Diamagnetic CEST Agents

Several molecules, including natural occurring molecules, possess exchangeable protons that can be indirectly detected within the CEST approach [39]. Most of these labile protons have chemical exchange rates that show a strong pH dependence. Hence differences in CEST contrast can be exploited for assessing the pH of the solution where they are dissolved. Due to the concomitant contribution of concentration and exchange rate to the observed CEST contrast, several approaches have been proposed to rule out the concentration term, based on the ratiometric method, that is, taking the ratio of the observed contrast, providing accurate pH readouts [40, 41]. Most of the pH responsive diamagnetic molecules investigated so far in vivo are iodinated contrast agents used for radiographic procedures, since they have been used in the last 40 years in clinical examinations owing to their high safety profiles [42, 43]. The presence of amide groups in their chemical structure allow them to be exploited as CEST MRI contrast agents, upon selective irradiation of the mobile proton pool [44].

Among the radiographic contrast media, Iopamidol (Isovue®, Bracco Imaging, Italy) (Fig. 1) was the first agent exploited for mapping pH thanks to the presence of two amide groups with different resonance frequencies, at 4.2 ppm and at 5.5 ppm, respectively, that can be selectively irradiated [45–47]. This chemical peculiarity led to the development of a ratiometric approach based on the ratio of the CEST effects at these two frequencies to provide accurate pH measurements. In vitro experiments showed a high pH responsiveness within the physiological range and accurate pH measurements (Fig. 2a, b). Following intravenous administration, it can provide selective contrast at specific frequency offsets and from the ratio of these two parametric maps it is possible to measure renal pH map (Fig. 2c–f). To validate the approach and test the pH-responsiveness of the agent, induced alkalinisation or acidification of urine was obtained in mice upon providing acidic or alkaline drinking water for a week. For control mice, mean pH values calculated for cortex, medulla and calyx regions were: 7.0 ± 0.11; 6.85 ± 0.15 and 6.6 ± 0.20, respectively. In mice drinking acidic water a significant acidification of renal pH values was obtained. Conversely, a marked increase of renal pH values was

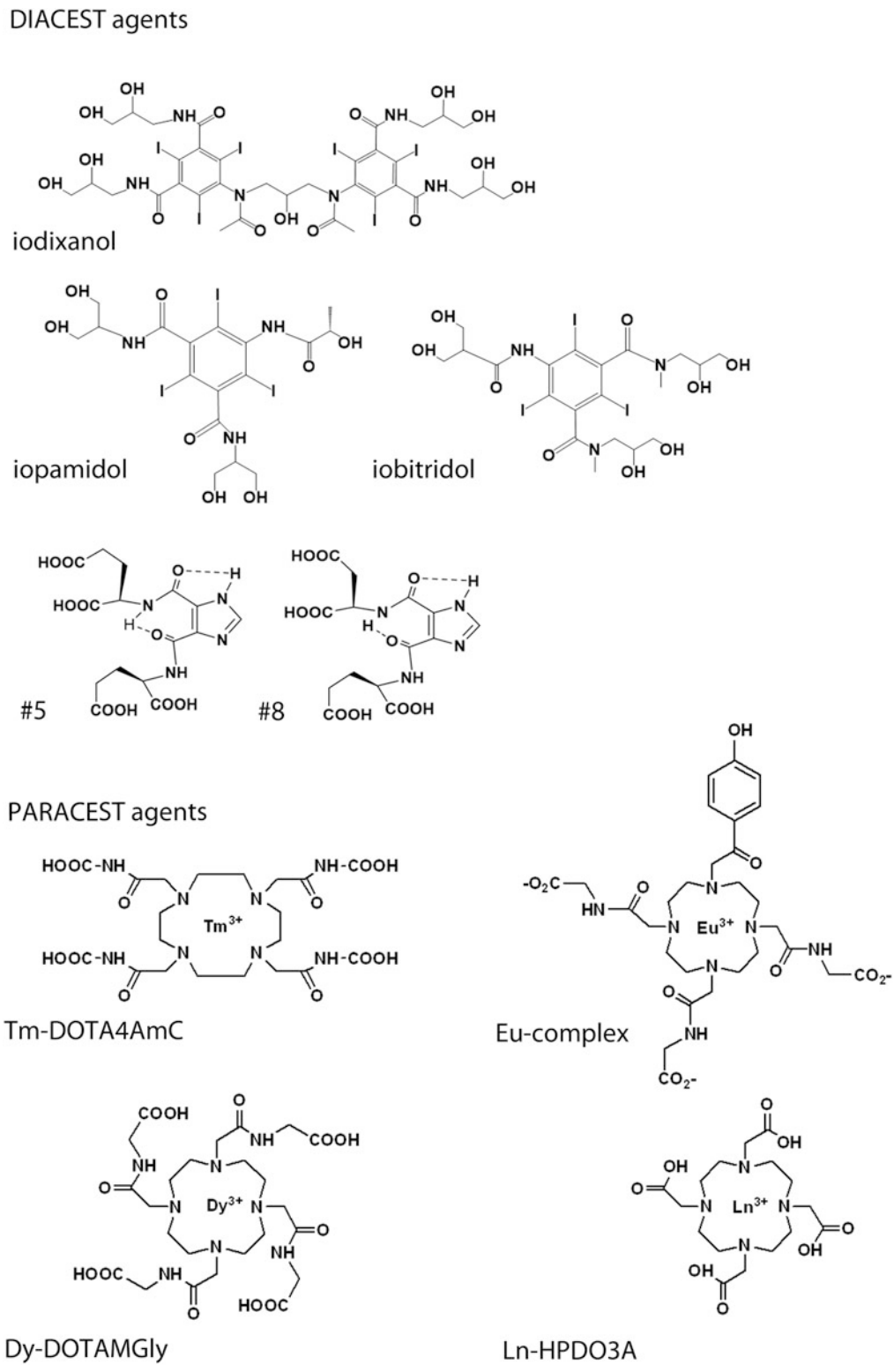

Fig. 1 Chemical structures of the reported pH-responsive CEST agents investigated for renal pH mapping

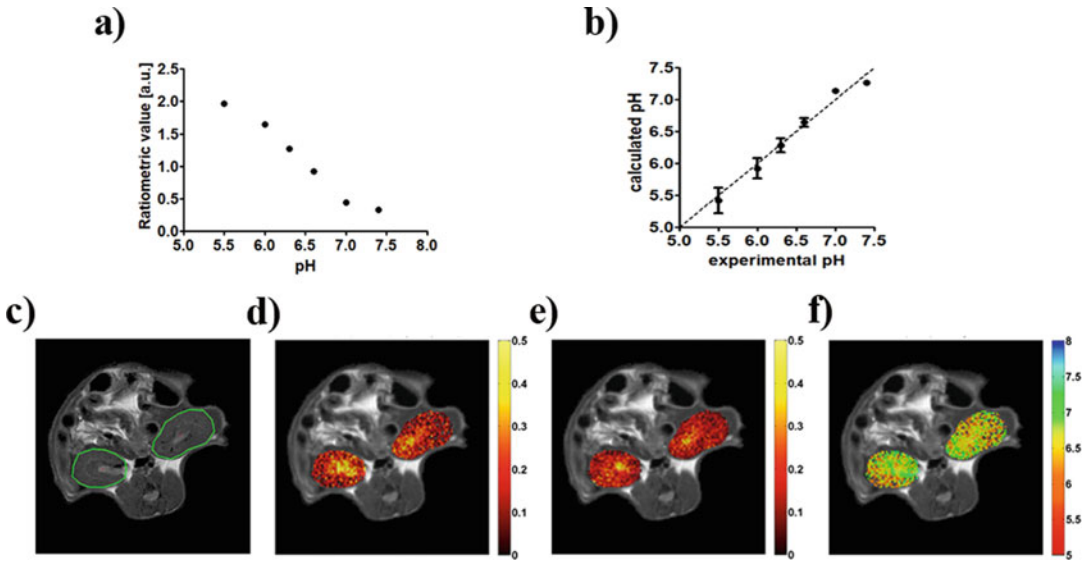

Fig. 2 Iopamidol ratiometric curve obtained from the rations of the CEST contrast upon irradiating at 4.2 and 5.5 ppm, respectively, showing the high pH responsiveness of Iopamidol. Irradiation power levels of 3 μT, Iopamidol 30 mM, 7.05 T, 310 K, irradiation time 5 s (**a**). Calculated pH values obtained by the ratiometric method (Iopamidol 30 mM, 7.05 T, 310 K, irradiation time 5 s, B_1 3 μT) are compared with the values read on the pH-meter (**b**). Representative images of in vivo renal pH mapping showing the anatomical image (**c**) and the CEST contrast parametric maps overlaid to the anatomical image at 4.2 ppm (**d**) and 5.5 ppm (**e**) and the observed pH map (**f**) obtained by ratioing maps (**d**) and (**e**) and using the calibration curve in (**a**) for calculating the pH values. (Adapted with permission from *Magnetic Resonance in Medicine* 2011 (Iopamidol as a responsive MRI-chemical exchange saturation transfer contrast agent for pH mapping of kidneys: in vivo studies in mice at 7 T. Volume: 65, Issue: 1, Pages: 202–211, DOI: https:/doi.org/10.1002/mrm.22608))

observed upon alkaline water administration. Both observations demonstrate the capability to measure in vivo renal pH changes with CEST MRI.

Since the accuracy in measuring pH depends on several factors, including chemical exchange rate, irradiation conditions (saturation power and duration), and main magnetic field, quantification of multisite pH-dependent chemical exchange properties is needed to improve pH accuracy [48]. This characterization of chemical exchange rates and optimal irradiation RF pulses led to the development of an optimized saturation for each single amide proton pools, hence resulting in a higher pH sensitivity. As a result, the capability to measure pH was demonstrated also at magnetic field strengths of 4.7 T, where amide resonances partially overlap. In the study of Wu and coworkers, they demonstrated an improved pH sensitivity, extending the pH detection range from 5.5 to 7.5, with high resolution pH maps of the kidneys in healthy rats (Fig. 3) [49]. More recently, the exploitation of the same ratiometric approach for measuring in vivo pH was also demonstrated at magnetic fields as low as 3 T, which still preserved good pH accuracy [50].

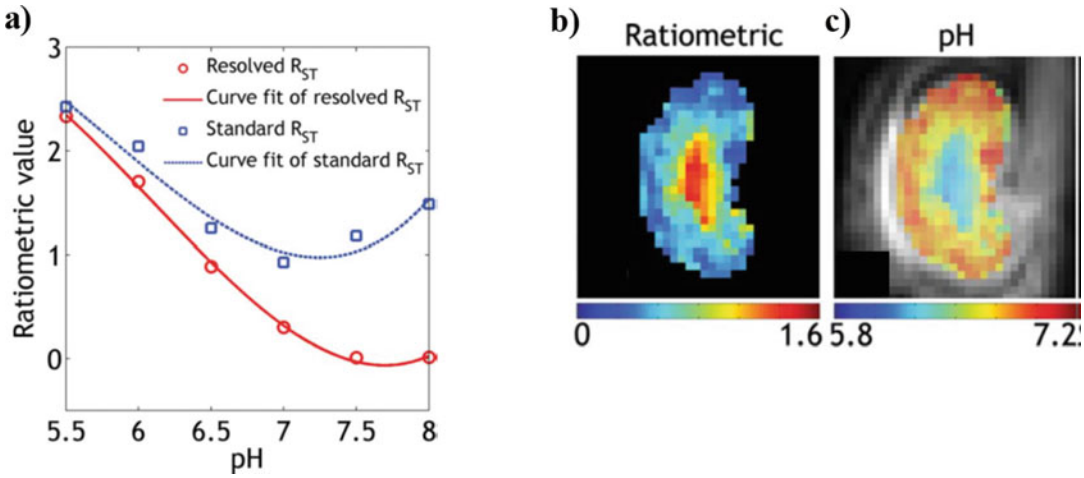

Fig. 3 Extension of pH detection range using the modified ratiometric analysis (red circles) versus the standard ratiometric approach (blue squares) (**a**). Representative in vivo ratiometric map for the proposed approach (**b**). pH map shows the renal pH gradually decreasing from the cortex, medulla to calyx (**c**). Maps are overlaid on the corresponding T_2-weighted image. (Adapted with permission from *Magnetic Resonance in Medicine* 2018 (A generalized ratiometric chemical exchange saturation transfer (CEST) MRI approach for mapping renal pH using Iopamidol, Volume: 79, Issue: 3, Pages: 1553–1558, DOI: https:/doi.org/10.1002/mrm.26817))

Another similar iodinated contrast media, Iopromide (Ultravist®, Bayer Healthcare, Germany), was also demonstrated and compared to Iopamidol for measuring pH, with a pH sensitivity that was not substantially different, although Iopamidol allows for more precise pH measurements [51].

The exploitation of the ratiometric approach requires two distinguishable protons pools on the same molecule, therefore it is limited to a select group of compounds possessing this feature. To overcome this limitation, Longo and Sun proposed a novel approach based on the irradiation of a single pool under different radiofrequency powers [52]. The proposed approach, called ratio of RF power mismatch or RPM, was demonstrated by using Iobitridol (Omnipaque®, GE Healthcare, USA), a radiographic contrast medium possessing only one amide proton pool resonating at 5.5 ppm (Fig. 1). Since the measured CEST contrast is dependent on both pH and irradiation power (B_1), a strong pH dependence was demonstrated by calculating the ratio of the CEST contrast at two different B_1 power levels. In comparison to the conventional ratiometric approach, a good pH accuracy and an even higher pH sensitivity were demonstrated. When investigated in healthy kidneys, the measured pH values upon iobitridol injection strongly correlated with the pH values obtained following iopamidol injection. Recently, to overcome the specific absorption rate (SAR) limitations when using a continuous wave (CW) irradiation of the mobile proton pools, a pulsed ratiometric approach has been

exploited and tested on the Iodixanol (Visipaque®, GE Healthcare, USA) X-ray contrast medium for CEST pH imaging [53].

Diamagnetic contrast agents possess resonances that are close in frequency to the bulk water signal resulting in a reduction of sensitivity (due to an inefficient labeling selectivity) when moving from high to low magnetic fields. Following previous investigations, McMahon and colleagues developed new diamagnetic systems based on the imidazole, salicylate or anthranilate moieties which possess mobile protons shifted very far from the bulk water peak [54–56]. In particular, candidate compounds derived from imidazole-4,5-dicarboxamides (#5 and #8, Fig. 1) show a CEST signal shifted up to 7.8 ppm upfield by exploiting the presence of intramolecular bond shifted hydrogens. Besides the large chemical shift, a good pH sensitivity and a high-water solubility made compound **#5** suitable as a pH sensor and so it has been tested in vivo [57]. pH imaging of the kidneys at 11.7 T resulted in average pH values for the whole kidneys of 6.5 ± 0.1, consistent with renal pH values reported by radiographic contrast agents (Fig. 4).

2.2.2 Paramagnetic CEST Agents

Paramagnetic chemical exchange saturation transfer (paraCEST) agents typically consist of a paramagnetic metal ion and an organic chelate based on a macrocyclic cage due to the high kinetic stability of these metal chelates to prevent the release of the toxic free lanthanide cation [58]. The CEST signal is therefore generated by selective irradiation of the bound water molecule, or of the slowly exchanging ligand protons, such as hydroxyl, amine, or amide groups [59–62]. The main advantage of paraCEST agents in comparison to diamagnetic ones relies in the exceptionally large chemical shifts (MR frequency relative to the water frequency) due to the hypershift contribution of the lanthanide metal ion. This large range of chemical shifts increases the specificity of the exchanging proton pools, hence reducing the adverse contributions of direct saturation and of the endogenous semisolid macromolecular effects [63]. Since the chemical exchange rate of the paraCEST agent can be altered by environmental factors such as pH, changes in CEST amplitudes can be used as well for deriving pH values.

The first demonstration of CEST detection in kidneys using a paraCEST agent (TmDOTA-4AmC, Fig. 1) was provided by Vinogradov et al., showing good detectability in the whole kidney regions [64]. Later on, a Europium paraCEST pH responsive agent (europium(III) DO3A-tris(amide) complex, Fig. 1) was exploited to measure pH in mouse kidneys [65]. Owing to its chemical structure, a quite large frequency shift of the ion-bound water molecule due to the delocalization of negative charge coming from deprotonation of phenolic residue was observed. This shift is pH dependent, therefore an alkalinisation from 6.0 to 7.6 at 298 K leads to a 4 ppm shift in frequencies, from 50.5 to

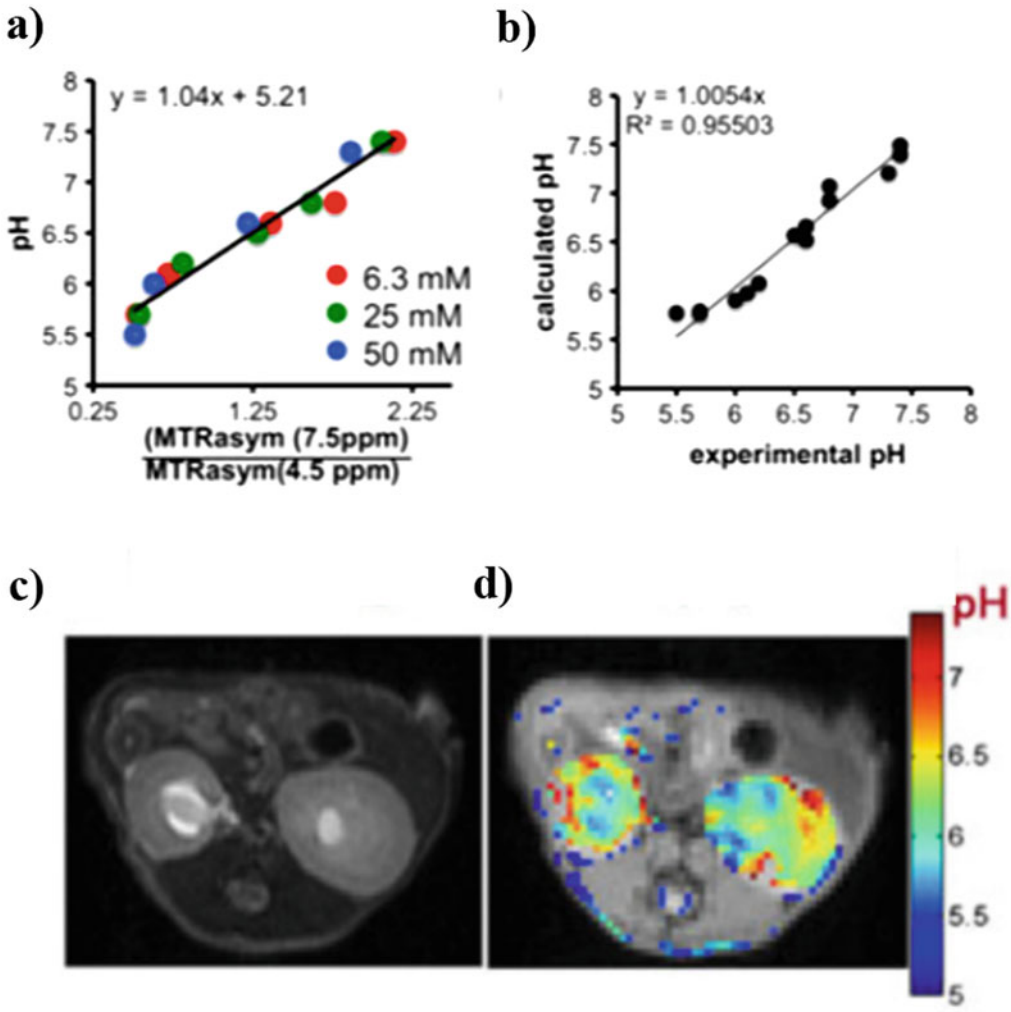

Fig. 4 pH calibration curve of compound #5 (**a**) and calibration plot using all tubes in the phantom showing experimental versus calculated pH (**b**). Experimental conditions: CEST data were obtained at 6.25 mM, 25 mM, or 50 mM concentration, saturation time = 3 s, saturation power = 5.9 μT and 37 °C. pH measurements were made with a precision of ±0.1 unit. T_2-weighted image (**c**) and pH map (**d**) following administration of compound #5. (Adapted with permission from *Contrast Media Molecular Imaging* 2016 (Developing imidazoles as CEST MRI pH sensors, Volume: 11, Issue: 4, Pages: 304–312, DOI: https:/doi.org/10.1002/cmmi.1693))

54.5 ppm, respectively, that can be exploited for assessing pH. By exploiting a 9.4 T MR scanner and ensuring stable temperature homogeneity, in vivo pH measurements were feasible in kidneys upon the administration of a dose of 0.4 mmol/kg [66].

2.3 Imaging Readout

CEST MRI techniques includes continuous wave (CW) or pulsed train RF saturation to prepare the magnetization followed by a fast image readout such as echo planar imaging (EPI), Rapid Imaging with Refocused Echoes (RARE) and/or fast imaging with steady-

state precession (FISP) [45, 67, 68]. More advanced methods now provide more sophisticated sampling schemes, such as 3D radial or spiral acquisitions, but those are currently available only on clinical scanners and not on preclinical scanners, thus limiting CEST acquisition in mice and rats to single slice based approaches [69, 70]. However, recent studies have utilized multislice acquisition schemes on preclinical scanners as well [67, 71, 72].

2.3.1 Rapid Imaging with Refocused Echoes (RARE)

Fast spin echo (FSE) or rapid imaging with refocused echoes (RARE) are commonly used because of the strong SNR (signal-to-noise ratio), high tolerance to B_0 inhomogeneities and moderate to short acquisition times. These methods allow acquisitions of several lines for full sampling the k-space for a single slice within a single TR, which greatly reduces the acquisition time and still preserves SNR. With single shot acquisitions, usually centric encoding is exploited to maximize the SNR. Further reductions in acquisition time can be achieved by adjusting the bandwidth (hence reducing the echo times or the distance between each refocused echo time) or by partial Fourier approaches (i.e., by acquiring only a portion of the k-space).

2.3.2 Fast Imaging with Steady-State Precession (FISP)

FISP readout has been used with CEST MRI that provides robust image readout with little distortion, although more sensitive to B_0 inhomogeneity than RARE. B_0 inhomogeneity might be an important issue particularly for body applications like the kidneys.

2.3.3 Spin-Echo Echo Planar Imaging (EPI)

CEST MRI is often combined with EPI acquisition, which provides fast image readout after a relatively long RF saturation. Whereas both gradient echo and spin echo EPI have been used, SE EPI is often preferred for body application because it is less susceptible to mild magnetic field inhomogeneity distortions that are common in body applications. The use of an EPI readout also enables multislice acquisitions in reasonable times.

3 Overview of Applications

CEST imaging has been exploited for assessing renal pH values in healthy and in several models of renal damage, including either bilateral or unilateral acute kidney injury models. Both endogenous CEST approaches and exogenous CEST approaches have been proposed and validated in vivo.

3.1 Endogenous CEST Methods for Assessing Renal Diseases

Since diabetic nephropathies (DNs) are associated with changes in renal metabolites, the utility of CEST MRI to detect changes in glucose/glycogen hydroxylic protons was investigated in murine models of diabetic nephropathies. The study was conducted longitudinally from 8 to 24 weeks on two groups of diabetic mice and on nondiabetic mice as control. Based on the variation of glucose/

glycogen composition and the consequent CEST effects measured in kidney regions, a significantly increased CEST of hydroxyl metabolites was observed in diabetic mice during the progression of DN [73].

3.2 CEST pH Imaging for Assessing Renal Diseases

Most of the studies reported so far have exploited the pH-responsiveness of Iopamidol for investigating the changes in pH homeostasis following renal injuries. In one of these studies, the pH evolution in an acute kidney injury model induced by intramuscular glycerol injection and consequent rhabdomyolysis was monitored [74]. Renal pH maps acquired at 1, 3, 7, 14, 21 days after the injury reported a marked increase of pH values during the damage evolution up to 3–7 days, followed by recovery of pH toward baseline values at 14 and 21 days. These results were in good agreement with morphological and Blood Urean Nitrogen (BUN) quantification supporting this CEST MRI pH mapping approach for investigating renal function. Furthermore, along with the progression of the damage, a reduction of pixels where Iopamidol was detectable was observed, suggesting that also the percentage of CEST-detected pixels can be used as an imaging biomarker of renal injury.

In another study, Longo and coworkers investigated a unilateral kidney ischemia reperfusion injury (KIRI) model to validate MRI-CEST pH mapping for assessing single kidney functionality [75]. Two different times of ischemia duration, 20 and 40 min, were applied to model moderate or severe KIRI, respectively. Following the damage evolution at days 0, 1, 2, 7, a significant increase in renal pH values was observed even at day 1 in both cases. Furthermore, in the following MRI acquisitions a clear distinction between moderate and severe AKI is possible since a recovery of normal acid-base balance was observed only in the moderate KIRI mice whereas in severe KIRI mice the increased pH values did not restore to baseline values (Fig. 5a, b). In additions, as in the previous study, the percentage of CEST detected pixels, representing a marker of the filtration fraction, showed significant differences between the injured kidneys and the contralateral ones, reflecting the different evolution of moderate-to-severe damage (Fig. 5c, d).

3.3 GlucoCEST Imaging for Assessing Renal Diseases

Since the capability of CEST imaging to detect hydroxyl protons, native glucose has also been proposed as a tracer for MRI GlucoCEST imaging [76–78]. Besides its exploitation in oncological applications, it has been applied for monitoring allograft rejection [79]. In this study, Brown Norway rat kidneys were transplanted into Lewis rats and imaged 4 days following the surgery, before and after glucose administration. By calculating the cortex-to-medulla CEST ratio (CESTR), dependent on the accumulation of the administered glucose, rats that underwent allogeneic transplant showed the highest CESTR values compared to syngeneic transplant group and to control mice.

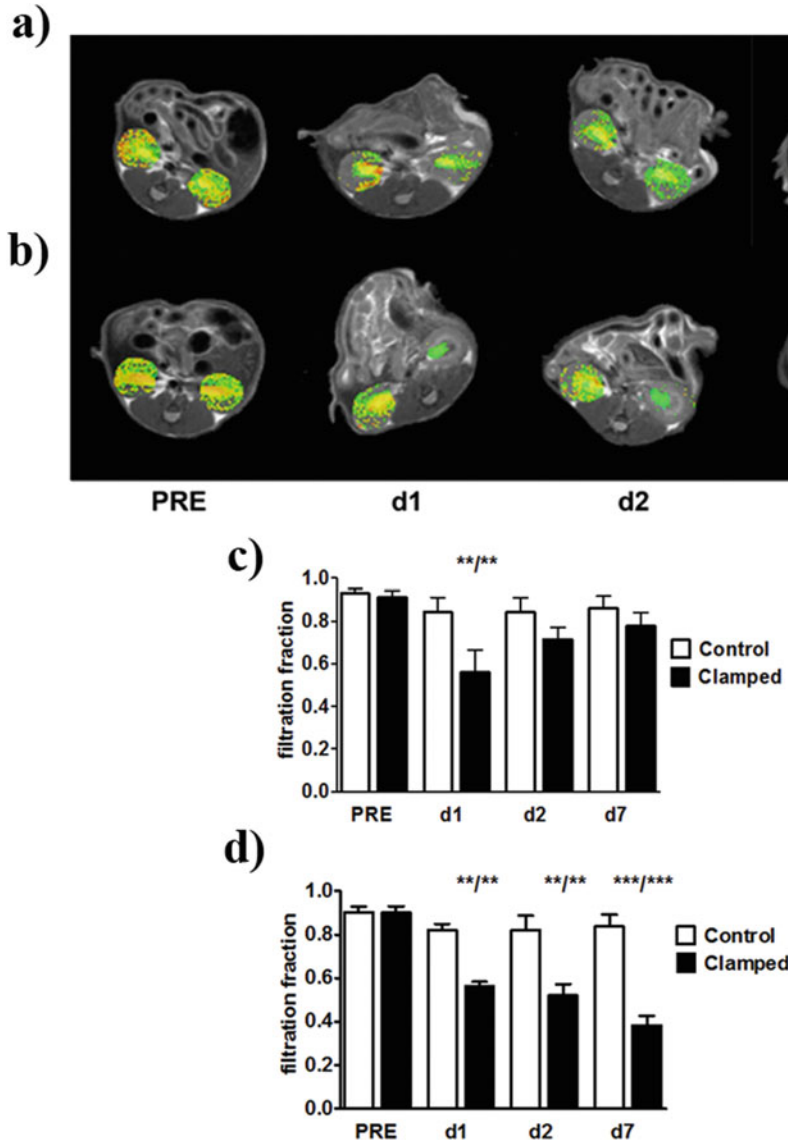

Fig. 5 MRI-CEST pH mapping detects renal pH changes and regional distribution of damage after moderate and severe unilateral kidney ischemia reperfusion injury (KIRI) showing clamped (right) and contralateral normal kidney (left). Representative MRI-CEST pH maps overimposed onto anatomical images before and after moderate (**a**) and severe (**b**) KIRI at different time points (day 1, day 2, and day 7) showing pronounced alkalinization and reduced filtration (noncolored pixels within the renal region, **c**, **d**) of the pH-responsive contrast agent in clamped kidney in comparison to contralateral kidney. (Adapted with permission from: *NMR in Biomedicine* 2017 (Noninvasive evaluation of renal pH homeostasis after ischemia reperfusion injury by CEST-MRI, Volume: 30, Issue: 7, DOI: https:/doi.org/10.1002/nbm.3720))

Acknowledgments

The Italian Ministry for Education and Research (MIUR) is gratefully acknowledged for yearly FOE funding to the Euro-BioImaging Multi-Modal Molecular Imaging Italian Node (MMMI).
This chapter is based upon work from COST Action PARENCHIMA, supported by European Cooperation in Science and Technology (COST). COST (www.cost.eu) is a funding agency for research and innovation networks. COST Actions help connect research initiatives across Europe and enable scientists to enrich their ideas by sharing them with their peers. This boosts their research, career, and innovation.
PARENCHIMA (renalmri.org) is a community-driven Action in the COST program of the European Union, which unites more than 200 experts in renal MRI from 30 countries with the aim to improve the reproducibility and standardization of renal MRI biomarkers.

References

1. Al Malla M, Varghese NV, AlAbdullatif M, Narchi H, Khassawneh M (2017) Prevalence and outcome of acute kidney injury, as defined by the new kidney disease improving global outcomes guideline, in very low birth weight infants. World J Nephrol 6(5):229–235. https://doi.org/10.5527/wjn.v6.i5.229
2. Kassebaum NJ, Lopez AD, Murray CJ, Lozano R (2014) A comparison of maternal mortality estimates from GBD 2013 and WHO. Lancet 384(9961):2209–2210. https://doi.org/10.1016/S0140-6736(14)62421-1
3. Zollner FG, Kalayciyan R, Chacon-Caldera J, Zimmer F, Schad LR (2014) Pre-clinical functional magnetic resonance imaging part I: the kidney. Z Med Phys 24(4):286–306. https://doi.org/10.1016/j.zemedi.2014.05.002
4. Neugarten J, Golestaneh L (2014) Blood oxygenation level-dependent MRI for assessment of renal oxygenation. Int J Nephrol Renovasc Dis 7:421–435. https://doi.org/10.2147/IJNRD.S42924
5. Zimmer F, Zollner FG, Hoeger S, Klotz S, Tsagogiorgas C, Kramer BK, Schad LR (2013) Quantitative renal perfusion measurements in a rat model of acute kidney injury at 3T: testing inter- and intramethodical significance of ASL and DCE-MRI. PLoS One 8(1):e53849. https://doi.org/10.1371/journal.pone.0053849
6. Ichikawa S, Motosugi U, Ichikawa T, Sano K, Morisaka H, Araki T (2013) Intravoxel incoherent motion imaging of the kidney: alterations in diffusion and perfusion in patients with renal dysfunction. Magn Reson Imaging 31(3):414–417. https://doi.org/10.1016/j.mri.2012.08.004
7. Clatworthy MR, Kettunen MI, Hu DE, Mathews RJ, Witney TH, Kennedy BW, Bohndiek SE, Gallagher FA, Jarvis LB, Smith KG, Brindle KM (2012) Magnetic resonance imaging with hyperpolarized [1,4-(13)C2]fumarate allows detection of early renal acute tubular necrosis. Proc Natl Acad Sci U S A 109(33):13374–13379. https://doi.org/10.1073/pnas.1205539109
8. Warner L, Yin M, Glaser KJ, Woollard JA, Carrascal CA, Korsmo MJ, Crane JA, Ehman RL, Lerman LO (2011) Noninvasive in vivo assessment of renal tissue elasticity during graded renal ischemia using MR elastography. Investig Radiol 46(8):509–514. https://doi.org/10.1097/RLI.0b013e3182183a95
9. Oostendorp M, de Vries EE, Slenter JM, Peutz-Kootstra CJ, Snoeijs MG, Post MJ, van Heurn LW, Backes WH (2011) MRI of renal oxygenation and function after normothermic ischemia-reperfusion injury. NMR Biomed 24(2):194–200. https://doi.org/10.1002/nbm.1572

10. Notohamiprodjo M, Reiser MF, Sourbron SP (2010) Diffusion and perfusion of the kidney. Eur J Radiol 76(3):337–347. https://doi.org/10.1016/j.ejrad.2010.05.033
11. Prasad PV (2006) Evaluation of intra-renal oxygenation by BOLD MRI. Nephron Clin Pract 103(2):c58–c65. https://doi.org/10.1159/000090610
12. Kline TL, Edwards ME, Garg I, Irazabal MV, Korfiatis P, Harris PC, King BF, Torres VE, Venkatesh SK, Erickson BJ (2018) Quantitative MRI of kidneys in renal disease. Abdom Radiol (NY) 43(3):629–638. https://doi.org/10.1007/s00261-017-1236-y
13. Zhang JL, Morrell G, Rusinek H, Sigmund EE, Chandarana H, Lerman LO, Prasad PV, Niles D, Artz N, Fain S, Vivier PH, Cheung AK, Lee VS (2014) New magnetic resonance imaging methods in nephrology. Kidney Int 85(4):768–778. https://doi.org/10.1038/ki.2013.361
14. Zhang JL, Rusinek H, Chandarana H, Lee VS (2013) Functional MRI of the kidneys. J Magn Reson Imaging 37(2):282–293. https://doi.org/10.1002/jmri.23717
15. Grenier N, Pedersen M, Hauger O (2006) Contrast agents for functional and cellular MRI of the kidney. Eur J Radiol 60(3):341–352. https://doi.org/10.1016/j.ejrad.2006.06.024
16. Liu G, Song X, Chan KW, McMahon MT (2013) Nuts and bolts of chemical exchange saturation transfer MRI. NMR Biomed 26(7):810–828. https://doi.org/10.1002/nbm.2899
17. Kogan F, Hariharan H, Reddy R (2013) Chemical exchange saturation transfer (CEST) imaging: description of technique and potential clinical applications. Curr Radiol Rep 1(2):102–114. https://doi.org/10.1007/s40134-013-0010-3
18. Jones KM, Pollard AC, Pagel MD (2018) Clinical applications of chemical exchange saturation transfer (CEST) MRI. J Magn Reson Imaging 47(1):11–27. https://doi.org/10.1002/jmri.25838
19. Anemone A, Consolino L, Arena F, Capozza M, Longo DL (2019) Imaging tumor acidosis: a survey of the available techniques for mapping in vivo tumor pH. Cancer Metastasis Rev 38(1-2):25–49. https://doi.org/10.1007/s10555-019-09782-9
20. Ward KM, Aletras AH, Balaban RS (2000) A new class of contrast agents for MRI based on proton chemical exchange dependent saturation transfer (CEST). J Magn Reson 143(1):79–87. https://doi.org/10.1006/jmre.1999.1956
21. Sun PZ, Benner T, Copen WA, Sorensen AG (2010) Early experience of translating pH-weighted MRI to image human subjects at 3 Tesla. Stroke 41(10 Suppl):S147–S151. https://doi.org/10.1161/STROKEAHA.110.595777
22. Aime S, Castelli DD, Crich SG, Gianolio E, Terreno E (2009) Pushing the sensitivity envelope of lanthanide-based magnetic resonance imaging (MRI) contrast agents for molecular imaging applications. Acc Chem Res 42(7):822–831. https://doi.org/10.1021/ar800192p
23. McMahon MT, Gilad AA, DeLiso MA, Berman SM, Bulte JW, van Zijl PC (2008) New "multicolor" polypeptide diamagnetic chemical exchange saturation transfer (DIACEST) contrast agents for MRI. Magn Reson Med 60(4):803–812. https://doi.org/10.1002/mrm.21683
24. Sun PZ, Zhou J, Huang J, van Zijl P (2007) Simplified quantitative description of amide proton transfer (APT) imaging during acute ischemia. Magn Reson Med 57(2):405–410. https://doi.org/10.1002/mrm.21151
25. McMahon MT, Gilad AA, Zhou J, Sun PZ, Bulte JW, van Zijl PC (2006) Quantifying exchange rates in chemical exchange saturation transfer agents using the saturation time and saturation power dependencies of the magnetization transfer effect on the magnetic resonance imaging signal (QUEST and QUESP): Ph calibration for poly-L-lysine and a starburst dendrimer. Magn Reson Med 55(4):836–847. https://doi.org/10.1002/mrm.20818
26. Jones CK, Schlosser MJ, van Zijl PC, Pomper MG, Golay X, Zhou J (2006) Amide proton transfer imaging of human brain tumors at 3T. Magn Reson Med 56(3):585–592. https://doi.org/10.1002/mrm.20989
27. Sun PZ, Wang E, Cheung JS (2012) Imaging acute ischemic tissue acidosis with pH-sensitive endogenous amide proton transfer (APT) MRI--correction of tissue relaxation and concomitant RF irradiation effects toward mapping quantitative cerebral tissue pH. NeuroImage 60(1):1–6. https://doi.org/10.1016/j.neuroimage.2011.11.091
28. Haris M, Nath K, Cai K, Singh A, Crescenzi R, Kogan F, Verma G, Reddy S, Hariharan H, Melhem ER, Reddy R (2013) Imaging of glutamate neurotransmitter alterations in Alzheimer's disease. NMR Biomed 26(4):386–391. https://doi.org/10.1002/nbm.2875
29. Longo DL, Di Gregorio E, Abategiovanni R, Ceccon A, Assfalg M, Molinari H, Aime S

(2014) Chemical exchange saturation transfer (CEST): an efficient tool for detecting molecular information on proteins' behaviour. Analyst 139(11):2687–2690. https://doi.org/10.1039/c4an00346b

30. Ceccon A, D'Onofrio M, Zanzoni S, Longo DL, Aime S, Molinari H, Assfalg M (2013) NMR investigation of the equilibrium partitioning of a water-soluble bile salt protein carrier to phospholipid vesicles. Proteins 81 (10):1776–1791. https://doi.org/10.1002/prot.24329
31. Castelli DD, Terreno E, Longo D, Aime S (2013) Nanoparticle-based chemical exchange saturation transfer (CEST) agents. NMR Biomed 26(7):839–849. https://doi.org/10.1002/nbm.2974
32. Dastru W, Longo D, Aime S (2011) Contrast agents and mechanisms. Drug Discov Today 8 (2–4):e109–e115. https://doi.org/10.1016/j.ddtec.2011.11.013
33. Sherry AD, Woods M (2008) Chemical exchange saturation transfer contrast agents for magnetic resonance imaging. Annu Rev Biomed Eng 10:391–411. https://doi.org/10.1146/annurev.bioeng.9.060906.151929
34. Zaiss M, Windschuh J, Goerke S, Paech D, Meissner JE, Burth S, Kickingereder P, Wick W, Bendszus M, Schlemmer HP, Ladd ME, Bachert P, Radbruch A (2016) Downfield-NOE-suppressed amide-CEST-MRI at 7 Tesla provides a unique contrast in human glioblastoma. Magn Reson Med 77 (1):196–208. https://doi.org/10.1002/mrm.26100
35. Rivlin M, Navon G (2016) Glucosamine and N-acetyl glucosamine as new CEST MRI agents for molecular imaging of tumors. Sci Rep 6:32648. https://doi.org/10.1038/srep32648
36. Li Y, Chen H, Xu J, Yadav NN, Chan KW, Luo L, McMahon MT, Vogelstein B, van Zijl PC, Zhou S, Liu G (2016) CEST theranostics: label-free MR imaging of anticancer drugs. Oncotarget 7(6):6369–6378. https://doi.org/10.18632/oncotarget.7141
37. Desmond KL, Mehrabian H, Chavez S, Sahgal A, Soliman H, Rola R, Stanisz GJ (2017) Chemical exchange saturation transfer for predicting response to stereotactic radiosurgery in human brain metastasis. Magn Reson Med 78(3):1110–1120. https://doi.org/10.1002/mrm.26470
38. Goerke S, Breitling J, Zaiss M, Windschuh J, Kunz P, Schuenke P, Paech D, Longo DL, Klika KD, Ladd ME, Bachert P (2018) Dual-frequency irradiation CEST-MRI of endogenous bulk mobile proteins. NMR Biomed 31 (6):e3920. https://doi.org/10.1002/nbm.3920
39. Longo DL, Moustaghfir FZ, Zerbo A, Consolino L, Anemone A, Bracesco M, Aime S (2017) EXCI-CEST: exploiting pharmaceutical excipients as MRI-CEST contrast agents for tumor imaging. Int J Pharm 525 (1):275–281. https://doi.org/10.1016/j.ijpharm.2017.04.040
40. Ward KM, Balaban RS (2000) Determination of pH using water protons and chemical exchange dependent saturation transfer (CEST). Magn Reson Med 44(5):799–802. https://doi.org/10.1002/1522-2594
41. Longo D, Aime S (2017) Iodinated contrast media as pH-responsive CEST agents. In: McMahon MT, Gilad AA, Bulte JBM, Van Zijl PCM (eds) Chemical exchange saturation transfer imaging, Advances and applications. Pan Stanford Publishing, Singapore, pp 447–466. https://doi.org/10.1201/9781315364421-20
42. McDonald RJ, McDonald JS, Bida JP, Carter RE, Fleming CJ, Misra S, Williamson EE, Kallmes DF (2013) Intravenous contrast material-induced nephropathy: causal or coincident phenomenon? Radiology 267 (1):106–118. https://doi.org/10.1148/radiol.12121823
43. McDonald JS, McDonald RJ, Comin J, Williamson EE, Katzberg RW, Murad MH, Kallmes DF (2013) Frequency of acute kidney injury following intravenous contrast medium administration: a systematic review and meta-analysis. Radiology 267(1):119–128. https://doi.org/10.1148/radiol.12121460
44. Aime S, Calabi L, Biondi L, De Miranda M, Ghelli S, Paleari L, Rebaudengo C, Terreno E (2005) Iopamidol: exploring the potential use of a well-established x-ray contrast agent for MRI. Magn Reson Med 53(4):830–834. https://doi.org/10.1002/mrm.20441
45. Longo DL, Dastru W, Digilio G, Keupp J, Langereis S, Lanzardo S, Prestigio S, Steinbach O, Terreno E, Uggeri F, Aime S (2011) Iopamidol as a responsive MRI-chemical exchange saturation transfer contrast agent for pH mapping of kidneys: in vivo studies in mice at 7 T. Magn Reson Med 65(1):202–211. https://doi.org/10.1002/mrm.22608
46. Anemone A, Consolino L, Longo DL (2017) MRI-CEST assessment of tumour perfusion using X-ray iodinated agents: comparison with a conventional Gd-based agent. Eur Radiol 27 (5):2170–2179. https://doi.org/10.1007/s00330-016-4552-7
47. Longo DL, Michelotti F, Consolino L, Bardini P, Digilio G, Xiao G, Sun PZ, Aime S

(2016) In vitro and in vivo assessment of non-ionic iodinated radiographic molecules as chemical exchange saturation transfer magnetic resonance imaging tumor perfusion agents. Investig Radiol 51(3):155–162. https://doi.org/10.1097/RLI.0000000000000217

48. Sun PZ, Longo DL, Hu W, Xiao G, Wu R (2014) Quantification of iopamidol multi-site chemical exchange properties for ratiometric chemical exchange saturation transfer (CEST) imaging of pH. Phys Med Biol 59 (16):4493–4504. https://doi.org/10.1088/0031-9155/59/16/4493
49. Wu Y, Zhou IY, Igarashi T, Longo DL, Aime S, Sun PZ (2018) A generalized ratiometric chemical exchange saturation transfer (CEST) MRI approach for mapping renal pH using iopamidol. Magn Reson Med 79 (3):1553–1558. https://doi.org/10.1002/mrm.26817
50. Longo DL, Bartoli A, Consolino L, Bardini P, Arena F, Schwaiger M, Aime S (2016) In vivo imaging of tumor metabolism and acidosis by combining PET and MRI-CEST pH imaging. Cancer Res 76(22):6463–6470. https://doi.org/10.1158/0008-5472.CAN-16-0825
51. Moon BF, Jones KM, Chen LQ, Liu P, Randtke EA, Howison CM, Pagel MD (2015) A comparison of iopromide and iopamidol, two acidoCEST MRI contrast media that measure tumor extracellular pH. Contrast Media Mol Imaging 10(6):446–455. https://doi.org/10.1002/cmmi.1647
52. Longo DL, Sun PZ, Consolino L, Michelotti FC, Uggeri F, Aime S (2014) A general MRI-CEST ratiometric approach for pH imaging: demonstration of in vivo pH mapping with iobitridol. J Am Chem Soc 136 (41):14333–14336. https://doi.org/10.1021/ja5059313
53. Arena F, Irrera P, Consolino L, Colombo Serra S, Zaiss M, Longo DL (2018) Flip-angle based ratiometric approach for pulsed CEST-MRI pH imaging. J Magn Reson 287:1–9. https://doi.org/10.1016/j.jmr.2017.12.007
54. Song X, Walczak P, He X, Yang X, Pearl M, Bulte JW, Pomper MG, McMahon MT, Janowski M (2016) Salicylic acid analogues as chemical exchange saturation transfer MRI contrast agents for the assessment of brain perfusion territory and blood-brain barrier opening after intra-arterial infusion. J Cereb Blood Flow Metab 36(7):1186–1194. https://doi.org/10.1177/0271678X16637882
55. Song X, Yang X, Ray Banerjee S, Pomper MG, McMahon MT (2015) Anthranilic acid analogs as diamagnetic CEST MRI contrast agents that feature an intramolecular-bond shifted hydrogen. Contrast Media Mol Imaging 10 (1):74–80. https://doi.org/10.1002/cmmi.1597
56. Yang X, Song X, Li Y, Liu G, Ray Banerjee S, Pomper MG, McMahon MT (2013) Salicylic acid and analogues as diaCEST MRI contrast agents with highly shifted exchangeable proton frequencies. Angew Chem Int Ed Engl 52 (31):8116–8119. https://doi.org/10.1002/anie.201302764
57. Yang X, Song X, Ray Banerjee S, Li Y, Byun Y, Liu G, Bhujwalla ZM, Pomper MG, McMahon MT (2016) Developing imidazoles as CEST MRI pH sensors. Contrast Media Mol Imaging 11(4):304–312. https://doi.org/10.1002/cmmi.1693
58. Zhang S, Merritt M, Woessner DE, Lenkinski RE, Sherry AD (2003) PARACEST agents: modulating MRI contrast via water proton exchange. Acc Chem Res 36(10):783–790. https://doi.org/10.1021/ar020228m
59. Hancu I, Dixon WT, Woods M, Vinogradov E, Sherry AD, Lenkinski RE (2010) CEST and PARACEST MR contrast agents. Acta Radiol 51(8):910–923. https://doi.org/10.3109/02841851.2010.502126
60. Liu G, Ali MM, Yoo B, Griswold MA, Tkach JA, Pagel MD (2009) PARACEST MRI with improved temporal resolution. Magn Reson Med 61(2):399–408. https://doi.org/10.1002/mrm.21863
61. Aime S, Delli Castelli D, Terreno E (2005) Highly sensitive MRI chemical exchange saturation transfer agents using liposomes. Angew Chem Int Ed Engl 44(34):5513–5515. https://doi.org/10.1002/anie.200501473
62. Srivastava K, Ferrauto G, Harris SM, Longo DL, Botta M, Aime S, Pierre VC (2018) Complete on/off responsive ParaCEST MRI contrast agents for copper and zinc. Dalton Trans 47(33):11346–11357. https://doi.org/10.1039/c8dt01172a
63. Woods M, Woessner DE, Sherry AD (2006) Paramagnetic lanthanide complexes as PARACEST agents for medical imaging. Chem Soc Rev 35(6):500–511. https://doi.org/10.1039/b509907m
64. Vinogradov E, He H, Lubag A, Balschi JA, Sherry AD, Lenkinski RE (2007) MRI detection of paramagnetic chemical exchange effects in mice kidneys in vivo. Magn Reson Med 58 (4):650–655. https://doi.org/10.1002/mrm.21393
65. Wu Y, Soesbe TC, Kiefer GE, Zhao P, Sherry AD (2010) A responsive europium(III) chelate that provides a direct readout of pH by MRI. J Am Chem Soc 132(40):14002–14003. https://doi.org/10.1021/ja106018n

66. Wu Y, Zhang S, Soesbe TC, Yu J, Vinogradov E, Lenkinski RE, Sherry AD (2016) pH imaging of mouse kidneys in vivo using a frequency-dependent paraCEST agent. Magn Reson Med 75(6):2432–2441. https://doi.org/10.1002/mrm.25844
67. Sun PZ, Cheung JS, Wang E, Benner T, Sorensen AG (2011) Fast multislice pH-weighted chemical exchange saturation transfer (CEST) MRI with unevenly segmented RF irradiation. Magn Reson Med 65(2):588–594. https://doi.org/10.1002/mrm.22628
68. Sheth VR, Li Y, Chen LQ, Howison CM, Flask CA, Pagel MD (2012) Measuring in vivo tumor pHe with CEST-FISP MRI. Magn Reson Med 67(3):760–768. https://doi.org/10.1002/mrm.23038
69. Zaiss M, Ehses P, Scheffler K (2018) Snapshot-CEST: optimizing spiral-centric-reordered gradient echo acquisition for fast and robust 3D CEST MRI at 9.4 T. NMR Biomed 31 (4):e3879. https://doi.org/10.1002/nbm.3879
70. Zhu H, Jones CK, van Zijl PC, Barker PB, Zhou J (2010) Fast 3D chemical exchange saturation transfer (CEST) imaging of the human brain. Magn Reson Med 64 (3):638–644. https://doi.org/10.1002/mrm.22546
71. Sun PZ, Murata Y, Lu J, Wang X, Lo EH, Sorensen AG (2008) Relaxation-compensated fast multislice amide proton transfer (APT) imaging of acute ischemic stroke. Magn Reson Med 59(5):1175–1182. https://doi.org/10.1002/mrm.21591
72. Randtke EA, Granados JC, Howison CM, Pagel MD, Cardenas-Rodriguez J (2017) Multislice CEST MRI improves the spatial assessment of tumor pH. Magn Reson Med 78 (1):97–106. https://doi.org/10.1002/mrm.26348
73. Wang F, Kopylov D, Zu Z, Takahashi K, Wang S, Quarles CC, Gore JC, Harris RC, Takahashi T (2016) Mapping murine diabetic kidney disease using chemical exchange saturation transfer MRI. Magn Reson Med 76 (5):1531–1541. https://doi.org/10.1002/mrm.26045
74. Longo DL, Busato A, Lanzardo S, Antico F, Aime S (2013) Imaging the pH evolution of an acute kidney injury model by means of iopamidol, a MRI-CEST pH-responsive contrast agent. Magn Reson Med 70(3):859–864. https://doi.org/10.1002/mrm.24513
75. Longo DL, Cutrin JC, Michelotti F, Irrera P, Aime S (2017) Noninvasive evaluation of renal pH homeostasis after ischemia reperfusion injury by CEST-MRI. NMR Biomed 30(7). https://doi.org/10.1002/nbm.3720
76. Walker-Samuel S, Ramasawmy R, Torrealdea F, Rega M, Rajkumar V, Johnson SP, Richardson S, Goncalves M, Parkes HG, Arstad E, Thomas DL, Pedley RB, Lythgoe MF, Golay X (2013) In vivo imaging of glucose uptake and metabolism in tumors. Nat Med 19 (8):1067–1072. https://doi.org/10.1038/nm.3252
77. Xu X, Chan KW, Knutsson L, Artemov D, Xu J, Liu G, Kato Y, Lal B, Laterra J, McMahon MT, van Zijl PC (2015) Dynamic glucose enhanced (DGE) MRI for combined imaging of blood-brain barrier break down and increased blood volume in brain cancer. Magn Reson Med 74 (6):1556–1563. https://doi.org/10.1002/mrm.25995
78. Chan KW, McMahon MT, Kato Y, Liu G, Bulte JW, Bhujwalla ZM, Artemov D, van Zijl PC (2012) Natural D-glucose as a biodegradable MRI contrast agent for detecting cancer. Magn Reson Med 68(6):1764–1773. https://doi.org/10.1002/mrm.24520
79. Kentrup D, Bovenkamp P, Busch A, Schuette-Nuetgen K, Pawelski H, Pavenstadt H, Schlatter E, Herrmann KH, Reichenbach JR, Loffler B, Heitplatz B, Van Marck V, Yadav NN, Liu G, van Zijl PCM, Reuter S, Hoerr V (2017) GlucoCEST magnetic resonance imaging in vivo may be diagnostic of acute renal allograft rejection. Kidney Int 92(3):757–764. https://doi.org/10.1016/j.kint.2017.04.015

Chapter 15

Sodium (^{23}Na) MRI of the Kidney: Basic Concept

James T. Grist, Esben Søvsø Hansen, Frank G. Zöllner, and Christoffer Laustsen

Abstract

The handling of sodium by the renal system is a key indicator of renal function. Alterations in the corticomedullary distribution of sodium are considered important indicators of pathology in renal diseases. The derangement of sodium handling can be noninvasively imaged using sodium magnetic resonance imaging (^{23}Na MRI), with data analysis allowing for the assessment of the corticomedullary sodium gradient. Here we introduce sodium imaging, describe the existing methods, and give an overview of preclinical sodium imaging applications to illustrate the utility and applicability of this technique for measuring renal sodium handling.

This chapter is based upon work from the COST Action PARENCHIMA, a community-driven network funded by the European Cooperation in Science and Technology (COST) program of the European Union, which aims to improve the reproducibility and standardization of renal MRI biomarkers. This introduction chapter is complemented by two separate chapters describing the experimental procedure and data analysis.

Key words Magnetic resonance imaging (MRI), Kidney, Mice, Rats, ^{23}Na, Sodium

1 Introduction

In this chapter, we describe renal sodium imaging, as acquired with magnetic resonance imaging (MRI). An introduction to the many methods that can be used to acquire sodium (23Na) signal is presented, as well as the postprocessing required to quantitatively describe the signal in terms of relaxation or concentration. Example applications of sodium renal imaging are discussed—ranging from the action of diuretic drugs to early sodium handling alterations in acute kidney injury. This introduction is complemented by two separate chapters describing the experimental procedure and data analysis, which are part of this book.

This chapter is part of the book Pohlmann A, Niendorf T (eds) (2020) Preclinical MRI of the Kidney—Methods and Protocols. Springer, New York.

Andreas Pohlmann and Thoralf Niendorf (eds.), *Preclinical MRI of the Kidney: Methods and Protocols*, Methods in Molecular Biology, vol. 2216, https://doi.org/10.1007/978-1-0716-0978-1_15, © The Author(s) 2021

2 Measurement Concept

2.1 Basic Concept of Sodium Imaging

Sodium imaging can provide quantitative measures of the ^{23}Na concentration in tissue [1]. It utilizes the signal from the sodium nucleus, found in both the intra- and extracellular compartments, to acquire images of the ^{23}Na biodistribution. Due to the low natural abundance of biological sodium, in comparison to water, as well as a rapid quadrupolar relaxation and lower gyromagnetic ratio (spin $= \frac{3}{2}$, $\gamma = 11.262 \frac{\text{MHz}}{\text{T}}$), approximately ¼ of protons, the signal available is much lower than that of conventional ^{1}H MRI [2]. The fast quadrupolar relaxation recovers some of the disadvantages of imaging ^{23}Na, as very short repetition times (TR) can be used, albeit the ultrafast T_2^* relaxation imposing constraints on the imaging technique used. Commonly, the total (meaning from both the intra- and extracellular compartments) sodium signal is acquired through the use of surface or RF volume coils, at high magnetic field strengths (3–9.4 T) using gradient echo-based imaging technique [3–6]. It is possible to suppress some of the extracellular signal, to give an "intracellular weighted" image, with advanced techniques such as inversion signal nulling or triple quantum filtering (TQF) [7, 8]. An estimate of the difference in the intra- and extracellular compartment sizes is feasible through the use of T_2^* mapping [9]. It is noted that no current use of TQF or inversion recovery signal nulling have been undertaken in renal studies; however, there are a number of publications in neurological work [8, 10, 11].

2.2 Sodium Imaging Methods

There are a number of imaging methods available for mapping the biodistribution of sodium in the renal system. The sodium signal detected in a simple imaging experiment is a combination of intra- and extracellular compartments, termed the "total" sodium signal. The three main methods used to differentiate the intra- and extracellular sodium signals are triple quantum filtering, inversion recovery fluid attenuation (IR), and T_2^* mapping.

2.2.1 Sodium MRI Hardware

For signal reception, the MR scanners need to be equipped by RF transmitters and receive RF coils tuned to the resonance frequency of the sodium nuclei at the respective magnetic field strength. Today, such extensions are supported by some vendors of preclinical systems. In the following, hardware developments for quantitative ^{23}Na-MRI in preclinical are briefly outlined.

For the first time, Barberi et al. introduced the transmit-only receive-only (TORO) system, the so-called dual radiofrequency (RF) resonator, which is based on the idea of separated transmit and receive RF elements [12]. In contrast to the standard RF resonators in transceiver (TXRX) mode (e.g., surface coil or

birdcage), the dual RF resonator allows for both a homogeneous transmit B_1^+ field and a highly sensitive receive B_1^- field [12, 13].

Kalacycian et al. developed a homogeneous transmit-only volume resonator and a highly sensitive RO surface resonator for renal ^{23}Na-MRI for 3 T or 9.4 T MRI scanners [14]. For this setup the sensitivity correction needs to be performed only for the receive profile. Furthermore, the dual resonator allows for increased ^{23}Na-MR signal sensitivity due to the localized signal detection using RO surface coils. For the dedicated task of bilateral kidney imaging, a dual resonator system (TORO) including a two-element phased array at 9.4 T and a receiver saddle shaped RF resonator at 3 T was implemented [13]. These systems were tailored for measuring the absolute renal TSC in rat kidney models with high spatiotemporal resolution, and high concentration measurement accuracy.

2.2.2 Total Sodium Imaging

Total sodium imaging is typically performed using a gradient echo-based technique. To ensure that the conversion from the imaging signal to the sodium concentration is accurate, a repetition time of approximately 2.5 times the T_1 of tissue sodium (approximately 25 ms at 3 T, and longer at higher field strengths) is essential. Further optimization of the sequence readout can be undertaken to capture the fast T_2^* relaxation of the sodium nucleus. For example, an ultrashort echo time (UTE) approach such as radial or twisted projection imaging is preferred over conventional Cartesian strategies. Due to the inherent low SNR of sodium acquisitions, it is common to average a number of sodium scans from the same subject; however, this may lead to long scan times.

An example of total sodium imaging pulse sequence, and renal images, are provided in Figs. 1a and 2.

2.2.3 Triple Quantum Filtering (TQF)

Due to the $\frac{3}{2}$ spin of the sodium nucleus, a biexponential T_2^* is exhibited by the isotope. A single excitation with a 90-degree hard pulse causes a transition of spins between the outer spin states ($\frac{3}{2}$ to $\frac{1}{2}$ and $-\frac{1}{2}$ to $-\frac{3}{2}$) as well as the inner states ($\frac{1}{2}$ to $-\frac{1}{2}$). The outer spin states exhibit a faster T_2^* decay than the inner. Using phase-cycled radiofrequency pulses it is possible to isolate the signal of slow-moving spins in the intracellular compartment, while removing the extracellular contribution [15].

There are a number of limitations to TQF though. The challenges include long scan times and high energy deposition required due to a large SNR penalty of the TQF technique. Furthermore, inhomogeneity in main magnetic field distribution can lead to spurious results, with corrections in reconstruction required to counter the B_0-nonuniformity effects [10]. An example triple quantum filtering sodium imaging pulse sequence is shown in Fig. 1b.

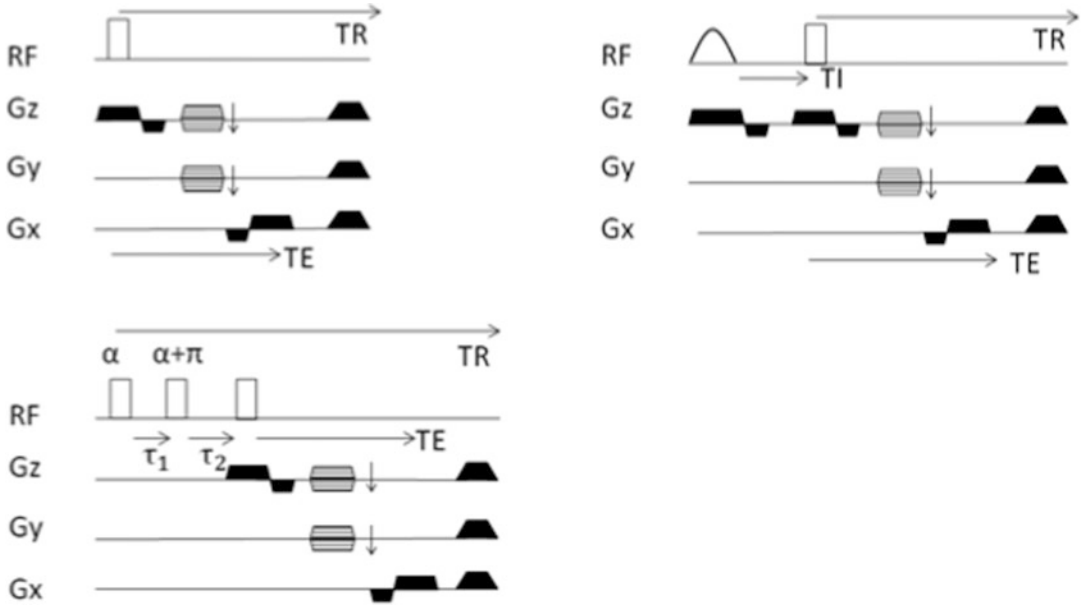

Fig. 1 Sodium imaging pulse sequences. (**a**) Total sodium imaging sequence using a 3D GRE readout. TR = Repetition time, TE = Echo time. (**b**) Triple Quantum Filtered sodium imaging pulse sequence using a 3D GRE readout. α = phase of pulse 1, T1 = Mixing time 1, T2 = Mixing time 2. (**c**) Inversion prepared sodium imaging pulse sequence. TI = Inversion preparation time (determined experimentally)

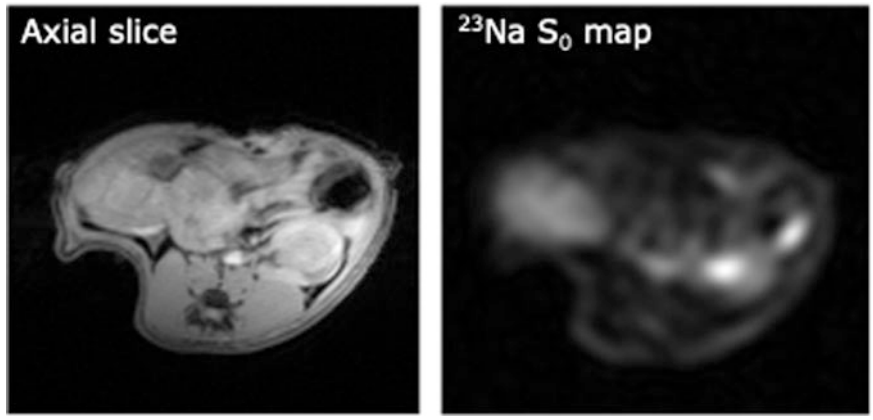

Fig. 2 Example rodent renal ^{1}H (left) and sodium (right) imaging acquired at 9.4 T

2.2.4 Inversion Recovery Utilizing the difference in T_1 between bound and unbound sodium, it is possible to null the signal contribution fluid compartment using an inversion pulse, whilst retaining the bound signal, as described through Eqs. 1 and 2 [7].

$$S(\mathrm{TI}) = S_0\left(1 - \exp\left(-\frac{\mathrm{TI}}{T_1}\right)\right) \tag{1}$$

$$\mathrm{TI}_{\mathrm{null}} = \ln(2)\, T_1^{\mathrm{Fluid}} \tag{2}$$

where TI is the inversion time, T_1 is the relaxation constant of free sodium, S_0 is the initial sodium NMR signal, and S(TI) is the signal at TI. An example of an inversion recovery sodium imaging technique is illustrated in Fig. 1c.

2.2.5 T2* Mapping

T_2^* mapping is performed with either a multiecho based gradient echo sequence, or many individual scans with an incremented echo time (TE). It is currently thought that the shorter T_2^* component (1-5 ms at 3 T) is derived from the intracellular compartment, and the longer (10–30 ms at 3 T) from the extracellular compartment [9, 16]. T2* mapping therefore could be sensitive to changes in the intracellular–extracellular renal sodium balance.

A multiecho or incremented echo series can be used to derive both the pool sizes and T_2^* time constant for each compartment through Eq. 3.

$$S(\mathrm{TE}) = \left(a \exp\left(-\frac{\mathrm{TE}}{T^*_{2,\mathrm{Short}}} \right) + b \exp\left(-\frac{\mathrm{TE}}{T^*_{2,\mathrm{Long}}} \right) \right) \quad (3)$$

where S(TE) is the signal at a given echo time, a and b are the intra- and extracellular pool sizes, respectively, and $T^*_{2,\mathrm{Short}}$ and $T^*_{2,\mathrm{Long}}$ are the biexponential relaxation constants.

2.3 Imaging Readout

Due to the rapid decay of the sodium signal, fast gradient echo-based imaging methods are commonly employed for data acquisition. A large number of encoding schemes are present in the literature, encompassing Cartesian and non-Cartesian imaging [17]. Below is a summary of most frequently applied methods.

2.3.1 3D Cartesian Imaging

The majority of preclinical imaging has been undertaken with 3D gradient echo Cartesian imaging, whereby a volume of k-space is sampled using trapezoidal readout gradients. Due to the ease of implementation on a preclinical system, this has been the sequence of choice for a number studies in rodents [3–5]. However, as Cartesian imaging requires encoding in k_y and k_z directions prior to data acquisition, the minimum echo time available for imaging is substantially longer than in other methods available for use in future studies.

2.3.2 Ultrashort Echo Time (UTE) Imaging

In order to shorten the echo time of acquisition, thereby increasing the total signal available for sampling, non-Cartesian imaging trajectories can be employed. Non-Cartesian trajectories are less commonly used in imaging, and require special design of magnetic field gradient waveforms and a more sophisticated reconstruction process. However, with a very short minimum echo time, 3D non-Cartesian trajectories are better suited for probing the fast-relaxing sodium signal. Where a 3D Cartesian sequence requires localisation in k_y and k_z prior to data acquisition, a 3D non-Cartesian acquisition starts each excitation at the center of k-space, and data are simultaneously acquired in k_x, k_y, and k_z. To

ensure short TE in UTE imaging a hard RF pulse is commonly used to excite all spins in the imaging volume. A number of trajectories used for non-Cartesian data readout are available from literature, for example radial imaging, twisted projection imaging (TPI), density adapted radial (DAR) imaging, and 3D CONES, briefly described in the following.

Twisted projection imaging (TPI) was first described by Fernando Boada in 1997, as an extension to 2D TWIRL imaging [18]. The technique utilizes a hybrid radial-spiral sampling of k-space, allowing for acceleration in comparison to radial imaging with an underdamping factor defined during trajectory construction. TPI requires high gradient slew rates for image acquisition, due to the sharp transition between the radial and spiral potions of the trajectory. Further optimizations to the trajectory can be made by optimizing maximum gradient amplitudes throughout scan time [19].

Density adapted radial (DAR) trajectories are described in work by Nagel, whereby concentric rings of k-space are acquired with a radial readout. DAR allows for under sampling of k-space, shortening acquisition times in comparison to radial imaging [20].

The 3D cones approach was initially described for UTE proton imaging and has found applications in sodium acquisitions [21, 22]. Due to the high *k*-space efficiency of the trajectory, it is possible to acquire a full imaging volume in a very short time, leading to rapid high resolution imaging [23]. However, due to the high k-space efficiency, the SNR of each volume is lower than a radial acquisition; therefore, it is common practice to perform a number of spatial averages in a single acquisition.

2.4 Reconstruction

There are three main methods for reconstruction of sodium imaging data, depending on the acquisition scheme used. If Cartesian data is acquired, a Fourier transform is applied in all dimensions (x, y,z,t). If non-Cartesian acquisitions are employed more complex reconstruction strategies such as gridding or nonuniform fast Fourier transforms are used. Compensation for the oversampling of the center of k-space is performed in non-Cartesian imaging using precalculated density compensation functions (*see* **Note 1**).

2.5 Sodium Phantoms

External calibration phantoms are used to convert sodium imaging data to quantitative maps, with voxels fitted to a calibration curve formed from measurements of signal from known concentration phantoms as well as from regions of noise in the image.

Phantoms are generally made from agarose doped with sodium chloride, to ensure a T_1 and T_2 that mimic that of tissue. However, other designs are also possible. Phantoms are placed within the imaging field of view before the start of the experiment to ensure that signal is acquired from both tissue and calibration standards in the same exam.

2.6 Segmentation

Segmentation of the kidney is commonly achieved through region of interests initially drawn on proton anatomical imaging and transferred to the sodium images. Other methods have been proposed for the segmentation of the renal system, in particular to measure the corticomedullary sodium gradient, focusing on defining layers of the kidney from an initial whole kidney region [24].

3 Overview of Applications

3.1 Total sodium Imaging for Assessing Alterations in the Corticomedullary sodium Gradient

The corticomedullary sodium gradient has been studied with sodium imaging in a number of healthy and pathological scenarios [3–5, 25–29]. Broadly, the current preclinical literature focuses either on the action of diuretic drugs upon the sodium gradient, or upon acute tubular necrosis. The action of furosemide has been estimated by acquiring longitudinal imaging before and after the introduction of the acute diuretic. Furosemide acts as a loop diuretic, halting reabsorption of sodium through the loop of Henley, leading to acute diuresis. Results from studies have shown the capability of sodium MRI to detect the acute renal sodium alterations induced by furosemide, revealing a flattening of the corticomedullary sodium gradient within minutes of administration [3, 4, 26].

Studies focusing upon the early formation of acute kidney injury through tubular necrosis have revealed alterations in the sodium gradient, with a decreased gradient in the damaged kidney [5].

3.2 Potential Future Applications of sodium Imaging

Although the literature is limited to the current applications of renal sodium imaging, there is a large scope for further preclinical studies demonstrating the power of this technique to probe disease formation. In particular, the formation of acute kidney disease and chronic kidney disease remain prime targets for further ^{23}Na MRI studies.

3.3 Acute Kidney Disease

Acute kidney disease is heralded by a sudden loss of renal function, and impaired reabsorption of electrolytes such as urea and sodium [30]. Indeed, this is a key clinical problem, with a number of patients diagnosed upon admission with AKI and leads to high mortality rates. AKI can occur over a number of hours or days, and is heralded by an decrease of the glomerular filtration rate, leading to retention of nitrogenous waste [31]. Due to the increase in waste retention, common methods for diagnosis are serum-based measures of creatinine clearance and blood nitrogen [31]. Further to the increase in the retention of waste, sodium reabsorption is impaired in AKI. An initial sodium imaging study showed a flattening of the corticomedullary sodium gradient [32]. A particular challenge in diagnosis and management of AKI is the direct estimation of renal health and function pre- and post-therapy, with many imaging methods either requiring the

introduction of potentially hazardous contrast agents, or unable to provide physiological information [33]. Here sodium imaging may provide a more specific measure of renal health. The initial imaging study, mentioned above, offers a potential for further studies assessing therapeutic response [32]. Assessing the angle of the corticomedullary sodium gradient may also provide insights in to the degree of the insult that the disrupted kidney is facing.

3.4 Chronic Kidney Disease

Chronic kidney disease (CKD) is characterized by a gradual loss of kidney function over time, leading to a decrease in the intrarenal transport of metabolites such as urea and sodium [34, 35]. A challenge in this disease is, as with AKI, both monitoring disease progression and estimating therapeutic response. Sodium imaging has the potential to evaluate renal function via the corticomedullary sodium gradient, to differentiate the earliest changes in the metabolic and functional mismatch that occur in the renal system prior to the development of kidney disease [28, 32, 36]. The use of a combined multimodal anatomical and functional imaging approach with methods such as sodium, arterial spin labeling, BOLD, dynamic contrast enhanced imaging, and diffusion weighted imaging may provide a more complete picture of the alterations in renal function in relation to chronic kidney disease [24, 36–42].

4 Notes

1. Example gridding and density compensation calculation functions used for the reconstruction of data acquired with non-Cartesian trajectories can be found at https://www.ismrm.org/mri_unbound/sequence.htm.

Acknowledgments

The authors would like to thank Andreas Pohlmann and Thoralf Niendorf for assistance in preparing this chapter (Max-Delbrück Center for Molecular Medicine in the Helmholtz Association, Berlin, Germany.
This chapter is based upon work from COST Action PARENCHIMA, supported by European Cooperation in Science and Technology (COST). COST (www.cost.eu) is a funding agency for research and innovation networks. COST Actions help connect research initiatives across Europe and enable scientists to enrich their ideas by sharing them with their peers. This boosts their research, career, and innovation.
PARENCHIMA (renalmri.org) is a community-driven Action in the COST program of the European Union, which unites more than 200 experts in renal MRI from 30 countries with the aim to improve the reproducibility and standardization of renal MRI biomarkers.

References

1. Christensen JD, Barrère BJ, Boada FE et al (1996) Quantitative tissue sodium concentration mapping of normal rat brain. Magn Reson Med 36:83–89
2. Zöllner FG, Konstandin S, Lommen J et al (2016) Quantitative sodium MRI of kidney. NMR Biomed 29:197–205
3. Maril N, Margalit R, Mispelter J, Degani H (2004) Functional sodium magnetic resonance imaging of the intact rat kidney. Kidney Int 65:927–935
4. Maril N, Margalit R, Mispelter J, Degani H (2005) Sodium magnetic resonance imaging of diuresis: spatial and kinetic response. Magn Reson Med 53:545–552
5. Maril N, Margalit R, Rosen S et al (2006) Detection of evolving acute tubular necrosis with renal 23Na MRI: studies in rats. Kidney Int 69:765–768
6. Zöllner FG, Kalayciyan R, Chacón-Caldera J et al (2014) Pre-clinical functional magnetic resonance imaging part I: the kidney. Z Med Phys 24:286–306
7. Stobbe R, Beaulieu C (2005) In vivo sodium magnetic resonance imaging of the human brain using soft inversion recovery fluid attenuation. Magn Reson Med 54:1305–1310
8. Benkhedah N, Bachert P, Semmler W, Nagel AM (2012) Three-dimensional biexponential weighted (23) Na imaging of the human brain with higher SNR and shorter acquisition time. Magn Reson Med 765:754–765
9. Riemer F, Solanky BS, Wheeler-Kingshott CAM, Golay X (2018) Bi-exponential ^{23}Na T_2* component analysis in the human brain. NMR Biomed 31(5):e3899
10. Tsang A, Stobbe RW, Beaulieu C (2013) Evaluation of B0-inhomogeneity correction for triple-quantum-filtered sodium MRI of the human brain at 4.7 T. J Magn Reson 230:134–144
11. Hancu I, Boada FE, Shen GX (1999) Three-dimensional triple-quantum-filtered 23Na imaging of in vivo human brain. Magn Reson Med 42:1146–1154
12. Ackerman JJH, Grove TH, Wong GG et al (1980) Mapping of metabolites in whole animals by 31P NMR using surface coils. Nature 283:2–5
13. Mueller OM, Hayes CE, Eash M et al (2006) An efficient, highly homogeneous radiofrequency coil for whole-body NMR imaging at 1.5 T. J Magn Reson 63:622–628
14. Kalayciyan R, Malzacher M, Neudecker S, Gretz N SL (2013) 23Na/1H in-vivo renal MRI of rodent kidney at 3T by using a double-tuned transceiver resonator system. In: International Society for Magnetic Resonance in Medicine. Salt-Lake City, p 4355
15. Hancu I, Boada FE, Shen GX (1999) Three-dimensional triple-quantum – filtered 23 Na imaging of in vivo human brain. Magn Reson Med 42(6):1146–1154
16. Qian Y, Panigrahy A, Laymon CM et al (2014) Short-T2 imaging for quantifying concentration of sodium ((23) Na) of bi-exponential T2 relaxation. Magn Reson Med 00:00–00
17. Konstandin S, Nagel AM (2014) Measurement techniques for magnetic resonance imaging of fast relaxing nuclei. MAGMA 27:5–19
18. Boada FE, Gillen JS, Shen GX et al (1997) Fast three dimensional sodium imaging. Magn Reson Med 37:706–715
19. Angelica MD, Fong Y (2008) Quantitative sodium imaging with a flexible twisted projection pulse sequence. Magn Reson Med 141:520–529
20. Nagel AM, Laun FB, Weber M-A et al (2009) Sodium MRI using a density-adapted 3D radial acquisition technique. Magn Reson Med 62:1565–1573
21. Riemer F, Solanky BS, Stehning C et al (2014) Sodium (23Na) ultra-short echo time imaging in the human brain using a 3D-Cones trajectory. MAGMA 27:35–46
22. Gurney PT, Hargreaves BA, Nishimura DG (2006) Design and analysis of a practical 3D cones trajectory. Magn Reson Med 55:575–582
23. Grist JT, Riemer F, McLean MA et al (2018) Imaging intralesional heterogeneity of sodium concentration in multiple sclerosis: initial evidence from 23Na-MRI. J Neurol Sci 387:111–114
24. Milani B, Ansaloni A, Sousa-Guimaraes S et al (2016) Reduction of cortical oxygenation in chronic kidney disease: evidence obtained with a new analysis method of blood oxygenation level-dependent magnetic resonance imaging. Nephrol Dial Transplant 32 (12):2097–2105
25. Maril N, Rosen Y, Reynolds GH et al (2006) Sodium MRI of the human kidney at 3 tesla. Magn Reson Med 56:1229–1234
26. Neuberger T, Gulani V, Webb A (2007) Sodium renal imaging in mice at high magnetic fields. Magn Reson Med 58:1067–1071
27. Haneder S, Juras V, Michaely HJ et al (2014) In vivo sodium (23Na) imaging of the human

kidneys at 7 T: preliminary results. Eur Radiol 24:494–501
28. Qi H, Nørlinger TS, Nielsen PM et al (2016) Early diabetic kidney maintains the corticomedullary urea and sodium gradient. Physiol Rep 4:1–6
29. Giovannetti G, Pingitore A, Positano V et al (2014) Improving sodium magnetic resonance in humans by design of a dedicated 23Na surface coil. Measurement 50:285–292
30. Hansell P, Welch WJ, Blantz RC, Palm F (2013) Determinants of kidney oxygen consumption and their relationship to tissue oxygen tension in diabetes and hypertension. Clin Exp Pharmacol Physiol 40:123–137
31. Basile DP, Anderson MD, Sutton TA (2012) Pathophysiology of acute kidney injury. Compr Physiol 2:1303–1353
32. Nielsen PM, Szocska Hansen ES, Nørlinger TS et al (2016) Renal ischemia and reperfusion assessment with three-dimensional hyperpolarized13C,15N2-urea. Magn Reson Med 76:1524–1530
33. Perazella MA (2015) Gadolinium-contrast toxicity in patients with kidney disease: nephrotoxicity and nephrogenic systemic fibrosis. Curr Drug Saf 3:67–75
34. McFarland JG (1999) Perioperative blood transfusions: indications and options. Chest 115:113S–121S
35. Thomas R, Kanso A, Sedor JR (2008) Chronic kidney disease and its complications. Prim Care 35:329–344
36. Bertelsen LB, Nielsen PM, Qi H et al (2017) Diabetes induced renal urea transport alterations assessed with 3D hyperpolarized13C,15N-urea. Magn Reson Med 77:1650–1655
37. Cox EF, Buchanan CE, Bradley CR et al (2017) Multiparametric renal magnetic resonance imaging: validation, interventions, and alterations in chronic kidney disease. Front Physiol 8:1–15
38. Piskunowicz M, Hofmann L, Zuercher E et al (2015) A new technique with high reproducibility to estimate renal oxygenation using BOLD-MRI in chronic kidney disease. Magn Reson Imaging 33:253–261
39. Pruijm M, Milani B, Burnier M (2017) Blood oxygenation level-dependent mri to assess renal oxygenation in renal diseases: progresses and challenges. Front Physiol 7:1–7
40. Nielsen PM, Eldirdiri A, Bertelsen LB et al (2017) Fumarase activity: an in vivo and in vitro biomarker for acute kidney injury. Sci Rep 7:40812
41. Zimmer F, Zöllner FG, Hoeger S et al (2013) Quantitative renal perfusion measurements in a rat model of acute kidney injury at 3T: testing inter- and intramethodical significance of ASL and DCE-MRI. PLoS One 8:e53849
42. Zhou HY, Chen TW, Zhang XM (2016) Functional magnetic resonance imaging in acute kidney injury: present status. Biomed Res Int 2016:2027370

Chapter 16

Hyperpolarized Carbon (^{13}C) MRI of the Kidneys: Basic Concept

Cornelius von Morze, Galen D. Reed, Zhen J. Wang, Michael A. Ohliger, and Christoffer Laustsen

Abstract

Existing clinical markers for renal disease are limited. Hyperpolarized (HP) ^{13}C MRI is based on the technology of dissolution dynamic nuclear polarization (DNP) and provides new avenues for imaging kidney structure, function, and most notably, renal metabolism, addressing some of these prior limitations. Changes in kidney structure and function associated with kidney disease can be evaluated using [^{13}C]urea, a metabolically inert tracer. Metabolic changes can be assessed using [1-^{13}C]pyruvate and a range of other rapidly metabolized small molecules, which mainly probe central carbon metabolism. Results from numerous preclinical studies using a variety of these probes demonstrated that this approach holds great potential for monitoring renal disease, although more work is needed to bridge intelligently into clinical studies. Here we introduce the general concept of HP ^{13}C MRI and review the most relevant probes and applications to renal disease, including kidney cancer, diabetic nephropathy and ischemic kidney injury.

This chapter is based upon work from the PARENCHIMA COST Action, a community-driven network funded by the European Cooperation in Science and Technology (COST) program of the European Union, which aims to improve the reproducibility and standardization of renal MRI biomarkers. This introduction chapter is complemented by two separate chapters describing the experimental procedure and data analysis.

Key words Dynamic nuclear polarization, Kidney, Preclinical models, Carbon-13

1 Introduction

While renal MRI has traditionally been limited largely to morphologic depiction of vascular disease and neoplasia, hyperpolarized (HP) ^{13}C MRI supplies new metabolic and/or functional insight that could be valuable for a range of kidney diseases. The high renal delivery of intravenously injected small molecules, which provides extraordinary sensitivity for renal imaging of HP ^{13}C MRI probes, suggests great potential for application of this nascent medical imaging modality to kidney disease.

Andreas Pohlmann and Thoralf Niendorf (eds.), *Preclinical MRI of the Kidney: Methods and Protocols*, Methods in Molecular Biology, vol. 2216, https://doi.org/10.1007/978-1-0716-0978-1_16,

Commonly used clinical markers for kidney disease have significant limitations, especially in the context of early disease. Serum creatinine is frequently utilized as a functional marker, but has a wide reference interval, and the mathematical corrections applied for the estimation of glomerular filtration rate (GFR) are inexact. For example, GFR is unpredictably overestimated in glomerulopathic patients as a result of increased creatinine secretion [1]. Even accurately measured GFR, such as by the "gold standard" inulin clearance, is insensitive to early disease [2]. Blood urea nitrogen (BUN) fluctuates due to factors unrelated to kidney function, such as hydration status and diet. Proteinuria at baseline is a significant risk factor for renal disease, but has poor negative predictive value [3]. In general, clinical markers do not exhibit definitive changes until a significant fraction of kidney function is already lost.

Medical imaging has clear potential to address these limitations by providing localized functional data, but this has yet to be translated on a large scale. Nuclear medicine plays a significant role, with (mercaptoacetyltriglycine) MAG_3 scintigraphy estimated to account for >400,000 renograms per year [4], commonly for evaluation of renal function (often pre- or post-transplant), split function, collecting duct/urinary tract obstruction, renovascular hypertension, and renal artery stenosis. However, nuclear scans typically have relatively poor spatial resolution and lack the rich tissue contrast of MRI. Furthermore, these studies carry the risks of exposure to ionizing radiation. Ultrasound is also commonly used for assessing kidney disease [5], but is generally limited to evaluating advanced damage reflected in alterations in kidney size and shape, and to some extent blood flow. For patients with impaired renal function, iodinated Computer Tomography (CT) contrast media carry an increased risks of acute kidney injury [6]. Gadolinium based MRI contrast media are associated with nephrogenic systemic fibrosis [7].

HP ^{13}C MRI has unique potential for improved, safer clinical imaging studies of renal structure and function, and perhaps most notably offers an unprecedented avenue toward assessing renal metabolism in vivo. Indeed, results of numerous preclinical studies conducted to date, as summarized below, show the clear potential of this new approach to fill pressing unmet clinical needs for improved markers of various diseases affecting the kidneys, both malignant and nonmalignant. More preclinical work with realistic renal disease models is, however, needed in order to bridge effectively into clinical studies.

This introduction chapter is complemented by two separate chapters describing the experimental procedure and data analysis, which are part of this book.

This chapter is part of the book Pohlmann A, Niendorf T (eds) (2020) Preclinical MRI of the Kidney—Methods and Protocols. Springer, New York.

2 Measurement Concept

2.1 Basic Concept of HP ^{13}C MRI

HP ^{13}C MRI is based on a transient enhancement of the nuclear magnetism of ^{13}C-enriched liquids, by up to five orders of magnitude over states readily attainable in a clinical MRI magnet, thereby offsetting the limitation of poor sensitivity that previously hampered in vivo ^{13}C MRI. Although multiple alternate approaches exist for producing HP material, the method of dissolution dynamic nuclear polarization (DNP) [8] provides an especially robust avenue for hyperpolarizing a wide variety of ^{13}C-labeled substrates, using commercially available instruments. In this approach, the ^{13}C substrate is first prepolarized in a separate magnet at low temperature (*see* **Note 1**), primarily through microwave irradiation applied near the electron paramagnetic resonance (EPR) frequency in the presence of a stable organic free radical (aka electron paramagnetic agent or EPA, usually a trityl radical) (*see* **Note 2**). Following a period of polarization buildup, the solid sample is rapidly dissolved into a liquid state where it temporarily maintains its hyperpolarization, and is quickly transferred to the MRI scanner for intravenous injection and imaging (*see* **Note 3**). The overall process is illustrated in Fig. 1. The transient hyperpolarized state persists for a period of time determined by the substrate's T_1 relaxation time, an exponential time constant governing the rate of decay of polarization (*see* **Note 4**). Inverse scaling of T_1 with molecular size limits the scope of applicable probes to small molecules, with labels preferably located distal to bonded hydrogen atoms, which can destroy the ^{13}C magnetization via ^{13}C-^{1}H dipolar coupling (*see* **Note 5**). During the decay period, ^{13}C MRI data is collected, capitalizing on the sensitivity enhancement afforded by hyperpolarization. Specific methods for data acquisition and processing of HP ^{13}C MRI data are described in the relevant sections to follow.

2.2 Renal Functional and Metabolic Investigations Using HP ^{13}C MRI

HP ^{13}C MRI offers many new possibilities for renal functional and metabolic investigations. Dynamic images of the real-time delivery of metabolically inert tracers such as ^{13}C urea from arterial vasculature to the kidneys can be used to quantify renal function. Real-time in vivo processing of metabolically active HP probes by the kidneys can be tracked by spectroscopic imaging, which yields separate images of injected tracer(s) and their downstream metabolic product(s) based on chemical shift differences. Notably, multiple probes can also be simultaneously copolarized to yield multiparametric data sets [9], for example spanning both renal functional and metabolic parameters. In this section, we review the most promising HP ^{13}C MRI probes of renal function/metabolism proposed to date, and the relevant associated principles. These probes and their metabolic pathways are illustrated in Fig. 2.

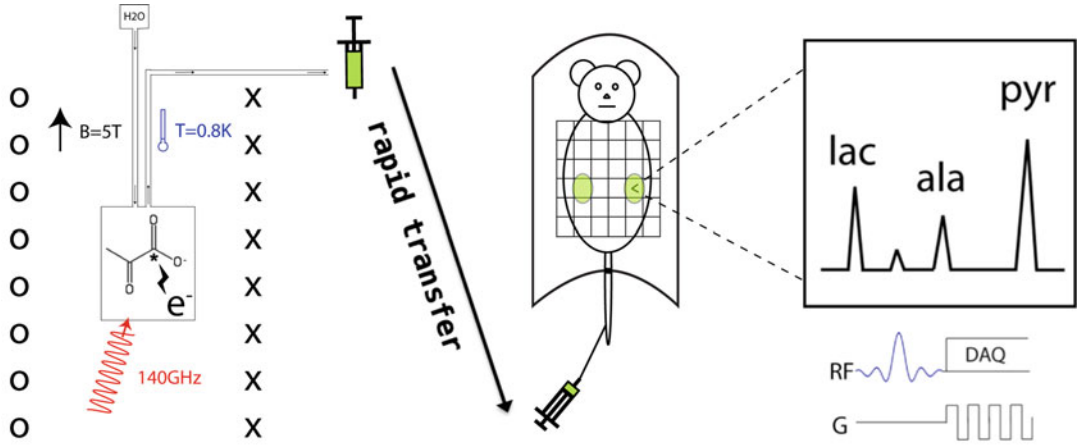

Fig. 1 Illustration of the process of HP ^{13}C MRI via dissolution dynamic nuclear polarization. The agent (e.g., [1-^{13}C]pyruvate) is mixed with the EPA and cooled to 0.8 K in a magnetic field of 5 T, then irradiated at 140GHz to transfer polarization from unpaired electrons in the EPA to the ^{13}C nuclei. The sample is then rapidly dissolved and transferred to the MRI scanner for intravenous injection and MR imaging

2.2.1 [^{13}C]Urea

The key osmolyte and metabolic end product urea was one of the first ^{13}C-labeled molecules to be hyperpolarized ($T_1 = 45$ s at 3 T) [8] and imaged in vivo [10], and high quality dynamic images of the kidneys and the feeding arterial vasculature can readily be generated [11–13]. Quantitative estimates of renal function require dynamic measurements from both the renal parenchyma and arterial vasculature [11, 14]. Urea is largely reabsorbed by urea transporters (UTs) expressed at the inner medullary collecting ducts (IMCD), and accordingly renal imaging shows distinct modulation by hydration state [13, 15], based on differential action of vasopressin. Despite this significant reabsorption, it has been suggested that urea can also be used to estimate glomerular filtration rate (GFR) [14], based on the first-order transfer coefficient between arterial vasculature and renal parenchyma. Secondary labeling of [^{13}C]urea with $^{15}N_2$ is helpful in terms of prolonging both T_1 (at low magnetic fields only) [16] and T_2 relaxation times [12] of urea, with the latter factor allowing imaging rat kidneys at spatial resolutions approaching 1 mm isotropic (using refocused image acquisition) [13]. Furthermore, relaxation mapping shows great promise for improved contrast between the individual kidney compartments and various functional states [12, 13, 17]. Urea is distinguished by an exceptionally good safety profile among medical imaging contrast agents, even in patients with reduced kidney function, and therefore has potential for clinical translation for imaging patients with kidney diseases.

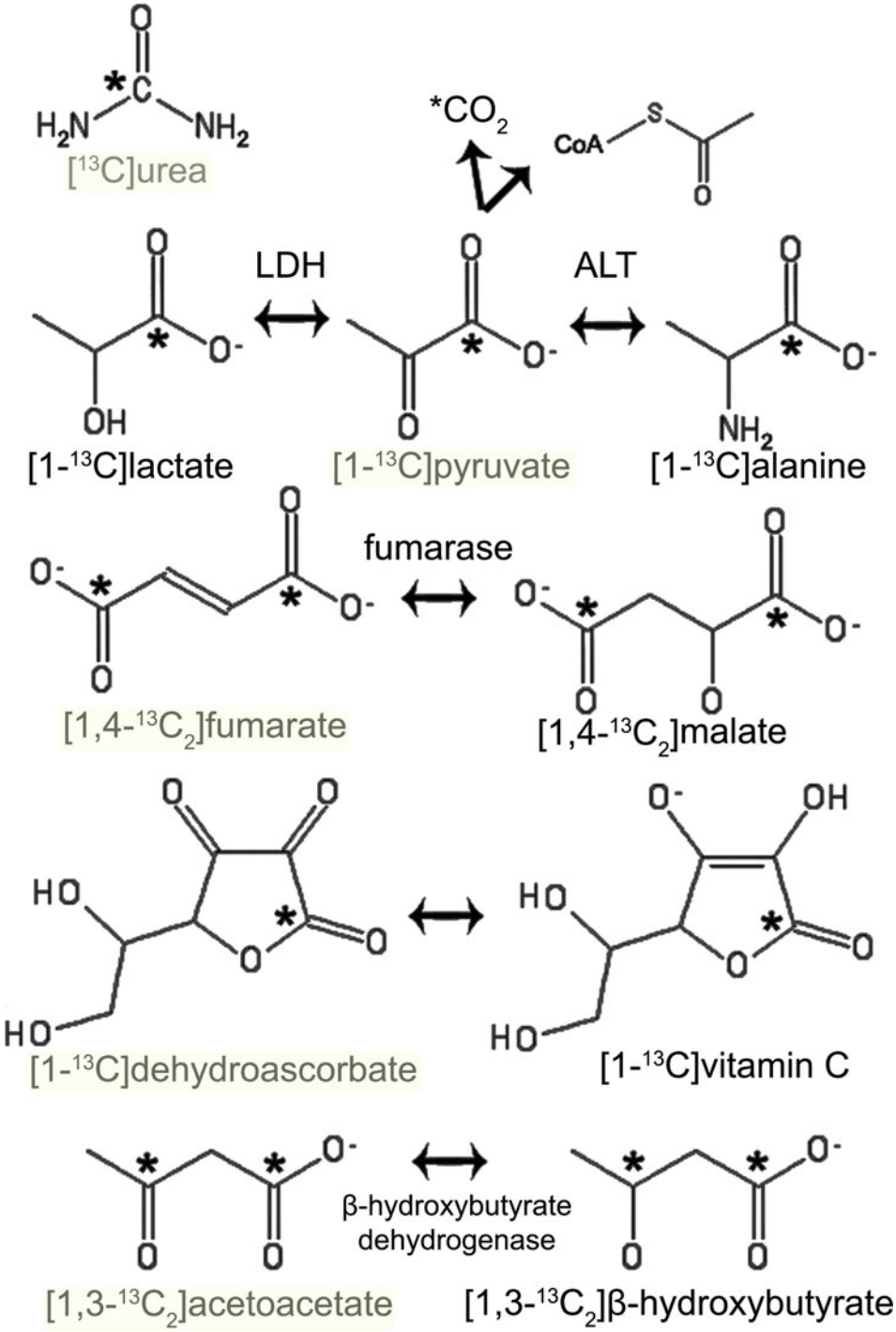

Fig. 2 HP ^{13}C MRI probes of interest for monitoring renal disease, and the associated metabolic conversions (if any). Positions of the ^{13}C labels are indicated by stars

2.2.2 [1-^{13}C]Pyruvate

Pyruvate, the end product of glycolysis and key metabolic intermediate, is the most widely studied ^{13}C probe, in C_1-labeled form (T_1 = 60s at 3 T) [18]. In the kidneys, its interconversions with lactate (via lactate dehydrogenase, LDH) and alanine (via alanine transaminase, ALT), as well as its decarboxylation yielding [^{13}C] bicarbonate (via pyruvate dehydrogenase or PDH) can readily be tracked by spectroscopic imaging. The extent of metabolic conversion observed reflects a complex series of biophysical processes, including vascular delivery, cellular uptake (via monocarboxylate transporters), and finally enzymatic conversion, which in turn may be influenced by multiple factors. For the conversion via LDH, the lactate pool size is especially important [19, 20]. For quantitative comparison among subjects, all of these factors are usually grouped into simple parameters such as metabolite area-under-the-curve (AUC) ratios or related apparent first-order conversion rates (e.g., $k_{pyruvate\text{-}to\text{-}lactate}$ or k_{pl}) [21, 22], derived from a series of dynamic spectroscopic imaging data. From a metabolic perspective, while the conversion to bicarbonate is clearly a net flux, the conversions to lactate and alanine via the respective bidirectional, highly active enzymes appear to represent largely isotopic exchange fluxes into the respective product metabolite pools [19, 20, 23]. Because of the high bidirectional activity of LDH (which is restricted to cytoplasm), the ratio of lactate to pyruvate has frequently been interpreted as a marker for the cytosolic free NADH/NAD$^+$ ratio [24]. This suggests that the conversion of HP pyruvate to lactate is driven by this NAD(H) redox state, a parameter that is fundamentally inter-connected with numerous related biochemical reactions.

2.2.3 [1,4-$^{13}C_2$]Fumarate

Cellular uptake of injected fumarate, a tricarboxylic acid (TCA) cycle intermediate, is ordinarily highly restricted on the timescale of HP experiments, due to its dicarboxylate structure. Compromise of the cellular membrane (e.g., due to necrosis) allows access of injected HP [1,4-$^{13}C_2$]fumarate (a singlet due to molecular symmetry, with T_1 = 58 s at 3 T) [25] to cellular fumarase, and consequently detectable conversion of product HP [1,4-$^{13}C_2$] malate. Thus, HP fumarate has been investigated as a specific marker of cellular necrosis with potentially significant applicability to detection of renal tubular necrosis [26].

2.2.4 [1-^{13}C] Dehydroascorbate

HP [1-^{13}C]dehydroascorbate (T_1 = 56 s at 3 T) [27, 28] can be used to probe oxidative stress in a direct manner. Vitamin C, a key physiologic antioxidant, exists in a NADP(H)-mediated equilibrium with its oxidized form, dehydroascorbate (DHA). Conversion of injected HP [1-^{13}C]DHA, which is rapidly taken up by glucose transporters, to [1-^{13}C]vitamin C is detectable in vivo. The observed extent of conversion of HP DHA to vitamin C, a reaction whose reducing power is likely mostly derived from reduced glutathione (GSH), is attenuated by oxidative stress.

2.2.5 [^{13}C]Acetoacetate

The ketone body acetoacetate, a universal oxidative fuel, rapidly interconverts with its reduced form, beta-hydroxybutyrate, in mitochondria via beta-hydroxybutyrate dehydrogenase. In analogy with lactate/pyruvate, the BOHB–AcAc ratio has frequently been interpreted as a marker of the free mitochondrial NADH–NAD$^+$ ratio, suggesting an analogous interpretation of conversion of HP acetoacetate [29, 30] as being driven by the mitochondrial NAD(H) redox state. Metabolic conversion of injected [1,3-$^{13}C_2$]acetoacetate (58 s at 3 T, C_1 position) can be detected in rat kidney in vivo (via the C_1 label) [29], suggesting applicability of this new probe to interrogate mitochondrial-driven kidney disease.

3 Overview of Applications

3.1 Kidney Cancer

Multiple studies have reported elevated conversion of HP [1-^{13}C]pyruvate to [1-^{13}C]lactate and rapid export of [1-^{13}C]lactate in renal cell carcinoma (RCC), in both RCC cells ex vivo [31–33] and in vivo in mice orthotopically implanted with human RCC cells [34]. These findings suggest that HP [1-^{13}C]pyruvate MRI could have clinical value for improved characterization of kidney cancer in patients. Moreover, a recent study showed that HP [1-^{13}C]pyruvate MRI could be used to predict RCC treatment response to mTOR inhibition, which varies greatly among individual patients, thus potentially informing treatment decisions [35].

3.2 Diabetic Nephropathy

Diabetes results in profound shifts in central carbon metabolism, directly shifting several pathways accessible to HP ^{13}C MRI. Although diabetes is detectable using relatively simple testing, sustained hyperglycemia over time leads to serious end-organ complications including diabetic nephropathy, a significant source of morbidity, the detection/prediction of which is a difficult clinical problem where HP ^{13}C MRI could be valuable. Though cancer has been the main focus of the HP ^{13}C MRI community, several recent studies have reported differences in renal HP ^{13}C signals detected in type 1 and type 2 diabetes models as compared to normal controls, based on multiple HP probes including [1-^{13}C]pyruvate [23, 36, 37], [^{13}C]urea [38, 39], and [1-^{13}C]DHA [40]. Not surprisingly, standard antidiabetic agents including insulin and metformin have been found to induce large renal HP signal changes as well [29, 41, 42]. Renal HP lactate levels are attenuated with hyperbaric [43] and antioxidant treatment [44] in diabetic rats. HP [^{13}C]acetate has so far failed to show any significant metabolic change associated with the diabetic kidney [45]. Further work is needed in animal models of frank diabetic nephropathy, which may display changes additive to the fundamental metabolic shifts observed in diabetes, to address this important clinical problem.

3.3 Ischemic Kidney Injury

Effective detection of acute kidney injury (AKI) is an unresolved clinical problem especially affecting hospitalized patients. Rapid treatment of AKI is critical but is impeded by existing clinical indicators which are poor in diagnosing early AKI. Several studies of models of ischemia reperfusion injury (i.e., unilateral renal artery clamp) have shown clear effects of AKI on renal HP ^{13}C MRI using [^{13}C]urea [46, 47], pyruvate [48], and [1-^{13}C]pyruvate–[1-^{13}C] DHA combination [49], and fumarate [50]. However, these relatively simple models likely do not reflect the etiology of ischemic injuries more frequently encountered in patients, such as those resulting from atherosclerotic disease. Further work using more realistic models of ischemic kidney injury is needed to answer, for example, the important question of predicting treatment response in renal artery stenosis. Finally, HP [1,4-$^{13}C_2$]fumarate has also been investigated as a probe of tissue necrosis in a toxic folic acid model of acute tubular necrosis (ATN) [26]. A nonzero urinary fumarase activity could potentially be used as a clinical indicator for a hyperpolarized fumarate examination to investigate the extent and the origin of the renal damage [50].

4 Notes

1. The state-of-the-art GE SPINLab polarizer operates at 5 T and a temperature of 0.8 K. Microwave irradiation is applied near the EPR frequency corresponding to this magnetic field (~140 GHz), with a typical power of ~20 mW. A buildup time of ~3 h is typically required.
2. Urea and many other agents including fumarate and acetoacetate require the addition of a glassing agent such as glycerol or DMSO to prevent crystallization upon freezing, which impedes the polarization process.
3. The ^{13}C concentration is made as high as possible in the starting material (in the molar range), facilitating efficient polarization, but the concentration typically drops >10-fold on dissolution. In contrast, the concentration of the radical is only ~15 mM in the starting material.
4. The T_1 exponential decay constant of HP ^{13}C probe is directly proportional to its "half-life," by a factor of ln 2 (i.e., $t_{1/2} = 0.69 \times T_1$).
5. T_1 values of 30–60 s are typical for the most useful probes, and T_1 values are magnetic field- and temperature-dependent.

Acknowledgments

Grant support from National Institutes of Health (NIH) K01DK099451 is gratefully acknowledged.
This chapter is based upon work from COST Action PARENCHIMA, supported by European Cooperation in Science and Technology (COST). COST (www.cost.eu) is a funding agency for research and innovation networks. COST Actions help connect research initiatives across Europe and enable scientists to enrich their ideas by sharing them with their peers. This boosts their research, career, and innovation.
PARENCHIMA (renalmri.org) is a community-driven Action in the COST program of the European Union, which unites more than 200 experts in renal MRI from 30 countries with the aim to improve the reproducibility and standardization of renal MRI biomarkers.

References

1. Shemesh O, Golbetz H, Kriss JP, Myers BD (1985) Limitations of creatinine as a filtration marker in glomerulopathic patients. Kidney Int 28:830–838
2. Metcalfe W (2007) How does early chronic kidney disease progress? A background paper prepared for the UK Consensus Conference on early chronic kidney disease. Nephrol Dial Transplant 22(Suppl 9):ix26–ix30. https://doi.org/10.1093/ndt/gfm446
3. Ishani A, Grandits GA, Grimm RH, Svendsen KH, Collins AJ, Prineas RJ, Neaton JD (2006) Association of single measurements of dipstick proteinuria, estimated glomerular filtration rate, and hematocrit with 25-year incidence of end-stage renal disease in the multiple risk factor intervention trial. J Am Soc Nephrol 17:1444–1452. https://doi.org/10.1681/ASN.2005091012
4. Esteves FP, Taylor A, Manatunga A, Folks RD, Krishnan M, Garcia EV (2006) 99mTc-MAG3 renography: normal values for MAG3 clearance and curve parameters, excretory parameters, and residual urine volume. AJR Am J Roentgenol 187:W610–W617. https://doi.org/10.2214/AJR.05.1550
5. O'Neill WC (2014) Renal relevant radiology: use of ultrasound in kidney disease and nephrology procedures. Clin J Am Soc Nephrol 9:373–381. https://doi.org/10.2215/CJN.03170313
6. PA MC, Stacul F, Becker CR, Adam A, Lameire N, Tumlin JA, Davidson CJ, CIN Consensus Working Panel (2006) Contrast-induced nephropathy (CIN) consensus working panel: executive summary. Rev Cardiovasc Med 7:177–197
7. Kuo PH, Kanal E, Abu-Alfa AK, Cowper SE (2007) Gadolinium-based MR contrast agents and nephrogenic systemic fibrosis. Radiology 242:647–649. https://doi.org/10.1148/radiol.2423061640
8. Ardenkjaer-Larsen JH, Fridlund B, Gram A, Hansson G, Hansson L, Lerche MH, Servin R, Thaning M, Golman K (2003) Increase in signal-to-noise ratio of > 10,000 times in liquid-state NMR. Proc Natl Acad Sci U S A 100:10158–10163. https://doi.org/10.1073/pnas.1733835100
9. Wilson DM, Keshari KR, Larson PEZ, Chen AP, Hu S, Van Criekinge M, Bok R, Nelson SJ, Macdonald JM, Vigneron DB, Kurhanewicz J (2010) Multi-compound polarization by DNP allows simultaneous assessment of multiple enzymatic activities in vivo. J Magn Reson 205:141–147. https://doi.org/10.1016/j.jmr.2010.04.012
10. Golman K, Ardenkjaer-Larsen JH, Petersson JS, Månsson S, Leunbach I (2003) Molecular imaging with endogenous substances. Proc Natl Acad Sci U S A 100:10435–10439. https://doi.org/10.1073/pnas.1733836100
11. von Morze C, Larson PEZ, Hu S, Keshari K, Wilson DM, Ardenkjaer-Larsen JH, Goga A, Bok R, Kurhanewicz J, Vigneron DB (2011) Imaging of blood flow using hyperpolarized [C-13] urea in preclinical cancer models. J

Magn Reson Imaging 33:692–697. https://doi.org/10.1002/jmri.22484

12. Reed GD, von Morze C, Bok R, Koelsch BL, Van Criekinge M, Smith KJ, Shang H, Larson PEZ, Kurhanewicz J, Vigneron DB (2014) High resolution (13)C MRI with hyperpolarized urea: in vivo T(2) mapping and (15)N labeling effects. IEEE Trans Med Imaging 33:362–371. https://doi.org/10.1109/TMI.2013.2285120
13. Reed GD, von Morze C, Verkman AS, Koelsch BL, Chaumeil MM, Lustig M, Ronen SM, Bok RA, Sands JM, Larson PEZ, Wang ZJ, Larsen JHA, Kurhanewicz J, Vigneron DB (2016) Imaging renal urea handling in rats at millimeter resolution using hyperpolarized magnetic resonance relaxometry. Tomography 2:125–135. https://doi.org/10.18383/j.tom.2016.00127
14. Østergaard Mariager C, Nielsen PM, Qi H, Schroeder M, Bertelsen LB, Laustsen C (2017) Can hyperpolarized 13C-urea be used to assess glomerular filtration rate? A retrospective study. Tomography 3:146–152. https://doi.org/10.18383/j.tom.2017.00010
15. von Morze C, Bok RA, Sands JM, Kurhanewicz J, Vigneron DB (2012) Monitoring urea transport in rat kidney in vivo using hyperpolarized C-13 magnetic resonance imaging. Am J Physiol Renal Physiol 302:F1658–F1662. https://doi.org/10.1152/ajprenal.00640.2011
16. Chiavazza E, Kubala E, Gringeri CV, Düwel S, Durst M, Schulte RF, Menzel MI (2013) Earth's magnetic field enabled scalar coupling relaxation of 13C nuclei bound to fast-relaxing quadrupolar 14N in amide groups. J Magn Reson 227:35–38. https://doi.org/10.1016/j.jmr.2012.11.016
17. Laustsen C, Stokholm Nørlinger T, Christoffer Hansen D, Qi H, Mose Nielsen P, Bonde Bertelsen L, Henrik Ardenkjaer-Larsen J, Stødkilde Jørgensen H (2016) Hyperpolarized 13C urea relaxation mechanism reveals renal changes in diabetic nephropathy. Magn Reson Med 75:515–518. https://doi.org/10.1002/mrm.26036
18. Golman K, in 't Zandt R, Thaning M (2006) Real-time metabolic imaging. Proc Natl Acad Sci U S A 103:11270–11275. https://doi.org/10.1073/pnas.0601319103
19. Day SE, Kettunen MI, Gallagher FA, Hu D-E, Lerche M, Wolber J, Golman K, Ardenkjaer-Larsen JH, Brindle KM (2007) Detecting tumor response to treatment using hyperpolarized 13C magnetic resonance imaging and spectroscopy. Nat Med 13:1382–1387. https://doi.org/10.1038/nm1650
20. Hurd RE, Spielman D, Josan S, Yen Y-F, Pfefferbaum A, Mayer D (2013) Exchange-linked dissolution agents in dissolution-DNP (13)C metabolic imaging. Magn Reson Med 70:936–942. https://doi.org/10.1002/mrm.24544
21. Hill DK, Orton MR, Mariotti E, Boult JKR, Panek R, Jafar M, Parkes HG, Jamin Y, Miniotis MF, Al-Saffar NMS, Beloueche-Babari M, Robinson SP, Leach MO, Chung Y-L, Eykyn TR (2013) Model free approach to kinetic analysis of real-time hyperpolarized 13C magnetic resonance spectroscopy data. PLoS One 8:e71996. https://doi.org/10.1371/journal.pone.0071996
22. Daniels CJ, McLean MA, Schulte RF, Robb FJ, Gill AB, McGlashan N, Graves MJ, Schwaiger M, Lomas DJ, Brindle KM, Gallagher FA (2016) A comparison of quantitative methods for clinical imaging with hyperpolarized (13)C-pyruvate. NMR Biomed 29:387–399. https://doi.org/10.1002/nbm.3468
23. von Morze C, Allu PKR, Chang GY, Marco-Rius I, Milshteyn E, Wang ZJ, Ohliger MA, Gleason CE, Kurhanewicz J, Vigneron DB, Pearce D (2018) Non-invasive detection of divergent metabolic signals in insulin deficiency vs. insulin resistance in vivo. Sci Rep 8:2088. https://doi.org/10.1038/s41598-018-20264-w
24. Williamson D, Lund P, Krebs H (1967) Redox state of free nicotinamide-adenine dinucleotide in cytoplasm and mitochondria of rat liver. Biochem J 103:514–527
25. Gallagher FA, Kettunen MI, Hu D-E, Jensen PR, I' nt Zandt R, Karlsson M, Gisselsson A, Nelson SK, Witney TH, Bohndiek SE, Hansson G, Peitersen T, Lerche MH, Brindle KM (2009) Production of hyperpolarized [1,4-13C2]malate from [1,4-13C2]fumarate is a marker of cell necrosis and treatment response in tumors. Proc Natl Acad Sci U S A 106:19801–19806. https://doi.org/10.1073/pnas.0911447106
26. Clatworthy MR, Kettunen MI, Hu D-E, Mathews RJ, Witney TH, Kennedy BWC, Bohndiek SE, Gallagher FA, Jarvis LB, Smith KGC, Brindle KM (2012) Magnetic resonance imaging with hyperpolarized [1,4-(13)C2]fumarate allows detection of early renal acute tubular necrosis. Proc Natl Acad Sci U S A 109:13374–13379. https://doi.org/10.1073/pnas.1205539109
27. Keshari KR, Kurhanewicz J, Bok R, Larson PEZ, Vigneron DB, Wilson DM (2011) Hyperpolarized 13C dehydroascorbate as an endogenous redox sensor for in vivo metabolic

imaging. Proc Natl Acad Sci U S A 108:18606–18611. https://doi.org/10.1073/pnas.1106920108

28. Bohndiek SE, Kettunen MI, Hu D-E, Kennedy BWC, Boren J, Gallagher FA, Brindle KM (2011) Hyperpolarized [1-13C]-ascorbic and dehydroascorbic acid: vitamin C as a probe for imaging redox status in vivo. J Am Chem Soc 133:11795–11801. https://doi.org/10.1021/ja2045925
29. von Morze C, Ohliger MA, Marco-Rius I, Wilson DM, Flavell RR, Pearce D, Vigneron DB, Kurhanewicz J, Wang ZJ (2018) Direct assessment of renal mitochondrial redox state using hyperpolarized 13 C-acetoacetate. Magn Reson Med 79(4):1862–1869. https://doi.org/10.1002/mrm.27054
30. Miller JJ, Ball DR, Lau AZ, Tyler DJ (2018) Hyperpolarized ketone body metabolism in the rat heart. NMR Biomed 31:e3912. https://doi.org/10.1002/nbm.3912
31. Keshari KR, Sriram R, Koelsch BL, Van Criekinge M, Wilson DM, Kurhanewicz J, Wang ZJ (2013) Hyperpolarized 13C-pyruvate magnetic resonance reveals rapid lactate export in metastatic renal cell carcinomas. Cancer Res 73:529–538. https://doi.org/10.1158/0008-5472.CAN-12-3461
32. Sriram R, Van Criekinge M, Hansen A, Wang ZJ, Vigneron DB, Wilson DM, Keshari KR, Kurhanewicz J (2015) Real-time measurement of hyperpolarized lactate production and efflux as a biomarker of tumor aggressiveness in an MR compatible 3D cell culture bioreactor. NMR Biomed 28:1141–1149. https://doi.org/10.1002/nbm.3354
33. Sriram R, Van Criekinge M, Delos Santos J, Keshari KR, Wilson DM, Peehl D, Kurhanewicz J, Wang ZJ (2016) Non-invasive differentiation of benign renal tumors from clear cell renal cell carcinomas using clinically translatable hyperpolarized 13C pyruvate magnetic resonance. Tomography 2:35–42. https://doi.org/10.18383/j.tom.2016.00106
34. Sriram R, Gordon J, Baligand C, Ahamed F, Delos Santos J, Qin H, Bok RA, Vigneron DB, Kurhanewicz J, Larson PEZ, Wang ZJ (2018) Non-invasive assessment of lactate production and compartmentalization in renal cell carcinomas using hyperpolarized 13C pyruvate MRI. Cancers (Basel) 10:313. https://doi.org/10.3390/cancers10090313
35. Dong Y, Eskandari R, Ray C, Granlund KL, Dos Santos-Cunha L, Miloushev VZ, Tee SS, Jeong S, Aras O, Chen Y-B, Cheng EH, Hsieh JJ, Keshari KR (2019) Hyperpolarized MRI visualizes Warburg effects and predicts treatment response to mTOR inhibitors in patient-derived ccRCC xenograft models. Cancer Res 79(1):242–250. https://doi.org/10.1158/0008-5472.CAN-18-2231
36. Laustsen C, Østergaard JA, Lauritzen MH, Nørregaard R, Bowen S, Søgaard LV, Flyvbjerg A, Pedersen M, Ardenkjaer-Larsen JH (2013) Assessment of early diabetic renal changes with hyperpolarized [1-13C]pyruvate. Diabetes Metab Res Rev 29:125–129. https://doi.org/10.1002/dmrr.2370
37. von Morze C, Chang GY, Larson PE, Shang H, Allu PK, Bok RA, Crane JC, Olson MP, Tan CT, Marco-Rius I, Nelson SJ, Kurhanewicz J, Pearce D, Vigneron DB (2017) Detection of localized changes in the metabolism of hyperpolarized gluconeogenic precursors 13C-lactate and 13C-pyruvate in the kidneys and liver. Magn Reson Med 77(4):1429–1437
38. Qi H, Nørlinger TS, Nielsen PM, Bertelsen LB, Mikkelsen E, Xu Y, Stødkilde Jørgensen H, Laustsen C (2016) Early diabetic kidney maintains the corticomedullary urea and sodium gradient. Physiol Rep 4:e12714. https://doi.org/10.14814/phy2.12714
39. Bertelsen LB, Nielsen PM, Qi H, Nørlinger TS, Zhang X, Stødkilde Jørgensen H, Laustsen C (2017) Diabetes induced renal urea transport alterations assessed with 3D hyperpolarized 13 C,15 N-urea. Magn Reson Med 77:1650–1655. https://doi.org/10.1002/mrm.26256
40. Keshari KR, Wilson DM, Sai V, Bok R, Jen K-Y, Larson P, Van Criekinge M, Kurhanewicz J, Wang ZJ (2015) Noninvasive in vivo imaging of diabetes-induced renal oxidative stress and response to therapy using hyperpolarized 13C dehydroascorbate magnetic resonance. Diabetes 64:344–352. https://doi.org/10.2337/db13-1829
41. Laustsen C, Lipsø K, Østergaard JA, Nørregaard R, Flyvbjerg A, Pedersen M, Palm F, Ardenkjaer-Larsen JH (2014) Insufficient insulin administration to diabetic rats increases substrate utilization and maintains lactate production in the kidney. Physiol Rep 2:e12233. https://doi.org/10.14814/phy2.12233
42. Qi H, Nielsen PM, Schroeder M, Bertelsen LB, Palm F, Laustsen C (2018) Acute renal metabolic effect of metformin assessed with hyperpolarised MRI in rats. Diabetologia 61:445–454. https://doi.org/10.1007/s00125-017-4445-6
43. Nørlinger TS, Nielsen PM, Qi H, Mikkelsen E, Hansen K, Schmidt NH, Pedersen M, Agger P, Palm F, Laustsen C (2017) Hyperbaric oxygen therapy reduces renal lactate production.

Physiol Rep 5:e13217. https://doi.org/10.14814/phy2.13217

44. Laustsen C, Nielsen PM, Nørlinger TS, Qi H, Pedersen UK, Bertelsen LB, Østergaard JA, Flyvbjerg A, Ardenkjaer-Larsen JH, Palm F, Stødkilde Jørgensen H (2017) Antioxidant treatment attenuates lactate production in diabetic nephropathy. Am J Physiol Renal Physiol 312:F192–F199. https://doi.org/10.1152/ajprenal.00148.2016
45. Koellisch U, Laustsen C, Nørlinger TS, Østergaard JA, Flyvbjerg A, Gringeri CV, Menzel MI, Schulte RF, Haase A, Stødkilde Jørgensen H (2015) Investigation of metabolic changes in STZ-induced diabetic rats with hyperpolarized [1-13C]acetate. Physiol Rep 3:e12474. https://doi.org/10.14814/phy2.12474
46. Nielsen PM, Szocska Hansen ES, Nørlinger TS, Nørregaard R, Bonde Bertelsen L, Stødkilde Jørgensen H, Laustsen C (2016) Renal ischemia and reperfusion assessment with three-dimensional hyperpolarized 13 C,15 N2-urea. Magn Reson Med 76:1524–1530. https://doi.org/10.1002/mrm.26377
47. Mariager CØ, Nielsen PM, Qi H, Ringgaard S, Laustsen C (2018) Hyperpolarized 13 C,15 N2 -urea T2 relaxation changes in acute kidney injury. Magn Reson Med 80:696–702. https://doi.org/10.1002/mrm.27050
48. Nielsen PM, Laustsen C, Bertelsen LB, Qi H, Mikkelsen E, Kristensen MLV, Nørregaard R, Stødkilde Jørgensen H (2017) In situ lactate dehydrogenase activity: a novel renal cortical imaging biomarker of tubular injury? Am J Physiol Renal Physiol 312:F465–F473. https://doi.org/10.1152/ajprenal.00561.2015
49. Baligand C, Qin H, True-Yasaki A, Gordon JW, von Morze C, Delos Santos J, Wilson DM, Raffai R, Cowley PM, Baker AJ, Kurhanewicz J, Lovett DH, Wang ZJ (2017) Hyperpolarized C-13 magnetic resonance evaluation of renal ischemia reperfusion injury in a murine model. NMR Biomed 30(10). https://doi.org/10.1002/nbm.3765
50. Nielsen PM, Eldirdiri A, Bertelsen LB, Jørgensen HS, Ardenkjaer-Larsen JH, Laustsen C (2017) Fumarase activity: an in vivo and in vitro biomarker for acute kidney injury. Sci Rep 7:40812. https://doi.org/10.1038/srep40812

Chapter 17

Functional Imaging Using Fluorine (^{19}F) MR Methods: Basic Concepts

Sonia Waiczies, Christian Prinz, Ludger Starke, Jason M. Millward, Paula Ramos Delgado, Jens Rosenberg, Marc Nazaré, Helmar Waiczies, Andreas Pohlmann, and Thoralf Niendorf

Abstract

Kidney-associated pathologies would greatly benefit from noninvasive and robust methods that can objectively quantify changes in renal function. In the past years there has been a growing incentive to develop new applications for fluorine (^{19}F) MRI in biomedical research to study functional changes during disease states. ^{19}F MRI represents an instrumental tool for the quantification of exogenous ^{19}F substances in vivo. One of the major benefits of ^{19}F MRI is that fluorine in its organic form is absent in eukaryotic cells. Therefore, the introduction of exogenous ^{19}F signals in vivo will yield background-free images, thus providing highly selective detection with absolute specificity in vivo. Here we introduce the concept of ^{19}F MRI, describe existing challenges, especially those pertaining to signal sensitivity, and give an overview of preclinical applications to illustrate the utility and applicability of this technique for measuring renal function in animal models.

This chapter is based upon work from the COST Action PARENCHIMA, a community-driven network funded by the European Cooperation in Science and Technology (COST) program of the European Union, which aims to improve the reproducibility and standardization of renal MRI biomarkers. This introduction chapter is complemented by two separate chapters describing the experimental procedure and data analysis.

Key words Magnetic resonance imaging (MRI), Fluorine (^{19}F), Kidney, Inflammation, Tissue oxygenation

1 Introduction

The need for methods to assess renal function that are both robust and noninvasive is increasingly becoming recognized. One approach is to use MRI in combination with contrast agents that are responsive to physiological changes [1]. The most common type of MR contrast agents are paramagnetic agents that enhance contrast on MR images. These contrast agents act by modulating proton (^{1}H) relaxation, either during recovery (T_1 component) or

Andreas Pohlmann and Thoralf Niendorf (eds.), *Preclinical MRI of the Kidney: Methods and Protocols*, Methods in Molecular Biology, vol. 2216, https://doi.org/10.1007/978-1-0716-0978-1_17, © The Author(s) 2021

decay (T_2 component) of the MR signal. In order for a contrast agent to be useful to identify changes in a specific physiological phenomenon, its sensitivity to detect and quantify physiological changes on MRI and its pharmacokinetic properties must be balanced [2].

From a technical point of view, paramagnetic contrast agents have a concomitant effect on all components of MR relaxation; the interplay between T_1 and T_2 relaxation depends on the dose and location of the contrast agent as well as the MR imaging sequence used [3]. This complexity is exacerbated by intrinsic factors such as deoxygenated blood or air cavities that may confound the signal being investigated [4]. A case in point is when imaging cells labeled with contrast agent: changes in contrast created by such intrinsic tissue factors could render the labeled cells indistinguishable from the surrounding tissue. This drawback is heightened by the signal sensitivity constraints due to the low concentrations of contrast agent (<μM range). As a result, any quantification of the physiological observation is hampered, and in some cases, no definitive conclusions can be made.

The use of fluorinated agents in combination with fluorine (^{19}F) MRI overcomes the hurdle of signal ambiguity because the ^{19}F MR signal is specific to the administered ^{19}F agent. While the ^{19}F nucleus has similar MR sensitivity and resonance frequency as ^{1}H, unlike ^{1}H, it is practically absent in vivo, that is, there are no endogenous ^{19}F organic forms in vivo. Therefore, any exogenous fluorinated compounds introduced in vivo can be detected with high selectivity and absolute specificity. This has been exploited to noninvasively track cells in vivo using ^{19}F MRI after labeling them with ^{19}F compounds, typically in the form of nanoparticles (NP). Interestingly, the chemical shift range for ^{19}F is much larger than that of ^{1}H. Organofluorine compounds span a chemical shift range of over 350 ppm [5]. Thus multiple ^{19}F nuclei resonances for organofluorine compounds can be easily separated, even under rather inhomogeneous conditions [6]. The unique properties of ^{19}F nuclei as well as ^{19}F compounds have been the driving force behind the increasing interest in ^{19}F MRI. However, the application of ^{19}F MRI to a wide range of biomedical research fields has been restricted by the low abundance of ^{19}F nuclei in vivo following exogenous administration. This constraint is compounded by the fact that the signal sensitivity of current MR hardware remains limited, making the detection of ^{19}F compounds present at low concentrations extremely challenging. Therefore, one strategy in ^{19}F MRI to circumvent this is to boost the signal-to-noise ratio (SNR) as a function of time, that is, the SNR efficiency to enhance signal sensitivity and improve detection limits.

From a biological perspective, several key components must be considered when using contrast agents to study renal function. Among other physicochemical properties, size will determine the pharmacokinetic properties of the contrast agent as well as its uptake

by cells in vivo. For example, low-molecular-weight-gadolinium-based contrast agents (GBCAs) are filtered through the glomerulus and are not reabsorbed by the renal tubule. Conversely, larger contrast agents such as paramagnetic iron oxide particles or ^{19}F nanoparticles commonly follow a one-compartment pharmacokinetic model within the blood [7]. These nanoparticles are too large to be filtered by the glomerulus and are eventually taken up by phagocytic blood cells. Such nanoparticles including the iron replacement therapy ferumoxytol have a long intravascular half-life (>14 h) and are therefore useful for vascular and perfusion-weighted MRI [8]. Unless inflammatory processes are ongoing, these particles will localize primarily in the liver and will eventually undergo elimination via hepatic clearance. The clearance of nanoparticles via liver or kidney is dependent on their size and surface properties [9] but also on the health status of these organs, such that clearance should be critically studied [10] especially prior to patient studies.

This introduction chapter is complemented by two separate chapters describing the experimental procedure and data analysis, which are part of this book.

This chapter is part of the book Pohlmann A, Niendorf T (eds) (2020) Preclinical MRI of the Kidney—Methods and Protocols. Springer, New York.

2 Overview of Applications

Quantitative measurements of renal function are necessary to detect changes already during the early stages of kidney disease, to support disease staging and to screen emerging therapeutic strategies. Non-invasive and rapid MR methods are needed to quantify disease components such as inflammation, hypoxia and tissue damage. While commonly available MR contrast agents act by modulating ^{1}H relaxation, contrast agents containing ^{19}F have also been developed to investigate disease components such as inflammation and to quantify pathological changes in the tissue microenvironment (e.g., changes in tissue oxygenation (pO_2) or pH) using ^{19}F MRI.

2.1 ^{19}F MRI to Study Environmental Changes in the Kidney In Vivo

There is an abundant repertoire of exogenous MRI contrast agents that act by modulating ^{1}H relaxation and which are triggered by changes in pO_2, pH or temperature as well as changes in protein, metabolite or metal ion concentrations (reviewed elsewhere [1]). Here we focus on the application of ^{19}F probes that elicit a desired MR signal following changes in pO_2 and pH and hold promise as tools for screening kidney disease.

2.1.1 Renal Tissue Oxygenation

Healthy kidneys operate under relatively low O_2 conditions, requiring extensive extraction of O_2 from flowing blood. While several regulatory mechanisms act to maintain oxygenation within homeostatic limits, the kidneys are nonetheless particularly susceptible to

hypoxic injury [11]. While O_2 consumption determines perfusion in most nonrenal tissue such as the brain, perfusion determines O_2 consumption in the kidney [12]. Therefore, a sudden temporary impairment of the blood flow to the kidney results in acute kidney injury (AKI) as a result of impaired O_2 delivery. Approaches for identifying and treating AKI as early as possible should aim at detecting and restoring imbalances the homeostasis between renal oxygenation and factors such as nitric oxide that control the renal microcirculation [13].

Noninvasive methods to measure kidney function in vivo, specifically tissue pO_2 and blood perfusion, are crucial. Arterial spin labeling MRI determines intrarenal perfusion without the need of exogenous contrast agents, and will be reviewed in a separate chapter of this book. MRI techniques that utilize the native ^{1}H contrast from blood—blood-oxygenation-level-dependent (BOLD) MRI—have been proposed [14]. The level of renal oxygenation within each voxel is quantified by mapping the shortening of ^{1}H T_2^* induced by deoxyhemoglobin—deoxyHb [15]. However, the relation of T_2^* to tissue pO_2 may be confounded by factors such as hematocrit, oxyHb dissociation curve, and the vascular volume fraction. This underscores the need for careful scrutiny of this relation in order to make quantitative interpretations [16].

Perfluorocarbon (PFC) emulsions offer an alternative to quantify changes in tissue pO_2 during vascular pathology [17, 18]. More recently PFC NPs were also employed as a theranostic strategy for studying perfusion and treating AKI [19]. Primarily PFC NPs have been used to assess perfusion in the renal microvasculature following AKI [20]. ^{19}F MRI sensitively detected decreased RBV and pO2 in the cortical–medullary (CM) junction 24 h following unilateral (left) renal ischemia–reperfusion [20], where increased T_2^* was also observed by ^{1}H BOLD MRI (Fig. 1a). The T_2^*, ^{19}F signal, and pO_2 in the renal cortex of injured kidneys were all comparable to the contralateral control kidney, suggesting recovery of perfusion and oxygenation in this region. In the inner medulla, however, vascular leakage and hemorrhage-induced extravascular retention of PFC NPs (Fig. 1b, c) resulted in a false readout of reduced ^{1}H T_2^*, increased ^{19}F signal intensity, and unchanged pO2.

PFCs and oxygen exhibit similarly low cohesive energy densities, such that both require little energy for mutual solubility [21]. The high oxygen-dissolving capacity of PFC emulsions makes them ideal as O_2 carriers. PFCs were, in fact, considered as artificial blood substitutes [22]. Fluosol-DA—a mixture of perfluorodecalin (PFD) and perfluorotributylamine—was the first PFC emulsion studied in humans in a trial of Japanese patients [23]. It was soon recalled due to its rather low oxygen transport capacity compared to that of red blood cells [24]. PFCs ultimately failed as blood substitutes (even as next generation products

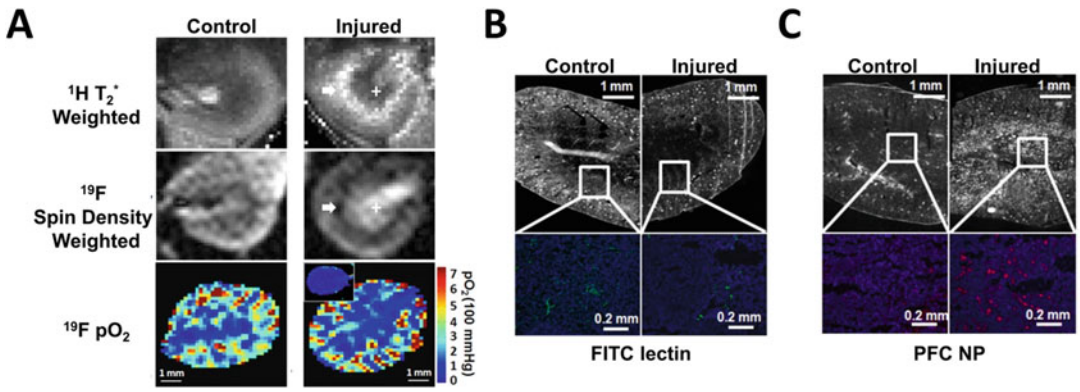

Fig. 1 Assessing perfusion in the renal microvasculature following acute kidney injury using PFCs. (**a**) Composite Representative ^{1}H T2*-weighted image (top row), ^{19}F spin density weighted image (middle row), and pO_2 map (bottom row) in the left control and right injured kidneys of the same mouse. (**b**) Fluorescence images showing FITC-lectin labeled perfused blood vessels in control and injured kidneys (top row) and zoom-in view of FITC-lectin (green) labeled perfused vessels in the CM junction (bottom row). (**c**) Fluorescence images showing rhodamine labeled PFC NPs in injured and control kidneys (top row) and zoom-in view showing PFC NPs (red) in the renal medulla (bottom row). Adapted from Hu L. et al. (2013) [20] with permission from John Wiley & Sons Inc.

appeared in the clinic). Although O_2-deprived tissues easily extract O_2 in PFCs, the oxygen dissociation curve of PFC emulsions is linear and monotonic, in contrast to the sigmoidal hemoglobin dissociation curve. Therefore, most of the O_2 dissolved in PFCs is released at high O_2 partial pressure in the arteries, with little O_2 being available for the capillaries where O_2 partial pressure is low but needed the most [22]. Interestingly Fluosol-DA (the first PFC that was used in patients [23]) was also used to acquire the first ^{19}F MR images in vivo, showing its accumulation in the rat liver [25]. The PFC in this emulsion gives complex MR spectra and has since been replaced by other PFCs with better imaging properties [26].

The longitudinal relaxation rate ($1/T_1$) of ^{19}F in PFCs was shown to depend linearly on O_2 partial pressure [27]. This led to the first noninvasive in vivo tissue O_2 assessments in tumor tissue and liver [28] and later in myocardial tissue [29]. The latter study provided the first proof of concept study for rapid, noninvasive measurements of O_2 oxygen tension changes in response to ischemia and reperfusion [29]. It is claimed that the size of PFC nanoparticles (>100 nm) confers upon them a good safety profile without renal toxicity, since they are not expected to be cleared through glomerular filtration. Therefore, unlike other imaging agents that undergo renal clearance (e.g., iodinated CT compounds, gadolinium MRI chelates), PFC emulsions do not increase the workload of the kidney and are not immediately considered as nephrotoxic [10].

2.1.2 Acid–Base Homeostasis in the Kidney and pH Sensors

The kidney plays a major role in acid–base homeostasis; this balance depends on its capacity to reabsorb filtered bicarbonate, mainly from the proximal tubule, and to excrete an equivalent amount of protons at the distal tubule [30]. CEST MRI was originally developed to measure pH with exogenous pH-responsive MRI contrast agents [31]. The pH in the kidney following AKI gradually increased from 6.7 to 7.2 as measured with CEST-MRI pH-responsive probes [32]. A major drawback of paramagnetic probes is that signal intensity is not only proportional to the pH but also to contrast agent concentration. Particularly in tumors, in vivo pH mapping assumes a constant contrast agent concentration across tissue notwithstanding poor perfusion where acidolysis occurs [33].

Approaches such as ratiometric $^{19}F/^{1}H$ probes have been developed to overcome the issue of quantification; the signal is normalized to the concentration of the contrast agent by means of a concentration reporting (^{19}F) moiety [34]. Another advantage of ^{19}F MR probes is the larger range in chemical shifts in ^{19}F (compared to ^{1}H). These chemical shifts are highly sensitive to the immediate surroundings, such that small chemical changes can lead to dramatic changes in chemical shift [6]. The first ^{19}F MR probe identified as a candidate to probe cellular pH was the vitamin B6 analog 6-fluoropyridoxol (6-FPOL) reported to have a pK_a in the physiological range and large chemical shift response [35]. Subsequently the feasibility of using 6-FPOL to probe cellular pH was demonstrated in whole blood [36]. The concept of employing ^{19}F MR probes for in vivo imaging was introduced when a series of fluorinated vitamin B6 analogs with a chemical shift sensitivity in the range 7.4–12 ppm were synthesized as pH indicators [37]. The sensitivity of ^{19}F MRS probes can be further improved by incorporating paramagnetic metal ions that further amplify the chemical shift between protonated and deprotonated forms by the presence of covalent and dipolar contributions [38, 39]. Iron (II) complexes were also explored to exploit the pH-dependent spin-state population change; the ^{19}F NMR chemical shift was in a sensitivity range of 13.9 ppm per pH unit at 37 °C [40]. More recently fluorinated nickel (II) complexes with diamagnetic and paramagnetic properties were designed for ratiometric pH mapping by ^{19}F MRI [41]. Supramolecular nanostructures formed by fluorinated peptide amphiphiles transitioning from cylindrical to ribbon-like shape as pH increases from 4.5 to 8.0 resulting in enhanced MR signals. These nanostructures represent a good strategy to design stimulus-responsive ^{19}F MRI contrast agents for responses to pH changes in vivo [42].

2.2 ^{19}F MRI to Study Renal Inflammation In Vivo

Together with renal tissue hypoxia and tubular injury, inflammation is one underlying component in the pathology of AKI [43]. Studies suggest that systemic inflammation causes ischemic injury in one organ and that repercussions follow in distant organs downstream

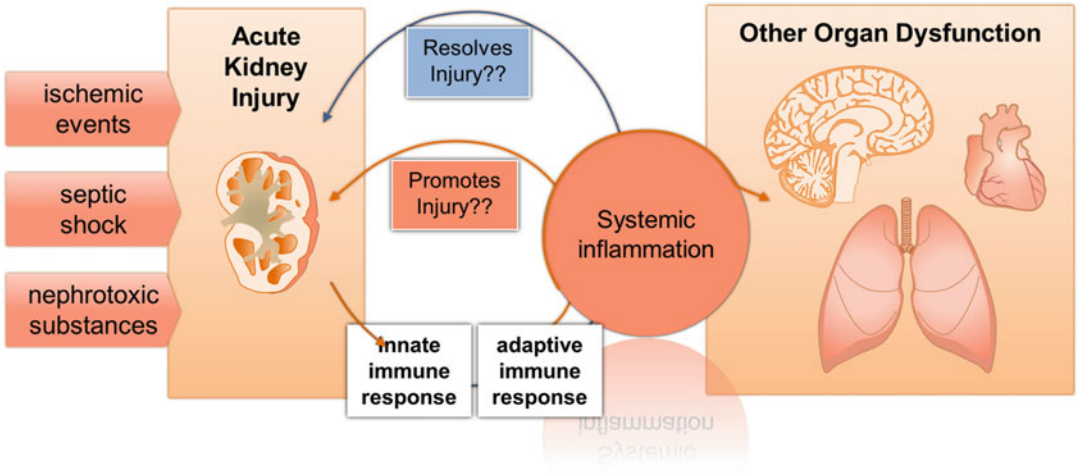

Fig. 2 Inflammation as one underlying factor in the pathology of AKI. AKI can be triggered by a variety of clinical disorders ranging from renal ischemic events to sepsis and exposure to nephrotoxic substances. The kidney is tightly connected with the interior milieu of the body such that even the slightest of changes will be rapidly detected and communicated between the kidney and the rest of the body

of the ischemic event [44–46] (Fig. 2). Therefore, methods that can non-invasively quantify the level of inflammation in different organs would be crucial to identify the causality and significance of inflammation during both systemic and kidney-specific disease.

^{19}F MRI is commonly used in association with an intravenous administration of PFC emulsions to study the distribution of inflammatory cells in vivo [26, 47–51]. ^{19}F MRI is performed after an in vivo labeling of inflammatory cells with a ^{19}F compound—typically in nanoparticle (NP) form. The ^{19}F-NPs are administered intravenously in order for them to be taken up by inflammatory cells that are migrating through the systemic circulation into inflamed organs. Typically, PFCs such as perfluoro-15-crown-5 ether (PFCE) are used to prepare NPs for cell labeling. PFCE is biologically stable and provides a high payload of ^{19}F nuclei since it contains 20 chemically equivalent ^{19}F spins.

In a rat model of orthotopic kidney transplantation, ^{19}F MRI was used to study inflammation in the kidney undergoing rejection [48]. Three days following transplantation, PFCE NPs were administered intravenously and ^{1}H/^{19}F images acquired 2 and 24 h following NP infusion (Fig. 3a). At the earlier time point, the ^{19}F signal was mainly found in the circulation but also in small but roughly equal amounts in both the native and transplanted kidneys (Fig. 3a). By day 4 posttransplantation (i.e., 24 h following PFCE NP), the transplanted kidney underwent moderate (Grade 2) rejection and showed an intense signal in the allograft kidney and in liver and spleen, but the ^{19}F signal was virtually undetectable above the level of image noise in the native kidney (Fig. 3a). T_2*-weighted

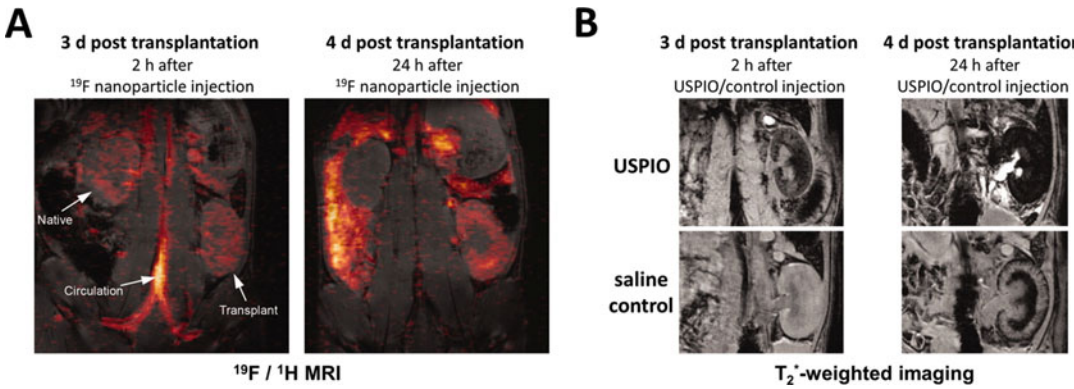

Fig. 3 Inflammation in the kidney in a rat model of orthotopic kidney transplantation experiencing rejection. (**a**) Composite $^{1}H/^{19}F$ images of an orthotopic kidney transplant recipient ~2 h post–PCE injection on POD 3 with ^{19}F signal found in the vasculature and equally in both the native (upper) and graft (lower) kidneys (left) and ~24 h post–PCE injection with ^{19}F signal in the allograft kidney, as well as other organs (right). (**b**) Allograft kidney on POD 4 following an injection (left) of 6 mg/kg BW USPIO (upper row) or following an injection of saline (lower row) and 24 h later (right). Adapted from Hitchens T.K. et al. (2011) [48] with permission from John Wiley & Sons Inc.

imaging reveals hemorrhaging in the medulla on day 4 post-kidney transplantation, which can be detected both in animals administered ultrasmall superparamagnetic iron oxide (USPIO) NPs but also in transplants without USPIO (saline control) (Fig. 3b). This can confound the detection of USPIO-labeled macrophages and exhibits one of the advantages of ^{19}F MRI over iron oxide-based NPs.

Apart from labeling inflammatory cells in vivo, NPs have been used to label specific immune cell types such as dendritic cells (DCs) ex vivo, prior to their administration in vivo [52–54]. This kind of labeling is particularly useful to label cellular therapies that will be administered in patients as part of a treatment strategy [55]. In addition to cancer patients, kidney transplantation patients would also benefit from cell-based therapies, specifically the types of cells inducing tolerance [56]. Monocyte-derived suppressor cell products are currently being investigated alongside immunosuppressive therapies in kidney transplant recipients with promising results [57]. These candidate therapies would benefit from a labeling strategy that will enable them to be tracked in vivo over time with ^{19}F MRI. The possibility of quantifying the ^{19}F MR signal would allow an objective assessment of the spatial and temporal cellular distribution within the same individual. This kind of labeling and ^{19}F MRI would result in absolute cell quantification, since the ^{19}F MR signal is generated from the cells alone, by direct detection of the ^{19}F spins in the cells labeled with ^{19}F NPs, without any confounding background MR signal. However, several biological and technical considerations need to be made, in order to achieve a truly absolute MR signal quantification: not all cell types can be labeled with the ^{19}F NPs currently available (Subheading 3.1.1).

3 Basic Concepts of ^{19}F MRI

3.1 ^{19}F imaging Probes

The design and synthesis of novel fluorine-rich molecular labels and imaging probes is an important domain for ^{19}F MRI. For several years, a wide range of fluorine probes has been available for experimental and even clinical applications [58, 59].

3.1.1 ^{19}F Probes for Cellular Uptake

Current procedures used to label cells with nanoparticles take advantage of the intrinsic nature of cells to engulf foreign bodies, a cellular property known as phagocytosis. Dendritic cells are intrinsically phagocytic and therefore ideal candidates for tracking with ^{19}F MRI [52, 53, 55, 60–62]. Cells labeled with clinical grade ^{19}F nanoparticles have been administered as immunotherapies in cancer patients [55]. This tracking method could support several other cell therapy studies, including those dealing with kidney transplantation [63].

Enhancing cellular uptake is desirable, even for cells that are intrinsically phagocytic. Several studies have investigated the incorporation of phosphatidylserine (PS) in nanoparticle-based therapeutics to enhance their uptake [64]. After renal ischemia–reperfusion, the signal from PS-containing microbubbles was two-fold higher than that for standard lipid microbubbles [65]. Phospholipids such as PS and phosphatidylethanolamine (PE) are important components of biological cell membranes and are important components for endocytosis in phagocytic cells such as DCs [66]. We previously reported that enrichment of ^{19}F nanoparticles with 1,2-dipalmitoyl-sn-glycero-3-PE (DPPE) resulted in a striking increase (at least one order of magnitude) in cytoplasmic uptake in DCs [62]. Interestingly, membrane lipid-raft processes have been proposed as trafficking mechanisms for transporting therapeutic cargo such as siRNA [67] or targeting ligands [68] into the cytoplasm, circumventing the usual endosomal uptake pathway.

Labeling cells with low intrinsic phagocytic properties (such as T cells) will prove more difficult using the above strategy, even if the nanoparticle size is lower than 180 nm [69]. Some research groups claim to have labeled T cells using the same above principles [70]. T cells are not able to internalize nanoparticles, even small iron oxide nanoparticles (core diameter = 12.5 nm), as has been clearly shown by transmission electron microscopy (TEM), considered to be a definitive method, and also by confocal microscopy [71]. For the latter method nanoparticles with fluorescent tags were used to corroborate the in vivo ^{19}F signals with ex vivo fluorescence microscopy signals, but the authors also included a cell membrane stain [71]. This is a necessary control to distinguish membrane association from intracellular distribution, in light of the point spread function contribution [72]. Another key point is that the fluorescent tag dissociates from the fluorine label over time, both in vitro and in vivo [73]. This has a critical impact on the interpretation of long-term experiments validated by standard fluorescent techniques.

Before taking the next steps toward administering cells in vivo, it is essential to understand how nanoparticles are recognized, internalized, trafficked, and distributed within the specific host cell [74]. This is critical when contemplating labeling of cells that may ultimately be applied in vivo to patients in a therapeutic context. Cells that are not intrinsically phagocytic will not readily internalize NPs but might still exhibit a ^{19}F MR signal ex vivo, due to reasons such as transitional binding of NPs to the cell membrane or incomplete clearing of noninternalized NPs from the cell culture medium. The ^{19}F MR signals following administration of ineffectively labeled cells with contaminating NPs would be misrepresentative of the actual distribution of the cells in vivo. Therefore, we need to ask the right questions regarding the specific cell type to be labeled, and the methods used prior to transfer of the cells into living organisms [75].

3.1.2 ^{19}F Probes with Increased Signal Sensitivity

Fluorinated probes are commonly designed with the goal of improving signal strength by increasing the number of fluorine atoms per molecule [59]. Linear ^{19}F polymers such as perfluoropolyethers (PFPEs) are the simplest choice to achieve increased fluorine content but the NPs produced with these polymers are polydisperse and the presence of multiple chemical shifts presents several peaks in the ^{19}F spectra [76]. Superfluorinated branched ^{19}F probes such as ^{19}FIT [77] and PERFECTA [78] promise several advantages, specifically a very high fluorine nuclei density with a single ^{19}F spectral peak. These probes therefore afford enhanced sensitivity and better imaging performance than linear perfluoropolymers. Unlike PERFECTA [78], the bispherical fluorocarbon ^{19}FIT is water soluble [77] and therefore possesses low organ retention, but it cannot be emulsified into nanoparticles for cell labeling strategies. Increasing the density of ^{19}F nuclei can only go so far in terms of increased sensitivity of ^{19}F probes. Ultimately, a limit to this density will be reached.

Another strategy to promote ^{19}F MR signal is to manipulate the MR properties of the ^{19}F probes in order to favor ideal conditions for MR signal acquisition. One approach is to decrease the T_1 of the ^{19}F nuclei, which is typically in the range of 0.5–3 s for diamagnetic compounds. Paramagnetic metal ions such as lanthanides(III) or iron(II) reduce the T_1 of ^{19}F compounds [38]. Paramagnetic centers affect the relaxation of ^{19}F nuclei (paramagnetic relaxation enhancement or PRE effect) via a number of mechanisms, most notably electron–nucleus dipole–dipole interaction and Curie relaxation [39], both of which are influenced by the effective magnetic moment (μ_{eff}) of the paramagnetic metal [79]. Other than the μ_{eff} of the metal ion, the PRE effect is also influenced by the distance separating the ^{19}F nuclei and the paramagnetic metal ion [39]. While long distances will severely diminish PRE, short

distances will substantially shorten the spin–spin relaxation time T_2. Thus T_1 reduction by molecular design should be dealt with carefully since it could also lead to a reduction in the T_2 and thereby line broadening of the resonance, which ultimately affects sensitivity [80]. The most sensitive metal-based probes are, in fact, not those whose metal ions have the highest μ_{eff}, but rather those who have the ideal distance separating ^{19}F from the paramagnetic metal ion (4.5–7.5 Å) thus resulting in higher T_2/T_1 ratios [81]. Nonetheless even at larger ^{19}F–M distances (>10 Å), the PRE effect can still be notable as is the case for a DOTA-based ^{19}F chelator [82]. In paramagnetic PFC nanoparticles, the ^{19}F MR relaxation enhancement has also been explained by diffusion mechanisms attributed to the changes in Brownian motion of PFC molecules inside the NP in conjunction with their ability to permeate into the lipid surfactant coating [83].

Introduction of paramagnetic metals in the design of ^{19}F probes not only results in a decrease T_1 of ^{19}F nuclei but also leads to paramagnetic induced chemical shifts. The CEST signal generated by paramagnetic involvement (PARACEST) will also be modulated by pH (Subheading 2.1.2). A macrocyclic Fe (II) complex bearing both exchangeable ^{1}H and ^{19}F was shown to behave as a ratiometric pH-responsive MRI contrast agent, whereby the CEST, but not the ^{19}F MR signal was pH-dependent [84]. This enables accurate pH mapping without the use of multiple probes. More recently a DOTA macrocyclic structure complexed with Ni(II) metal was shown to exhibit larger separations between the ^{1}H CEST signal and water [85]. Though the in vivo application of ^{19}F PARACEST probes remains to be investigated, the available complexes will likely provide valuable information in the near future when probing pH changes in vivo.

3.2 MR Data Acquisition

3.2.1 Pulse Sequence Optimization

One way of improving signal sensitivity is to avoid signal losses such as those occurring during spin relaxation. Most fluorinated compounds generally have long T_1 relaxation times, which effectively increases the acquisition time. Together with the fact that there is a large range of relaxation times for ^{19}F MR, this motivates more reliable optimization of pulse sequences that is informed by the MR properties of the ^{19}F compounds under investigation. Sequence performance is largely dependent on the relaxation times of the addressed spin system but also on the conditions the nuclei are in, such as tissue oxygenation level [17].

The choice of the best pulse sequence and acquisition method is dictated by the MR properties, particularly the relaxation times, of the nuclei being measured. The acquisition protocol for each sequence should be optimized by tailoring detection schemes to the properties of the nucleus—also in relation to its environment—using relationships empirically drawn from simulations [86]. Relaxation times determine the time frames of signal losses, so the time

orchestration for data acquisition should be assigned correctly. Other parameters, such as acquisition bandwidths, should also be properly planned to avoid recording unnecessary noise and to achieve the highest possible SNR [87].

A number of ^{19}F MR studies using different pulse sequences have aimed to optimize the acquisition method to promote SNR efficiency and signal sensitivity [17, 87–90]. A large proportion of ^{19}F MR studies, especially those applying perfluorocarbons (PFCs) in vivo, have employed the turbo spin echo (SE) rapid acquisition using relaxation enhancement (RARE) sequence [26, 47, 50, 51, 91]. This method reduces acquisition time by accumulating multiple echoes (dictated by the turbo factor) within a single repetition time [92]. Optimal settings for echo train lengths and repetition time (TR) according to measured relaxation times (T_1/T_2 combinations) were calculated for RARE to improve sensitivity thresholds [90].

Although RARE is commonly been for studying PFCs in vivo, other sequences will be better suited for ^{19}F compounds that unlike typical PFCs have short T_2 relaxation times. In such cases signal detection might be technically challenging and will demand acquisition strategies properly adapted for the compound and its environment. Gradient echo (GE) sequences were used to maximize SNR efficiency for imaging paramagnetic macrocyclic ^{19}F molecules complexed to lanthanides [87]. These molecules exhibit T_1 values in the order of 1–15 ms and T_2* values in the order of 0.4–12 ms [88]. In the latter study a radial zero echo time (ZTE) sequence yielded a sensitivity gain of 27-fold when compared to nonparamagnetic molecules, while the GE sequence yielded a gain of 11-fold [88]. Additionally, the highest SNR efficiency gain was achieved when T_2/T_1 were close to 1, particularly for the ZTE pulse sequence, and when T_1 was in the range of 1–5 ms [88]. Even ^{19}F molecules with unique spectral properties will require a more individualized adjustment of the MR parameters; such molecules might benefit from sequences such as ultrashort echo time (UTE) that acquire signal before the spins dephase, taking into consideration destructive phase interference [93]. An efficient k-space sampling strategy will be necessary to achieve maximal SNR and artifact-free MR images [94]. To image perfluorooctyl bromide (PFOB) that has a rich spectrum with large chemical shifts, a radial UTE with a balanced steady-state free precession (bSSFP) pulse sequence showed superiority above other sequences, such as SE, GE, or bSSFP with Cartesian sampling [89]. However, radial sampling might not always be viable since k space sampling pattern effects need to be considered, which might altogether result in reduced SNR efficiency [86]. Another way to speed up data acquisition is synchronous multinuclear imaging. For this, the MR system needs to have the architecture suited to acquire images from more than one nucleus in a single pulse sequence [95]. Simultaneous proton

and ^{19}F MRI was performed in a preclinical model using a clinical MR scanner at 3 T [95].

3.3 Hardware Considerations

The similarity between ^{19}F and ^{1}H MR properties with respect to sensitivity and resonance frequency is an advantage, from an engineering perspective since similar pulse power settings can be used, and dual-tuned radio frequency (RF) coils for ^{19}F and ^{1}H MRI are more convenient to design [50, 96]. One way of improving the ^{19}F MR signal in vivo is to increase SNR by improving the sensitivity of the measuring instrument. Two hardware strategies to improve sensitivity for ^{19}F MR are to increase the strength of the static magnetic field (B_0), and to increase the sensitivity of the RF coil by cryogenic cooling.

3.3.1 Cryogenic Cooling

The sensitivity of the RF coil is an important factor limiting SNR and thereby the level of spatial and temporal resolution that is targeted for ^{19}F MRI [97]. Even when employing an RF coil with a homogeneous transmit field (B_1^+) distribution and dedicated for brain ^{19}F and ^{1}H MRI, the spatial resolution of in vivo ^{19}F MRI was limited to approximately 600 μm [50]. This level of spatial resolution prohibits a detailed understanding of inflammation dynamics. To overcome the sensitivity constraints in ^{19}F MR and improve detail of inflammatory cell location, we applied the concept of cryogenically cooling RF coil hardware to improve SNR by reducing thermal noise [98–100]. The cryogenically cooled RF coil (CryoProbe™) technology is commercially available for small animal MRI of ^{1}H and X-nuclei such as carbon (^{13}C) and phosphorous (^{31}P). For these X-nuclei this technology is expected to be particularly useful for increasing SNR. A gain in SNR of 3.0- to 3.5-fold was reported for the ^{13}C CryoProbe [101]. We recently compared a ^{19}F CryoProbe with a room temperature ^{19}F RF coil of similar size and reported on a maximal SNR gain of 15-fold and were able to study inflammation at an isotropic resolution of 150 μm [100].

Surface RF coils provide a very high SNR close to the region where they are applied. However, a decrease in signal amplitude with increasing distance from their surface is inherent to the geometry of their design. Inhomogeneities in the transmit (B_1^+) field cause a spatially varying flip angle (FA) and as a result signal quantification is hampered. Likewise, the receive (B_1^-) field of surface RF coils is position-dependent [102]. In the particular case of the ^{19}F CryoProbe, we observed a strong FA decrease with increasing distance from the surface of the coil [100]. Using a receive-only surface RF coil in combination with a volume resonator used for transmission would overcome B_1^+ inhomogeneities. With this configuration the transmitted FAs will be homogeneous, thus enabling quantification [103]. This option is not available when using CryoProbes, since they are typically built in the form of transceive (transmit–receive) RF coils with no active decoupling.

Particularly for quantitative ^{19}F MRI, a correction of the B_1^+ inhomogeneity will be necessary when comparing concentrations of PFC in vivo with an external standard of known ^{19}F concentration. Differences in the B_1^+ field between the region of interest in vivo and the external standard will result in errors when quantifying in vivo ^{19}F signals. Several approaches have been implemented to correct B_1^+ inhomogeneities retrospectively, even for ^{19}F MRI [104, 105]. These approaches typically include RF pulse sequences for which an analytical knowledge of the signal intensity dependency on the FA exists.

3.3.2 Magnetic Field Strengths

Increasing the strength of the static magnetic field (B_0) will increase SNR of the measured signal [106], a strategy which is actively being pursued for clinical application [107]. Intrinsic SNR is expected to grow at least linearly with increasing B_0 strengths [97, 108, 109]. The principle of reciprocity can be used at low field strengths to calculate the receive field (B_1) sensitivity of a single channel RF coil in terms of the transmit field (B_1^+) that can be easily measured [110]. In studies performed at frequency (f) <1 MHz the maximum sensitivity was calculated to be proportional to the f: sensitivity $\propto f1.75$ [97, 108]. When going to higher magnetic field strengths, the increasing f and the influence of wave propagation need to be considered [106]. The homogeneity of the B_1^+ field is expected to decline with increasing B_0, thereby influencing the overall SNR gain. An experimental study investigating SNR dependency on B_0 in the human brain revealed that SNR $\propto B_0 1.65$ in the range of 3.0–9.4 T [109]. A recent simulation study also showed that SNR grows superlinearly with frequency, particularly in deeper regions of the sample; in less deep regions the SNR versus B_0 trend approached linearity [111].

An increase in magnetic field strength is particularly beneficial for X-nuclei imaging. An increase in B_0 from 9.4 to 21.1 T results in an SNR gain of ~3 compared to a gain of ~2 for ^{1}H MR [112]. We recently studied the influence of increasing B_0 on improving ^{19}F MR signal sensitivity [113]. Prior to the practical experiments, we estimated the expected SNR gain when moving from 9.4 to 21.1 T to be 2.7 [113]. We estimated SNR gain using the principle of reciprocity [110] and ignoring all flip angle, sequence and relaxation-dependent effects. The estimated SNR gain represents a baseline expectation, based on the information available for the specific hardware of each system. When introducing the relationship of the reference power for both MR systems, we estimated an SNR gain of ~3.8. In our practical experiments the ratio in SNR efficiency (SNR/$\sqrt{t}$ ratio) was estimated to be 7.29, when comparing the best possible conditions for both 21.1 and 9.4 T, and when including T_1 relaxation effects [113]. Differences between the actual SNR gains determined experimentally and those expected

from simulations are conceivable, due to minor inaccuracies in the assumptions made for the EMF simulations.

All research efforts ranging from new ^{19}F probe design, through optimization of ^{19}F MR data acquisition methods up to hardware developments hinge on the need for promoting ^{19}F MR signal in vivo, in order to answer crucial questions during pathology including kidney disease. Most of the efforts devoted to discovery and proof-of-principle research will benefit from an integration of all available tools and technologies, in order to reach the maximum potential for practical applications for patient health care.

Acknowledgments

This work was funded in part (Thoralf Niendorf, Sonia Waiczies, Andreas Pohlmann) by the German Research Foundation (Gefoerdert durch die Deutsche Forschungsgemeinschaft (DFG), Projektnummer 394046635, SFB 1365, RENOPROTECTION. Funded by the Deutsche Forschungsgemeinschaft (DFG, German Research Foundation), Project number 394046635, SFB 1365, RENOPROTECTION).

Also, our research is funded by the Deutsche Forschungsgemeinschaft to S.W. (DFG WA2804) and A.P. (DFG PO1869), by the European Research Council, ERC to T.N. (ThermalMR, EU project 743077), by the State of Florida and National Science Foundation Cooperative Agreement No. DMR-1157490 and DMR-1644779 to J.R. and the Visiting Scientist Program of the NHMFL to S.W. and H.W. (227000-110, Project 12643). We thank Professor Samuel Wickline from the University of South Florida for valuable feedback on the manuscript.

This publication is based upon work from COST Action PARENCHIMA, supported by European Cooperation in Science and Technology (COST). COST (www.cost.eu) is a funding agency for research and innovation networks. COST Actions help connect research initiatives across Europe and enable scientists to enrich their ideas by sharing them with their peers. This boosts their research, career, and innovation.

PARENCHIMA (renalmri.org) is a community-driven Action in the COST program of the European Union, which unites more than 200 experts in renal MRI from 30 countries with the aim to improve the reproducibility and standardization of renal MRI biomarkers.

References

1. Hingorani DV, Bernstein AS, Pagel MD (2015) A review of responsive MRI contrast agents: 2005–2014. Contrast Media Mol Imaging 10(4):245–265. https://doi.org/10.1002/cmmi.1629

2. Grenier N, Merville P, Combe C (2016) Radiologic imaging of the renal parenchyma structure and function. Nat Rev Nephrol 12 (6):348–359

3. Martinez GV, Zhang X, García-Martín ML, Morse DL, Woods M, Sherry AD, Gillies RJ (2011) Imaging the extracellular pH of tumors by MRI after injection of a single cocktail of T1 and T2 contrast agents. NMR Biomed 24(10):1380–1391. https://doi.org/10.1002/nbm.1701
4. Brooks RA, Brunetti A, Alger JR, Di Chiro G (1989) On the origin of paramagnetic inhomogeneity effects in blood. Magn Reson Med 12(2):241–248
5. Günther H (2013) NMR spectroscopy: basic principles, concepts and applications in chemistry. John Wiley & Sons, Hoboken, NJ
6. Dolbier WR (2009) Guide to fluorine NMR for organic chemists. John Wiley & Sons, Hoboken, NJ
7. Arami H, Khandhar A, Liggitt D, Krishnan KM (2015) In vivo delivery, pharmacokinetics, biodistribution and toxicity of iron oxide nanoparticles. Chem Soc Rev 44 (23):8576–8607. https://doi.org/10.1039/c5cs00541h
8. Toth GB, Varallyay CG, Horvath A, Bashir MR, Choyke PL, Daldrup-Link HE, Dosa E, Finn JP, Gahramanov S, Harisinghani M, Macdougall I, Neuwelt A, Vasanawala SS, Ambady P, Barajas R, Cetas JS, Ciporen J, DeLoughery TJ, Doolittle ND, Fu R, Grinstead J, Guimaraes AR, Hamilton BE, Li X, McConnell HL, Muldoon LL, Nesbit G, Netto JP, Petterson D, Rooney WD, Schwartz D, Szidonya L, Neuwelt EA (2017) Current and potential imaging applications of ferumoxytol for magnetic resonance imaging. Kidney Int 92(1):47–66. https://doi.org/10.1016/j.kint.2016.12.037
9. Feng Q, Liu Y, Huang J, Chen K, Huang J, Xiao K (2018) Uptake, distribution, clearance, and toxicity of iron oxide nanoparticles with different sizes and coatings. Sci Rep 8 (1):2082. https://doi.org/10.1038/s41598-018-19628-z
10. Longmire M, Choyke PL, Kobayashi H (2008) Clearance properties of nano-sized particles and molecules as imaging agents: considerations and caveats. Nanomedicine (Lond) 3(5):703–717. https://doi.org/10.2217/17435889.3.5.703
11. O'Connor PM (2006) Renal oxygen delivery: matching delivery to metabolic demand. Clin Exp Pharmacol Physiol 33(10):961–967. https://doi.org/10.1111/j.1440-1681.2006.04475.x
12. Hansell P, Welch WJ, Blantz RC, Palm F (2013) Determinants of kidney oxygen consumption and their relationship to tissue oxygen tension in diabetes and hypertension. Clin Exp Pharmacol Physiol 40(2):123–137. https://doi.org/10.1111/1440-1681.12034
13. Le Dorze M, Legrand M, Payen D, Ince C (2009) The role of the microcirculation in acute kidney injury. Curr Opin Crit Care 15 (6):503–508. https://doi.org/10.1097/MCC.0b013e328332f6cf
14. Ries M, Basseau F, Tyndal B, Jones R, Deminière C, Catargi B, Combe C, Moonen CWT, Grenier N (2003) Renal diffusion and BOLD MRI in experimental diabetic nephropathy. J Magn Reson Imaging 17 (1):104–113. https://doi.org/10.1002/jmri.10224
15. Prasad PV (2006) Evaluation of intra-renal oxygenation by BOLD MRI. Nephron Clin Pract 103(2):c58–c65. https://doi.org/10.1159/000090610
16. Niendorf T, Pohlmann A, Arakelyan K, Flemming B, Cantow K, Hentschel J, Grosenick D, Ladwig M, Reimann H, Klix S, Waiczies S, Seeliger E (2015) How bold is blood oxygenation level-dependent (BOLD) magnetic resonance imaging of the kidney? Opportunities, challenges and future directions. Acta Physiol 213(1):19–38. https://doi.org/10.1111/apha.12393
17. Dardzinski BJ, Sotak CH (1994) Rapid tissue oxygen tension mapping using 19F inversion-recovery echo-planar imaging of P erfluoro-15-crown-5-ether. Magn Reson Med 32 (1):88–97
18. Noth U, Morrissey SP, Deichmann R, Adolf H, Schwarzbauer C, Lutz J, Haase A (1995) In vivo measurement of partial oxygen pressure in large vessels and in the reticuloendothelial system using fast 19F-MRI. Magn Reson Med 34(5):738–745
19. Chen J, Vemuri C, Palekar RU, Gaut JP, Goette M, Hu L, Cui G, Zhang H, Wickline SA (2015) Antithrombin nanoparticles improve kidney reperfusion and protect kidney function after ischemia-reperfusion injury. Am J Physiol Renal Physiol 308(7):28
20. Hu L, Chen J, Yang X, Senpan A, Allen JS, Yanaba N, Caruthers SD, Lanza GM, Hammerman MR, Wickline SA (2013) Assessing intrarenal nonperfusion and vascular leakage in acute kidney injury with multinuclear 1H/19F MRI and perfluorocarbon nanoparticles. Magn Reson Med. https://doi.org/10.1002/mrm.24851
21. Riess JG (2005) Understanding the fundamentals of perfluorocarbons and perfluorocarbon emulsions relevant to in vivo oxygen

delivery. Artif Cell Blood Sub Biotechnol 33 (1):47–63

22. Schmieder AH, Caruthers SD, Keupp J, Wickline SA, Lanza GM (2015) Recent advances in (19)fluorine magnetic resonance imaging with perfluorocarbon emulsions. Engineering (Beijing, China) 1(4):475–489. https://doi.org/10.15302/j-eng-2015103
23. Mitsuno T, Ohyanagi H, Naito R (1982) Clinical studies of a perfluorochemical whole blood substitute (Fluosol-DA) summary of 186 cases. Ann Surg 195(1):60–69. https://doi.org/10.1097/00000658-198201001-00010
24. Gould SA, Rosen AL, Sehgal LR, Sehgal HL, Langdale LA, Krause LM, Rice CL, Chamberlin WH, Moss GS (1986) Fluosol-DA as a red-cell substitute in acute anemia. N Engl J Med 314(26):1653–1656. https://doi.org/10.1056/nejm198606263142601
25. McFarland E, Koutcher JA, Rosen BR, Teicher B, Brady TJ (1985) In vivo 19F NMR imaging. J Comput Assist Tomogr 9 (1):8–15
26. Jacoby C, Temme S, Mayenfels F, Benoit N, Krafft MP, Schubert R, Schrader J, Flögel U (2014) Probing different perfluorocarbons for in vivo inflammation imaging by 19F MRI: image reconstruction, biological half-lives and sensitivity. NMR Biomed 27 (3):261–271. https://doi.org/10.1002/nbm.3059
27. Parhami P, Fung B (1983) Fluorine-19 relaxation study of perfluoro chemicals as oxygen carriers. J Phys Chem 87(11):1928–1931
28. Mason RP, Nunnally RL, Antich PP (1991) Tissue oxygenation: a novel determination using 19F surface coil NMR spectroscopy of sequestered perfluorocarbon emulsion. Magn Reson Med 18(1):71–79. https://doi.org/10.1002/mrm.1910180109
29. Mason RP, Jeffrey FMH, Malloy CR, Babcock EE, Antich PP (1992) A noninvasive assessment of myocardial oxygen tension: 19f nmr spectroscopy of sequestered perfluorocarbon emulsion. Magn Reson Med 27(2):310–317. https://doi.org/10.1002/mrm.1910270210
30. Pereira PCB, Miranda DM, Oliveira EA, Silva ACSE (2009) Molecular pathophysiology of renal tubular acidosis. Curr Genomics 10 (1):51–59. https://doi.org/10.2174/138920209787581262
31. Zhang S, Wu K, Sherry AD (1999) A novel pH-sensitive MRI contrast agent. Angew Chem Int Ed 38(21):3192–3194. https://doi.org/10.1002/(sici)1521-3773(19991102)38:21<3192::aid-anie3192>3.0.co;2-#
32. Longo DL, Busato A, Lanzardo S, Antico F, Aime S (2013) Imaging the pH evolution of an acute kidney injury model by means of iopamidol, a MRI-CEST pH-responsive contrast agent. Magn Reson Med 70 (3):859–864. https://doi.org/10.1002/mrm.24513
33. Raghunand N, Gatenby RA, Gillies RJ (2003) Microenvironmental and cellular consequences of altered blood flow in tumours. Br J Radiol 76(Suppl_1):S11–S22. https://doi.org/10.1259/bjr/12913493
34. Gianolio E, Napolitano R, Fedeli F, Arena F, Aime S (2009) Poly-β-cyclodextrin based platform for pH mapping via a ratiometric 19F/1H MRI method. Chem Commun 40:6044–6046. https://doi.org/10.1039/B914540K
35. Chang YC, Graves DJ (1985) Use of 6-fluoroderivatives of pyridoxal and pyridoxal phosphate in the study of the coenzyme function in glycogen phosphorylase. J Biol Chem 260(5):2709–2714
36. Mehta VD, Kulkarni PV, Mason RP, Constantinescu A, Aravind S, Goomer N, Antich PP (1994) 6-Fluoropyridoxol: a novel probe of cellular pH using 19F NMR spectroscopy. FEBS Lett 349(2):234–238. https://doi.org/10.1016/0014-5793(94)00675-x
37. He S, Mason RP, Hunjan S, Mehta VD, Arora V, Katipally R, Kulkarni PV, Antich PP (1998) Development of novel 19F NMR pH indicators: synthesis and evaluation of a series of fluorinated vitamin B6 analogues. Bioorg Med Chem 6(9):1631–1639. https://doi.org/10.1016/S0968-0896(98)00104-7
38. Neubauer AM, Myerson J, Caruthers SD, Hockett FD, Winter PM, Chen J, Gaffney PJ, Robertson JD, Lanza GM, Wickline SA (2008) Gadolinium-modulated 19F signals from perfluorocarbon nanoparticles as a new strategy for molecular imaging. Magn Reson Med 60(5):1066–1072
39. Chalmers KH, De Luca E, Hogg NHM, Kenwright AM, Kuprov I, Parker D, Botta M, Wilson JI, Blamire AM (2010) Design principles and theory of paramagnetic fluorine-labelled lanthanide complexes as probes for 19F magnetic resonance: a proof-of-concept study. Chem Eur J 16(1):134–148. https://doi.org/10.1002/chem.200902300
40. Gaudette AI, Thorarinsdottir AE, Harris TD (2017) pH-dependent spin state population and 19F NMR chemical shift via remote ligand protonation in an iron(ii) complex.

Chem Commun 53(96):12962–12965. https://doi.org/10.1039/C7CC08158H

41. Xie D, Ohman LE, Que EL (2018) Towards Ni(II) complexes with spin switches for 19F MR-based pH sensing. MAGMA. https://doi.org/10.1007/s10334-018-0698-4
42. Preslar AT, Tantakitti F, Park K, Zhang S, Stupp SI, Meade TJ (2016) 19F magnetic resonance imaging signals from peptide amphiphile nanostructures are strongly affected by their shape. ACS Nano 10 (8):7376–7384. https://doi.org/10.1021/acsnano.6b00267
43. Liu KD, Glidden DV, Eisner MD, Parsons PE, Ware LB, Wheeler A, Korpak A, Thompson BT, Chertow GM, Matthay MA (2007) Predictive and pathogenetic value of plasma biomarkers for acute kidney injury in patients with acute lung injury. Crit Care Med 35 (12):2755–2761
44. Levy EM, Viscoli CM, Horwitz RI (1996) The effect of acute renal failure on mortality. A cohort analysis. JAMA 275 (19):1489–1494
45. Jorres A, Gahl GM, Dobis C, Polenakovic MH, Cakalaroski K, Rutkowski B, Kisielnicka E, Krieter DH, Rumpf KW, Guenther C, Gaus W, Hoegel J (1999) Haemodialysis-membrane biocompatibility and mortality of patients with dialysis-dependent acute renal failure: a prospective randomised multicentre trial. International Multicentre Study Group. Lancet 354 (9187):1337–1341
46. Brouns R, De Deyn PP (2004) Neurological complications in renal failure: a review. Clin Neurol Neurosurg 107(1):1–16. https://doi.org/10.1016/j.clineuro.2004.07.012
47. Flögel U, Ding Z, Hardung H, Jander S, Reichmann G, Jacoby C, Schubert R, Schrader J (2008) In vivo monitoring of inflammation after cardiac and cerebral ischemia by fluorine magnetic resonance imaging. Circulation 118(2):140–148
48. Hitchens TK, Ye Q, Eytan DF, Janjic JM, Ahrens ET, Ho C (2011) 19F MRI detection of acute allograft rejection with in vivo perfluorocarbon labeling of immune cells. Magn Reson Med 65(4):1144–1153. https://doi.org/10.1002/mrm.22702
49. Temme S, Bonner F, Schrader J, Flögel U (2012) 19F magnetic resonance imaging of endogenous macrophages in inflammation. Wiley Interdiscip Rev Nanomed Nanobiotechnol 4(3):329–343. https://doi.org/10.1002/wnan.1163
50. Waiczies H, Lepore S, Drechsler S, Qadri F, Purfurst B, Sydow K, Dathe M, Kuhne A, Lindel T, Hoffmann W, Pohlmann A, Niendorf T, Waiczies S (2013) Visualizing brain inflammation with a shingled-leg radiofrequency head probe for 19F/1H MRI. Sci Rep 3:1280. https://doi.org/10.1038/srep01280
51. Flögel U, Burghoff S, van Lent PL, Temme S, Galbarz L, Ding Z, El-Tayeb A, Huels S, Bonner F, Borg N, Jacoby C, Muller CE, van den Berg WB, Schrader J (2012) Selective activation of adenosine A2A receptors on immune cells by a CD73-dependent prodrug suppresses joint inflammation in experimental rheumatoid arthritis. Sci Transl Med 4 (146):146ra108. https://doi.org/10.1126/scitranslmed.3003717
52. Ahrens ET, Flores R, Xu H, Morel PA (2005) In vivo imaging platform for tracking immunotherapeutic cells. Nat Biotechnol 23 (8):983–987
53. Waiczies H, Lepore S, Janitzek N, Hagen U, Seifert F, Ittermann B, Purfurst B, Pezzutto A, Paul F, Niendorf T, Waiczies S (2011) Perfluorocarbon particle size influences magnetic resonance signal and immunological properties of dendritic cells. PLoS One 6(7):e21981
54. Waiczies H, Guenther M, Skodowski J, Lepore S, Pohlmann A, Niendorf T, Waiczies S (2013) Monitoring dendritic cell migration using 19F/1H magnetic resonance imaging. J Vis Exp 73:e50251. https://doi.org/10.3791/50251
55. Ahrens ET, Helfer BM, O'Hanlon CF, Schirda C (2014) Clinical cell therapy imaging using a perfluorocarbon tracer and fluorine-19 MRI. Magn Reson Med 72 (6):1696-1701. https://doi.org/10.1002/mrm.25454
56. Ten Brinke A, Hilkens CMU, Cools N, Geissler EK, Hutchinson JA, Lombardi G, Lord P, Sawitzki B, Trzonkowski P, Van Ham SM, Martinez-Caceres EM (2015) Clinical use of tolerogenic dendritic cells-harmonization approach in european collaborative effort. Mediat Inflamm 2015:8. https://doi.org/10.1155/2015/471719
57. Hutchinson JA, Riquelme P, Sawitzki B, Tomiuk S, Miqueu P, Zuhayra M, Oberg HH, Pascher A, Lützen U, Janßen U, Broichhausen C, Renders L, Thaiss F, Scheuermann E, Henze E, Volk H-D, Chatenoud L, Lechler RI, Wood KJ, Kabelitz D, Schlitt HJ, Geissler EK, Fändrich F (2011) Cutting edge: immunological consequences and trafficking of human regulatory

macrophages administered to renal transplant recipients. J Immunol 187(5):2072–2078. https://doi.org/10.4049/jimmunol.1100762

58. Ruiz-Cabello J, Barnett BP, Bottomley PA, Bulte JW (2011) Fluorine (19F) MRS and MRI in biomedicine. NMR Biomed 24 (2):114–129. https://doi.org/10.1002/nbm.1570
59. Jirak D, Galisova A, Kolouchova K, Babuka D, Hruby M (2018) Fluorine polymer probes for magnetic resonance imaging: quo vadis? MAGMA. https://doi.org/10.1007/s10334-018-0724-6
60. Helfer BM, Balducci A, Nelson AD, Janjic JM, Gil RR, Kalinski P, de Vries IJ, Ahrens ET, Mailliard RB (2010) Functional assessment of human dendritic cells labeled for in vivo (19)F magnetic resonance imaging cell tracking. Cytotherapy 12(2):238–250. https://doi.org/10.3109/14653240903446902
61. Bonetto F, Srinivas M, Heerschap A, Mailliard R, Ahrens ET, Figdor CG, de Vries IJ (2011) A novel (19)F agent for detection and quantification of human dendritic cells using magnetic resonance imaging. Int J Cancer 129(2):365–373. https://doi.org/10.1002/ijc.25672
62. Waiczies S, Lepore S, Sydow K, Drechsler S, Ku MC, Martin C, Lorenz D, Schutz I, Reimann HM, Purfurst B, Dieringer MA, Waiczies H, Dathe M, Pohlmann A, Niendorf T (2015) Anchoring dipalmitoyl phosphoethanolamine to nanoparticles boosts cellular uptake and fluorine-19 magnetic resonance signal. Sci Rep 5:8427. https://doi.org/10.1038/srep08427
63. Hutchinson JA, Ahrens N, Riquelme P, Walter L, Gruber M, Böger CA, Farkas S, Scherer MN, Broichhausen C, Bein T, Schlitt H-J, Fändrich F, Banas B, Geissler EK (2014) Clinical management of patients receiving cell-based immunoregulatory therapy. Transfusion 54(9):2336–2343. https://doi.org/10.1111/trf.12641
64. Bagalkot V, Deiuliis JA, Rajagopalan S, Maiseyeu A (2016) "Eat me" imaging and therapy. Adv Drug Deliv Rev 99(Pt A):2–11. https://doi.org/10.1016/j.addr.2016.01.009
65. Lindner JR, Song J, Xu F, Klibanov AL, Singbartl K, Ley K, Kaul S (2000) Noninvasive ultrasound imaging of inflammation using microbubbles targeted to activated leukocytes. Inflammation 102:2745–2750
66. Steinman RM, Mellman IS, Muller WA, Cohn ZA (1983) Endocytosis and the recycling of plasma membrane. J Cell Biol 96(1):1–27
67. Kaneda MM, Sasaki Y, Lanza GM, Milbrandt J, Wickline SA (2010) Mechanisms of nucleotide trafficking during siRNA delivery to endothelial cells using perfluorocarbon nanoemulsions. Biomaterials 31 (11):3079–3086
68. Partlow KC, Lanza GM, Wickline SA (2008) Exploiting lipid raft transport with membrane targeted nanoparticles: a strategy for cytosolic drug delivery. Biomaterials 29 (23):3367–3375
69. Chapelin F, Capitini CM, Ahrens ET (2018) Fluorine-19 MRI for detection and quantification of immune cell therapy for cancer. J Immunother Cancer 6(1):105. https://doi.org/10.1186/s40425-018-0416-9
70. Chapelin F, Gao S, Okada H, Weber TG, Messer K, Ahrens ET (2017) Fluorine-19 nuclear magnetic resonance of chimeric antigen receptor T cell biodistribution in murine cancer model. Sci Rep 7(1):17748. https://doi.org/10.1038/s41598-017-17669-4
71. Sanz-Ortega L, Rojas JM, Marcos A, Portilla Y, Stein JV, Barber DF (2019) T cells loaded with magnetic nanoparticles are retained in peripheral lymph nodes by the application of a magnetic field. J Nanobiotechnol 17(1):14. https://doi.org/10.1186/s12951-019-0440-z
72. Stephens DJ, Allan VJ (2003) Light microscopy techniques for live cell imaging. Science 300(5616):82–86. https://doi.org/10.1126/science.1082160
73. Bouvain P, Flocke V, Krämer W, Schubert R, Schrader J, Flögel U, Temme S (2018) Dissociation of 19F and fluorescence signal upon cellular uptake of dual-contrast perfluorocarbon nanoemulsions. MAGMA. https://doi.org/10.1007/s10334-018-0723-7
74. Gustafson HH, Holt-Casper D, Grainger DW, Ghandehari H (2015) Nanoparticle uptake: the phagocyte problem. Nano Today 10(4):487–510. https://doi.org/10.1016/j.nantod.2015.06.006
75. Waiczies S, Niendorf T, Lombardi G (2017) Labeling of cell therapies: how can we get it right? Oncoimmunology 2017:e1345403. https://doi.org/10.1080/2162402x.2017.1345403
76. Tirotta I, Dichiarante V, Pigliacelli C, Cavallo G, Terraneo G, Bombelli FB, Metrangolo P, Resnati G (2015) 19F magnetic resonance imaging (MRI): from design of materials to clinical applications. Chem Rev 115(2):1106–1129. https://doi.org/10.1021/cr500286d
77. Jiang ZX, Liu X, Jeong EK, Yu YB (2009) Symmetry-guided design and fluorous synthesis of a stable and rapidly excreted imaging

tracer for 19F MRI. Angew Chem Int Edn 48 (26):4755–4758. https://doi.org/10.1002/anie.200901005

78. Tirotta I, Mastropietro A, Cordiglieri C, Gazzera L, Baggi F, Baselli G, Bruzzone MG, Zucca I, Cavallo G, Terraneo G, Baldelli Bombelli F, Metrangolo P, Resnati G (2014) A superfluorinated molecular probe for highly sensitive in vivo(19)F-MRI. J Am Chem Soc 136(24):8524–8527. https://doi.org/10.1021/ja503270n
79. Peterson KL, Srivastava K, Pierre VC (2018) Fluorinated paramagnetic complexes: sensitive and responsive probes for magnetic resonance spectroscopy and imaging. Front Chem 6:160–160. https://doi.org/10.3389/fchem.2018.00160
80. Kislukhin AA, Xu H, Adams SR, Narsinh KH, Tsien RY, Ahrens ET (2016) Paramagnetic fluorinated nanoemulsions for sensitive cellular fluorine-19 magnetic resonance imaging. Nat Mater 15:662. https://doi.org/10.1038/nmat4585. https://www.nature.com/articles/nmat4585#supplementary-information
81. Harvey P, Kuprov I, Parker D (2012) Lanthanide complexes as paramagnetic probes for 19F magnetic resonance. Eur J Inorg Chem 2012(12):2015–2022
82. Jiang Z-X, Feng Y, Yu YB (2011) Fluorinated paramagnetic chelates as potential multichromic 19 F tracer agents. Chem Commun 47(25):7233–7235
83. Hu L, Zhang L, Chen J, Lanza GM, Wickline SA (2011) Diffusional mechanisms augment the fluorine MR relaxation in paramagnetic perfluorocarbon nanoparticles that provides a “relaxation switch” for detecting cellular endosomal activation. J Magn Reson Imaging 34(3):653–661
84. Srivastava K, Ferrauto G, Young VG, Aime S, Pierre VC (2017) Eight-coordinate, stable Fe (II) complex as a dual 19F and CEST contrast agent for ratiometric pH imaging. Inorg Chem 56(20):12206–12213. https://doi.org/10.1021/acs.inorgchem.7b01629
85. Yu M, Bouley BS, Xie D, Que EL (2019) Highly fluorinated metal complexes as dual 19F and PARACEST imaging agents. Dalton Trans. https://doi.org/10.1039/C9DT01852B
86. Faber C, Schmid F (2016) Pulse sequence considerations and schemes. Fluorine magnetic resonance imaging. Pan Stanford Publishing, Singapore, pp 1–28
87. Chalmers KH, Kenwright AM, Parker D, Blamire AM (2011) 19F-lanthanide complexes with increased sensitivity for 19F-MRI: optimization of the MR acquisition. Magn Reson Med 66(4):931–936. https://doi.org/10.1002/mrm.22881
88. Schmid F, Höltke C, Parker D, Faber C (2013) Boosting 19F MRI—SNR efficient detection of paramagnetic contrast agents using ultrafast sequences. Magn Reson Med 69(4):1056–1062. https://doi.org/10.1002/mrm.24341
89. Goette MJ, Keupp J, Rahmer J, Lanza GM, Wickline SA, Caruthers SD (2015) Balanced UTE-SSFP for 19F MR imaging of complex spectra. Magn Reson Med 74(2):537–543. https://doi.org/10.1002/mrm.25437
90. Mastropietro A, De Bernardi E, Breschi GL, Zucca I, Cametti M, Soffientini CD, de Curtis M, Terraneo G, Metrangolo P, Spreafico R, Resnati G, Baselli G (2014) Optimization of rapid acquisition with relaxation enhancement (RARE) pulse sequence parameters for (1)(9)F-MRI studies. J Magn Reson Imaging 40(1):162–170
91. Srinivas M, Morel PA, Ernst LA, Laidlaw DH, Ahrens ET (2007) Fluorine-19 MRI for visualization and quantification of cell migration in a diabetes model. Magn Reson Med 58 (4):725–734. https://doi.org/10.1002/mrm.21352
92. Hennig J, Nauerth A, Friedburg H (1986) RARE imaging: a fast imaging method for clinical MR. Magn Reson Med 3:823–833. https://doi.org/10.1002/mrm.1910030602
93. Rahmer J, Börnert P, Groen J, Bos C (2006) Three-dimensional radial ultrashort echo-time imaging with T2 adapted sampling. Magn Reson Med 55(5):1075–1082. https://doi.org/10.1002/mrm.20868
94. Hennig J (1999) K-space sampling strategies. Eur Radiol 9(6):1020–1031. https://doi.org/10.1007/s003300050788
95. Keupp J, Rahmer J, Grässlin I, Mazurkewitz PC, Schaeffter T, Lanza GM, Wickline SA, Caruthers SD (2011) Simultaneous dual-nuclei imaging for motion corrected detection and quantification of 19F imaging agents. Magn Reson Med 66(4):1116–1122. https://doi.org/10.1002/mrm.22877
96. Hu L, Hockett FD, Chen J, Zhang L, Caruthers SD, Lanza GM, Wickline SA (2011) A generalized strategy for designing (19)F/(1)H dual-frequency MRI coil for small animal imaging at 4.7 Tesla. J Magn Reson Imaging 34(1):245–252
97. Hoult DI, Richards RE (1976) The signal-to-noise ratio of the nuclear magnetic resonance experiment. J Magn Reson 24(1):71–85
98. Kovacs H, Moskau D, Spraul M (2005) Cryogenically cooled probes – a leap in NMR

technology. Prog Nucl Magn Reson Spectrosc 46(2–3):131–155

99. Baltes C, Radzwill N, Bosshard S, Marek D, Rudin M (2009) Micro MRI of the mouse brain using a novel 400 MHz cryogenic quadrature RF probe. NMR Biomed 22 (8):834–842
100. Waiczies S, Millward JM, Starke L, Delgado PR, Huelnhagen T, Prinz C, Marek D, Wecker D, Wissmann R, Koch SP, Boehm-Sturm P, Waiczies H, Niendorf T, Pohlmann A (2017) Enhanced fluorine-19 MRI sensitivity using a cryogenic radiofrequency probe: technical developments and ex vivo demonstration in a mouse model of neuroinflammation. Sci Rep 7(1):9808. https://doi.org/10.1038/s41598-017-09622-2
101. Sack M, Wetterling F, Sartorius A, Ende G, Weber-Fahr W (2014) Signal-to-noise ratio of a mouse brain 13C CryoProbe™ system in comparison with room temperature coils: spectroscopic phantom and in vivo results. NMR Biomed 27(6):709–715. https://doi.org/10.1002/nbm.3110
102. Axel L, Hayes C (1985) Surface coil magnetic resonance imaging. Arch Int Physiol Biochim 93(5):11–18. https://doi.org/10.3109/13813458509080620
103. Crowley MG, Evelhoch JL, JJH A (1985) The surface-coil NMR receiver in the presence of homogeneous B1 excitation. J Magn Reson 64(1):20–31. https://doi.org/10.1016/0022-2364(85)90026-5
104. Goette MJ, Lanza GM, Caruthers SD, Wickline SA (2015) Improved quantitative (19) F MR molecular imaging with flip angle calibration and B1 -mapping compensation. J Magn Reson Imaging 42(2):488–494. https://doi.org/10.1002/jmri.24812
105. Vernikouskaya I, Pochert A, Lindén M, Rasche V (2018) Quantitative 19F MRI of perfluoro-15-crown-5-ether using uniformity correction of the spin excitation and signal reception. MAGMA. https://doi.org/10.1007/s10334-018-0696-6
106. Ladd ME (2018) The quest for higher sensitivity in MRI through higher magnetic fields. Z Med Phys 28(1):1–3. https://doi.org/10.1016/j.zemedi.2017.12.001
107. Niendorf T, Barth M, Kober F, Trattnig S (2016) From ultrahigh to extreme field magnetic resonance: where physics, biology and medicine meet. Magma (New York, NY) 29 (3):309–311. https://doi.org/10.1007/s10334-016-0564-1
108. Hoult DI, Lauterbur PC (1979) Sensitivity of the zeugmatographic experiment involving human samples. J Magn Reson 34 (2):425–433
109. Pohmann R, Speck O, Scheffler K (2016) Signal-to-noise ratio and MR tissue parameters in human brain imaging at 3, 7, and 9.4 tesla using current receive coil arrays. Magn Reson Med 75(2):801–809. https://doi.org/10.1002/mrm.25677
110. Hoult DI (2000) The principle of reciprocity in signal strength calculations—a mathematical guide. Concept Magn Reson 12 (4):173–187. https://doi.org/10.1002/1099-0534(2000)12:4<173::AID-CMR1>3.0.CO;2-Q
111. Guérin B, Villena JF, Polimeridis AG, Adalsteinsson E, Daniel L, White JK, Wald LL (2017) The ultimate signal-to-noise ratio in realistic body models. Magn Reson Med 78 (5):1969–1980. https://doi.org/10.1002/mrm.26564
112. Schepkin VD, Brey WW, Gor'kov PL, Grant SC (2010) Initial in vivo rodent sodium and proton MR imaging at 21.1 T. Magn Reson Imaging 28(3):400–407. https://doi.org/10.1016/j.mri.2009.10.002
113. Waiczies S, Rosenberg JT, Prinz C, Starke L, Millward JM, Ramos Delgado P, Pohlmann A, Kühne A, Waiczies H, Niendorf T (2018) Fluorine-19 magnetic resonance at 21.1 Tesla to detect brain inflammation. Proc Intl Soc Mag Reson Med 26:3314

Chapter 18

MR Elastography of the Abdomen: Basic Concepts

Suraj D. Serai and Meng Yin

Abstract

Magnetic resonance elastography (MRE) is an emerging imaging modality that maps the elastic properties of tissue such as the shear modulus. It allows for noninvasive assessment of stiffness, which is a surrogate for fibrosis. MRE has been shown to accurately distinguish absent or low stage fibrosis from high stage fibrosis, primarily in the liver. Like other elasticity imaging modalities, it follows the general steps of elastography: (1) apply a known cyclic mechanical vibration to the tissue; (2) measure the internal tissue displacements caused by the mechanical wave using magnetic resonance phase encoding method; and (3) infer the mechanical properties from the measured mechanical response (displacement), by generating a simplified displacement map. The generated map is called an elastogram.

While the key interest of MRE has traditionally been in its application to liver, where in humans it is FDA approved and commercially available for clinical use to noninvasively assess degree of fibrosis, this is an area of active research and there are novel upcoming applications in brain, kidney, pancreas, spleen, heart, lungs, and so on. A detailed review of all the efforts is beyond the scope of this chapter, but a few specific examples are provided. Recent application of MRE for noninvasive evaluation of renal fibrosis has great potential for noninvasive assessment in patients with chronic kidney diseases. Development and applications of MRE in preclinical models is necessary primarily to validate the measurement against "gold-standard" invasive methods, to better understand physiology and pathophysiology, and to evaluate novel interventions. Application of MRE acquisitions in preclinical settings involves challenges in terms of available hardware, logistics, and data acquisition. This chapter will introduce the concepts of MRE and provide some illustrative applications.

This publication is based upon work from the COST Action PARENCHIMA, a community-driven network funded by the European Cooperation in Science and Technology (COST) program of the European Union, which aims to improve the reproducibility and standardization of renal MRI biomarkers. This introduction chapter is complemented by another separate chapter describing the experimental protocol and data analysis.

Key words Magnetic resonance elastography (MRE), Stiffness, Kidney, Preclinical imaging, MRI, Fibrosis

1 Introduction

Elastography based imaging techniques have received substantial attention in recent years for noninvasive assessment of tissue mechanical properties. These techniques take advantage of changed

Andreas Pohlmann and Thoralf Niendorf (eds.), *Preclinical MRI of the Kidney: Methods and Protocols*,
Methods in Molecular Biology, vol. 2216, https://doi.org/10.1007/978-1-0716-0978-1_18,

soft tissue elasticity in various pathologies to yield qualitative and quantitative information that can be used for diagnostic purposes. Measurements are acquired in specialized imaging modes that can detect tissue stiffness in response to an applied mechanical force (compression or shear wave). Elasticity reflects the ability of tissue to deform and resume its normal shape under an applied stress and relates to tissue stiffness. Tissue stiffness in turn reflects tissue composition and structure. The primary desired output is to measure the level of stiffness. The measurement that helps differentiate if the tissue is hard or soft can give diagnostic information about the presence of the disease.

In the liver, tissue stiffness has been shown to be elevated with advanced fibrosis and to correlate with various stage of fibrosis [1–3]. Tissue stiffness can be estimated by imaging with either ultrasound (US) or magnetic resonance imaging (MRI). US-based elastography techniques include strain-based imaging, transient elastography (TE), and shear wave elastography (SWE). MRI measures tissue stiffness with magnetic resonance elastography (MRE). Other than strain-based imaging, which has largely been abandoned in the liver, all of these techniques (TE, SWE, and MRE) estimate tissue stiffness by measuring the speed of a shear wave traversing the tissue. In MRI, elastography encompasses imaging techniques that noninvasively estimate tissue elasticity and related mechanical properties through the application of external forces [4]. MRE is a phase contrast-based MRI technique for observing strain waves propagating in soft tissues (e.g., brain, heart, liver, spleen, breast, kidney, and muscle). Mechanical shear waves with frequencies of 40 to 200 Hz are induced using either a piezoelectric transducer or speaker coil oscillator directly coupled to the region of interest. By using multiple phase offsets and motion encoding gradients, MRE acquires data that allows the generation of images that depict shear wave motion and the calculation of local values of the tissue viscoelastic properties. In this chapter, we will provide an overview of MRE including the basic concepts involved, and a few illustrative applications of MRE in preclinical imaging.

This introduction chapter is complemented by a separate publication describing the experimental procedure and data analysis, which is part of this book.

This chapter is part of the book Pohlmann A, Niendorf T (eds) (2020) Preclinical MRI of the Kidney—Methods and Protocols. Springer, New York.

2 Measurement Concept

2.1 Basic Concept of Stiffness Measured Using MRE

MRE uses mechanical shear waves to evaluate the viscoelastic properties of tissues. In the abdomen, mechanical shear waves produced by an external driver are propagated into the tissue using an abdominal driver placed over the region of interest and in contact with the

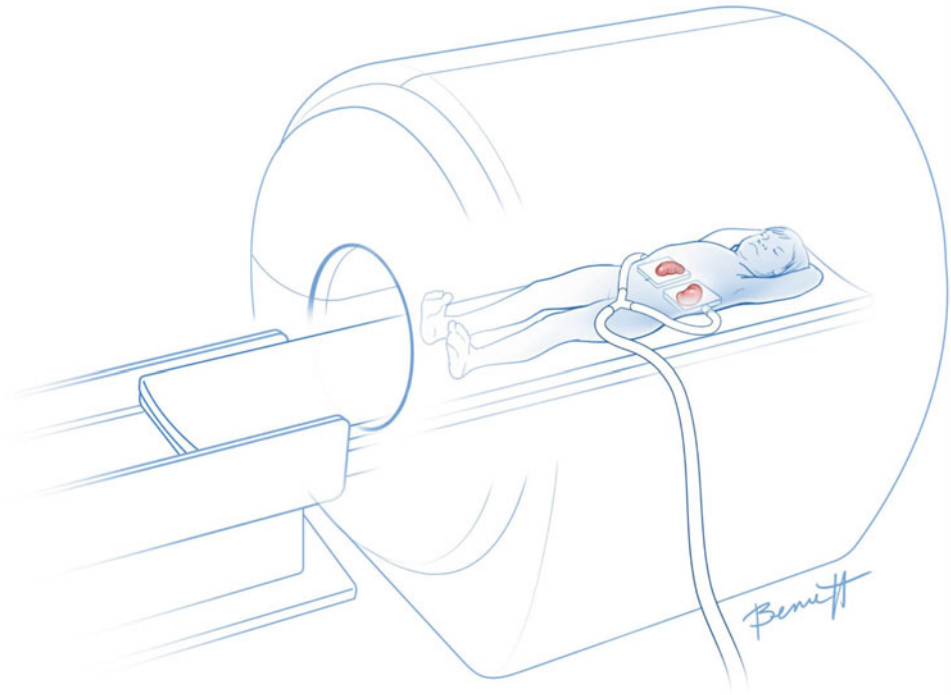

Fig. 1 Clinical MRE set up for the kidney

specific abdominal organ. Tissue displacements in the range of microns produced by propagating shear waves can be detected because phase shifts are encoded with motion encoding gradients in the MRE sequence. In liver, the typical frequency of shear waves used for clinical liver MRE is 60 Hz [5]. An accurate and reproducible stiffness measurement of organs such as pancreas and kidney, given their small size, complex geometry and boundary conditions, heterogeneous nature of the organ, and deeply seated location, requires 3D analysis of wave field data. For this reason, 3D MRE is recommended for such imaging. In 3D MRE, the propagating shear waves are imaged with a 2D multislice spin-echo echo-planar imaging (SE-EPI) pulse sequence modified to include the motion encoding gradients (MEG) in the X, Y, and Z directions. This is different from the 2D MRE typically utilized for liver imaging in which motion is encoded only in a single direction. An inversion algorithm automatically produces stiffness maps using the phase shift information. Shear stiffness values in kilopascals (kPa) are displayed for selected regions of interest in the target tissue. In renal MRE, the wave transmitting paddle is placed close to the kidney, preferably on the dorsal side (Fig. 1).

2.2 Generating Propagating Shear Waves

It is now well known that the MRE-measured shear modulus of soft tissue is dependent on the frequency of applied mechanical waves [6, 7]. That is why the term "shear stiffness" is often used to describe the shear modulus at a specific frequency. However, it should be fully understood that the formula that calculates the shear modulus from the measured velocity of the waves ($\mu = \rho c^2$, where μ = shear modulus, ρ = density of tissue, and c = wave speed) is valid only in purely elastic tissues.

In a typical MR elastography configuration, an active pneumatic mechanical wave driver is located outside the MR elastography room and is connected, by way of a flexible plastic (polyvinyl chloride) tube, to a passive driver that is fastened onto the abdominal wall or the abdominal organ or interest. The passive driver generates a continuous acoustic vibration that is transmitted through the abdomen, with a focus on the region of interest, at a fixed frequency, which typically lies in the range 40–400 Hz. A phase-contrast MRI pulse sequence with motion encoding gradients is synchronized to the frequency of mechanical waves created by the passive driver. This sequence is then used to image the micron-level cyclic displacements caused by the propagating shear waves to create a magnitude image, which provides anatomic information, and a phase difference image, which provides wave motion information. After the magnitude and phase images are created, an inversion algorithm can be used to processes these raw data images to create several additional images and maps. The gray-scale elastogram is commonly used to provide quantitative stiffness measurement, in kiloPascals. The color elastogram is generally used for qualitative tissue stiffness evaluation. The color elastogram used clinically has a stiffness range of 0–8 kPa. A 0–20 kPa color elastogram is also created and is useful for appreciating tissue stiffness heterogeneity. For research purposes, the range can also be adjusted as desired. More details on image acquisition, postprocessing, and analysis are included in the chapter by Serai SD et al. "MR Elastography of the Abdomen: Experimental Protocols."

2.3 Pulse Sequence for MRE Motion Encoding

The two types of acquisition sequences currently in use to obtain liver stiffness values are the gradient-recalled-echo (GRE) based (Fig. 2a) and the spin echo (SE) based with echo-planar readout (Fig. 2b); both of which have been shown to have excellent performance on both 1.5 and 3 T MRI scanners [8, 9]. The use of GRE-based sequence has been demonstrated to correlate with histological grading of liver fibrosis in previous studies and in a recent meta-analysis [8, 10]. The traditional GRE-based MRE acquisition works well on a 1.5 T scanner. However, the inherent limitations of GRE-based acquisition on field strengths at 3 T or higher are (1) enhanced sensitivity to susceptibility; T1 is longer at the higher field strength and hence signal drops off due to a longer echo time (TE); and (2) T2 and T2* are shorter at field strengths of 3 T and higher; hence, the relatively shorter T_2 and T_2* relaxation

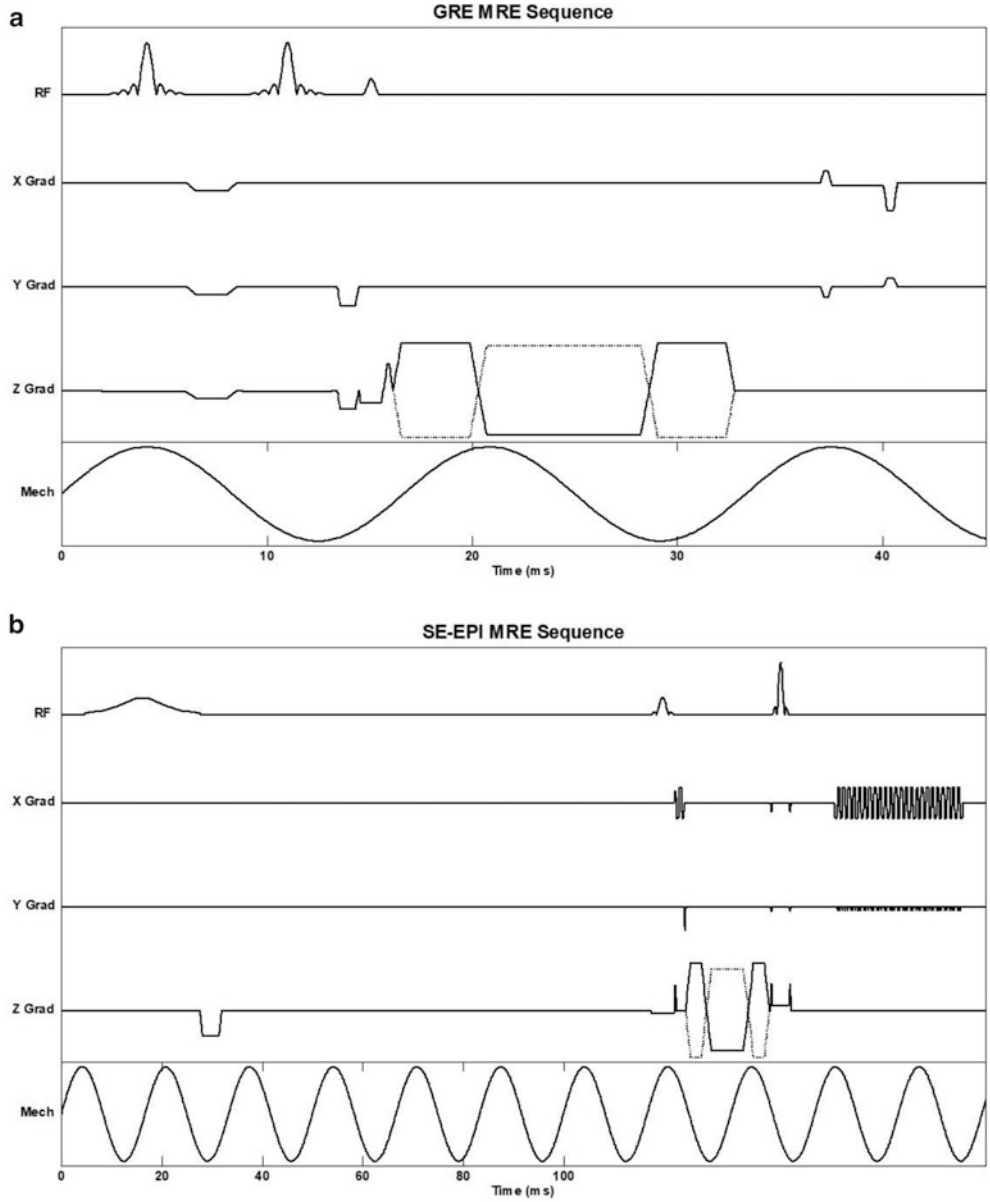

Fig. 2 (**a**) Pulse sequence diagram of a typical GRE-based MRE acquisition sequence and (**b**) SE-EPI-based MRE

time of the liver requires an even shorter TE. GRE-based MRE also has relatively lower accuracy in obese patients due to the increased distance from the driver to the liver. Thicker layers of fat can limit the acoustic penetration depth in the liver and produce limitations for encoding shear waves in the deeper areas of the liver, hence reducing the measurable area [9]. SE-EP–based acquisition overcomes this limitation by encoding more wavelengths per TR and hence can show more acoustic penetration. Since chronic liver

disease is quite frequently associated with obesity, radiologists should be aware of the limitations of GRE-based acquisitions in such cases. GRE-based MRE acquisition also requires relatively longer periods of acquisition and have a higher susceptibility to breathing motion artifacts. The current GRE-based protocol for MRE image acquisition requires a breath hold of approximately 20 s for a single slice. Echo-planar imaging (EPI), on the other hand, is a faster magnetic resonance imaging technique that obtains all spatial-encoding information in a single radiofrequency (RF) pulse, allowing shorter acquisition times with reduced motion artifacts. SE-EPI-based images are advantageous in patients with limited breath-holding capacity because they allow image acquisition of multiple slices within only one breath hold, and also enable measuring larger areas of the liver due to the greater number of waves encoded per relaxation time (TR). The drawback of SE-EPI–based acquisition is the potential increase in susceptibility artifacts due to an EPI-based readout. While technically more demanding, 3D-MRE offers advantages that might provide even higher diagnostic performance [11, 12].

3 Applications of MRE to the Abdomen

3.1 MRE for Evaluation of Liver Fibrosis

Liver fibrosis is an important pathological and pathogenic feature, and the assessment of fibrosis is often necessary for prognosis, risk stratification, clinical decision-making, and disease severity monitoring. Hepatic fibrosis eventually leads to cirrhosis, which is associated with a 50% 5-year mortality due to severe complications including variceal bleeding, hepatic failure, and development of hepatocarcinoma. Approximately 170 million people world-wide (3% of the global population) are infected with chronic hepatitis C (HCV), and 10–15% will develop cirrhosis within 20 years of infection [13]. Needle liver biopsy analyzed with connective tissue stains has long been considered the "gold standard" to detect and quantify hepatic fibrosis. Because of the cost, sampling variability, need for sedation, and risk associated with biopsy, noninvasive methods to assess liver fibrosis such as elastography are needed [14, 15]. MRE uses low-frequency (40–80 Hz) sound waves to induce shear waves in the liver, visualizes the shear waves by tracking tissue displacement using a modified phase-contrast sequence, and measures the speed of the propagating wave with specialized software called an inversion algorithm (Fig. 3) [16]. In Fig. 3, it can be seen that the red to blue region is a wavelength and this wavelength becomes longer in the presence of a stiff region for a given excitation frequency (Fig. 4). Then these wave images are converted into spatial stiffness maps (elastograms) using an inversion algorithm. Clinically MRE of the liver is FDA approved for human use and available on major MRI scanners. In the commercial version, the sound waves are generated by an acoustic subwoofer

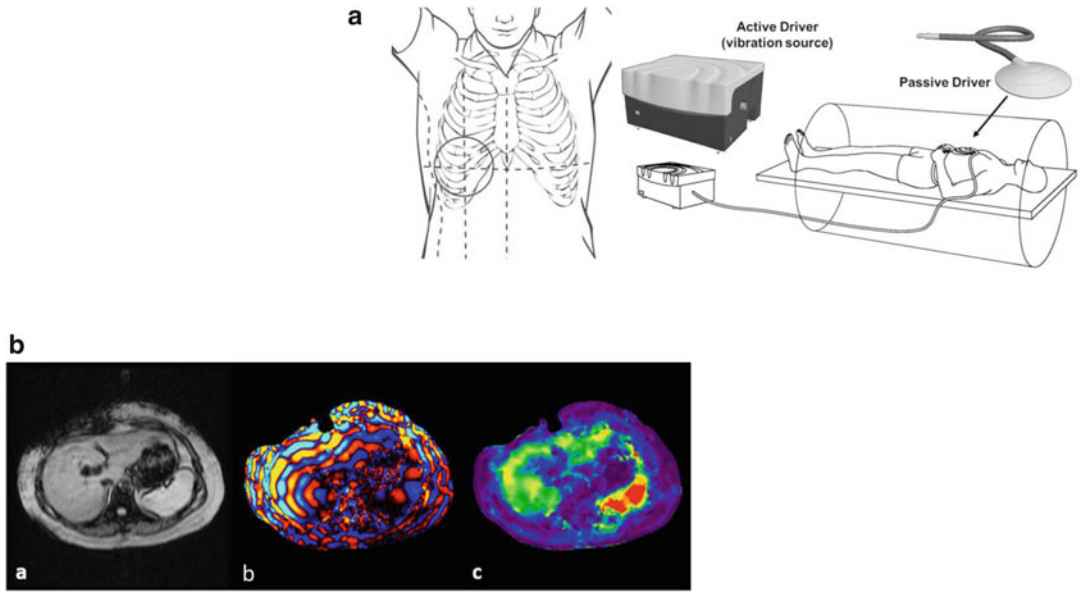

Fig. 3 Clinical MRE of the liver: (**A**) The passive driver should be placed over the right lower anterior chest wall at the level of the xiphisternum, centered on the mid-clavicular line. Once positioned, the passive driver should be held firmly against the chest wall by a wide elastic band, placed around the torso. Check to ensure that the band is stretched sufficiently so that the driver is not loose during full expiration. Note that the passive driver is connected via a plastic tube to the active driver (vibration source), which is located outside the scan room. (**B**) Magnitude and color-coded wave images of a successful MRE showing excellent illumination of waves through the liver. Stiffness map shows elevated liver stiffness consistent with significant fibrosis

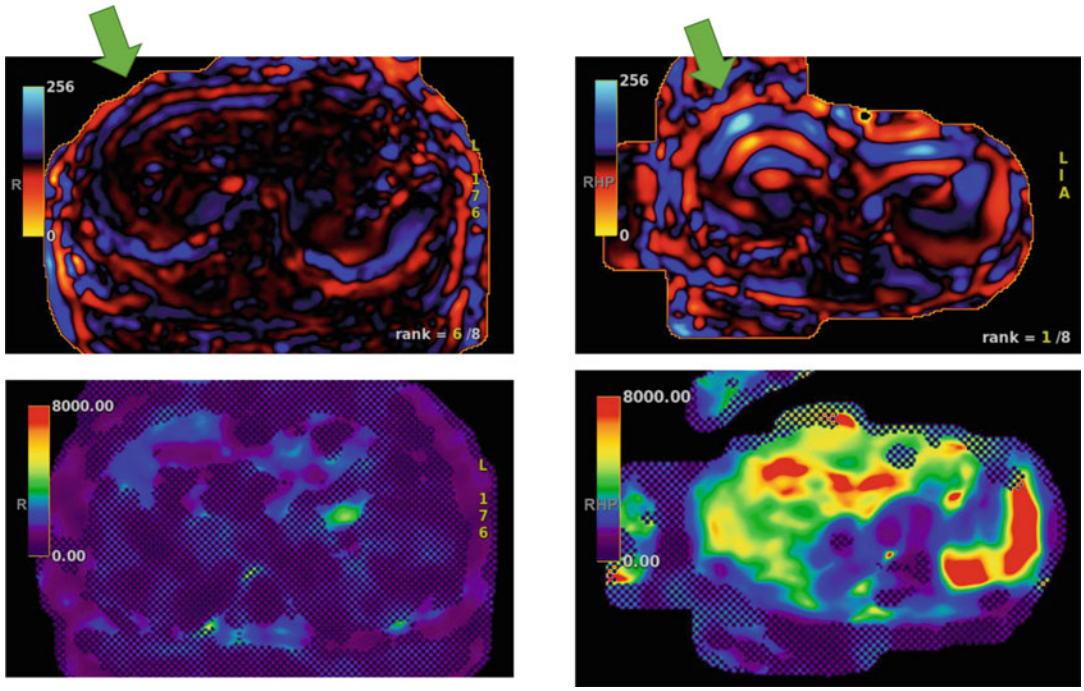

Fig. 4 Color (red and blue) wave images and its corresponding elastogram showing the difference in wavelength (green arrow) of a relatively "normal" subject vs. a patient with fibrosis

(called as "active driver") outside the scan room and are transmitted to a plastic disk (called as "passive driver") via a plastic tube passing through a wave guide [5]. During liver MRE image acquisition, the passive driver is secured by an elastic band over the right lower anterior chest wall. Most patients can feel the vibrations generated by the disk but do not find them uncomfortable. Identical MRE hardware and inversion algorithms are available on scanners manufactured by the three major MR vendors (GE, Philips, and Siemens) [10, 17]. MRE, as used clinically, currently has advantages over other tissue elastographic techniques. These advantages include the ability to further characterize tissue in terms of fat and iron content as well as standardization across manufacturer platforms, since the vast majority elastography hardware and software currently comes from a single manufacturer (Resoundant Inc.; Rochester, MN). Peer reviewed studies have shown that MRE is a robust, reliable, repeatable, and reproducible technique for detection and staging of liver fibrosis [10]. The accuracy of MRE has been reported to range from 0.85 to 0.99 for differentiating different stages of liver fibrosis [18]. The performance of MRE for differentiating mild fibrosis (stage 1) from normal liver or inflammation is lower and the performance is highest for diagnosis of cirrhosis (stage 4) [3, 10].

3.2 MRE for Evaluation of Liver Tumors

Motivated by the successful implementation of MRE for the study of diffuse changes in hepatic stiffness due to fibrosis, studies have been conducted to evaluate the potential role of MRE in characterizing hepatic tumors as malignant tumors appear to be stiffer than benign tumors [19–21]. In a preliminary work by Venkatesh et al., patients with 44 hepatic masses were evaluated with MRE and the results were correlated with pathological diagnosis or other accepted diagnostic criteria [20]. The stiffness of benign masses (nine hemangiomas, three focal nodular hyperplasia, and one hepatic adenoma) averaged 2.7 kPa, slightly higher than the mean stiffness of normal liver parenchyma (2.3 kPa). The mean stiffness of the malignant tumors was reported to be 10.1 kPa. The authors reported that a cutoff value of 5 kPa completely separated all benign liver masses from malignant lesions. Their results indicate that MRE shows substantial promise for aiding the characterization of liver tumors, which provides motivation for exploring the potential for evaluating other mass lesions in the abdomen as well.

3.3 MRE of the Spleen for Evaluation of Portal Hypertension

A study of 12 normal volunteers and 38 liver patients with biopsy-proven chronic liver diseases performed by Talwalkar et al., demonstrated higher spleen stiffness in patients with chronic liver disease and a very strong correlation between hepatic and splenic stiffness in these patients [22]. This may suggest that the bulk stiffness of the spleen is strongly affected by the portal venous pressure through a poroelasticity effect. A preclinical MRE study was performed on two adult mongrel dogs immediately after and 4 weeks

after initiating cholestatic liver disease by common bile duct ligation [23]. This preclinical model is known to have portal hypertension within 4 weeks. In this study subcutaneous vascular access ports were placed with catheter tips in the portal vein and the right hepatic vein allowing measurement of hepatic venous pressure gradient [23]. The MRE-assessed splenic stiffness in these dogs rose from a mean value of 1.8 kPa to an average of 3.4 kPa. The MRE study from the authors provide evidence to support the hypothesis that in the absence of confounding effects, the MRE-assessed stiffness of the spleen reflects the magnitude of the hepatic venous pressure gradient. This also provides motivation for the development of improved MRE techniques for the assessment of the spleen as well as the development and validation of poroelastic models that may allow the hepatic venous pressure gradient to be estimated noninvasively from MRE-based measurements of splenic stiffness. This would be a very significant development because knowledge of the hepatic venous pressure gradient is considered to be very important in the management of chronic liver disease and is very difficult to determine noninvasively. In a cross-sectional study of 25 patients with autosomal recessive polycystic kidney disease (ARPKD) and 25 healthy controls, ARFI based elastography was able to distinguish between participants without and with clinical signs of portal hypertension, namely splenomegaly or low platelets [24].

3.4 MRE of the Kidney

Many different disease mechanisms induce glomerular injury, including glomerulonephritis, hypertensive nephrosclerosis and diabetic nephropathy [25]. However, once renal damage reaches a certain threshold, progression of renal disease is consistent, and largely independent of the initial insult. This common pathway to end-stage renal failure is mainly due to tubulointerstitial damage characterized by tubular atrophy, loss of peritubular capillaries, and interstitial fibrosis. Mechanisms leading to kidney failure via tubulointerstitial damage and development of fibrosis are mostly massive proteinuria and chronic hypoxia [26]. Fibrosis further impairs oxygen diffusion and supply to tubular cells. This in turn exacerbates fibrosis of the kidney, rendering it into a vicious cycle.

Renal fibrosis is the excessive accumulation and deposition of extracellular matrix in the interstitial space of the kidneys. The process of fibrogenesis in kidneys is very complicated and cannot be attributed to any single type of cellular activity. However, it can be described as an overall result of the kidney's incapability to properly regenerate the damaged tissues after renal injury. When kidneys suffer injury, extracellular matrix deposition is an integral part of the damage repair process. However, certain processes can lead to excessive matrix to be deposited in the interstitial space, which leads to scarring of the kidneys. This interferes with the normal functioning of the kidneys and causes progressive loss of

renal function over time due to the reduction in the number of renal tubules. Renal fibrosis is a significant hallmark in the progression of CKD and can lead to end stage renal disease (ESRD), which necessitates dialysis or kidney transplant Thus, in the assessment of chronic renal failure, fibrosis is a major histological feature and may be an important surrogate endpoint for prognosis and monitoring of treatment response. Besides, some investigations suggest that fibrosis might be reversible, when the cause is treated, emphasizing the need for early detection and quantification of this fibrosis [27–33]. Currently, renal biopsy is the gold standard for diagnosing kidney fibrosis. In this procedure, the kidneys of the patient are located with help of ultrasonography or X-rays. After determining the location, a needle is inserted in the kidney either percutaneously (called percutaneous biopsy) or after performing a cut near the region of kidney being observed under local anesthesia (called open biopsy) to obtain tissue samples [32, 33]. These samples are used for histological analysis to determine the presence of renal fibrosis.

Kidney biopsy has several limitations. It is invasive and causes pain to the patients after the procedure is performed. It is also associated with a prolonged hospital stay and higher costs and the procedure suffers from intra- and inter- observer variability. Since, only a small region from the entire kidney is used to obtain samples leading to potential sampling error [34]. Thus a noninvasive, truly quantitative method of interstitial renal fibrosis monitoring would be desirable. Diffusion-weighted and Blood Oxygenation Level Dependent (BOLD) MRI findings have been shown to be correlated to renal function [35–39], but no data has been published as to their correlation with the degree of fibrosis. Blood or urinary markers of fibrosis are also currently evaluated but neither is used in clinical practice yet [40].

MRI and ultrasound (US)-based methods can estimate tissue stiffness (and thus the degree of fibrosis) by measuring the velocity of shear waves traveling through the organ of interest [41, 42]. US-based elastography techniques are mainly classified under strain imaging (SI) or shear wave imaging (SWI). The basic principle of SI is application of stress to the tissue and measuring the resulting normal strain which is reported as Young's modulus. SWI-based techniques use either a dynamic vibrating device or acoustic radiation force to generate shear waves in the tissues, which are reported either as shear wave speed or Young's modulus. Techniques based on SI include strain elastography (SE) and acoustic radiation force impulse strain imaging (ARFI), whereas SWI-based techniques include point shear wave elastography (pSWE), 2D shear wave elastography (SWE), and 1D transient elastography (TE).

Studies have used both SI and SWI to investigate renal fibrosis. SI-based techniques are found to be beneficial for diagnosing renal

fibrosis in allografts than native kidneys [43]. This is because external compression can be efficiently applied to allografts located superficially than to native kidneys which are located retroperitoneally thereby limiting accuracy of this technique. A study by Menzilcioglu et al. reported that even though SE reported higher mean strain index in CKD patients when compared to healthy subjects, it could not differentiate between various stages of CKD [44].

SWI-based techniques have an advantage over SI-based techniques since they do not depend on external compression. However, studies using SWI have reported conflicting results. A study by Wang et al. reported that shear wave velocity measurements did not show any correlation with degree of renal fibrosis [45]. Few studies have reported lower shear wave velocities in patients with CKD than in healthy subjects [46]. It has been observed that there is a negative correlation between shear wave velocity and progression of CKD in kidneys whereas a positive correlation has been observed in liver using the same SWI-based techniques [43]. Apart from these conflicting results, US-based elastography techniques have following limitations: (1) only provides 1D or 2D stiffness of the kidneys; (2) requires extensive training of technicians and is still prone to inter- and intraobserver variability; (3) highly dependent on the body mass index of subjects; and (4) anisotropy of the kidney can impact the results. The US-based transient elastography (Fibroscan™ device) is able to discriminate the different stages of liver fibrosis with a quadratic trend of the curve plotting histologic scores versus elasticity measurements [47]. Among patients with cirrhosis, stiffness thresholds predicting the onset of specific complications (ascites, oesophageal bleeding, hepatocarcinoma, etc.) have been identified. However, as explained with the limiations of US based studies, this technique is limited by its 1D nature in that it does not allow the exploration of the entire liver. MRI has advantages over US since it can image organs located deep in the human body with good image contrast and spatial resolution thereby improving the diagnosis. It also does not involve use of any radiation and therefore can be used to monitor progression of diseases over a period of time. MRE has been successfully used to assess and stage liver fibrosis. The shear stiffness of normal liver was found to be approximately 2.2 kPa by several independent groups, using vibrating frequencies of 60 Hz [1, 3]. MRE has been shown to sucessfully discriminate the different stages of liver fibrosis, with the same quadratic trend of the fibrosis/elasticity curve and a recommended cut-off value derived from a large group of patients [18]. MRE has the advantage of being intrinsically a 2D technique and can be associated to conventional liver imaging at the same time. In the kidney, evaluation of interstitial fibrosis is crucial to the assessment of prognosis and to guide therapy for most kidney diseases. However, how best to measure kidney fibrosis remains

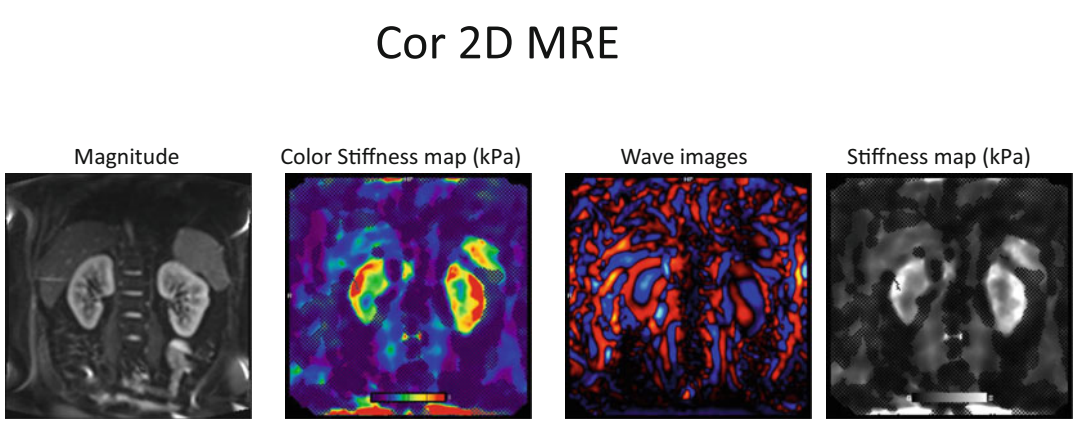

Fig. 5 MRE of the kidney of a healthy volunteer performed at 60 Hz. Magnitude, stiffness map and color-coded wave images of a successful MRE showing excellent illumination of waves through the kidney. The stiffness of the normal kidneys at 60 Hz ranged from 3.5 to 5 kPa

uncertain. An MRE-based technique that measures tissue stiffness, would be a novel application for assessment of renal fibrosis. The resulting microscopic vibrational waves passing through the organ generate shear waves that can be imaged with motion-synchronized MRI. The velocity of wave propagation is dependent on organ stiffness, with stiffer fibrotic tissue leading to more rapidly moving waves with longer wavelength. Exploratory MRE of the kidneys in healthy volunteers has demonstrated that shear waves can be readily generated and imaged in this organ. Unlike the liver and spleen, the patterns of wave propagation in these structures are extremely complex and include significant components propagating at oblique angles relative to an axial plane of section. Given these characteristics, it is necessary to image the pattern of wave propagation in three dimensions and to obtain data from all three polarizations of motion, which requires longer imaging times. This kind of 3D/3-axis MRE acquisition is problematic if the imaging is to be conducted during suspended respiration and using a GRE-based acquisition method. One approach to this is to use respiratory gating, though this can make the total acquisition times quite long. As an alternative, EPI-based techniques can be used to significantly reduce acquisition times. EPI-based MRE sequence have been shown to be capable of acquiring 12 wave images (four phase offsets at each of three motion-encoding directions) with an acquisition time of 8 s per slice. This technique has successfully generated 3D wave data sets with typical voxel dimensions of 4 mm (Figs. 5, 6, and 7). With a 3D extension of the inversion software, including 3D spatial filtering, the preliminary results indicate that it is quite feasible to image tissue stiffness throughout a larger 3D region of interest in the abdomen and has yielded provocative preliminary results in the kidneys that motivate further development in this organ.

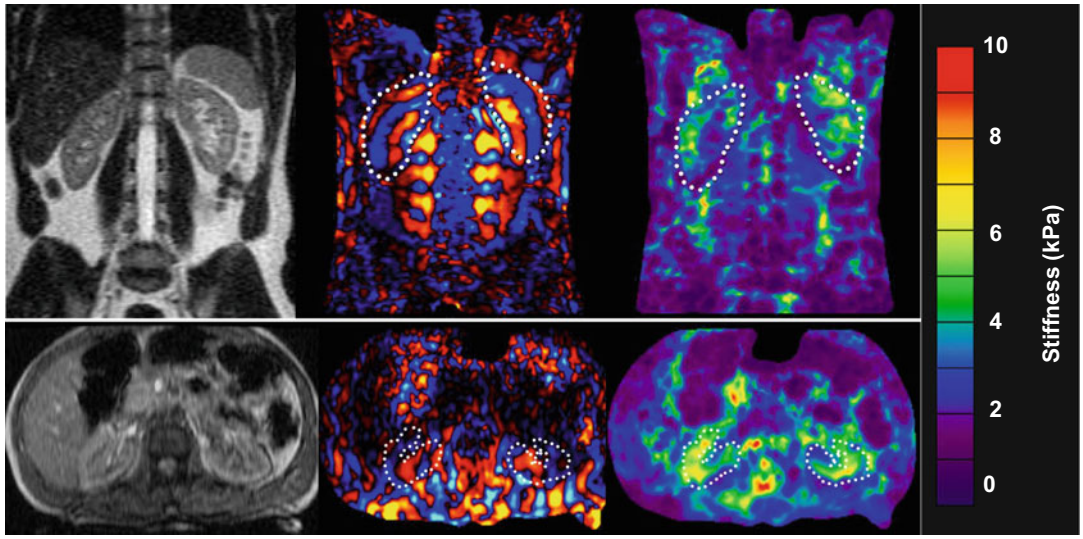

MRE of kidneys performed in two normal healthy volunteers.
MRE performed in coronal and axial planes at 90Hz. The dotted lines on the wave images and stiffness maps outline the kidneys. The stiffness of the normal kidneys ranged from 5 to 7.5 kPa

Fig. 6 MRE performed in coronal and axial planes at 90 Hz. The dotted lines on the wave images and stiffness maps outline the kidneys. The stiffness of the normal kidneys at 90 Hz ranged from 5 to 7.5 kPa (Image courtesy of Dr. Sudhakar Venkatesh, Mayo Clinic, Rochester, Minnesota, USA)

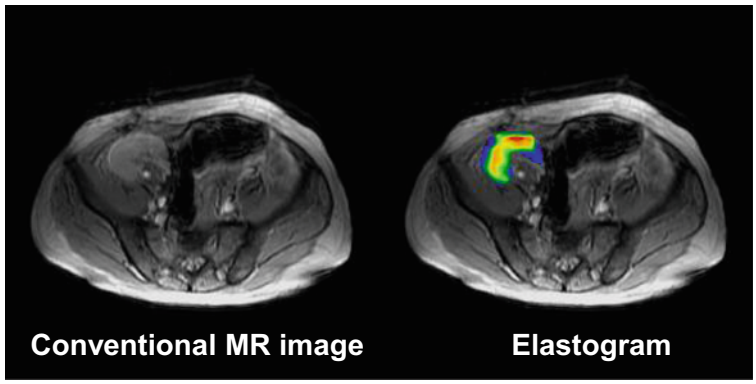

MRE of renal graft in the right iliac fossa 4-months following transplantation.
Stiffness is similar to normal kidneys. The renal function was normal. Biopsy showed no interstitial fibrosis or tubular atrophy.

Fig. 7 MRE of renal graft in the right iliac fossa acquired 4-months following transplantation. Stiffness is similar to normal kidneys. The renal function was normal. Biopsy showed no interstitial fibrosis or tubular atrophy (Image courtesy of Dr. Sudhakar Venkatesh, Mayo Clinic, Rochester, Minnesota, USA)

Pilot studies of MRE have been performed in native kidneys and kidney allografts, attempting to correlate kidney stiffness with either fibrosis burden or kidney function [48]. Although MRE in porcine kidneys showed a correlation between stiffness and fibrosis in the medulla, the results of small pilot human studies have so far been conflicting, and no studies, as yet, have assessed whether stiffness measured by MRE predicts progression of kidney dysfunction [49]. MRE may also be helpful in the evaluation and follow-up of patients undergoing renal transplant [50]. In a study by Orlachio et al., real-time elastography was able to evaluate kidney fibrosis in a noninvasive way and could be used as complementary imaging during follow-up of renal transplant patients [51].

3.5 MRE of the Pancreas

Pancreatic fibrosis is often associated with chronic pancreatitis, pancreatic ductal cancer, or inflammatory pseudotumor [52]. Since pancreatic fibrosis may affect decisions of surgical interventions and prognosis in such pathologies [53], MRE techniques could be exploited for information concerning pancreatic fibrosis reflected by its stiffness. Serai et al. have demonstrated that 3D MRE of the pancreas is feasible in children with and without pancreatic disease, in a small cohort of pediatric patients, referred for clinical imaging with history of acute recurrent pancreatitis (APR) or CP [12]. In this preliminary study, they observed statistically significant lower pancreas stiffness values derived from 3D MRE in children with a history of ARP or CP as compared to healthy control children (1 kPa vs. 1.7 kPa) [12]. The finding of lower pancreas stiffness in ARP/CP than controls is contrary to the findings reported in a small series of adults (mean age 55.6 years) by An et al. [54]. In their study, a mean stiffness value of 1.1 kPa was reported for healthy controls compared to a mean stiffness of 1.5 kPa in five patients with chronic pancreatitis. Further, a study by Wang et al. reported mean stiffness values of 1.5 and 1.9 kPa in adults with mild ($n = 30$) and moderate to severe ($n = 16$) chronic pancreatitis respectively as classified by the Cambridge criteria [55]. Reported stiffness values in patients were higher than the values in healthy patients in the same study.

3.6 Other MRE Body Applications

Since MRE is a new, multistep MR technique, there is potential for improvement, expansion and exploration. Breast tumors are known to be stiffer than normal breast tissue and hence manual palpation is a recommended part of routine screening that helps in the detection of tumors [56]. MRE is being investigated in breast imaging for the detection of breast cancer since this disease is one of the leading causes of death in women and the current diagnostic methods are not satisfactory [57, 58]. Skeletal muscle MRE can be used for studying the physiological response of diseased and pathological muscles [59]. For instance, it has been found that there is a difference in the stiffness of muscles with and without neuromuscular

disease [60]. In a recent study on patients with Duchenne muscular dystrophy, the authors concluded that shear wave elastography could be considered a useful noninvasive tool to monitor muscle changes in early stages of the disease [61].

4 Influence of Perfusion on Abdominal Organs

Preliminary results from the studies relating splenic stiffness to hepatic venous pressure gradient (HVPG) suggests that the stiffness of abdominal organs may have two components: a static component reflecting intrinsic structural properties and a dynamic component reflecting extrinsic perfusion changes [62, 63]. To investigate the influence of perfusion on the shear stiffness of abdominal organs, studies of specific conditions of the liver and kidneys are being actively pursued [64].

4.1 Post-prandial Influence on Liver Stiffness

Food intake is known to cause an increase in mesenteric blood flow, which may lead to a postprandial increase in hepatic stiffness that is different in patients with hepatic fibrosis than in normal volunteers [65]. It has been observed that MRE-assessed liver stiffness increases significantly (average increment of 18% with ranges from 5% up to 48%) following a test meal in patients with advanced hepatic fibrosis, whereas fasting and postprandial liver stiffness are similar in the normal state [65]. This finding suggests that there is a dynamic component to the liver stiffness that is dependent on the portal pressure. Therefore, it is very important to have hepatic MRE examinations performed consistently in a fasting state. The postprandial augmentation in hepatic stiffness after a test meal known to increase mesenteric blood flow is likely due to the transiently increased portal pressure in patients with hepatic fibrosis. It is thought that mechanical distortion of the intrahepatic vasculature caused by fibrosis impairs the autoregulatory mechanism for the portal venous pressure, which may cause acceleration of the development of portal systemic varies and stretching of hepatic parenchyma and stellate cells that are instrumental in the progression of hepatic fibrosis. This promising observation provides motivation for further studies to determine the potential value of assessing postprandial hepatic stiffness augmentation for predicting progression of fibrotic disease and the development of portal varices. It may also provide new insights into the natural history and pathophysiology of chronic liver disease.

4.2 Influence of Hydration on Renal Stiffness

Stiffness plays an important role in diagnosing renal fibrosis. However, kidney stiffness is altered by perfusion changes in many kidney diseases. A study by Clark et al. suggests that increasing water intake is recommended for patients with CKD as it helps to preserve renal function [66]. Water intake before a MRE scan can act also as a confounding factor to estimate the stiffness of kidneys. In a recent

study, Gandhi et al. observed a negative correlation between difference in stiffness values and changes in bladder volumes before and after water intake [67]. This suggests that at lower bladder volume the kidneys are still filtering the water where perfusion pressure is high leading to an increased stiffness in the kidneys.

4.3 Stenotic Kidney MRE

The kidney is a richly perfused organ receiving 25% of the cardiac output. Renal occlusions, such as renal arterial stenosis, threaten the viability of the kidney by diminishing blood flow leading to irreversible tissue fibrosis and ultimately kidney failure. Preliminary research has been performed to study the impact of renal arterial stenosis on kidney stiffness in a porcine model of acute renal arterial stenosis [68]. MRE measurements showed that the stiffness of the kidney progressively decreased as the renal artery stenosis was increased. The authors reported that the stiffness of the contralateral kidney was observed to increase progressively, which indicates that hemodynamics can significantly affect the mechanical properties of renal parenchyma. Fibrosis is associated with elevated tissue stiffness. However, studies have indicated the rich perfusion of the kidney may affect its distension and, in turn, stiffness [68]. In order to determine the interdependent relationship between perfusion, fibrosis and stiffness, an acute renal arterial stenosis model was established in adult pigs by isolating the renal artery to insert a vascular occluder and an embedded Doppler flow probe. The renal blood flow (RBF) was gradually reduced from the baseline level to total occlusion of 100% with MRE acquisitions performed at each step. The cortex of the acutely stenotic kidney decreased in stiffness as the degree of stenosis was increased to 40% and above. The systemic blood pressure also rose during each decrement in the RBF (from 75 $\pm$ 3 to 96 $\pm$ 3 mmHg). These preliminary renal MRE results encourage the further evaluation of renal hemodynamics on tissue stiffness, which may be due, in part, to perfusion pressure applied to the organ. These factors may also play a complicating role in detecting the presence of fibrosis due to renal arterial stenosis, and hence may lead to new techniques to assess tissue stiffness. The use of MRE to assess changes in tissue mechanics associated with the dynamic perfusion of tissue may also provide new insights into the natural history and pathophysiology of renal diseases (Table 1).

5 Preclinical MRE

Increasing evidence has demonstrated that, unlike cirrhosis, the early stages of fibrosis are treatable and reversible if appropriate antifibrotic treatment is given [69, 70]. As antifibrotic therapies evolve, a reliable, noninvasive assessment of hepatic fibrosis is needed to manage patients with chronic liver disease. Being able

Table 1
Factors confounding the tissue stiffness measured using MRE

Confounding factor	Direction of effect	Examples scenarios
Iron/T_2*	Loss of SNR	Patients with B-Thalassemia
Inflammation	Positive	Patients with AIH
Congestion	Positive	Patients with Fontan
Magnetic-field (B_0) inhomogeneity	Positive	Bowel gas, poor shim
Steatosis/fat	Negative	Patients with NAFLD, NASH
Renal stenosis	Negative	Patients with renal artery stenosis or perfusion defects
Renal perfusion	Positive	Large hydration volume or higher renal perfusion pressure can alter renal stiffness

A "positive" direction of the effect means that an increase in the confounding factor leads to an increase in measured stiffness and hence an overestimation of the fibrosis, and a "negative" direction of the effect means that decreases the confounding factor lead to a potential under estimation of stiffness

to noninvasively monitor the progression of liver fibrosis helps in understanding the natural history of liver fibrosis in patients with chronic liver disease, determining which patients require antiviral therapy, predicting the approximate time to the development of cirrhosis, and discovering new directions of scientific inquiry. Similarly, being able to early diagnose renal fibrosis or parencyma damage would help in understanding the natural history of renal fibrosis in patients with CKD, determining which patients require which therapy, predicting the approximate time to the development of renal failure, and discovering new directions of scientific inquiry. Therefore, there are ongoing investigations using preclinical models with a reliable, noninvasive method to assess fibrosis, not only to detect and stage the disease itself but also to monitor treatment efficacy and optimize dosing. In recent work by Yin et al. [2] feasibility of MRE was demonstrated on a mouse model of autosomal recessive polycystic kidney disease (ARPKD), which is an inherited disorder of the kidneys and liver caused by mutations in the PKHD1 gene and an important cause of congenital hepatic fibrosis (CHF) in humans. A renal wrapping surgery performed on eight pigs to induce sytemic arterial hypertension, showed that MRE derived aortic stiffness increased with mean arterial pressure [71].

5.1 Considerations Regarding Animal Preparation

- Bowel gas can create susceptibility artifacts in renal imaging; right lateral position helps minimize susceptibility artifacts from bowel gas.
- Respiratory motion can create artifacts and if necessary free breathing methods may be needed to minimize them. Alternately, respiratory triggering could be used, but this may increase the acquisition time [72].
- Studies indicate the choice of anesthesia may have an effect on quantitative MR measurements. This may be partly due to known effects of anesthesia on respiration, temperature, blood pressure, and pO_2.
- Hemodynamic variables may modulate kidney stiffness measured by MRE and may mask the presence of fibrosis [68].
- In liver imaging, elevated stiffness is observed "after meal" due to postprandial effect. Such effects have not yet been reported in measuring kidney stiffness [65].
- While performing renal MRE, renal perfusion status should be taken into account to ensure reproducible detection [73]. Confounding stiffness changes due to excess water intake have been reported [67].
- In the preclinical setting, motion artifacts can usually be minimized using multiple averages.

6 Conclusion

Renal fibrosis causes a change in the anatomy of kidneys wherein there is an excess accumulation of interstitial extracellular matrix and reduction in the number of tubules. Elasticity imaging is an imaging field that has received considerable attention due to its intuitive mechanical contrast based on "palpation" and its great diagnostic potential. Elasticity imaging techniques are based on measuring the response of tissues to an applied excitation and different approaches have been proposed and investigated toward this goal. Elastography encompasses imaging techniques that noninvasively estimate tissue elasticity and the related mechanical properties through the application of external forces. Elasticity reflects the ability of tissue to deform and resume its normal shape under an applied stress and relates to tissue stiffness. Tissue stiffness in turn reflects tissue composition and structure. Fibrosis is an important pathologic and pathogenic feature of each of these conditions, and the assessment of fibrosis is often necessary for prognosis, risk stratification, clinical decision-making, and disease severity monitoring. Due to the cost, need for sedation, and risk associated with biopsy, noninvasive methods such as elastography to assess tissue fibrosis are needed.

US-based methods only provide 1-D stiffness, have lower penetration depth and are highly dependent on body mass index, anisotropy of tissues, transducer force, and intra- and inter-observer variability. Numerous investigations have shown that it is readily possible to perform MRE in abdominal organs for detecting specific diseases, such as hepatic fibrosis and portal hypertension, which increase the stiffness of the liver and spleen. Other preliminary studies have demonstrated that is possible to evaluate the mechanical properties of other abdominal structures, such as the pancreas and kidneys. These results will further motivate future studies incorporating MRE to study the normal and pathological mechanics and physiology of abdominal organs.

MRE has been shown to be capable of detecting alterations in the tissue mechanical properties of kidneys in vivo preclinical and clinical studies. In the kidney, shear wave elastography has been shown to be helpful in early noninvasive detection and management of patients with chronic kidney disease (CKD). Renal MRE is a promising noninvasive technique that might have pathologic and prognostic significance.

Acknowledgments

This publication is based upon work from COST Action PARENCHIMA, supported by European Cooperation in Science and Technology (COST). COST (www.cost.eu) is a funding agency for research and innovation networks. COST Actions help connect research initiatives across Europe and enable scientists to enrich their ideas by sharing them with their peers. This boosts their research, career, and innovation.

PARENCHIMA (renalmri.org) is a community-driven Action in the COST program of the European Union, which unites more than 200 experts in renal MRI from 30 countries with the aim to improve the reproducibility and standardization of renal MRI biomarkers.

References

1. Yin M, Talwalkar JA, Glaser KJ, Manduca A, Grimm RC, Rossman PJ, Fidler JL, Ehman RL (2007) Assessment of hepatic fibrosis with magnetic resonance elastography. Clin Gastroenterol Hepatol 5(10):1207–1213.e1202. https://doi.org/10.1016/j.cgh.2007.06.012
2. Yin M, Woollard J, Wang X, Torres VE, Harris PC, Ward CJ, Glaser KJ, Manduca A, Ehman RL (2007) Quantitative assessment of hepatic fibrosis in an animal model with magnetic resonance elastography. Magn Reson Med 58 (2):346–353. https://doi.org/10.1002/mrm.21286
3. Xanthakos SA, Podberesky DJ, Serai SD, Miles L, King EC, Balistreri WF, Kohli R (2014) Use of magnetic resonance elastography to assess hepatic fibrosis in children with chronic liver disease. J Pediatr 164 (1):186–188. https://doi.org/10.1016/j.jpeds.2013.07.050

4. Muthupillai R, Ehman RL (1996) Magnetic resonance elastography. Nat Med 2 (5):601–603
5. Serai SD, Towbin AJ, Podberesky DJ (2012) Pediatric liver MR elastography. Dig Dis Sci 57 (10):2713–2719. https://doi.org/10.1007/s10620-012-2196-2
6. Fung YC (1993) Biomechanics mechanical properties of living tissues. Springer, New York, NY
7. Papazoglou S, Hirsch S, Braun J, Sack I (2012) Multifrequency inversion in magnetic resonance elastography. Phys Med Biol 57 (8):2329–2346. https://doi.org/10.1088/0031-9155/57/8/2329
8. Serai SD, Dillman JR, Trout AT (2017) Spin-echo echo-planar imaging MR elastography versus gradient-echo MR elastography for assessment of liver stiffness in children and young adults suspected of having liver disease. Radiology 282(3):761–770. https://doi.org/10.1148/radiol.2016160589
9. Calle-Toro JS, Serai SD, Hartung EA, Goldberg DJ, Bolster BD Jr, Darge K, Anupindi SA (2019) Magnetic resonance elastography SE-EPI vs GRE sequences at 3T in a pediatric population with liver disease. Abdom Radiol. https://doi.org/10.1007/s00261-018-1884-6
10. Serai SD, Obuchowski NA, Venkatesh SK, Sirlin CB, Miller FH, Ashton E, Cole PE, Ehman RL (2017) Repeatability of MR elastography of liver: a meta-analysis. Radiology 285 (1):92–100. https://doi.org/10.1148/radiol.2017161398
11. Loomba R, Cui J, Wolfson T, Haufe W, Hooker J, Szeverenyi N, Ang B, Bhatt A, Wang K, Aryafar H, Behling C, Valasek MA, Lin GY, Gamst A, Brenner DA, Yin M, Glaser KJ, Ehman RL, Sirlin CB (2016) Novel 3D magnetic resonance elastography for the non-invasive diagnosis of advanced fibrosis in NAFLD: a prospective study. Am J Gastroenterol 111(7):986–994. https://doi.org/10.1038/ajg.2016.65
12. Serai SD, Abu-El-Haija M, Trout AT (2019) 3D MR elastography of the pancreas in children. Abdom Radiol. https://doi.org/10.1007/s00261-019-01903-w
13. Mohamed AA, Elbedewy TA, El-Serafy M, El-Toukhy N, Ahmed W, Ali El Din Z (2015) Hepatitis C virus: a global view. World J Hepatol 7(26):2676–2680. https://doi.org/10.4254/wjh.v7.i26.2676
14. Ratziu V, Charlotte F, Heurtier A, Gombert S, Giral P, Bruckert E, Grimaldi A, Capron F, Poynard T (2005) Sampling variability of liver biopsy in nonalcoholic fatty liver disease. Gastroenterology 128(7):1898–1906
15. Regev A, Berho M, Jeffers LJ, Milikowski C, Molina EG, Pyrsopoulos NT, Feng ZZ, Reddy KR, Schiff ER (2002) Sampling error and intraobserver variation in liver biopsy in patients with chronic HCV infection. Am J Gastroenterol 97(10):2614–2618. https://doi.org/10.1111/j.1572-0241.2002.06038.x
16. Venkatesh SK, Ehman RL (2014) Magnetic resonance elastography of liver. Magn Reson Imaging Clin N Am 22(3):433–446. https://doi.org/10.1016/j.mric.2014.05.001
17. Trout AT, Serai S, Mahley AD, Wang H, Zhang Y, Zhang B, Dillman JR (2016) Liver stiffness measurements with MR elastography: agreement and repeatability across imaging systems, field strengths, and pulse sequences. Radiology 281(3):793–804. https://doi.org/10.1148/radiol.2016160209
18. Yin M, Glaser KJ, Talwalkar JA, Chen J, Manduca A, Ehman RL (2016) Hepatic MR elastography: clinical performance in a series of 1377 consecutive examinations. Radiology 278(1):114–124. https://doi.org/10.1148/radiol.2015142141
19. Pepin KM, McGee KP (2018) Quantifying tumor stiffness with magnetic resonance elastography: the role of mechanical properties for detection, characterization, and treatment stratification in oncology. Top Magn Reson Imaging 27(5):353–362. https://doi.org/10.1097/rmr.0000000000000181
20. Venkatesh SK, Yin M, Glockner JF, Takahashi N, Araoz PA, Talwalkar JA, Ehman RL (2008) MR elastography of liver tumors: preliminary results. AJR Am J Roentgenol 190 (6):1534–1540. https://doi.org/10.2214/ajr.07.3123
21. Garteiser P, Doblas S, Daire JL, Wagner M, Leitao H, Vilgrain V, Sinkus R, Van Beers BE (2012) MR elastography of liver tumours: value of viscoelastic properties for tumour characterisation. Eur Radiol 22 (10):2169–2177. https://doi.org/10.1007/s00330-012-2474-6
22. Talwalkar JA, Yin M, Venkatesh S, Rossman PJ, Grimm RC, Manduca A, Romano A, Kamath PS, Ehman RL (2009) Feasibility of in vivo MR elastographic splenic stiffness measurements in the assessment of portal hypertension. AJR Am J Roentgenol 193(1):122–127. https://doi.org/10.2214/AJR.07.3504
23. Yin M, Chen J, Glaser KJ, Talwalkar JA, Ehman RL (2009) Abdominal magnetic resonance elastography. Top Magn Reson Imaging 20 (2):79–87. https://doi.org/10.1097/RMR.0b013e3181c4737e
24. Hartung EA, Wen J, Poznick L, Furth SL, Darge K (2019) Ultrasound elastography to

quantify liver disease severity in autosomal recessive polycystic kidney disease. J Pediatrics 209:107–115.e105. https://doi.org/10.1016/j.jpeds.2019.01.055

25. Nangaku M (2004) Mechanisms of tubulointerstitial injury in the kidney: final common pathways to end-stage renal failure. Intern Med 43(1):9–17. https://doi.org/10.2169/internalmedicine.43.9
26. Hodgkins KS, Schnaper HW (2012) Tubulointerstitial injury and the progression of chronic kidney disease. Pediatr Nephrol 27 (6):901–909. https://doi.org/10.1007/s00467-011-1992-9
27. Alukal JJ, Thuluvath PJ (2019) Reversal of NASH fibrosis with pharmacotherapy. Hepatol Int 13(5):534–545. https://doi.org/10.1007/s12072-019-09970-3
28. Ismail MH, Pinzani M (2009) Reversal of liver fibrosis. Saudi J Gastroenterol 15(1):72–79. https://doi.org/10.4103/1319-3767.45072
29. Schuppan D, Ashfaq-Khan M, Yang AT, Kim YO (2018) Liver fibrosis: direct antifibrotic agents and targeted therapies. Matrix Biol 68-69:435–451. https://doi.org/10.1016/j.matbio.2018.04.006
30. Tampe D, Zeisberg M (2014) Potential approaches to reverse or repair renal fibrosis. Nat Rev Nephrol 10(4):226–237. https://doi.org/10.1038/nrneph.2014.14
31. Bledsoe G, Shen B, Yao Y, Zhang JJ, Chao L, Chao J (2006) Reversal of renal fibrosis, inflammation, and glomerular hypertrophy by kallikrein gene delivery. Hum Gene Ther 17 (5):545–555. https://doi.org/10.1089/hum.2006.17.545
32. Klinkhammer BM, Goldschmeding R, Floege J, Boor P (2017) Treatment of renal fibrosis-turning challenges into opportunities. Adv Chronic Kidney Dis 24(2):117–129. https://doi.org/10.1053/j.ackd.2016.11.002
33. Lee SY, Kim SI, Choi ME (2015) Therapeutic targets for treating fibrotic kidney diseases. Transl Res 165(4):512–530. https://doi.org/10.1016/j.trsl.2014.07.010
34. Menn-Josephy H, Lee CS, Nolin A, Christov M, Rybin DV, Weinberg JM, Henderson J, Bonegio R, Havasi A (2016) Renal interstitial fibrosis: an imperfect predictor of kidney disease progression in some patient cohorts. Am J Nephrol 44 (4):289–299. https://doi.org/10.1159/000449511
35. dos Santos EA, Li LP, Ji L, Prasad PV (2007) Early changes with diabetes in renal medullary hemodynamics as evaluated by fiberoptic probes and BOLD magnetic resonance imaging. Investig Radiol 42(3):157–162. https://doi.org/10.1097/01.rli.0000252492.96709.36
36. Li LP, Halter S, Prasad PV (2008) Blood oxygen level-dependent MR imaging of the kidneys. Magn Reson Imaging Clin N Am 16 (4):613–625. https://doi.org/10.1016/j.mric.2008.07.008
37. Pruijm M, Mendichovszky IA, Liss P, Van der Niepen P, Textor SC, Lerman LO, Krediet CTP, Caroli A, Burnier M, Prasad PV (2018) Renal blood oxygenation level-dependent magnetic resonance imaging to measure renal tissue oxygenation: a statement paper and systematic review. Nephrol Dial Transplant 33 (Suppl_2):ii22–ii28. https://doi.org/10.1093/ndt/gfy243
38. Caroli A, Schneider M, Friedli I, Ljimani A, De Seigneux S, Boor P, Gullapudi L, Kazmi I, Mendichovszky IA, Notohamiprodjo M, Selby NM, Thoeny HC, Grenier N, Vallee JP (2018) Diffusion-weighted magnetic resonance imaging to assess diffuse renal pathology: a systematic review and statement paper. Nephrol Dial Transplant 33(Suppl_2): ii29–ii40. https://doi.org/10.1093/ndt/gfy163
39. Ljimani A, Caroli A, Laustsen C, Francis S, Mendichovszky IA, Bane O, Nery F, Sharma K, Pohlmann A, Dekkers IA, Vallee JP, Derlin K, Notohamiprodjo M, Lim RP, Palmucci S, Serai SD, Periquito J, Wang ZJ, Froeling M, Thoeny HC, Prasad P, Schneider M, Niendorf T, Pullens P, Sourbron S, Sigmund EE (2019) Consensus-based technical recommendations for clinical translation of renal diffusion-weighted MRI. MAGMA. https://doi.org/10.1007/s10334-019-00790-y
40. Mansour SG, Puthumana J, Coca SG, Gentry M, Parikh CR (2017) Biomarkers for the detection of renal fibrosis and prediction of renal outcomes: a systematic review. BMC Nephrol 18(1):72. https://doi.org/10.1186/s12882-017-0490-0
41. Serai SD, Trout AT, Miethke A, Diaz E, Xanthakos SA, Dillman JR (2018) Putting it all together: established and emerging MRI techniques for detecting and measuring liver fibrosis. Pediatr Radiol 48(9):1256–1272. https://doi.org/10.1007/s00247-018-4083-2
42. Serai SD, Trout AT, Sirlin CB (2017) Elastography to assess the stage of liver fibrosis in children: concepts, opportunities, and challenges. Clin Liver Dis 9(1):5–10. https://doi.org/10.1002/cld.607

43. Sigrist RMS, Liau J, Kaffas AE, Chammas MC, Willmann JK (2017) Ultrasound elastography: review of techniques and clinical applications. Theranostics 7(5):1303–1329. https://doi.org/10.7150/thno.18650
44. Menzilcioglu MS, Duymus M, Citil S, Avcu S, Gungor G, Sahin T, Boysan SN, Altunoren O, Sarica A (2015) Strain wave elastography for evaluation of renal parenchyma in chronic kidney disease. Br J Radiol 88(1050):20140714. https://doi.org/10.1259/bjr.20140714
45. Wang L, Xia P, Lv K, Han J, Dai Q, Li XM, Chen LM, Jiang YX (2014) Assessment of renal tissue elasticity by acoustic radiation force impulse quantification with histopathological correlation: preliminary experience in chronic kidney disease. Eur Radiol 24(7):1694–1699. https://doi.org/10.1007/s00330-014-3162-5
46. Bob F, Bota S, Sporea I, Sirli R, Popescu A, Schiller A (2015) Relationship between the estimated glomerular filtration rate and kidney shear wave speed values assessed by acoustic radiation force impulse elastography: a pilot study. J Ultrasound Med 34(4):649–654. https://doi.org/10.7863/ultra.34.4.649
47. Bota S, Herkner H, Sporea I, Salzl P, Sirli R, Neghina AM, Peck-Radosavljevic M (2013) Meta-analysis: ARFI elastography versus transient elastography for the evaluation of liver fibrosis. Liver Int 33(8):1138–1147. https://doi.org/10.1111/liv.12240
48. Lee CU, Glockner JF, Glaser KJ, Yin M, Chen J, Kawashima A, Kim B, Kremers WK, Ehman RL, Gloor JM (2012) MR elastography in renal transplant patients and correlation with renal allograft biopsy: a feasibility study. Acad Radiol 19(7):834–841. https://doi.org/10.1016/j.acra.2012.03.003
49. Zhang X, Zhu X, Ferguson CM, Jiang K, Burningham T, Lerman A, Lerman LO (2018) Magnetic resonance elastography can monitor changes in medullary stiffness in response to treatment in the swine ischemic kidney. MAGMA 31(3):375–382. https://doi.org/10.1007/s10334-017-0671-7
50. Grenier N, Poulain S, Lepreux S, Gennisson JL, Dallaudiere B, Lebras Y, Bavu E, Servais A, Meas-Yedid V, Piccoli M, Bachelet T, Tanter M, Merville P, Couzi L (2012) Quantitative elastography of renal transplants using supersonic shear imaging: a pilot study. Eur Radiol 22(10):2138–2146. https://doi.org/10.1007/s00330-012-2471-9
51. Orlacchio A, Chegai F, Del Giudice C, Anselmo A, Iaria G, Palmieri G, Di Caprera E, Tosti D, Costanzo E, Tisone G, Simonetti G (2014) Kidney transplant: usefulness of real-time elastography (RTE) in the diagnosis of graft interstitial fibrosis. Ultrasound Med Biol 40(11):2564–2572. https://doi.org/10.1016/j.ultrasmedbio.2014.06.002
52. Itokawa F, Itoi T, Sofuni A, Kurihara T, Tsuchiya T, Ishii K, Tsuji S, Ikeuchi N, Umeda J, Tanaka R, Yokoyama N, Moriyasu F, Kasuya K, Nagao T, Kamisawa T, Tsuchida A (2011) EUS elastography combined with the strain ratio of tissue elasticity for diagnosis of solid pancreatic masses. J Gastroenterol 46(6):843–853. https://doi.org/10.1007/s00535-011-0399-5
53. Erkan M, Hausmann S, Michalski CW, Schlitter AM, Fingerle AA, Dobritz M, Friess H, Kleeff J (2012) How fibrosis influences imaging and surgical decisions in pancreatic cancer. Front Physiol 3:389. https://doi.org/10.3389/fphys.2012.00389
54. An H, Shi Y, Guo Q, Liu Y (2016) Test-retest reliability of 3D EPI MR elastography of the pancreas. Clin Radiol 71(10):1068.e1012–1068.e1012. https://doi.org/10.1016/j.crad.2016.03.014
55. Wang M, Gao F, Wang X, Liu Y, Ji R, Cang L, Shi Y (2018) Magnetic resonance elastography and T1 mapping for early diagnosis and classification of chronic pancreatitis. J Magn Reson Imaging. https://doi.org/10.1002/jmri.26008
56. Barton MB, Harris R, Fletcher SW (1999) The rational clinical examination. Does this patient have breast cancer? The screening clinical breast examination: should it be done? How? JAMA 282(13):1270–1280. https://doi.org/10.1001/jama.282.13.1270
57. Lorenzen J, Sinkus R, Lorenzen M, Dargatz M, Leussler C, Roschmann P, Adam G (2002) MR elastography of the breast:preliminary clinical results. Rofo 174(7):830–834. https://doi.org/10.1055/s-2002-32690
58. McKnight AL, Kugel JL, Rossman PJ, Manduca A, Hartmann LC, Ehman RL (2002) MR elastography of breast cancer: preliminary results. AJR Am J Roentgenol 178(6):1411–1417. https://doi.org/10.2214/ajr.178.6.1781411
59. Kim HK, Lindquist DM, Serai SD, Mariappan YK, Wang LL, Merrow AC, McGee KP, Ehman RL, Laor T (2013) Magnetic resonance imaging of pediatric muscular disorders: recent advances and clinical applications. Radiol Clin N Am 51(4):721–742. https://doi.org/10.1016/j.rcl.2013.03.002
60. Basford JR, Jenkyn TR, An KN, Ehman RL, Heers G, Kaufman KR (2002) Evaluation of healthy and diseased muscle with magnetic resonance elastography. Arch Phys Med Rehabil

83(11):1530–1536. https://doi.org/10.1053/apmr.2002.35472

61. Pichiecchio A, Alessandrino F, Bortolotto C, Cerica A, Rosti C, Raciti MV, Rossi M, Berardinelli A, Baranello G, Bastianello S, Calliada F (2018) Muscle ultrasound elastography and MRI in preschool children with Duchenne muscular dystrophy. Neuromuscul Dis 28 (6):476–483. https://doi.org/10.1016/j.nmd.2018.02.007
62. Buechter M, Manka P, Theysohn JM, Reinboldt M, Canbay A, Kahraman A (2018) Spleen stiffness is positively correlated with HVPG and decreases significantly after TIPS implantation. Dig Liver Dis 50(1):54–60. https://doi.org/10.1016/j.dld.2017.09.138
63. Song J, Huang J, Huang H, Liu S, Luo Y (2018) Performance of spleen stiffness measurement in prediction of clinical significant portal hypertension: a meta-analysis. Clin Res Hepatol Gastroenterol 42(3):216–226. https://doi.org/10.1016/j.clinre.2017.11.002
64. Yin M, Kolipaka A, Warner L, Talwalkar JA, Manduca A, Ehman RL (2010) Influence of perfusion on tissue stiffness assessed with MR elastography. Proc Int Soc Magn Reson Med 18:256
65. Yin M, Talwalkar JA, Glaser KJ, Venkatesh SK, Chen J, Manduca A, Ehman RL (2011) Dynamic postprandial hepatic stiffness augmentation assessed with MR elastography in patients with chronic liver disease. AJR Am J Roentgenol 197(1):64–70. https://doi.org/10.2214/AJR.10.5989
66. Clark WF, Sontrop JM, Moist L, Huang SH (2015) Increasing water intake in chronic kidney disease: why? Safe? Possible? Ann Nutr Metab 66(Suppl 3):18–21. https://doi.org/10.1159/000381241
67. Gandhi D, Kalra P, Raterman B, Mo X, Dong H, Kolipaka A (2019) Magnetic resonance elastography-derived stiffness of the kidneys and its correlation with water perfusion. NMR Biomed 33:e4237. https://doi.org/10.1002/nbm.4237
68. Warner L, Yin M, Glaser KJ, Woollard JA, Carrascal CA, Korsmo MJ, Crane JA, Ehman RL, Lerman LO (2011) Noninvasive in vivo assessment of renal tissue elasticity during graded renal ischemia using MR elastography. Investig Radiol 46(8):509–514. https://doi.org/10.1097/RLI.0b013e3182183a95
69. Ramachandran P, Iredale JP (2009) Reversibility of liver fibrosis. Ann Hepatol 8(4):283–291
70. Campana L, Iredale JP (2017) Regression of liver fibrosis. Semin Liver Dis 37(1):1–10. https://doi.org/10.1055/s-0036-1597816
71. Dong H, Mazumder R, Illapani VSP, Mo X, White RD, Kolipaka A (2017) In vivo quantification of aortic stiffness using MR elastography in hypertensive porcine model. Magn Reson Med 78(6):2315–2321. https://doi.org/10.1002/mrm.26601
72. Morin CE, Dillman JR, Serai SD, Trout AT, Tkach JA, Wang H (2018) Comparison of Standard Breath-Held, Free-Breathing, and Compressed Sensing 2D Gradient-Recalled Echo MR Elastography Techniques for Evaluating Liver Stiffness. AJR American journal of roentgenology:1–9. doi:https://doi.org/10.2214/ajr.18.19761
73. Liu X, Li N, Xu T, Sun F, Li R, Gao Q, Chen L, Wen C (2017) Effect of renal perfusion and structural heterogeneity on shear wave elastography of the kidney: an in vivo and ex vivo study. BMC Nephrol 18(1):265. https://doi.org/10.1186/s12882-017-0679-2

Part IV

Experimental Protocols

Chapter 19

Monitoring Renal Hemodynamics and Oxygenation by Invasive Probes: Experimental Protocol

Kathleen Cantow, Mechthild Ladwig-Wiegard, Bert Flemming, Andreas Pohlmann, Thoralf Niendorf, and Erdmann Seeliger

Abstract

Renal tissue hypoperfusion and hypoxia are early key elements in the pathophysiology of acute kidney injury of various origins, and may also promote progression from acute injury to chronic kidney disease. Here we describe methods to study control of renal hemodynamics and tissue oxygenation by means of invasive probes in anesthetized rats. Step-by-step protocols are provided for two setups, one for experiments in laboratories for integrative physiology and the other for experiments within small-animal magnetic resonance scanners.

This publication is based upon work from the COST Action PARENCHIMA, a community-driven network funded by the European Cooperation in Science and Technology (COST) program of the European Union, which aims to improve the reproducibility and standardization of renal MRI biomarkers. This experimental protocol chapter is complemented by a separate chapter describing the basic concepts of quantitatively assessing renal perfusion and oxygenation with invasive probes.

Key words Renal hemodynamics and oxygenation, In vivo methods, Rats, Magnetic resonance imaging (MRI)

1 Introduction

Kidney diseases are a global health burden with steadily increasing incidence [1–5]. Animal studies indicate that acute kidney injuries (AKI) of various origins share one common link in the pathophysiological chain of events, ultimately leading to AKI, as well as to progression from AKI to chronic kidney diseases (CKD): imbalance between renal oxygen delivery and oxygen demand [3, 6–13]. Renal tissue hypoperfusion and hypoxia have also been suggested to play a pivotal role in the pathophysiology of other kidney diseases including diabetic nephropathy [14–18].

The majority of the preclinical studies that generated this concept utilized a set of invasive probes to measure renal hemodynamics and oxygenation in anaesthetized rats [12, 14–16, 19–22]. These probes

Andreas Pohlmann and Thoralf Niendorf (eds.), *Preclinical MRI of the Kidney: Methods and Protocols*, Methods in Molecular Biology, vol. 2216, https://doi.org/10.1007/978-1-0716-0978-1_19,

typically include (1) a perivascular flow probe for measurement of total renal blood flow, (2) laser-Doppler-probes for assessment of local tissue perfusion, (3) Clark-type electrodes or fluorescence-quenching optodes for measurements of local tissue partial pressure of oxygen (pO_2), and (4) devices for invasive measurement of arterial blood pressure. These methods are considered the gold standard for the study of renal hemodynamics and oxygenation because the methods—with the exception of the laser-Doppler—provide calibrated quantitative data [23–25]. The methodological principles of these techniques are detailed in the chapter by Cantow K et al. "Quantitative Assessment of Renal Perfusion and Oxygenation by Invasive Probes: Basic Concepts." Besides the study of the pathophysiology of AKI and CKD, these methods have also been used to study (1) mechanisms of control of renal hemodynamics and oxygenation in healthy rats, (2) the effects of various substances on this control, and (3) several putative preventive or therapeutic approaches for AKI and CKD [20–22, 26–30].

It is well known that, due to the considerable capacity of the organism's homeostatic control systems to—at least partially—compensate for disturbances of, or injury to, certain control elements, these alterations are often not easily detectable when studied by measuring baseline data only. Therefore, the control systems must be "challenged" in order to unmask such alterations. This is done by dedicated test interventions (*see* the chapter by Cantow K et al. "Reversible (Patho)Physiologically Relevant Test Interventions: Rationale and Examples") [19, 27, 28, 31].

As all established modalities available in today's experimental and translational research, these techniques have shortcomings and methodological restraints, in particular, the invasiveness that preclude the survival of the animals and therefor the implementation in long-term studies, and, of course, their use in humans. Magnetic resonance imaging (MRI) offers noninvasive techniques to obtain insight into renal perfusion and oxygenation under (patho)-physiological conditions. MRI affords full kidney coverage, soft tissue contrast that helps to differentiate the renal layers, seconds to minutes temporal resolution, support of longitudinal studies, and high anatomical detail [24, 25, 32–34].

However, the validity and efficacy of functional MRI techniques for quantitative characterization of renal tissue perfusion and oxygenation and its changes in various (patho)physiological scenarios remains to be established [24, 33, 35–37]. In particular, the weakness of MRI, its qualitative nature, needs to be addressed by calibration with quantitative methods, that is, the gold standard physiological techniques. Realizing the need of tracking invasive physiological parameters and MR parameters simultaneously for the same kidney, an integrated multimodality approach designated as MR-PHYSIOL was developed by our group [24, 33, 38]. It combines the measurements by the invasive probes described above

(hereafter called *PHYSIOL*) with renal functional MRI data acquired by an ultrahigh field small animal scanner. By means of this hybrid setup, the first steps toward calibration of the blood oxygenation-sensitive parameter T_2* (so-called blood oxygenation level-dependent MRI, BOLD-MRI) were done. Dedicated (patho)physiologically relevant test intervention including short periods of suprarenal aortic occlusion, hypoxia, and hyperoxia were applied to modulate renal perfusion and oxygenation, in order to detail the relationship between renal T_2* and tissue oxygenation [24, 33, 39]. Of course, the MR-PHYSIOL setup can be used for calibration of functional MR parameters other than oxygenation-sensitive T_2* as well.

In the following, step-by-step protocols are provided for two setups, one for stand-alone experiments in laboratories for integrative physiology (*PHYSIOL*) and the other for experiments within dedicated small-animal magnetic resonance scanners by use of the hybrid setup (*MR-PHYSIOL*).

This experimental protocol chapter is complemented by a separate chapter describing the basic concepts, which is part of this book.

This chapter is part of the book Pohlmann A, Niendorf T (eds) (2020) Preclinical MRI of the Kidney—Methods and Protocols. Springer, New York.

2 Materials

2.1 Animals

For *PHYSIOL*, male Wistar rats with body mass of 300–400 g are used. For *MR-PHYSIOL*, the spatial constraints dictated by the MR environment require the use of relatively small rats ($\leq$350 g). The rats are allowed ad libitum food (standard maintenance diet) and water and must be housed at standardized conditions (e.g., group housed in Makrolon type IV cages with elevated lids under conventional SPF conditions; for cage enrichment paper towels as nesting material and pieces of wood for gnawing should be provided).

2.2 Surgical Preparation

1. Anesthesia: urethane solution (Sigma-Aldrich, Steinheim, Germany; 20% in distilled water).
2. Temperature controlled operation table.
3. Operation microscope (e.g., Leica MZ6; Leica Microsystems, Wetzlar, Germany) with magnification range between 6.3× and 40×.
4. Set of microsurgical instruments (including dissecting scissors, microsurgical forceps, needle holders) and threads (including Vicryl polyglactin 910, 4/0; Prolene 6/0; Ethicon, Norderstedt, Germany).
5. For blood pressure measurement: (a) a pressure transducer (e.g., DT-XX, Viggo-Spectramed, Swindon, UK) connected

to an amplifier (TAM-A Plugsys, Hugo Sachs Elektronik—Harvard Apparatus, March, Germany); (b) a femoral artery catheter designed and custom-made in our laboratory using Portex Tubing (polythene). For *MR-PHYSIOL* the catheter must be longer than 1 m to allow placing the pressure transducer well outside the bore of the MR scanner. Safety information: Make sure that the positioning of the amplifier meets the safety requirements of the MR environment.

6. For monitoring of total renal blood flow for *PHYSIOL*: a perivascular flow probe (1RB, Transonic Systems, Ithaca, NY, USA), for *MR-PHYSIOL* a perivascular flow probe (MCV2PSB-MRI; Transonic Systems) as depicted in Fig. 1. Please note that the flow probe employed in *MR-PHYSIOL* uses an acoustic reflector made of Macor ceramics instead of a stainless steel or brass reflector to meet the safety and compatibility requirements of MRI. The respective flow probe is connected to a perivascular flow module (TS420; Transonic Systems). Safety information: Make sure that the positioning of the flow module meets the safety requirements of the MR environment.
7. Combined optical laser-Doppler-Flux and pO_2 probes (pO_2 E-Series Sensor; Oxford Optronix, Oxford, UK) for measurements of local tissue oxygenation and local tissue perfusion as

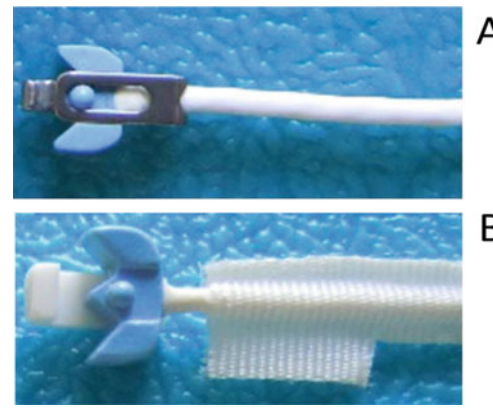

Fig. 1 Probes for monitoring of total renal blood flow. (**a**) Perivascular flow probe (1RB, Transonic Systems, Ithaca, NY, USA) for *PHYSIOL*: the acoustic reflector is made of steel; closing the probe's steel "lock" prevents detachment from the renal artery. (**b**) perivascular flow probe (MV2PSB-MRI; Transonic Systems) for *MR-PHYSIOL*: due to the long extension leads necessary to meet MR safety requirements, this probe has a larger body size. The reflector is made of ceramics (it does not induce MR artifacts), is L-shaped and offers no mechanism to lock the vessel. Therefore, a gauze is attached to the probe's cable, which will be fixed to the retroperitoneal muscles by means of sutures to avoid probe displacement

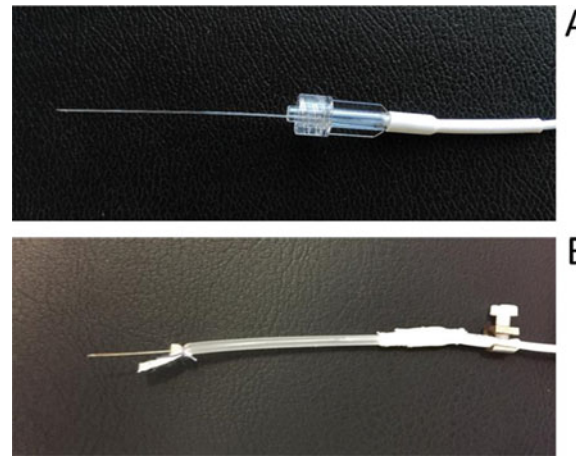

Fig. 2 Probes for monitoring of tissue laser-Doppler-flux and pO_2 (pO_2 E-Series Sensor; Oxford Optronix, Oxford, UK). (**a**) Unmodified probe for *PHYSIOL*. (**b**) Modified probe for *MR-PHYSIOL*: the customary Luer-Lock connector is removed, the fiber glass cores are fixed to the sheathing by means of a clamp. Silicone tubing with its length adjusted to the distance between the caudal and the cranial extremities of the individual kidney enables the exact placement of the cortical probe. A patche of gauze attached to the end of silicone tubing is used to fixed the probe on the kidney surface by Histoacryl glue to prevent displacement

depicted in Fig. 2. The probes are attached to an OxyLite/OxyFlo-apparatus (Oxford Optronics, Oxford, UK). Safety information: For *MR-PHYSIOL* make sure that the positioning of the OxyLite/OxyFlo-apparatus meets the safety requirements of the MR environment.

8. For continuous logging of the signals from the probes for arterial blood pressure, renal blood flow, cortical and medullary pO_2 and flux, their analog outputs must be digitized and recorded. An analog–digital converter (e.g., DT 9800-16SE-BNC, Data Translation GmbH, Bietigheim-Bissingen, Germany) permits connection to the USB port of a PC. A dedicated data acquisition software (HAEMODYN, Hugo Sachs Elektronik—Harvard Apparatus, March, Germany) allows for calibration of the probe signals and their continuous recording.
9. A vascular occluder (*see* Fig. 3): the remotely controlled hydraulic occluder is custom-made; it was designed and manufactured in our laboratory. The occluder consists of an inflatable tube ("head" of the occluder) connected by a catheter to a syringe. The "head" of the occluder is made of a high-grade silicone elastomer tube (Silikonkautschuk, Detakta Isolier-und Messtechnik GmbH & Co KG, Germany). For the connection between the "head" of the occluder and a regulative syringe an inextensible extension catheter (Portex Polythene Tubing; Ref

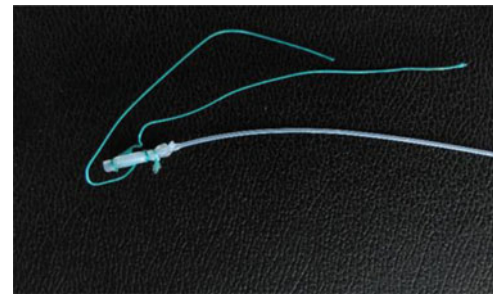

Fig. 3 Custom-made remotely controlled hydraulic vascular occluder as designed and manufactured in our laboratory. An inflatable tube ("head" of the occluder) is connected by an inextensible catheter (about 1 m length for *MR-PHYSIOL*) to a syringe. Inflation of the "head" (which is made of a high-grade silicone elastomer tube) compresses the respective vessel due to its fixation to the vessel by means of the (green) surgical threads

800/110/200; inner diameter 0.58 mm) is used. For *MR-PHYSIOL*, the extension catheter must be longer than 1 m to allow remote control of the occluder from outside the bore of the MR scanner.

10. Vascular catheter(s) for administration of fluids (e.g., isotonic saline) and/or solutions of substances used for selective test interventions (e.g., drugs), and for repeated blood sampling (e.g., for measurements of blood gases and hemoximetry). Catheters for venous and arterial insertion are made in our laboratory using Portex Tubing (polythene).
11. For fixation and stabilization of the probes for *PHYSIOL*: two micromanipulators (e.g., type M-44 and MN-153, Narishige group, Tokyo, Japan) mounted on a rotatable magnetic pedestal (e.g., type M9, World Precision Instruments, Sarasota, FL, USA) as depicted in Fig. 4. The operation table needs a steel surface (e.g., type Micro-g, Technical Manufacturing Corporation, Peabody, MA, USA) to fixate the magnetic pedestals in positions required by the individual placements of the probes within the rat. For *MR-PHYSIOL*: to achieve stabile positions of the probes and to ensure safe transfer of the animal equipped with the probes to the scanner, a custom-made portable animal holder must be used (*see* Fig. 5). It was designed and built in our laboratory using 3D CAD (Autodesk Inventor 2012; Autodesk, San Rafael, CA, USA) and rapid prototyping (BST 1200es; Alphacam GmbH, Schorndorf, Germany). The holder must meet the geometry of the MR setup; it has a half-pipe shape with a section of reduced diameter to allow for the 4-element surface RF coil to be placed beneath. A mark on the holder indicates the center of the RF coil. A bridge-like construction, positioned at the end of the hind paws of the rat, enables fixation of all leads that connect the physiological

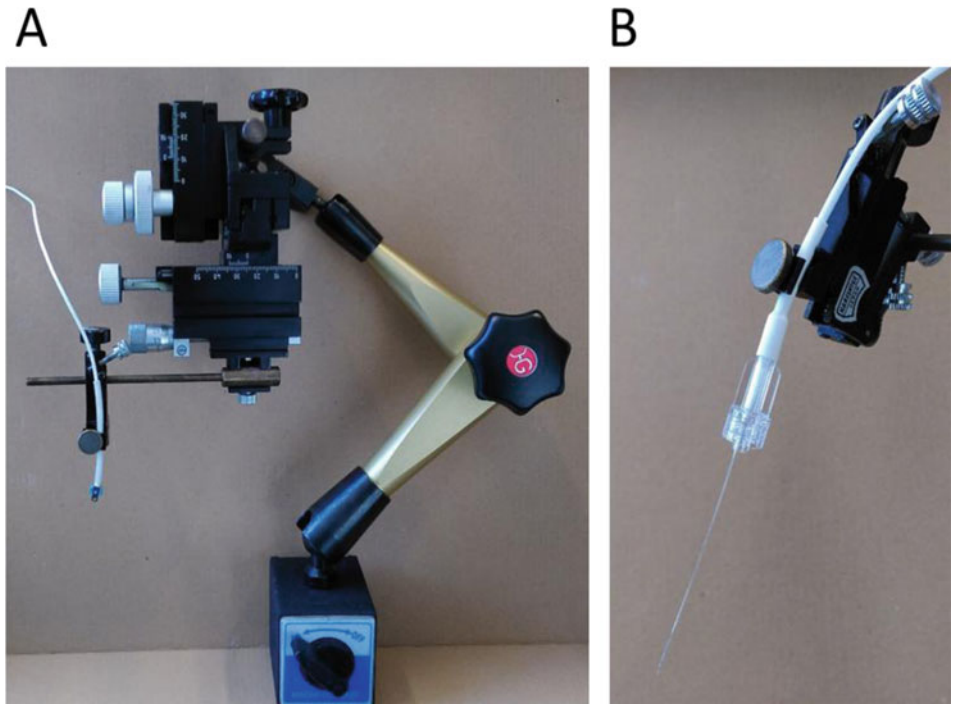

Fig. 4 Micromanipulators used for placement/insertion and fixation of probes for *PHYSIOL*. (**a**) micromanipulator (type M-44 and MN-153, Narishige group, Tokyo, Japan) mounted on a rotatable magnetic pedestal (type M9, World Precision Instruments, Sarasota, FL, USA). A perivascular flow probe (1RB, Transonic Systems, Ithaca, NY, USA) is attached to its "clutch" (type M-44). (**b**) Detail of the "clutch" with a laser-Doppler-flux and pO_2 probe (pO_2 E-Series Sensor; Oxford Optronix, Oxford, UK) attached

Fig. 5 Portable animal holder for *MR-PHYSIOL*. The holder enables fixation and stabilization of the probes and a safe transfer to the scanner of the animal equipped with the probes. To meet the geometry of the MR setup, it is custom-made by our lab in a half-pipe shape with a section of reduced diameter to allow for the surface RF coil. A bridge-like construction, positioned at the caudal end, enables fixation of all leads that connect the physiological probes with the equipment positioned outside the MR scanner room

probes with the equipment positioned outside the MR scanner room. The portable rigid animal holder in conjunction with the adjustable cable support bridge enables a safe transport of the animal to the MR scanner.

12. A respiratory (anesthetic) mask through which the spontaneously breathing rat is provided with air or other gas mixtures at

a supply rate of about 1000 mL/min. Such a mask can be easily built: take a 20 mL plastic syringe, cut off the tip approximately 15 mm from the bottom of the syringe, yielding a funnel shaped mask. Finally deflash and smooth the cutting edges of the mask using a file. The cone of the syringe can be connected to the gas supplying tube (*see* **Note 1**).

13. Patches of Dacron gauze (Woven Mesh Spacer; Merck Millipore, Billerica, USA).
14. Histoacryl glue (Braun Surgical GmbH, Melsungen, Germany).
15. Medical sticky tape.
16. Silicone elastomer tubes (Silikonkautschuk, Detakta Isolier- und Messtechnik GmbH & Co KG, Germany).

2.3 Magnetic Resonance Imaging (for MR-PHYSIOL)

Magnetic resonance imaging (MRI) requires access to an ultrahigh field MRI system including suitable accessories for the MR acquisition (radio frequency antennas), positioning, warming, and monitoring of physiological parameters, as well as trained personnel for operating the MRI system. The general hardware requirements for renal ^{1}H MRI on rats and mice are described in the chapter by Ramos Delgado P et al. "Hardware Considerations for Preclinical Magnetic Resonance of the Kidney." The methods described in this chapter were tailored for in vivo studies in rats by means of the dedicated MR-PHYSIOL techniques.

Due to the small size of rats in comparison with humans a much higher spatial resolution is required to depict the kidney with adequate detail. This, in turn, demands a high signal-to-noise ratio (SNR), which must be achieved by use of tailored MR equipment.

1. MR system: a dedicated small animal MR system with a magnetic field strength of 7 T and higher is recommended. We use a 9.4 T 20 cm bore system (Biospec 94/20, Bruker Biospin, Ettlingen, Germany) equipped with a gradient system with integrated shim set (B-GA12S2, Bruker Biospin, Ettlingen, Germany; gradient amplitude 440 mT/m, max. Slew rate 3440 T/m/s).
2. Radio frequency (RF) coils: use RF coils (antennas for RF transmission and reception) suitable for abdominal imaging, such as a transmit/receive rat body volume coil (72 mm inner diameter, quadrature; Bruker Biospin, Ettlingen, Germany) or preferably a transmit only *rat body volume coil* (72 mm inner diameter, linear; model T10325V3, Bruker Biospin, Ettlingen, Germany) in combination with a receive only *rat heart RF coil array* (curved, 2 × 2 elements; model T12814V3, Bruker Biospin, Ettlingen, Germany). Use of the latter coil setup is assumed here, as it allows for much higher spatial resolution

due to its superior SNR when compared with the transmit/receive *volume coil.*

3. Animal holder: an MRI animal holder designed for the size of the rats and the geometry of the RF coils (here model T11739 with 68 mm diameter, Bruker Biospin, Ettlingen, Germany).
4. Device for sustaining the rat's body temperature: use a circulating warm-water based heating system, consisting of a flexible rubber blanket with integrated tubing (part no. T10964, Bruker Biospin, Ettlingen, Germany) connected to a conventional warm water bath (SC100-A10, ThermoFisher, Dreieich, Germany). For alternative coil setups water pipes may be integrated into the animal holder.
5. Monitoring of physiological parameters: for monitoring of respiration and core body temperature throughout the entire MR experiment use a small animal monitoring system (Model 1025, Small Animal Instruments, Inc., Stony Brook, NY, USA), including a rectal temperature probe and pneumatic pillow.

2.4 Test Interventions

1. Gases: O_2, N_2, and compressed air, as well as a gas-mixing system (e.g., Föhr Medical Instruments GmbH, Seeheim-Ober Beerbach, Germany) to achieve required changes in the oxygen fraction of inspired gas mixture (FiO_2). The following gas mixtures are required during the experiment: (a) for hypoxia: 10% O_2–90% N_2; (b) for hyperoxia: 100% O_2; (c) for normoxia: 21% O_2 (air) (*see* **Note 2**).
2. Device for monitoring FiO_2 and $FiCO_2$ in gas mixtures: for example Capnomac AGM-103 (Datex GE, Chalfont St Gils, UK).
3. Vascular occluder as listed under 2.2.9. already.
4. Vascular catheters as listed under 2.2.10. already.
5. Solutions for fluid supplementation (e.g., isotonic saline) and drug administration for dedicated test intervention according to the scientific purpose of the respective study.
6. Equipment for blood sampling via vascular catheters (e.g., capillaries for hemoximetry).
7. Instruments for analyses of blood samples according to the scientific purpose of the respective study, for example, regarding blood gases and hemoximetry (e.g., ABL80 FLEX CO-OX, Radiometer, Copenhagen, Denmark).

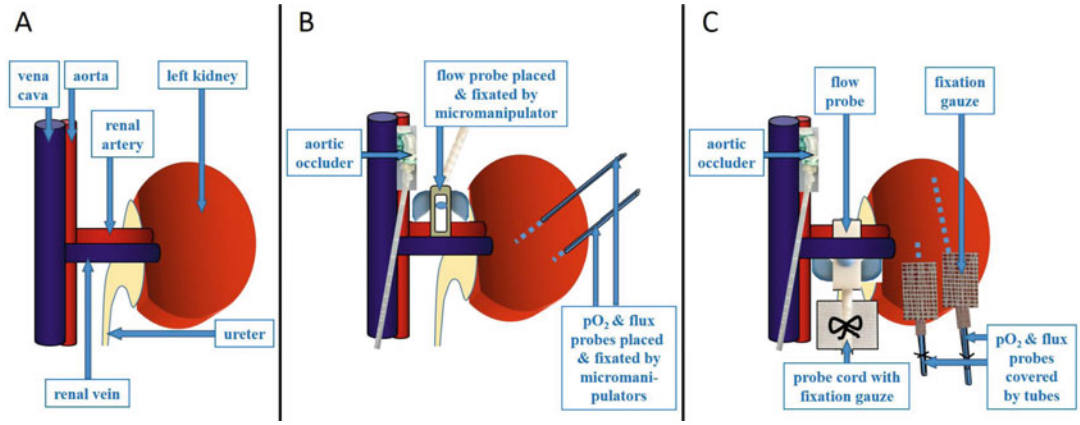

Fig. 6 Schemes depicting (**a**) the rat anatomy relevant for the placing of probes, (**b**) positions and fixations of probes for *PHYSIOL*, and (**c**) positions and fixations of probes for *MR-PHYSIOL*. For details see text

3 Methods

Figure 6 provides schemes of (a) the rat anatomy relevant for the placing of probes, (b) positions and fixations of probes for *PHYSIOL*, and (c) positions and fixations of probes for *MR-PHYSIOL*.

3.1 Surgical Preparation

For *PHYSIOL*, surgery is performed at the same operation table at which the subsequent experiment is executed. For *MR-PHYSIOL*, surgery must be performed outside the MR scanner room (in a neighboring preparation room) for safety reasons.

1. Anesthetize the animal by intraperitoneal injection of urethane (20% solution, 6 mL/kg body mass) (*see* **Note 3**).
2. After reaching the required depth of anesthesia, that is, the state of surgical tolerance (determined by specific physiological signs such as muscle relaxation degree, absence of the paw withdrawal and eye lid reflexes, absence of the swallowing reflex, and whisker movement), carefully shave the coat in the abdominal, inguinal, and ventral neck areas of the rat (hair clipper Elektra II GH2, Aesculap AG, Tuttlingen, Germany).
3. Place the rat in supine position on a warmed-up (39 °C) temperature-controlled operating table and fix the extremities of the animal to the table by means of sticky tapes.
4. Make an incision into the skin of the left inguinal area (approx. 12 mm) along the natural angle of the hind leg by lifting a fold of the skin in order to avoid an injury of the underlying blood vessels.

5. Bluntly dissect the connective tissue until the femoral vein, artery, and nerve are exposed.
6. Gently separate the nerve. Do not cut or damage the nerval tissue.
7. Separate the vein from the artery by using fine tip forceps, while trying to release an approximately 7–8 mm length vein fragment from the surrounding tissue.
8. Place three pieces of 4.0 threads under the femoral artery: situate the *first* thread distal (i.e., toward the leg), the *second* thread proximal (i.e., toward the body) and the *third* one between them.
9. Pull the *first* thread toward the leg and tie a ligature to the distal artery by using a triple knot.
10. Prepare loops with loose surgical knots on the remaining two threads.
11. Pull the *second* thread slightly toward the body so that the blood flow from femoral artery is inhibited.
12. Make a tiny incision in the exposed segment of the femoral artery behind the third thread using fine tip scissors. Fill a catheter with tapered tip with saline.
13. Grasp the catheter with the forceps and gently insert through the incision into the lumen of the femoral artery.
14. Tie the *third* knot slightly, fix catheter and arterial wall with a forceps, relax the tensed *second* thread, and push the catheter with a second forceps slowly deeper (≈10 mm) into the artery in direction of the abdomen.
15. Rinse the catheter carefully with saline, and make sure that it is patent.
16. Tie the prepared loose knot of the *third* and *second* threads.
17. Start the monitoring of arterial blood pressure.
18. For insertion of additional vascular catheters for volume supplementation (e.g., by saline infusion), for test interventions by drugs, and for blood sampling (if warranted by the specific scientific goal of the experiment) surgically prepare the proximal external jugular vein (catheter tip toward vena brachiocephalica) and/or the left common carotid artery (catheter tip toward aorta) similar to **steps 5–16** detailed for the femoral artery catheter implantation.
19. Open the abdominal cavity by a midventral incision (4–5 cm) into the skin. Then open the abdominal cavity by an incision along the linea alba, thereby preventing damage to the abdominal organs. Carefully displace the bowel to the right side of the abdomen to expose the aorta and the left kidney. Carefully detach the aorta directly cranial of the renal arteries from the

surrounding tissues without damaging the very tender lymphatic vessels of that area.

20. Fix the hydraulic occluder around the aorta cranial of the renal arteries in a manner, that the occluder is well attached to the aorta without impairing the blood flow while being deflated (*see* **Note 4**).
21. Carefully separate the left renal artery from the renal vein using fine tip forceps. Try to expose an approximately 6–7 mm long fragment. Do not cut or damage the nerves.
22. For *MR-PHYSIOL*, transfer the animal onto the portable animal holder such that the kidney is aligned with the mark on the holder that indicates the center of the RF coil.
23. Start the HAEMODYN software (*see* Subheading 3.3).
24. Place the Transonic flow probe around the left renal artery and start monitoring RBF. It is important that the head of the flow probe is filled with fluid. For *PHYSIOL*, attach the cable of the probe on the "clutch" of a micromanipulator (*see* Fig. 4a). Position and fixate the probe (Type 1RB) by means of the micromanipulator in the appropriate position of the artery (*see* Fig. 6b). For *MR-PHYSIOL*, the placement of the probe upon the artery must be done without the benefit of a micromanipulator. A gauze is attached to the probe cable (Type MV2PSB-MRI) as shown in Fig. 1b. To avoid displacements of the probe, the gauze is fixed to the retroperitoneal muscles by sutures (*see* Fig. 6c) (*see* **Note 5**).
25. For *PHYSIOL*, attach the cortical and medullary laser-flux-pO_2 probes, respectively, at one of the two "clutches" (*see* Fig. 4b) of a micromanipulator. With the help of the micromanipulator, the probes are placed into the renal cortex (depth about 1–1.5 mm below the capsule) and the medulla (3–4 mm below the capsule), respectively, as shown in Fig. 6b (*see* **Note 6**).
26. For *MR-PHYSIOL*, remove the customary Luer-Lock connectors of the laser-flux-pO2 probes and carefully fix the fiber glass cores to the sheathing using a clamp. Provide the probe with a customary silicone tubing; its length must be adjusted to the distance between the caudal and the cranial extremities of the left kidney. Attach tailored patches of gauze to the end of silicone tubing (*see* Fig. 2b). Measure the distance between the caudal and the cranial extremities of the left kidney by a caliper gauge. Based on this measurement, the cortical laser-flux-pO2-probe must be carefully prepared so that the distance between insertion point and the tip exactly matches the individual kidney's diameter minus 1.5 mm.

27. For *MR-PHYSIOL*, advance the cortical laser-flux-pO_2-probe meticulously from the caudal extremity of the kidney along the caudocranial axis (*see* Fig. 6c). To prevent craniocaudal displacement, the patch of gauze fixed to the silicone tubing of the probe (*see* Fig. 2b) must be stuck to the capsule of kidney's ventral surface by a thin layer of Histoacryl glue.
28. For *MR-PHYSIOL*, prepare the medullary laser-flux-pO_2-probe so that the distance between insertion point and the tip exactly matches the distance 3–4 mm. Carefully advance the medullary laser-flux-pO_2-probe from the caudal extremity of the kidney along the caudocranial axis. Stick the patch of gauze fixed to the silicone tubing of the probe to the capsule of kidney's ventral surface by Histoacryl glue (*see* Fig. 6c).
29. For *MR-PHYSIOL*, carefully fix the two probes' tubing to the retroperitoneal muscles by sutures in order to prevent displacement (*see* Fig. 6c).
30. Fill the abdominal cavity with warm saline (37 °C). For *PHYSIOL*, intermittent exchange of this fluid throughout the experiment is done via the open abdominal wall. As the abdomen will be closed for *MR-PHYSIOL* (see below), for replenishment of abdominal saline a catheter must be placed into the abdominal cavity. Furthermore, for *MR-PHYSIOL*, a fiber-optical temperature probe is placed in close proximity to the left kidney, in order to monitor the temperature of the kidney throughout the experiment.
31. Connect the probes with OxyLite/OxyFlo-apparatus and start the monitoring of tissue pO_2 and laser-Doppler-flux.
32. For *MR-PHYSIOL*, mark the localization of the investigated kidney's upper and lower pole from the outside on the abdominal skin using a pen. Check that the kidney (pen markings on skin) is still aligned with the mark on the portable animal holder that indicates the center of the RF coil—if necessary carefully correct the animal's position. This is essential for optimal positioning of the rat in the MRI scanner (i.e., optimal position of the rat's kidney relative to the MR coil).
33. For *MR-PHYSIOL*, place the special bridge of the portable animal holder right behind the rat's hind paws and fix all the technical extensions (temperature probe, Transonic probe, laser-flux-pO_2-probes, aortic occluder line and abdominal flushing catheter) to the bridge (*see* Fig. 5). Close the abdominal cavity of the rat by continuous suture while passing all extensions through the caudal cutting edge of the median abdominal incision. The extensions of the laser-flux-pO_2-probes must be led through the abdominal wall using a small incision in the left inguinal region.

34. Place a respiratory mask loosely around the muzzle of the spontaneously breathing rat. Open air supply to a rate of 1000 mL/min.
35. Restart the HAEMODYN software (to start a new data file) and check the quality of all physiological signals, that is, arterial pressure (measured caudal the aortic occlude and therefore equivalent to renal artery pressure, RAP), renal blood flow (RBF), cortical and medullary laser-Doppler-flux, and cortical and medullary pO_2.

3.2 Setting Up Animal for MR-PHYSIOL Examination

1. Transfer the animal into the MR scanner room using the portable animal holder (*see* **Note 7**). Position portable animal holder with the rat on the MR scanner's animal bed.
2. Switch on the small animal monitoring system. Place the pneumatic pillow on the abdomen, and cover the animal with the warming blanket. Watch the respiration trace on the monitor of the small animal monitoring system and adjust pillow position until the respiratory motion is captured well (*see* **Note 8**). Set the trigger options of the small animal monitoring system such that the trigger gate opens for the duration of the expiratory phase.
3. Position the animal bed in the MR scanner such that the kidney of interest is located at the isocenter of the magnet.
4. Perform anatomical imaging as described in the chapter by Pohlmann A et al. "Essential Practical Steps for MRI of the Kidney in Experimental Research."
5. Perform localized shimming on the kidney imaging as described in the chapter by Pohlmann A et al. "Essential Practical Steps for MRI of the Kidney in Experimental Research."

3.3 Experimental Procedures

A number of dedicated test procedures and the rationale behind the usage of the respective procedure is detailed in the chapter by Cantow K et al. "Reversible (Patho)Physiologically Relevant Test Interventions: Rationale and Examples." If adequate for the specific purpose of the study, reversible procedures (such as short periods of hypoxia, hyperoxia, and suprarenal aortic occlusion) are preferred, to keep the number of animals as small as possible as required by the 3R principle (*see* the chapter by Hosszu A et al. "Animal Models of Renal Pathophysiology and Disease"). Following each reversible intervention, appropriate time is given for complete recovery. The exact duration of the reversible intervention is dictated by the duration and number of MR measurements. Because MRI can interfere with parameters acquired by invasive probes (as has been observed for laser-Doppler flux), short intervals without MR measurements must be implemented. In the following, an exemplary protocol is given for an *MR-PHYSIOL*

experiment. It must be noted, that for these experiments, the closest coordination among the operator(s) of the MR scanner, the person(s) who perform the test interventions and those who run the electronic data storage (including setting markers for events such as start and end of an intervention) is of the essence.

1. On the PC that acquires the physiological data set a "START" marker in the HAEMODYN software to monitor and store a first set of baseline data.
2. On the MR system run the protocol(s) of your choice (T_1-, T_2-, T_2*-mapping, DWI, etc.) to acquire a set of baseline data. Duplicate these scans for repeated measurements during/between/after the test interventions and ensure that all parameters remain identical, including the shim and receiver gain.
3. *Start of hypoxia*. Change the gas flowing through the respiratory mask to 10% O_2–90% N_2.
4. Set markers and acquire both physiological and MR data during the hypoxic challenge.
5. *End of hypoxia*. Change the gas flowing through the respiratory mask back to air (21% O_2).
6. Set markers and acquire both physiological and MR data during the recovery.
7. *Start of hyperoxia*. Change the gas flowing through the respiratory mask to 100% O_2.
8. Set markers and acquire both physiological and MR data during the hyperoxic challenge.
9. *End of hyperoxia*. Change the gas flowing through the respiratory mask back to air (21% O_2).
10. Set markers and acquire both physiological and MR data during the recovery.
11. *Start of occlusion*. Inflate the remotely controlled suprarenal aortic occluder.
12. Set markers and acquire both physiological and MR data during the occlusion (*see* **Note 9**).
13. *End of occlusion*. Rapidly deflate the occluder.
14. Set markers and acquire both physiological and MR data during the recovery.

3.4 End of Experiment

1. Carefully remove the respiratory mask from the animal's muzzle.
2. Cut all sutures; remove the fluid from the abdominal cavity using a pipette.
3. Control and note the overall condition of the kidney after experiment (e.g., surface coloring and its homogeneity).

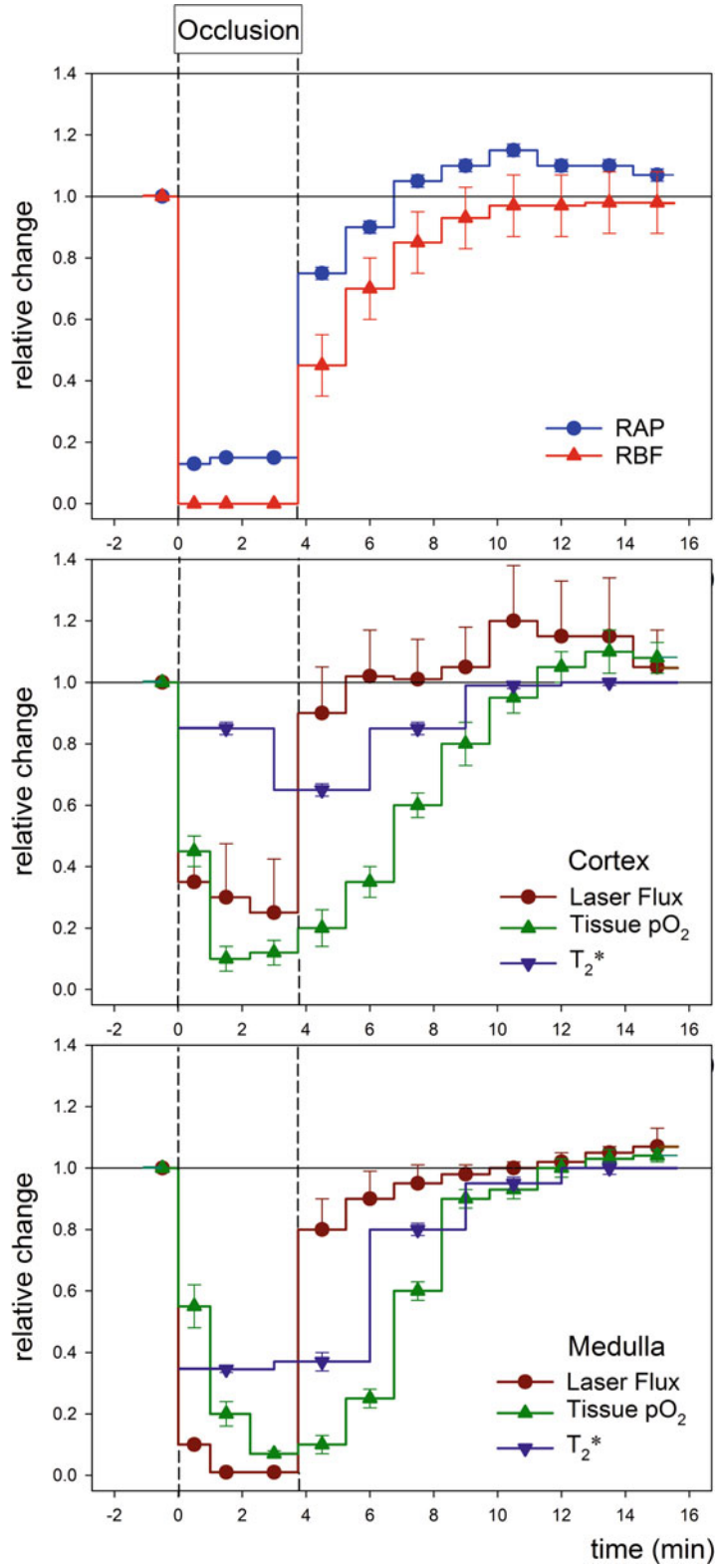

Fig. 7 Example of data obtained with *MR-PHYSIOL* in anesthetized rats (adapted from Ref. 39). Time courses of renal arterial pressure (RAP), total renal blood flow (RBF), cortical and medullary tissue perfusion (Laser Flux), cortical and

4. Carefully untie all sutures and knots; remove all probes and catheters, as well as the occluder.
5. Exsanguinate the animal by cutting the abdominal aorta.

3.5 Data Analysis

The analyses of MRI data acquired for *MR-PHYSIOL* experiments depend on the respective MR protocol and are detailed in dedicated analysis chapters for each MR method, which are part of the book Pohlmann A, Niendorf T (eds) (2020) Preclinical MRI of the Kidney—Methods and Protocols, Springer, New York.

Temporal alignment of MR and PHYSIOL data is achieved by identifying the starting point of the experiment within both data sets. For a direct comparison of the *MR-PHYSIOL* parameters only PHYSIOL data acquired during the relevant MRI acquisitions can be used. While the PHYSIOL parameters are measured with sub-second temporal resolution the acquisition of the MR parameters (derived from a MR image) requires much more time (e.g., about 60 s for a typical T_2* mapping). PHYSIOL and MR parameters can only be compared based on the (low) temporal resolution of the MRI. For this purpose the average value of each physiological parameter over the acquisition time of each MRI scan is calculated. For PHYSIOL data that are influenced by MR acquisition (such as Laser flux signals) the averages over the times without MR acquisition must be taken. Finally, group analyses of the results (e.g., relative changes of MR and PHYSIOL data; *see* **Note 10**) are done, as shown by exemplary data obtained by *MR-PHYSIOL* during a short suprarenal aortic occlusion and recovery in Fig. 7.

4 Notes

1. Instead of a respiratory (anesthetic) mask, a tracheal cannula can be used, as it is custom-made in our lab using designed and made in our laboratory using polythene tubing. The ventral region of the throat and the trachea are opened surgically, the cannula is inserted and fixated by suture.
2. As another dedicated test of control of hemodynamics and oxygenation, hypercapnia can be used with an inspiratory fraction of CO_2 of 5% in air.

Fig. 7 (continued) medullary tissue partial pressure of oxygen (Tissue pO_2) as monitored by invasive methods (PHYSIOL) simultaneously with cortical and medullary T_2* data (MR) acquired by a 9.4 T small animal MR scanner during suprarenal aortic occlusion and recovery. Date are given as relative changes (mean ± SEM) versus baseline (immediately before the occlusion)

3. Urethane supports anesthesia throughout the surgical preparation and the MRI examination (for several hours) and leaves cardiovascular and respiratory reflexes largely undisturbed.
4. (a) In order to prevent additional pressure on the aorta (and therefore development of an unintended kidney ischemia) the positioning and fixation of the aortic occluder must be performed under careful monitoring of the overall condition of the kidney (e.g., surface coloring and its homogeneity); (b) since the occluder consists of silicone and polyethylene and is positioned about 15 mm away from the kidney, it does not cause artefacts in MRI that affect the kidney.
5. (a) The signal of the probe used for *PHYSIOL* is too weak due to the long extension leads. For *MR-PHYSIOL* a probe with a larger body size and a reflector made of ceramics instead of metal must be used (*see* Fig. 1). Its reflector does not induce MR artifacts, is L-shaped and offers no mechanism to lock the vessel, which presents a significant challenge for the implantation if the probe. (b) The bulk of the intestine bears the risk to cause additional pressure that can dislocate the probe and cause probe pressure on the aorta, the renal artery and vein, or the kidney itself. (c) Since Transonic measurements rely on ultrasound an appropriate coupling into tissue is of high relevance. To this end the abdominal cavity must be filled with saline solution (37 °C) and no air bubbles must remain between probe and vessel. An additional catheter was placed in the abdominal cavity to replenish saline leakage in time course of the experiment.
6. Before inserting the tip of the respective probe, a small incision about the diameter of the probe is made into the renal capsule by means of the tip of a hypodermic needle to facilitate insertion of the rather dull tip probe.
7. Special attention during transfer must be paid to the tube/cable extensions (aortic occluder, abdominal flushing, and all probes). Make sure to keep tubes or cable close to the animal bed so they cannot get caught anywhere on the way into the magnet!
8. The peak-to-peak amplitude of the respiratory trace should span about 2/3 of the vertical axis on the display. Any gross movement (for instance during repositioning the pillow) will lead to large peaks and force the monitoring system to adapt the signal amplification, so that temporarily the signal will become much smaller on the display. Keep an eye on the magnification, which is given left next to the display, this will drop to a low value such as 15×—wait until it recovered back to a value around 100× before further adjusting it.

9. If unsuccessful, repeat the occlusion and inflate the occluder with higher hydraulic pressure and make sure that the fluid reservoir for the inflation is sufficiently filled. Always check that the inflation is sufficient to bring total renal blood flow (RBF) rapidly toward zero.
10. It is usually more practical and useful to compare relative changes in the parameters rather than absolute changes. To do this divide all parameter values by that of the last baseline value (e.g., *see* Fig. 7).

Acknowledgments

The authors wish to thank Ariane Anger, Andrea Gerhardt, Stefanie Münchberg, Yvonne Balke, and Victoria Prochnov for expert technical assistance.

This work was funded in part (Kathleen Cantow, Thoralf Niendorf, Andreas Pohlmann and Erdmann Seeliger) by the German Research Foundation (Gefoerdert durch die Deutsche Forschungsgemeinschaft (DFG), Project number / Projektnummer 394046635, SFB 1365, RENOPROTECTION).

This publication is based upon work from COST Action PARENCHIMA, supported by European Cooperation in Science and Technology (COST). COST (www.cost.eu) is a funding agency for research and innovation networks. COST Actions help connect research initiatives across Europe and enable scientists to enrich their ideas by sharing them with their peers. This boosts their research, career, and innovation.

PARENCHIMA (renalmri.org) is a community-driven Action in the COST program of the European Union, which unites more than 200 experts in renal MRI from 30 countries with the aim to improve the reproducibility and standardization of renal MRI biomarkers.

References

1. Fortrie G, de Geus HRH, Betjes MGH (2019) The aftermath of acute kidney injury: a narrative review of long-term mortality and renal function. Crit Care 23(1):24. https://doi.org/10.1186/s13054-019-2314-z
2. Selby NM, Taal MW (2019) Long-term outcomes after AKI-a major unmet clinical need. Kidney Int 95(1):21–23. https://doi.org/10.1016/j.kint.2018.09.005
3. Zuk A, Bonventre JV (2019) Recent advances in acute kidney injury and its consequences and impact on chronic kidney disease. Curr Opin Nephrol Hypertens. https://doi.org/10.1097/mnh.0000000000000504
4. Levin A, Tonelli M, Bonventre J, Coresh J, Donner JA, Fogo AB, Fox CS, Gansevoort RT, Heerspink HJL, Jardine M, Kasiske B, Kottgen A, Kretzler M, Levey AS, Luyckx VA, Mehta R, Moe O, Obrador G, Pannu N, Parikh CR, Perkovic V, Pollock C, Stenvinkel P, Tuttle KR, Wheeler DC, Eckardt KU (2017) Global kidney health 2017 and beyond: a roadmap for closing gaps in care, research, and policy. Lancet 390(10105):1888–1917. https://doi.org/10.1016/s0140-6736(17)30788-2
5. Bello AK, Levin A, Tonelli M, Okpechi IG, Feehally J, Harris D, Jindal K, Salako BL, Rateb A, Osman MA, Qarni B, Saad S,

Lunney M, Wiebe N, Ye F, Johnson DW (2017) Assessment of global kidney health care status. JAMA 317(18):1864–1881. https://doi.org/10.1001/jama.2017.4046

6. Brezis M, Rosen S (1995) Hypoxia of the renal medulla—its implications for disease. N Engl J Med 332:647–655
7. Fähling M, Seeliger E, Patzak A, Persson PB (2017) Understanding and preventing contrast-induced acute kidney injury. Nat Rev Nephrol 13(3):169–180
8. Evans RG, Ince C, Joles JA, Smith DW, May CN, O'Connor PM, Gardiner BS (2013) Haemodynamic influences on kidney oxygenation: the clinical implications of integrative physiology. Clin Exp Pharmacol Physiol 40:106–122
9. Evans RG, Ow CP, Bie P (2015) The chronic hypoxia hypothesis: the search for the smoking gun goes on. Am J Physiol Renal Physiol 308 (2):F101–F102
10. Shu S, Wang Y, Zheng M, Liu Z, Cai J, Tang C, Dong Z (2019) Hypoxia and hypoxia-inducible factors in kidney injury and repair. Cell 8(3). https://doi.org/10.3390/cells8030207
11. Hultstrom M, Becirovic-Agic M, Jonsson S (2018) Comparison of acute kidney injury of different etiology reveals in-common mechanisms of tissue damage. Physiol Genomics 50 (3):127–141. https://doi.org/10.1152/physiolgenomics.00037.2017
12. Calzavacca P, Evans RG, Bailey M, Bellomo R, May CN (2015) Cortical and medullary tissue perfusion and oxygenation in experimental septic acute kidney injury. Crit Care Med 43 (10):e431–e439
13. Ma S, Evans RG, Iguchi N, Tare M, Parkington HC, Bellomo R, May CN, Lankadeva YR (2019) Sepsis-induced acute kidney injury: a disease of the microcirculation. Microcirculation 26(2):e12483. https://doi.org/10.1111/micc.12483
14. Palm F, Carlsson PO, Hansell P, Hellberg O, Nygren A, Liss P (2003) Altered response in renal blood flow and oxygen tension to contrast media in diabetic rats. Acta Radiol 44 (3):347–353
15. Palm F, Cederberg J, Hansell P, Liss P, Carlsson PO (2003) Reactive oxygen species cause diabetes-induced decrease in renal oxygen tension. Diabetologia 46(8):1153–1160
16. dos Santos EA, Li LP, Ji L, Prasad PV (2007) Early changes with diabetes in renal medullary hemodynamics as evaluated by fiberoptic probes and BOLD magnetic resonance imaging. Investig Radiol 42(3):157–162. https://doi.org/10.1097/01.rli.0000252492.96709.36
17. Calvin AD, Misra S, Pflueger A (2010) Contrast-induced acute kidney injury and diabetic nephropathy. Nat Rev Nephrol 6 (11):679–688
18. Hansell P, Welch WJ, Blantz RC, Palm F (2013) Determinants of kidney oxygen consumption and their relationship to tissue oxygen tension in diabetes and hypertension. Clin Exp Pharmacol Physiol 40(2):123–137
19. Seeliger E, Flemming B, Wronski T, Ladwig M, Arakelyan K, Godes M, Mockel M, Persson PB (2007) Viscosity of contrast media perturbs renal hemodynamics. J Am Soc Nephrol 18 (11):2912–2920
20. Hoff U, Lukitsch I, Chaykovska L, Ladwig M, Arnold C, Manthati VL, Fuller TF, Schneider W, Gollasch M, Muller DN, Flemming B, Seeliger E, Luft FC, Falck JR, Dragun D, Schunck WH (2011) Inhibition of 20-HETE synthesis and action protects the kidney from ischemia/reperfusion injury. Kidney Int 79(1):57–65
21. Cantow K, Flemming B, Ladwig-Wiegard M, Persson PB, Seeliger E (2017) Low dose nitrite improves reoxygenation following renal ischemia in rats. Sci Rep 7(1):14597–15058
22. Seeliger E, Cantow K, Arakelyan K, Ladwig M, Persson PB, Flemming B (2014) Low-dose nitrite alleviates early effects of an X-ray contrast medium on renal hemodynamics and oxygenation in rats. Investig Radiol 49(2):70–77
23. Evans RG, Gardiner BS, Smith DW, O'Connor PM (2008) Methods for studying the physiology of kidney oxygenation. Clin Exp Pharmacol Physiol 35(12):1405–1412
24. Pohlmann A, Cantow K, Hentschel J, Arakelyan K, Ladwig M, Flemming B, Hoff U, Persson PB, Seeliger E, Niendorf T (2013) Linking non-invasive parametric MRI with invasive physiological measurements (MR-PHYSIOL): towards a hybrid and integrated approach for investigation of acute kidney injury in rats. Acta Physiol (Oxf) 207 (4):673–689
25. Hirakawa Y, Tanaka T, Nangaku M (2017) Renal hypoxia in CKD; pathophysiology and detecting methods. Front Physiol 8:99. https://doi.org/10.3389/fphys.2017.00099
26. Seeliger E, Wronski T, Ladwig M, Dobrowolski L, Vogel T, Godes M, Persson PB, Flemming B (2009) The renin-angiotensin system and the third mechanism of renal blood flow autoregulation. Am J Physiol Renal Physiol 296(6):F1334–F1345

27. Flemming B, Seeliger E, Wronski T, Steer K, Arenz N, Persson PB (2000) Oxygen and renal hemodynamics in the conscious rat. J Am Soc Nephrol 11(1):18–24
28. Ferrara F, Cantow K, Flemming B, Skalweit A, Ladwig M, Fähling M, Seeliger E (2017) Effects of liraglutide on control of renal hemodynamics and oxygenation in diabetic rats. Acta Physiol (Oxf) 219(Suppl 711):38
29. Cantow K, Pohlmann A, Flemming B, Ferrara F, Waiczies S, Grosenick D, Niendorf T, Seeliger E (2016) Acute effects of ferumoxytol on regulation of renal hemodynamics and oxygenation. Sci Rep 6:29965. https://doi.org/10.1038/srep29965
30. Emans TW, Janssen BJ, Pinkham MI, Ow CP, Evans RG, Joles JA, Malpas SC, Krediet CT, Koeners MP (2016) Exogenous and endogenous angiotensin-II decrease renal cortical oxygen tension in conscious rats by limiting renal blood flow. J Physiol 594(21):6287–6300. https://doi.org/10.1113/jp270731
31. Grosenick D, Cantow K, Arakelyan K, Wabnitz H, Flemming B, Skalweit A, Ladwig M, Macdonald R, Niendorf T, Seeliger E (2015) Detailing renal hemodynamics and oxygenation in rats by a combined near-infrared spectroscopy and invasive probe approach. Biomed Opt Express 6(2):309–323
32. Li LP, Halter S, Prasad PV (2008) Blood oxygen level-dependent MR imaging of the kidneys. Magn Reson Imaging Clin N Am 16 (4):613–625. viii
33. Niendorf T, Pohlmann A, Arakelyan K, Flemming B, Cantow K, Hentschel J, Grosenick D, Ladwig M, Reimann H, Klix S, Waiczies S, Seeliger E (2015) How bold is blood oxygenation level-dependent (BOLD) magnetic resonance imaging of the kidney? Opportunities, challenges and future directions. Acta Physiol (Oxf) 213(1):19–38
34. Grenier N, Merville P, Combe C (2016) Radiologic imaging of the renal parenchyma structure and function. Nat Rev Nephrol 12 (6):348–359
35. Niendorf T, Flemming B, Evans RG, Seeliger E (2016) What do BOLD MR imaging changes in donors' remaining kidneys tell us? Radiology 281(2):653–655
36. Brix S, Cantow K, Flemming B, Pohlmann A, Niendorf T, Seeliger E (2018) Interpretation of functional renal MRI findings: where physiology and imaging sciences need to talk across domains. J Magn Reson Imaging 47 (4):1140–1141. https://doi.org/10.1002/jmri.25829
37. Evans RG, Leong CL, Anderson WP, O'Connor PM (2007) Don't be so BOLD: potential limitations in the use of BOLD MRI for studies of renal oxygenation. Kidney Int 71 (12):1327–1328
38. Cantow K, Arakelyan K, Seeliger E, Niendorf T, Pohlmann A (2016) Assessment of renal hemodynamics and oxygenation by simultaneous magnetic resonance imaging (MRI) and quantitative invasive physiological measurements. Methods Mol Biol 1397:129–154. https://doi.org/10.1007/978-1-4939-3353-2_11
39. Pohlmann A, Arakelyan K, Hentschel J, Cantow K, Flemming B, Ladwig M, Waiczies S, Seeliger E, Niendorf T (2014) Detailing the relation between renal T2* and renal tissue pO2 using an integrated approach of parametric magnetic resonance imaging and invasive physiological measurements. Investig Radiol 49(8):547–560

Chapter 20

Essential Practical Steps for MRI of the Kidney in Experimental Research

Andreas Pohlmann, João S. Periquito, and Thoralf Niendorf

Abstract

Magnetic resonance imaging (MRI) is an emerging method to obtain valuable functional and structural information about the kidney noninvasively. Before performing specialized MR measurements for probing tissue structure and function, some essential practical steps are needed, which are common for most applications. Here we describe in a step-by-step manner how to (1) achieve the double-oblique slice orientation coronal-to-the-kidney, (2) adapt the scan protocol for avoiding aortic flow artifacts and covering both kidneys, (3) perform localized shimming on the kidney, and (4) check perfusion in the large renal blood vessels using time-of-flight (TOF) angiography. The procedures are tailored to preclinical MRI but conceptionally are also applicable to human MRI.

This chapter is based upon work from the COST Action PARENCHIMA, a community-driven network funded by the European Cooperation in Science and Technology (COST) program of the European Union, which aims to improve the reproducibility and standardization of renal MRI biomarkers. This experimental protocol chapter explains the initial and essential MRI steps that precede specific functional and structural MR imaging techniques (T_1- and T_2*-mapping, DWI, ASL, etc.), which are described in separate chapters.

Key words Magnetic resonance imaging (MRI), Kidney, Mice, Rats, Shimming, Time-of-flight (TOF) angiography

1 Introduction

Magnetic resonance imaging (MRI) is a state-of-the-art noninvasive method to obtain valuable functional and structural information about the kidney. The wide range of available contrast agent mechanisms and the corresponding MR techniques can enable a comprehensive characterization of the kidney. This includes morphology (e.g., kidney size), tissue microstructure (e.g., diffusion-weighted MRI, T1 mapping, elastography), and function (e.g., arterial spin labeling MRI for perfusion mapping or mapping of T_2* for probing blood oxygenation).

Before carrying out these specialized MR measurements, some essential practical steps are required, which are common for most

Andreas Pohlmann and Thoralf Niendorf (eds.), *Preclinical MRI of the Kidney: Methods and Protocols*, Methods in Molecular Biology, vol. 2216, https://doi.org/10.1007/978-1-0716-0978-1_20,

applications. Here we describe in a step-by-step manner how to (1) achieve the double oblique slice orientation coronal-to-the-kidney, (2) adapt the scan protocol for avoiding aortic flow artifacts and covering both kidneys, (3) perform localized shimming on the kidney, and (4) check perfusion in the large renal blood vessels using time-of-flight (TOF) angiography. The procedures are tailored to preclinical MRI but are also conceptually applicable to human MRI.

This experimental protocol chapter is complemented by separate chapters describing the basic concepts, experimental protocol and data analysis of numerous renal MR techniques, which are part of this book.

This chapter is part of the book Pohlmann A, Niendorf T (eds) (2020) Preclinical MRI of the Kidney—Methods and Protocols. Springer, New York.

2 Materials

2.1 Animals

These experimental protocols are tailored for rats (e.g., Wistar, Sprague-Dawley, or Lewis) with a body mass of 250–350 g. Advice for adaptation to mice is given where necessary.

2.2 Lab Equipment

Anesthesia: For nonrecovery experiments urethane solution (Sigma-Aldrich, Steinheim, Germany; 20% in distilled water) can provide anesthesia for several hours with comparatively little side effects on renal physiology, which is an important issue. For an in-depth description and discussion of the anesthesia please refer to the chapter by Kaucsar T et al. "Preparation and Monitoring of Small Animals in Renal MRI."

Monitoring several physiological parameters of the animal is essential to ensure the anesthesia works and while the animal is unconscious and does not feel pain, it is physiologically as close to the normal nonanesthetized state as possible. For an in-depth description of physiological monitoring please refer to the chapter by Kaucsar T et al. "Preparation and Monitoring of Small Animals in Renal MRI."

2.3 MRI Hardware

The general hardware requirements for renal ^{1}H MRI on mice and rats are described in the chapter by Ramos Delgado P et al. "Hardware Considerations for Preclinical Magnetic Resonance of the Kidney." The techniques described in this chapter are tailored for a 9.4 T MR system (Biospec 94/20, Bruker Biospin, Ettlingen, Germany), but advice for adaptation to other field strengths and systems is given where necessary. No special or additional hardware is required, except for the following:

A physiological monitoring system that can track the respiration, and which is connected to the MR system such that it can be used to trigger the image acquisition.

2.4 MRI Techniques

This protocol requires only standard MR techniques that should be available on any commercial system. The shimming capabilities and procedure are specific to the MR hardware and each vendors software platform; in this protocol we focus on describing the shimming on a Bruker BioSpec system running ParaVision 6.0.1.

1. 2D spoiled gradient-echo sequence ("FLASH" on Bruker systems).
2. 2D spoiled gradient-echo sequence with flow compensation and angio-mode (only one slice excitation per TR) ("FcFLASH" on Bruker systems).
3. 2D fast spin echo sequence ("RARE" on Bruker systems).

3 Methods

3.1 MR Protocol Setup

The basic protocols described here are based on default protocols available in Bruker ParaVision, which have been adapted to the geometry of the rat abdomen. Although it is one of the aims of this book to also describe the reasons for the choice of parameters, we have refrained from doing so here because the choice of parameters is not crucial for these protocols. Here we present working protocols for rats on a Bruker 9.4 T system. For MRI at lower field strengths the reduced signal-to-noise ratio (SNR) may be compensated by signal averaging and/or reducing the spatial resolution. For MRI of mice a good starting point is to reduce the FOV used in the rat protocols to the smaller body size of the mouse while keeping the matrix size the same. In this way the relative resolution (voxels per animal/organ dimensions) is similar. Despite the smaller voxel size the SNR is often not much worse than for the rat protocol, because the smaller size of the mouse RF coil improves the SNR (e.g., mouse heart four-element surface coil vs rat heart four-element surface coil).

3.1.1 Multislice Tripilot Scan (R01_TriPilotmulti)

1. Pulse sequence: 2D spoiled gradient-echo sequence (FLASH).
2. Contrast: TR = 126 ms, TE = 2 ms, flip angle = 90°, averages = 3.
3. Spatial resolution: in plane of (234 × 234) μm^2; three packages of seven slices with 1.0 mm thickness, slice distances of 5.0/4.5/4.0 mm and hence slice gaps of 4.0/3.5/3.0 mm (axial/coronal/sagittal); FOV = (60 × 60) mm^2; matrix size = 256 × 256 derived from a 85 × 128 acquisition matrix.

4. Acceleration: 2.0 in phase encoding and frequency encoding directions by zero-filling, 1.72 in frequency encoding direction by partial-Fourier.
5. Sequence: bandwidth = 89 kHz, trigger = off, fat suppression = off, flip-back = on, dummy scans = 10, motion suppression = on, duration: TA = 49 s.

3.1.2 Axial Multislice Pilot Scan

1. Pulse sequence: 2D fast spin echo sequence (RARE).
2. Contrast: TR = 540 ms, TE = 12 ms, effective TE = 24, flip angle = 90°, averages = 1.
3. Spatial resolution: in plane of (407 × 406) μm^2; eight slices of 1.0 mm thickness, a slice distance of 2.2 mm and hence a slice gap of 1.2 mm; FOV = (70 × 52) mm^2; matrix size = 172 × 128 identical to the 172 × 128 acquisition matrix.
4. Acceleration: RARE factor (echo train length or number of echoes per excitation) = 4.
5. Sequence: bandwidth = 63 kHz, trigger = on (per phase step), fat suppression = on, flip-back = on, dummy scans = 2, duration: TA = 17 s.

3.1.3 Coronal Pilot Scan

1. Pulse sequence: 2D fast spin echo sequence (RARE).
2. Contrast: TR = 540 ms, TE = 12 ms, effective TE = 24, flip angle = 90°, averages = 1.
3. Spatial resolution: in plane of (407 × 406) μm^2; one slice of 1.0 mm thickness; FOV = (70 × 52) mm^2; matrix size = 172 × 128 identical to the 172 × 128 acquisition matrix.
4. Acceleration: RARE factor = 4.
5. Sequence: bandwidth = 63 kHz, trigger = on (per phase step), fat suppression = on, flip-back = on, duration: TA = 17 s.

3.1.4 Abdominal Time-of-Flight (TOF) Angiography

1. Pulse sequence: Flow compensated 2D spoiled gradient-echo sequence (FcFLASH).
2. Contrast: TR = 13 ms, TE = 2.3 ms, flip angle = 80°, averages = 1.
3. Spatial resolution: in plane of (200 × 200) μm^2; nine slices of 1.4 mm thickness, a slice distance of 2.1 mm and hence a slice gap of 0.7 mm; FOV = (51.2 × 51.2) mm^2; matrix size = 256 × 256 derived from a 183 × 172 acquisition matrix.
4. Acceleration: 1.5 in phase encoding direction by zero-filling, 1.4 in frequency encoding direction by partial-Fourier.
5. Sequence: bandwidth = 75 kHz, angio mode = yes, trigger = off, fat suppression = off, duration: TA = 20 s.

3.1.5 Kidney TOF-Angiography

1. Pulse sequence: Flow compensated 2D spoiled gradient-echo sequence (FcFLASH).
2. Contrast: TR = 7 ms, TE = 3 ms, flip angle = 80°, averages = 1.
3. Spatial resolution: in plane of (200 × 208) μm^2; 15 slices of 1.0 mm thickness, a slice distance of 0.5 mm and hence a slice gap of −0.5 mm (overlapping); FOV = (60 × 40) mm^2; matrix size = 300 × 192 derived from a 214 × 128 acquisition matrix.
4. Acceleration: 1.5 in phase encoding direction by zero-filling, 1.4 in frequency encoding direction by partial-Fourier.
5. Sequence: bandwidth = 75 kHz, angio mode = yes, trigger = off, fat suppression = off, duration: TA = 14 s.

3.2 Animal Preparation

Anesthetize the animal and transfer it to scanner. For more information on the choice and use of anesthesia please refer to the chapter by Kaucsar T et al. "Preparation and Monitoring of Small Animals in Renal MRI".

Start the temperature monitoring system, apply some surgical lubricant to the temperature probe and place it in the rectum of the animal.

Attach the respiration sensor (e.g., balloon) to the abdomen of the animal using adhesive tape. Start and setup the respiratory monitoring system. If necessary, adjust the position of the respiration sensor until the amplitude of the respiration trace is sufficiently large for the system to reliably detect the trigger points at the beginning of expiration.

3.3 Pilot Scans and Slice Positioning Coronal to tthe Kidney

3.3.1 Slice Planning: From Pilot Scan to the Coronal-to-the-Kidney Image

Here we describe how to acquire a single image slice in coronal-to-the-kidney orientation, which is the best approach if only one kidney is of interest. If both kidneys are of interest, each kidney may be imaged separately using the steps described below.

However, if the experimental conditions do not allow for imaging each kidney separately, then a compromise must be made. This could be the case if, for instance, the available scan time is limited: slice planning, shimming, and acquiring images twice may take too long. Also, the experimental procedure might demand acquisition of the images for both kidneys simultaneously (multislice scan), for example when monitoring dynamic physiological processes. In these cases shimming should be performed on a voxel enclosing both kidneys and the image slice package orientation should be chosen such that it depicts both kidneys in a view that is as close as possible to coronal-to-the-kidney orientation.

1. Start with acquiring a fast pilot scan to obtain images in the three orthogonal planes *x*, *y*, and *z*: load the *multislice tripilot* protocol and run it with the default slice geometry and the usual automatic adjustments (shimming and adjustments of the

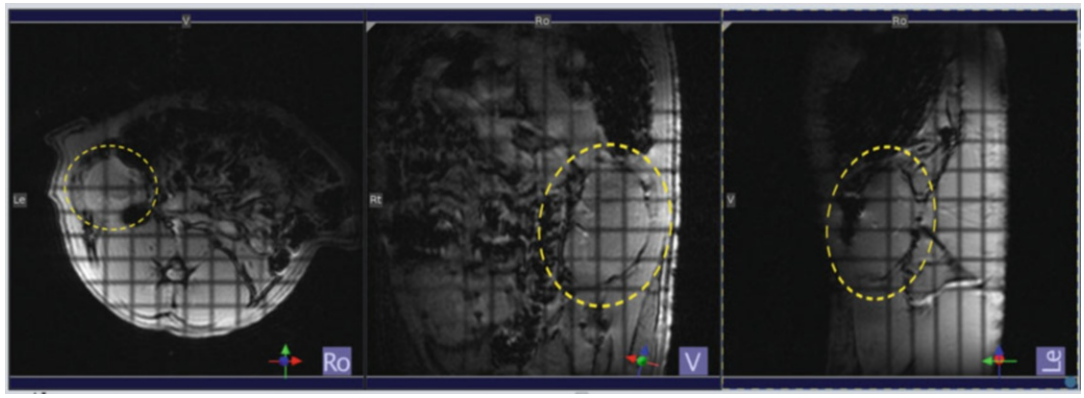

Fig. 1 Slice planning on a small animal MR system (here 9.4 T Bruker Biospec with ParaVision 6. Images obtained from the very first MR scan, a fast *multislice tripilot*: Shown are three selected image slices in strictly axial (left), coronal (center), and sagittal (right) orientation with respect to the scanner coordinates. The location of the left kidney is highlighted by the dashed yellow line. The dark stripes are saturation effects occurring at the intersection of the slices (*see* **Note 1**)

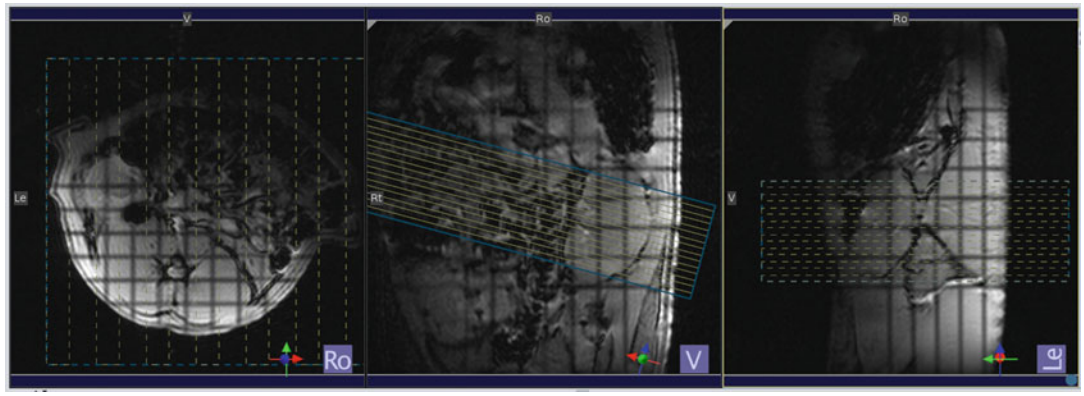

Fig. 2 Images obtained from the fast *multislice tripilot* showing the planning of the *axial multislice pilot scan*: The slice package should be rotated such that it is axial to the kidney in the coronal *multislice tripilot* images (center)

base frequency, the RF pulse reference power, and the receiver gain). Example images are shown in Fig. 1 (*see* **Note 1**).

2. Keep a record of the reference power in the lab notebook for later reference. Comparing the reference power to those used in previous studies with the same setup is very helpful for early identifying possible technical issues in an in-vivo study.
3. Load the *axial multislice pilot scan*, adapt the slice package position and orientation such that it is centered on the kidney and axial to the kidney (not to the animal's body) (Fig. 2).
4. In the monitoring unit set the trigger delay so that the trigger starts at the beginning of the expiratory plateau and the

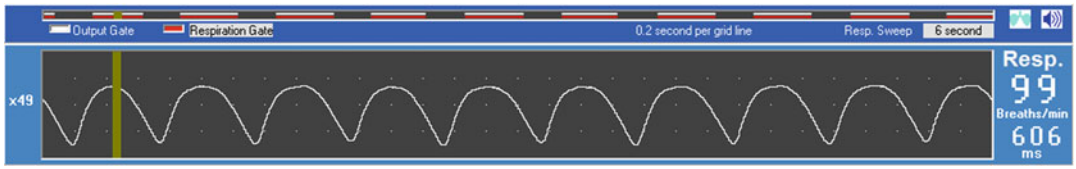

Fig. 3 Setup of the respiratory triggering in the physiological monitoring system. The respiratory gate is defined such that it spans across the expiratory phase and avoids the inspiratory motion. The above trace is for a urethane anesthetized rat. With isoflurane anesthesia the respiratory rate is lower and a long expiratory plateau is typical

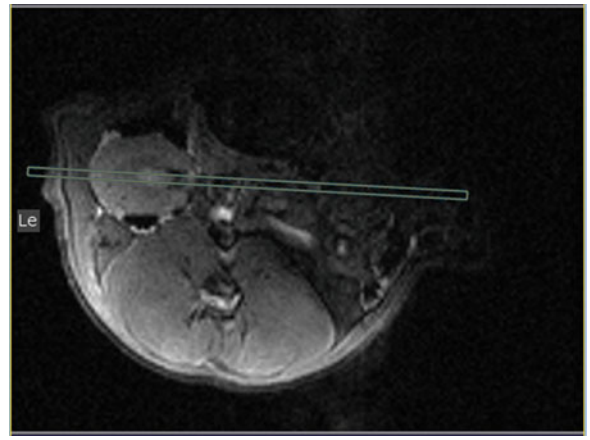

Fig. 4 Image obtained from the fast *axial multislice pilot scan* showing the planning of the *coronal pilot scan*: The slice should be perpendicular to the *axial multislice pilot scan* and rotated such that it runs through the center of the kidney

duration such that it covers the entire expiratory phase (Fig. 3, *see* **Note 2**).

5. If you use a RARE protocol like described here, adjust the TR so that it is longer that the respiratory trigger window but shorter than the current respiration period. For the example shown in Fig. 3, TR should be set to a value within the range 400–570 ms, in order to lie safely between 370 ms (respiratory trigger window) and 606 ms (respiration period). Run the scan. An example image slice is shown in Fig. 4.
6. Load the *coronal pilot scan* protocol and adjust the geometry: the slice should be perpendicular to the *axial multislice pilot scan* and rotated such that it runs through the center of the kidney (Fig. 4). The frequency encoding direction should be rostral–caudal in order to avoid aliasing. Run the scan. An example image is shown in Fig. 5.

Fig. 5 Image obtained from the *coronal pilot scan* showing the planning of the *sagittal pilot scan*: The slice should be perpendicular to the *coronal pilot scan* and rotated such that it runs along the long axis of the kidney

7. To acquire a *sagittal pilot scan*, duplicate the previous scan protocol and adapt the slice orientation: The slice should be perpendicular to the *coronal pilot scan* and rotated such that it runs along the long axis of the kidney (Fig. 5). Run the scan. An example image is shown in Fig. 6.
8. For the *coronal-to-the-kidney scan*, duplicate the *coronal pilot scan* protocol and fine-adjust the slice orientation: The slice should be rotated such that it runs along the long axis of the kidney in the *sagittal pilot scan* (Fig. 6). Run the scan. An example of the final image acquired in double-oblique *coronal-to-the-kidney* orientation is shown in Fig. 7.

3.3.2 Transferring the Coronal-to-the-Kidney Geometry to Other Scans

1. Start from the pilot scan with coronal-to-the-kidney geometry (Fig. 7).
2. From this protocol copy the slice orientation (*see* **Note 3**) to the first of your special scans (e.g., DWI, T_2*-mapping). Pay attention not to copy the entire slice package geometry, because this typically would include the FOV, slice thickness, and number of slices, which are usually different between the pilot scans and functional scans.
3. To illustrate how a typical result should look like, Fig. 8 shows an example of a coronal-to-the-kidney T_2-weighted image from a multispin echo scan.

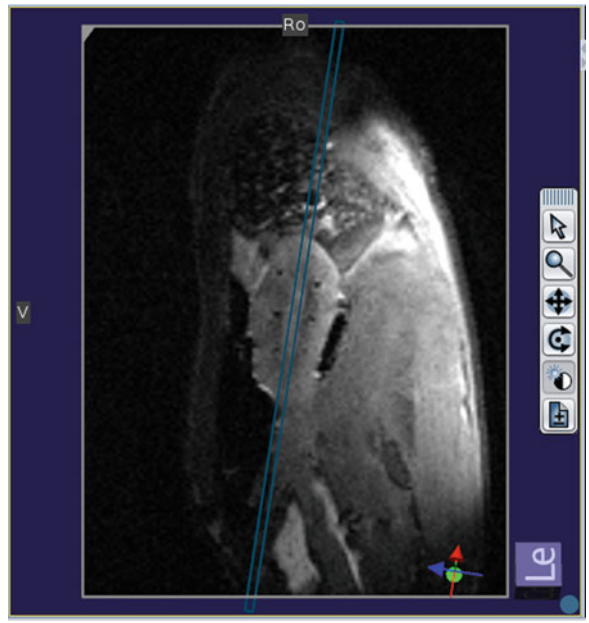

Fig. 6 Image obtained from the *sagittal pilot scan* showing the planning of the *coronal-to-the-kidney scan*: The slice should be rotated such that it runs along the long axis of the kidney

Fig. 7 Final image acquired in double-oblique *coronal-to-the-kidney* orientation (The black tubular structures caudal to the kidney are implanted probes that are not relevant in this context)

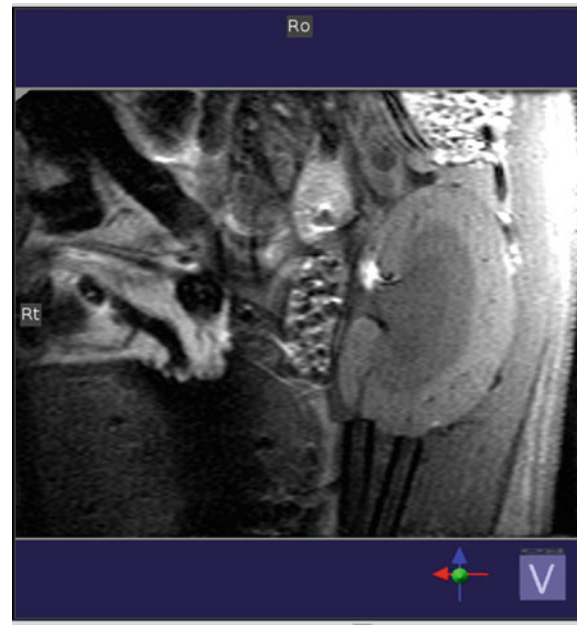

Fig. 8 T_2-weighted image acquired in double-oblique *coronal-to-the-kidney* orientation

3.3.3 Reducing Aortic Flow Artifacts (Optional)

The coronal-to-the-kidney slice orientation will naturally vary from animal to animal and of course between the right and left kidney. Sometimes the aorta lies within the image slice, which can result in unwanted flow artifacts. These artifacts can be reduced using a saturation slice, where a block of repeated excitation and spoiling is applied just before the imaging block in order to suppress the signal:

1. In the protocol setup look for the field-of-view saturation option (e.g., "FOV sat") and enable it. This will add a saturation slice with default geometry.
2. Load the *abdominal TOF-angiography* scan. Copy the slice orientation (*see* **Note 3**) from the *axial multislice pilot* and run the scan. An example image is shown in Fig. 9.
3. Load the following images to the viewer: the *axial pilot* scan, *coronal-to-the-kidney* scan, and the *abdominal TOF-angiography* scan (Fig. 9).
4. In the image viewer enable the display of saturation slices (gray in Fig. 9).
5. Adjust the saturation slice thickness and orientation: place it in approximately sagittal orientation and rotate it such that it covers the aorta without intersecting the kidney(!).

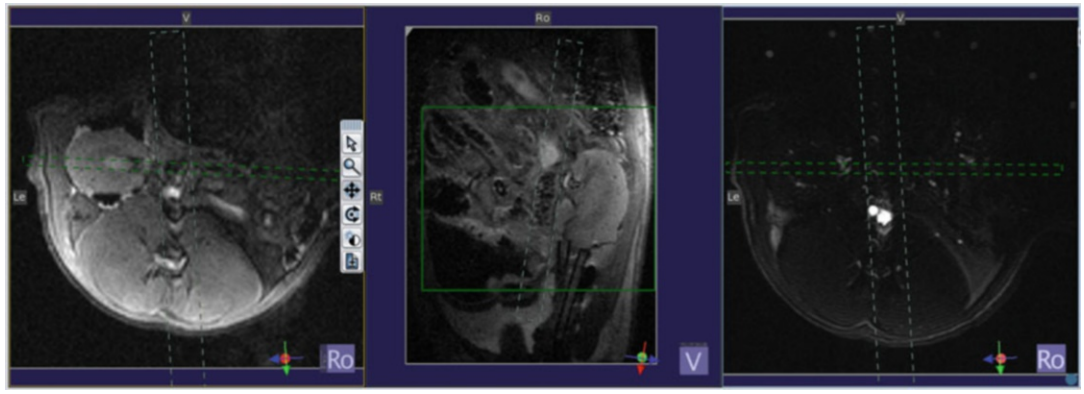

Fig. 9 Images obtained from the *axial pilot* scan (left), *coronal-to-the-kidney* scan (center), and an *abdominal TOF-angiography* scan (right) showing the planning of an optional *FOV saturation slice* (gray dashed lines). The saturation slice has the purpose of reducing possible flow artifacts from the aorta, and hence should be placed in approximately sagittal orientation and rotated such that it covers the aorta without intersecting the kidney. Please note that in this example the aorta was not within the kidney image slice, but, nevertheless, placing a saturation slice was performed as part of our standard operating procedure (SOP)

3.3.4 Multislice and Covering Both Kidneys (Optional)

1. To set up a multislice protocol, simply follow the steps for a single slice and subsequently change the number of slices to the desired number. This should be an odd number (3,5,7, . . .), so that the original single slice remains in the center.
2. For acquiring coronal-to-the-kidney images from both kidneys with the same scan protocol add a second slice package. This allows you to acquire two slice packages with arbitrary orientation, one coronal to the left kidney and one coronal to the right kidney.
3. First plan the geometry of the slice package for one kidney and afterward repeat the same steps for the other kidney.
4. Pay attention to where the two slice packages intersect. In the rare case when the slices of the right and left kidney cross within the kidney, adjust the slice orientation slightly to move the intersection to outside of the kidney. This is important, because otherwise the saturation effect would lead to a dark stripe artifact in the kidney. Alternatively, split the protocol into two, one for each kidney. This will permit acquiring images in the desired orientations without artifacts; however, it also doubles the scan time.

3.4 Localized Shimming

Shimming is particularly important for T_2*-mapping, since macroscopic magnetic field inhomogeneities shorten T_2*, but provide no tissue specific information—rather they overshadow the microscopic T_2* effects of interest and hinder quantitative intra- and intersubject comparisons. But a good shim is also relevant for other imaging techniques, such diffusion weighted imaging

(DWI) or perfusion measurements with arterial-spin-labeling (ASL), because they are commonly based on an echo-planar-imaging (EPI) sequence due to its fast imaging speed. EPI is prone to magnetic susceptibility artifacts, which increase with the number of echoes acquired after each excitation. Hence, this can particularly become a problem when the number of segments is small or one in the case of single-shot acquisition. These artifacts appear as T_2* induced signal loss (or even signal voids) in areas with very high B_0 gradients, image distortion due to the inherently low phase encoding bandwidth, and off-resonance effects caused by frequency dispersions. Therefore, EPI is in kidney regions adjacent to bowels or in close proximity to skin/fat/muscle boundaries is particularly challenging. To this end, it is often beneficial not to use the default standard shim (usually on the entire field-of-view), but to perform additional shimming tailored to the kidney.

Ideally, shimming is performed on a voxel enclosing only the kidney of interest. When a good shim is crucial, the shim volume may be reduced even further to a volume that is smaller than the kidney and just a little thicker than the slice package (*see* **Note 4**). This is the procedure we describe in the following.

However, if both kidneys are of interest and the available scan time or experimental procedure does not allow for imaging each kidney separately, then shimming should be performed instead on a voxel enclosing both kidneys.

Field map-based shimming has become the standard shimming method on preclinical and clinical MR systems. It consists of (1) the manual definition of a shim volume, (2) the acquisition of a 3D B_0 field map (usually with a dual-echo gradient-echo method), and (3) the calculation of the shim currents needed to make the B_0 field within the shim volume as homogeneous as possible. This is the approach we recommend and describe in the following step-by-step instructions. Yet, in our experience, simple iterative linear (first-order) shimming on the selected volume is usually sufficient.

The main limiting factor for achieving a good shim is the capability of the shim coil set. For first-order (linear) shimming no additional shim coils are needed, since the standard *x/y/z* gradient coils used for imaging can double as shim coils. Higher-order shimming (nonlinear spatial harmonics) requires additional coils, typically one for each spatial harmonic (newer designs are more efficient), that is, a minimum of five separate coils are employed for second-order field correction. Therefore, it is usually impossible to correct complex and small B_0 inhomogeneities caused by for example by bowel gas, invasive measurement probes, or trapped air bubbles (from surgery). Considering the very small size of a rat and mouse kidney, in practice the shimming cannot compensate much more than a linear B_0 gradient within the rodent kidney.

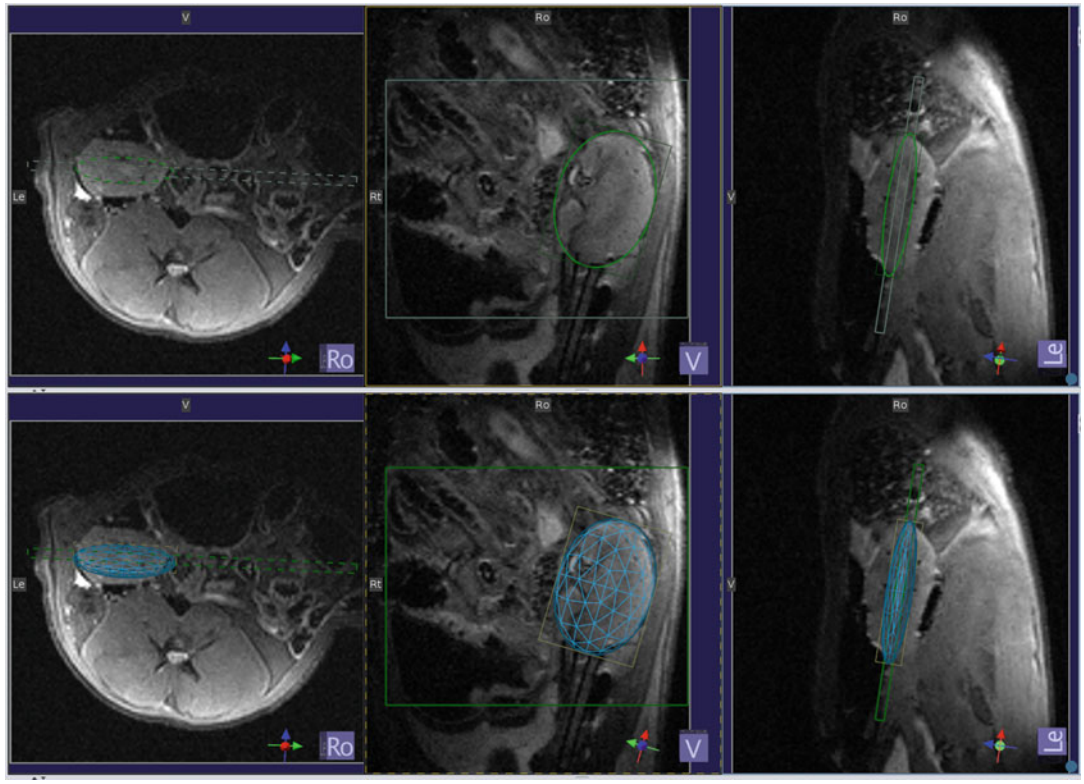

Fig. 10 Shimming on a rat kidney on a small animal MR system (here 9.4 T Bruker Biospec with ParaVision 6). Images obtained from the *axial pilot* scan (left), *coronal-to-the-kidney* scan (center), and an *sagittal pilot* scan (right) showing the planning of the double-oblique *shim volume*. The shim volume tightly encloses the kidney in "coronal" view and is about twice as thick as the imaging slice. Top panel: green outline of the ellipsoid shim volume. Bottom panel: ellipsoid shim volume shown as blue 2D grid

3.4.1 Planning the Shim Volume (Bruker ParaVision)

1. Load into the viewer the images obtained from the *axial pilot* scan, *coronal-to-the-kidney* scan, and *sagittal pilot* scan, as shown in Fig. 10.
2. Open the scan protocol for which the shimming should be performed and go to the *Adjustment* section of the protocol.
3. In the *Adjustment* > *Automatic Shim* tab select *Mapshim*.
4. In the *Adjustment* > *Automatic Shim* tab select *Default Shim Volume*, then deselect it again. You now have a shim volume geometry that is identical to the slice geometry.
5. In the *Adjustment* > *Automatic Shim* tab select a cuboid or better the *ellipsoid* volume, which fits very well to the shape of the kidney.
6. Adjust the geometry of the double-oblique shim volume, such that the volume tightly encloses the kidney in the "coronal" view and that it is about twice as thick as the image slice

package. Figure 10 shows the ellipsoid shim volume with a thickness of 4 mm for one image slice of 1.5 mm).

3.4.2 Shimming (Bruker ParaVision)

1. Finish all other changes you may want to make to the scan protocol.
2. In the *Adjustment Platform* select the *B0 map* and in the protocol parameters enable the respiratory triggering. It is usually OK to use the default FOV, but check that all the visible part of the animal lies within in (*see* **Note 5**).
3. Start the acquisition of the B_0 map, this usually takes a couple of minutes. When the acquisition has finished, exit the *Adjustment Platform* and return to the scan protocol.
4. In the *Adjustment* > *Automatic Shim* tab select *Mapshim* (you probably did that already during the shim volume planning).
5. In the *Adjustment* > *Automatic Shim* tab enable *Iterative Correction* of the first order shims.
6. It should be displayed that a B_0 map is available (if it does not, go back to acquiring the B_0 map).
7. *Apply* the changes to the protocol and run the scan—shimming will be performed as the first step of the data acquisition, followed by a frequency adjustment (necessary after shimming).
8. For repeating the same scan later in the experiment, copy this protocol and make sure to change the selection of *Mapshim* to *Current Shim* in the *Adjustment* > *Automatic Shim* tab.
9. To use the new shim for subsequent measurements, select *Current Shim* in the *Adjustment* > *Automatic Shim* tab of each of these protocols.

3.4.3 Shimming on a Clinical MR System (Siemens Syngo)

1. Load into the viewer localizer images acquired in the *coronal-to-the-kidney* orientation, and the *sagittal-to-the-kidney* orientation.
2. Open the scan protocol for which the shimming should be performed.
3. Click on the icon for the *Position Toolbar* to open it.
4. In the *Position Toolbar* click on the *Adjust Volume on/off* button. The default shim volume geometry that is identical to the slice geometry is now displayed as a green frame (Fig. 11).
5. Adjust the geometry of the shim volume, such that the volume encloses the kidney in the "coronal" view and that it is about twice as thick as the image slice package. Figure 11 shows the cuboid shim volume with a thickness of 4 mm.

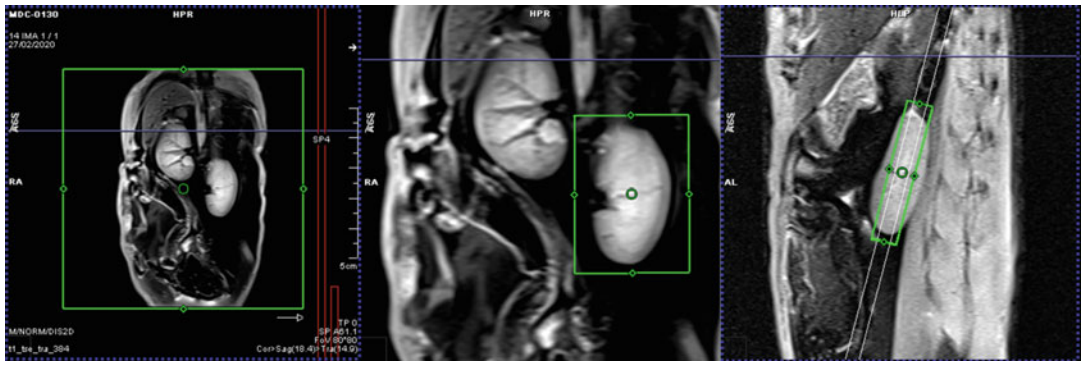

Fig. 11 Shimming on a rat kidney on a clinical MR system (here 3 T Siemens Skyra with Syngo). After clicking on the *Adjust Volume on/off* button in the *Position Toolbar* the default shim volume geometry is displayed as a green frame (left). Then the geometry of the shim volume was adjusted, such that it encloses the kidney in the coronal-to-the-kidney view (center) and that it is about twice as thick as the image slice, as can be seen in the *sagittal-to-the-kidney* scan (right). Here the size of the shim volume was (20 × 16 × 4) mm^3

6. In the scan protocol parameter setup click on the *System* tab and then the *Adjustments* tab. Select as the *B0 Shim Mode* = *Standard* or *Abdominal*.
7. *Apply* the changes to the protocol and start the scan—B_0 mapping (if not already done) and shimming will be performed as the first step of the data acquisition, followed by a frequency adjustment (necessary after shimming).

3.5 Fast and Simple Test of Renal Blood Flow (Optional)

Time-of-flight (TOF) angiography is a simple technique to check the perfusion in the large renal blood vessels. Acquiring a TOF angiogram only requires a few seconds and it can provide very valuable information in experiments that involve major changes in renal blood flow, such as short-time reversible occlusions of the renal artery, renal vein, or aorta as well as ischemia–reperfusion. One can confirm that the vessel occlusion and reperfusion are successful, or otherwise repeat the procedure. TOF angiography is also essential in MRI experiments that include implanted invasive probes (e.g., fiber-optical pO_2 probes, ultrasound flow probes, near-infrared probes) or devices for physiological interventions, such as inflatable balloons that serve as remotely controllable blood-vessel occluders. The reason is that these devices are relatively large and if they are placed in proximity to a blood vessel they may apply too much pressure on it, hindering or even stopping the blood flow within it. TOF angiography can help to detect such hypoperfusion early in the experiment, when a surgical correction may still be possible.

3.5.1 Measurement Concept

For correct interpretation of the TOF angiogram it is important to understand the measurement concept. The measurement uses a conventional gradient echo (GRE) pulse sequence with a high flip angle (FA) and very short repetition time (TR). After a few

excitations this results in saturation, that is, a suppression of the signal (from stationary protons), because there is too little time for T_1 recovery from the previous excitation leading to almost no signal being available for the next excitation. However, the fast-moving spins of blood flowing in large vessels that cross the image slice are not stationary—under normal blood flow conditions the blood present in the image slice during one excitation has been entirely replaced with new blood (from outside of the slice) before the next excitation. That means that the water protons of the blood are still fully "relaxed" when the excitation RF pulse is applied—these spins have never seen an RF pulse before and hence give maximum signal. The signal of the blood is not suppressed, because the effective TR is infinitely long—unlike for stationary protons in tissue to which the very short nominal TR applies.

The TOF contrast is not a quantitative measure. While in theory there is a window of flow velocities that will create intermediate blood signal intensities (between maximum signal from fresh blood to almost no signal from stationary blood), in practice the TOF contrast has an approximately binary character: you see signal or you do not. What flow velocity is needed to see the maximum blood signal can be roughly estimated from the distance that blood needs to flow (i.e., the image slice/slab thickness) and the available time (i.e., TR). However, the vessel orientation and flow profile in the vessel also play a role, so one cannot draw conclusions about the actual blood flow velocity; it rather serves as a simple tool for qualitative comparison of blood flow between (patho)physiological states.

3.5.2 Protocol

Here we describe how to perform a TOF angiography to check for (ab)normal perfusion in the large renal blood vessels.

Please note that this protocol is not designed for creating a 3D depiction of the renal vascular architecture via maximum-intensity projections (MPIs)—this would require whole kidney coverage, a higher spatial resolution, and hence a longer acquisition time.

1. In the viewer open the images obtained from the *axial pilot* scan, *coronal-to-the-kidney* scan, and the *sagittal pilot* scan (Fig. 12).
2. Load the *kidney TOF-angiography* protocol.
3. If you have acquired a *sagittal pilot scan* at the beginning of the experiment, then copy the slice orientation from that scan (*see* **Note 3**). Otherwise start with a default sagittal slice orientation.
4. Plan the slice geometry sagittal with regard to the kidney, as shown in Fig. 12.
5. Start the scan. Figure 13 shows an example image in which six major vessels are clearly visible (in Wistar rat kidneys typically 6 or 8 vessels are seen). During temporary occlusions of the

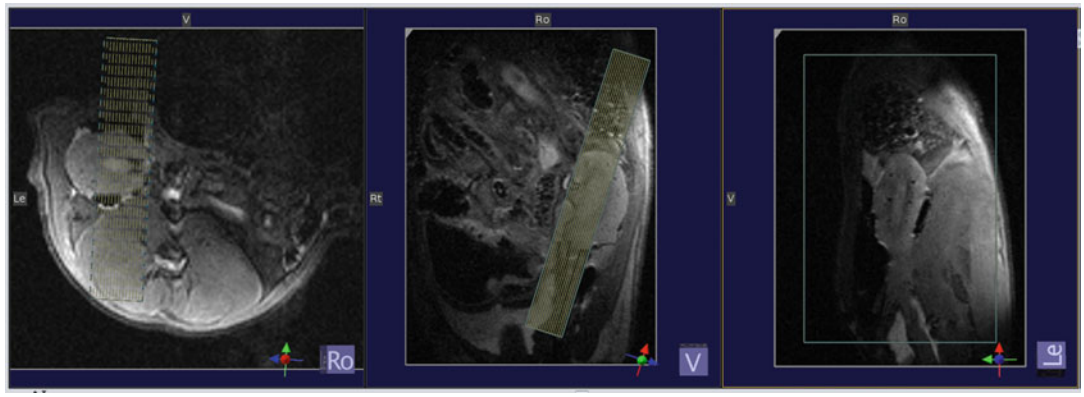

Fig. 12 Basic TOF angiography of a rat kidney on a small animal MR system (here 9.4 T Bruker Biospec with ParaVision 6). Images obtained from the *axial pilot* scan (left), *coronal-to-the-kidney* scan (center), and an *sagittal pilot* scan (right) showing the planning of the *kidney TOF-angiography*. The slice package is positioned sagittal with regard to the kidney

Fig. 13 Selected images slice obtained from the *kidney TOF-angiography*. Six major vessels can be clearly seen. In experiments where a temporary occlusion of the renal artery, vein, or aorta via a remote controlled hydraulic occluder is performed, this scan is very useful to confirm vessel occlusion was successful (vessels are not visible anymore) and reperfusion was successful (vessels are visible again like above)

renal artery, vein, or aorta (via a remote controlled hydraulic occluder) the vessels will disappear and reappear after successful reperfusion.

4 Notes

1. The saturation effect is an inevitable artifact that occurs when several crossing slices are acquired in an interleaved manner, that is, excitation of all slices during one TR. This effect can be avoided be acquiring all slices consecutively, however, that significantly increases the scan time. For the initial scan this artifact is acceptable because it only serves to localize the kidney, so speed is given preference.
2. If you use a RARE protocol like described here, the TR needs to be relatively long to allow for sufficient T_1-recovery and hence acceptable signal-to-noise ratio (SNR). Due to the long TR it is advisable to have only one excitation per breath. To ensure that there will be only one triggered acquisition per breath, adjust the TR so that it is longer than the respiratory trigger window but shorter than the current respiration period. Alternatively, you could adjust the trigger window in the monitoring software to be very short (e.g., 10 ms), but then you will have to reverse this change for every gradient echo scan. You must monitor the respiration continuously throughout the entire experiment and, if necessary, adapt the TR accordingly.
3. With "copying the slice orientation" we mean copying the spatial location of the center of the slice package as well as copying its spatial orientation, that is, the angulation in all three directions x, y, and z (or left–right, anterior–posterior, rostral–caudal). On a system running Bruker ParaVision this is achieved by copying the slice orientation; in contrast, copying the slice geometry includes the FOV, slice thickness, and number of slices.
4. Considering the small size of a rat and mouse kidney and the limited capabilities of shim coils, it is unrealistic to expect that a "perfect" shim on the kidney can be achieved. In practice, one aims to remove a linear B_0 gradient in the kidney. Nonlinear B_0 gradients within the kidney are very challenging to compensate for, because they are only a few millimeters in size. This would require a high-end gradient set with very high-order shims.
5. For rats the default shim volume has a reasonable size, but you must check for your particular setup (RF coil, rat size) that it is large enough so that there will be no aliasing artifacts in the two phase encoding directions. If the default shim volume is much larger than the object (possible for small mice) one can reduce the size of the shim volume. As this will reduce the signal-to-

noise ratio of the B_0 map and hence it may be useful to increase the number of averages. When you modify the shim volume FOV try to maintain the *isotropic* voxel size, as this permits capturing the B_0 inhomogeneities in all spatial directions with equal accuracy.

Acknowledgments

This work was funded in part (Thoralf Niendorf, Andreas Pohlmann, Joao Periquito) by the German Research Foundation (Gefoerdert durch die Deutsche Forschungsgemeinschaft (DFG), Projektnummer 394046635, SFB 1365, RENOPROTECTION. Funded by the Deutsche Forschungsgemeinschaft (DFG, German Research Foundation), Project number 394046635, SFB 1365, RENOPROTECTION).

This chapter is based upon work from COST Action PARENCHIMA, supported by European Cooperation in Science and Technology (COST). COST (www.cost.eu) is a funding agency for research and innovation networks. COST Actions help connect research initiatives across Europe and enable scientists to grow their ideas by sharing them with their peers. This boosts their research, career and innovation.

PARENCHIMA (renalmri.org) is a community-driven Action in the COST program of the European Union, which unites more than 200 experts in renal MRI from 30 countries with the aim to improve the reproducibility and standardization of renal MRI biomarkers.

Chapter 21

Assessment of Renal Volume with MRI: Experimental Protocol

Andreas Müller and Martin Meier

Abstract

Renal length and volume are important parameters in the clinical assessment of patients with diabetes mellitus, kidney transplants, or renal artery stenosis. Kidney size is used in primary diagnostics to differentiate between acute (rather swollen kidneys) and chronic (rather small kidney) pathophysiology. Total kidney volume is also an established biomarker in studies for the treatment of autosomal dominant polycystic kidney disease (ADPKD). There are several factors influencing kidney size, and there is still a debate on the value of the measured kidney size in terms of renal function or cardiovascular risk. The renal volume is most often calculated by measuring the three axes of the kidney, on the assumption that the organ resembles an ellipsoid. By default, the longitudinal and transverse diameters of the kidney are measured. In animal models renal length and volume[1] are also important parameters in the assessment of organ rejection after transplantation and in determination of kidney failure due to renal artery stenosis, recurrent urinary tract infections, or diabetes mellitus. In general total kidney volume (TKV) is a valuable parameter for predicting prognosis and monitoring disease progression in animal models of human diseases like polycystic kidney disease (PKD) or acute kidney injury (AKI) and chronic kidney disease (CKD).

This chapter is based upon work from the COST Action PARENCHIMA, a community-driven network funded by the European Cooperation in Science and Technology (COST) program of the European Union, which aims to improve the reproducibility and standardization of renal MRI biomarkers. This analysis protocol is complemented by two separate chapters describing the basic concept and experimental procedure.

Key words Magnetic resonance imaging (MRI), Kidney, Mice, Rats, T_2, T_1, Volume

1 Introduction

Kidney size is used in primary diagnostics to differentiate between acute (rather swollen kidneys) and chronic (rather small kidney) pathophysiologies. Renal length and volume are important parameters in the clinical assessment of patients with diabetes mellitus, kidney transplants, or renal artery stenosis. Total kidney volume (TKV) is also qualified as a biomarker in studies for treatment of autosomal dominant polycystic kidney disease (ADPKD). According to the nonbinding recommendations of the FDA this

Andreas Pohlmann and Thoralf Niendorf (eds.), *Preclinical MRI of the Kidney: Methods and Protocols*, Methods in Molecular Biology, vol. 2216, https://doi.org/10.1007/978-1-0716-0978-1_21,

biomarker can be used by drug developers for the qualified context of use in submissions of investigational new drug applications, new drug applications, and biologics license applications (www.fda.gov/media/93105/download). There are many factors governing kidney size and volume.

In patients, renal volume is probably one of the most important predictive parameters for the loss of renal function. Therefore, a determination of kidney size is recommended for patients at risk. For example in ADPKD patients <30 years with a combined renal volume >1500 mL and an estimated glomerular filtration rate (eGFR) <90 mL/min are at high risk even with otherwise normal renal function. Such patients will need renal replacement therapy within 20 years. In ADPKD patients renal volume measurements have been studied extensively and provide a method for patient stratification, monitoring of disease progression and therapeutic efficacy [1–3].

Also, therapeutic decisions are frequently based on the size of the kidney, and for example routinely assessed in follow-up of patients with renal stenosis or for assessment of renal transplant candidates [4, 5]. Therefore it is important to employ a measuring method that provides accurate and precise results in vivo.

In animal models renal length and volume are also important parameters in the assessment of organ rejection after transplantation and in determination of kidney failure due to renal artery stenosis, recurrent urinary tract infections, or diabetes mellitus. In general total kidney volume (TKV) is a valuable parameter for predicting prognosis and monitoring disease progression in models of polycystic kidney disease (PKD). Still, so far, no gold standard exists for renal volumetry in vivo.

The renal volume is most often calculated by measuring the three axes of the kidney, on the assumption that the organ resembles an ellipsoid. By default, the longitudinal and transverse diameters of the kidney are measured. The kidney volume is calculated according to the following approximation formula (in humans these kidney volume data correlate well with the body length and age) (*see* Fig. 1):

$$\text{volume} = \text{length} \times \text{width} \times \text{average depth} \times 0.5.$$

Conventional anatomic MRI offers easy access to high quality image data. Kidney volume is reliably reproduced, and measurements can be performed with minimal bias and low inter- and intraoperator variability [6]. In the voxel-count method accurate calculation is facilitated by acquisition of multiple consecutive images sectioning the kidney. After identification of the organ boundaries, summation of all voxel volumes lying within the organ boundaries provides the total renal volume. While such an approach is highly accurate, it is also time-consuming. Transferring TKV measurement into everyday practice requires imaging techniques and protocols that are widely available while easy to employ

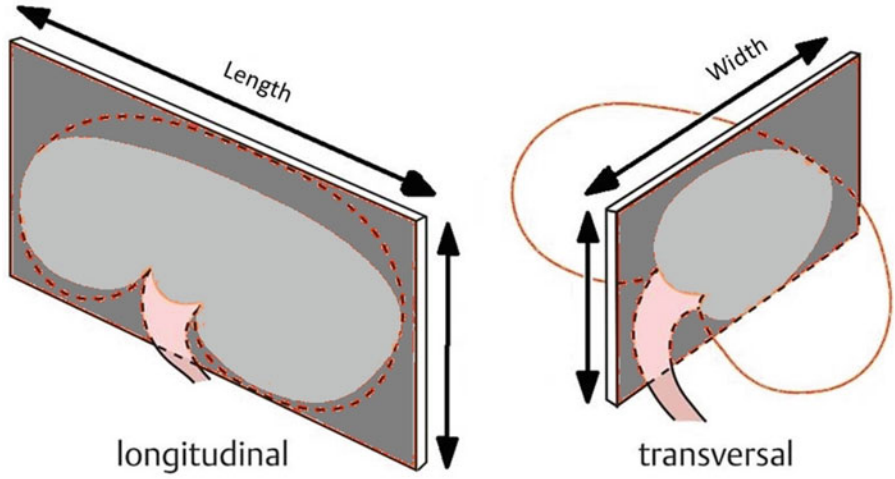

Fig. 1 Depicting standard measurement of length and width for ellipsoidal volume approximation of a kidney

and fast. Furthermore methods for interpretation of results are needed that are feasible and easy to apply. For this purpose open source image analysis tools are available that facilitate fast and easy determination of TKV.

For anatomical MRI of the kidney T_2 weighted MRI sequences are the modality of choice. They provide excellent contrast between different tissues and for the different compartments of the kidney itself. Standard spin-echo T_2 weighted imaging sequences are time-consuming due to the long repetition times TR. However, they still offer best image quality with respect to reproducibility and inter slice variability. Additionally such sequences can be modified easily to perform multiecho imaging, resulting in a set of images with different weighting that even can be used to calculate T_2 maps. In this tutorial we demonstrate the applicability of a 2D T_2 weighted multi echo MRI for accurate determination of kidney volume and compare different standardized TKV measurement techniques using MRI scanners developed for clinical routine imaging or dedicated to (preclinical) small animal imaging.

This chapter is part of the book Pohlmann A, Niendorf T (eds) (2020) Preclinical MRI of the Kidney—Methods and Protocols. Springer, New York.

2 Materials

2.1 Animals

These experimental protocols are tailored for mice (C57BL/6J) with a body mass of 20–30 g. Advice for adaptation to rat (Wistar, Sprague-Dawley or Lewis) is given in Subheading 4 where necessary.

2.2 Lab Equipment

1. Anesthesia: For standard experiments isoflurane inhalation (CP-Pharma, Baxter) provides robust anesthesia for up to 2 h with comparatively little side-effects on renal physiology. For a detailed description and discussion of the anesthesia please refer to the chapter by Kaucsar T et al. "Preparation and Monitoring of Small Animals in Renal MRI."
2. Gases: O_2 or compressed air, as delivering system for evaporated isoflurane. Besides air for use with pulse oximetry systems for monitoring blood oxygenation, O_2 gas is preferred during the experiment on diseased animals.
3. Devices for physiological monitoring ECG, temperature and respiration, to trigger the image acquisition: for example SAI (Model 1030, SAII, Stony Brook, NY, US).

2.3 MRI Hardware

The general hardware requirements for renal ^{1}H MRI on mice and rats are described in the chapter by Ramos Delgado P et al. "Hardware Considerations for Preclinical Magnetic Resonance of the Kidney" (open-access). The technique described in this chapter was tailored for a 9.4 T MR system (Biospec 94/20, Bruker Biospin, Ettlingen, Germany) but advice for adaptation to other field strengths and systems (e.g., 4.7 T Varian and 3 T Siemens Skyra human MR scanner using a wrist RF coil (for signal reception) or knee RF coil (transmit-receive)) is given where necessary.

With preclinical MRI systems volume RF coils covering the entire mouse or rat bodies can be used for signal transmission and reception. However, if needed signal-to-noise ratio (SNR) can be elevated by using dedicated surface receive RF coils (i.e., mouse heart four-element surface RF coil or rat heart four-element surface RF coil) in combination with linear polarized transmit only volume RF coils.

No other special or additional hardware is required.

2.4 MRI Protocols

For anatomical MRI of the kidney T_2-weighted MRI sequences are the modality of choice. Accelerated imaging techniques are available on all MRI systems. On Bruker systems they are identified by acronyms "RARE" or "turboRARE" (for *r*apid *a*cquisition *r*elaxation *e*nhanced). On Philips and Siemens scanners such sequences usually are denoted "FSE" or "TSE" (for *f*ast *s*pin *e*cho or *t*urbo *s*pin *e*cho).

2.5 Image Analysis Tools

MRI data can be analyzed easily by manual planimetry or by calculating TKV from length and width measurements with different standardized equations[2] (the "Traditional Ellipsoid," the "Mayo Ellipsoid," and the "Mid-slice Method"). For this we recommend employing the open source imaging tools ImageJ or IcY:

1. ImageJ (https://imagej.nih.gov/ij/) and the Versatile Wand Tool (https://imagej.nih.gov/ij/plugins/versatile-wand-tool/index.html).
2. IcY (http://icy.bioimageanalysis.org/).

For providing the ex vivo gold standard, kidney volumes can be additionally measured post mortem, using the fluid displacement method.

3 Methods

Renal volumes can be calculated in several ways, using the ellipsoid formula or the voxel-count method. For the ellipsoid formula calculation, the length is determined on the sagittal scans. The width and thickness will be measured at the hilum on the transverse scans. Width can also be measured at the largest transverse diameter. Both volume-hilum and volume-maximum will be calculated. Volume measurements using the ellipsoid formula can easily be done in less than 2 min. In most clinical studies, the ellipsoid method is commonly applied for renal volume assessment. With this method, it is assumed that the kidney resembles an ellipsoid structure. This leads to systematic underestimation of the renal volume. In fact the kidney is not a true ellipsoid structure.

With the voxel-count method, the volumes of all voxels within the boundary of the kidney are summated, thus giving the true total volume of the kidney so that obtaining inaccurate results is highly unlikely. For the voxel-count method, the kidney has to be segmented manually. Segmentations can be done by tracing the boundaries of the kidney on each slice. The total renal volume will then be calculated by summation of all voxel volumes lying within the boundaries of the kidney. Partial volume effects, which occur if voxels contain both kidney and surrounding tissue, could lead to overestimation of the kidney volume, if such voxels are included within the boundaries of the kidney. To avoid such an overestimation, the segmentation line can be drawn halfway along the change in signal intensity between the kidney and surrounding tissues. Semiautomatic segmentation techniques, such as region-growing, can save time. However, such methods are not really practical to use for most available software. Neighboring tissues with very similar signal intensity still have to be separated manually. Fat within the kidneys might perturb the segmentation of the boundaries due to fat-water chemical shift artifacts when using region-growing segmentation technique, leading to an underestimation of the total volume. Semiautomatic segmentation techniques are also challenging to perform on images obtained with accelerated T_2 weighted MRI sequences. While accelerated T_2 weighted imaging yields good results when organ morphology is

considered, signal to noise ratio fluctuations between the individual slices due to spatial changes in the noise amplification intrinsic to parallel imaging techniques cannot be entirely prevented. For this reason, selection of threshold values and propagation has to be done individually for each slice and is a source for investigator bias and experimental error. Newer segmentation techniques, like automatic contour detection, might be an option in future software implementations.

Calculating renal volume from both coronal and sagittal scans can help eliminating differences due to aberrations in slice positioning.

Furthermore there is a simplified Mid-Slice Technique for MRI. In this technique, the renal volume is calculated from the area of a single middle slice image of the kidney multiplied by the number of slices. The kidney volumes correlate well with stereology and have high reproducibility comparable with manual planimetry. However, when calculating single kidney volumes, both the mid-slice technique and the ellipsoid formula are less accurate than stereology and manual or semiautomatic planimetry. Although significantly faster than manual tracing for calculating kidney volume, this technique is slower than the standard ellipsoid method. Volume estimates are based on a multiplier linked to the hypothesis that the shape of the kidney is ellipsoidal.

All these approaches rely on geometrical assumptions, that might not be true.

3.1 MR Protocol Setup

3.1.1 Multislice Multiecho Sequence for T_2 Imaging

1. Load the 2D multislice multiecho sequence (MSME). (preferred *see* **Note 1**)
2. Set the shortest echo time (TE) and echo spacing (ΔTE) possible, under the condition that fat and water are in phase (*see* **Note 2**). The last TE should be close to the largest expected $T_2^{(*)}$ in the kidney multiplied by 1.5 (*see* **Note 3**). The aim is to acquire at least five echo images. Consider increasing the acquisition bandwidth and using half Fourier acceleration to shorten the first TE and ΔTE (*see* **Note 4**).
3. Choose the shortest possible repetition time (TR) for good signal-to-noise per time (SNR/t) efficiency. TR will be limited by the length of the echo train and the number of slices you acquire.
4. Adapt the flip angle (FA) to the TR and T_1 in order to achieve the best possible SNR. Use the Ernst angle $\alpha_E = \arccos(\exp(-TR/T_1))$ as a good starting value. Then try a few smaller and larger FAs and determine the optimal FA experimentally by comparing the measured SNRs.
5. Set a high acquisition bandwidth (BW) to shorten ΔTE, while keeping an eye on the SNR, which decreases with the square

root of BW. Low SNR may be balanced out with averaging (*see* **Note 5**).

6. Enable fat saturation. On ultrahigh field systems this works well to avoid fat signal overlaying the kidney due to chemical shift. At lower field strengths it might work less efficient.
7. Enable the respiration trigger (per phase step or per slice). This is essential to reduce motion artifacts (*see* also **Note 6**), reduce motion blurring and unwanted intensities variations among the images acquired with different TEs.
8. Choose as phase-encoding direction the L-R direction and adapt the geometry so that the FOV in this direction includes the entire animal (approx. 40 mm).
9. Use frequency encoding in head-feet (rostral-caudal) direction to avoid severe aliasing. Adjust the FOV to your needs keeping in mind that in this direction the FOV can be smaller than the animal and a smaller FOV permits a smaller acquisition matrix, and in turn a shorter echo-spacing.
10. Use an appropriate slice thickness, typically around 1.0 mm.
11. Use high in-plane resolution that the SNR allows, typically between 100 and 200 μm. Zero-filling in phase encoding direction can be helpful to speed up acquisition. One may use half Fourier in read direction (asymmetric echo) to further shorten the first TE, if very short T_2* (<5 ms) can occur. Reducing the excitation pulse length to below 1 ms would then also help to shorten TE.
12. A spin echo sequence (MSME) with an echo time of >20 ms is very sensitive for instabilities of your system. If the system is not stable for any reason, this can often be observed directly at the time signal.
13. For examples of specific parameter sets please *see* **Notes 9–13**.

3.2 In Vivo MR Imaging

After obtaining scout images in the *x*, *y*, and *z* planes, T_2-weighted MRI should be performed in sagittal and coronal orientation.

When selecting a certain type of MRI sequence and its parameters, an optimum should be established between spatial resolution, signal-to-noise ratio, and scan duration. Accuracy of the volume measurements can be enhanced by reducing slice thickness and/or choosing an additional section orientation transverse to the major axis of the kidney, mostly in axial orientation.

While theoretically beneficial for discrimination of kidney size differences, measurements in multiple orthogonal planes across the kidney prolong examination times and increase the time required for segmentation, thus hampering both clinical and preclinical practice. This holds also true for application of sophisticated high resolution T_2 weighted 3D imaging techniques instead of standard

(multislice) 2D T_2 weighted MRI covering the entire kidney. Especially in preclinical studies of diseased animals, it is often more appropriate to use solely a single slice orientation 2D MRI approach to gather standardized images in minimum time (i.e., to reduce length of anesthesia). If reduction of imaging time is of particular importance, accelerated imaging techniques are recommended. Such sequences should be available on all MRI systems. On Bruker systems they are identified by acronyms "RARE" or "turboRARE" (for rapid acquisition relaxation enhanced). On Siemens scanners such sequences usually are denoted "FSE" or "TSE" (for fast spin echo or turbo spin echo). In these measurement techniques acceleration is facilitated mainly by recording of multiple lines of k-space, that is, performing multiple phase-encoding steps on the echo train.

3.2.1 Scanner Adjustments and Anatomical Imaging

1. Acquire a fast pilot scan to obtain images in the three orthogonal planes *x*, *y*, and *z*.
2. Acquire anatomical images in several oblique orientations to facilitate planning a coronal slice orientation with regard to the long axis of the kidney, as described in the chapter by Pohlmann A et al. "Essential Practical Steps for MRI of the Kidney in Experimental Research."
3. Perform localized shimming on the kidney as described in the chapter by Pohlmann A et al. "Essential Practical Steps for MRI of the Kidney in Experimental Research."

3.2.2 Morphometric MR Imaging

1. Load the MSME sequence, adapt the slice orientation to provide a coronal or axial view with respect to the kidney (in scanner coordinates this is double-oblique). (caveat *see* **Note 8**)
2. In the monitoring unit set the trigger delay so that the trigger starts at the beginning of the expiratory plateau (no chest or diaphragm motion) and the duration such that it covers the entire expiratory phase, that is, until just before inhalation starts (1/2 to 2/3 of breath-to-breath interval) (*see* **Note 7**).
3. Adapt TR to be a little shorter (about 100 ms) than the average respiration interval that is displayed on the physiological monitoring unit.
4. Run the MSME scan. Example images are shown in Figs. 2, 3, and 4.

A demonstration of the volume changes that can be expected in pathophysiological scenarios is given in Fig. 4.

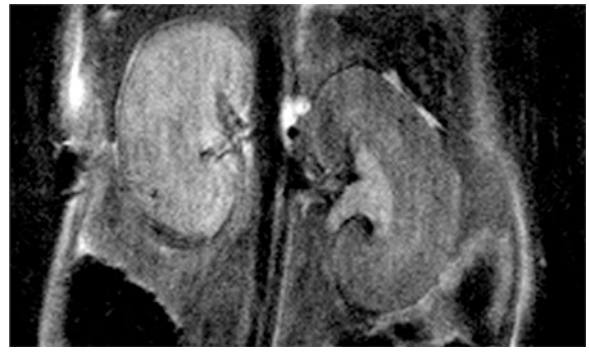

Fig. 2 T_2 weighted image of mouse kidneys in coronal view. For the quantification of kidney volume, respiratory triggered, fat-saturated T2-weighted turbo spin echo (TSE) sequences were acquired in axial and coronal planes, covering both kidneys. The coronal plane was adjusted to the long axis of both kidneys. Scan parameters were: TR/TE = 1500/33 ms, averages = 2, matrix = 256x256, field of view = 35x35 mm2, slice thickness = 1 mm

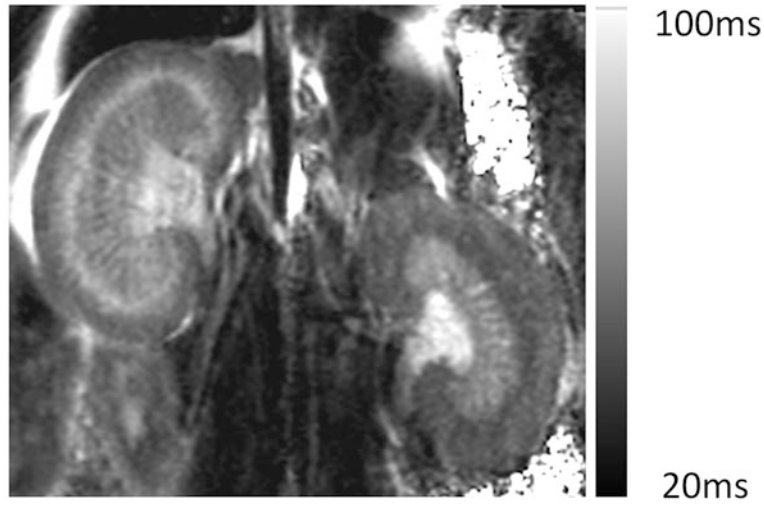

Fig. 3 T_2 map of mouse kidneys with AKI (left). Note the different T_2 values in cortex and medulla between left and right kidney

4 Notes

1. A 3D version of the turboRARE sequence is also available, which allows thinner slices with better SNR, but tends to be too slow for most in vivo applications.
2. The fat signal has a slightly different Larmor frequency (fat-water shift: Δf = 3.5 ppm × Larmor frequency or

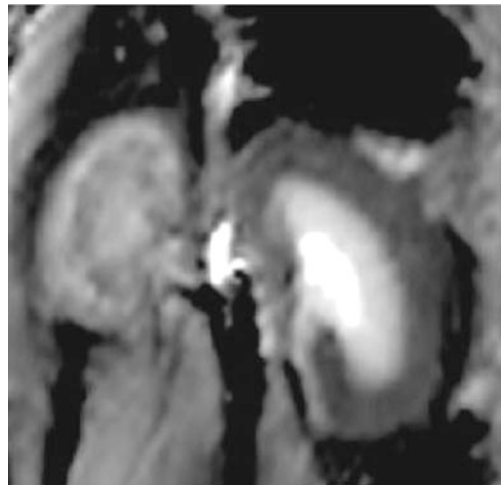

Fig. 4 MSME permits easy detection of size differences in kidneys after acute kidney failure

146 Hz/T, for example: $\Delta f = 220$ Hz at 1.5 T) than the water signal. The faster precession of the fat protons means that with increasing time the fat and water signal fractions within a voxel are sometimes in phase (signals add up) and sometime out of phase (signals subtract). This can lead to an unwanted fat-water shift induced signal intensity modulation along the exponential signal decay curve. This is mostly relevant for diseased kidneys with increased fat content (e.g., diabetes), but we recommend to generally take this into account, that is, also for healthy kidneys. The TEs at which fat and water are in phase depend on the field strength: TE [ms] $= n \times (6.7069/B_0[T])$.

3. When establishing the MR technique you need to define an SNR acceptance threshold for the image with the shortest TE. The aim is to have at least three (better five or more) number of echoes with an SNR > 5. This threshold will depend on the expected $T_2^{(*)}$ values, which in turn depends on parameters like the magnetic field strength, shim quality, and tissue properties (pathology). Example: For a rat imaged at 9.4 T using a four-element rat heart array receive surface RF coil together with a volume RF resonator for excitation in combination with interventions leading to strong hypoxia, an SNR > 60 was needed.
4. For rats increase the FOV to the body width and keep the matrix size the same. The relative resolution is then identical and the SNR should also be similar, because the smaller mouse RF coil provides better SNR.

5. A good starting point is to use the same relative resolution as for rats. For this, reduce the FOV to the mouse body width and keep the matrix size the same.
6. If no specific animal holder is used, it is preferable to position the animals in left or right decubitus position to keep the bowels away from the kidneys to mitigate susceptibility artifacts.
7. You must monitor the respiration continuously throughout the entire experiment and if necessary adapt the TR accordingly.
8. Acquiring more echoes with smaller echo spacing will be beneficial because it improves the fitting when calculating a T_2 map (*see* Fig. 3), but keep in mind the specific absorption rate (SAR) associated with sending many 180° RF pulses in a short time could heat up the tissue. This will usually not be detectable via a rectal temperature probe, but measurements with a temperature probe placed in the abdomen next to the kidney showed that significant temperature increases are possible with a multi-spin echo sequence.
9. Ellipsoid based calculation: Example parameters for a 300 g rat at 9.4 T (Bruker small animal system): TR = [respiration interval] -100 ms; receiver bandwidth = 50 kHz; number of echoes = 12; first echo = 10.0 ms; echo spacing 10.0 ms; TE = 10, 20, 30, 40, 50, 60, 70, 80, 90, 100, 110, 120 ms; averages = 1; slice orientation = coronal to kidney; frequency encoding = head-feet; FOV = (38.2 × 48.5) mm; matrix size = 169 × 115 zero-filled to 169 × 215; resolution = (0.226 × 0.421) mm; 1 slice with 1.4 mm thickness; fat suppression = on; respiration trigger = per slice; acquisition time = 55–75 s (with triggering under urethane anesthesia).
10. *Ellipsoid based calculation: Example parameters for a 30 g mouse at 4.7 T (Agilent small animal system)*: TR = [respiration interval] − 100 ms; receiver bandwidth = 50 kHz; number of echoes = 12; first echo = 10.0 ms; echo spacing 10.0 ms; TE = 10, ..., 120 ms; averages = 1; slice orientation = coronal to kidney; frequency encoding = head-feet; FOV = (30 × 30) mm; matrix size = 128 × 128; resolution = (0.230 × 0.230) mm; 1 slice with 1.0 mm thickness; fat suppression = on; respiration trigger = on; acquisition time = 3.5–9.0 min (with triggering under isoflurane anesthesia).
11. *Ellipsoid based calculation: Example parameters for a 300 g rat at 3.0 T (Siemens Skyra^{fit}, a clinical system)*: Animal position: Right decubitus; Coil: Knee; TR = [respiration interval] − 500 ms; receiver bandwidth = 399 Hz/pixel; number of echoes = 12; first echo = 10.0 ms; echo spacing 10.0 ms; TE = 10, ..., 120 ms; averages = 2; slice orientation = axial;

frequency encoding = left-right; FOV = (120x60) mm; matrix size = 256 × 128; resolution = (0.470 × 0.470) mm; 1 slice with 2.0 mm thickness; fat suppression = on; respiration trigger = off; acquisition time ~ 2 min. If no specific animal holder is used, it is preferable to position the animals in left of right decubitus position to keep the bowels away from the kidneys to mitigate susceptibility artifacts.

12. *Planimetry based calculation: Example parameters for a 300 g rat at 9.4 T (Bruker small animal system)*: TR = 1700 ms; receiver bandwidth = 50 kHz; number of echoes = 12; first echo = 10.0 ms; echo spacing 10.0 ms; TE = 10, 20, 30, 40, 50, 60, 70, 80, 90, 100, 110, 120 ms; averages = 1; slice orientation = coronal to kidney; frequency encoding = head-feet; FOV = (38.2 × 48.5) mm; matrix size = 169 × 115 zero-filled to 169 × 215; resolution = (0.226 × 0.421) mm; 13 slices at 1 mm thickness; fat suppression = on; respiration trigger = per slice; acquisition time = 220–300 s (with triggering under isoflurane anesthesia).

    The following images should be acquired: coronal and transverse T2-weighted fast spin-echo sequence (TSE) and coronal T1-weighted TSE.

    The following images should be acquired: coronal and transverse T2-weighted fast spin-echo sequence (TSE) and coronal T1-weighted TSE.

    The parameters for coronal position TSE can be as follows: slice thickness, 2.0 mm; slice interval, 0.2 mm.

    For T_1 weighted turbo spin-echo (TSE): repetition time (TR), 650 ms; echo time (TE), 10 ms; field of view (FOV), 120 mm × 120 mm; band width, 250 Hz/Px; matrix, 256 × 256; and number of excitations (NEX), 4.0;

    For T_2 weighted TSE you can use: TR, 3460 ms; TE, 35 ms; FOV, 120 mm × 120 mm; band width, 250 Hz/Px; matrix, 256 × 256; and NEX, 4.0.

    The parameters for the transverse position T_2 TSE can be as follows: slice thickness, 2.0 mm; slice interval, 0.2 mm; TR, 650 ms; TE, 10 ms; FOV, 120 mm × 120 mm; band width, 250 Hz/Px; matrix, 256 × 256; and NEX, 4.0.

    Shimming is particularly important, since macroscopic magnetic field inhomogeneities shorten T_2*, but provide no tissue specific information—rather they overshadow the microscopic T_2* effects of interest and hinder quantitative intra- and intersubject comparisons. Shimming should be performed on a voxel enclosing only the kidney using either the default iterative shimming method or based on previously recorded field maps (recommended).

13. If the height adjusted total kidney volume (HtTKV) must be calculated it can be done by measuring the kidneys in three

axes. To calculate HtTKV a structural MRI or at least CT scan is required. The height of the patient is also required for the calculation. The total kidney volume (TKV) is determined using an ellipsoid equation. This is clinically validated for patients with polycystic disease, with bilateral and diffuse small to medium sized cysts. The ellipsoid equation requires only three measurements from both kidneys:

- Kidney length.
- Kidney width.
- Kidney depth.

If you are viewing images on PACs or any DICOM-Viewer it is easiest to calculate the HtTKV with all planes of the kidney visible at the same time. To do this, you mostly have to select "MPR" under the available "View Options" in the specific menu.With this you can view the kidney in the coronal, sagittal, and axial planes. The maximum length of the kidney should be measured in the sagittal plane.

The width and depth can be measured in the axial plane in a slice that shows the greatest kidney width and depth.Repeat this for both kidneys. Once you have all six measurements and the patient's height, you can calculate HtTKV or use one of the available online calculators for kidney volume.

Acknowledgments

This chapter is based upon work from COST Action PARENCHIMA, supported by European Cooperation in Science and Technology (COST). COST (www.cost.eu) is a funding agency for research and innovation networks. COST Actions help connect research initiatives across Europe and enable scientists to enrich their ideas by sharing them with their peers. This boosts their research, career, and innovation.

PARENCHIMA (renalmri.org) is a community-driven Action in the COST program of the European Union, which unites more than 200 experts in renal MRI from 30 countries with the aim to improve the reproducibility and standardization of renal MRI biomarkers.

References

1. King BF, Reed JE, Bergstralh EJ, et al (2000) Quantification and longitudinal trends of kidney, renal cyst, and renal parenchyma volumes in autosomal dominant polycystic kidney disease. 11:1505–1511
2. Sise C, Kusaka M, Wetzel LH et al (2000) Volumetric determination of progression in autosomal dominant polycystic kidney disease by computed tomography. Kidney Int 58:2492–2501
3. Grantham JJ, Torres VE (2016) The importance of total kidney volume in evaluating progression of polycystic kidney disease. Nat Rev Nephrol 12:667–677

4. Hederström E, Forsberg L (1985) Kidney size in children assessed by ultrasonography and urography. Acta Radiol Diagn (Stockh) 26:85–91
5. Ferrer FA, McKenna PH, Bauer MB et al (1997) Accuracy of renal ultrasound measurements for predicting actual kidney size. J Urol 157:2278–2281
6. Sharma K, Caroli A, Quach LV et al (2017) Kidney volume measurement methods for clinical studies on autosomal dominant polycystic kidney disease. PLoS One 12:e0178488

Chapter 22

Experimental Protocols for MRI Mapping of Renal T_1

Philippe Garteiser, Octavia Bane, Sabrina Doblas, Iris Friedli, Stefanie Hectors, Gwenaël Pagé, Bernard E. Van Beers, and John C. Waterton

Abstract

The water proton longitudinal relaxation time, T_1, is a common and useful MR parameter in nephrology research. Here we provide three step-by-step T_1-mapping protocols suitable for different types of nephrology research. Firstly, we provide a single-slice 2D saturation recovery protocol suitable for studies of global pathology, where whole-kidney coverage is unnecessary. Secondly, we provide an inversion recovery type imaging protocol that may be optimized for specific kidney disease applications. Finally, we also provide imaging protocol for small animal kidney imaging in a clinical scanner.

This chapter is based upon work from the COST Action PARENCHIMA, a community-driven network funded by the European Cooperation in Science and Technology (COST) program of the European Union, which aims to improve the reproducibility and standardization of renal MRI biomarkers. This analysis protocol chapter is complemented by two separate chapters describing the basic concept and experimental procedure.

Key words Magnetic resonance imaging (MRI), Kidney, Mice, Rats, Longitudinal relaxation time (T_1), Spin-lattice relaxation time (T_1)

1 Introduction

The water proton longitudinal (or spin-lattice) relaxation time, T_1 (s), is a MR parameter commonly used in biomedical imaging. Unlike machine-dependent metrics such as "signal intensity in T_1-weighted MRI," T_1 measures a real physical process (i.e., the return to Boltzmann equilibrium of water proton longitudinal magnetisation) measured in absolute units (s) and, for any given magnetic field strength, independent of the machine used. Renal pathology often results in abnormal T_1 either globally (e.g., in renal failure) or focally (e.g., in renal cancer). Moreover, disease-induced changes in T_1 can often be assigned, at least qualitatively, to pathological changes such as fibrosis, inflammation, and oedema [1]. A second motivation to measure T_1 is in so-called dynamic experiments. In

Andreas Pohlmann and Thoralf Niendorf (eds.), *Preclinical MRI of the Kidney: Methods and Protocols*, Methods in Molecular Biology, vol. 2216, https://doi.org/10.1007/978-1-0716-0978-1_22,

this case the object under investigation in the MRI scanner for a short period (e.g., 10 min) while T_1 is measured repetitively, during some intervention to perturb T_1 (e.g., contrast agent administration). After administration of a contrast agent such as manganese, a gadolinium chelate, or dioxygen, changes in T_1 are linearly related to the contrast agent concentration, which could not reliably be determined from signal intensity changes alone.

Here we describe MRI protocols for mapping and monitoring T_1 in the kidney of small rodents in a step-by-step experimental protocol. The rationale for choosing different acquisition parameters depending to the aims of the study is discussed, together with specific parameter examples. T_1 measurements for dynamic studies are discussed in the chapter by Irrera P et al. "Dynamic Contrast Enhanced (DCE) MRI-Derived Renal Perfusion and Filtration: Experimental Protocol."

1.1 Motivation for Measuring T_1 in Animal Kidneys

Imaging provides many useful metrics in animal models of kidney physiology and pathophysiology. These include "extensive" or size variables, such as renal volume (ml) or thickness (mm) of renal cortex, and "intensive" or tissue characterisation variables, such as the longitudinal relaxation time, T_1 (s). Some investigators prefer to report the longitudinal relaxation rate R_1, the reciprocal of T_1, because from a metrology perspective R_1 is a "ratio variable" while T_1 is merely an "interval variable" [2]. In this work we use T_1. "Intensive" variables can be mapped, the maps themselves being a type of image. Such image metrics used in animal studies are valuable in translational research, as they are directly comparable with the imaging markers [3–5] used in studies of human subjects.

1.2 Study Design Concepts

Great care is needed in the choice of method to map T_1. No single method is optimal for all in vivo studies. The most accurate methods (e.g., inversion recovery with long TR and short TE readout) are neither fast nor efficient. In vivo studies involve complex tradeoffs between accuracy, speed, spatial resolution, field of view, need for fat suppression, sensitivity to inflow, sensitivity to motion artifact, biexponential T_1 decay, and other confounding tissue magnetisation behaviours such as transverse relaxation and magnetisation transfer. Moreover, even after a specific method is chosen, errors can be very sensitive to pulse sequence parameters such as delays, flip angles, spoiling and refocussing strategies, mis-set RF pulses and so on. For the renal investigator the first question in designing a study to measure T_1 must always be: *what is the aim of the study?*

1. For studies of global pathology, very high spatial and temporal resolution may be unnecessary provided that the cortex, the zones of the medulla, and the papilla can be resolved. In such studies a 2D image with voxel size of around 0.25 mm (in mice, e.g., [6–8]) or around 0.5 mm (in rats, e.g., [9–12]) may be adequate. It is often desirable to acquire T_1 with low

uncertainty so that small early pathological changes can be detected, and also to acquire accurate T_1 values that are reproducible between centers so that findings are generalizable. A saturation recovery sequence with ten or more inversion times, a 2D RARE readout, moderate spatial resolution, and a two- or three-parameter fit, should provide T_1 values which are not biased by B_1^+ errors. Alternately an inversion recovery sequence with a 2D echo-planar readout [6, 8] may be used although this is less time-efficient. The accuracy of the T_1 acquisition and analysis method should be verified using phantoms of known T_1 [2].

2. Studies of focal pathology may require high spatial resolution in 3D appropriate to the disease under investigation. Low uncertainty, high accuracy, and high reproducibility are also likely to be important so that scan times may be relatively long. 3D variable flip angle sequences are convenient, although they are quite vulnerable to B_1^+ errors. In these cases, phantom studies are highly desirable to mitigate B_1^+ errors, although phantom studies do not mitigate the motion artifact error to which these sequences are also highly vulnerable.
3. Longitudinal studies, during the development and/or treatment of disease have similar demands on spatial and temporal resolution, although if the study endpoint is the change in T_1, requirements for accuracy may be relaxed: in a significance test of post vs pre, or treated vs untreated, systematic errors from biased T_1 measurement may partly cancel out.
4. Dynamic studies have similar demands on spatial resolution (e.g., high 3D resolution for focal disease) together with very good temporal resolution to allow dynamic changes to be quantitated. In consequence accuracy may be compromised, but since the study endpoint relies on T_1 change during the dynamic run, bias may partly cancel out. Propagation of errors in these cases can be exceedingly complex and requires careful simulation.

1.3 Data Quality

It is highly desirable to verify the accuracy and repeatability of T_1 using phantoms [2], before experimental animals are exposed to study procedures. The design of MR phantoms can be challenging, and while validated traceable phantoms have been developed by metrologists for clinical MR [13–15], these are usually too large for use in rodent MR scanners. Design considerations should include biological, chemical, and physical stability, temperature independence, convenience, and cost. The phantom should cover both the expected T_1 range and the spatial range, since it may be advantageous to position the kidneys offset relative to the magnet's isocenter [16]. Nickel-doped agarose gels [17–19] are particularly convenient as simple liquid flood phantoms may introduce artifacts from unfamiliar MR phenomena such as radiation damping, convection, excessive T_2 or self-diffusion, standing waves, or abrupt boundaries.

This chapter is part of the book Pohlmann A, Niendorf T (eds) (2020) Preclinical MRI of the Kidney—Methods and Protocols. Springer, New York.

2 General Considerations

2.1 Magnetic Field Strengths

Animal kidney MRI has been performed at a wide range of magnetic field strengths (B_0) between at least 0.4 T [20] and 16.4 T [21]. T_1 increases with B_0 [22]. Hence it is important to consider B_0 as an important factor in experiment design, although in practice B_0 may not be an adjustable parameter since many facilities only have a single MRI machine operated at a single magnetic field strength available. Higher magnetic field strengths are not always preferable, as the scan times required to properly sample the recovery of longitudinal magnetization will be somewhat longer, and problems from motion artifact, chemical shift artifact or susceptibility variation may increase. For an investigator who wishes to use rodent renal T_1 changes to study, say, the development of fibrosis or inflammation, the relevant metric is T_1 contrast-to-noise ratio per unit time, which does not necessarily improve as field strength increases: a high-field ($\geq$9.4 T) magnet may be no better than a conventional 3-7 T magnet. On the other hand, for an investigator who measures the uptake of a relaxive substance such as dioxygen, manganese, or gadolinium chelate, a high-field magnet provides a lower baseline R_1, making the induced changes ΔR_1 more evident.

2.2 Physiologic Motion

Acquisition parameters should ensure that interference from physiologic motion on the signal is kept to a minimum. Indeed, although kidneys are positioned quite low in the abdomen, they are still subject to mild respiratory motion artifacts. It is possible to acquire continuously under shallow breathing, taking advantage of the slow speed of breathing in anesthetized animals [23]. With such datasets, some of this motion can be corrected for during image processing with appropriate coregistration strategies or by intentionally skipping frames presenting a high degree of respiratory motion from the analysis. However, because this strategy potentially removes important datapoints or because it introduces physiological noise into the quantitative estimation, it is still recommended to implement motion compensation strategies at the acquisition level. In particular, respiratory motion compensation takes advantage of a respiratory signal (acquired externally or with MR signals such as navigators) to only allow acquisition during the long periods of breathing motion arrest that are typical of anesthetized animals. An example of such a setup applied to a clinical scanner, is depicted in Fig. 1. Special care is needed to ensure such triggering approaches are compatible with T_1 mapping protocols. In such protocols, sequence timing dictates the effective repetition time, upon which the accuracy of the T_1 computation is

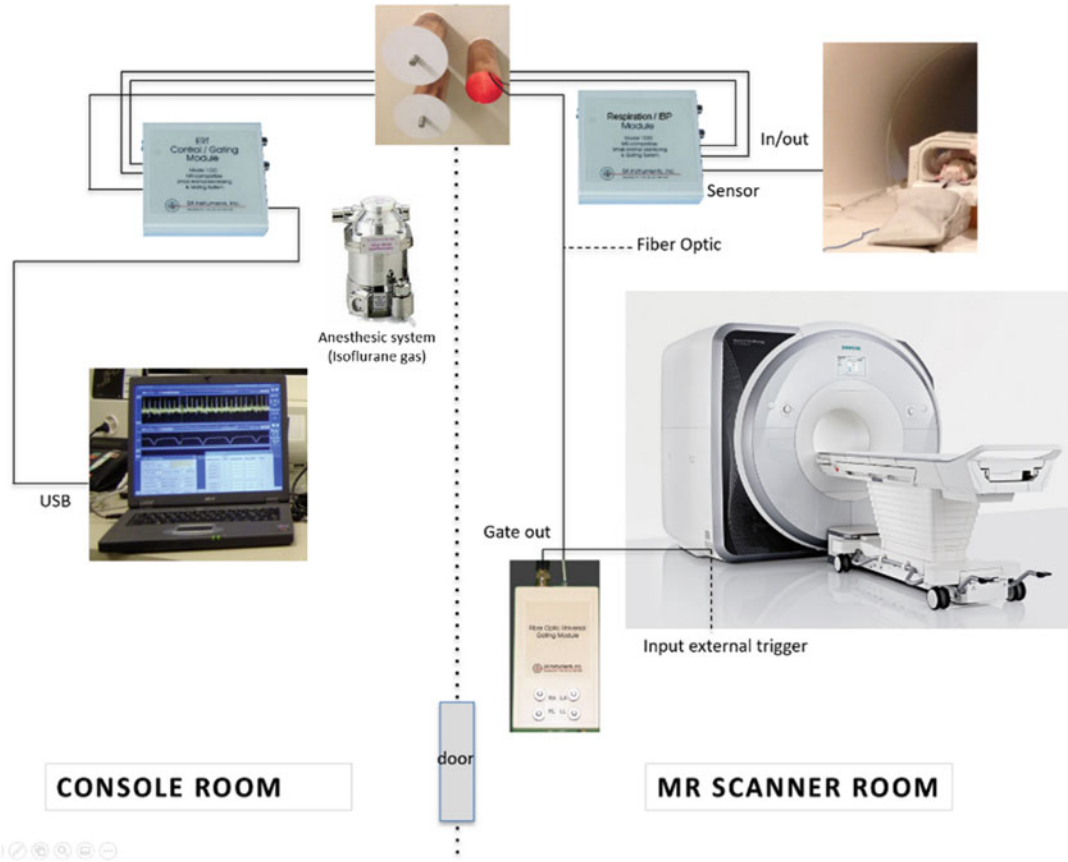

Fig. 1 Scheme of the experimental setup for a respiratory-gated implementation with monitoring small animal system SA Instruments, Inc., Stony Brook, NY11790 USA

based. It is sometimes preferred to position the trigger on the inversion (or saturation) RF pulse rather than on the slice selection or other imaging loops [16] so that the timing of image acquisition relative to inversion is guaranteed. The only timing affected in this strategy is the delay between saturation or inversion slices. In inversion recovery protocols this delay is already very long, (often more than 10 s), so any additional delay incurred will not significantly affect T_1 accuracy, while in saturation recovery the saturation pulse destroys the longitudinal magnetization so that preceding delays are unable to affect T_1 accuracy.

An alternative approach for respiratory motion compensation is retrospective gating or self-gating, which is compatible with gradient echo methods such as Variable Flip Angle (VFA). In this case, data are acquired continuously but an additional "navigator" signal allows data displaced by respiration to be sorted or discarded. This is marketed under the brand-name "IntraGate" (Bruker Biospin, Ettlingen, Germany).

Because kidneys are anatomically close to the bowels, some authors favor imaging sessions done after fasting periods [10]. Fasting should only be done after considering the physiologic

consequences, and from the animal welfare perspective should be of the minimum duration consistent with the imaging aims.

3 Imaging Techniques

Conventionally, for T_1 measurement, signal intensity is probed at different time points during exponential decay back to Boltzmann equilibrium following inversion or saturation of the longitudinal magnetization: inversion recovery or saturation recovery. Saturation can be achieved using a specific saturation pulse, or simply by varying the repetition time TR of a conventional spin echo or gradient echo acquisition which also incidentally saturates the magnetization. To reduce the total acquisition time, the Look Locker (LL) sequence can be used. With LL sequences, the magnetization is also prepared with an inversion or saturation pulse [24], but instead of a single sample of the recovery curve per TR, multiple samples are taken using a train of low flip angle pulses [25].

The inversion recovery sequence is the reference method to calculate T_1 but it suffers from long acquisition times. Therefore, the use of Look-Locker inversion recovery is advantageous, but is limited to single 2D slice acquisition: if multiple slices are needed, they must be acquired sequentially.

The alternative approach involves repeating a gradient echo acquisition at varying flip angles (VFA) while keeping TR and other sequence parameters constant: since the signal depends sinusoidally on flip angle but decays exponentially with T_1, the T_1 can be calculated from the Ernst equation (chapter by Garteiser P et al. "Analysis Protocols for MRI Mapping of Renal T_1"). Three-dimensional acquisition (3D) can be performed with VFA, but since VFA is sensitive to B_1^+ inhomogeneity, the B_1^+ field should be mapped to allow correction (chapter by Garteiser P et al. "Analysis Protocols for MRI Mapping of Renal T_1"). Although 3D VFA is familiar in clinical imaging, it is not commonly employed in rodent kidney studies, and we have not provided a protocol here.

3.1 RARE-VTR

3.1.1 Protocol Description

Rapid acquisition with relaxation enhancement at variable TR (RARE-VTR) is a type of saturation recovery sequence. Data are acquired as 2D slices, so this sequence is ideal when a single slice provides an adequate sample of the kidney, for example in the case of homogeneous global pathology. If volumetric data are required then a stack of slices must be acquired sequentially, which is time-consuming.

The RARE-VTR protocol is based on the multiecho RARE protocol, with a slice-selective 90° rf pulse followed by a train of slice-selective 180° refocusing pulses separated by an inter-echo time TE (Fig. 2). Each 180° pulse induces a refocused echo comprising spin-echo and stimulated echo contributions, which is

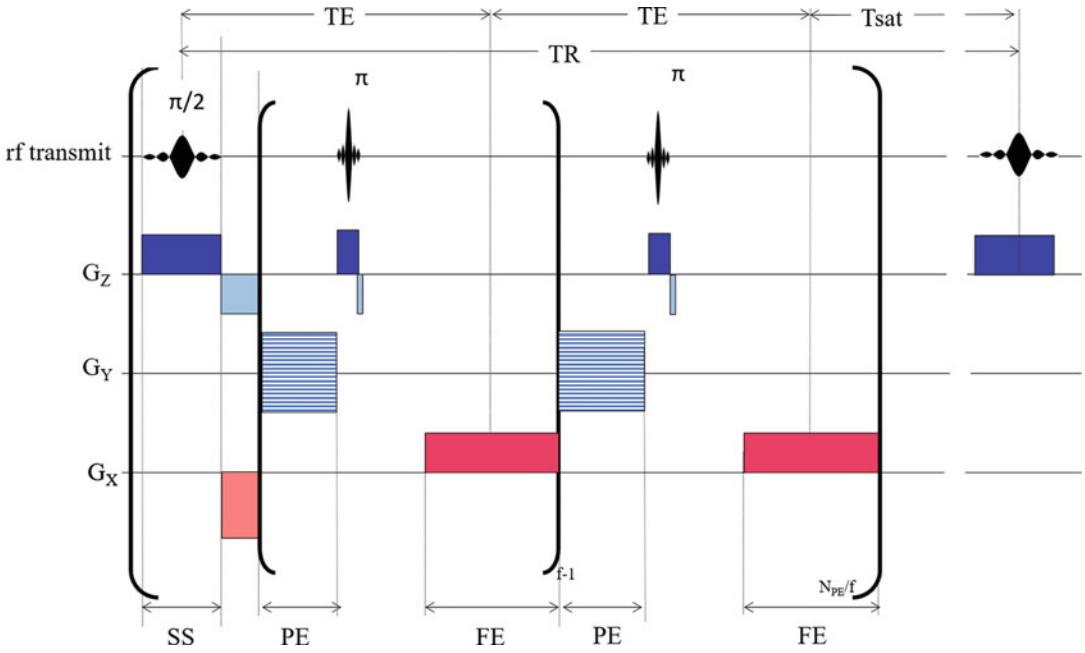

Fig. 2 Simplified timing diagram for 2D saturation recovery sequence with RARE readout. A series of 180° pulses creates *f* echoes at TE, 2 × TE, 3 × TE, and so on, where *f* is the RARE factor, typically $f = 8$. During the phase encoding (PE) step, spatial location is encoded by incrementing the *Y* gradient N_Y times so that each echo is encoded with a different phase, thereby accelerating the k-space coverage. During the frequency encoding (FE) readout periods, the spatial location is encoded in the frequency content of the digitized signal from the echo. If the pulses are perfect and if neglecting the longitudinal regrowth occurring during the echo train, all the magnetization is effectively kept in the transverse plane until the last echo (Phase cycling and spoiling not shown)

digitized, and each echo experiences a different phase encode gradient. Following the last echo there is a delay following which the sequence is repeated with a repetition time TR. The number of 180° pulses is called the echo train length (ETL) or RARE factor: a typical value is 8. TR is then varied to sample the magnetization recovery. A saturation recovery time T_{sat} is defined as TR − (ETL × TE). Thus if an investigator requires a 128^2 matrix, the entire acquisition duration would be $\Sigma TR \times 128/ETL$, where ΣTR is the sum of all the TR values used to sample the longitudinal magnetization recovery. Recommended acquisition parameters are given in section 4 below.

Because of the presence of refocusing RF pulses, this protocol is relatively insensitive to B_0 imperfections and susceptibility artifacts. For 2D single-slice T_1 mapping it is quite time-efficient, but acquisition of a multislice stack requires rather long acquisition times.

3.1.2 *Repetition Times*

The set of repetition times that are sampled needs careful consideration. The TR values should be rationally selected during preliminary studies with the animal model under investigation. In

saturation recovery experiments, the signal starts at $S_0 \sim 0$ at short TRs ($TR \ll T_1$) and increases with approximately linear S_∞/T_1 dependence on TR. At longer TRs ($TR \approx T_1$), the signal enters a transition regime where the increase in signal per unit TR diminishes. Finally at large TRs ($TR \gg T_1$), the signal asymptotically approaches S_∞. Hence, proper TR sampling strategy should be adopted to cover both regimes and the transition in between.

In determining the set of repetition times to use, the first question may be to select the highest TR that is required. This choice is mainly dictated by the expected T_1 in the tissue of interest, the available scan time and the planned postprocessing strategy.

For the first constraint, literature values or preliminary studies may help in the determination of the expected tissue T_1 at the corresponding magnetic field strength. The longest TR should be substantially larger than the longest expected tissue T_1. Typical T_1 values for cortex and medulla are in the range 1–2 s and for urine around 3 s. There is no generally accepted consensus, but authors typically have the maximal TR be 3–5 times the longest expected T_1, typically 8–12 s. If the investigator finds this makes the overall study duration too long then spatial resolution can be reduced, particularly when small focal changes are not of interest. Alternatively a maximal TR of two times the longest expected T_1 could be considered, but in this case it is recommended to perform careful simulations to ensure the propagated errors are at an acceptable level. A special case arises in contrast agent injection studies. Here, the distribution of the agent into the tissue of interest is quantified by looking at the absolute change in R_1 after vs before injection. Hence, care should be taken to consider that the T_1 value may be significantly shorter after injection. It may be necessary to adopt a different maximal TR for the pre- and postinjection scans. Contrast agents decrease T_1, hence the possible decrease in longest TR that is afforded has the additional consequence of shortening the scan duration. This is potentially advantageous, especially when the dynamics of contrast agent distribution needs to be interrogated and is slow (on the order of minutes). In this case it becomes feasible to monitor the contrast agent distribution dynamically by repetitively acquiring T_1 maps. Temporal resolutions of under 2 min can reasonably be achieved by trading off, for example, spatial resolution. This strategy is compatible with some contrast agent dynamics such as in manganese-enhanced MRI [21].

The choice of the longest TR should be done in harmony with the particular postprocessing solution that is planned. Indeed, the dataset obtained with the longest applied TR may be used to provide an estimate for the total equilibrium signal S_∞. In that case, the mathematical problem to be solved is reduced since S_∞ can be inserted in the fitting equation, thereby removing a degree of freedom and making the fit more robust. This comes at the cost

of the necessity to acquire a scan at very long TR to ensure the signal is close enough to equilibrium values. When such an estimate of S_∞ is available, it may no longer be necessary to sample other TRs longer than the tissue T_1, concentrating instead on TR values at and below the tissue T_1 [21].

Once the largest TR to acquire has been selected, the number of TRs should be determined. The set of TR values should span the range of expected T_1. Depending on the fitting equation that is used, a larger number of repetition times may be required to provide sufficient overdetermination for the fitting procedure. In other words, there should be significantly more TRs sampled than there are free parameters in the fitted equation. In an ideal situation with negligible experimental noise, it may be sufficient to select only a number of TR values equal to the number of free parameters in the fit. However, with experimental noise, this rapidly becomes insufficient and introduces bias into the results. Hence, when signal to noise ratio is limited, it is recommended to acquire a larger number of TR values. This comes at the cost of increased scan time, since each TR is generally acquired sequentially. In saturation recovery sequences, the fitting equation only has a limited number of parameters (i.e., S_∞, R_1, and maybe S_0 and/or an error term); hence, as few as four TR values are acceptable providing sufficient signal to noise is available and sampling is appropriately selected.

In disease models the pathology evolves slowly over days or weeks, the scan duration becomes less important, and it is possible to increase the number of TR values to 6, 8, or even 12, although from an ethical perspective the duration of the procedures should always be as short as possible. The choice of TR values can even be done a priori using Cramer-Rao lower-bound methodology. This technique optimizes the distribution of the sampled variable (in that case TR), for a given number of samples, an expected noise distribution and a signal model. It was used already with some success for cardiac T_1 mapping, where it was found that at constant number of acquired averages, increasing the SNR by averaging a carefully selected subset of TR values could prove beneficial relative to a set of uniformly distributed TR values [26]. A similar approach can be proposed to optimize the repetition times to use in kidney T_1 mapping.

In typical MRI scanners, the specific TR values can be set manually with a TR table having a user-specified number of TR entries. Manufacturers also often provide utilities that assist the user in prescribing the TR series. These utilities query from the user only a minimal value, a maximal value and a number of steps, or a minimal value, a number of steps and an estimate of the tissue T_1. These input values are then used to generate the series of TR values to use during the acquisition.

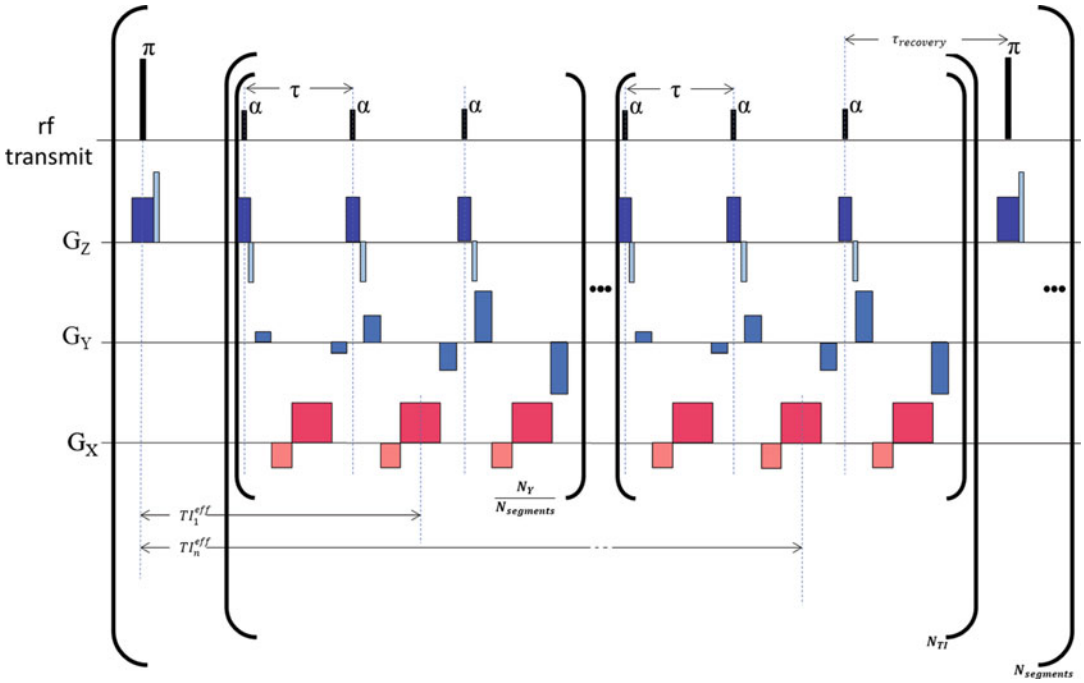

Fig. 3 Schematic view of the look-locker inversion recovery pulse sequence (fast low flip angle spoiled gradient echoes variant with spoiler gradient pulses omitted for simplicity). τ repetition time, N_y prescribed number of k-space lines, $N_{segments}$ number of k space segments (acceleration factor), *TI* inversion recovery time. Effective recovery times are considered at the centerline of each imaging segment. $\tau_{recovery}$: delay added to enable full recovery of the longitudinal magnetization before the subsequent inversion pulse is applied. In other variants, the fast low angle shots can be replaced by steady state free precession modules or EPI modules (Accessory gradient lobes are not shown for clarity)

3.2 Recovery Techniques: Look-Locker and Derivatives

3.2.1 Protocol Description

Look-Locker (LL) is a variant of inversion recovery or saturation recovery sequence. Data are acquired as 2D slices, and if volumetric data are required, a stack of slices must be acquired sequentially. LL involves sampling the magnetization using rapid, small angle imaging readouts while it recovers from the inversion or a saturation RF pulse (Fig. 3). The temporal spacing between imaging readouts provides a rapid way to sample the longitudinal regrowth. Indeed, each imaging shot will occur at a different time during regrowth, hence many different recovery times can be sampled during a single recovery event. Full longitudinal regrowth takes longer after an inversion RF pulse than after a saturation RF pulse, however, adopting an inversion RF pulse increases the dynamic range of the sampled signal. Thus the choice between saturation or inversion for the preparation of magnetization in a recovery sequence may be dictated by the experimental necessity for short acquisition time (for instance in dynamic experiments involving contrast agents with rapid kinetics) or higher measurement precision.

The Modified Look-Locker Inversion Recovery (MOLLI) sequence is an alternative when small animal renal T_1 mapping is

performed using a clinical MR system. One rationale for choosing a clinical platform for preclinical studies is the similarity between MR protocol played out on small animals and human kidneys. MOLLI was initially designed for myocardial T_1 mapping at 1.5 T [27]. A typical MOLLI sequence can be performed by acquiring single shot True FISP images at different inversion times after a single inversion pulse. MOLLI is routinely used clinically for T_1 mapping and is usually available on clinical MR systems equipped with a cardiac package. The original MOLLI sequence provided by the manufacturers' library is a good starting point for MOLLI optimization in the rodent kidney. However, translating the MOLLI technique for scanning rodent models on a clinical MR scanner requires a specific implementation. In human, MOLLI is usually acquired in breath hold. In rodent, a physiological monitoring system to track the respiration and synchronize the sequence is needed (*see* Fig. 1).

3.2.2 Types of Readouts, and Corresponding Specific Points of Attention

In recovery-type sequences, several options are possible for the imaging shots that are performed to sample the recovery period.

Fast low angle shots, where magnetization is spoiled before subsequent RF pulses, can be used. They have the advantage of a short TR (~3 ms) that is compatible with low flip angles (<10°) [9]. As such, they perturb the longitudinal regrowth of the magnetization only to a small extent.

Balanced readouts such as steady-state free precession (SSFP) can also be used, as they tend to yield higher signal to noise due to the conservation of magnetization from preceding shots [28]. The SSFP condition links the TE and TR. Because FISP involves radiofrequency phase coherence between shots, acquisition can be true-FISP, fid mode or echo mode. It acquires innermost the phase encoding (in-segments), then slices, then phase encoding (segments), then (optionally) averaging. SSFP is especially sensitive to careful shimming of the B_0. The segmenting can be performed either sequentially or by interleaving phase encode steps. The interleaved mode is recommended for inversion recovery experiments. The T_1 recovery sampling must then be setup by adjusting the time between the inversion pulse and the first imaging shot. This delay is incompressible due to the need for stabilizing the steady state condition of the magnetization. This is either done with a half flip angle pulse or with a starter (dummy) sequence, at the cost of a longer delay. Unfortunately for these reasons, the implementation of respiratory or cardiac triggering is challenging, and it is recommended to proceed by gating on the saturation or inversion pulse.

Finally, echoplanar imaging (EPI) readouts have also been proposed in that context [6, 7, 16, 29, 30]. Although they are quite advantageous due to their speed (in single shot EPI, a full k-space image may be acquired after a single excitation pulse), EPI sequences for kidney T_1 mapping are vulnerable to problems associated with EPI in general, particularly if both kidneys are to be

assessed. In particular, the EPI train is sensitive to B_0 inhomogeneity, which can become problematic at higher magnetic field strengths and in large bore systems. This effect is more important for long echo train EPIs such as single shot EPI. In this situation there is also a long effective echo time to accommodate the train length required by the single shot mode. This can be detrimental because it can increase the point spread function diameter ("smearing"), thus reducing the effective spatial resolution [30]. The long echo time of single shot EPI also comes at a disadvantage in kidneys with short T_2^* such as kidneys after injection of high concentrations of contrast agents. EPI is also associated with signal dropouts and geometric distortions at regions of strong magnetic susceptibility gradients, which sometimes occur at the kidney edges [30].

These disadvantages can be mitigated by performing segmented EPI acquisitions. In segmented EPI, full k-space acquisition is subdivided over several recovery periods, thereby enabling for decreased echo times. Segmentation will, however, increase the acquisition time, since full k-space coverage will be performed over a greater number of recovery periods. Finally, EPI image quality is also adversely affected by the presence of fat, which may be abundant in some kidney disease models such as obesity-related disease models. This can be remedied by applying fat saturation pulses [7].

3.2.3 Duration of Imaging Readouts

The duration of the imaging readouts should be short relatively to the duration of the recovery. This enables to interrogate precise inversion recovery delays rather than long intervals during which the longitudinal magnetization does vary substantially. Furthermore, short imaging readout durations are also advantageous because more imaging shots can be positioned during longitudinal regrowth. The increased number of data points yields better numerical stability during the subsequent fitting procedure.

3.2.4 Number of Imaging Readouts

The total number of imaging readouts that can be fit in a single regrowth is limited by several factors. First, the imaging sequence (excitation and readout) itself takes an incompressible minimum amount of time. Second, there is a requirement to acquire full images at each of the recovery delays. Hence, if only a single k-space line is acquired at each recovery delay, this also means that to acquire the appropriate number of k-space lines for image reconstruction (e.g., 128), an equal number of saturation or inversion recovery periods will be necessary. Since full relaxation needs to be reached (typically 10 s or more) before the next inversion RF pulse can be applied, this implies very long acquisition times (20 min or more). Hence it is important to consider acceleration schemes such as echoplanar imaging, where partial k-spaces are acquired during the regrowth rather than single k-space lines. Finally, the image acquisition readouts perturb the growing longitudinal

magnetization: the application of the imaging RF pulses slightly saturates the signal, which makes the signal regrow with a biased apparent T_1 (sometimes denoted T_1*) that is different than the true tissue T_1. This effect can be mitigated by using smaller flip angles and longer RF pulse repetition intervals. Postprocessing strategies are also available to correct for that effect (cf. the chapter by Garteiser P et al. "Analysis Protocols for MRI Mapping of Renal T_1").

3.2.5 Repetition Time

In saturation or inversion recovery type sequences, it is important to distinguish the time between RF inversion pulses and the time between imaging RF pulses. The time between saturation or inversion must take into account the T_1 of the kidney at the considered field strength. A sufficiently long recovery period must be taken into account to prevent to saturate the magnetization. Typically inversion pulses are separated by 10 s [16, 28], 18 s [6, 7] or even 20 s [30].

The repetition time between imaging segments represents the precision with which the inversion recovery will be sampled. If a high accuracy is required for the T_1, only short imaging segments with a few to a single k-space line can be adopted. This will ensure that there is only little confounding factor arising from the longitudinal regrowth occurring during each imaging segment. Conversely if a lower T_1 recovery sampling is acceptable, then imaging can be noticeably accelerated by k-space segmenting.

3.2.6 Inversion Pulses

Adiabatic passage pulses can be advantageous to ensure saturation (adiabatic half passage) or inversion (adiabatic full passage). These pulses maintain their rotation properties invariant to the B_1^+ field, provided that the pulse B_1 exceeds an adiabaticity threshold. This is of importance in the field of kidney imaging, where the presence of intraabdominal fat can be challenging for B_1 homogeneity. Hence adiabatic RF pulses such as the hyperbolic secant RF pulse, are often used in T_1-mapping protocols, as half passage for saturation recovery experiments [23, 31] or as full passage for inversion recovery experiments [16, 30]. However, these RF pulses tend to require long duration and RF power levels, which may not be compatible with all RF coils, and unless provided by the manufacturer, their frequency and phase modulation shapes may require careful design.

Generally non selective inversion RF pulses are used. Indeed, slice selective inversion RF pulses are exposed to inflow artifacts. Indeed, when a slice selective RF pulse is applied, the spins entering the imaging slice via perfusion effects, have not been resonantly exposed to the RF pulse. Hence their presence in the imaging slice will contribute to increase on average the magnetization. This effect will be higher if perfusion is elevated, and is in fact the basis for FLAIR sequences. Whenever the true tissue T_1 is the parameter

of interest, perfusion becomes a confounding factor, and inflow artifacts should be minimized. This can be achieved either by selecting an inversion slice that is significantly larger than the imaging slice to minimize the inflow artifact by creating a large region adjacent to the imaging slice that the noninverted spins need to cross before entering the imaged slice. Alternately, a nonselective saturation pulse may be adopted. In this case, even the spins that enter the imaging slice by perfusion during the imaging train are inverted, and hence they will not modify the apparent tissue T_1. Some authors recommend offsetting the position of the kidney within the radiofrequency coil to ensure that the heart is present within the effective region of the coil, to ensure maximally inverted spins throughout the entire body of the animal [16].

Recommended acquisition parameters are given in section 4 below.

3.3 Variable Flip Angle Techniques

Variable flip angle (VFA) sequences vary the flip angle of the rf excitation pulse but keep TR constant. Data can be acquired in 3D volume, so such sequences are ideal when the entire kidney must be sampled, for example in the case of heterogeneous or focal pathology (Fig. 4). However, data acquisition takes longer than for 2D sequences, and they are not robust in the presence of B_1^+ inhomogeneity.

Variable flip angle sequences are usually based on spoiled gradient echo sequences (fast low angle shot) [12, 32, 33], but the same principles can be applied with UTE sequences [34]. By virtue of their 3D nature, they are well suited for analyzing entire kidney volumes. However, the acquisition scheme where a single angle is acquired at a time also limits the number of different flip angle acquisitions that can be achieved within reasonable scanning durations. A linearization of the VFA signal provides T_1 estimates based on as little as two flip angles, although this technique is prone to noise bias. In a study at clinical field strength of 3.0 T using a wrist coil, flip angles of 5° and 26° were proposed for a rat model of acute kidney injury [12]. The use of VFA-based protocols for kidney mapping is not yet widespread at higher magnetic field strengths, but this type of sequence is applicable in other organs [34] or in tumor models [32, 33]. VFA schemes are also prone to B_1^+ field heterogeneity. Indeed, the effectively achieved flip angle at a specific location in the kidney is function of not only pulse amplitude, but also the shape and electromagnetic properties of the animal, the radiofrequency pulse design and (to a lesser extent when volume RF coils are used for RF transmission) RF coil coverage homogeneity. Thus, the B_1 field may require to be mapped first. For instance a reference T_1 map using a recovery-based sequence can be obtained and then injected into the signal equation to extract the effective flip angle [35]. Another acquisition strategy consists of measuring the B_1^+ field directly with dual angle spin echo sequence

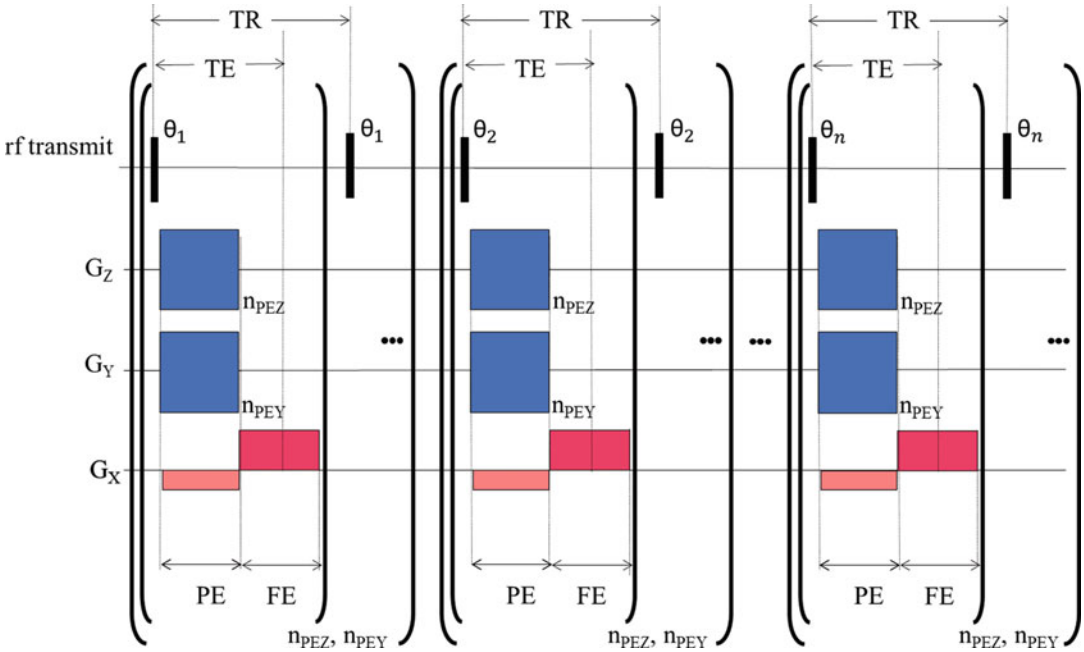

Fig. 4 3D variable flip angle protocol. *TR* repetition time (maintained constant for the duration of the acquisition), *TE* echo time, θ flip angle (flip angle is varied during the protocol), n_{PEY}, n_{PEZ} number of prescribed phase encoding lines in the *Y* and *Z* dimensions, *PE* phase encoding, *FE* frequency encoding. While the TR is maintained and constant during acquisition, the flip angle is varied several times until a complete dataset has been fully acquired for each prescribed flip angle. Accessory gradient lobes are not shown for clarity. Often, investigators need to suppress the signal from fat, in which case the hard pulse would be replaced by a spectrally selective "soft" pulse to excite ^1H_2O but not C^1H_2 or C^1H_3. During the phase-encoding (PE) step, spatial location is encoded by incrementing *X* and *Y* gradients i_X and G_Y multiple times n_{PEX} and n_{PEY}, typically 64 or 128. During this period magnetization is prephased using the *Z* gradient G_Z, so that a gradient echo may be formed by inverting the polarity of the gradient, yielding a return to phase at TE at the mid-point of the gradient echo. TE is set as short as possible, typically ~2–3 ms, in order to avoid T_2^* weighting, and to minimize total acquisition time. Practically, this is limited by the specification and performance of the gradient coils and amplifiers available to the investigator. TR is also set as short as possible, ~5 ms, in order to minimize the overall acquisition time

[36, 37]. Recommended acquisition parameters are given in section 4 below.

4 Methods

4.1 MR Protocol Setup

4.1.1 2D RARE VTR in Bruker ParaVision 6

1. Use the ParaVision RARE T1 saturation-recovery METHOD "T1map_RARE protocol" (Rat/Head/Relaxometry, or Mouse/Head/Relaxometry).
2. Set the geometry to coronal, 58 × 58 mm FOV (rat) or 40 × 30 mm FOC (mouse). These may need adjustment in studies on large (e.g., obese) animals.

3. Set the matrix size to 128 × 128; if acquisition length is too large, you may decrease the phase encoding resolution.
4. Use a single 90° 1.16 mm slice selection (optionally, apply spectrally selective fat suppression).
5. Select an180° train RARE factor 8, matching pulse bandwidths of 90° and 180°, effective TE 30 ms, echo spacing 7.5 ms.
6. Set five dummy scans; no signal averaging.
7. Set TR = 5500, 2000, 1200, 750, 500, 300, 200, and 100 ms.
8. A manufacturer-provided macro is available for data processing.

4.1.2 Inversion Recovery Sequence in Bruker ParaVision 6

1. Use the ParaVision Fluid-Attenuated Inversion Recovery (FLAIR) method using only the global inversion mode (FairMode set to Nonselective), using Flow-sensitive Alternating Inversion Recovery FAIR-RARE or FAIR-EPI Bruker methods.
2. Set the geometry to axial or coronal, 58 × 58 mm FOV (rat) or 40 × 30 mm FOV (mouse). These may need adjustment on large (e.g., obese) animals.
3. Use a single 1 mm slice selection.
4. Set the matrix size to 128 × 128 matrix; if acquisition is too long, you may diminish the spatial resolution and adopt partial Fourier acceleration.
5. Set an TE of 36 ms (FAIR-RARE) or longer (FAIR-EPI).
6. Set the inversion pulse properties to calculated, as this provides a full passage adiabatic pulse with appropriately good flip angle homogeneity.
7. Use 21 inversion times starting at 30 ms with increments of 200 ms (to be adapted to the particular study at hand).
8. Select a recovery time of 10 s or greater.
9. Adjust the number of averages based on the available scan time.
10. In case of EPI usage, a careful shimming of B0 is paramount. The manufacturer-recommended method is MapShim using an ellipsoidal shim volume, in which a B_0 map is measured (accessible in the adjustments platform) and used to correct the B_0 with the shims coils available on the system.
11. A manufacturer-provided macro is provided for data processing.

1. Install rat in a wrist coil with conventional pressure pad to monitor breath rate. Figure 1 illustrates a dedicated small animal SA Instruments system connected to a Siemens clinical MR system.

4.1.3 Modified Look-Locker Inversion Recovery (MOLLI) [27] Sequence for Rats on a Siemens Clinical Scanner

2. Load the MOLLI sequence provided by the MRI system. The original MOLLI 3(3)3(3)5 scheme can be applied for kidney imaging. In this sampling scheme, multiple images are acquired at 11 time points on the recovery curve, with three inversions with slightly shifted inversion times, enabling a pixel-based T_1 quantification.
3. Start TI at 117 ms with TI increments (ΔTI) between inversion of 80 ms.
4. The slice thickness and in-plane resolution are particularly important to avoid partial volume effects. Use a slice with the lowest thickness and the highest in-plane resolution allowed by the MR system typically resulting voxel size around $0.7 \times 1.1 \times 3.5$ mm at 3 T.
5. Set TR/TE around 711/1.09 ms.
6. Set flip angle from 28° to 35° (default flip angle of 35°) T1 map relies on kidney being aligned between all TI images. As a consequence it is important to provide an additional motion correction method to mitigate residual respiratory motion. It is recommended to perform at least a rigid registration algorithm between images from various inversion times before the pixel-wise analysis of the relaxation curve (cf. the chapter by Garteiser P et al. "Analysis Protocols for MRI Mapping of Renal T_1"). Some vendors proposed on line motion correction algorithm, such as MOCCO from Siemens, during the reconstruction process.

4.2 Calibrated Phantom Acquisitions

1. Construct or procure a set of filled nickel/agarose phantoms without air bubbles. Each phantom should use a vial appropriate for the size of the animal abdomen (e.g., 25 mm diameter × 40 mm high for a mouse or 50 mm diameter × 80 mm high for a rat). Use 2% agarose, and a different concentration of nickel chloride in each phantom. Suitable nickel concentrations are 0 mM, 0.5 M, 1 mM, 2 mM, and 4 mM: 8 mM, and 16 mM can be added if very short T_1 values are expected (e.g., in DCEMRI). Add a preservative, such as 0.05% sodium azide, and seal.
2. Measure T_1 for each phantom using the method of Subheading 4.3 and the chapter by Garteiser P et al. "Analysis Protocols for MRI Mapping of Renal T_1." Repeat the measurements on a different day. Temperature should be controlled carefully, for instance by isolating the T_1 phantom in an ice–water mixture, or by inserting the phantom in a larger structure with high thermal inertia and preequilibrated at the target temperature.
3. In consultation with a professional statistician, calculate the repeatability and ensure the sample size is adequate to test the

hypothesis of interest. From an ethical perspective, this is mandatory before living animals are entered into the procedures.

4. Repeat **steps 2** and **3** in a group of living animals. The group size should be determined in consultation with a professional statistician: group sizes of between 6 and 15 are common.

4.3 Animal Experiments (Dedicated Small Animal MR Systems)

1. Use a volume RF coil of suitable diameter. In dedicated preclinical MRI, volume RF coils with an inner diameter of 38 mm for mice or 72 mm for rats could be used.
2. Anesthetize the animal with isoflurane as described in the chapter by Kaucsar T et al. "Preparation and Monitoring of Small Animals in Renal MRI" and transfer it to the scanner.
3. Set up the temperature monitoring (rectal probe) and respiratory monitoring (balloon on chest) unit.
4. Perform anatomical imaging as described in the chapter by Pohlmann A et al. "Essential Practical Steps for MRI of the Kidney in Experimental Research."
5. Perform localized shimming on the kidney imaging as described in the chapter by Pohlmann A et al. "Essential Practical Steps for MRI of the Kidney in Experimental Research." Wherever possible, appropriate tuning and matching of the used RF coil should be done.
6. Make sure the respiratory gating is setup properly, and that the anesthesia is stable.
7. Ensure that B_1^+ is correct, that is, that the relationship between the RF power and the desired flip angle is known in the region of space occupied by the kidneys. In *ParaVision* this is performed as part of the initial sequence adjustments when the reference pulse power is calibrated.

Acknowledgments

We thank Dr. Sascha Koehler (Bruker Biospin, Ettlingen, Germany) for helpful discussions.

This chapter is based upon work from COST Action PARENCHIMA, supported by European Cooperation in Science and Technology (COST). COST (www.cost.eu) is a funding agency for research and innovation networks. COST Actions help connect research initiatives across Europe and enable scientists to enrich their ideas by sharing them with their peers. This boosts their research, career, and innovation.

PARENCHIMA (renalmri.org) is a community-driven Action in the COST program of the European Union, which unites more than 200 experts in renal MRI from 30 countries with the aim to improve the reproducibility and standardization of renal MRI biomarkers.

References

1. Friedli I, Crowe LA, Berchtold L, Moll S, Hadaya K, de Perrot T et al (2016) New magnetic resonance imaging index for renal fibrosis assessment: a comparison between diffusion-weighted imaging and T1 mapping with histological validation. Sci Rep 6:30088
2. Waterton JC, Hines CDG, Hockings PD, Laitinen I, Ziemian S, Campbell S et al (2019) Repeatability, and reproducibility of longitudinal relaxation rate in 12 small-animal MRI systems. Magn Reson Imaging 59:121–129
3. Dekkers IA, Lamb HJ (2018) Clinical application and technical considerations of T1 & T2 (*) mapping in cardiac, liver, and renal imaging. Br J Radiol 91(1092):20170825
4. Waterton JC (2013) Translational magnetic resonance imaging and spectroscopy: opportunities and challenges. In: Garrido L, Beckmann N (eds) New applications of NMR in drug discovery and development. Royal Society of Chemistry, London, pp 333–360
5. O'Connor JP, Aboagye EO, Adams JE, Aerts HJ, Barrington SF, Beer AJ et al (2017) Imaging biomarker roadmap for cancer studies. Nat Rev Clin Oncol 14(3):169–186
6. Hueper K, Peperhove M, Rong S, Gerstenberg J, Mengel M, Meier M et al (2014) T1-mapping for assessment of ischemia-induced acute kidney injury and prediction of chronic kidney disease in mice. Eur Radiol 24(9):2252–2260
7. Tewes S, Gueler F, Chen R, Gutberlet M, Jang MS, Meier M et al (2017) Functional MRI for characterization of renal perfusion impairment and edema formation due to acute kidney injury in different mouse strains. PLoS One 12(3):e0173248
8. Hueper K, Hensen B, Gutberlet M, Chen R, Hartung D, Barrmeyer A et al (2016) Kidney transplantation: multiparametric functional magnetic resonance imaging for assessment of renal allograft pathophysiology in mice. Investig Radiol 51(1):58–65
9. Kierulf-Lassen C, Nielsen PM, Qi H, Damgaard M, Laustsen C, Pedersen M et al (2017) Unilateral nephrectomy diminishes ischemic acute kidney injury through enhanced perfusion and reduced pro-inflammatory and pro-fibrotic responses. PLoS One 12(12): e0190009
10. Wang JJ, Hendrich KS, Jackson EK, Ildstad ST, Williams DS, Ho C (1998) Perfusion quantitation in transplanted rat kidney by MRI with arterial spin labeling. Kidney Int 53 (6):1783–1791
11. Ogbron MR, Sareen S, Prychitko J, Buist R, Peeling J (1997) Altered organic anion and osmolyte content and excretion in rat polycystic kidney disease: an NMR study. Am J Phys 272(1 Pt 2):F63–F69
12. Ko SF, Yip HK, Zhen YY, Lee CC, Lee CC, Huang SJ et al (2017) Severe bilateral ischemic-reperfusion renal injury: hyperacute and acute changes in apparent diffusion coefficient, T1, and T2 mapping with immunohistochemical correlations. Sci Rep 7(1):1725
13. Keenan KE, Ainslie M, Barker AJ, Boss MA, Cecil KM, Charles C et al (2018) Quantitative magnetic resonance imaging phantoms: a review and the need for a system phantom. Magn Reson Med 79(1):48–61
14. Captur G, Gatehouse P, Keenan KE, Heslinga FG, Bruehl R, Prothmann M et al (2016) A medical device-grade T1 and ECV phantom for global T1 mapping quality assurance-the T1 mapping and ECV standardization in cardiovascular magnetic resonance (T1MES) program. J Cardiovasc Magn Reson 18(1):58
15. Lerski RA, McRobbie DW, Straughan K, Walker PM, de Certaines JD, Bernard AM (1988) Multi-center trial with protocols and prototype test objects for the assessment of MRI equipment. EEC Concerted Research Project. Magn Reson Imaging 6(2):201–214
16. Rajendran R, Lew SK, Yong CX, Tan J, Wang DJ, Chuang KH (2013) Quantitative mouse renal perfusion using arterial spin labeling. NMR Biomed 26(10):1225–1232
17. Christoffersson JO, Olsson LE, Sjoberg S (1991) Nickel-doped agarose gel phantoms in MR imaging. Acta Radiol 32(5):426–431
18. Kraft KA, Fatouros PP, Clarke GD, Kishore PR (1987) An MRI phantom material for quantitative relaxometry. Magn Reson Med 5 (6):555–562
19. Howe FA (1988) Relaxation times in paramagnetically doped agarose gels as a function of temperature and ion concentration. Magn Reson Imaging 6(3):263–270
20. Finney JS, Bach PH, Bushell MC, Gregg NM, Taylor DG (1990) The application of proton nuclear magnetic resonance imaging for the in vivo characterisation of chemically induced renal lesions in rats over a prolonged time study. Magn Reson Imaging 8(6):713–721
21. Jiang K, Tang H, Mishra PK, Macura SI, Lerman LO (2018) A rapid T1 mapping method for assessment of murine kidney viability using

dynamic manganese-enhanced magnetic resonance imaging. Magn Reson Med 80 (1):190–199
22. Korb JP, Bryant RG (2002) Magnetic field dependence of proton spin-lattice relaxation times. Magn Reson Med 48(1):21–26
23. Zhang J, Chamberlain R, Etheridge M, Idiyatullin D, Corum C, Bischof J et al (2014) Quantifying iron-oxide nanoparticles at high concentration based on longitudinal relaxation using a three-dimensional SWIFT Look-Locker sequence. Magn Reson Med 71 (6):1982–1988
24. Chow K, Flewitt JA, Green JD, Pagano JJ, Friedrich MG, Thompson RB (2014) Saturation recovery single-shot acquisition (SASHA) for myocardial T(1) mapping. Magn Reson Med 71(6):2082–2095
25. Stikov N, Boudreau M, Levesque IR, Tardif CL, Barral JK, Pike GB (2015) On the accuracy of T1 mapping: searching for common ground. Magn Reson Med 73(2):514–522
26. Akcakaya M, Weingartner S, Roujol S, Nezafat R (2015) On the selection of sampling points for myocardial T1 mapping. Magn Reson Med 73(5):1741–1753
27. Messroghli DR, Radjenovic A, Kozerke S, Higgins DM, Sivananthan MU, Ridgway JP (2004) Modified Look-Locker inversion recovery (MOLLI) for high-resolution T1 mapping of the heart. Magn Reson Med 52(1):141–146
28. Little RA, Jamin Y, Boult JKR, Naish JH, Watson Y, Cheung S et al (2018) Mapping hypoxia in renal carcinoma with oxygen-enhanced MRI: comparison with intrinsic susceptibility MRI and pathology. Radiology 288 (3):739–747
29. Hueper K, Gutberlet M, Rong S, Hartung D, Mengel M, Lu X et al (2014) Acute kidney injury: arterial spin labeling to monitor renal perfusion impairment in mice-comparison with histopathologic results and renal function. Radiology 270(1):117–124
30. Pastor G, Jimenez-Gonzalez M, Plaza-Garcia S, Beraza M, Reese T (2017) Fast T1 and T2 mapping methods: the zoomed U-FLARE sequence compared with EPI and snapshot-FLASH for abdominal imaging at 11.7 Tesla. MAGMA 30(3):299–307
31. Zhang J, Ring HL, Hurley KR, Shao Q, Carlson CS, Idiyatullin D et al (2017) Quantification and biodistribution of iron oxide nanoparticles in the primary clearance organs of mice using T1 contrast for heating. Magn Reson Med 78(2):702–712
32. Subashi E, Choudhury KR, Johnson GA (2014) An analysis of the uncertainty and bias in DCE-MRI measurements using the spoiled gradient-recalled echo pulse sequence. Med Phys 41(3):032301
33. Vautier J, Heilmann M, Walczak C, Mispelter J, Volk A (2010) 2D and 3D radial multi-gradient-echo DCE MRI in murine tumor models with dynamic R*2-corrected R1 mapping. Magn Reson Med 64(1):313–318
34. Alamidi DF, Smailagic A, Bidar AW, Parker NS, Olsson M, Hockings PD et al (2018) Variable flip angle 3D ultrashort echo time (UTE) T1 mapping of mouse lung: a repeatability assessment. J Magn Reson Imaging. https://doi.org/10.1002/jmri.25999
35. Marques JP, Kober T, Krueger G, van der Zwaag W, Van de Moortele PF, Gruetter R (2010) MP2RAGE, a self bias-field corrected sequence for improved segmentation and T1-mapping at high field. NeuroImage 49 (2):1271–1281
36. Yoon JH, Lee JM, Kim E, Okuaki T, Han JK (2017) Quantitative liver function analysis: volumetric T1 mapping with fast multisection B1 inhomogeneity correction in hepatocyte-specific contrast-enhanced liver MR imaging. Radiology 282(2):408–417
37. Stollberger R, Wach P (1996) Imaging of the active B1 field in vivo. Magn Reson Med 35 (2):246–251

Chapter 23

Experimental Protocol for MRI Mapping of the Blood Oxygenation-Sensitive Parameters T_2* and T_2 in the Kidney

Andreas Pohlmann, Kaixuan Zhao, Sean B. Fain, Pottumarthi V. Prasad, and Thoralf Niendorf

Abstract

Renal hypoxia is generally accepted as a key pathophysiologic event in acute kidney injury of various origins, and has also been suggested to play a role in the development of chronic kidney disease. Here we describe a step-by-step experimental protocol for indirect monitoring of renal blood oxygenation in rodents via the deoxyhemoglobin sensitive MR parameters T_2* and T_2—a contrast mechanism known as the blood oxygenation level dependent (BOLD) effect. Since an absolute quantification of renal oxygenation from T_2*/T_2 remains challenging, the effects of controlled and standardized variations in the fraction of inspired oxygen are used for bench marking. This MRI method may be useful for investigating renal blood oxygenation of small rodents in vivo under various experimental (patho)physiological conditions.

This chapter is based upon work from the COST Action PARENCHIMA, a community-driven network funded by the European Cooperation in Science and Technology (COST) program of the European Union, which aims to improve the reproducibility and standardization of renal MRI biomarkers. This experimental protocol chapter is complemented by two separate chapters describing the basic concept and data analysis.

Key words Magnetic resonance imaging (MRI), Kidney, Mice, Rats, T_2, T_2*, BOLD

1 Introduction

Renal tissue oxygenation relies on a delicate balance between delivery of O_2, as determined by renal blood flow and arterial O_2 content, and consumption of O_2, which is predominantly determined by energy-dependent tubular reabsorption. Even under physiological conditions, tissue partial pressure of O_2 is low in the medulla. Hence renal tissue hypoxia may result from even a small detrimental imbalance between O_2 delivery and consumption. Based largely upon studies on animal models, intrarenal hypoxia is generally accepted as a key pathophysiologic event in acute kidney injury of various origins, and has also been suggested to promote its progression to chronic kidney disease CKD.

Andreas Pohlmann and Thoralf Niendorf (eds.), *Preclinical MRI of the Kidney: Methods and Protocols*, Methods in Molecular Biology, vol. 2216, https://doi.org/10.1007/978-1-0716-0978-1_23,

The parametric mapping of the transverse relaxation times T_2^* and T_2 (or relaxation rates $R_2^* = 1/T_2^*$ and $R_2 = 1/T_2$) has the potential to allow inferences about renal oxygenation, because both parameters are sensitive to blood oxygenation. The underlying mechanism is the inherent difference in the magnetic properties of oxygenated hemoglobin (diamagnetic) vs. deoxygenated hemoglobin (paramagnetic). The presence of deoxyhemoglobin in a voxel decreases both relaxation times, T_2^* and T_2. Additional factors that influence this relationship between renal venous blood oxygenation and renal T_2^* include the blood volume fraction, the hematocrit and the oxygen binding curve.

Here we describe quantitative mapping of the blood oxygenation sensitive parameter T_2^* in the kidney of small rodents in a step-by-step experimental protocol. The rationale for the chosen acquisition parameters is given in generic terms, together with specific parameter examples.

Mapping of renal T_2 is described as an optional component of the experiment. This may serve two purposes. Firstly, T_2^* includes the dynamic (irreversible) dephasing effects described by T_2 plus the additional effects that are due to static (reversible) dephasing effects described by T_2'. Hence, the additional measurement of T_2 permits calculation of $R_2' = R_2^* - R_2 = 1/T_2^* - 1/T_2$.

Secondly, blood oxygenation affects primarily T_2^* (often referred to as blood oxygenation level dependent, BOLD) but also T_2 to a lesser extent. The T_2 effect is via water diffusion within the magnetic field gradient created by deoxyhemoglobin. This contrast mechanism results in T_2 being dominated by blood oxygenation effects in the microvasculature, which makes it a valuable complement to conventional T_2^* measurements.

The effects of controlled and standardized variations in T_2^* relaxation parameters in response to the fraction of inspired oxygen (hypoxia, hyperoxia) are used for benchmarking. This MRI method may be useful for investigating renal blood oxygenation of rodents in vivo under various experimental (patho)physiological conditions.

This experimental protocol chapter is complemented by two separate chapters describing the basic concept and data analysis, which are part of this book.

This chapter is part of the book Pohlmann A, Niendorf T (eds) (2020) Preclinical MRI of the Kidney—Methods and Protocols. Springer, New York.

2 Materials

2.1 Animals

These experimental protocols are tailored for rats (Wistar, Sprague-Dawley, or Lewis) with a body mass of 250–350 g. Advice for adaptation to mice is given in where necessary.

2.2 Lab Equipment

Anesthesia: For nonrecovery experiments urethane solution (Sigma-Aldrich, Steinheim, Germany; 20% in distilled water) can provide anesthesia for several hours with comparatively little side effects on renal physiology, which is an important issue. For an in-depth description and discussion of the anesthesia please refer to the chapter by Kaucsar T et al. "Preparation and Monitoring of Small Animals in Renal MRI."

Gases: O_2, N_2, and compressed air, as well as a gas-mixing system (FMI Föhr Medical Instruments GmbH, Seeheim-Ober Beerbach, Germany) to achieve required changes in the oxygen fraction of inspired gas mixture (FiO_2). Besides air, the following gas mixtures are required during the experiment: 10% O_2–90% N_2 for hypoxia and 100% O_2 for hyperoxia.

Device for FiO_2 monitoring in gas mixtures: for example Capnomac AGM-103 (Datex GE, Chalfont St Gils, UK).

2.3 MRI Hardware

The general hardware requirements for renal ^{1}H MRI on mice and rats are described in the chapter by Ramos Delgado P et al. "Hardware Considerations for Preclinical Magnetic Resonance of the Kidney." The technique described in this chapter was tailored for a 9.4 T MR system (Biospec 94/20, Bruker Biospin, Ettlingen, Germany) but advice for adaptation to other field strengths and systems (e.g., 3 T Siemens Skyra or GE MR 750 human MR scanner using a wrist coil for signal reception or transmit-receive knee RF coil is given where necessary. No special or additional hardware is required, except for the following:

1. A physiological monitoring system that can track the respiration, and which is connected to the MR system such that it can be used to trigger the image acquisition.

2.4 MRI Techniques

Repeated measurements with a gradient-echo or spin-echo method and variable echo times (TE) would provide the most accurate T_2* and T_2 but require very long acquisition times. Here we describe fast multiecho MRI methods: multi-gradient-echo (MGE) for T_2* measurement and multi–spin-echo (also called "MSME") for T_2 assessment. They provide relaxation times that underestimate T_2* and overestimate T_2. With increasing echo number additional diffusion weighting is added due to the repeated magnetic field gradients (NB: this effect is much more pronounced in small animal systems because of the much stronger magnetic field gradients used compared to clinical systems). The superposition of stimulated echoes in multi–spin-echo imaging may lead to an overestimation of T_2. Although these biases depend on the acquisition parameters, they are fixed and reproducible for each protocol and hence acceptable in studies of relative differences/changes in T_2* and T_2, where precision is far more important than accuracy. If needed, more accurate T_2 values can be obtained from multiecho data using sophisticated postprocessing [1].

1. 2D multi-gradient-echo sequence for T_2*-mapping. This is a standard sequence that should be available on all MRI systems. (Bruker "MGE," Siemens "gre"; HE Healthcare 2D ME SPGR or ME FGRE) (*see* **Note 1**).
2. 2D multi-spin-echo sequence for T_2-mapping (optional; Bruker "MSME," Siemens "se_mc"; GE Healthcare "T2 Map" within the 2D ME FGRE family of sequences).
3. 3D double gradient echo sequence for acquiring a quantitative map of the static magnetic field B_0 (optional; Bruker "FieldMap"). The reconstruction performs a phase difference calculation, phase unwrapping, and a conversion to a frequency map. A similar sequence exists with Siemens ("AdjGreSeq"), however there is no reconstruction applied to the data. Choosing Magnitude and Phase under Reconstruction will save both Magnitude and Phase information, but no processing is performed to correct for the B_0 map. Similarly, for GE Healthcare clinical MR systems "IDEAL-IQ" allows for return of fat, water, R_2*, in-phase and out-of-phase water/fat images, but research mode is required to obtain magnitude, phase, and B_0 images.

3 Methods

3.1 MR Protocol Setup

3.1.1 Multi-gradient-Echo Sequence for T_2*-Mapping

1. Load the 2D multi–gradient-echo sequence.
2. Set the shortest echo time (TE) and echo spacing (ΔTE) possible, under the condition that fat and water are in phase (*see* **Note 2**). The last TE should be close to the largest expected $T_2^{(*)}$ in the kidney multiplied by 1.5 (*see* **Note 3**). The aim is to acquire ten or more echo images. Fewer TEs or larger ΔTE are not advisable because during strong hypoxia the SNR in the kidney at high TEs can be so low that only a few data points above the noise level are available for the analysis. Consider increasing the acquisition bandwidth and using half Fourier acceleration to shorten the first TE and ΔTE (*see* **Note 4**).
3. Choose the shortest possible repetition time (TR) for good signal-to-noise per time (SNR/t) efficiency. TR will be limited by the length of the echo train and the number of slices you acquire.
4. Adapt the flip angle (FA) to the TR and T_1 in order to achieve the best possible SNR. Use the Ernst angle $\alpha_E = \arccos(\exp(-TR/T_1))$ as a good starting value. Then try a few smaller and larger FAs and determine the optimal FA experimentally by comparing the measured SNRs in a phantom with a T_1 comparable to that of the renal cortex (1–1.2 s at 3 T).

5. Set a high acquisition bandwidth (BW) to shorten ΔTE, while keeping an eye on the SNR, which decreases with the square root of BW. SNR may be increased with signal averaging. (*see* **Note 5**).
6. Enable fat saturation. On ultrahigh field systems this works well to avoid fat signal overlaying the kidney due to chemical shift. At lower clinical field strengths fat saturation is less efficient.
7. Enable the respiration trigger (per slice). This is essential to reduce motion artefacts, reduce motion blurring and unwanted intensity variations between the images acquired with different TEs.
8. Choose as phase-encoding direction the L-R direction and adapt the geometry so that the FOV in this direction includes the entire animal (approx. 40 mm).
9. Use frequency encoding in head-feet (rostral-caudal) direction to avoid severe aliasing. Adjust the FOV to your needs keeping in mind that in the frequency encoding direction the FOV can be smaller than the animal and a smaller FOV permits a smaller acquisition matrix, and in turn a shorter echo-spacing.
10. Use the lowest slice thickness the SNR allows, typically around 1.5 mm. The thinner the slices the better, as this reduces the unwanted T_2^*-effects of macroscopic field inhomogeneities associated with the large voxel size in slice direction. For adaptation of the geometry to mice *see* **Note 6**.
11. Use highest in-plane resolution that the SNR allows, typically between 100 and 200 μm. The higher the resolution the better, as this reduces the unwanted T_2^*-effects of macroscopic field inhomogeneities. Zero-filling in phase encoding direction can be helpful to speed up acquisition when monitoring of fast oxygenation changes is required. One may use half Fourier in the frequency encoding direction (asymmetric echo) to further shorten the first TE, if very short T_2^* (<5 ms) can occur. Reducing the excitation pulse length to below 1 ms would then also help to shorten TE. For adaptation to mice *see* **Note 7**.
12. For examples of a specific parameter set please *see* **Notes 8–10**.

3.1.2 Multi-spin-Echo Sequence for T_2-Mapping (Optional)

1. Load the 2D multi–spin-echo sequence.
2. Use the same FOV, matrix size and slice thickness as for the multi–gradient-echo sequence.
3. Adapt the repetition time (TR) to the respiration: The effective TR will be given by the respiration trigger and will be the respiration interval, that is, one excitation per breath. Choose TR to be a little shorter (about 100 ms) than the average

respiration interval that is displayed on the physiological monitoring unit (*see* **Note 11**).

4. Set the number of echoes to 12 (*see* **Note 12**.).
5. Set the echo spacing (ΔTE) as small as possible (more echoes are effectively more data points for the analysis and reduce the error; consider that with increasing number of echoes also the SAR increases) and that the last TE is close to the largest expected T_2 in the kidney multiplied by 1.5 (*see* **Note 3**).
6. Due to the artificial increase in signal intensity of fat with a multi–spin-echo sequence, enable fat saturation. Note that the spectral fat saturation does not usually suppress the fat signal completely with some of residual fat signal overlaying the kidney due to chemical shift (Fig. 2).
7. Enable the respiration trigger (per slice).
8. For an example of a specific parameter set please *see* **Notes 13–15**.

3.1.3 Field Map (Optional)

1. Load the field map sequence.
2. Store the field mapping scan protocol with the default parameters when using a small animal system (*see* **Note 16**) or those adapted for a clinical system (*see* **Notes 17** and **18**). Make sure the 3D B_0 field-map has isotropic resolution and a FOV that includes the entire MR-visible part of the animal.

3.2 In Vivo Blood Oxygenation Sensitive Imaging

3.2.1 Animal Preparation

1. Anesthetize the animal and transfer it to scanner. For more information on the choice and use of anesthesia please refer to the chapter by Kaucsar T et al. "Preparation and Monitoring of Small Animals in Renal MRI."
2. Start the temperature monitoring system, apply some surgical lubricant to the temperature probe and place it in the rectum of the animal.
3. Attach the respiration sensor (e.g., balloon) to the chest of the animal using adhesive tape. Start and setup the respiratory monitoring system. If necessary, adjust the position of the respiration sensor until the amplitude of the respiration trace is sufficiently large for the system to reliably detect the trigger points at the beginning of expiration.

3.2.2 Scanner Adjustments and Anatomical Imaging

1. Acquire a fast pilot scan to obtain images in the three orthogonal planes *x*, *y*, and *z*.
2. Acquire anatomical images in several oblique orientations to facilitate planning a coronal slice orientation with regard to the long axis of the kidney, as described in the chapter by Pohlmann A et al. "Essential Practical Steps for MRI of the Kidney in Experimental Research."

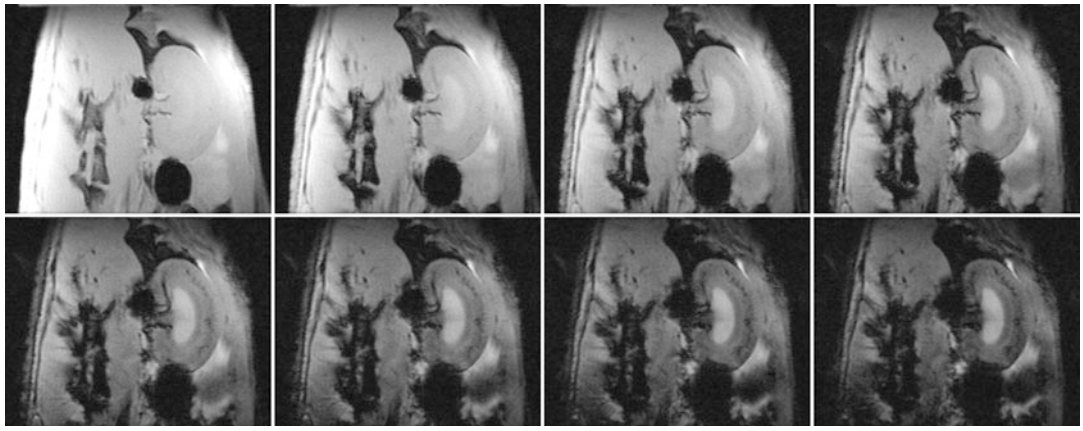

Fig. 1 Series of 8 T_2*-weighted images of a healthy rat kidney acquired with a multi–gradient-echo sequence at 9.4 T. Images correspond to TE = 1.43, 3.57, 5.71, 7.85 ms (top row), TE = 9.99, 12.13, 14.27, 16.41 ms (bottom row)

3. Perform localized shimming on the kidney as described in the chapter by Pohlmann A et al. "Essential Practical Steps for MRI of the Kidney in Experimental Research" (*see* **Note 19**).
4. Acquire a 3D B0 field-map without adaptation of the geometry (optional; *see* **Note 20**).

3.2.3 Baseline Condition

1. Load the T_2*-mapping sequence, adapt the slice orientation to provide a coronal or axial view with respect to the kidney (in scanner coordinates this is double-oblique).
2. In the monitoring unit set the trigger delay so that the trigger starts at the beginning of the expiratory plateau (no chest or diaphragm motion) and the duration such that it covers the entire expiratory phase, that is, until just before inhalation starts (1/2 to 2/3 of breath-to-breath interval) (*see* **Note 11**).
3. Run the T_2*-mapping scan. Example images are shown in Fig. 1.
4. Load the T_2-mapping sequence, adapt the slice orientation to provide a coronal or axial view with respect to the kidney (in scanner coordinates this is double-oblique).
5. Adapt TR to be a little shorter (about 100 ms) than the average respiration interval that is displayed on the physiological monitoring unit.
6. In the monitoring unit set the trigger delay so that the trigger starts at the beginning of the expiratory plateau (no chest or diaphragm motion) and the duration to a short value, such as 10 ms (**Note 11**).
7. Run the T_2-mapping scan. Example images are shown in Fig. 2.

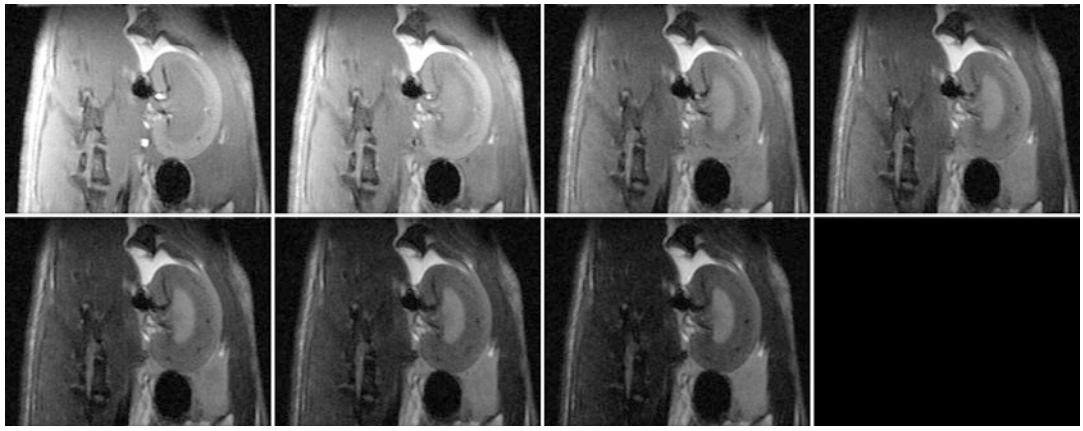

Fig. 2 Series of 7 T_2-weighted images of a healthy rat kidney acquired with a 2D multi-spin-echo sequence at 9.4 T. Images correspond to TE = 10, 20, 30, 40 ms (top row) and TE = 50, 60, 70 ms (bottom row)

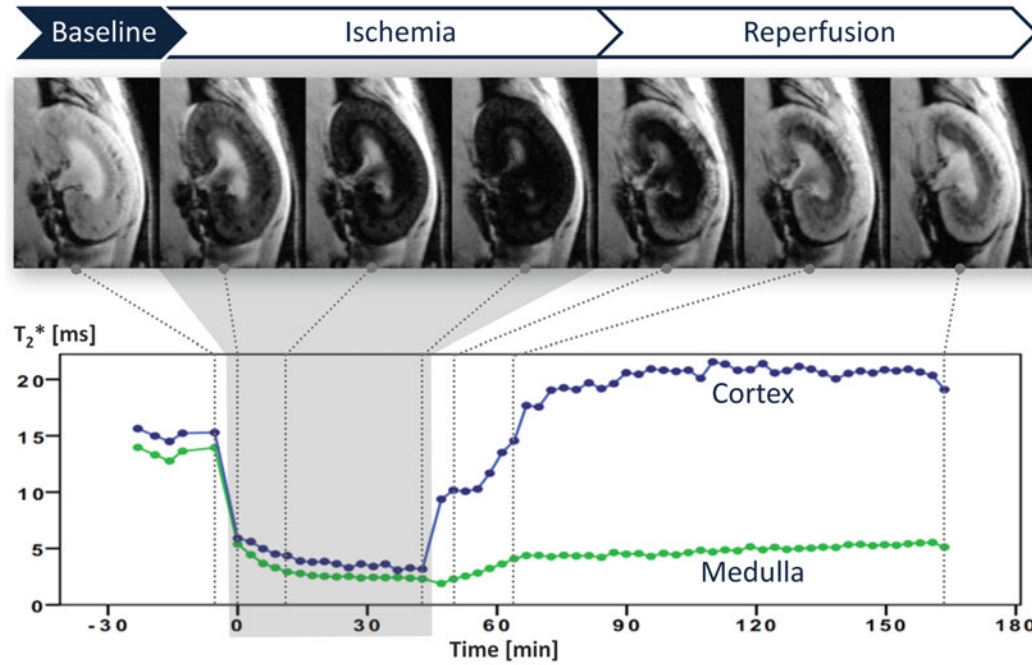

Fig. 3 Demonstration of the contrast changes that can be expected in pathophysiological scenarios. T_2*-weighted images (from a 2D multi–gradient-echo acquisition, TE = 3.57 ms) of rat kidneys throughout an ischemia–reperfusion experiment, together with a plot of T_2* in regions-of-interest in renal cortex and medulla

A demonstration of the contrast changes that can be expected in pathophysiological scenarios is given in Fig. 3. Example parametric maps of T_2* and T_2 are shown in Fig. 4.

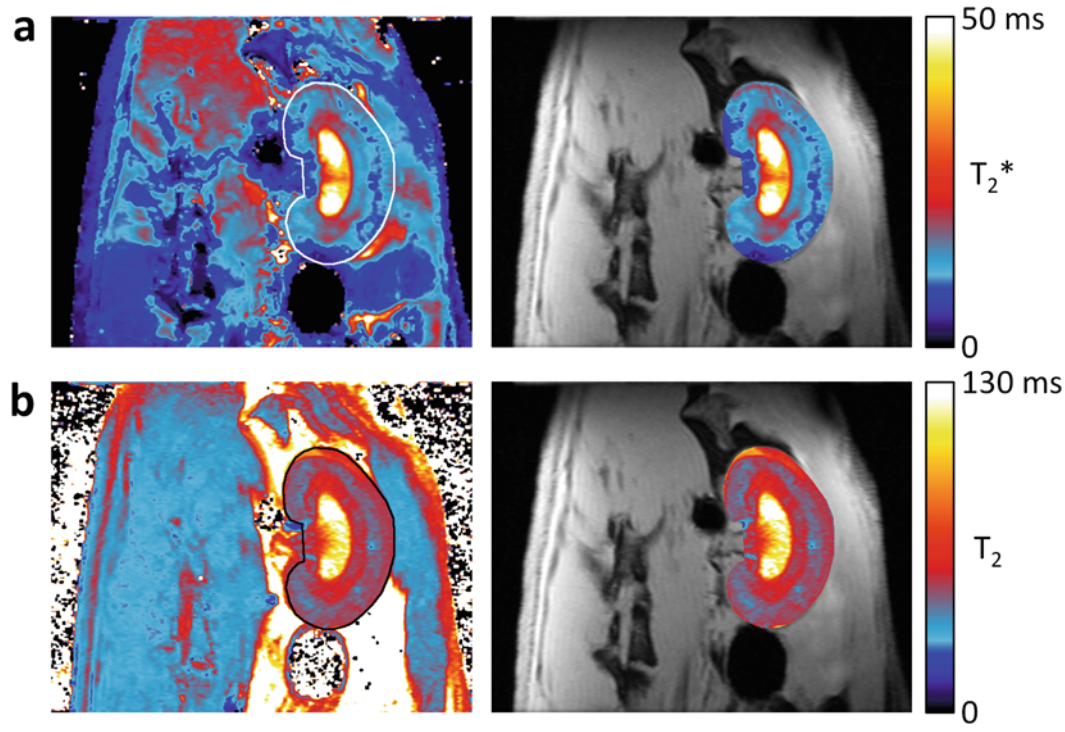

Fig. 4 Example parametric maps of T_2^* (**a**) and T_2 (**b**) acquired in a rat at 9.4 T. Shown are the entire map with the kidney outlined (left) as well as an overlay of the map onto an anatomical MR image (right). While the overlays are preferable because they focus on the relevant part and do not distract the eye, looking at the entire map can sometimes help to identify extra-renal sources of susceptibility artefacts, like here the bowel gas below the kidney and an implanted device near the hilus, which cast "shadows" onto the renal cortex. Beware to exclude from the ROI analysis any regions with overlaid fat signal due to chemical shift, here seen as a thin stripe at the rostral end of the kidney

3.2.4 Hypoxia/Hyperoxia for Benchmarking (optional)

1. Duplicate the two scans (T_2^*-mapping and T_2-mapping) and disable all adjustments (e.g., receiver gain, shimming) so that they are not changed from the previous scan.
2. Start hypoxia by changing the gas flowing through the respiratory mask to 10% O_2/90% N_2.
3. Three minutes after the start of hypoxia run the T_2^*-mapping and T_2-mapping scans. Hypoxia should not exceed 5 min in order to avoid long lasting effects.
4. Immediately after the two scans end, change the gas flowing through the respiratory mask back to air (21% O_2).
5. Wait for a recovery time of at least 5 min.
6. Start hyperoxia by changing the gas flowing through the respiratory mask to 100% O_2.
7. Two minutes after the start of hyperoxia run the T_2^*-mapping and T_2-mapping scans.

8. Immediately after the two scans end change the gas flowing through the respiratory mask back to air (21% O_2).
9. Wait for a recovery time of at least 5 min before conducting any further interventions.

3.2.5 Noise Scan

We highly recommend acquiring one scan with the T_2*-mapping protocol and T_2-mapping protocol that only contains noise. This is the best way to estimate the noise standard deviation, which is needed for correcting the noise bias during the data analysis (*see* **Note 21**). Alternatively it is possible to estimate the noise standard deviation from an ROI in the "background" of the study images, but it is often difficult to find a suitable region outside the subject that is large enough and artefact free.

1. Create a copy of the T_2*-mapping protocol.
2. Open the protocol and in the parameter setting set either the flip angle to 0° degrees or the reference power for the flip angle calibration to 0 W.
3. Run the T_2*-mapping scan.
4. Repeat **steps 1–3** for the T_2-mapping protocol.

4 Notes

1. A 3D version of this sequence is also available, which allows for thinner slices with better SNR, but tends to be too slow for most in vivo applications.
2. The fat signal has a slightly different Lamor frequency ($\Delta f = 220$ Hz/Tesla) than the water signal. The faster precession of the fat protons means that with increasing time the fat and water signal fractions within a voxel are sometimes in phase (signals add up) and sometimes out of phase (signals subtract). This can lead to an additional unwanted variation in the signal along the exponential decay curve. This is mostly relevant for diseased kidneys with increased fat content (e.g., diabetes), but we recommend to generally take this into account, that is, also for healthy kidneys. The TEs at which fat and water are in phase depend on the field strength: $\mathrm{TE}\,[\mathrm{ms}] = n \cdot (6.7069/B_0[T])$.
3. Larger TEs are needed to accurately calculate longer $T_2^{(*)}$ under normal or hyperoxic conditions. We recommend using the largest expected $T_2^{(*)}$ in the kidney multiplied by 1.5 as the largest TE. Since the largest $T_2^{(*)}$ is typically in the inner medulla—if this region is not relevant to your research then use the largest $T_2^{(*)}$ in the cortex/outer medulla. With increasing TE the signal intensity decreases and may reach the noise floor at large TEs. This can introduce a noise bias during data

analysis. To account for this we recommend performing a retrospective noise correction (preferred) or exclude images acquired at larger TEs from the analysis. Both approaches are described in the chapter by Periquito JS et al. "Analysis Protocols for MRI Mapping of the Blood Oxygenation–Sensitive Parameters T_2^* and T_2 in the Kidney."

4. Renal T_2* may be quite short at ultrahigh field strengths and in particular under hypoxia, which is what one wishes to detect. One needs to consider the shortest renal T_2* that could occur during experiment; under extreme conditions this could be only a few milliseconds, so several TEs around that value are needed.
5. When establishing the MR technique you need to define an SNR acceptance threshold for the image with the shortest TE. The aim is to have at least three (better five or more) number of echoes with an SNR > 5. This threshold will depend on the expected $T_2^{(*)}$ values, which in turn depends on parameters like the magnetic field strength, shim quality, and tissue properties (pathology). Example: for a rat imaged at 9.4 T using a 4-element rat heart array receive surface coil together with a volume resonator for excitation in combination with interventions leading to strong hypoxia, an SNR > 60 was needed.
6. For mice reduce the FOV to the body width and keep the matrix size the same. The relative resolution is then identical and the SNR should also be similar, because the smaller mouse RF coil gives better SNR, for example, mouse heart four-element surface coil vs rat heart four-element surface coil.
7. A good starting point is to use the same relative resolution as for rats. For this, reduce the FOV to the mouse body width and keep the matrix size the same.
8. *Example parameters for T_2* mapping of a 300 g rat at 9.4 T (Bruker small animal system)*: TR = 50 ms; flip angle = 16°; pulse length 1.0 ms; pulse bandwidth 5.4 kHz; receiver bandwidth = 109 kHz; number of echoes = 12; first echo = 2.14 ms; echo spacing 2.14 ms; TE = 2.14, 4.28, 6.42, 8.56, 10.7, 12.84, 14.98, 17.12, 19.26, 21.40, 23.54, 25.68 ms; averages = 4; slice orientation = coronal to kidney; frequency encoding = head-feet; FOV = (38.2 × 48.5) mm; matrix size = 169 × 115 zero-filled to 169 × 215; resolution = (0.226 × 0.421) mm; 1–3 slices with 1.4 mm thickness; fat suppression = on; respiration trigger = per slice; acquisition time = 40–60 s (with triggering under urethane anaesthesia).
9. *Example parameters for T_2* mapping of a 30 g mouse at 4.7 T (Agilent small animal system)*: TR = 350 ms; flip angle = 30°; receiver bandwidth = 100 kHz; number of echoes = 32; first

echo = 2.0 ms; echo spacing 2.4 ms; TE = 2.00, 4.40, 6.80, 9.20, 11.60, 14.00, 16.40, 18.80, 21.20, 23.60, 26.00, …, 76.40 ms; averages = 4; slice orientation = coronal to kidney; frequency encoding = head-feet; FOV = (30 × 30) mm; matrix size = 128 × 128; resolution = (0.230 × 0.230) mm; 1 slice with 1.0 mm thickness; fat suppression = on; respiration trigger = on; acquisition time = 3.5–9.0 min (with triggering under isoflurane anaesthesia).

10. *Example parameters for T_2* mapping of a 300 g rat at 3.0 T (Siemens Skyra^{fit}, a clinical system)*: Animal position: Right decubitus; Coil: Knee; TR = 69 ms; flip angle = 30°; receiver bandwidth = 320 Hz/pixel; number of echoes = 12; first echo = 3.56 ms; echo spacing 3.43 ms; TE = 3.56, 6.99, 10.42, 13.85, 17.28, 20.71, 24.14, 27.57, 31.00, 34.43, 37.86, 41.29 ms; averages = 20; slice orientation = axial; frequency encoding = anterior-posterior; FOV = (120 × 60) mm; matrix size = 256 × 128; resolution = (0.470 × 0.470) mm; 3 slices with 2.0 mm thickness; fat suppression = on; respiration trigger = off; acquisition time ~ 3 min. If one desires in-phase echoes, use first echo = 4.92 and echo spacing = 4.92 ms. If no specific animal holder is used, it is preferable to position the animals in left of right decubitus position to keep the bowels away from the kidneys to mitigate susceptibility artifacts.
11. You must monitor the respiration continuously throughout the entire experiment and if necessary adapt the TR accordingly.
12. Acquiring more echoes with smaller echo spacing will be beneficial because it improves the fitting, but keep in mind the SAR associated with sending many 180° RF pulses in a short time could heat up the tissue. This will usually not be detectable via a rectal temperature probe, but measurements with a temperature probe placed in the abdomen next to the kidney showed that significant temperature increases are possible with a multi–spin-echo sequence.
13. *Example parameters for T_2 mapping of a 300 g rat at 9.4 T (Bruker small animal system)*: TR = [respiration interval] − 100 ms; receiver bandwidth = 50 kHz; number of echoes = 12; first echo = 10.0 ms; echo spacing 10.0 ms; TE = 10, 20, 30, 40, 50, 60, 70, 80, 90, 100, 110, 120 ms; averages = 1; slice orientation = coronal to kidney; frequency encoding = head-feet; FOV = (38.2 × 48.5) mm; matrix size = 169 × 115 zero-filled to 169 × 215; resolution = (0.226 × 0.421) mm; 1 slice with 1.4 mm thickness; fat suppression = on; respiration trigger = per slice; acquisition time = 55–75 s (with triggering under urethane anaesthesia).

14. *Example parameters for T_2 mapping of a 30 g mouse at 4.7 T (Agilent small animal system)*: TR = [respiration interval] -100 ms; receiver bandwidth = 50 kHz; number of echoes = 12; first echo = 10.0 ms; echo spacing 10.0 ms; TE = 10, ..., 120 ms; averages = 1; slice orientation = coronal to kidney; frequency encoding = head-feet; FOV = (30 × 30) mm; matrix size = 128 × 128; resolution = (0.230 × 0.230) mm; 1 slice with 2.0 mm thickness; fat suppression = on; respiration trigger = on; acquisition time = 2–4 min (with triggering under isoflurane anaesthesia).
15. *Example parameters for T_2 mapping of a 300 g rat at 3.0 T (Siemens Skyra^{fit}, a clinical system)*: Animal position: Right decubitus; Coil: Knee; TR = [respiration interval] − 500 ms; receiver bandwidth = 399 Hz/pixel; number of echoes = 12; first echo = 10.0 ms; echo spacing 10.0 ms; TE = 10, ..., 120 ms; averages = 2; slice orientation = axial; frequency encoding = left-right; FOV = (120 × 60) mm; matrix size = 256 × 128; resolution = (0.470 × 0.470) mm; 1 slice with 2.0 mm thickness; fat suppression = on; respiration trigger = off; acquisition time ~2 min. If no specific animal holder is used, it is preferable to position the animals in left of right decubitus position to keep the bowels away from the kidneys to mitigate susceptibility artifacts.
16. *Example parameters for field mapping of a 300 g rat at 9.4 T (Bruker small animal system)*: use the vendors default protocol *AnyObject > AnyRegion > Adjustments > ADJ_B0MAP*. TR = 20 ms; flip angle = 30°; first echo = 1.60 ms; echo spacing = 3.57 ms; fat/water in-phase = on; slice orientation = main orientations (no angles) and offset = 0; FOV = (58 × 58 × 58) mm; matrix size = 64 × 64 × 64; resolution = (0.906 × 0.906 × 0.906) mm; respiration trigger = off; acquisition time = 1–2 min.
17. *Example parameters for field mapping of a 300 g rat at 3.0 T (Siemens Skyra^{fit}, a clinical system)*: The default setup uses the BODY Coil. TR = 20 ms; flip angle = 15°; in-phase echo times, first echo = 4.78 ms, and second echo = 7.17 ms; slice orientation = main orientations (no angles) and offset = 0; FOV = (350 × 350) mm; matrix size = 96 × 96; resolution = (3.6 × 3.6 × 8.0) mm; GRAPPA factor = 2; respiration trigger = off; acquisition time = 17 s.
18. *Example parameters for field mapping of a 300 g rat at 4.7 T (Agilent small animal system)*: TR = 34 ms; flip angle = 30°; number of echoes = 8; first echo = 4.23 ms; echo spacing 0.4 ms; averages = 8; slice orientation = coronal to kidney; frequency encoding = head-feet; FOV = (30 × 30) mm; matrix size = 128 × 128; resolution = (0.230 × 0.230) mm;

1 slice with 2.0 mm thickness; fat suppression = on; respiration trigger = on; acquisition time = 7.0–11.0 min (with triggering under isoflurane anaesthesia).

19. Shimming is particularly important, since macroscopic magnetic field inhomogeneities shorten T_2*, but provide no tissue specific information—rather they overshadow the microscopic T_2* effects of interest and hinder quantitative intra- and inter-subject comparisons. Shimming should be performed on a voxel enclosing only the kidney using either the default iterative shimming method or the Mapshim technique (recommended).
20. This serves to keep a record of the B_0 influence on the measured T_2*. It allows explanation of unusually small T_2* due to a bad shim. It may also be used later during the prost-processing for calculating a corrected T_2* by removing the influence B_0 inhomogeneities.
21. During the data analysis care must be taken to avoid noise biasing the mapping of T_2* and T_2. With increasing echo time the signal intensity in the images approaches more and more the noise floor, where the signal is so small that it is not detectable anymore. However, even though only noise is detected the signal is still above 0, because of the Ricean nature of the noise (negative values are "flipped" to the positive side). This means that the shape of the exponential curve will not fit well, as it expects the signal to decay toward 0. Adding an offset parameter to the fitted curve does not solve the problem because an offset will affect the signal intensities of all echoes, but the noise bias only affects those echoes where the true signal is very small. Instead a noise bias correction should be performed, which is described in the chapter by Periquito JS et al. "Analysis Protocols for MRI Mapping of the Blood Oxygenation–Sensitive Parameters T_2* and T_2 in the Kidney." Please note that you may not need to perform such a noise correction if all echo images are well above the noise floor.

Acknowledgments

This work was funded, in part (Thoralf Niendorf and Andreas Pohlmann), by the German Research Foundation (Gefoerdert durch die Deutsche Forschungsgemeinschaft (DFG), Projektnummer 394046635, SFB 1365, RENOPROTECTION. Funded by the Deutsche Forschungsgemeinschaft (DFG, German Research Foundation), Project number 394046635, SFB 1365, RENOPROTECTION).

This publication is based upon work from COST Action PARENCHIMA, supported by European Cooperation in Science and

Technology (COST). COST (www.cost.eu) is a funding agency for research and innovation networks. COST Actions help connect research initiatives across Europe and enable scientists to grow their ideas by sharing them with their peers. This boosts their research, career and innovation.

PARENCHIMA (renalmri.org) is a community-driven Action in the COST program of the European Union, which unites more than 200 experts in renal MRI from 30 countries with the aim to improve the reproducibility and standardization of renal MRI biomarkers.

Reference

1. Ben-Eliezer N, Sodickson DK, Block KT (2015) Rapid and accurate T2 mapping from multi-spin-echo data using bloch-simulation-based reconstruction. Magn Reson Med 73:809–817

Chapter 24

Renal MRI Diffusion: Experimental Protocol

João S. Periquito, Martin Meier, Thoralf Niendorf, Andreas Pohlmann, and Neil Peter Jerome

Abstract

Renal diffusion-weighted imaging (DWI) can be used to obtain information on the microstructure of kidney tissue, and has the potential to provide MR-biomarkers for functional renal imaging. Here we describe in a step-by-step experimental protocol the MRI method for measuring renal diffusion coefficients in rodents using ADC or IVIM models. Both methods provide quantification of renal diffusion coefficients; however, IVIM, a more complex model, allows for the calculation of the pseudodiffusion and fraction introduced by tissue vascular and tubular components. DWI provides information of renal microstructure contributing to the understanding of the physiology and the underlying processes that precede the beginning of pathologies.

This chapter is based upon work from the COST Action PARENCHIMA, a community-driven network funded by the European Cooperation in Science and Technology (COST) program of the European Union, which aims to improve the reproducibility and standardization of renal MRI biomarkers. This experimental protocol chapter is complemented by two separate chapters describing the basic concept and data analysis.

Key words Magnetic resonance imaging (MRI), Kidney, Mice, Rats, Diffusion, ADC, IVIM

1 Introduction

Diffusion weighting imaging (DWI) is an MR imaging technique sensitive to the motion of water molecules within a voxel of tissue. The random movement, also known as Brownian motion, of fluid molecules makes them spread out until a boundary stops them. In general, extracellular water molecules will have a larger net displacement over time than intracellular molecules. Intracellular molecules have more chances to collide with cell walls, organelles, and macromolecules. Diseases and pathologies that influence tissue properties and structure may either increase or decrease the diffusion behavior of water in tissues, which can be quantified using DWI [1, 2].

In DWI, the image contrast is based on the displacement of water molecules. Voxels where molecules present a larger

Andreas Pohlmann and Thoralf Niendorf (eds.), *Preclinical MRI of the Kidney: Methods and Protocols*, Methods in Molecular Biology, vol. 2216, https://doi.org/10.1007/978-1-0716-0978-1_24,

displacement during the diffusion-sensitization preparation will appear darker on the resulting image.

Sensitization to diffusion can be achieved by using an extra pair of magnetic field gradients during the pulse sequence, generating images with diffusion-weighting determined by the magnitude, duration, and separation of the gradients, which can be quantified by the acquisition parameter *b*-value [3].

The DWI signal decay across a series of images with different diffusion-weightings can then be analyzed, using more or less complex mathematical models, to quantify the diffusion parameters. Ideally, the acquisition should be designed considering the signal model one wishes to use. The simplest model considers only the apparent diffusion coefficient (ADC), an empirical parameter reflecting the overall water molecule motion in the tissue averaged over one or more directions using a small number of *b*-values. ADC can be estimated by fitting a monoexponential curve to the DWI signal as a function of b-value, and fitting signal curves on a pixel-by-pixel basis allows construction of diffusion parameter maps [4].

Perfusion in tissue introduces a pseudodiffusion component to the DWI signal, which cannot be quantified using the ADC model (but it will influence the calculated ADC if low b-values are included). A more complex model is needed to take separate out this effect. Intravoxel incoherent motion (IVIM) intends to model flow processes, which manifest as pseudodiffusion with a larger coefficient, by assuming the DWI signal as a function of the *b*-value is not monoexponential but biexponential. This method requires the acquisition of several *b*-values before the pseudodiffusion decays away, especially between *b*-values of 0 and 200 s/mm^2 [5].

This experimental protocol chapter is complemented by two separate chapters describing the basic concept and data analysis, which are part of this book.

This chapter is part of the book Pohlmann A, Niendorf T (eds) (2020) Preclinical MRI of the Kidney—Methods and Protocols. Springer, New York.

2 Materials

2.1 Animals

This experimental protocol is tailored for mice (variants of C57BL/6) with a body mass of 15–35 g. Advice for adaptation to rats is given as *Notes* where necessary.

2.2 Lab Equipment and Chemicals

1. Anesthesia: typically, 0.5–1.5% isoflurane is used for anesthesia administered to the mice using an anesthetic gas vaporizer (Leica Biosystems, Maryland, USA). For nonrecovery experiments, urethane solution (Sigma-Aldrich, Steinheim,

Germany; 20% in distilled water) can provide anesthesia for several hours with comparatively fewer side effects on renal physiology, which is an important issue. For nonrecovery experiments urethane solution (Sigma-Aldrich, Steinheim, Germany; 20% in distilled water) can provide anesthesia for several hours with comparatively fewer side effects on renal physiology, which is an important issue. For an in-depth description and discussion of the anesthesia please refer to the chapter by Kaucsar T et al. "Preparation and Monitoring of Small Animals in Renal MRI."

2. Gases: O_2, N_2, and compressed air, as well as a gas-mixing system (FMI Föhr Medical Instruments GmbH, Seeheim-Ober Beerbach, Germany) or general inhalation anesthesia equipment, including an anesthetic vaporizer, a flow meter, and an induction chamber.

2.3 MRI Hardware

The general hardware requirements for renal ^{1}H MRI on mice and rats are described in the chapter by Ramos Delgado P et al. "Hardware Considerations for Preclinical Magnetic Resonance of the Kidney." The technique described in this chapter has been tailored for MR preclinical systems at magnetic fields higher than 3 T but advice for adaptation to other field strengths is given where necessary. No special or additional hardware is required, except for the following:

A physiological monitoring system that can track the respiration and which is connected to the MR system such that it can be used to trigger the MRI scanner with respiration. Typically, we use the MR-compatible rodent monitoring and gating system (Small Animal Instruments, New York, USA) equipped with an air-pillow to monitor breathing rate.

2.4 MRI Techniques

The diffusion MRI pulse sequence includes a diffusion preparation responsible for the diffusion sensitization. Specifically, sensitisation to diffusion and/or other motion of water molecules is achieved by inclusion of an extra pair of magnetic field gradients during the acquisition, generating images with varying degrees of diffusion-weighting. The degree of diffusion weighting depends on the area of each of the diffusion gradients (amplitude G and duration δ) as well as the time spacing between the pair (Δ); the resulting weighting is commonly specified by the compound parameter *b*-value (Fig. 1). The diffusion module is followed by fast image readout such as echo planar imaging (EPI). Other readouts are available for DWI (*see* **Note 1**), but DW-EPI is the standard since it provides the higher SNR in acceptable acquisition times, and so will be used in this chapter.

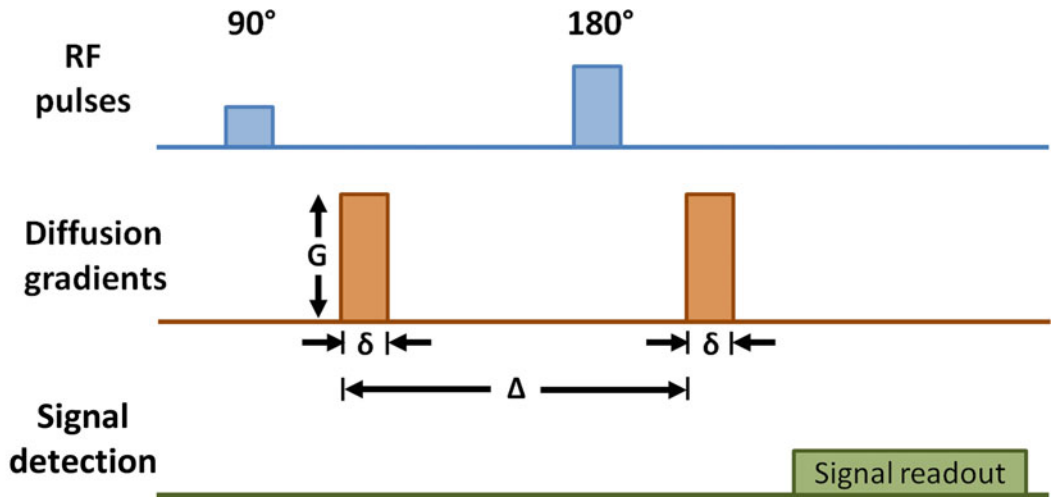

Fig. 1 Diffusion preparation ("Diffusion gradients"). The degree of diffusion weighting (measured by the "*b*-value" [mm/s^2]) depends on the area of the extra pair of gradients (amplitude *G* and duration δ) as well as the time spacing between them (Δ): $b = \gamma^2 G^2 \delta^2 \left(\Delta - \frac{\delta}{3}\right)$

3 Methods

3.1 MR Protocol Setup

All the mentioned MR parameters are adjustable; the provided suggestions are based on experience, but the end protocol is likely to be adjusted from these values. For more details on what goes toward making these decisions please refer to the chapter by Jerome NP et al. "Renal Diffusion-Weighted Imaging (DWI) for Apparent Diffusion Coefficient (ADC), Intravoxel Incoherent Motion (IVIM), and Diffusion Tensor Imaging (DTI): Basic Concepts"of this book.

3.1.1 DW-EPI for ADC

1. Load the DW-EPI sequence.
2. Sequence type: 2D Echo Planar Imaging sequence with diffusion preparation module that has a defined Δ and δ and a *G* which can be incremented within a single scan. This is a standard sequence on Bruker MRI systems, called "DW-EPI."
3. The diffusion parameters are then adjusted to allow detection of incoherent movement of molecules. The range of displacements measured with DWI is typically in the order of 1–20 μm, allowing for quantitative measurements that reflect micromorphological and physiological changes in tissues. As a recommendation a $\delta = 3.5$ ms and a $\Delta = 8.5$ ms should be used (*see* **Note 2**).
4. Set up your *b*-values to the following values: 0, 200, 600 s/mm^2 over three orthogonal directions *x*: (1,0,0), *y*: (0,1,0) and *z*: (0,0,1).

5. Repetition time (TR): choose ~500 ms for good signal stability and signal-to-noise per time (SNR/t) efficiency. TR will be limited by the length of the excitation pulse, length of echo train and the number of slices you acquire.
6. Echo time (TE): use the shortest TE. Acquisition bandwidth should be considered to shorten the inter-echo-time.
7. Segments: as low as possible to reduce scan time, however 1 segment (single-shot) might create unacceptable distortions on phase encoding. A high number of segments will increase scan time and makes the acquisition more prone to motion artifacts. As a recommendation two segments should be used (multishot DW-EPI) with a matrix size of 172 × 172 with an FOV of 30 × 30 mm.
8. Acquisition bandwidth (BW): ~ 350.000 Hz, one wants to acquire as many lines of k-space as possible to minimize motion distortions of the images. For that reason, it is advantageous to have a low inter-echo-time. Larger inter-echo-times are not advisable because the SNR in the kidney will be so low that these images must be excluded.
9. Enable fat saturation. On ultrahigh field systems this works well to avoid fat signal overlaying the kidney due to chemical shift. At lower field strengths it might work less efficient.
10. Enable the respiration trigger (per slice). This is essential to reduce motion artefacts, reduce motion blurring and unwanted intensities variations among the images acquired with different *b*-values (*see* **Note 3**).
11. Choose as phase-encoding direction the L-R direction and adapt the geometry so that the FOV in this direction includes the entire animal.
12. Use frequency encoding in head-feet (rostral-caudal) direction to avoid severe aliasing. Adjust the FOV to your needs keeping in mind that in this direction the FOV can be smaller than the animal and a smaller FOV permits a smaller acquisition matrix, and in turn a shorter echo-spacing.
13. Increase the number of averages to improve signal-to-noise ratio by a factor of $\sqrt{}$averages, especially important for higher *b*-values (use nine averages as a recommendation).
14. To reach a steady-state magnetization is advisable to use dummy scans, two as a recommendation.
15. For an example of a specific parameter set please *see* **Notes 4** and **5**.
16. For adaptation of the geometry to rats (*see* **Note 6**).

3.1.2 DW-EPI for IVIM

1. Load the DW-EPI sequence.
2. Use the same parameters as DWI-EPI for ADC (TE, TR, matrix size, dummy scans, averages, bandwidth, segments).
3. Keep the same diffusion parameters as for the ADC but increase the number of *b*-values from 3 to at least 7 (e.g., 0, 50, 100, 200, 400, 600, and 740 s/mm^2) to probe fast diffusion from blood perfusion.

3.2 In Vivo DWI

3.2.1 Animal Preparation

1. Anesthetize the animal and transfer it to scanner. For an in-depth description and discussion of the anesthesia please refer to the chapter by Kaucsar T et al. "Preparation and Monitoring of Small Animals in Renal MRI."
2. Start the temperature monitoring system, apply some surgical lubricant to the temperature probe and place it in the rectum of the animal.
3. Attach the respiration sensor (e.g., balloon) to the chest of the animal using adhesive tape. Start and set up the respiratory monitoring system. If necessary, adjust the position of the respiration sensor until the amplitude of the respiration trace is sufficiently large for the system to reliably detect the trigger points at the beginning of expiration (*see* **Note 3**).

3.2.2 Scanner Adjustments and Anatomical Imaging

1. Acquire a fast pilot scan to obtain images in three orthogonal planes *x*, *y*, and *z*.
2. Acquire anatomical images in several oblique orientations to facilitate planning a coronal slice orientation with regard to the long axis of the kidney, as described in the chapter by Pohlmann A et al. "Essential Practical Steps for MRI of the Kidney in Experimental Research" (open-access).
3. Perform localized shimming on the kidney as described in the chapter by Pohlmann A et al. "Essential Practical Steps for MRI of the Kidney in Experimental Research" (open-access). NB: shimming is crucial for DW-EPI (*see* **Note 7**), because a poor shim can lead to large distortions and add errors in the measured diffusion coefficients.
4. Acquire a 3D B_0 field-map without adaptation of the geometry (optional; *see* **Notes 8** and **9**).

3.2.3 Baseline Condition

1. Load the 2D multishot EPI sequence, adapt the slice orientation to provide a coronal or axial view with respect to the kidney (in scanner coordinates this is double-oblique).
2. In the monitoring unit set the trigger delay so that the trigger starts at the beginning of the expiratory plateau (no chest or diaphragm motion) and the duration such that it covers the

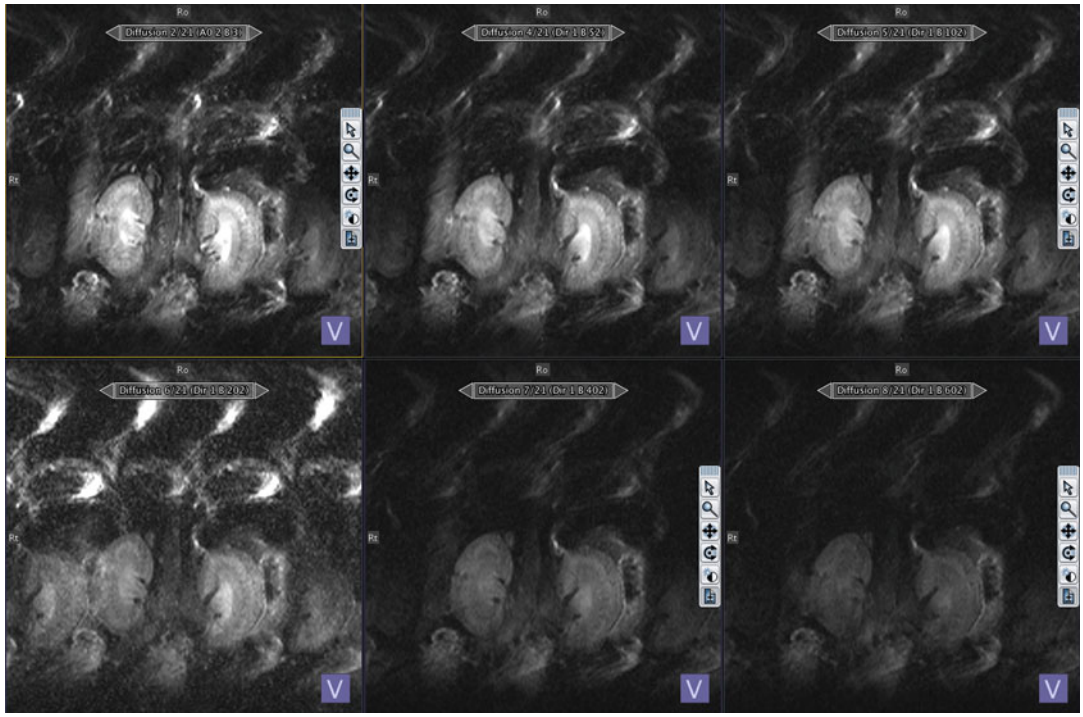

Fig. 2 Series of six diffusion-weighted images of a healthy mouse kidney acquired with DW-EPI sequence at 7.0 T. Images correspond to *b*-values: 0, 50, 100, 200, 400, and 600 mm/s^2. EPI readouts are prone to magnetic susceptibility artifacts, low-phase encoding bandwidth leads to ΔB_0 induced frequency dispersions which causes image distortion. When using a segmented EPI readout a phase deviation occurs between the different segments in k-space leading to ghosting artefacts visible in the above images [7]

entire expiratory phase, that is, until just before inhalation starts (1/2–2/3 of breath-to-breath interval) (*see* **Note 3**).

3. In the monitoring unit set the trigger delay so that the trigger starts at the beginning of the expiratory plateau (no chest or diaphragm motion) and the duration to a short value, such as 10 ms (*see* **Note 3**).
4. Run the EPI scan. Example images are shown in Fig. 2.

4 Notes

1. Other readouts apart from EPI can be use in DWI such as rapid acquisition with relaxation enhancement (RARE) (Fig. 3) which is less prone to suffering from geometric distortion specially at ultrahigh magnetic fields [6].
2. Gradients systems might differ from MR scanner to MR scanner even for the same magnetic field. If the gradient system cannot reach *b*-value of 600, consider to adjust $\delta = 3.5$ ms and

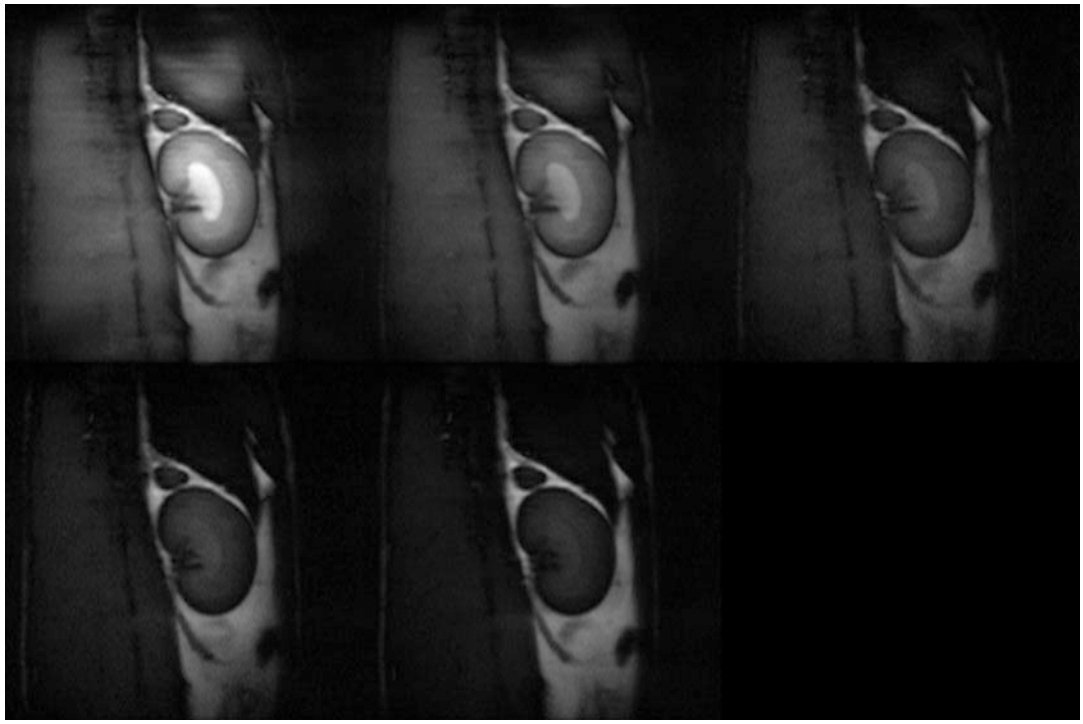

Fig. 3 Series of five diffusion-weighted images of a healthy mouse kidney acquired with single-shot DW-RARE sequence at 9.4 T. Images correspond to *b*-values: 0, 200, 300, 400, and 600 mm/s^2. A RARE readout can be used to minimize the magnetic susceptibility artifacts which cause geometric distortions on DW-EPI. DW-RARE is not commercially available, pulse programming skills are needed to implement it [6]

a $\Delta = 8.5$ to higher values. Record and report all diffusion parameters used.

3. You must monitor the respiration continuously throughout the entire experiment.
4. *Example for ADC of a 30 g mouse at 7 T (Bruker small animal system)*: TR = 500 ms; 3 *b*-values: 0, 200, 600 s/mm^2, diffusion directions: 3 (orthogonal), effective TE = 56.87 ms; Segments = 2; averages = 9; slice thickness = 1.2 mm; slice orientation = axial; frequency encoding = head-feet; FOV = 30 × 30 mm; matrix size = 172 × 172; Bandwidth = 350.000 Hz; fat suppression = on; scan time ≈ 80 s.
5. *Example for ADC of a 270 g rat at 9.4 T (Bruker small animal system)*: TR = 500 ms; 3 *b*-values: 0, 200, 600 s/mm^2, diffusion directions: 3 (orthogonal), effective TE = 56.87 ms; Segments = 2; averages = 9; slice thickness = 1.2 mm; slice orientation = axial; frequency encoding = head-feet; FOV = 45 × 45 mm; matrix size = 172 × 172; Bandwidth = 350.000 Hz; fat suppression = on;, scan time ≈ 80 s.

6. For rats increase the FOV to the body width and keep the matrix size the same or similar. The relative resolution is then identical and the SNR should also be similar, because the larger rat RF coil provides worse SNR (e.g., eight-channel rat body phase array receive coil vs eight-channel mouse body phase array receive coil).
7. Shimming is particularly important, since macroscopic magnetic field inhomogeneities affect EPI readout and might create severe geometric distortions. Shimming should be performed on a voxel enclosing the kidney using either the default iterative shimming method or the Mapshim technique (recommended).
8. *Example parameters for field mapping of a 30 g mice at 9.4 T (Bruker small animal system)*: use the vendors default protocol *AnyObject* > *AnyRegion* > *Adjustments* > *ADJ_B0MAP*. TR = 20 ms; flip angle = 30°; first echo = 1.60 ms; echo spacing = 3.57 ms; fat/water in-phase = on; slice orientation = main orientations (no angles) and offset = 0; FOC = (58 × 58 × 58) mm; matrix size =64 × 64 × 64; resolution = (0.904 × 0.904 × 0.904) mm; respiration trigger = off; acquisition time = 1–2 min.
9. This serves to keep a record of the B_0 influence on the measured DW-EPI images. It allows explanation of unusually distortions due to an imperfect shim.

Acknowledgments

This work was funded, in part (Thoralf Niendorf, Andreas Pohlmann, and Joao Periquito), by the German Research Foundation (Gefoerdert durch die Deutsche Forschungsgemeinschaft (DFG), Projektnummer 394046635, SFB 1365, RENOPROTECTION. Funded by the Deutsche Forschungsgemeinschaft (DFG, German Research Foundation), Project number 394046635, SFB 1365, RENOPROTECTION).

This chapter is based upon work from COST Action PARENCHIMA, supported by European Cooperation in Science and Technology (COST). COST (www.cost.eu) is a funding agency for research and innovation networks. COST Actions help connect research initiatives across Europe and enable scientists to enrich their ideas by sharing them with their peers. This boosts their research, career, and innovation.

PARENCHIMA (renalmri.org) is a community-driven Action in the COST program of the European Union, which unites more than 200 experts in renal MRI from 30 countries with the aim to improve the reproducibility and standardization of renal MRI biomarkers.

References

1. Hahn EL (1950) Spin echoes. Phys Rev 80:580–594
2. Carr HY, Purcell EM (1954) Effects of diffusion on free precessions in nuclear magnetic resonance experiments. Phys Rev 94:630–635
3. Stejskal EO, Tanner JE (1965) Spin diffusion measurements: spin echoes in the presence of a time-dependent field gradient. J Chem Phys 42:288–292. https://doi.org/10.1063/1.1695690
4. Le Bihan D et al (1950) Imagerie de diffusion in-vivo par resonance magnetique. CR Acad Sci 15:1109–1112
5. Le Bihan D et al (1988) Separation of diffusion and perfusion in intravoxel incoherent motion MR imaging. Radiology 168(2):497–505
6. Periquito J et al (2020) Diffusion-weighted renal MRI at 9.4 Tesla using RARE to improve anatomical integrity. *Scientific Reports* 9(1):1–12
7. Paul K et al (2015) Diffusion-sensitized ophthalmic magnetic resonance imaging free of geometric distortion at 3.0 and 7.0 T: a feasibility study in healthy subjects and patients with intraocular masses. Investig Radiol 50:309–321

Chapter 25

Dynamic Contrast Enhanced (DCE) MRI-Derived Renal Perfusion and Filtration: Experimental Protocol

Pietro Irrera, Lorena Consolino, Walter Dastrù, Michael Pedersen, Frank G. Zöllner, and Dario Livio Longo

Abstract

Dynamic contrast-enhanced magnetic resonance imaging (DCE-MRI) can provide a noninvasive way for assessing renal functional information following the administration of a small molecular weight gadolinium-based contrast agent. This method may be useful for investigating renal perfusion and glomerular filtration rates of rodents in vivo under various experimental (patho)physiological conditions. Here we describe a step-by-step protocol for DCE-MRI studies in small animals providing practical notes on acquisition parameters, sequences, T_1 mapping approaches and procedures.

This chapters is based upon work from the COST Action PARENCHIMA, a community-driven network funded by the European Cooperation in Science and Technology (COST) program of the European Union, which aims to improve the reproducibility and standardization of renal MRI biomarkers. This experimental protocol chapter is complemented by two separate chapters describing the basic concept and data analysis.

Key words Magnetic resonance imaging (MRI), Kidney, Mice, Rats, Dynamic contrast-enhanced (DCE), Contrast agent, T_1 map

1 Introduction

Kidneys play an important role in fluid regulation, waste products elimination, and homeostasis of salts and pH. Therefore, accurate measurement of kidney function is essential for monitoring early renal injuries, disease progression, renal transplantation and in assessing therapeutic efficacy after renal failure [1, 2]. Magnetic resonance imaging (MRI) has emerged as a powerful technique that combines anatomical details with functional information. In recent years, various MRI techniques have been investigated for assessing renal function, including dynamic contrast-enhanced (DCE) MRI, arterial spin labelling (ASL), blood oxygenation level dependent (BOLD), diffusion weighted imaging (DWI), sodium imaging, chemical exchange saturation

Andreas Pohlmann and Thoralf Niendorf (eds.), *Preclinical MRI of the Kidney: Methods and Protocols*, Methods in Molecular Biology, vol. 2216, https://doi.org/10.1007/978-1-0716-0978-1_25,

transfer (CEST), and hyperpolarized MRI [3–9]. These techniques have shown promising results for the noninvasive evaluation of several renal function, including filtration, perfusion, oxygenation, pH, homeostasis, and others [10–27]. Among them, DCE-MRI or MR renography has emerged as a reliable method to reveal renal pathophysiology, functional and hemodynamic parameters. DCE-MRI relies on bolus administration of a gadolinium-based contrast agent (CA) [16], which changes the intrinsic longitudinal (T_1) and transversal (T_2) relaxation rates of protons in tissue. This means that administration of CA leads to an increased signal intensity on T_1-weighted images or decreased signal intensity on T_2-weighted images. DCE-MRI usually refers to T_1-weighted MR imaging techniques combined with a gadolinium-based CA using an acquisition scheme with a high temporal resolution. In the kidney the acquired signal over time leads to an MRI renogram, where the absolute signal intensity, in complex manner, depends on the native T_1 value, MRI sequence parameters, the specific magnetic relaxivity constant of the CA (the contrast agent efficiency, dependent also on its chemical structure [28–34]) and the concentration of the CA residing in the tissue [35, 36].

The main purpose of DCE-MRI is to reveal information about extravascular permeability, blood perfusion and compartmental kinetics. In practice, this method provides images prior and following the administration of the CA using a continuous image acquisition protocol. In kidneys, DCE-MRI is suitable for assessing kidney function in terms of filtration and perfusion [17]. Different post-processing methods allow estimations of kidney function and perfusion, either from simple semiquantitative approaches to more elaborated model-based analyses [37–42].

Here we describe step-by-step an experimental dynamic contrast enhanced (DCE) MRI protocol for monitoring the passage of a Gd-based tracer in the kidneys of rodents. The rationale for the choosing acquisition parameters is given in generic terms, together with specific parameter examples.

This experimental protocol chapter is complemented by two separate chapters describing the basic concepts and data analysis, which are part of this book.

This chapter is part of the book Pohlmann A, Niendorf T (eds) (2020) Preclinical MRI of the Kidney—Methods and Protocols. Springer, New York.

2 Materials

2.1 Animals

This experimental protocol was tailored for immune-competent (typically C57BL/6 and Balb/C) or immune-compromised (nude, NOD-SCID) mice with a body mass of 15–35 g. Advice for adaptation to rats is given as *Notes* where necessary. All animal

studies have to be carried out in compliance with specific legislation covering the use of animals for scientific purposes. Therefore, all experiments must be authorized under national regulations.

2.2 Lab Equipment and Chemicals

1. Mouse tail illuminator/restrainer for catheterizing the tail vein.
2. Saline solution or heparin solution, 1-ml syringe, catheter (e.g., PE 20 polyethylene tubing) of known inner diameter to hold the saline flush and for contrast agent bolus is required.
3. Anesthesia: please refer to the chapter by Kaucsar T et al. "Preparation and Monitoring of Small Animals in Renal MRI" for an in-depth description and discussion of the anesthesia. Typically, 0.5–1.5% isoflurane is used for anesthesia administered to the mice using an anesthetic gas vaporizer (Leica Biosystems, Maryland, USA). For nonrecovery experiments, urethane solution (Sigma–Aldrich, Steinheim, Germany; 20% in distilled water) can provide anesthesia for several hours with comparatively fewer side effects on renal physiology, which is an important issue. For intramuscular anesthesia, please refer to **Note 1**.
4. Gases: O_2, N_2, and compressed air, as well as a gas-mixing system or general inhalation anesthesia equipment, including an anesthetic vaporizer, a flow meter, and an induction chamber.
5. Mouse cradle.
6. Gd-based contrast agents: typically, small molecular weight FDA-approved gadolinium-based contrast agents are employed, such as gadoteridol (Prohance®, Bracco Imaging SpA, Milano, Italy), gadobutrol (Gadovist®, Bayer Healthcare Pharmaceuticals, Germany), or gadoteric acid (Dotarem®, Guerbert, France). Such clinically available contrast agents have stock concentrations of 0.5–1.0 mol/l that need to be diluted for handling volumes with less error (*see* **Note 2**).
7. Small animal ventilator: animals (rats) needs to be ventilated so the DCE-MRI acquisition can be gated to minimize the respiratory motion artifacts.
8. Syringe infusion pump: an MRI-compatible single syringe pump (Harvard Bioscience, Holliston, USA) for contrast agent administration for allowing precise timing infusion.

2.3 MRI Hardware

The general hardware requirements for renal 1H MRI on mice and rats are described in the chapter by Ramos Delgado P et al. "Hardware Considerations for Preclinical Magnetic Resonance of the Kidney." The technique described in this chapter was tailored for MRI preclinical systems at a magnetic field strength of 7 T but advice for adaptation to other magnetic field strengths is given where necessary (*see* **Note 3**). No special or additional hardware is required, except for the following:

1. A physiological monitoring system that can track the respiration and which is connected to the MRI system such that it can be used to synchronize DCE-MRI with respiration. Typically, we use an MRI-compatible rodent monitoring and gating system equipped with an air-pillow to monitor breath rate (Small Animal Instruments, New York, USA).

2.4 MRI Techniques

DCE-MRI experiments are performed by dynamic acquisitions of a strongly T_1-weighted imaging technique. The acquired signal following the CA administration is converted to relative concentrations of the gadolinium agent using either phantom calibration scales or by mathematical calculation of the sequence equation that describes the relationship between signal and MRI sequence parameters. The MRI sequence parameters, required volume coverage, spatial resolution, and SNR will determine the final temporal resolution. Several T_1 mapping approaches can be exploited for measuring the longitudinal relation times, a detailed description of different methods is provided in the chapter by Garteiser P et al. "Experimental Protocols for MRI Mapping of Renal T_1."

3 Methods

3.1 MR Protocol Setup

3.1.1 Variable Repetition Time (VTR) Acquisition for T_1 Mapping

1. Use a 2D RARE (rapid acquisition with refocused echoes) sequence with variable repetition times (RAREVTR on a Bruker MR system).
2. Set the acceleration factor (RARE-factor or echo train length, ETL) to at least 4 in order to shorten the acquisition time; an acceleration factor of 8–16 can be used to further shorten the acquisition time by sampling more k-space lines within a single repetition period (TR). Centric encoding can be exploited to minimize T_2 effects with increasing doses, but at the expenses or "blurred" images.
3. Set the echo time (TE) as short as possible for pure T_1-weight; in our setup an effective TE of 25 ms (defined by the acquisition of the central k-space line) was used.
4. Choose enough averages in order to have a sufficient signal to noise ratio (SNR) of above 30.
5. Repeat the RARE acquisition a number of times by changing the value of the repetition time (TR) to sample changes in signal intensities according to the expected T_1 values of the kidneys.
6. Because of the variability of the T_1 values inside the kidney regions, choose the TRs values to span a range large enough to permit an accurate calculation of T_1 by selecting 3–7 TR values in the range 100–10,000 ms (*see* **Note 4**).

7. For in vivo experiments, keep the overall acquisition time as short as possible by considering a trade-off between number of TRs, averages and matrix size (or spatial resolution).
8. For an example of a specific parameter set please *see* **Note 5**.

3.1.2 Variable Flip Angle (VFA) Acquisition for T_1 Mapping

1. Use a 2D gradient-echo sequence (FLASH on a Bruker system).
2. Set the echo time (TE) as short as possible for heavily T_1 weighting; in our setup a TE of 1.5 ms was used.
3. In order to have a sufficient signal to noise ratio, at least two averages have been acquired or enough averages for SNR > 30.
4. Repeat the FLASH acquisition a number of times by changing the value of the flip angle (FA). The changes in signal intensities will follow a parabolic curve, thus low flip angles and higher flip angles are needed to sample both side of this curve. Acquire a minimum of 2–3 flip angles, considering that experiments with more flip angles will improve the goodness of the T_1 estimate.
5. Set the TR in the range 10–100 ms for providing good T_1 weighting. Shorter TR increases T_1 weighting, but with detrimental SNR values; thus, a trade-off must be chosen, even considering number of averages and overall acquisition time.
6. For an example of a specific parameter set please *see* **Note 6**.

3.1.3 Fast Low Angle Shot (FLASH) T1-Weighted Sequence for DCE-MRI Experiments

1. Use a T_1-weighted sequence as a fast low angle shot (FLASH) sequence (in Bruker systems, this sequence refers to a dubbed FLASH sequence).
2. Use short TR to increase T_1-weighting, but this will decrease SNR. Therefore, a good balance should be found between strongly T_1-weighted images and image quality with sufficient SNR. Besides, TE and FA affect T_1-weighting and SNR. A good TR range could be between 5 and 100 ms (usually shorter values for 3D imaging and longer for 2D multislice acquisition).
3. Use the shortest echo time (TE) possible for pure T_1 weight.
4. Flip Angle (FA): high FA corresponds to a strong T_1 weighting, but at expenses of reduced SNR, therefore a good balance may result in FAs in the range 10–60°.
5. Use Partial Fourier acceleration to reduce the size of the acquired matrix and improve the time efficiency of data acquisition.
6. Use a high acquisition bandwidth (BW) to shorten TE, while keeping an eye on the SNR, which decreases with the square root of the increasing BW. For the image with the shortest TE an SNR of at least 30 is recommended.

7. Employ Fat Saturation modules. It is important to avoid fat signal overlaying with the kidney due to chemical shift.
8. Respiration trigger: there is no need to use respiratory triggering (per slice).
9. Adapt the geometry (or slice position) so that animal fits into FOV in Left-Right direction (approximately 30–40 mm according to the inner coil diameter) and use frequency encoding in Head-Feet direction. Use a slice with the lowest thickness the SNR allows, typically around 1–2 mm. The thinner the slices the better, as this improves the resolution which can be readily found on the raw images.
10. Use the highest in-plane resolution that the SNR allows, typically around 96×96 to 128×128 for FOV of 30×30 mm^2 or 40×40 mm^2. This resolution should be balanced by the need for sufficient SNR in the images. Zero-filling or use of partial Fourier techniques in the phase encoding direction can be helpful to speed up acquisition to minimize motion artifacts and contrast agent concentration changes during the acquisition. One may use half-Fourier acquisition schemes in read direction (asymmetric echo) to further shorten the TE. Reducing the excitation and refocusing pulse lengths to below 1.5 ms can then also help to shorten TE.
11. For an example of specific parameter sets for a 7 T MRI system, please *see* **Notes 7** and **8**, whereas for a scanner operating at 3 T please *see* **Note 9.**

3.2 Preparations of the Contrast Agent Injection and of the Catheter

1. Fill the 1-ml syringe with the contrast agent solution (*see* **Note 2**).
2. Prepare the catheter by filling the PE20 tubing with the contrast agent solution, and with 20–40 μl of a heparin solution (or a saline solution), between the needle (the animal) and the contrast agent solution to prevent clotting before the contrast agent will be injected.
3. According to the length of the catheter (usually 60–100 cm to exit from the magnet bore) the contrast agent solution can be injected directly from the syringe containing the contrast agent or by changing the syringe with one filled with a (heparin-free) saline solution for the postinjection flush.

3.3 Preparations of the Mouse

1. Place the mouse on a mouse tail illuminator restrainer for catheterizing the tail vein. The tail vein can be catheterized by placing a 27/29-G needle in the animal.
2. Induce anesthesia in animals via isoflurane in an induction box. Then transfer the animal to the MRI system (*see* **Note 10**).
3. Set up the temperature monitoring (rectal probe) and respiratory monitoring (balloon on chest) unit. During imaging, keep

the animal's respiration rate at 35–80 breaths per min by adjusting the dose of anesthesia (approximately 1–1.5% isoflurane with air and oxygen mixed at a 3:1 ratio administered through a nose cone attached to the animal bed and ophthalmic ointment will be applied to the eyes) (*see* **Note 11**).

4. Perform anatomical imaging as described in the chapter by Pohlmann A et al. "Essential Practical Steps for MRI of the Kidney in Experimental Research."
5. Since the AIF should be sampled with the same temporal resolution of the DCE-MRI experiment, selection of anatomical slices including large vessels near the kidneys should be considered.
6. Perform localized shimming on the kidney imaging as described in the chapter by Pohlmann A et al. "Essential Practical Steps for MRI of the Kidney in Experimental Research."

3.4 In Vivo T_1 Mapping

Typically, a T_1 map is acquired before the injection of Gd-based agent.

1. Select the same geometry of the anatomical images, with the same number of slices and position.
2. Load or select one of the several T_1 mapping sequences previously described (3.1). Adapt the same slice orientation as for the anatomical image with coronal or axial view with respect to the kidneys.
3. Run the T_1-mapping scan. Examples images are shown in Fig. 1 and Fig. 2.

3.4.1 DCE-MRI Experiment

1. Load the T_1-weighted sequence, adapt the slice orientation to provide a coronal or axial view with respect to the kidney (in scanner coordinates this is double-oblique) by importing the same geometry as for the anatomical (and T_1 mapping sequence).
2. Set the required number of repetitions accordingly to the sampling time and to the duration of the dynamic acquisition. Typically, 50–100 repetitions provide enough points to be exploited by any of the analysis procedures.
3. Initiate the DCE-MRI scan.
4. After some baseline image acquisition (5–10 images before the injection are enough to derive average baseline values and signal oscillations) perform an intravenous bolus injection of the Gd-based CA through the tail vein at a dose of 0.02–0.1 mmol Gd /kg b.w. by using a power injector to maintain the exact administration rate for each imaged mouse.
5. A demonstration of the signal intensity changes that can be expected for the DCE-MRI experiment across the kidneys is

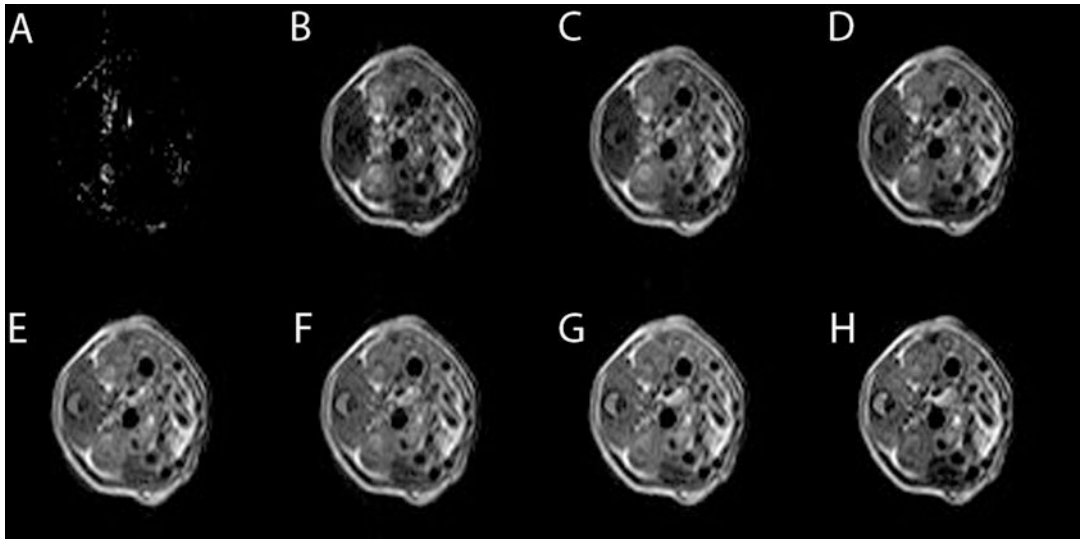

Fig. 1 Representative T_1-weighted images in kidneys obtained with the VTR scheme at different repetition times (TR) values: 75 ms (**a**), 534 ms (**b**), 1076 ms (**c**), 1738 ms (**d**), 2589 ms (**e**), 3782 ms (**f**), 5791 ms (**g**), and 15000 ms (**h**). Acquisition details are provided in **Note 5**

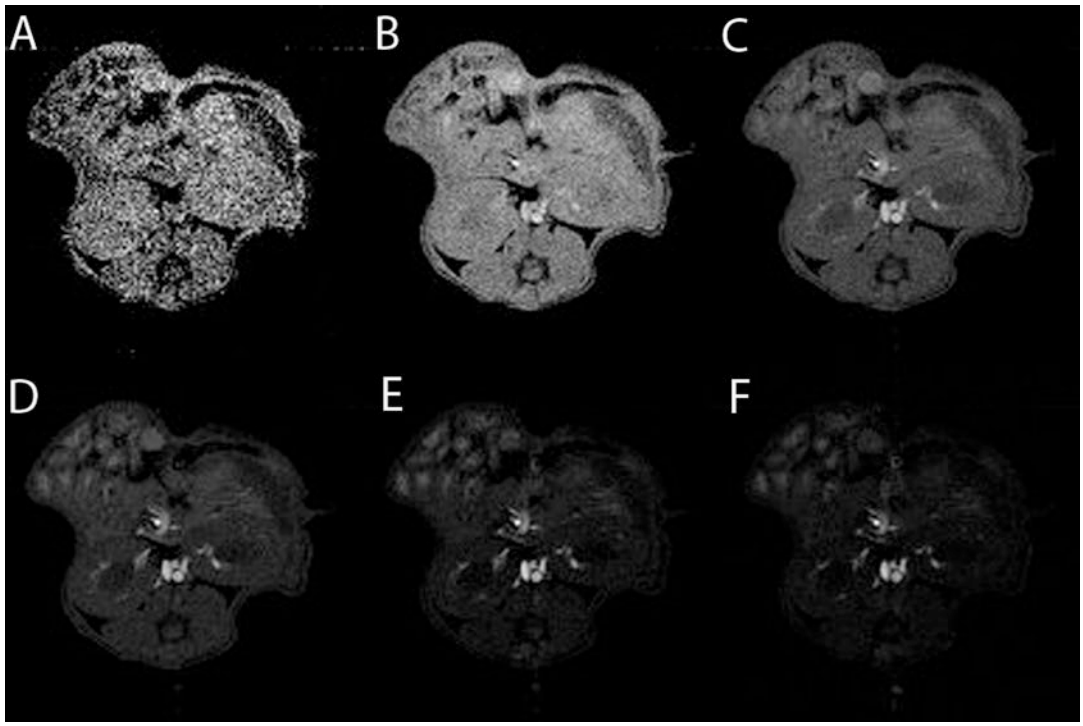

Fig. 2 Representative T_1-weighted images in kidneys obtained with VFA T_1 mapping approach by varying the excitation pulse flip angle values: 5° (**a**), 15° (**b**), 30° (**c**), 45° (**d**), 60° (**e**), and 75° (**f**) with a 7 T MRI system. Acquisition details are provided in **Note 6**

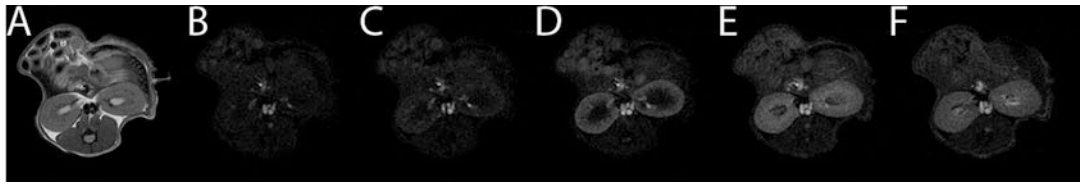

Fig. 3 Representative DCE-MRI images in kidneys (transversal orientation) at different time points following Gd-based contrast agent injection with a 7 T MRI scanner. Anatomical T_2-weighted (**a**) and GRE-FLASH T_1-weighted images before (**b**) and 4 s (**c**), 30 s (**d**), 5 min (**e**), and 10 min (**f**) after gadoteridol injection (dose 0.1 mmol Gd/kg b.w.). Acquisition details are provided in **Note 7**

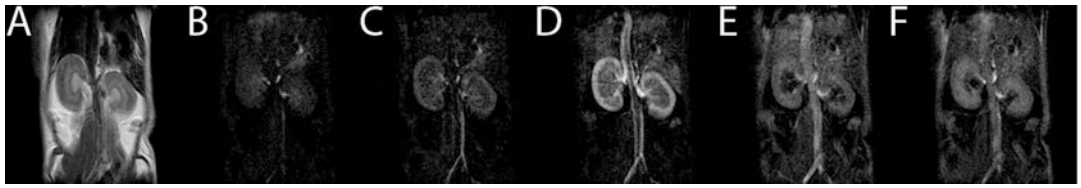

Fig. 4 Representative DCE-MRI images in kidneys (coronal orientation) at different time points following Gd-based contrast agent injection with a 7 T MRI scanner. Anatomical T_2-weighted (**a**) and GRE-FLASH T_1-weighted images before (**b**) and 4 s (bc), 30 s (**d**), 5 min (**e**), and 10 min (**f**) after gadoteridol injection (dose 0.1 mmol Gd/kg b.w.). Acquisition details are provided in **Note 8**

given in Fig. 3 (axial orientation) and Fig. 4 (coronal orientation).

4 Notes

1. Intramuscular anesthesia can be administered as a mixture of xylazine 5 mg/kg (Rompun, Bayer, Italy) and tiletamine/zolepan 20 mg/kg (Zoletil 100, Virbac, Italy) with a dose dependent on the length of the MRI session. Usually, a 40–80 μl volume allows for a sleeping time of 30–60 min for a 25 g mouse.
2. A required dose for DCE-MRI in the kidneys is in the range 0.01–0.1 mmol Gd/kg b.w. that would require too small volumes of the stock solution. Therefore, it is advisable to dilute stock solutions to ca. 50 mmol/l. For instance, a 25 g mouse would receive 50 μl of 50 mmol/l Gd-complex to achieve a dose of 0.1 mmol Gd/kg. Please avoid the inclusion of air bubbles in the catheter filled with the saline solution or with the contrast agent solution that will be injected into the animals.
3. DCE-MRI experiments are described for Bruker MRI systems, such as Avance 300 (7 T) and Biospec (3 T), (Bruker, Ettlingen, Germany) or for a Magnetom Skyra 3 T (Siemens Healthcare, Erlangen, Germany). Standard ^{1}H radiofrequency-coils

(birdcage, quadrature) or phased-array ^{1}H coils can be used for data reception.

4. Within the Bruker method, specific TR values can be suggested according to the estimated T_1 values of the tissue.
5. For estimated T_1 of 1–3 s, 10 TR values can be used (580, 810, 1075, 1380, 1740, 2180, 2740, 3525, 4830, and 10,000 ms) to correctly follow signal intensities recovery until plateau. With 10 TR values complete acquisition lasted 8:40 min (for 96 × 96 matrix and 8 slices).
6. For estimated T_1 values of 1–3 s, we used six different FA values (5°, 15°, 30°, 45°, 60°, and 75°). With a TR of 80 ms and matrix size of 96 × 96, the single image acquisition lasted more than 15 s (8 slices). The complete acquisition time of the VFA T_1 map with six FA values is approximately 2 min.
7. Example for DCE-MRI using a FLASH readout at 7 T: TR: 16 ms; TE: 1.6 ms; FA: 30°; scan averages: 2; slice thickness: 1.5 mm; slice number: 1; slice orientation: axial; frequency encoding: head-feet; FOV = 30 × 30 mm^2; matrix size = 128 × 128; fat suppression = on; acquisition time per image: 4 s; number of repetitions: 150.
8. Example for DCE-MRI using a FLASH readout at 7 T: TR: 15 ms; TE: 1.7 ms; FA: 30°; scan averages: 2; slice thickness: 1.5 mm; slice number: 1; slice orientation: coronal; frequency encoding: head-feet; FOV = 30 × 30 mm^2; matrix size = 128 × 128; fat suppression = on; acquisition time per image: 4 s; number of repetitions: 150.
9. Example for DCE-MRI using a 3D time-resolved angiography with stochastic trajectories (TWIST) sequence at 3 T: TR = 3.4 ms, TE = 1.4 ms, FA: 20°, FOV = 114 × 50 mm^2, generalized autocalibrating partially parallel acquisition (GRAPPA) of factor 2, matrix = 192 × 84; slice number: 2, voxel resolution = 0.6 × 0.6 × 1.2 mm^3. TWIST view sharing: 15% central region, 20% sampling density in the outer region, nominal temporal resolution 0.9 s per volume. Images were continuously acquired for 6 min.
10. Mice can be alternatively anesthetized with intramuscular anesthesia, tail veins heated with hot water/heater equipment at 37 °C and catheter placed in the animal.
11. It is important to monitor the respiration continuously throughout the entire experiment.

Acknowledgments

The Italian Ministry for Education and Research (MIUR) is gratefully acknowledged for yearly FOE funding to the Euro-BioImaging Multi-Modal Molecular Imaging Italian Node (MMMI).

This chapter is based upon work from COST Action PARENCHIMA, supported by European Cooperation in Science and Technology (COST). COST (www.cost.eu) is a funding agency for research and innovation networks. COST Actions help connect research initiatives across Europe and enable scientists to enrich their ideas by sharing them with their peers. This boosts their research, career, and innovation.

PARENCHIMA (renalmri.org) is a community-driven Action in the COST program of the European Union, which unites more than 200 experts in renal MRI from 30 countries with the aim to improve the reproducibility and standardization of renal MRI biomarkers.

References

1. Sawhney S, Mitchell M, Marks A, Fluck N, Black C (2015) Long-term prognosis after acute kidney injury (AKI): what is the role of baseline kidney function and recovery? A systematic review. BMJ Open 5(1):e006497. https://doi.org/10.1136/bmjopen-2014-006497
2. Joannidis M, Druml W, Forni LG, Groeneveld ABJ, Honore PM, Hoste E, Ostermann M, Oudemans-van Straaten HM, Schetz M (2017) Prevention of acute kidney injury and protection of renal function in the intensive care unit: update 2017: expert opinion of the Working Group on Prevention, AKI section, European Society of Intensive Care Medicine. Intensive Care Med 43(6):730–749. https://doi.org/10.1007/s00134-017-4832-y
3. Kline TL, Edwards ME, Garg I, Irazabal MV, Korfiatis P, Harris PC, King BF, Torres VE, Venkatesh SK, Erickson BJ (2018) Quantitative MRI of kidneys in renal disease. Abdom Radiol (NY) 43(3):629–638. https://doi.org/10.1007/s00261-017-1236-y
4. Zhang JL, Morrell G, Rusinek H, Sigmund EE, Chandarana H, Lerman LO, Prasad PV, Niles D, Artz N, Fain S, Vivier PH, Cheung AK, Lee VS (2014) New magnetic resonance imaging methods in nephrology. Kidney Int 85(4):768–778. https://doi.org/10.1038/ki.2013.361
5. Zhang JL, Rusinek H, Chandarana H, Lee VS (2013) Functional MRI of the kidneys. J Magn Reson Imaging 37(2):282–293. https://doi.org/10.1002/jmri.23717
6. Mannelli L, Maki JH, Osman SF, Chandarana H, Lomas DJ, Shuman WP, Linnau KF, Green DE, Laffi G, Moshiri M (2012) Noncontrast functional MRI of the kidneys. Curr Urol Rep 13(1):99–107. https://doi.org/10.1007/s11934-011-0229-6
7. Attenberger UI, Morelli JN, Schoenberg SO, Michaely HJ (2011) Assessment of the kidneys: magnetic resonance angiography, perfusion and diffusion. J Cardiovasc Magn Reson 13:70. https://doi.org/10.1186/1532-429X-13-70
8. Grenier N, Pedersen M, Hauger O (2006) Contrast agents for functional and cellular MRI of the kidney. Eur J Radiol 60(3):341–352. https://doi.org/10.1016/j.ejrad.2006.06.024
9. Ebrahimi B, Textor SC, Lerman LO (2014) Renal relevant radiology: renal functional magnetic resonance imaging. Clin J Am Soc Nephrol. https://doi.org/10.2215/CJN.02900313
10. Zollner FG, Konstandin S, Lommen J, Budjan J, Schoenberg SO, Schad LR, Haneder S (2016) Quantitative sodium MRI of kidney. NMR Biomed 29(2):197–205. https://doi.org/10.1002/nbm.3274
11. Zimmer F, Klotz S, Hoeger S, Yard BA, Kramer BK, Schad LR, Zollner FG (2017) Quantitative arterial spin labelling perfusion

measurements in rat models of renal transplantation and acute kidney injury at 3T. Z Med Phys 27(1):39–48. https://doi.org/10.1016/j.zemedi.2016.02.004

12. Hueper K, Peperhove M, Rong S, Gerstenberg J, Mengel M, Meier M, Gutberlet M, Tewes S, Barrmeyer A, Chen R, Haller H, Wacker F, Hartung D, Gueler F (2014) T1-mapping for assessment of ischemia-induced acute kidney injury and prediction of chronic kidney disease in mice. Eur Radiol 24(9):2252–2260. https://doi.org/10.1007/s00330-014-3250-6
13. Zollner FG, Schock-Kusch D, Backer S, Neudecker S, Gretz N, Schad LR (2013) Simultaneous measurement of kidney function by dynamic contrast enhanced MRI and FITC-sinistrin clearance in rats at 3 tesla: initial results. PLoS One 8(11):e79992. https://doi.org/10.1371/journal.pone.0079992
14. Hueper K, Rong S, Gutberlet M, Hartung D, Mengel M, Lu X, Haller H, Wacker F, Meier M, Gueler F (2013) T2 relaxation time and apparent diffusion coefficient for noninvasive assessment of renal pathology after acute kidney injury in mice: comparison with histopathology. Investig Radiol 48(12):834–842. https://doi.org/10.1097/RLI.0b013e31829d0414
15. Inoue T, Kozawa E, Okada H, Inukai K, Watanabe S, Kikuta T, Watanabe Y, Takenaka T, Katayama S, Tanaka J, Suzuki H (2011) Noninvasive evaluation of kidney hypoxia and fibrosis using magnetic resonance imaging. J Am Soc Nephrol 22(8):1429–1434. https://doi.org/10.1681/ASN.2010111143
16. Notohamiprodjo M, Reiser MF, Sourbron SP (2010) Diffusion and perfusion of the kidney. Eur J Radiol 76(3):337–347. https://doi.org/10.1016/j.ejrad.2010.05.033
17. Sourbron SP, Michaely HJ, Reiser MF, Schoenberg SO (2008) MRI-measurement of perfusion and glomerular filtration in the human kidney with a separable compartment model. Investig Radiol 43(1):40–48. https://doi.org/10.1097/RLI.0b013e31815597c5
18. Prasad PV (2006) Evaluation of intra-renal oxygenation by BOLD MRI. Nephron Clin Pract 103(2):c58–c65. https://doi.org/10.1159/000090610
19. Dujardin M, Sourbron S, Luypaert R, Verbeelen D, Stadnik T (2005) Quantification of renal perfusion and function on a voxel-by-voxel basis: a feasibility study. Magn Reson Med 54(4):841–849. https://doi.org/10.1002/mrm.20608
20. Longo DL, Dastru W, Digilio G, Keupp J, Langereis S, Lanzardo S, Prestigio S, Steinbach O, Terreno E, Uggeri F, Aime S (2011) Iopamidol as a responsive MRI-chemical exchange saturation transfer contrast agent for pH mapping of kidneys: in vivo studies in mice at 7 T. Magn Reson Med 65(1):202–211. https://doi.org/10.1002/mrm.22608
21. Longo DL, Busato A, Lanzardo S, Antico F, Aime S (2013) Imaging the pH evolution of an acute kidney injury model by means of iopamidol, a MRI-CEST pH-responsive contrast agent. Magn Reson Med 70(3):859–864. https://doi.org/10.1002/mrm.24513
22. Longo DL, Sun PZ, Consolino L, Michelotti FC, Uggeri F, Aime S (2014) A general MRI-CEST ratiometric approach for pH imaging: demonstration of in vivo pH mapping with iobitridol. J Am Chem Soc 136(41):14333–14336. https://doi.org/10.1021/ja5059313
23. Longo DL, Cutrin JC, Michelotti F, Irrera P, Aime S (2017) Noninvasive evaluation of renal pH homeostasis after ischemia reperfusion injury by CEST-MRI. NMR Biomed 30(7). https://doi.org/10.1002/nbm.3720
24. Longo D, Aime S (2017) Iodinated contrast media as pH-responsive CEST agents. In: Mcmahon MT, Gilad AA, JBM B, PCM VZ (eds) Chemical exchange saturation transfer imaging. Vol. Advances and applications. Pan Stanford Publishing, Singapore, pp 447–466. https://doi.org/10.1201/9781315364421-20
25. Wu Y, Zhou IY, Igarashi T, Longo DL, Aime S, Sun PZ (2018) A generalized ratiometric chemical exchange saturation transfer (CEST) MRI approach for mapping renal pH using iopamidol. Magn Reson Med 79(3):1553–1558. https://doi.org/10.1002/mrm.26817
26. Mariager CO, Nielsen PM, Qi HY, Schroeder M, Bertelsen LB, Laustsen C (2017) Can hyperpolarized C-13-urea be used to assess glomerular filtration rate? A retrospective study. Tomography 3(3):146–152. https://doi.org/10.18383/j.tom.2017.00010
27. Duwel S, Hundshammer C, Gersch M, Feuerecker B, Steiger K, Buck A, Walch A, Haase A, Glaser SJ, Schwaiger M, Schilling F (2017) Imaging of pH in vivo using hyperpolarized (13)C-labelled zymonic acid. Nat Commun 8:15126. https://doi.org/10.1038/ncomms15126
28. Aime S, Botta M, Terreno E (2005) Gd(III)-based contrast agents for MRI. Adv Inorgan

Chem 57(57):173–237. https://doi.org/10.1016/S0898-8838(05)57004-1

29. Sherry AD, Caravan P, Lenkinski RE (2009) Primer on gadolinium chemistry. J Magn Reson Imaging 30(6):1240–1248. https://doi.org/10.1002/jmri.21966
30. Longo DL, Arena F, Consolino L, Minazzi P, Geninatti-Crich S, Giovenzana GB, Aime S (2016) Gd-AAZTA-MADEC, an improved blood pool agent for DCE-MRI studies on mice on 1 T scanners. Biomaterials 75:47–57. https://doi.org/10.1016/j.biomaterials.2015.10.012
31. Geninatti-Crich S, Szabo I, Alberti D, Longo D, Aime S (2011) MRI of cells and mice at 1 and 7 Tesla with Gd-targeting agents: when the low field is better! Contrast Media Mol Imaging 6(6):421–425. https://doi.org/10.1002/cmmi.436
32. Avedano S, Botta M, Haigh JS, Longo DL, Woods M (2013) Coupling fast water exchange to slow molecular tumbling in Gd3+ chelates: why faster is not always better. Inorg Chem 52(15):8436–8450. https://doi.org/10.1021/ic400308a
33. Botta M, Avedano S, Giovenzana GB, Lombardi A, Longo D, Cassino C, Tei L, Aime S (2011) Relaxometric study of a series of monoaqua Gd-III complexes of rigidified EGTA-like chelators and their noncovalent interaction with human serum albumin. Eur J Inorg Chem 6:802–810. https://doi.org/10.1002/ejic.201001103
34. Botta M, Tei L (2012) Relaxivity enhancement in macromolecular and nanosized GdIII-based MRI contrast agents. Eur J Inorg Chem 12:1945–1960. https://doi.org/10.1002/ejic.201101305
35. Grenier N, Merville P, Combe C (2016) Radiologic imaging of the renal parenchyma structure and function. Nat Rev Nephrol 12(6):348–359. https://doi.org/10.1038/nrneph.2016.44
36. Winter KS, Helck AD, Ingrisch M, Staehler M, Stief C, Sommer WH, Braunagel M, Kazmierczak PM, Reiser MF, Nikolaou K, Notohamiprodjo M (2014) Dynamic contrast-enhanced magnetic resonance imaging assessment of kidney function and renal masses: single slice versus whole organ/tumor. Investig Radiol 49(11):720–727. https://doi.org/10.1097/RLI.0000000000000075
37. Sourbron SP, Buckley DL (2013) Classic models for dynamic contrast-enhanced MRI. NMR Biomed 26(8):1004–1027. https://doi.org/10.1002/nbm.2940
38. Zollner FG, Daab M, Sourbron SP, Schad LR, Schoenberg SO, Weisser G (2016) An open source software for analysis of dynamic contrast enhanced magnetic resonance images: UMMPerfusion revisited. BMC Med Imaging 16:7. https://doi.org/10.1186/s12880-016-0109-0
39. Beeman SC, Osei-Owusu P, Duan C, Engelbach J, Bretthorst GL, JJH A, Blumer KJ, Garbow JR (2015) Renal DCE-MRI model selection using Bayesian Probability Theory. Tomography 1(1):61–68. https://doi.org/10.18383/j.tom.2015.00133
40. Zollner FG, Zimmer F, Klotz S, Hoeger S, Schad LR (2014) Renal perfusion in acute kidney injury with DCE-MRI: deconvolution analysis versus two-compartment filtration model. Magn Reson Imaging 32(6):781–785. https://doi.org/10.1016/j.mri.2014.02.014
41. Zöllner FG, Zimmer F, Klotz S, Hoeger S, Schad LR (2015) Functional imaging of acute kidney injury at 3 Tesla: investigating multiple parameters using DCE-MRI and a two-compartment filtration model. Z Med Phys 25(1):58–65. https://doi.org/10.1016/j.zemedi.2014.01.002
42. Zollner FG, Weisser G, Reich M, Kaiser S, Schoenberg SO, Sourbron SP, Schad LR (2013) UMMPerfusion: an open source software tool towards quantitative MRI perfusion analysis in clinical routine. J Digit Imaging 26(2):344–352. https://doi.org/10.1007/s10278-012-9510-6

Chapter 26

Renal Blood Flow Using Arterial Spin Labeling (ASL) MRI: Experimental Protocol and Principles

Kai-Hsiang Chuang, Martin Meier, María A. Fernández-Seara, Frank Kober, and Min-Chi Ku

Abstract

A noninvasive, robust, and reproducible method to measure renal perfusion is important to understand the physiology of kidney. Arterial spin labeling (ASL) MRI technique labels the endogenous blood water as freely diffusible tracers to measure perfusion quantitatively without relying on exogenous contrast agent. Therefore, it alleviates the safety concern involving gadolinium chelates. To obtain quantitative tissue perfusion information is particularly relevant for multisite and longitudinal imaging of living subjects.

This chapter is based upon work from the PARENCHIMA COST Action, a community-driven network funded by the European Cooperation in Science and Technology (COST) program of the European Union, which aims to improve the reproducibility and standardization of renal MRI biomarkers. This experimental protocol chapter is complemented by two separate chapters describing the basic concept and data analysis.

Key words Magnetic resonance imaging (MRI), Kidney, Mice, Arterial spin labeling (ASL)

1 Introduction

Arterial spin labeling (ASL) is a magnetic resonance imaging (MRI) method for measuring tissue perfusion [1, 2]. The term perfusion refers to the delivery of blood to capillary beds, and is quantified by the amount of blood delivered to the tissue per unit time, per unit volume or mass of tissue. The quantification of renal tissue perfusion is essential because it determines the rate of nutrients (e.g., oxygenation and glucose) to the renal tissue, and the rate of clearance of waste products.

The principle of ASL-MRI is to label the arterial blood as an endogenous diffusible tracer. Before the blood flows into the target tissue, the blood proton spins are "labeled" (tagged) by inverting the longitudinal magnetization using radiofrequency (RF) pulses. The labeled blood then flows into the kidney tissue, resembling direct exogenous contrast more than MRI contrast agents that act

Andreas Pohlmann and Thoralf Niendorf (eds.), *Preclinical MRI of the Kidney: Methods and Protocols*, Methods in Molecular Biology, vol. 2216, https://doi.org/10.1007/978-1-0716-0978-1_26,

on relaxation times. The labeled blood, however, loses its contrast on its way to kidney tissue within a few seconds due to the T_1 relaxation of blood. This makes ASL only suitable for probing renal perfusion, but not later processes in the kidney such as glomerular filtration. On the other hand, the intrinsic signals from the static kidney tissue have to be eliminated. For this, a control image without labeling arterial blood is acquired, and subtraction of the two images with and without labeling would result in an image enhanced with only the labeled arterial blood.

The most frequently used ASL technique for kidney imaging is flow-sensitive alternating inversion recovery (FAIR) which uses an inversion pulse for spin labeling [3]. Its principle is illustrated in the chapter by Ku M-C et al. "Noninvasive Renal Perfusion Measurement Using Arterial Spin Labeling (ASL) MRI: Basic Concept." In this technique, two acquisitions with different inversions are alternatingly applied: one acquisition with selective inversion of a slab that is slightly larger than the imaging slice (no labeling of in-flowing blood) and a second acquisition with global inversion of all blood within the RF coil (nonselective inversion). Subtraction of the image with global inversion from the image with spatially selective inversion results in a perfusion-weighted image, as the difference between the two images is caused by the noninverted blood spins moving from outside the selective inversion slab into the imaging plane.

Here we describe ASL-MRI using FAIR method for monitoring of the renal blood flow in the kidney of rodents in a step-by-step experimental protocol. The rationale for the chosen acquisition parameters is given in generic terms, together with specific parameter examples.

This experimental protocol chapter is complemented by two separate chapters describing the basic concept and data analysis, which are part of this book.

This chapter is part of the book Pohlmann A, Niendorf T (eds) (2020) Preclinical MRI of the Kidney—Methods and Protocols. Springer, New York.

2 Materials

2.1 Animals

This experimental protocol is tailored to mice (e.g., wild type C57BL/6 or disease model in immune-deficient nude mice) with a body mass of 20–40 g. Some advice for adaptation to other rodents such as rats is given as *Notes* when necessary.

2.2 Lab Equipment

1. Anesthesia: For an in-depth description and discussion of anesthesia please refer to the chapter by Kaucsar T et al. "Preparation and Monitoring of Small Animals in Renal MRI." Typically 0.5–1.5% isoflurane is used for anesthesia administered to the mice using an anesthetic gas vaporizer (Dräger Vapor® FMI Föhr Medical Instruments GmbH, Seeheim-Ober Beerbach, Germany).

2. Gases: O_2, N_2 and compressed air, as well as a gas-mixing system or general inhalation anesthesia equipment, including an anesthetic vaporizer, a flow meter and an induction chamber.

2.3 MRI Hardware

The general hardware requirements for renal ^{1}H MRI on mice and rats are described in the chapter by Ramos Delgado P et al. "Hardware Considerations for Preclinical Magnetic Resonance of the Kidney." The technique described in this chapter was tailored for a 7 T MR system (Biospec 70/20, Bruker Biospin, Ettlingen, Germany) but advice for adaptation to other field strengths is given where necessary. No special or additional hardware is required, except for:

1. A physiological monitoring system that can track the respiration, and is connected to the MR system such that it can be used to trigger the image acquisition. Typically, the MR-compatible rodent monitoring and gating system (Small Animal Instruments, New York, USA) equipped with an air-pillow to monitor breath rate can be used.
2. Mouse cradle and RF-antenna (*see* **Note 1**): The 2 × 2 cardiac coil array (Bruker), originally designed for mouse heart is integrated into corresponding animal cradle tips. The combination of receive-only coil array and a circularly polarized volume transmitter coil (Bruker) will improve signal to noise ratio (SNR). Alternatively, a single-loop surface coil could be used for receiving provided that a volume coil is used for transmit in any case.

2.4 MRI Sequences

1. *Sequence type*: For the choice of type of sequence to use for renal ASL in rodents please refer to the chapter by Ku M-C et al. "Noninvasive Renal Perfusion Measurement Using Arterial Spin Labeling (ASL) MRI: Basic Concept." A 2D sequence composed by FAIR for labeling and EPI for image acquisition is described in this chapter. This is a standard sequence on Bruker MRI systems, where it is called "FAIR-EPI." To minimize the susceptibility artifact and geometric distortion in the abdomen, spin-echo EPI or RARE acquisition is desirable as alternative ("FAIR-RARE").
2. *Echo time (TE)*: To preserve signal from T_2/T_2^* decay, a minimum TE should always be used (~10 ms) to maximize SNR.

   Avoid crusher gradients: Although they reduce flow-related artifacts, they require prolongation of the minimum TE. They would reduce SNR and introduce more T_2 (T_2^*) contrast into the ASL image. Crusher gradients also remove potentially important information, such as the presence of delayed or collateral flow.

3. *Repetition time (TR)*: There are two considerations on choosing appropriate TR. First, to allow substantial relaxation of labeled spins between acquisitions, TR should be long enough (~10,000 ms). Since T_1 time is field dependent, TR as well. The long TR (~10,000 ms) is recommended for a 7 T system. For other field strength this value need to be justified. Second, if respiratory induced artifact is severe and the respiratory trigger is needed, a long TR that is at least five times greater than the tissue T_1 (e.g., 10 s) can be used to minimize the variable T_1-weighting due to irregular respiration rate. If the respiratory trigger is not needed, a shorter TR that has good signal-to-noise per time (SNR/t) efficiency could be used. TR will be limited by the maximum inversion time (TI) and the number of acquired slices.
4. *TR mode*: TR must allow tag washout and refreshing, TE should be short to minimize T2 contamination.
5. *Repetition spacing*: Choose "Const_Rep" to use the same TR.
6. *FAIR Experiment Mode*: Choose "Interleaved (TI loop outside)" to measure control-label pairs, followed by different TI.
7. *Inversion mode (TI Setting)*: Set for "User" TIR.
8. *Inversion time* (TI): TI should be long enough to permit tagging to leave tagging region and ensure tag exchange with tissue water (i.e., the arterial arrival time), but short enough to reduce loss of tag. TI should be increased whenever slow arterial flows (i.e., long arterial arrival time) are expected. For example, in the case of poor cardiac output. Shorter TI values are recommended in case of more rapid circulation times (this depends on the anesthesia level). Unless the arterial arrival time is known, measurement with multiple TI is recommended, e.g., from 25, 50, 100, 150, 200, 300, 500, 1000, 1500, 2000, to 5000 ms. The arrival time increases with the selective inversion slab thickness. For single slice FAIR, the arrival time is typically very short (*see* **Note 2**).
9. *Inversion pulse*: For inversion, an adiabatic full passage frequency-selective inversion pulse (e.g., hyperbolic secant-shaped pulse) should be used with a high bandwidth of 5190 Hz. A calculated adiabatic pulse can be used as well.
10. *Inversion slab thickness*: This depends on the imaging slice thickness. Usually at least 2.5 times of slice package thickness. For example, the slice package margin should be at least 1.5 mm resulting in a 5 mm inversion slice when you use 2 mm slice thickness.
11. *Acquisition bandwidth (BW)*: Use a high BW (e.g., 200 kHz) for EPI readout to shorten TE. Keep an eye on the SNR while modifying BW. SNR decreases with increasing BW. Low SNR

may be balanced out with more averages or repetitions. For scanning with a short TE, an SNR of at least 60 is recommended (*see* **Note 3**).

12. *Fat saturation*: Turn on. Important to avoid fat signal overlaying the kidney due to chemical shift.
13. *Geometry*: this is a tricky part. To cover the whole kidney in one slice, an oblique coronal slice will be needed. It is important to avoid the selective inversion slab crossing the feeding arteries (aorta) as this will reduce the labeled arterial blood spins. Use a rectangular field of view (FOV) and use a frequency encoding in H-F direction to avoid aliasing (*see* **Note 4**).
14. *Respiration trigger*: Turn on (per repetition). This is essential when respiration is very irregular or motion artifact is induced in multishot imaging such as RARE.
15. *Number of slice and thickness*: Slice thickness is typically no less than 1 mm in mice or rats due to the low SNR of ASL. The number of slices and thickness determines the selective inversion slab thickness. It should be noted that ASL using FAIR is not suitable for multislice imaging per se, because the labeled blood magnetization decreases with increasing inversion slab thickness. This is due to relaxation during transit, but also to the excitation pulses related to imaging readout in the various slices. Therefore, usually no more than three slices are recommended. Besides, ASL has generally low SNR due to a relatively small fractional magnetization of available labeled arterial blood (1–5%). Therefore, rather thick imaging slices ($\geq$1 mm) are needed to reduce noise.
16. *T_1 map*: A T_1 map is useful to improve the quantification accuracy as it provides a measured tissue T_1 (which is different in medulla and cortex) and inversion efficiency. It can be adapted from the ASL sequence by selecting the "nonselective inversion" mode in "FAIR Experiment." Set up at least six TI in logarithmic order (e.g., 10, 50, 200, 1000, 2000, 5000, 9000 ms) with long constant TR (e.g., 10 s). A few (e.g., 3) data averaging will be needed to increase SNR.

3 Methods

3.1 Animal Preparations and Initial Setups for Imaging

1. Anesthetize the animal with isoflurane in an induction box (approximately 3–3.5% isoflurane for induction with air and oxygen mixed at a 3:1 ratio) and then transfer the animal to the scanner (*see* **Note 5**).
2. Set up the temperature monitoring (rectal probe) and respiratory monitoring (balloon on chest) unit. Ophthalmic ointment should be applied to the eyes of the animal.

3. If isoflurane is used, adjust anesthesia level (e.g., 1.5–2%) to maintain regular respiration rate around 90 breaths per minute (bpm) in mouse or 60 bpm in rat during the scan. The level of isoflurane may need to be adjusted regularly to maintain a rather constant respiration rate (*see* **Note 6**).
4. Carefully position the RF-antenna to be near the kidney and place it to the magnet isocenter based on the initial anatomical imaging.
5. Perform coil tuning/matching and *global* shimming (*see* **Note 7**).
6. Acquire kidney anatomical imaging (i.e., routine respiratory triggered T_2-weighted turbo spin echo sequences in axial and coronal planes) as described in the chapter by Pohlmann A et al. "Essential Practical Steps for MRI of the Kidney in Experimental Research" (*see* **Note 8**).
7. In the case of use a sequence with FAIR for labeling and EPI for image readout (FAIR-EPI), please perform the trajectory adjustment (*see* **Note 9**).

3.2 Renal Perfusion Imaging

3.2.1 Baseline Condition (Healthy Animal)

1. Load the ASL (FAIR-EPI) sequence (*see* **Note 10**), adapt the slice orientation to provide either a coronal or axial view with respect to the kidney (in scanner coordinates this is double-oblique). Adjust the geometry of a flow saturation slice onto aorta and perpendicular to the ASL imaging slices (Fig. 1) (*see* **Note 11**).
2. Acquire a pilot scan to evaluate slice location and image quality by setting repetition and average to 1. Fine tune the slice position based on the pilot scan to maximize the coverage of

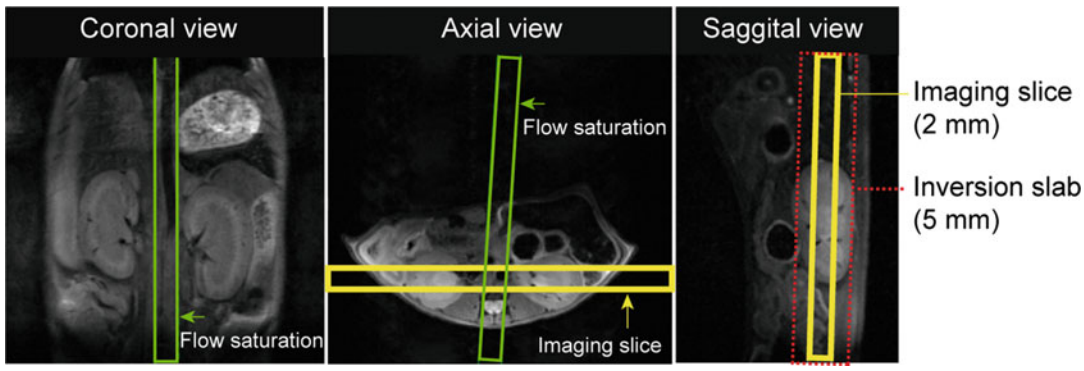

Fig. 1 Anatomical images with 3 planes (coronal, axial and sagittal views of mouse kidneys). Imaging is performed in a central coronal plane, adjusted to the long axis of the kidneys. The green box outlines slice position for a saturation slice. The yellow box outlines the imaging slice for a coronal view. The red dotted box outlines the inversion slab. Please note that the inversion slab has to be thicker than the imaging slice

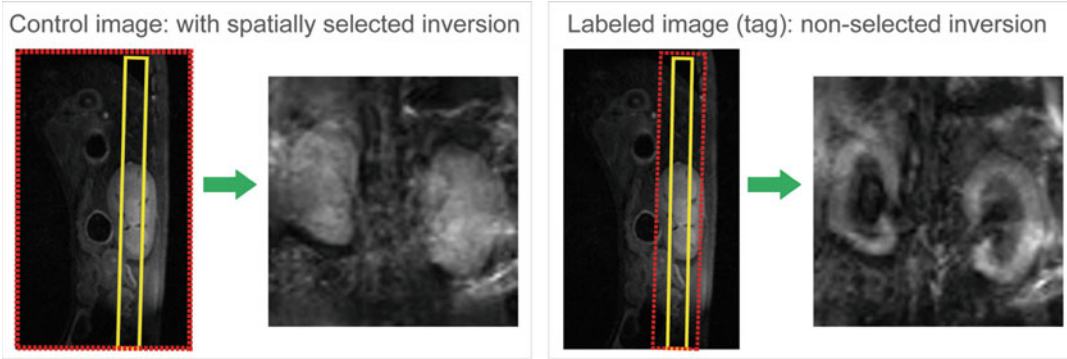

Fig. 2 Left: A resulted ASL image with coronal view from nonselective inversion pulse. Right: A resulted ASL image with coronal view from selective inversion

kidney while avoiding the selective inversion slab (imaging slab) to cross the feeding arteries (Fig. 2).

3. Perform subtraction between label and control images to evaluate the level of perfusion signal.
4. Acquire ASL scans with multiple repetitions. Increase repetition if SNR is not optimal (*see* **Note 12**).
5. Inspect the acquired image time series. If motion artifacts are severe, use respiratory trigger and then repeat scans (*see* **Note 13**).
6. When use respiration triggering: in the monitoring unit set the trigger delay so that the trigger starts at the beginning of the expiratory plateau (no chest motion) and the duration such that it covers the entire expiratory phase, that is, until just before the next inhalation starts.
7. Clone (duplicate) the ASL scan and set all the optimized parameters. Run the sequence for ASL scanning.
8. Load the T_1-mapping (IR-EPI) scan using the same slice geometry and resolution.

3.2.2 Hypoxia/Hyperoxia/Hypercapnia for Benchmarking (Optional)

1. Duplicate the ASL (FAIR-EPI) scan.
2. Start of hypoxia: Change the gas flowing through the respiratory mask to 10% O_2/90% N_2.
3. Exactly 5 min after the start of hypoxia run the ASL and T_1-mapping scans.
4. End of Hypoxia: Change the gas flowing through the respiratory mask back to air (21% O_2).
5. Similarly, hyperoxia and hypercapnia conditions could be assessed by switching to 100% O_2 and 5% CO_2 in air, respectively.

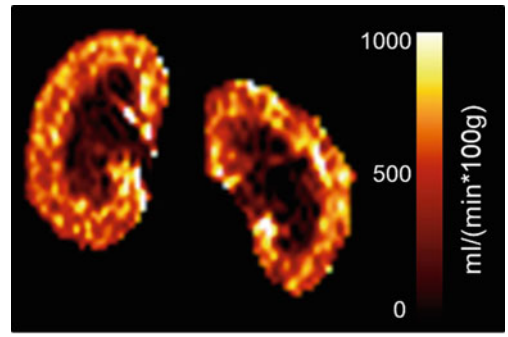

Fig. 3 A noninvasive, robust, and reproducible functional MRI method to characterize the physiology of kidney: An example of resulted renal perfusion maps in C57BL/6 mouse

3.2.3 Perfusion Map

1. The demonstration of a perfusion map that can be expected in physiological condition is shown in Fig. 3. Please note that the detailed protocol for the image analysis is given in the chapter by Chuang K-H et al. "Quantitative Analysis of Renal Perfusion by Arterial Spin Labeling." Briefly, the perfusion-weighted signals at different TIs, $\Delta M(\mathrm{TI})$, can be fitted to a kinetic function by a nonlinear least square routine in Matlab (Mathworks, MA, USA) [4–6]:

$$\Delta M(\mathrm{TI}) = 2M_0\alpha f/\lambda\left[\frac{\exp\left(-\mathrm{TI}/T_{1\mathrm{app}}\right) - \exp\left(-\mathrm{TI}/T_{1\alpha}\right)}{\left(1/T_{1\alpha} - 1/T_{1\mathrm{app}}\right)}\right],$$

   where $1/T_{1\mathrm{app}} = 1/T_1 + f/\lambda$, f is the perfusion (when lambda is in ml/100 g and T_1 in minutes), T_{1a} is the arterial blood T_1, and λ is the blood/tissue partition coefficient. In this equation, three parameters can be derived from the additional T_1 mapping: M_0 represents the equilibrium magnetization, T_1 the tissue longitudinal relaxation time, and α the inversion efficiency. They can be calculated by three-parameter curve fitting of the inversion recovery T_1 mapping data. Please note that the above equation assumes minimal and negligible arterial transit time.
2. In the Macro manager, choose Calculate Global T_1 Map. Note that if there is a bug, you need to select each map twice in the macro.
3. Step through the macro by first loading the ASL experiment.
4. Before selecting Compute Perfusion Map, check the T_1 of blood [7] (Fig. 3).

4 Notes

1. The ASL technique is SNR limited. Multichannel array coils or cryoprobes are a better choice. Particularly, as FAIR requires a global inversion, a volume transmit coil is necessary. Using surface transmit/receive coil would lead to underestimation of perfusion. Parallel acceleration should be avoided due to its SNR penalty. For mice reduce the FOV to the body width and keep the matrix size the same as that used in rats. The relative resolution in resolving kidney is then comparable to that in rats. The SNR would also be similar because the smaller mouse RF coil gives better SNR, that is, mouse heart four-element surface coil vs rat heart four-element surface coil.
2. For using CASL or pCASL instead of FAIR, depending on the field strength and expected flow velocities, the labeling duration and postlabeling delay should be adapted. Labeling durations of $\geq$1600 ms for (p)CASL with *postlabeling delay* $<=$500 ms are suitable.
3. As the labeling effect of ASL on image contrast is weak, SNR considerations mandate acquisition of images that are of lower spatial resolution. For ASL in plane matrices are in the range of 64×64 to 128×128. To maintain acceptable SNR at reasonable imaging times (2–6 min), multiple signal averages/repetitions are required ($N >= 3$).
4. In CASL or pCASL but not for FAIR, the labeling plane should be perpendicular to the feeding artery. As the labeling plane in CASL is typically designed to be in parallel to the imaging plane, that would limit the images to be acquired in transverse planes so that labeling can be perpendicular to the aorta.
5. The renal oxygen (O_2) demand is associated primarily with renal tubular O_2 consumption necessary for solute reabsorption. Increasing O_2 delivery such as giving pure oxygen to the animals makes animal hyperoxia and leads to vasoconstriction which changes the basal physiology.
6. The respiration rate must be monitored continuously throughout the entire experiment and if necessary adapt the TR accordingly to ensure full relaxation (~5 times of T_1).
7. Shimming is particularly important for nonselective (global) inversion, since adiabatic condition depends on B0 field homogeneity. If localized or high-order shim is used, the global field uniformity required for nonselective inversion (which is for labeling arterial spins) will be compromised and leads to inferior inversion (and spin labeling). Shimming should be performed on a global level to optimize uniformity over the whole

body. Neither the default iterative shimming method nor the Mapshim technique is recommended.

8. Example for a 25 g mouse at 7 T: Anatomical images can be acquired with routine respiratory-triggered T_2-weighted turbo spin echo (RARE) sequences in axial and coronal planes. Additionally, bSSFP is a fast imaging that could be used for acquiring anatomical image with minimal motion artefact, with parameters such as TR = 3 ms, TE = 1.07 ms, flip angle of 70°, matrix = 128 × 128 and 16 averages (TA = 6.2 s for one slice without trigger).
9. EPI sequence is highly depending on the gradient system therefore a good trajectory measurement is recommended.
10. Example for a 25 g mouse at 7 T [4, 5, 8, 9]: a respiratory triggered, FAIR sequence with an EPI readout: TR = 16,000 ms; TE = 16.6 ms; TIR = 30, 100, 200, 300, 500, 700, 1000, 1200, 1500, 2000, 3000, 5000, 8000 ms; calculated inversion pulse; effective bandwidth 350 kHz; pulse bandwidth = 2000 Hz; FOV = 3.5 × 3.5 mm^2, slice thickness = 2 mm, inversion slab = 5 mm, IR-spoiler duration = 10 ms, IR-Spoiler amplitude = 40%. As kidney has very high perfusion, the perfusion signal is expected to be high even with just a single pair of ASL scan. If perfusion signal is weak, the nonselective inversion may not be effective. Try increasing the bandwidth of the inversion pulse (i.e., from 2000 to 5000 Hz or higher). This will increase the RF power demand so be mindful about the safe limit of the RF coil and the amplifier.
11. Optional: The flow saturation slice shown in Fig. 1 is a spatially selective saturation band applied to suppress unwanted flow artifacts from vessels entering a slice. This is not the most optimal way of suppressing when using FAIR, but it reduces flow artifacts significantly.
12. Use repetition instead of averaging as repetition allows image registration in post-processing before averaging to minimize residual motion artefacts, whereas direct averaging on the scanner may lead to a blurred image in the presence of motion.
13. If SE-EPI readout causes severe distortion, consider using RARE acquisition instead.

Acknowledgments

This chapter is based upon work from COST Action PARENCHIMA, supported by European Cooperation in Science and Technology (COST). COST (www.cost.eu) is a funding agency for research and innovation networks. COST Actions help connect

research initiatives across Europe and enable scientists to enrich their ideas by sharing them with their peers. This boosts their research, career, and innovation.

PARENCHIMA (renalmri.org) is a community-driven Action in the COST program of the European Union, which unites more than 200 experts in renal MRI from 30 countries with the aim to improve the reproducibility and standardization of renal MRI biomarkers.

References

1. Williams DS, Detre JA, Leigh JS, Koretsky AP (1992) Magnetic resonance imaging of perfusion using spin inversion of arterial water. Proc Natl Acad Sci U S A 89:212–216
2. Kwong KK, Belliveau JW, Chesler DA, Goldberg IE, Weisskoff RM, Poncelet BP, Kennedy DN, Hoppel BE, Cohen MS, Turner R et al (1992) Dynamic magnetic resonance imaging of human brain activity during primary sensory stimulation. Proc Natl Acad Sci U S A 89:5675–5679
3. Kim SG (1995) Quantification of relative cerebral blood flow change by flow-sensitive alternating inversion recovery (FAIR) technique: application to functional mapping. Magn Reson Med 34:293–301
4. Hueper K, Gutberlet M, Rong S, Hartung D, Mengel M, Lu X, Haller H, Wacker F, Meier M, Gueler F (2014) Acute kidney injury: arterial spin labeling to monitor renal perfusion impairment in mice-comparison with histopathologic results and renal function. Radiology 270:117–124
5. Rajendran R, Lew SK, Yong CX, Tan J, Wang DJ, Chuang KH (2013) Quantitative mouse renal perfusion using arterial spin labeling. NMR Biomed 26:1225–1232
6. Pell GS, Thomas DL, Lythgoe MF, Calamante F, Howseman AM, Gadian DG, Ordidge RJ (1999) Implementation of quantitative FAIR perfusion imaging with a short repetition time in time-course studies. Magn Reson Med 41:829–840
7. Rane SD, Gore JC (2013) Measurement of T1 of human arterial and venous blood at 7T. Magn Reson Imaging 31:477–479
8. Hueper K, Schmidbauer M, Thorenz A, Brasen JH, Gutberlet M, Mengel M, Hartung D, Chen R, Meier M, Haller H, Wacker F, Rong S, Gueler F (2017) Longitudinal evaluation of perfusion changes in acute and chronic renal allograft rejection using arterial spin labeling in translational mouse models. J Magn Reson Imaging 46:1664–1672
9. Tewes S, Gueler F, Chen R, Gutberlet M, Jang MS, Meier M, Mengel M, Hartung D, Wacker F, Rong S, Hueper K (2017) Functional MRI for characterization of renal perfusion impairment and edema formation due to acute kidney injury in different mouse strains. PLoS One 12: e0173248

Chapter 27

Renal pH Mapping Using Chemical Exchange Saturation Transfer (CEST) MRI: Experimental Protocol

Kowsalya Devi Pavuluri, Lorena Consolino, Dario Livio Longo, Pietro Irrera, Phillip Zhe Sun, and Michael T. McMahon

Abstract

Chemical exchange saturation transfer (CEST) is recognized as one of the premier methods for measuring pH with this environmental variable expected to be an excellent biomarker for kidney diseases. Here we describe step-by-step CEST MRI experimental protocols for producing pH and perfusion maps for monitoring kidney pH homeostasis in rodents after administering iopamidol as contrast agent. Several CEST techniques, acquisition protocols and ratiometric approaches are described. The impact of length of acquisition time on the quality of the maps is detailed. These methods may be useful for investigating progression in kidney disease in vivo for rodent models.

This chapter is based upon work from the COST Action PARENCHIMA, a community-driven network funded by the European Cooperation in Science and Technology (COST) program of the European Union, which aims to improve the reproducibility and standardization of renal MRI biomarkers. This experimental protocol is complemented by two separate chapters describing the basic concepts and data analysis.

Key words Magnetic resonance imaging (MRI), Kidney, Mice, Rats, Chemical exchange saturation transfer (CEST), pH imaging, Iopamidol, Contrast agent, Responsive contrast agent

1 Introduction

The kidneys are responsible for filtration of plasma in order to remove waste and toxins and for maintaining the acid–base balance of the body through regulation of systemic HCO_3^- concentrations [1]. The kidneys can either reabsorb or generate new HCO_3^- through acid excretion. Renal control of pH could be impacted by a number of factors including whether or not there are abnormalities in perfusion, filtration, amino acid metabolism or if renal tissue edema or inflammation are present. Based on a number of studies relating changes in acid production, secretion or reduced NH_4^+ with pathological conditions [2–8], pH should be a good biomarker for assessing renal function. A number of methods are

Andreas Pohlmann and Thoralf Niendorf (eds.), *Preclinical MRI of the Kidney: Methods and Protocols*, Methods in Molecular Biology, vol. 2216, https://doi.org/10.1007/978-1-0716-0978-1_27, © The Author(s) 2021

now established for determining local pH in vivo, including use of pH micro electrodes [9–11], fluorescence imaging [12, 13], ^{1}H, ^{31}P, ^{19}F MRS [14–21] hyperpolarized ^{13}C MRS [22], pH-dependent MR relaxometry [23], and chemical exchange saturation transfer (CEST) MRI [24, 25]. CEST is a novel MRI contrast mechanism allowing detection of low concentrations of contrast agent through the application of saturation radiofrequency (RF) pulses on their labile protons to destroy their magnetization with the resulting signal loss transferred to water through chemical exchange which has now emerged as the premier MRI method for pH imaging [7, 26–32].

Here we describe CEST MRI for monitoring of the local pH variation found in the kidney of rodents in a step-by-step experimental protocol. The rationale for the choosing acquisition parameters is given in generic terms, together with specific parameter examples.

Mapping of contrast agent renal perfusion is described as an optional component of the experiment. Contrast agent perfusion is a functional parameter that is also sensitive to kidney damage. Currently CT, SPECT and gadolinium based MR imaging are available for assessing renal perfusion in patients, each with its own limitations [33]. CEST MRI contrast enables production of high resolution images of perfusion without need of using ionizing radiation making mapping of perfusion a valuable complement to pH imaging [34].

The protocols contained in this chapter were tested on healthy control mice using Iopamidol as the contrast agent to standardize the pH mapping and tested for both an axial slice and a coronal slice for bench marking. These methods may be useful for investigating renal pH and perfusion variations found in vivo for various rodent models with acute kidney injuries or which progress to chronic kidney disease.

This experimental protocol chapter is complemented by two separate chapters describing the basic concepts and data analysis, which are part of this book.

This chapter is part of the book Pohlmann A, Niendorf T (eds) (2020) Preclinical MRI of the Kidney—Methods and Protocols. Springer, New York.

2 Materials

2.1 Animals

This experimental protocol is tailored for immunocompetent (typically C57BL/6 and Balb/C) or immunocompromised (nude, NOD-SCID) mice with a body mass of 15–35 g. Advice for adaptation to rats is given as *Notes* where necessary. All animal studies have to be carried out in compliance with specific legislation covering the use of animals for scientific purposes. Therefore, all experiments must be authorized under national regulations.

2.2 Lab Equipment and Chemicals

1. Mouse tail illuminator/restrainer for catheterizing the tail vein.
2. Saline solution or heparin solution, 1-ml syringe, catheter (e.g., PE 20 polyethylene tubing) of known inner diameter to hold the saline flush and for contrast agent bolus is required.
3. Anesthesia: please refer to the chapter by Kaucsar T et al. "Preparation and Monitoring of Small Animals in Renal MRI" for an in-depth description and discussion of the anesthesia. Typically, 0.5–1.5% isoflurane is used for anesthesia administered to the mice using an anesthetic gas vaporizer (Leica Biosystems, Maryland, USA). For nonrecovery experiments, urethane solution (Sigma-Aldrich, Steinheim, Germany; 20% in distilled water) can provide anesthesia for several hours with comparatively few side effects on renal physiology, which is an important issue. For intramuscular anesthesia, please refer to **Note 1**.
4. Gases: O_2, N_2, and compressed air, as well as a gas-mixing system or general inhalation anesthesia equipment, including an anesthetic vaporizer, a flow meter and an induction chamber.
5. Mouse cradle.
6. pH imaging contrast agent: typically iodinated-based contrast media are employed, as Iopamidol (Isovue® 370, Bracco Imaging SpA, Milano, Italy), Iopromide (300 mg iodine/ml Ultravist®, Bayer Healthcare, Germany) or Iobitridol (Omnipaque®, GE Healthcare, USA). Such clinically available contrast agents have stock concentrations of 0.9–1 M that can be directly used (*see* **Note 2**).
7. Small Animal Ventilator: animals (rats) needs to be ventilated so the CEST MRI acquisition can be gated to minimize the respiratory motion artifacts. We used a TOPO Dual Mode Rodent/Small Animal Ventilator (Kent Scientific, Torrington, CT).
8. Syringe Infusion Pump: an MR-compatible single syringe pump (Harvard Bioscience, Holliston, MA) for contrast agent administration.

2.3 MRI Hardware

The general hardware requirements for renal ^{1}H MRI on mice and rats are described in the chapter by Ramos Delgado P et al. "Hardware Considerations for Preclinical Magnetic Resonance of the Kidney." The technique described in this chapter has been tailored for MR preclinical systems at magnetic fields higher than 3 T but advice for adaptation to other field strengths is given where necessary (*see* **Note 3**). No special or additional hardware is required, except for the following:

1. A physiological monitoring system that can track the respiration and which is connected to the MR system such that it can be used to synchronize CEST MRI with respiration. Typically, we use the MR-compatible rodent monitoring and gating system (Small Animal Instruments, New York, USA) equipped with an air-pillow to monitor breath rate.

2.4 MRI Sequences

The CEST MRI sequence includes continuous wave (CW) RF saturation followed by fast image readout such as echo planar imaging (EPI), Rapid Imaging with Refocused Echoes (RARE) and/or fast imaging with steady-state precession (FISP) [6, 35–37]. Herein we describe those based on fast refocused multiecho sequences since they provide the higher SNR in acceptable acquisition times and are without geometrical distortions. The same sequence readout is described for B_0 mapping, for full Z-spectrum acquisition and for dynamic acquisition applications.

3 Methods

3.1 MR Protocol Setup

3.1.1 Rapid Acquisition with Refocused Echoes Sequence for External B_0 Mapping Using WASSR

1. Select a 2D Rapid Acquisition with Refocused Echoes sequence in conjunction with a magnetization transfer preparation module that has a frequency offset which can be incremented within a single scan. This is a standard sequence on Bruker MRI systems, called "RARE."
2. Switch on the magnetization transfer module. The magnetization transfer pulse parameters are then adjusted to allow detection of direct water saturation vs. excitation frequency and also the signal-to-noise >50:1 when the saturation pulse is 500 Hz or more away from water. Typically, we employ $N = 11{,}000$ ms rectangular shaped pulse with saturation power (amplitude) of 1–1.5 μT, similar to what was previously described for the WASSR Scheme [38].
3. Sample several frequency offsets around the frequency of bulk water signal (commonly set at 0 ppm, in contrast to the 4.8 ppm as in conventional NMR experiments). Usually the sampled range is between −3 and +3 ppm with different step size, according to the available acquisition time and expected B_0 inhomogeneity. Please *see* **Note 4** for an example of the frequency list used in B_0 mapping.
4. Choose a repetition time (TR) of ~5–6 s for good signal stability and signal-to-noise per time (SNR/t) efficiency. TR will be limited by the length of the saturation pulse, length of echo train and the number of slices to be acquired, and saturation pulse(s)'s field strength.

5. Use the shortest echo time (TE) and echo spacing (ΔTE) possible. One wants to acquire as many lines of k space as possible to minimize motion distortions of the images. For that reason, it is advantageous to have ΔTE well below 10 ms. Larger ΔTE are not advisable because the SNR in the kidney will be so low that these images must be excluded. Acquisition bandwidth should be considered to shorten the ΔTE.
6. Set the rare factor as high as possible to reduce scan time. Same as the CEST acquisition scan (Subheading 3.1.2).
7. Set the acquisition bandwidth (BW) as for the CEST contrast scan (Subheading 3.1.2).
8. Switch on the fat saturation module.
9. Do not use the respiration trigger since this will increase the overall acquisition time.
10. Set the same geometry as for the CEST contrast scan (Subheading 3.1.2).
11. Set the matrix size/acceleration the same as for the CEST contrast scan (Subheading 3.1.2).
12. For an example of a specific parameter set please *see* **Note 5**.

3.1.2 Full Z-Spectrum Acquisition for CEST-pH Mapping

1. Select a 2D Rapid Acquisition with Refocused Echoes sequence with magnetization transfer preparation module. This is a standard sequence on Bruker MRI systems, called "RARE." RARE sequence with centric encoding is used. More details on CEST sequences for Bruker scanners are provided in **Note 6**.
2. Switch on the Magnetization transfer module. The magnetization transfer pulse parameters are then adjusted to allow detection of CEST contrast while keeping the current within limits given by the RF transmit coil and the ^{1}H RF power amplifier. For CEST pH mapping, Z-spectra are acquired by applying a 1.5–6 μT continuous wave (CW) block shaped (bp) presaturation pulse for 2–5 seconds or by applying a pulsed saturation scheme (*see* Subheading 2.4.3.35).
3. Acquire a series of 30–50 frequencies in the range of ±10 ppm for the whole CEST Z-spectrum acquisition. A macro file containing the MR frequencies is manually implemented by the operator in Bruker systems, by creating a list of frequencies covering the positive and negative side of CEST spectra. At the resonating frequencies of mobile protons (4.2/4.3 ppm and 5.5 ppm for Iopamidol and Iopromide, 5.6 ppm for Iobitridol) a denser sampling is usually applied (frequency resolution of 0.1 ppm). Please *see* **Note 7** for an example of the frequency list.

4. Choose the Repetition Time (TR) in the range 4–6 s for good signal stability and signal-to-noise per time (SNR/t) efficiency, also according to the duration of the saturation pulse.
5. Use the shortest TE and echo spacing (ΔTE) possible.
6. Set the Rare factor to 64–96. Typically, a single shot acquisition (Rare Factor equal to Matrix Size) to reduce the acquisition time for each frequency. Partial Fourier acceleration should be considered to reduce the size of the matrix and improve the time efficiency of data acquisition and centric encoding to maximize SNR. Reconstruction to higher matrix size may be also considered to improve spatial resolution.
7. Use a high acquisition bandwidth (BW) to shorten ΔTE, while keeping an eye on the SNR, which decreases with increasing BW.
8. Switch on the fat saturation module. Important to avoid fat signal overlaying with the kidney due to chemical shift.
9. Set off the respiration trigger.
10. Adapt the geometry of the slice(s) so that animal fits into FOV in L-R direction (approx. 30–40 mm, according to the coil inner diameter) and use frequency encoding in H-F direction. Use a slice with the lowest thickness the SNR allows, typically around 1.5–2.0 mm. The thinner the slices the better, as this improves the resolution—which can be readily seen on the raw images.
11. Use the highest in-plane resolution that the SNR allows. A typical matrix size of 64 × 64, 96 × 96, or 128 × 128 is used for CEST images, with in-plane spatial resolution of 468, 312, or 234 μm (for an FOV of 30 mm). This has to be balanced by the need for sufficient SNR in the images. Zero-filling or use of partial Fourier techniques in the phase encoding direction can be helpful to speed up acquisition to minimize motion artifacts and contrast agent concentration changes during the acquisition.
12. For an example of a specific parameter set for mice please *see* **Note 8** or for rats please *see* **Note 9**.

3.1.3 Rapid Acquisition with Refocused Echoes Sequence for CEST pH and Perfusion Measurements

1. Select a 2D rapid acquisition with refocused echoes sequence (RARE) with magnetization transfer preparation module.
2. Switch on the magnetization transfer module. The magnetization transfer pulse parameters are then adjusted to allow detection of CEST contrast while keeping the current within the limits given by the RF transmit coil, the ^{1}H RF power amplifier and the signal-to-noise >50:1 at the frequency of the labile protons of interest on the CEST agent. Typically, we employ signal averaging with $N = 10$, 300 ms rectangular shaped RF

pulses with an amplitude between 3 and 4 μT. The saturation frequency is alternated between 4.2 ppm, 5.5 ppm for collection of signal with saturation on resonance with the two labile protons in iopamidol and for the last ten images −100 ppm for collection of S_0 (signal with no saturation).

3. Choose a repetition time (TR) between 7 and 12 s for good signal stability and signal-to-noise per time (SNR/*t*) efficiency.
4. Use the shortest TE and echo spacing (ΔTE) possible (*see* Subheading 3.1.2).
5. Use a rare factor of 20–32. Typically, 20–32 TEs are sensible and allow acquiring a 32 × 32 matrix slice or 48 × 48 with partial Fourier acceleration in a single shot. Partial Fourier acceleration should be considered to reduce the size of the matrix and improve the time efficiency of data acquisition.
6. Use a high acquisition bandwidth (BW) to shorten ΔTE, while keeping an eye on the SNR, which decreases with increasing BW. For the image with the shortest TE an SNR of at least 60 is recommended.
7. Switch on the fat saturation module. Important to avoid fat signal overlaying with the kidney due to chemical shift.
8. Use an FOV saturation of 4 mm thickness above 9–13 mm from the kidneys for coronal slices. This is not required for axial slices.
9. Set off the respiration trigger.
10. Adapt the geometry of the acquisition slices so that the animal fits into FOV in L-R direction (approx. 30–40 mm according to the coil inner diameter) and use frequency encoding in H-F direction. Use a slice with the lowest thickness the SNR allows, typically around 1.5 mm. The thinner the slices the better, as this improves the resolution—which can be readily seen on the raw images. For adaptation to rats *see* **Note 10**.
11. Use highest in-plane resolution that the SNR allows, typically around 600 × 400 um^2 for axial slices or 200 × 500 μm^2 for coronal slices. This has to be balanced by the need for sufficient SNR in the images. Use zero-filling or partial Fourier techniques in the phase encoding direction to speed up acquisition and to minimize motion artifacts and contrast agent concentration changes during the acquisition. One may use half Fourier in read direction (asymmetric echo) to further shorten the first TE. Reducing the excitation and refocusing pulse lengths to below 1.5 ms can then also help to shorten TE.
12. For an example of a specific parameter set please *see* **Note 11**.

3.2 Setting of the pH Calibration Curve

Prepare multiple vials of Iopamidol phosphate-buffered solution (PBS 1×, 10 mM of inorganic phosphates) or human blood serum solutions, with pH titrated to physiological relevant renal pH values: 5.5, 6.0, 6.5, 7.0, 7.5, 8.0 and place them in a plastic container (e.g., 30–50 ml falcon tube) filled with water. Such a phantom calibration experiment is crucial for in vivo pH quantification at different experimental conditions such as magnetic field strength and CEST irradiation Schemes [39]. A more detailed description for pH calibration curve can be found in the chapter by Kim H et al. "Analysis Protocol for the Quantification of Renal pH Using Chemical Exchange Saturation Transfer (CEST) MRI."

1. Acquire the CEST Z-spectrum by sweeping RF saturation to a series of frequency offsets around the bulk water resonance. Note that the magnitude of the saturation field (B_1) and duration can be adjusted serially to facilitate Z-spectral acquisition. For an example of specific parameters at 7 T please *see* **Note 12**, whereas for an example of specific parameters at 4.7 T please *see* **Note 13** and for the same at 11.7 T please *see* **Note 14**.

3.3 Preparations of the Contrast Agent Injection and of the Catheter

1. Fill the 1-ml syringe with the contrast agent stock solution.
2. Prepare the catheter by filling the PE20 tubing with the contrast agent solution, and with 20–60 μl of a heparin solution (or a saline solution), between the needle (the animal) and the contrast agent solution to prevent clotting before the contrast agent will be injected.
3. According to the length of the catheter (usually 60–100 cm to exit from the magnet bore) the contrast agent solution can be injected directly from the syringe containing the contrast agent or by changing the syringe with one filled with a (heparin-free) saline solution for the postinjection flush.

3.4 Preparation of the Mouse

1. Place the mouse on a mouse tail illuminator restrainer for catheterizing the tail vein. Catheterize the tail vein by placing a 27/29-G needle in the animal.
2. Induce anesthesia via isoflurane in an induction box. Transfer the animal to the scanner (**Note 15**).
3. Set up the temperature monitoring (rectal probe) and respiratory monitoring (balloon on chest) unit. Keep the animal's respiration rate during imaging at 35–80 breaths per min by adjusting the dose of anesthesia (approximately 1–1.5% isoflurane with air and oxygen mixed at a 3:1 ratio administered through a nose cone attached to the animal bed and ophthalmic ointment will be applied to the eyes) (*see* **Note 16**).
4. Perform anatomical imaging as described in the chapter by Pohlmann A et al. "Essential Practical Steps for MRI of the Kidney in Experimental Research."

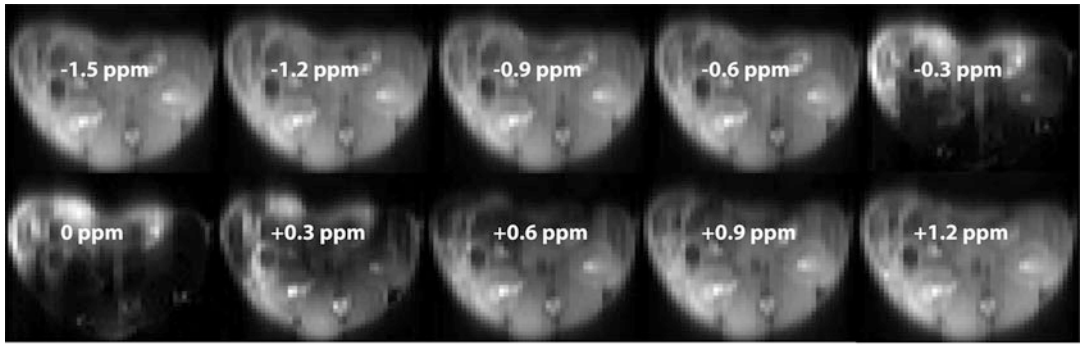

Fig. 1 Series of ten saturation weighted images of a healthy mouse kidney acquired with a 2D CEST-RARE sequence at 11.7 T. Images correspond to saturation frequencies = −1.5, −1.2, −0.9, −0.6, −0.3 ppm (top row) and saturation frequencies = 0, 0.3, 0.6, 0.9, 1.2 ppm (bottom row)

5. Perform localized shimming on the kidney imaging as described in the chapter by Pohlmann A et al. "Essential Practical Steps for MRI of the Kidney in Experimental Research" (*see* **Note 17**).

3.5 B_0 Mapping

3.5.1 External B_0 Mapping

1. Load the B_0 mapping sequence and adapt the slice orientation to provide a coronal or axial view of the two kidneys based on the tripilot/scout and anatomical images collected.
2. Run the B_0 mapping scan using 42 offsets from −1.5 to +1.5 ppm and B_1 = 1.5 μT. Example images are shown in Fig. 1.

3.5.2 Internal B_0 Mapping

1. Acquire a full Z-spectrum with some frequency offsets sampled around 0 ppm to exploit the Z-spectrum for internal measurement of B_0 shifts as described in the chapter by Kim H et al. "Analysis Protocol for the Quantification of Renal pH Using Chemical Exchange Saturation Transfer (CEST) MRI."

3.6 CEST Acquisition for pH Mapping

1. Perform the CEST experiment by acquiring CEST images before, (during) and after injection of the contrast agent. Choose among the different pH mapping procedures by conventional ratiometric approach (Subheading 3.5.1), pH mapping with power ratiometric method (Subheading 3.5.2) or dynamic CEST perfusion and pH mapping (Subheading 3.5.3).

3.6.1 pH Mapping with Conventional Ratiometric Method (Full Z-Spectrum)

1. Load the pH mapping sequence, using the same geometry as used for anatomical and B_0 mapping. Switch off the magnetization module and use this sequence to set the receiver gain.
2. Load the pH mapping sequence, using the same geometry as used for anatomical and B_0 mapping. Set the receiver gain as calculated by the magnetization off sequence (*see* Subheading

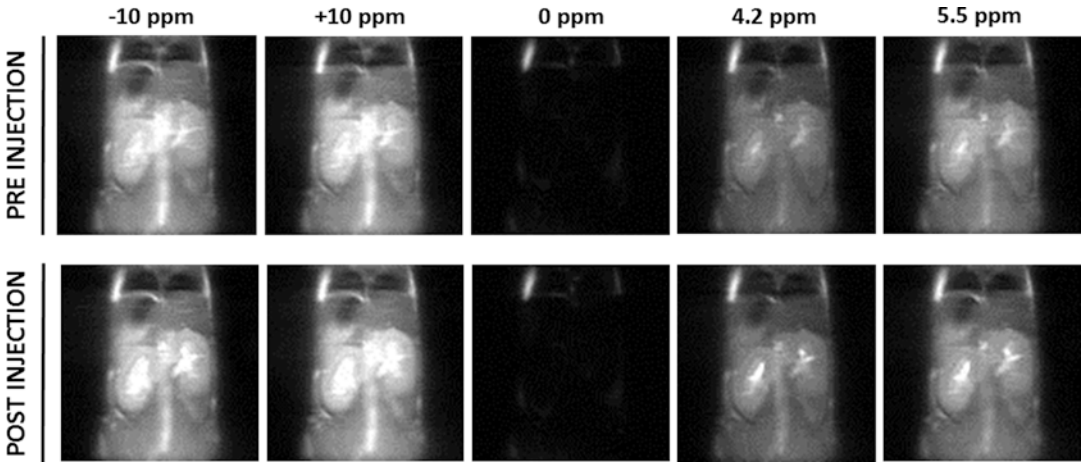

Fig. 2 Series of saturated weighted images of a healthy mouse kidney acquired with a 2D CEST-RARE sequence at 7 T before (up panel) and after (bottom panel) the injection of iopamidol at 1.5 mg I/kg b.w. Images correspond to saturation frequencies of −10, +10, 0, +4.2, and +5.5 ppm

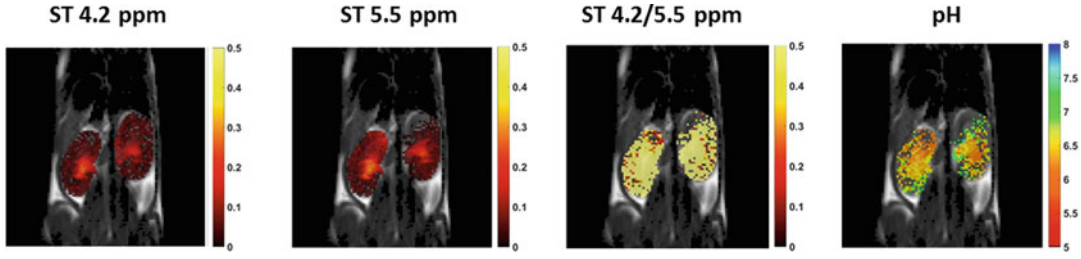

Fig. 3 From left to right: parametric maps of saturation transfer (ST) contrast obtained at 4.2 ppm, at 5.5 ppm, ratiometric 4.2/5.5 map and calculated pH map in kidney regions. The parametric color maps are superimposed on a T_{2w} anatomical image (gray scale)

3.5.1.15). Load the macro file containing the offset frequencies to be saturated and run the sequence for CEST preinjection scanning.

3. Clone the pH mapping scans, at least one time for acquiring one CEST postinjection scan.
4. After the acquisition of the CEST prescan, perform a bolus injection of iodine contrast agent through the tail vein catheter at a dose of 1.0–1.5 iodine/kg b.w. (*see* **Note 18**).
5. Run the postinjection scans.
6. A demonstration of the acquired images at different offsets and of CEST contrast that can be expected for the pH mapping scans are given in Fig. 2 and Fig. 3, respectively.

3.6.2 pH Mapping with Power Ratiometric Method (Full Z-Spectrum)

1. Load the pH mapping sequence, using the same geometry as used for anatomical and B_0 mapping. Switch off the magnetization module and use this sequence to set the receiver gain.
2. Load the pH mapping sequence, using the same geometry as used for anatomical and B_0 mapping. Set the receiver gain as calculated by the magnetization off sequence (*see* Subheading 3.6.1.15). Load the macro file containing the offset frequencies to saturate at a first selected power pulse (1.5 μT) and run the sequence for CEST preinjection scanning.
3. Clone the scan and set the second selected saturation power pulse (6 μT). Run the sequence for CEST preinjection scanning.
4. Clone two times the scans with 1.5 and 6 μT saturation power pulse for acquiring the postinjection scans.
5. Perform a bolus injection of iodine contrast agent with single amide exchanging pool (e.g., iobitridol) through the tail vein catheter at a dose of 1.0–1.5 iodine/kg b.w. (*see* **Note 18**).
6. Run the postinjection scans.

3.6.3 pH and Perfusion Mapping with Two Offset Sampling

1. Load the pH mapping sequence, using the same geometry as used for B_0 mapping and setting up a collection to run for 1 h, 5 min alternating the saturation frequency between 4.2 ppm (labile proton #1 for iopamidol), 5.5 ppm (labile proton #2 for iopamidol), and for the final ten images at −100 ppm (S_0 image) (*see* **Note 19**).
2. Initiate the pH mapping scans.
3. Exactly 5 min after starting the pH mapping scans, perform a bolus injection of contrast agent: inject iopamidol through the tail vein at a dose of 1.0 g iodine/kg using ~100–150 μl.
4. Approximately 1 h after injection, end the pH mapping scan collection.
5. A demonstration of the contrast changes that can be expected for the pH mapping scans are given in Fig. 4.

4 Notes

1. Intramuscular anesthesia can be administered as a mixture of xylazine 5 mg/kg (Rompun, Bayer, Milan, Italy) and tiletamine/zolepan 20 mg/kg (Zoletil 100, Virbac, Milano, Italy).
2. To reduce the viscosity of these solutions, hence the pressure needed to infuse these solutions, syringes can be warmed at 37 °C before the injection. Please avoid the inclusion of air bubbles in the catheter filled with the saline solution or with the contrast agent solution that will be injected into the animals.

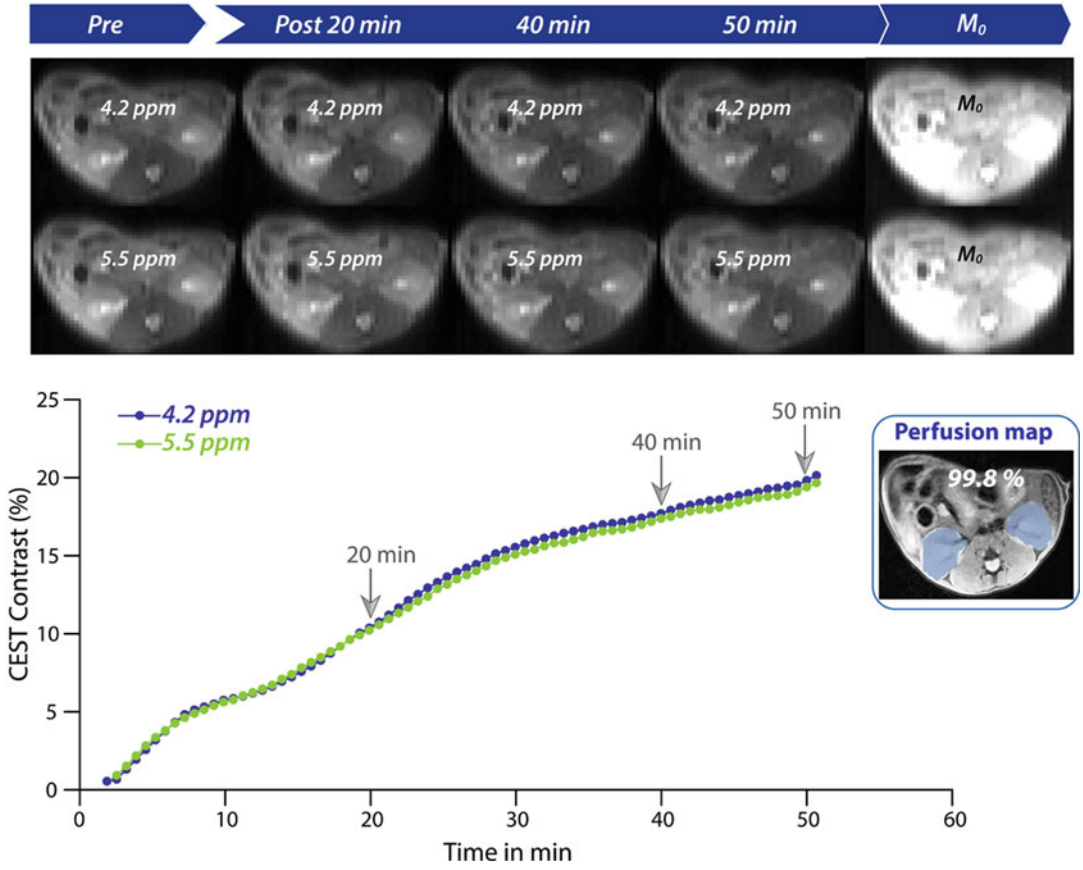

Fig. 4 Demonstration of the contrast changes that can be expected in pH mapping. CEST weighted images (from a 2D RARE acquisition, effective TE = 3.5 ms) of the kidneys throughout a pH measurement experiment, together with a final processed image of perfusion. A moving average filter was applied on the time series data to remove fluctuations in signal due to motion. The percentage of kidney pixels with >20% of maximum contrast were calculated to obtain the perfusion or filtration fraction map

3. CEST pH measurements are basically performed on Bruker MR systems as Biospec 117/20 (11.7 T), Avance 300 (7 T), Pharmascan 70/16 (7 T), or Biospec (3 T) (Bruker, Ettlingen, Germany). Standard 1H transmit/receive coils (birdcage, quadrature) or phased-array coils (4- or 8-channel mouse body phase array receive coil) to improve SNR can be used.
4. WASSR B_0 mapping frequency list (in ppm): −1.5, −1.4, −1.3, −1.2, −1.1, −1.0, −0.9, −0.8, −0.7, −0.6, −0.5, −0.4, −0.3, −0.2, −0.1, 0, 0.1, 0.2, 0.3, 0.4, 0.5, 0.6, 0.7, 0.8, 0.9, 1.0, 1.1, 1.2, 1.3, 1.4, and 1.5.
5. Scan acquisition parameters for B_0 mapping: TR = 5000 ms; magnetization transfer power = 1.5 μT; magnetization transfer module time = 3 s; MT offset mode = Sequential_Offset; effective TE = 3.49 ms; RARE Factor = 32; averages = 1;

centric encoding; slice thickness = 1.5 mm; slice orientation = axial; frequency encoding = head-feet; FOV = 28 × 19 mm; matrix size = 48 × 48 reconstructed to 128 × 128; fat suppression = on.

6. Standard Bruker sequences for the software versions PV5 and PV6 include only a Magnetization Transfer module that allows the saturation of a single frequency offset. As a consequence, full Z-spectrum acquisition can only be acquired by cloning the same scan and modifying for each scan the irradiated frequency offset. Therefore, for in vivo experiments this may lead to acquisition times that are not feasible in reasonable time. Bruker sequences for PV5 and PV6 that have been modified to accept a frequency list for acquiring the full Z-spectrum in a single scan are available upon request to the authors (dario.longo@unito.it; mtmcmaho@gmail.com; pzhesun@emory.edu). Starting from PV360 a new CEST module has been implemented with different readout sequences (RARE, EPI, Spiral) that allows to fix this issue. MR Solutions vendor has already a CEST module that can be applied with an EPI-based readout scheme.
7. Frequency list (in ppm) for a full Z-spectrum acquisition (43 offsets): 0, 0.5, −0.5, 1.0, −1.0, 1.5, −1.5, 2.0, −2.0, 3.0, −3.0, 3.9, −3.9, 4.0, −4.0, 4.1, −4.1, 4.2, −4.2, 4.3, −4.3, 4.4, −4.4, 4.5, −4.5, 5.2, −5.2, 5.3, −5.3, 5.4, −5.4, 5.5, −5.5, 5.6, −5.6, 5.7, −5.7, 5.8, −5.8, 7.5, −7.5, 10.0, and −10.0.
8. Example for a 30 g mouse at 7 T: TR = 6000 ms; magnetization transfer power = 3 μT; magnetization transfer module time = 5 s; MT offset mode = from file; effective TE = 4.14 ms; RARE Factor = 96; averages = 1; centric encoding; slice thickness = 1.5 mm; slice orientation = axial; frequency encoding = head-feet; FOV = 30 mm; matrix size = 96 × 96 reconstructed to 128 × 128; fat suppression = on.
9. Example for a 150 g rat at 4.7 T: Z-spectra are collected with moderate saturation RF power (B_1) levels of 1.0 and 2.0 μT. The in vivo CEST MRI parameters were as the following: RF saturation offsets from −7.0 to 7.0 ppm with intervals of 0.125 ppm, and TR, TS and TE were 6 s, 3 s, and 18 ms, respectively, for an image matrix of 48 × 48.
10. For rats increase the FOV to the body width and keep the matrix size the same or similar. The relative resolution is then identical and the SNR should also be similar, because the larger rat RF coil provides worse SNR (e.g., eight-channel rat body phase array receive coil vs eight-channel mouse body phase array receive coil).

11. Example for a 30 g mouse at 11.7 T: TR = 9000 ms; magnetization transfer power = 4 μT; magnetization transfer pulse number = 10; magnetization transfer inter pulse delay = 10 μs; magnetization transfer pulse length = 300 ms; magnetization transfer module time = 3 s; MT offset mode = from file; effective TE = 3.49 ms; RARE Factor = 32; averages = 1; centric encoding; slice thickness = 1.5 mm; slice orientation = axial; frequency encoding = head-feet; FOV = 28 × 19 mm^2; matrix size = 48 × 48 using partial Fourier of 1.5; fat suppression = on.
12. Phantom CEST acquisition parameters at 7 T: RF saturation offsets from −10.0 to 10.0 ppm with intervals of 0.1–0.2 ppm. TR = 10s, TE = 4.8 ms, saturation = 3 μT × 5 s, matrix size = 64 × 64, FOV = 30 × 30 mm^2 with centric encoding.
13. Phantom CEST acquisition parameters at 4.7 T: RF saturation offsets from −7 to 7 ppm with intervals of 0.25 ppm. TR = 12 s, TE = 39.5 ms, saturation: 1, 1.5, 2, 2.5, 3 and 4 μT × 5 s, matrix size = 64 × 64, FOV =48 × 48 mm with centric encoding.
14. Phantom CEST acquisition parameters at 11.7 T:: 25 mm transmit/receive volume coil; TR = 5000 ms; magnetization transfer power = six different saturation power (B_1) from 1 to 6 μT; magnetization transfer module time = 3 s; MT offset mode = Sequential_Offset; 71 CEST offsets between ±7 ppm plus one at +40 ppm for M_0; effective TE = 3.39 ms; RARE Factor = 16; averages = 1; centric encoding; slice - thickness = 1.0 mm; slice orientation = axial; frequency encoding = head-feet; FOV = 28 × 19 mm^2; matrix size = 64 × 48.
15. Mice can be alternatively anesthetized with intramuscular anesthesia, tail veins heated with hot water/heater equipment at 37 °C and catheter placed in the animal.
16. You must monitor the respiration continuously throughout the entire experiment.
17. B_0 Shimming is particularly important, since macroscopic magnetic field inhomogeneities affect the exact resonance frequency of the labile protons in a voxel, and can impact the pH and perfusion measurements and hinder quantitative intra- and inter-subject comparisons. Shimming should be performed on a voxel enclosing both kidneys using either the default iterative shimming method or the Mapshim technique (recommended).
18. Injections can be manually or automatically performed. For manual injection, keep injection constant within 20–30 s. Automatic injection can be performed with dedicated injection pumps, by setting injection speed of contrast agent at 400 μl/

min. For instance, a 25 g mouse would receive ca 70 μl to achieve a dose of 1 g iodine/kg b.w. with a stock solution of 370 mg iodine/ml.

19. The exact list of frequencies used here can be adjusted based on the B_0 shimming conditions of the kidneys and the saturation power applied. For example, if the B_0 varies by more than say 0.1 ppm, additional frequencies around each labile proton should be added to allow B_0 correction at the expense of SNR due to the reduced redundancy of the data collected.

Acknowledgments

This work was supported by the Maryland Stem Cell Research Foundation MSCRF#2829 and NIH P41EB024495. The Italian Ministry for Education and Research (MIUR) is gratefully acknowledged for yearly FOE funding to the Euro-BioImaging Multi-Modal Molecular Imaging Italian Node (MMMI).
This chapter is based upon work from COST Action PARENCHIMA, supported by European Cooperation in Science and Technology (COST). COST (www.cost.eu) is a funding agency for research and innovation networks. COST Actions help connect research initiatives across Europe and enable scientists to enrich their ideas by sharing them with their peers. This boosts their research, career, and innovation.
PARENCHIMA (renalmri.org) is a community-driven Action in the COST program of the European Union, which unites more than 200 experts in renal MRI from 30 countries with the aim to improve the reproducibility and standardization of renal MRI biomarkers.

References

1. Hamm LL, Nakhoul N, Hering-Smith KS (2015) Acid-base homeostasis. Clin J Am Soc Nephrol 10(12):2232–2242
2. Soleimani M, Rastegar A (2016) Pathophysiology of renal tubular acidosis: core curriculum 2016. Am J Kidney Dis 68(3):488–498. https://doi.org/10.1053/j.ajkd.2016.03.422
3. Gil-Peña H, Mejía N, Santos F (2014) Renal tubular acidosis. J Pediatr 164(4):691–698. https://doi.org/10.1016/j.jpeds.2013.10.085
4. Gillies RJ, Raghunand N, Garcia-Martin ML, Gatenby RA (2004) pH imaging. IEEE Eng Med Biol Mag 23(5):57–64
5. Raghunand N, Howison C, Sherry AD, Zhang S, Gillies RJ (2003) Renal and systemic pH imaging by contrast-enhanced MRI. Magn Reson Med 49(2):249–257
6. Longo DL, Busato A, Lanzardo S, Antico F, Aime S (2013) Imaging the pH evolution of an acute kidney injury model by means of iopamidol, a MRI-CEST pH-responsive contrast agent. Magn Reson Med 70(3):859–864
7. Longo DL, Cutrin JC, Michelotti F, Irrera P, Aime S (2017) Noninvasive evaluation of renal pH homeostasis after ischemia reperfusion injury by CEST-MRI. NMR Biomed 30(7). https://doi.org/10.1002/nbm.372
8. Hashim AI, Zhang XM, Wojtkowiak JW, Martinez GV, Gillies RJ (2011) Imaging pH and metastasis. NMR Biomed 24(6):582–591. https://doi.org/10.1002/nbm.1644

9. Ashby BS (1966) pH studies in human malignant tumours. Lancet 288(7458):312–315
10. Prescott DM, Charles HC, Poulson JM, Page RL, Thrall DE, Vujaskovic Z, Dewhirst MW (2000) The relationship between intracellular and extracellular pH in spontaneous canine tumors. Clin Cancer Res 6(6):2501–2505
11. Wike-Hooley JL, van den Berg AP, van der Zee J, Reinhold HS (1985) Human tumour pH and its variation. Eur J Cancer Clin Oncol 21(7):785789–787791
12. Li C, Xia J, Wei X, Yan H, Si Z, Ju S (2010) pH-activated near-infrared fluorescence nanoprobe imaging tumors by sensing the acidic microenvironment. Adv Funct Mater 20(14):2222–2230
13. Hassan M, Riley J, Chernomordik V, Smith P, Pursley R, Lee SB, Capala J, Amir HG (2007) Fluorescence lifetime imaging system for in vivo studies. Mol Imaging 6 (4):7290.2007.00019
14. García-Martín M-L, Hérigault G, Rémy C, Farion R, Ballesteros P, Coles JA, Cerdán S, Ziegler A (2001) Mapping extracellular pH in rat brain gliomas in vivo by H magnetic resonance spectroscopic imaging: comparison with maps of metabolites. Cancer Res 61 (17):6524–6531
15. Gillies R, Liu Z, Bhujwalla Z (1994) 31P-MRS measurements of extracellular pH of tumors using 3-aminopropylphosphonate. Am J Phys Cell Phys 267(1):C195–C203
16. Gillies RJ, Morse DL (2005) In vivo magnetic resonance spectroscopy in cancer. Annu Rev Biomed Eng 7:287–326
17. Vermathen P, Capizzano AA, Maudsley AA (2000) Administration and 1H MRS detection of histidine in human brain: application to in vivo pH measurement. Magn Reson Med 43(5):665–675
18. Bhujwalla ZM, McCoy C, Glickson J, Gillies R, Stubbs M (1998) Estimations of intra-and extracellular volume and pH by 31P magnetic resonance spectroscopy: effect of therapy on RIF-1 tumours. Br J Cancer 78(5):606
19. Aoki Y, Akagi K, Tanaka Y, Kawai J, Takahashi M (1996) Measurement of intratumor pH by pH indicator used in 19F-magnetic resonance spectroscopy: measurement of extracellular pH decrease caused by hyperthermia combined with hydralazine. Investig Radiol 31 (11):680–689
20. Zhou R, Bansal N, Leeper DB, Glickson JD (2000) Intracellular acidification of human melanoma xenografts by the respiratory inhibitor m-iodobenzylguanidine plus hyperglycemia: a 31P magnetic resonance spectroscopy study. Cancer Res 60(13):3532–3536
21. Ojugo AS, McSheehy PM, McIntyre DJ, McCoy C, Stubbs M, Leach MO, Judson IR, Griffiths JR (1999) Measurement of the extracellular pH of solid tumours in mice by magnetic resonance spectroscopy: a comparison of exogenous 19F and 31P probes. NMR Biomed 12(8):495–504
22. Gallagher FA, Kettunen MI, Day SE, Hu D-E, Ardenkjær-Larsen JH, Jensen PR, Karlsson M, Golman K, Lerche MH, Brindle KM (2008) Magnetic resonance imaging of pH in vivo using hyperpolarized 13C-labelled bicarbonate. Nature 453(7197):940–943
23. Garcia-Martin ML, Martinez GV, Raghunand N, Sherry AD, Zhang S, Gillies RJ (2006) High resolution pHe imaging of rat glioma using pH-dependent relaxivity. Magn Reson Med 55(2):309–315
24. McMahon MT, Gilad AA, Bulte JWM, van Zijl PCM (2017) Chemical exchange saturation transfer imaging: advances and applications, 1st edn. Pan Stanford Publishing, Singapore
25. Longo D, Aime S (2017) Iodinated contrast media as pH-responsive CEST agents. In: McMahon MT, Gilad AA, JBM B, PCM VZ (eds) Chemical exchange saturation transfer imaging. Vol. Advances and applications. Pan Stanford Publishing, Singapore, pp 447–466. https://doi.org/10.1201/9781315364421-20
26. Pavuluri K, McMahon MT (2017) pH imaging using chemical exchange saturation transfer (CEST) MRI. Isr J Chem 57(9):862–879. https://doi.org/10.1002/ijch.201700075
27. Longo DL, Dastrù W, Digilio G, Keupp J, Langereis S, Lanzardo S, Prestigio S, Steinbach O, Terreno E, Uggeri F (2011) Iopamidol as a responsive MRI-chemical exchange saturation transfer contrast agent for pH mapping of kidneys: In vivo studies in mice at 7 T. Magn Reson Med 65(1):202–211
28. Longo DL, Sun PZ, Consolino L, Michelotti FC, Uggeri F, Aime S (2014) A general MRI-CEST ratiometric approach for pH imaging: demonstration of in vivo pH mapping with iobitridol. J Am Chem Soc 136 (41):14333–14336
29. Wu RH, Longo DL, Aime S, Sun PZ (2015) Quantitative description of radiofrequency (RF) power-based ratiometric chemical exchange saturation transfer (CEST) pH imaging. NMR Biomed 28(5):555–565. https://doi.org/10.1002/nbm.3284
30. Yang X, Song X, Ray Banerjee S, Li Y, Byun Y, Liu G, Bhujwalla ZM, Pomper MG, McMahon

MT (2016) Developing imidazoles as CEST MRI pH sensors. Contrast Media Mol Imaging 11(4):304–312

31. McMahon MT, Gilad AA, Zhou J, Sun PZ, Bulte JW, van Zijl P (2006) Quantifying exchange rates in chemical exchange saturation transfer agents using the saturation time and saturation power dependencies of the magnetization transfer effect on the magnetic resonance imaging signal (QUEST and QUESP): pH calibration for poly-L-lysine and a starburst dendrimer. Magn Reson Med 55(4):836–847
32. Anemone A, Consolino L, Arena F, Capozza M, Longo DL (2019) Imaging tumor acidosis: a survey of the available techniques for mapping in vivo tumor pH. Cancer Metastasis Rev. https://doi.org/10.1007/s10555-019-09782-9
33. Grenier N, Cornelis F, Le Bras Y, Rigou G, Boutault JR, Bouzgarrou M (2013) Perfusion imaging in renal diseases. Diagn Interv Imaging 94(12):1313–1322. https://doi.org/10.1016/j.diii.2013.08.018
34. Anemone A, Consolino L, Longo DL (2017) MRI-CEST assessment of tumour perfusion using X-ray iodinated agents: comparison with a conventional Gd-based agent. Eur Radiol 27(5):2170–2179. https://doi.org/10.1007/s00330-016-4552-7
35. Sheth VR, Li Y, Chen LQ, Howison CM, Flask CA, Pagel MD (2012) Measuring in vivo tumor pHe with CEST-FISP MRI. Magn Reson Med 67(3):760–768. https://doi.org/10.1002/mrm.23038
36. Sun PZ, Cheung JS, Wang E, Benner T, Sorensen AG (2011) Fast multislice pH-weighted chemical exchange saturation transfer (CEST) MRI with unevenly segmented RF irradiation. Magn Reson Med 65(2):588–594. https://doi.org/10.1002/mrm.22628
37. Pavuluri K, Manoli I, Pass A, Li Y, Vernon HJ, Venditti CP, McMahon MT (2019) Noninvasive monitoring of chronic kidney disease using pH and perfusion imaging. Sci Adv. https://doi.org/10.1126/sciadv.aaw8357
38. Kim M, Gillen J, Landman BA, Zhou J, van Zijl PC (2009) Water saturation shift referencing (WASSR) for chemical exchange saturation transfer (CEST) experiments. Magn Reson Med 61(6):1441–1450. https://doi.org/10.1002/mrm.21873
39. Sun PZ, Longo DL, Hu W, Xiao G, Wu R (2014) Quantification of iopamidol multi-site chemical exchange properties for ratiometric chemical exchange saturation transfer (CEST) imaging of pH. Phys Med Biol 59(16):4493

Chapter 28

Sodium (^{23}Na) MRI of the Kidney: Experimental Protocol

James T. Grist, Esben Søvsø Hansen, Frank G. Zöllner, and Christoffer Laustsen

Abstract

Sodium handling is a key physiological hallmark of renal function. Alterations are generally considered a pathophysiologic event associated with kidney injury, with disturbances in the corticomedullary sodium gradient being indicative of a number of conditions. This experimental protocol review describes the individual steps needed to perform ^{23}Na MRI; allowing accurate monitoring of the renal sodium distribution in a step-by-step experimental protocol for rodents.

This chapter is based upon work from the PARENCHIMA COST Action, a community-driven network funded by the European Cooperation in Science and Technology (COST) program of the European Union, which aims to improve the reproducibility and standardization of renal MRI biomarkers. This experimental protocol chapter is complemented by two separate chapters describing the basic concept and data analysis.

Key words Magnetic resonance imaging (MRI), Kidney, Mice, Rats, ^{23}Na, Sodium

1 Introduction

Sodium is an essential body fluid electrolyte, with serum concentration tightly controlled by the renal proximal and distal tubules, the loop of Henle, and the collecting duct through a complex process of active reabsorption via transport proteins [1]. Electrolyte reabsorption requires large quantities of adenosine triphosphate (ATP), to move ions against the concentration gradient, produced via the mitochondrial tricarboxylic acid (TCA) cycle [1–3]. To fuel TCA activity, oxygen is delivered via a network of arterial vessels to the renal system. However, should the renal system undergo injury, for example in acute kidney injury or chronic renal disease, the delivery of oxygen to local tissues may be disrupted, and subsequently the gradient of sodium from the cortex to the medulla impaired [4].

In this chapter we describe the process of undertaking sodium MRI for assessing alterations of the corticomedullary sodium

Andreas Pohlmann and Thoralf Niendorf (eds.), *Preclinical MRI of the Kidney: Methods and Protocols*, Methods in Molecular Biology, vol. 2216, https://doi.org/10.1007/978-1-0716-0978-1_28,

gradient in the kidney of rodents in a step-by-step experimental protocol. We also describe the rationale for acquisition parameter selection, with generic terms, with specific examples for rodent imaging on a small-bore animal MR system (Bruker Biospin, Ettlingen, Germany), and porcine imaging on whole body human MR scanner (General Electric, Waukesha, USA). Finally, we discuss the effects of acute diuretics such as furosemide to demonstrate alterations in renal sodium handling.

This experimental protocol chapter is complemented by two separate chapters describing the basic concept and data analysis, which are part of this book.

This chapter is part of the book Pohlmann A, Niendorf T (eds) (2020) Preclinical MRI of the Kidney—Methods and Protocols. Springer, New York.

2 Materials

2.1 Calibration Phantom Preparation: Rodent

2.1.1 Lab Equipment and Components

1. 5 mL Eppendorf tubes.
2. Agarose.
3. 5 g Sodium chloride.
4. Microwave oven.
5. Beaker (microwave safe).
6. Deionized water.

2.1.2 Process to Make 4% Agarose Phantoms (Example 60 and 150 mmol/L Phantoms)

1. Weigh 350 mg sodium chloride.
2. Weight 25 g agarose.
3. Add both to a beaker with 100 mL of deionized water and stir until dissolved.
4. Heat solution in a microwave oven in 30 s intervals, until thickened.
5. Pipette 5 mL of solution in to Eppendorf tubes.
6. Repeat for 150 mmol/L phantom, weighing 875 mg sodium chloride for an equivalent volume of water.
7. Leave Eppendorf tubes to cool for 24 h and seal with Parafilm.

2.2 Animals

This experimental protocol is tailored for rats (Wistar, Sprague-Dawley or Lewis) with a body mass of 300–350 g or pigs 20–40 kg.

2.3 Lab Equipment

1. Anesthesia: please refer to the chapter by Kaucsar T et al. "Preparation and Monitoring of Small Animals in Renal MRI" for an in-depth description and discussion of the anesthesia. For nonrecovery experiments urethane solution (Sigma-Aldrich, Steinheim, Germany; 20% in distilled water) can provide anesthesia for several hours with comparatively fewer side effects on renal physiology, which is an important issue.

2. Gases: O_2, N_2, and compressed air, as well as a gas-mixing system (FMI Föhr Medical Instruments GmbH, Seeheim-Ober Beerbach, Germany) to achieve required changes in the oxygen fraction of inspired gas mixture (FiO_2).
3. Device for FiO_2 monitoring in gas mixtures: for example, Capnomac AGM-103 (Datex GE, Chalfont St Gils, UK).
4. A physiological monitoring system that can track the respiration, and which is connected to the MR system such that it can be used to trigger the image acquisition.

2.4 MRI Hardware

The general hardware requirements for renal ^1H MRI on mice and rats are described in the chapter by Ramos Delgado P et al. "Hardware Considerations for Preclinical Magnetic Resonance of the Kidney." The technique described in this chapter has been tailored for a 7 and 3 T MR system (Biospec 94/20, Bruker Biospin, Ettlingen, Germany and MR750, General Electric, Milwaukee, USA), but advice for adaptation to other field strengths is given where necessary. An additional dual or single tuned $^1H/^{23}Na$ surface or volume coil is required, as well as multinuclear capabilities of the MR system.

3 Methods

3.1 MR Protocol Setup

3.1.1 Total Sodium Imaging (BRUKER)

1. Sequence type: 3D gradient echo sequence. This is a standard sequence on Bruker MRI systems. *See* **Notes 1–3** for details.
2. Repetition time (TR): Choose 2.5× greater than the T_1 of sodium in free fluid (T_1 approx. 70 ms at 7 T).
3. Flip angle (FA): 90°.
4. Echo time (TE): The minimum TE achievable on the system is used to acquire the rapidly decaying signal.
5. Acquisition bandwidth (BW): Use the highest acquisition bandwidth possible to shorten the echo time; however, this will lead to a decrease in SNR. Low SNR may be countered by signal averaging.
6. Respiration trigger: on (per excitation).
7. Geometry: adapt so that animal fits into FOV in L-R direction.
8. Spatial resolution: adapt to the physiological resolution aimed for in the study at hand. Recommend 1 mm × 1 mm in rats.
9. Crushing: Ensure signal is crushed at the end of each readout, to ensure spoiling of latent T_2^* signal.

3.1.2 Total Sodium Imaging (General Electric)

1. Sequence type: Fidall. This is a research pulse sequence from GE. *See* **Notes 4–6** for sequence details.
2. Calibration can be performed using the inbuilt Bloch–Siegert calibration sequence.

3. Readout type: 3D cones. Waveforms can be generated using code available online (http://www-mrsrl.stanford.edu/~ptgurney/cones.php).
4. Repetition time (TR): Choose 2.5× greater than the T_1 of sodium in free fluid (T_1 approx. 50 ms at 3 T).
5. Flip angle (FA): Ernst-angle (typically 70–90°).
6. Echo time (TE): The minimum TE achievable on the system is used to acquire the rapidly decaying signal.
7. Acquisition bandwidth (BW): Use the highest acquisition bandwidth possible to shorten TE, however this will lead to a decrease in SNR. Low SNR may be countered by signal averaging.
8. Respiration trigger: on (minimum 6 per excitation).
9. Geometry: adapt so that animal fits into FOV in L-R direction.
10. Crushing: Ensure signal is crushed at the end of each readout, to ensure spoiling of latent T_2^* signal using crusher gradients.

3.1.3 T_2^* Mapping (BRUKER)

1. Sequence type: 3D gradient echo sequence. This is a standard sequence on Bruker MRI systems, where it is called "3D gradient echo" (*see* **Note 1** for sequence details).
2. Repetition time (TR): Choose 2.5× greater than the T_1 of sodium in free fluid (T_1 approx. 70 ms at 7 T).
3. Flip angle (FA): 90°.
4. Echo time (TE): The minimum TE achievable on the system is used to acquire the rapidly decaying signal.
5. Acquisition bandwidth (BW): Use the highest acquisition bandwidth possible to shorten TE, however this will lead to a decrease in SNR. Low SNR may be countered by signal averaging.
6. Geometry: adapt so that animal fits into FOV in L-R direction.
7. Spatial resolution: adapt to the physiological resolution aimed for in the study at hand. Recommend 1 mm × 1 mm in rats.
8. Crushing: Ensure signal is crushed at the end of each readout to ensure spoiling of latent T_2^* signal using crusher gradients.
9. Repeat acquisition using same prescan parameters with incremented TE, ensuring at least five echo times are collected. We recommended eight echo times: 0.5, 1, 2, 4, 5, 10, 15, and 20 ms.

3.1.4 Total Sodium Imaging Agilent)

1. Sequence type: 2D or 3D chemical shift imaging sequence. This is a standard sequence on preclinical MRI and clinical MRI systems. *See* **Notes 7** and **8** for sequence details.

2. Repetition time (TR): Choose 2.5× greater than the T_1 of sodium in free fluid (T_1 approx. 70 ms at 7 T).
3. Echo time (TE): choose the shortest possible for good signal-to-noise.
4. Flip angle (FA): 90° or according to the Ernst angle.
5. Acquisition bandwidth (BW): Choose BW and NP to ensure sufficient resolution and acquisition time of approximately $2.5 \times T_2^*$.

3.1.5 Calibration Scans

1. Perform a reference scan with above given parameters using a homogeneous phantom to acquire the receive sensitivity of the RF coils and gradient trajectory (*see* **Note 8**).
2. Coregistration of reference and the scans of Subheading 3.1.1–3.1.4.
3. Obtain sensitivity corrected images by the quotient image of both coregistered images concentration.
4. For B_1 mapping (double angle method) perform a measurement using a homogeneous phantom and scan parameters reported in Subheading 3.1.1 and flip angles of $\alpha_1 = 40°$, $\alpha_2 = 80°$.

3.2 In Vivo Sodium Imaging

1. Anesthetize the animal, obtained venous access (tail vein for rat and ear vein for pig) and transfer it to scanner.

3.2.1 Preparations

2. Set up the temperature monitoring (rectal probe) and respiratory monitoring (balloon on chest) unit.
3. Fixate the sodium phantoms to the animal near the imaging area.
4. Perform anatomical imaging as described in the chapter by Pohlmann A et al. “Essential Practical Steps for MRI of the Kidney in Experimental Research.”

3.2.2 Baseline Condition

1. Load the 3D GRE sequence, altering the slice orientation to the desired acquisition plane.
2. Triggering: in the monitoring unit set the trigger delay so that the trigger starts at the beginning of the expiratory plateau (no chest motion) and the duration such that it covers the entire expiratory phase, that is, until just before inhalation starts.
3. Run the sodium scan. Example images are shown in Fig. 1.

3.2.3 Imaging Furosemide Action

1. Duplicate the sodium scan.
2. Introduction of furosemide: Inject 10 mg/kg furosemide via tail vein catheter and begin image acquisition.

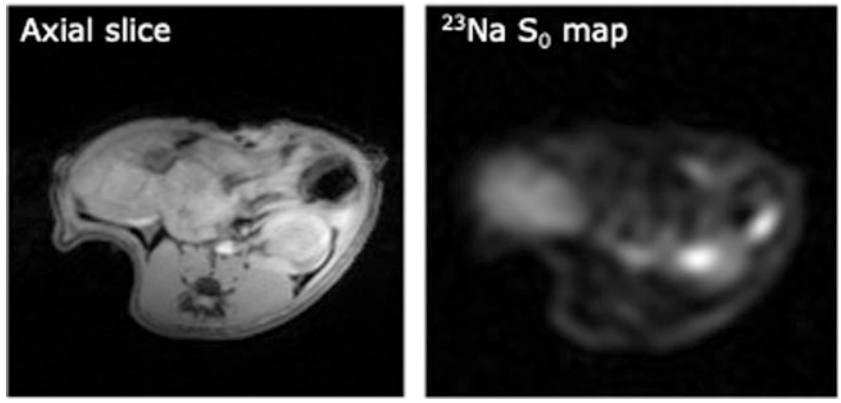

Fig. 1 Example ^{1}H (left) and ^{23}Na (right) rodent renal imaging acquired at 9.4 T, acquisition time = 3.5 min

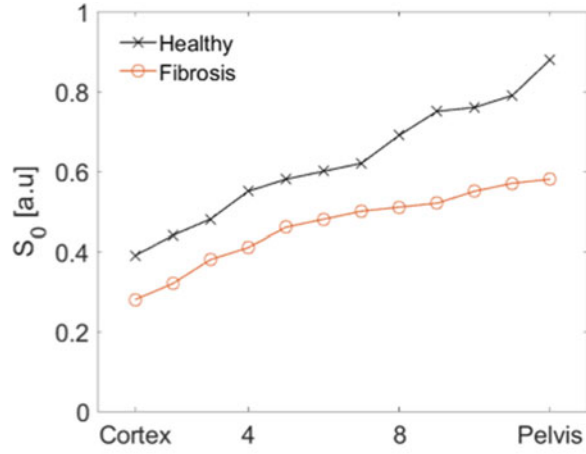

Fig. 2 Example corticomedullary sodium gradient, healthy (black) and impaired rodent kidney (orange)

3. Continue to acquire sodium imaging for up to one hour post the introduction of furosemide.
4. A demonstration of the sodium changes that can be expected in pathophysiological scenarios is given in Fig. 2.

3.2.4 T_2^* Mapping

1. Load the 3D GRE multiecho sequence, altering the slice orientation to the desired acquisition plane.
2. Triggering: in the monitoring unit set the trigger delay so that the trigger starts at the beginning of the expiratory plateau (no chest motion) and the duration such that it covers the entire expiratory phase, that is, until just before inhalation starts.
3. Run the sodium scan.

4 Notes

1. *Example 3D gradient echo sequence parameters at 4.7 T*: 90° sine/cosine adiabatic pulse, echo-time/repetition-time (TE/TR) of 1.7/60 ms, FOV 12 × 12 × 5–8 cm^3, and a matrix of 128 × 128 × 16 with ten scans (20 min scan time).
2. *Example 3D gradient echo sequence parameters at 7 T*: 90° sine/cosine adiabatic pulse, echo-time/repetition-time (TE/TR) of 1.7/180 ms, FOV 12 × 12 × 5–8 cm^3, and a matrix of 128 × 128 × 16 with ten scans (60 min scan time).
3. *Example dynamic imaging protocol at 4.7 T*: 90° sine/cosine adiabatic pulse, echo-time/repetition-time (TE/TR) of 1.7/60 ms, FOV 12 × 12 × 5–8 cm^3, and a matrix of 128 × 128 × 16 with two scans (4 min scan time).
4. *3D cones sequence parameters at 3 T*: TR = 48 ms; TE = 0.5 ms, flip angle = 90°; pulse length 500 μs; receiver bandwidth = 250 kHz; readout length = 30 ms, averages = 10; slice orientation = coronal oblique; FOV = (240 × 240 × 240) mm; matrix size = 60 × 60 × 60 zero-filled to 120 × 120 × 120 (10 min scan time).
5. *Example dynamic imaging protocol at 3 T*: TR = 48 ms; TE = 0.5 ms, flip angle = 90°; pulse length 500 μs; receiver bandwidth = 250 kHz; readout length = 30 ms, averages = 5; slice orientation = coronal oblique; FOV = (240 × 240 × 240) mm; matrix size = 60 × 60 × 60 zero-filled to 120 × 120 × 120 (5 min scan time).
6. *Example 3D radial UTE protocol at 9.4 T*: TR = 150 ms; TE = 185 μs; 90° block pulse length of 350 μs; each radial projection was recorded in 6.4 ms of read out time (Tro) using a low acquisition bandwidth of 5 kHz; undersampling factor of 3; number of projections to 4206, nominal anisotropic resolution of (1 × 1 × 4) mm^3, and FOV = 64 mm × 64 mm × 64 mm; TR = 50 ms.
7. *2D CSI sequence parameters at 9.4 T*: Example for a 300 g rat at 9.4 T: TR = 65 ms; TE = 0.65 ms, flip angle = 90°; pulse length 500 μs; receiver bandwidth = 8 kHz; number of points = 256 complex points, averages = 8; slice orientation = axial oblique; FOV = (60 × 60) mm; matrix size = 32 × 32 zero-filled to 64 × 64; 1 slice with 1–2 cm thickness; TA = 67 s (without triggering).
8. Rapid MR-imaging sequences using non-Cartesian sampling are known to be sensitive to gradient hardware imperfections and eddy-current effects that can superimpose acquired data. This is a common problem on preclinical MRI systems which compared with human MRI systems are equipped with

approximately 20-fold stronger (740 mT/m maximal gradient amplitude) and 30-fold faster gradient systems (6900 T/m/s gradient slew rate). To overcome this a calibration by measuring the readout trajectory on a phantom should be performed. For further details please *see* [5].

Acknowledgments

This chapter is based upon work from COST Action PARENCHIMA, supported by European Cooperation in Science and Technology (COST). COST (www.cost.eu) is a funding agency for research and innovation networks. COST Actions help connect research initiatives across Europe and enable scientists to enrich their ideas by sharing them with their peers. This boosts their research, career, and innovation.
PARENCHIMA (renalmri.org) is a community-driven Action in the COST program of the European Union, which unites more than 200 experts in renal MRI from 30 countries with the aim to improve the reproducibility and standardization of renal MRI biomarkers.

References

1. Kiil F (1977) Renal energy metabolism and regulation of sodium reabsorption. Kidney Int 11:153–160
2. Klahr S, Hamm LL, Hammerman MR, Mandel LJ (2011) Renal metabolism: integrated responses. Compr Physiol. https://doi.org/10.1002/cphy.cp080249
3. Deng A, Miracle CM, Suarez JM et al (2005) Oxygen consumption in the kidney: effects of nitric oxide synthase isoforms and angiotensin II. Kidney Int 68:723–730
4. Hansell P, Welch WJ, Blantz RC, Palm F (2013) Determinants of kidney oxygen consumption and their relationship to tissue oxygen tension in diabetes and hypertension. Clin Exp Pharmacol Physiol 40:123–137
5. Zhang Y, Hetherington HP, Stokely EM et al (1998) A novel k-space trajectory measurement technique. Magn Reson Med 39:999–1004

Chapter 29

Hyperpolarized Carbon (^{13}C) MRI of the Kidney: Experimental Protocol

Christoffer Laustsen, Cornelius von Morze, and Galen D. Reed

Abstract

Alterations in renal metabolism are associated with both physiological and pathophysiologic events. The existing noninvasive analytic tools including medical imaging have limited capability for investigating these processes, which potentially limits current understanding of kidney disease and the precision of its clinical diagnosis. Hyperpolarized ^{13}C MRI is a new medical imaging modality that can capture changes in the metabolic processing of certain rapidly metabolized substrates, as well as changes in kidney function. Here we describe experimental protocols for renal metabolic [1-^{13}C]pyruvate and functional ^{13}C-urea imaging step-by-step. These methods and protocols are useful for investigating renal blood flow and function as well as the renal metabolic status of rodents in vivo under various experimental (patho)physiological conditions.

This chapter is based upon work from the COST Action PARENCHIMA, a community-driven network funded by the European Cooperation in Science and Technology (COST) program of the European Union, which aims to improve the reproducibility and standardization of renal MRI biomarkers. This experimental protocol is complemented by two separate chapters describing the basic concept and data analysis.

Key words Magnetic resonance imaging (MRI), Kidney, Mice, Rats, Hyperpolarization, 13C, DNP

1 Introduction

The causal link between renal blood flow (RBF) and glomerular filtration rate (GFR), tubular reabsorption and thus oxygen/metabolic demand and the development of renal dysfunction is well-known [1]. Therefore, diagnostic modalities able to image RBF, GFR, and the metabolic effects have long been sought for.

One such method is hyperpolarized ^{13}C MR, described in the chapter by von Morze C et al. "Hyperpolarized Carbon (^{13}C) MRI of the Kidneys: Basic Concept." In short, a transient enhancement of more than 10.000 times in spin polarization of a substrate molecule, such as [1-^{13}C]pyruvate, is achieved by irradiating a supercooled mixture of ^{13}C spins and electron spins with a microwave frequency obeying the nuclear Overhauser condition—and subsequently rapidly dissolved by superheated water [2]. The

Andreas Pohlmann and Thoralf Niendorf (eds.), *Preclinical MRI of the Kidney: Methods and Protocols*, Methods in Molecular Biology, vol. 2216, https://doi.org/10.1007/978-1-0716-0978-1_29,

resulting mixture retains the high polarization and allows injection of metabolic and functional active molecules and subsequent imaging of the substrate and potential metabolic derivatives following cellular uptake and enzymatic conversion [3, 4]. We will describe basic experiments using hyperpolarized ^{13}C MRS and MRI for monitoring of the metabolic conversion of [1-^{13}C]pyruvate and the intra-renal distribution of ^{13}C-urea in the kidney of rodents in a step-by-step experimental protocol. The rationale for choosing acquisition parameters is given in generic terms, together with specific parameter examples for 3 T, 4.7 T and 9.4 T MRI. Several imaging sequences to map renal metabolism and function are described as optional components of the experiment.

This experimental protocol chapter is complemented by two separate chapters describing the basic concept and data analysis, which are part of this book.

This chapter is part of the book Pohlmann A, Niendorf T (eds) (2020) Preclinical MRI of the Kidney—Methods and Protocols. Springer, New York.

2 Materials

2.1 Animals

This experimental protocol is tailored for rats (Wistar, Sprague-Dawley, or Lewis) with a body mass of 200–350 g. Advice for adaptation to mice is given as *Notes* where necessary.

2.2 Lab Equipment

1. Anesthesia has been shown to impact renal metabolism using hyperpolarized MRI [5]; An appropriate and convenient choice is the use of gas anesthesia. For in-depth description, *see* the chapter by Kaucsar T et al. "Preparation and Monitoring of Small Animals in Renal MRI."
2. Gases: O_2 with or without additional N_2, as well as a gas-mixing system to achieve required blood oxygen saturation level.
3. Hyperpolarizer equipment, typically the commercial preclinical polarizer HyperSense (Oxford Instruments Molecular Biotools, Oxford, United Kingdom) or newer variants of this design [6, 7] as well as the clinical intent polarizer, the so-called SPINLAB (GE Healthcare, Milwaukee, WI, USA).
4. Vein or artery access, typically tail vein access for fast bolus infusion of the hyperpolarized substrate either by manual injection or by infusion pumps [7] (*see* **Note 1**).
5. Phantom: A ^{13}C containing phantom is needed to confirm center frequency and power calibration. A typical phantom used: 8 M ^{13}C-urea (Sigma, St. Louis, MO, USA) in 90% H_2O and 10% Glycerol with 3 μl/ml Gd contrast agent (Dotarem; Guerbet, Roissy, France) (*see* **Note 2**).

2.3 MRI Hardware

The general hardware requirements for renal ^{1}H MRI on mice and rats are described in the chapter by Ramos Delgado P et al. "Hardware Considerations for Preclinical Magnetic Resonance of the Kidney." The technique described in this chapter was tailored for a 3 T clinical system (GE Healthcare, Milwaukee, WI, USA) and a 9.4 Tesla MR system (Agilent, Yarnton, UK) but advice for adaptation to other field strengths is given where necessary. Additional hardware is required, for excitation and reception of ^{13}C: X-band RF amplifiers and signal preamplifiers supporting the resonance frequency of ^{13}C, ^{13}C transmit and receive RF coils, such as ^{1}H/^{13}C volume RF coils [8–10] as well as transmit/receive switches adjusted to the resonance frequency of ^{13}C.

1. A physiological monitoring system that can track the respiration, and which is connected to the MR system such that it can be used to trigger the image acquisition.

3 Methods

3.1 MRI Protocol Setup

3.1.1 Prescan

1. Single pulse and acquire sequence to identify ^{13}C phantom frequency and calibration of the ^{13}C transmitter power for a given pulse shape, width, and amplitude (*see* **Note 3**).

3.1.2 2D/3D Slice Selective Chemical Shift Imaging (CSI)

1. Sequence type: 2D or 3D chemical shift imaging sequence. This is a standard sequence on preclinical MRI and clinical MRI systems [9, 11, 12].
2. Repetition time (TR): choose the shortest possible with sufficient spectral resolution (which is inversely related to the duration of the data sampling window), for efficient temporal resolution.
3. Echo time (TE): choose the shortest possible for good signal-to-noise and reduction of first order phase effects (*see* **Note 4**).
4. Flip angle (FA): adapt to ensure a good compromise between SNR, T_1 relaxation and sufficient signal following repeated excitations. FA is often a low flip angle of $\Theta = 5–10^{\circ}$ leaving a factor of $\cos(\theta)^n$ longitudinal magnetization remaining, with n being the number of excitations (*see* **Note 5**).
5. Acquisition bandwidth (BW): set to a value in the typically range of 4000–20,000 Hz, Number of acquisition points (NP): 256–2048 [9, 11, 12]. Choose BW and NP to ensure sufficient resolution and acquisition time of approximately $2.5 \times T_2$*.

6. K-space ordering: use conventional view ordering, which will result in the center of k-space being sampled late in the acquisition (*see* **Note 6**).
7. For an example of a specific parameter set, please *see* **Note 7**.

3.1.3 2D/3D Echo-Planar Spectroscopic Imaging (EPSI)

1. Sequence type: 2D or 3D echo-planar spectroscopic imaging (EPSI) with or without double spin echo refocusing. This approach superimposes an oscillating readout gradient onto CSI acquisition, replacing one of the phase encoding dimensions needed for CSI. This is not a standard sequence on most preclinical or clinical MRI systems [9, 13, 14].
2. Spectral bandwidth (BW): set spectral BW in the order of 500–600 Hz. The EPSI readout is limited by gradient switching and thus only much lower spectral acquisition bandwidths than CSI are achievable, with outside resonances potentially aliasing into the spectral window. Spectral bandwidth can be traded for spatial resolution but is typically in the order of 500–600 Hz (*see* **Note 8**) for a spatial resolution of ~5 mm.
3. Flip angle (FA): adapt to ensure a good compromise between SNR, T_1 relaxation, and sufficient signal following repeated excitations. FA is often a low flip of $\Theta = 5–10^\circ$ leaving a factor of $\cos(\theta)^n$ longitudinal magnetization remaining, with n being the number of excitations (*see* **Note 5**).
4. Respiration trigger: can be added to improve the spatial localization.
5. Geometry: adapt so that animal fits into FOV and both kidneys are covered. Axial or coronal directions are most often used.
6. For an example of a specific parameter set, please *see* **Note 9**.

3.1.4 Multi-echo Gradient-Echo Sequence for IDEAL Mapping

1. Sequence type: 2D multi-gradient echo sequence. This is a standard sequence on preclinical MRI systems; alternatively, single timepoint acquisitions such as EPI or spiral readout can be used [15–18] (*see* **Note 10**).
2. Repetition time (TR): choose the shortest possible with sufficient distinct echo times, for highest temporal resolution.
3. Flip angle (FA): adapt to ensure a good compromise between SNR, T_1 relaxation and sufficient signal following repeated excitations. FA is often a low flip of $\Theta = 5–10^\circ$ utilizing $\cos(\theta)^n$ of excitations of the nonrecoverable magnetization. n being the number of excitations.
4. Echo time (TE): set the number of echoes to $N+1$ echoes with N being the number of peaks to be resolved. TE is determined by the ability to separate the a priori known peaks to resolve. This can be calculated using the number of signal averages

(NSA) [17]. A rule of thumb is that minimally $N+1$ echoes are needed to accurately resolve N peaks.

5. Acquisition bandwidth (BW): use a high BW to shorten ΔTE, to ensure good separation of the peaks according to NSA.
6. Respiration trigger: on (per slice), can be added to improve the spatial localization.
7. Geometry: adapt so that animal fits into FOV and both kidneys are covered. Axial or coronal directions are most often used.
8. For an example of a specific parameter set, please *see* **Note 11**.
9. Use double spin echo (DSE) or flow gradients to suppress flowing spins [19, 20] (optional).

3.1.5 Spectral-Spatial Imaging

1. Sequence type: 2D spectral-spatial excitation with Cartesian, EPI or spiral trajectory readout [8, 21–23] or 3D sequences with or without slice selection and thus spectrally selective narrow band pulses [24] (*see* **Note 12**).
2. Repetition time (TR): adapt to the respiration. If respiration is triggered, the effective TR will be given by the respiration trigger and will be the respiration interval, that is, one excitation per breath. Choose TR to be a little shorter (about 100 ms) than the average respiration interval that is displayed on the physiological monitoring unit (*see* **Note 13**).
3. Flip angle (FA): use a low FA (in the range of 3–8°) on the substrate peak ([1-^{13}C]pyruvate) and high FA (in the range of 30–90°) on the metabolic derivatives, to preserve magnetization for metabolic conversions allowing a longer temporal window in dynamic studies, and allowing saturation recovery kinetics to be fitted.
4. For an example of a specific parameter set, please *see* **Note 14**.

3.1.6 Perfusion Imaging

1. Sequence type: 2D/3D balanced steady state free precession (bSSFP) sequence [25–27].
2. Repetition time (TR): use shortest possible TR for high temporal resolution. If triggering respiration, adapt to the respiration. The effective TR will be given by the respiration trigger and will be the respiration interval, that is, one frame per breath. Ideally choose NP × TR to be shorter (about 100 ms) than the average respiration interval that is displayed on the physiological monitoring unit.
3. For perfusion assessment use full saturation of the inflowing spins or (optional) a lower flip angle (in the range of 10–30°) [28, 29].

Table 1
bSSFP sequence parameters [23–25]

Sequence	TR/TE, ms	Matrix size	FOV, mm	Acquisition bandwidth, kHz	Flip angle (°)	Preparation	References
2D at 3 T	11.5/5.7	32 × 32	80	20	15	$\alpha/2$	[23]
2D at 9.4 T	4.8/2.4	32 × 32	60		15	–	[24]
3D at 9.4 T	5.4/2.7	48 × 48 × 48	60	20	15	–	[25]

4. Use preparation pulses (optional) to improve magnetization utilization; typically, $\alpha/2$ pulses before and after the bSSFP train to achieve faster pseudo-steady state and to retain the magnetization for subsequent scans [30].
5. For an example of a specific parameter set, please *see* Table 1.

3.2 *In Vivo ^{13}C MR*

3.2.1 *Preparations*

1. Anesthetize the animal and transfer it to the scanner.
2. Place ^{13}C enriched phantom in the FOV (*see* **Note 15**).
3. Set up the temperature monitoring (rectal probe) and respiratory monitoring (balloon on chest) unit.
4. Perform anatomical imaging as described in the chapter by Pohlmann A et al. "Essential Practical Steps for MRI of the Kidney in Experimental Research."
5. Perform localized shimming on the kidney imaging as described in the chapter by Pohlmann A et al. "Essential Practical Steps for MRI of the Kidney in Experimental Research" (*see* **Note 16**).
6. Perform ^{13}C frequency calibration and ^{13}C power calibration (*see* **Note 17**).

3.2.2 *Hyperpolarized ^{13}C Metabolic and Functional Imaging*

1. Load the ^{13}C sequence of choice, adapt the slice orientation to provide a coronal or axial view with respect to the kidney (in scanner coordinates this is double-oblique).
2. Triggering (^{13}C): in the monitoring unit set the trigger delay so that the trigger starts at the beginning of the expiratory plateau (no chest motion) and the duration such that it covers the entire expiratory phase, that is, until just before inhalation starts.
3. Run the ^{13}C imaging scan (*see* **Note 18**). Examples of images are shown in Figs. 1, 2, 3, and 4.

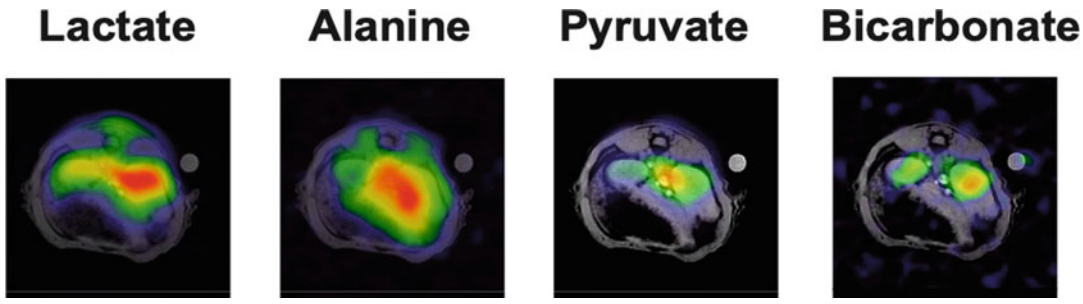

Fig. 1 Series of axial metabolic maps (color) from a 2D CSI overlaid on ^{1}H anatomical scans (grayscale), showing the individual metabolites after integration of the individual peaks

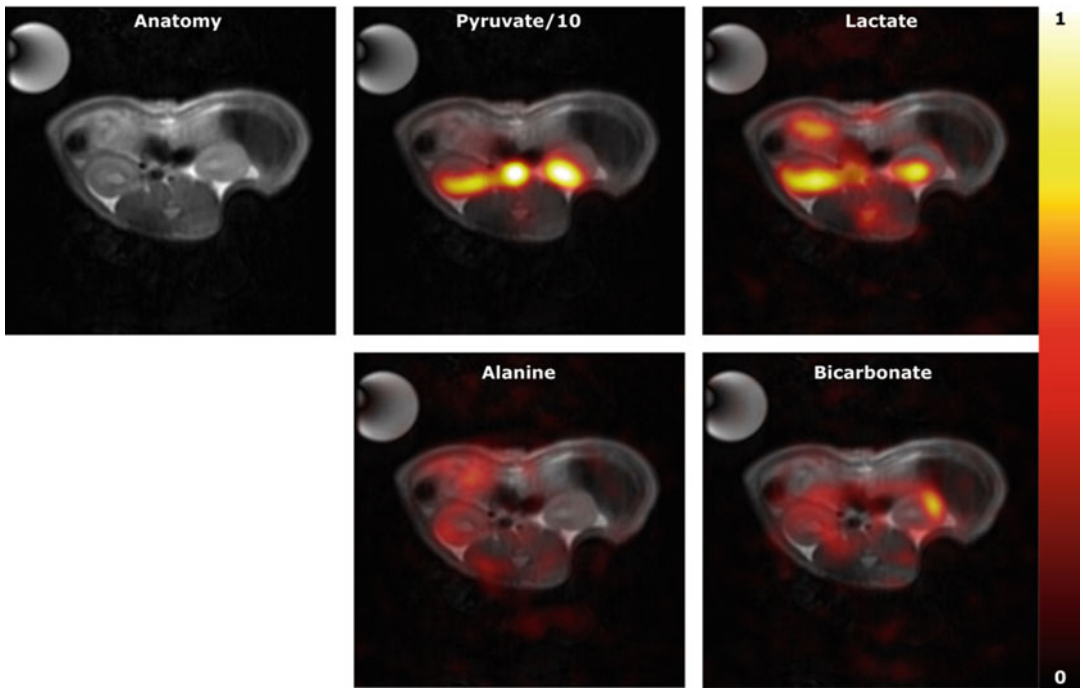

Fig. 2 Examples of axial IDEAL spiral sequence in the kidney at 3 T

3.3 Emerging Sequences

Several novel alternative strategies have been proposed for various imaging applications and just to mention a few there are control of the inflowing spins with bolus tracking [31, 32], spatiotemporal encoding [33], improved resolution by spatially shaped excitations [32, 34]. Variations of the balanced steady state sequences [35, 36] hold potential for further improvement by optimally designing the imaging strategy toward the long T_2's seen in most ^{13}C molecules. Relaxation contrast is another potential renal contrast mechanism, showing substantial promise to improve the diagnostic potential of hyperpolarized MR [37–40].

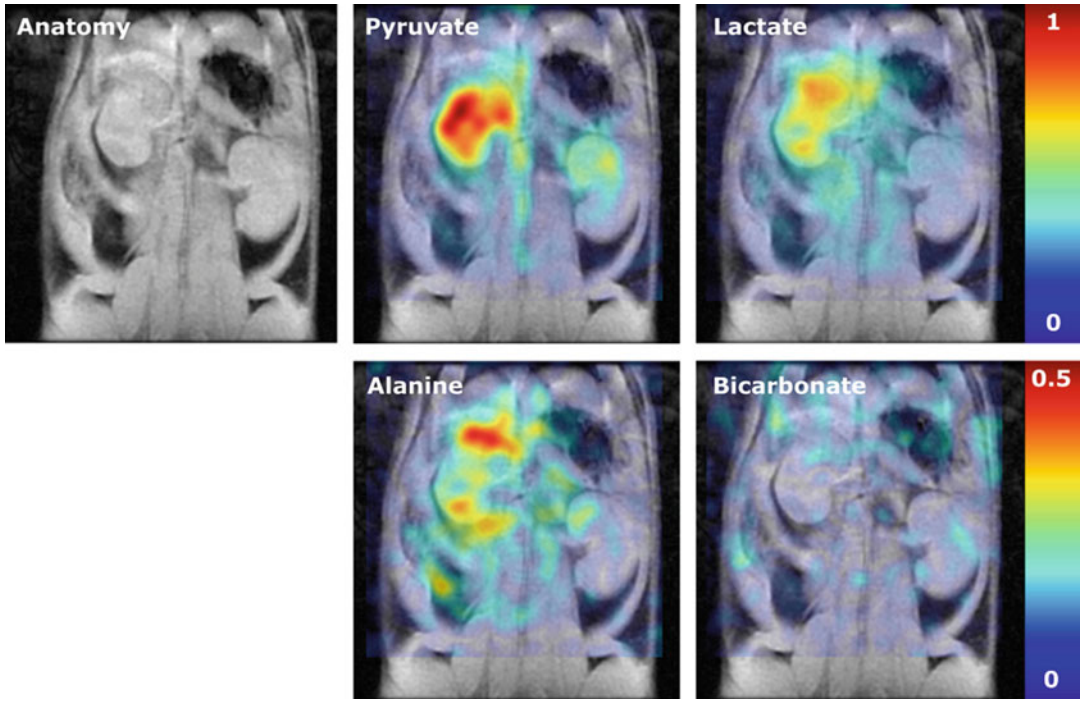

Fig. 3 Examples of coronal spectral spatial (spsp) excitation sequence in the kidney at 3 T

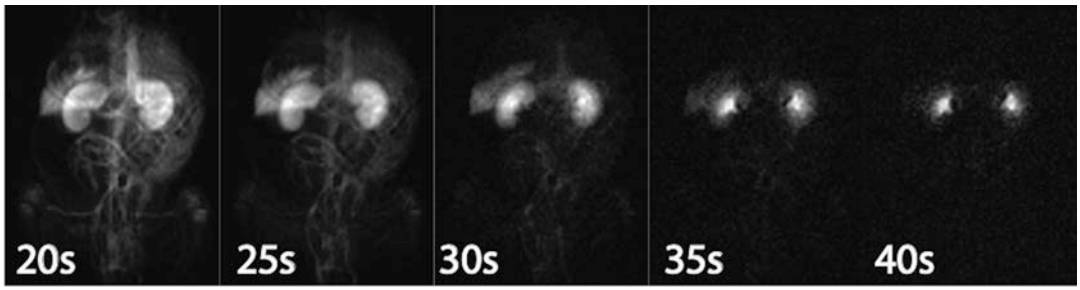

Fig. 4 2D BSSFP dynamic coronal imaging of hyperpolarized [^{13}C,$^{15}N_2$]urea at 3 T. Using a 180 flip angle, 0.92 mm in plane resolution, no slice select. The imaging durations were 1 s separated by 4 s delays, with catalyzation/decatalyzation pulses before and after each image

4 Notes

1. In order to allow optimal usage of the substrate, keep dead-volume as small as possible for injection line; injection speed is typically 0.1 ml/s and up to 2 ml for a rat. If the sequence is single timepoint imaging method or flow artifacts are corrupting the images with a minimum of 20 s time delay from start of injection it is an appropriate choice for intrarenal metabolism and function of the rodent kidneys.

2. Ensure short enough T_1 of the ^{13}C phantom to allow rapid frequency and power calibration. Caution, due to B_0 variation the reference ^{13}C peak is not always representative of the in vivo position.
3. Frequency calibration and power calibration can be done in a similar manner as any ^{1}H experiment with a centering on the phantom peak and running a power calibration using a standard nutation experiment. Calibrating with a 180 pulse is desirable as the signal changes more rapidly as a function of applied power than with a 90 pulse. Alternatively, a Bloch–Siegert shift method can be used [41].
4. As the RF pulse length contributes to the TE and the RF flip often is very low, it is often possible to shorten the TE by reducing the RF pulse length.
5. Signal decay over the phase encoding steps, either due to T_1 decay or consumption of magnetization due to RF pulses (i.e., T_2). Constant flip angle excitation constitutes a k-space filter that can introduce significant image blurring. Alternatively, an increasing flip angle can be employed to compensate for such effects [42].
6. A variety of CSI sampling patterns can be adopted to optimize temporal constraints, SNR, and partial volume effects [9].
7. Example *for a 300 g rat at 9.4 T*: TR = 70 ms; TE = 0.68 ms, flip angle = 10°; pulse length 500 us; receiver bandwidth = 8 kHz; number of points = 512 complex points (i.e., 1024), averages = 1; slice orientation = axial oblique; FOV = (60 × 60) mm; matrix size = 16 × 16 zero-filled to 32 × 32; 1 slice with 1–2 cm thickness; TA = 17 s (without triggering).
8. The low bandwidth will typically require prior knowledge of the peaks of interest and their folding patterns to fully recover the spectral information [9].
9. Example 3D EPSI for a 300 g rat at 3 T: An EPSI sequence with double spin echo refocusing (13). Images are acquired with (8 × 8 × 8) mm^3 voxel size and a matrix size of 18 × 10 × 8, coronal view, with a TR of 215 ms, TE of 140 ms, and a spectral width 543 Hz.
10. The multispectral signals are resolved by fitting to a signal model with unknown components at known frequency offsets. B_0 offset is typically an important component of the model and is fitted along with the spectral components or estimated separately (see https://github.com/LarsonLab/hyperpolarized-mri-toolbox).
11. Example: *2D IDEAL-spiral for a 300 g rat at 3 T (18)*: TR = 100 ms; TE = 0.9 ms; flip angle = 10°; 11 IDEAL

echoes with ΔTE values 0.9 ms, determined by the NSA formalism to resolve [1-^{13}C]pyruvate, [1-^{13}C]lactate, [1-^{13}C]alanine, [1-^{13}C]pyruvate hydrate, [^{13}C]bicarbonate. Slice orientation = axial oblique; FOV = (80 × 80) mm^2; matrix size = 32 × 32; 5 mm × 5 mm real spatial resolution; 1 slice with 1–2 cm thickness covering both kidneys. Dynamic acquisition over 60–80 s.

12. Offset frequencies for individual metabolites must be specified a priori. It is important to note that the frequency might be different than the in vivo version of a given phantom metabolite and thus it is important to verify the correct frequency.
13. Monitor the respiration continuously throughout the entire experiment and if necessary adapt the TR accordingly for the ^{13}C examination.
14. Example: *2D spectral-spatial for a 300 g rat at 3 T (20)*: TR = 1 s; TE = 10 ms; flip angle = 90° on [1-^{13}C]lactate, flip angle = 15° on [1-^{13}C]pyruvate;, flip angle = 90° on [^{13}C]bicarbonate and flip angle = 90° on [1-^{13}C]alanine; slice orientation = axial oblique; FOV = (80 × 80) mm; matrix size = 32 × 32; 5 mm × 5 mm real spatial resolution; 1 slice with 1–2 cm thickness covering both kidneys. Dynamic acquisition over 60–80 s.
15. Be careful with the frequency shift between in vivo and ex vivo phantom conditions.
16. B_0 shimming is particularly important, since macroscopic magnetic field inhomogeneities shorten T_2*, and potentially shift the peak positions relative to the main magnetic field. Shimming should be performed on a voxel enclosing only the kidney using either the default iterative shimming method or manual shimming.
17. It is often possible to retain a similar B_1 amplitude for similar sized animals. ^{13}C Tx gain and Tx/Rx frequency is largely similar in rats and mice and thus the differences should be small between experiments (typically below 1 dB and 50 Hz).
18. A good starting point is to use the same relative resolution as for rats. For this, reduce the FOV to the mouse body width and keep the matrix size the same.

Acknowledgments

This chapter is based upon work from COST Action PARENCHIMA, supported by European Cooperation in Science and Technology (COST). COST (www.cost.eu) is a funding agency for research and innovation networks. COST Actions help connect research initiatives across Europe and enable scientists to enrich

their ideas by sharing them with their peers. This boosts their research, career, and innovation.

PARENCHIMA (renalmri.org) is a community-driven Action in the COST program of the European Union, which unites more than 200 experts in renal MRI from 30 countries with the aim to improve the reproducibility and standardization of renal MRI biomarkers.

References

1. Blantz RC, Deng A, Miracle CM, Thomson SC (2007) Regulation of kidney function and metabolism: a question of supply and demand. Trans Am Clin Climatol Assoc 118:23–43
2. Ardenkjaer-Larsen JH, Fridlund B, Gram A, Hansson G, Hansson L, Lerche MH, Servin R, Thaning M, Golman K (2003) Increase in signal-to-noise ratio of > 10,000 times in liquid-state NMR. Proc Natl Acad Sci U S A 100(18):10158–10163. https://doi.org/10.1073/pnas.1733835100
3. Kurhanewicz J, Vigneron DB, Ardenkjaer-Larsen JH, Bankson JA, Brindle K, Cunningham CH, Gallagher FA, Keshari KR, Kjaer A, Laustsen C, Mankoff DA, Merritt ME, Nelson SJ, Pauly JM, Lee P, Ronen S, Tyler DJ, Rajan SS, Spielman DM, Wald L, Zhang X, Malloy CR, Rizi R (2018) Hyperpolarized (13)C MRI: path to clinical translation in oncology. Neoplasia 21(1):1–16. https://doi.org/10.1016/j.neo.2018.09.006
4. Laustsen C (2016) Hyperpolarized renal magnetic resonance imaging: potential and pitfalls. Front Physiol 7:72. https://doi.org/10.3389/fphys.2016.00072
5. Qi H, Mariager CO, Lindhardt J, Nielsen PM, Stodkilde-Jorgensen H, Laustsen C (2018) Effects of anesthesia on renal function and metabolism in rats assessed by hyperpolarized MRI. Magn Reson Med 80(5):2073–2080. https://doi.org/10.1002/mrm.27165
6. Ardenkjaer-Larsen JH, Bowen S, Petersen JR, Rybalko O, Vinding MS, Ullisch M, Nielsen NC (2018) Cryogen-free dissolution dynamic nuclear polarization polarizer operating at 3.35 T, 6.70 T, and 10.1 T. Magn Reson Med. https://doi.org/10.1002/mrm.27537
7. Comment A, van den Brandt B, Uffmann K, Kurdzesau F, Jannin S, Konter JA, Hautle P, Wenckebach WT, Gruetter R, van der Klink JJ (2007) Design and performance of a DNP prepolarizer coupled to a rodent MRI scanner. Concepts Magn Reson B Magn Reson Eng 31B(4):255–269. https://doi.org/10.1002/cmr.b.20099
8. Xu T, Mayer D, Gu M, Yen YF, Josan S, Tropp J, Pfefferbaum A, Hurd R, Spielman D (2011) Quantification of in vivo metabolic kinetics of hyperpolarized pyruvate in rat kidneys using dynamic 13C MRSI. NMR Biomed 24(8):997–1005. https://doi.org/10.1002/nbm.1719
9. Yen YF, Kohler SJ, Chen AP, Tropp J, Bok R, Wolber J, Albers MJ, Gram KA, Zierhut ML, Park I, Zhang V, Hu S, Nelson SJ, Vigneron DB, Kurhanewicz J, Dirven HA, Hurd RE (2009) Imaging considerations for in vivo 13C metabolic mapping using hyperpolarized 13C-pyruvate. Magn Reson Med 62(1):1–10. https://doi.org/10.1002/mrm.21987
10. Bertelsen LB, Nielsen PM, Qi H, Norlinger TS, Zhang X, Stodkilde-Jorgensen H, Laustsen C (2016) Diabetes induced renal urea transport alterations assessed with 3D hyperpolarized 13 C,15 N-Urea. Magn Reson Med. https://doi.org/10.1002/mrm.26256
11. Laustsen C, Østergaard JA, Lauritzen MH, Nørregaard R, Bowen S, Søgaard LV, Flyvbjerg A, Pedersen M, Ardenkjær-Larsen JH (2013) Assessment of early diabetic renal changes with hyperpolarized [1-13C]pyruvate. Diabetes Metab Res Rev 29(2):125–129. https://doi.org/10.1002/dmrr.2370
12. Laustsen C, Hansen ES, Kjaergaard U, Bertelsen LB, Ringgaard S, Stodkilde-Jorgensen H (2015) Acute porcine renal metabolic effect of endogastric soft drink administration assessed with hyperpolarized [1-13c]pyruvate. Magn Reson Med. https://doi.org/10.1002/mrm.25692
13. Ohliger MA, von Morze C, Marco-Rius I, Gordon J, Larson PEZ, Bok R, Chen HY, Kurhanewicz J, Vigneron D (2017) Combining hyperpolarized (13) C MRI with a liver-specific gadolinium contrast agent for selective assessment of hepatocyte metabolism. Magn Reson Med 77(6):2356–2363. https://doi.org/10.1002/mrm.26296
14. Cunningham CH, Chen AP, Albers MJ, Kurhanewicz J, Hurd RE, Yen YF, Pauly JM, Nelson SJ, Vigneron DB (2007) Double spin-echo sequence for rapid spectroscopic imaging of hyperpolarized 13C. J Magn Reson 187

(2):357–362. https://doi.org/10.1016/j.jmr.2007.05.014

15. Leupold J, Månsson S, Stefan Petersson J, Hennig J, Wieben O (2009) Fast multiecho balanced SSFP metabolite mapping of 1H and hyperpolarized 13C compounds. Magn Reson Mater Phys 22(4):251–256
16. Niles DJ, Gordon JW, Huang G, Reese S, Adamson EB, Djamali A, Fain SB (2018) Evaluation of renal metabolic response to partial ureteral obstruction with hyperpolarized (13) C MRI. NMR Biomed 31(1). https://doi.org/10.1002/nbm.3846
17. Wiesinger F, Weidl E, Menzel MI, Janich MA, Khegai O, Glaser SJ, Haase A, Schwaiger M, Schulte RF (2012) IDEAL spiral CSI for dynamic metabolic MR imaging of hyperpolarized [1-13C]pyruvate. Magn Reson Med 68 (1):8–16. https://doi.org/10.1002/mrm.23212
18. Qi H, Nielsen PM, Schroeder M, Bertelsen LB, Palm F, Laustsen C (2018) Acute renal metabolic effect of metformin assessed with hyperpolarised MRI in rats. Diabetologia 61 (2):445–454. https://doi.org/10.1007/s00125-017-4445-6
19. Josan S, Yen Y-F, Hurd R, Pfefferbaum A, Spielman D, Mayer D (2011) Application of double spin echo spiral chemical shift imaging to rapid metabolic mapping of hyperpolarized [1-^{13}C]-pyruvate. J Magn Reson 209 (2):332–336. https://doi.org/10.1016/j.jmr.2011.01.010
20. Gordon JW, Niles DJ, Adamson EB, Johnson KM, Fain SB (2016) Application of flow sensitive gradients for improved measures of metabolism using hyperpolarized (13) c MRI. Magn Reson Med 75(3):1242–1248. https://doi.org/10.1002/mrm.25584
21. Shang H, Sukumar S, von Morze C, Bok RA, Marco-Rius I, Kerr A, Reed GD, Milshteyn E, Ohliger MA, Kurhanewicz J, Larson PEZ, Pauly JM, Vigneron DB (2017) Spectrally selective three-dimensional dynamic balanced steady-state free precession for hyperpolarized C-13 metabolic imaging with spectrally selective radiofrequency pulses. Magn Reson Med 78(3):963–975. https://doi.org/10.1002/mrm.26480
22. Schulte RF, Sperl JI, Weidl E, Menzel MI, Janich MA, Khegai O, Durst M, Ardenkjaer-Larsen JH, Glaser SJ, Haase A, Schwaiger M, Wiesinger F (2013) Saturation-recovery metabolic-exchange rate imaging with hyperpolarized [1-13C] pyruvate using spectral-spatial excitation. Magn Reson Med 69 (5):1209–1216. https://doi.org/10.1002/mrm.24353
23. Lau AZ, Chen AP, Hurd RE, Cunningham CH (2011) Spectral-spatial excitation for rapid imaging of DNP compounds. NMR Biomed 24(8):988–996. https://doi.org/10.1002/nbm.1743
24. Eichhorn TR, Takado Y, Salameh N, Capozzi A, Cheng T, Hyacinthe JN, Mishkovsky M, Roussel C, Comment A (2013) Hyperpolarization without persistent radicals for in vivo real-time metabolic imaging. Proc Natl Acad Sci U S A 110 (45):18064–18069. https://doi.org/10.1073/pnas.1314928110
25. von Morze C, Bok RA, Sands JM, Kurhanewicz J, Vigneron DB (2012) Monitoring urea transport in rat kidney in vivo using hyperpolarized 13C magnetic resonance imaging. Am J Physiol Ren Physiol. https://doi.org/10.1152/ajprenal.00640.2011
26. Qi H, Norlinger TS, Nielsen PM, Bertelsen LB, Mikkelsen E, Xu Y, Stodkilde Jorgensen H, Laustsen C (2016) Early diabetic kidney maintains the corticomedullary urea and sodium gradient. Physiol Rep 4(5). https://doi.org/10.14814/phy2.12714
27. Nielsen PM, Szocska Hansen ES, Norlinger TS, Norregaard R, Bonde Bertelsen L, Stodkilde Jorgensen H, Laustsen C (2016) Renal ischemia and reperfusion assessment with three-dimensional hyperpolarized (13) C, (15) N2-urea. Magn Reson Med 76 (5):1524–1530. https://doi.org/10.1002/mrm.26377
28. Johansson E, Olsson LE, Månsson S, Petersson JS, Golman K, Ståhlberg F, Wirestam R (2004) Perfusion assessment with bolus differentiation: a technique applicable to hyperpolarized tracers. Magn Reson Med 52(5):1043–1051. https://doi.org/10.1002/mrm.20247
29. von Morze C, Larson PE, Hu S, Keshari K, Wilson DM, Ardenkjaer-Larsen JH, Goga A, Bok R, Kurhanewicz J, Vigneron DB (2011) Imaging of blood flow using hyperpolarized [(13)C]urea in preclinical cancer models. J Magn Reson Imaging 33(3):692–697. https://doi.org/10.1002/jmri.22484
30. Svensson J, Mansson S, Johansson E, Petersson JS, Olsson LE (2003) Hyperpolarized 13C MR angiography using trueFISP. Magn Reson Med 50(2):256–262. https://doi.org/10.1002/mrm.10530
31. Durst M, Koellisch U, Gringeri C, Janich MA, Rancan G, Frank A, Wiesinger F, Menzel MI, Haase A, Schulte RF (2014) Bolus tracking for improved metabolic imaging of hyperpolarised compounds. J Magn Reson (San Diego, CA: 1997) 243:40–46. https://doi.org/10.1016/j.jmr.2014.02.011

32. Tang S, Jiang W, Chen HY, Bok R, Vigneron DB, Larson PE (2015) A 2DRF pulse sequence for bolus tracking in hyperpolarized 13C imaging. Magn Reson Med 74(2):506–512. https://doi.org/10.1002/mrm.25427
33. Schmidt R, Laustsen C, Dumez J-N, Kettunen MI, Serrao EM, Marco-Rius I, Brindle KM, Ardenkjaer-Larsen JH, Frydman L (2014) In vivo single-shot 13C spectroscopic imaging of hyperpolarized metabolites by spatiotemporal encoding. J Magn Reson 240:8–15. https://doi.org/10.1016/j.jmr.2013.12.013
34. Vinding MS, Laustsen C, Maximov II, Sogaard LV, Ardenkjaer-Larsen JH, Nielsen NC (2013) Dynamic nuclear polarization and optimal control spatial-selective 13C MRI and MRS. J Magn Reson (San Diego, CA: 1997) 227:57–61. https://doi.org/10.1016/j.jmr.2012.12.002
35. Varma G, Wang X, Vinogradov E, Bhatt RS, Sukhatme VP, Seth P, Lenkinski RE, Alsop DC, Grant AK (2016) Selective spectroscopic imaging of hyperpolarized pyruvate and its metabolites using a single-echo variable phase advance method in balanced SSFP. Magn Reson Med 76(4):1102–1115. https://doi.org/10.1002/mrm.26004
36. Mansson S, Petersson JS, Scheffler K (2012) Fast metabolite mapping in the pig heart after injection of hyperpolarized 13C-pyruvate with low-flip angle balanced steady-state free precession imaging. Magn Reson Med 68 (6):1894–1899. https://doi.org/10.1002/mrm.24183
37. Reed GD, von Morze C, Bok R, Koelsch BL, Van Criekinge M, Smith KJ, Hong S, PEZ L, Kurhanewicz J, Vigneron DB (2014) High resolution ^{13}C MRI with hyperpolarized urea: in vivo T_2 mapping and ^{15}N labeling effects. IEEE Trans Med Imaging 33(2):362–371. https://doi.org/10.1109/TMI.2013.2285120
38. Reed GD, von Morze C, Verkman AS, Koelsch BL, Chaumeil MM, Lustig M, Ronen SM, Sands JM, Larson PEZ, Wang ZJ, Ardenkjær Larsen JH, Kurhanewicz J, Vigneron DB (2015) Imaging renal urea handling in rats at millimeter resolution using hyperpolarized magnetic resonance relaxometry. ArXiv 1511:200
39. Laustsen C, Stokholm Norlinger T, Christoffer Hansen D, Qi H, Mose Nielsen P, Bonde Bertelsen L, Henrik Ardenkjaer-Larsen J, Stodkilde Jorgensen H (2015) Hyperpolarized C urea relaxation mechanism reveals renal changes in diabetic nephropathy. Magn Reson Med. https://doi.org/10.1002/mrm.26036
40. Qi H, Mariager CO, Nielsen PM, Schroeder M, Lindhardt J, Norregaard R, Klein JD, Sands JM, Laustsen C (2019) Glucagon infusion alters the hyperpolarized (13) C-urea renal hemodynamic signature. NMR Biomed 32(1):e4028. https://doi.org/10.1002/nbm.4028
41. Schulte RF, Sacolick L, Deppe MH, Janich MA, Schwaiger M, Wild JM, Wiesinger F (2011) Transmit gain calibration for nonproton MR using the Bloch-Siegert shift. NMR Biomed 24(9):1068–1072. https://doi.org/10.1002/nbm.1657
42. Zhao L, Mulkern R, Tseng CH, Williamson D, Patz S, Kraft R, Walsworth RL, Jolesz FA, Albert MS (1996) Gradient-echo imaging considerations for hyperpolarized 129Xe MR. J Magn Reson B 113:179–183

Chapter 30

Fluorine (^{19}F) MRI for Assessing Inflammatory Cells in the Kidney: Experimental Protocol

Min-Chi Ku, Adrian Schreiber, Paula Ramos Delgado, Philipp Boehm-Sturm, Ralph Kettritz, Thoralf Niendorf, Andreas Pohlmann, and Sonia Waiczies

Abstract

Inflammation is one underlying contributing factor in the pathology of acute and chronic kidney disorders. Phagocytes such as monocytes, neutrophils and dendritic cells are considered to play a deleterious role in the progression of kidney disease but may also contribute to organ homeostasis. The kidney is a target of life-threatening autoimmune disorders such as the antineutrophil cytoplasmic antibody (ANCA)-associated vasculitides (AAV). Neutrophils and monocytes express ANCA antigens and play an important role in the pathogenesis of AAV. Noninvasive in vivo methods that can quantify the distribution of inflammatory cells in the kidney as well as other organs in vivo would be vital to identify the causality and significance of inflammation during disease progression. Here we describe an noninvasive technique to study renal inflammation in rodents in vivo using fluorine (^{19}F) MRI. In this protocol we chose a murine ANCA-AAV model of renal inflammation and made use of nanoparticles prepared from perfluoro-5-crown-15-ether (PFCE) for renal ^{19}F MRI.

This chapter is based upon work from the COST Action PARENCHIMA, a community-driven network funded by the European Cooperation in Science and Technology (COST) program of the European Union, which aims to improve the reproducibility and standardization of renal MRI biomarkers. This experimental protocol chapter is complemented by two separate chapters describing the basic concept and data analysis.

Key words Magnetic resonance imaging (MRI), Fluorine (^{19}F), Nanoparticles (NPs), Inflammation, Kidney, Mice

1 Introduction

Inflammation is one underlying contributing factor in the pathology of acute and chronic kidney disorders [1]. Studies also suggest that systemic inflammation can cause ischemic injury in a vital organ, such as the kidney, which could then result in repercussions in another distant organ downstream of the ischemic event, such as the heart [2–4]. Early inflammatory events governed by cells of the innate immune system, such as macrophages, probably promote

Andreas Pohlmann and Thoralf Niendorf (eds.), *Preclinical MRI of the Kidney: Methods and Protocols*, Methods in Molecular Biology, vol. 2216, https://doi.org/10.1007/978-1-0716-0978-1_30,

renal tissue injury but may also support repair [5–8]. Phagocytes such as dendritic cells (DC) and macrophages are considered to play a deleterious role in the inflammatory outcome of chronic kidney disease but may also contribute to organ homeostasis [9].

The kidney is often a target of systemic autoimmune disorders that are compounded by complex inflammatory processes [10]. Examples of life-threatening autoimmune disorders that affect the kidneys are the antineutrophil cytoplasmic antibody (ANCA)-associated vasculitides (AAV) manifesting as rapidly progressive necrotizing crescentic glomerulonephritis (NCGN) [11]. Neutrophils and monocytes express ANCA antigens and ANCA induces neutrophil extracellular traps that cause RIPK1-dependent endothelial cell (EC) damage via activation of the alternative complement pathway [12]. While the central role of neutrophil activation in ANCA-associated vasculitis and NCGN is clear, the role of monocytes/macrophages was only recently uncovered in a renal ANCA-associated vasculitis model [13].

Noninvasive in vivo methods that can quantify the level of inflammation in the kidney as well as other organs in system autoimmune disorders such as ANCA-associated vasculitides would be vital to identify the causality and significance of inflammation during the course of disease. One method to visualize inflammation by MRI makes use of MR contrast agents that modulate T_2^* and that are easily taken up by phagocytic inflammatory cells [14, 15]. Iron oxide particles including ultrasmall iron oxide agents (USPIO) have been used as susceptibility (T_2^*) MR contrast agents to target inflammatory cell populations. These particles are engulfed by phagocytic cells in the blood. Drawbacks of USPIO-based T_2^* studies include MR signal quantification and difficulty to distinguish contrast created by labeled cells from other intrinsic tissue contrasts [14].

Here we describe an alternative noninvasive technique to study inflammation in rodents in vivo using fluorine (^{19}F) MRI. ^{19}F MRI is performed in association with intravenous injections of perfluorocarbon (PFC) nanoparticles (NPs). These NPs are taken up by cells of the immune system traveling through the circulation into the inflammatory regions. Thus ^{19}F MRI is ideal for studying distribution of inflammatory cell in vivo. In this protocol we chose a murine AAV model of renal inflammation that has been described in greater depth elsewhere [16] and made use of nanoparticles prepared from perfluoro-5-crown-15-ether (PFCE).

This experimental protocol chapter is complemented by two separate chapters describing the basic concept (please *see* the chapter by Waiczies S et al. "Functional Imaging Using Fluorine (^{19}F) MR Methods: Basic Concepts") and data analysis (please *see* the chapter by Starke L et al. "Data Preparation Protocol for Low Signal-to-Noise Ratio Fluorine-19 MRI"), which are both part of this book.

This chapter is part of the book Pohlmann A, Niendorf T (eds) (2020) Preclinical MRI of the Kidney—Methods and Protocols. Springer, New York.

2 Materials

2.1 Animals

This experimental protocol is tailored for mice with a body mass of 20-30 g (e.g., wild type C57BL/6 mice or a disease model of renal inflammation). Here we describe briefly how to generate the AAV animal model. More thorough detail on the immunization, bone marrow transplantation as well purification of mouse MPO is given in the study establishing the MPO-AAV animal model [16]. Wild-type (WT) C57BL/6J mice (B6) (Jackson Laboratories, Bar Harbor, ME) and myeloperoxidase-deficient ($MPO^{-/-}$) mice (generated by Aratani et al. [17]) were used in this protocol. $MPO^{-/-}$ mice were immunized with murine MPO at the age of 8–10 weeks, subjected to lethal irradiation, and then transplanted with MPO-expressing bone marrow cells. Animal experiments should be approved by animal welfare authorities and guidelines to minimize discomfort to animals (86/609/EEC).

2.1.1 Lab Equipment

1. NP preparation: Ultrasonic device with ultrasonic power (400 W) and frequency (24 kHz) for stand-mounted operation such as UP400S (Hielscher, Teltow, Germany) to prepare PFCE nanoparticles.
2. NP preparation: Titanium sonotrode for emulsifying samples from 5 to 200 ml (e.g., H3 from Hielscher, Teltow, Germany).
3. NP characterization: Dynamic light scattering instrument such as Zetasizer Nano (Malvern Instruments, Malvern, Worcestershire, UK) to characterize particle size (Z-average) and polydispersity index (PDI) of the PFCE nanoparticles.
4. NP application: Mouse restrainer for intravenous administering the PFCE nanoparticles.
5. Anesthesia: Isoflurane inhalation system which can adjust different levels of isoflurane such as Isoflurane Vapor 19.1 (Draeger, Draegerwerk, Luebeck, Germany). The range of isoflurane level that is used for anesthesia in mice is 0.5–1.5%. Please refer to the chapter by Kaucsar T et al. "Preparation and Monitoring of Small Animals in Renal MRI" for an in-depth description and discussion of the anesthesia.
6. Anesthesia: Mouse chamber connected to isoflurane inhalation system and gas-mixing system to anesthetize mice by inhalation narcosis prior to transfer to the MR scanner.
7. Gases: O_2, and compressed air, as well as a gas-mixing system such as FMI (Föhr Medical Instruments GmbH, Seeheim-Ober Beerbach, Germany) to achieve the required physiological O_2/air mixture in combination with the isoflurane gas.

2.2 MRI Hardware

The general hardware requirements for renal ^{1}H MRI on mice and rats are described in the chapter by Ramos Delgado P et al. "Hardware Considerations for Preclinical Magnetic Resonance of the Kidney." The technique described in this chapter was tailored for a 9.4 T MR system (Biospec 94/20, Bruker Biospin, Ettlingen, Germany) but advice for adaptation to other field strengths is given where necessary.

1. $^{1}H/^{19}F$ dual-tunable volume RF coil (35 mm inner diameter, 50 mm length; Rapid Biomed, Würzburg, Germany).
2. $^{1}H/^{19}F$ dual-tunable volume RF coil (18 mm inner diameter, 39 mm length) for ex vivo imaging [18].
3. ^{19}F cryogenic quadrature RF surface probe (^{19}F-CRP) operated at ~28 K (*see* **Note 1**).
4. A physiological monitoring system that can track respiration and temperature during the MR procedure such as the Monitoring & Gating System and PC-sam software from SA Instruments (SAII, Stony Brook, NY, USA).
5. Mouse sled with a breathing mask connected to the isoflurane system.

2.3 MRI Techniques

Typically, ^{19}F MR studies applying PFC compounds such as PFCE to study inflammation in vivo employ the turbo spin echo (SE) rapid acquisition using relaxation enhancement (RARE) sequence [18–22]. This method reduces acquisition time by accumulating multiple echoes within a single repetition time [23]. Typically T_1 of these ^{19}F compounds is in the range of 0.5–3 s, depending on the compound and also magnetic field strength (B_0). However, if employing paramagnetic macrocyclic PFC compounds complexed to lanthanides, T_1 values can be reduced to the order of 1–15 ms and T_2* values correspondingly reduced to 0.4–12 ms and a radial zero echo time (ZTE) sequence might be better suited [24].

1. *^{1}H MR sequence*: 2D and 3D FLASH protocols are standard sequences on Bruker MRI systems, where they are called "FLASH_2D", "FLASH_3D" or "1_Localizer_multi_slice" (*see* **Note 2**).
2. *^{19}F spectroscopy sequence*: Block pulse for nonlocalized (global) is a standard sequence on Bruker MRI systems, where it is called "SINGLEPULSE" (*see* **Note 3**).
3. *^{19}F MR sequence*: 3D RARE protocol for measurements. This is a standard sequence on Bruker MRI systems, where it is called "TurboRARE_3D" in Paravision 5, "T2_TurboRARE_3D" in Paravision 6 (*see* **Note 4**).

3 Methods

3.1 MR Protocol Setup

3.1.1 ^{19}F MR Imaging

Typically T_1 of PFC compounds is in the range of 0.5–3 s, depending on the compound and also magnetic field strength (B_0). When working with a standard diamagnetic PFC such as PFCE that is documented in the literature, it is recommended that the T_1 and T_2 of the compound be studied at 37 °C before starting with the first in vivo experiments to study inflammation. According to the measured relaxation times (T_1/T_2), the optimal settings for RARE, namely echo train lengths (ETL) and repetition time (TR) should be calculated to improve sensitivity thresholds.

1. *Repetition time (TR)*: for RARE, TR will be limited by ETL and the number of slices. A short TR is desirable for SNR efficiency (0.8–1.5 s depending on T_1) keeping in mind that T_1 will change with changes in oxygenation status (*see* **Note 5**).
2. *Flip angle (FA)*: for the block pulse and RARE sequence, the FA for the excitation pulse should be at 90°. Additionally the RARE sequence has a refocusing pulse with a FA of 180°. To maximize the SNR and contrast, the flip angle has to be separately calculated for FLASH considering the Ernst angle: $\alpha_E = \cos^{-1}\left(e^{-TR/T_1}\right)$ which relates FA, T_1 and TR (*see* **Note 6**).
3. *Echo train length (ETL)*: in RARE, use a value as high as possible to reduce scan time. In the TurboRARE sequence on Bruker MRI systems, ETL is referred to as "rare factor".
4. *Echo time (TE)*: use the shortest effective TE and echo spacing (ΔTE) possible. Especially for very high ETL, TE can become very long. Centric encoding can be used to reduce the effective TE, generally at the cost of introducing minor image artifacts.
5. *Acquisition bandwidth (BW)*: long enough to shorten the ΔTE without compromising the SNR, which decreases with increasing BW as a result of increased noise level.
6. *Geometry*: Adapt so that whole abdomen fits into FOV in L-R direction (approx. 25 mm for mice) and use frequency encoding in H-F- direction. Choose a 3D volume suited to cover the whole body width and as much of the length of the mouse that the RF coil can afford as possible. With a typical mouse body resonator as the one used in this protocol one could use a FOV of 60 × 30 × 30 mm and matrix size of 400 × 200 × 200 (for ^{1}H) and 128 × 64 × 64 (for ^{19}F).
7. *Resolution/acceleration*: Use the highest in-plane resolution that the SNR allows, typically around 100–150 μm for ^{1}H MR scans and 250–500 μm for ^{19}F MR scans. Zero-filling in phase encoding direction can be helpful to speed up acquisition while increasing the number of averages to improve SNR

especially for ^{19}F MR scans. One may use half Fourier in read direction (asymmetric echo) to further shorten the first TE. Reducing the excitation pulse length to below 1 ms would then also help to shorten TE.

8. For an example of parameters used in this chapter, please *see* **Notes 7** and **13**.

3.2 ^{19}F Nanoparticle Preparation, Characterization, and Application

1. *NP preparation*: Emulsify 1.2 M PFCE (Fluorochem, Derbyshire, UK) in Pluronic F-68 (Sigma-Aldrich, Germany) for 10 min using a cell disrupting titanium sonotrode connected to an ultrasonic device and employing a continuous pulse program for 60 s. Use ear protection while sonicating the mixture to avoid hearing damage and loss.
2. *NP characterization*: Measure mean particle size (in nm), polydispersity index (PdI), and zetapotential (mV) by using a dynamic light scattering machine such as the one listed above. Use the *z*-average diameter for particle size since it gives an intensity-weighted harmonic diameter and is ideal for comparing different analyses. The nanoparticles should have a PdI < 0.3 indicating a relatively low polydispersity and narrow size distribution (*see* **Note 8**).
3. *NP application*: Administer ^{19}F nanoparticles via tail vein at a dose of 5–80 μmol of PFCE molecules, depending on the frequency of the bolus injections. Start administering ^{19}F nanoparticles at relevant time-points of your inflammatory model, for example, in MPO immunized $MPO^{-/-}$ mice subjected to lethal irradiation we started intravenous application of PFCE nanoparticles 4–8 weeks following transplantation of MPO-expressing bone marrow cells (*see* **Note 9**).

3.3 Preparation Prior to $^{19}F/^{1}H$ MRI Scans

Four to 18 h following the last intravenous administration of ^{19}F nanoparticles prepare the mice for $^{19}F/^{1}H$ MRI:

1. First anesthetize the mice by inhalation narcosis using a mouse chamber connected to a isoflurane inhalation system and gas-mixing system (*see* **Note 10**).
2. Adjust the flow rate for air and O_2 at 0.2 and 0.1 l/min respectively and 3% isoflurane (adjusted from a vaporizer) for about 2 min until the required level of anesthesia is reached (no response following toe pinch).
3. Transfer mice to the MR scanner. Should a quantification of inflammation be required, a reference tube with a known concentration of ^{19}F nanoparticles should be placed in proximity to the region of interest. For quantification of signal please refer to the chapter by Starke L et al. "Data Preparation Protocol for Low Signal-to-Noise Ratio Fluorine-19 MRI."

4. While keeping the flow rate for air and O_2 constant, adjust the isoflurane vaporizer to 0.8–1.5% until an optimal breathing pattern is reached.
5. Set up the temperature monitoring (rectal probe) and respiratory monitoring (balloon on chest) unit. A respiratory rate of 70–90 breaths per minute is recommended. Keep the body temperature at 36–37 °C during the experiment by employing a warm water (or alternatively warm air) circulation system.
6. Tune the RF coil to both the ^{1}H resonance frequency (e.g., 400.1 MHz for 9.4 T) and to the ^{19}F resonance frequency (e.g., 376.3 MHz for 9.4 T) and match the characteristic impedance of the coil to 50 Ω using the tuning monitor of the animal MR scanner.
7. Perform anatomical imaging as described in the chapter by Pohlmann A et al. "Essential Practical Steps for MRI of the Kidney in Experimental Research." Set up a 2D FLASH protocol for the acquisition of anatomical kidney ^{1}H scans (*see* **Note 7**).
8. Perform localized shimming on the kidney imaging as described in the chapter by Pohlmann A et al. "Essential Practical Steps for MRI of the Kidney in Experimental Research" (*see* **Note 11**).
9. Save the parameters of all adjustments (such as iterative shimming calculations and reference power values) performed during the first ^{1}H scans for application into the ^{19}F scans.

3.4 ^{19}F/^{1}H MRI of the Kidney

Following acquisition of the anatomical ^{1}H kidney scans, in vivo ^{19}F MR images of the kidney can be acquired and later overlaid onto the ^{1}H MR images. An example of an in vivo ^{1}H/^{19}F MRI is shown in Fig. 1.

3.4.1 In Vivo ^{19}F/^{1}H MRI Using a Room Temperature Mouse Body Volume ^{19}F/^{1}H RF Resonator

1. Load the SINGLEPULSE FID-sequence with a TR of at least 1000 ms.
2. Set nucleus to ^{19}F (e.g., in "Open Edit Scan" in Bruker's Paravision 5.1 or "System" tab in Bruker's Paravision 6). Since the ^{19}F MR signal is too low for automatic adjustments, apply the same settings used for the ^{1}H anatomical scans (*see* **Note 12**).
3. Deselect the automatic reference gain (RG) and set on maximum (e.g., in Edit Method in Bruker's Paravision 5.1 or using the "Instruction" tab (GOP) and "Setup" tab in Paravision 6).
4. Start the SINGLEPULSE sequence using setup mode. If the ^{19}F spectral signal within the acquisition-window is too low, add more averages until a signal is clearly visible. Adjust the basic frequency in order to center the ^{19}F spectral peak at 0 Hz in the acquisition window. Apply this basic frequency, press Stop and apply.

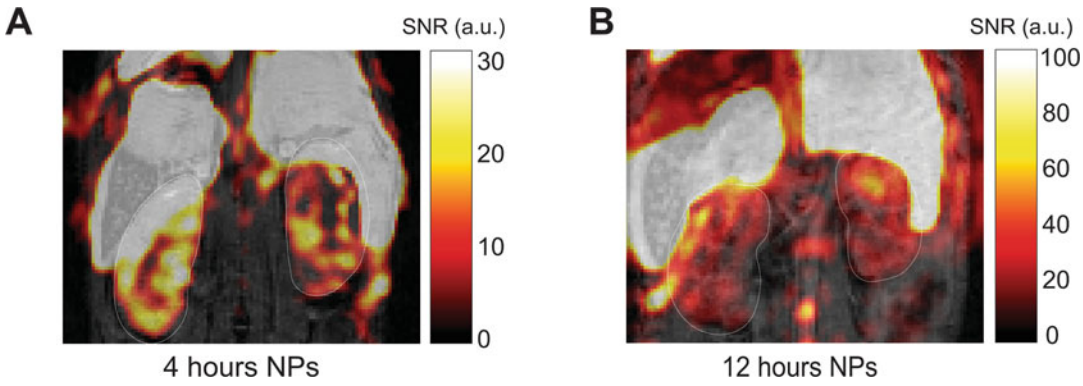

Fig. 1 In vivo $^{19}F/^{1}H$ MRI of a murine ANCA-AAV model of renal inflammation using the $^{1}H/^{19}F$ dual-tunable volume RF coil (35 mm inner diameter). Eight weeks following transplantation of bone marrow cells, MPO-AAV mice were administered one bolus of PFCE nanoparticles (NPs) intravenously (80 μmol in 100 μl) and $^{19}F/^{1}H$ MRI was performed 4 h (**a**) and 12 h (**b**) thereafter. (1) ^{1}H 2D FLASH protocol: TR = 579.4 ms, TE = 5 ms, FA = 75, matrix = 256 × 128. (2) ^{19}F 3D RARE protocol: TR = 800 ms, TE = 6.16 ms, Matrix = 256 × 128 × 128, RARE Factor = 32

5. Setup a TurboRARE 3D protocol for the ^{19}F scans.
6. Use the same geometry used for anatomical ^{1}H imaging but reduce the matrix size for increased SNR and use a rare factor of at least 32. Set nucleus to ^{19}F. Deselect automatic adjustments (as above). For an example of parameters, please *see* **Note 7**.
7. When the scans are finished retract the mouse-holder from the MR scanner. Disconnect the mouse carefully from the holder. If the mouse is not sacrificed for ex vivo analysis (e.g., high resolution ^{19}F MRI of the kidney, see below) following the MR scans, closely monitor until it has completely recovered from anesthesia. Body temperature regulation might still be affected after the anesthesia, so during the recovery process, put the mouse in a separate cage that is placed on a warm temperature regulated pad. Once the mouse has completely recovered from anesthesia, you may return it to its holding cage and to the animal room.

3.4.2 High Spatial Resolution ^{19}F MRI of Ex Vivo Kidney Using a ^{19}F CryoProbe

Kidney inflammation can also be studied with high spatial resolution ex vivo ^{19}F MRI, for example, by using a transceive ^{19}F CryoProbe, which we previously used to study brain inflammation in a model of CNS autoimmunity [25]. An example of a high resolved ex vivo $^{1}H/^{19}F$ MRI of the kidney is shown in Fig. 2.

1. At the end of the in vivo experiment, anesthetize mice with a terminal dose of ketamine and xylazine. Ensure the required level of anesthesia is reached (no response following toe pinch).
2. Transcardially perfuse mouse with 20 ml PBS followed by 20 ml 4% paraformaldehyde.

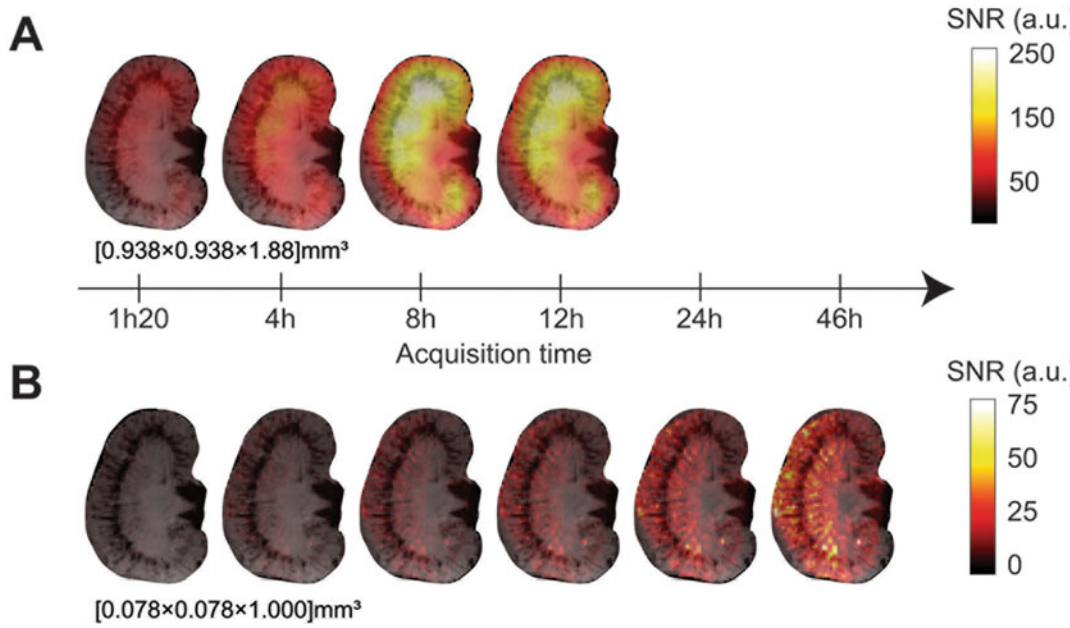

Fig. 2 Ex vivo ^{19}F/^{1}H MRI of an inflamed kidney from the ANCA-AAV model. (**a**) Low spatial resolution images acquired using the ^{1}H/^{19}F dual-tunable volume RF coil (18 mm inner diameter). At this resolution [0.938 × 0.938]mm^2, a high ^{19}F signal can be achieved already after 1 h acquisition time. However, anatomical detail is lacking in the ^{19}F MR images. (**b**) High spatial resolution images acquired with the ^{19}F cryogenic quadrature RF surface probe (^{19}F-CRP). The gain in SNR achieved by the ^{19}F-CRP was used to increase the in plane spatial resolution [0.078 × 0.078]mm^2

3. Harvest relevant organs (e.g., kidney, liver, and spleen).
4. Transfer organs to a container filled with 4% PFA and store at 4 °C.
5. Prior to the high resolution ^{19}F MRI of the kidney, embed the kidney in 1% low melting agarose in a 1.5 ml Eppendorf tube.
6. ^{19}F-CRP adjustments: since the ^{19}F signal is too low for automatic adjustments, use a ^{19}F calibration phantom (fill highly fluorinated substance such as trifluoroethanol with water in a 1.5 ml Eppendorf tube. Place the ^{19}F calibration tube under the ^{19}F-CRP and repeat steps 13–16 to calculate the working frequency. Load and run a 1_Localizer_multi_slice sequence (see above). Adjust the reference power using the adjustments platform: select a coronal slice of 2 mm thickness and place it close to the RF coil's surface. Select an initial power two orders of magnitude smaller than what is usually expected and press start. Run the rest of the adjustments using the same sequence. Save the shim settings.
7. ^{19}F-CRP imaging: place the ex vivo kidney embedded in a 1.5 ml Eppendorf tube under the ^{19}F-CRP surface. Run the working frequency adjustments as per 13–16, load the shim

calculations, and adjust the reference power as described above. Set the RG to maximum. Load a 2D FLASH protocol and set it up for ^{19}F imaging. Examples for high and medium resolution ^{19}F imaging are given in **Note 13**.

8. Set up a 2D FLASH protocol for the acquisition of anatomical kidney ^{1}H scans. Use the same geometry used for ^{19}F imaging (*see* **Note 13**).

4 Notes

1. The transceive ^{19}F cryogenic quadrature RF surface probe (^{19}F CryoProbe) operates at ~28 K with a dual cooled preamplifier at the base running at ~77 K. It has a similar geometry to the existing Bruker ^{1}H quadrature CryoProbes. More details on the ^{19}F CryoProbe are available in our previous study [25].
2. The FLASH_3D protocol is especially adapted for whole-body imaging of mice (the gradient-system and the volume-resonator need to have a linear region of about 8 cm).
3. The block pulse program (SINGLEPULSE) contains the necessary elements for a simple transmit/receive experiment, sending a pulse and acquiring an FID afterward.
4. A 2D version of this sequence is also available, which allows thicker slices for a general overview but suffers from low SNR for most in vivo applications.
5. Special attention should be given when studying inflammation in models where tissue oxygen levels are likely to change, for example, following ischemic events. In these cases, T_1 weighting needs to be reduced at cost of SNR efficiency by increasing $TR \gg T_1$ (typically $TR = 3–5 \times T_1$).
6. When using transmit-receive surface coils a B_1 correction should be considered in order to compensate for the intrinsic spatial gradient in coil sensitivity (B_1^-) and excitation field (B_1^+ inhomogeneity), which results is signification variation in the excitation FA, decreasing with increasing distance from the RF coil surface. This severely reduces image homogeneity and hampers the acquisition of the absolute signal intensity values for ^{19}F quantification techniques.
7. Example for a 30 g mouse at 9.4 T and FOV of 50 × 25 × 25 mm, (1) ^{1}H 2D FLASH protocol: TR = 579.4 ms, TE = 5 ms, FA = 75, matrix = 256 × 128. (2) ^{19}F 3D RARE protocol: TR = 800 ms, TE = 6.16 ms, Matrix = 256 × 128 × 128, RARE Factor = 32–64.

8. The polydispersity index (PdI) is extrapolated from the DLS function and quantitatively describes the particle size distribution best. PdI ranges from 0.01 for monodispersed particles to 0.7 for particles that have a very broad size distribution. The *z*-average diameter gives the mean diameter based on intensity of scattered light and sensitive to presence of large particles, peak diameter, peak width, and PdI.
9. In MPO-AAV mice we administered one bolus of PFCE nanoparticles intravenously (80 μmol in 100 μl) 8 weeks following transplantation of bone marrow cells.
10. Mice can be alternatively anesthetized with an intraperitoneal injection of ketamine and xylazine.
11. Shimming is particularly important, since macroscopic magnetic field inhomogeneities affect the exact resonance frequency of the PFCE compounds and might affect quantification of the ^{19}F MR signal. Shimming should be performed on a voxel enclosing both kidneys using either the default iterative shimming method or the Mapshim technique (recommended). However, the Mapshim technique is not available for X-nuclei-only RF coils. An alternative in this case is to use a highly fluorinated sample to calculate the shims.
12. Since the NMR properties of ^{19}F and ^{1}H are similar, the same MR setup and MR parameter settings can be used for both nuclei.
13. Example for ex vivo *high-resolved ^{19}F MRI* at 9.4 T using the ^{19}F-CRP and a 2D FLASH: TR = 11 ms, TE = 2.7 ms, FA = 30, Avg = 2250, Repetitions = 35, FOV = 20 × 20, matrix = 256 × 256, 1 mm slice thickness. Example for ex vivo *low-resolved ^{19}F MRI* at 9.4 T using the ^{1}H/^{19}F dual-tunable volume RF coil (18 mm inner diameter) and a 3D RARE method: TR = 800 ms, TE = 5 ms, Avg = 256, Repetitions = 13, FOV = 60 × 30 × 30, matrix = 64 × 32 × 16. ^{1}H 2D FLASH protocol: TR = 18.7 ms, TE = 5.5 ms, FA = 25, matrix = 171 × 256, 1 mm slice thickness.

Acknowledgments

This work was funded, in part (Adrian Schreiber, Ralph Kettritz, Thoralf Niendorf, Sonia Waiczies, and Andreas Pohlmann), by the German Research Foundation (Gefoerdert durch die Deutsche Forschungsgemeinschaft (DFG), Projektnummer 394046635, SFB 1365, RENOPROTECTION. Funded by the Deutsche Forschungsgemeinschaft (DFG, German Research Foundation), Project number 394046635, SFB 1365, RENOPROTECTION).

Also, our research is funded by the Deutsche Forschungsgemeinschaft to SW (DFG WA2804), AP (DFG PO1869), and AS (DFG SCHR7718).
This chapter is based upon work from COST Action PARENCHIMA, supported by European Cooperation in Science and Technology (COST). COST (www.cost.eu) is a funding agency for research and innovation networks. COST Actions help connect research initiatives across Europe and enable scientists to enrich their ideas by sharing them with their peers. This boosts their research, career, and innovation.
PARENCHIMA (renalmri.org) is a community-driven Action in the COST program of the European Union, which unites more than 200 experts in renal MRI from 30 countries with the aim to improve the reproducibility and standardization of renal MRI biomarkers.

References

1. Chawla LS, Eggers PW, Star RA, Kimmel PL (2014) Acute kidney injury and chronic kidney disease as interconnected syndromes. N Engl J Med 371(1):58–66. https://doi.org/10.1056/NEJMra1214243
2. Levy EM, Viscoli CM, Horwitz RI (1996) The effect of acute renal failure on mortality. a cohort analysis. JAMA 275(19):1489–1494
3. Jorres A, Gahl GM, Dobis C, Polenakovic MH, Cakalaroski K, Rutkowski B, Kisielnicka E, Krieter DH, Rumpf KW, Guenther C, Gaus W, Hoegel J (1999) Haemodialysis-membrane biocompatibility and mortality of patients with dialysis-dependent acute renal failure: a prospective randomised multicentre trial. International Multicentre Study Group. Lancet 354(9187):1337–1341
4. Brouns R, De Deyn PP (2004) Neurological complications in renal failure: a review. Clin Neurol Neurosurg 107(1):1–16. https://doi.org/10.1016/j.clineuro.2004.07.012
5. Chawla LS, Bellomo R, Bihorac A, Goldstein SL, Siew ED, Bagshaw SM, Bittleman D, Cruz D, Endre Z, Fitzgerald RL, Forni L, Kane-Gill SL, Hoste E, Koyner J, Liu KD, Macedo E, Mehta R, Murray P, Nadim M, Ostermann M, Palevsky PM, Pannu N, Rosner M, Wald R, Zarbock A, Ronco C, Kellum JA (2017) Acute kidney disease and renal recovery: consensus report of the Acute Disease Quality Initiative (ADQI) 16 Workgroup. Nat Rev Nephrol 13(4):241–257
6. Humphreys BD, Cantaluppi V, Portilla D, Singbartl K, Yang L, Rosner MH, Kellum JA, Ronco C (2016) Targeting endogenous repair pathways after AKI. J Am Soc Nephrol 27 (4):990–998
7. Kurts C, Panzer U, Anders H-J, Rees AJ (2013) The immune system and kidney disease: basic concepts and clinical implications. Nat Rev Immunol 13:738. https://doi.org/10.1038/nri3523. https://www.nature.com/articles/nri3523-supplementary-information
8. Bellomo R, Kellum JA, Ronco C, Wald R, Martensson J, Maiden M, Bagshaw SM, Glassford NJ, Lankadeva Y, Vaara ST, Schneider A (2017) Acute kidney injury in sepsis. Intensive Care Med 43(6):816–828
9. Weisheit CK, Engel DR, Kurts C (2015) Dendritic cells and macrophages: sentinels in the kidney. Clin J Am Soc Nephrol 10 (10):1841–1851. https://doi.org/10.2215/cjn.07100714
10. Kurts C, Panzer U, Anders H-J, Rees AJ (2013) The immune system and kidney disease: basic concepts and clinical implications. Nat Rev Immunol 13:738. https://doi.org/10.1038/nri3523. https://www.nature.com/articles/nri3523-supplementary-information
11. Furuta S, Jayne DRW (2013) Antineutrophil cytoplasm antibody–associated vasculitis: recent developments. Kidney Int 84 (2):244–249. https://doi.org/10.1038/ki.2013.24
12. Schreiber A, Rousselle A, Becker JU, von Mässenhausen A, Linkermann A, Kettritz R (2017) Necroptosis controls NET generation and mediates complement activation, endothelial damage, and autoimmune vasculitis. Proc Natl Acad Sci 114(45):E9618–E9625. https://doi.org/10.1073/pnas.1708247114

13. Rousselle A, Kettritz R, Schreiber A (2017) Monocytes promote crescent formation in anti-myeloperoxidase antibody–induced glomerulonephritis. Am J Pathol 187 (9):1908–1915. https://doi.org/10.1016/j.ajpath.2017.05.003
14. Grenier N, Merville P, Combe C (2016) Radiologic imaging of the renal parenchyma structure and function. Nat Rev Nephrol 12 (6):348–359
15. Hueper K, Gutberlet M, Bräsen JH, Jang M-S, Thorenz A, Chen R, Hertel B, Barrmeyer A, Schmidbauer M, Meier M, von Vietinghoff S, Khalifa A, Hartung D, Haller H, Wacker F, Rong S, Gueler F (2016) Multiparametric functional MRI: non-invasive imaging of inflammation and edema formation after kidney transplantation in mice. PLoS One 11(9): e0162705. https://doi.org/10.1371/journal.pone.0162705
16. Schreiber A, Xiao H, Falk RJ, Jennette JC (2006) Bone marrow-derived cells are sufficient and necessary targets to mediate glomerulonephritis and vasculitis induced by anti-myeloperoxidase antibodies. J Am Soc Nephrol 17(12):3355–3364. https://doi.org/10.1681/asn.2006070718
17. Aratani Y, Koyama H, Nyui S, Suzuki K, Kura F, Maeda N (1999) Severe impairment in early host defense against *Candida albicans* in mice deficient in myeloperoxidase. Infect Immun 67(4):1828–1836
18. Waiczies H, Lepore S, Drechsler S, Qadri F, Purfurst B, Sydow K, Dathe M, Kuhne A, Lindel T, Hoffmann W, Pohlmann A, Niendorf T, Waiczies S (2013) Visualizing brain inflammation with a shingled-leg radiofrequency head probe for 19F/1H MRI. Sci Rep 3:1280. https://doi.org/10.1038/srep01280
19. Srinivas M, Morel PA, Ernst LA, Laidlaw DH, Ahrens ET (2007) Fluorine-19 MRI for visualization and quantification of cell migration in a diabetes model. Magn Reson Med 58 (4):725–734. https://doi.org/10.1002/mrm.21352
20. Flögel U, Ding Z, Hardung H, Jander S, Reichmann G, Jacoby C, Schubert R, Schrader J (2008) In vivo monitoring of inflammation after cardiac and cerebral ischemia by fluorine magnetic resonance imaging. Circulation 118 (2):140–148
21. Jacoby C, Temme S, Mayenfels F, Benoit N, Krafft MP, Schubert R, Schrader J, Flögel U (2014) Probing different perfluorocarbons for in vivo inflammation imaging by 19F MRI: image reconstruction, biological half-lives and sensitivity. NMR Biomed 27(3):261–271. https://doi.org/10.1002/nbm.3059
22. Flögel U, Burghoff S, van Lent PL, Temme S, Galbarz L, Ding Z, El-Tayeb A, Huels S, Bonner F, Borg N, Jacoby C, Muller CE, van den Berg WB, Schrader J (2012) Selective activation of adenosine A2A receptors on immune cells by a CD73-dependent prodrug suppresses joint inflammation in experimental rheumatoid arthritis. Sci Transl Med 4(146):146ra108. https://doi.org/10.1126/scitranslmed.3003717
23. Hennig J, Nauerth A, Friedburg H (1986) RARE imaging: a fast imaging method for clinical MR. Magn Reson Med 3:823–833. https://doi.org/10.1002/mrm.1910030602
24. Schmid F, Höltke C, Parker D, Faber C (2013) Boosting 19F MRI—SNR efficient detection of paramagnetic contrast agents using ultrafast sequences. Magn Reson Med 69 (4):1056–1062. https://doi.org/10.1002/mrm.24341
25. Waiczies S, Millward JM, Starke L, Delgado PR, Huelnhagen T, Prinz C, Marek D, Wecker D, Wissmann R, Koch SP, Boehm-Sturm P, Waiczies H, Niendorf T, Pohlmann A (2017) Enhanced fluorine-19 MRI sensitivity using a cryogenic radiofrequency probe: technical developments and ex vivo demonstration in a mouse model of neuroinflammation. Sci Rep 7(1):9808. https://doi.org/10.1038/s41598-017-09622-2

Chapter 31

Fluorine (^{19}F) MRI to Measure Renal Oxygen Tension and Blood Volume: Experimental Protocol

Lingzhi Hu, Hua Pan, and Samuel A. Wickline

Abstract

Fluorinated compounds feature favorable toxicity profile and can be used as a contrast agent for magnetic resonance imaging and spectroscopy. Fluorine nucleus from fluorinated compounds exhibit well-known advantages of being a high signal nucleus with a natural abundance of its stable isotope, a convenient gyromagnetic ratio close to that of protons, and a unique spectral signature with no detectable background at clinical field strengths. Perfluorocarbon core nanoparticles (PFC NP) are a class of clinically approved emulsion agents recently applied in vivo for ligand-targeted molecular imaging. The objective of this chapter is to outline a multinuclear $^{1}H/^{19}F$ MRI protocol for functional kidney imaging in rodents for mapping of renal blood volume and oxygenation (pO_2) in renal disease models.

This chapter is based upon work from the COST Action PARENCHIMA, a community-driven network funded by the European Cooperation in Science and Technology (COST) program of the European Union, which aims to improve the reproducibility and standardization of renal MRI biomarkers. This experimental protocol chapter is complemented by a separate chapter describing the basic concept of functional imaging using fluorine (^{19}F) MR methods.

Key words Perfluorocarbon, Fluorine, Oxygenation, Perfusion, MRI, Kidney, Mice, Rats

1 Introduction

In healthy kidneys, the countercurrent design of blood vessels and tubules maintains the necessary osmolar gradient to permit efficient urinary concentration, yet the system operates under conditions of a relatively hypoxic environment in some regions that requires extensive extraction of oxygen from flowing blood [1, 2]. During acute and chronic kidney injury, ischemia challenges effective O_2 delivery to the capillary beds of the renal tubules where extraction of extra oxygen is marginal, resulting in heightened susceptibility to ischemic damage that may culminate in renal failure [3]. Besides the traditional biochemical metrics for assessing renal failure (e.g., blood urea nitrogen, creatinine), $^{1}H/^{19}F$ imaging offers a multiparametric quantifiable approach to functional imaging in kidney

Andreas Pohlmann and Thoralf Niendorf (eds.), *Preclinical MRI of the Kidney: Methods and Protocols*, Methods in Molecular Biology, vol. 2216, https://doi.org/10.1007/978-1-0716-0978-1_31,

injury that avoids the use of potentially nephrotoxic gadolinium (Gd) based contrast agents [3].

Perfluorocarbon core nanoparticles (PFC NP) are a class of emulsion agents clinically approved as blood substitutes that have been applied recently for in vivo for targeted molecular imaging and noninvasive oxygen tension (pO_2) assessment [1–3]. As compared with standard iodinated or Gd contrast agents, PFC NP are biologically inert and exhibit a good safety profile with no renal toxicity reported in both animals and human [3]. Because PFC NP (nominal size 200–250 nm) are not cleared through glomerular filtration, they do not increase kidney workload, which is a major risk factor for kidney failure with the use of other agents that undergo renal clearance [3]. For imaging purposes, the unique ^{19}F MR signal emanating from the fluorine core of PFC NP can be measured directly in vivo in quite sparse concentrations (e.g., picomolar voxel amounts) with no background signal, as contrasted with other paramagnetic or superparamagnetic moieties that exert indirect contrast effects on circulating protons [4–6]. PFC NP have been demonstrated as effective functional probes for regional blood volume as the detected ^{19}F signal intensity directly reflects the actual quantity of PFC NP within a voxel. Furthermore, for pO_2 measurements, the ^{19}F longitudinal relaxation rate (R_1) responds directly to local oxygen content in a linear manner [1, 2].

Herein we describe $^{1}H/^{19}F$ MRI for monitoring of renal perfusion in the kidney of rodents in a step-by-step experimental protocol. The rationale for choosing acquisition parameters is described in generic terms, together with specific parameter examples.

This experimental protocol chapter is complemented by a separate chapter describing the basic concept of functional imaging using fluorine (19F) MR methods, which is part of this book.

This chapter is part of the book Pohlmann A, Niendorf T (eds) (2020) Preclinical MRI of the Kidney—Methods and Protocols. Springer, New York.

2 Materials

2.1 Animals

This experimental protocol is applicable to mice and rats.

2.2 Lab Equipment

Enumerated below are the contrast agents and equipment components needed:

1. Perfluorocarbon Nanoparticle Preparation: PFC NP (~200–250 nm) can be formulated with a variety of PFC that are liquid at body temperature. Here we describe either perfluorooctylbromide (PFOB) or perfluoro-15-crown-5-ether (CE). The PFOB or CE emulsions are composed of 20% or 40% (v/v) of PFOB or CE, 2.0% (w/v) of a surfactant commixture, and 1.7% (w/v) glycerin in water (*see* **Note 1**).

2. Gases: O_2, N_2, and compressed air, as well as a gas-mixing system to achieve required changes in the oxygen fraction of inspired gas mixture (FiO_2). In addition to room air, the following gas mixtures are required during the experiment: 10% O_2–90% N_2 for hypoxia and 100% O_2 for hyperoxia.
3. Anesthesia: An MRI-compatible slow infusion system is needed for anesthesia with ketamine–xylazine (e.g., syringe pump). Isoflurane is not recommended for ^{19}F imaging as it could interfere with the detected ^{19}F MRI signal from PFC NP.
4. Small Animal Monitoring System: An MRI-compatible small animal physiological monitoring system (e.g., SAI Inc., USA) is needed for real time respiratory monitoring and respiratory triggering and/or gating. Respiratory gating is recommended during ^{19}F MRI acquisition because it reduces motion artifact and preserves ^{19}F signal intensity in the final images, which could otherwise be degraded by motion.
5. Small Animal Holder: a dedicated customer built small animal holder is needed to accommodate animal imaging and for maintenance of body temperature at 37 °C. A warm water blanket or warm air blower can be used for maintaining body temperature of animals (*see* **Note 2**).
6. Animal Surgery Suite: A fully equipped animal surgery suite is needed for preparing animal models of renal injury (*see* **Note 3**).

2.3 MRI Hardware

The technique described in this chapter is tailored for an 11.7 T MR system (e.g., Varian, USA) but advice for adaptation to other field strengths is given where necessary. In general, the MRI scanner should be equipped with a wide band spectrometer and a wide band RF power amplifier. The scanner needs to be functional at both ^{1}H and ^{19}F frequencies.

1. $^{1}H/^{19}F$ dual-tuned Coils: use actively decoupled coil pair for renal imaging applications. Such coils can be custom-built as described in our prior publications [7] or obtained from commercial coil manufacturers (*see* **Note 4**).
2. Transmit Coils: use a volume transmit coil to generate a homogeneous B_1 field that covers both kidneys. Tune and match to the ^{19}F frequency.
3. Receive Coils: Place a surface receive coil on the dorsal side of the animal to achieve high sensitivity to ^{19}F signal from the two kidneys. Tune and match to the ^{19}F frequency.

2.4 MRI Techniques

1. ^{1}H MRI: a gradient echo sequence is employed to locate two imaging slices with 2 mm thickness, positioned 1–2 mm apart, and centered respectively at the left and right kidney.

2. ^{1}H MRI: a multiecho gradient-echo blood oxygenation level dependent (BOLD) scan can be performed. For an example of parameters used for a specific setting (*see* **Note 5**).
3. ^{19}F MRI: For spin density ^{19}F MRI, TR is set to 4 s. For T_1-weighted MRI, TR is set to two respiration periods, or ~300 ms. All other imaging parameters are identical in these two sets of ^{19}F MRI (*see* **Note 6**)
4. ^{19}F MRI Oxygenation Measurement: For PFC NP dependent oxygenation measurements in fast flowing blood of major blood vessels, a Blood Flow-Enhanced-Saturation-Recovery (BESR) sequence [8] can be utilized to minimize in-flow effects on the image (*see* **Note 7**).

3 Methods

3.1 PFC Nanoparticle Formulation

1. Prepare PFC NP emulsifying 40% (v/v) of CE (Exfluor Research Corp, Round Rock, TX), 2.0% (w/v) of a surfactant commixture, and 1.7% (w/v) glycerin, in distilled water using a microfluidic apparatus (e.g., benchtop LV1 fluidizer, Microfluidics Corporation, Westwood, MA) (*see* **Note 8**).
2. Determine size and charge with a submicron particle analyzer (e.g., Zetasizer, Malvern, UK) [9, 10].

3.2 PFC NP Injection and Imaging

1. Inject PFC NP for functional perfusion imaging to quantify blood volume and oxygenation.
2. Prepare an external reference for ^{19}F signal quantification. Place the external reference close to the animal within the field of view (*see* **Note 9**).
3. Perform ^{1}H and ^{19}F imaging 10 min to 1 h after NP injection. A shorter circulation time is preferred to maximize the intravascular ^{19}F signal (*see* **Note 10**).

3.3 Coil Sensitivity Profiling for Quantification of ^{19}F Signal Intensity

1. Acquire an RF coil sensitivity map using a saline phantom positioned at the selected imaging location to correct for the signal bias created by surface coil receive profile inhomogeneity. The saline phantom is prepared to cover the entire region of imaging FOV (*see* **Note 11**).
2. Compensate for the spatial inhomogeneity of the RF coil sensitivity profile by multiplying the correction factor obtained from the phantom image (*see* **Note 12**) with the in vivo measured image signal intensity at the corresponding locations.

3.4 Calibration of ^{19}F R_1 vs. pO_2 Curve In Vitro

1. Perform an in vitro calibration of ^{19}F relaxation time (R_1) as a function of pO_2 using at least three different O_2 concentrations (e.g., 0%, 21%, 100% O_2 balanced with N_2) by bubbling gas

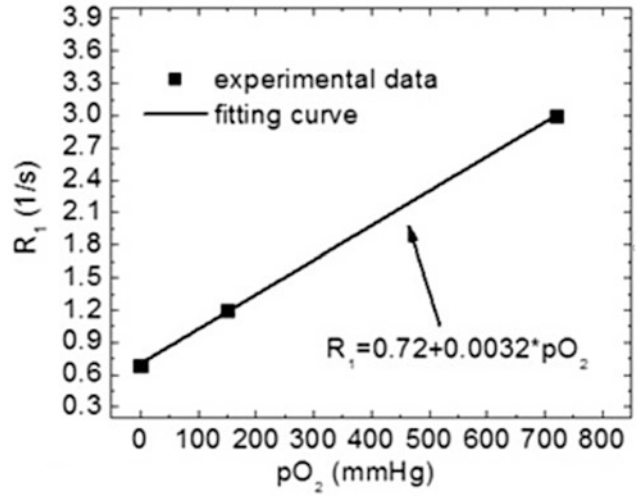

Fig. 1 In vitro calibration shows the ^{19}F R_1 ($=1/T_1$) of PFC NP as a function of pO_2. Data were collected at 11.7 T using a PFC NP phantom. Temperature of the PFC NP phantom was maintained at 37 °C. The correlation coefficient $R > 0.99$ (From Hu et al. [1])

mixtures into a PFC emulsion sample for 30 min at 37 °C (Fig. 1).

2. Perform ^{19}F T_1 measurements with inversion recovery spectroscopy at TR > 10 s, and at least ten different inversion delays (T_I) ranging from 3 ms to 5 s. Use exponential fitting to extract R_1 from T_1 measurements and linear fitting to calibrate the relationship between ^{19}F R_1 and pO_2.

3.5 Quantification of ^{19}F Based pO_2 Measurement In Vivo

1. Create two sets of images, one using a short TR and one using a long TR, for T_1 mapping (*see* **Note 13**).
2. Determine the actual TR using the external ^{19}F standard (*see* **Note 14**).
3. After determining the actual short TR, perform voxel-wise T_1 mapping of the kidney using the standard saturation recovery signal model:

$$S = S_0\left(1 - e^{\frac{TR}{T_1}}\right). \quad (1)$$

4. Translate T_1 values into corresponding pO_2 levels according to the predetermined calibration curve.

4 Notes

1. The CE signal intensity is effectively greater for narrow band reception as all fluorine atoms contribute to a single spectral peak, as compared to PFOB where chemical shifts apportion

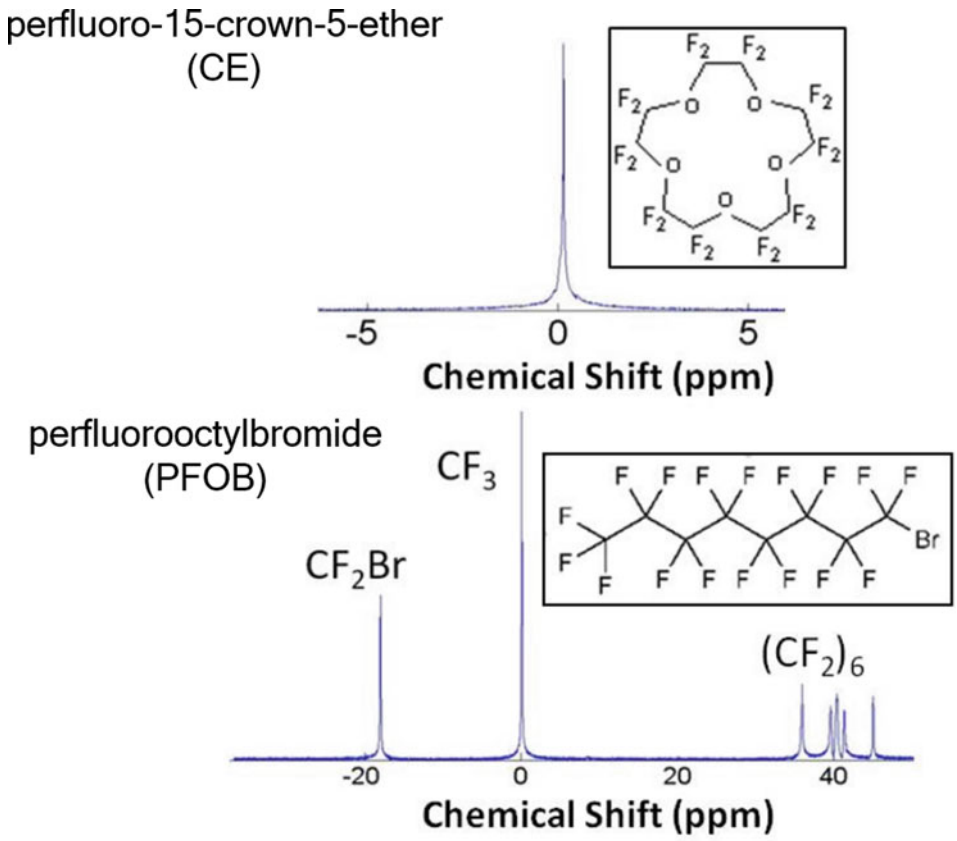

Fig. 2 Chemical structure and magnetic resonance chemical shift of perfluoro-15-crown-5-ether (CE) and perfluorooctylbromide (PFOB)

the signal into several peaks (Fig. 2). Suppliers of PFC include Exfluor Research Corporation (Round Rock, TX). The clearance half-life for PFOB is ~3–5 h depending on species and whether the PFC contrast material is molecularly targeted or not [11]. The CE materials exhibit a longer tissue residence time in bloodstream than PFOB compounds, which makes them problematic for clinical use or repeat studies. For the present protocol, no targeting ligands are attached to the surface of the PFC NP to avoid changing the pharmacokinetics of the contrast agent.

2. Potential MRI in-flow artifacts may be present on ^{1}H but not ^{19}F MR images if a warm water blanket is used. Special attention should be given when choosing the animal holder and the MRI coils as reduced animal motion during lengthy MRI acquisitions will improve image quality.
3. In general, ischemic renal injury can be produced unilaterally or bilaterally by exposing the kidneys either through the abdomen or retroperitoneally, and then clamping the renal artery for a

selected interval [1, 2]. The animal surgery suite does not need to be located in the MRI facility but should be close enough for imaging a short time after surgery and later for tissue harvest after imaging is completed if indicated.

4. Despite being slightly off-resonance for ^{1}H imaging, the ^{19}F coil pair should be sufficient to generate high quality anatomic images within <1 min scan time. The size of the transmit and receive coils should be designed to match the animal size, so that different coil sizes will be needed for imaging mice and rats. For imaging at field strengths lower than 11.7 T, it is recommended to use double tuned receive coils that simultaneously function at ^{1}H and ^{19}F frequency to assure maximal detection efficiency while avoiding potential image mismatches between ^{1}H and ^{19}F images that may occur as a result of manual coil retuning.
5. The imaging parameters of BOLD at 4.7 T are: TR = 100 ms, TE = 1.96 ms with 1.75 ms increment for every echo, flip angle = 10°, field of view = 26 × 26 mm^2, voxel size = 0.2 × 0.2 × 2 mm^3. Field of view and voxel size should be adjusted based on animal size to achieve optimal image quality.
6. ETL = 4, TE = 11.5 ms, receiver bandwidth = 20 kHz, voxel size = 0.4 × 0.4 × 2 mm^3, and the field of view is identical to that for ^{1}H BOLD imaging.
7. For an example of parameters used at 4.7 T, the imaging parameters of BESR sequence are: TR = 2.5 s; TE = 2.2 ms; number of points along recovery curve = 8; number of averages = 16; in plane resolution = 1.5 mm × 0.75 mm; slice thickness = 2 mm
8. PFC NP can be colabeled with Alexa Fluor 594 for ex vivo fluorescence microscopy examination.
9. As reference, a tube of another PFC NP formulation (e.g., perfluorodecalin) at a similar PFC concentration to that administered in vivo for the imaging studies can be used.
10. In healthy tissues, PFC NP are generally constrained to the intravascular space because of their large particle size (200–250 nm), which ensures that the measured ^{19}F signal intensity correlates linearly with intravascular blood volume. One has to also consider that during injury, PFC NP will escape from the circulation and will get trapped in tissue compartments. In this case the total fluorine signal would comprise both stationary (i.e., trapped in tissue) and flowing (i.e., in blood) PFC NP. Employ spin labeling [12] to eliminate the signal from trapped PFC NP, leaving only the signal from the flowing blood compartment. Apply diffusion gradients to suppress the signal from flowing blood [13] and acquire distinct

signal from either compartment. For O_2 measurements, a mixture of signals could occur where trapped PFC NP exist under hypoxic conditions and the flowing PFC NP under more normoxic conditions. In this case the ^{19}F relaxation times would represent an average of the two situations.

11. At 11.7 T, imaging parameters are as follows: TR = 100 ms, TE = 1.96 ms, and flip angle = 10°. For other field strengths, minimize TE and select similar TR and flip angle.
12. For each voxel location, the phantom image defines a correction factor matrix $R(x,y,z)$ that is the inverse of local signal intensity $I(x,y,z)$: $R(x,y,z) = 1/I(x,y,z)$.
13. In vivo quantification of renal T_1 and pO_2 is based on the general assumption that image signal intensity in a fast spin echo sequence follows a saturation-recovery process (Fig. 3). Because short TR or T_1-weighed ^{19}F MRI is gated with respiration, the actual short TR can vary from animal to animal.
14. Given that the ^{19}F T_1 of PFC standard is 0.9–1 s at room air oxygen tension, the signal acquired with a long TR = 4 s, that is, $>3 \times T_1$, should approximate the ^{19}F spin-density signal of PFC NP at room temperature (Fig. 4).

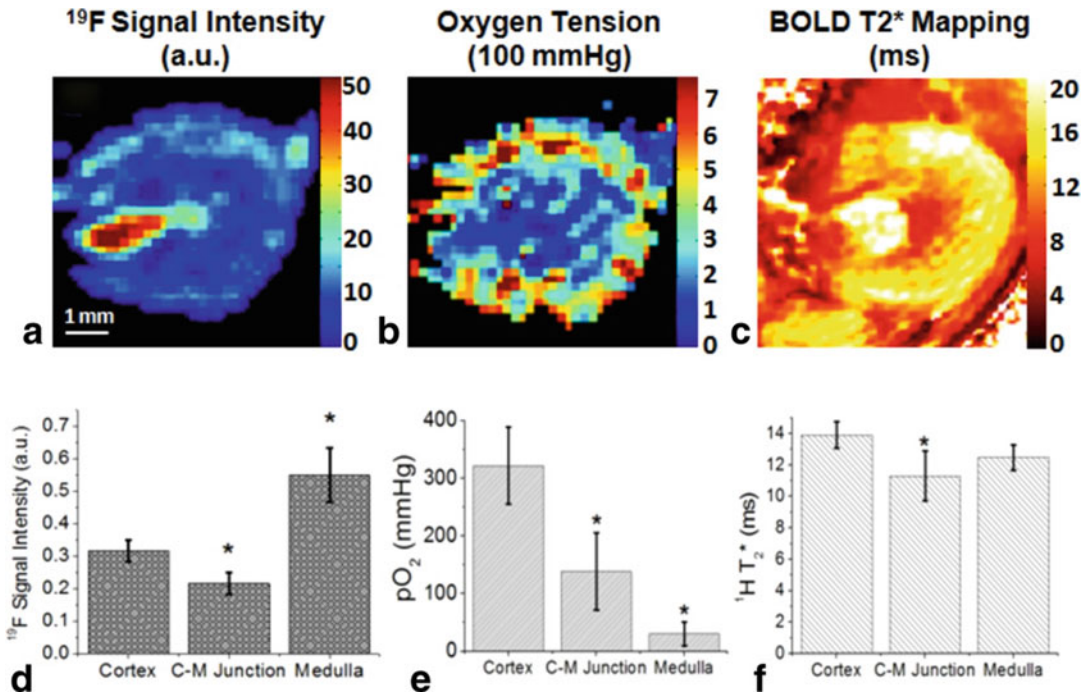

Fig. 3 (**a**, **b**) Representative renal blood volume and pO_2 mapping of healthy kidneys determined by quantitative ^{19}F MRI. (**c**) Representative ^{1}H T2* (BOLD) mapping of healthy kidneys. (**d**–**f**) Quantification of functional indexes in different anatomical regions. *$P < 0.05$ compared with cortex (From Hu et al. [1])

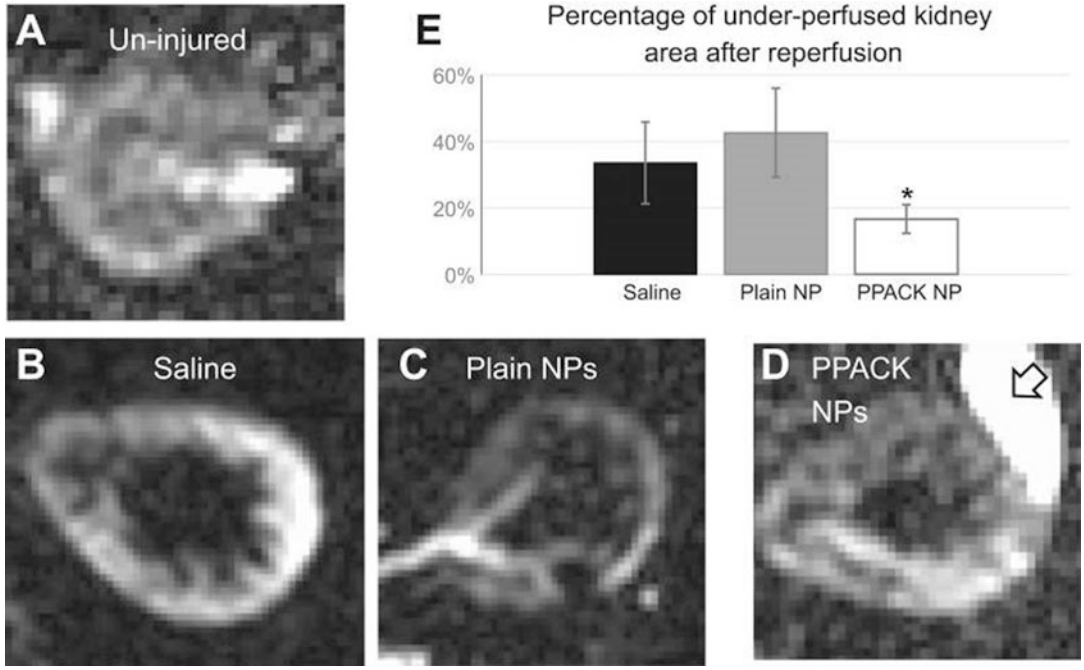

Fig. 4 Imaging of improved renal medullary perfusion after antithrombin PFC NP treatments. Here the thrombin inhibitor PPACK (phenylalanine-proline-arginine-chloromethylketone) was conjugated to the PFC NP. Mice were pretreated with PFOB PPACK NP, plain PFOB NP, or saline before ischemia induction. At 3 h after reperfusion, a single dose of CE NP was injected i.v. for ^{19}F MRI. The ^{19}F signal from circulating CE NP of uninjured kidney illustrates normal kidney perfusion (**a**). In contrast, all injured kidneys exhibited reduced ^{19}F signal in the medulla (**b**–**d**) reflecting the severity of regional nonreperfusion. Compared to kidneys pretreated with saline or plain NP (**b**, **c**), the improved medullary perfusion in PPACK NP treated kidneys is visually appreciable (**d**). Using in vivo ^{19}F MRI data, the ratio of nonperfused kidney area after reperfusion was determined. The PPACK NP treated kidneys ($n = 4$) developed less regional nonreperfusion than did saline ($n = 6$) or plain NP ($n = 6$) treated kidneys. *$p < 0.05$ compared to saline or plain NP treated kidneys. Note that the arrow in d indicates the partial overlay of ^{19}F signal from the adjacent spleen (From Chen et al. [2])

Acknowledgments

This chapter is based upon work from COST Action PARENCHIMA, supported by European Cooperation in Science and Technology (COST). COST (www.cost.eu) is a funding agency for research and innovation networks. COST Actions help connect research initiatives across Europe and enable scientists to enrich their ideas by sharing them with their peers. This boosts their research, career, and innovation.

PARENCHIMA (renalmri.org) is a community-driven Action in the COST program of the European Union, which unites more than 200 experts in renal MRI from 30 countries with the aim to improve the reproducibility and standardization of renal MRI biomarkers.

References

1. Hu LZ et al (2014) Assessing intrarenal non-perfusion and vascular leakage in acute kidney injury with multinuclear H-1/F-19 MRI and perfluorocarbon nanoparticles. Magn Reson Med 71(6):2186–2196
2. Chen JJ et al (2015) Antithrombin nanoparticles improve kidney reperfusion and protect kidney function after ischemia-reperfusion injury. Am J Physiol Renal Physiol 308(7): F765–F773
3. Chen JJ et al (2013) Perfluorocarbon nanoparticles for physiological and molecular imaging and therapy. Adv Chronic Kidney Dis 20 (6):466–478
4. Goette MJ et al (2015) Balanced UTE-SSFP for 19F MR imaging of complex spectra. Magn Reson Med 74(2):537–543
5. Goette MJ et al (2015) Improved quantitative 19 F MR molecular imaging with flip angle calibration and B1-mapping compensation. J Magn Reson Imaging 42(2):488–494
6. Palekar RU et al (2015) Quantifying progression and regression of thrombotic risk in experimental atherosclerosis. FASEB J 29 (7):3100–3109
7. Hu LZ et al (2011) A generalized strategy for designing (19)F/(1)H dual-frequency MRI coil for small animal imaging at 4.7 Tesla. J Magn Reson Imaging 34(1):245–252
8. Hu LZ et al (2013) Rapid quantification of oxygen tension in blood flow with a fluorine nanoparticle reporter and a novel blood flow-enhanced-saturation-recovery sequence. Magn Reson Med 70(1):176–183
9. Winter PM et al (2003) Molecular imaging of angiogenesis in nascent Vx-2 rabbit tumors using a novel alpha(nu)beta3-targeted nanoparticle and 1.5 tesla magnetic resonance imaging. Cancer Res 63(18):5838–5843
10. Winter PM et al (2003) Molecular imaging of angiogenesis in early-stage atherosclerosis with alpha(v)beta3-integrin-targeted nanoparticles. Circulation 108(18):2270–2274
11. Kaneda MM et al (2009) Perfluorocarbon nanoemulsions for quantitative molecular imaging and targeted therapeutics. Ann Biomed Eng 37(10):1922–1933
12. Wu WC et al (2011) Renal perfusion 3-T MR imaging: a comparative study of arterial spin labeling and dynamic contrast-enhanced techniques. Radiology 261(3):845–853
13. Ichikawa S et al (2013) Intravoxel incoherent motion imaging of the kidney: alterations in diffusion and perfusion in patients with renal dysfunction. Magn Reson Imaging 31 (3):414–417

Chapter 32

MR Elastography of the Abdomen: Experimental Protocols

Suraj D. Serai and Meng Yin

Abstract

Application of MRE for noninvasive evaluation of renal fibrosis has great potential for noninvasive assessment in patients with chronic kidney disease (CKD). CKD leads to severe complications, which require dialysis or kidney transplant and could even result in death. CKD in native kidneys and interstitial fibrosis in allograft kidneys are the two major kidney fibrotic pathologies where MRE may be clinically useful. Both these conditions can lead to extensive morbidity, mortality, and high health care costs. Currently, biopsy is the standard method for renal fibrosis staging. This method of diagnosis is painful, invasive, limited by sampling bias, exhibits inter- and intraobserver variability, requires prolonged hospitalization, poses risk of complications and significant bleeding, and could even lead to death. MRE based methods can potentially be useful to noninvasively detect, stage, and monitor renal fibrosis, reducing the need for renal biopsy. In this chapter, we describe experimental procedure and step by step instructions to run MRE along with some illustrative applications. We also includes sections on how to perform data quality check and analysis methods.

This publication is based upon work from the COST Action PARENCHIMA, a community-driven network funded by the European Cooperation in Science and Technology (COST) program of the European Union, which aims to improve the reproducibility and standardization of renal MRI biomarkers.

Key words Magnetic resonance elastography (MRE), Stiffness, Kidney, Preclinical imaging, MRI, Fibrosis, Chronic kidney disease (CKD)

1 Introduction

1.1 Magnetic Resonance Elastography

Magnetic resonance elastography (MRE) based imaging techniques are now being routinely used for noninvasive assessment of tissue mechanical properties. In MRI, elastography encompasses imaging techniques that noninvasively estimate tissue elasticity and related mechanical properties through the application of external forces [1]. MRE induces harmonic vibrations of acoustic-range frequencies in the tissue of interest and images the propagation of these vibrations in the tissues to calculate quantitative values of mechanical parameters. The desired output is to measure the level of stiffness. The elastogram differentiate if the tissue is hard or soft can give diagnostic information about the presence of the disease. In

Andreas Pohlmann and Thoralf Niendorf (eds.), *Preclinical MRI of the Kidney: Methods and Protocols*, Methods in Molecular Biology, vol. 2216, https://doi.org/10.1007/978-1-0716-0978-1_32,

liver, tissue stiffness has been shown to be elevated with advanced fibrosis and to correlate with the stage of fibrosis [2–4]. Renal fibrosis is a pathological process common to all chronic kidney diseases (CKD) and thereby represents an excellent treatment target. A large number of molecular pathways involved in renal fibrosis have been identified in preclinical studies, some of them being similar among different organs and some with available drugs in various phases of clinical testing [5]. CKD may lead to end-stage renal failure, with extensive morbidity, mortality, and increasing health costs. Primary and secondary prevention requires a better knowledge of mechanisms underlying renal scarring, the development of specific therapies to slow down the progression of the disease and the development of noninvasive diagnostic tools to characterize the process.

Among imaging methods, MRE, that has been successfully demonstrated in the liver, is an attractive alternative for staging of renal fibrosis. Application of MRE to kidney has been shown to be possible and initial results are encouraging. MRE methods are advantageous as compared to ultrasound based elastography methods because the kidneys are usually located deeply in the body and therefore there is no direct access to apply an external compression easily. An increase in the extracellular matrix synthesis, with excessive fibrillary collagens, characterizes the development of chronic lesions in the glomerular, interstitial, and vascular compartments, leading progressively to end-stage renal failure [6]. Mechanisms participating in these processes are increasingly identified and various therapeutic interventions have been shown to prevent or to favor regression of fibrosis in several experimental models. Therefore, development of new noninvasive MRE based methods for identification and quantification of fibrosis is worthwhile.

1.2 Modulus of Elasticity

The shear modulus (μ) and Young's modulus (E) are two parameters often used for describing tissue mechanical properties and are used as contrast parameters in elasticity imaging. Poisson's ratio (ν), another widely used parameter, is the ratio of lateral strain to longitudinal strain. Among these parameters, only two are independent. The shear modulus is known to be related to Young's modulus and one can be estimated from the other by knowing the Poisson's ratio. In general, soft tissues can be assumed to be incompressible and hence the Poisson's ratio can be assumed to be 0.5. The relationship between shear modulus and Young's modulus can be written as $E = 3\mu$, which means that the calculation of Young's modulus or shear modulus provides the same information. MRE is a dynamic elasticity imaging technique capable of calculating quantitative values of shear modulus of tissues and is clinically approved to be used for the assessment of liver fibrosis. MRE uses low-frequency (40–80 Hz) sound waves to induce shear waves in the liver, visualizes the shear waves by tracking tissue displacement

using a modified phase-contrast sequence, and measures the speed of the propagating wave with specialized software called an inversion algorithm [7]. In the commercial version of MRE supplied by Resoundant, the mechanical waves are generated by a subwoofer ("active driver") outside the scan room and are transmitted to a plastic disk ("passive driver") via a plastic tube passing through a wave guide [8]. For preclinical imaging, the same subwoofer active driver may be used or alternatively a functional generator may be used for generating a low frequency sinusoidal mechanical motion (typical range: 20–400 Hz). When the shear stresses (amplitude of microns) are applied to the top surface of a material with certain frequency, the induced waves are propagating into the tissue and every point in the tissue reciprocates in this micromotion. During clinical MRE image acquisition, the passive driver is secured by an elastic band over the abdominal organ of interest [8, 9]. In general, most patients can feel the vibrations generated by the disk but do not find them uncomfortable. For clinical image postprocessing, identical MRE hardware and inversion algorithms are commercially available on scanners manufactured by major MR vendors [10, 11]. Several studies have shown that MRE is a robust, reliable, repeatable, and reproducible technique for detection and staging of liver fibrosis [10]. The accuracy of MRE ranges from 0.85 to 0.99 for differentiating different stages of liver fibrosis [2]. The performance of MRE for differentiating mild fibrosis (stage I) from normal liver or inflammation is lower and the performance is highest for diagnosis of cirrhosis (stage 4) [4, 10]. For preclinical MRE, an actuator, replicating the use of passive driver may be used to couple to the tissue of interest to generate propagating shear waves within a soft tissue material [12]. The electrical signal for the drivers is created by a signal generator synchronized with the MRI pulse sequence triggered and is amplified by an audio amplifier before being fed into the mechanical driver. After the mechanical excitation, a phase-contrast based pulse sequence is used to encode the shear wave motion into the MR phase signal by using a series of magnetic field gradients called motion-encoding gradients (MEG). The MEG, synchronized with the mechanical excitations, is applied after RF excitation [13]. Postprocessing may be done on the scanner or images may be taken offline for analysis. Details of data processing and image reconstruction are covered in the following sections.

1.3 Need for Preclinical MRE

Renal fibrosis causes a change in the structure of the kidney wherein there is an excess accumulation of interstitial extracellular matrix and reduction in the number of tubules. Increasing evidence has demonstrated that, unlike cirrhosis, the early stages of fibrosis are treatable and reversible if appropriate antifibrotic treatment is given [5, 14]. As antifibrotic therapies evolve, a reliable, noninvasive assessment of fibrosis is needed to manage patients with chronic

disease. Being able to noninvasively monitor the progression of fibrosis would help in understanding the natural history in patients with chronic disease, determining which patients require antiviral therapy, predicting the approximate time to the development of high-grade fibrosis, and discovering new directions of scientific inquiry. Therefore, there are ongoing investigations using preclinical models with a reliable, noninvasive method to assess organ inflammation and fibrosis, not only to detect and stage the disease itself but also to monitor treatment efficacy and optimize dosing. The feasibility of MRE has been demonstrated on a mouse model of autosomal recessive polycystic kidney disease (ARPKD) which is an inherited disorder of the kidneys and liver caused by mutations in the PKHD1 gene and an important cause of congenital hepatic fibrosis in humans [3].

1.4 Quest for Renal MRE

Many different mechanisms induce glomerular injury, including glomerulonephritis, hypertensive nephrosclerosis and diabetic nephropathy. However, once renal damage reaches a certain threshold, progression of renal disease is consistent, and largely independent of the initial insult. This common pathway to end-stage renal failure is mainly due to tubulointerstitial damage characterized by tubular atrophy, loss of peritubular capillaries and interstitial fibrosis. Mechanisms leading to kidney failure via tubulointerstitial damage and development of fibrosis are mostly massive proteinuria and chronic hypoxia. Fibrosis further impairs oxygen diffusion and supply to tubular cells, rendering a vicious cycle. Thus, in the assessment of chronic renal failure, fibrosis is a major histological feature and may be an important surrogate endpoint for prognosis and monitoring of treatment response. Besides, some investigations suggest that fibrosis might be reversible, when the cause is treated, emphasizing the need for an early detection and quantification of this fibrosis [14–19]. Currently, the extent of interstitial fibrosis is evaluated by renal biopsy which has several drawbacks: it is a semiquantitative approach with wide interobserver variability, and it is prone to sampling errors and associated with significant morbidity. Thus a noninvasive, truly quantitative method of interstitial fibrosis monitoring would be desirable. Diffusion-weighted and blood oxygenation level dependent (BOLD) MRI findings have been shown to be correlated to renal function, but no data have been published as to their correlation with the degree of fibrosis. Blood or urinary markers of fibrosis are also currently evaluated but none is used in clinical practice yet. MRE based methods can estimate tissue stiffness (and thus, the degree of fibrosis) by measuring the velocity of shear waves traveling through the organ of interest. Clinically, they have been mostly used in liver. The ultrasound-based transient elastography (Fibroscan™ device) is able to discriminate the different stages of liver fibrosis with a quadratic trend of the curve plotting histologic scores versus

elasticity measurements. Among patients with cirrhosis, stiffness thresholds predicting the onset of specific complications (ascites, esophageal bleeding, hepatocarcinoma, etc.) have been identified. However, this technique is limited by its 1D nature that does not allow the exploration of the entire liver. MRE has been successfully used to assess liver fibrosis. The shear stiffness of normal liver was found to be approximately 2.2 kPa by independent groups, using vibrating frequencies of 60 Hz [4]. As with ultrasound-based transient elastography, MRE can discriminate the different stages of liver fibrosis, with the same quadratic trend of the fibrosis/elasticity curve [2]. MRE has the advantage of being intrinsically a 2D technique and can be associated with conventional liver imaging at the same time. MRE has also been used for applications in the abdomen such as characterizing focal liver lesions, and in organs such as pancreas, breast, muscle, prostate, and kidney [9].

Currently, the most definitive means of assessing renal fibrosis is a kidney biopsy. The invasiveness of a biopsy coupled with its small sampling size have limited its utility in quantifying and monitoring changes in renal fibrosis, especially because fibrosis can be heterogeneously distributed. Accordingly, a noninvasive modality that assesses fibrosis on a kidney-wide scale would be of clinical utility. By replacing soft healthy tissue with stiff extracellular matrix, fibrosis stiffens organs, a phenomenon that has led multiple groups to explore whether tissue stiffness could be used as a surrogate measure for fibrosis. MRE based technique that measures tissue stiffness, would be a novel application for assessment of renal fibrosis. During MRE, the organ of interest is gently vibrated by applying acoustic waves through a pad placed on the overlying skin. The resulting microscopic vibrational waves passing through the organ generate shear waves that can be imaged with motion-synchronized MRI. The velocity of wave propagation is dependent on organ stiffness, with stiffer fibrotic tissue leading to more rapidly moving waves with longer wavelength. Capturing shear waves at multiple time points enables the reconstruction of a quantitative stiffness map. MRE is already a well-established, gold standard technique for liver fibrosis imaging, having been shown to accurately reflect biopsy-derived liver fibrosis measurements. In contrast, MRE for nonhepatic applications is still early in its development, and its technique has not yet been standardized. Small pilot studies of MRE have been performed in native kidneys and kidney allografts, attempting to correlate kidney stiffness with either fibrosis burden or kidney function. Although MRE in porcine kidneys showed a correlation between stiffness and fibrosis in the medulla, the results of small pilot human studies thus far have been conflicting, and no studies as yet have assessed whether stiffness measured by MRE predicts progression of kidney dysfunction. In this chapter, we provide recommended MRE protocols for applications in the abdomen with a focus on the kidney, and a few illustrative applications of MRE in preclinical imaging.

This introduction chapter is complemented by a separate chapter describing the concepts of MRE in the abdomen, which is part of this book.

This chapter is part of the book Pohlmann A, Niendorf T (eds) (2020) Preclinical MRI of the Kidney—Methods and Protocols. Springer, New York.

2 Materials

MRE is an MR-based elastography technique that uses mechanical shear waves to evaluate viscoelastic properties of tissues. Mechanical shear waves produced by an external driver are propagated into the organ of interest using a passive abdominal driver placed over the organ and in contact with the abdominal wall. Tissue displacements in the range of microns produced by propagating shear waves because phase shifts that can be detected with motion encoding gradients in the MRE sequence. The frequency of shear wave applied ranges from 40 to 400 Hz. In liver, the frequency of shear waves used for clinical liver MRE is 60 Hz. A lower frequency is used for organs that are situated deep in the body and a higher frequency may be used for regions of interest that may be closer to the body surface. A lower frequency wave has deeper penetration and spatial lower resolution. A higher frequency wave has higher attenuation and higher spatial frequency. Once decided on the resolution and frequency, these parameters must stay consistent for the duration of the study and must not be changed. Stiffness values measured with one particular frequency are not convertible with those measured with a different frequency. An inversion algorithm automatically produces stiffness maps using the phase shift information. Shear stiffness values can be obtained by drawing regions of interest over the tissue of interest in the stiffness maps and expressed in kiloPascals (kPa).

2.1 Animals

The experimental protocols in this section are tailored for rats (Wistar, Sprague-Dawley or Lewis) with a body mass of 250–350 g. Advice for adaptation to other smaller animals (e.g., mice) or larger animals (e.g., pigs) are given in the sections where necessary.

2.2 Lab Equipment

1. Anesthesia: For nonrecovery experiments urethane solution (Sigma-Aldrich, Steinheim, Germany; 20% in distilled water) can provide anesthesia for several hours with comparatively few side effects on renal physiology, which is an important issue. For an in-depth description and discussion of anesthesia please refer to the chapter by Kaucsar T et al. "Preparation and Monitoring of Small Animals in Renal MRI."
2. Gases: O_2, N_2, and compressed air, as well as a gas-mixing system (FMI Föhr Medical Instruments GmbH, Seeheim-Ober Beerbach, Germany) to achieve required changes in the

oxygen fraction of inspired gas mixture (FiO_2). Besides air, the following gas mixtures are required during the experiment: 10% O_2–90% N_2 for hypoxia and 100% O_2 for hyperoxia.

3. Device for FiO_2 monitoring in gas mixtures: for example Capnomac AGM-103 (Datex GE, Chalfont St Gils, UK).

2.3 MRI Hardware

The general hardware requirements for renal 1H MRI on mice and rats are described in the chapter by Ramos Delgado P et al. "Hardware Considerations for Preclinical Magnetic Resonance of the Kidney." The technique described in this chapter is tailored for a standard 1.5 T or a 3.0 T MR scanner using a head coil or small flex coil (for signal reception) or knee RF coil (transmit–receive) is given where necessary but advice for adaptation to other field strengths and systems (e.g., 9.4 T MR system Biospec 94/20, Bruker Biospin, Ettlingen, Germany). No special or additional hardware is required, except for the following:

1. A physiological monitoring system that can track the respiration, and which is connected to the MR system such that it can be used to trigger the image acquisition.
2. MRE hardware to generate shear waves in the abdomen, details explained in the following section. The experimental protocols are tailored for using a FDA approved and commercially available subwoofer-based system for generating shear waves (Resoundant, MN, USA). Advice for options on using other in-house custom-made MR conditional hardware is included where necessary.

2.3.1 Generating Propagating Shear Waves in the Abdomen: Hardware

MRE has received considerable attention due to the flexibility of MR in acquiring arbitrary 2D images and 3D volumes and its capability to measure motion in all three directions. Though the application of excitation to the tissue of interest could be either internal or external, and either static or dynamic, MRE typically uses dynamic vibrations of a single frequency (within the audio frequency range) induced by external drivers. The electrical signal for these drivers is created signal generator synchronized with MRI pulse sequence triggered and is amplified by an audio amplifier before being fed into the mechanical driver. The mechanical vibrations applied to tissue fall into three categories: transient, quasi-static, or harmonic. It is now well known that the MRE-measured shear modulus of soft tissue is dependent on the frequency of applied mechanical waves. That is why the term "shear stiffness" is often used to describe the shear modulus at a specific frequency. However, it should be fully understood that the formula that calculates the shear modulus from the measured velocity of the waves ($\mu = \rho c^2$, where μ = shear modulus, ρ = density of tissue, and c = wave speed) is valid only in purely elastic tissues. MRE

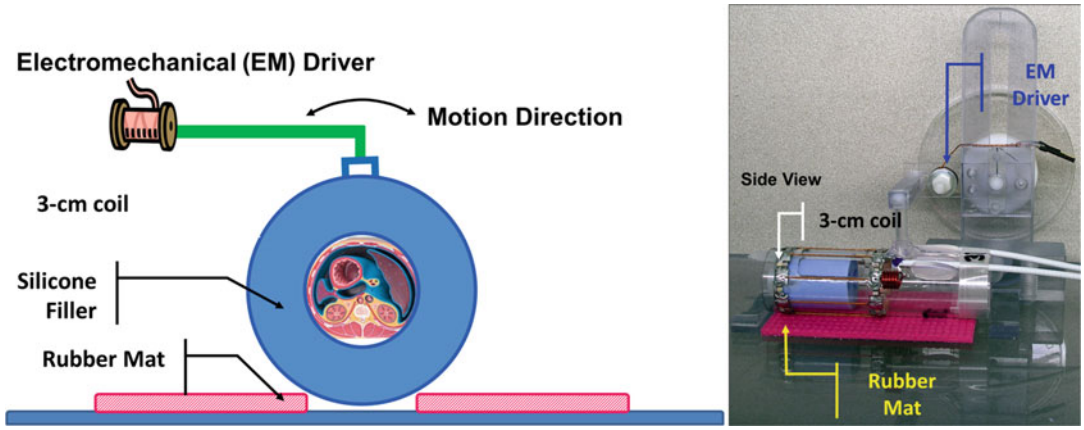

Fig. 1 For smaller animals, an electromechanical driver setup may be used for shear wave generation. Rotational vibrations generated by the electromechanical driver are transmitted into the entire body of the animal. The transmitted shear wave frequency range can be set between 50 and 400 Hz

typically uses harmonic vibrations generated by an external driver device to perturb the tissue. In harmonic excitation, a low-frequency acoustic wave (20–400 Hz) is transmitted within the tissue using a sinusoidal mechanical source. When performing MR elastography, the goal is to acquire tissue stiffness maps for each imaging slice, with a large area of the tissue of interest not covered by the 95% confidence map so that a large portion of the tissue can be measured. The confidence maps are calculated during the stiffness inversion, as the fit of a smooth polynomial to the phase images. In a typical MR elastography configuration, to create a sinusoidal mechanical motion, an active pneumatic wave driver, which is a subwoofer, is located outside the MR scanner room and is connected, by way of a flexible plastic (polyvinyl chloride) tube, to a passive driver that is fastened onto the abdominal wall or the organ or interest. For the most part, three kinds of active driver mechanical driving mechanisms have been used in the literature. They are electromechanical drivers, piezoelectric drivers, and acoustic speaker-based driver systems [20–22]. Electromechanical drivers were one of the initially developed driver systems (Fig. 1). They use the Lorentz force between the induced magnetic moment created by voice coils, and the static magnetic field of the main MRI magnet to create the motion [20]. Piezoelectric and needle-based drivers have commonly been used in preclinical or MRE of tissues [12, 21]. This is primarily because of the advantages of the ease of positioning of the driver in comparison to the electromechanical drivers and the avoidance of an additional magnetic field, leading to a reduction of artifacts [22]. Also, these drivers can create more reliable waveforms with less ringing effects, which becomes especially useful in situations where a single transient wave needs to be induced in the tissue or sample of interest. Acoustic speaker-based

driver systems are commercially available and are commonly used for clinical MRE scans. The vibrations in the acoustic systems are again produced by the Lorentz force, but the static magnetic field is from a devoted permanent magnet present in an acoustic speaker. These speakers, with their own permanent magnets, that are much weaker than the static field B_0 of the MR system, are designed such that they are placed away from the main magnet. Thus, this system necessitates an additional component to couple the vibrations produced by the speakers to the tissue of interest. The active driver is coupled to a passive driver that is positioned on the abdominal organ of interest. The passive driver transfers a continuous acoustic vibration that is transmitted through the entire abdomen, at a fixed low frequency, which is typically 60 Hz for the liver. Choice of frequency is a balance between wave penetration and desired spatial resolution. A higher frequency improves spatial resolution while a low frequency improves wave penetration. The advantage of this system is that the passive drivers can be developed according to the application in different organs and can thus be used to effectively propagate shear waves within the desired organ of interest with comfort to the patient. For preclinical images in small animals such as mice or rats, a frequency of up to 400 Hz may be used to get the desired spatial resolution. A modified phase-contrast based pulse sequence with motion encoding gradient pairs synchronized to oscillate at the same frequency of mechanical waves created by the passive driver are used to encode the motion of the tissues in the phase of an MR image. This sequence is then used to image the micron-level cyclic displacements caused by the propagating shear waves to create a magnitude image, which provides anatomic information, and a phase image, which provides wave motion information. The phase or "wave" images, containing wave-propagation information, are then inverted to calculate quantitative stiffness maps (elastograms).

2.3.2 Pulse Sequence for MRE Motion Encoding: Software

The two main pulse sequence groups in MRI are spin echo (SE) and gradient recalled echo (GRE). In the early 1980s, the SE sequence was the main magnetic resonance sequence in clinical imaging [23]. Later, the GRE sequence proposed by Mansfield and Maudsley became an essential technique and a good alternative to SE sequences [24]. The two types of acquisition sequences currently in use to obtain abdomen organ stiffness values are the GRE based and the SE based with echo-planar readout; both of which have been shown to have excellent correlation on both 1.5 and 3.0 T MRI scanners [13, 25, 26]. The use of GRE-based sequence has demonstrated to correlate with histological grading of liver fibrosis in previous studies and a recent meta-analysis [10, 13]. However, the inherent limitations of GRE-based acquisition on field strengths of 3.0 T or higher in addition to enhanced sensitivity to

susceptibility, is the signal drop off due to longer echo time (TE) and relatively shorter T2 relaxation time of the liver. GRE-based MRE also has relatively lower accuracy in obese patients due to the increased distance from the driver to the liver. Thicker layers of fat can result in signal loss and produce limitations for encoding shear waves in the deeper areas of the liver, hence reducing the resulting stiffness measurable area [25]. Since chronic liver disease is quite frequently associated with obesity, radiologists should be aware of the limitations of GRE-based acquisition in such cases. GRE-based MRE acquisition also require relatively longer periods of acquisition and have higher susceptibility to breathing motion. Clinically, the current GRE-based protocol, for MRE image acquisition requires a breath-hold of approximately 20 s for a single slice. Echo-planar imaging (EPI), on the other hand, is a fast magnetic resonance imaging technique that obtains all spatial-encoding information in a single radiofrequency (RF) pulse, allowing for faster acquisition times with less motion artifacts. SE-EPI MRE has several advantages over the GRE MRE sequence: (1) It allows for acquisition of multiple slices in a single breath-hold covering entire kidney as compared to GRE MRE, which allowed for acquisition of only a single slice per breath-hold; (2) Entire 3D acquisition with three motion encoding directions can be performed in three breath-holds, which enables completion of the study in patients who cannot perform more than three breath-holds and cannot lay flat for longer period of time in the scanner; (3) SE-EPI MRE can avoid problems such as data misregistration caused due to multiple breath-holds when acquiring multiple slices compared to GRE MRE. SE-EPI-based images are also advantageous because it enables measuring larger areas of the organ due to higher waves encoded per relaxation time (TR). Despite these advantages, use of SE-EPI MRE sequence has a few limitations such as it is prone to the distortion artifacts arising from the eddy currents caused by gradients switching on and off rapidly. These distortions may cause increase in the apparent wavelength of the waves propagating through the kidneys thereby causing an increase in the stiffness estimations. Care must be taken to correct for the distortions when observed. Additionally, SE-EPI MRE is also very sensitive to chemical shift and ghosting artifacts. Appropriate steps need to be taken during acquisition by application of spatial spectral frequency pulses and phase correction to correct for these artifacts, respectively for accurate estimate of MRE-derived stiffness values.

The tissue response to the applied harmonic excitation is represented in terms of waves propagating within the tissue. After the mechanical excitation, the phase-contrast based pulse sequence is used to encode the shear wave motion into the MR phase signal by using a series of magnetic field gradients called MEG. The MEG is typically applied after RF excitation pulses and before signal

2.4 Image Postprocessing: Generating Elastograms for Stiffness Estimation

acquisition. From the acquired wave images, inverse reconstruction algorithms are applied to convert the displacement data to mechanical properties [27]. The mechanical quantity that MRE characterizes typically is shear modulus (μ), which describes the proportionality relationship between the shear stress and strain. In MRE excitation is primarily shear and the displacements in MRE are very small (~microns). Therefore, it is a good approximation to model tissue as a linear, viscoelastic solid. It can be assumed that there is no volume change as layers of material move in shear, perpendicular to the direction of the wave propagation. The shear stiffness, μ, can be calculated if the wavelength, λ, is measured, as the frequency is known and the density of most soft tissues is close to the density of water (1000 kg/m^3). Assuming an isotropic material, this reduces to two independent quantities, the Lame constants λ and μ related to longitudinal and shear deformation respectively. If local homogeneity is assumed, λ and μ become single unknowns, and the equation for harmonic motion becomes an algebraic matrix equation that can be solved locally: $\mu\nabla 2u + (\lambda + \mu)\nabla(\nabla \cdot u) = -\rho\omega 2u$ [28], with ρ the density, ω the angular frequency of the mechanical oscillation, and u the displacement vector. Approaches such as local frequency estimation (LFE), phase gradient (PG), and direct inversion (DI) have been used to estimate the localized wavelength [28, 29]. The algorithms assume that the waves are propagating in a uniform, infinite, homogeneous medium. The LFE algorithm can estimate the spatial frequency of the propagating shear waves. LFE is a robust method for estimating isotropic tissue stiffness even in the presence of noise when compared to other methods, as it is performed in the k-space domain. However, it suffers from edge effects where the estimates values at the sharp boundaries can be inaccurate. Hence, if LFE is used, the ROIs on the elastograms must be drawn away from the edges. DI is another inversion algorithm where lower order polynomials are fit to the displacement field data to obtain its Laplacian; and solving the Helmholtz wave equation by plugging the Laplacian generates the stiffness map. However, DI is also sensitive to noise because of the Laplacian operator.

2.5 Periodic Quality Assurance (QA)

Recommended QA: Measurements of organ stiffness (magnitude of the complex shear modulus) obtained with MRE depend on the spatial fidelity of the acquired phase images. Therefore, the validity of the field of view and image linearity should be assessed and confirmed on an ongoing basis, as is already routine for all clinical scanners, using manufacturer-recommended procedures.

While other instrumental causes of drift in stiffness measurements have not been documented in the literature, technical failures such as faulty synchronization of the driver system or incorrect driver frequency settings can cause incorrect measurement.

Performing and documenting a routine QA process also helps in preparation of local institutional research guidelines.

Optional QA: Correct user setup and proper functioning of the MRE system can be confirmed using a phantom with known stiffness properties. These usually consist of a uniform, tissue-simulating material with known stiffness and known stability over time and storage conditions. An MRE phantom can be used to confirm proper functioning of the MRE system after initial installation and as a periodic test of correct functioning. There is as yet no consensus on recommendations for the frequency of phantom testing. Optional QA testing with a phantom should employ a protocol recommended by the phantom manufacturer.

3 Methods

3.1 Animal Setup on the Scanner

1. As described in Subheading 2, in a typical preclinical MRE study, animals are anesthetized by intraperitoneal injections of ketamine hydrochloride (50 mg/kg) and xylazine hydrochloride (5 mg/kg).
2. After shaving and preparation of the abdomen, animals are placed and fixed on a plastic table in the supine position. It is important to position the animal as close to the isocenter as possible to avoid any B_0 or B_1 inhomogeneity artifacts.
3. Start the temperature monitoring system, apply some surgical lubricant to the temperature probe and place it in the rectum of the animal.
4. Attach the respiration sensor to the upper abdomen of the animal using adhesive tape. Start and setup the respiratory monitoring system. If necessary, adjust the position of the respiration sensor until the amplitude of the respiration trace is sufficiently large for the system to reliably detect the trigger points at the beginning of expiration.
5. A silver needle (disposable silver acupuncture needles, Asahi Medical Instrument Co., Kawaguchi, Saitama, Japan) can be used in lieu of a passive driver and gently inserted gently into the target tissue through the anterior body wall (Figs. 2 and 3). The other end of the needle is attached to an electromechanical driver that generated longitudinally orientated sinusoidal vibrations at low frequency.

3.2 Scanner Adjustments and Anatomical Imaging

1. MR image acquisitions may be performed with a standard 1.5 T or a 3.0 T whole body MRI scanner using a receiving surface coil.
2. Acquire a fast pilot scan to obtain images in the three orthogonal planes *x*, *y*, and *z*.

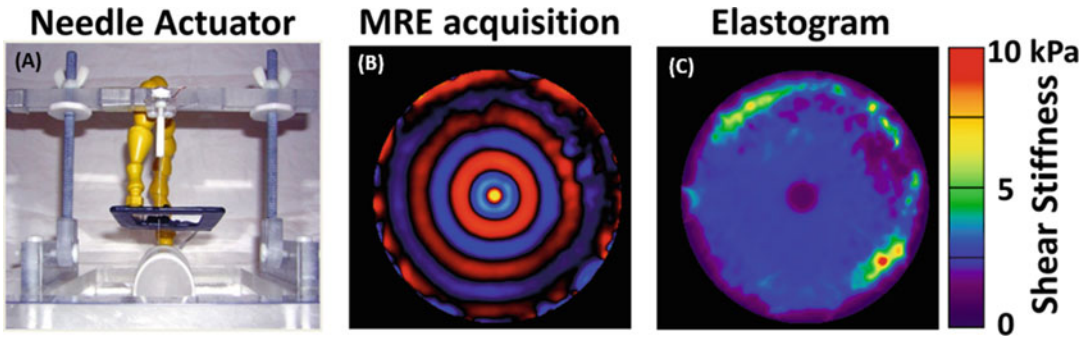

Fig. 2 (**a**) Drawing illustrates a typical experimental setup of a mouse or rat MR elastography configuration. A passive driver, a needle, is used to generate circular shear wave fields. A plastic connecting tube connects the passive driver to the active driver, which is located behind a wall outside the imaging room. This setup is relatively easy to apply for preclinical imaging. The active driver used may be a standard commercially available equipment. (**b**) Images acquired during a MRE phantom scan. Magnitude and phase images yield raw data: The magnitude images provide anatomic information, and the phase images provide wave motion information. After postprocessing, color wave images and (**c**) stiffness maps, also known as elastograms, are generated

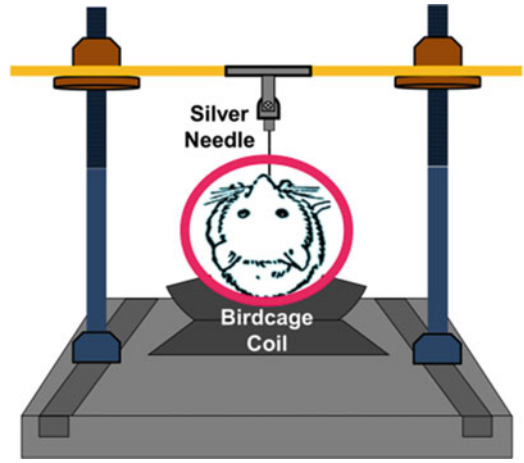

Fig. 3 A typical experimental setup for a mouse MRE study. A silver needle is used to generate circular shear wave field in the mouse liver in vivo

3. Acquire anatomical images in several oblique orientations to facilitate planning a coronal slice orientation with regards to the long axis of the kidney, as described in the chapter by Pohlmann A et al. "Essential Practical Steps for MRI of the Kidney in Experimental Research."
4. Perform localized shimming on the kidney as described in the chapter by Pohlmann A et al. "Essential Practical Steps for MRI of the Kidney in Experimental Research" (*see* **Note 16**).

Table 1
Recommended 2D MRE protocol parameters

Parameter	2D GRE MRE	2D SE-EPI MRE
TR (ms)	50	1000
TE (ms)	23.7	30
Matrix size	128 × 64 interpolated to 128 × 128	100 × 100 (true)
Voxel size (mm)	1.2 × 1.2	1.5 × 1.5
Slice thickness (mm)	6	6
Bandwidth (Hz/Px)	399	2380
No. of averages	1	1
No. of slices	4	4
MEG frequency (Hz)	60	60
MEG direction	*Z* axis (slice)	*Z* axis (slice)
Echo spacing (ms)	24.7	0.5
EPI factor	NA	100
Acceleration factor	2	2
Scan time (min: s)	1:00	0:11

3.3 MRE Imaging

1. A gradient echo (GRE) MRE sequence may be used for wave image acquisition with the following parameters: matrix size of 256 × 64, TR/TE of 33.3 ms/17.8 ms, flip angle of 30°, slice thickness of 5 mm, field of view of 10 cm × 10 cm, one pair of 1.76 G/cm trapezoidal motion-encoding gradients (MEG) at 120 Hz (8.33 ms duration). The repetition time is typically set as an integer multiple of the mechanical wave period to allow for continuous shear wave motion during the scan via the customary synchronized trigger pulses. Details of protocol parameters for relevant acquisition sequence choices are provided in Tables 1, 2 and 3.
2. It should be noted that the trigger pulses are moved during the scan to obtain images at four different phase offsets between the motion and the MEG, equally spaced over one cycle of the motion.
3. Perpendicular to the driving needle, several sequential imaging planes containing tissue of interest should be chosen for MRE wave data collection. The number of slices to be acquired depends on the size of the organ of interest, but is typically 2–4.
4. The MEG should be set to sensitize the shear motion along the through-plane direction (i.e., the anterior–posterior or slice-select direction for these coronal images). Typically, respiratory

Table 2
Recommended imaging protocol for propagating shear waves in the abdomen (small animal 3D MRE protocol parameters)

Parameter	3D MRE
Pulse sequence type	2D SE-EPI
Matrix	128 × 128
No. of averages	1–16
No. of EPI shots	1
TR (ms)	1000
TE (ms)	Minimum
No. of slices	12–20
Slice thickness (mm)	1
Gap (mm)	0, Interleave
No. of phases	3–4
MEG frequency (Hz)	200–400
MEG direction	*X*, *Y*, and *Z* axes
MEG Power per axis	25 G/cm
Field of view (cm)	3–4

If available on the scanner, it is strongly recommended to use 3D MRE protocol parameters
GRE gradient recalled echo, *SE-EPI* spin-echo echo-planar imaging, *2D* two dimensional, *MRE* magnetic resonance elastography, *MEG* motion encoding gradients, *msec* milliseconds, *mm* millimeters, *Hz* hertz, *mT/m* milliTesla/meter, *Px* pixel, *min* minutes, *s* seconds, *NA* not applicable

or cardiac gating is not needed for lower abdomen organs such as liver and kidneys but this may be added if significant motion is observed. With a fixed needle inserted into the liver tissue, anaesthetized animals only performed shallow and fast upper-chest breathing instead of deep and slow diaphragm breathing. Therefore, the tissue do not move much during respiration. In addition, the phase-encoding direction is chosen to be right-left (frequency-encoding direction superior-inferior), which prevents possible motion artifacts from the chest wall and the heart from corrupting the tissue signal. In preclinical setting, motion artifacts can also be minimized by using multiple averages. As a reference for mice MRE imaging, preclinical MRE studies on ten ARPKD mice, with ages ranging from 3 to 12 months were used in the study by Yin et al. [3].

An accurate and reproducible stiffness measurement of the kidney, given its small size, and deeply seated location, requires

Table 3
Recommended 3D MRE imaging protocol parameters for clinical renal imaging

Parameter	3D MRE
Pulse sequence type	2D SE-EPI
Matrix	96 × 96
No. of averages	1
No. of EPI shots	1
TR (ms)	2400
TE (ms)	Minimum
No. of slices	42
Slice thickness (mm)	3.6
Gap (mm)	0, Interleave
No. of phases	3
MEG frequency (Hz)	120
Wave frequency (Hz)	60/90
MEG direction	*X*, *Y*, and *Z* axes
No. of breath-holds	6
Acceleration factor	3
Driver amplitude range	30–50%

3D analysis of wave field data. For this reason, if available on the scanner, 3D MRE is recommended to be utilized for renal imaging. In 3D MRE, the propagating shear waves are imaged with a 2D multislice spin-echo echo-planar imaging (SE-EPI) pulse sequence modified to include the motion encoding gradients (MEG) in the *X*, *Y*, and *Z* directions. MEGs can be applied in one or more directions to encode the motion in those specific directions. This is different from the 2D MRE typically utilized for commercial MRE imaging in which motion is encoded only in a single direction.

A typical small animal preclinical 3D MRE protocol is shown in Table 2.

Figures 4, 5, and 6 show cross sectional spin echo anatomical images of the animal abdomen, more specifically of the mouse liver region and its respective wave displacement images along the *x*, *y*, and *z* directions and the absolute values of the complex shear modulus.

In 3D MRE, the propagating shear waves are imaged with a 2D multislice spin-echo echo-planar imaging (SE-EPI) pulse sequence

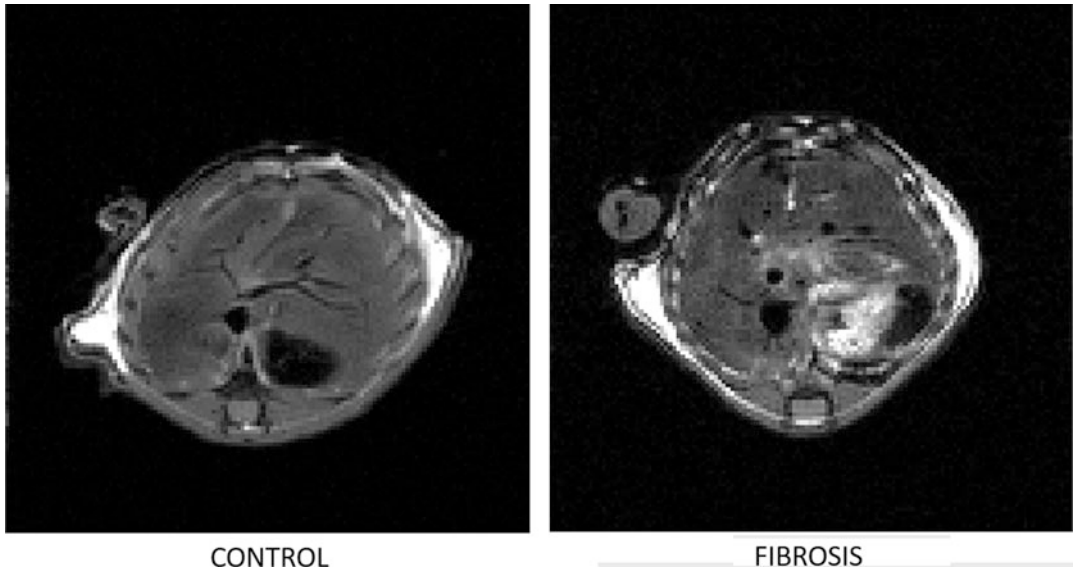

Fig. 4 Cross-sectional spin-echo anatomical images of the mouse abdomen, more specifically of the liver region (Image courtesy of Dr. S. Majumdar and Dr. D. Klatt from the Motion-encoding MRI Lab at the University of Illinois at Chicago, Chicago, Illinois, USA)

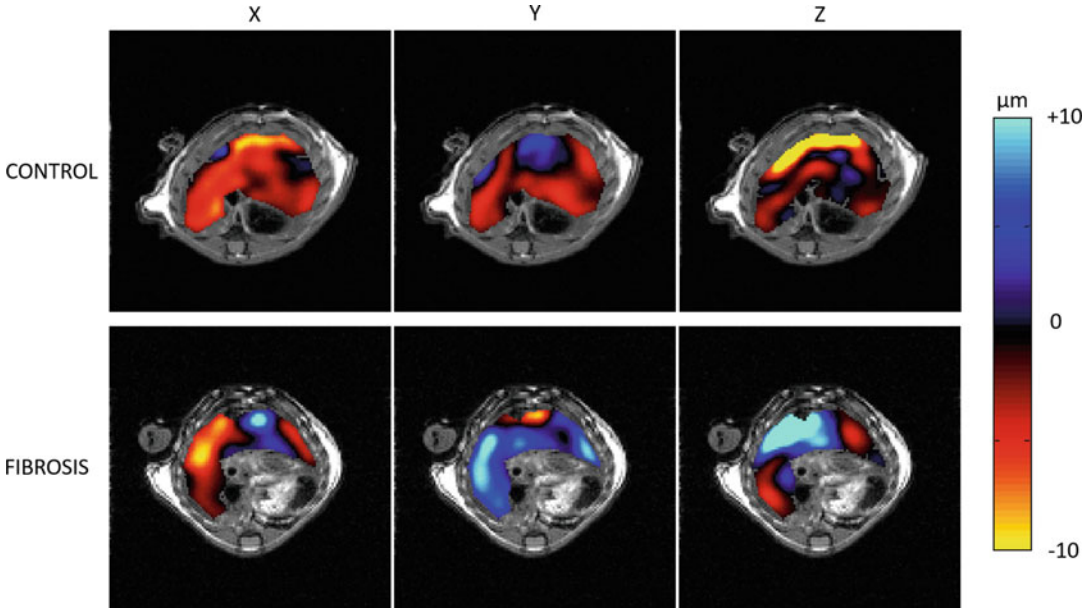

Fig. 5 Wave-displacement images along the *x*, *y*, and *z* directions (Image courtesy of Dr. S. Majumdar and Dr. D. Klatt from the Motion-encoding MRI Lab at the University of Illinois at Chicago, Chicago, Illinois, USA)

modified to include the motion encoding gradients (MEG) in the X, Y, and Z directions. Since kidney is a viscoelastic material, the stiffness varies with excitation frequency (i.e., stiffness increases with an increase in frequency). Once decided, it is important to keep the MEG frequency consistent for the duration of the study.

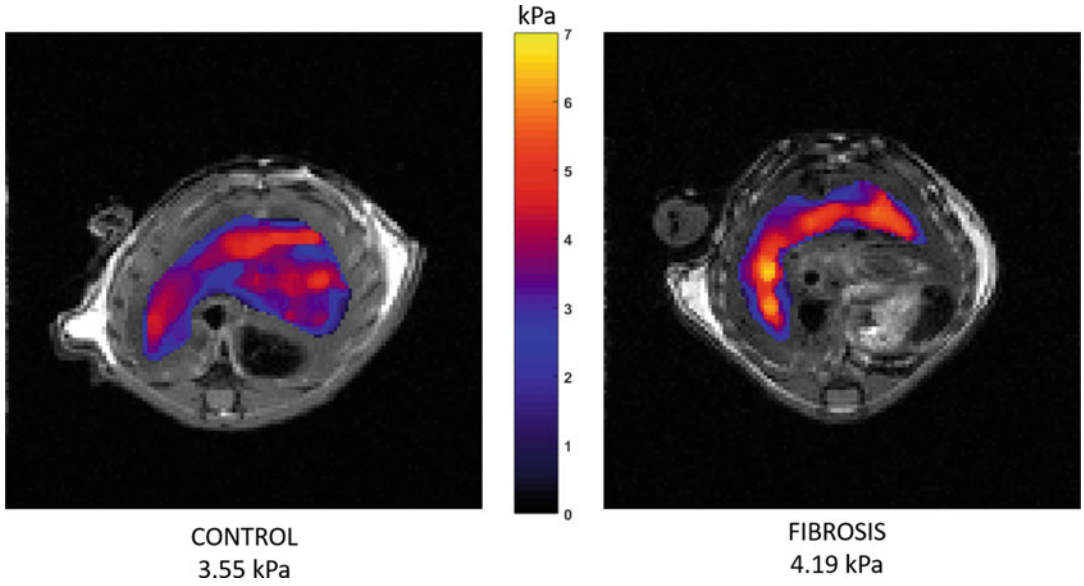

Fig. 6 |G*| or the absolute value of the complex shear modulus (Image courtesy of Dr. S. Majumdar and Dr. D. Klatt from the Motion-encoding MRI Lab at the University of Illinois at Chicago, Chicago, Illinois, USA)

At a frequency of 60 Hz, the average kidney stiffness range of 3.5–5 kPa has been reported on normals in the literature by multiple groups [30, 31]. At a frequency of 90 Hz, a higher kidney stiffness range of 5–7.5 kPa was measured.

3.4 Image Review to Ensure Technical Success

The raw magnitude and phase images obtained from the MRE acquisition should be reviewed on the scanner console at the time of the exam. The magnitude images should show signal loss in the subcutaneous fat just below the passive driver placement, confirming that mechanical waves are being applied. The signal loss is due to the phase images (also known as wave images) should demonstrate shear waves in the specific abdominal organ of interest. In the color phase images, red to blue region is a wavelength and this wavelength becomes longer in the presence of a stiff region for a given excitation frequency. Then these wave images are converted into spatial stiffness maps using an inversion algorithm known as elastograms. If no waves are seen in the tissue of interest, then the driver system should be checked. A phantom scan of known stiffness may be performed if needed to validate driver system. Shear wave images represent an instantaneous snapshot of the mechanical waves propagating through the tissue. After the magnitude and phase images are created, an inversion algorithm is applied to processes these raw data images to create several additional images and maps.

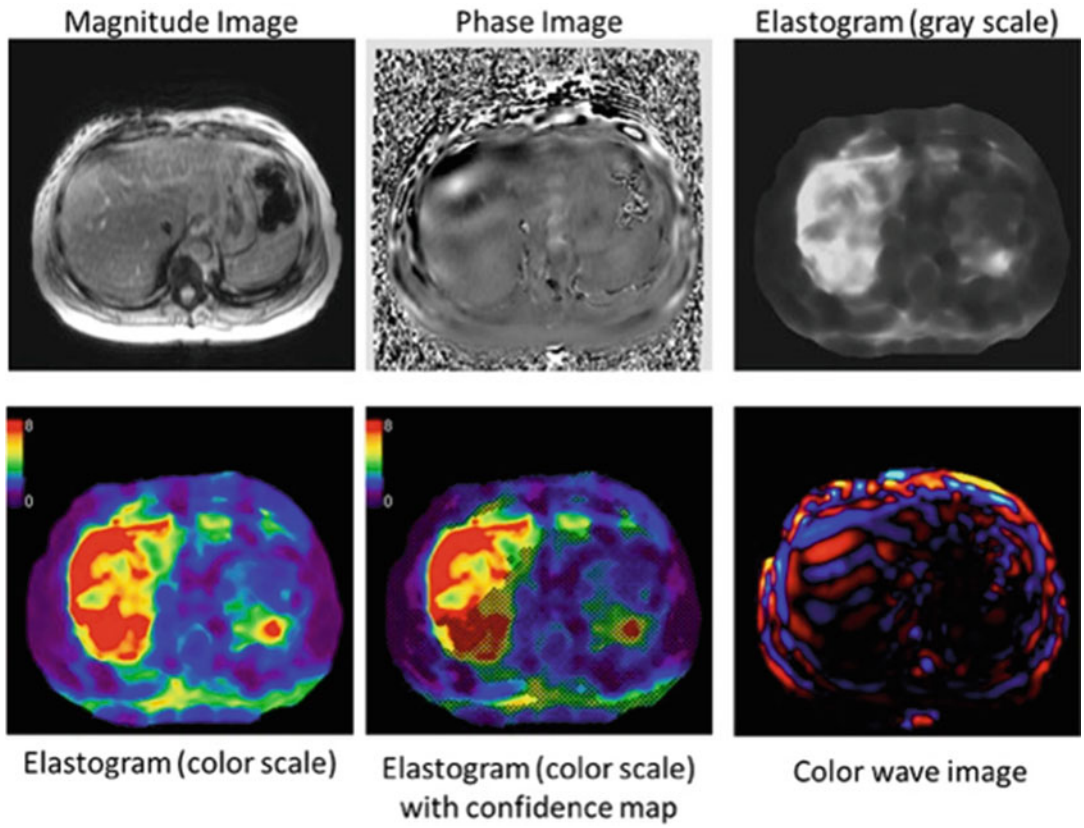

Fig. 7 Representation of typical postprocessed images generated in a clinical liver MRE study. Additional postprocessed images may be generated offline depending on the software version of the pulse sequence installed on the scanner

3.5 Color Display of Images

This section is tailored for images acquired using an FDA approved and commercially available subwoofer-based system for generating shear waves (Resoundant, MN, USA). For images generated using other in-house developed hardware and software, image display should be optimized as recommended by the manufacturer.

For image viewing purposes, the following information should preferably be generated (Fig. 7).

1. Unwrapped wave images clearly depicting the propagation of shear waves through the abdomen. Phase wrapping occurs when the shear wave motion is large. Since MRE is a phase-based technique, the displacement data typically must be unwrapped before subsequent processing is performed.
2. A gray-scale elastogram without a superimposed 95% confidence map.

3. A gray-scale elastogram with a super imposed 95% confidence map. The confidence map displayed is a statistical derivation used to overlay a "checkerboard" on the stiffness map to exclude regions that have less reliable (i.e., noisy and discontinuous) stiffness data so that a high-quality and valid stiffness measurement can be obtained.
4. A color elastogram without a superimposed 95% confidence map. The color elastogram, typically generated in JPEG format is generally used for qualitative stiffness evaluation and visual purposes. However, if the color elastograms are generated in DICOM format, then they can also be used to obtain quantitative measurements.
5. And a color elastogram with a superimposed 95% confidence map.

The gray-scale elastogram, generated and saved in DICOM format is commonly used to obtain quantitative stiffness measurement, in kiloPascals (kPa). The color elastogram used clinically has a stiffness display range of 0–8 kPa. A 0–20 kPa color elastogram display range may also be created and is useful for appreciating tissue stiffness heterogeneity across the larger region. For research purposes, the range may be adjusted as desired.

3.6 Drawing Regions of Interest to Measure Stiffness

Mean shear stiffness of the organ is calculated using manually specified regions of interest (ROIs). Skilled interpretation of the magnitude and wave images is currently required to select a ROI from which the average hepatic stiffness can be calculated from the elastogram. Areas with wave interference and noise, as well as partial volume effects and hepatic blood vessels, can bias the stiffness calculation and need to be avoided when selecting this ROI. The ROIs are drawn manually in the largest possible area of organ parenchyma in which coherent shear waves are visible. To avoid areas of incoherent waves, avoid regions immediately under the paddle and stay ~1 cm inside the organ boundary and contain a minimum of 500 pixels per slice. ROIs should be placed in individual slices. The ROI should also exclude areas of low confidence, as seen by the checkerboard pattern in the masked elastogram images. The procedure needs to be repeated for every slice, with magnitude, phase, and elasticity images all needing to be analyzed. The confidence maps calculated during the stiffness inversion as the fit of a smooth polynomial to the phase images may be helpful in guiding the ROIs across multiple slices. The mean value is calculated from all slices and reported as stiffness in kPa. In practice, the ROIs may be drawn in a single step, keeping these principles in mind. If available, an automated tool capable of deriving ROIs from MRE images and accurately calculating stiffness may be helpful to reduce measurement variability [32, 33].

3.7 Image Interpretation

Overall mean stiffness of organ is reported by recording the mean stiffness value of each ROI and then calculating the mean value, weighted by ROI size.

Example: Slice 1: mean stiffness = 2.42 kPa and ROI size = 2000 mm^2; Slice 2: mean stiffness = 2.55 kPa and ROI size = 1800 mm^2; Slice 3: mean stiffness = 2.92 kPa and ROI size = 800 mm^2; and Slice 4: mean stiffness = 4.22 kPa and ROI size = 1000 mm^2; then the weighted mean = $((2.42 \times 2000) + (2.55 \times 1800) + (2.92 \times 800) + (4.22 \times 1000))/(2000 + 1800 + 800 + 1000) = 2.85$ kPa.

3.8 Role of Preclinical MRE

Since MRE is a relatively new, multistep MR technique, there is room for improvement of efficacy, expansion and exploration. There is evidently a need for preclinical applications of the method, primarily to validate the technique against invasive measures and better understand changes in different diseases. Preclinical work helps to realize some of this potential with the exploration of novel driving and contrast mechanisms to improve the efficiency of MRE and to test and provide clinical capabilities that are otherwise unavailable.

3.9 Application to Renal Disease Models

Acute kidney injury (AKI) is a sudden episode of kidney failure or kidney damage that happens within a few hours or a few days of an insult such as administration of nephrotoxins. AKI is common in patients who are hospitalized, have underlying kidney disease and especially in older adults. Medullary hypoxic injury plays a major role in the pathogenesis of AKI [34], as has been studied by MRE.

A typical hardware setup for pig MRE is shown in Fig. 8**.** In a study by Warner et al., the authors tested the hypothesis that renal blood flow (RBF) is an important determinant of renal stiffness as measured by MRE [35]. In this study, in six anesthetized pigs with renal artery stenosis, MRE studies were performed to determine cortical and medullary elasticity during acute graded decreases in RBF (by 20%, 40%, 60%, 80%, and 100% of baseline) achieved by a vascular occlusion (Figs. 9 and 10). Three sham-operated swine, that served as control pigs, were anesthetized (telazol 5 mg/kg and xylazine 2 mg/kg) and maintained with mechanical ventilation of 1–2% isoflurane in room air. An ear vein catheter was introduced for saline infusions (5 mL/min). MRE studies were performed on a standard clinical 3.0 T MRI system (GE Healthcare, Waukesha, WI) using a standard multichannel phased array coil. After localization, a renal volume series was performed in the axial plane with a T2 weighted fast spin echo sequence using the following parameters: TR/TE = 2000 ms/88 ms; Flip angle = 90; FOV = 35 cm; imaging matrix = 384 × 320 × 40; thickness = 2.5 mm; NEX = 1. The MRE acquisition sequence used was SE-EPI method. Shear waves were induced by two cylindrical passive pneumatic drivers aligned along the posterior body wall. Continuous vibrations at a

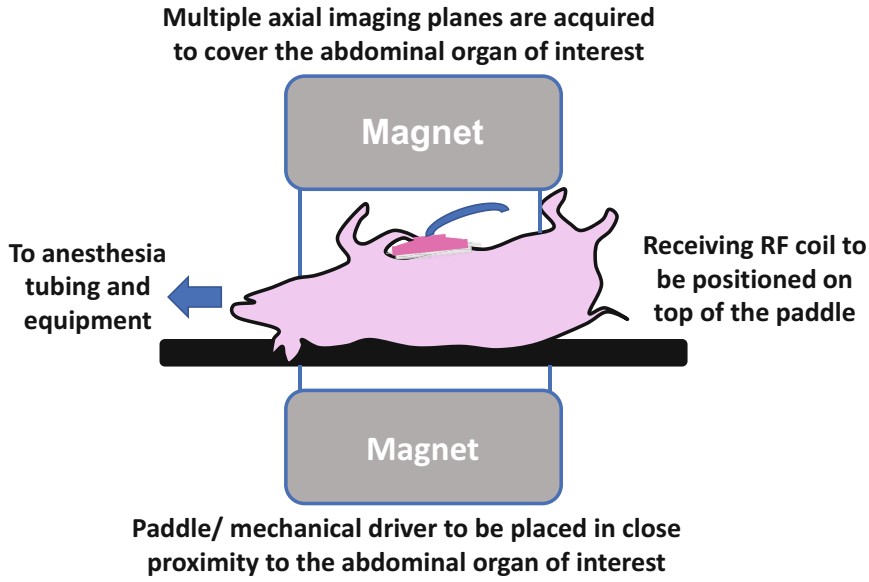

Fig. 8 A typical experimental setup for a pig MRE study

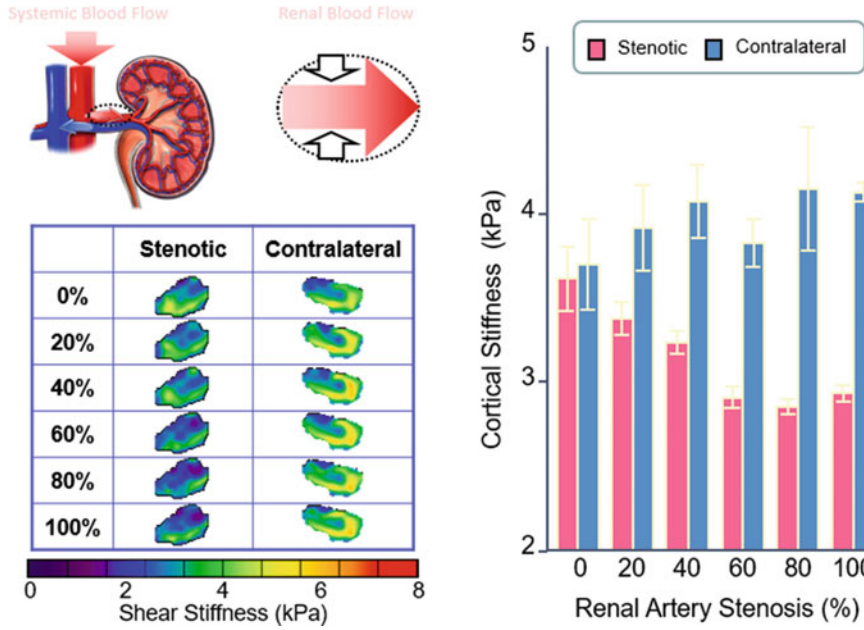

Fig. 9 A representative example from one of the pigs' kidney MRE is shown. The stenosis extent changed gradually from 0% to 100%. Meanwhile, the systemic blood pressure also rose during the acute decrements in renal blood flow from 75 $\pm$ 3 to 96 $\pm$ 3 mmHg. The kidney's elastograms at six different extents of acute stenosis are shown. The chart summarizes the mean kidney stiffness measurements in stenotic and contralateral sides respectively. From the left elastograms and the right chart, the authors observed that the renal cortex stiffness decreased progressively as the degree of stenosis increased. It is another evidence that less perfusion causes reduced stiffness. Conversely, the contralateral kidney slightly increased in the stiffness during the same period. It is caused by increased systemic blood pressure

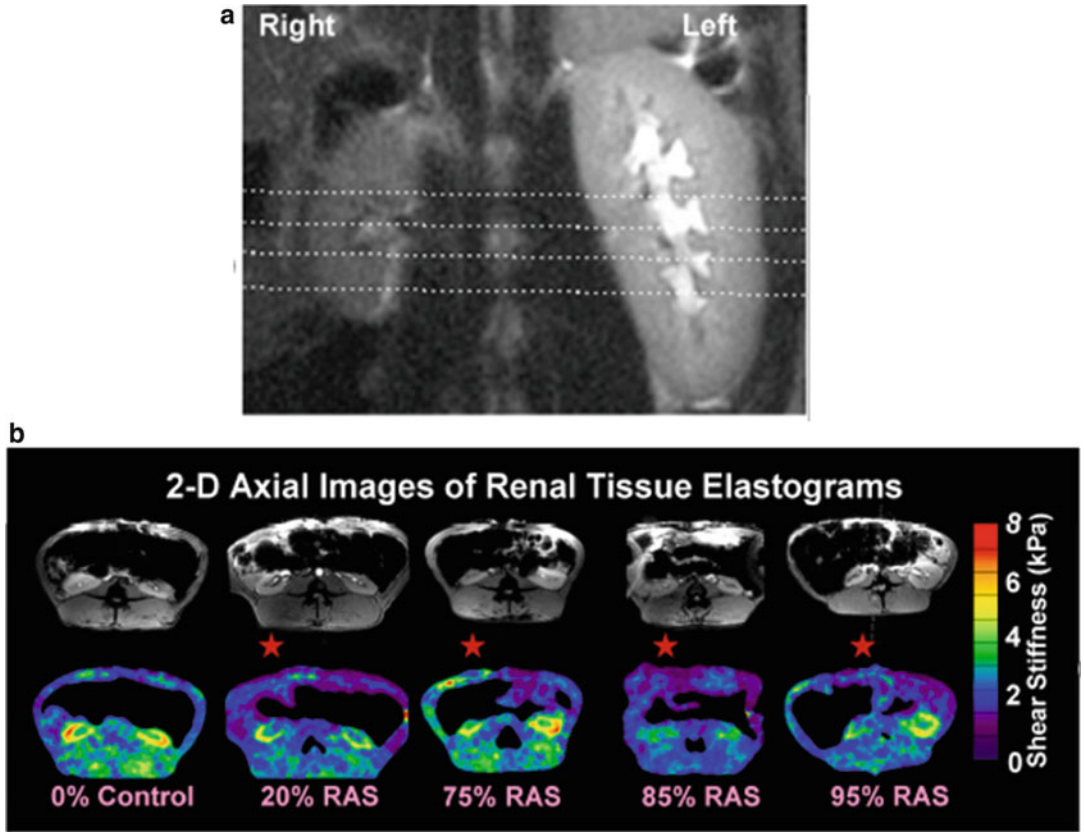

Fig. 10 (**a**) Right (stenotic) and left (contralateral) kidneys in experimental renal artery stenosis. (**b**) 2D axial magnitude and elastograms for normal (control) and variable renal artery stenosis at 10 weeks. The elastogram shear stiffness legend is on the far right. Red stars indicate stenotic kidneys. The images were oriented to show the stenotic kidney on the left

motion encoding gradient (MEG) frequency of 120 Hz generated shear waves throughout the abdominal tissues. MRI parameters used were: TR/TE = 2334 ms/48 ms; FOV = 35 × 35 cm^2; Imaging Matrix = 96 × 96; Slice thickness = 3 mm; NEX = 1; Number of shots = 2; parallel imaging ASSET factor = 2; four phase offsets through one cycle of motion, six pairs of tetrahedral trapezoidal motion encoding gradients in three orthogonal directions with one motion encoding gradient on each side of the refocusing pulse synchronized with motion. The main finding of their study was that acute decreases in renal blood flow with no fibrosis lead to a decrease in renal cortical shear stiffness. Similarly, in chronic renal arterial stenosis the decrease in renal blood flow offsets a likely increase in stiffness secondary to development of renal fibrosis. Decreased renal stiffness may therefore mask the presence of renal fibrosis, but nevertheless stiffness is a marker of renal hypoperfusion.

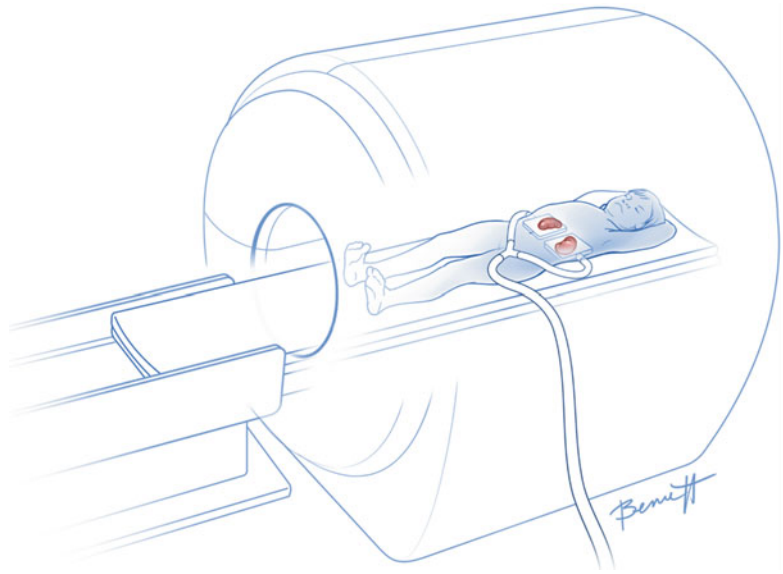

Fig. 11 MRE paddle placement on dorsal side

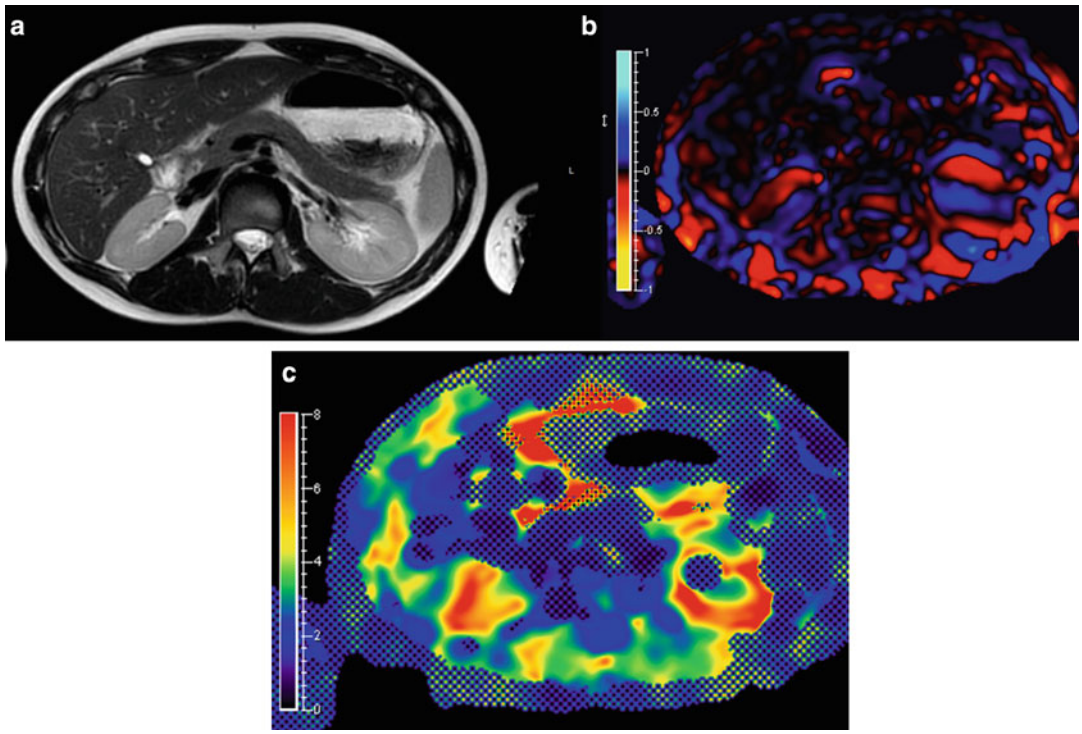

Fig. 12 MRE of the kidneys in a normal 15-year-old male volunteer. (**a**) T2W images in axial plane. (**b**) Wave illumination and (**c**) corresponding stiffness map. Note good illumination of waves in both kidneys (Image courtesy of Dr. Jonathan R. Dillman, Cincinnati, Ohio, USA)

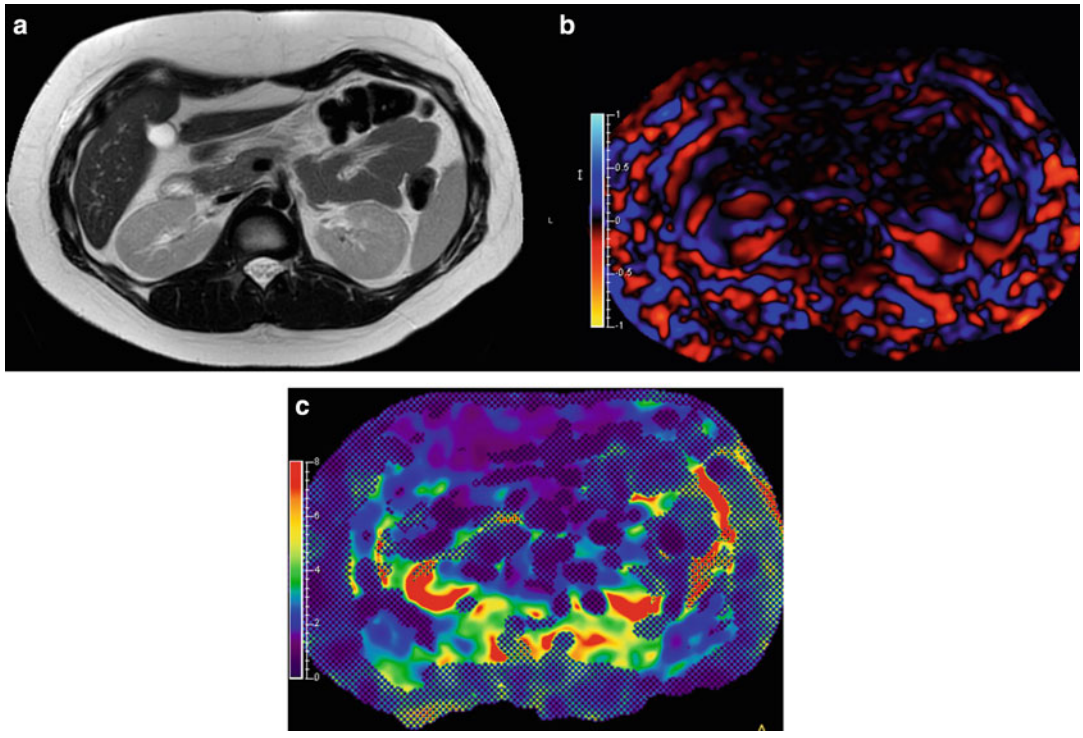

Fig. 13 MRE of the kidneys of a 13-year-old female patient with loss of corticomedullary differentiation; chronic kidney disease. (**a**) T2W images in axial plane. (**b**) Wave illumination and (**c**) corresponding stiffness map (Image courtesy of Dr. Jonathan R. Dillman, Cincinnati, Ohio, USA)

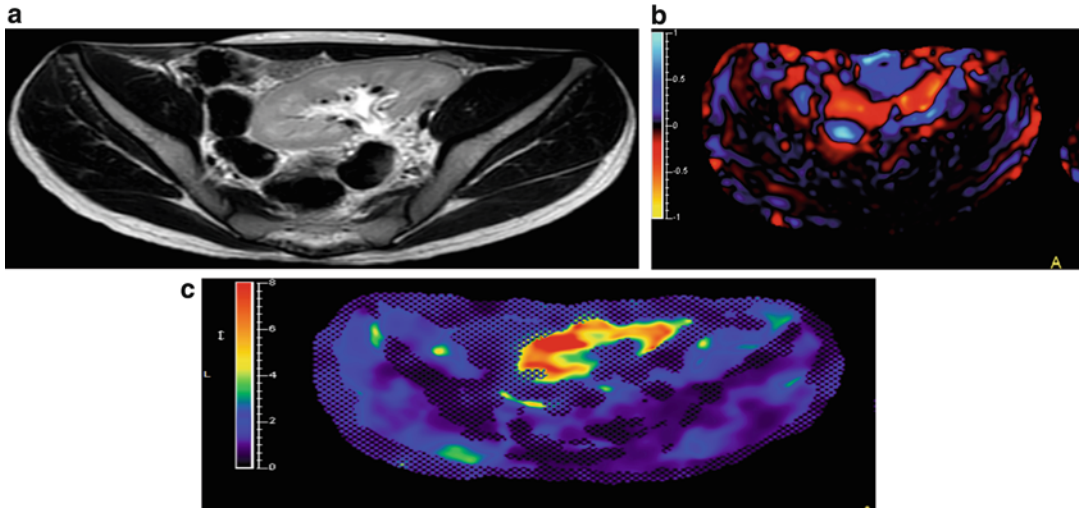

Fig. 14 MRE of the kidneys in a 20-year-old patient with transplant rejection. (**a**) T2W images in axial plane. (**b**) Wave illumination and (**c**) corresponding stiffness map (Image courtesy of Dr. Jonathan R. Dillman, Cincinnati, Ohio, USA)

Renal MRE has also been demonstrated to provide clinical utility in humans. In clinical renal MRE, the paddle is recommended to be placed on the dorsal side with the patient lying in supine position (Fig. 11). Preliminary results show successful transmission of waves by placing the driver in this position (Figs. 12, 13, and 14). In a recent study by Kirpalani et al., the authors examined whether MRE could noninvasively estimate allograft fibrosis and predict progression of allograft dysfunction [36]. In this study, renal MRE was performed on a standard clinical 3.0 T MRI scanner (Skyra, Siemens Healthineers, USA). Patients were positioned head first and supine, and they were imaged with a standard 18-channel torso phased array coil centered over the allograft. The mechanical vibrations required for MRE were supplied by an active pneumatic driver system. MRE acquisitions were performed using a MEG of 60 Hz vibrations and a free-breathing, flow-compensated two-dimensional gradient echo coronal MRE pulse sequence to derive magnitude images and a corresponding stiffness map. The imaging orientation was standardized to the coronal plane, with the frequency encoding direction superior to inferior. Other imaging parameters were as follows: field of view, 32×40 cm^2; acquisition matrix, 128×128 reconstructed to 1.48×1.48 mm^2 in-plane resolution; no parallel imaging; five two-dimensional slices through the allograft, with each slice being 5-mm thick with a 1-mm interslice gap; TR/TE = 50 ms/21 ms. Four time points of the motion and three mutually perpendicular directions of the vector motion were sampled. The acquisition time per scan was reported to be approximately 5 min. This study is based on the hypothesis that fibrosis stiffens organs as soft healthy tissue is replaced by stiff extracellular matrix and suggests the potential of renal MRE as a new noninvasive way to assess whole-allograft fibrosis burden; one that may predict future changes in kidney function.

Renal fibrosis causes an increase in the interstitial extracellular matrix and reduction in the number of tubules, thereby making the kidneys stiffer. Previous studies suggest that renal fibrosis is a distinctive feature of progressive kidney diseases such as chronic kidney disease (CKD), a change that increases the risk of cardiovascular diseases. Therefore, renal fibrosis is an important hallmark for diagnosing CKD. Noninvasive MRE is attractive for clinical use in humans.

Existing imaging technologies have been very successful in the noninvasive assessment of many focal diseases of the kidneys, but they have been somewhat less helpful for evaluating diffuse (medical) renal disease such as glomerulonephritis, and renal biopsy remains the diagnostic tool of choice in many situations. It is now feasible to quantitatively image the shear stiffness of both kidneys with an MRE employing a large, posteriorly located passive acoustic driver. Wave images and the corresponding elastograms can be relatively easily acquired in axial, coronal, and sagittal planes.

Preliminary results provide a basis and motivation for investigating the potential to use MRE as a diagnostic tool for characterizing renal parenchyma in diffuse and focal diseases of the kidneys.

References

1. Muthupillai R, Ehman RL (1996) Magnetic resonance elastography. Nat Med 2 (5):601–603
2. Yin M, Talwalkar JA, Glaser KJ, Manduca A, Grimm RC, Rossman PJ, Fidler JL, Ehman RL (2007) Assessment of hepatic fibrosis with magnetic resonance elastography. Clin Gastroenterol Hepatol 5(10):1207–1213.e1202. https://doi.org/10.1016/j.cgh.2007.06.012
3. Yin M, Woollard J, Wang X, Torres VE, Harris PC, Ward CJ, Glaser KJ, Manduca A, Ehman RL (2007) Quantitative assessment of hepatic fibrosis in an animal model with magnetic resonance elastography. Magn Reson Med 58 (2):346–353. https://doi.org/10.1002/mrm.21286
4. Xanthakos SA, Podberesky DJ, Serai SD, Miles L, King EC, Balistreri WF, Kohli R (2014) Use of magnetic resonance elastography to assess hepatic fibrosis in children with chronic liver disease. J Pediatr 164 (1):186–188. https://doi.org/10.1016/j.jpeds.2013.07.050
5. Klinkhammer BM, Goldschmeding R, Floege J, Boor P (2017) Treatment of renal fibrosis—turning challenges into opportunities. Adv Chronic Kidney Dis 24 (2):117–129. https://doi.org/10.1053/j.ackd.2016.11.002
6. El Nahas M (2005) The global challenge of chronic kidney disease. Kidney Int 68 (6):2918–2929. https://doi.org/10.1111/j.1523-1755.2005.00774.x
7. Venkatesh SK, Ehman RL (2014) Magnetic resonance elastography of liver. Magn Reson Imaging Clin N Am 22(3):433–446. https://doi.org/10.1016/j.mric.2014.05.001
8. Serai SD, Towbin AJ, Podberesky DJ (2012) Pediatric liver MR elastography. Dig Dis Sci 57 (10):2713–2719. https://doi.org/10.1007/s10620-012-2196-2
9. Venkatesh SK, Ehman RL (2015) Magnetic resonance elastography of abdomen. Abdom Imaging 40(4):745–759. https://doi.org/10.1007/s00261-014-0315-6
10. Serai SD, Obuchowski NA, Venkatesh SK, Sirlin CB, Miller FH, Ashton E, Cole PE, Ehman RL (2017) Repeatability of MR elastography of liver: a meta-analysis. Radiology 285 (1):92–100. https://doi.org/10.1148/radiol.2017161398
11. Trout AT, Serai S, Mahley AD, Wang H, Zhang Y, Zhang B, Dillman JR (2016) Liver stiffness measurements with MR elastography: agreement and repeatability across imaging systems, field strengths, and pulse sequences. Radiology 281(3):793–804. https://doi.org/10.1148/radiol.2016160209
12. Othman SF, Curtis ET, Plautz SA, Pannier AK, Butler SD, Xu H (2012) MR elastography monitoring of tissue-engineered constructs. NMR Biomed 25(3):452–463. https://doi.org/10.1002/nbm.1663
13. Serai SD, Dillman JR, Trout AT (2017) Spin-echo echo-planar imaging MR elastography versus gradient-echo MR elastography for assessment of liver stiffness in children and young adults suspected of having liver disease. Radiology 282(3):761–770. https://doi.org/10.1148/radiol.2016160589
14. Schuppan D, Ashfaq-Khan M, Yang AT, Kim YO (2018) Liver fibrosis: direct antifibrotic agents and targeted therapies. Matrix Biol 68-69:435–451. https://doi.org/10.1016/j.matbio.2018.04.006
15. Alukal JJ, Thuluvath PJ (2019) Reversal of NASH fibrosis with pharmacotherapy. Hepatol Int 13(5):534–545. https://doi.org/10.1007/s12072-019-09970-3
16. Ismail MH, Pinzani M (2009) Reversal of liver fibrosis. Saudi J Gastroenterol 15(1):72–79. https://doi.org/10.4103/1319-3767.45072
17. Lee SY, Kim SI, Choi ME (2015) Therapeutic targets for treating fibrotic kidney diseases. Transl Res 165(4):512–530. https://doi.org/10.1016/j.trsl.2014.07.010
18. Tampe D, Zeisberg M (2014) Potential approaches to reverse or repair renal fibrosis. Nat Rev Nephrol 10(4):226–237. https://doi.org/10.1038/nrneph.2014.14
19. Bledsoe G, Shen B, Yao Y, Zhang JJ, Chao L, Chao J (2006) Reversal of renal fibrosis, inflammation, and glomerular hypertrophy by kallikrein gene delivery. Hum Gene Ther 17 (5):545–555. https://doi.org/10.1089/hum.2006.17.545
20. Braun J, Braun K, Sack I (2003) Electromagnetic actuator for generating variably oriented shear waves in MR elastography. Magn Reson

Med 50(1):220–222. https://doi.org/10.1002/mrm.10479

21. Chan QC, Li G, Ehman RL, Grimm RC, Li R, Yang ES (2006) Needle shear wave driver for magnetic resonance elastography. Magn Reson Med 55(5):1175–1179. https://doi.org/10.1002/mrm.20856
22. Tse ZT, Chan YJ, Janssen H, Hamed A, Young I, Lamperth M (2011) Piezoelectric actuator design for MR elastography: implementation and vibration issues. Int J Med Robot Comput Assist Surg 7(3):353–360. https://doi.org/10.1002/rcs.405
23. Mansfield P (1977) Multi-planar image formation using NMR spin echoes. J Phys C Solid State Phys 10(3):L55. https://doi.org/10.1088/0022-3719/10/3/004
24. MAUDSLEY PMAA (1977) Planar spin imaging by NMR. J Magn Reson Imaging 27:101–119
25. Calle-Toro JS, Serai SD, Hartung EA, Goldberg DJ, Bolster BD Jr, Darge K, Anupindi SA (2019) Magnetic resonance elastography SE-EPI vs GRE sequences at 3T in a pediatric population with liver disease. Abdom Radiol. https://doi.org/10.1007/s00261-018-1884-6
26. Gandhi D, Kalra P, Raterman B, Mo X, Dong H, Kolipaka A (2019) Magnetic resonance elastography of kidneys: SE-EPI MRE reproducibility and its comparison to GRE MRE. NMR Biomed 32(11):e4141. https://doi.org/10.1002/nbm.4141
27. Doyley MM (2012) Model-based elastography: a survey of approaches to the inverse elasticity problem. Phys Med Biol 57(3): R35–R73. https://doi.org/10.1088/0031-9155/57/3/r35
28. Oliphant TE, Manduca A, Ehman RL, Greenleaf JF (2001) Complex-valued stiffness reconstruction for magnetic resonance elastography by algebraic inversion of the differential equation. Magn Reson Med 45(2):299–310. https://doi.org/10.1002/1522-2594(200102)45:2<299::aid-mrm1039>3.0.co;2-o
29. Manduca A, Oliphant TE, Dresner MA, Mahowald JL, Kruse SA, Amromin E, Felmlee JP, Greenleaf JF, Ehman RL (2001) Magnetic resonance elastography: non-invasive mapping of tissue elasticity. Med Image Anal 5 (4):237–254. https://doi.org/10.1016/s1361-8415(00)00039-6
30. Low G, Owen NE, Joubert I, Patterson AJ, Graves MJ, Glaser KJ, Alexander GJ, Lomas DJ (2015) Reliability of magnetic resonance elastography using multislice two-dimensional spin-echo echo-planar imaging (SE-EPI) and three-dimensional inversion reconstruction for assessing renal stiffness. J Magn Reson Imaging 42(3):844–850. https://doi.org/10.1002/jmri.24826
31. Gandhi D, Kalra P, Raterman B, Mo X, Dong H, Kolipaka A (2019) Magnetic resonance elastography-derived stiffness of the kidneys and its correlation with water perfusion. NMR Biomed 33(4):e4237. https://doi.org/10.1002/nbm.4237
32. Dzyubak B, Venkatesh SK, Glaser K, Yin M, Talwalkar J, Chen J, Manduca A, Ehman RL (2013) Stable automated segmentation of liver MR elastography images for clinical stiffness measurement. Proceedings of SPIE—the international society for optical engineering 8672. https://doi.org/10.1117/12.2006943
33. Dzyubak B, Venkatesh SK, Manduca A, Glaser KJ, Ehman RL (2016) Automated liver elasticity calculation for MR elastography. J Magn Reson Imaging 43(5):1055–1063. https://doi.org/10.1002/jmri.25072
34. Hultstrom M, Becirovic-Agic M, Jonsson S (2018) Comparison of acute kidney injury of different etiology reveals in-common mechanisms of tissue damage. Physiol Genomics 50 (3):127–141. https://doi.org/10.1152/physiolgenomics.00037.2017
35. Warner L, Yin M, Glaser KJ, Woollard JA, Carrascal CA, Korsmo MJ, Crane JA, Ehman RL, Lerman LO (2011) Noninvasive in vivo assessment of renal tissue elasticity during graded renal ischemia using MR elastography. Investig Radiol 46(8):509–514. https://doi.org/10.1097/RLI.0b013e3182183a95
36. Kirpalani A, Hashim E, Leung G, Kim JK, Krizova A, Jothy S, Deeb M, Jiang NN, Glick L, Mnatzakanian G, Yuen DA (2017) Magnetic resonance elastography to assess fibrosis in kidney allografts. Clin J Am Soc Nephrol 12(10):1671–1679. https://doi.org/10.2215/cjn.01830217

Part V

Protocols for Advanced Analyses

Chapter 33

Subsegmentation of the Kidney in Experimental MR Images Using Morphology-Based Regions-of-Interest or Multiple-Layer Concentric Objects

Leili Riazy, Bastien Milani, João S. Periquito, Kathleen Cantow, Thoralf Niendorf, Menno Pruijm, Erdmann Seeliger, and Andreas Pohlmann

Abstract

Functional renal MRI promises access to a wide range of physiologically relevant parameters such as blood oxygenation, perfusion, tissue microstructure, pH, and sodium concentration. For quantitative comparison of results, representative values must be extracted from the parametric maps obtained with these different MRI techniques. To improve reproducibility of results this should be done based on regions-of-interest (ROIs) that are clearly and objectively defined.

Semiautomated subsegmentation of the kidney in magnetic resonance images represents a simple but very valuable approach for the quantitative analysis of imaging parameters in multiple ROIs that are associated with specific anatomic locations. Thereby, it facilitates comparing MR parameters between different kidney regions, as well as tracking changes over time.

Here we provide detailed step-by-step instructions for two recently developed subsegmentation techniques that are suitable for kidneys of small rodents: i) the placement of ROIs in cortex, outer and the inner medulla based on typical kidney morphology and ii) the division of the kidney into concentrically oriented layers.

This chapter is based upon work from the COST Action PARENCHIMA, a community-driven network funded by the European Cooperation in Science and Technology (COST) program of the European Union, which aims to improve the reproducibility and standardization of renal MRI biomarkers.

Key words Magnetic resonance imaging (MRI), Kidney, Mice, Rats, Segmentation, ROI

1 Introduction

The potential of magnetic resonance imaging (MRI) for the diagnosis and monitoring of renal disease remains largely untapped. Functional renal MRI promises access to a wide range of (patho)-physiologically relevant parameters via techniques such as blood oxygenation sensitive T_2*-mapping (aka blood oxygenation level-dependent MRI, BOLD), perfusion measurement by arterial spin

Andreas Pohlmann and Thoralf Niendorf (eds.), *Preclinical MRI of the Kidney: Methods and Protocols*, Methods in Molecular Biology, vol. 2216, https://doi.org/10.1007/978-1-0716-0978-1_33,

labeling (ASL), and diffusion weighted imaging (DWI). Insights into microstructural changes can be obtained with DWI and T_1-mapping, for example to probe for renal fibrosis. Emerging techniques including pH-mapping via chemical exchange saturation transfer (CEST) and sodium (^{23}Na) imaging complement the renal MRI portfolio. For quantitative comparison of results, representative values must be extracted from the parametric maps obtained with any of these MRI techniques. To improve reproducibility of results this should be done based on regions-of-interest (ROIs) that are clearly and objectively defined.

Semiautomated subsegmentation of the kidney in MRI represents a simple but very valuable approach for the quantitative analysis of imaging parameters in multiple ROIs that are associated with specific anatomic locations, for example, the distinct layers: cortex, outer medulla, and inner medulla. Thereby, it facilitates comparing MR parameters between different kidney regions, as well as tracking changes over time. Here we use the term *subsegmentation* in order to make a clear distinction between segmenting the kidney into smaller subregions and the identification of the kidney organ borders within an image, for which commonly the term *segmentation* is used.

In this chapter we provide detailed step-by-step instructions for two recently proposed subsegmentation techniques [1, 2], which are suitable for kidneys of small rodents: (1) the placement of ROIs in cortex, outer and the inner medulla based on typical kidney morphology (used in [1, 3–8]) and (2) the division of the kidney into concentrically oriented layers (used in [2, 9–13]). They work independent of the actual image contrasts or parameter map values and hence are well suited for a wide range of MRI mapping techniques. Both techniques allow for the exclusion of one or several regions in the kidney from the analysis, for example regions that show obvious image artefacts. Changes in kidney size are accommodated for by both techniques, but results should be treated with due caution if the relative sizes of the renal layers are significantly different from naive healthy kidneys or change throughout the experiment.

The first method described here is the *Segmentation of Morphology-Based Renal Regions-of-Interest* (SOMBRERO) [1]. Quantitative histomorphological data on the dimensions of the renal layers were obtained from a number of freshly excised kidneys of adult male rats, where anatomical structures were identified to be distributed in certain proportions. The percentages referring to the corresponding locations exclude the rather broad (and in case of the cortical–medullary border zone undulating) transition regions among the layers that are prone to partial volume effects. The percentages are adapted to MRI images by determining a standardized location, length, width and angle of the kidney in the image. Subsequently, ROIs at anatomical locations such as the cortex, outer medulla, and inner medulla are returned

automatically in form of masks. These masks can then easily be applied to the user's parameter maps.

The strength of this technique is that it creates ROIs whose positions have been carefully chosen to provide representative values for the renal cortex, outer medulla and inner medulla, leaving a generous "buffer zone" at the transition regions between the renal layers. Also, access to five (or three) ROIs in each layer allow assessment of inter-layer and intra-layer variability. Differences between the parameters in the three renal layers can be expressed as ratios, such as T_2*(cortex)/T_2*(outer medulla). The transition regions between the renal layers are not accessible with this approach at present, but such a feature could be included without difficulty in the future, even by the user. ROI locations have been defined for rat kidneys in coronal view (with respect to the kidney). However, this method is in principle applicable to mouse and rat kidneys in axial, sagittal, and coronal view. An extension to other orientations or mice would only require some additional careful morphometric measurements to define the relative ROI positions.

The second technique is the *multiple-layer concentric objects* segmentation (MLCO; for human MRI proposed as 12-layer concentric objects, TLCO) [2, 9]. A series of concentrically oriented layers is generated after a manual retracing of the outline of the kidney in the respective MR image. The desired number of concentric objects (COs) can be freely chosen by the user, although most publications have used twelve layers in humans thus far.

This technique was developed for human kidney MRI; although the COs do not refer to specific anatomic locations, they approximately reflect the layered structure of the kidney through their concentric nature. This makes it suited for MRI of rodent kidneys, whose simpler anatomic structure is better represented by the concentric layers than that of the human kidney. While the outermost and innermost COs are straightforward to interpret and are generally considered as a proxy of respectively cortex and medulla, a clear association of the intermediate concentric objects with the renal layers remains challenging, in particular, because the broad transition zones and, thereby, probable partial volume effects are neglected. Differences between the parameters in the three renal layers can only be indirectly expressed by the slope of the curve when plotting the COs' mean values against their position. This technique is applicable to mouse and rat kidneys in axial, sagittal, and coronal view (with respect to the kidney). One of its strengths is its applicability to human kidneys. A direct comparison between human results and those from rodent kidneys would, however, require a carefully calibrated conversion, due to the morphological differences.

Notwithstanding their limitations, both kidney subsegmentation techniques are very valuable semiautomated tools for the quantitative analysis of imaging parameters, specifically for comparing MR

parameters between groups, between different kidney regions and monitoring changes over time. Use of these objectively defined ROIs (rather than manually drawn ROIs) should help to improve reproducibility and comparability of results in future studies.

This chapter is part of the book Pohlmann A, Niendorf T (eds) (2020) Preclinical MRI of the Kidney—Methods and Protocols. Springer, New York.

2 Materials

2.1 Software Requirements

2.1.1 Essential Tools

The SOMBRERO method is provided in Python (3.6) programming language. It has been implemented and tested using the following software, which is available for macOS 10.14.5 (used for development), Windows and Linux operating systems.

1. Spyder 3.2.4, installed through Anaconda (https://www.anaconda.com), which is open-source.

   The MLCO method requires the following software:

2. The MATLAB® programming environment (MathWorks, Natick, MA, USA, https://www.mathworks.com/products/matlab.html). It may also be possible to use the open-source alternative Octave (https://www.gnu.org/software/octave/), but this has not been tested and may require some adaptations in the MLCO toolbox.

2.1.2 Toolboxes

The provided software for SOMBRERO requires the installation of the following packages: *numpy*, *matplotlib*, *cv2*, *math*, *pydicom*, *os*, and *pickle*.

These can be conveniently installed one-by-one through the *Anaconda Navigator* for Windows. For Linux or MacOS the following line in the terminal will install all them at once:

```
pip install numpy matplotlib cv2 math pydicom os pickle
```

2.1.3 Software

SOMBRERO: The software is provided online at GitHub: https://github.com/lriazy/sombrero/

MLCO: The software is provided online at GitHub: https://github.com/bmilani/conObj

2.2 Source Data: Format Requirements

2.2.1 Imaging Planes

Common MRI imaging planes are sagittal, coronal, and axial slices as displayed in Fig. 1. For the sake of this tutorial we will focus on coronal slices. Other imaging planes are possible for these segmentations as well (*see* **Note 1**).

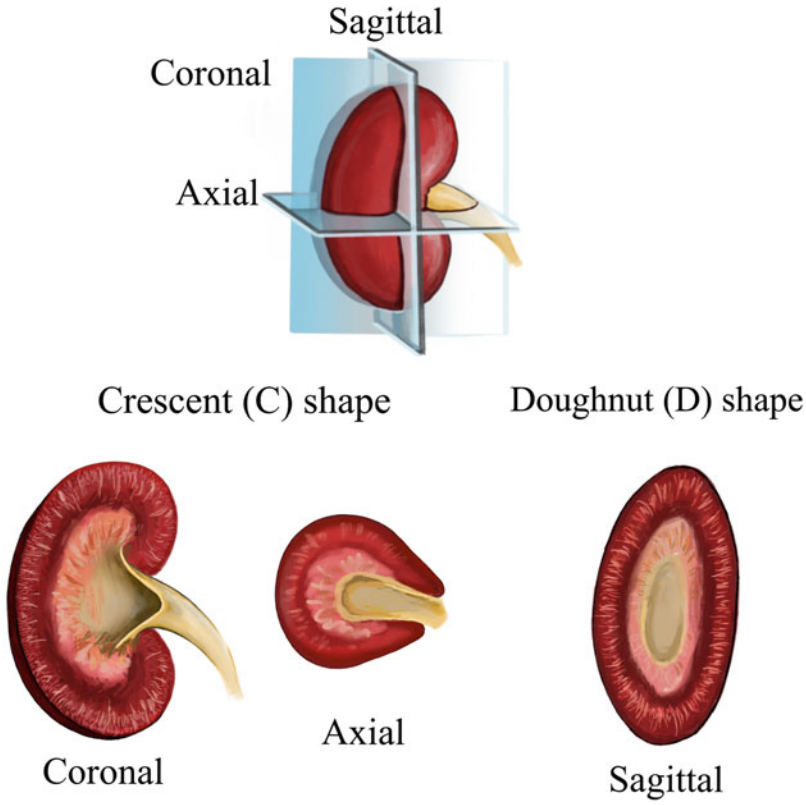

Fig. 1 Typical MR imaging planes and their resulting kidney shapes. The coronal, axial, and sagittal planes do not correspond to the scanner coordinate system, but instead are defined with respect to the double-oblique spatial orientation of the kidney. "C" stands for crescent and "D" doughnut

2.2.2 Input Requirements In this chapter, all input files are assumed to be Dicoms. However, any way to import an image as a matrix to Matlab or NumPy array to Python will work equivalently.

3 Methods

3.1 Segmentation of Morphology-Based Renal Regions-of-Interest (SOMBRERO)

3.1.1 Settings

In order to display interactive plots, make sure your graphics backend is set on "automatic."

This can be looked up in Preferences > IPython console > Graphics > Graphics backend.

3.1.2 Loading Images

1. Open the script roirect.py, which is executed cell-by-cell. Running a cell can be done by a button or by pressing CTRL + ENTER.
2. The images are loaded by the line:

```
im = pydicom.dcmread('EnIm1.dcm')
```

in the script. Modify 'EnIm1.dcm' to be the path to your dicom file. In this case, the file is located in the same directory as the script. Therefore the filename is sufficient.

3.1.3 Definition of Bounding Box

1. Execute the first cell in `roirect.py`.
2. Drag on the image to draw a new rectangle (Fig. 2a).
3. Use the edge markers to adjust the height and width of the rectangle
4. Shift the rectangle using the central marker.

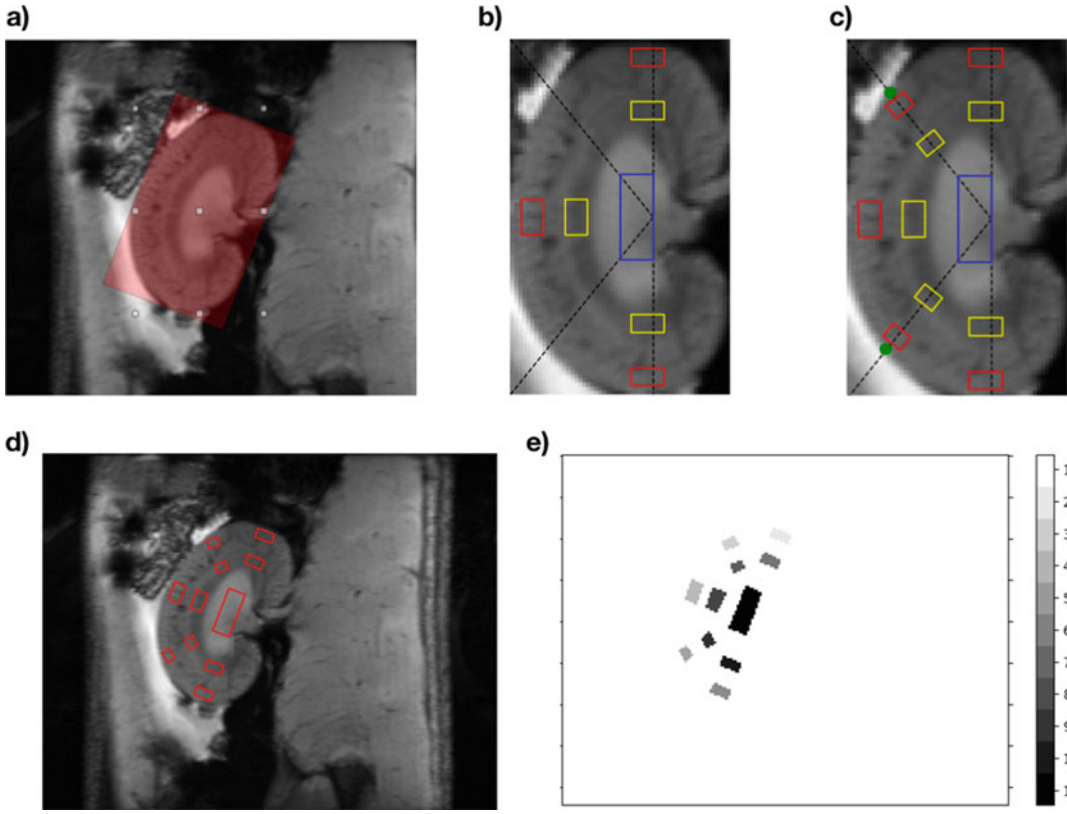

Fig. 2 (**a**) Manual selection of the kidney with the rectangle tool. (**b**) Cropped and straightened kidney image with reference lines. The red boxes are located in the cortex, the yellow box in the outer medulla and the blue box in the inner medulla. (**c**) Display of the successful selection of two border points (in green) at the intersection of the kidney border and the diagonal line. (**d**) The ROIs after transformation to the locations in the original image (without cropping or other processing). (**e**) The final mask of ROIs as an image of the same size as the original image with coded regional masks

5. Tip the rectangle using one of the edge markers (Note: A finer adjustment of the angle can be done by pressing the UP and DOWN buttons).
6. Press ENTER to end the adjustments and proceed.

3.1.4 Diagonal Boundary Selection

1. A new window opens up automatically (Fig. 2b).
2. Mark two points marking the end of the kidney on the black diagonal lines.
3. The resulting image should look like Fig. 2c).

3.1.5 Generation of Mask for Imaging Series

1. Execute the next section to transform the morphologic ROIs back to their locations in the original image (Fig. 2d).
2. Execute the next section to generate and visualize the variable roimask, which contains numbered masks for each ROI (Fig. 2e).

3.1.6 Saving Mask

1. Generate a path to the file by connecting the path (`path="` and `filename=1` will save the file `1.pickle` in the current folder).

```
pfile = os.path.join(path,filename+'pickle')
```

2. Write the file using the following commands:

```
with open(pfile,'wb') as f:
pickle.dump([S, roimask], f)
```

3.1.7 Loading Mask

1. Generate a path to the file by connecting the path just as in saving the file:

```
pfile = os.path.join(path,filename+'pickle')
```

2. Read the file into the variables `S` and `roimask`:

```
S, roimask = pickle.load(open(pfile,"rb"))
```

3.2 Multilayer Concentric Objects (MLCO) Segmentation

Given the character of in-house developed programs, the MLCO toolbox allows the user the freedom and obligation to specify all details exactly. Subheadings 3.2.1–3.2.4 describe essential steps, where any of the proposed options have to be chosen. Finally, Subheading 3.2.5 shows an example for each choice made as in the preceding sections and composes a script, which is ready to run.

3.2.1 Load an Image or a List of Images in a Matlab Array

1. Open the matlab script called demo_script.m.
2. Note that you can execute a cell of a matlab script by pressing CTRL + ENTER.

3. Load a list of images by executing for example the following line:

```
myImageList = conObjDicomRead('Dir','C:\Users\conObj\myGRE\');
```

4. This loads the image list stored in C:\Users\conObj\myGRE\.
5. The variable `myImageList`, is now a three-dimensional array containing a list of matrices that each corresponds to a gray scale image.
6. You can visualize this image list by executing the line

```
conObjImage(myImageList);
```

   This function plots the first image in the image stack. If you would like to display the mean of all images. The file has to be opened and modified. Line 41 has to be modified from

```
imagesc(argIm(:,:,curImNum));
```

   to

```
imagesc(mean(argIm(:,:,:),3))
```

7. You can navigate through the images with the up and down arrow of your keyboard.

3.2.2 Defining the Number of Layers

In order to realize the concentric object technique, you have to choose a mask-number, which is the number of masks that will patch the chosen segmented area of you images. We also call this number the "number of layers" and we gave the name `nLayers` to this number in our script (*see* **Note 2**). If you want 9 layers, execute the line

```
nLayers = 9;
```

The number of layers is inevitably limited by the image resolution. For experimental MR, 9 layers are recommended, whereas MR images of human kidneys were usually divided into 12 layers.

3.2.3 Segmenting the Area of Your Choice in the Image

In the following, the segmentation of "C"-shaped kidney slices from MR images will be described. This applies to coronal (Fig. 3) and axial (Fig. 4) slices as shown in Fig. 1.

1. Execute the line

```
[myBound_ext,myBound_int] = conObjBound_C(myImageList);
```

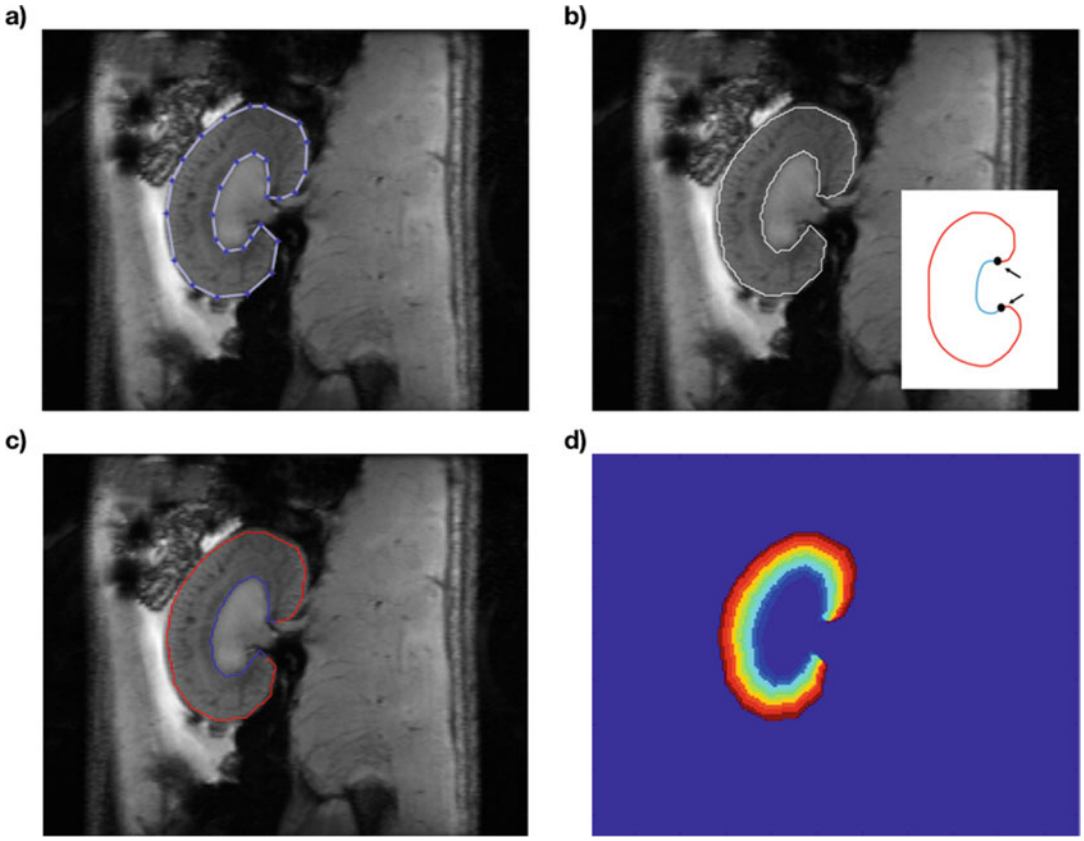

Fig. 3 (**a**) Closed manual contour of the kidney. Modification of the contour at the blue points is still possible at this stage. (**b**) The contour of the kidney turns white, after the contour is finished. The required input of two points describe the inner and outer borders. (**c**) After the two points have been entered, the inner and outer contour can be automatically separated into blue and red contours. (**d**) Output of the finished MLCO procedure

2. A matlab figure appears displaying the first image stored in myImageList.
3. Navigate through the images with the up and down arrow of your keyboard.
4. Adjust the contrast by pressing on CTRL+D and fix the change by pressing on CTRL+F.
5. By clicking on the picture, you can manually segment the area of your choice (Fig. 3a).
6. Note that pressing the key ESC allows you to reset your selection. You can also zoom in the picture with the available Matlab tools. If any problem appears during this manual segmentation, pressing the key ESC often solves the problem!
7. Double click on the picture to close the polygon. You can still modify the position of its vertices interactively on the picture (Fig. 3a).

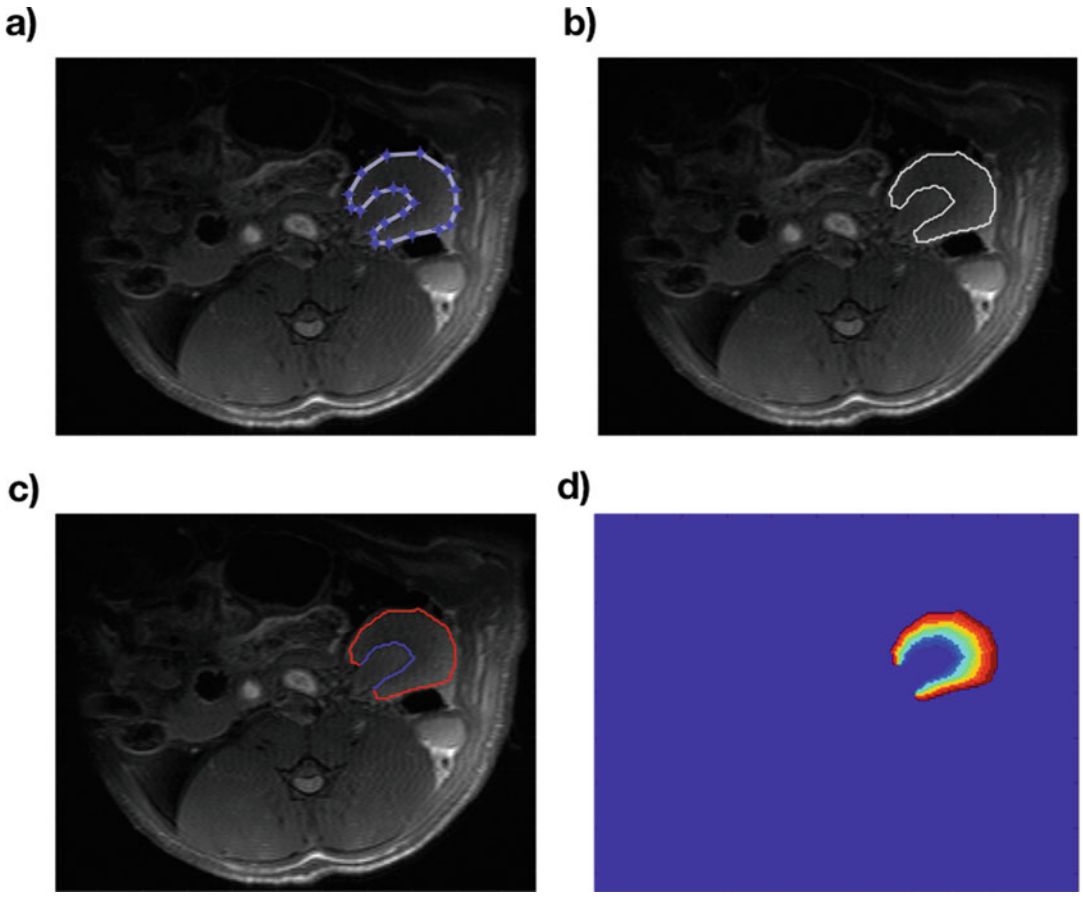

Fig. 4 (**a**) Manual contouring of the outer kidney boundary in the MLCO method. (**b**) The contour of the kidney turns white, after the contour is finished. (**c**) After the two points have been entered, the inner and outer contour can be automatically separated into blue and red contours. (**d**) Output of the finished MLCO procedure

8. When you are finished, double-click inside the polygon.
9. The contour of your segmentation will now appear in white (Fig. 3b).
10. Click near the white line at two different locations to indicate where the separation between the inner part and the outer part of the contour should occur. (Note: You do not need to press exactly on the white line because the program will choose the location on the white line that is the closest to your click.) (Fig. 3b)
11. The inner and outer part of the contour appear now in blue and red respectively (Fig. 3c).
12. You can now close the figure. The polygon of the outer contour is now stored in the variable myBound_ext and the polygon of the inner contour is now stored in myBound_int.

The same procedure can be applied for axial slices (Fig. 4). We describe in the following how to segment an area that contains a

hole. The procedure is very similar to the previous one but the function conObjBound_D has to be used instead of conObjBound_C (C for crescent and D for doughnut).

1. First execute the line

```
[myBound_ext, myBound_int] = conObjBound_D(myImageList);
```

2. As previously, segment manually the area of your choice (Fig. 5a) and double-click in the polygon to validate it. The contour of the polygon is now white and you can choose another closed polygon that has to lie inside the first one (Fig. 5b).
3. Once the second area is segmented, double-click inside it such that its polygon also appears in white (Fig. 5c).
4. As previously, you have to indicate which contour is the outer one and which contour is the inner one. For that purpose, click first near the outer contour and then click near the inner one.

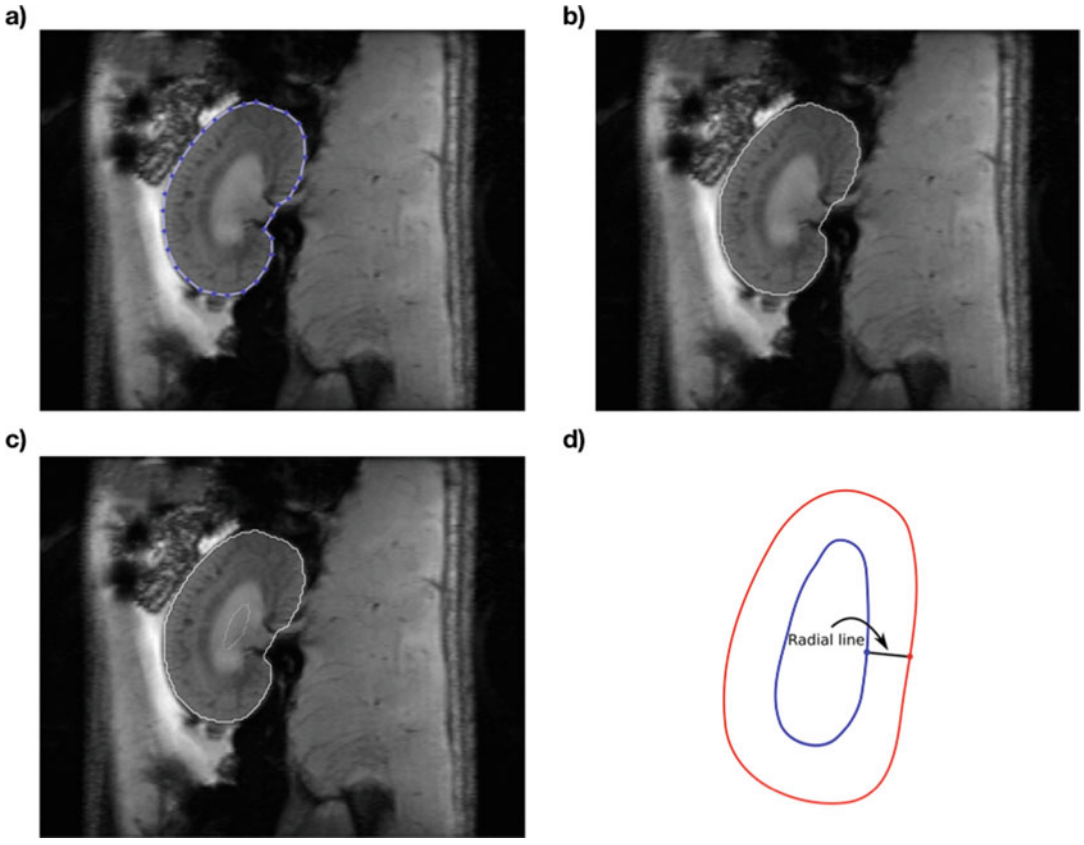

Fig. 5 (**a**) Outer contour for the "D"-shaped kidneys. (**b**) Entered contour in white. (**c**) Inner contour added manually, which is different from the previous "C"-shape procedure. (**d**) The required input of two points describe a radial line

But the two location you click on must be approximately on the same radial line (as on Fig. 5d) to allow the algorithm to work correctly.

5. Once the two location are chosen, the outer and inner contour appear in red and blue respectively (Fig. 6a). This closes the step of the segmentation.

3.2.4 Build the List of Masks That Realizes the Concentric Object Technique

1. Execute the following line:

```
myCO_mask = conObjMask(myImageList, myBound_ext ,
myBound_int,.nLayers);
```

2. You can visualize the masks with the command

```
conObjImage(myCO_mask);
```

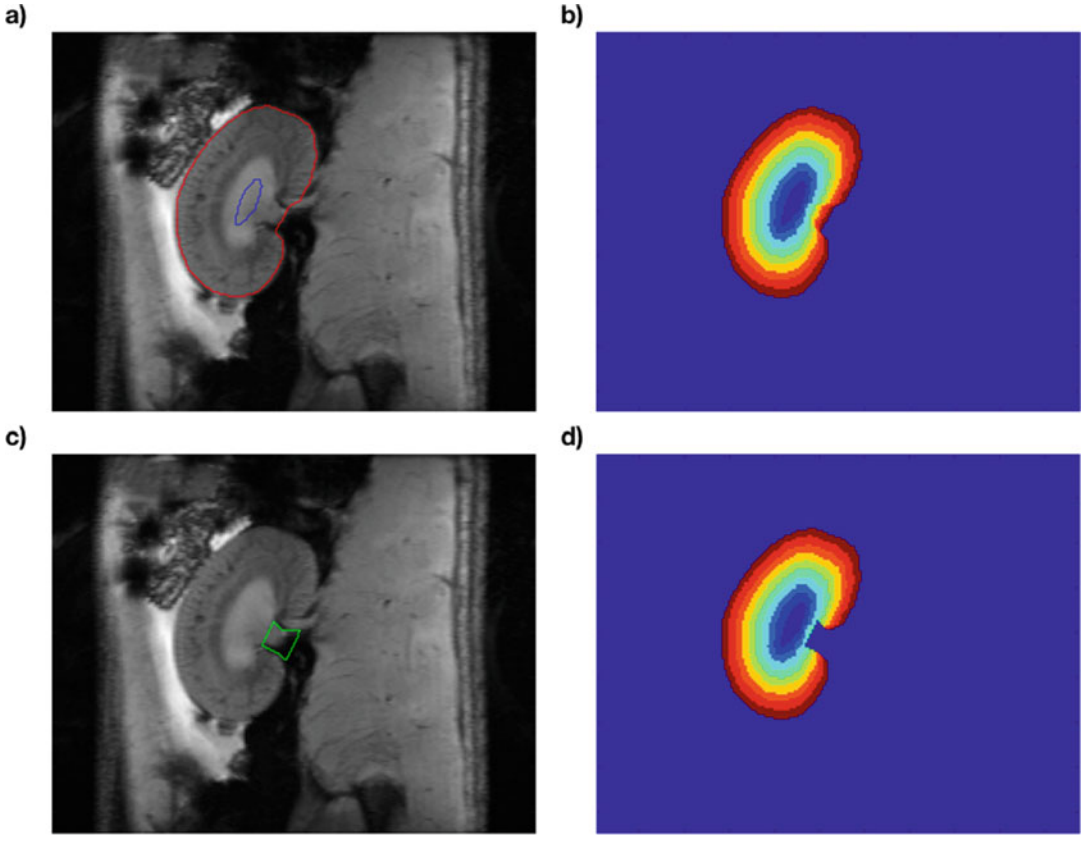

Fig. 6 (**a**) Inner and outer contour can again be identified after two points are entered. (**b**) The finished output from the MLCO method for "D"-shaped kidneys. (**c**) Exclusion of regions. (**d**) Result from MLCO method after excluding the regions specified in (**c**)

3. Browse through the different masks with the up and down arrow of the keyboard. Alternatively, you can visualize the list of masks by executing

```
conObjMaskImage(myCO_mask)
```

or

```
conObjMaskImage(myCO_mask,'jet')
```

The last line results for example in Figs. 3d and 4d for the segmentation in the crescent shape and in Fig. 6b) for the segmentation in the doughnut shape.

3.2.5 Basic Script for Applying the Concentric Object Technique

Assuming the location of the images to be in the folder 'C:\Users\conObj\myGRE\', a basic script could look as follows:

```
myImageList = conObjDicomRead('Dir' ,'C:\Users\conObj\myGRE\');

[myBound_ext,myBound_int] = conObjBound_C(myImageList);

myCO_mask = conObjMask(myImageList, myBound_ext , myBound_int,...nLayers);
```

3.2.6 Exclusion of Regions

This part describes multiple possibilities, which are optional for modifying the list. The only steps required are the first and the second.

1. Create an object of the class conObjExclusion.m in the *conObj* folder by executing: myExclusion = conObjExclusion;
2. Manually segment some region of the image to exclude from the analysis and to store these exclusion regions in the object myExclusion. For that purpose, execute: myExclusion.stack (myImageList);
3. A figure appears.
4. Segment the area of your choice.
5. Double-click to close the polygon and double-click again in the polygon to validate it. (You can execute **steps 2–5** as many times as you want to add new exclusion regions.)
6. Execute myExclusion.show(myImageList);
   to visualize all the exclusion mask that are in the object myExclusion (Fig. 6c).
7. Execute myExclusion.remove[2];
   to remove the exclusion mask number 2.
8. Execute myExclusion.clear;
   to empty the object `myExclusion`.

9. To construct a new list of masks from the previous list of masks myCO_mask but excluding the region stored in the object myExclusion, simply execute

```
myCO_mask_new = myExclusion.crop(myCO_mask);
```

10. The new list of masks myCO_mask_new can be displayed by executing the following line

```
conObjMaskImage(myCO_mask_new);
```

which results in Fig. 6d.

4 Notes

1. The orientation of the kidney was assumed to be coronal throughout this chapter. However, the MLCO method does not refer to specific anatomical locations and can therefore be used in any of the cases displayed in Fig. 1. The SOMBRERO method can potentially be used in other planes as well but would need new percentage values from kidney histology as a reference.
2. For human renal MRI the use of 12 layers was proposed [2]. For rats and mice another number of layers may be more suitable. This also depends on the spatial resolution that can be achieved with that particular MRI technique and available hardware, because it would probably not make much sense to have layers with a width of less than one (noninterpolated) pixel. As a default we recommend to use the proposed number of 12 layers.

Acknowledgments

This work was funded in part (Kathleen Cantow, Erdmann Seeliger, Thoralf Niendorf, Andreas Pohlmann, Joao Periquito) by the German Research Foundation (Gefoerdert durch die Deutsche Forschungsgemeinschaft (DFG), Projektnummer 394046635, SFB 1365, RENOPROTECTION . Funded by the Deutsche Forschungsgemeinschaft (DFG, German Research Foundation), Project number 394046635, SFB 1365, RENOPROTECTION).
This chapter is based upon work from COST Action PARENCHIMA, supported by European Cooperation in Science and Technology (COST). COST (www.cost.eu) is a funding agency for research and innovation networks. COST Actions help connect research initiatives across Europe and enable scientists to enrich their ideas by sharing them with their peers. This boosts their research, career, and innovation.

PARENCHIMA (renalmri.org) is a community-driven Action in the COST program of the European Union, which unites more than 200 experts in renal MRI from 30 countries with the aim to improve the reproducibility and standardization of renal MRI biomarkers.

References

1. Pohlmann A, Cantow K, Huelnhagen T, Grosenick D, Periquito S, Boehmert L, Gladytz T, Waiczies S, Flemming B, Seeliger E, Niendorf T (2017) Experimental MRI monitoring of renal blood volume fraction variations en route to renal magnetic resonance oximetry. Tomography 3:188–200. https://doi.org/10.18383/j.tom.2017.00012
2. Milani B, Ansaloni A, Sousa-Guimaraes S, Vakilzadeh N, Piskunowicz M, Vogt B, Stuber M, Burnier M, Pruijm M (2016) Reduction of cortical oxygenation in chronic kidney disease: evidence obtained with a new analysis method of blood oxygenation level-dependent magnetic resonance imaging. Nephrol Dial Transplant 32:2097–2105. https://doi.org/10.1093/ndt/gfw362
3. Pohlmann A, Hentschel J, Fechner M, Hoff U, Bubalo G, Arakelyan K, Cantow K, Seeliger E, Flemming B, Waiczies H (2013) High temporal resolution parametric MRI monitoring of the initial ischemia/reperfusion phase in experimental acute kidney injury. PLoS One 8: e57411
4. Arakelyan K, Cantow K, Hentschel J, Flemming B, Pohlmann A, Ladwig M, Niendorf T, Seeliger E (2013) Early effects of an x-ray contrast medium on renal T2*/T2 MRI as compared to short-term hyperoxia, hypoxia and aortic occlusion in rats. Acta Physiol 208:202–213
5. Pohlmann A, Arakelyan K, Hentschel J, Cantow K, Flemming B, Ladwig M, Waiczies S, Seeliger E, Niendorf T (2014) Detailing the relation between renal T2* and renal tissue pO2 using an integrated approach of parametric magnetic resonance imaging and invasive physiological measurements. Invest Radiol 49:547–560
6. Pohlmann A, Arakelyan K, Seeliger E, Niendorf T (2016) Magnetic resonance imaging (MRI) analysis of ischemia/reperfusion in experimental acute renal injury. In: Kidney research. Springer, New York, NY, pp 113–127
7. Cantow K, Arakelyan K, Seeliger E, Niendorf T, Pohlmann A (2016) Assessment of renal hemodynamics and oxygenation by simultaneous magnetic resonance imaging (MRI) and quantitative invasive physiological measurements. In: Kidney research. Springer, New York, NY, pp 129–154
8. Hoff U, Bubalo G, Fechner M, Blum M, Zhu Y, Pohlmann A, Hentschel J, Arakelyan K, Seeliger E, Flemming B (2019) A synthetic epoxyeicosatrienoic acid analogue prevents the initiation of ischemic acute kidney injury. Acta Physiol 227(2):e13297
9. Piskunowicz M, Hofmann L, Zuercher E, Bassi I, Milani B, Stuber M, Narkiewicz K, Vogt B, Burnier M, Pruijm M (2015) A new technique with high reproducibility to estimate renal oxygenation using BOLD-MRI in chronic kidney disease. Magn Reson Imaging 33:253–261. https://doi.org/10.1016/j.mri.2014.12.002
10. Ponikowski P, Voors AA, Anker SD, Bueno H, Cleland JGF, Coats AJS, Falk V, González-Juanatey JR, Harjola V-P, Jankowska EA, Jessup M, Linde C, Nihoyannopoulos P, Parissis JT, Pieske B, Riley JP, Rosano GMC, Ruilope LM, Ruschitzka F et al (2016) 2016 ESC guidelines for the diagnosis and treatment of acute and chronic heart failure. Eur J Heart Fail 18:891–975. https://doi.org/10.1002/ejhf.592
11. Vakilzadeh N, Muller M-E, Forni V, Milani B, Hoffman L, Piskunowicz M, Maillard M, Zweiacker C, Pruijm M, Burnier M (2015) Comparative effect of a renin inhibitor and a thiazide diuretic on renal tissue oxygenation in hypertensive patients. Kidney Blood Press Res 40:542–554. https://doi.org/10.1159/000368530
12. Pruijm M, Milani B, Pivin E, Podhajska A, Vogt B, Stuber M, Burnier M (2018) Reduced cortical oxygenation predicts a progressive decline of renal function in patients with chronic kidney disease. Kidney Int

93:932–940. https://doi.org/10.1016/j.kint.2017.10.020

13. Vakilzadeh N, Zanchi A, Milani B, Ledoux J-B, Braconnier P, Burnier M, Pruijm M (2019) Acute hyperglycemia increases renal tissue oxygenation as measured by BOLD-MRI in healthy overweight volunteers. Diabetes Res Clin Pract 150:138–143. https://doi.org/10.1016/j.diabres.2019.03.009

Chapter 34

Denoising for Improved Parametric MRI of the Kidney: Protocol for Nonlocal Means Filtering

Ludger Starke, Karsten Tabelow, Thoralf Niendorf, and Andreas Pohlmann

Abstract

In order to tackle the challenges caused by the variability in estimated MRI parameters (e.g., T_2* and T_2) due to low SNR a number of strategies can be followed. One approach is postprocessing of the acquired data with a filter. The basic idea is that MR images possess a local spatial structure that is characterized by equal, or at least similar, noise-free signal values in vicinities of a location. Then, local averaging of the signal reduces the noise component of the signal. In contrast, nonlocal means filtering defines the weights for averaging not only within the local vicinity, bur it compares the image intensities between *all* voxels to define "nonlocal" weights. Furthermore, it generally compares not only single-voxel intensities but small spatial patches of the data to better account for extended similar patterns. Here we describe how to use an open source NLM filter tool to denoise 2D MR image series of the kidney used for parametric mapping of the relaxation times T_2* and T_2.

This chapter is based upon work from the COST Action PARENCHIMA, a community-driven network funded by the European Cooperation in Science and Technology (COST) program of the European Union, which aims to improve the reproducibility and standardization of renal MRI biomarkers.

Key words Magnetic resonance imaging (MRI), Kidney, Mice, Rats, Parametric mapping, T_2, T_2*, Diffusion

1 Introduction

Mapping of the transverse relaxation times T_2* and T_2 (or relaxation rates R_2* $= 1/T_2$* and $R_2 = 1/T_2$) requires series of MR images with different echo times TE: The maps are obtained by fitting the exponential model curve $S(\mathrm{TE}) = S_0 \exp(-\mathrm{TE}/T_2^{(*)})$ to the signal intensities of each image pixel with increasing TE. This approach is inherently associated with decreasing signal-to-noise ratio (SNR) for the image volumes obtained for longer echo times. Similarly, there is a substantial signal attenuation and SNR reduction in diffusion-weighted MRI versus images acquired without diffusion-sensitizing gradients. Low SNR basically poses two

Andreas Pohlmann and Thoralf Niendorf (eds.), *Preclinical MRI of the Kidney: Methods and Protocols*, Methods in Molecular Biology, vol. 2216, https://doi.org/10.1007/978-1-0716-0978-1_34, © The Author(s) 2021

general problems: First, it leads to a variability for the parameter estimates in the quantitative maps or derived model parameters. Second, it induces a systematic bias for the estimated parameter maps [1]. Please *see* Polzehl and Tabelow [2] for an elaboration of the issues and possible solutions.

In order to tackle the challenges caused by the variability in the estimated parameters due to low SNR a number of strategies can be followed. The obvious one is hardware related and includes improvements on the MR scanner side, such as dedicated RF coils or the use of cryogenically cooled RF probes [3]. Then, SNR is increased by reducing the variability of the measurement. Since the magnitude of the MR signal is directly related to the voxel volume [4], SNR increase can be achieved by reducing the spatial resolution of the image acquisition. This is obviously a very unfavorable solution. Alternatively, signal variability can be reduced by averaging of the signal over multiple acquisitions. This approach comes at the cost of prolonged acquisition times. Acceleration techniques like parallel imaging [5, 6] or compressed sensing [7] allow for more signal averaging within the same time span. Image postprocessing provides another alternative for reducing the variability of the data. Within this chapter, we specifically consider a class of methods that post-processes the acquired data, that is, smoothing. The basic idea is that MR images (like all images) possess a local spatial structure that is characterized by equal, or at least similar, noise-free signal values in vicinities of a location. Then, local averaging of the signal reduces the noise component of the signal. The simplest approach is the application of a Gaussian filter which performs a local averaging with weights defined by a (Gaussian) kernel function and a bandwidth. Due to its simple mathematical formulation it can be performed very fast on data volumes independent of the spatial dimensionality of the data. However, it comes with the blurring of the images, which is evident at edges between different tissues, especially hindering the analysis of fine structures within the volumes.

Alternatively, adaptive smoothing methods have been developed that aim to take the local properties of the specific data at hand into account. The specific methods are based on different methodologies, like anisotropic diffusion [8–11], nonlocal means [12], penalization techniques [13, 14] wavelet filtering [15], model-based methods [16, 17], the propagation-separation approach [18, 19], or other local techniques [20, 21]. Many of these techniques have been applied to diffusion-weighted MRI data but are also applicable for relaxometry measurements. Depending on the specific method and the input data at adaptive smoothing is performed on each image volume separately or uses the combined information from all available raw data. In contrast to nonadaptive filters such as the Gaussian filter, these methods typically require longer computation times and the choice of one or more

smoothing parameters. Furthermore, in a similar way as the Gaussian filter induced blurring of images, adaptive filters might impose artifacts depending on their assumptions on the data like a cartoonesque appearance due to a step-function reconstruction of the images.

Here, we specifically consider the nonlocal means (NLM) filter [22, 23], which is of proven value for MRI. In contrast to defining the weights for averaging within the local vicinity of a location depending on the spatial distance only, it compares the image intensities between *all* voxels to define "nonlocal" weights for averaging intensities. Furthermore, it generally compares not only single-voxel intensities but small spatial patches of the data to better account for extended similar patterns. It is related to the bilateral filtering [24], where the *local* weights are refined by a factor related to local intensity differences; nonlocal means can thus be considered as a bilateral filter with infinite spatial bandwidth making it nonlocal. The filter can be applied to images in two dimensions but also in 3D or for multispectral [25] such as multiecho imaging techniques used in MR relaxometry.

Advantages of the application of the NLM filter are manifold: As a purely postprocessing method it does not require special hardware or sophisticated image acquisition techniques but can be applied offline. Many implementations and extensions of the original algorithm as open-source software are freely available. Examples are provided under: https://sites.google.com/site/pierrickcoupe/softwares/denoising-for-medical-imaging/dwi-denoising/dwi-denoising-software. Most of the implementations require MATLAB. Although smoothing parameters need to be tuned, default settings provide a very good starting point. Images processed with the NLM filter exhibit an improved SNR, show no extra blurring of the edges and preserve effective spatial resolution. Occasional and slight introduction of large-scale structures along the coordinate axis is a recognized limitation of the NLM filter because the comparison of spatial patches is in favor of these directions.

In this protocol we describe the application of a purpose-build implementation of the NLM filter for 2D MRI relaxometry data (*see* **Note 1** for implementation details). The open source tool comes in two versions: (1) each echo time is filtered independently (*2D-NLM*) (2) similarities between image patches are estimated jointly for the complete stack of echo images (*stackNLM*). While the first is a straightforward block-wise implementation of the NLM filter, the second proposes a novel method exploiting the redundancy of information in MR relaxometry data (*see* **Note 1** for implementation details). Both filters reduce the noise level in low SNR relaxometry data with version 2 offering slightly superior results (*see* **Note 2** for a detailed example). Additionally, application of the MATLAB Image Processing toolbox function imnlmfilt is

described. This function performs similar to 2D-NLM while being considerably faster. To complete the preprocessing of MRI relaxometry data, correction of the Rician noise bias is described.

This chapter is part of the book Pohlmann A, Niendorf T (eds) (2020) Preclinical MRI of the Kidney—Methods and Protocols. Springer, New York.

2 Materials

2.1 Software Requirements

The processing steps outlined in this protocol require the following:

1. The software development environments *MATLAB*® (The MathWorks, Natick, Massachusetts, USA; mathworks.com) or *Octave* (gnu.org/software/octave).
2. The MATLAB/Octave implementation of the NLM filter downloadable from github.com/LudgerS/MRIRelaxometryNLM
3. Optional: The MATLAB Image Processing Toolbox release R2018b or newer.
4. A MATLAB/Octave tool for noise bias correction downloadable from github.com/LudgerS/MRInoiseBiasCorrection. This tool includes detailed documentation to facilitate adaptation for other software development environments or use with multichannel coil data.
5. A tool for data import. This tool will depend on the data format:
   DICOM data—MATLAB contains a build in function to import dicom data: dicomread. For Octave support is offered by the following package octave.sourceforge.io/dicom/.

   Bruker data—Bruker also offers a toolbox to import data into MATLAB directly. To obtain Bruker's *pvtools* contact Bruker software support (mri-software-support@bruker.com).

2.2 Data Requirements

1. The following protocol assumes that a pure noise scan was acquired to reliable estimate the data noise level.
2. *See* **Note 3** for comments on noise scan acquisition.

3 Methods

3.1 Data Import

These steps should be executed for both the relaxometry data and the noise scan data. In the following sections it is assumed that the relaxometry data was stored in variable relaxData and the noise scan in variable noiseData.

3.1.1 DICOM Data

1. To import dicom data execute the command

```
data = dicomread(filePath);
```

where 'filePath' is a string containing the relative or absolute path of the .dcm file.

3.1.2 Bruker Data

For a Linux or MacOS system, substitute the file separator \ by /.

1. Ensure that pvtools is on the search path:

```
addpath(genpath(...\pvtools))
```

where '...\pvtools' specifies the path of the pvtools folder.

2. Store the path to the scan you want to load in variable scanFolder.
3. Read the visu_pars parameter file:

```
visuPars = readBrukerParamFile([scanFolder,
'\visu_pars']);
```

4. Load the Paravision reconstruction:

```
[data, ~] = readBruker2dseq([scanFolder, '\pdata
\1\2dseq'], visuPars);
```

3.2 Correct Data Scaling

The data scaling needs to be corrected in some cases depending on the data format and vendor if the relaxometry data and noise scan were acquired with different numbers of averages. For example, in Bruker data, the individual averages are simply added instead of computing the mean (*see* **Note 4** for a procedure to test the scaling convention). Assuming the noise scan was acquired with a single average and the relaxometry data with NA averages, use the following processing step:

1. `relaxData = relaxData/NA`

3.3 Noise Level Estimation

We assume the availability of a pure noise scan. In this case the complete noise data constitutes a background region. Assuming that the noise scan was acquired with a single average and the relaxometry data with NA averages, the noise level can be computed as

1. `sigma = std(noiseData(:))/(0.6551*sqrt(NA));`

The factor 0.6551 accounts for the different standard deviations in background and high SNR regions in MR magnitude images [1, 26, 27]. For data from multichannel coils *see* **Note 5**.

3.4 Application of the NLM Filter

To apply the provided NLM filter implementation, use a loop over all echo times. It is assumed that the relaxometry images are two dimensional and that the echoes are stored along the third dimension of relaxData.

3.4.1 Filtering of Individual Echoes with 2D-NLM

1. Set the parameters of the filter (*see* **Note 6** for an explanation of choices)

```
params.centerDistance = 1; % distance between individual blocks

params.blockRadius = 1; % size of the blocks;

params.searchRadius = 10; % determines the number of searched blocks

params.beta = 0.5; % adjusts the filter strength
```

2. Prealocate memory for the filtered data

```
filteredData = zeros(size(relaxData));
```

3. Apply the filter to every echo individually

```
for ii = 1:size(relaxData, 3)

filteredData(:,:,ii) = nlmFilter2D(relaxData(:,:,ii), sigma, params);

end
```

3.4.2 Filtering Using stackNLM

1. Set the paramters of the filter (*see* **Note 4** for an explanation of choices)

```
params.centerDistance = 1; % distance between individual blocks

params.blockRadius = 1; % size of the blocks;

params.searchRadius = 10; % determines the number of searched blocks

params.beta = 0.3; % adjusts the filter strength
```

2. Directly apply the filter to all echoes

```
filteredData(:,:,ii) = stackNlmFilter(relaxData, sigma, params);
```

3.4.3 Filtering Using MATLAB's Imnlmfilt

MATLAB's imnlmfilt works on 2D images. Again a loop over the echo times is used:

1. Prealocate memory for the filtered data

```
filteredData = zeros(size(relaxData));
```

2. Apply the filter to every echo individually

```
for ii = 1:size(relaxData, 3)
filteredData(:,:,ii) = imnlmfilt(relaxData(:,:,ii),
degreeOfSmoothing, sigma);
end
```

3.5 Bias Correction

To correct the Rician noise bias, the MRInoiseBiasCorrection toolbox is used. Importantly, the noise level sigma of the original data and not that of the filtered image needs to be given as an input parameter.

1. Ensure that the toolbox is on the search path

```
addpath(...\MRInoiseBiasCorrection)
```

   where '...\MRInoiseBiasCorrection' specifies the path of the toolbox folder.

2. Apply the noise bias correction

```
correctedImage = correctNoiseBias(imageData,
sigma, 1);
```

   The last argument specifies the number of channels in the RF coil.

4 Notes

1. The provided tool follows the block-wise implementation of the NLM filter outlined by Coupé et al. for 3D data [28]. The noise level σ is expected to be provided by separate means such as the noise scan described in this protocol. The filtering parameter h is set to $\sqrt{2\beta\sigma^2 n}$, where n is the number of pixels in the compared blocks and β a parameter which can be controlled by the user (*see* **Note 5**). Noise bias correction was not integrated into the filter but is recommended as a subsequent step.
2. We present an example application to showcase the potential of the NLM filter for T_2* relaxometry. For this purpose the kidney of an ex vivo rat phantom was scanned with a multiecho gradient-echo (MGE) sequence (TR = 50 ms, TE = 2.14 ms, 2.47 ms echo spacing, ten echoes, [38.2 × 48.5] mm^2 FOV, 1 mm slice thickness, [202 × 256] image matrix, 80 repetitions, one average per repetition). The average of all 80 repetitions was used as a reference measurement. T_2* maps were computed from unfiltered data and data filtered following the protocols of Subheading 3.4.1 (2D-NLM) and Subheading 3.4.2 (stackNLM).

   Figure 1 shows maps for a single repetition (NA = 1), the average of four repetitions (NA = 4) and the reference data

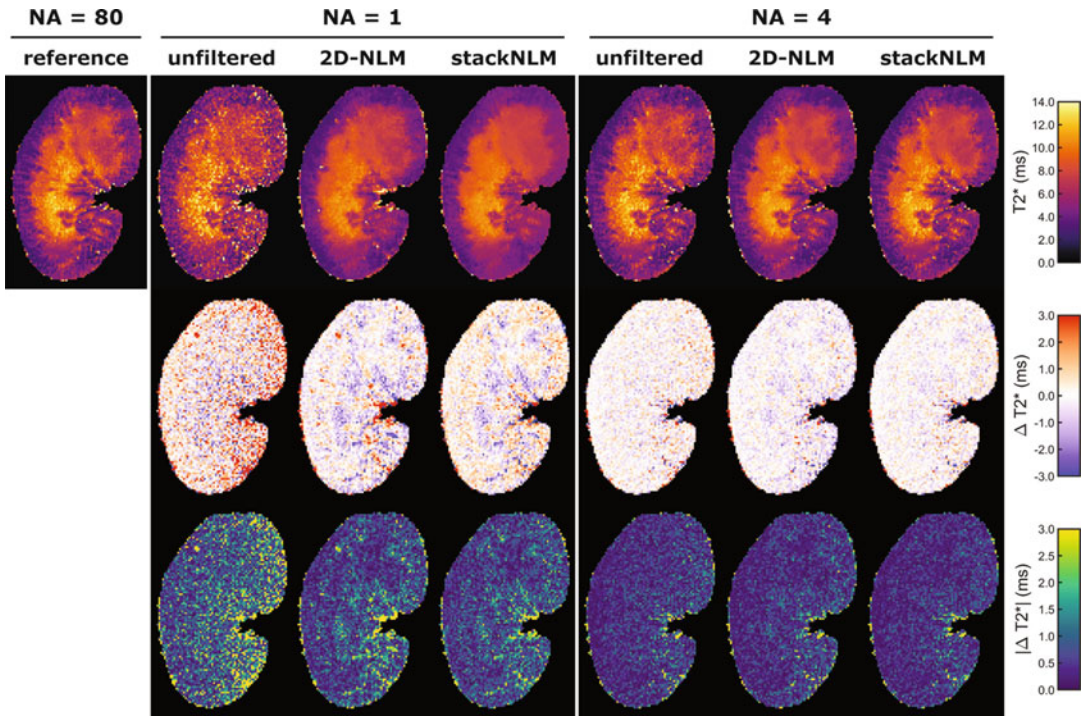

Fig. 1 Filtered and unfiltered kidney T_2* maps acquired in an ex vivo rat phantom. The reference was computed from unfiltered data and NA denotes the number of averages. The second row shows the T_2* deviation from the reference while the third row shows the magnitude of the T_2* deviation

with 80 averages. Maps showing the deviation from the reference (ΔT_2*) and the magnitude deviation ($|\Delta T_2$*$|$) highlight the strongly reduced noise level in filtered images for NA = 1. No bias is introduced and edges are preserved. The filter working on the complete stack of echoes (stackNLM) is more robust regarding outliers. For NA = 4 only very little improvement is achieved due to the already good data quality, yet also no artifacts are introduced.

The root-mean-square deviations (RMSD) of the T_2* maps from the reference support this visual assessment (Fig. 2a). At low SNR (low number of averages) the filtered data outperform the maps computed without filtering. The improvement exceeds the gain achieved by doubling the measurement time. At higher SNR filtered and unfiltered data perform similarly. stackNLM consistently performs better than 2D-NLM. Figure 2b shows selected echoes for NA = 1 and the reference. Here the improved performance of stackNLM becomes obvious for data acquired with TE = 19.4 ms where signal is recovered with sharper detail.

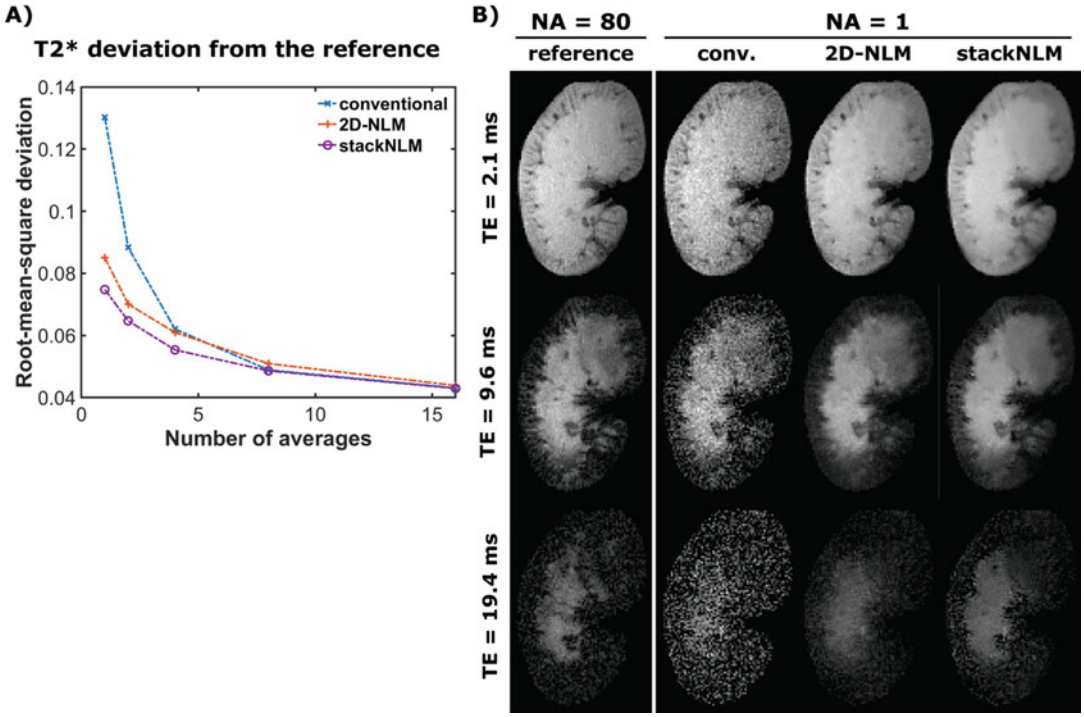

Fig. 2 (**a**) Root-mean-square deviation (RMSD) from the reference (NA = 80, unfiltered) for T_2* maps computed from filtered and unfiltered data. (**b**) Image data for selected echo times (TE). The scaling is set individually for each row

Figure 3 shows an in vivo example for both T_2* and T_2 data. Here little filtering is performed for the high SNR T_2* data, whereas the T_2 map is effectively denoised.

3. A pure noise scan is acquired by setting the excitation flip angle and reference power to zero so that no excitation occurs and pure noise is acquired. The receiver gain needs to be set identical to all other scans for which the noise level should be determined. The number of averages can be reduced to one, as the resulting change in noise level is easily compensated. Alternatively, the output of the RF power supply can be disconnected following the system adjustments.
4. To determine the employed convention of averaging, acquire high SNR phantom data with varying numbers of averages while keeping all other parameters fixed. Import the data as described in Subheading 3.1. If all scans show the same signal magnitude, the scaling step described in Subheading 3.2 should be omitted. However if for example doubling the number of averages also doubles the signal amplitude, rescaling should be performed.

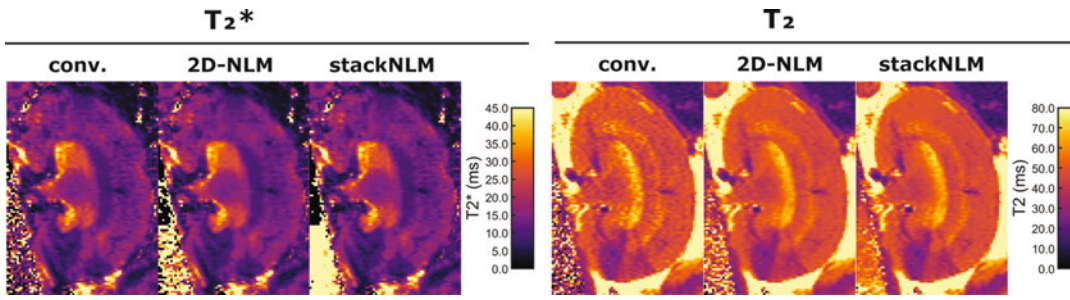

Fig. 3 Filtered and unfiltered T_2 and T_2* maps acquired in a rat in vivo. In this experimental set-up (a healthy naive rat kidney being imaged using a dedicated 9.4T small animal MR system) the SNR is sufficiently high for the denoising to have only minor denoisng effect. The parameter β was set to 0.4 for the stackNLM filter to increase the smoothing effect

5. Assuming a sum-of-squares reconstruction, the factor 0.6551 should be replaced by 0.6824, 0.6953, 0.7014 or 0.7043 for 2, 4, 8 or 16 receive element coil data [29].
6. The block-wise NLM filter compares overlapping square image patches or blocks. The larger the distance between block centers (params.centerDistance), the fewer blocks are in the image. Reducing the number of blocks will accelerate the filter but might lead to artifacts in the vicinity of contrast edges. params.blockRadius determines the size of the blocks and must always be larger than params.centerDistance to ensure overlap. The block is a square patch of area $(\text{params.centerDistance} + 1)^2$. Increasing the size of blocks will improve performance in homogeneous areas but prevent the filter from finding similar blocks in areas with small features. params.searchRadius specifies the number of compared image blocks: each block is compared with the adjacent $(\text{params.searchRadius} + 1)^2$ blocks to determine the corresponding filter weights. In the ideal case the algorithm would always search the complete image for similar blocks; however, the computational cost to do so would be prohibitive while the benefit diminishes fast with increasing search radius. params.beta specifies the parameter β introduced in **Note 1**. While theoretical considerations suggest a value close to 1, the optimal value of β is known to vary with the noise level [28]. Increasing the value of β will increase the smoothing effect. The proposed values of 0.5 for 2D-NLM and 0.3 for stackNLM were found to perform well over a wide range of noise levels.

Acknowledgments

This work was funded, in part (S.W. and A.P.; DFG WA2804, DFG PO1869), by the Deutsche Forschungsgemeinschaft and, in part (Thoralf Niendorf and Andreas Pohlmann), by the German Research Foundation (Gefoerdert durch die Deutsche Forschungsgemeinschaft (DFG), Projektnummer 394046635, SFB 1365, RE NOPROTECTION . Funded by the Deutsche Forschungsgemeinschaft (DFG, German Research Foundation), Project number 394046635, SFB 1365, RENOPROTECTION).
This chapter is based upon work from COST Action PARENCHIMA, supported by European Cooperation in Science and Technology (COST). COST (www.cost.eu) is a funding agency for research and innovation networks. COST Actions help connect research initiatives across Europe and enable scientists to enrich their ideas by sharing them with their peers. This boosts their research, career, and innovation.
PARENCHIMA (renalmri.org) is a community-driven Action in the COST program of the European Union, which unites more than 200 experts in renal MRI from 30 countries with the aim to improve the reproducibility and standardization of renal MRI biomarkers.

References

1. Gudbjartsson H, Patz S (1995) The Rician distribution of noisy MRI data. Magn Reson Med 34:910–914
2. Polzehl J, Tabelow K (2016) Low SNR in diffusion MRI models. J Am Stat Assoc 111 (516):1480–1490
3. Niendorf T, Pohlmann A, Reimann HM et al (2015) Advancing cardiovascular, neurovascular, and renal magnetic resonance imaging in small rodents using cryogenic radiofrequency coil technology. Front Pharmacol 6:255
4. Edelstein W, Glover G, Hardy C, Redington R (1986) The intrinsic signal-to-noise ratio in NMR imaging. Magn Reson Med 3 (4):604–618
5. Pruessmann KP, Weiger M et al (1999) SENSE: sensitivity encoding for fast MRI. Magn Reson Med 42(5):952–962
6. Griswold MA, Jakob PM et al (2002) Generalized autocalibrating partially parallel acquisitions (GRAPPA). Magn Reson Med 47 (6):1202–1210
7. Lustig M, Donoho D, Pauly JM (2007) Sparse MRI: the application of compressed sensing for rapid MR imaging. Magn Reson Med 58:1182–1195
8. Ding Z, Gore J, Anderson A (2005) Reduction of noise in diffusion tensor images using anisotropic smoothing. Magn Reson Med 53 (2):485–490
9. Parker G, Schnabel J, Symms M, Werring D, Barker G (2000) Nonlinear smoothing for reduction of systematic and random errors in diffusion tensor imaging. J Magn Reson Imaging 11:702–710
10. Xu Q, Anderson AW, Gore JC, Ding Z (2010) Efficient anisotropic filtering of diffusion tensor images. Magn Reson Imaging 28 (2):200–211
11. Duits R, Franken E (2011) Left-invariant diffusions on the space of positions and orientations and their application to crossing-preserving smoothing of HARDI images. Int J Comput Vis 92(3):231–264
12. Manjón JV, Thacker NA, Lull JJ, Garcia-Martí G, Martí-Bonmatí L, Robles M (2009) Multicomponent MR image denoising. Int J Biomed Imaging 2009:756897
13. McGraw T, Vemuri B, Özarslan E, Chen Y, Mareci T (2009) Variational denoising of diffusion weighted MRI. Inverse Probl Imaging 3:625–648

14. Haldar JP (2014) Low-rank modeling of local k-space neighborhoods (LORAKS) for constrained MRI. IEEE Trans Med Imaging 33 (3):668–681
15. Lohmann G, Bohn S, Müller K, Trampel R, Turner R (2010) Image restoration and spatial resolution in 7-Tesla magnetic resonance imaging. Magn Reson Med 64(1):15–22
16. Fletcher PT (2004) Statistical variability in nonlinear spaces: application to shape analysis and DT-MRI, Ph.D. thesis. University of North Carolina at Chapel Hill, Chapel Hill, NC
17. Tabelow K, Polzehl J, Spokoiny V, Voss HU (2008) Diffusion tensor imaging: structural adaptive smoothing. Neuroimage 39:1763–1773
18. Becker SMA, Tabelow K, Voss HU, Anwander A, Heidemann RM, Polzehl J (2012) Position-orientation adaptive smoothing of diffusion weighted magnetic resonance data (POAS). Med Image Anal 16 (6):1142–1155
19. Becker SMA, Tabelow K, Mohammadi S, Weiskopf N, Polzehl J (2014) Adaptive smoothing of multi-shell diffusion-weighted magnetic resonance data by msPOAS. Neuroimage 95:90–105
20. Aja-Fernández S, Niethammer M, Kubicki M, Shenton ME, Westin C-F (2008) Restoration of DWI data using a Rician LMMSE estimator. IEEE Trans Med Imaging 27:1389–1403
21. Tristán-Vega A, Aja-Fernández S (2010) DWI filtering using joint information for DTI and HARDI. Med Image Anal 14(2):205–218
22. Buades A, Coll B, Morel J (2005) A non-local algorithm for image denoising. In: IEEE Computer Society conference on computer vision and pattern recognition (CVPR'05), San Diego, CA, vol 2. IEEE Computer Society, Washington, DC, pp 60–65
23. Wiest-Daesslé N, Prima S, Coupe P, Morrissey SP, Barillot C (2007) Nonlocal means variants for denoising of diffusion-weighted and diffusion tensor MRI. MICCAI 10(2):344–351
24. Tomasi C, Manduchi R (1998) Bilateral filtering for gray and color images. In: Proceedings of the sixth international conference on computer vision (ICCV '98). IEEE Computer Society, Washington, DC
25. Bouhrara M, Bonny J-M, Ashinsky BG, Maring MC, Spencer RG (2017) Noise estimation and reduction in multispectral magnetic resonance images. IEEE Trans Med Imaging 36 (1):181–193
26. National Electrical Manufacturers Association (2001) Determination of signal-to-noise ratio (SNR) in diagnostic magnetic resonance imaging. NEMA standards publication MS 1–200. NEMA, Arlington, VA
27. Henkelman RM (1985) Measurement of signal intensities in the presence of noise in MR images. Med Phys 12(2):232–233
28. Coupe P, Yger P, Prima S, Hellier P, Kervrann C, Barillot C (2008) An optimized blockwise nonlocal means denoising filter for 3-D magnetic resonance images. IEEE Trans Med Imaging 27(4):425–441
29. Constantinides CD, Atalar E, McVeigh ER (1997) Signal-to-noise measurements in magnitude images from NMR phased arrays. Magn Reson Med 38(5):852–857

Chapter 35

Analysis Protocols for MRI Mapping of Renal T_1

Philippe Garteiser, Gwenaël Pagé, Sabrina Doblas, Octavia Bane, Stefanie Hectors, Iris Friedli, Bernard E. Van Beers, and John C. Waterton

Abstract

The computation of T_1 maps from MR datasets represents an important step toward the precise characterization of kidney disease models in small animals. Here the main strategies to analyze renal T_1 mapping datasets derived from small rodents are presented. Suggestions are provided with respect to essential software requirements, and advice is provided as to how dataset completeness and quality may be evaluated. The various fitting models applicable to T_1 mapping are presented and discussed. Finally, some methods are proposed for validating the obtained results.

This chapter is based upon work from the COST Action PARENCHIMA, a community-driven network funded by the European Cooperation in Science and Technology (COST) program of the European Union, which aims to improve the reproducibility and standardization of renal MRI biomarkers. This analysis protocol chapter is complemented by two separate chapters describing the basic concept and experimental procedure.

Key words Magnetic resonance imaging (MRI), Kidney, Mice, Rats, T_1 mapping, Processing, Fitting

1 Introduction

The computation of T_1 maps from MR datasets represents an important step towards the precise characterization of kidney disease models in the small animal. Although some concepts pertaining to T_1 mapping are relatively general, there are some important points that need to be observed specifically for each different acquisition strategy. In this section we will describe in more detail the three main classes of data fitting procedures corresponding to saturation recovery, inversion recovery, and variable flip angle protocols.

This analysis protocol chapter is complemented by two separate chapters describing the basic concept and experimental procedure, which are part of this book.

This chapter is part of the book Pohlmann A, Niendorf T (eds) (2020) Preclinical MRI of the Kidney—Methods and Protocols. Springer, New York.

Andreas Pohlmann and Thoralf Niendorf (eds.), *Preclinical MRI of the Kidney: Methods and Protocols*, Methods in Molecular Biology, vol. 2216, https://doi.org/10.1007/978-1-0716-0978-1_35,

2 Materials

2.1 Software Requirements

The method described in this chapter does require the following software tools:

1. For Bruker users, the availability of a Bruker post-processing station with Bruker Paravision fitting tools ("ISA Tools") installed, or if an independent console is not available, the scanner console. It may not always be possible or practical to alter the vendor-proposed routines to adapt to a particular use case.
2. A programming environment capable of applying fitting models, such as MATLAB® including the curve fitting toolbox (MathWorks, https://www.mathworks.com/products/matlab.html), Octave (https://www.gnu.org/software/octave/), ...
3. An image processing software (e.g., Image J, we recommend using Fiji, which is ImageJ with a wide range of plugins already included, https://fiji.sc/, open source), as a practical tool for the image quality check or for measuring the SNR.
4. For region based approaches, analysis can be done in the R language [1].
5. To speed up computation time, it may be necessary to use optimized compiled code executables or to take advantage of parallel computing.

2.2 Source Data: Format Requirements and Quality Check

2.2.1 Input Requirements

To be able to calculate T_1 maps, multiple images with different repetition times, inversion times or flip angles are needed. It is necessary to have access to some scan parameters, including matrix size and number of slices, scaling information (offset and slope), and the values of the repetition times, inversion times or flip angle. Additional time delays may also be required. In the case of protocols with multiple acquisitions, the receiver gain should also be accessible. Consistency in the acquisition parameters is paramount, especially the parameter that is varied, which should sample the same interval for each animal in the study. The completeness of the data needs to be verified ahead of the processing, by checking that the matrices have the expected size and dimensionality, or in the case of multiple protocols datasets, by ensuring that each expected protocol has indeed been acquired.

2.2.2 Physiologic Motion Check

Physiological motion is an important source of image error. Because it is difficult to avoid entirely in vivo, even in the presence of triggered acquisitions, it represents an important determinant of the dataset quality. The amount of physiologic motion can be assessed visually or via quantitative estimators (see below). Frames displaying high respiratory motion may be either discarded altogether, or they may be weighted differently in the fitting procedure.

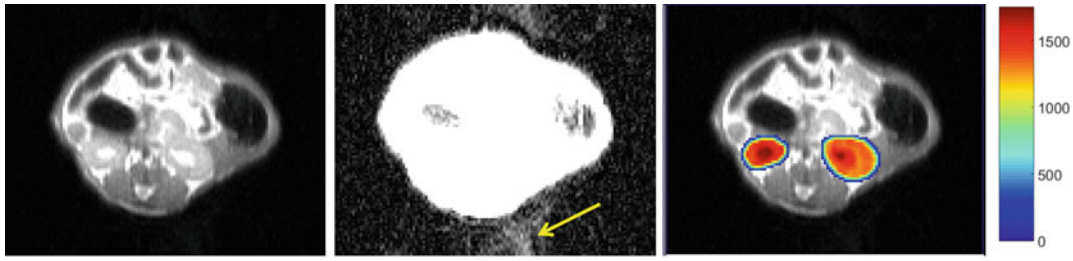

Fig. 1 Illustration of physiologic respiration-based noise. Left: original image. Middle: same image with a different windowing applied. Respiratory noise is evident as a signal smeared in the phase-encoding direction (vertical) only in the image with a strong windowing applied. Different amounts of noise may be tolerated depending on the final intended use of the data. Right: image with T_1 map overlay on the kidneys (color scale in ms)

In the simplest cases (especially with cartesian sampling schemes), respiratory motion can be identified as high intensity regions in the air surrounding the animal, corresponding to smeared projection of the signal along the phase-encoding direction (Fig. 1). Such motion may not be immediately visible and instead require to enhance the image windowing. Varying degrees of physiologic motion may be tolerated depending on the application. Automated methods can be put in place, to selectively remove frames where the noise level in the air region surrounding the animal exceeds a certain limit, in a retrospective fashion [2].

2.2.3 Acquisition Geometry Check

The geometry of the acquisition also needs to be set and verified prior to processing.

1. Verify the slice position and orientation to ensure that an optimal delineation of the kidneys is possible. A coronal orientation is often chosen, because it enables to have large regions of interest that depict all the anatomical regions of the kidney in a single image.
2. Visually check image centering to ensure that the dataset can be exploited.

2.2.4 Acquisition Parameters Consistency Check (Multiple Scans Case Only)

Regardless of the technique which is applied, it is preferable to acquire a single protocol where the parameter of interest varies.

1. Assume that the acquisition parameters are the same for all acquired images and move on to the next step.

If such a protocol is not available on the system, the same scan has to be acquired several times while varying the parameter of interest. This is the case typically for T_1 mapping with variable flip angle approach.

2. Check that all parameters (other than the varied parameter of interest) have stayed the same.

2.2.5 Receiver Gain Consistency Check (Multiple Scans Case Only)

1. Check that the receiver gain setting is identical for each scan when merging data from separate protocols.
2. If the receiver gain is not the same: contact the manufacturer to obtain receiver gain amplification tables.
3. Use the receiver gain amplification tables to calculate correcting factors.
4. Apply the correction factors to set each image at a common amplification level.

This exposes the user to noise compression or amplification and should only be used as a last resort.

2.2.6 Data Intensity Scaling Consistency Check (Multiple Scans Case Only)

The data should also be rescaled to the same intensity mapping. This ensures comparability of data coming from different datasets. For Bruker-generated data, it is recommended to use the absolute mapping option in the reconstruction options. If this has not been done during acquisition, additionally for Bruker-generated data, at the console, the user must:

1. Duplicate the processing.
2. Activate "Prototype Reconstruction".
3. Set output mapping to "User Scale".
4. Set parameters "Output Slope/Output Offset" accordingly to the setting of the first scan of the series. The setting of the first scan of the series can be checked in the "Single Parameter" parameter editor.

3 Methods

3.1 Data Exclusion

1. Check that all data points have sufficient signal to noise (SNR of 5 or higher).
2. If not all data points have high SNR then consider the necessity to only use data points with sufficient signal to noise (see next two steps).
3. For variable repetition time protocols, eliminate the data points at low repetition times (TR) that have insufficient SNR.
4. For inversion recovery protocols eliminate the data points close to the zero-crossing that have sufficient signal to noise.

3.2 Data Coregistration

To improve dataset quality, coregistration of images can be implemented to correct for respiratory motion, if such tools are available. The elastix package [3], MATLAB's built-in imregtform function, SPM [4], or AIR [5] (among others) can be used toward that objective.

3.3 Model Fitting

With contemporary computing hardware, fast fitting of the model to the signal intensity magnitude images can be performed on each pixel of the initial dataset. A region-based approach (wherein the fitting procedure is applied to ROI averages), can also be applied, but by construction it will lack the ability to examine the local spatial variations of tissue T_1.

3.3.1 Fitting Data for Saturation Recovery Experiments

1. Select an appropriate fitting equation. For the VTR protocol, the following equation is applicable (under the assumption of a perfect pulse) [6]:

$$S = S_0\left(1 - e^{-TR/T_1}\right) + \varepsilon \quad (1)$$

   where S is the signal magnitude, S_0 is the maximal available signal magnitude (including amplification factors), TR is the repetition time, T_1 is the longitudinal relaxation time, and ε is an additive noise component with Rician distribution.
2. If S_0 is known, linearize the fitting equation. A plot of $\ln(1 - S/S_0)$ against TR yields a straight line of slope $-1/T_1$ from which T_1 can be extracted with linear regression (*see* **Note 1**).
3. If the longest TR is significantly longer than T_1, please refer to **Note 3**.
4. If S_0 is not known, Eq. 1 can be fitted with nonlinear regression.
5. Initialize the fit with appropriate starting values for S_0 (*see* **Note 2**), using the signal obtained at the longest TR (*see* **Notes 3** and **4**).
6. Initialize the fit with appropriate starting values for T_1 (*see* **Note 2)** using the value obtained by linear regression if applicable (*see* **item 2**).
7. Perform the fit with the Levenberg-Marquardt, the trust region or the maximum likelihood algorithms (*see* **Note 5**).

3.3.2 Fitting Data for Inversion Recovery Experiments

1. Select an appropriate fitting equation. For the inversion-recovery protocol, the following equation is applicable (assuming perfect pulses and absence of relaxation during pulses) [6, 7]:

$$S = \left|S_0\left(1 - 2e^{-TI/T_1}\right) + \varepsilon\right| \quad (2)$$

   where S is the signal magnitude, S_0 is the maximal available signal magnitude (including amplification factors), TI is the inversion time, T_1 is the longitudinal relaxation time, and ε is an additive noise component with Rician distribution.
2. If S_0 is known, linearize the fitting equation. A plot of $\ln((S_0 - S)/(2 \cdot S_0))$ against TI yields a straight line of slope $-1/T_1$ from which T_1 can be extracted with linear regression (*see* **Note 1**).

3. Optionally, apply a corrective formula to account for the perturbation in recovery caused by the small angle imaging pulses (*see* **Note 6**):

$$\frac{1}{T_1} = \frac{1}{T_1^*} + \frac{\ln(\cos(\theta))}{\tau} \tag{3}$$

4. Optionally, the following equation is also applicable (assuming perfect pulses and absence of relaxation during pulses) [2, 8–11] and adds a saturation-correcting factor (*see* **Notes 7** and **8**):

$$S = S_0\left(1 - \beta \cdot e^{-TI/T_1^*}\right) \tag{4}$$

5. If S_0 is known, linearize fitting Eq. 4. A plot of $\ln(1 - S/S_0)$ against TI yields a straight line of intercept $\ln(\beta)$ and of slope $-1/T_1$ from which $T_1{}^*$ can be extracted with linear regression. The actual T_1 is subsequently recovered from the values of T_1^* and β as follows:

$$T_1 = T_1^* \cdot (\beta - 1) \tag{5}$$

6. If S_0 is not known, Eqs. 2 and 4 can be fitted with nonlinear regression using S_0, T_1 and β as adjustable parameters and if applicable the correction of Eq. 5.
7. Initialize the fit with appropriate starting values (*see* **Note 2**) for S_0, using the signal obtained at the longest TI (*see* **Notes 3** and **4**).
8. Initialize the fit with appropriate starting values (*see* **Note 2**) for T_1 using the value obtained by linear regression if applicable (*see* **Note 4**), or using the graphical procedure outlined in **Note 9**.
9. If the longest TR is significantly longer than T_1, please refer to **Note 10**.
10. Perform the fit with the Levenberg-Marquardt, the trust region or the maximum likelihood algorithms (*see* **Note 5**).

3.3.3 Fitting Data for Variable Flip Angle Experiments

1. If only two flip angles are available, use the following simplified equation involving α_1 and α_2 the two flip angles used, β the ratio image obtained between the two flip angles, and TR the repetition time TR [12] to compute the T_1:

$$T_1 = \frac{TR}{\ln\left(\frac{\beta \cdot \sin(\alpha_2) \cdot \cos(\alpha_1) - \sin(\alpha_1) \cdot \cos(\alpha_2)}{\beta \cdot \sin(\alpha_2) - \sin(\alpha_1)}\right)} \tag{6}$$

2. In the more general case, the following equation is applicable (*see* **Notes 11** and **12**):

$$S(\theta) = S_0 \cdot \sin(\theta) \cdot ((1 - E_1)/(1 - E_1 \cdot \cos(\theta))) \tag{7a}$$

where

$$E_1 = exp(-TR/T_1) \tag{7b}$$

3. Determine T_1 using linear regression on the linear form of Eqs. 7a and 7b [13]:
   Plot $S(\theta)/\sin(\theta)$ against $S(\theta)/\tan(\theta)$.
4. Retrieve the slope of the plot from the linear regression. This is E_1 (definition in Eq. 7b).
5. Compute the T_1 estimate directly as $-1/\ln(E_1)$.
6. Retrieve the intercept of the plot from the linear regression. This is $S_0(1 - E_1)$. The S_0 value is estimated by dividing the intercept value that was found by $1 - E_1$ (using for E_1 the value obtained previously).
7. Alternately, determine T_1 using a nonlinear fitting procedure.
8. Initialize the fit with starting values (*see* **Note 2**) for S_0 and T_1 obtained using the linearization described previously (*see* **Note 4**).
9. Perform the fit with the Levenberg-Marquardt, the trust region or the maximum likelihood algorithms (*see* **Note 5**).

3.4 Visual Display

T_1 maps can be shown as gray-scaled or color-coded maps. T_1 maps from the region of interest can be superimposed after coregistration on a morphological image or on an image acquired with the T_1 mapping protocol to better illustrate anatomical location. Window scales, usually run from $T_1 = 0$ to $T_1 = 3000$ ms, should be provided with the map and should be kept constant between figures.

3.5 Quantification

The fitting algorithm is usually applied on a voxel-by-voxel basis to yield a T_1 map. Mean T_1 is then calculated by averaging T_1 values within a region of interest. It is recommended to define a region of interest for each anatomical subregion of the kidney, as the pathology of interest can affect differently these subregions [14]. Typical ROIs are cortex, outer medulla and inner medulla, using morphological images as references to draw these ROIs. Provided sufficient spatial resolution is available, finer structures such as the outer and inner stripes of the outer medulla [15], or the corticomedullary junction [7], may be distinguished. It is also common to report T_1 changes relative to baseline or to the contralateral kidney.

3.6 Results Validation

3.6.1 Evaluation of Analysis Errors and Variability Using Synthetic Data

Synthetic datasets of various complexities should be generated to test the validity of the processing solution. Artificial noise can be added to assess the stability of the fitting procedure. T_1 of the numeric phantom should match the expected T_1. This approach is, however, limited by the signal equation, which may or may not recapitulate the real situation complexity. Hence, the use of physical phantoms can also be recommended (*see* procedure outlines in the chapter by Irrera P et al. "Dynamic Contrast Enhanced (DCE) MRI-Derived Renal Perfusion and Filtration: Experimental Protocol").

3.6.2 Comparison with Reference Values from the Literature

Relatively few studies have reported T_1 values for kidney acquired in animal models at high magnetic fields (4.7 T and higher). Typical ranges for normal kidney tissue are $T_1 = 1000–1700$ ms at magnetic field strengths of 7 or 9.4 T [14–16], with significant differences reported between mouse strains [16]. Acute kidney injury and unilateral nephrectomy have been reported to increase T_1 values in kidney, up to $T_1 = 1944$ ms at 7 T for severe acute injury [15] and well above $T_1 = 2000$ ms at 9.4 T for unilateral nephrectomy [14].

4 Notes

1. The accurate estimation of S_0 is, not trivial. Indeed, in Eqs. 1 and 2, signal evolution is asymptotic and even at very high TR or TI values, the signal only approaches the actual S_0 value. Furthermore, in these protocols, TR or TI directly affect the acquisition duration. Hence, the precision of the estimation of S_0 directly affects scan duration. In the linearization approach, the available precision on S_0 dictates the precision with which T_1 is recovered (error propagation). Hence with this approach, increased acquisition time is needed to improve the precision of the measurement. If the duration of the experiment is a concern (dynamic studies, animal models of severe diseases, difficult anesthesia), it may be preferable to leave S_0 as free parameter and to use a nonlinear fitting procedure.
2. In nonlinear fitting algorithms it can be advantageous to provide starting points that are close to the final values. Indeed, this allows to decrease the number of iterations required to reach convergence, and hence can limit the computation time. Furthermore, using starting values close to the true values also helps identifying the global minimum rather than a distant local minimum. Hence, strategies can be adopted to provide as accurate as possible initial estimates for the free parameters of the nonlinear fitting procedure.

3. In some cases, an initial S_0 estimate for fitting initialization can be obtained from the highest signal available (at the latest saturation or inversion recovery delays for instance). This estimate will only be precise if the longest delay that is sampled is sufficiently long.
4. The outlined strategies for determining reasonable starting values may not work in all cases. For instance, in the presence of high experimental noise or in the case of poorly controlled acquisition conditions, the initial estimates may prove unreliable. In this case, reasonable starting values for the T_1 may be alternately obtained from the literature. Special care should be taken to select literature reference values from studies where similar magnetic field strength, protocol type and experimental disease models were used.
5. Careful comparison of the performance of the fitting algorithms should be conducted on datasets obtained on the disease model and hardware setup used in the study. The various algorithms may be compared in terms of computation speed and goodness-of-fit figures of merit such as the root-mean-squared error before a final choice is made.
6. In inversion recovery protocols, the T_1 relaxation process is sampled several times after an inversion RF pulse using small gradient echo shots, EPI readouts or FISP readouts. Thus, the natural longitudinal recovery is perturbed by the application of the imaging RF pulses of flip angle θ and separated by a repetition interval τ. The effect can be accounted for by correcting T_1^*, the apparent T_1 resulting from the fit, using the expression given in Eq. 3 [17–19].
7. With inversion-recovery protocols followed by multiple shots, it would be preferable to use long delays between the imaging RF pulses, to drive down the saturation effect of the fast repeating gradient echo excitation RF pulses. This is not always practical, since short delays are required to fit a large number of imaging shots within a single inversion recovery interval. This is linked to the requirement that no transverse magnetization remains at the end of an imaging shot once the subsequent imaging shot is acquired, that is, that the condition of spoiled magnetization is applicable. The generally accepted condition is thus to ensure that $\tau \gg T_2^*$. Thus, although not ideal, it is acceptable to shorten the repetition time between imaging RF pulses, to reach an optimal situation where the two conflicting constraints of having both a large number of imaging shots per inversion recovery and a sufficiently good spoiling of magnetization between consecutive imaging shots are met. Similarly, it can be advantageous to work at low flip angle, to minimize the perturbation to the natural magnetization recovery relative to

the ideal case when no imaging RF pulses are applied after the inversion RF pulse. This comes at a disadvantage of having a smaller signal to noise ratio. However, this may be preferable when exactness of the recovered T_1 is important. In conclusion, the selection of the most appropriate fitting equation should be guided by careful examination of the specific acquisition protocol that was used, and of values of the imaging delays, flip angles, and typical expected tissue magnetic properties in the disease model at hand.

8. More complete correction schemes can be applied in the case of Look–Locker protocols. In particular, the delay between the inversion RF pulse and the first imaging RF pulse may be different than the delay between subsequent sequential imaging RF pulses. The imperfections in the inversion profile may also be modelled in the equation. Expressions taking this delay into account are available. Furthermore, in inversion recovery protocols, some variants may be segmented. For instance, partial k-space segments can be acquired by groups of imaging shots at several times post inversion. The various individual shots in a segment are used to reconstruct an image at a single inversion delay (the delay between the inversion RF pulse and the half of the imaging segment). Imaging segments may be separated by arbitrary delays. Expressions are available to take into account these delays [20–22].
9. In the case of inversion recovery protocols, a simpler method may be used to provide a reasonable estimate of T_1 to be used as starting point. Indeed, the signal has the typical shape where the image magnitude first drops down to zero, then comes back up (*see* Fig. 2). This is due to the fact that the image magnitude is gotten from the transverse component of the magnetization, without discerning whether the magnetization is below or above the transverse plane. This offers a graphical way to determine rapidly the T_1 by identifying the point at which the signal is minimal. The recovery delay at which this condition is verified is an approximation of the time when the longitudinal magnetization crosses the transverse plane. The precision of this estimate will be improved if the sampling of inversion times is dense around this point. The delay of the zero-crossing is equal to $T_1 \times \ln(2)$. Hence the true T_1 can be identified by dividing the zero crossing delay by $\ln(2)$. This can be useful to obtain a rapid estimate of the T_1 during parameter optimization. This computation can be performed very simply at each voxel by identifying the index of the signal vector where the smallest signal intensity is obtained. This strategy is, however, limited when only few points are available along the regrowth or when the signal to noise is low. Both cases can

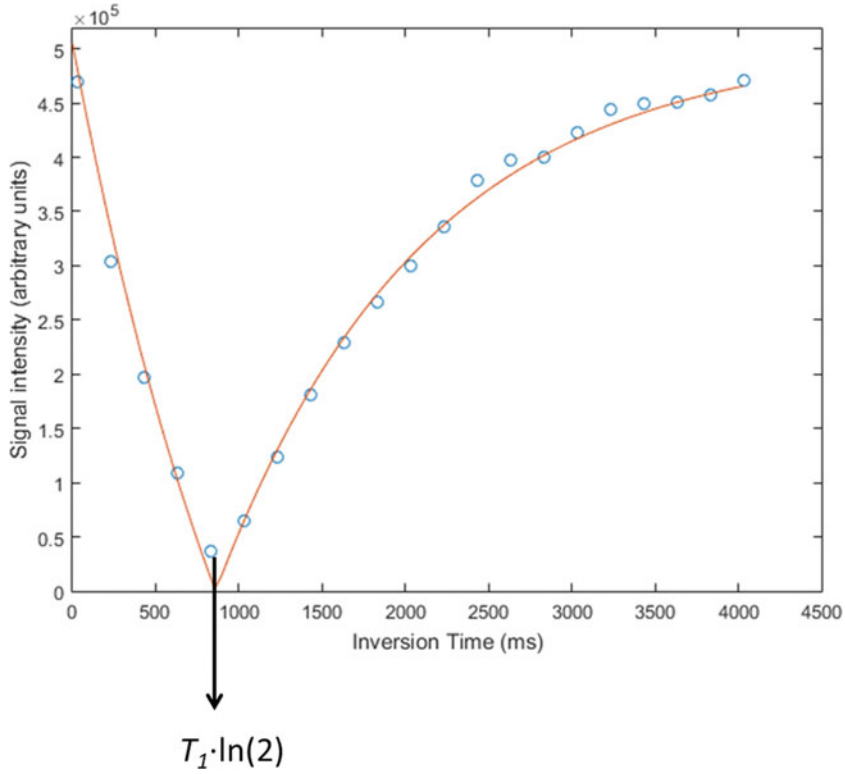

Fig. 2 Inversion recovery plot depicting the graphical method to identify T_1. An estimate of T_1 is obtained by identification of the inversion time yielding the smallest available signal, and dividing this value by ln(2). Although this quantification is not optimally accurate, it may prove useful in determining sufficiently close values to serve as a good initialization point for nonlinear fitting procedures

alter the accuracy of the estimation of the delay time yielding zero crossing.

10. Depending on the acquisition conditions, images are available at TI (or TR) $\gg T_1$. In that case, Eqs. 1 and 2 collapse to $S = S_0$. Such images can be used to normalize the data, and the nonlinear fitting procedure can be carried out on S/S_0 rather than S. By suppressing the free parameter S_0 from the fitting procedure, the numeric stability of the fit is improved, at the expense of the longer acquisition time required for the acquisition of the TI $\gg T_1$ protocol. This approach is also subject to the problem of error propagation from the S_0 estimation into the T_1 term exposed previously.
11. The true signal behavior may differ significantly from this expression, especially if the applied flip angle is not homogeneous. In that case, a corrective, smoothly spatial-varying $\zeta\left(B_1^+\right)$ term may need to be applied to account for excitation radiofrequency field heterogeneity. The effectively obtained flip angles, θ_{eff}, are in that case a modulation of the prescribed

flip angle series, θ, such that $\theta_{\text{eff}} = \zeta\left(B_1^+\right) \cdot \theta$. The evaluation of the ζ field is not trivial, and becomes especially important at higher field strengths. Post-processing methods based on large scale features in the image such as low pass filtering, or fitting of slowly spatially varying functions, can be proposed, but only extract the combined effects of transmit (B_1^+) and receive (B_1^-) heterogeneities [23]. The modulation fields can be subtracted out before performing the fit, provided that the reception field is sufficiently homogeneous. Of note, this assumption is quite difficult to validate, especially at high field strengths or when single receive RF coil elements are used as the detection circuitry.

12. Alternately, a reference T_1 map acquired with a Look–Locker protocol at lower spatial resolution and short acquisition time can be used to correct B_1 heterogeneity. Indeed, such protocol is much less prone to B_1 heterogeneity artifacts, hence the T_1 it provides can be assumed to be precise [19]. This low spatial resolution reference T_1 map is fed into a separate fit of Eq. 7a expressed as function of $\theta_{\text{eff}} = \zeta\left(B_1^+\right) \cdot \theta$ rather than merely θ, and letting ζ as free parameter. Finally, the modulation map ζ determined in that way can be injected back into Eq. 7a, this time letting T_1 and S_0 as free parameters to be determined, and operating at the full spatial resolution of the VFA dataset. This approach enables a more precise quantification of T_1 because the $B_1{}^+$ and $B_1{}^-$ effects are effectively separated out into the ζ and the S_0 maps, respectively. However, this approach is more complex and requires to acquire separate reference T_1 map, increasing the overall scan time duration.

Acknowledgments

This chapter is based upon work from COST Action PARENCHIMA, supported by European Cooperation in Science and Technology (COST). COST (www.cost.eu) is a funding agency for research and innovation networks. COST Actions help connect research initiatives across Europe and enable scientists to enrich their ideas by sharing them with their peers. This boosts their research, career, and innovation.
PARENCHIMA (renalmri.org) is a community-driven Action in the COST program of the European Union, which unites more than 200 experts in renal MRI from 30 countries with the aim to

improve the reproducibility and standardization of renal MRI biomarkers.

References

1. Team RC (2015) R: a language and environment for statistical computing. R Foundation for Statistical Computing, Vienna
2. Ramaswamy R, Campbell-Washburn AE, Wells JA, Johnson SP, Pedley RB, Walker-Samuel S et al (2015) Hepatic arterial spin labelling MRI: an initial evaluation in mice. NMR Biomed 28(2):272–280
3. Klein S, Staring M, Murphy K, Viergever MA, Pluim JP (2010) elastix: a toolbox for intensity-based medical image registration. IEEE Trans Med Imaging 29(1):196–205
4. Huhdanpaa H, Hwang DH, Gasparian GG, Booker MT, Cen Y, Lerner A et al (2014) Image coregistration: quantitative processing framework for the assessment of brain lesions. J Digit Imaging 27(3):369–379
5. Woods RP, Grafton ST, Holmes CJ, Cherry SR, Mazziotta JC (1998) Automated image registration: I. General methods and intrasubject, intramodality validation. J Comput Assist Tomogr 22(1):139–152
6. Haacke EM, Brown RW, Thompson MR, Venkatesan R (2014) Magneticresonance imaging, physical principles and sequence design. Wiley, Hoboken, NJ
7. Bosch CS, Ackerman JJ, Tilton RG, Shalwitz RA (1993) In vivo NMR imaging and spectroscopic investigation of renal pathology in lean and obese rat kidneys. Magn Reson Med 29 (3):335–344
8. Jiang K, Tang H, Mishra PK, Macura SI, Lerman LO (2018) A rapid T1 mapping method for assessment of murine kidney viability using dynamic manganese-enhanced magnetic resonance imaging. Magn Reson Med 80 (1):190–199
9. Pastor G, Jimenez-Gonzalez M, Plaza-Garcia S, Beraza M, Reese T (2017) Fast T1 and T2 mapping methods: the zoomed U-FLARE sequence compared with EPI and snapshot-FLASH for abdominal imaging at 11.7 Tesla. MAGMA 30(3):299–307
10. Rajendran R, Lew SK, Yong CX, Tan J, Wang DJ, Chuang KH (2013) Quantitative mouse renal perfusion using arterial spin labeling. NMR Biomed 26(10):1225–1232
11. Wang JJ, Hendrich KS, Jackson EK, Ildstad ST, Williams DS, Ho C (1998) Perfusion quantitation in transplanted rat kidney by MRI with arterial spin labeling. Kidney Int 53 (6):1783–1791
12. Ko SF, Yip HK, Zhen YY, Lee CC, Lee CC, Huang SJ et al (2017) Severe bilateral ischemic-reperfusion renal injury: hyperacute and acute changes in apparent diffusion coefficient, T1, and T2 mapping with immunohistochemical correlations. Sci Rep 7 (1):1725
13. Cheng HL, Wright GA (2006) Rapid high-resolution T(1) mapping by variable flip angles: accurate and precise measurements in the presence of radiofrequency field inhomogeneity. Magn Reson Med 55(3):566–574
14. Kierulf-Lassen C, Nielsen PM, Qi H, Damgaard M, Laustsen C, Pedersen M et al (2017) Unilateral nephrectomy diminishes ischemic acute kidney injury through enhanced perfusion and reduced pro-inflammatory and pro-fibrotic responses. PLoS One 12(12): e0190009
15. Hueper K, Peperhove M, Rong S, Gerstenberg J, Mengel M, Meier M et al (2014) T1-mapping for assessment of ischemia-induced acute kidney injury and prediction of chronic kidney disease in mice. Eur Radiol 24(9):2252–2260
16. Tewes S, Gueler F, Chen R, Gutberlet M, Jang MS, Meier M et al (2017) Functional MRI for characterization of renal perfusion impairment and edema formation due to acute kidney injury in different mouse strains. PLoS One 12(3):e0173248
17. De Graaf R (2007) In vivo NMR spectroscopy, principles and techniques, 2nd edn. Wiley-Interscience, Hoboken, NJ
18. van Schie JJ, Lavini C, van Vliet LJ, Vos FM (2015) Feasibility of a fast method for B1-inhomogeneity correction for FSPGR sequences. Magn Reson Imaging 33 (3):312–318
19. Zhang J, Chamberlain R, Etheridge M, Idiyatullin D, Corum C, Bischof J et al (2014) Quantifying iron-oxide nanoparticles at high concentration based on longitudinal

relaxation using a three-dimensional SWIFT Look-Locker sequence. Magn Reson Med 71 (6):1982–1988

20. Nkongchu K, Santyr G (2005) An improved 3-D Look-Locker imaging method for T (1) parameter estimation. Magn Reson Imaging 23(7):801–807
21. Henderson E, McKinnon G, Lee TY, Rutt BK (1999) A fast 3D Look-Locker method for volumetric T1 mapping. Magn Reson Imaging 17(8):1163–1171
22. Nkongchu K, Santyr G (2007) Phase-encoding strategies for optimal spatial resolution and T1 accuracy in 3D Look-Locker imaging. Magn Reson Imaging 25(8):1203–1214
23. Marques JP, Kober T, Krueger G, van der Zwaag W, Van de Moortele PF, Gruetter R (2010) MP2RAGE, a self bias-field corrected sequence for improved segmentation and T1-mapping at high field. NeuroImage 49 (2):1271–1281

Chapter 36

Analysis Protocols for MRI Mapping of the Blood Oxygenation–Sensitive Parameters T_2* and T_2 in the Kidney

João S. Periquito, Ludger Starke, Carlota M. Santos, Andreia C. Freitas, Nuno Loução, Pablo García Polo, Rita G. Nunes, Thoralf Niendorf, and Andreas Pohlmann

Abstract

Renal hypoxia is generally accepted as a key pathophysiologic event in acute kidney injury of various origins and has also been suggested to play a role in the development of chronic kidney disease. Here we describe step-by-step data analysis protocols for MRI monitoring of renal oxygenation in rodents via the deoxyhemoglobin concentration sensitive MR parameters T_2* and T_2—a contrast mechanism known as the blood oxygenation level dependent (BOLD) effect.

This chapter describes how to use the analysis tools provided by vendors of animal and clinical MR systems, as well as how to develop an analysis software. Aspects covered are: data quality checks, data exclusion, model fitting, fitting algorithm, starting values, effects of multiecho imaging, and result validation.

This chapter is based upon work from the PARENCHIMA COST Action, a community-driven network funded by the European Cooperation in Science and Technology (COST) program of the European Union, which aims to improve the reproducibility and standardization of renal MRI biomarkers. This experimental protocol chapter is complemented by two separate chapters describing the basic concept and data analysis.

Key words Magnetic resonance imaging (MRI), Kidney, Mice, Rats, T_2, T_2*, BOLD

1 Introduction

The parametric mapping of the transverse relaxation times T_2* and T_2 (or relaxation rates $R_2 = 1/T_2$* and $R_2 = 1/T_2$) has the potential to yield inferences regarding renal oxygenation, since both parameters are sensitive to blood oxygenation [1]. The underlying mechanism rests on the inherent difference in the magnetic properties of oxygenated hemoglobin (diamagnetic) vs. deoxygenated hemoglobin (paramagnetic) [2]. The presence of deoxyhemoglobin in a voxel decreases both relaxation times, T_2* and T_2, which are the time constants governing the exponential signal decays due to spin

Andreas Pohlmann and Thoralf Niendorf (eds.), *Preclinical MRI of the Kidney: Methods and Protocols*, Methods in Molecular Biology, vol. 2216, https://doi.org/10.1007/978-1-0716-0978-1_36, © The Author(s) 2021

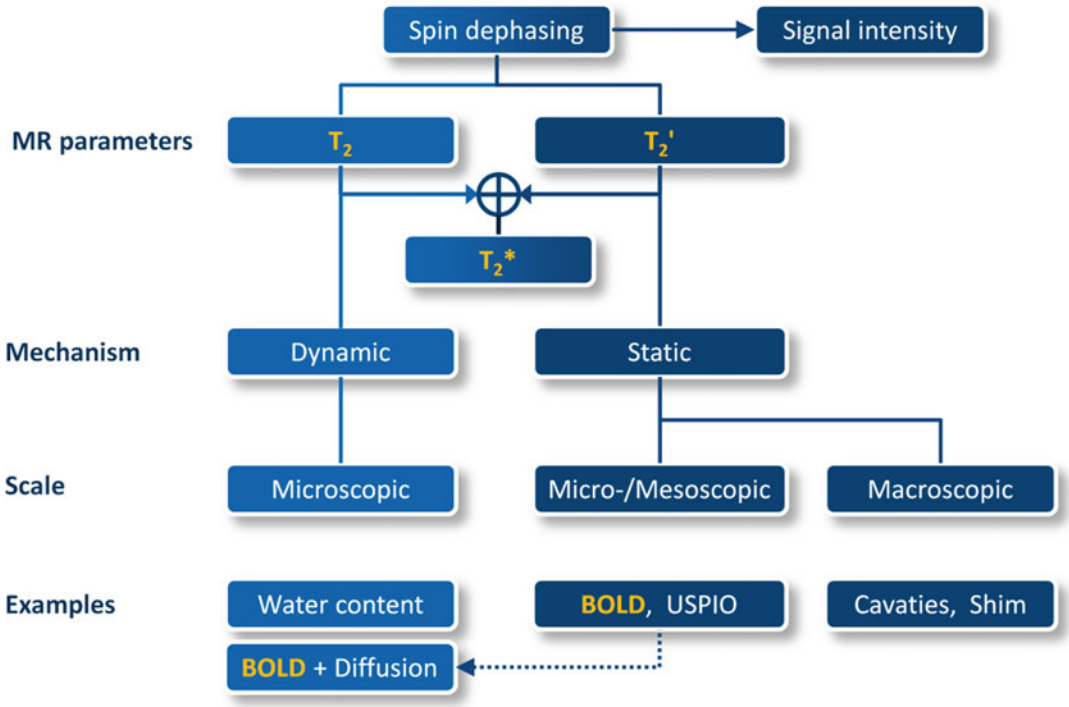

Fig. 1 Spin dephasing due to dynamic (irreversible; represented by the parameter T_2) and static (reversible; represented by the parameter T_2') sources can be quantified by calculation of T_2^* and T_2 from series of MRI images with different echo times using $1/T_2^* = 1/T_2 + 1/T_2'$. The possible sources for this dephasing range from the microscopic to the macroscopic scale and their level dictates the observed attenuation in the signal intensity. Blood oxygenation affects primarily T_2^* (often referred to as Blood Oxygenation Level Dependent, BOLD), but to a lesser extend also T_2 via diffusion effects in the proximity of blood vessels. USPIO: Ultra-small Superparamagnetic Particles of Iron Oxide, which can be used as intravascular contrast agents

dephasing in gradient-echo (GRE) and spin-echo (SE) MR measurements, respectively.

Possible sources for this dephasing are magnetic field inhomogeneities ranging from the microscopic to the macroscopic scale, which can be classified with respect to the echo time into microscopic dynamic spin–spin interactions—T_2, that is, typically ranging a time span between 1 and 100 ms (Fig. 1) and static mesoscopic interactions—T_2'. In fact, T_2^* includes the dynamic (irreversible) dephasing effects described by T_2 plus the additional effects that are due to static (reversible) dephasing effects described by T_2'. Blood oxygenation affects primarily T_2^* (often referred to as Blood Oxygenation Level Dependent, BOLD), but to a lesser extend also T_2, via water diffusion effects in the proximity of blood vessels due to local magnetic field gradients [1].

Calculation of T_2^* and T_2 requires a series of MR images with different echo times. Repeated measurements with a single echo

sequence using either a GRE or SE method and variable echo times (TE) would provide the most accurate T_2* and T_2 values but would require very long acquisition times [2]. In order to address this shortcoming fast multiecho MRI methods are commonly used for in vivo studies: multi-gradient-echo (MGE) for T_2* and multi-spin-echo (also called "MSME") for T_2. They provide relaxation times that slightly underestimate T_2* and overestimate T_2 (*see* **Note 1**).

The core of $T_2^{(*)}$ mapping consists of fitting the exponential model curve $S(\mathrm{TE}) = S_0 \exp.(-\mathrm{TE}/T_2^{(*)})$ to the signal intensities of each image pixel at increasing TE. For the calculation of such parameter maps from a series of $T_2^{(*)}$-weighted images software tools and plugins are provided by the MR system vendors but they may lack some features instrumental for precise $T_2^{(*)}$ mapping. For example, some important preprocessing steps may not be available, such as eliminating the first echo of T_2 data, removing echoes acquired at high TEs that may have too low signal-to-noise ratio (SNR) or applying Rician noise bias correction. Also, details about the used processing and curve fitting algorithms may not be available. It is also a limitation that the algorithms are fixed and cannot be modified for specific purposes. Therefore, depending on application, it may be advantageous to develop a dedicated analysis software program in-house. The analysis software is developed assuming 2D data was acquired, for 3D data (multiple slices) data set are separated into individual slices.

The pixel-wise signal fitting with a monoexponential model is known to introduce T_2 bias, and so for studies that require an extremely rigorous T_2 value (error $< 1\%$) a dictionary-based method has been suggested. In dictionary-matching methodologies, T_2 maps are calculated by matching the T_2 signal decay to precomputed Echo Modulation Curve (EMC), therefore accounting for all echo pathways. The use of dictionary-based methods has been suggested to improve T_2 accuracy, accounting for the stimulated echoes and effective B_1^+ field [3]. The use of dictionary-based methods is still fairly novel and its implementation and use is not covered in this chapter.

This chapter will describe both how to use the vendor's analysis tools and how to develop your own analysis software conceptually. An example of a MATLAB script described in this chapter together with a data sample (*T2analysis.m* and *data.mat*) can be downloaded from https://github.com/JoaoPeriquito/T2-s-Mapping.

This data analysis protocol is complemented by two separate chapters describing the basic concept and experimental, which are part of this book.

This chapter is part of the book Pohlmann A, Niendorf T (eds) (2020) Preclinical MRI of the Kidney—Methods and Protocols. Springer, New York.

2 Materials

2.1 Software Requirements

To calculate the parametric maps using existing tools, a software such as the following is required:

2.1.1 Essential Tools

1. MR system software *ParaVision* (version 5 or higher; Bruker Biospin, Ettlingen, Germany).
2. MR system software *Syngo* (versions MR B17 or higher; Siemens Healthineers, Erlangen, Germany). The optional toolbox *MapIt* is not necessary.
3. MR system software *Ready View* (General Electric Healthcare, Milwaukee, USA).
4. MR system software from Philips (Philips Medical Systems, Best, Netherlands).

To develop custom software for calculating the parametric maps one of the following, or other equivalent, software development environments (SDE) is required:

5. *MATLAB*® including the *Curve Fitting* toolbox (The MathWorks, Natick, Massachusetts, USA; www.mathworks.com/products/MATLAB).
6. *Python* (https://www.python.org/).
7. *Octave* (http://www.gnu.org/software/octave).
8. A MATLAB tool for Rician noise bias correction can be downloaded from https://github.com/LudgerS/MRInoiseBiasCorrection. It is also compatible with Octave and includes detailed documentation to facilitate adaptation for, for example, Python.

2.1.2 Optional Tools

An image processing software for checking data quality, such as ImageJ (free Java-based image processing program developed at the National Institutes of Health and the University of Wisconsin; https://imagej.net/). We recommend and describe here the use of Fiji (https://fiji.sc/ [4]), which is ImageJ packaged with a wide range of plugins included.

2.2 Source Data: Format Requirements and Quality Check

Before the analysis it is highly recommended to check the image quality. This check should include SNR measurements, particularly for the images with longest echo times, and the assessment of geometric image distortions, motion artifacts, or susceptibility artifacts.

The steps in this section can be performed either on the scanner console using the MR vendors system viewing software, or offline using a software such as *Fiji* (recommended as a practical tool).

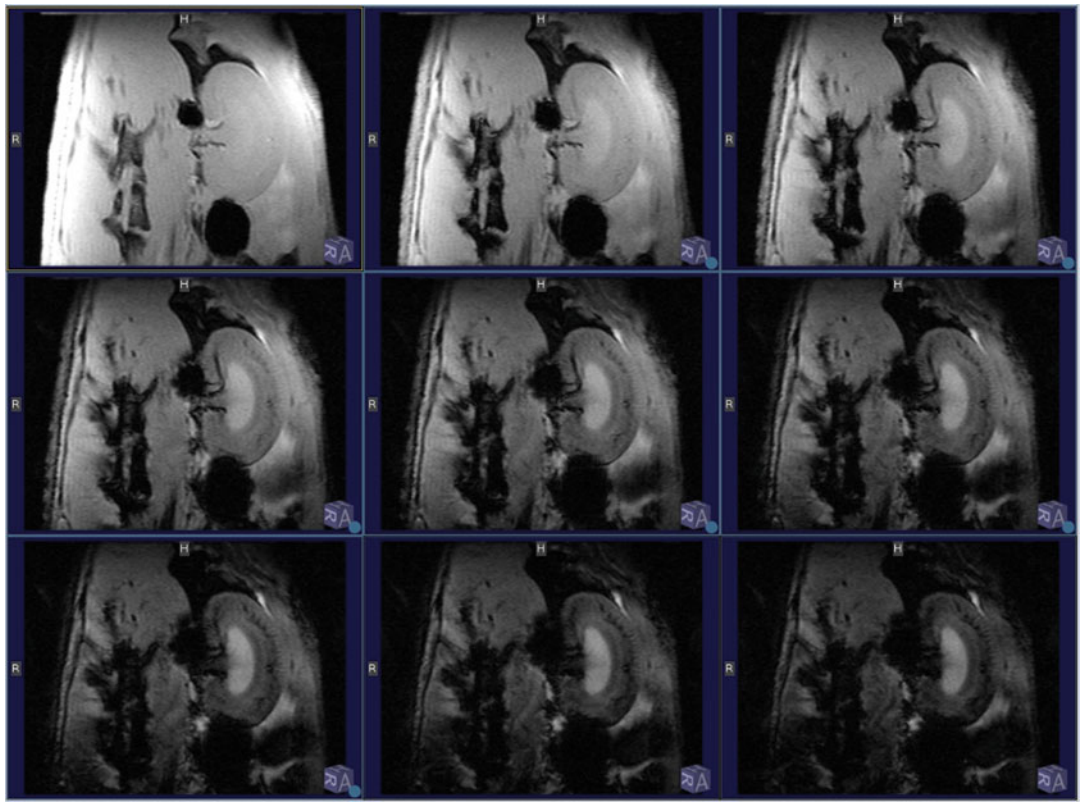

Fig. 2 Series of nine T_2*-weighted images of a healthy rat kidney acquired with a 2D MGE sequence at 9.4 T. From left to right and top to bottom, images correspond to TE = 2.14, 4.28, 6.42 ms (top row), TE = 8.56, 10.70, 12.84 ms (middle row), and TE = 14.98, 17.12, 19.26 ms (bottom row)

2.2.1 Input Requirements

As already mentioned, in order to be able to calculate $T_2^{(*)}$-maps, multiple images acquired with different echo times are needed. As an example, please refer to Fig. 2 and Fig. 3, where a series of T_2*- and T_2-weighted images suitable for mapping is presented (*see* **Note 2**). Access to specific acquisition parameters is also necessary, namely the TE of each image and in some cases the image intensity scaling parameters (offset, slope) used when storing the image data.

2.2.2 Open/Import Images

When using the scanner console:

1. Open the $T_2^{(*)}$-weighted image series in the image viewer.

When using *Fiji* for DICOM images:

2. Import the DICOM image series using the DICOM import plugin.

When using *Fiji* for images in Bruker format:

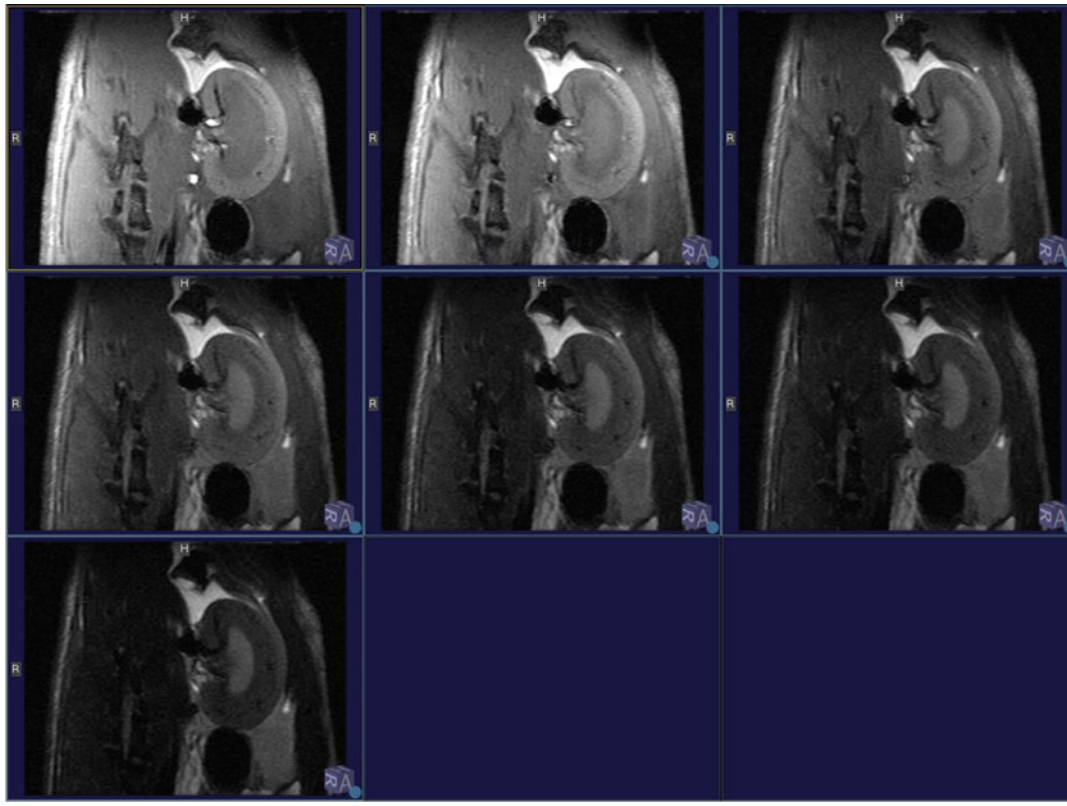

Fig. 3 Series of seven T2-weighted images of a healthy rat kidney acquired with a 2D MSME sequence at 9.4 T. Images correspond to TE = 10.0, 20.0, 30.0 ms (top row), TE = 40.0, 50.0, 60.0 ms (middle row), and TE = 70.0 ms (bottom row)

3. Browse to the data directory for the scan containing the $T_2^{(*)}$-weighted image series: /opt/PV6.0.1/data/[user_name]/[session_name]/[scan_number]/.
4. Open the "*method*" file of the scan in a text editor or by dragging it to the *Fiji* window.
5. Get the following parameters: number of slices, matrix size (e.g., 128 × 128) image type (e.g., little-endian) and byte order (e.g., 16-bit unsigned).
6. Load the image series using the RAW import function (*Import > RAW*) and providing the above parameters. The MR data file is called 2dseq and located in the subfolder "pdata/nr" (number of reconstruction) of the data directory.

2.2.3 Motion Artifacts Check

Abdominal imaging comes with complex bulk physiological motion due to the interplay of respiratory and bowel movement. If respiratory triggering of the data acquisition was used (recommended) there should only be minor motion artifacts. Check

images for artifacts from motion (nontriggered acquisition) or possible residual motion (triggered acquisition).

In the image viewer or *Fiji* go to the central slice and scroll rapidly from the first to the last echo image.

1. Check for motion between the echoes. If motion is noticeable then information close to structure boundaries may not be reliable and image registration should be used for motion correction (registration is a separate topic that is not explained in this chapter).

2.2.4 Susceptibility Artifacts Check on T_2*-Weighted Images

Kidney regions adjacent to bowels or in close proximity to skin/fat/muscle boundaries or air cavities are particularly challenging to T_2* imaging and prone to loss of anatomical integrity due to geometric distortions and signal loss created by susceptibility artifacts induced by the air-filled bowels, cavities and tissue interfaces surrounding the kidneys.

1. Scroll to the images acquired at the later echoes, where susceptibility artifacts are more severe.
2. Check areas affected by susceptibility artifacts, that is, areas in the kidney with unusual and severe hypointensities (typically in the form of spherical dark "shadows"; Fig. 4).
3. Make a record of areas affected by such artifacts (notes, screenshots). They must be excluded from the analysis or at least be considered during interpretation of the result.

2.2.5 Signal-to-Noise Ratio Check

Before the analysis it is highly recommended to define an SNR acceptance threshold (*see* **Note 3**).

1. Draw a region-of-interest (ROI) over the inner medulla in the first echo image (in *Fiji* use the "Freehand Selection" tool) (*see* **Note 4**).

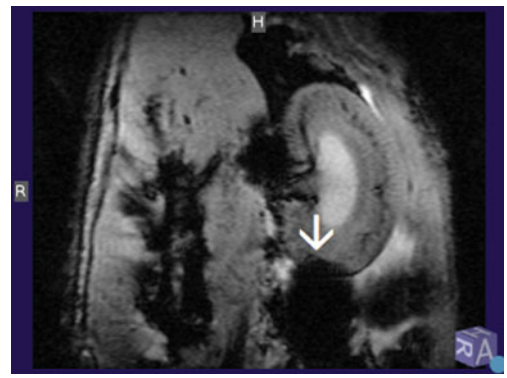

Fig. 4 T_2*-weighted image of a rat kidney that shows a susceptibility artifact at the caudal end (white arrow); image acquired with TE = 10.70 ms at B_0 = 9.4 T

2. Measure the mean signal intensity of the ROI (in *Fiji*: *Analyze* > *Set Measurements*; select mean and standard deviation; *Analyze* > *Measure*).
3. Draw an ROI over a region in the background that contains only noise without any signal or artifacts (*see* **Note 5**).
4. Measure the standard deviation of the signal within this background ROI.
5. Divide this value by 0.655 to obtain the noise standard deviation. This is necessary because the background noise in MR magnitude images differs from noise in signal regions (*see* **Note 6** if you use a multichannel RF array).
6. Calculate the SNR by dividing the mean signal of the inner medulla ROI by the noise standard deviation.
7. If the SNR is significantly below your predefined acceptance threshold, this indicates that there might be a technical problem or that the animal is not positioned correctly relative to the receiver RF coils. For more information on adequate SNR thresholds refer to **Note 7**.

3 Methods

Tools for calculating $T_2^{(*)}$-maps are provided by most MRI vendors, but, as mentioned in the introduction, we recommend creating your own analysis tool to have the maximum level of control over the processing steps and freedom to adapt them to your specific needs. Hence, this section will describe both how to use vendor's analysis tools and how to develop your own analysis software.

In both cases, mapping of T_2 and T_2*, it may be required to exclude some data from the analysis, such as data points with insufficient SNR in the tail of the exponential decay. In the case of T_2-mapping from data acquired with a MSME method, it is also recommended to discard the first echo (*see* **Note 8**).

3.1 Data Exclusion and Model Fitting (Siemens Syngo)

When using the Siemens scanner console this is currently not possible, but one can manually select the echo images that should be included when computing the fit. Using this feature, one can exclude entire images at high TEs. We recommend using a cut-off for echo images with low SNR. Please exclude all echo images with SNR < 2.6 in the ROI of interest (*see* **Note 7**). When performing T_2-mapping, the first echo should also be excluded from the data analysis (*see* **Note 8**).

1. Load image series in the *Viewing Task Card*.
2. Using the *ROI* tool to draw an ROI on the image with the largest TE over the region of interest, and register the mean signal.

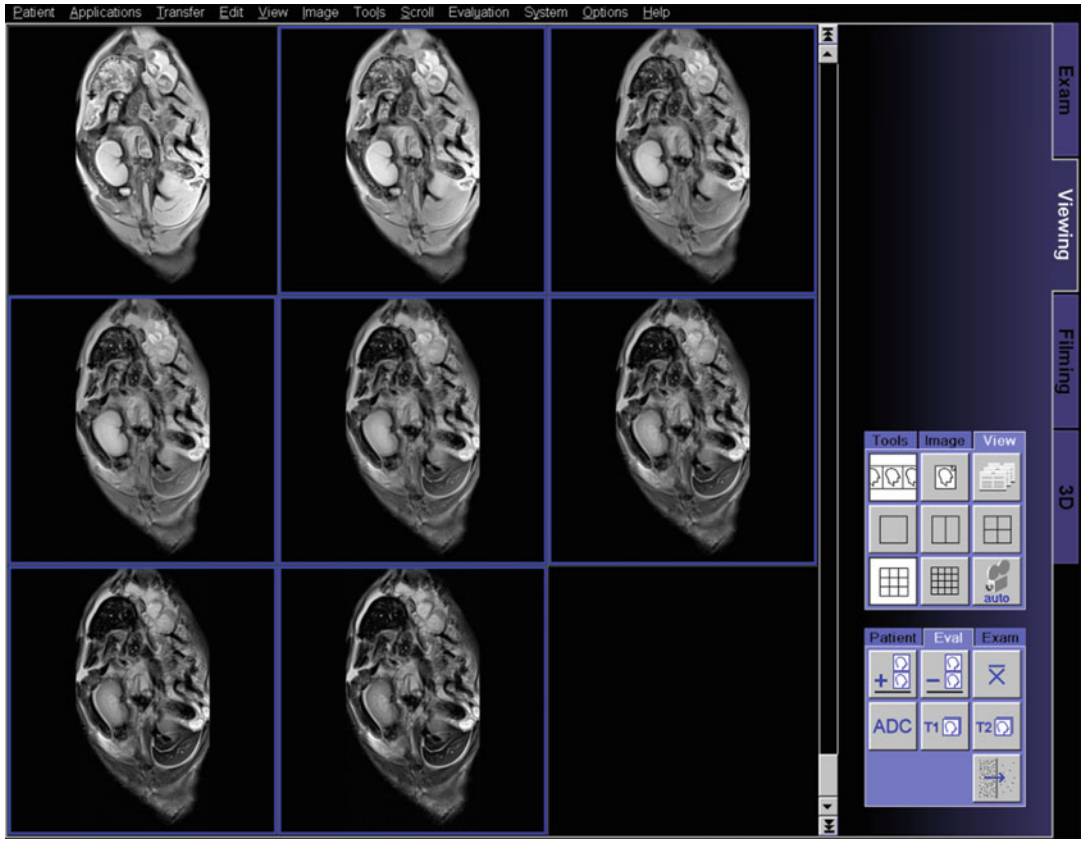

Fig. 5 Selection of echo images for $T_2^{(*)}$-mapping of a rat kidney in Siemens *Syngo*. Here T_2-mapping was performed, for which the first echo image must be excluded. Then start the $T_2^{(*)}$-map calculation with the *T2* button in the *Eval* tab in the *Control Area* panel on the bottom right

3. On the same image, use the *ROI* tool draw an ROI on the background, and register the standard deviation of the signal. Divide this value by 0.655 to obtain the noise standard deviation (*see* **Note 6** if you use a multichannel RF array).
4. Calculate the SNR by dividing the mean signal ROI by the noise standard deviation. If the SNR is below 2.6 this image should be excluded on step "8" (*see* **Note 7**).
5. Select a 3 × 3 or 4 × 4 layout in the *View* tab of the *Control Area* (right panel) in order to see all acquired echo images.
6. Select all echo images for T_2*-mapping or all echo images except the first for T_2-mapping (Fig. 5).
7. In the *Control Area* choose *Eval* > T_2 > *OK*. Two new images will appear in the viewer, the $T_2^{(*)}$-map and the S_0-map.
8. Exclude all echo images that have a SNR < 2.6 (*see* **Note 7**).

Fig. 6 T_2-map of a rat kidney calculated using the *T2-analysis* tool of Siemens *Syngo* from data acquired with a clinical 3 T scanner

9. In the *Control Area* choose *Eval* > T_2 > *OK*. A $T_2{}^{(*)}$-map will appear in the viewer. Use this new map for further analysis/quantification (Fig. 6).

3.2 Model Fitting (General Electric $T_2{}^{(*)}$ Map Ready View)

On a GE system a similar tool is used for mapping of T_2 and T_2*. The *Ready View T2 Map* protocol post processes data sets acquired using the *Cartigram* (T_2 Map) application. The *T2 Map* layout is comprised of four viewports: upper-left Map viewport: source image, upper-right viewport: curve displaying signal intensity (vertical axis) and the echo number (horizontal axis). A data point for each echo is plotted when an ROI is deposited on any of the three images. Lower left viewport: *T2 Map* Preset-1 parametric image. Lower right viewport: *T2 Map* Preset-2 parametric map.

Use these steps to post-process data sets acquired using the *Cartigram* application. The $T_2{}^{(*)}$ relaxation time color map is

coded to capture $T_2^{(*)}$ values from the TE range of the acquired images. Blue and green reflect the longer $T_2^{(*)}$ values, yellow the intermediate $T_2^{(*)}$ values, and red and orange the shorter $T_2^{(*)}$ values. The functional $T_2^{(*)}$ map units are ms.

1. Open *ReadyView* and start the *T2map* protocol.
2. Adjust the *W/L* (window width and level) and magnification—to adjust the *W/L*, middle-click and drag over the image. To adjust the magnification factor, place the cursor over the red *DFOV* and middle-click and drag right to left.
3. Locate the desired images to view—press the Up and Down arrows to move through the images to locate the image with the area of interest. Or click and drag the red slice Location annotation. Press the Right and Left arrows to select the desired echo or click and drag the red echo annotation.
4. Open the *T2 Map* Settings screen.
5. Adjust the settings on the *T2 Map Settings* screen. Typically, the Preset Color Level sliders for both the $T_2^{(*)}$ map and parametric image are within a 10 and 90 ms range and the Threshold is 20. Typically, the Confidence Level is 0.05. A default smoothing kernel of 2 is recommended.
6. Click Compute.
7. If necessary, use the *Clip Min & Max* values. By default (25–75).
8. In the measurements panel, select the ROI icon and draw the desired region of interest. An annotation with the area, mean value and standard deviation of the ROI will appear.

3.3 Model Fitting (Philips)

1. When acquiring a $T_2^{(*)}$ (mTSE/MGE) dataset, select the *Post-proc* tab and choose the option $T2^{(*)}$ or $R2^{(*)}$ ($1/T_2^{(*)}$) under the field *Calculated images* (Fig. 7).
2. Insert the maximum expected $T_2^{(*)}$ or its reciprocal ($1/T_2^{(*)}$) under the field *T2 clip value* or its reciprocal $R2^{(*)}$ *clip value* to specify the maximum calculated $T_2^{(*)}/R_2^{(*)}$ value for the SE sequence. Larger $T_2^{(*)}/R_2^{(*)}$ values are clipped to this value.
3. By default, T_2/T_2* reconstruction includes the first echo and performs a MLE fitting of the signal curve. Research customers can modify these parameters under the *Scan Control Parameters* panel select *Reconstruction* and choose the option *Include first echo for (SE) T2,R2 calc (yes/no)*, and reconstruction method (*MLE* [5, 6] or Least squares (*RLSQ*)) for $T_2^{(*)}$, $R_2^{(*)}$. If available we recommend to use *Include first echo = no* and the default *MLE* calculation method (*see* **Note 9**)—Warning: changing these options affects every scan until reset of the system (Fig. 8). After the acquisition, drag and drop the images in the viewer.

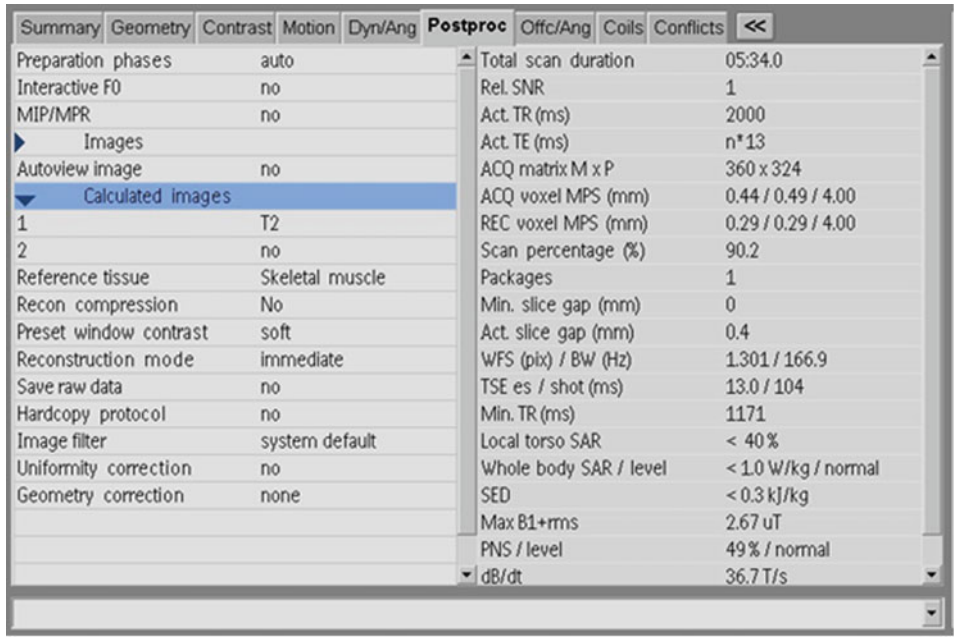

Fig. 7 Philips acquisition software *Postproc* tab. Here T_2-mapping can be performed by choosing the option *T2* or *R2* ($1/T_2$) under the field *Calculated images*

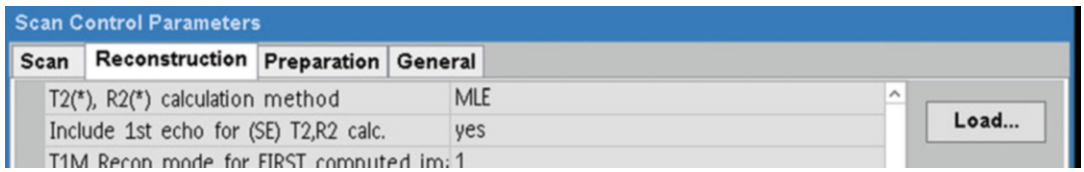

Fig. 8 Philips acquisition software *Scan Control Parameters* panel—only accessible for research customers. Here under the *Reconstruction* tab select *no* on the option *Include first echo for (SE) T2/R2 calc.* to exclude the first echo image on T_2 mapping and select *MLE* for *T2(*), R2(*) calculation method* (*see* **Note 9**)

3.4 Data Preparation and Model Fitting (Custom Program)

The following custom program for $T_2^{(*)}$ relaxometry contains code examples following MATLAB syntax. These were tested to be compatible with Octave and should be easily reproducible in Python or an equivalent SDE.

3.4.1 Data Import and Exclusion of First TE (Only for T_2)

1. Import your scan with the images obtained for different TEs.

   Bruker data: in MATLAB use the import function provided by Bruker's *pvtools*—to obtain Bruker's *pvtools* send an e-mail to Bruker mri-software-support@bruker.com.

   DICOM data: in MATLAB use the dicomread function—https://mathworks.com/help/images/ref/dicomread.html; in Python use dcmread from the pydicom package—https://pydicom.github.io/). As input you need to provide a string containing the full path of the DICOM file.

2. As previously explained, when performing T_2-mapping using a multiecho sequence, the first echo must be excluded from data analysis (*see* **Note 8**). For example, that could mean that for a series of T_2 weighted data acquired at TE = 10.0, 20.0, 30.0, 40.0, 50.0, 60.0, 70.0 ms one would only be able to fit the model curve to the TE = 20.0, 30.0, 40.0, 50.0, 60.0 ms data points: store your data in a different variable excluding the first TE (`imgData_forAnalysis = imgDataT2w(:,:,2:end); TE_forAnalysis = TE(2:end)`).

3.4.2 Rician Noise Bias Correction

MR signal intensities are overestimated in low SNR magnitude images. This bias is due to the Rician distribution of noisy MR magnitude data and can be corrected in post-processing. We can understand the processing step as multiplication with a signal-level dependent correction factor, which approaches 1 as higher SNRs are reached. To incorporate Rician noise bias correction into our custom program, we first need to determine the noise level and then utilize a MATLAB/Octave tool provided for this book under https://github.com/LudgerS/MRInoiseBiasCorrection:

1. Add the downloaded noise correction tool to the search path.

   ```
   Addpath(genpath('...\MRInoiseBiasCOrrection)).
   ```

2. Compute unbiased data by executing the following:

   ```
   imgData_corrected=correctNoiseBias(imgData_forA-
   nalysis,sigma,1)
   ```

   If you work with data from a multichannel RF array, change the last argument of the function to the number of receive elements.

3.4.3 Fitting Model

The most common method is to iteratively fit the model of the $T_2^{(*)}$ decay to the signal intensity (SI) data of each pixel using the following equation:

$$S(\mathrm{TE}) = S_0 . \exp\left(-\frac{\mathrm{TE}}{T_2^{(*)}}\right) \quad (1)$$

where S_0 is a scaling factor that includes many parameters such as the proton density together with the signal gain of the system.

3.4.4 Starting Values

An important step of the curve fitting process is the choice of suitable starting values for each parameter that will be determined by the fitting algorithm (NB: different starting values may lead to different results!). Here we describe how to derive starting values from the SI of each pixel.

1. Step through all pixels in the images using for loops for the pixel coordinates x and y.

2. Store the SI of that pixel at all TEs in a vector (in MATLAB: `SI_vector = imgData_forFitting(xPix, yPix,:)`).
3. As starting value for the parameter S_0 use the first and largest SI (`startVal_S0 = SI_vector(1)`).

For estimating a starting value for $T_2^{(*)}$, one can exploit the fact that at TE = $T_2^{(*)}$ the SI has fallen to 37% of its value at TE = 0. Estimate the starting value by determining the TE whose SI is closest to 37% of the largest SI value:

4. Normalize the SI vector to a maximum value of 1 (divide by the largest SI value).
5. Subtract 0.63 from the SI vector.
6. Get the absolute values of the SI vector (resulting in only positive values).
7. Find the index of the smallest value in the vector (in MATLAB: `[min_Value,min_Index] = min(SI_norm_abs_37pct)`).
8. Get the respective echo from your echoes using the index from the last step (`startVal_T2=TE_forFitting(min_Index)`).

3.4.5 Fitting Algorithm

Least squares algorithms, such as the Levenberg–Marquardt [7] and Trust-region methods [8], are the most commonly used curve fitting algorithms for $T_2^{(*)}$-mapping. They work by minimizing a cost function, which describes the deviation of the fitted curve from the corresponding data points. With starting values near the optimal solution they quickly converge, but with starting values far away from the solution, the Levenberg–Marquardt algorithm will slow down significantly. Also, there is the risk that it may converge to a local minimum (rather than the global minimum) and hence produce an erroneous result.

In contrast, the Trust-region method (a further development of the Levenberg–Marquardt algorithm) will quickly converge, even with suboptimal starting values, and it will always find the global minimum. However, it does require the definition of lower and upper limits for the parameters to be fitted. Hence, for $T_2^{(*)}$-mapping, where such limits can easily be defined, the Trust-region method is well suited (*see* **Note 10**)

1. Create for loops for pixel coordinates *x* and *y* to step through all pixels of the image.
2. Store the SI of that pixel at all TEs in a vector (in MATLAB: `SI_vector = imgData_forFitting(xPix, yPix,:)`).
3. Define the model for the function using Equation1 (in MATLAB: `T2model = fittype('a*exp.(-x*b)', 'independent', 'x', 'dependent', 'y')`).

4. Choose the function for the fitting algorithm, that is, Trust-region or, if not available, then Levenberg–Marquardt (in MATLAB: `opts.Algorithm = 'Trust-Region'`).
5. Provide the starting values for S_0 and $T_2^{(*)}$ (in MATLAB, e.g., `opts.StartPoint = [startVal_S0 startVal_T2]`).
6. Define lower and upper limits for the fit parameters. Use for T_2* [0.1 150], for T_2 [1 1000], and for S_0 the possible range of SI in the image data (this depends on the system; for 16-bit integer it may be [1 65536]). In MATLAB, for example, `opts.Lower = [1 0.1]; opts.Upper = [65,536 150].`
7. Execute the curve fitting for each pixel data (in MATLAB: `[fitresult, gof] = fit(TE_forFitting, SI_vector, T2model, opts);`).
8. Save the fit result for each variable in parameter maps: `mapS0(xPix, yPix) = fitresult.a; mapT2(xPix, yPix) = fitresult.b; rsquare(xPix, yPix) = gof.rsquare.`

3.4.6 Visual Display

1. Display the parameter map, which is a matrix with floating point numbers, as an image (in MATLAB: `imagesc(mapT2);`).
2. Remove axis labels and ensure that the axes are scaled such that the aspect ratio of the image is identical to that of the acquired FOV (For the case of square pixels in MATLAB: `axis off; axis equal;`).
3. Select the color map and display a color bar (in MATLAB: colormap(jet(256)); `colorbar;`) (*see* **Note 11**).
4. Set the display range for the color coding, for example, for T_2* [0 25]; and for T_2 [0 80]; (in MATLAB: `caxis([0 25]);`). An example is shown in Fig. 9.

3.5 Quantification

Quantitative values can be obtained from the parameter maps using manually drawn ROI for the different morphological regions (cortex, outer medulla, and inner medulla). Because manual ROI drawing can introduce unwanted additional variability or bias, we recommend the use of semiautomated methods, such as the concentric objects technique [9] or the morphology-based ROI placement technique [10]. For further details and step-by-step protocols for these two techniques please refer to the chapter by Riazy L et al. "Subsegmentation of the Kidney in Experimental MR Images Using Morphology-Based Regions-of-Interest or Multiple-Layer Concentric Objects."

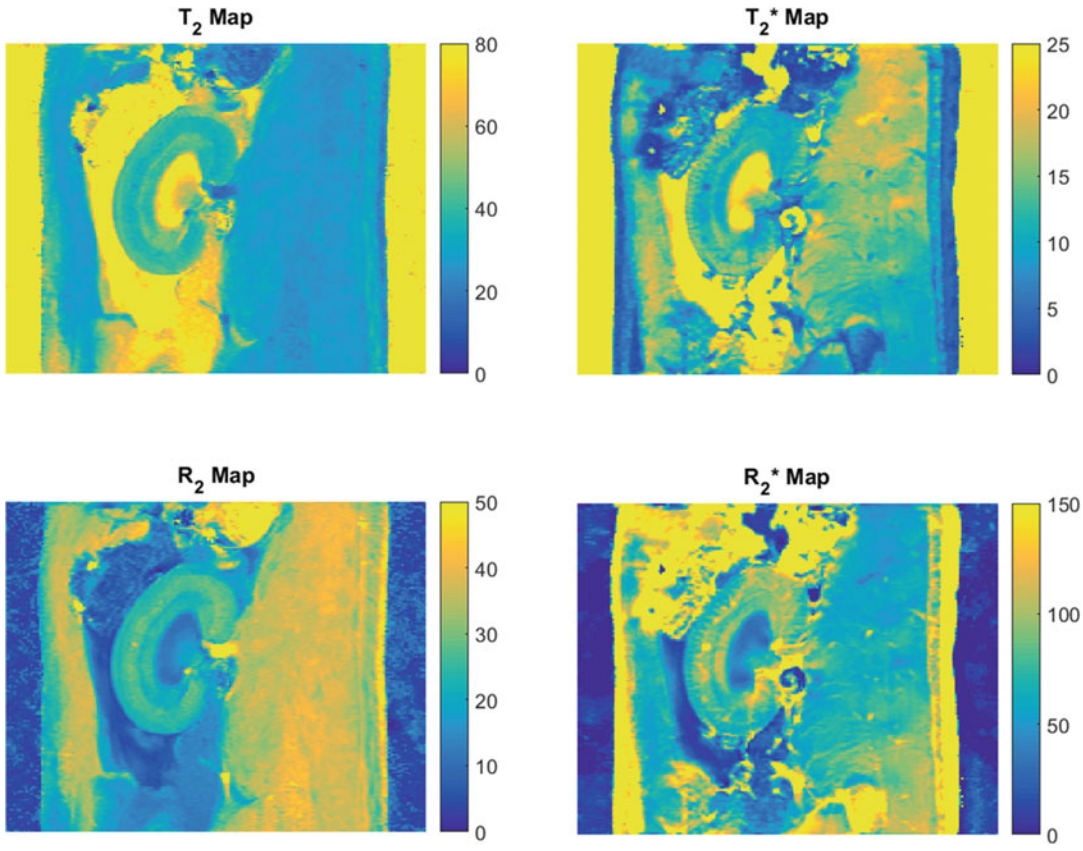

Fig. 9 $T_2^{(*)}$ in ms and $R_2^{(*)}$ in ms^{-1} maps of an healthy rat kidney calculated using a custom program developed in MATLAB (displayed using colormap *parula*) from data acquired with a preclinical 9.4 T scanner

3.6 Methods for Result Validation

3.6.1 Evaluation of Analysis Errors and Variability Using Synthetic Data

A simple approach to validate the data analysis procedure is to generate synthetic image data and then evaluate how close the results produced by the analysis are to the known true value. A series of artificial images could be created (using an in-house software program) that mimic a multiecho MR experiment. Each image could represent a chosen TE for which the signal intensity in a virtual phantom (could simply be a circle in the center of the image) has been calculated using the known exponential equation that describes the $T_2^{(*)}$ relaxation. Alternatively, more sophisticated simulation approaches as previously described in [3] could be used, accounting for the timings and characteristics of the used RF pulses so as to evaluate the effect of using the simpler monoexponential decay model. Having generated the images, Rician noise is added. This synthetic data could then be analyzed, evaluating both accuracy (how close the resulting $T_2^{(*)}$ is to the true $T_2^{(*)}$) and precision (evaluating dispersion over multiple instances with the same level of SNR).

Table 1
Typical values of T_2 and T_2^* for each specific renal tissue for a healthy rat at 9.4 T [11] and 3 T [12]

Map	Inner medulla	Outer medulla	Cortex
9.4 T [8]			
R_2 [1 s^{-1}]	11.0–14.6	20.0–23.2	23.0–27.3
R_2^* [1 s^{-1}]	32.1–47.2	73.9–101.1	64.8–93.6
3.0 T [9]			
R_2 [1 s^{-1}]	5.5–7.0	9.6–12.5	13.8–16.3
R_2^* [1 s^{-1}]	12.8–19.8	28.3–30.3	29.5–37.5

3.6.2 Comparison with Reference Values from the Literature

The obtained values can be compared with those reported for healthy animals in the literature. Table 1 provides ranges of T_2^* and T_2 for different magnetic field strengths based on current literature.

4 Notes

1. With increasing echo number additional diffusion weighting is added due to the repeated magnetic field gradients used for spatial encoding (NB: this effect is much more pronounced in small animal systems, which use much stronger gradients than clinical systems). A greater bias is introduced by the superposition of stimulated echoes in multi-spin-echo imaging, which leads to significant overestimation of T_2. It also demands the exclusion of the first echo (pure spin echo) from the analysis, because its magnitude is usually much smaller than that of the following echoes, which are combinations of spin-echoes and stimulated echoes. Although these biases depend on the acquisition parameters, they are fixed and reproducible for each protocol and hence acceptable in studies focusing on relative differences/changes, where precision is far more important than accuracy. If needed, more accurate T_2 values can be obtained from multiecho data using sophisticated post-processing, such as dictionary-matching methodologies [3].
2. Make sure your data is ordered from the lowest to the highest TE as in Figs. 2 and 3.
3. When establishing the MR technique, define an SNR acceptance threshold. The aim is to have at least three (preferably five or more) number of echoes with an SNR > 5. This threshold will depend on the expected $T_2^{(*)}$ values, which in turn depend on parameters like the magnetic field strength, shim quality, and tissue properties (pathology). Example: for a rat imaged at 9.4 T using a 4-element rat heart array receiver surface RF coil

together with a volume resonator for excitation in combination with interventions leading to strong hypoxia an SNR > 60 was needed for the image with the lowest TE. Always draw the ROI over the same region of the kidney, that is, cortex, outer medulla, or inner medulla (we use the inner medulla, which is the brightest region of the kidney). If reaching a sufficiently high SNR is a problem, consider creating ROIs and performing the $T_2^{(*)}$-fitting on the average values of these ROIs in order to boost the SNR (SNR scales with the square root of the number of pixels). Another option is to modify the acquisition protocol, reducing the attained spatial resolution to gain SNR.

4. As a good practice you should always save your ROIs for later reference. After creating an ROI click on Analyze > Tools > ROI Manager > Add. Then rename your ROI to a meaningful name (using the button "Rename on the ROI Manager).
5. When you create an ROI over a region with no signal make sure no artifacts are present. Click on Image > Adjust > Brightness and Contrast and drag the scroll bar "Minimum" to the left.
6. Sum-of-squares reconstruction of multichannel data changes the distribution of noisy MR magnitude data. Substitute the factor 0.655 by 0.682 or 0.695 for two channel and four channel data, respectively [13].
7. The Rician distribution of MR magnitude images introduces a signal level-dependent positive bias. The relative error introduced by this bias increases with decreasing SNR. For single receive element coils, an error of 10% is reached at SNR = 2.6. For two-channel or four-channel coils, the corresponding threshold is at SNR = 4.2 or 6.4, respectively, assuming sum-of-squares reconstruction. Under pathophysiological conditions $T_2^{(*)}$ can become significantly shorter and images acquired at high TEs may have a rather low SNR or may even reach noise level. This could result in a poor model curve fit and overestimate the calculated $T_2^{(*)}$. Therefore, data points at high TEs below a predefined SNR threshold should be excluded from the data analysis. Data exclusion can be done either during the acquisition (by not acquiring some echoes) or performed prior to data analysis. The latter is advantageous because the SNR cutoff to exclude data from the fitting can also be adjusted for each pixel individually.
8. When a multiecho sequence is used for T_2-mapping, the first echo must be excluded from the data analysis. The reason is that the first echo is a pure spin echo, unlike all following echoes, which are superpositions of spin-echoes and stimulated echoes. As a result, the first echo has significantly smaller amplitude than the second echo and fitting the model curve to all data points would produce a poor curve fit and an inaccurate T_2 value [10].

9. MLE option refers to "Maximum-likelihood estimator" that takes into account the Rician noise. The noise level is measured as part of the scan. This approach should be robust against noise floor estimation bias and therefore there is no need to exclude later echoes from the analysis [5, 6].
10. An approach to increase the speed of the curve fitting is using a fast mono exponential fit [14]. The MATLAB implementation of the following fit can be downloaded from https://github.com/JoaoPeriquito/T2-s-Mapping under the name *fastExpoFit.m*. The result of a simulation comparing the recommended fast mono exponential fit and the trust-region can be found at the same location under the name *fastExpoFit_Simulation.png*.
11. Pseudocolor representations can be extremely useful for analyzing $T_2^{(*)}$-maps, since they generally enhance the perception of differences within the value range of the parameter. But one needs to be careful when choosing a color map. Parameter maps displayed as images in pseudocolor can potentially be misleading. Small differences in the underlying values may be artificially emphasised by a change in color hue, or a significant parameter difference that can easily be seen in a gray-scale image may be flattened or hidden if there is little change of hue or brightness over a certain range of the color-scale. It is recommended to always use the same color map and scale to improve comparability.

Acknowledgments

The authors wish to thank Dr. Torben Schneider and Dr. Anabea Solana for the contribute of the $T_2^{(*)}$ mapping protocol for Philips and GE scanner, respectively. Portuguese Foundation for Science and Technology (FCT—UID/EEA/50009/2019), and POR Lisboa 2020 (LISBOA-01-0145-FEDER-029686).
This work was funded in part (Thoralf Niendorf, Andreas Pohlmann, Joao Periquito) by the German Research Foundation (Gefoerdert durch die Deutsche Forschungsgemeinschaft (DFG), Projektnummer 394046635, SFB 1365, RENOPROTECTION. Funded by the Deutsche Forschungsgemeinschaft (DFG, German Research Foundation), Project number 394046635, SFB 1365, R ENOPROTECTION).
This chapter is based upon work from COST Action PARENCH IMA, supported by European Cooperation in Science and Technology (COST). COST (www.cost.eu) is a funding agency for research and innovation networks. COST Actions help connect research initiatives across Europe and enable scientists to enrich their ideas by sharing them with their peers. This boosts their research, career, and innovation.

PARENCHIMA (renalmri.org) is a community-driven Action in the COST program of the European Union, which unites more than 200 experts in renal MRI from 30 countries with the aim to improve the reproducibility and standardization of renal MRI biomarkers.

References

1. Niendorf T, Pohlmann A et al (2015) How bold is blood oxygenation level-dependent (BOLD) magnetic resonance imaging of the kidney? Opportunities, challenges and future directions. Acta Physiol (Oxf) 213(1):19–38. https://doi.org/10.1111/apha.12393
2. Pohlmann A et al (2014) Detailing the relation between renal T2* and renal tissue pO2 using an integrated approach of parametric magnetic resonance imaging and invasive physiological measurements. Investig Radiol 49:547–560
3. Ben-Eliezer N, Sodickson DK, Block KT (2015) Rapid and accurate T2 mapping from multi-spin-echo data using Bloch-simulation-based reconstruction. Magn Reson Med 73:809–817
4. Schindelin J, Arganda-Carreras I, Frise E et al (2012) Fiji: an open-source platform for biological-image analysis. Nat Methods 9 (7):676–682. https://doi.org/10.1038/nmeth.2019
5. Senegas J, Knopp T, Dahnke H (2007) Dealing with spatially varying noise in T2* mapping with SENSE. Proceedings of the International Society of Magnetic Resonance in Medicine, Berlin
6. Hedström E et al (2017) Automatic T2* determination for quantification of iron load in heart and liver: a comparison between automatic inline maximum likelihood estimate and the truncation and offset methods. Clin Physiol Funct Imaging 37(3):299–304
7. Moré JJ (1978) The Levenberg-Marquardt algorithm: implementation and theory. Numerical analysis. Springer, Berlin, pp 105–116
8. Byrd RH, Schnabel RB, Shultz GA (1987) A trust region algorithm for nonlinearly constrained optimization. SIAM J Numer Anal 24(5):1152–1170
9. Piskunowicz M et al (2015) A new technique with high reproducibility to estimate renal oxygenation using BOLD-MRI in chronic kidney disease. Magn Reson Imaging 33(3):253–261
10. Pohlmann A, Cantow K, Huelnhagenm T, Grosenick D, dos Santos Periquito J et al (2017) Experimental MRI monitoring of renal blood volume fraction variations en route to renal magnetic resonance oximetry. Tomography 3(4):188–200
11. Pohlmann A et al (2013) High temporal resolution parametric MRI monitoring of the initial ischemia/reperfusion phase in experimental acute kidney injury. PLoS One 8(2):e57411
12. Thacker J, Zhang JL, Franklin T, Prasad P (2017) BOLD quantified renal pO2 is sensitive to pharmacological challenges in rats. Magn Reson Med 78(1):297–302
13. Constantinides CD, Atalar E, McVeigh ER (1997) Signal-to-noise measurements in magnitude images from NMR phased arrays. Magn Reson Imaging 38(5):852–857
14. Pei M et al (2015) Algorithm for fast monoexponential fitting based on auto-regression on linear operations (ARLO) of data. Magn Reson Med 73:843–850

Chapter 37

Analysis of Renal Diffusion-Weighted Imaging (DWI) Using Apparent Diffusion Coefficient (ADC) and Intravoxel Incoherent Motion (IVIM) Models

Neil Peter Jerome and João S. Periquito

Abstract

Analysis of renal diffusion-weighted imaging (DWI) data to derive markers of tissue properties requires careful consideration of the type, extent, and limitations of the acquired data. Alongside data quality and general suitability for quantitative analysis, choice of diffusion model, fitting algorithm, and processing steps can have consequences for the precision, accuracy, and reliability of derived diffusion parameters. Here we introduce and discuss important steps for diffusion-weighted image processing, and in particular give example analysis protocols and pseudo-code for analysis using the apparent diffusion coefficient (ADC) and intravoxel incoherent motion (IVIM) models. Following an overview of general principles, we provide details of optional steps, and steps for validation of results. Illustrative examples are provided, together with extensive notes discussing wider context of individual steps, and notes on potential pitfalls.

This publication is based upon work from the COST Action PARENCHIMA, a community-driven network funded by the European Cooperation in Science and Technology (COST) program of the European Union, which aims to improve the reproducibility and standardization of renal MRI biomarkers. This analysis protocol chapter is complemented by two separate chapters describing the basic concepts and experimental procedure.

Key words MRI, Kidney, Diffusion, Diffusion-weighted imaging (DWI), Apparent diffusion coefficient (ADC), Intravoxel incoherent motion (IVIM), Mouse, Rat, Analysis, Algorithm

1 Introduction

Diffusion-weighted imaging (DWI) can be implemented in many forms, and similarly analysis of DWI data is more complex than for other common quantitative modalities such as T_1, T_2, and T_2* [1, 2]. The overall goal of deriving robust biomarkers for renal function, disease identification and response, as well as monitoring of transplants and so forth [3] relies not only on the suitability of the acquisition for the question being asked, but also how that data are handled in post-processing and analysis.

Andreas Pohlmann and Thoralf Niendorf (eds.), *Preclinical MRI of the Kidney: Methods and Protocols*, Methods in Molecular Biology, vol. 2216, https://doi.org/10.1007/978-1-0716-0978-1_37,

The basic concepts underlying DWI, and example experimental protocols, are discussed in the chapters by Jerome NP et al. "Renal Diffusion-Weighted Imaging (DWI) for Apparent Diffusion Coefficient (ADC), Intravoxel Incoherent Motion (IVIM), and Diffusion Tensor Imaging (DTI): Basic Concepts" and by Periquito J et al. "Renal MRI Diffusion: Experimental Protocol" of this book. This chapter will cover general elements of data quality and analysis, with a view to providing example protocols for the main models employed for renal DWI. As mentioned in the chapter by Jerome NP et al. "Renal Diffusion-Weighted Imaging (DWI) for Apparent Diffusion Coefficient (ADC), Intravoxel Incoherent Motion (IVIM), and Diffusion Tensor Imaging (DTI): Basic Concepts," however, it is critical to note that analysis choices are intrinsically linked to the acquisition strategy itself, most prominently in number and direction of chosen *b*-values used, which means not only that the available choices of analysis are limited by the type of data collected but also that intended analysis should be an integral part of study planning. Analysis itself is naïve to the suitability of the choices of model and algorithm used, for example, and so this responsibility rests with the researcher.

Alternative diffusion models, as well as other mathematical signal representations without explicit physiological meaning, to the ones discussed here are numerous, and include the increasingly popular stretched exponential and kurtosis descriptions, and this field is constantly developing [4–8]. In addition to general considerations, this chapter provides explicit methods for two common diffusion models, namely, the apparent diffusion coefficient (ADC) and the intravoxel incoherent motion (IVIM) models, and describes the estimation of the corresponding diffusion parameters. While the assumption has been made that suitable data has been acquired (*see* the chapter by Periquito J et al. "Renal MRI Diffusion: Experimental Protocol"), no two datasets are alike, and these protocols are presented as guidelines that claim to be neither complete nor sufficient, and are intended only to provide a basic framework whereby a full analysis protocol can be developed. The advantages of more sophisticated algorithms than are presented here are becoming more apparent, and while the full details of these techniques are beyond the scope of this chapter, the reader is encouraged to investigate their potential when considering both analysis protocols and, where possible, study design. When retrospective analysis is performed outside the original study plan, understanding associated limitations and potential problems is crucial to delivering sound conclusions.

Once DWI data has been acquired, an appreciable portion of the available choices has already been made about how the data are presented and packaged. Analysis is thus a purely computational process that can be performed either "manually" using routines developed in-house, ideally in collaboration with specialist MR

physicists or mathematicians, or by using commercially available software packages (including those available on the scanners themselves). The pros and cons of these two approaches are inversions of each other, essentially revolving around transparency of the processes and the ability to design bespoke interrogations of the data, versus using more developed and optimized analysis using tools that require less "up-front" investment of time but which can act as inscrutable "black boxes."

While many of the same issues arise for renal imaging, is it useful to remember that much of current DWI acquisition and analysis development has been in the brain and for neurological applications. While this affords a large amount of literature and advanced techniques, translating from one tissue to another requires a certain degree of circumspection regarding assumptions and reoptimization, if not protocol redesign. Finally, it should be remembered that no level of analysis can ever provide more information than is contained in the data itself, and care should be taken to avoid over-interpretation.

This analysis protocol chapter is complemented by two separate chapters describing the basic concepts and experimental procedure, which are part of this book.

This chapter is part of the book Pohlmann A, Niendorf T (eds) (2020) Preclinical MRI of the Kidney—Methods and Protocols. Springer, New York.

2 Materials

2.1 Data Format and Quality

MRI, including DWI, data are stored as either a manufacturer-specific format (e.g., Bruker) or as a medical imaging standard (e.g., DICOM, NifTI), but in essence contains a series of matrices of intensity values constituting the images, with each image indexed against the acquisition parameters including the diffusion-weighting *b*-value. The exact details of where the *b*-value is stored varies by image format, or the *b*-value may need to be explicitly added (*see* **Note 1**). Commonly, DWI schemes acquire a set of three images for nonzero *b*-value magnitudes, with the diffusion-sensitizing gradients applied in orthogonal directions; this allows for calculation of a *trace image*, where any anisotropy of diffusion is averaged out by taking the geometric mean of the intensities. If possible, the separate images should be used for analysis, since this allows for finer quality control before processing, and will retain the intrinsic weighting (i.e., more data at nonzero points) assumed by fitting algorithms.

A brief visual inspection should identify corrupted data or individual images that need to be excluded on account of severe artifacts or signal dropout, or from insufficient signal-to-noise (SNR). Images and/or cases that display gross motion or distortion may require additional processing steps before being included [9], or can be excluded (*see* Fig. 1).

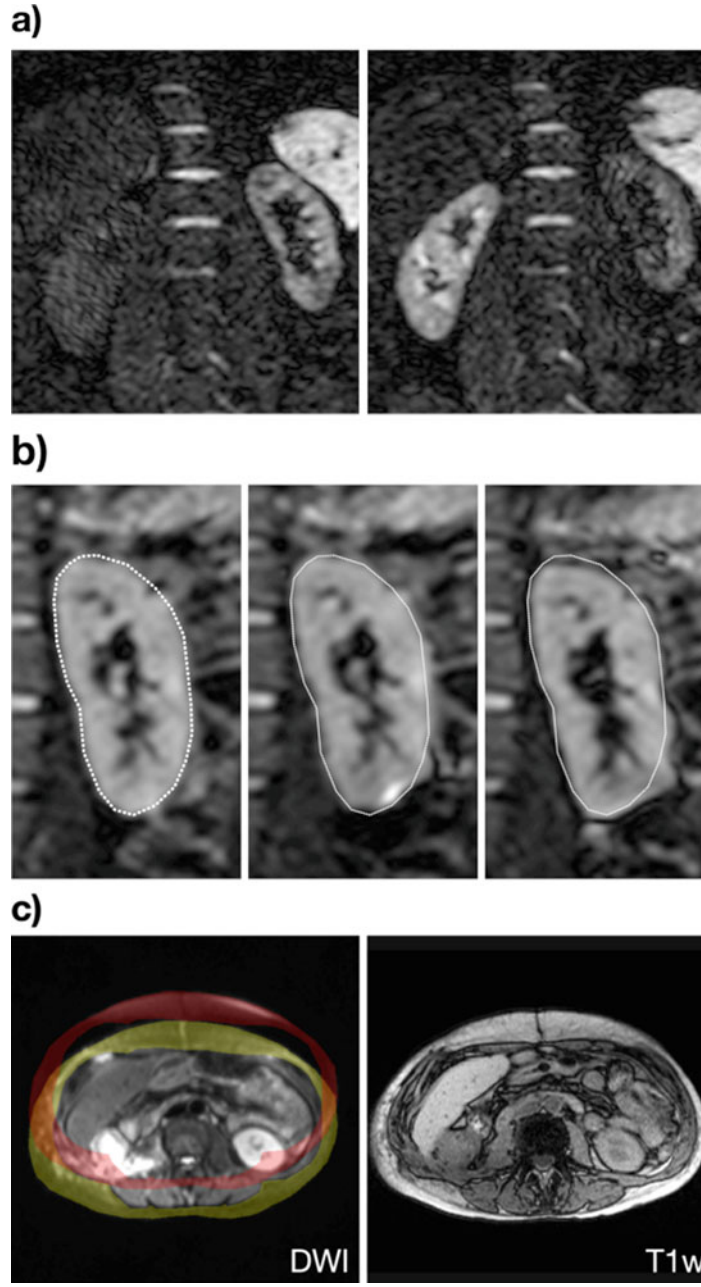

Fig. 1 Examples of images that might be considered for exclusion from analysis. (**a**) Signal drop, which can be uneven across the image, may arise from excessive movement during image readout; these images are the same *b*-value and were acquired in the same sequence, but show markedly different signal in each kidney. (**b**) Three images from the same sequence showing different degrees of distortion around the kidney edge; distortion is a dominant artifact in DWI where EPI is used, and is most prominent at magnetic susceptibility boundaries. (**c**) Imperfect fat suppression in the diffusion-weighted image across the body, combined with the chemical shift displacement of fat protons,

2.2 Software Requirements

Many common mathematical algorithms used for signal fitting are available across many software platforms with limited expertise needed to implement them, meaning analysis routines can be designed and written as needed. Commercial software such as *Matlab* include curve fitting toolboxes, whereas platforms such as *Python* and *R* contain equivalent functions and, being freely available, may present a more accessible or portable choice. In addition, these environments have the ability to handle image data (reading, sorting, displaying) and create figures, though a basic level of programming ability is required. The trade-off is more direct control versus the extra investment required to obtain proficiency with the software environment.

Several freely available software packages are able to perform both image processing and curve fitting, but attempt to give a more intuitive graphical user interface that allows out-of-the-box use, perhaps at the expense of tailored functionality. Environments such as *Fiji* (based on *ImageJ*, with additional plugins), as well as the brain-centric *FSL* and the OSX-only DICOM viewers *Horos* and *OsiriX*, provide different degrees of functionality and automation, and the option for bespoke plugins to at least some degree. The MR scanner itself and associated workstations also offer some options for processing of diffusion images, for example *ParaVision* on Bruker scanners or *SyngoVia* on Siemens, although the available choices and customizability on these systems can be limited.

In the following we present detailed instructions for implementing a custom-made analysis program.

2.3 Fitting Algorithms, Limits, and Initialization

In well-behaved systems with high quality data and appropriate models, choice of fitting algorithm is unlikely to influence the resulting parameters. In many cases, however, data are sufficiently noisy, or there may be cross-correlation between parameters in the model being used, which can mean that choice of fitting algorithm and initialization values can affect the result. These choices are subjective and are made as part of the analysis procedure, so should be reported in publications. Similarly, whether parameters are constrained to physical or anticipated physiological limits may have an effect on reported metrics. Analysis protocols should critically consider these choices as well as report them in scientific articles so that the results can be communicated within the appropriate context.

It is difficult to prescribe "best practice" in diffusion-weighted image processing, since organs and pathologies give a wide-ranging spectrum of situations. Given the highly perfused nature of the

Fig. 1 (continued) may give incorrect intensities from overlap of fat signal with target areas; here, the subcutaneous fat around the abdomen (overlay in yellow; T1w is given for comparison) is shifted up in the image (overlay in red), and will alter the observed image intensity seen for part of the kidney

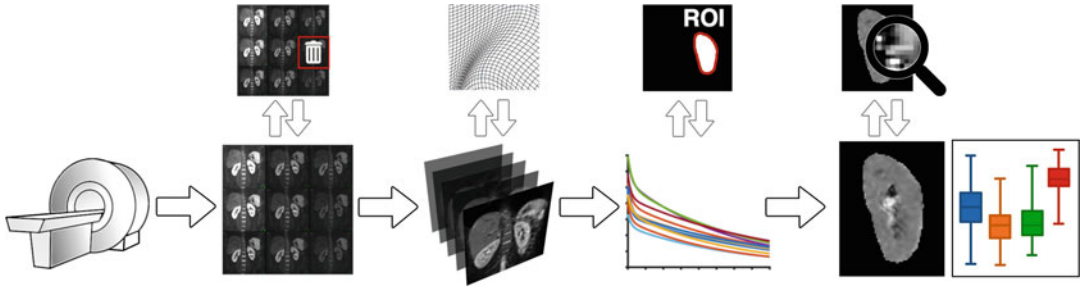

Fig. 2 General overview of the diffusion-weighted imaging pipeline, left to right: Export from the scanner gives the diffusion-weighted images, which should be reviewed for quality (SNR, artifacts, excessive motion, or distortion). The resulting data matrix can be preprocessed using registration, and corrections for eddy currents, distortion, and motion if desired. The fitting algorithm for the chosen model is run either on a region of interest, or on the whole image and the ROI drawn on the parameter maps. A further quality check on the maps and extracted results is recommended

kidney, together with the tubular structures, models such as IVIM that attempt to quantify pseudodiffusion (*see* **Note 2**) are potentially more informative than simple *ADC* measurements, although the analysis is more complex commensurate with the model, and may not give sufficient repeatability for detection of small changes [10]. Overall, standardization of protocols across studies has a value to be balanced against optimization at a local level, where translation of preclinical work into clinical use is the ultimate goal.

3 Methods

3.1 Generalized Steps for Diffusion-Weighted Image Processing

The steps listed here outline a general approach for DWI analysis (Fig. 2). The sections immediately following give more specific instructions for the ADC and IVIM models respectively, which are sufficiently different in complexity to warrant separate presentation and discussion. Notes at the end of the chapter, referenced throughout, give further detail on aspects that may need to be considered.

1. *Retrieve DWI data* to analysis platform: verify *b*-value information, and expected number of images (*see* **Note 1**).
2. *Initial quality check*: SNR threshold (*see* **Notes 3** and **4**) for exclusion of poor images, excessive signal drop-out, distortion, motion, failed fat suppression, and so on.
3. *Preprocessing*: motion correction, distortion correction, and registration if desired/applicable (*see* **Note 5**).
4. *Fitting of the model* to observed signal intensities against their acquisition parameters, normally *b*-value magnitude (*see* **Note 6**).

5. *Second quality check*: visual inspection of parameter maps, extreme values, visualization of fitted curves against the data (*see* **Note 7**).
6. *Extraction of diffusion parameters*. Summary statistics, histogram moments, and so on from a region of interest (*see* **Notes 8** and **9**).

The example protocols below are the constituent parts of a custom-made analysis program, designed to illustrate each step clearly and explicitly (and are thus not optimized for speed), and are presented in pseudo-code using functions and syntax in Matlab (Mathworks, Natick, USA). The wide number of equivalent choices and flexibility of some steps involved in DWI analysis are ignored in favor of presenting the main thread of a workflow that is easy to recreate, and so the reader is encouraged to appreciate the purpose of each step, which can usually be performed in a number of ways with different functions, rather than the specific implementation.

3.2 Diffusion Weighted Imaging: Apparent Diffusion Coefficient (ADC)

3.2.1 Preparation of Image Data for Fitting

1. Retrieve the data to the required folder structure and verify contents.
2. Load image data to matrix structure, aiming to create a 3D matrix of stacked images for each slice (a single slice is presented for simplicity here), with *b*-value in the 3rd dimension (*see* **Note 10**).

```
DICOM: matrix(:,:,i) = dicomread(<i_th_DICOM_filename>);
Bruker: [img,hdr] = read_2dseq(<series/pdata/1>);
```

3. Create a 'bVals' vector variable with the corresponding *b*-values, checking for the correct number of repetitions and the correct order (*see* **Notes 11** and **12**).
4. Review the images for quality: sufficient SNR, artifacts, and so on. Identify and remove any nonqualifying images from the img matrix, and correct bVals to match.

```
exclude = [0 0 0 1 0 0 0 1 1 0 0];
img = img(:,:,~logical(exclude));
bVals = bVals(~logical(exclude));
```

Optional steps at this stage include distortion, eddy current, and motion correction, and image registration (*see* **Notes 5** and **13**).

3.2.2 Least Squares Fitting for Apparent Diffusion Coefficient ADC

1. Define the model for fitting, where the two variables in *X* are *S0* and *ADC* (*see* **Note 14**):

```
curveADC = @(X,bVals) (X(1)*exp(-bVals*X(2)));
```

2. Assign empty matrices for the two resulting maps, using the dimensions of the images (*see* **Note 15**):

```
S0map = NaN(nRows,nCols);
ADCmap = NaN(nRows,nCols);
```

3. For each voxel, loop through each row (i) and column (j) and extract the signal data

```
for i = 1:nRows; for j = 1:nCols;
Sb = img(i,j,:);
```

4. Estimate initial values for the variables to be fitted; use the $b = 0$ s/mm^2 value for *S0*, and approximate *ADC* by taking the gradient of the log signal between two points (*see* **Notes 16** and **17**). *See* also Subheading 3.2.4 for discussion of linearization of *ADC* estimation and fitting.

```
S0_est = Sb(1);
ADC_est = (log(max(Sb))-log(min(Sb)))/
(max(bVals)-min(bVals));
X_est = [S0_est ADC_est];
```

5. Run the least-squares curve fitting routine, using the initial estimates and providing lower and upper boundaries for the estimates if desired (*see* **Note 18**). Assign the results to the allocated results maps:

```
limL = [0 0]; limU = [Inf Inf];
res = lsqcurvefit(curveADC,X_est,bVals,Sb,LimL,LimU);
S0map(i,j) = res(1);
ADCmap(i,j) = res(2);
end; end; % close the row/column loops
```

Some of the options available for least-squares curve fitting include the choice of algorithm, boundary conditions, stopping criteria, number of iterations, and so forth. In general, for well-behaved data the initial estimates will be good and the fitting should converge quickly.

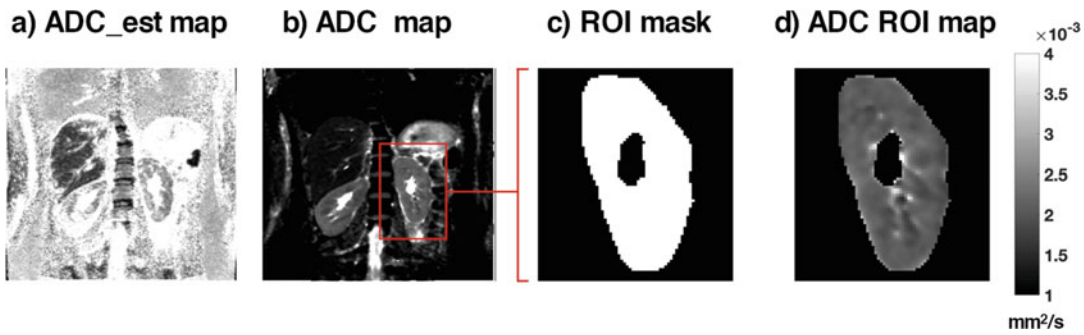

Fig. 3 Example maps from a healthy volunteer illustrating the steps for *ADC* analysis. (**a**) Initial linear estimate of *ADC* gives initial values for least-squares fitting. (**b**) Resulting *ADC* map. (**c**) A binary mask for the region-of-interest drawn on the *ADC* image. (**d**) *ADC* values ready for extraction

3.2.3 Extraction of Parameter Results

1. Review the results maps to visually inspect the results. Data plotted against a signal curve generated from the fitted values for any voxel in the image (i,j) should alert to any issues with either the fitting process or the data itself.

```
Sb = img(i,j,:);
S0 = S0map(i,j);
ADC = ADCmap(i,j);
figure; hold on;
plot(bVals, Sb, 'o'); % show the data
% show the fitted curve
plot(0:max(bVals), S0*exp(-ADC*(0:max(bVals))), 'r-');
```

2. Define the region of interest on the *ADC* map and use this to create a list of voxel coordinates within the ROI. For display, creating a binary mask is also useful (Fig. 3).

```
imagesc(ADCmap);
roi = impoly(); % draw ROI on image
mask = createMask(roi);
ADCmask = ADCmap .* mask;
```

3. Extract the *ADC* values from the ROI to a single matrix for summarizing (mean, median, percentiles, etc.).

```
ADClist = ADCmask(find(ADCmask));
ADC_mean = mean(ADClist);
```

3.2.4 Linear Regression and Matrix Inversion for ADC

Fitting of DWI to the monoexponential ADC model can be achieved with either nonlinear fitting of the signal directly, as above, but can also be treated as a linear regression fitting problem (which is computationally faster) if the natural log of the signal intensities is used (*see* **Note 17**). For the minimal acquisition of

only two *b*-values, there is no ambiguity and the initial estimate calculation shown in Subheading 3.2.2 gives the result.

Taking the signal logarithm also allows for the use of matrix manipulations to perform the linear fitting, which again is computationally faster and handles the whole image simultaneously (*see* **Note 19**).

3.2.5 Computed Diffusion Images

Following calculation of *S0* and *ADC* maps, it becomes possible to create synthetic images at any desired *b*-value based on these values, which may increase conspicuity of lesions at higher *b*-values where noise would dominate in experimentally acquired images. Extension of this technique using an additional echo time *TE* allows similar control for computed T_2 weighting, which may assist with T_2 shine-through from fluid [11, 12].

3.3 Intravoxel Incoherent Motion (IVIM)

Fitting of the more complex IVIM model introduces associated complexity on the analysis, in particular the initialization and algorithm used for fitting [13]. Notably, the fitting for IVIM is inherently nonlinear, and cannot be easily linearized for speed. While more advanced fitting routines become popular (*see* Subheading 3.3.6), the major obstacle to successful IVIM fitting is ultimately the appropriateness of the model to the quality of data available.

In the protocol below, which shares much with the *ADC* protocol in Subheading 3.2, we present the segmented method as a method of initializing a full least-squares fit. The segmented method benefits from speed and stability, and can be used as an estimator in its own right, although it relies on prior assumptions. Parameters from segmented fitting may be fixed for the subsequent least-squares fitting if desired [14–16]. In all cases, the user is strongly encouraged to critically examine the results from IVIM fitting.

3.3.1 Preparation of Image Data for Fitting

This is identical to the preparation steps for *ADC* in Subheading 3.2.1.

1. Retrieve the data to the required folder structure and verify contents.
2. Load image data to matrix structure, aiming to create a 3D matrix of stacked images for each slice (a single slice is presented for simplicity here), with *b*-value in the third dimension (*see* **Note 10**).

```
DICOM: matrix(:,:,i) = dicomread(<ith_DICOM_filename>);
Bruker: [img,hdr] = read_2dseq(<series/pdata/1>);
```

3. Create a bVals vector variable with the corresponding *b*-values, checking for the correct number of repetitions and the correct order (*see* **Notes 11** and **12**).

4. Review the images for quality: sufficient SNR, artifacts, and so on. Identify and remove any nonqualifying images from the img matrix, and correct bVals to match.

```
exclude = [0 0 0 1 0 0 0 1 1 0 0];
img = img(:,:,~logical(exclude));
bVals = bVals(~logical(exclude));
```

Optional steps at this stage include distortion, eddy current, and motion correction, and image registration (*see* **Notes 5** and **13**).

3.3.2 Segmented Fitting for Diffusion Coefficient D

This section is largely the same as fitting for *ADC* in Subheading 3.2.2, with the exception that it is on a subset of the data in order to derive *D*. The parameter *SD* is the equivalent of *S0* but for the *D* compartment only, and is used to estimate *f* in the next section.

1. Choose a threshold *b*-value beyond which it is assumed that the pseudodiffusion signal contribution is negligible; this is commonly around 200 s/mm^2. Create a new (not overwritten) data matrix containing only these images, and matching bVals vector.

```
Bcut = 200;
imgD = img(:,:,[find(bVals >= Bcut)]);
bValsD = bVals(find(bVals >= Bcut));
```

2. Define the model for fitting, directly analogous to *ADC*, where the two variables in X are *SD* and *D*:

```
curveD = @(X,bVals) (X(1)*exp(-bVals*X(2)));
```

3. Assign empty matrices for the two resulting maps, using the dimensions of the images (*see* **Note 15**):

```
SDmap = NaN(nRows,nCols);
Dmap = NaN(nRows,nCols);
```

4. For each voxel, loop through each row (i) and column (j) and extract the signal data:

```
for i = 1:nRows; for j = 1:nCols;
Sb = imgD(i,j,:);
```

5. Estimate initial values for *SD* and *D* by taking the gradient of the log signal between two points (*see* **Note 16**).

```
SD_est = Sb(1);
D_est = (log(max(Sb))-log(min(Sb)))...
/(max(bValsD)-min(bValsD));
X_est = [SD_est D_est];
```

6. Run the least-squares curve fitting routine, using the initial estimates and providing boundaries for the estimates if desired (*see* **Note 18**). Assign the results to the allocated results maps:

```
limL = [0 0]; limU = [Inf Inf];
res = lsqcurvefit(curveD,X_est,bValsD,Sb,limL,limU);
SDmap(i,j) = res(1);
Dmap(i,j) = res(2);
end; end; % close the row/column loops
```

3.3.3 Segmented Fitting for Pseudodiffusion Fraction f

The calculation (not strictly a fitting) of *f*, similar to fitting for *D**, that follows, can also be performed on a voxelwise basis within the loops used for the fitting of *D*. The presentation here is to emphasize the stepwise nature of this procedure.

1. Derive estimate of *f* by calculating the fraction of *S0* (the signal at $b = 0$ s/mm^2) that does not arise from the *D* component. Use the mean $b = 0$ s/mm^2 image if there are more than one.

```
b0img = mean(img(:,:,find(bVals == 0)),3);
fmap = (b0img - SDmap) ./ b0img;
```

3.3.4 Fitting for Pseudodiffusion Coefficient D*

Having estimated *D* and *f* using the segmented method above, *D** can be estimated by a second fitting process of the residuals after subtracting the calculated signal from the *D* component. Though not exactly equivalent, it is common to fix the *D* and *f* values and perform a least-squares fit only for *D** using all the data (*see* **Note 20**). These estimates can be sufficient on their own to provide a result, or they can be used as initial estimates for subsequent nonlinear fitting of all the parameters in the IVIM model (*see* Subheading 3.3.5).

The dependency of IVIM parameters on the specific details of the fitting process is not simple [17], and pseudodiffusion parameters in particular are known to be less repeatable [18]. It is worth reiterating here that DWI acquisition and analysis are closely interwoven, and the utility of derived parameters is ultimately reliant on the acquisition of suitable data.

1. Allocate a matrix for the D^* values (*see* **Note 21**) and the pseudodiffusion fraction signal intensity.

```
Dsmap = NaN(nRows,nCols); SDsmap = NaN(nRows,nCols);
```

2. Define the IVIM model for fitting of D^* (*see* **Note 20**). Note that this uses the fixed values for SD and D so is placed inside the voxel loops.

```
for i = 1:nRows; for j = 1:nCols;
SD = SDmap(i,j); D = Dmap(i,j); F = fmap(i,j);
curveDs = @(X,bVals) ( X(1)*exp(-bVals*X(2)) +...
SD*exp(-bVals*D) );
```

3. Extract the voxel data for the fitting.

```
Sb = img(i,j,:);
```

4. Estimate initial values for the fitted parameters; in this case D^* can be initialized as $10 \times D$, and *SDs* is derived from f from the $b = 0$ s/mm^2 image.

```
SDs_est = F*b0img(i,j); Ds_est = 10*D;
X_est = [SDs_est Ds_est];
```

5. Run the fitting routine, assign the results to maps, and close the loops.

```
limL = [0 0]; limU = [Inf Inf];
res = lsqcurvefit(curveDs,X_est,bVals,Sb,limL,limU);
SDsmap(i,j) = res(1); Dsmap(i,j) = res(2);
end; end;
```

3.3.5 Least-Squares Fitting for Full IVIM Model

The segmented fitting described above should provide good initial values for a full least-squares fitting, using the same framework. Approximation of f and D^* is more challenging than for D (Fig. 4).

1. Define model.

```
curveIVIM = @(X,bVals) ( X(1)*(X(2)*exp(-bVals*X(3)) +...
(1-X(2))*exp(-bVals*X(4)) ));
```

2. Assign matrices for maps.

```
S0full = NaN(nRows,nCols);
ffull = NaN(nRows,nCols);
```

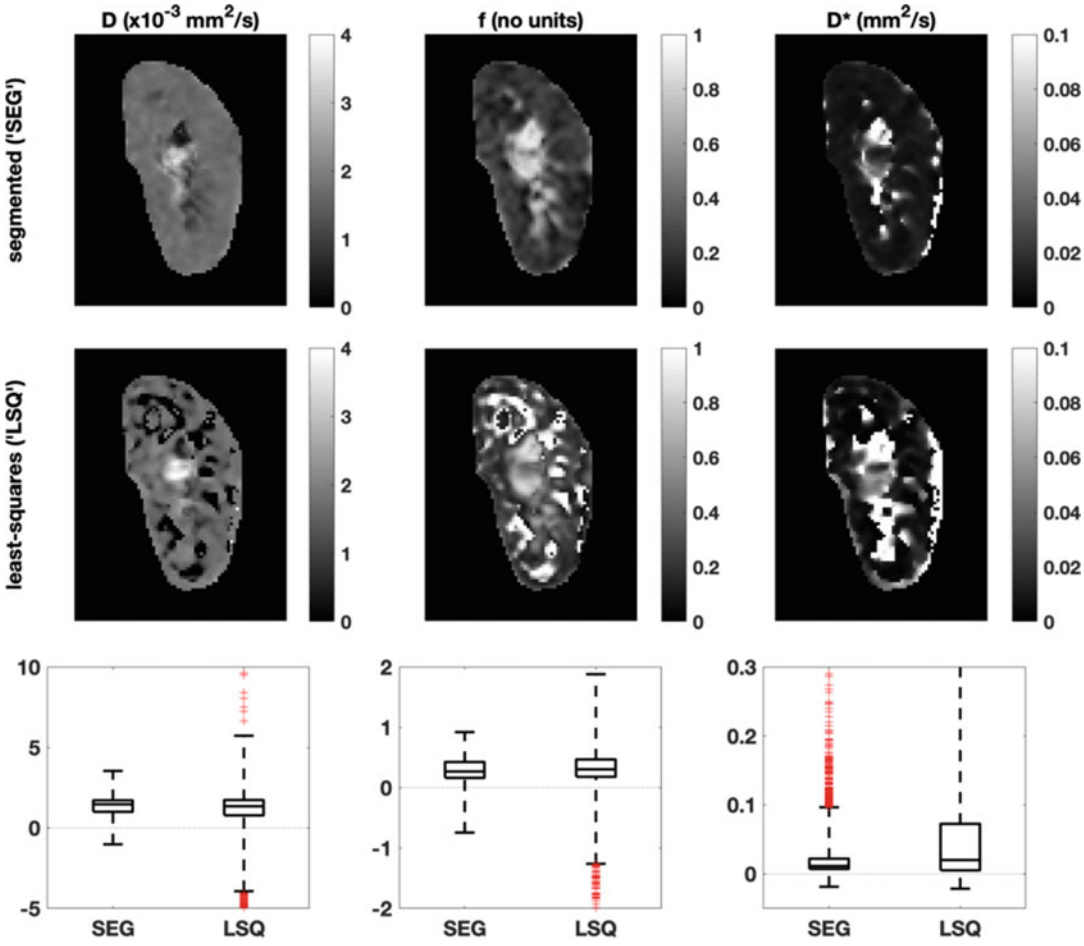

Fig. 4 IVIM parameter maps derived from (top row) segmented approach and (middle row) least-squares using segmented values for initialization. Box plots of the parameter values for the ROI (bottom row, outliers indicated in red) show the voxel spread in more detail and illustrate the relationship between returned parameters and the specifics of the analysis protocol, although the summary parameters are largely similar

```
Dsfull = NaN(nRows,nCols);
Dfull = NaN(nRows,nCols);
```

3. Begin voxel loop and assign initial values.

```
for i = 1:nRows; for j = 1:nCols;
X_est = [b0img(i,j) fmap(i,j) Dsmap(i,j) Dmap(i,j)];
```

4. Run fitting routine.

```
Sb = img(i,j,:);
limL = [0 0 0 0]; limU = [Inf Inf Inf Inf];
res = lsqcurvefit(curveIVIM,X_est,bVals,Sb,limL,limU);
```

5. Assign results to maps and close loops.

```
S0full(i,j) = res(1);
ffull(i,j) = res(2);
Dsfull(i,j) = res(3);
Dfull(i,j) = res(4);
end; end;
```

3.3.6 Spatial Information and Bayesian Fitting Algorithms

Another class of algorithms that have found promising applications for IVIM data are Bayesian methods that utilize additional information not normally considered in conventional fitting strategies [19, 20]. If each voxel is fitted independently, as for the segmented and least-squares approaches outlined above, it is implicitly assumed there is no interrelation between different voxels; in reality, voxels that are either adjacent or within the same tissue (or lesion) are likely to share diffusion and pseudodiffusion characteristics, at least to some degree.

The assumption of spatial similarity can be leveraged against the IVIM model with the view to improving the performance of the fitting, by allowing cross-talk between voxels throughout a series of iterations. These algorithms, by their nature, require many more calculations and so take substantially longer to run; nevertheless, they require no extra data to be acquired and so can be performed retrospectively, and have been shown to produce not only more visually appealing parameter maps but also more meaningful results [17, 21].

4 Methods for Results Validation

4.1 Validation of Fitting Algorithm

One simple way to validate the fitting procedure is to run (and initially develop) the code on synthetic data, generated using known parameters, and to compare the results [21, 22]. A more rigorous validation of the entire pipeline, including data acquisition and transfer, can be performed by scanning a test object with known diffusion parameters [23] using the study protocol.

Curve fitting routines should be able to supply additional output, such as stopping condition and number of iterations used, and these may be useful for troubleshooting, for example identifying where results have hit boundaries or found local minima.

4.2 Visualization of Fitted Curves

Generating signal curves using the derived parameters, and comparing against the original data, is a straightforward way of validating results, and allows examination of areas of interest or apparently spurious results (extreme or suspect values commonly arise from

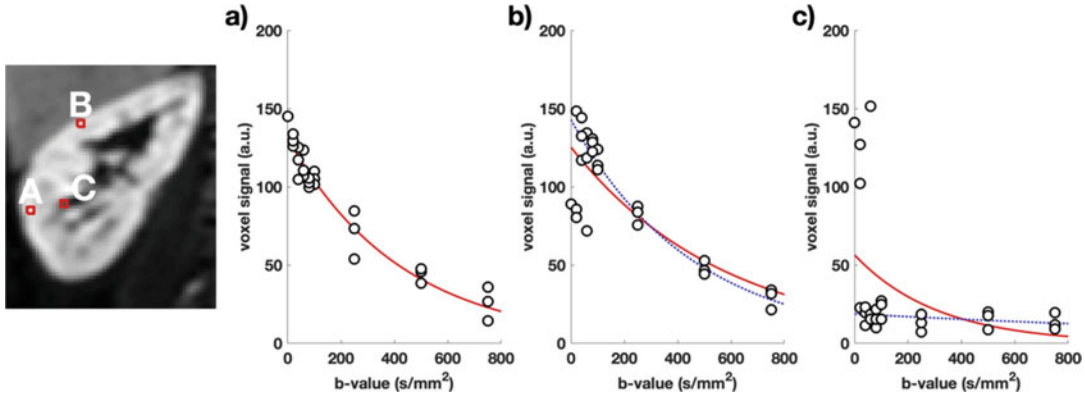

Fig. 5 Typical fitted curves overlaid on the experimental data from voxels in the healthy kidney, with locations indicated in the calculated S0 map shown. (**a**) Good fitting within the kidney parenchyma. (**b**) A voxel near the boundary is susceptible to respiratory motion, with some samples coming from within the liver tissue; the ADC from all the data (red curve) is an underestimation compared to excluding images with substantial motion (blue curve). (**c**) A similar effect is responsible for returning an incorrect curve for a voxel in the renal hilum. Note that exclusion of the same four images would avoid both of these problems, or alternatively registration may ameliorate it to some degree

partial volume or motion in voxels at tissue boundaries, *see* Fig. 5). Identification of particular issues may suggest changes to the analysis routine or, in more severe cases, amendments to the analysis or acquisition protocols. In particular for IVIM results, if the underlying pseudodiffusion fraction is limitingly small (or very large, though this is not expected), the parameter D^* can take essentially any value without affecting the associated signal curve and thus the quality of the fit. This is an intrinsic problem with the model performance in this region of the parameter space, and cannot be solved by acquiring better data.

4.3 Residuals and Systematic Bias

Examining the residuals from the fitting, which are expected to be normally distributed if the model correctly describes the underlying signal, may also highlight bias in the model. Systematic deviation of the residuals over b-values is an indication that the selected signal representation is not optimal, though this does not necessarily preclude it from providing useful parameters (Fig. 6).

4.4 Information Criteria and Model Selection

It may become apparent, from examination of the data, that original assumptions made about the applicability of different models may not be valid. Comparisons of different models must take account of the complexity of the model (number of variable parameters) as well as the number of samples, since additional parameters will always provide a better fit if only residual signal is considered.

There are several forms of such measures, the dominant one being the Akaike information criteria (AIC), formulated using the

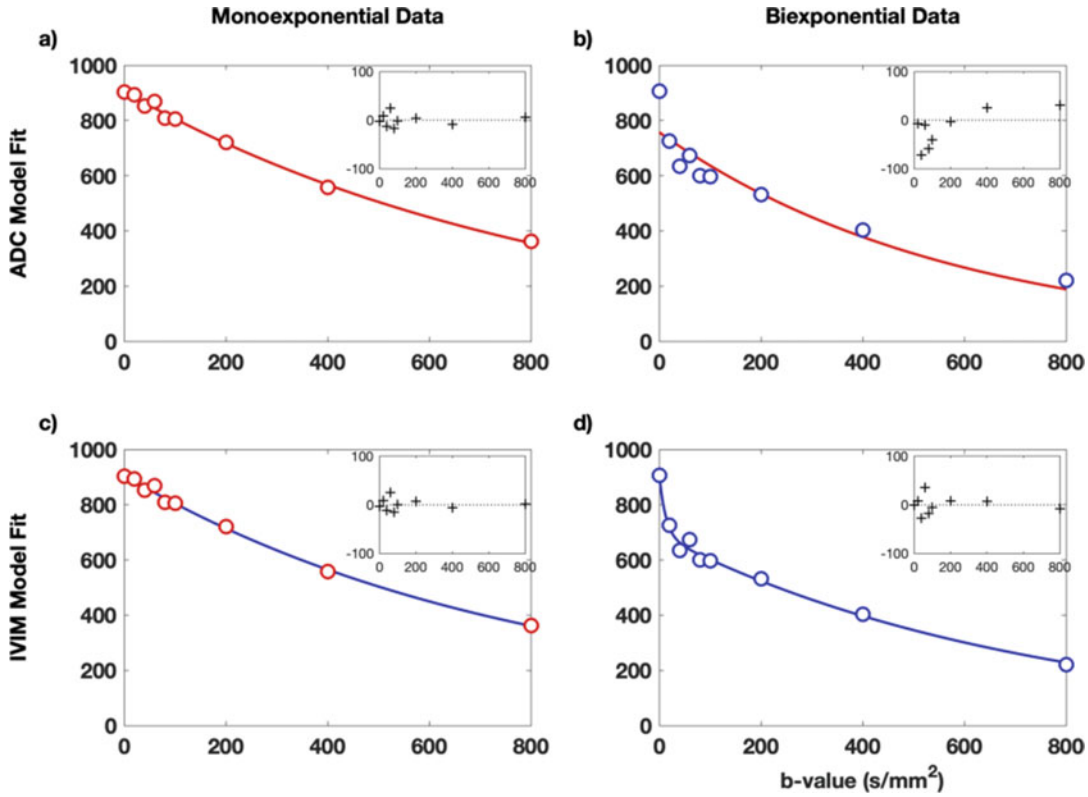

Fig. 6 Example sample fits for synthetic monoexponential (left column, data in red) and biexponential (right column, data in blue) data, fitted with the ADC (top row, curve in red) and IVIM (bottom row, curve in blue) models. Residual signal from each fitting are inset. Where the model matches the underlying signal curve, in (**a**) and (**d**), the residuals are normally distributed. Underfitting the model in (**b**) shows bias in the residuals. Overfitting the data in (**c**) gives a visually acceptable curve and comparable residuals to ADC, but returns $f = 0.98$, $D^* = 0.0012$ mm^2/s, and $D = -0.005$ mm^2/s, which should be flagged as problematic; critical assessment of results should highlight such issues

residual sum-of-squares differences between the observed data and the fitted values at those points (RSS) and the number of data points k:

$$\mathrm{AIC} = -2 \cdot \ln(\mathrm{RSS}) + 2k \tag{1}$$

The AIC thus gives a numerical value that can be compared across models, with lower (or more negative) values being preferred, although the relationship of the AIC to model validation is not straightforward and is sometimes criticised for being too liberal in favoring overly complex models. Nevertheless, it can often provide evidence for questioning assumptions about suitability. Note that an assessment by AIC indicates only which model is best supported by the data, and is not a validation of the model (Fig. 7).

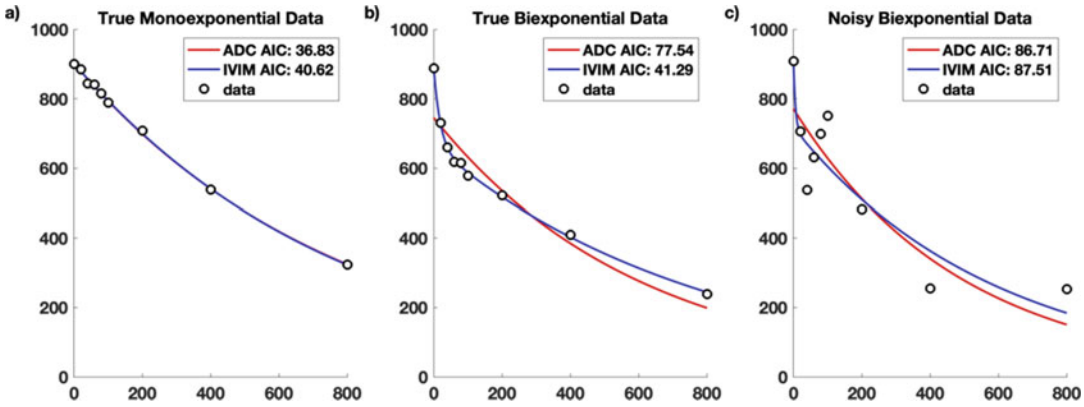

Fig. 7 Comparison of models using the Akaike information criterion (AIC) illustrates what complexity of model is supported by the data but does not necessarily indicate the underlying truth if the data are not of high quality. For (**a**) monoexponential and (**b**) biexponential synthetic data with low noise, the appropriate model fit gives the favorable (lower) AIC value for ADC and IVIM models, respectively, indicated by the lower AIC values in the legend. In (**a**), ADC and IVIM curves are identical, but the simpler ADC model (fewer variables) is favoured. (**c**) With enough noise added, however, the underlying biexponential nature is obscured, and the monoexponential fit with fewer parameters is favored. Axes shown are x: b-value (mm^2s^{-1}) and y: signal (a.u.)

4.5 Covariance and Repeatability

It is critical in quantitative studies to assess the robustness of the derived metrics, and the gold standard for this is to include repeatability studies where the same objects are measured (at least, but commonly only) twice in the same way, and the resulting metrics compared [24]. This is more achievable in preclinical studies, and helps to establish the scale of changes in metrics that can be reliably interpreted as arising from underlying physiological changes. Previous work on the *ADC* in extracranial cancer has shown it to be generally robust [25], whereas there is less certainty about the repeatability of parameters arising from more complex models [10, 18].

Without the benefit of repeated measurements, analyzing the covariance matrix of fitted parameters—that is to say, the extent to which combinations of parameters have the same effect on the fitted curve, can be illuminating. The covariance matrix is a standard output from many fitting routines; high values indicate redundancy between parameters, which in itself is not disqualifying but may indicate a mis-match between the chosen model and the available information in the data.

4.6 Final Analysis Quality Check

Critical assessment of DWI results, no less than the principles of good study design, is essential to avoid wasted time and effort, not to mention the animals used for study, in generating meaningless results. Diffusion-weighted imaging is extremely sensitive to spin motion, which is not simple, and the complexity of the diffusion signal curve is compounded by the additional subtleties of modeling and analysis. In general, mistakes arise as a result of incorrect

assumptions; a review of such assumptions—including attempting to identify those made unconsciously, for example the role of parameters automatically set by the scanner (*see* **Note 22**)—is therefore a vital part of any diffusion analysis protocol.

5 Notes

1. *Location of b-values*. For Bruker data, the method file in the experiment directory contains the full acquisition parameter list; this file is human-readable but is best treated as a reference list where *b*-values can be found by searching for the text "Bval." Export of Bruker data to DICOM varies by software version but may not include the *b*-value in the export. For DICOM files extracted from clinical scanners, the *b*-value is normally located in a private field—for example (0019,100c) in Siemens data—and can be accessed using functions such as dicominfo(<DICOM_filename>) with an appropriate dictionary file. NIfTI files do not contain *b*-value information as standard in their header.
2. *Pseudodiffusion*, rather than perfusion, is a more accurate name for the volume fraction and coefficient associated with the second compartment of the IVIM model, given that it describes only the phenomenon and avoids physiological inference. Particularly in the kidney, the pseudodiffusion observed may arise from both vascular and tubular structures. Even in tissues without the complication of tubular or ductal structures, the term pseudodiffusion should be used, since the apparent pseudodiffusion fraction is known to be dependent on acquisition parameters [26].
3. *A review of images* prior to processing should be performed to ensure that assumptions made about the format and packaging of the data are valid. This includes any naming and/or export order conventions; incorrect assumptions about data presentation and provenance may also introduce errors into results or interfere with smooth processing.
4. *Signal-to-noise* (SNR) for the relevant region is calculated as the mean of the signal divided by the standard deviation of the background noise signal, found from a comparable region containing only noise (i.e., outside the object). This should be tested at the highest *b*-values in particular; it is common to require SNR above a suitable threshold (e.g., 5) for inclusion in the calculation, unless a noise contribution is explicitly included in the model.
5. *Image registration* to account for motion and distortion is a large topic in its own right and there are many strategies available, essentially divided into rigid and non-rigid

techniques. It is useful to avoid averaging within the scanner, for example of separate diffusion directions to form trace images, which can lock in motion errors. Prospective motion correction acquisitions (e.g., gating to respiration) may still require motion correction; more efficient sampling with increased averaging alleviates this problem overall, and allows a wider range of processing options [27, 28].

6. Conventionally, all parameters except *b*-value remain constant through the acquisition, and so *b*-value is the only independent variable. For more complex acquisitions, fitting across several parameters such at *TE* or Δ are needed [26, 29]. For DTI, direction of diffusion-weighting is fitted as well as *b*-value.
7. An *additional quality or "sanity" check* is advised after the fitting procedure; invalid assumptions about model applicability or data quality should become apparent either in the resulting values, or from visual inspection of the parameter maps or fitted curves. Resulting values should always be critically assessed and not just accepted.
8. *Region of interest definition*. Depending on the research question, it may be appropriate to define a region of interest (ROI) based on a calculated parameter map (e.g., *ADC*) or a representative high-*b*-value image, or to transfer an ROI from another modality (e.g., DCE). In the latter cases, it is not necessary to perform diffusion modeling over the whole image, which can save considerable computation where more complex models and algorithms are used. In general, calculation of the parameter map across the whole image gives a better visual overview and may reveal features otherwise missed.
9. The *definition of regions of interest* (ROIs) can be done before or after the model fitting. If done before, the signal through the ROI can be summed (or averaged) and fitted to give a single parameter set to reflect the entire ROI. This approach minimizes the influence of noise, but is predicated on all ROI voxels being the same class of tissue and discards spatial information. Conversely, calculation of entire-image parameter maps can highlight spatial features and help guide to ROI definition. Summary statistics drawn from voxel-wise maps after fitting also discards spatial information, and each voxel fit will be subject to more noise but allows for reporting and analysis of ROI histogram moments.
10. *Reading Bruker format* data into Matlab is not a standard function; the read_2dseq suggested here is available for download from Mathworks [30]. Another alternative, with more direct equivalents in other programming languages, is to read the file directly:

```
file = fopen('<2dseqFile>', 'r');
data = fread(file, 'int16');
img = reshape(data,imageDim1,imageDim2,nSlices,nBVals);
thisSlice = squeeze(img(:,:,sliceNumber,:));
fclose(file);
Other platforms are able to read Bruker format directly, or
convert to a more accessible format (e.g., NIfTI).
```

11. *The order of b-values* is irrelevant for the fitting, but it is convention to handle them in a consistent (usually ascending) order. If the *b*-values are known but without assignation to specific images, the correct assignment can be inferred from the overall image signal intensity if there is sufficient change in contrast between successive images. *b*-value magnitude cannot be inferred from the images if the values are not recorded.
12. *b-values* are usually specified as nominal values entered on the console (e.g., 100 s/mm^2) but, in reality, are modified by the use of the imaging readout gradients themselves (which, like the diffusion-encoding gradients pulses, have both magnitude and direction). It is more correct to use the full *b*-value matrix in the fitting [31], although the imaging gradient contributions are often considered small (e.g., "100" = 105 s/mm^2).
13. *Registration* and/or motion correction can be applied within the diffusion series, or to a separate reference image (e.g., T2w). Distortion correction from eddy currents in EPI images can also be ameliorated by registration to T2w images, or by using phase reversed image pairs if acquired [32].
14. *The S0 maps* from ADC and IVIM fitting are expected to be qualitatively similar to the $b = 0$ s/mm^2 images (for DWI acquisitions with two *b*-values they are equivalent) and are often not considered to be interesting. Nevertheless, the *S0* map is generated using all data and thus may have less influence from confounding factors (noise, distortion, etc.) and may highlight issues arising from the fitting process.
15. When using *custom fitting routines*, certain programming practices such as memory preallocation can save substantial computation time and are worth the extra investment of effort. Full optimization of code is a much larger task, and will give diminishing returns beyond a certain level.
16. *Division by zero*, for example in voxels outside the object (and which are not of interest), may result in infinities or errors that halt the routine. These can be excluded from the fitting loop, assigned an arbitrary default value, or values in Sb can be incremented to an arbitrary small value (e.g., 1) that will not appreciably affect the outcome.

```
Sb = 1 + img(i,j,:);
```

17. *Normalization of signal data* to the $b = 0$ s/mm^2 value is not necessary, and may introduce inaccuracy if the observed signal value at $b = 0$ s/mm^2 is not representative of the underlying *S0* (e.g., in the presence of appreciable perfusion).
18. *Imposing limits* on fitted variables, perhaps to physiological or physical, is possible in many fitting algorithms. One potential pitfall with this approach is if limit values returned from a failed fitting are treated as legitimate (i.e., converged) values, they may bias summary measures. This is an easy oversight if summary statistics are taken and parameter maps/histograms are not examined.
19. *Matrix inversion* is an efficient implementation of linear regression (using the log signal). The whole image can be used at once, although since the 3D data matrix is reshaped for the calculation, care must be taken to reconstruct the resulting maps with the correct dimensions.

```
si = size(img);
dataVect = reshape(img+1,(si(1)*si(2)),si(3));
dataVectLog = log(dataVect');
A = [ones(length(bVals),1) -bVals'];
res = inv(A'*A)*A'*dataVectLog;
res(1,:) = exp(res(1,:));
ADCmap_MI = reshape(res(2,:),si(1),si(2));
```

20. *Segmented fitting for D** can take many flavors, essentially revolving around which parameters are allowed to be free and which are fixed. For example in this implementation, f is already fixed but could be recalculated following fitting for *SDs*. The use of the segmented method as initialization for a full least-squares fitting is an iterative process and can minimize the influence of noise in the $b = 0$ s/mm^2 image, and uncertainty in choosing a suitable Bcut threshold [33].
21. One major need in the IVIM community is the standardization of terminology, including the exact formulation of the model, and even the parameter symbols. This article uses D^* to denote pseudodiffusion coefficient, but owing to the use of the asterisk in Matlab to denote the product, D^* is written Ds in the code.
22. The effect of *diffusion time* (delay between the gradient-encoding pulses, Δ) is yet to be fully described, although it is known to influence IVIM parameters in a similar way to echo time, *TE* [26, 29]. It is thus important to fix, record, and report this during acquisition, similar to *TE*.

Acknowledgments

N.P.J. wishes to acknowledge support from the liaison Committee between the Central Norway Regional Health Authority and the Norwegian University of Science and Technology (Project nr. 90065000).
This work was funded in part (Joao Periquito) by the German Research Foundation (Gefoerdert durch die Deutsche Forschungsgemeinschaft (DFG), Projektnummer 394046635, SFB 1365, RE NOPROTECTION . Funded by the Deutsche Forschungsgemeinschaft (DFG, German Research Foundation), Project number 394046635, SFB 1365, RENOPROTECTION).
This publication is based upon work from COST Action PAR ENCHIMA, supported by European Cooperation in Science and Technology (COST). COST (www.cost.eu) is a funding agency for research and innovation networks. COST Actions help connect research initiatives across Europe and enable scientists to enrich their ideas by sharing them with their peers. This boosts their research, career, and innovation.
PARENCHIMA (renalmri.org) is a community-driven Action in the COST program of the European Union, which unites more than 200 experts in renal MRI from 30 countries with the aim to improve the reproducibility and standardization of renal MRI biomarkers.

References

1. Wolf M, de Boer A, Sharma K et al (2018) Magnetic resonance imaging T1- and T2-mapping to assess renal structure and function: a systematic review and statement paper. Nephrol Dial Transplant 33:ii41–ii50
2. Pruijm M, Mendichovszky IA, Liss P et al (2018) Renal blood oxygenation level-dependent magnetic resonance imaging to measure renal tissue oxygenation: a statement paper and systematic review. Nephrol Dial Transplant 33:ii22–ii28
3. Caroli A, Schneider M, Friedli I et al (2018) Diffusion-weighted magnetic resonance imaging to assess diffuse renal pathology: a systematic review and statement paper. Nephrol Dial Transplant 33:ii29–ii40
4. Taouli B, Beer AJ, Chenevert T et al (2016) Diffusion-weighted imaging outside the brain: consensus statement from an ISMRM-sponsored workshop. J Magn Reson Imaging 44:521–540
5. Notohamiprodjo M, Chandarana H, Mikheev A et al (2014) Combined intravoxel incoherent motion and diffusion tensor imaging of renal diffusion and flow anisotropy. Magn Reson Med 1532:1526–1532
6. Rosenkrantz AB, Padhani AR, Chenevert TL et al (2015) Body diffusion kurtosis imaging: basic principles, applications, and considerations for clinical practice. J Magn Reson Imaging 42:1190–1202
7. Jensen JH, Helpern J, Ramani A et al (2005) Diffusional kurtosis imaging: the quantification of non-Gaussian water diffusion by means of magnetic resonance imaging. Magn Reson Med 53:1432–1440
8. Bennett KM, Schmainda KM, Bennett RT et al (2003) Characterization of continuously distributed cortical water diffusion rates with a stretched-exponential model. Magn Reson Med 50:727–734
9. Le Bihan D, Poupon C, Amadon A, Lethimonnier F (2006) Artifacts and pitfalls in diffusion MRI. J Magn Reson Imaging 24:478–488
10. Orton MR, Jerome NP, Rata M, Koh D-M (2018) IVIM in the body: a general overview. In: Le Bihan D, Iima M, Federau C, Sigmund EE (eds) Intravoxel incoherent Motion MRI. Pan Stanford Publishing Pte. Ltd., Singapore, pp 145–174
11. Cheng L, Blackledge MD, Collins DJ et al (2016) T2-adjusted computed diffusion-

weighted imaging: a novel method to enhance tumour visualisation. Comput Biol Med 79:92–98

12. Blackledge MD, Leach MO, Collins DJ, Koh D-M (2011) Computed diffusion-weighted MR imaging may improve tumor detection. Radiology 261:573–581
13. Gurney-Champion OJ, Klaassen R, Froeling M et al (2018) Comparison of six fit algorithms for the intravoxel incoherent motion model of diffusionweighted magnetic resonance imaging data of pancreatic cancer patients. PLoS One 13:1–18
14. Meeus EM, Novak J, Withey SB et al (2017) Evaluation of intravoxel incoherent motion fitting methods in low-perfused tissue. J Magn Reson Imaging 45:1325–1334
15. Barbieri S, Donati OF, Froehlich JM, Thoeny HC (2016) Impact of the calculation algorithm on biexponential fitting of diffusion-weighted MRI in upper abdominal organs. Magn Reson Med 75:2175–2184
16. Park HJ, Sung YS, Lee SS et al (2017) Intravoxel incoherent motion diffusion-weighted MRI of the abdomen: the effect of fitting algorithms on the accuracy and reliability of the parameters. J Magn Reson Imaging 45:1637–1647
17. Vidić I, Jerome NP, Bathen TF et al (2019) Accuracy of breast cancer lesion classification using intravoxel incoherent motion diffusion-weighted imaging is improved by the inclusion of global or local prior knowledge with bayesian methods. J Magn Reson Imaging 50 (5):1478–1488
18. Jerome NP, Miyazaki K, Collins DJ et al (2016) Repeatability of derived parameters from histograms following non-Gaussian diffusion modelling of diffusion-weighted imaging in a paediatric oncological cohort. Eur Radiol 27:345–353
19. Orton MR, Collins DJ, Koh DM, Leach MO (2014) Improved intravoxel incoherent motion analysis of diffusion weighted imaging by data driven Bayesian modeling. Magn Reson Med 71:411–420
20. Freiman M, Perez-Rossello JM, Callahan MJ et al (2013) Reliable estimation of incoherent motion parametric maps from diffusion-weighted MRI using fusion bootstrap moves. Med Image Anal 17:325–336
21. While PT (2017) A comparative simulation study of bayesian fitting approaches to intravoxel incoherent motion modeling in diffusion-weighted MRI. Magn Reson Med 78:2373–2387
22. Meeus EM, Novak J, Dehghani H, Peet AC (2018) Rapid measurement of intravoxel incoherent motion (IVIM) derived perfusion fraction for clinical magnetic resonance imaging. Magn Reson Mater Phys Biol Med 31:269–283
23. Jerome NP, Papoutsaki M-V, Orton MR et al (2016) Development of a temperature-controlled phantom for magnetic resonance quality assurance of diffusion, dynamic, and relaxometry measurements. Med Phys 43:2998–3007
24. Shukla-Dave A, Obuchowski NA, Chenevert TL et al (2018) Quantitative imaging biomarkers alliance (QIBA) recommendations for improved precision of DWI and DCE-MRI derived biomarkers in multicenter oncology trials. J Magn Reson Imaging. https://doi.org/10.1002/jmri.26518
25. Winfield JM, Tunariu N, Rata M et al (2017) Extracranial soft-tissue tumors: repeatability of apparent diffusion coefficient estimates from diffusion-weighted MR imaging. Radiology 284:88–99
26. Jerome NP, D'Arcy JA, Feiweier T et al (2016) Extended T2-IVIM model for correction of TE dependence of pseudo-diffusion volume fraction in clinical diffusion-weighted magnetic resonance imaging. Phys Med Biol 61: N667–N680
27. Jerome NP, Orton MR, D'Arcy JA et al (2014) Comparison of free-breathing with navigator-controlled acquisition regimes in abdominal diffusion-weighted magnetic resonance images: effect on ADC and IVIM statistics. J Magn Reson Imaging 39:235–240
28. Jerome NP, Orton MR, D'Arcy JA et al (2015) Use of the temporal median and trimmed mean mitigates effects of respiratory motion in multiple-acquisition abdominal diffusion imaging. Phys Med Biol 60:N9–N20
29. Clark C, Hedehus M, Moseley ME (2001) Diffusion time dependence of the apparent diffusion tensor in healthy human brain and white matter disease. Magn Reson Med 45:1126–1129
30. Yen C. read_2dseq :quickly reads Bruker's 2dseq MRI images. In: MATLAB Cent File Exch. https://www.mathworks.com/matlabcentral/fileexchange/69177-read_2dseq-quickly-reads-bruker-s-2dseq-mri-images
31. Zubkov M, Stait-Gardner T, Price WS (2014) Efficient and precise calculation of the b-matrix elements in diffusion-weighted imaging pulse sequences. J Magn Reson 243:65–73
32. Holland D, Kuperman JM, Dale AM (2010) Efficient correction of inhomogeneous static

magnetic field-induced distortion in echo planar imaging. Neuroimage 50:175–183
33. Wurnig MC, Kenkel D, Filli L, Boss A (2016) A standardized parameter-free algorithm for combined intravoxel incoherent motion and diffusion kurtosis analysis of diffusion imaging data. Invest Radiol 51:203–210

Chapter 38

Analysis Protocol for Dynamic Contrast Enhanced (DCE) MRI of Renal Perfusion and Filtration

Frank G. Zöllner, Walter Dastrù, Pietro Irrera, Dario Livio Longo, Kevin M. Bennett, Scott C. Beeman, G. Larry Bretthorst, and Joel R. Garbow

Abstract

Here we present an analysis protocol for dynamic contrast enhanced magnetic resonance imaging (DCE-MRI) data of the kidneys. It covers comprehensive steps to facilitate signal to contrast agent concentration mapping via T_1 mapping and the calculation of renal perfusion and filtration parametric maps using model-free approaches, model free analysis using deconvolution, the Toft's model and a Bayesian approach.

This chapter is based upon work from the COST Action PARENCHIMA, a community-driven network funded by the European Cooperation in Science and Technology (COST) program of the European Union, which aims to improve the reproducibility and standardization of renal MRI biomarkers. This analysis protocol chapter is complemented by two separate chapters describing the basic concept and experimental procedure.

Keywords Magnetic resonance imaging (MRI), Dynamic contrast enhanced (DCE), Contrast agent, Kidney, Mice, Rats, Deconvolution, Toft's model, T_1 mapping, Perfusion, Filtration

1 Introduction

Contrast enhanced imaging is based on the use of endogenous tracers (or contrast agents) with para- or ferromagnetic properties and was proposed in the mid-1980s. The aim was to measure or derive the tissue perfusion and capillary permeability from the signal changes caused by the tracer. Based on the employed imaging technique, this concept is called dynamic susceptibility contrast (DSC) or dynamic contrast-enhanced (DCE) MRI whereby the first is used in conjunction with T_2-weighted imaging techniques whereas the latter is used in T_1-weighted imaging. During such DCE-MRI exams a signal time curve (STC) is recorded that reflects the passage of the tracer through tissue and therefore also the perfusion and filtration of the renal tissue. To analyze the tracer

Andreas Pohlmann and Thoralf Niendorf (eds.), *Preclinical MRI of the Kidney: Methods and Protocols*, Methods in Molecular Biology, vol. 2216, https://doi.org/10.1007/978-1-0716-0978-1_38,

kinetics and the STC various approaches were proposed comprising semiquantitative, model-free, and model based approaches which will be outlined in this chapter [1–6].

Theoretical considerations and acquisition protocols are detailed in the chapters by Pedersen M et al. "Dynamic Contrast Enhancement (DCE) MRI–Derived Renal Perfusion and Filtration: Basic Concepts" and by Irrera P et al. "Dynamic Contrast Enhanced (DCE) MRI-Derived Renal Perfusion and Filtration: Experimental Protocol."

A typical workflow for analyzing DCE-MRI data and for calculating parametric maps of renal perfusion and filtration comprises the segmentation of the kidney and the delineation of the arterial input function (AIF), calculation of T_1 maps to convert voxel-wise STCs to concentration time curves (CTC), model selection, and eventually the calculation of perfusion and filtration parameters [7–10]. There are several existing software packages that can calculate renal perfusion and filtration from a dynamic contrast enhanced MRI scan. However, none of the packages provide a complete solution so that the user has to select the package(s) that fit(s) his needs most.

This analysis protocol chapter is complemented by two separate chapters describing the basic concept and experimental procedure, which are part of this book.

This chapter is part of the book Pohlmann A, Niendorf T (eds) (2020) Preclinical MRI of the Kidney—Methods and Protocols. Springer, New York.

2 Materials

2.1 Software Requirements

The methods described in this chapter require the following software tools:

1. A recent version of the DICOM workstation OsiriX (www.pixmeo.com) or Horos (https://horosproject.org/).
2. UMMPerfusion Plugin version 1.5.3 (http://www.opossumm.de/redmine/projects/ummperfusion).
3. Bayesian Data-Analysis Toolbox (a working manual of the entire Bayesian Data-Analysis Toolbox, including server- and client-side installation and operation instructions, descriptions and operating instructions for software packages and an overview of Bayesian Probability Theory can be found at: http://bayes.wustl.edu/Manual/BayesManual.pdf). Information on server-side and client-side configurations may be found below in **Notes 1** and **2**.

2.2 Source Data: Format Requirements and Quality Check

2.2.1 Input Requirements

To analyze preclinical data with UMMPerfusion, the image data need to be converted into DICOM prior to the analysis [11, 12]. It is recommended to convert DICOM to NIFTI first, then use the NIFTI images for all processing within ROCKETSHIP [13]. Data can be imported into DCE@ur-Lab from DICOM format, Bruker Biospin MRI data format (http://www.bruker.com/products/mr/mri.html), as well as from binary unformatted data [14]. MITK-model fit can import various data formats like DICOM or NIFTI [15].

2.2.2 Prequality Check

Visual inspection is required to check that all slices are aligned as time advances. Slices with clear motion artifacts should be removed. More robustly, data with slight movements can be recovered by coregistration images to suitable baseline image(s).

3 Methods

3.1 Segmentation

For the calculation of whole kidney GFR it is necessary to segment the kidneys and to determine their volume.

3.2 T_1 Mapping

According to the software chosen for performing the analysis the series of images acquired may be converted to a convenient format (e.g., DICOM).

The calculations should be performed only on the pixels obtained from renal segmentation (*see* Subheading 3.1).

More detailed descriptions of T_1 mapping calculations are described in the chapter by Garteiser P et al. "Analysis Protocols for MRI Mapping of Renal T_1."

3.2.1 VTR Analysis

For the analysis of the VTR images a pixel-by-pixel fitting procedure is used to fit the intensities of every renal pixel in the images as a function of TR against the following signal equation

$$S = A + S_o\left(1 - e^{-TR/T_1}\right) \tag{1}$$

where TR is the repetition time, A is a bias intensity, and S_0 is the intensity once reached a plateau.

For every pixel a T_1 value can be obtained according to the fitting of Eq. 1 (an example of T_1 map fitting within the Bruker Paravision® software is shown in Fig. 1).

3.2.2 VFA Analysis

For the analysis of the VFA images a pixel by pixel fitting procedure is used to fit the intensities of every renal pixel in the images as a function of FA against the following signal equation

$$S = A + S_o\left[\frac{\sin FA \times \left(1 - e^{-TR/T_1}\right)}{1 - \cos FA \times e^{-TR/T_1}}\right] \tag{2}$$

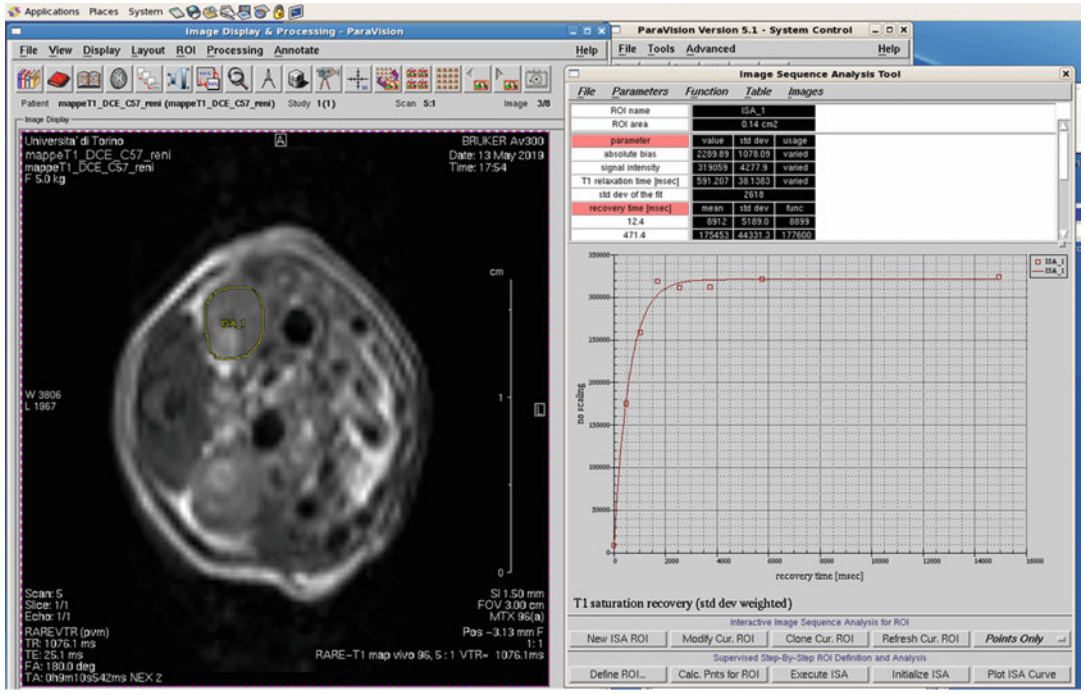

Fig. 1 T_1 map fitting under the VTR scheme performed within the Bruker Paravision 5.1® software for a selected ROI

where FA is the flip angle, TR is the repetition time, A is a bias intensity and S_0 is the intensity reached a plateau.

For every pixel a T_1 value can be obtained according to the fitting of Eq. 2.

3.3 Model Selection and Quantification

Several methods for DCE-MRI analysis have been proposed, with different mathematical representation of physiologic system interpretation through kinetic modeling [1]. Due to the large number of these methods and models, herein we describe only those that are mostly used and that can be easily exploited due to the availability of free software for these analyses. Among them we will consider deconvolution approaches (*see* Subheading 3.4) and extended Toft's model (*see* Subheading 3.5). In addition, a description on how to select the best model based on Bayesian approaches according to the acquired data is also provided (*see* Subheading 3.6).

3.4 Deconvolution Approach

The following steps are based on the UMMPerfusion plugin [12] and the DICOM workstation OsiriX.

1. Open the dataset in the Osirix 4D-viewer (*see* **Note 3**):
2. OsiriX will check if the data selected are a 4D data set (3D spatial plus 1D temporal), however, sometimes this internal check fails. Therefore, an intermediate step might be

Fig. 2 Selecting the UMMPerfusion plugin from the plugin menu of OsiriX

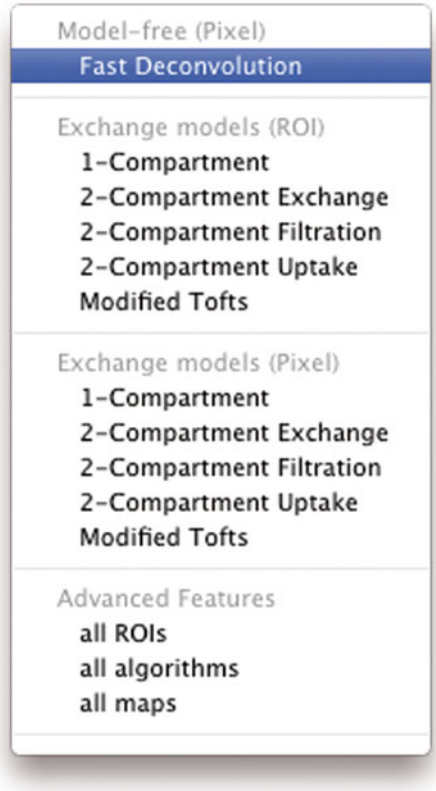

Fig. 3 UMMperfusion drop down menu to select a perfusion model

necessary to load the data into the UMMPerfusion plugin. To do so, select the series in the database window. Press the Alt-Key and click the 2D-viewer's icon at the same time. A window will open. Select/click on the 4D-viewer button, the series will appear within the 4D viewer, although it was not designed for it initially.

3. Start the plugin via the Osirix plugin menu (*see* Fig. 2):
   Plugins → image filter → UMMPerfusion
4. Select algorithm from the tool bar (*see* Fig. 3).

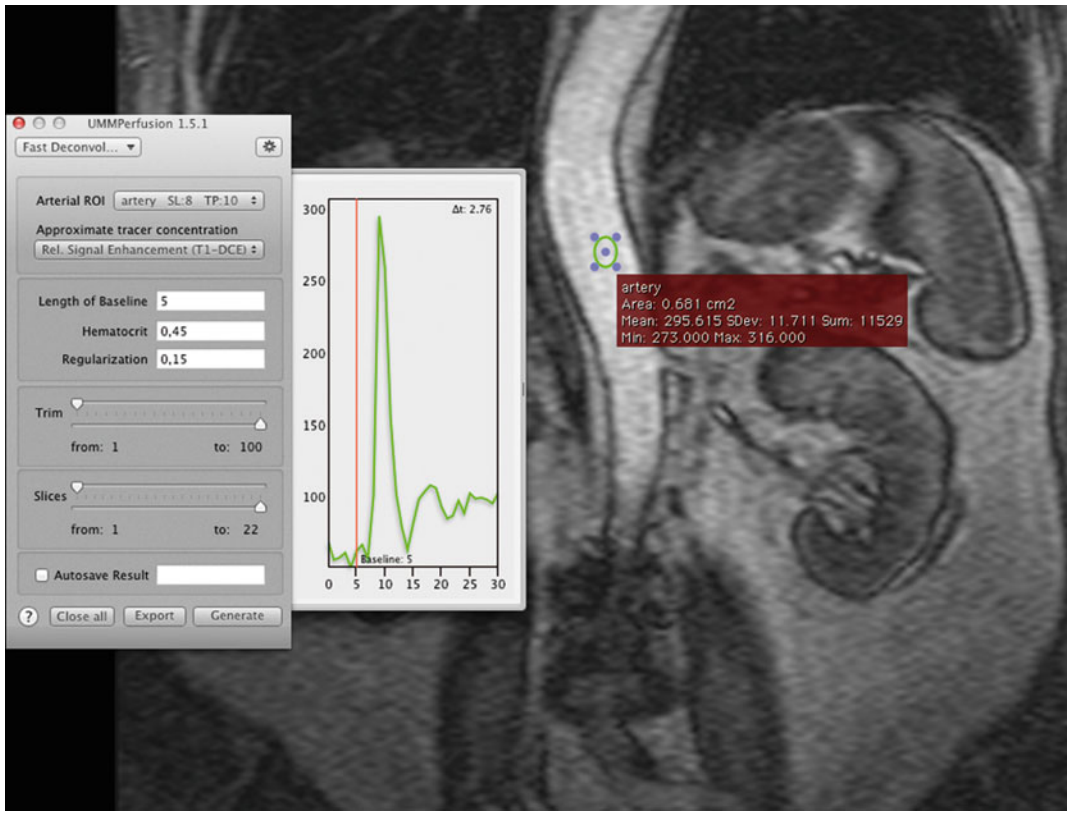

Fig. 4 Example of placing a ROI to select the AIF. The AIF is displayed as a chart next to the plugin

5. Place a ROI on a clearly visible artery in order to receive an arterial input function.
6. For ensuring correct results all algorithms require an arterial input function (AIF). This function is defined by using the Osirix ROI-tool and by placing/designating a "region of interest" (ROI) on the abdominal artery. An oval is used as a standard, however all ROI-tools offered by Osirix are supported by UMMPerfusion.
7. Upon placing a ROI, a chart will appear on the right-hand side of the plugin window, depicting the arterial input function. The aif-color corresponds to the current ROI border color, whereas the vertical line, the base line will always be in red. When a ROI is created, it will be attached to the popup-menu. If several ROIs have been created within this dataset, the desired ROI has to be assigned to its determined position. If only one pixel shall be the source of the AIF, the ROI-Brush-Tool with the size of 1px is to be used in order to specify the smallest ROI possible (Fig. 4).

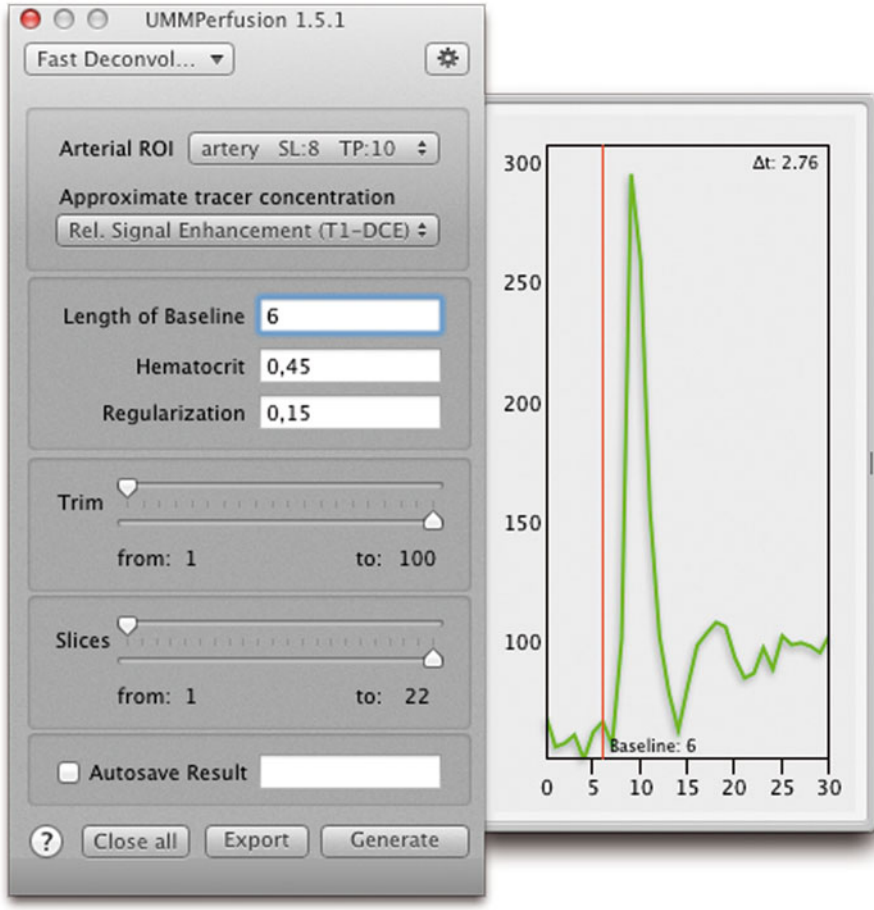

Fig. 5 Selection of the baseline

8. Make sure that the desired ROI is selected in the popup menu called "Arterial."
9. A good ROI selection can be recognized by a large peak on the chart to the right of the plugin-window.
10. Drag the baseline to a desired position or simply enter the value in the respective text field.
11. The length of baseline represents the number of images during a certain period of time that are used for signal normalization. For attaining correct results, the baseline should be chosen in a way that the tracer is not yet visible at that point of time. The easiest way to set the baseline is to drag the baseline with the mouse to its desired timeframe in the AIF-chart. The value can alternatively be inserted into the baseline textfield (*see* **Note 4**, and Fig. 5).
12. Set limits to the relevant scope by using the trim-sliders if necessary.

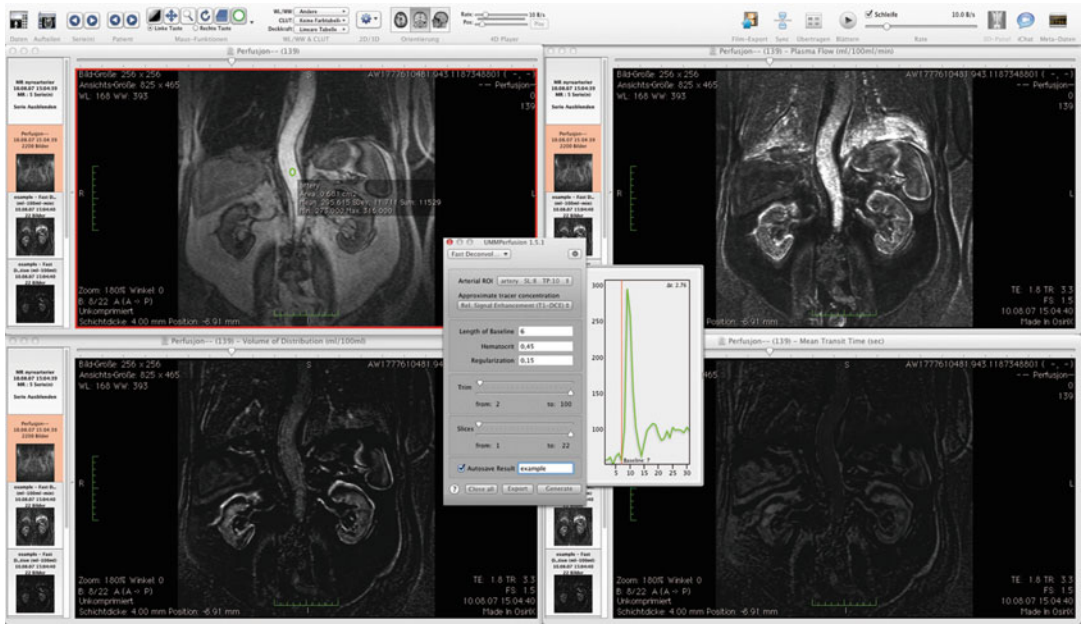

Fig. 6 Example of the result of the deconvolution model implemented in UMMPerfusion. Besides the original DCE-MRI data (top left), three additional viewers are opened presenting parametric maps of blood flow, blood volume, and mean transit time

13. Before hitting the generate-button, there is the opportunity to activate the autosave-checkbox to automatically save the results and to generate a report.
14. The calculation begins after using the generate-button.
15. As a result, three new views/viewers are created in which the calculated data are presented. Each viewer shows one parametric map calculated by the deconvolution approach: blood flow (perfusion) in ml/100 ml/min, the blood volume (ml/100 ml) and the mean transit time (s) (Fig. 6).
16. If the autosave function has not been activated before using the generate button, it is still possible to save the results as well as the report after the calculation. In this case, use the export button next to the generate-button.

3.5 Toft's Model

Three open source packages for renal perfusion and filtration quantification implement the Toft's model, namely, UMMPerfusion [12], ROCKETSHIP [13], MITK-model fit [15], and DCE@urLAB [14]. In the following, the processing steps are given for UMMPerfusion; however, the other three tools can be used in exchange. For details on using them please refer to the respective documentation.

1. Open the dataset in the Osirix 4D-viewer.

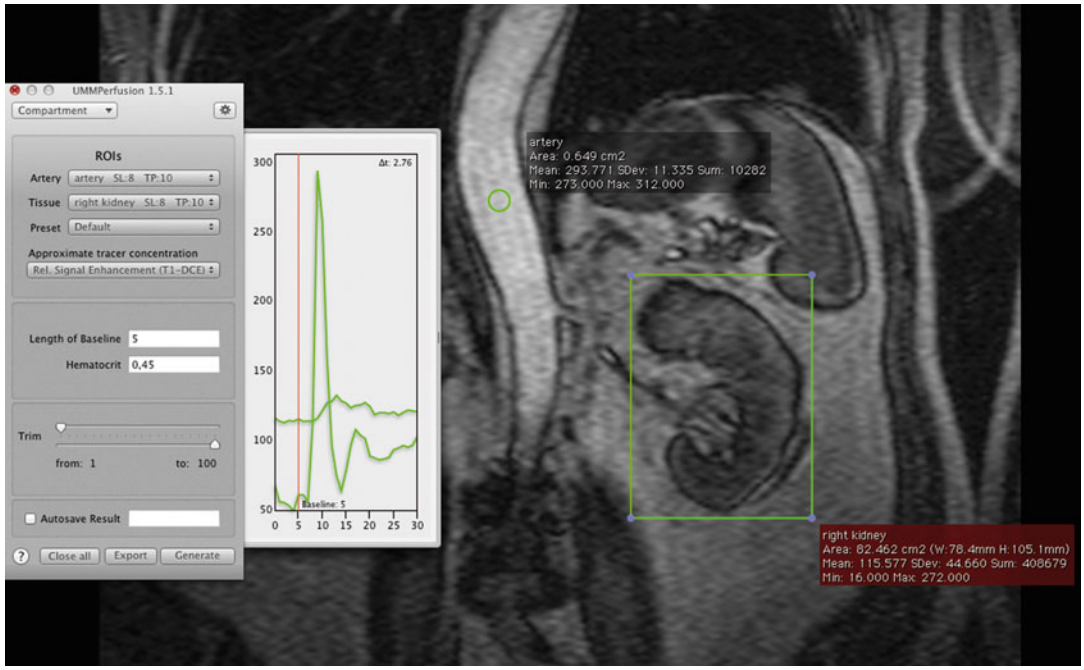

Fig. 7 Example of rectangular ROI placed tight around the kidney. Within this ROI, a voxel-wise fit of the Toft's model is performed, all pixels outside the ROI are not considered

2. Start the plugin via the Osirix plugin menu:
   Plugins → image filter → UMMPerfusion.
3. Select algorithm from the tool bar.
   UMMperfusion implements the extended Toft's model. It can be calculated either ROI-based (*see* **Note 5**) or pixel-wise. The latter is described in the following.
4. Place a ROI on a clearly visible artery in order to receive an arterial input function. The recommended shape of the ROI is oval.
   Please *see* Subheading 3.4 for more details.
5. Place a rectangular ROI on the relevant tissue. When using the pixel-based compartment model algorithms, only a rectangular ROI shape is supported at the moment by UMMPerfusion.
6. The pixelwise calculation might require some time to calculate. To save time, the ROI should be accurately fitting around the tissue that is to be analyzed (*see* Fig. 7).
7. The arterial-ROI and the tissue-ROI do not have to be on the same slice.
8. Make sure that the desired arterial-ROI is selected in the popup menu called "Arterial."
9. Make sure that the desired tissue-ROI is selected in the popup menu called "Tissue."

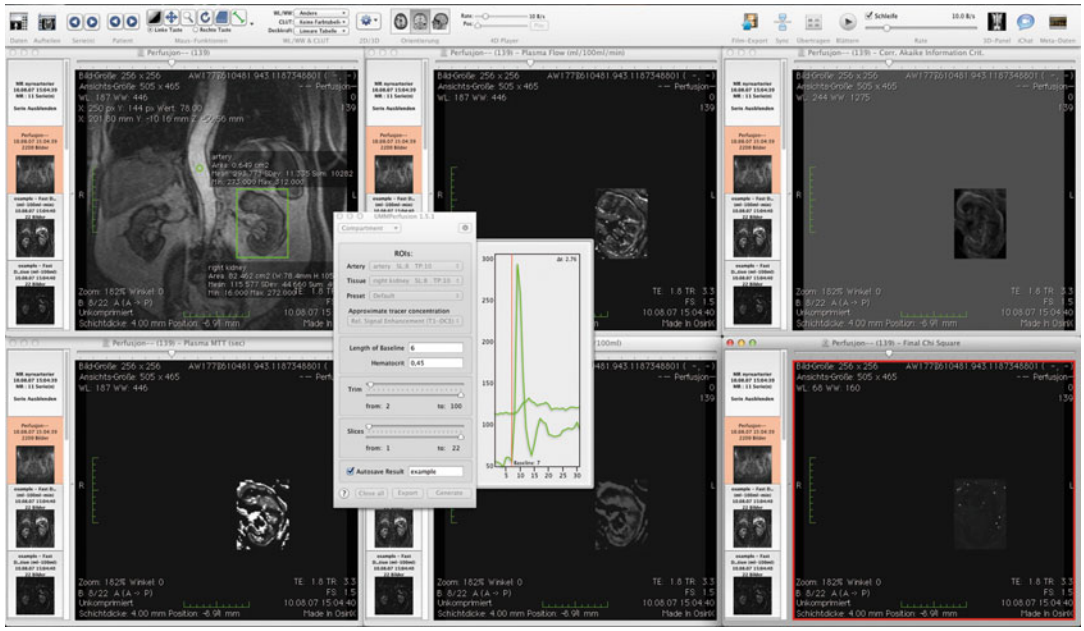

Fig. 8 Example of different parametric maps calculated by the Toft's model. Based on the ROI drawn around the kidney, only voxels within this ROI are used during model fit. Voxels outside the ROI are not taken into account

10. Select the tracer approximation, baseline, and spatiotemporal trimming of the data as described in Subheading 3.4.
11. The calculation begins after using the generate-button. A new window will appear, in which the desired viewers (parametric maps) can be chosen.
12. Upon approval with the OK button the selected viewers will appear and show the specified area (*see* Fig. 8).
13. If the autosave function has not been activated before using the generate button, it is still possible to save the results, as well as the report. In that case, use the export button next to the generate-button. The dataset's name will be appended on your specified name.

3.6 Bayesian Model Selection

3.6.1 Analyzing Regions of Interest Data Using the Enter ASCII Model Package

From the client-side Java interface:

1. Select the "enter ASCII Model" option under the "Package" menu.
2. Load your signal model.
   - Your own signal model can be loaded using the "User" button (links to the client-side .../Bayes/BayesAsciiModels folder, where you should store you model and parameter files).

- A prepackaged "System" model can be loaded using the "System" button (links to Server-side models).

3. Load ASCII data using widgets.
   - File → Load ASII → File.
   - Data file must be in ASCII format.
   - Data are typically in 2-column ASCII format (abscissa, ordinate), however, the software package allows both multicolumn abscissas and ordinates.
4. Build your model using the "Build" button.
5. OPTIONAL: If you believe that your data contains outliers, you can check the "Find Outliers" option under "Analysis Options."
6. Under the "Prior Viewer" tab, review your user-defined prior probability distributions and parameter ranges.
7. If you have multiple servers running the Bayesian Data-Analysis Toolbox, select the desired server for processing the analysis using the "Select" button.
8. OPTIONAL: You can check the status of the selected server using the "Status" button.
9. Run the analysis using the "Run" button.
10. You can monitor the status of the analysis using the Status button or the button bearing a picture of an eye at the bottom left of the window.
11. Once the analysis is complete, retrieve the results using the "Get Job" button or the job will be automatically retrieved when the job status is checked and the job is completed.

3.6.2 Model Selection and Analysis of Region of Interest Data Using the Enter ASCII Model Selection Package

From the client-side Java interface:

1. Select the "enter ASCII Model Selection" option under the "Package" menu.
2. Load all of the signal models that you would like to compare.
   - Your own signal models can be loaded using the "User" button (links to the client-side ../Bayes/BayesAsciiModels folder, where a model and parameter files are stored).
   - Prepackaged "System" models can be loaded using the "System" button (links to Server-side models).
3. Load your data.
   - File → Load ASII → File.
   - Data file must be in ASCII format.
   - Data are typically in 2-column ASCII format (abscissa, ordinate), however, the software package allows for

multicolumn data and abscissaes (See the Bayesian Data-Analysis Toolbox manual, Appendix A for details).

4. Build your models using the "Build" button.
5. OPTIONAL: If you believe that your data contain outliers, you can check the "Find Outliers" option under "Analysis Options."
6. Under the "Fortran/C Model Viewer" → "Parameters" tabs, review your user-defined prior probability distributions.
7. If you have multiple servers running the Bayesian Data-Analysis Toolbox, select desired server for processing the analysis using the "Select" button.
8. OPTIONAL: You can check the status of the selected server using the "Status" button.
9. Run the analysis using the "Run" button.
10. You can monitor the status of the analysis with the Button bearing a picture of an eye at the bottom left of the window, or using the status button.
11. Once the analysis is complete, retrieve the results using the "Get Job" button. The job is automatically retrieved when the job status is checked and the job is completed.

3.7 Voxel-Wise Image Analysis

3.7.1 Analyzing Image Data Using the Analyze Image Pixels Package

From the client-side Java interface:

1. Select the "Analyze Image Pixels" option under the "Package" menu.
2. Load your signal model.
   - Your own signal model can be loaded using the "User" button (links to the client-side ../Bayes/BayesAsciiModels folder, where you should store you model and parameter files).
   - A prepackaged "System" model can be loaded using the "System" button (links to Server-side models).
3. Load your data.
   - File → Load Image.
   - Select the file format of your data.
4. Load an abscissa file (your vector specifying the time at which data were collected, *b*-values, echo times, etc.).
5. Set the noise standard deviation of the data.
   - An acceptable approximation of the noise standard deviation for this purpose would be to draw an ROI in a region of no signal of an image and input the RMS value of this ROI. Tools to make this measurement are available in the main window once data have been loaded—Do not use the standard deviation of the data.

6. Compile your signal model using the "Build" button.
7. OPTIONAL: If you believe that your data contains outliers, you can check the "Find Outliers" option under "Analysis Options."
8. OPTIONAL: If you want a much faster analysis, you can select the "Max Probability" option. The option comes at the cost of only returning the max probability parameter value. No posterior probability distribution information is available if you use this option.
9. Under the "Prior Viewer" tab, review the prior probability distributions.
10. If you have multiple servers running the Bayesian Data-Analysis Toolbox, select desired server for processing the analysis using the "Select" button.
11. OPTIONAL: You can check the status of the selected server using the "Status" button.
12. Run the analysis using the "Run" button.
13. You can monitor the status of the analysis with the status button or the button bearing a picture of an eye at the bottom left of the window.
14. Once the analysis is complete, retrieve the results using the "Get Job" button. The job is automatically retrieved when the job status is checked and the job is completed.

3.7.2 Model Selection and Analysis of Image Data Using the Image Model Selection Package

From the client-side Java interface:

1. Select the "Analyze Image Pixels" option under the "Package" menu.
2. Load all of the signal models that you would like to compare.
   - Your own signal models can be loaded using the "User" button (links to the client-side ../Bayes/BayesAsciiModels folder, where you should store you model and parameter files).
   - Prepackaged "System" models can be loaded using the "System" button (links to Server-side models).
3. Load your data.
   - File → Load Image.
   - Select the file format of your images.
4. Load an abscissa file (your vector specifying the time at which data were collected, b-values, echo times, etc.).
5. Set the noise standard deviation of the data.
   - An acceptable approximation of the noise standard deviation for this purpose would be to draw an ROI in a region of no

signal of an image and input the RMS value of this ROI. Tools to make this measurement are available in the main window once data have been loaded.

6. Build your signal models using the "Build" button.
7. Under the "Fortran/C Model Viewer" → "Parameters" tabs, review your user-defined prior probability distributions.
8. If you have multiple servers running the Bayesian Data-Analysis Toolbox, select desired server for processing the analysis using the "Select" button.
9. OPTIONAL: You can check the status of the selected server using the "Status" button.
10. Run the analysis using the "Run" button.
11. You can monitor the status of the analysis using the status button, or with the Button bearing a picture of an eye at the bottom left of the window.
12. Once the analysis is complete, retrieve the results using the "Get Job" button. The job is automatically retrieved when the job status is checked and the job is completed.

3.8 Results Validation

3.8.1 Evaluation of Analysis Errors and Variability Using Synthetic Data

UMMPerfusion has been in-house certified by the authors and comes with a set of simulated data to test the technical validity of the algorithms. Also, the other software packages provide example data for testing. The Bayesian Data-Analysis Toolbox provides an estimation of uncertainty, even for a single measurement and it has been validated with simulated data for which ground truth is known [4].

Table 1
Values of renal blood flow (RBF) reported in the literature for different animal models and field strengths

Animal model	RBF (ml/100 ml/min)	Field strength, T	Reference
Lewis rats		3	Zimmer et al. [16]
Healthy	542 ± 85		
AKI	407 ± 119		
SD rats		3	Sadick et al. [17]
Healthy	440 ± 86		
PKD	156 ± 40		
PCK	69 ± 23		
Swiss mice		7	Oostendorp et al. [18]
Healthy	481 ± 26		
AKI	451 ± 24		

AKI acute kidney injury, *PKD* polycystic kidney disease, *PCK* autosomal polycystic kidney disease

3.8.2 Comparison with Reference Values from the Literature

Table 1 surveys reference values from the literature for renal blood flow in small rodents. Please note that these values might vary versus those obtained by the reader following this chapter due to different AIF selection and acquisition parameters.

4 Notes

1. Recommended server configuration and server-side installation of the Bayesian Data-Analysis Toolbox: Multicore LinuxPC (32 or 64 cores); 32- or 64-bit processor; Operating system: Linux (CentOS 4.7 or higher) or Sun Solaris 9 or 10; Installing Fortran and C is strongly recommended (required to build and analyze data with your own signal model). Server-side installation instruction can be found at: http://bayesiananalysis.wustl.edu/install.html.
2. Recommended client-side configuration for the Bayesian Data-Analysis Toolbox: any operating system that can run Java 6 or higher. Note that the client machine only runs a Java graphical user interface that the sends and receives jobs from the server-side Bayesian Data-Analysis Toolbox. Through this interface, data can be loaded and visualized, mathematical models can be written in Fortran and tested, jobs can be sent to the server-side software for analysis, and completed jobs can be retrieved from the server-side Bayesian Data-Analysis Toolbox and visualized.
3. If T_1-mapping is available, please convert signal intensities to concentrations beforehand and save this back into DICOM files.
4. If concentration time curves are used, please select the option "Signal enhancement."
5. For examples to perform ROI based analysis with UMMperfusion please see http://www.opossumm.de/redmine/projects/ummperfusion/wiki/Tutorials__How_to_.

Acknowledgments

The Italian Ministry for Education and Research (MIUR) is gratefully acknowledged for yearly FOE funding to the Euro-BioImaging Multi-Modal Molecular Imaging Italian Node (MMMI).

This chapter is based upon work from COST Action PARENCH IMA, supported by European Cooperation in Science and Technology (COST). COST (www.cost.eu) is a funding agency for research and innovation networks. COST Actions help connect research initiatives across Europe and enable scientists to enrich

their ideas by sharing them with their peers. This boosts their research, career, and innovation.

PARENCHIMA (renalmri.org) is a community-driven Action in the COST program of the European Union, which unites more than 200 experts in renal MRI from 30 countries with the aim to improve the reproducibility and standardization of renal MRI biomarkers.

References

1. Sourbron SP, Buckley DL (2013) Classic models for dynamic contrast-enhanced MRI. NMR Biomed 26(8):1004–1027. https://doi.org/10.1002/nbm.2940
2. Sourbron S, Dujardin M, Makkat S, Luypaert R (2007) Pixel-by-pixel deconvolution of bolus-tracking data: optimization and implementation. Phys Med Biol 52(2):429–447. https://doi.org/10.1088/0031-9155/52/2/009
3. Duan C, Kallehauge JF, Bretthorst GL, Tanderup K, Ackerman JJ, Garbow JR (2017) Are complex DCE-MRI models supported by clinical data? Magn Reson Med 77(3):1329–1339. https://doi.org/10.1002/mrm.26189
4. Beeman SC, Osei-Owusu P, Duan C, Engelbach J, Bretthorst GL, Ackerman JJH, Blumer KJ, Garbow JR (2015) Renal DCE-MRI model selection using Bayesian Probability Theory. Tomography 1(1):61–68. https://doi.org/10.18383/j.tom.2015.00133
5. Sourbron SP, Michaely HJ, Reiser MF, Schoenberg SO (2008) MRI-measurement of perfusion and glomerular filtration in the human kidney with a separable compartment model. Investig Radiol 43(1):40–48. https://doi.org/10.1097/RLI.0b013e31815597c5
6. Baumann D, Rudin M (2000) Quantitative assessment of rat kidney function by measuring the clearance of the contrast agent Gd(DOTA) using dynamic MRI. Magn Reson Imaging 18(5):587–595
7. Eikefjord E, Andersen E, Hodneland E, Hanson EA, Sourbron S, Svarstad E, Lundervold A, Rørvik JT (2017) Dynamic contrast-enhanced MRI measurement of renal function in healthy participants. Acta Radiol 58(6):748–757. https://doi.org/10.1177/0284185116666417
8. Ebrahimi B, Textor SC, Lerman LO (2014) Renal relevant radiology: renal functional magnetic resonance imaging. Clin J Am Soc Nephrol. https://doi.org/10.2215/CJN.02900313
9. Sourbron SPMH, Reiser MF, Schoenberg SO (2008) MRI-measurement of perfusion and glomerular filtration in the human kidney with a separable compartment model. Invest Radiol 43(1):40–48
10. Buckley DL, Shurrab AE, Cheung CM, Jones AP, Mamtora H, Kalra PA (2006) Measurement of single kidney function using dynamic contrast-enhanced MRI: comparison of two models in human subjects. J Magn Reson Imaging 24(5):1117–1123. https://doi.org/10.1002/jmri.20699
11. Zollner FG, Daab M, Sourbron SP, Schad LR, Schoenberg SO, Weisser G (2016) An open source software for analysis of dynamic contrast enhanced magnetic resonance images: UMMPerfusion revisited. BMC Med Imaging 16:7. https://doi.org/10.1186/s12880-016-0109-0
12. Zollner FG, Weisser G, Reich M, Kaiser S, Schoenberg SO, Sourbron SP, Schad LR (2013) UMMPerfusion: an open source software tool towards quantitative MRI perfusion analysis in clinical routine. J Digit Imaging 26(2):344–352. https://doi.org/10.1007/s10278-012-9510-6
13. Barnes SR, Ng TS, Santa-Maria N, Montagne A, Zlokovic BV, Jacobs RE (2015) ROCKETSHIP: a flexible and modular software tool for the planning, processing and analysis of dynamic MRI studies. BMC Med Imaging 15:19. https://doi.org/10.1186/s12880-015-0062-3
14. Ortuno JE, Ledesma-Carbayo MJ, Simoes RV, Candiota AP, Arus C, Santos A (2013) DCE@urLAB: a dynamic contrast-enhanced MRI pharmacokinetic analysis tool for

preclinical data. BMC Bioinformatics 14:316. https://doi.org/10.1186/1471-2105-14-316

15. Debus C, Floca R, Ingrisch M, Kompan I, Maier-Hein K, Abdollahi A, Nolden M (2019) MITK-ModelFit: a generic open-source framework for model fits and their exploration in medical imaging - design, implementation and application on the example of DCE-MRI. BMC Bioinformatics 20(1):31. https://doi.org/10.1186/s12859-018-2588-1
16. Zimmer F, Zollner FG, Hoeger S, Klotz S, Tsagogiorgas C, Kramer BK, Schad LR (2013) Quantitative renal perfusion measurements in a rat model of acute kidney injury at 3T: testing inter- and intramethodical significance of ASL and DCE-MRI. PLoS One 8(1). https://doi.org/10.1371/journal.pone.0053849
17. Sadick M, Schock D, Kraenzlin B, Gretz N, Schoenberg SO, Michaely HJ (2009) Morphologic and dynamic renal imaging with assessment of glomerular filtration rate in a pcy-mouse model using a clinical 3.0 Tesla scanner. Investig Radiol 44(8):469–475. https://doi.org/10.1097/RLI.0b013e3181a8afa1
18. Oostendorp M, de Vries EE, Slenter JM, Peutz-Kootstra CJ, Snoeijs MG, Post MJ, van Heurn LW, Backes WH (2011) MRI of renal oxygenation and function after normothermic ischemia-reperfusion injury. NMR Biomed 24(2):194–200. https://doi.org/10.1002/nbm.1572

Chapter 39

Quantitative Analysis of Renal Perfusion by Arterial Spin Labeling

Kai-Hsiang Chuang, Frank Kober, and Min-Chi Ku

Abstract

The signal intensity differences measured by an arterial-spin-labelling (ASL) magnetic resonance imaging (MRI) experiment are proportional to the local perfusion, which can be quantified with kinetic modeling. Here we present a step-by-step tutorial for the data post-processing needed to calculate an ASL perfusion map. The process of developing an analysis software is described with the essential program code, which involves nonlinear fitting a tracer kinetic model to the ASL data. Key parameters for the quantification are the arterial transit time (ATT), which is the time the labeled blood takes to flow from the labeling area to the tissue, and the tissue T_1. As ATT varies with vasculature, physiology, anesthesia and pathology, it is recommended to measure it using multiple delay times. The tutorial explains how to analyze ASL data with multiple delay times and a T_1 map for quantification.

This chapter is based upon work from the COST Action PARENCHIMA, a community-driven network funded by the European Cooperation in Science and Technology (COST) program of the European Union, which aims to improve the reproducibility and standardization of renal MRI biomarkers. This analysis protocol chapter is complemented by two separate chapters describing the basic concept and experimental procedure.

Key words Magnetic resonance imaging (MRI), Kidney, Rodent, ASL, Blood flow, Perfusion

1 Introduction

The signal intensity differences measured by an arterial-spin-labelling (ASL) magnetic resonance imaging (MRI) experiment are proportional to the local perfusion, which can be quantified with kinetic modeling. To calculate the perfusion map, an additional T_1 relaxation map should be obtained from inversion recovery data acquired with the same image acquisition method (eg, Spin-Echo EPI or RARE) and geometry setting.

Creation of perfusion maps involves nonlinear fitting of a tracer kinetic model to the ASL data. Depending on the type of ASL sequence—pulsed or (pseudo)continuous—the model is slightly different. Two key parameters in the quantification are the arterial transit time (ATT), which is the time the labeled blood taken to

Andreas Pohlmann and Thoralf Niendorf (eds.), *Preclinical MRI of the Kidney: Methods and Protocols*, Methods in Molecular Biology, vol. 2216, https://doi.org/10.1007/978-1-0716-0978-1_39,

flow from the labeling area to the tissue, and the tissue T_1. As ATT varies with vasculature, physiology, anesthesia, and pathology, it is recommended to measure it using multiple delay times (i.e., multiple TI in pulsed ASL, or multiple postlabeling delays in continuous ASL). In the kidney, the cortex and medulla have different T_1. T_1 could also change depending on the pathological conditions. Therefore acquiring a T_1 map is desirable. This chapter focuses on how to analyze ASL data with multiple delay times and a T_1 map for quantification.

This analysis protocol chapter is complemented by two separate chapters describing the basic concept and experimental procedure, which are part of this book.

This chapter is part of the book Pohlmann A, Niendorf T (eds) (2020) Preclinical MRI of the Kidney—Methods and Protocols. Springer, New York.

2 Materials

2.1 Software Requirements

The method described in this chapter provides a detailed description for a solution in MATLAB, but can be adopted to other platforms:

1. A programming environment capable of applying fitting models, such as Python, Octave, R or MATLAB®.
2. A software to convert the data format from DICOM or vendor proprietary format (eg, Bruker 2dseq) to the NifTi format, such as dcm2nii (for DICOM; https://people.cas.sc.edu/rorden/mricron/dcm2nii.html), or Bru2Nii (for Bruker 2dseq; https://github.com/neurolabusc/Bru2Nii).
3. An image viewing software such as Fiji (www.fiji.sc) or MRIcro (https://www.mccauslandcenter.sc.edu/crnl/mricro).
4. A software for motion correction, such as SPM, FSL, or AFNI.

2.2 Source Data: Format Requirements

2.2.1 Input Requirements

To be able to calculate perfusion maps, ASL data with interleaved control and label images and multiple delay times, and a T_1 mapping acquired with inversion recovery are needed. For more details on the basic concept of ASL please refer to the chapter by Ku M-C et al. "Noninvasive Renal Perfusion Measurement Using Arterial Spin Labeling (ASL) MRI: Basic Concept." The data acquisition is described in a step-by-step manner in the chapter by Chuang K-H et al. "Renal Blood Flow Using Arterial Spin Labeling (ASL) MRI: Experimental Protocol and Principles."

2.2.2 Intensity Scaling of Multiple Delay ASL Data

If the ASL data of multiple delay times was acquired by separate scans (eg, one delay time for one scan) but not all within the same scan, there could be a difference in the intensity scaling among separate scans due to changes in receiver gain and/or internal scaling factor during image reconstruction. Such a difference

could lead to artifactual intensity among delay times leading to bias in the model fitting and inaccurate perfusion quantification.

On Bruker MRI systems, the default intensity scaling is set to maximize the dynamic range of the output format. Therefore scans with lower signal would be magnified. The intensity scaling method in the "Reconstruction" class should be changed to "User Scaling" with a scaling factor of 1 for all the scans.

To ensure the same intensity scaling of the ASL data, the receiver gain may be extracted from the header information ("RG" variable in the "acqp" file) and used to rescale the data.

2.2.3 Format Conversion

Convert all data into 4D NifTi format. Consider magnifying the voxel size by 10 in the image header if motion correction tools designed for humans (eg, FSL or SPM) will be used (*see* **Note 1**).

3 Methods

3.1 Quality Control/ Data Exclusion

During the ASL image acquisition, movement of the body or kidney itself can occur. Artifacts may also arise from ASL labeling pulses. In order to construct accurate perfusion maps, it is important to ensure that the scan series don't show severe movement, spikes, banding artifacts, or sudden changes in SNR. Scans with poor quality or large movement should be discarded.

1. Open each dataset by a NifTi image viewer.
2. Adjust the window/level (or reduce the maximum intensity range) to visualize the image better.
3. Scroll through each time frame to visually check whether there are sudden changes in intensity or movement.

3.2 Motion Correction

ASL perfusion imaging, due to its subtraction between label and control images, is very sensitive to movement. Despite respiratory trigger, slight movement between scans could still be present. Motion artifact maybe reduced by rigid-body motion correction tools in many software packages. Since most motion correction algorithms (regardless correlation or square error based cost function) rely on intensity changes for detecting movement, the intensity changes between control and label images and between scans of different delay times (particularly for FAIR ASL) could lead to pseudo motion. Besides, the T_1 mapping data should also be coregistered to the ASL data. Therefore, it is recommended to realign images to the same reference target, (e.g., the M_0 image or an averaged image). Additionally, use "cost functions" that are less dependent on the global intensity difference, such as normalized correlation or mutual information, and avoid using least square error (*see* **Note 2**).

1. Use FSL mcflirt to do motion correction on the ASL data (ASL_DATA_TI1.nii) using the mean image as the reference target, normalized correlation as the cost function, and spline for interpolation:
   mcflirt -in ASL_DATA_TI1.nii -out rASL_DATA_TI1 -cost normcorr -meanvol -spline_final.
2. Do motion correction on another ASL data set (ASL_DATA_TI2.nii). This time using the mean image generated from the first step as the reference target:
   mcflirt -in ASL_DATA_TI2.nii -out rASL_DATA_TI2 -cost normcorr -reffile ASL_DATA_TI1_meanvol.nii -spline_final.
3. Repeat the same procedures until all the ASL data are coregistered.
4. Similarly, do motion correction on T_1 mapping data (T1MAP.nii) also using the mean image generated from the first step as the reference target:
   mcflirt -in T1MAP.nii -out rT1MAP -cost normcorr -reffile ASL_DATA_TI1_meanvol.nii -spline_final.

3.3 Quantification of M_0 and T_1

Both M_0 and T_1 are important parameters needed in ASL kinetic model. Besides, the inversion efficiency will be used for FAIR ASL quantification to correct its "labeling efficiency."

3.3.1 Model Equations

The most common method to obtain these parameters is to fit the model of an inversion recovery experiment to the signal intensity data of each pixel at various TI, $M(\mathrm{TI})$, using the following equation:

$$M(\mathrm{TI}) = \mathrm{abs}\left[M_0\left(1 - 2\alpha e^{-\frac{TI}{T_1}}\right)\right], \quad (1)$$

where M_0 is the fully relaxed magnetization signal which is a scaling factor that includes many parameters such as the proton density together with the coil sensitivity and the signal gain of the system. α is the inversion efficiency of the inversion pulse ($\alpha = 1$ for a perfect inversion), and T_1 is the longitudinal relaxation time.

3.3.2 Starting Values

An important step of the curve fitting process is the choice of suitable starting values for each parameter that will be determined by the fitting algorithm (NB: different starting values may lead to different results!). Here we describe how to derive starting values from the SI of each pixel.

1. Step through all pixels in the images using for loops for the pixel coordinates x and y.
2. Store the SI of that pixel at all TIs in a vector (in Matlab: SI_vector = imgData_forFitting(xPix, yPix,:)).

3. As starting value for the parameter M0 use the largest SI (in Matlab: startVal_M0 = max(SI_vector)).
4. For estimating a starting value for T1, one can exploit the fact that the null point of an inversion recovery, where the SI is 0, is $TI = \ln 2 \times T_1 = 0.693 \times T_1$. Estimate the starting T_1 value by finding the TI whose SI is minimal:
5. Find the index of the smallest value in the vector (in Matlab: [min_Value,min_Index] = min(SI_vector)).
6. Get the respective TI using the index from the last step and divide by ln2 to estimate T_1 (in Matlab: startVal_T1 = TI_forFitting(min_Index)/0.693).

As for a starting value for α, one can assume that is close to 1 (in Matlab: startVal_alpha = 1).

3.3.3 Fitting Algorithm

Least squares algorithms, such as the Levenberg–Marquardt and Trust-region methods, are the most commonly used curve fitting algorithms for T_1-mapping. They work by minimizing a cost function, which describes the deviation of the fitted curve from the data points. With starting values near the optimal solution they quickly converge, but with starting values far away from the solution, the Levenberg–Marquardt algorithm will slow down significantly. Also, there is the risk that it may converge to a local minimum (rather than the global minimum) and hence produce a wrong result.

In contrast, the Trust-region method (a further development of the Levenberg–Marquardt algorithm) will quickly converge, even with suboptimal starting values, and it will always find the global minimum. However, it does require the definition of lower and upper limits for the parameters to be fitted. Hence, for T_1-mapping, where such limits can easily be defined, the Trust-region method is well suited (*see* **Note 3**).

1. Create for loops for pixel coordinates x and y to step through all pixels of the image.
2. Store the SI of that pixel at all TIs in a vector (in Matlab: SI_vector = imgData_forFitting(xPix, yPix,:)).
3. Define the model for the function using Eq. 1 (in Matlab: T1model = fittype('abs(a*(1-2*c*exp.(−x*b)))', 'independent', 'x', 'dependent', 'y')).
4. Initialize the fitting options in Matlab: opts = fitoptions (T1model);
5. Choose the function for the fitting algorithm, that is, Trust-region or, if not available, then Levenberg–Marquardt (in Matlab: opts.Algorithm = 'Trust-Region').
6. Provide the starting values for M_0 and T_1 (in Matlab, e.g., opts. StartPoint = [startVal_M0 startVal_T1 startVal_alpha]).

7. Define lower and upper limits for the fit parameters. Use T1 [1 9000], α [0 1] and for M_0 the possible range of SI in the image data (this depends on the system; for 16-bit integer it may be [1 65536]). In Matlab, for example, opts.Lower = [1 1 0]; opts.Upper = [65536 9000 1].
8. Execute the curve fitting for each pixel data (in Matlab: [fitresult, gof] = fit(TI_forFitting, SI_vector, T1model, opts);).
9. Save the fit result for each variable in parameter maps: mapM0(xPix, yPix) = fitresult.a; mapT1(xPix, yPix) = fitresult.b; mapAlpha(xPix, yPix) = fitresult.c; rsquare(xPix, yPix) = gof.rsquare.

Besides using Matlab, inversion recovery T_1 curve fitting can be done by using ImageJ. QuickVol II (http://www.quickvol.com/launch2.html) is a powerful ImageJ plugin that supports fitting the inversion recovery data and other user defined equation. The reader should refer to the user's manual on how to use the plugin.

3.3.4 Visual Display

1. Display the parameter map, which is a matrix with floating point numbers, as an image (in Matlab: imagesc(mapT1);).
2. Remove axis labels and ensure that the axes are scaled equally, so that pixels are square and not rectangular (in Matlab: axis off; axis equal;).
3. Select the color map and display a color bar (in Matlab: colormap(jet(256)); colorbar;) (*see* **Note 4**).
4. Set the display range for the color coding, for example, for T_1 [0 2000]; (in Matlab: caxis([0 2000]);).

3.4 Quantification of Perfusion

3.4.1 Model Equation for FAIR-ASL

The pairwise subtracted perfusion-weighted signals at different TIs, ΔM(TI), can be fitted to the following kinetic function [1] (*see* Fig. 1):

$$\Delta M(\mathrm{TI}) = 2M_0\alpha f/\lambda\left[\frac{\exp\left(-\mathrm{TI}/T_{1\mathrm{app}}\right) - \exp\left(-\mathrm{TI}/T_{1\mathrm{a}}\right)}{\left(1/T_{1\mathrm{a}} - 1/T_{1\mathrm{app}}\right)}\right] \quad (2)$$

where $1/T_{1\mathrm{app}} = 1/T_1 + f/\lambda$, f is the quantified perfusion in ml/100 g/min, λ is the blood–tissue partition coefficient. In the above equation, M_0 represents the equilibrium magnetization derived from T_1 mapping, T_1 the tissue longitudinal relaxation time, and α (the inversion efficiency) are all determined from the curve fitting of the inversion recovery T_1 mapping data. λ is a value typically derived from literature which ranges between 0.52 and 0.94 have been reported in [2]. Here, $\lambda = 0.9$ ml/g can be used based on studies in the brain [3]. However, the suitable value for the kidney remains to be determined. $T_{1\mathrm{a}}$ is the longitudinal relaxation time of arterial blood, which is field strength dependent. A

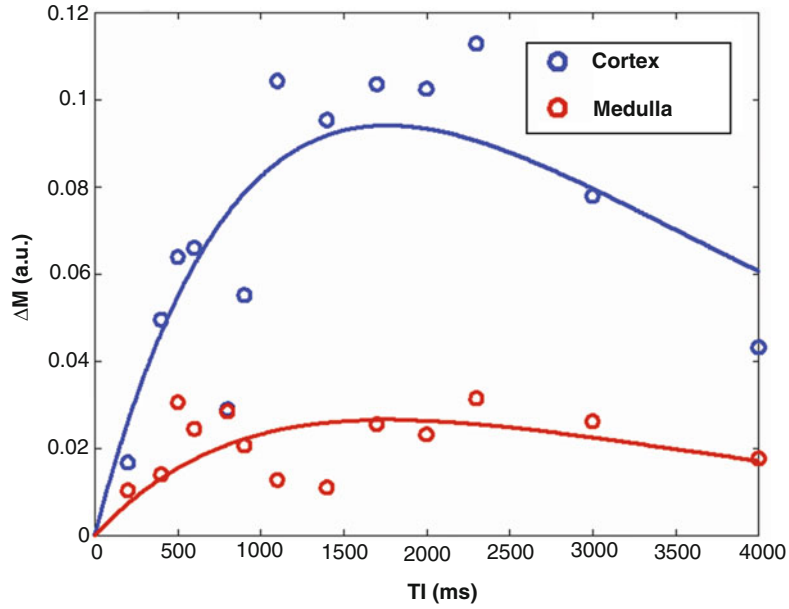

Fig. 1 Fitting perfusion-weighted signal from ROIs in the renal cortex and medulla to the FAIR-ASL kinetic model described in Eq. 2

value of 2.21 s can be used at 7 T [4]. And the blood T_1 at other field strength can be calculated using the equation in [4] (*see* **Note 5**).

3.4.2 Pairwise Subtraction

The first step is to generate the ΔM image of each TI, and then concatenate the results of different TI together to form a 4D time-series data:

1. Use the following FSL command to do pairwise subtraction:

```
asl_file --data = rASL_DATA_TI1 --ntis = 1 --iaf = tc --diff
--out = rASL_DeltaM_TI1 --mean = rASL_DeltaM_TI1_mean
```

Note that the --iaf option is to specify the order of label–control pair where tc means the label (tag) image is acquired first and then followed by control image. Use --iaf = ct if the data is acquired with the opposite order.

2. Concatenate the mean difference images of all the TIs together:

```
fslmerge -t rASL_DeltaM_mean rASL_DeltaM_TI1_mean rASL_DeltaM_TI2_mean ... rASL_DeltaM_TIn_mean
```

   where n is the number of TI.

3. If the data is acquired with varying TIs in one scan, the command could be:

```
asl_file --data = rASL_DATA --ntis = n --iaf = tc --diff --out = rASL_DeltaM --mean = rASL_DeltaM_mean
```

   The resulted rASL_DeltaM_mean image will then be used in the following fitting process.

3.4.3 Starting Values

Deriving the starting value of perfusion from the SI of each pixel is not trivial. Therefore one can just use a literature value (e.g., 300 ml/100 g/min).

1. The starting value for perfusion (startVal_f = 300).

3.4.4 Fitting Algorithm

Similar to T_1 fitting, the Trust-region method can be used.

1. Create for loops for pixel coordinates x and y to step through all pixels of the image.
2. Store the SI of that pixel at all TIs in a vector (in Matlab: SI_vector = imgData_forFitting(xPix, yPix,:)).
3. Change T_1 value from millisecond to second (in Matlab: mapT1(xPix,yPix) = mapT1(xPix,yPix)/1000).
4. The model for the function using Eq. 2 (in Matlab: FAIRmodel = fittype('mapM0(xPix,yPix) * mapAlpha(xPix,yPix) * a * (exp(−x * (1/mapT1(xPix,yPix) + a)) − exp.(−x/0.221))/(1/0.221 − (1/mapT1(xPix,yPix) + a)) ', 'independent', 'x', 'dependent', 'y')).
5. Initialize the fitting options in Matlab: opts = fitoptions (FAIRmodel);
6. Choose the function for the fitting algorithm, that is, Trust-region or, if not available, then Levenberg–Marquardt (in Matlab: opts.Algorithm = 'Trust-Region').
7. Provide the starting values for perfusion (in Matlab, e.g., opts. StartPoint = [startVal_f]).
8. Define lower and upper limits for the fit parameters. Assuming perfusion will be below 900 ml/100 g/min, use for f [0 900/6000]. In Matlab, for example, opts.Lower = [0]; opts. Upper = [0.15] (*see* **Note 6**).

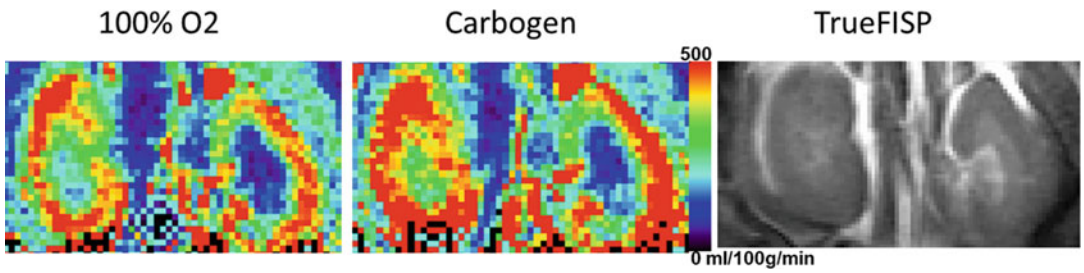

Fig. 2 Quantitative perfusion maps show lower perfusion under hyperoxia than that under carbogen (5% CO_2 + 95% O_2). Anatomical image was acquired with TrueFISP showing contrast between the cortex (dark) and medulla

9. Execute the curve fitting for each pixel data (in Matlab: [fitresult, gof] = fit(TI_forFitting, SI_vector, FAIRmodel, opts);).
10. Save the fit result in parameter maps and rescale by $2/\lambda$ and unit conversion factor: mapF(xPix, yPix) = fitresult.a * 0.9/2 * 6000; rsquare(xPix, yPix) = gof.rsquare (*see* **Note 6**).

3.4.5 Visual Display

1. Display the parameter map, which is a matrix with floating point numbers, as an image (in Matlab: imagesc(mapF);) (*see* Fig. 2).
2. Remove axis labels and ensure that the axes are scaled equally, so that pixels are square and not rectangular (in Matlab: axis off; axis equal;).
3. Select the color map and display a color bar (in Matlab: colormap(jet(256)); colorbar;) (*see* **Note 4**).
4. Set the display range for the color coding, for example, for perfusion [0 500] (in Matlab: caxis([0 500]);).

3.5 Regional Analysis

To obtain quantitative medulla and cortex perfusion, the kidney can be manually or automatically segmented based on the T_1 map or other kinds of structural images.

3.6 Results Validation

Further validation of imaging derived results can be performed using datasets acquired under physiological manipulations that alter blood flow, such as hypercapnia or hyperoxia. As CO_2 is a potent vasodilator, the blood flow under hypercapnia condition should be higher than that in normal gas condition. Hyperoxia is expected to lead to the opposite result with O_2 acting like a vasoconstrictor (*see* Fig. 2).

3.6.1 Comparison with Tissue Values Under Hypercapnia or Hyperoxia

3.6.2 Comparison with Reference Values from the Literature

Obtained values for both cortex and medulla tissue segmentation can be compared against reference values, shown in Table 1. It should be noted that blood flow is also modulated by anesthesia. For example, the commonly used isoflurane is a vasodilator and can increase blood flow depending on dosage. Therefore, the

Table 1
Comparison of renal blood flow measured by ASL-MRI in rodents

Cortex (ml/100 g/min)	Medulla (ml/100 g/min)	Animal strain, anesthesia and gas	Reference
338–452	123–240	C57BL/6 mouse, 1–1.5% isoflurane in 100% O_2	[5]
550–750	140–230	C57BL/6J mouse, 1.5% isoflurane (gas unknown)	[6]
344–575	ND	C57BL/6N mouse, isoflurane (dose and gas unknown)	[7]
288.4 ± 51.3	ND	Spraque-Dawley rat, 1.5% isoflurane (gas unknown)	[8]
750 ± 80	ND	Fisher 344 rat, thiobutabarbitural, 69-135 mg/kg (gas unknown)	[9]

comparison with literature values should be done with comparable anesthesia dosage.

4 Notes

1. Processing is typically performed in software packages such as MATLAB (The MathWorks, MA) or open source platforms as R programming language (http://r.org). The data can either be processed as DICOM images or if available as the raw data format from the scanner. As some motion correction tools (e.g., FSL, SPM) works on NiFti format, the data may need to be converted to that format during the processing. At the end of the processing pipeline, finalizing the data in the DICOM format would allow for further analysis and comparison to other image data on clinical viewers.
2. To correct for respiratory induced motion, resulted ASL images can be coregistered using Elastix (open source software, http://elastix.isi.uu.nl/) and a rigid registration algorithm.
3. An approach that is frequently used to increase the speed of the curve fitting, is to fit a linear model to the log of the SI data. This only requires a few simple modifications to the protocol described here. We recommend using exponential fitting (unless speed is very important), because the log-scaling leads to the noise error at each TI being scaled differently and this will impact on the fitted curve. If you do want to use linear fitting it would be good to initially perform both, exponential and linear fitting, on a few data sets and compare the results so as to better appreciate the impact of this choice.
4. Pseudocolor representations can be extremely useful for analyzing T_1-maps or perfusion maps, since they generally enhance

the perception of differences within the value range of the parameter. But one needs to be careful when choosing a color map. Parameter maps displayed as images in pseudocolor can potentially be misleading. Small differences in the underlying values may be artificially emphasized by a change in color hue, or a significant parameter difference that can easily be seen in a gray-scale image may be flattened or hidden if there is little change of hue or brightness over a certain range of the color-scale. It is recommended to always use the same color map and scale to improve comparability.

5. The transit time is ignored in the above equation as the delivery of spins is almost instantaneous with a small gap between the imaging and inversion slices used in FAIR ASL. Whether the transit time is negligible can be verified by adding the transit time into the kinetic model.
6. To get the correct unit, the T_1, T_{1a} and T_{1app} should be expressed in "second" and the perfusion value, f, will need to be multiplied by 6000 to convert to per 100 g/min.

Acknowledgments

This chapter is based upon work from COST Action PARENCHIMA, supported by European Cooperation in Science and Technology (COST). COST (www.cost.eu) is a funding agency for research and innovation networks. COST Actions help connect research initiatives across Europe and enable scientists to enrich their ideas by sharing them with their peers. This boosts their research, career, and innovation.
PARENCHIMA (renalmri.org) is a community-driven Action in the COST program of the European Union, which unites more than 200 experts in renal MRI from 30 countries with the aim to improve the reproducibility and standardization of renal MRI biomarkers.

References

1. Pell GS, Thomas DL, Lythgoe MF, Calamante F, Howseman AM, Gadian DG et al (1999) Implementation of quantitative FAIR perfusion imaging with a short repetition time in time-course studies. Magn Reson Med 41 (4):829–840
2. Kudomi N, Koivuviita N, Liukko KE, Oikonen VJ, Tolvanen T, Iida H et al (2009) Parametric renal blood flow imaging using [15O]H2O and PET. Eur J Nucl Med Mol Imaging 36 (4):683–691
3. Herscovitch P, Raichle ME (1985) What is the correct value for the brain–blood partition coefficient for water? J Cereb Blood Flow Metab 5 (1):65–69
4. Dobre MC, Ugurbil K, Marjanska M (2007) Determination of blood longitudinal relaxation time (T1) at high magnetic field strengths. Magn Reson Imaging 25(5):733–735
5. Rajendran R, Lew SK, Yong CX, Tan J, Wang DJ, Chuang KH (2013) Quantitative mouse renal perfusion using arterial spin labeling. NMR Biomed 26(10):1225–1232

6. Duhamel G, Prevost V, Girard OM, Callot V, Cozzone PJ (2014) High-resolution mouse kidney perfusion imaging by pseudo-continuous arterial spin labeling at 11.75T. Magn Reson Med 71(3):1186–1196
7. Hueper K, Gutberlet M, Rong S, Hartung D, Mengel M, Lu X et al (2014) Acute kidney injury: arterial spin labeling to monitor renal perfusion impairment in mice-comparison with histopathologic results and renal function. Radiology 270(1):117–124
8. Romero CA, Cabral G, Knight RA, Ding G, Peterson EL, Carretero OA (2018) Noninvasive measurement of renal blood flow by magnetic resonance imaging in rats. Am J Physiol Renal Physiol 314(1):F99–F106
9. Wang JJ, Hendrich KS, Jackson EK, Ildstad ST, Williams DS, Ho C (1998) Perfusion quantitation in transplanted rat kidney by MRI with arterial spin labeling. Kidney Int 53 (6):1783–1791

Chapter 40

Analysis Protocol for the Quantification of Renal pH Using Chemical Exchange Saturation Transfer (CEST) MRI

Hahnsung Kim, Yin Wu, Daisy Villano, Dario Livio Longo, Michael T. McMahon, and Phillip Zhe Sun

Abstract

The kidney plays a major role in maintaining body pH homeostasis. Renal pH, in particular, changes immediately following injuries such as intoxication and ischemia, making pH an early biomarker for kidney injury before the symptom onset and complementary to well-established laboratory tests. Because of this, it is imperative to develop minimally invasive renal pH imaging exams and test pH as a new diagnostic biomarker in animal models of kidney injury before clinical translation. Briefly, iodinated contrast agents approved by the US Food and Drug Administration (FDA) for computed tomography (CT) have demonstrated promise as novel chemical exchange saturation transfer (CEST) MRI agents for pH-sensitive imaging. The generalized ratiometric iopamidol CEST MRI analysis enables concentration-independent pH measurement, which simplifies in vivo renal pH mapping. This chapter describes quantitative CEST MRI analysis for preclinical renal pH mapping, and their application in rodents, including normal conditions and acute kidney injury.

This publication is based upon work from the COST Action PARENCHIMA, a community-driven network funded by the European Cooperation in Science and Technology (COST) program of the European Union, which aims to improve the reproducibility and standardization of renal MRI biomarkers. This analysis protocol chapter is complemented by two separate chapters describing the basic concepts and experimental procedure.

Key words Chemical exchange saturation transfer (CEST), Magnetic resonance imaging (MRI), pH, Rats, Mice, Iopamidol, Kidney, Contrast agents, pH imaging

1 Introduction

Chemical exchange saturation transfer (CEST) MRI provides a sensitive means to image microenvironment properties such as tissue pH, temperature, metabolites, and enzyme activities via dilute labile protons [1–12]. Endogenous CEST MRI has been increasingly adopted for imaging a host of disorders including acute ischemic stroke [13–22], tumor [23–27], and epilepsy [28, 29]. In addition, CEST MRI contrast agents have been developed for exogenous CEST imaging that may provide more sensitive

Andreas Pohlmann and Thoralf Niendorf (eds.), *Preclinical MRI of the Kidney: Methods and Protocols*, Methods in Molecular Biology, vol. 2216, https://doi.org/10.1007/978-1-0716-0978-1_40,

CEST detection which is specific to the administered agents [30–34]. This is because the labile proton exchange rate and chemical shifts can be designed/preselected to optimize these for exogenous CEST MRI contrast [35–38]. There has been an emerging library of iodinated-based CEST agents such as iopamidol, iobitridol, iopromide, and iodixanol, which have been approved by the U.S. Food and Drug Administration (FDA) for computed tomography (CT) head and body imaging applications [39–47]. Such FDA-approved iodinated contrast agents are promising for translational CEST imaging to characterize renal dysfunction, diagnose regional kidney injury before symptom onset, and help guide treatment before irreversible damage [48–50].

Because the CEST MRI effect depends on not only pH-dependent exchange rates but also on the labile proton ratio, relaxation rates and experimental conditions such as magnetic field strength, saturation power, and duration, CEST-weighted MRI contrast is often complex [51–55]. As such, it remains challenging to quantify CEST MRI toward tissue indices such as absolute pH and/or total protein concentration. Persistent progress has been achieved toward simplified and quantitative in vivo pH mapping [56–61]. In particular, ratiometric CEST MRI refers to a specific type of CEST MRI analysis that takes multiple CEST measurements, the ratio of which normalizes common confounding factors such as tissue labile proton concentration and relaxation effects, therefore enabling quantitative in vivo CEST mapping [42, 56, 62–67]. Although pH imaging is more straightforward at high magnetic fields ($B_0 \geq 7$ T) due to the large frequency shift difference between labile and bulk tissue water protons, it is important to extend pH MRI to magnetic fields such as 3 and 4.7 T [68, 69]. Due to the complexity of the source of the MRI CEST signal, multiple approaches have been established for a better quantification of the CEST contrast [54, 60]. In this chapter, we describe variant ratiometric pH CEST MRI analysis techniques, image down-sampling expedited adaptive least-squares (IDEAL) fitting algorithm, smoothing splines interpolation algorithm and use of iodinated CEST agents for mapping renal pH in vivo [50, 70].

This analysis protocol chapter is complemented by two separate describing the basic concepts and experimental procedure, which are part of this book.

This chapter is part of the book Pohlmann A, Niendorf T (eds) (2020) Preclinical MRI of the Kidney—Methods and Protocols. Springer, New York.

2 Materials

2.1 Software Requirements

2.1.1 Essential Tools

1. Matlab/Python: The method described in this chapter requires MATLAB (MathWorks, Natick, MA, https://www.mathworks.com/products/matlab.html) for data analysis of applying fitting models and measuring ratiometric. Because Matlab functions used in the data processing can also be implemented in python (https://www.python.org/), python can be used instead.
2. An image processing software (e.g., Image J, we recommend using Fiji, which is ImageJ with a wide range of plugins already included, https://fiji.sc/, open-source), as a practical tool for the image quality check or to measure SNR.

2.1.2 Optional Tools

A statistical analysis software (e.g., SPSS, SPSS Inc., Chicago, IL or Prism, GraphPad, USA) as a practical tool for the statistical significance calculation.

2.2 Source Data: Format Requirements and Data Preprocessing

The CEST images can be retrieved directly from the MRI scanner as raw binary images or in DICOM format (*see* **Note 1**). To be able to perform CEST analysis different scans are needed:

2.2.1 Input Requirements

- Anatomical image (optional).
- Unsaturated image (optional).
- CEST images or Z-spectra.
- CEST images (Z-spectra) before and after contrast agent (CA) injection for in vivo acquisitions.

Information about some scan acquisition parameters is also necessary as is the frequency offsets vector.

2.2.2 Background Removal

In order to avoid the analysis outside the object of interest and to shorten the analysis duration a first segmentation between the background and the imaged object is suggested. Manual thresholding or automatic thresholding (as by the Otsu method) can be easily applied within the Matlab environment.

3 Methods

3.1 Motion Correction

If needed, postprocessing motion correction can be applied to coregister images to correct for motion artifacts.

3.2 Z-Spectra Analysis

Z-spectra can be analyzed as mean contribution inside one or more regions of interest, that can be drawn on an anatomical image reference, or preferentially, by a voxel-by-voxel analysis. Different approaches for Z-spectra analysis will be described in detail.

3.2.1 Multi Pool Lorentzian Fitting

The Z-spectra are numerically described using a multipool Lorentzian model [24, 71–74]:

$$Z(\omega) = 1 - \frac{M_z}{M_0} = \sum_{i=1}^{N} L_i(\omega) \tag{1}$$

where ω is the frequency offset from the water resonance, N is the total number of proton pools, and L_i is the Lorentzian spectrum of the ith pool. The Lorentzian lineshape is represented by the following equation:

$$L(\omega) = \frac{A}{1 + 4\left(\frac{\omega - \omega_0}{\sigma}\right)^2} \tag{2}$$

where A, ω_0, and σ are the amplitude, center frequency, and linewidth of the ith saturation transfer effects, respectively.

1. Map B_0 inhomogeneity with water saturation shift referencing (WASSR) using external acquired B_0 maps, by field maps or by interpolation procedures looking to the minimum of the Z-spectrum (internal B_0 mapping) [75–79].
2. Shift CEST MRI Z-spectrum based on the field inhomogeneity, per voxel, for correction.
3. Normalize the Z-spectra (i_z) by the signal without RF irradiation (M_0).
4. Fit the Z-spectrum using a five pool Lorentzian model (two pools for iopamidol amide groups at 4.3 and 5.5 ppm, one for bulk tissue water (0 ppm), and two pools for the hydroxyl groups at 0.8 and 1.8 ppm) [80, 41]. Representative multipool Lorentzian fitting is described in Fig. 1.

3.2.2 Image Down-Sampling Expedited Adaptive Least-Squares (IDEAL) Fitting Algorithm

1. Initially down-sample the B_0 field inhomogeneity-corrected CEST images to one or a few pixels and calculate the global Z-spectrum by averaging the Z-spectra of all voxel within an ROI to substantially improve the signal-to-noise ratio (SNR) for the numerical fitting.
2. Set the boundaries to be between 1% and 100 times of the initial values for the amplitude and linewidth of each chemical pool, with their peak frequency shift within ±0.2 ppm of the initial chemical shift. The relaxed boundary constraints ensure that the initial fitting provides a reasonable estimation of the multiple Lorentzian pools under the condition of sufficiently high SNR.
3. Fit the down-sampled image exploiting.
4. Resample the CEST images to 2 × 2 matrix size.

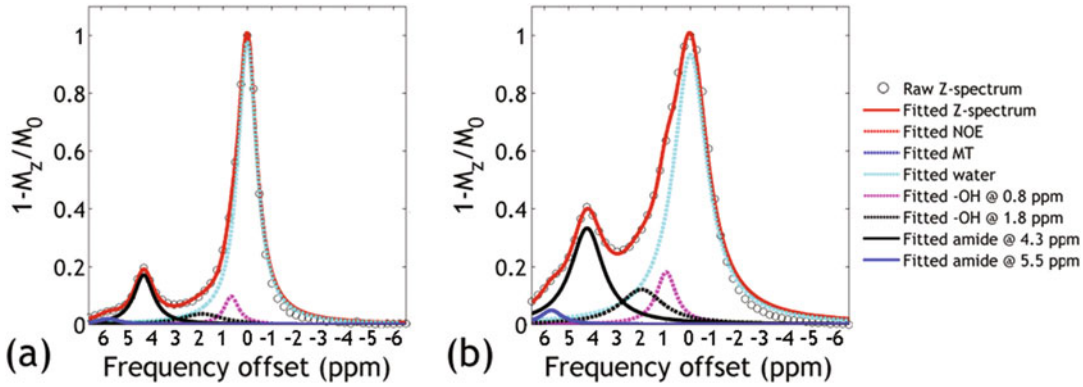

Fig. 1 Multipool Lorentzian fitting of representative CEST Z-spectra from a 40 mM iopamidol solution vial with a pH of 7.0. CEST Z-spectrum obtained from under (**a**) $B_1 = 1$ μT and (**b**) 2 μT under body temperature. A five-pool Lorentzian model was used to describe the CEST spectrum [Adapted with permission from *Magnetic Resonance in Medicine* 2018 (A generalized ratiometric chemical exchange saturation transfer (CEST) MRI approach for mapping renal pH using Iopamidol, Volume: 79, Issue: 3, Pages: 1553–1558, DOI: https:/doi.org/10.1002/mrm.26817)]

5. Take the initial values for the fitting of each voxel of the resampled image from the results of the previous image with lower spatial resolution.
6. Set the boundary constraints relatively loose albeit narrower than the initial fitting, to be 10% and ten times of the initial values.
7. Use a nonlinearly constrained fitting algorithm with twofold overweighting applied for Z-spectra between 4.0 and 5.8 ppm to increase the fitting accuracy of Iopamidol CEST effects at 4.3 and 5.5 ppm.
8. Resample the CEST images, 4 × 4, 8 × 8, 12 × 12, 24 × 24 until the original resolution of 48 × 48 or voxel-wise multipool Lorentzian fitting and repeat from **step 5** until you get the desired final resolution.
9. Figure 2 shows the flowchart of the IDEAL fitting algorithm.

3.2.3 Smoothing Splines Interpolation

The cubic smoothing splines estimate the interpolating function f, minimizing the following expression, linearly composed by two parts:

$$p\sum_{j=1}^{N}\left|y_j - f(x_j)\right|^2 + (1-p)\int \left|D^2 f(t)\right|^2 \mathrm{d}t \qquad (3)$$

The first addend represents the mean square error between data y_j and the interpolating cubic spline $f(x_j)$ calculated in x_j measure

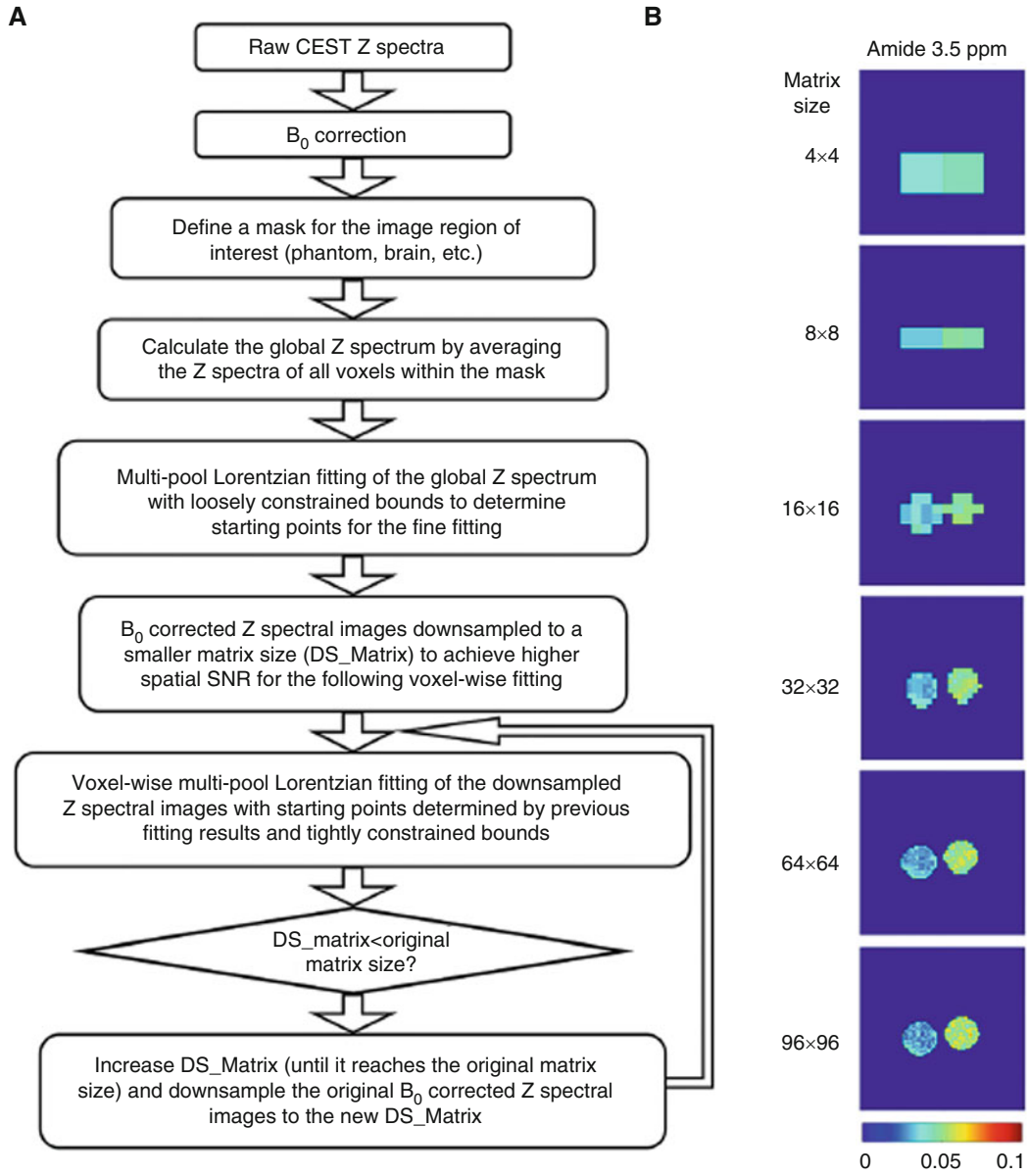

Fig. 2 Illustration of the Image Downsampling Expedited Adaptive Least Squares (IDEAL) CEST analysis algorithm. (**a**) Flow chart of data processing steps of the IDEAL fitting algorithm. (**b**) The intermediate fitting results of iteratively less downsampled images from a two-compartment CEST phantom [Adapted with permission from *Scientific Reports*. 2017 (Quantitative chemical exchange saturation transfer (CEST) MRI of glioma using Image Downsampling Expedited Adaptive Least-squares (IDEAL) fitting, Volume: 7, Issue: 1, Pages: 84, DOI: https:/doi.org/10.1038/s41598-017-00167-y)]

points. The second term consists of the integral of the squared second-order derivative of f and is a measure of function flexibility.

p is a smoothing parameter and determines the relative weight you would like to place on the contradictory demands of having

f be smooth *vs* having f be close to the data. Its value ranges between 0 and 1. For $p = 1$, the curvature constraint is nullified, f passes for all data points and converges to the interpolating spline, while, at the other extreme, for $p = 0$, f curvature is minimized and f results in a linear least square fit.

1. Normalize pre- and postinjection Z-spectra to the maximum intensity value of the free water signal, generally corresponding to the most distant offset or to the unsaturated image (M_0) [79].
2. Interpolate each voxel Z-spectra data with a cubic spline function paying action to regularization factor selection (*see* **Note 2**) and ignoring the background pixels/voxels (in Matlab use csasp function).
3. Find in the fitted spectra the absolute minimum corresponding to bulk water frequency offset (in Matlab use fnmin function).
4. Use the minimum position (corresponding to water peak shift from zero) to correct B_0 inhomogeneity shifting the frequency offsets vector.
5. Save minimum position in a matrix to construct the B_0 shift map.

To exclude noisy data points from the analysis a filtration step is suggested:

6. Construct R^2 matrix evaluating the distance of the interpolating function to data in each pixel.
7. Define a R^2 threshold (in our application R^2 ranges between 0.97 and 0.99).
8. Ignore pixel for which the R^2 value is lower than the threshold.

Smoothing spline algorithm workflow is described in Fig. 3.

3.3 CEST Quantification

After having fitted the Z-spectra by smoothing splines or Lorenzian fitting, CEST contrast quantification can be evaluated and ratiometric values (ratio between two CEST contrast quantifications to remove the concentration effect) can be calculated.

3.3.1 CEST Ration Calculation by Asymmetry Analysis

The CEST ratio (CESTR) is calculated by asymmetry analysis:

$$\mathrm{CESTR}(\omega) = \frac{M_z(-\omega) - M_z(\omega)}{M_0} \tag{4}$$

where ω is the labile proton chemical shift from the bulk water resonance (for Iopamidol ω = 4.2 ppm and 5.5 ppm). For the in vivo images, contrast was calculated by subtracting contrast after CA injection from the contrast before the injection at the different frequency offsets.

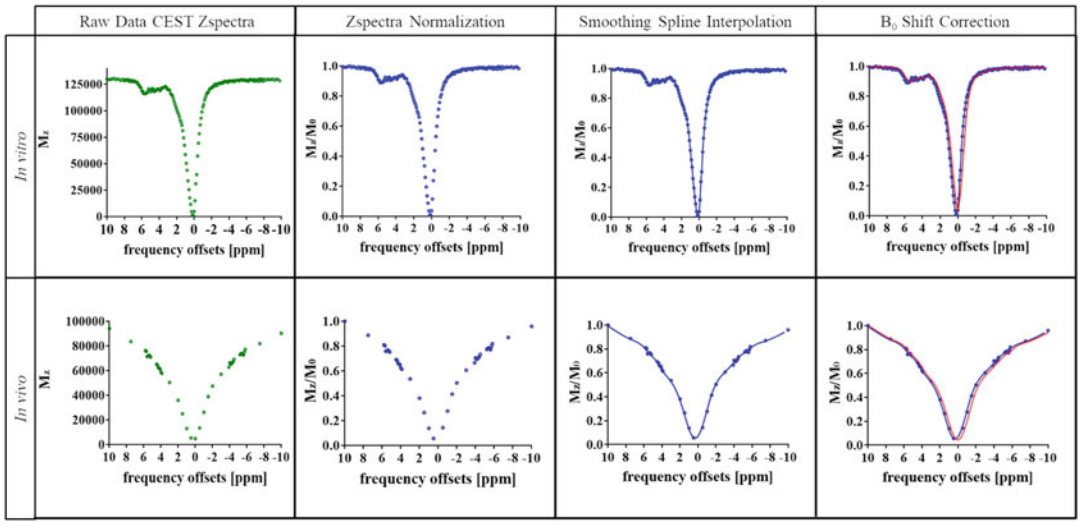

Fig. 3 Representative z-spectra from in vitro (bottom) and in vivo (top) images showing the analysis steps for data normalization, smoothing splines interpolation and B_0 shift correction (from left to right)

1. Calculate CEST contrast according to Eq. 4 for the two pools of Iopamidol (4.2 and 5.5 ppm).

3.3.2 CEST Ratio Calculation from Lorentzian Fitting

1. Calculate CEST contrast from the amplitude obtained from the Lorentzian fitting according to Eq. 4 for the two pools of Iopamidol (4.2 and 5.5 ppm).

3.3.3 Chemical Shift-Based Ratiometric CEST Analysis

Because the direct saturation is relatively small at the magnetic field at or above 7 T, the coupling between multiple CEST effects is relatively small, and a ratiometric analysis of two CEST effects obtained under the same RF irradiation power level can be calculated for pH calibration, as

$$R_{\mathrm{ST}}(\mathrm{pH}) = \frac{\mathrm{CESTR}(\delta 1)}{\mathrm{CESTR}(\delta 2)} \tag{5}$$

3.3.4 RF Power-based Ratiometric CEST Analysis

For CEST agent of a single labile proton group, the conventional ratiometric analysis does not apply. It has been shown that the ratiometric analysis can be generalized by taking the ratio of CEST effects obtained under two RF power levels as [42].

$$R_{\mathrm{ST}}(\mathrm{pH}) = \frac{\mathrm{CESTR}(B_{1b})}{\mathrm{CESTR}(B_{1a})} \tag{6}$$

If the direct water saturation is not negligible, the saturation effect can be calculated/removed to improve the precision of RF power-based ratiometric analysis [56, 64].

3.3.5 The Generalized RF Power- and Chemical Shift-Hybrid Ratiometric CEST Analysis

When CEST MRI is performed at lower magnetic field strengths ($B_0 < 7.0$ T) or the RF saturation power induces nonnegligible direct saturation effect, the coupling between multiple CEST effects (i.e., CEST and direction water saturation) become nonnegligible. Under such conditions, the routine ratiometric analysis (chemical shift- and RF power-based methods) may be susceptible to the coupling. In addition, the coupling depends on the transverse relaxation rate, which may be the difference between phantom calibration and in vivo experiments. To minimize such confounding coupling effect, the CEST effect can be decoupled with the multipool Lorentzian model, and their ratio is more reproducible and specific to pH. As such, the ratiometric analysis is generalized to a ratio of CEST effects of different chemical shift obtained under different saturation power levels.

$$R_{ST}(\mathrm{pH}) = \frac{\mathrm{CESTR}(\delta 1, B_{1b})}{\mathrm{CESTR}(\delta 2, B_{1a})} \tag{7}$$

1. Calculate the ratiometric values following one of the previously described Eqs. 5–7.

3.4 Set-Up of pH Calibration Curve

To investigate the relation between the R_{ST} value and the pH a calibration is needed. In the following steps the calibration done for Iopamidol on a pH varying phantom is described. Two examples of pH calibration curves obtained at 7 T and at 4.7 T are shown in Fig. 4.

1. Acquire CEST spectra images of the pH varying phantom;
2. Draw the ROI including only the pH compartment;
3. Evaluate mean CESTR at 4.2 and 5.5 ppm inside each compartment;
4. Calculate R_{ST};
5. Fit the R_{ST} as function of the titrated pH (usually a polynomial fit of the third order is selected).

It is worth to observe that by decoupling the CEST effects at 4.2 and 5.5 ppm, the generalized ratiometric CEST MRI index provides an extended range of pH measurement at 4.7 T (Fig. 4b). Note that such a calibration experiment is important to ensure that the pH dynamic range is sufficient to cover tissue pH of interest. The polynomial regression enables the derivation of the absolute pH map of renal images.

6. From the calculated ratiometric value derives the pH value according to the used calibration curve.

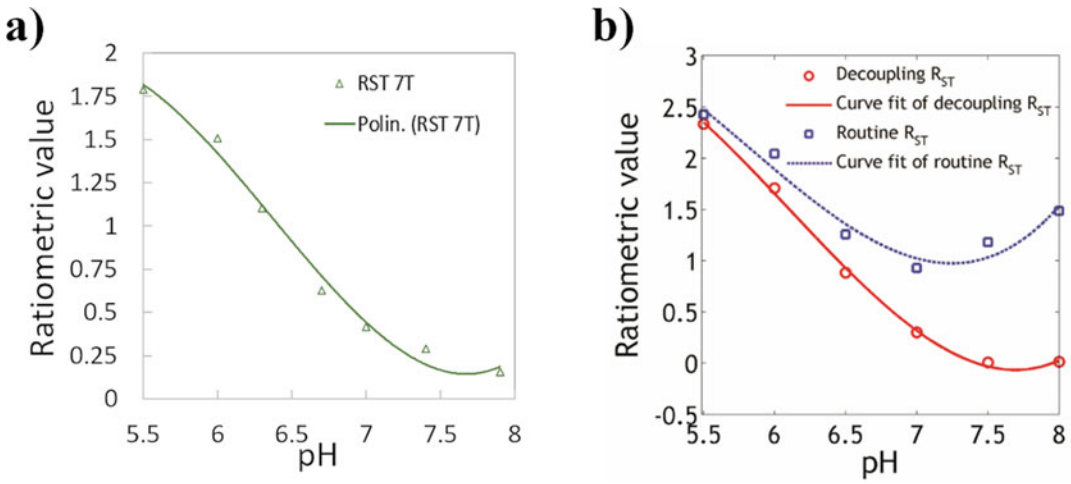

Fig. 4 Comparison of ratiometric analysis of Iopamidol at high magnetic field of 7 T (**a**) and at sub-high magnetic field of 4.7 T (**b**). Note that the routine R_{ST} of 5.5 and 4.3 ppm provides a limited pH MRI range below pH = 7 due to the CEST MRI effect coupling at high pH. In comparison, the modified approach extends the pH imaging range to 7.5 [Adapted with permission from *Magnetic Resonance in Medicine* 2018 (A generalized ratiometric chemical exchange saturation transfer (CEST) MRI approach for mapping renal pH using Iopamidol, Volume: 79, Issue: 3, Pages: 1553–1558, DOI: https:/doi.org/10.1002/mrm.26817)]

3.5 In Vivo Application for pH Mapping

3.5.1 pH Mapping by Lorentzian Fitting or IDEAL Approach

1. Obtain two representative in vivo CEST Z-spectra from a normal rat (or mouse) kidney during Isovue infusion under two RF saturation power levels of 1 and 2 μT at 4.7 T as shown in Fig. 5.
2. Apply the IDEAL algorithm and perform Lorentzian decoupling to resolve Iopamidol CEST effects at 4.3 and 5.5 ppm.
3. Outline the renal cortex, medulla, and calyx based on T_2-weighted MRI.
4. Z-spectra are broadened at a higher RF power level due to more prominent direct RF saturation effect. Notably, the CEST effect increases from the cortex, medulla to calyx. This is because pH gradually reduces from the cortex, medulla to the calyx, which causes a persistent reduction in the Iopamidol CEST exchange rate. As such, the saturation efficiency increases when the exchange rate becomes comparable to the saturation field. In addition, the kidney concentrates and excretes Isovue, resulting in a concentration gradient across the kidney.
5. Describe the CEST effect by a six-pool Lorentzian model (i.e., five-pool model plus semisolid macromolecule magnetization transfer (MT) effect in tissue). Corresponding parametric images for CEST contrast and pH mapping in rat kidneys are shown in Fig. 6.

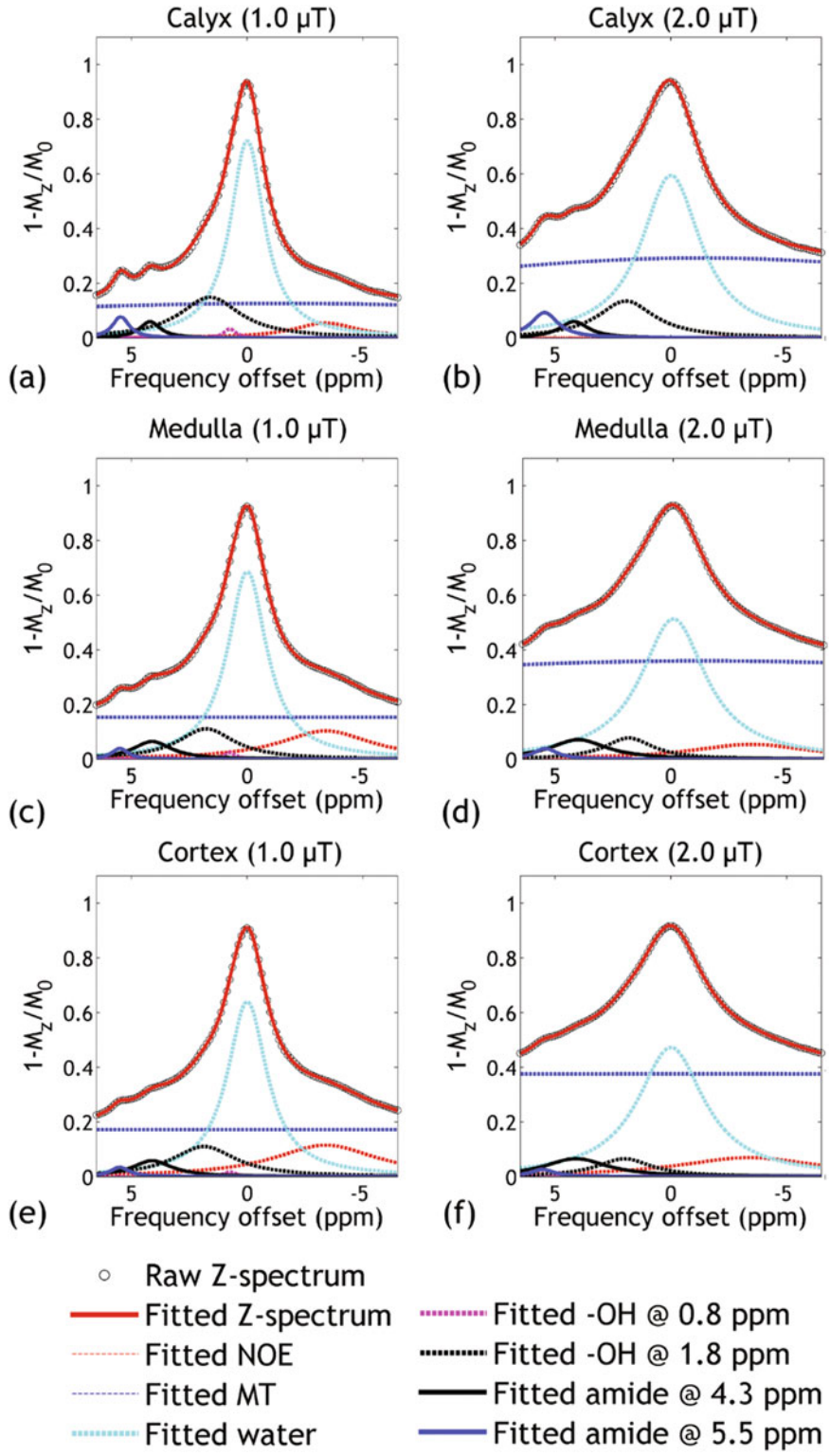

Fig. 5 Demonstration of regional CEST Z-spectra of calyx (**a**, **b**), medulla (**c**, **d**), and cortex (**e**, **f**) at 1 and 2 μT, respectively [Adapted with permission from *Magnetic Resonance in Medicine* 2018 (A generalized ratiometric chemical exchange saturation transfer (CEST) MRI approach for mapping renal pH using Iopamidol, Volume: 79, Issue: 3, Pages: 1553–1558, DOI: https:/doi.org/10.1002/mrm.26817)]

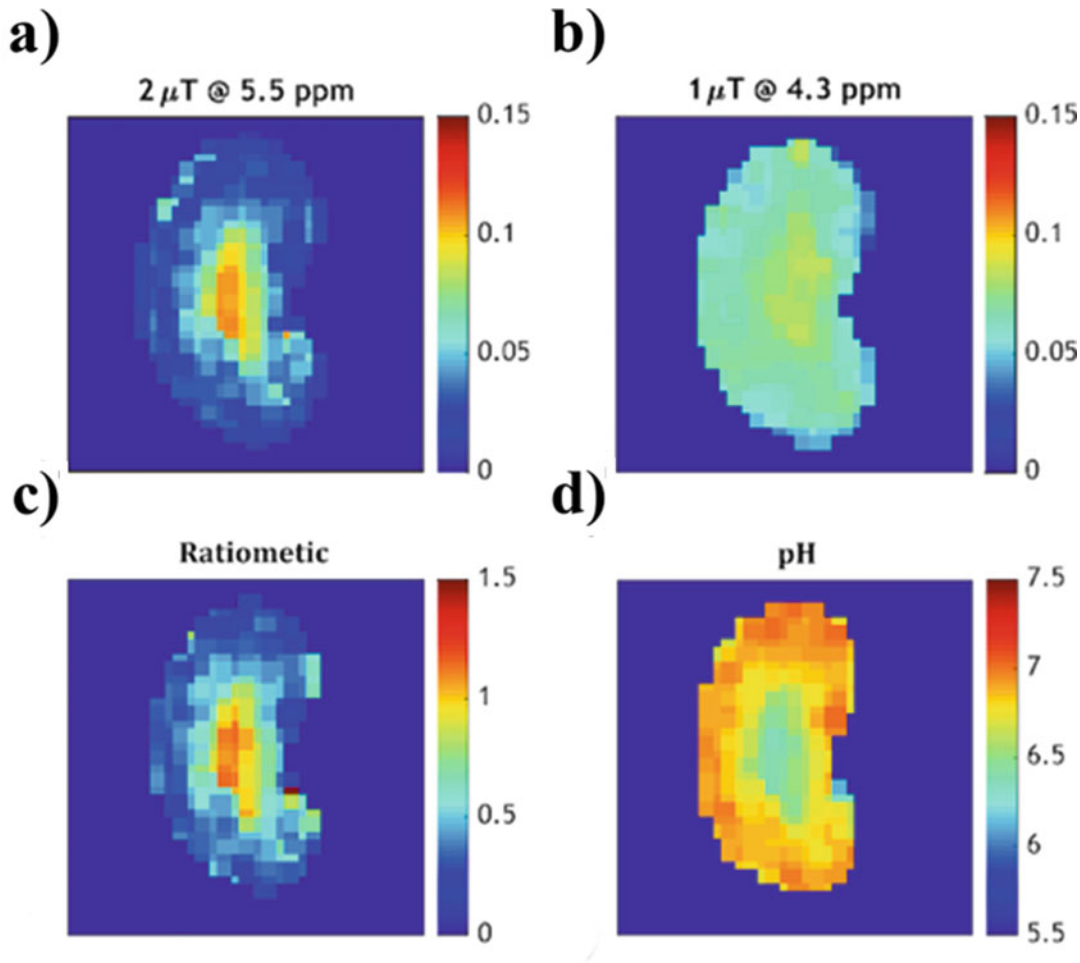

Fig. 6 Demonstration of a renal pH map from a representative rat following Iopamidol injection at 4.7 T. The resolved maps of ST effects at 5.5 ppm (**a**) and 4.3 ppm (**b**) were obtained with the IDEAL fitting algorithm, from which the ratiometric map was obtained (**c**). (**d**) pH map overlaid on the corresponding T_2-weighted image show the renal pH gradually decreasing from the cortex, medulla to calyx

3.5.2 pH Mapping by Using the Smoothing Splines Approach

1. Import your scans (anatomical image, pre- and postinjection CEST images) and save them in a matrix.
2. Use cubic spline algorithm to interpolate both pre- and post-injection Z-spectra as described in Subheading 3.2.3.
3. Use cubic spline interpolated Z-spectra to calculate CESTR at specific ω (+4.2 and +5.5 ppm for Iopamidol) or/and B_1 levels before and after the CA injection and save CEST contrast values in a matrix to construct CESTR maps (in Matlab use fnval function to evaluate interpolating cubic spline values at ω corrected for calculated B_0 shift).

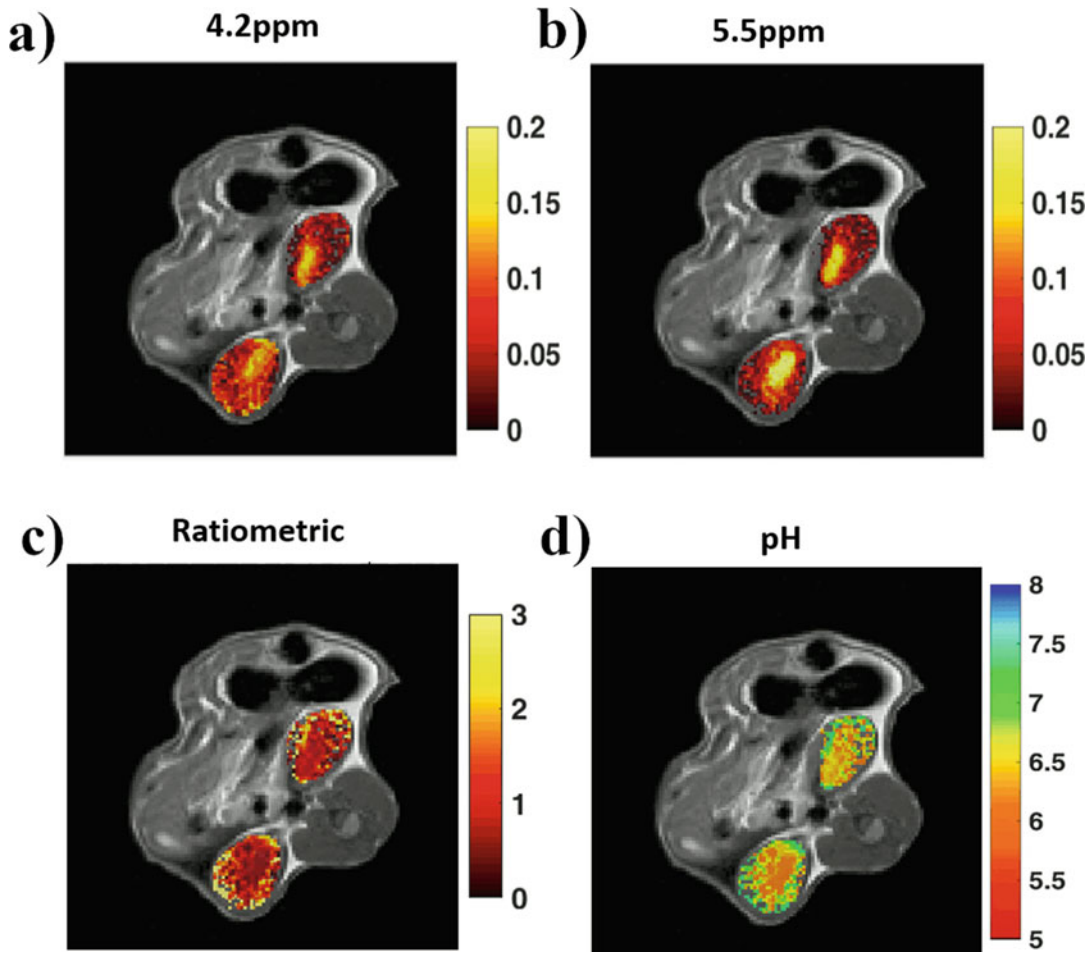

Fig. 7 Demonstration of a physiologic renal pH map from a representative mouse following Iopamidol injection at 7 T. The resolved maps of ST effects at 4.2 ppm (**a**) and 5.5 ppm (**b**) were obtained with the smoothing splines algorithm, from which the ratiometric map was obtained (**c**). (**d**) pH map overlaid on the corresponding T_2-weighted anatomical image show the renal pH gradually decreasing from the cortex, medulla to calyx

4. To remove endogenous effects and to isolate contrast agent contribution, subtract postinjection CEST contrast map to preinjection CEST contrast map (Fig. 7a, b).
5. Calculate the ratio map ratioing difference CEST contrast maps obtained at different ω values (Fig. 7c) or/and B_1 levels.
6. Derive pH map from the ratio map using the experimental calibration curve calculated in Subheading 3.4, **step 6** (Fig. 7d).

3.6 Representation

The obtained Z-spectra and pH maps can be represented as averaged values in a region of interest (ROI) or as parametric pixel-by-pixel maps. Before the representation, in order to remove residual noise, contrast and pH maps can be filtered, by applying a threshold

corresponding to the measured signal intensities variability of the exploited MRI scanner to discriminate between enhanced and nonenhanced voxels, following CA injection (*see* **Note 3**).

1. Select a noise threshold.
2. Set to 0 or to NaN all pixels inside the map for which the contrast increment is lower than the threshold.
3. Use the anatomical image (or alternatively the first CEST image) to identify and draw one or more ROIs (in Matlab use the `roipoly` function).
4. Create a mask from the ROI(s), a matrix that contains 1 value inside the region of interest and 0 or NaN values outside.

   For representing mean Z-spectra:

5. Calculate mean Z-spectra (pre- and postinjection), ignoring values outside the ROI.

   For representing parametric maps:

6. Represent contrast and pH maps overimposed to the anatomical image for having a morphological reference.

Representative mean spectra are shown in Fig. 8, whereas parametric images for CEST contrast quantification and pH values calculated in rat kidneys at 4.7 T and in murine kidneys at 7 T are shown in Fig. 6 and Fig. 7, respectively.

3.7 Quantitative Analysis

Statistics values as mean, median, and standard deviation can be obtained evaluating maps inside different ROI (cortex, medulla, and calyx) to have a quantitative description of the analysis results.

3.8 Results Validation

3.8.1 Evaluation of Analysis Errors

The quality of CEST fitting can be evaluated by the following three methods: (1) coefficient of variation (standard deviation/mean) within ROI, (2) contrast-to-noise ratio (CNR) between the two vials in the phantom study calculated by $\mathrm{CNR} = |S_1 - S_2|/\sqrt{(\sigma_1{}^2 + \sigma_2{}^2)}$, where $S_{1,\,2}$ are the mean values for the two ROIs and $\sigma_{1,\,2}$ are their standard deviations, and (3) goodness of fit (R^2) maps.

3.8.2 Comparison with Reference Values from the Literature

It has been documented that kidney pH values are heterogeneous, with a gradient from the cortex, medulla to calyx due to filtration and blood volume difference. MRI-based pH imaging reveals significant different pH values among the three layers, with more neutral pH values (7–7.4) for the cortex region, mild acidic pH values (6.6–7.0) for the medulla, and acidic pH values for the calyx (6.3–6.7). Please consider Table 1 for average pH values measured in specific kidney regions.

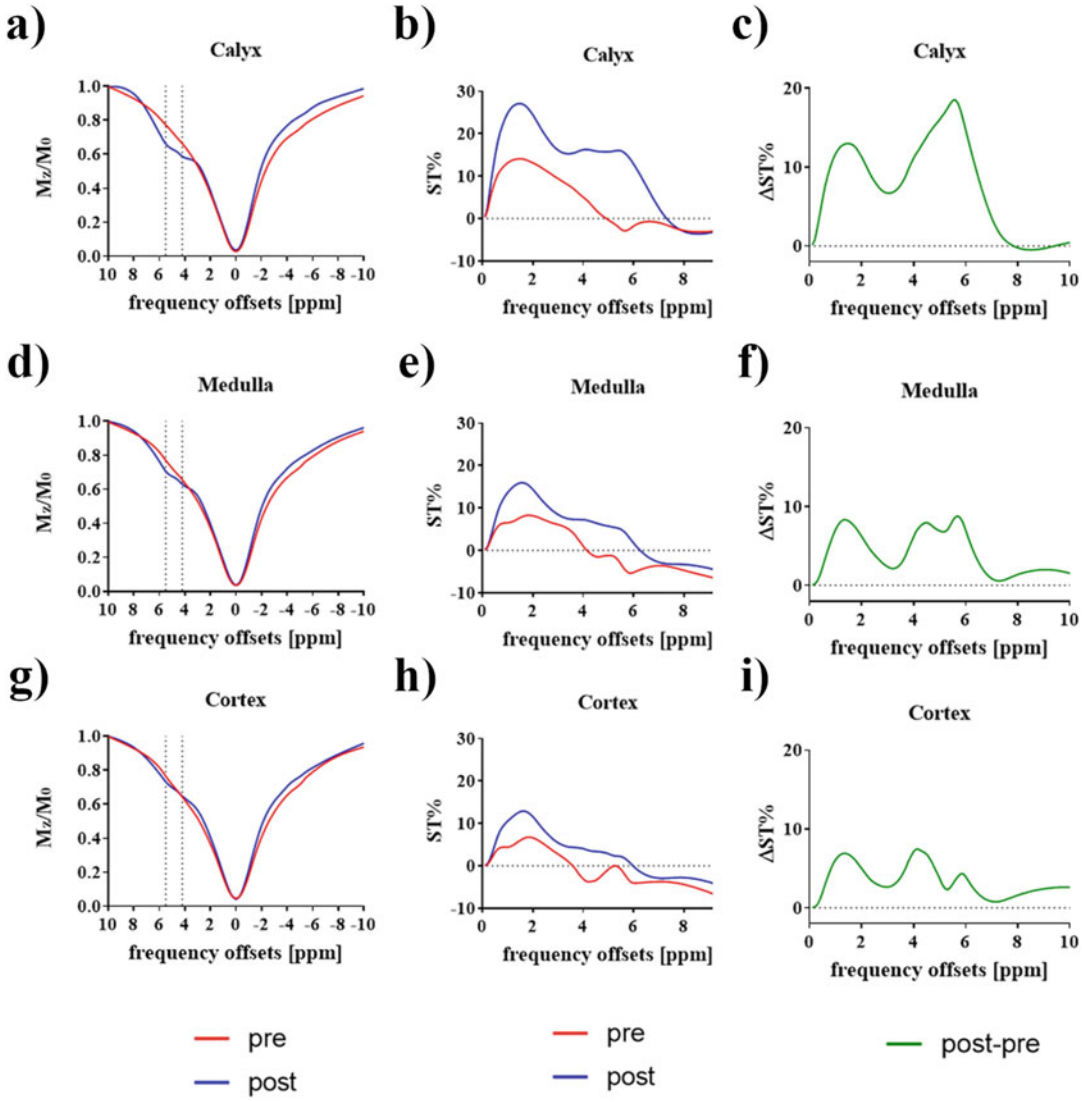

Fig. 8 Demonstration of regional CEST Z-spectra and contrast of calyx (**a**, **b**), medulla (**c**, **d**), and cortex (**e**, **f**) at 3 μT. Described CEST contrast became higher from calyx, trough medulla, to cortex, due to pH variation

Table 1
Typical pH values for each specific renal tissue for healthy mice and rats (literature values)

pH				
Inner medulla	**Outer medulla**	**Cortex**	**Field strength, T**	**Reference**
6.3 ± 0.45	7.0 ± 0.29	7.3 ± 0.13	4.7	[81]
6.6 ± 0.2	6.85 ± 0.15	7.0 ± 0.11	7	[69]
6.5 ± 0.2	6.8 ± 0.1	7.0 ± 0.1	4.7	[80]
6.6 ± 0.1	6.7 ± 0.08	6.8 ± 0.1	7	[49, 50]

4 Notes

1. Data are stored in the 2dseq file for Bruker scanners or in .img file for ASPECT MRI instrumentations. In both cases metadata files (method, acqp and reco for Bruker scanner or dat file for Aspect systems) need to be read for retrieving all the information needed to correctly read the raw binary file. Bruker import file plugins are available in ImageJ for directly opening raw Bruker files (for PV5). Matlab-based scripts for importing Bruker images and for the CEST analysis described in this chapter can be made available upon sending a request to the authors (dario.longo@unito.it; mtmcmaho@gmail.com; pzhesun@emory.edu). More information on the software can be found at the following links: http://www.cim.unito.it/website/research/research_processing.php http://godzilla.kennedykrieger.org/CEST/.
2. The choice of the regularization factor plays a key role in calculating CEST spectra and contrast; in particular, a trade-off between the "zero" estimation, noise suppression and peak identification is needed for an optimal choice [78]. Z-spectra and resulting CEST contrast obtained with different p values are shown in Fig. 9: when the regularization factor increases, the flexibility of the interpolating curve increases, yielding more evident peaks, but at the same time the smoothing of the raw data decreases. In our application p ranged between 0.90 and 0.99.
3. Signal variations (or fluctuations), as a measure of scanner instability, can be evaluated by repeating the same CEST acquisition (without saturation) several times (10–100 repetitions) and then evaluating the oscillation (or standard deviation) of

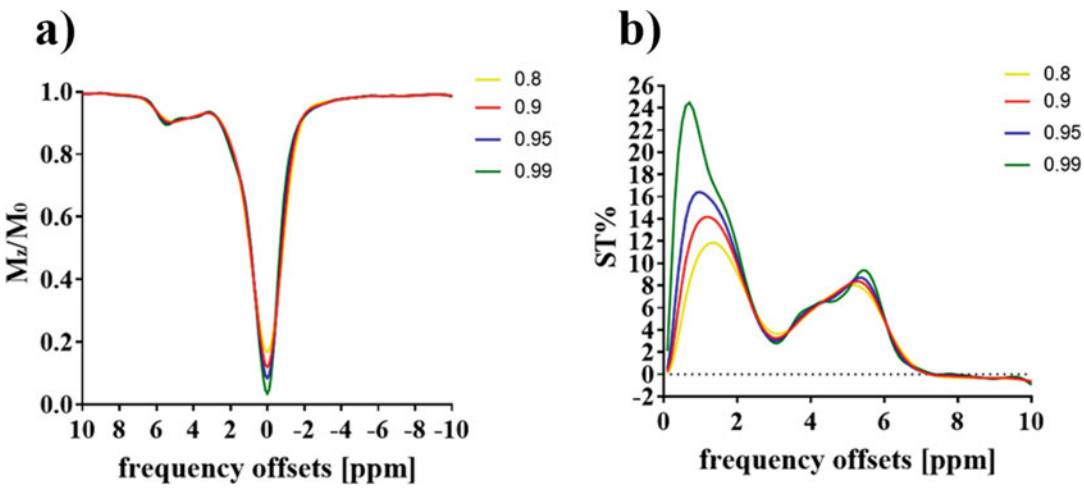

Fig. 9 Z-Spectra (**a**) and CEST contrast (**b**) obtained with different smoothing factors. The contrast decreases with a decrease of the smoothing factor value

the average signal along the repetition. Such value can be exploited to set a threshold for evaluating CEST contrast increase following contrast agent injection due to the contrast agent itself and not due to signal oscillation (i.e., it acts as a detection threshold). Signal fluctuation can be expected to be less than 0.2–1% with slight constant increase with the age of the scanner.

Acknowledgments

The Italian Ministry for Education and Research (MIUR) is gratefully acknowledged for yearly FOE funding to the Euro-BioImaging Multi-Modal Molecular Imaging Italian Node (MMMI).

This chapter is based upon work from COST Action PARENCH IMA, supported by European Cooperation in Science and Technology (COST). COST (www.cost.eu) is a funding agency for research and innovation networks. COST Actions help connect research initiatives across Europe and enable scientists to enrich their ideas by sharing them with their peers. This boosts their research, career, and innovation.

PARENCHIMA (renalmri.org) is a community-driven Action in the COST program of the European Union, which unites more than 200 experts in renal MRI from 30 countries with the aim to improve the reproducibility and standardization of renal MRI biomarkers.

References

1. Forsen S, Hoffman RA (1963) Study of moderately rapid chemical exchange reactions by means of nuclear magnetic double resonance. J Chem Phys 39(11):2892. https://doi.org/10.1063/1.1734121
2. Wolff SD, Balaban RS (1990) Nmr imaging of labile proton-exchange. J Magn Reson 86 (1):164–169. https://doi.org/10.1016/0022-2364(90)90220-4
3. Dagher AP, Aletras A, Choyke P, Balaban RS (2000) Imaging of urea using chemical exchange-dependent saturation transfer at 1.5T. J Magn Reson Imaging 12:745–748
4. Sun PZ, Zhou J, Huang J, van Zijl P (2007) Simplified quantitative description of amide proton transfer (APT) imaging during acute ischemia. Magn Reson Med 57(2):405–410. https://doi.org/10.1002/mrm.21151
5. Aime S, Delli Castelli D, Fedeli F, Terreno E (2002) A paramagnetic MRI-CEST agent responsive to lactate concentration. J Am Chem Soc 124(32):9364–9365
6. Jokivarsi KT, Grohn HI, Grohn OH, Kauppinen RA (2007) Proton transfer ratio, lactate, and intracellular pH in acute cerebral ischemia. Magn Reson Med 57(4):647–653. https://doi.org/10.1002/mrm.21181
7. Zhang L, Martins AF, Mai Y, Zhao P, Funk AM, Clavijo Jordan MV, Zhang S, Chen W, Wu Y, Sherry AD (2017) Imaging extracellular lactate in vitro and in vivo using CEST MRI and a paramagnetic shift reagent. Chemistry 23 (8):1752–1756. https://doi.org/10.1002/chem.201604558
8. Liu G, Li Y, Pagel MD (2007) Design and characterization of a new irreversible responsive PARACEST MRI contrast agent that detects nitric oxide. Magn Reson Med 58 (6):1249–1256. https://doi.org/10.1002/mrm.21428

9. Li Y, Sheth VR, Liu G, Pagel MD (2011) A self-calibrating PARACEST MRI contrast agent that detects esterase enzyme activity. Contrast Media Mol Imaging 6(4):219–228. https://doi.org/10.1002/cmmi.421
10. McVicar N, Li AX, Suchy M, Hudson RH, Menon RS, Bartha R (2013) Simultaneous in vivo pH and temperature mapping using a PARACEST-MRI contrast agent. Magn Reson Med 70(4):1016–1025. https://doi.org/10.1002/mrm.24539
11. Zhang S, Malloy CR, Sherry AD (2005) MRI thermometry based on PARACEST agents. J Am Chem Soc 127(50):17572–17573. https://doi.org/10.1021/ja053799t
12. Liu G, Li Y, Sheth VR, Pagel MD (2012) Imaging in vivo extracellular pH with a single paramagnetic chemical exchange saturation transfer magnetic resonance imaging contrast agent. Mol Imaging 11(1):47–57
13. Zhou J, Payen JF, Wilson DA, Traystman RJ, van Zijl PC (2003) Using the amide proton signals of intracellular proteins and peptides to detect pH effects in MRI. Nat Med 9 (8):1085–1090. https://doi.org/10.1038/nm907
14. Harston GW, Tee YK, Blockley N, Okell TW, Thandeswaran S, Shaya G, Sheerin F, Cellerini M, Payne S, Jezzard P, Chappell M, Kennedy J (2015) Identifying the ischaemic penumbra using pH-weighted magnetic resonance imaging. Brain 138(Pt 1):36–42. https://doi.org/10.1093/brain/awu374
15. Wang E, Wu Y, Cheung JS, Igarashi T, Wu L, Zhang X, Sun PZ (2019) Mapping tissue pH in an experimental model of acute stroke – determination of graded regional tissue pH changes with non-invasive quantitative amide proton transfer MRI. NeuroImage. https://doi.org/10.1016/j.neuroimage.2019.02.022
16. Sun PZ, Wang E, Cheung JS (2012) Imaging acute ischemic tissue acidosis with pH-sensitive endogenous amide proton transfer (APT) MRI—correction of tissue relaxation and concomitant RF irradiation effects toward mapping quantitative cerebral tissue pH. NeuroImage 60(1):1–6. https://doi.org/10.1016/j.neuroimage.2011.11.091
17. Sun PZ, Cheung JS, Wang E, Lo EH (2011) Association between pH-weighted endogenous amide proton chemical exchange saturation transfer MRI and tissue lactic acidosis during acute ischemic stroke. J Cereb Blood Flow Metab 31(8):1743–1750. https://doi.org/10.1038/jcbfm.2011.23
18. Sun PZ, Zhou J, Sun W, Huang J, van Zijl PC (2007) Detection of the ischemic penumbra using pH-weighted MRI. J Cereb Blood Flow Metab 27(6):1129–1136. https://doi.org/10.1038/sj.jcbfm.9600424
19. McVicar N, Li AX, Goncalves DF, Bellyou M, Meakin SO, Prado MA, Bartha R (2014) Quantitative tissue pH measurement during cerebral ischemia using amine and amide concentration-independent detection (AACID) with MRI. J Cereb Blood Flow Metab 34(4):690–698. https://doi.org/10.1038/jcbfm.2014.12
20. Heo HY, Zhang Y, Burton TM, Jiang S, Zhao Y, van Zijl PCM, Leigh R, Zhou J (2017) Improving the detection sensitivity of pH-weighted amide proton transfer MRI in acute stroke patients using extrapolated semi-solid magnetization transfer reference signals. Magn Reson Med 78(3):871–880. https://doi.org/10.1002/mrm.26799
21. Jin T, Wang P, Hitchens TK, Kim SG (2017) Enhancing sensitivity of pH-weighted MRI with combination of amide and guanidyl CEST. NeuroImage 157:341–350. https://doi.org/10.1016/j.neuroimage.2017.06.007
22. Zhou J, van Zijl PC (2011) Defining an acidosis-based ischemic penumbra from pH-weighted MRI. Transl Stroke Res 3 (1):76–83. https://doi.org/10.1007/s12975-011-0110-4
23. Heo HY, Zhang Y, Jiang S, Lee DH, Zhou J (2016) Quantitative assessment of amide proton transfer (APT) and nuclear overhauser enhancement (NOE) imaging with extrapolated semisolid magnetization transfer reference (EMR) signals: II. Comparison of three EMR models and application to human brain glioma at 3 Tesla. Magn Reson Med 75 (4):1630–1639. https://doi.org/10.1002/mrm.25795
24. Cai K, Singh A, Poptani H, Li W, Yang S, Lu Y, Hariharan H, Zhou XJ, Reddy R (2015) CEST signal at 2ppm (CEST@2ppm) from Z-spectral fitting correlates with creatine distribution in brain tumor. NMR Biomed 28(1):1–8. https://doi.org/10.1002/nbm.3216
25. Zhou J, Tryggestad E, Wen Z, Lal B, Zhou T, Grossman R, Wang S, Yan K, Fu DX, Ford E, Tyler B, Blakeley J, Laterra J, van Zijl PC (2011) Differentiation between glioma and radiation necrosis using molecular magnetic resonance imaging of endogenous proteins and peptides. Nat Med 17(1):130–134. https://doi.org/10.1038/nm.2268
26. Zhao X, Wen Z, Huang F, Lu S, Wang X, Hu S, Zu D, Zhou J (2011) Saturation power dependence of amide proton transfer image contrasts in human brain tumors and strokes at 3 T. Magn Reson Med 66(4):1033–1041. https://doi.org/10.1002/mrm.22891

27. Zhao X, Wen Z, Zhang G, Huang F, Lu S, Wang X, Hu S, Chen M, Zhou J (2013) Three-dimensional turbo-spin-echo amide proton transfer MR imaging at 3-Tesla and its application to high-grade human brain tumors. Mol Imaging Biol 15(1):114–122. https://doi.org/10.1007/s11307-012-0563-1
28. Davis KA, Nanga RP, Das S, Chen SH, Hadar PN, Pollard JR, Lucas TH, Shinohara RT, Litt B, Hariharan H, Elliott MA, Detre JA, Reddy R (2015) Glutamate imaging (GluCEST) lateralizes epileptic foci in nonlesional temporal lobe epilepsy. Sci Transl Med 7 (309):309ra161. https://doi.org/10.1126/scitranslmed.aaa7095
29. Lee D-H, Lee D-W, Kwon J-I, Woo C-W, Kim S-T, Lee JS, Choi CG, Kim KW, Kim JK, Woo D-C (2018) In vivo mapping and quantification of creatine using chemical exchange saturation transfer imaging in rat models of epileptic seizure. Mol Imaging Biol. https://doi.org/10.1007/s11307-018-1243-6
30. Zhang S, Merritt M, Woessner DE, Lenkinski RE, Sherry AD (2003) PARACEST agents: modulating MRI contrast via water proton exchange. Acc Chem Res 36(10):783–790. https://doi.org/10.1021/ar020228m
31. Aime S, Carrera C, Delli Castelli D, Geninatti Crich S, Terreno E (2005) Tunable imaging of cells labeled with MRI-PARACEST agents. Angew Chem Int Ed Engl 44 (12):1813–1815. https://doi.org/10.1002/anie.200462566
32. Vinogradov E, Zhang S, Lubag A, Balschi JA, Sherry AD, Lenkinski RE (2005) On-resonance low B1 pulses for imaging of the effects of PARACEST agents. J Magn Reson 176(1):54–63. https://doi.org/10.1016/j.jmr.2005.05.016
33. Winter PM, Cai K, Chen J, Adair CR, Kiefer GE, Athey PS, Gaffney PJ, Buff CE, Robertson JD, Caruthers SD, Wickline SA, Lanza GM (2006) Targeted PARACEST nanoparticle contrast agent for the detection of fibrin. Magn Reson Med 56(6):1384–1388. https://doi.org/10.1002/mrm.21093
34. Yoo B, Raam MS, Rosenblum RM, Pagel MD (2007) Enzyme-responsive PARACEST MRI contrast agents: a new biomedical imaging approach for studies of the proteasome. Contrast Media Mol Imaging 2(4):189–198. https://doi.org/10.1002/cmmi.145
35. Sun PZ, van Zijl PC, Zhou J (2005) Optimization of the irradiation power in chemical exchange dependent saturation transfer experiments. J Magn Reson 175(2):193–200. https://doi.org/10.1016/j.jmr.2005.04.005
36. Woessner DE, Zhang S, Merritt ME, Sherry AD (2005) Numerical solution of the Bloch equations provides insights into the optimum design of PARACEST agents for MRI. Magn Reson Med 53(4):790–799. https://doi.org/10.1002/mrm.20408
37. Zaiss M, Bachert P (2013) Exchange-dependent relaxation in the rotating frame for slow and intermediate exchange – modeling off-resonant spin-lock and chemical exchange saturation transfer. NMR Biomed 26 (5):507–518
38. Zhou J, van Zijl PCM (2006) Chemical exchange saturation transfer imaging. Prog Nucl Magn Reson Spectrosc 48:109–136
39. Aime S, Calabi L, Biondi L, De Miranda M, Ghelli S, Paleari L, Rebaudengo C, Terreno E (2005) Iopamidol: exploring the potential use of a well-established x-ray contrast agent for MRI. Magn Reson Med 53(4):830–834. https://doi.org/10.1002/mrm.20441
40. Muller-Lutz A, Khalil N, Schmitt B, Jellus V, Pentang G, Oeltzschner G, Antoch G, Lanzman RS, Wittsack HJ (2014) Pilot study of Iopamidol-based quantitative pH imaging on a clinical 3T MR scanner. MAGMA 27 (6):477–485. https://doi.org/10.1007/s10334-014-0433-8
41. Sun PZ, Longo DL, Hu W, Xiao G, Wu R (2014) Quantification of iopamidol multi-site chemical exchange properties for ratiometric chemical exchange saturation transfer (CEST) imaging of pH. Phys Med Biol 59(16):4493
42. Longo DL, Sun PZ, Consolino L, Michelotti FC, Uggeri F, Aime S (2014) A general MRI-CEST ratiometric approach for pH imaging: demonstration of in vivo pH mapping with iobitridol. J Am Chem Soc 136 (41):14333–14336. https://doi.org/10.1021/ja5059313
43. Chen LQ, Howison CM, Jeffery JJ, Robey IF, Kuo PH, Pagel MD (2014) Evaluations of extracellular pH within in vivo tumors using acidoCEST MRI. Magn Reson Med 72 (5):1408–1417. https://doi.org/10.1002/mrm.25053
44. Randtke EA, Chen LQ, Corrales LR, Pagel MD (2014) The Hanes-Woolf linear QUESP method improves the measurements of fast chemical exchange rates with CEST MRI. Magn Reson Med 71(4):1603–1612. https://doi.org/10.1002/mrm.24792
45. Anemone A, Consolino L, Longo DL (2017) MRI-CEST assessment of tumour perfusion using X-ray iodinated agents: comparison with a conventional Gd-based agent. Eur Radiol 27 (5):2170–2179. https://doi.org/10.1007/s00330-016-4552-7

46. Longo DL, Michelotti F, Consolino L, Bardini P, Digilio G, Xiao G, Sun PZ, Aime S (2016) In vitro and in vivo assessment of non-ionic iodinated radiographic molecules as chemical exchange saturation transfer magnetic resonance imaging tumor perfusion agents. Investig Radiol 51(3):155–162. https://doi.org/10.1097/RLI.0000000000000217
47. Longo DL, Bartoli A, Consolino L, Bardini P, Arena F, Schwaiger M, Aime S (2016) In vivo imaging of tumor metabolism and acidosis by combining PET and MRI-CEST pH imaging. Cancer Res 76(22):6463–6470. https://doi.org/10.1158/0008-5472.CAN-16-0825
48. Longo D, Aime S (2017) Iodinated contrast media as pH-responsive CEST agents. In: McMahon MT, Gilad AA, JBM B, PCM VZ (eds) Chemical exchange saturation transfer imaging. vol advances and applications. Pan Stanford Publishing, Singapore, pp 447–466. https://doi.org/10.1201/9781315364421-20
49. Longo DL, Busato A, Lanzardo S, Antico F, Aime S (2013) Imaging the pH evolution of an acute kidney injury model by means of iopamidol, a MRI-CEST pH-responsive contrast agent. Magn Reson Med 70(3):859–864. https://doi.org/10.1002/mrm.24513
50. Longo DL, Cutrin JC, Michelotti F, Irrera P, Aime S (2017) Noninvasive evaluation of renal pH homeostasis after ischemia reperfusion injury by CEST-MRI. NMR Biomed 30(7). https://doi.org/10.1002/nbm.3720
51. Jin T, Autio J, Obata T, Kim SG (2011) Spin-locking versus chemical exchange saturation transfer MRI for investigating chemical exchange process between water and labile metabolite protons. Magn Reson Med 65(5):1448–1460. https://doi.org/10.1002/mrm.22721
52. Jiang W, Zhou IY, Wen L, Zhou X, Sun PZ (2016) A theoretical analysis of chemical exchange saturation transfer echo planar imaging (CEST-EPI) steady state solution and the CEST sensitivity efficiency-based optimization approach. Contrast Media Mol Imaging 11(5):415–423. https://doi.org/10.1002/cmmi.1699
53. Ji Y, Zhou IY, Qiu BS, Sun PZ (2017) Progress toward quantitative in vivo chemical exchange saturation transfer (CEST) MRI. Israel J Chem 57(9):809–824. https://doi.org/10.1002/ijch.201700025
54. Kim J, Wu Y, Guo Y, Zheng H, Sun PZ (2015) A review of optimization and quantification techniques for chemical exchange saturation transfer MRI toward sensitive in vivo imaging. Contrast Media Mol Imaging 10(3):163–178. https://doi.org/10.1002/cmmi.1628
55. Liu G, Song X, Chan KW, McMahon MT (2013) Nuts and bolts of chemical exchange saturation transfer MRI. NMR Biomed 26(7):810–828. https://doi.org/10.1002/nbm.2899
56. Sun PZ, Xiao G, Zhou IY, Guo Y, Wu R (2016) A method for accurate pH mapping with chemical exchange saturation transfer (CEST) MRI. Contrast Media Mol Imaging 11(3):195–202. https://doi.org/10.1002/cmmi.1680
57. Sun PZ, Sorensen AG (2008) Imaging pH using the chemical exchange saturation transfer (CEST) MRI: Correction of concomitant RF irradiation effects to quantify CEST MRI for chemical exchange rate and pH. Magn Reson Med 60(2):390–397. https://doi.org/10.1002/mrm.21653
58. Dixon WT, Ren J, Lubag AJ, Ratnakar J, Vinogradov E, Hancu I, Lenkinski RE, Sherry AD (2010) A concentration-independent method to measure exchange rates in PARACEST agents. Magn Reson Med 63(3):625–632. https://doi.org/10.1002/mrm.22242
59. Yang X, Song X, Ray Banerjee S, Li Y, Byun Y, Liu G, Bhujwalla ZM, Pomper MG, McMahon MT (2016) Developing imidazoles as CEST MRI pH sensors. Contrast Media Mol Imaging 11(4):304–312. https://doi.org/10.1002/cmmi.1693
60. Kujawa A, Kim M, Demetriou E, Anemone A, Livio Longo D, Zaiss M, Golay X (2019) Assessment of a clinically feasible Bayesian fitting algorithm using a simplified description of Chemical Exchange Saturation Transfer (CEST) imaging. J Magn Reson 300:120–134. https://doi.org/10.1016/j.jmr.2019.01.006
61. Pavuluri K, Manoli I, Pass A, Li Y, Vernon HJ, Venditti CP, McMahon MT (2019) Noninvasive monitoring of chronic kidney disease using pH and perfusion imaging. Sci Adv. https://doi.org/10.1126/sciadv.aaw8357
62. Sun PZ (2012) Simplified quantification of labile proton concentration-weighted chemical exchange rate (kws) with RF saturation time dependent ratiometric analysis (QUESTRA): normalization of relaxation and RF irradiation spillover effects for improved quantitative chemical exchange saturation transfer (CEST) MRI. Magn Reson Med 67(4):936–942

63. Ward KM, Balaban RS (2000) Determination of pH using water protons and chemical exchange dependent saturation transfer (CEST). Magn Reson Med 44(5):799–802
64. Wu R, Longo DL, Aime S, Sun PZ (2015) Quantitative description of radiofrequency (RF) power-based ratiometric chemical exchange saturation transfer (CEST) pH imaging. NMR Biomed 28(5):555–565. https://doi.org/10.1002/nbm.3284
65. Arena F, Irrera P, Consolino L, Colombo Serra S, Zaiss M, Longo DL (2018) Flip-angle based ratiometric approach for pulsed CEST-MRI pH imaging. J Magn Reson 287:1–9. https://doi.org/10.1016/j.jmr.2017.12.007
66. Anemone A, Consolino L, Arena F, Capozza M, Longo DL (2019) Imaging tumor acidosis: a survey of the available techniques for mapping in vivo tumor pH. Cancer Metastasis Rev. https://doi.org/10.1007/s10555-019-09782-9
67. Anemone A, Consolino L, Conti L, Reineri F, Cavallo F, Aime S, Longo DL (2017) In vivo evaluation of tumour acidosis for assessing the early metabolic response and onset of resistance to dichloroacetate by using magnetic resonance pH imaging. Int J Oncol 51(2):498–506. https://doi.org/10.3892/ijo.2017.4029
68. Sheth VR, Li Y, Chen LQ, Howison CM, Flask CA, Pagel MD (2012) Measuring in vivo tumor pHe with CEST-FISP MRI. Magn Reson Med 67(3):760–768. https://doi.org/10.1002/mrm.23038
69. Longo DL, Dastru W, Digilio G, Keupp J, Langereis S, Lanzardo S, Prestigio S, Steinbach O, Terreno E, Uggeri F, Aime S (2011) Iopamidol as a responsive MRI-chemical exchange saturation transfer contrast agent for pH mapping of kidneys: in vivo studies in mice at 7 T. Magn Reson Med 65(1):202–211. https://doi.org/10.1002/mrm.22608
70. Zhou IY, Wang E, Cheung JS, Zhang X, Fulci G, Sun PZ (2017) Quantitative chemical exchange saturation transfer (CEST) MRI of glioma using Image Downsampling Expedited Adaptive Least-squares (IDEAL) fitting. Sci Rep 7(1):84. https://doi.org/10.1038/s41598-017-00167-y
71. Li AX, Hudson RH, Barrett JW, Jones CK, Pasternak SH, Bartha R (2008) Four-pool modeling of proton exchange processes in biological systems in the presence of MRI-paramagnetic chemical exchange saturation transfer (PARACEST) agents. Magn Reson Med 60(5):1197–1206. https://doi.org/10.1002/mrm.21752
72. Zhou IY, Fuss TL, Igarashi T, Jiang W, Zhou X, Cheng LL, Sun PZ (2016) Tissue characterization with quantitative high-resolution magic angle spinning chemical exchange saturation transfer Z-spectroscopy. Anal Chem 88(21):10379–10383. https://doi.org/10.1021/acs.analchem.6b03137
73. Xu J, Zaiss M, Zu Z, Li H, Xie J, Gochberg DF, Bachert P, Gore JC (2014) On the origins of chemical exchange saturation transfer (CEST) contrast in tumors at 9.4 T. NMR Biomed 27(4):406–416
74. Zaiss M, Xu J, Goerke S, Khan IS, Singer RJ, Gore JC, Gochberg DF, Bachert P (2014) Inverse Z-spectrum analysis for spillover-, MT-, and T1-corrected steady-state pulsed CEST-MRI—application to pH-weighted MRI of acute stroke. NMR Biomed 27(3):240–252. https://doi.org/10.1002/nbm.3054
75. Kim M, Gillen J, Landman BA, Zhou J, van Zijl PC (2009) Water saturation shift referencing (WASSR) for chemical exchange saturation transfer (CEST) experiments. Magn Reson Med 61(6):1441–1450. https://doi.org/10.1002/mrm.21873
76. Wei W, Jia G, Flanigan D, Zhou J, Knopp MV (2014) Chemical exchange saturation transfer MR imaging of articular cartilage glycosaminoglycans at 3 T: accuracy of B0 field inhomogeneity corrections with gradient echo method. Magn Reson Imaging 32(1):41–47. https://doi.org/10.1016/j.mri.2013.07.009
77. Sun PZ, Farrar CT, Sorensen AG (2007) Correction for artifacts induced by B(0) and B(1) field inhomogeneities in pH-sensitive chemical exchange saturation transfer (CEST) imaging. Magn Reson Med 58(6):1207–1215. https://doi.org/10.1002/mrm.21398
78. Stancanello J, Terreno E, Castelli DD, Cabella C, Uggeri F, Aime S (2008) Development and validation of a smoothing-splines-based correction method for improving the analysis of CEST-MR images. Contrast Media Mol Imaging 3(4):136–149. https://doi.org/10.1002/cmmi.240
79. Terreno E, Stancanello J, Longo D, Castelli DD, Milone L, Sanders HM, Kok MB, Uggeri F, Aime S (2009) Methods for an improved detection of the MRI-CEST effect.

Contrast Media Mol Imaging 4(5):237–247. https://doi.org/10.1002/cmmi.290

80. Wu Y, Zhou IY, Igarashi T, Longo DL, Aime S, Sun PZ (2018) A generalized ratiometric chemical exchange saturation transfer (CEST) MRI approach for mapping renal pH using iopamidol. Magn Reson Med 79 (3):1553–1558. https://doi.org/10.1002/mrm.26817
81. Raghunand N, Howison C, Sherry AD, Zhang S, Gillies RJ (2003) Renal and systemic pH imaging by contrast-enhanced MRI. Magn Reson Med 49(2):249–257. https://doi.org/10.1002/mrm.10347

Chapter 41

Analysis Protocol for Renal Sodium (^{23}Na) MR Imaging

James T. Grist, Esben Søvsø Szocska Hansen, Frank G. Zöllner, and Christoffer Laustsen

Abstract

The signal acquired in sodium (^{23}Na) MR imaging is proportional to the concentration of sodium in a voxel, and it is possible to convert between the two using external calibration phantoms. Postprocessing, and subsequent analysis, of sodium renal images is a simple task that can be performed with readily available software. Here we describe the process of conversion between sodium signal and concentration, estimation of the corticomedullary sodium gradient and the procedure used for quadrupolar relaxation analysis.

This chapter is based upon work from the COST Action PARENCHIMA, a community-driven network funded by the European Cooperation in Science and Technology (COST) program of the European Union, which aims to improve the reproducibility and standardization of renal MRI biomarkers. This analysis protocol chapter is complemented by two separate chapters describing the basic concept and experimental procedure.

Key words Magnetic resonance imaging (MRI), Kidney, Rats, ^{23}Na, Sodium

1 Introduction

The signal acquired in sodium (^{23}Na) MR imaging is proportional to the concentration of sodium in a voxel, and it is possible to convert between the two using external calibration phantoms. To calculate sodium concentration maps, an imaging volume including the tissue of interest and external calibration phantoms is required, using a gradient echo (GRE) sequence for data acquisition. T_2^* relaxation maps can be calculated from multiecho GRE data acquired in the same acquisition. Theoretical considerations and acquisition protocols are detailed in the chapters by Grist JT et al. "Sodium (^{23}Na) MRI of the Kidney: Basic Concept" and "Sodium (^{23}Na) MRI of the Kidney: Experimental Protocol." Creation of sodium concentration maps can be performed with several commercially available software packages (*see* **Note 1**). In general, a linear fit is performed between the mean signal intensity of each

Andreas Pohlmann and Thoralf Niendorf (eds.), *Preclinical MRI of the Kidney: Methods and Protocols*, Methods in Molecular Biology, vol. 2216, https://doi.org/10.1007/978-1-0716-0978-1_41,

calibration phantoms and a region of noise. The fitting coefficients are used to convert sodium signal to sodium concentration. This chapter focuses on how to do this, conceptually.

This analysis protocol chapter is complemented by two separate chapters describing the basic concept and experimental procedure, which are part of this book.

2 Materials

2.1 Software Requirements

1. To calculate parameter maps: A programming environment capable of applying fitting models, such as Python (www.python.org), Octave (www.gnu.org/software/octave) or MATLAB (The MathWorks, Natick, MA, USA) with a curve fitting capability. The method described in this chapter provides a detailed description for a solution in MATLAB, but can be adopted to other platforms.
2. Optional: A image processing software such as Fiji (www.fiji.sc) or Horos (www.horosproject.org).

2.2 Source Data: Format Requirements and Quality Check

2.2.1 Input Requirements

To be able to calculate sodium concentration maps, images including sodium calibration phantoms acquired during an experiment are required, as well as the known absolute concentration of sodium in the calibration phantoms.

2.2.2 Data Exclusion

When sodium imaging is acquired, it commonly has a low signal-to-noise ratio (SNR). In order to construct accurate sodium T_2* maps, it is important to ensure that the signal of kidneys is greater than that of the background noise, else a poor fit will occur. Therefore, data with SNR lower than a threshold (e.g., SNR < 5) should be discarded.

This step should be avoided for concentration mapping, as a region of noise is required to calculate an assumed 0 mmol/L signal value.

2.2.3 SNR Check for T_2* Mapping

To check SNR in renal sodium imaging in MATLAB (NB: example code for SNR measurements assumes a single slice and absolute value data):

1. Draw an ROI, using the "roipoly" command, over a region of background noise free of artefacts.

```
Region = poly2mat(roipoly(mat2gray(image_slice)));
Masked_Region = Region .* image_slice;
```

2. Calculate the standard deviation of the noise using the "std" command.

```
NoiseSTD = std(Masked_Region(Masked_Region >0));
```

3. Divide the original image by 0.66 multiplied by the standard deviation of the noise to produce SNR maps.

```
Image_SNR = image_slice ./ (sqrt(2)*NoiseSTD);
```

4. SNR maps can then be used to form a mask to remove signal less than a predefined SNR value (e.g., 5).

```
Image_SNR(Image_SNR<5) = 0;
Image_SNR(Image_SNR>1) = 1;
Masked_Image_Slice = Image_slice .* Image_SNR
```

2.2.4 Dual Flip Angle B_1 Mapping for Sodium Concentration Mapping

Furthermore, if local send and receive RF coils are used, B_1 mapping to correct for signal inhomogeneity due to coil profiles can be performed (*see* **Note 2**).

3 Methods

3.1 Sodium Concentration Mapping

The mean signal from phantoms in the images can be derived using regions of interest (ROIs). Furthermore, a mean image noise value should be defined on a slice by slice basis using signal outside of the body.

Once the mean signal of each phantom, as well as noise, has been calculated, a linear fit should be performed between the known concentration values and the phantom/noise signal (assuming noise represents 0 mmol/L sodium).

The coefficients derived from the fit (offset and slope) can then be used to convert each voxel in the image from signal intensity to concentration using Eq. 1, below.

$$\text{Sodium concentration}\left(\text{mmolL}^{-1}\right) = \frac{\text{signal} - \text{offset}}{\text{slope}} \qquad (1)$$

3.1.1 Algorithm for Sodium Concentration Mapping

1. Define region of noise on a slice-by-slice basis using either automated (selecting voxels in a specific region of each image) or via ROI placement on a slice-by-slice basis.
2. Calculate the mean of each noise region and store this value in a vector (e.g., *meannoise*).
3. Segment sodium calibration phantoms using ROIs and calculate the mean signal for each phantom.
4. Perform concentration mapping by calculating a linear fit between the noise, phantom signals, and the known

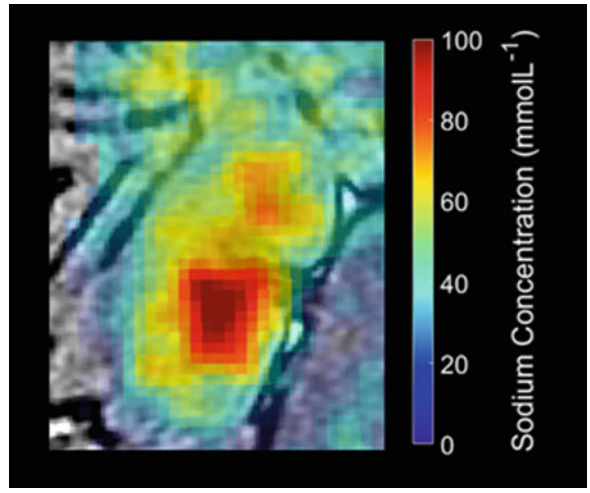

Fig. 1 Example images of sodium signal in the healthy porcine kidney, acquired at 3T, demonstrating increase sodium signal in the medulla, in comparison to the cortex

concentrations of the phantoms (example code presented below) on a slice by slice basis

3.1.2 Example Matlab Code

```
  for zslice = 1:Number_Of_Z_Slices
        fitting = polyfit([0,conc1,conc2],[meannoise(zslice),
Phantom1, Phantom2],1);
      slope = fitting(1);
      offset = fitting(2);
      Image(:,:,zslice) = (Image(:,:,zslice) - offset)./slope;
  End
```

Example sodium concentration mapping data of the porcine kidney can be seen in Fig. 1.

3.1.3 Biexponential T_{2^*} Mapping

In order to map the biexponential T_2^* of the kidney (separating the restricted quadrupolar spins and the freely moving spins), a more complicated process of signal fitting is required. Utilizing multi-echo GRE data, acquired in the same imaging acquisition, a non-linear fitting routine is employed to determine the behavior of the sodium signal, as described in Eq. 2.

$$s(\mathrm{TE}) = \left(a\, e^{-\frac{\mathrm{TE}}{\mathrm{T}^*_{2,\mathrm{Short}}}} + b\, e^{-\frac{\mathrm{TE}}{\mathrm{T}^*_{2,\mathrm{Long}}}} \right) \tag{2}$$

where a and b are the relative pool sizes, and $\mathrm{T}^*_{2,\mathrm{Short}}$ and $\mathrm{T}^*_{2,\mathrm{Long}}$ are the pool T_2^* constants (ms), with the constraints that $a + b = 1$, and $\mathrm{T}^*_{2,\mathrm{Short}} > \mathrm{T}^*_{2,\mathrm{Long}}$. Assuming five or more data sets are acquired, the following MATLAB code can be used to fit the above curve. An example fit is shown in Fig. 2.

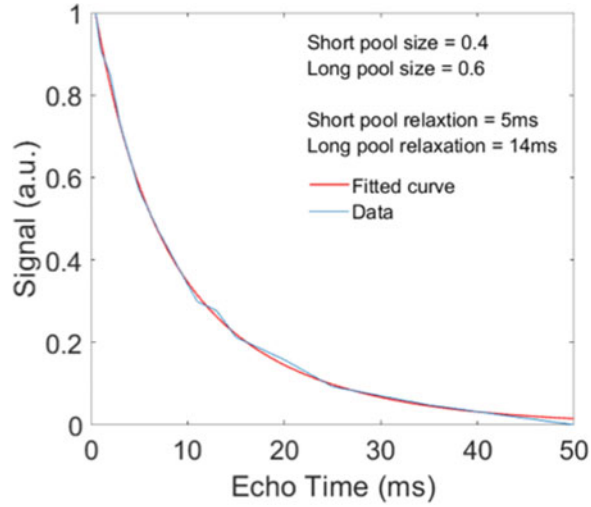

Fig. 2 Example fit of biexponential data acquired from an agar phantom

3.1.4 Algorithm for T2 Mapping*

1. Perform SNR thresholding as detailed in Subheading 2.2.3.
2. Loop biexponential curve-fitting code (example Matlab code presented below) over all SNR masked regions in the image. The fit algorithm used here is trust region reflective.
3. Store data either as DICOM, proprietary (e.g., .mat), or text files.

3.1.5 Example Matlab Fitting Code

```
%% List of echo times acquired during imaging
TE_List = [TE1, TE2, TE3,...];
%% Setting up fit options
fopts = fitoptions('Method','NonlinearLeastSquares',...
                   'Lower',[0,0,0,5],...
                   'Upper',[1,1,5,55]
                   'StartPoint',[0.2 1,10]);
% Fit curve equation
ft = fittype('a*exp(-x/b) + (1-a)*exp(-x/c)','coefficients',
{'a', 'T21','T22'},'independent','x','options',fopts);
%% Pre-allocation of memory to speed up fitting
ShortPoolSize(xvoxel,yvoxel,zvoxel) = ...
 zeros(size(Imaging_Data,1),size(imageing_Data,2),size(Ima-
ging_Data,3));
LongPoolSize(xvoxel,yvoxel,zvoxel) = ...
 zeros(size(Imaging_Data,1),size(imageing_Data,2),size(Ima-
ging_Data,3));
ShortPoolRelaxation(xvoxel,yvoxel,zvoxel) = ...
 zeros(size(Imaging_Data,1),size(imageing_Data,2),size(Ima-
ging_Data,3));
LongPoolRelaxation(xvoxel,yvoxel,zvoxel) = ...
 zeros(size(Imaging_Data,1),size(imageing_Data,2),size(Ima-
ging_Data,3));
```

```
%% Fitting loop core
for zslice = 1:Number_Of_Z_Slices
   for yvoxel = 1:Number_Of_Y_Voxels
      for xvoxel = 1:Number_Of_X_Voxels
         if (Masked_Image_Slice ~= 0)
            % Extract data vector for one pixel
            Data_Vector = Imaging_Data (xvoxel,yvoxel,zlice,:);
            % Do curve fitting for one voxel
            [Fit,gof] = fit(TE_List,Data_Vector, ft);
            % Store results
            ShortPoolSize(xvoxel,yvoxel,zvoxel) = Fit.a;
            LongPoolSize(xvoxel,yvoxel,zvoxel) = 1 - Fit.a;
            ShortPoolRelaxation(xvoxel,yvoxel,zvoxel) = Fit.b;
            LongPoolRelaxation(xvoxel,yvoxel,zvoxel) = Fit.c
         end
      end
   end
end
```

If data are acquired at higher magnetic field strengths ($B_0 \geq 3$T), it is advisable to alter the pool constraints for the parameter *fopts* to reflect the shorter $T^*_{2,Short}$ and $T^*_{2,Long}$ components.

3.2 Visual Display

There is no current consensus on the best colour map to use when displaying sodium concentration images. T_1- or T_2-weighted images acquired in the same slice position can provide guidance for the interpretation as well as base layer for presenting the images as a set of fused images, *see* Fig. 1.

An example display option for MATLAB is described below:

1. Display the parameter map, which is a matrix with floating point numbers, as an image (in MATLAB: imagesc (ShortPoolRelaxation)).
2. Remove axis labels and ensure the axis are scaled equally, so that pixels are square and not rectangular (in MATLAB: axis off; axis equal;).
3. Select the color map and display a color bar (in MATLAB: colormap(hot(256)); colorbar;).
4. Set the display range for the color coding, for example, for short and long T_2* [0 5] and [5 60], respectively; (in MATLAB: caxis([0 5]);).

3.3 Quantification

In order to obtain quantitative medulla and cortex values from sodium concentration maps, the kidney can be segmented using either concentric objects or semiautomated ROI placement [1, 2]. To assess the corticomedullary sodium gradient, a linear fit can be performed across concentration values derived from the

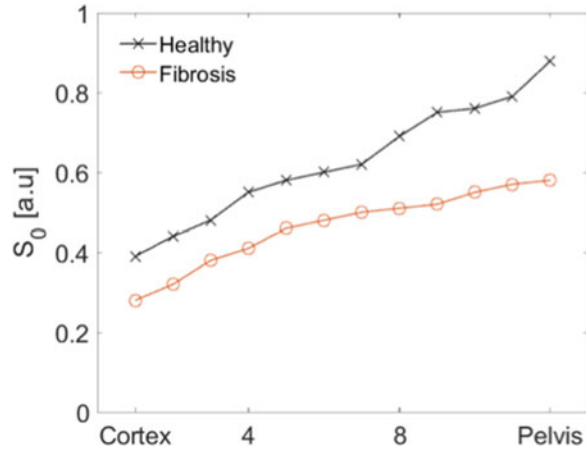

Fig. 3 Example corticomedullary sodium gradient, healthy (black) and impaired rodent kidney (orange)

Table 1
Example sodium concentration values from renal compartments, derived from post-sacrifice kidneys [5]

Tissue type	Total sodium concentration (mmol/L)
Cortex	29 ± 7
Outer-medullar	75 ± 20
Inner-medullar	161 ± 29

concentric objects method, providing the slope of the gradient. An example corticomedullary sodium gradient in both healthy and fibrosis impaired rodent kidney can be seen in Fig. 3.

3.4 Results Validation

Further validation of imaging derived results can be performed using biopsy derived tissue samples, using methods such as flame photometry, mass spectrometry, or *ex vivo* spectroscopy.

3.4.1 Comparison with Tissue Values from Biopsy

3.4.2 Comparison with Reference Values from the Literature

If biopsy derived results cannot be obtained, for example due to longitudinal studies, obtained values for both tissue segmentation can be compared against reference values, shown in Table 1.

4 Notes

1. Processing is typically performed in software packages such as MATLAB (The MathWorks, MA) or open source platforms as python programming language (python.org). The data can either

be processed as DICOM images or if available as the raw data format from the scanner (dicomstandard.org/using/cds/). Finalizing the data in the DICOM format pipelines the data for further analysis and comparison to conventional MRI images.

2. The linear proportionality of the NMR signal to the spin density allows for the absolute quantification of the Total Sodium Concentration (TSC) on the basis of a known concentration reference. However, TSC measurements are distorted by hardware-dependent influences and by typical ^{23}Na-NMR properties. This can be determined and corrected with the help of B_1 mapping methods [3]. Mapping methods which allow short TE are the double-angle and the phase-sensitive method [4].

Acknowledgments

This chapter is based upon work from COST Action PARENCHIMA, supported by European Cooperation in Science and Technology (COST). COST (www.cost.eu) is a funding agency for research and innovation networks. COST Actions help connect research initiatives across Europe and enable scientists to enrich their ideas by sharing them with their peers. This boosts their research, career, and innovation.
PARENCHIMA (renalmri.org) is a community-driven Action in the COST program of the European Union, which unites more than 200 experts in renal MRI from 30 countries with the aim to improve the reproducibility and standardization of renal MRI biomarkers.

References

1. Milani B, Ansaloni A, Sousa-Guimaraes S et al (2017) Reduction of cortical oxygenation in chronic kidney disease: evidence obtained with a new analysis method of blood oxygenation level-dependent magnetic resonance imaging. Nephrol Dial Transplant 32(12):2097–2105
2. Mikheev A, Lim RP (2016) A semi-automated "blanket" method for renal segmentation from non-contrast T1-weighted MR images. MAGMA 29:197–206
3. Gatzeva-topalova PZ, Warner LR, Pardi A, Carlos M (2011) Quantitative sodium imaging with a flexible twisted projection pulse sequence. Magn Reson Med 18:1492–1501
4. Morrell GR, Schabel MC (2010) An analysis of the accuracy of magnetic resonance flip angle measurement methods. Phys Med Biol 55:6157–6174
5. Saikia TC (1964) Composition of the renal cortex and medulla of rats during water diuresis and antidiuresis. J Clin Invest 51:1145–1151

Chapter 42

Analysis Methods for Hyperpolarized Carbon (^{13}C) MRI of the Kidney

Galen D. Reed, Natalie J. Korn, Christoffer Laustsen, and Cornelius von Morze

Abstract

Hyperpolarized ^{13}C MR is a novel medical imaging modality with substantially different signal dynamics as compared to conventional ^{1}H MR, thus requiring new methods for processing the data in order to access and quantify the embedded metabolic and functional information. Here we describe step-by-step analysis protocols for functional renal hyperpolarized ^{13}C imaging. These methods are useful for investigating renal blood flow and function as well as metabolic status of rodents in vivo under various experimental physiological conditions.

This chapter is based upon work from the COST Action PARENCHIMA, a community-driven network funded by the European Cooperation in Science and Technology (COST) program of the European Union, which aims to improve the reproducibility and standardization of renal MRI biomarkers. This analysis protocol chapter is complemented by two separate chapters describing the basic concept and experimental procedure.

Key words Magnetic resonance imaging (MRI), Kidney, Mice, Rats, Hyperpolarization, ^{13}C, Dynamic nuclear polarization (DNP)

1 Introduction

Hyperpolarized ^{13}C imaging experiments can yield a wide variety of metabolic, structural, and functional information which is extracted via analysis of time-varying NMR signals. The choice of analysis strategy depends on numerous factors, including the imaging agent, the organ of interest, the acquisition strategy, and imaging parameter being measured. In general, much of the image-formation pipelines are nearly identical to those for ^{1}H MRI; particularly, the steps of Fourier transforming k-space data, reconstructing under-sampled data using parallel imaging afforded by RF coil arrays, etc. are nearly identical and will not be discussed in detail here. Instead, we describe some of the applications more specific to hyperpolarized ^{13}C data analysis, and we guide the reader through

Andreas Pohlmann and Thoralf Niendorf (eds.), *Preclinical MRI of the Kidney: Methods and Protocols*, Methods in Molecular Biology, vol. 2216, https://doi.org/10.1007/978-1-0716-0978-1_42,

details and attempt to point out pitfalls. We select a few applications which will be interesting for researchers studying renal physiology and function in a preclinical setting, and where available, we point to links to source code for image processing pipelines.

Beginning at the steps of image formation, there are some key attributes differentiating hyperpolarized from conventional MRI. One of the primary differences is the constant depolarization of the contrast agent during imaging. Image encoding requires radio frequency (RF) excitation of z polarization that is typically nonrenewable, meaning it does not recover with T_1 relaxation. Instead, T_1 relaxation imposes an exponential decay envelope which decreases the z polarization over time. In addition to potentially degrading image resolution, this window has the consequence that physiological parameters calculated from the time course of image pixel intensity may be biased, either by RF flip angle (θ) nonuniformity or by influence of relaxation times which are almost never known precisely beforehand in vivo. In some of the subsequent examples of this chapter, this effect is accounted for, or it may be compensated for through the use of acquisition-based signal compensation. However, a thorough error propagation of parameter estimation is extremely difficult as is the estimation of all ancillary parameters influencing the measurements. For instance, although precise flip angle knowledge is key to the estimation of virtually every parameter measured here, θ is typically estimated using an external reference phantom during imaging. Furthermore, it is extremely difficult to map out the transmitter profile due to the low natural ^{13}C abundance *in vivo*. In general, the nuances of hyperpolarized MRI may complicate image processing and could potentially bias parameters that are calculated from images if not properly taken into account.

This analysis protocol chapter is complemented by two separate chapters describing the basic concept and experimental procedure, which are part of this book.

2 Materials

2.1 Software Analysis Tools

There are numerous publicly shared, open-source MRI processing code written on the MATLAB platform which can be directly ported to the open source platform GNU Octave. Processing requiring nonlinear optimization, signal processing, image manipulations, or DICOM reading/writing will require installation of additional toolboxes. Octave and MATLAB provide excellent prototyping platforms since the file input/output interface for most vendors' raw data formats can be found on online repositories or via the vendor directly. For example, the files for reading the GE P-file format are distributed with the EPIC software development kit (SDK) software release via the MR collaboration community portal

[1]. Within this SDK is the set of MATLAB scripts in the folder read_MR that may be invoked as

```
[rawdata, header] = read_MR_rawdata(filename)
```

Where filename is the name of the raw file (P-file), and rawdata and header are the parsed outputs. The variable rawdata is parsed as

```
rawdata(yres, xres, phases, echoes, slices, receivers)
```

Note that GE P-files are stored on the scanner directory /usr/g/mrraw. An example 2D Fourier Transform reconstruction of a single slice, single coil image will look like

```
singleSliceImage = abs(fftnc(rawdata(:, :, 1, 1, sliceIndex, coilIndex)));
```

Aside from vendor-specific items, the vast majority of publicly shared source code is on a github repository. To interact with this code base, git should be loaded on your localhost. On Mac, this can be done with the MacPorts utility (www.macports.org) via terminal command

```
sudo port install git
```

Note that all MacPorts-installed code can be conveniently updated via the single command sudo port selfupdate. The example code-base for this book chapter [2] can be cloned from the github repository by running the following in your terminal:

```
git clone https://github.com/galenreed/renalC13MRIBook.git
```

This will clone the repository and create a folder called renalC13MRIBook with subfolders and scripts that can be run and modified locally.

3 Methods

3.1 Quantitative Perfusion Imaging

Noninvasive determination of perfusion has been of significant interest in contrast-enhanced MRI and has numerous applications in oncology and cerebral blood flow mapping. Unlike contrast-enhanced MRI using gadolinium (Gd) based agents, hyperpolarized ^{13}C images contain no background signal contribution and thus have the desirable characteristic that their signal intensity is proportional to the agent concentration. Commonly used hyperpolarized ^{13}C perfusion targets are [^{13}C]urea [3], [^{13}C, ^{15}N]urea

[4], bis-1,1-(hydroxymethylcyclopropane-D_8) (commonly referred to as HP001) [5], and [^{13}C]tert-butanol [6]. These molecules differ greatly in their tissue permeability [7], biodistribution, and relaxation time-based contrast [4]. Furthermore, the endogenous nature of many hyperpolarized probes makes them highly attractive as a potential agent which may be delivered to patients with impaired renal function. Data for perfusion imaging typically consist of time- and space resolved magnitude images of nonexchanging molecular probes which are acquired with gradient echo (GRE) or steady state free precession (SSFP) pulse sequences. Since the initial tissue uptake is an important piece of the curve for data processing, data acquisition is typically initiated before or at the beginning of contrast agent injection, and temporal resolution should be adequate to encode the uptake and washout curves.

In this section, we walk through the processing script example_perfusion.m that contains the essential processing elements of data from this experiment. The goal this problem is to solve the convolution integral

$$C_{\mathrm{VOI}}(t) = F\int_0^\infty C_{\mathrm{a}}(\tau)R(t-\tau)\mathrm{d}\tau \tag{1}$$

for the product of the residue function $R(t)$ and flow rate F. This model uses the bolus tracking theory which is described in depth in ref. 8. In this approach, the concentration of the tracer in the tissue $C_{\mathrm{VOI}}(t)$ is modeled as a convolution integral with the arterial input function $C_{\mathrm{a}}(t)$ and the residue function. Since $C_{\mathrm{VOI}}(t)$ and $C_{\mathrm{a}}(t)$ are measured directly off the time course images, the $F{\cdot}R(t)$ can be estimated via deconvolution. The product $F{\cdot}R(t)$ serves as the tissue impulse response in this framework. The essential steps in the processing pipeline are as follows:

1. Delineate the arterial pixels. In the example code, a single coordinate from the center of the artery is stored in the array AIFPixels with a single index per slice. Note that this processing script creates a rectangular ROI centered around the pixel coordinate to reduce noise. The intensity of these pixels is used as the function $C_{\mathrm{a}}(t)$.
2. Create the matrix A which whose columns consist of $C_{\mathrm{a}}(t)$, where each subsequent column is translated one time point (see line 58 in example_perfusion.m and equation 11 in ref. 8). This is for discretizing the convolution integral in order to recast it as a matrix multiplication, which can then be inverted to measure the product $F{\cdot}R(t)$. *See* refs. 8–10 for details
3. Loop through all pixels within the image and create the temporal curve to create $C_{\mathrm{VOI}}(t)$
4. Invert the linear system to estimate $F{\cdot}R(t)$. The code example gives two examples of how to do this: the first uses Tikhonov

regularization, the second uses singular value decomposition (SVD)-based thresholding.

5. Compute the maximum of this function to obtain the flow rate, then normalize by Δt to recast the value in standard mL/mL/s units.

A few nuances of the computation are discussed. The tissue residue function $R(t)$ tends to have a monotonically decreasing shape and is often approximated as a single exponential decay in model-dependent deconvolution techniques. By definition, $R(0) = 1$, since it depends on the cumulative distribution of the tracer transit times in the tissue. Therefore, the flow F can be solved for once $R(t)$ is estimated.

$$F = \frac{\max\left(FR(t)\right)}{\Delta t} \tag{2}$$

Note that the maximum operation is used rather than taking the value $R(t = 0)$ to account for possible imaging/infusion delays. Hyperpolarized ^{13}C images are proportional to the concentration which simplifies the estimation of $C_{vol}(t)$ and $C_a(t)$ since they can be directly measured from image ROIs. However, the polarization level constantly decreases post injection, so the signal proportionality is not constant over time. To compensate this effect, $R(t)$ has been modelled as a product $R_t(t)P(t)$, where $R_t(t)$ is the true residue function and $P(t)$ is an exponential decay which models the T_1 decay and RF depolarization [9]. Alternatively, an acquisition-based compensation using progressively increasing flip angles on subsequent time-points can be used to offset this signal decay over a fixed horizon [10]. As ref. 8 points out, it is highly important to handle noise amplification in this inversion by using techniques such as singular value decomposition- (SVD) based thresholding or regularization. Figure 1 shows the effects of Tikhonov regularization on the calculated flow images and highlights its importance. When no regularization is used, the estimated $F{\cdot}R(t)$ product shows large oscillations over the time course. Adding regularization not only smooths the time-course curve but also yields a residue function closely resembling the expected exponential decay.

3.2 Relaxation Mapping

Preliminary measurements of NMR relaxation times (T_1 and T_2) of hyperpolarized ^{13}C contrast agents show interesting in vivo renal tissue contrast. The T_2 of [1-^{13}C]lactate after injection of hyperpolarized [1-^{13}C]pyruvate has been shown to increase in tumor regions in preclinical models [11]. The T_2 of [^{13}C, ^{15}N]urea has been shown to greatly increase in the rat kidney [4], and this signal change has been linked to the glomerular filtration process [12]. Anatomically, an inward, cortex-to-medulla T_2 gradient is observed. This gradient becomes disrupted in diabetic nephropathy

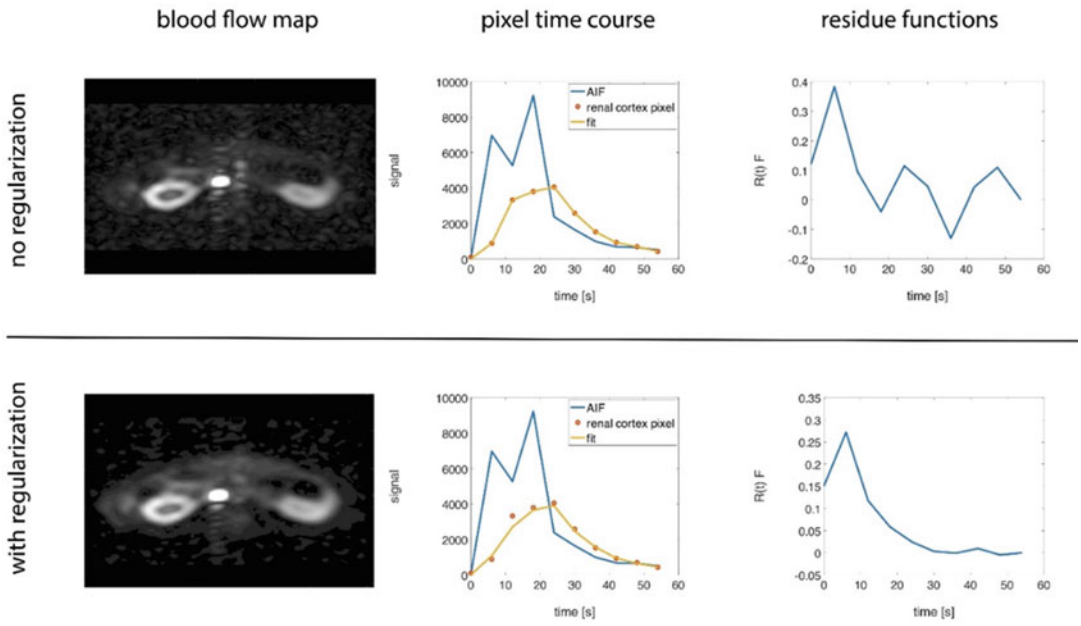

Fig. 1 Estimating blood flow from dynamic hyperpolarized [^{13}C]urea images of a rat kidney. The top and bottom panels show the problem solved with and without using regularization. The blood flow maps (left) are calculated from solving the deconvolution of the arterial input function (AIF) and the tissue uptake curves (center). Note that there is a dip in the AIF due to a chase infusion of saline. The curves on the right highlight the need for some degree of regularization. The top solution, derived without regularization, shows large-amplitude fluctuations, while the bottom curve, derived with regularization, shows a much cleaner curve more closely resembling an exponential decay. Regularization does slightly decrease curve fit/data consistency; this can be seen on the orange curves in the center plot, where the regularized curve (bottom) deviates slightly more from the nonregularized curves (top). However, it generally produces cleaner images with reduces noise sensitivity

[13] as well as in ischemic injury [14]. T_2 mapping is performed on magnitude images which are spatially and echo-time-resolved. Acquisitions are based on multiple spin-echo acquisitions that must be specifically tailored to the hyperpolarized experiment. To best utilize the nonrenewable magnetization, acquisitions start with a 90° excitation followed by a train of spin echo RF pulses and encoding gradients. Hyperpolarized ^{13}C T_2 values reported in the literature are long compared to those of ^{1}H, ranging from hundreds of milliseconds to several seconds. The effective T_2 measured can have some dependence on the inhomogeneity of the transmit field (B_1^+), but the dependency is not strong unless the deviation from 180° is very large [12].

Modeling multiexponential T_2, decay in NMR signals is typically performed by matching the signal to an expression of the form

$$S = S_0 + \sum_{i=i}^{n} a_i e^{-t/T_{2,i}} \tag{3}$$

where S_0 is a bias term, a_i is the signal amplitude of the ith T_2 component, and $T_{2,i}$ is the decay time constant. Typically, a_i and $T_{2,i}$ are all unknown beforehand and must be solved for. If SNR is sufficiently high, the bias term can be ignored. The T_2NNLS algorithm [15] casts the estimation of multiple T_2 decays as a matrix inversion problem:

$$\begin{pmatrix} S(\mathrm{TE}_1) \\ \vdots \\ S(\mathrm{TE}_n) \end{pmatrix} = \begin{pmatrix} e^{-\mathrm{TE}_1/T_{2,1}} & \cdots & e^{-\mathrm{TE}_1/T_{2,m}} \\ \vdots & \ddots & \vdots \\ e^{-\mathrm{TE}_n/T_{2,1}} & \cdots & e^{-\mathrm{TE}_n/T_{2,m}} \end{pmatrix} \begin{pmatrix} a_1 \\ \vdots \\ a_m \end{pmatrix} \tag{4}$$

Note that this is a standard problem of the form

$$y = Ax \tag{5}$$

where the matrix A is constructed from selecting m logarithmically spaced T_2 values from within a defined range, then computing an idealized T_2 decay curve sampled at each acquired echo time. These idealized single-exponential decays constitute the columns of the A matrix. The column vector x contains the amplitudes which are solved for, and y contains the measurements. Equation 5 is solved for using regularized, nonnegative least squares.

$$\underset{x}{\operatorname{argmin}} \quad \|Ax - y\|^2 + \lambda \|x\|^2 \tag{6}$$

Similar to the perfusion measurement, the use of the L2 norm for the regularization term is required as detecting multiple T_2 values that are different but close in value can be exceedingly susceptible to noise amplification.

In the example script example_t2nnls.m, the following steps are used to demonstrate the T_2 nonnegative least squares algorithm on rat kidney data:

1. Reconstruct spatially and echo-time-resolved magnitude images.
2. Is spatial resolution is sufficient to resolve respiratory motion, an image alignment via rigid translation may be applied [12].
3. Create a list of echo times (TElist in the script) corresponding to the TE of each image.
4. Create a T_2 axis which is a vector of logarithmically spaced T_2 values spanning the expected solution range.
5. Create the matrix A from Eqs. 4 and 5 as is performed in the script t2nnls.m (where the matrix is stored as the variable T2DecayMatrix).
6. Extract signal intensity of a single pixel over TEs ($S(\mathrm{TE})_1 \ldots S(\mathrm{TE})_n$).
7. Compute the best fit solution $S(T_2)$. This function can be created at each pixel. Figure 2 shows example $S(T_2)$

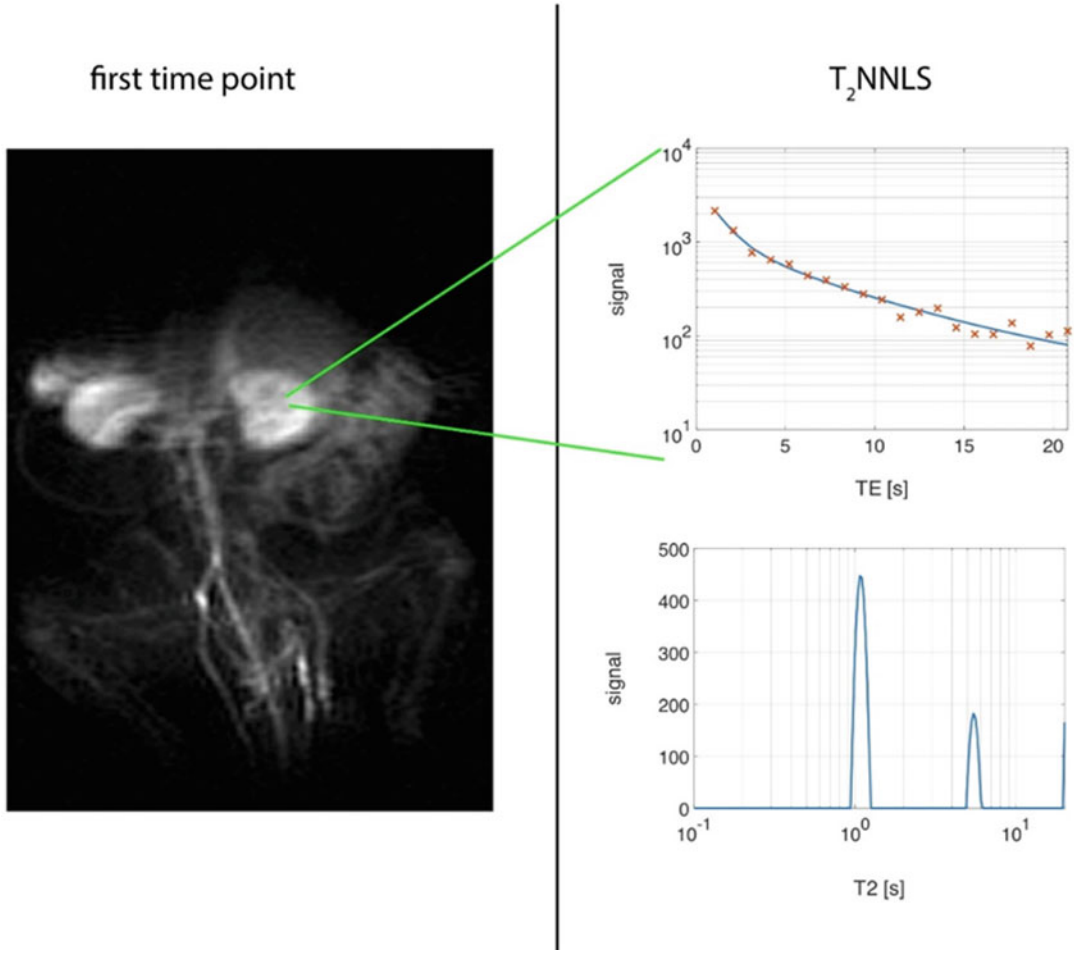

Fig. 2 Multiexponential analysis of a hyperpolarized T_2 mapping experiment. Left: coronal [^{13}C, ^{15}N]urea image of a rat at the earliest echo time (500 ms). Right, top: T_2 decay curve from a single pixel inside the kidney. Right, bottom: multiexponential analysis using the T2NNLS algorithm. Using L2 regularization penalty causes broadened peaks in the T_2 spectrum. Note that bias offsets are captured as signal at the high extremum of the T_2 domain. Hyperpolarized [^{13}C, ^{15}N]urea images of the rat kidney show two distinct decay modes representing the vascular and renal filtrate pools of the contrast agent

distributions calculated from a single pixel within the kidney calculated differing values of the regularization parameter.

8. $S(T_2)$ can be treated as a spectrum, so the signal intensity within some given T_2 bounds may be integrated to find the intensity within that range. Alternatively, the expectation value $\langle T_2 \rangle$ can be calculated by treating $S(T_2)$ as a probability distribution function and computing moments. This is demonstrated in Eq. 2, ref. 16 for estimating water content in vivo.

3.3 Glomerular Filtration Rate Estimation

A key component of renal function is the glomerular filtration rate (GFR), and nearly all hyperpolarized ^{13}C probes are sufficiently small to be freely filtered at the glomerulus. Molecules which are metabolically inert, not appreciably reabsorbed in the nephron, and have T_1 values sufficiently long to be detected in the renal medulla may be good targets for GFR measurement. Although urea is reabsorbed to some degree, there is a strong appeal of using this molecule as a hyperpolarized GFR marker due to its extremely low toxicity. Data for GFR estimation are spatially and temporally resolved magnitude images with spatial resolution sufficient to resolve the renal cortex from the medulla and temporal resolution sufficient to trace the medullary uptake curve with several data points. Since the current example uses data only from the uptake phase, the effects of transmitter-based depolarization are likely small.

GFR estimation using hyperpolarized ^{13}C imaging has been demonstrated by retrospectively processing datasets using the Baumann–Rudin model [17]. This technique was originally developed for measuring renal clearance of Gd agents in rats [18] and uses the time-varying signals from the renal cortex (C_{cortex}) and medulla (C_{medulla}) to estimate an effective exchange rate.

$$\frac{\mathrm{d}C_{\text{medulla}}}{\mathrm{d}t} = KC_{\text{cortex}}(t). \tag{7}$$

Here the constant K represents the one-way exchange rate from cortex to medulla. Although one-way exchange is an invalid assumption for probes that are reabsorbed, the model is assumed to hold true in the initial uptake phase. Solving Eq. 7 analytically requires initial conditions for the concentration variables which, therefore, requires an additional arterial input model parameter. To avoid this computational complexity, this model can instead be solved algebraically by normalizing the mean slope ($\mathrm{d}C_{\text{medulla}}/\mathrm{d}t$) during the uptake phase by the mean cortex signal and scaling by the medullary volume [19]. The script example_GFR.m demonstrates the following steps for calculating GFR from a dynamic set of [^{13}C]urea images

1. Time-dependent, magnitude images are reconstructed.
2. The renal cortical and medullary ROIs are delineated, and a mean taken over these ROIs is used to create $C_{\text{medulla}}(t)$ and $C_{\text{cortex}}(t)$.
3. The initial uptake period of the time domain is isolated (uptakeInds in the script).
4. A linear fit is performed on $C_{\text{medulla}}(t)$ to estimate its slope $\frac{\mathrm{d}C_{\text{medulla}}}{\mathrm{d}t}$ during the uptake period. These curves and the slope estimates are shown in Fig. 3.

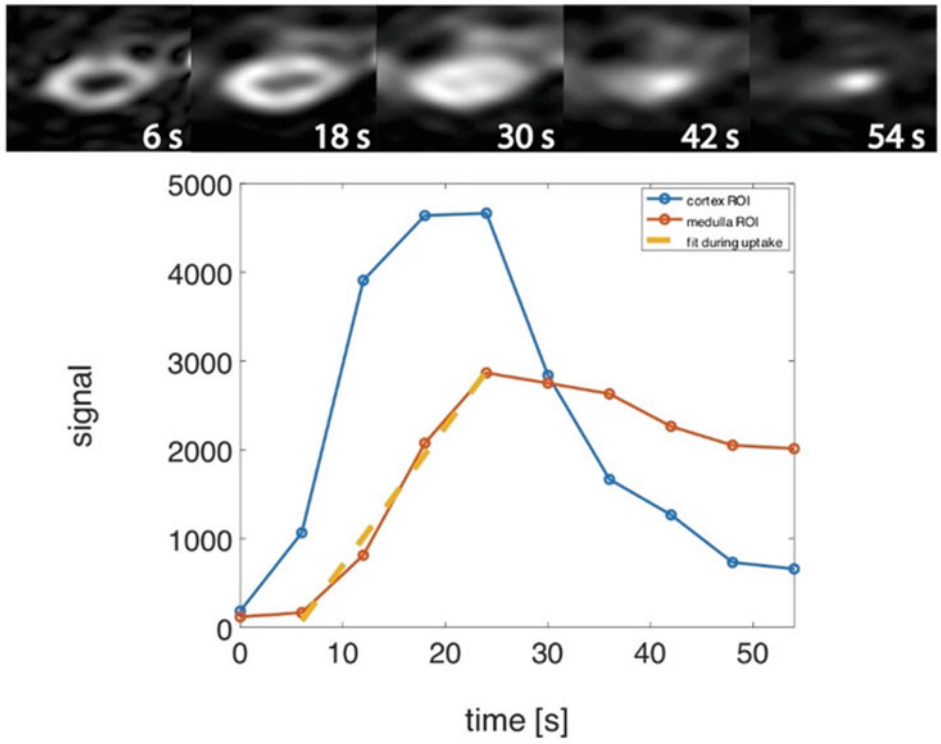

Fig. 3 Estimating glomerular filtration rate from dynamic [13]C urea images of a rat. The top frame shows every other time point of the acquisition, and the bottom plot gives the uptake curves from the renal cortex and medulla. The yellow trace shows the best linear fit of the medulla signal during uptake; the rate from this fit is used for GFR estimation

5. The parameter K from Eq. 7 is estimated via $K = \frac{\mathrm{d}C_{\mathrm{medulla}}}{\mathrm{d}t} / \langle C_{\mathrm{cortex}}(t) \rangle$, where $\langle C_{\mathrm{cortex}}(t) \rangle$ is the mean value of $C_{\mathrm{cortex}}(t)$ during the uptake phase.
6. The GFR can then be estimated as $\mathrm{GFR} = K \cdot V_{\mathrm{medulla}} \cdot 60$, where V_{medulla} is the medullary volume in mL, making GFR in mL/min.

3.4 Metabolic Rate Constant Estimation

The estimation of the metabolic flux from a hyperpolarized substrate to some metabolic products which are distinguished from the substrate via chemical shift is a topic of paramount interest. The metabolic conversion of hyperpolarized ^{13}C substrates can be an extremely complex process. For instance, the conversion of hyperpolarized [1-^{13}C]pyruvate to hyperpolarized [1-^{13}C]lactate depends on arterial input to the tissue, the monocarboxylate transporter-mediated transport into the cell where the substrate undergoes a Michaelis–Menten exchange with lactate. Therefore, the net conversion of the substrate depends not only on the rate of each transport step but also the availability of the enzyme and

cofactor, and the size of the steady-state lactate pool [20]. Using hyperpolarized ^{13}C NMR to capture this effect requires fitting signal amplitudes of data acquired from a spectroscopic readout. The data may be spatially resolved, but frequently a "slice dynamic" acquisition is used which greatly simplifies setting up the acquisition protocol and maximizes the probability of detecting low SNR metabolic products. A typical in vivo experiment will acquire a spectrum over 1–10 kHz sweep width using a slice selective pulse, and this acquisition is repeated until the polarization is presumed to be depleted. This type of acquisition gives data of the form $S(f,t)$, where f is the Fourier transform of the FID domain, and t is a variable proportional to the number of repetitions. The substrate and products have time-dependent signals $S(t)$ and $P(t)$, respectively. The hyperpolarized signals may be matched to functions of the form

$$\frac{\mathrm{d}S(t)}{\mathrm{d}t} = -\left(k_{\mathrm{SP}} + \frac{1}{T_{1,S}}\right)S(t) + k_{\mathrm{PS}}P(t) + u(t), \tag{8}$$

$$\frac{\mathrm{d}P(t)}{\mathrm{d}t} = -\left(k_{\mathrm{PS}} + \frac{1}{T_{1,P}}\right)P(t) + k_{\mathrm{SP}}S(\mathrm{t}) \tag{9}$$

where $T_{1,\mathrm{S}}$ and $T_{1,\mathrm{P}}$ are the spin lattice relaxation times of the substrate and product, respectively, k_{SP} and k_{PS} are the forward and reverse rate constants, and $u(t)$ is a function that models substrate delivery to the tissue. A frequently made simplification made when modeling conversion of [1-^{13}C]pyruvate to [1-^{13}C]lactate is to assume both molecules have nearly identical relaxation times ($T_{1,\mathrm{P}} = T_{1,\mathrm{S}}$) and that no significant backward flux occurs during measurement ($k_{\mathrm{PS}} = 0$). This reduces the number of unknowns to be fitted from 4 to 2 and greatly improves the noise conditioning of the problem.

Typical steps in processing 2D, slice-dynamic spectroscopy and estimating metabolic conversion metrics are summarized here:

1. Raw spectra are typically apodized in the spectral domain using a filter matched to the T_2* of the compound (on the order of 50–500 ms) to reduce noise.
2. Apodized spectra are Fourier transformed along the FID axis giving spectra of the form $S(f,t,$ coils).
3. If data are displayed in magnitude, then a sum-of-squares over the coil axis may be performed giving $|S(f,t)|$ Phase sensitive detection may be used, but it requires phasing each channel individually before combination. Although phase-sensitive processing adds complexity, it simplifies detection of low-SNR metabolites, and may reduce contamination of large amplitude resonance on neighboring peaks due to apparent line-narrowing.

4. A further de-noising step may be performed on the 2D $|S(f,t)|$ data by using SVD-thresholding [21]. This step can be motivated by subsequent processing steps which can greatly enhance noise if poorly conditioned.
5. The peak amplitudes are then tracked over time to generate 1D curves of substrate $S(t)$ and product $P(t)$. This may be performed by taking the maximum value or integrating over a small frequency band.
6. A flip angle correction may be applied to account for RF-induced depolarization, but this requires accurate knowledge of the flip angle applied at each time point (*see* ref. 22 for an in-depth treatment of this topic).
7. Estimating the forward rate constant k_{SP} requires fitting the experimental data to the kinetic models such as those given in Eqs. 8 and 9. However, a frequently applied model free analysis of Hill et al. vastly simplifies the analysis of hyperpolarized metabolic kinetic data [23]. The model free approach is based on the fact that integrating $S(t)$ and $P(t)$ over time and taking their ratios gives a value proportional to this rate constant, so no deconvolution or curve fitting is required. This model free approach is simply implemented by taking the area under the curve (AUC) of the product and normalizing this value to the AUC of the substrate (*see* Fig. 4, right, for example traces of such an experiment).
8. For a more detailed treatment, the readers are referred to the open source hyperpolarized MRI toolbox scripts from UCSF.

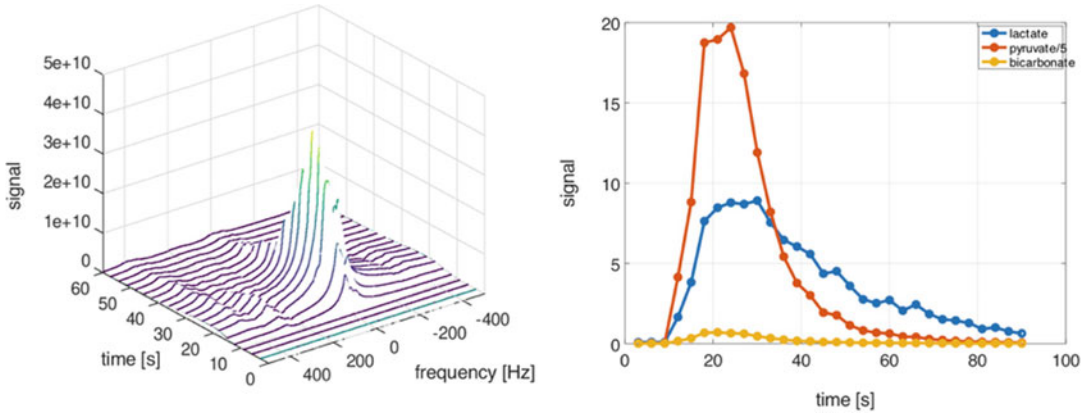

Fig. 4 Left: a typical slab-dynamic spectroscopy acquisition on a 3T scanner captures the conversion of [1-^{13}C]pyruvate (large peak on resonance) to [1-^{13}C]lactate (left, at 390 Hz) and [^{13}C]bicarbonate. Right: the traces of these three metabolites over time generated by integrating over the line width at each point. A simple measure of metabolic flux can be derived from these traces by taking the area under the curve (AUC) of a metabolic product and dividing it by the AUC of the substrate

A review paper covers the topics of kinetic modeling in great detail [22]. This toolbox can be cloned via git clone https://github.com/LarsonLab/hyperpolarized-mri-toolbox.git

9. Within this toolbox, the subfolder kinetic_modeling contains numerous scripts for fitting kinetic curves with a variety of options. See example_exchangeModel.m for a sample invocation of the main wrapper function fit_kPL() in the toolbox.

3.5 Results Validation

Most of the analysis methods outlined here will output values in physical units, so cross referencing measurements with values quoted in the literature is the chief method for validation of results. For instance, renal blood flow measurements in the range 4–10 mL/mL/min have been reported using hyperpolarized contrast agents [17]. Preliminary results show hyperpolarized-MRI-derived GFR measurements in the range of 2–3 mL/min for the rat kidney which are in close agreement with GFR measured with other modalities. A wider variation of relaxation times has been reported. For instance, [^{13}C, ^{15}N]urea T_2 values have been reported ranging from 400–800 ms to greater than 4 s [12, 13]. A further study is required to elucidate the influence of acquisition on the variance of findings in the literature.

Acknowledgments

This chapter is based upon work from COST Action PARENCHIMA, supported by European Cooperation in Science and Technology (COST). COST (www.cost.eu) is a funding agency for research and innovation networks. COST Actions help connect research initiatives across Europe and enable scientists to enrich their ideas by sharing them with their peers. This boosts their research, career, and innovation.
PARENCHIMA (renalmri.org) is a community-driven Action in the COST program of the European Union, which unites more than 200 experts in renal MRI from 30 countries with the aim to improve the reproducibility and standardization of renal MRI biomarkers.

References

1. GE MR Collaboration Community. https://collaborate.mr.gehealthcare.com
2. Reed GD accompanying source code examples for book chapter on renal MRI analysis. https://github.com/galenreed/renalC13MRIBook
3. Golman K, Ardenkjaer-Larsen JH, Petersson JS et al (2003) Molecular imaging with endogenous substances. Proc Natl Acad Sci 100:10435–10439
4. Reed GD, von Morze C, Bok R et al (2014) High resolution 13C MRI with hyperpolarized urea: in vivo T2 mapping and 15N labeling effects. IEEE Trans Med Imaging 33:362–371
5. Svensson J, Månsson S, Johansson E et al (2003) Hyperpolarized 13C MR angiography using trueFISP. Magn Reson Med 50:256–262
6. Grant AK, Vinogradov E, Wang X et al (2011) Perfusion imaging with a freely diffusible

hyperpolarized contrast agent. Magn Reson Med 66:746–755
7. von Morze C, Bok RA, Reed GD et al (2014) Simultaneous multiagent hyperpolarized 13C perfusion imaging. Magn Reson Med 72:1599–1609
8. Østergaard L, Weisskoff RM, Chesler DA et al (1996) High resolution measurement of cerebral blood flow using intravascular tracer bolus passages. Part I: mathematical approach and statistical analysis. Magn Reson Med 36:715–725
9. Johansson E, Månsson S, Wirestam R et al (2004) Cerebral perfusion assessment by bolus tracking using hyperpolarized 13C. Magn Reson Med 51:464–472
10. von Morze C, Larson PEZ, Hu S et al (2011) Imaging of blood flow using hyperpolarized [13C]Urea in preclinical cancer models. J Magn Reson Imaging 33:692–697
11. Yen Y-F, Le Roux P, Mayer D et al (2010) T2 relaxation times of 13C metabolites in a rat hepatocellular carcinoma model measured in vivo using 13C-MRS of hyperpolarized [1-13C]pyruvate. NMR Biomed 85:414–423
12. Reed GD, von Morze C, Verkman AS et al (2016) Imaging renal urea handling in rats at millimeter resolution using hyperpolarized magnetic resonance relaxometry. Tomography 2:125–137
13. Laustsen C, Stokholm Nørlinger T, Christoffer Hansen D et al (2016) Hyperpolarized 13C urea relaxation mechanism reveals renal changes in diabetic nephropathy. Magn Reson Med 75:515–518
14. Mariager CØ, Nielsen PM, Qi H et al (2017) Hyperpolarized 13C, 15N2-urea T2 relaxation changes in acute kidney injury. Magn Reson Med 80:696–702
15. Whittall KP, MacKay AL (1989) Quantitative interpretation of NMR relaxation data. J Magn Reson 84:134–152
16. Whittall KP, MacKay AL, Graeb DA et al (1997) In vivo measurement of T2 distributions and water contents in normal human brain. Magn Reson Med 37:34–43
17. Østergaard Mariager C, Nielsen PM, Qi H et al (2017) Can hyperpolarized 13C-urea be used to assess glomerular filtration rate? A retrospective study. Tomography 3:146–152
18. Baumann D, Rudin M (2000) Quantitative assessment of rat kidney function by measuring the clearance of the contrast agent Gd(DOTA) using dynamic MRI. Magn Reson Imaging 18:587–595
19. Krepkin K, Won E, Ramaswamy K et al (2014) Dynamic contrast-enhanced MR renography for renal function evaluation in ureteropelvic junction obstruction: feasibility study. Am J Roentgenol 202:778–783
20. Witney TH, Kettunen MI, Brindle KM (2011) Kinetic modeling of hyperpolarized 13C label exchange between pyruvate and lactate in tumor cells. J Biol Chem 286:24572–24580
21. Brender JR, Kishimoto S, Merkle H et al (2019) Dynamic imaging of glucose and lactate metabolism by 13C-MRS without hyperpolarization. Sci Rep 9:3410
22. Larson PEZ, Chen H, Gordon JW et al (2018) Investigation of analysis methods for hyperpolarized 13C-pyruvate metabolic MRI in prostate cancer patients. NMR Biomed 31:e3997
23. Hill DK, Orton MR, Mariotti E et al (2013) Model free approach to kinetic analysis of real-time hyperpolarized 13C magnetic resonance spectroscopy data. PLoS One 8:e71996

Chapter 43

Data Preparation Protocol for Low Signal-to-Noise Ratio Fluorine-19 MRI

Ludger Starke, Thoralf Niendorf, and Sonia Waiczies

Abstract

Fluorine-19 MRI shows great promise for a wide range of applications including renal imaging, yet the typically low signal-to-noise ratios and sparse signal distribution necessitate a thorough data preparation.

This chapter describes a general data preparation workflow for fluorine MRI experiments. The main processing steps are: (1) estimation of noise level, (2) correction of noise-induced bias and (3) background subtraction. The protocol is supplemented by an example script and toolbox available online.

This chapter is based upon work from the COST Action PARENCHIMA, a community-driven network funded by the European Cooperation in Science and Technology (COST) program of the European Union, which aims to improve the reproducibility and standardization of renal MRI biomarkers. This analysis protocol chapter is complemented by two separate chapters describing the basic concept and experimental procedure.

Key words Magnetic resonance imaging (MRI), Fluorine, Data preparation, Mice, Rats

1 Introduction

Fluorine-19 (^{19}F) MR methods have found their application in a wide range of biomedical research areas including renal imaging [1–8]. The sensitivity constraints, low signal-to-noise ratio (SNR) and sparse signal distribution typical of fluorine-19 MRI necessitate a thorough data preparation. The main processing steps are: (1) estimation of noise level, (2) correction of noise-induced bias and (3) background subtraction. While variations on this theme are common in fluorine MRI studies, a standardized method of data preparation and analysis with well-documented implementation will improve accuracy and reproducibility of reported results.

Estimating the noise level is a prerequisite for all subsequent processing steps. Assuming data from a single channel RF coil, the signal in MR magnitude images follows a Rician distribution [9, 10] (*see* **Note 1** for information on multichannel RF coils). At SNR > 10, this distribution closely resembles a Gaussian

Andreas Pohlmann and Thoralf Niendorf (eds.), *Preclinical MRI of the Kidney: Methods and Protocols*, Methods in Molecular Biology, vol. 2216, https://doi.org/10.1007/978-1-0716-0978-1_43,

distribution. Yet, when analyzing low SNR fluorine MRI data, its diverging properties need to be taken into account. The MRI magnitude signal is computed from complex data, which contain signal with positive and negative values, and is corrupted by zero mean Gaussian noise. Mapping positive and negative signals to the positive magnitude results in a pronounced upward bias at low SNRs. Additionally, the standard deviation of the measured signal is reduced (Fig. 1a). To ensure accurate measurement of signal intensities, the noise-induced bias must be corrected. It is also essential to consider the signal level-dependence of the measured standard deviation for correct noise level estimation.

Background subtraction is the process of classifying image voxels as either signal or noise. Most fluorine MRI studies are dealing with signals that are close to the detection threshold; in this case the background subtraction method strongly influences the sensitivity of the measurement and most importantly the reliability and reproducibility of the obtained results. Ideally, reporting of the used background subtraction method should include the expected false positive rate (FPR).

In this chapter we present a data preparation protocol for low SNR fluorine MRI data (Fig. 2). An open source toolbox is used for bias correction (Fig. 2b) of the magnitude data (Fig. 2a). We expand upon the common method of SNR-based thresholding [2, 4, 11] (Fig. 2c) by proposing an additional outlier removal processing step (Fig. 2d). The shown example is based on a dataset with fluorine nanoparticle labeled immune cells showing the sites of inflammation in a mouse model of multiple sclerosis (*see* Setup 4 in Starke et al. [12] for details). The data preparation protocol is equally applicable to low SNR ^{19}F MRI of the kidney.

A self-contained script reproducing Fig. 2 and illustrating the data preparation step-by-step, from noise level estimation to generation of a proton/fluorine-19 overlay is provided online together with the example data.

This analysis protocol chapter is complemented by separate chapters describing the basic concept and experimental procedure, which are part of this book.

2 Materials

2.1 Software Requirements

The processing steps outlined in this protocol require:

1. A software development environment. The provided code examples follow the syntax of *MATLAB*® (The MathWorks, Natick, Massachusetts, USA; mathworks.com) and *Octave* (gnu.org/software/octave). The code could also be adapted for other scientific software development environments like *Python* (python.org/) or *Julia* (julialang.org/).

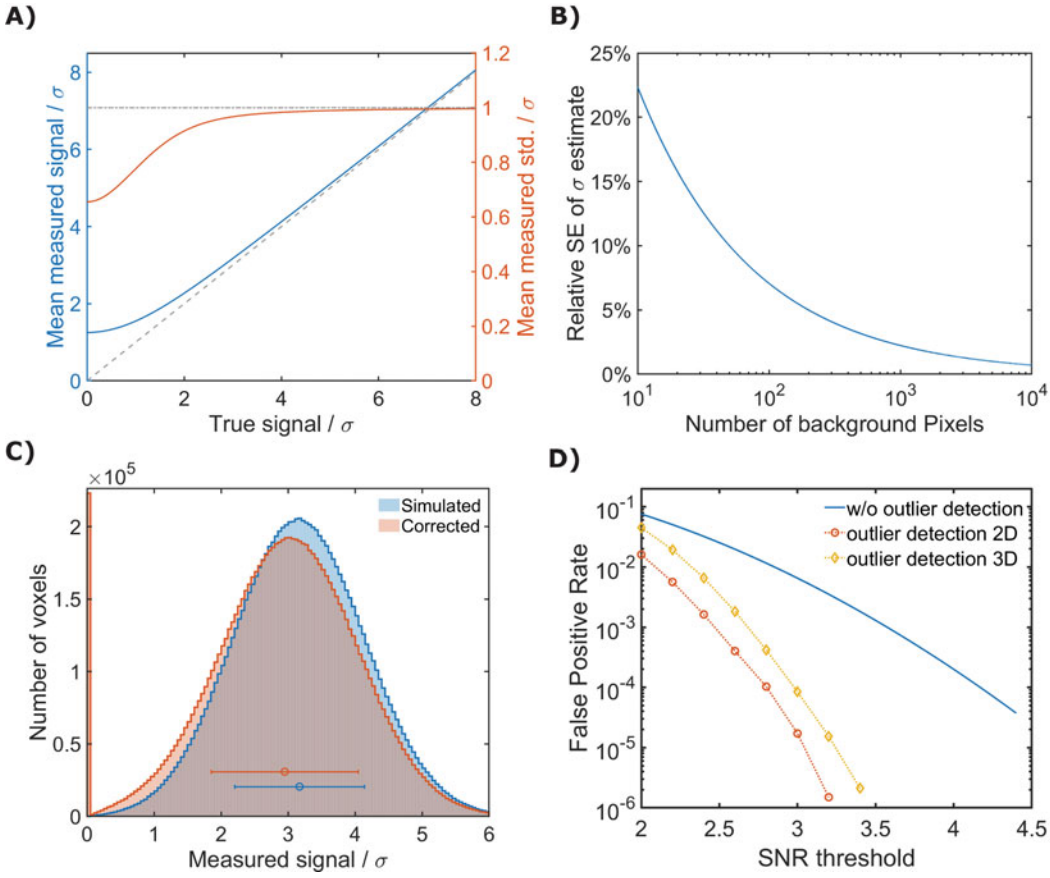

Fig. 1 (**a**) Mean measured signal and mean measured standard deviation (std.) of MR magnitude data. σ denotes the signal level independent standard deviation of the Gaussian noise in the underlying complex data. (**b**) The size of the used background region determines the uncertainty of the standard deviation estimate. The relative standard error (SE) shown here is defined as the standard deviation of the standard deviation estimate divided by σ itself. Note the logarithmic scale of the *x*-axis. (**c**) Histogram of simulated Rician data for true signal $= 3\sigma$ (blue). The corrected data was computed using the tool described in Subheading 3.3 (red). The circles and bars indicate the mean and standard deviations of the two distributions. (**d**) Expected false positive rate (FPR) for different SNR thresholds with and without outlier detection. The FPR is defined as number of false positive voxels divided by number of true negative voxels. Without outlier detection background subtraction is performed by simple thresholding. The expected FPR can be computed by the steps in **Note 5**. Outlier detection is performed by removing all groups of less than three connected signal voxels after SNR based thresholding. In 2D 8-connectivity is used and in 3D 18-connectivity. Here simulated data is shown

2. A MATLAB / Octave tool for noise bias correction downloadable from github.com/LudgerS/MRInoiseBiasCorrection. This tool includes detailed documentation to facilitate adaptation for other software development environments or use with multichannel RF coil data.
3. A collection of data preparation specific MATLAB / Octave subfunctions found under github.com/LudgerS/19fMRIdataPreparation. It is provided together with a script

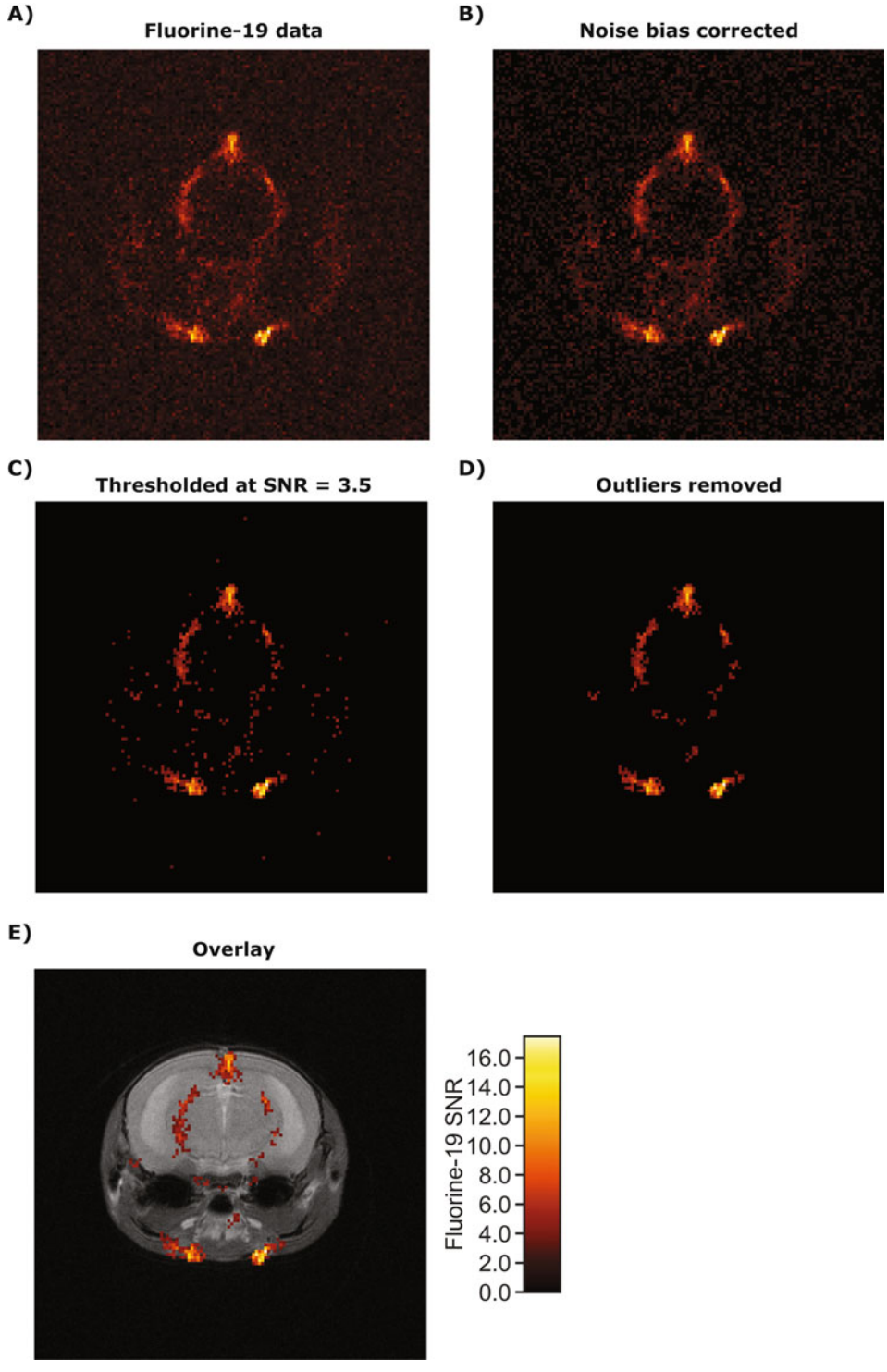

Fig. 2 Example analysis for fluorine-19 MRI data acquired in a mouse model of multiple sclerosis. Immune cells were labeled in situ with fluorine-19 nanoparticles such that fluorine signal shows sites of inflammation.

collecting all processing steps of this protocol as well as an example dataset allowing the reproduction of Fig. 2.

4. The MATLAB *Image Processing* toolbox is needed to run the function fluorineOverlay.m which creates proton/fluorine overlays and is part of the aforementioned 19fMRIdataPreparation repository.
5. A tool for data import. This tool will depend on the data format:

   DICOM data—MATLAB contains a built-in function to import dicom data: dicomread. For Octave, Python and Julia, dicom support is offered by supplemental packages (octave.sourceforge.io/dicom/, pydicom.github.io/, github.com/JuliaIO/DICOM.jl).

   Bruker data—Bruker also offers a toolbox to import data into MATLAB directly. To obtain Bruker's *pvtools*, contact Bruker software support (mri-software-support@bruker.com).

3 Methods

3.1 Data Import and Scaling

These steps should be executed for both the fluorine MRI data and the noise scan data. In the following sections it is assumed that the fluorine data was stored in variable `imageData` and the noise scan in variable `noiseData`.

3.1.1 DICOM Data

1. To import dicom data execute the command

```
data = dicomread('filePath');
```

   where `'filePath'` is a string containing the relative or absolute path of the .dcm file.

3.1.2 Bruker Data

For a Linux or MacOS system, substitute the file separator \ by /.

1. Ensure that pvtools is on the search path:

```
addpath(genpath('...\pvtools'))
```

   where `'...\pvtools'` specifies the path of the pvtools folder.

Fig. 2 (continued) Acquisition parameters: 2D-RARE, ETL = 32, [20 × 20] mm^2 FOV, 128 × 128 matrix, 3.2 mm slice thickness. The noise level was determined from a corresponding noise scan. Details regarding the animal model and acquisition can be found in Starke et al. [12] under Setup 4. (**a**) Fluorine-19 MRI magnitude data. (**b**) Data after application of the Rician noise bias correction. (**c**) Thresholding was performed at SNR = 3.5. (**d**) Removal of groups of <3 connected pixels. (**e**) Overlay of the fluorine data on an anatomical image

2. Store the path to the scan you want to load in variable `scanFolder`.
3. Read the visu_pars parameter file:

```
visuPars = readBrukerParamFile([scanFolder, '\visu_pars']);
```

4. Load the Paravision reconstruction:

```
[data, ~] = readBruker2dseq([scanFolder, '\pdata\1\2dseq'],
visuPars);
```

3.2 Correct Data Scaling

There are vendor-specific conventions regarding the averaging of multiple image acquisitions. In some cases, for example in Bruker data, the individual acquisitions are simply added instead of computing the mean. To ensure comparability between different scan times, determine the employed convention (*see* **Note 2**) and if necessary divide the data by the number of averages. This processing step will be required if a pure noise scan has been employed to determine the noise level.

1. Assuming `nAverages` is the number of averages acquired for the fluorine data and the noise scan was acquired with a single average, simply execute

```
imageData = imageData/nAverages;
```

3.3 Noise Level Estimation

The amount of random variation in MR magnitude images, as measured by the standard deviation, is signal level dependent (Fig. 1a). By convention, the noise level is reported as the asymptotic standard deviation at high SNR, which we denote by σ [13, 14]. This value is equal to the standard deviation of the Gaussian noise in the underlying complex data. While a larger number of noise level estimation methods has been proposed [13], two are of practical relevance for fluorine MRI: estimation based on a background region, which is known to be without signal, or estimation based on a dedicated pure noise scan. Although the former yields adequate results for most applications, we strongly recommend the use of a noise scan due to its independence of user input and improved accuracy. The uncertainty of the standard deviation estimate depends on the number of samples n. For $n > 10$, we can approximate the standard error as $\mathrm{SE}_\sigma \approx \frac{\sigma}{\sqrt{2n}}$ (Fig. 1b) [15].

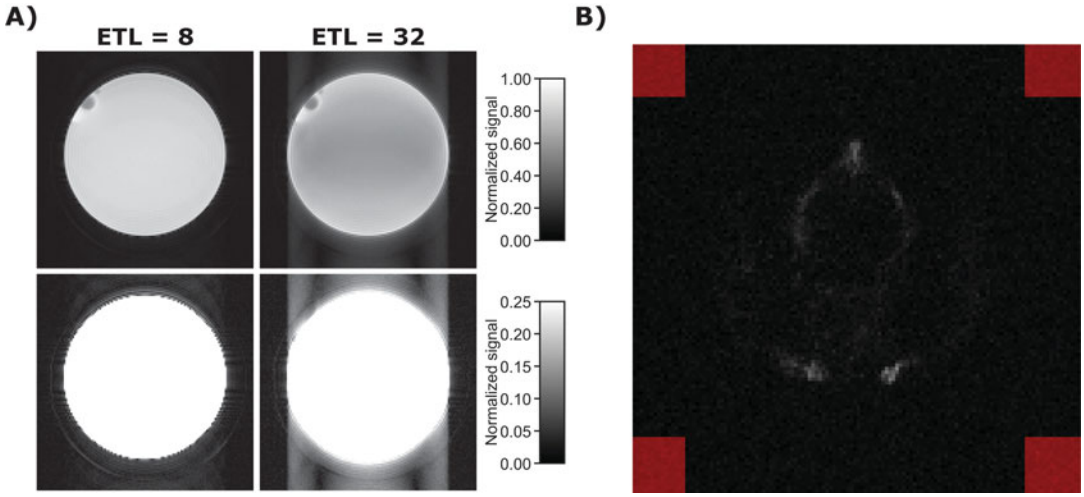

Fig. 3 (**a**) Point spread function artifacts can corrupt background regions without being visually obvious. In this water phantom example, the RARE image with echo train length 8 (ETL = 8, top left) does not show artifacts. However rescaling (bottom left) shows that a noise level estimate based on a background region would lead to erroneous values if the region is not chosen just in the corners of the image. The example on the right (ETL = 32) shows an exaggerated case where the effect is obvious in the image itself. (**b**) The red regions show a background mask that would yield reliable values for the example shown in Fig. 2

3.3.1 Estimation Based on a Background Region

The largest possible background region free of major signal artifacts should be used to improve accuracy (also *see* **Note 3**). However, point spread function artifacts can corrupt image regions even distal from signal features without being necessarily visible (Fig. 3a). We recommend using quadratic regions in all four corners of the image.

1. Create a mask of the background region for logical indexing

```
backgroundMask = createBackgroundMask(size(imageData), cornerSize);
```

   The argument `size(imageData)` determines the dimensions of the mask and `cornerSize` sets the size of the four corners (Fig. 3b).

2. The noise level can then be computed as

```
sigma = std(imageData(backgroundMask))/0.6551;
```

   where the factor 0.6551 accounts for the ratio between the background standard deviation and σ (Fig. 1a) [13]. It needs to be adjusted for data from multichannel RF coils (*see* **Note 4**).

3.3.2 Estimation Based on a Noise Scan

In this case the complete noise image constitutes the background region. It is not necessary to acquire the noise scan with multiple averages, as the dependence of the noise level on the number of

averages is well understood mathematically (*see* **Note 5** for further comments on noise scan acquisition).

1. If the noise scan was acquired with a single average and the number of averages of the image data is given by `nAverages`, the noise level can be computed as

```
sigma = std(noiseData(:))/(0.6551*sqrt(nAverages));
```

3.4 Bias Correction

Rician noise leads to a systematic upward bias in MR magnitude images at low SNR. Signal intensities need to be multiplied with a correction factor <1 to achieve correct signal estimation on average (Fig. 1a, c). While the expected measured signal $E[M]$ for a given true signal level A and noise level σ is known, there is no established inverse function $A(E[M], \sigma)$ [9, 10, 14]. The provided toolbox thus uses a lookup table to compute the correction factor [9]. Signal intensities below the mean background level are set to zero (Fig. 1c). Alternatively, the correction scheme of Koay and Basser could be used [14]. *See* **Note 6** for a comment on averaging over regions of interest (ROIs).

1. After determining the noise level, the corrected image (Fig. 2b) can simply be computed as

```
correctedImage = correctNoiseBias(imageData, sigma, 1);
```

   where the last argument specifies the number of receive elements in the RF coil (*see* **Note 1**).

3.5 Background Subtraction

In fluorine MRI, background subtraction commonly involves thresholding by removing all voxels below a certain SNR (Fig. 2c). However, the threshold necessary to prevent the occurrence of false positives could compromise sensitivity, especially for larger datasets such as those from 3D MR data (Fig. 1d, *see* **Note 7** for an analytical formula). Based on the assumption that all relevant fluorine features should at least comprise a minimum of three connected voxels, we recommend an additional outlier correction that excludes isolated voxels (Fig. 2d). To determine features with a minimum of three connected voxels, we recommend to use 8-connected neighborhoods (connection via edges or corners) for 2D images and 18-connected neighborhoods (connection via faces or edges but not corners) for 3D images. This additional processing step drastically reduces the expected FPR. In the 2D case, for example, thresholding at SNR = 2.74 with outlier detection reduces the FPR to the same level as thresholding at SNR = 4 without outlier detection (Fig. 1d).

1. Copy the bias corrected image to a new variable

```
thresholdedImage = correctedImage;
```

2. Set all voxels below the chosen threshold `snrThreshold` to zero

```
thresholdedImage(thresholdedImage < snrThreshold*sigma) = 0;
```

3. Then apply the provided function for outlier removal on the thresholded image:

```
cleanedImage = removeIsolatedVoxels(thresholdedImage, 3);
```

The second argument specifies the minimum size of preserved features.

3.6 Proton/ Fluorine-19 Overlays

In order to locate the source of fluorine signal within an in vivo context, it will need to be coregistered with an anatomical image. While it might be appealing to overlay transparent fluorine images to avoid concealing of anatomical detail, we advise against this practice for quantification purposes, as manipulation of the data will result in ambiguous readings. If no external standard is used to determine fluorine concentrations, it is best practice to show the fluorine signal in terms of the SNR as this also conveys a standard means of information. For the provided function the anatomical image should be acquired with the same field of view as the fluorine MR image.

1. An overlay of fluorine on proton MR images (Fig. 2e) can be achieved simply by calling

```
fluorineOverlay(anatomyData, cleanedImage, colorMap, resizeF, fileName)
```

`anatomyData` is the anatomical image, `colorMap` specifies the fluorine color map in the conventional MATLAB format, `resizeF` is a factor by which the image size is increased to ensure faithful display and `fileName` the file name of the saved image.

2. To complement the fluorine image with a corresponding color bar (Fig. 2e) execute

```
plotFluorineColorBar(colorMap, fileNameCB, max(cleanedImage(:))/sigma, 'Fluorine-19 SNR')
```

`fileNameCB` states the path and file name of the saved color bar image. The third argument specifies the range of the color map. Dividing the maximum of the fluorine image by σ establishes the SNR scaling. The fourth argument determines the label of the color bar.

4 Notes

1. In the case of multichannel RF coil data and sum-of-squares reconstruction, the MR signal follows a noncentral chi distribution instead of a Rician distribution. This case is described thoroughly in Constantinides et al. [16]. The bias correction toolbox used in this protocol also handles the more general case. It should be noted that the bias effects become more pronounced with increasing number of receive elements.
2. To determine the employed convention of averaging, acquire high SNR phantom data with varying numbers of averages while keeping all other parameters fixed. Import the data as described in Subheading 3.1. If all scans show the same signal magnitude, the scaling step described in Subheading 3.1 should be omitted. However, if, for example, doubling the number of averages also doubles the signal amplitude, rescaling should be performed.
3. Be aware that some vendors include heavy filtering and/or background masking into the automated reconstruction pipeline. This has a major impact on the background noise or sets background values to zero and hence renders estimation based on a background region not suitable for noise assessment.
4. Assuming a sum-of-squares reconstruction, the factor 0.6551 should be replaced by 0.6824, 0.6953, 0.7014 or 0.7043 for 2, 4, 8 or 16 receive element RF coil data [16].
5. A pure noise scan is acquired by setting the excitation flip angle and reference power to zero so that no excitation occurs and pure noise is acquired. The receiver gain needs to be set identical to all other scans for which the noise level should be determined. The number of averages can be reduced to one, as the resulting change in noise level is easily compensated. Instead of setting the reference power to zero in preparation of the noise scan, the output of the RF power supply can be disconnected following the system adjustments.
6. In a background region without true signal, the Rice distribution reduces to the Rayleigh distribution [10], which is equivalent to a chi-squared distribution. Thus the expected FPR can be computed via the cumulative distribution function of the chi-squared distribution. First calculate the expected signal [17] for the chosen SNR cutoff snrThreshold

   thresholdExpectation = sigma × sqrt(pi/2) × laguerreL (1/2,0,-snrThreshold.^2./(2 × sigma^2)).

   Then calculate the expected FPR as

   FPR = 1 − gammainc((thresholdExpectation/sigma)^2/ 2, 1, 'lower').

   This formula is valid for simple thresholding without outlier removal and data from single receive element RF coils.

7. Often fluorine-MRI studies involve calculating signal-to-noise ratios for specific regions of interest (ROIs). Averaging over all pixels in the region should be performed before applying the noise bias correction. This is particularly relevant for phantom studies where the number of voxels in the assumed to be homogeneous ROI is large enough to obtain accurate values even for regions with SNR < 2. *See* **Note 8** for a comment on the uncertainty of SNR estimates.
8. SNR is conventionally reported as the bias corrected signal level divided by the asymptotic standard deviation σ [14]. The uncertainty of the SNR estimate is determined by the signal level, the size of the ROI and the uncertainty of the noise level. A convenient formula for the standard error is $\frac{\mathrm{SE}_{\mathrm{SNR}}}{\mathrm{SNR}} \approx \sqrt{\frac{1}{m \cdot \mathrm{SNR}^2} + \frac{1}{2n}}$, where m denotes the number of voxels in the ROI and n the number of voxels in the background region used to estimate the noise level. At high SNRs the uncertainty of the SNR estimate is dominated by the uncertainty of the noise level estimate.

   Derivation: The standard errors of the mean ROI signal $\bar{S}$ and noise level σ are $\mathrm{SE}_{\bar{S}} = \frac{\sigma}{\sqrt{m}}$ and $\mathrm{SE}_{\sigma} \approx \frac{\sigma}{\sqrt{2n}}$ [15]. Assuming independence of $\bar{S}$ and σ, the variance formula [18] for the standard error of $\frac{\bar{S}}{\sigma}$ yields

$$\mathrm{SE}_{\mathrm{SNR}} \approx \sqrt{\left(\frac{1}{\sigma} \cdot \frac{\sigma}{\sqrt{m}}\right)^2 + \left(\frac{\bar{S}}{\sigma^2} \cdot \frac{\sigma}{\sqrt{2n}}\right)^2} = \sqrt{\frac{1}{m} + \frac{\mathrm{SNR}^2}{2n}} \ .$$

Acknowledgment

This study was funded, in part (Sonia Waiczies, Thoralf Niendorf; DFG WA2804, DFG PO1869), by the Deutsche Forschungsgemeinschaft and, in part (T.N. and S.W.), by the German Research Foundation (Gefoerdert durch die Deutsche Forschungsgemeinschaft (DFG), Projektnummer 394046635, SFB 1365, RENOPROTECTION. Funded by the Deutsche Forschungsgemeinschaft (DFG, German Research Foundation), Project number 394046635, SFB 1365, RENOPROTECTION).

This chapter is based upon work from COST Action PARENCHIMA, supported by European Cooperation in Science and Technology (COST). COST (www.cost.eu) is a funding agency for research and innovation networks. COST Actions help connect research initiatives across Europe and enable scientists to enrich their ideas by sharing them with their peers. This boosts their research, career, and innovation.

PARENCHIMA (renalmri.org) is a community-driven Action in the COST program of the European Union, which unites more than 200 experts in renal MRI from 30 countries with the aim to improve the reproducibility and standardization of renal MRI biomarkers.

References

1. Ruiz-Cabello J, Barnett BP, Bottomley PA, Bulte JW (2011) Fluorine (19F) MRS and MRI in biomedicine. NMR Biomed 24 (2):114–129
2. Ahrens ET, Helfer BM, O'Hanlon CF, Schirda C (2014) Clinical cell therapy imaging using a perfluorocarbon tracer and fluorine-19 MRI. Magn Reson Med 72(6):1696–1701
3. Prinz C, Delgado PR, Eigentler TW, Starke L, Niendorf T, Waiczies S (2019) Toward (19)F magnetic resonance thermometry: spin-lattice and spin-spin-relaxation times and temperature dependence of fluorinated drugs at 9.4 T. Magma 32(1):51–61
4. Waiczies S, Rosenberg JT, Kuehne A et al (2019) Fluorine-19 MRI at 21.1 T: enhanced spin-lattice relaxation of perfluoro-15-crown-5-ether and sensitivity as demonstrated in ex vivo murine neuroinflammation. Magma 32(1):37–49
5. Kuethe DO, Caprihan A, Fukushima E, Waggoner RA (1998) Imaging lungs using inert fluorinated gases. Magn Reson Med 39 (1):85–88
6. Hu LZ, Chen JJ, Yang XX et al (2014) Assessing intrarenal nonperfusion and vascular leakage in acute kidney injury with multinuclear H-1/F-19 MRI and perfluorocarbon nanoparticles. Magn Reson Med 71(6):2186–2196
7. Hitchens TK, Ye Q, Eytan DF, Janjic JM, Ahrens ET, Ho C (2011) 19F MRI detection of acute allograft rejection with in vivo perfluorocarbon labeling of immune cells. Magn Reson Med 65(4):1144–1153
8. Moore JK, Chen J, Pan H, Gaut JP, Jain S, Wickline SA (2018) Quantification of vascular damage in acute kidney injury with fluorine magnetic resonance imaging and spectroscopy. Magn Reson Med 79(6):3144–3153
9. Henkelman RM (1985) Measurement of signal intensities in the presence of noise in MR images. Med Phys 12(2):232–233
10. Gudbjartsson H, Patz S (1995) The Rician distribution of noisy MRI data. Magn Reson Med 34(6):910–914
11. van Heeswijk RB, Pilloud Y, Flögel U, Schwitter J, Stuber M (2012) Fluorine-19 magnetic resonance angiography of the mouse. PLoS One 7(7):e42236
12. Starke L, Pohlmann A, Prinz C, Niendorf T, Waiczies S (2019) Performance of compressed sensing for fluorine-19 magnetic resonance imaging at low signal-to-noise ratio conditions. Magn Reson Med 84(2):592–608
13. National Electrical Manufacturers Association (2001) Determination of signal-to-noise ratio (SNR) in diagnostic magnetic resonance imaging. NEMA standards publication MS 1-2001. NEMA, Arlington, VA
14. Koay CG, Basser PJ (2006) Analytically exact correction scheme for signal extraction from noisy magnitude MR signals. J Magn Reson 179(2):317–322
15. Ahn S, Fessler A (2003) Standard errors of mean, variance, and standard deviation estimators. EECS Department, The University of Michigan, Ann Arbor, MI. http://web.eecs.umich.edu/fessler/papers/files/tr/stderr.pdf
16. Constantinides CD, Atalar E, McVeigh ER (1997) Signal-to-noise measurements in magnitude images from NMR phased arrays. Magn Reson Med 38(5):852–857
17. Aja-Fernández S, Vegas-Sánchez-Ferrero G (2016) Statistical analysis of noise in MRI. Springer International Publishing, Cham
18. Ku HH (1966) Notes on the use of propagation of error formulas. J Res Natl Bur Stand 70 (4):263–273

INDEX

Andreas Pohlmann and Thoralf Niendorf (eds.), *Preclinical MRI of the Kidney: Methods and Protocols*, Methods in Molecular Biology, vol. 2216, https://doi.org/10.1007/978-1-0716-0978-1, © The Author(s) 2021

G

H

L

I

M

N

O

P

R

S

T

U

V